

C55,612:971/V.1

A UNITED STATES  
DEPARTMENT OF  
COMMERCE  
PUBLICATION



# U.S. DEPARTMENT OF COMMERCE

## National Oceanic and Atmospheric Administration

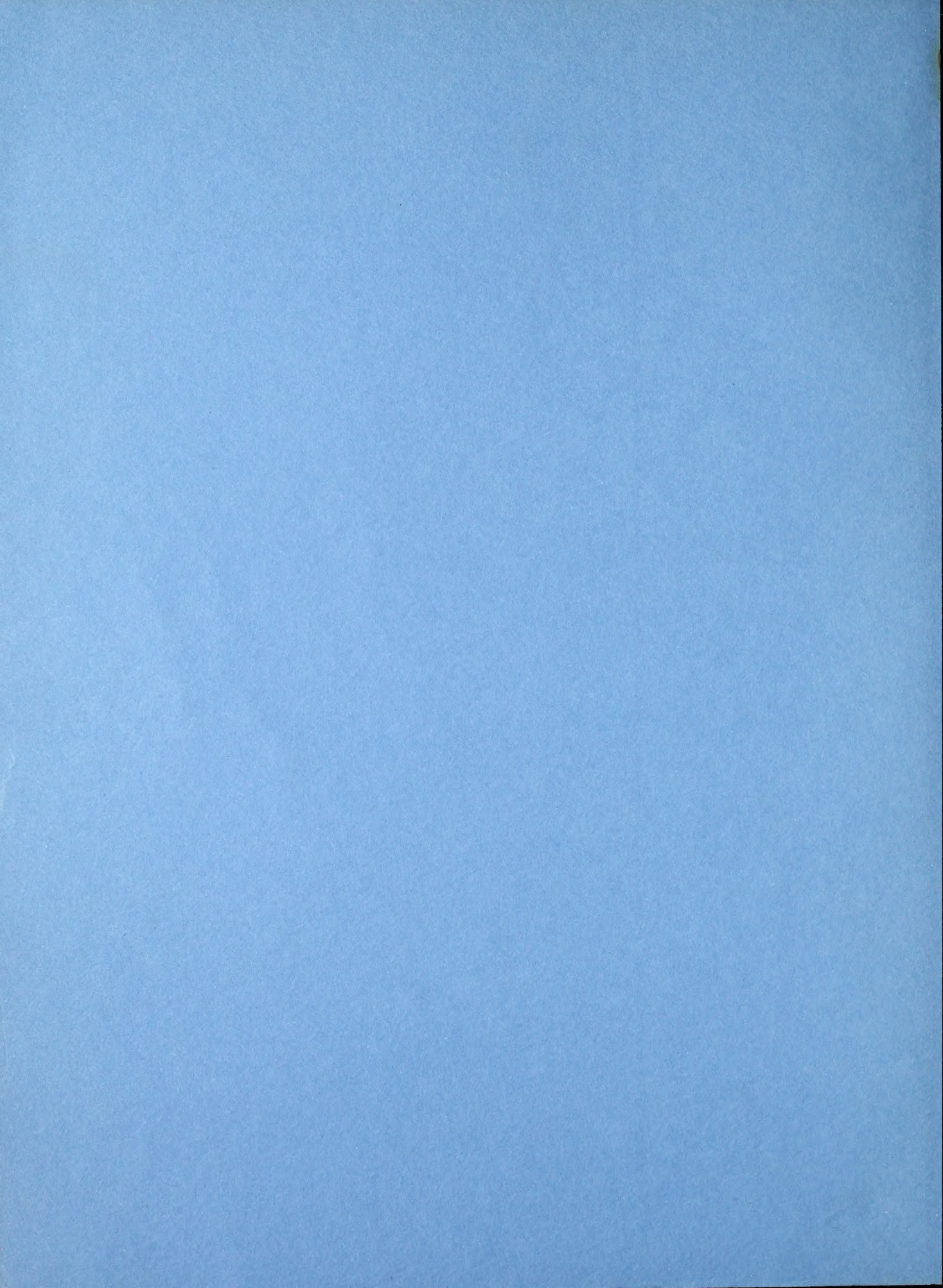
### COLLECTED REPRINTS-1971

### Volume I



ATLANTIC OCEANOGRAPHIC  
AND METEOROLOGICAL LABORATORIES









U.S. DEPARTMENT OF COMMERCE

Peter G. Peterson, Secretary

NATIONAL OCEANIC AND ATMOSPHERIC ADMINISTRATION

Robert M. White, Administrator

ENVIRONMENTAL RESEARCH LABORATORIES

Wilmot N. Hess, Director

## **Collected Reprints—1971**

### **Volume I**

#### **ATLANTIC OCEANOGRAPHIC AND METEOROLOGICAL LABORATORIES**


ISSUED JULY 1972

Atlantic Oceanographic and Meteorological Laboratories  
Miami, Florida 33149

---

For sale by the Superintendent of Documents, U. S. Government Printing Office, Washington, D. C. 20402





Digitized by the Internet Archive  
in 2012 with funding from  
LYRASIS Members and Sloan Foundation

<http://archive.org/details/collectedreprintv1atla>

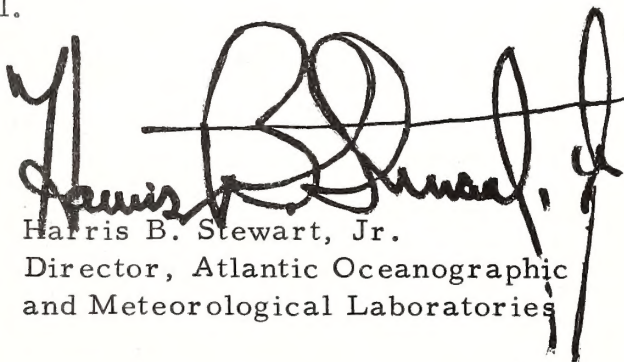


## FOREWORD

An increased understanding of the ocean and its processes, of the underlying geological and geophysical structures, and of the overlying atmosphere and its interactions with the sea will result in man's increased ability to deal intelligently with the problems of this environment.

The scientific and technical accomplishments of the National Oceanic and Atmospheric Administration's Environmental Research Laboratories are contributing to this understanding. Because the published results of the Atlantic Oceanographic and Meteorological Laboratories are broadly scattered through the literature, they are being brought together in a series of annual publications. These provide a convenient summary of the results of the work of these laboratories for researchers and interested laymen alike.

This volume, the sixth in the series, contains the published results of NOAA's Atlantic Oceanographic and Meteorological Laboratories for the year 1971.



Harris B. Stewart, Jr.  
Director, Atlantic Oceanographic  
and Meteorological Laboratories







## CONTENTS

### VOLUME I

#### General

1. Apel, John R.  
Wave Interactions in Solid State Plasmas: Book Review.  
Physics Today 24, No. 2, p. 47.
2. Stewart, Harris B. Jr.  
CICAR - An International Oceanographic Program in the  
Caribbean: Oceanic Citation Journal 8, No. 5, 2-5.
3. Stewart, Harris B. Jr.  
Ecological Aspects of Industrial Development: Muse  
News 11, No. 12, 411-413.
4. Stewart, Harris B. Jr.  
Exploring America's Mediterranean: NOAA 1, No. 2, 9-11.
5. Stewart, Harris B. Jr.  
Man and the Sea: Book Review. Bulletin of the American  
Meteorological Society 52, No. 8, 739-740.
6. Stewart, Harris B. Jr.  
Non-Food Resources as Viewed by: Federal Oceanographic  
Research: Third Proceedings of the Third Sea Grant  
Conference, sponsored by Oregon State University,  
March 1970, 47-48.
7. Stewart, Harris B. Jr.  
Ocean Symposium: AAAS Symposia Annual Meeting: Phila-  
delphia. Science 174, No. 4012, 964-965.
8. Staff  
Satellite Data Requirements of Atlantic Oceanographic  
and Meteorological Laboratories for Studies of Ocean  
Physics and Solid Earth. NOAA TR ERL 225-AOML 5.



## Physical Oceanography

9. Chew, Frank, and G. A. Berberion  
A Determination of Horizontal Divergence in the Gulf Stream Off Cape Lookout: *Journal of Physical Oceanography* 1, No. 1, 39-44.
10. Hansen, Donald V.  
Oceanography for the 1970's. *The Science Teacher* 38, No. 1.
11. Hansen, Donald V.  
Oceans from Space: Book Review. *Bulletin of the American Meteorological Society* 52, No. 8, 738-739.
12. Low, James K., and George A. Maul  
Precise Two-Point STD Calibrations: *Marine Technology Society Journal* 5, No. 5, 22-33.
13. Zetler, Bernard D.  
Earth Tides. *McGraw-Hill Yearbook of Science Technology*, 174-177.
14. Zetler, Bernard D., and George A. Maul  
Precision Requirements for a Spacecraft Tide Program: *Journal of Geophysical Research* 76, No. 27, 6601-6605.
15. Zetler, Bernard D.  
Radiational Ocean Tides Along the Coasts of the United States: *Journal of Physical Oceanography* 1, No. 1, 34-38.
16. Zetler, Bernard D., D. Cartwright, and W. Munk  
Tidal Constants Derived from Response Admittances: *Sixth International Symposium on Earth Tides, Strasbourg 1969*, 1-4.
17. Zetler, Bernard D.  
Tide: *Encyclopedia Americana*, 731-735.
18. Zetler, Bernard D.  
Tsunamis and the Seismic Sea Wave Warning System: *Man and the Sea*, American Museum of Natural History, 301-306.



## Meteorology

19. Anthes, Richard A.  
A Numerical Model of the Slowly Varying Tropical Cyclone in Isotropic Coordinates: Monthly Weather Review 99, No. 8, 617-635.
20. Anthes, Richard A.  
Iterative Solutions to the Steady-State Axisymmetric Boundary-Layer Equations under an Intense Pressure Gradient: Monthly Weather Review 99, No. 4, 261-268.
21. Anthes, Richard A.  
Numerical Experiments with a Slowly Varying Model of the Tropical Cyclone: Monthly Weather Review 99, No. 8, 636-643.
22. Anthes, Richard A.  
The Development of Asymmetries in a Three-Dimensional Numerical Model of the Tropical Cyclone: NOAA Tech Memo ERL NHRL-94.
23. Anthes, Richard A.  
The Response of a Three-Level Axisymmetric Hurricane Model to Artificial Redistribution of the Convective Heat Release: NOAA Tech Memo ERL NHRL-92.
24. Anthes, Richard A., Stanley L. Rosenthal, and James W. Trout  
Preliminary Results from an Asymmetric Model of the Tropical Cyclone: Monthly Weather Review 99, No. 10, 744-758.
25. Anthes, Richard A., James W. Trout, and Stellan S. Ostlund  
Three-Dimensional Particle Trajectories in a Model Hurricane: Weatherwise 24, No. 4, 174-178.
26. Anthes, Richard A., James W. Trout, and Stanley L. Rosenthal  
Comparisons of Tropical Cyclone Simulations With and Without the Assumption of Circular Symmetry: Monthly Weather Review 99, No. 10, 759-766.
27. Black, Peter G.  
Cumulonimbus Modification of Tropical Nature: Bulletin of the American Meteorological Society 52, No. 7, 562-565.



28. Black, Peter G., and Richard A. Anthes  
On the Asymmetric Structure of the Tropical Cyclone Outflow Layer: Journal of Atmospheric Sciences 28, No. 8, 1348-1366.
29. Carlson, Toby N.  
A Detailed Analysis of Some African Disturbances: NOAA Tech Memo ERL NHRL-90.
30. Carlson, Toby N.  
Weather Note: An Apparent Relationship Between the Sea-Surface Temperature of the Tropical Atlantic and the Development of African Disturbances into Tropical Storms: Monthly Weather Review 99, No. 4, 309-310.
31. Carlson, Toby N., and Robert C. Sheets  
Comparison of Draft Scale Vertical Velocities Computed from Gust Probe and Conventional Data Collected by a DC-6 Aircraft: NOAA Tech Memo ERL NHRL-91.
32. Gentry, R. Cecil  
To Tame a Hurricane: Science Journal, 49-55.
33. Koss, Walter James  
Numerical Integration Experiments with Variable-Resolution Two-Dimensional Cartesian Grids Using the Box Method: Monthly Weather Review 99, No. 10, 725-738.
34. Rosenthal, Stanley L.  
The Response of a Tropical Cyclone Model to Variations in Boundary Layer Parameters, Initial Conditions, Lateral Boundary Conditions and Domain Size: Monthly Weather Review 99, No. 10, 767-777.
35. Rosenthal, Stanley L., and Michael S. Moss  
Numerical Experiments of Relevance to Project Stormfury: NOAA Tech Memo ERL NHRL-95.
36. Rosenthal, Stanley L., and Michael S. Moss  
The Responses of a Tropical Cyclone Model to Radical Changes in Data Fields During the Mature Stage: NOAA Tech Memo ERL NHRL-96.



37. Scott, William D.  
Aerosol Sampling and Data Analysis with the NCAR Counter: The Second International Workshop on Condensation and Ice Nuclei sponsored by National Science Foundation, August 1970, 49-52.
38. Scott, William D., Robert M. Cunningham, Robert G. Knollenberg, and William R. Cotton  
Symposium on the Measurements of Cloud Elements: Bulletin of the American Meteorological Society 52, No. 9, 889-890.
39. Sugg, Arnold L., Leonard G. Pardue, and Robert L. Carrodus  
Memorable Hurricanes of the United States Since 1873: NOAA Tech Memo NWS SR-56.

Volume II

Meteorology (continued)

40. Staff  
Project Stormfury 1970 Annual Report.
41. Trout, James W., and Richard A. Anthes  
Horizontal Asymmetries in a Numerical Model of a Hurricane: NOAA Tech Memo ERL NHRL-93.
42. Barday, Robert J.  
Free-Air Gravity Anomalies South of Panama and Costa Rica (NOAA Ship Oceanographer - August 1969): NOAA Tech Memo ERL AOML-14.
43. Bassinger, B. G., R. N. Harbison, and L. Austin Weeks  
Marine Geophysical Study Northeast of Trinidad-Tobago: The American Association of Petroleum Geologists Bulletin 55, No. 10, 1730-1740.
44. Bennett, Richard H., and Douglas N. Lambert  
Rapid and Reliable Technique for Determining Unit Weight and Porosity of Deep-Sea Sediments: Marine Geology 11, 201-207.

45. Bennett, Richard H., Douglas N. Lambert, and Paul J. Grim  
Tables for Determining Unit Weight of Deep-Sea Sediments from Water Content and Average Grain Density Measurements: NOAA Tech Memo ERL AOML-13.
46. Dietz, Robert S.  
North Atlantic-Geology and Continental Drift (A Symposium): Marine Technology Society Journal 5, No. 5, 33.
47. Dietz, Robert S.  
Shatter Cones (Shock Fractures) in Astroblemes: Meteoritics 6, No. 4, 258-259.
48. Dietz, Robert S.  
Sudbury Astrobleme: A Review. Meteoritics 6, No. 4, 259-260.
49. Dietz, Robert S.  
The Sea: Ideas and Observations on Progress in the Study of the Seas. Book Review American Scientist 59, No. 5, 627.
50. Dietz, Robert S.  
Those Shifty Continents: Sea Frontiers 17, No. 4, 204-212.
51. Dietz, Robert S., and K. D. Emery  
Portrait of a Scientist: Francis Shepard. Earth-Science Reviews 7, No. 1, A9-A15.
52. Dietz, Robert S., and John C. Holden  
Pre-Mesozoic Oceanic Crust in the Eastern Indian Ocean (Wharton Basin): Nature 229, No. 5283, 309-312.
53. Dietz, Robert S., John C. Holden, and Walter P. Sproll  
Geotectonic Evolution and Subsidence of Bahama Platform: Reply. Geological Society of America Bulletin 82, 811-814.
54. Dietz, Robert S., and Harley J. Knebel  
Trou Sans Fond Submarine Canyon: Ivory Coast, Africa: Deep Sea Research 18, 441-447.



55. Freeland, George L., and Robert S. Dietz  
Plate Tectonic Evolution of Caribbean - Gulf of Mexico Region: Nature 232, 20-23.
56. Keller, George H.  
Engineering Properties of North Atlantic Deep-Sea Sediments: Interocean '70 2, 65-71.
57. Keller, George H.  
Mass Properties of the Sea Floor in a Selected Depositional Environment: Proceedings Civil Engineering in the Oceans II, Miami Beach, December 1969, 857-877.
58. Lattimore, R. K., L. Austin Weeks, and L. W. Mordock  
Marine Geophysical Reconnaissance of Continental Margin North of Paria Peninsula, Venezuela: The American Association of Petroleum Geologists Bulletin 55, No. 10, 1719-1729.
59. Peter, George and Omar E. DeWald  
Deformation of the Sea Floor off the North-west Coast of the United States: Nature Physical Science 232, No. 31, 97-98.
60. Peter, George, Barrett H. Erickson, and Paul J. Grim  
Magnetic Structure of the Aleutian Trench and Northeast Pacific Basin (1968): The Sea, Ed. A. E. Maxwell, Published by Wiley-Interscience, 4, pt. 2, 191-222, 1971. John Wiley & Sons, Inc., 1971.
61. Rona, Peter A.  
Bathymetry Off Central Northwest Africa: Deep Sea Research 18, 321-327.
62. Rona, Peter A.  
Deep Sea Salt Diapirs: Letter to editor Geotimes, p. 8.
63. Rona, Peter A.  
Depth Distribution in Ocean Basins and Plate Tectonics: Nature 231, 179-180.
64. Starr, Robert B., and Robert G. Bassinger  
Marine Geophysical Observations of the Eastern Puerto Rico-Virgin Islands Region: Trans-Fifth Caribbean Geological Conference, Geology Bulletin No. 5, Queens College Press, 25-29.

65. Weeks, L. Austin, and Robert K. Lattimore  
Continental Terrace and Deep Plain Offshore Central  
California: Marine Geophysical Research 1, 145-161.
66. Weeks, L. Austin, R. K. Lattimore, R. N. Harbison,  
B. G. Bassinger, and G. F. Merrill  
Structureal Relations Among Lesser Antilles, Venezuela,  
and Trinidad-Tobago: The American Association of  
Petroleum Geologists Bulletin 55, No. 10, 1741-1752.

#### Sea-Air Interaction

67. Hanson, Kirby J.  
Studies of Cloud and Satellite Parameterization of  
Solar Irradiance at the Earth's Surface: Proceedings  
of the Miami Workshop on Remote Sensing March 29-31,  
1971, Miami, Florida, 133-148.
68. McAlister, E. D., William McLeish, and Ernst A. Corduan  
Airborne Measurements of the Total Heat Flux from the  
Sea during BOMEX: Journal of Geophysical Research 76,  
No. 18, 4172-4180.
69. Nordbert, W., J. Conway, Duncan B. Ross, and T. Wilheit  
Measurements of Microwave Emission from a Foam-  
Covered Wind-Driven Sea: Journal of Atmospheric  
Sciences 28, No. 3, 429-435.
70. Ostapoff, F.  
Introductory Remarks - Sea-Air Interaction Instrumen-  
tation: IEEE Transactions on Geoscience Electronics  
GE-9, No. 4, 197-198.
71. Ostapoff, F.  
Ocean-Atmosphere Interaction in the Caribbean Sea:  
Viewed from the Oceanographer Side: Proceedings Sym-  
posium on Investigations and Resources of the Caribbean  
Sea and Adjacent Regions, 137-145.
72. Shinnars, Willard W., Gerald E. Putland, and Peter B.  
Connors  
Tests of Modified Radiosonde Hygristor Duct: NOAA  
Tech Memo ERL AOML-15.



## Wave Interactions in Solid State Plasmas

By Martin C. Steele, Bayram Vural

285 pp. McGraw-Hill, New York, 1969.

\$15.50

Solid-state plasma—nearly a contradiction in terms, after all—consists of mobile charge carriers (plus their neutralizing ionic background) as they co-exist in a semiconductor, semimetal or metal. The study of such a system from the plasma viewpoint is a relatively recent discipline whose practitioners have come from both gaseous plasma and solid-state physics and are driven by interest in modeling controlled thermonuclear reactors in the small, or by potential device applications or perhaps by the sheer good physics of it all.

Martin C. Steele and Bayram Vural, whose origins at RCA Laboratories betray their biases in this respect, have rendered the rest of us a valuable service by undertaking the onerous task of reducing the research literature in the field to an advanced monograph of high quality. The primary emphasis of

their book is on wave propagation and interactions in such a charged-particle ether, especially as regards the existence of unstable solutions.

The approach is summarized by the dielectric response tensor for electrokinetic waves in a magnetic field and encompasses passive and growing waves; their interactions with phonons, spin waves, and external circuits; negative resistance, and pinch effects. In level and content, and in its mix of both theory and experiment, the book serves as a connection between textbook and journal. Its primary lack is in photon-plasma interactions in solids at infrared through ultraviolet frequencies; but then this leaves something for others to do.

JOHN R. APEL  
*Johns Hopkins University*

# 15 Nations Join In CICAR Study Of Caribbean

*By Harris B. Stewart, Jr.*  
*U.S. National Coordinator for CICAR*

CICAR — the Cooperative Investigation of the Caribbean and Adjacent Regions — has moved smoothly from a collection of separate national efforts into a truly cooperative international program in which all participants are working in a synergistic arrangement to solve major scientific problems in the Gulf of Mexico and the Caribbean Sea that could not otherwise have been meaningfully attacked.

Sponsored by the Intergovernmental Oceanographic Commission, CICAR is a 15-nation investigation of the fisheries, marine biology, physical oceanography, marine geology and geophysics, sea-air interaction, and meteorology of the Caribbean and the Gulf.

The three-year field program, now underway, concludes in December 1972. The U.S. effort for the final year and a half is being supported primarily through the National Science Foundation, Office of the International Decade of Ocean Exploration (IDOE) as one of its first major thrusts.

A cooperative international Caribbean study was first proposed by the Netherlands at the fourth session of the Intergovernmental Oceanographic Commission meeting in Paris in 1966. CICAR was adopted as an official program of the Intergovernmental Oceanographic Commission in October of the following year, and the first meeting of delegations from the interested countries took place in Curacao, Netherlands Antilles, in November of 1968 immediately following the week-long symposium on Investigations and Resources of the Caribbean Sea and Adjacent Regions. Subsequent meetings of the CICAR International Coordination Group, made up of the numerous CICAR national coordinators, the international coordinator (Admiral Langeraar), subject leaders, and assistant international coordinators, were held in Washington, D.C. (June 1969), Mexico City (February 1970), and Trinidad (March-April 1971).

The actual field work on CICAR started in January of 1970 and is due to run through December of 1972. Although some 15 countries have joined the CICAR program to date, the field work has been carried out by nine of these fifteen countries with the facilities to operate at sea in the area: Brazil, Colombia, Cuba, Mexico, Netherlands, United Kingdom, USA, USSR, and Venezuela.

There is a well-founded feeling within the international oceanographic community that cooperative international projects should be undertaken only when the problems being addressed can not be solved by one country alone. Until the Trinidad CICAR meeting, in the winter of 1971, there was no overall defined scientific problem which required such cooperation; CICAR, until then, was essentially a collection of individual national programs taking place in the Caribbean and its adjacent regions.

This collection of individual national programs provided the background and experience at sea that made possible the truly cooperative international effort developed out of the Trinidad meetings in the winter of 1971.

Just what did happen at Trinidad to change that approach? First was a report made by Mamayev (UNESCO) and Kesteven (FAO) as a result of their visits to various CICAR countries. In effect, it said that there was little going on in the CICAR area that would not have been done anyway — CICAR or no CICAR. The effect was to shake up the meeting and to generate a note of resolute determination that would not otherwise have developed. This set the stage for the growth of a very real effort to show that the program could indeed be a success.

Although the definition and understanding of the overall circulation pattern and mechanism for the Gulf and Caribbean had been a CICAR goal from the outset, no concerted international program to attack this problem had until then materialized. At Trinidad, it developed that the United States was mounting a multi-ship operation in the Gulf of





*U.S. scientists, on board the OREGON II, demonstrate the use of "bongo nets" to Mexican oceanographers.*

Mexico, Yucatan Channel, and the northwestern Cayman Sea scheduled for August of 1971. This was to be the fourth multi-ship operation mounted by the US in the Gulf of Mexico — the so-called EGMEX cruises coordinated through the State University System Institute of Oceanography (SUSIO) of Florida.

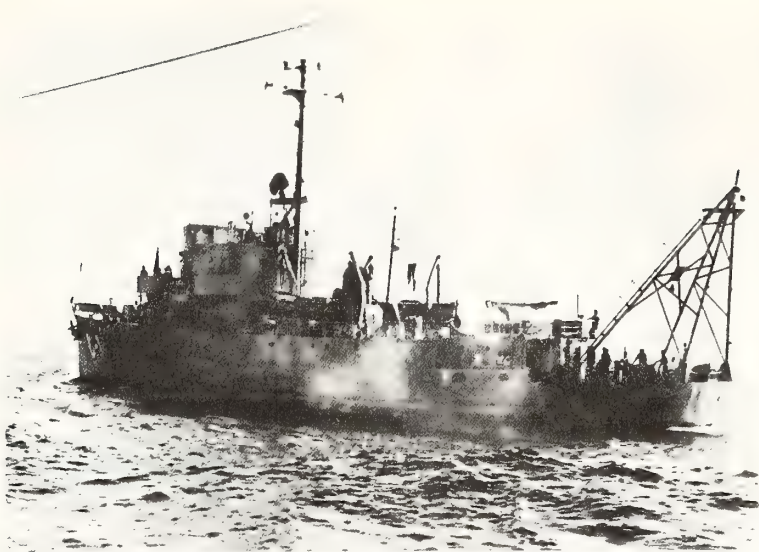
These EGMEX (for Eastern Gulf of Mexico) cruises had been incorporated as part of the United States CICAR effort, and the results of the first three have already added to our knowledge of the Loop Current in the Gulf and of the importance of the circulation system on the distribution of plankton in the Gulf.

The preliminary plans for EGMEX IV in August of 1971 were presented at Trinidad by the United States, and bit by bit the other pieces of what would be a truly cooperative quasi-synoptic operation fell into place. The Mexican delegation agreed to switch its planned work for the URIBE from geophysical work to physical oceanographic work and to be

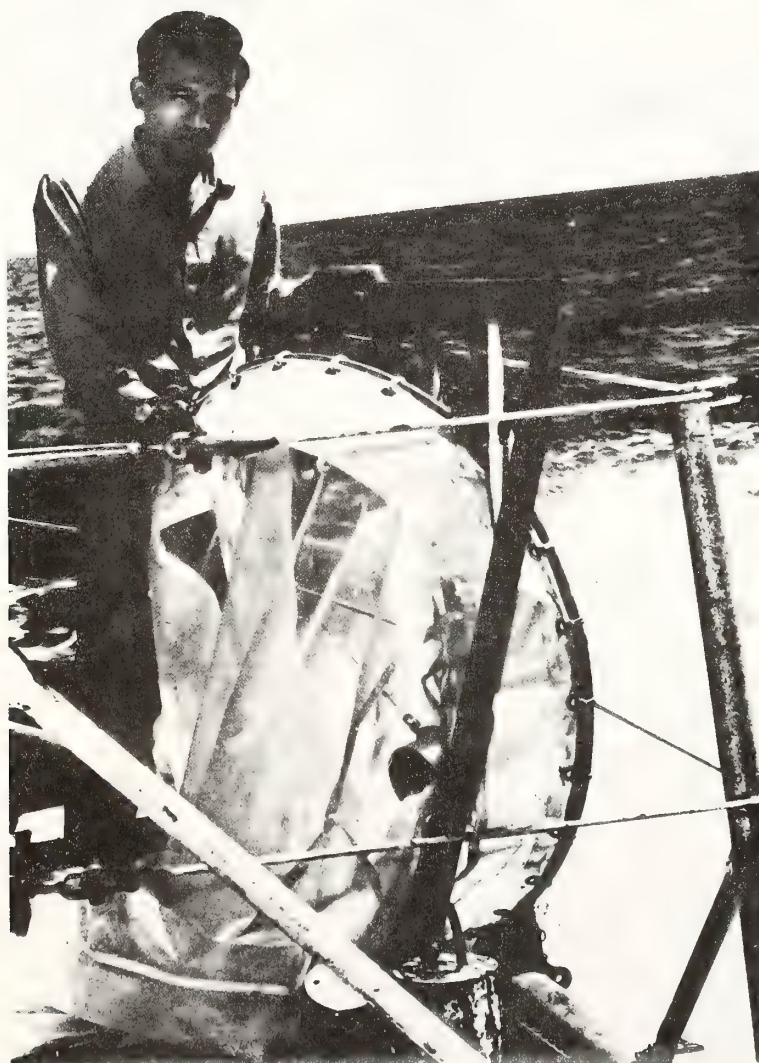
in the southern Gulf of Mexico and Yucatan Channel in August of 1971. The Cubans agreed to run their standard sections (physical and chemical data and biological collections) between Cabo San Antonio on the western tip of Cuba and the Yucatan peninsula and across the Straits of Florida between Havana and Key West and to carry them out also in August of 1971.

The UK then agreed to occupy the north-south section along  $60^{\circ}\text{W}$  just east of the Antilles in late July with the H.M.S. HECLA, and the Venezuelans agreed to modify their geophysical cruise planned for August to include a reoccupation of this same  $60^{\circ}\text{W}$  section up to  $15^{\circ}\text{N}$  in early August with the LASALLE and to follow this by occupying the north-south section along  $63^{\circ}\text{W}$  — just west of the Antilles. The Colombians then agreed to occupy the sections from Cartagena to Haiti, Haiti to Jamaica, Jamaica to the Honduras banks, and from there to Cartagena.

The U.S. Coast Guard Cutter



*The Mexican research vessel URIBE (left) has conducted surveys in conjunction with the NOAA ship DISCOVERER and the OREGON II. Photos: National Oceanic and Atmospheric Administration.*



ROCKAWAY, doing physical and chemical work as part of a training cruise in the southeastern Caribbean area, modified its earlier planned program to occupy one of the CICAR standard sections off northeastern South America in late July and to make observations on the section along 60°W on its return from the area in August.

Through Ingvar Emilsson in Mexico, subject leader for standard sections, and through John Cochran at Texas A&M, subject leader for circulation studies, the physical observations have been standardized insofar as possible among so many different ships, and the Netherlands-provided CICAR Operations Center at Curacao tries to keep track of what ships are in the area and where and what they are doing as well as providing a communications center for the whole operation.

The Trinidad meeting also resulted in the agreement to use a standard neuston net for biological tows, these nets in limited amounts to be furnished by the NOAA National Marine Fisheries Service to ships participating in the August operation. Agreement was also reached on adopting the 20-cm diameter bongo nets (0.125 and 0.250 mm mesh openings) for the standard CICAR biological station, and a double bongo array (two 20-cm nets and two 60-cm nets) as the standard sampler for ichthyoplankton. Thus standard biological samples would also be obtained during the CICAR Survey Month of August.

A CICAR drift-bottle program is under way with the NOAA-NMFS laboratory at Miami acting as the



central focus and providing the bottles at no cost to the participating ships and tallying the returns. The National Oceanographic Data Center is acting as the regional CICAR data center and through World Data Center-A (Oceanography) is funneling all CICAR data into the international data exchange mechanism. Standard data forms have been provided to all participating ships, and assistance in standardizing analytical procedures is available. Additional projects in tidal studies, meteorology, marine geology and geophysics, fisheries, bathymetry, data management, and in education and training are well along.

With support from the International Decade of Ocean Exploration program of the National Science Foundation, both the Geological Survey and NOAA's Atlantic Oceanographic and Meteorological Laboratories in Miami will be carrying out marine geological and geophysical work in the CICAR area during the present year. As part of the CICAR program to date, Woods Hole, the University of Rhode Island, Duke University, University of Miami, Geological Survey, Naval Oceanographic Office, and NOAA have carried out major geological and geophysical studies in the CICAR area.

Geophysicists from NOAA's Atlantic Oceanographic and Meteorological Laboratories have been working especially on the overall tectonic framework and geological structure of the Antillean island arc complex. They worked from the NOAA DISCOVERER first in the southeast corner of the Caribbean and

are gradually extending their studies up the island arc in cooperation with the UK geophysicists working aboard H.M.S. HECLA.

It is planned to assemble and eventually publish a complete bibliography of the published results of all U.S. CICAR projects, and an interim list is to be available in early 1972. The method whereby the results of the total CICAR program will be made available internationally has not yet been decided. As is so often the case, funding appears to be the

problem, and it may be that each participating country will prepare collected reprints of its own CICAR projects.

CICAR started slowly and primarily as an assemblage of individual national efforts. This phase has been supplanted by the development of a truly cooperative quasi-synoptic CICAR Survey Month in August of 1971 (CSM-I), and plans are being developed for comparable CSM-II and CSM-III operations in April and October of 1972 respectively.



*RESEARCHER is one of the ships participating in the Caribbean investigation.*

# ECOLOGICAL ASPECTS OF INDUSTRIAL DEVELOPMENT

by

*Harris B. Stewart, Jr.*

*Director Atlantic Oceanographies  
And Meteorological Laboratories,  
NOAA, U.S. Department of Commerce,  
Miami, Florida*

Words, their meaning, their use and misuse, have always fascinated me. Some of our misuses are popular but painful. The word "real" for example has within the past five years become increasingly used to modify adjectives: Real good, real fast. This is using the adjective "real" in place of the adverb "really." A generation ago such usage would have branded you as a grammatical dolt. Today this usage is widely accepted, although still wrong in my book. "Irregardless" is a delightful mistake that you actually hear used in all seriousness. It is a combination of "regardless" and "irrespective" both thoroughly legitimate words, but their coupling has given birth to a monster that seems to have many friends.

Speaking of words, we all have ones that we particularly like, and one that I am fond of is "shibboleth." First, it sounds nice. And the sounds that words make are often overlooked in our rush to communicate meaning. Gertrude Stein, for example, totally disregarded meaning to create pleasing sounds when she wrote, "It is as roses that cows commit suicide." You smile when you hear it, because you are so accustomed to look for meaning in words, and this is a nonsense phrase. But forget the meaning aspect and concentrate on the sounds: "It is as roses that cows commit suicide." You must admit, the sound is pleasant.

To me, "shibboleth" sounds nice, but its meaning is also interesting it comes from the Hebrew and literally means both an ear of corn and a stream. In the Bible in Judges, Chapter 12, verses 4-6, the word "shibboleth" was used by Jephthah as a password by which to distinguish the fleeing Ephraimites from the men of his own army, since the Ephraimites could not pronounce the "sh" sound—much like the use of such words as "lollapaluza" as a password in the Pacific during World War II which comes out "rarraparuza" when the Japanese say it. Originally used as a test word itself, Shibboleth has taken on the meaning of password and today means a watchword, key word, or pet phrase of a particular sect or group. Today we would say "shibboleth" means an "in" word or an "ok" word.

It now appears that we have two new shibboleths for the seventies, and these words are "environment" and "ecology." Let us look at both of these words for a short while as they relate to industrial development.

"Environment" comes from the French word "environ" meaning "around," and the transitive verb "to environ" means to form a ring around, to surround, to envelop. So our environment is that which surrounds or envelops us. "Environment" is a word that has come to have a very real meaning for those concerned with the



development of land for industry.

As little as five years ago, a developer was convinced that the break between the land and the sea needed to be a neat, sharp concrete break, and a concrete seawall was the answer. Today, however, such a plan would be developmental suicide, and the militant conservationists would be outside your office, droves carrying placards that told the world that the XYZ Development Company was destroying the environment. This you could live with, but they would probably back up their placards with a court case that they might win.

Before I get the local conservationists up in arms, let me make my position perfectly clear. I am myself a conservationist. I like green grass and I enjoy the uncluttered natural shoreline where it still exists. I want to have shallow areas preserved for the development of the larval stages of our sport and commercial fish species, and I think man as a busy, harried species needs a few places where he can sit and vegetate and commune with nature. However, I also feel that the really endangered species in our world today is man himself. My view of conservation is a man-oriented view. Our population is now doubling about every forty of fifty years, so it is man that we must be most concerned about. We must put an end to the hysterical approach to the problems of our environment, and we must look at them rationally. Conservation of the natural environment is just one of the many uses to which our lands can be put. It is a good and thoroughly legitimate use, but it can not hope to be the only use. It is one of many competing uses.

What are the environmental implications for the industrial developer? To me these mean that people, in my

man-oriented view of conservation, must have a pleasant and healthful environment in which to live. This means better than "adequate" means of disposal of municipal wastes. It means the incorporation of the "greenbelt concept" into any large-scale development planning. It means providing adequate transportation to and from the area. It means ample space for recreation for the people who will live and work in your development, and it means clean air, clean water, and an uncluttered landscape.

For the developer, the nation's present love affair with the environment can mean two things. First, it can mean that he must either keep his plans secret so that the militant conservationists, the hysterical environmentalists don't learn about them until it is too late for them to do anything or else he must throw enough bones to these hungry groups that they will be quiet and not interfere with his plans. Secondly, the present national concern with the environment can present to the developer a real opportunity to create more than just reinforcing rods and concrete. The people to whom he is selling his ideas or his product have within the past few years become educated environmentally. If you would capitalize on this market, you must meet the demands of your potential customers. You must have the greenbelts, the parks, the marinas, the open beaches, the conservation areas, the well-landscaped buildings.

Environment, then, must be of very real concern to you. Suddenly it has become an essential part of your bread and butter. An industrial or residential development plan that takes the environmental aspects into consideration will be a much easier one to get through the various zoning boards, city and county planning boards,

citizens' groups, and all the others that you have to face before you can put in the first bulldozer these days. The day of environmental concern is here. Learn how to live with it, even cater to it, and your own projects will be considerably more successful.

"Ecology" is another of the mis-used words, another of today's shibboleths. It derives from the Greek word "oikos" meaning "house" and actually means the study of houses or, in a broader sense, of environments. More specifically, ecology is that branch of biology which treats of the relations between organisms and their environment. So "ecology" is a branch of science and not something that can be destroyed by a jetport or by cooling waters from a power plant. But the word, like so many others, is losing its original meaning through misuse, and the "branch of biology which treats of" part of the definition has been dropped in common usage, and we tend to think of "ecology" as meaning the interrelationship of organisms and the environment rather than the study of it.

When we speak of the interrelationship between organisms and their environment—ecology—we must remember that man himself is one of those organisms. To me the very real ecological aspects of your profession must be not the effect of your works on the interrelation of turtle grass and

the overlying water, not the interrelationship of migratory ducks and the wetlands, but rather the interrelationships of man himself with the world around him. Every time a dozer blade rearranges the landscape, there are ecological effects. The question then is not is your work "changing the ecology"—of course it is. The question should be is the end result good or bad for man? Man likes to have wetlands preserved. He likes to have coastal mangroves preserved. He likes to be able to fish and swim and to sit and look at unspoiled nature. He does not want all construction, all progress to stop so that he can do these things; he just wants these elements taken into consideration, and the clever developer will do just that.

Today there are environmental constraints on every developer that were unheard of five years ago. My suggestion is not to fight them. Use them in your planning. Make sure your architects and engineers are aware of them. Utilize these constraints in your construction projects in your real estate and industrial developments. The developers that come our ahead in the next several years will be those that know what the public wants and caters to this. Today's public wants to be sure that the environmental aspects are considered. Capitalize on this and you are a winner. Disregard it at your peril.





*CICAR: Progress Report*

After years of scientific neglect,  
the Caribbean is being probed and  
measured in a cooperative study by fifteen nations.

## EXPLORING AMERICA'S MEDITERRANEAN

IT IS INTERESTING—if not discouraging—that so little scientific work has been done over the years in “the Mediterranean of the Americas.”

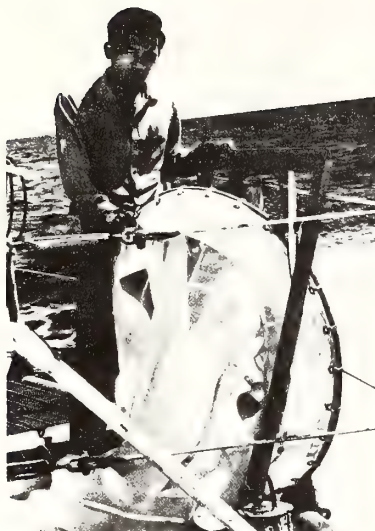
The Caribbean Sea with its adjacent Gulf of Mexico is, oceanographically speaking, still poorly described and even less well understood.

Now, its dynamics, its contained life, its bottom topography and tectonic framework, its interactions with the overlying atmosphere, and the dynamics of the atmosphere above it are the subjects of a cooperative international investigation sponsored by the Intergovernmental Oceanographic Commission.

Officially called the Cooperative Investigation of the Caribbean and Adjacent Regions—CICAR for short—its field phase began in 1970 and will continue through 1972. Originally proposed by Dutch oceanographers, the idea won quick accept-

BY HARRIS B. STEWART, JR.  
U.S. National Coordinator for the  
Cooperative Investigation of the  
Caribbean and Adjacent Regions

*continued*



*In the Cooperative Investigation of the Caribbean, the Mexican research vessel URIBE (top right) has conducted surveys in conjunction with the NOAA Ship DISCOVERER and the OREGON II. (Top left) Plankton samples were gathered to study the distribution of these organisms. (Bottom) U.S. scientists, on board the OREGON II, demonstrated the use of "bongo nets" to Mexican oceanographers.*



ance among the larger Caribbean countries and many of the maritime nations with or without territorial claims in the CICAR region. Since then, several of the smaller countries bordering the Caribbean have also joined in, so that as CICAR enters its second year of field operations some 15 countries are involved: Brazil, Colombia, Cuba, Germany, France, Guatemala, Jamaica, Mexico, Netherlands, Panama, Soviet Union, Trinidad and Tobago, United Kingdom, United States, and Venezuela.

Because so little is known of the oceanography of the Caribbean and the Gulf of Mexico, much of the CICAR effort is of a reconnaissance or survey nature. This is particularly true of the marine geophysics and the marine biological and fisheries programs.

The United Kingdom, the Dutch, and the United States are all involved in systematic surveys of the bathymetry, gravity, and magnetics of the Antillean arc and the A, B, C's, as the islands of Aruba, Bonaire, and Curacao are known.

The Cubans are deeply involved in standard repeat sections of observations along lines radiating out from their island, sections along which they make repeated collections of plankton and measurements of the physical and chemical properties.

The Colombians recently completed a successful cruise along several standard sections to evaluate the upwelling area off the north coast of South America, and NOAA's National Marine Fisheries Service with the OREGON II has made several cruises to evaluate the fisheries potential of the area.

Since the available data in the CICAR area are comparatively few, it has been difficult to identify specific research problems that would lure research oceanographers from their previously planned projects in other portions of the ocean. One outstanding exception among U.S. oceanographers has been the interest in determining circulation patterns in the Caribbean and the Gulf of Mexico. At a meeting held in Miami last summer, physical oceanographers from the eastern seaboard and the gulf coast identified two aspects of the overall circulation that they particularly wanted to investigate in view of the importance of the CICAR area as the source for the Florida Current and much of the water of the Gulf Stream. Highest priority was given to the currents in the Yucatan Channel and the circulation of the Gulf of Mexico. The second problem to be investigated is the complex movement of the waters through the passes between the Antillean Islands.

While the ATLANTIS II of the Woods Hole Oceanographic Institution investigated the currents in the passes, a large cooperative Mexican-U.S. effort was mounted in the Yucatan Channel and the eastern Gulf of Mexico. This latter effort, called the Eastern Gulf of Mexico Expedition, has consisted thus far of three carefully planned multi-ship operations, with a fourth one now in the planning stages. Ships from the several universities of the State University System of Florida, from Texas A&M, the University of Miami, NOAA's DISCOVERER and the URIBE from Mexico worked together to obtain data on the elusive Loop Current in the Gulf of Mexico and on the distribution of eggs, larvae, and other planktonic organisms.

A CICAR Tides Program under the international direction of Bernard Zetler of NOAA's Atlantic Oceanographic and

Meteorological Labs in Miami is well underway. Records from tide gages on the coasts of Cuba and Mexico have recently gone to the National Ocean Survey for analysis, and data from six Ocean Survey gages throughout the Lesser Antilles are being used to piece together the tidal picture for the whole region. A NOAA deep-sea tides projects will place bottom-mounted pressure-type tide gages at critical points throughout the area to help in determining the tidal characteristics of the entire basin. More specifically, two one-month sets of open-sea tide measurements will be made with bottom-mounted gages deployed by the NOAA Ship DISCOVERER this fall in the area of the semidiurnal amphidromic point in the eastern Caribbean. Tidal current analyses are even now being run on the data from near-bottom current observations obtained by the DISCOVERER in the Yucatan Channel in 1970, and analyses are planned on current data obtained by Woods Hole oceanographers in the passes between the Antillean Islands.

The United States' effort in CICAR is truly a cooperative one. From the federal government, personnel and facilities are committed from the Geological Survey, the Navy, the Coast Guard, the National Science Foundation, and NOAA's various components. From the university community, there is broad representation including Woods Hole, University of Rhode Island, Lamont-Doherty Geological Observatory, Princeton, Duke, Florida State University, University of South Florida, Florida Institute of Technology, University of Miami, Texas A&M, University of Puerto Rico, and the Scripps Institution of Oceanography.

The National Marine Fisheries Service, particularly with the OREGON II, is heavily involved in the fisheries aspects of the CICAR program. In January of this year, the OREGON II and the URIBE from Mexico met near Alacran Reef (22°30'N, 89°45'W) to intercalibrate various nets for sampling larval and juvenile fishes and to demonstrate the use of the so-called "bongo nets" to the Mexicans. This operation was under the direction of Ken Honey from the NMFS Lab at Boothbay Harbor, Maine, as Chief Scientist, and Bengt Arpi of the FAO mission in Mexico was in charge aboard the URIBE.

NOAA's Tropical Atlantic Biological Laboratory at Miami is serving as the central agency for the CICAR drift bottle program. Feodor Ostapoff of the Atlantic Oceanographic and Meteorological Laboratories is the International Coordinator for CICAR meteorology, and plans to conduct sea-air interaction research aboard the DISCOVERER in the CICAR area this fall. Zetler is the subject leader for tides, and his own project in this field is progressing well. NOAA's ships are participating. NOAA's physical oceanographers, NOAA's fisheries scientists, and NOAA's marine geophysicists are involved, and the National Oceanographic Data Center is heavily involved as the central data repository and distributory for CICAR.

Through the International Decade of Ocean Exploration, first-year funding has just become available from the National Science Foundation for the CICAR program, and it is anticipated that NOAA's role in CICAR will continue to be a large portion of the United States' contribution to this international cooperative venture. □

**Man and the Sea.** Edited by Bernard L. Gordon. The Natural History Press, Garden City, New York, 1970. 498 pages. \$9.95. Hardbound.

In this one volume, Prof. Gordon has collected the works of some 71 different contributors to our present state of knowledge of the global sea. His selections run the gamut from A to Z—literally, from Agassiz (directions for collecting fish—1853) to Zetler (tsunamis—1965). His time span covers something to over 4000 years, from the Genesis account of the flood (ca. 2348 B.C.) to the account of the Red Sea brines and “hot holes” (1969).

No two oceanographers would select the same set of 71 basic original works to include in one volume, so it is obvious that any reviewer would have his own ideas of just which 71 basic works should have been included. It is a tribute to Prof. Gordon that most oceanographers would have probably chosen more than half of the authors he chooses, and this one found that with something over half of the remaining ones he was totally unfamiliar and thoroughly enjoyed reading them.

Too often today's student of the oceanic and atmospheric sciences builds his knowledge of the field only on those most recent works that form the top of the pyramid of knowledge. Actually, he can survive professionally if he knows only the top, but the really well-rounded oceanographer or meteorologist wants to know the earlier thinking that forms the base and body of this pyramid. *Man and the Sea* provides a concise and singularly readable summary of this background, and it does so by including the actual writings of the men who block-by-block built the pyramid at whose top we now rest and—hopefully—build even higher.

Within the past 10 years, meteorologists have come to place increasing emphasis on the necessity to understand the intricate interactions between the sea and the atmosphere. For too long, meteorologists studied the atmosphere down to the sea surface and stopped, and the oceanographers studied the sea up to the same surface and stopped. There was considerably more interaction between the sea and the atmosphere than there was between the oceanographer and the meteorologist. Fortunately, that era is over, and both meteorologists and oceanographers are investigating each other's field where they come together at the sea surface. The editor of *Man and the Sea* has included several works that touch on the sea-air interaction phenomena. The first reference to this sea-air interaction process is a footnote ascribed to Aristotle (p. 10):

As the sun is continually evaporating the water of the sea, it must eventually be entirely dried up. But we have reason to believe that all the water which is evaporated by the solar heat, or any other natural process, is again deposited in the form of rain or dew.

William Ferrel (1817–1891) was an American meteorologist with the Coast Survey who did considerable research on winds, storms, currents, and tides. His “An essay on winds

and currents of the ocean” is included in the papers selected, and in this tract he takes a few swipes at Lieutenant Maury and then delves into the riddle of the Gulf Stream (p. 68):

It is proposed in this essay to inquire into the effects which are produced, both in the atmosphere and in the ocean, by this disturbance of equilibrium, and by means of a new force which has never been taken into account in any theory of winds and currents, to endeavor to account for certain phenomena in their motions, which have always been a puzzle to Meteorology and Hydrology.

Two more papers consider the ocean-atmosphere problem, Willard Pierson's “Understanding and forecasting phenomena at the air-sea interface” and John Isaacs' “The birth-place of weather.”

*Man and the Sea*, however, is primarily for oceanographers and students of oceanography, and the authors of the selections read like a Who's Who in marine science: Leonardo Da Vinci, Newton on Tides, Benjamin Franklin on the Gulf Stream, van Humboldt, Bowditch, Scoresby, Darwin, Agassiz, Maury, Secchi, John Murray of *H.M.S. Challenger* fame, Dittmar, Nansen, Herdman, Ekman, Wegener as the father of Continental Drift, Hjort, Henry Bigelow, Beebe, Iselin, Waksman, Sverdrup, Revelle, Schaefer, and a raft of today's oceanographers and writers of the sea who either have made significant contributions themselves or can write especially well of the contributions of others. It would be difficult to pick a better set of contributions, but there does seem to be an overabundance of selections on undersea vehicles. These include not only Da Vinci's early 16th century description of an “underwater device,” but one on Halley's 1716 diving bell, Jacob Bigelow's 1829 account of diving bells, Beebe's account of the Bathysphere, Anderson's record of the *Nautilus* at the North Pole, Don Walsh on the *Trieste*, Cousteau on the Diving Saucer, the voyage of the *Triton*, the *Thresher* search by Bracket Hersey, Bill Rainnie's account of the *Alvin*'s search for the H-bomb off Palameres, Scott Carpenter and *Sealab II*, and Piccard on the *Ben Franklin*.

The book also includes original articles related to marine biology, chemistry, geology, physical oceanography, marine optics, ocean mining, Mohole, the *Glomar Challenger* deep drilling project, continental drift, tides, the Arctic, radioactive waste disposal, marine archeology, desalination, fish-protein concentrate, international cooperation, marine fisheries, seaweeds, and power from the sea. It is a veritable oceanographic bouillabaisse, and everyone with a love of the sea will be sure to find in *Man and the Sea* at least one selection by his own personal marine hero, be it Nansen, Bigelow, Sverdrup, or Revelle. It is a book worth having on your shelf, for it does us all good to return to the sea from time to time, and to become acquainted or renew acquaintance with the men who made the contributions in the past on which today's marine scientists must build.—Harris B. Stewart, Jr.



*Reprinted from Third Proceedings of the Third Sea Grant Conference, sponsored by Oregon State University, March 1970, 47-48*

**Non-Food Resources as Viewed by: Federal Oceanographic Research**

*Harris B. Stewart, Jr.*

*Director, ESSA Atlantic Oceanographic and Meteorological Laboratories  
Miami, Florida*

I will recall the NASCO meeting a number of years ago when, during a long discussion on marine science education and training, Athelstan Spilhaus delivered a lengthy — and pithy — diatribe on the growing gap between “ivory tower ocean research” and the needs of the poor guys trying to make a buck out of the ocean or get something done at sea. He wound up with an — at the time — outlandish suggestion that what we should have are Sea Grant Colleges, a marine counterpart of the Land Grant Colleges that have worked so well. We have come a long way since then, along the route of hearings, draft legislation, more hearings, a bill, passage of the Sea Grant Act, appropriations, proposals and more proposals, and now we are well along the road of implementation. I believe the program has worked well to date; it has been money well spent.

One of the things that I particularly like about the Sea Grant concept is the involvement of capabilities other than marine science, and of people other than oceanographers. Oceanographers are interested primarily in finding out how that great, boiling, bubbling confusion, called the ocean, really works. Other views will broaden the scope of investigations. You will notice that I avoid the word “interdisciplinary.” That term has become one of the most overworked words and underworked concepts in science today, and I have come to loathe it. We tend to use the word as a crutch and forget the concept that the word supposedly embodies. Sea Grant has tried to correct this neglect by bringing many capabilities to bear on oceanic problems. I like the approach.

However, I feel that we have, as a country, done an extremely poor job in our approach to the increased utilization of marine resources. First, we have done a poor job in our public relations. We have for years shouted about “feeding the world’s starving millions from the ocean” and “utilizing the untapped treasure troves” of our continental shelves. We tried to use these slogans as justification for an increased federal program in marine sciences. Obviously this approach did not work on those in control, for the federal program in marine science and technology has been essentially level-funded for the past several years. The President’s budget submitted to Congress for fiscal year 1971 showed an increase of about \$23 million over 1970 for a total of some \$537 million for marine science and

technology. It is interesting to note that this is the first year in some time that the non-military oceanography budget is more than half of the total amount. So perhaps we have started. I was pleased to note that \$3.4 million of the increase was for Sea Grant and about \$15 million for the IDOE (International Decade of Ocean Exploration).

If our PR approach has been wrong, how do we correct it? The time has come for our public utterances to be realistic and factual. The solution to the problem of our present inadequate utilization of marine resources is not solely a scientific one, as many would have us believe. It is in large part dependent on the economics of the situation (can we get it cheaper from a land source?), in part dependent on modernizing the legal framework of resource development, and in part dependent on improved technology. Marine science can and will contribute, but the idea that marine science alone will solve the problems of increased resource utilization is mere dreaming. Our public relations, therefore, must be based on cold hard facts, not the flowery phrases and glowing generalities of the past 10 years, which implied that oceanography alone could provide the panacea for all our resource ills.

In addition to a poor public relations job, we have made, what I consider, a gross blunder in pushing for exploitation of marine resources without also pushing for the exploration that must precede it. We talk glibly of the importance of the sea for food, for mineral resources, for transportation, for improved weather forecasts, for national defense, and many other uses. The truth is, that the sea is so little explored and its magnificently complex processes so poorly understood, that we have been unable to utilize the sea for much of anything other than the same uses to which it has historically been put — and with relatively little improvement in these. For example, less than 5% of the seafloor is adequately mapped for nautical charting purposes, and we have yet to know enough about the distribution of wave conditions on a global scale to provide good ship-routing services. We still know so little of the interrelationship between the marine environment and the edible resources living there that “feeding the world’s starving millions from the wealth of the sea” is a veritable pipe dream today. We are still so unaware of the extent of the “untapped mineral resources” we talk so glibly about, that we do not know where they are, how extensive they

are, or even what they are. We know that the sea influences the weather and *vice versa*, but our ability to forecast the weather has improved little over the past 20 years, and marked improvements cannot be expected until we have been able to explore, untangle, and understand the complex interrelationship between sea and atmosphere. Our military knows so little of the marine environment that they still cannot find submarines, and new weapons systems that work in theory often do not work at sea. The Navy uses the term "environmentally limited" when referring to some of their marine equipment or systems. Actually, this is just a euphemism that means we still know so little about the environment of the sea that we are unable to build things that will work there.

Too long the United States has talked of the resources and the utilization of the sea without considering the fundamental initial steps of exploring, describing, and understanding. The recovery of food and minerals, the improvement of marine transportation, better national defense, improved forecasts, and all the other ways in which the sea will be utilized cannot be effectively realized until the basic exploration, description, and understanding have been accomplished. This fact is so simple and so basic that it has been almost completely overlooked in the rush to glamorize the benefits eventually accruing from the sea. Exploring, describing, and understanding are perhaps less exciting economically and politically than commerce, weather, food, minerals, and defense, but they are the *sine qua non* of all man's efforts to reap the harvest of the seas.

Man speaks of invading the sea and even now has several habitats in operation on the seafloor, but he knows practically nothing of the environmental constraints of the realm he is attempting to invade. One hears a lot of talk today about marine ecology — the study of the interrelationship of marine organisms and their environment. We know a good deal about the organisms, their life cycles, their eating habits, even the number of vertebrae in their backbones, but we know very little about the environmental variations to which they are subjected. Take for example a study of lobsters from a seafloor habitat — and just such a study is planned for TEKTITE II and was started in TEKTITE I last year. You can tag them. You can follow their travels with tricky electronics. You can watch their movements. You can watch when they eat and what they eat. You can count the numbers that are around a given "rock pile" each day. You can detail their comings and goings with great precision, but to know "why" you must know what changes are taking place in the world they live in. How does the visibility vary; how does the temperature of the water vary? What sort of current regime is in the area and how does it vary? Does the dissolved oxygen, salinity, or nutrient material vary with time, and, if so, how do they react to these changes? My point here is that we talk glibly about "ecology" and tend to neglect the environmental half.

Pollution and pollution control are fast becoming the watchwords for the seventies. Already many in political

office, or those aspiring to one, have latched onto pollution control or pollution abatement as their personal standard. To those who are serious and dedicated, I say "more power to you." But for those who are using this merely as a lever for their own political adornment, I have coined the term "polluticians." We will hear from many "polluticians" in the years ahead. Let us plan now to use them and educate them so their "pollutical" speeches make sense and will help the cause. Man eyes the sea as a convenient place to get rid of the wastes he creates on land. He thinks of the estuaries as convenient toilets that flush themselves in a half-hearted way a couple of times a day. In fact, it may be that one of the great resources of the sea is that they are just this — a big flushing hole in the ground and a great place to get rid of our wastes. You could spit in the Columbia River out here, and it wouldn't "pollute" it. Two people or even two hundred people could spit in the river, and it would not be polluted. So it is not a question of dumping or not dumping, but rather a question of how much of what can be dumped for how long before the other uses of the river are imperiled. To answer such questions for the Columbia River, for the nation's estuaries, and for our extensive nearshore areas, we must first undertake to explore, describe, and understand these dynamic systems. Once we know how they work, this information must be conveyed to the decision makers, so that valid judgments can be made on the basis of fact rather than on emotionalism, financial pressure, political influence, and the other grounds on which decisions are so often made in the absence of facts.

We want to protect our beaches and improve our harbors. We want to dispose of the cooling waters from our coastal power plants. We want to fish and play in the nearshore waters. We want to harvest fish commercially in our offshore waters and our rivers and estuaries. We want to launch our pleasure boats, to build our marinas, to develop our coastal lands for living and for industry. We want to build causeways to our offshore islands. We want to set aside coastal preserves and maintain our navigable waters. But, to do these things intelligently, we must first explore, describe, and understand the entire nearshore and estuarine regime.

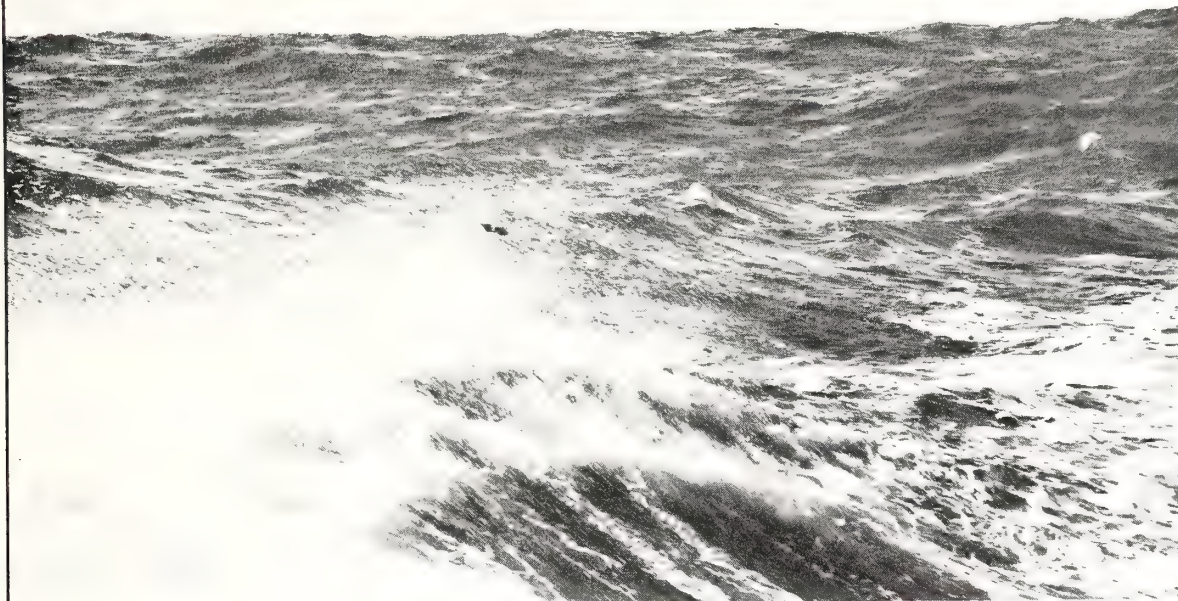
My point, then, is to stop kidding ourselves that we can just go to sea and harvest its resources. It is absolutely essential that our approach to utilizing marine resources be comparable to that for harvesting our resources on land. First we must map, describe, and understand, or the attempts at harvesting will continue to be in the hit-or-miss, catch-as-catch-can approach we have been using with just the poor results one would expect.

I am not advocating the termination of all resource-oriented activities at sea. I am, however, pleading for an appropriate amount of our effort, of the Sea Grant effort, being directed towards providing the basic environmental understanding on which intelligent utilization of our marine resources must depend.



# AAAS Symposia

Annual Meeting: Philadelphia



[National Oceanographic and Atmospheric Administration]

28-29 December

## Ocean Symposium

Over the past 10 years, the American scientific community, as well as the executive and legislative branches of the federal government, have been inundated with reports relating to the ocean, to oceanography, to marine technology, and to the importance of all of these fields within the framework of today's social, economic, and geopolitical problems. The present sequence started with the 12-chapter report of the National Academy of Sciences Committee on Oceanography entitled *Oceanography 1960 to 1970*. The sequence essentially ended with the outstanding report of the Stratton Commission, *Our Nation and the Sea*. An incredible number of man-hours has been spent both in producing these numerous documents and in reading and commenting on them. Most of the U.S. scientific community is now sated with reports on oceanography, and the question that is most often heard now is "What are we really doing about the oceans?"

The American Association for the Advancement of Science has planned a 2-day symposium on the oceans as part of their Annual Meeting in Philadelphia. This symposium is planned to bring us all up to date on the present status of ocean science; to provide a summary of the issues facing the coun-

try today insofar as the ocean is concerned; to discuss the future of the ocean insofar as the United States is concerned; and to describe and discuss the federal role in the national program in oceanography.

The best way to determine what, in fact, is happening in the ocean arena today and to predict what lies ahead is to have as speakers the top men in the ocean business, and this is indeed what the AAAS Section on Atmospheric and Hydrospheric Sciences has managed to accomplish. On the morning of 28 December, John Calhoun (chairman, National Academy of Sciences Ocean Affairs Board) will chair a session planned to bring the American scientific community up to date on the present status of our knowledge in the five major fields of marine science: physical oceanography, chemical oceanography, marine geology and geophysics, marine biology, and marine engineering. For too long, the marine scientists have been isolated from the engineers. This situation, in part, is because the results of marine scientific work have not generally been available to engineers nor have these results been translated into useful knowledge for the engineers who are involved in trying to accomplish something meaningful in

the ocean. That era, however, now appears to be ending, and the scientists and the engineers will brief us on the present state of the art in their respective fields (morning session on 28 December).

On the afternoon of 28 December, the session will be concerned with today's major issues in oceanography. Chaired by E. Seabrook Hull (editor, *Ocean Science News*), the session will include discussions on marine pollution, coastal zone management, the law and the sea, the role of industry, and international problems and opportunities.

In the English language there is probably no phase more internally contradictory than "the foreseeable future." The one thing that we know about the future is that it is not "foreseeable." Any discussion of the future of oceanography in the United States must be highly speculative at best. However, on the morning of 29 December the AAAS will hold a session entitled "The Oceans and the Future." What we have tried to do is corral the very best man in each area to give us his feelings on what the future holds in each of five specific areas: food from the sea, minerals from the sea, weather and the sea, national defense and the sea, and man in the sea.

The final session on the afternoon of 29 December is dedicated to "The Federal Role." This session will be chaired by George Reedy (former press secretary to President Johnson and mem-

ber of the Commission on Marine Science, Engineering and Resources). Robert M. White (administrator, National Oceanographic and Atmospheric Administration), has already agreed to participate for that agency. Representatives are also invited from the Environmental Protection Agency, the President's Office of Science and Technology, the House of Representatives, and the Senate. This last session could very well be the highlight of the 2-day meeting and might point the way toward this country's future direction in marine science.

Over the past several years, much has been said about the importance of the oceans to our national welfare; much has been written about the importance of the ocean to the future welfare—

even to the survival—of mankind. The AAAS wants this symposium to provide a rare insight into the present status of marine science, the marine issues which face the country today, the hope which we might expect for the future, and the role which the federal government must play in converting these hopes into marine realities.

The day of the "Madison Avenue" approach to the oceans is over. We have all heard of the "untapped treasure troves on our continental shelves," of the "potential of the ocean for feeding the world's starving millions," and the fact that "the seas cover 71 percent of the earth's surface." It is time that we cut through the flowery prose, the well-formed phrases, and the glowing rhetoric to get to the basic facts at issue. How

much do we know about the oceans today? What are the real problems we now face for which the solutions lie in the ocean? What does the future look like insofar as the oceans are concerned? And finally, what role does the federal government play in all of this? This symposium will answer these questions by bringing together in one place and at one time the top people in the field. This will be a good session, and hopefully from it will come the guidelines within which will be shaped the national policy relating to the oceans for the years ahead.

HARRIS B. STEWART, JR.  
*National Oceanographic and  
Atmospheric Administration, Atlantic  
Oceanographic and Meteorological  
Laboratory, Miami, Florida*





**U.S. DEPARTMENT OF COMMERCE**

Peter G. Peterson, Secretary

**NATIONAL OCEANIC AND ATMOSPHERIC ADMINISTRATION**

Robert M. White, Administrator

**ENVIRONMENTAL RESEARCH LABORATORIES**

Wilmot N. Hess, Director

**NOAA TECHNICAL REPORT ERL 225-AOML 5**

**Satellite Data Requirements of Atlantic  
Oceanographic and Meteorological  
Laboratories for Studies of Ocean Physics  
and Solid Earth**

**INVESTIGATORS:**

GEORGE MAUL  
BERNARD ZETLER  
DONALD HANSEN  
KIRBY HANSON  
DUNCAN ROSS  
GEORGE KELLER  
JOHN APEL

Physical Oceanographic Laboratory  
Physical Oceanographic Laboratory  
Physical Oceanographic Laboratory  
Sea-Air Interaction Laboratory  
Sea-Air Interaction Laboratory  
Marine Geology and Geophysics Laboratory  
Office of the Director

**BOULDER, COLO.  
September 1971**

For sale by the Superintendent of Documents, U. S. Government Printing Office, Washington, D. C. 20402  
Price 55 cents

# TABLE OF CONTENTS

	Page
SUMMARY OF REQUIREMENTS	v
PART I: OCEAN PHYSICS PROGRAM	
1. GLOBAL OCEAN RADIATION BUDGET	3
1.1 Background	3
1.2 Requirements	4
2. GLOBAL OCEAN SEA-SURFACE TEMPERATURE	5
2.1 Background	5
2.2 Requirements	10
3. WATER MASS IDENTIFICATION	10
3.1 Thermal Gradient Detection	11
3.2 Salinity Gradient Detection	12
3.3 Turbidity Gradient Detection	12
3.4 High Velocity Gradients	13
3.5 Other Applications	13
3.6 Platform Location and Interrogation	13
3.7 Development Studies	14
4. SURFACE WIND AND WAVE CONDITIONS	14
4.1 Problems	14
4.2 Requirements	15
4.3 Intended Use of Data	17
4.4 Justification	17
5. SEA-STATE, TIDES, AND OCEAN SLOPES	24
5.1 Problems	24
5.2 Requirements	24
PART II: SOLID EARTH PROGRAMS	
6. CHANGES IN SHORELINE AND SEAFLOOR FEATURES CAUSED BY STORMS	29
6.1 Objective	29
6.2 Problems	29
6.3 Approach	30
6.4 Benefits	30
6.5 Requirements	31



	Page
7. TURBID WATER MASS MOVEMENT	31
7.1 Objective	31
7.2 Problems	31
7.3 Approach	32
7.4 Benefits	32
7.5 Requirements	33
8. REFERENCES	35
APPENDIX A: Letter from J. W. Townsend, Jr., to L. Jaffe	41
APPENDIX B: Memo from J. R. Apel to H. B. Stewart, Jr.	45

## SUMMARY OF REQUIREMENTS

This document has been prepared by research scientists at the Atlantic Oceanographic and Meteorological Laboratories in response to the memorandum from the Associate Administrator of NOAA requesting NOAA Laboratory "Requirements for Ocean Physics and Solid Earth Data."

These Laboratories are broad based and interdisciplinary covering solid earth, oceanography, and meteorology. Although the requirements for meteorology are not included here, the range of requirements for application to ocean physics and solid earth is large. Table 1 shows that the investigators are asking for sensors covering a large range of the electromagnetic spectrum, from reflected solar radiation in the visible spectrum to both active and passive microwave systems. These measurements will provide data that can be used to describe the state, physical properties, and energetics of the surface and near-surface layer of all of the world's oceans.

Table 1. *Summary of Data Applications Related to the Electromagnetic Spectrum*

Spectrum	Date Application
Visible	{ Ocean Turbidity Detection Shoreline Topography Bottom Topography
Broadband Solar Broadband IR	Ocean/Atmosphere Energetics
IR "Window"	{ Ocean Currents Eckman Divergence and Wind Stress Long-Term, Sea-Air Interaction Teleconnections of World Oceans
Active Microwave	{ Sea State Tides Ocean Slopes
Passive Microwave	{ Salinity Surface Wind Waves



The programs that are envisioned to carry out these studies are listed in table 2; the purpose and the main investigator(s) are also included.

The sensor or measurement requirements are listed in table 3 together with categories for orbit, resolution, and accuracy desired. The ideas contained here have not been constrained to fit any particular satellite, orbit, or sensor system; however, there were some obvious matches of plans and requirements.

Some of the values in table 3 have been difficult to specify for several reasons. This means that although a single value (in some cases) has been given, it is simply the investigators "reasonable, first estimate" at the value based on his knowledge at this time. Obviously, some values should be adjusted as new information becomes available. Therefore, it would be desirable for those who may make use of table 3 in developing satellite systems to have further discussion with these investigators.

*Table 2. Proposed Programs for Studies of Ocean Physics and Solid Earth*

Purpose	Investigator	
Global Ocean Radiation Budget		
Determine Radiative Heat Sources and Sinks for World Oceans	Dr. K. Hanson	
Global Ocean Sea Surface Temperature		
Study Eckman Divergence Related to Surface Wind Stress	Dr. K. Hanson	
Diagnostic Studies of Long-Term Sea-Air Interaction Phenomena		
Study Large Scale Teleconnections Between World's Oceans		
Water Mass Identification		
Bioassay	Mr. G. Maul	
Current Boundaries and Advection of Pollutants		
Applications to Marine Transportation		
Estuarine Studies		
Surface Wind and Wave Conditions		
Prediction of Surge Associated with Storms and Hurricanes	Mr. D. Ross	
Studies Leading to Improved Operational Forecasting of Ocean Surface Winds, Wave, Surf Conditions, and Storm Surge		
Sea State Determination		
Research on Forecasting Techniques		Dr. J. Apel Mr. B. Zetler
Tidal Amplitudes		
Worldwide Tide Forecasting	Mr. B. Zetler Dr. J. Apel	
Ocean Slopes Over (a) Currents and (b) Deep Trenches		
Global Ocean Circulation	Dr. J. Apel Dr. D. Hansen	
Gravity Anomalies	Mr. B. Zetler	
Changes in Shoreline and Seafloor Features due to Storms		
Research on Storm Effects of Shoreline and Shallow Water Features		
Turbid Water Mass Movement		
Concentration, Composition, and Transport	Dr. G. Keller	



Table 3. Data Requirements for Studies of Ocean Physics and Solid Earth

Sensor or Measurement Requirements	Orbit		Resolution		Geophysical		
	Inclination (deg)	Altitude or Period (km)	Approx. Local Sun Time	Time	Space (km)	Accuracy	Precision
Program: Global Ocean Radiation Budget							
(a) Solar Radiation, 0.3-3.0 $\mu$ m	81 retro	1100-1500	1200 & 1430	2/day (daylight hr)	100	0.006*	0.003*
(b) IR Radiation, 3-50 $\mu$ m	81 retro	1100-1500	0000 & 1200	2/day	100	0.006*	0.003*
(c) IR Window, 10.5-12.5 $\mu$ m	81 retro	1100-1500	0000 & 1200	2/day	100	1 °K	0.5 °K
(d) Total Water Vapor	81 retro	1100-1500	0000 & 1200	2/day	100	0.2 cm	---
Program: Global Ocean Sea Surface Temperature							
Sea Surface Temperature (10.5-12.5 $\mu$ m)	81 retro	1100-1500	0000	1/day	100	1 °K	0.5 °K
Program: Water Mass Identification							
(a) Sea Surface Temperature HRIR (10.5-12.5 $\mu$ m)	81 retro	1100-1500	0930 or 1430	1/day	2	1 °K	0.5 °K
(b) Salinity, 1.4 GHz	81 retro	1100-1500	0930 or 1430	1/day	2	1(°/oo)	0.5 °K
(c) Ocean Turbidity, 0.46 $\mu$ m and 0.54 $\mu$ m (0.015 $\mu$ m spectral interval)	81 retro	1100-1500	0930 or 1430	1/day	2	3.0+	1.5+
Program: Surface Wind and Wave Conditions							
Multifrequency Microwave Radiometer 1-3, 5-8, 10, 15-19 GHz dual polarization.	81 retro	(Unspecified, depends on antenna)	0000, 0600, 1200 & 1800	4/day	20-100	Wind: 2 mps Waves: 0.5 m	Wind: 1 mps Waves: 0.5 m
Program: Sea State Determination							
Short-pulse Radar Altimeter, 10 GHz (3 ns pulse, power 2 kW)	~65	300-400	(see text)	1 look/12 sec over ocean, not continuous meas	4-8	0.5 m	0.5 m
Program: Tidal Amplitudes							
Precision Altimeter with radar/laser altimeter, plus vertical stabilization to 1°.	~65	300-400	(see text)	100/yr over 20 1° squares (to be specified)	4-8	5 m	1.0 m
Program: Ocean Slopes Over (a) Currents and (b) Deep Trenches							
Precision Altimeter with radar/laser altimeter, plus vertical stabilization to 1°.	~65	300-400	(see text)	(a) 1 obsr/3 days over Gulf Stream (b) 100 obsr/ trench for each major ocean trench	4-8	5 m	0.1 m
Program: Changes in Shoreline and Seafloor Features Due to Storms							
Multispectral Radiance 0.46 $\mu$ m, 0.54 $\mu$ m and 0.70 $\mu$ m (with 0.015 $\mu$ m spectral interval)	81 retro	(unspecified)	~0930 or 1430	1 obsr/15 days	20 m	3.0+	1.5+
Program: Turbid Water Mass Movement							
Multispectral Radiance 0.46 $\mu$ m, 0.54 $\mu$ m and 0.70 $\mu$ m (with 0.015 $\mu$ m spectral interval)	81 retro	(unspecified)	~0930 or 1430	1 obsr/15 days	20 m	3.0+	1.5+

$\mu$ cal cm<sup>-2</sup> min<sup>-1</sup>    +W m<sup>-2</sup> ster<sup>-1</sup>     $\mu$ m<sup>-1</sup>

\*cal cm<sup>-2</sup> min<sup>-1</sup> +W m<sup>-2</sup> ster<sup>-1</sup>  $\mu$ m<sup>-1</sup>

# 1. GLOBAL OCEAN RADIATION BUDGET

Kirby Hanson

## 1.1 Background

The global radiation budget at the earth's surface has been calculated by a number of investigators including Kimball (1928) as early as 1928. More recently, Budyko (1955, 1963), Black (1956), Ashbel (1961), and Wyrтки (1965) have made similar determinations. On comparing observed irradiance values in the tropical Pacific with values calculated by the investigators mentioned above, Quinn and Burt (1968) found the calculations were 15 to 27 percent too low at Canton Island and 15 to 18 percent too low at Wake Island.

From irradiance measurements in the Line Islands (near the equator, south of Hawaii), Cox and Hastenrath (1970) stated that the "downward-directed short-wave radiation at Palmyra is considerably larger than expected from available climatic mean maps. The climatic mean irradiance values were calculated from cloud observations and empirical relationships of irradiance as a function of cloudiness (Black, 1956; Bernhardt and Phillipps, 1958; and Budyko, 1963)."

At Swan Island in the Caribbean, this author found that calculated values of the solar irradiance by Ashbel (1961) and Budyko (1963) are 3 to 9 percent too low.

These scattered observations in the tropics are consistent, because they show more solar energy reaching and being absorbed in the tropical oceans than was previously thought. This recent finding is also consistent with satellite observations of the earth's radiation budget; these show that about 30 percent more solar radiation is absorbed by the earth-atmosphere system in the tropics than suggested by pre-satellite calculations (House, 1965; Vonder Haar, 1968; London and Sasamori, 1971; and Vonder Haar and Hanson, 1969).



From these surface and satellite observations, it now appears that the tropical oceans are receiving perhaps 10 to 20 percent more solar energy than is suggested by the climatic mean maps that have been published in the last 10 years.

Satellite measurements of the reflected solar irradiance leaving the atmosphere are now wrong by only a few percent, when averaged over seasonal and annual time scales. However, the error of *surface* irradiance calculations (based on cloud observations) on the same time scale is about an order of magnitude larger.

We propose to develop parameterization techniques based on satellite observed broadband solar irradiance, to apply these techniques to satellite data, and to determine the global ocean radiation budget over monthly, seasonal, and annual time scales. We also propose to do a similar parameterization for the IR irradiance at the earth's surface based on satellite observed IR radiance.

## 1.2 Requirements

The satellite data requirements for this section are specified in table 3. They are:

1. Upwelling broadband solar radiance (0.3 to 3  $\mu\text{m}$ )
  - complete global coverage at least two per day during *daylight* hours: one pass at local noon and one at 1430 UT/LT
  - horizontal resolution of 100 km
  - accuracy of 2 percent, or  $0.006 \text{ cal cm}^{-2} \text{ per min}$
  - precision of 1 percent, or  $0.003 \text{ cal cm}^{-2} \text{ per min}$ .
2. Upwelling broadband IR radiance (3 to 50  $\mu\text{m}$ )
  - complete global coverage at least two per day: one pass at local noon and one at midnight
  - horizontal resolution of 100 km
  - accuracy of 2 percent, or  $0.006 \text{ cal cm}^{-2} \text{ per min}$
  - precision of 1 percent, or  $0.003 \text{ cal cm}^{-2} \text{ per min}$ .

3. Upwelling IR window radiance (10.5 - 12.5  $\mu\text{m}$ )
  - complete global coverage at least two per day:  
one pass at local noon and one at midnight
  - horizontal resolution of 100 km
  - accuracy of 1°C (effective radiation temperature).
4. Total precipitable water vapor (cm)
  - complete global coverage at least two per day:  
one pass at local noon and one at midnight
  - horizontal resolution of 100 km
  - accuracy 0.2 cm.

Requirement 4 will be limited by clouds in the sensor's field of view. In those cases, a statistical estimate with higher resolution sensors (<100 km) should be made to determine clear sky total precipitable water.

Two observations of the upwelling broadband solar radiance are required during daylight. The hours suggested are 1200 and 1430 LST (local sun time). Polar orbiters are assumed at these hours.

The IR radiance, IR window, and total water vapor measurements are required at 0000 and 1200 LST. Thus, one polar orbiter is required.

## 2. GLOBAL OCEAN SEA-SURFACE TEMPERATURE

Kirby Hanson

### 2.1 Background

The "southern oscillation," a long-term sea-air interaction phenomenon, was first described by Sir Gilbert Walker in 1924. Following this, it received little attention until the 1960's when Austin (1960) examined mid-Pacific equatorial ocean temperatures, and Bjerknes (1966) suggested the importance of this tropical sea-air interaction phenomenon to the

predictability of the atmosphere in midlatitudes. Berlage (1966) has studied this phenomenon in relation to world weather for nearly 40 years.

The Eastern Pacific Ocean is the largest area of sub-normal temperatures observed anywhere in tropical oceans. As stated by Bjerknes (1969):

"The cause of the temperature deficiency is partly the cold water supplied by the Humbolt Current from southern sources, aided by upwelling along the Chilean and Peruvian coast. Even more important, though, is the upwelling along 10,000 km, more or less, of the Pacific equator.

"The upwelling in the open ocean along the equator is due to the prevailing easterly winds. In addition to the westward drift produced by these winds, a diverging Ekman drift is maintained, to the right north of the equator and to the left south of the equator, so as to pump upwelling water to the surface at the equator. As long as this process continues uninterruptedly, more and more upwelling water gathers at the surface and spreads sideways from the equator until a tongue of cold water establishes as wide as shown in figure 1."

Ocean temperature anomalies in this cold current can also lead to catastrophic conditions for some South American countries. The *El Niño* is an anomalously warm ocean temperature condition that occurs in the otherwise cold water along the west coast of South America. The occurrence of it and associated meteorological conditions can lead to torrential rains and flooding in the normally arid regions of Ecuador and Peru; red tide; invasion by tropical nekton; and mass mortality of various marine organisms including guano birds, sometimes with subsequent decomposition and release of hydrogen sulfide (Wooster, 1960) (cited by Quinn, 1970).

Ocean temperature anomalies also have a large effect on precipitation along the equatorial dry zone of the Pacific. A time plot of sea/air temperatures and precipitation at Canton Island (Bjerknes, 1969) is shown in figure 2. Many



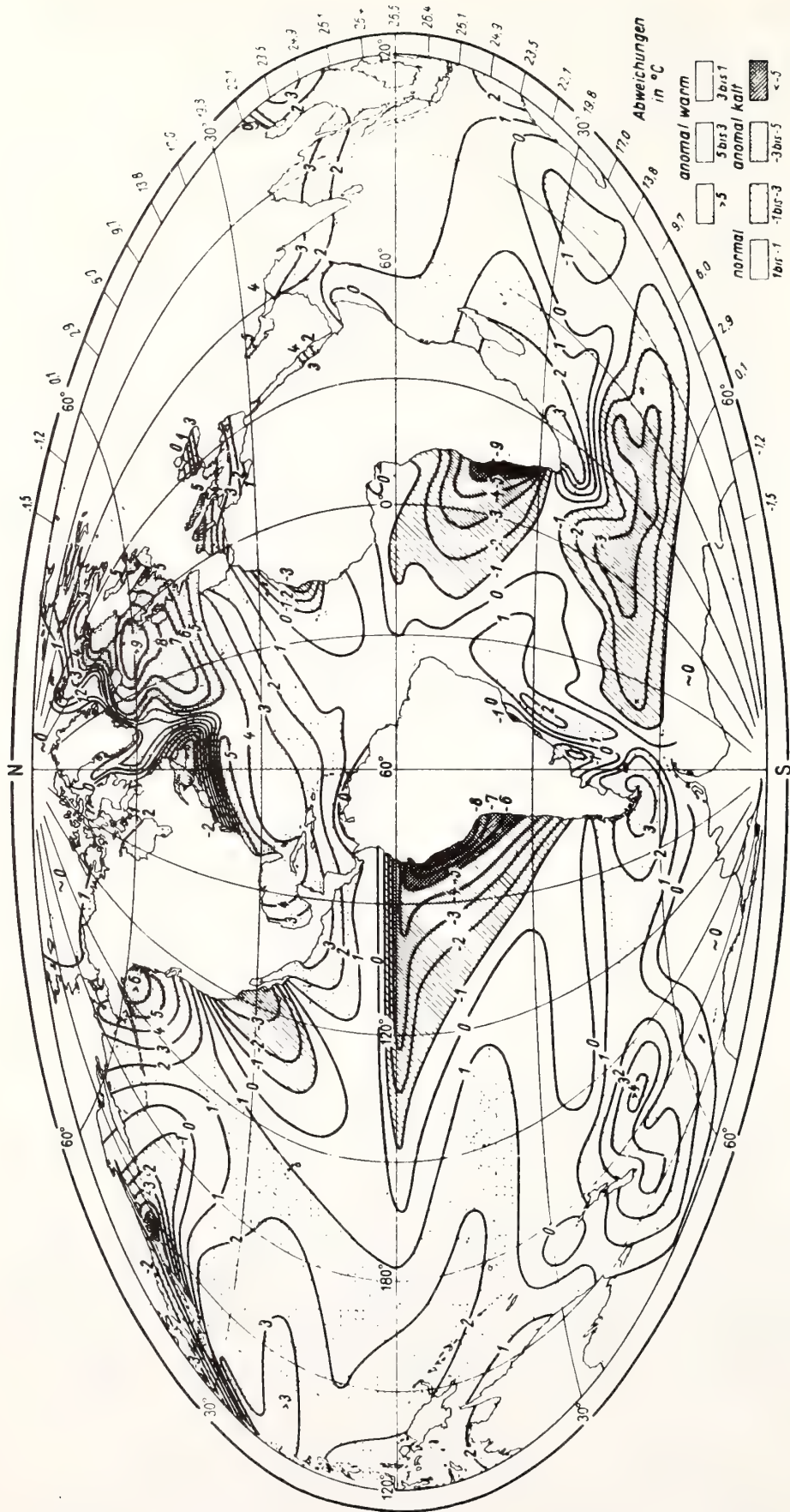


Figure 1. Sea-surface temperature represented as deviation from the average at each latitude (after Bjerknes, 1969; from Dietrich and Kalle, 1957).

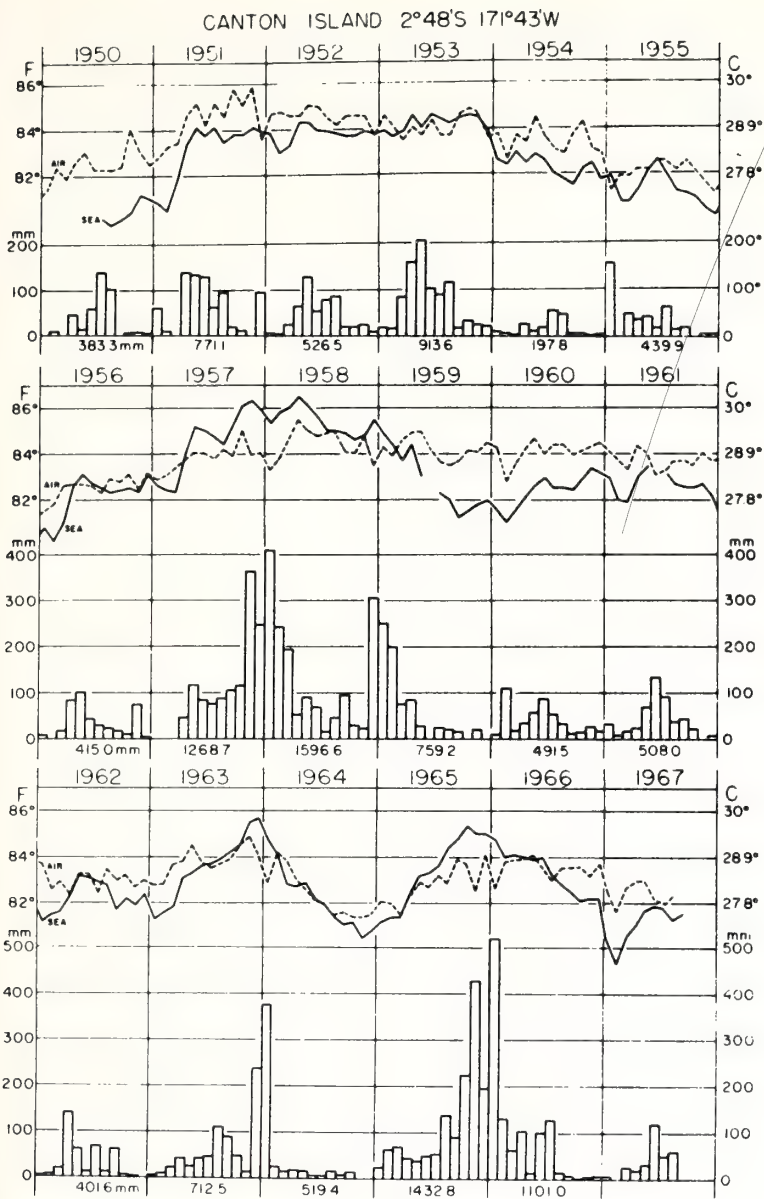


Figure 2. Time series of monthly air and sea temperatures and of monthly precipitation at Canton Island from 1950 to 1967 (from Bjerknes, 1969).

other investigators have examined this response of the tropical atmosphere (more precipitation) to warm surface waters and its self-amplification (Krueger and Gray, 1969; Quinn, 1970; and others). This increased precipitation has been suggested as an explanation for the midlatitude westerlies being stronger during periods of warm surface temperatures in the equatorial dry zone. The suggestion is that the greater heat supply

from the equatorial ocean is added to the atmospheric Hadley circulation by precipitation intensifying that circulation and producing more than the normal flux of angular momentum at the midlatitude belt of westerlies (Bjerknes, 1969).

The response of midlatitude circulation patterns to tropical (or extratropical) ocean temperature anomalies has obvious importance to the predictability of the atmosphere. Thus, the initial work by Berlage and Bjerknes has brought on a number of diagnostic studies during the past few years on teleconnections of the atmosphere and ocean (Krueger and Gray, 1969; Namias, 1969). These studies are very useful in establishing the global nature of this phenomena. Furthermore, they have shown the need for global satellite measurements to study these long-term, sea-air interaction phenomena.

Studies that should be undertaken when adequate satellite data are available are:

1. The Ekman divergence has been postulated as a response to the strength of the equatorial trade winds. The time development of sea surface temperature patterns in response to surface wind stress should be studied to verify this or offer another explanation.
2. The long-term sea surface temperature anomalies recorded at Canton Island need to be extended to all of the tropical and subtropical oceans. Unfortunately, only a few island stations record sea surface temperatures, and ships provide only limited data (time and space). Satellite sea surface temperature measurements (to required precision) are required on a global scale to provide the necessary sampling resolution and accuracy to study these anomalies. These will provide basic information for diagnostic studies of long-term sea surface temperature anomalies as a means for forcing (and interacting with) the circulation patterns in the atmosphere.
3. If there are large-scale teleconnections between the ocean and atmosphere, we can also expect to have large-scale teleconnections between the world's oceans (with the atmosphere as a link). Sea surface temperature data obtained by satellite will provide basic input for such studies.



## 2.2 Requirements

The requirement is for sea surface temperature, once a day at 0000 LST, a spatial resolution of 100 km, an accuracy of  $1^{\circ}\text{K}$ , and a precision of  $0.5^{\circ}\text{K}$ .

The satellite measurements required have not been specified in table 3 (only sea surface temperature has been specified). It is assumed that some organization with satellite data processing capability (such as NESS) will reduce the necessary measurements to sea surface temperature values. This requires eliminating the effect of the atmosphere and clouds on the measurement.

## 3. WATER MASS IDENTIFICATION

George Maul

Oceanic circulation is a fundamental geophysical phenomenon that affects every milligram of biota on this planet. The advection of heat and nutrients is the controlling influence in the primary biological production and hence the entire food web. Major weather systems, such as subtropical cyclones, are influenced (if not controlled) by the ability of the ocean to release thermal energy; regional climates are established because of this. Marine transportation, commercial fishing, deep-sea mining and drilling, national defense, and other such ocean-oriented activities of man are influenced by the surface and near-surface circulation.

If we are to use the ocean in an ecologically acceptable and commercially practical manner, the perturbations in the average surface flow are the meaningful properties that must be measured and eventually predicted. Fortunately, due to the intense baroclinicity of the important currents, there are several surface features that hold promise for detection by remote sensors.

Characteristically, the surface manifestation of major currents, such as the Gulf Stream, Kuroshio, Agulhas, Peru, and Somali, are (1) a high temperature gradient, (2) a high salinity gradient, (3) a high turbidity gradient, (4) a high velocity gradient, (5) a change in sea state, (6) a change in cloudiness or cloud patterns, and (7) a change in sea-surface slope. The possibility of remotely sensing these features and the requirements to do so are discussed in the following paragraphs. The goal is to make appropriate measurements of each of these features and by machine processing and decision, provide the maritime community with synoptic maps. The feasibility of machine processing and decision of multispectral scanner data has been demonstrated by Higer et al. (1970).

### 3.1 Thermal Gradient Detection

The surface thermal signature of the Gulf Stream has been documented as a reliable, year round, indication of the current (Hansen and Maul, 1970). Attempts to track routinely the thermal boundary by using Nimbus II data have led to the conclusion that the uncontaminated sea surface temperature must be known to  $\pm 1^\circ\text{K}$  (Maul, 1972). To accomplish this, we recommend that a high resolution infrared sensor (HRIR), response-limited to the range of oceanic surface temperatures with allowance for atmospheric attenuation (namely  $260^\circ\text{K} - 310^\circ\text{K}$ ), be flown. The subsatellite ground resolution should be about 2 km for meaningful location of the thermal field with respect to the velocity field, the attitude control requirements of the altimeter (discussed in sections 2.4 and 2.5) must keep the location of the HRIR ground spot in an area less than the spot size itself. A second channel that simultaneously measures the planetary albedo with the same resolution is required for cloud detection. The spectral range of the HRIR desired is 10.5 to 12.5  $\mu$ , because energy at earth temperatures is maximized, reflected energy is negligible, and atmospheric

attenuation due to  $H_2O$ ,  $CO_2$ , and  $O_3$  is small. The albedo channel specifications are less well-determined; however, 0.4 to 0.7  $\mu$  should be adequate. The multispectral approach (Anding and Kauth, 1970) seems to have the potential for very accurate measurements, but field tests have yet to be made.

### 3.2 Salinity Gradient Detection

Salinity changes across the Mississippi River outflow were measured by Droppleman et al. (1970) using a passive microwave radiometer operating on 1.4 GHz from a low-flying aircraft. Although this experiment is in its infancy, it is very promising for current boundary detection where changes of 2 ‰ may occur over several kilometers. It may prove especially valuable in the region of the ocean between 30°N and 30°S (about half the earth's surface), where surface thermal fronts are absent or seasonal.

The inclusion of a passive microwave radiometer on an oceanographic satellite is most desirable for applications in ice detection and sea state; one channel should operate on 1 to 1.5 GHz. The ground spot size and attitude control requirements discussed for temperature apply to the salinity discussion as well as the other observations discussed below.

### 3.3 Turbidity Gradient Detection

Clarke et al. (1969) showed that the differences in color of oceanic water masses could be detected from aircraft. These measurements have been linked to the chlorophyll content of the water and hence to its bioassay. Color change between water masses is independent of location, and thus is as valuable in the tropics as in midlatitude regions. The measurements of Clarke et al. (1969) suggest that two narrow (0.015  $\mu$ ) channels centered on 0.54 and 0.46  $\mu$  are necessary to perform these studies. Absolute accuracies needed correspond to the capability of measuring chlorophyll-A



concentrations of about  $0.2 \text{ mg m}^{-3}$  to precisions of  $\pm 0.1 \text{ mg m}^{-3}$ . This translates (Ramsey, 1968), to an accuracy of  $3.0 \text{ W m}^{-2} \text{ ster}^{-1} \mu\text{m}^{-1}$  and a precision of  $\pm 1.5 \text{ W m}^{-2} \text{ ster}^{-1} \mu\text{m}^{-1}$ .

### 3.4 High Velocity Gradients

The other features listed above are covered in sections 2.4 and 2.5 and come naturally out of those requirements, except for item (4), Velocity Gradients. McManus et al. (1968) have shown that a Doppler laser can give absolute current speeds. The adaptability of such a device enables an oceanographer to separate the barotropic flow from the baroclinic flow and, hence, obtain the entire current field from measurement of sea surface slope by an altimeter.

### 3.5 Other Applications

Being able to measure the thermal, salinity, and turbidity gradients in the open ocean to the required accuracies allows one to easily apply the techniques to estuarine and near-shore circulation problems. These areas are of immediate interest in problems of ocean waste disposal, pollution, and recreation. These capabilities also help geological interests solve such problems as longshore transport, and river plume sedimentation.

### 3.6 Platform Location and Interrogation

Finally, the basic need for Lagrangian drifters in ocean circulation studies must be promulgated. An oceanographic satellite system must be able to locate free drifting buoys and to telemeter basic measurements. Thus the system can also service moored buoys, which serve as operational ground

truth stations for the remote measurements. Without periodically comparing remotely sensed data with acceptable standards, we will not have the beginning of genuinely reliable synoptic oceanography.

### 3.7 Development Studies

Many of the items discussed in this section require further R&D before we attempt to integrate them into a satellite. We strongly recommended that a vigorous aircraft program be supported to determine, first, the optimum spectral bands needed for ocean sensing in order to simplify the satellite as much as possible, and second, to determine if these optimum bands can see through the atmosphere with adequate resolution to warrant integration at all.

## 4. SURFACE WIND AND WAVE CONDITIONS

Duncan Ross

### 4.1 Problems

The problem area here is in the general knowledge of surface wind and wave conditions as input to research programs studying the exchanges of heat, energy, and moisture at the sea-air interface. This study will also help the continued development of numerical forecasting of oceanic wind and wave conditions.

There are numerous organizations and programs that desire synoptic wind and wave observations over the oceans. These needs are documented in various reports of the World Meteorology Organization (WMO), World Weather Watch (WWW), etc.

Typical of these are the objectives stated by the WMO in Resolution 1721 (XVI) adopted at the United Nations General Assembly in December 1961:

- "1. To develop a deeper understanding of the global circulations of the atmosphere and the associated system of climates;
2. To place weather forecasting on a firmer scientific basis: to develop techniques for predictions on extended time scales and to provide knowledge needed to improve weather forecasts of small space-scales and time space;
3. To explore the extent to which weather and climate may be modified through artificial means."

These objectives have been addressed by numerous organizations, and current experimental programs gather data from ships, aircraft, and satellites. The system requirements stated here will provide additional input to these programs. Section 4 is concerned with the rationale behind the stated requirements; however, note that elements of those requirements are in the area of technology development.

#### 4.2 Requirements

A multi-frequency scanning microwave radiometer system is needed to provide data from which the aforementioned parameters can be inferred. The system should contain the following features:

1. Frequencies - approximately 1-3, 5-8, 10, and 15-19 GHz
2. Polarization - dual
3. Spatial resolution - 20-100 km
4. Scan -  $\pm 30$ - $50^\circ$  orthogonal to ground track and conical at  $50^\circ$
5. Accuracy - antenna temperatures  $\pm 1^\circ\text{K}$ .



The programs that are envisioned to carry out these studies are listed in table 2; the purpose and the main investigator(s) are also included.

The sensor or measurement requirements are listed in table 3 together with categories for orbit, resolution, and accuracy desired. The ideas contained here have not been constrained to fit any particular satellite, orbit, or sensor system; however, there were some obvious matches of plans and requirements.

Some of the values in table 3 have been difficult to specify for several reasons. This means that although a single value (in some cases) has been given, it is simply the investigators "reasonable, first estimate" at the value based on his knowledge at this time. Obviously, some values should be adjusted as new information becomes available. Therefore, it would be desirable for those who may make use of table 3 in developing satellite systems to have further discussion with these investigators.

*Table 2. Proposed Programs for Studies of Ocean Physics and Solid Earth*

Purpose	Investigator
Global Ocean Radiation Budget	
Determine Radiative Heat Sources and Sinks for World Oceans	Dr. K. Hanson
Global Ocean Sea Surface Temperature	
Study Eckman Divergence Related to Surface Wind Stress	Dr. K. Hanson
Diagnostic Studies of Long-Term Sea-Air Interaction Phenomena	
Study Large Scale Teleconnections Between World's Oceans	
Water Mass Identification	
Bioassay	Mr. G. Maul
Current Boundaries and Advection of Pollutants	
Applications to Marine Transportation	
Estuarine Studies	
Surface Wind and Wave Conditions	
Prediction of Surge Associated with Storms and Hurricanes	Mr. D. Ross
Studies Leading to Improved Operational Forecasting of Ocean Surface Winds, Wave, Surf Conditions, and Storm Surge	
Sea State Determination	
Research on Forecasting Techniques	Dr. J. Apel Mr. B. Zetler
Tidal Amplitudes	
Worldwide Tide Forecasting	Mr. B. Zetler Dr. J. Apel
Ocean Slopes Over (a) Currents and (b) Deep Trenches	
Global Ocean Circulation	Dr. J. Apel Dr. D. Hansen
Gravity Anomalies	Mr. B. Zetler
Changes in Shoreline and Seafloor Features due to Storms	
Research on Storm Effects of Shoreline and Shallow Water Features	
Turbid Water Mass Movement	
Concentration, Composition, and Transport	Dr. G. Keller

Table 3. Data Requirements for Studies of Ocean Physics and Solid Earth

Sensor or Measurement Requirements	Inclination (deg)	Orbit		Approx. Local Sun Time	Resolution		Geophysical	
		Altitude or Period (km)	Program:		Time	Space (km)	Accuracy	Precision
Program: Global Ocean Radiation Budget								
(a) Solar Radiance, 0.3-3.0 $\mu$ m	81 retro	1100-1500	1200 & 1430	2/day (daylight hr)	100	0.006*	0.003*	
(b) IR Radiance, 3-50 $\mu$ m	81 retro	1100-1500	0000 & 1200	2/day	100	0.006*	0.003*	
(c) IR Window, 10.5-12.5 $\mu$ m	81 retro	1100-1500	0000 & 1200	2/day	100	1 °K	0.5 °K	
(d) Total Water Vapor	81 retro	1100-1500	0000 & 1200	2/day	100	0.2 cm	---	
Program: Global Ocean Sea Surface Temperature								
Sea Surface Temperature (10.5-12.5 $\mu$ m)	81 retro	1100-1500	0000	1/day	100	1 °K	0.5 °K	
Program: Water Mass Identification								
(a) Sea Surface Temperature HRIR (10.5-12.5 $\mu$ m)	81 retro	1100-1500	0930 or 1430	1/day	2	1 °K	0.5 °K	
(b) Salinity, 1.4 GHz	81 retro	1100-1500	0930 or 1430	1/day	2	1(°/oo)	0.5 °K	
(c) Ocean Turbidity, 0.46 $\mu$ m and 0.54 $\mu$ m (0.015 $\mu$ m spectral interval)	81 retro	1100-1500	0930 or 1430	1/day	2	3.0+	1.5+	
Program: Surface Wind and Wave Conditions								
Multifrequency Microwave Radiometer 1-3, 5-8, 10, 15-19 GHz dual polarization.	81 retro	(Unspecified, depends on antenna)	0000, 0600, 1200 & 1800	4/day	20-100	Wind: 2 mps Waves: 0.5 m	Wind: 1 mps Waves: 0.5 m	
Program: Sea State Determination								
Short-pulse Radar Altimeter, 10 GHz (3 ns pulse, power 2 kW)	~65	300-400	(see text)	1 look/12 sec over ocean, not continuous meas	4-8	0.5 m	0.5 m	
Program: Tidal Amplitudes								
Precision Altimeter with radar/laser altimeter, plus vertical stabilization to 1°.	~65	300-400	(see text)	100/yr over 20 1° squares (to be specified)	4-8	5 m	1.0 m	
Program: Ocean Slopes Over (a) Currents and (b) Deep Trenches								
Precision Altimeter with radar/laser altimeter, plus vertical stabilization to 1°.	~65	300-400	(see text)	(a) 1 obsr/3 days over Gulf Stream (b) 100 obsr/ trench for each major ocean trench	4-8	5 m	0.1 m	
Program: Changes in Shoreline and Seafloor Features Due to Storms								
Multispectral Radiance 0.46 $\mu$ m, 0.54 $\mu$ m and 0.70 $\mu$ m (with 0.015 $\mu$ m spectral interval)	81 retro	(unspecified)	~0930 or 1430	1 obsr/15 days	20 m	3.0+	1.5+	
Program: Turbid Water Mass Movement								
Multispectral Radiance 0.46 $\mu$ m, 0.54 $\mu$ m and 0.70 $\mu$ m (with 0.015 $\mu$ m spectral interval)	81 retro	(unspecified)	~0930 or 1430	1 obsr/15 days	20 m	3.0+	1.5+	
†W m <sup>-2</sup> ster <sup>-1</sup> $\mu$ m <sup>-1</sup>								



# 1. GLOBAL OCEAN RADIATION BUDGET

Kirby Hanson

## 1.1 Background

The global radiation budget at the earth's surface has been calculated by a number of investigators including Kimball (1928) as early as 1928. More recently, Budyko (1955, 1963), Black (1956), Ashbel (1961), and Wyrтки (1965) have made similar determinations. On comparing observed irradiance values in the tropical Pacific with values calculated by the investigators mentioned above, Quinn and Burt (1968) found the calculations were 15 to 27 percent too low at Canton Island and 15 to 18 percent too low at Wake Island.

From irradiance measurements in the Line Islands (near the equator, south of Hawaii), Cox and Hastenrath (1970) stated that the "downward-directed short-wave radiation at Palmyra is considerably larger than expected from available climatic mean maps. The climatic mean irradiance values were calculated from cloud observations and empirical relationships of irradiance as a function of cloudiness (Black, 1956; Bernhardt and Phillipps, 1958; and Budyko, 1963)."

At Swan Island in the Caribbean, this author found that calculated values of the solar irradiance by Ashbel (1961) and Budyko (1963) are 3 to 9 percent too low.

These scattered observations in the tropics are consistent, because they show more solar energy reaching and being absorbed in the tropical oceans than was previously thought. This recent finding is also consistent with satellite observations of the earth's radiation budget; these show that about 30 percent more solar radiation is absorbed by the earth-atmosphere system in the tropics than suggested by pre-satellite calculations (House, 1965; Vonder Haar, 1968; London and Sasamori, 1971; and Vonder Haar and Hanson, 1969).

From these surface and satellite observations, it now appears that the tropical oceans are receiving perhaps 10 to 20 percent more solar energy than is suggested by the climatic mean maps that have been published in the last 10 years.

Satellite measurements of the reflected solar irradiance leaving the atmosphere are now wrong by only a few percent, when averaged over seasonal and annual time scales. However, the error of *surface* irradiance calculations (based on cloud observations) on the same time scale is about an order of magnitude larger.

We propose to develop parameterization techniques based on satellite observed broadband solar irradiance, to apply these techniques to satellite data, and to determine the global ocean radiation budget over monthly, seasonal, and annual time scales. We also propose to do a similar parameterization for the IR irradiance at the earth's surface based on satellite observed IR radiance.

## 1.2 Requirements

The satellite data requirements for this section are specified in table 3. They are:

1. Upwelling broadband solar radiance (0.3 to 3  $\mu\text{m}$ )
  - complete global coverage at least two per day during *daylight* hours: one pass at local noon and one at 1430 UT/LT
  - horizontal resolution of 100 km
  - accuracy of 2 percent, or  $0.006 \text{ cal cm}^{-2} \text{ per min}$
  - precision of 1 percent, or  $0.003 \text{ cal cm}^{-2} \text{ per min}$ .
2. Upwelling broadband IR radiance (3 to 50  $\mu\text{m}$ )
  - complete global coverage at least two per day: one pass at local noon and one at midnight
  - horizontal resolution of 100 km
  - accuracy of 2 percent, or  $0.006 \text{ cal cm}^{-2} \text{ per min}$
  - precision of 1 percent, or  $0.003 \text{ cal cm}^{-2} \text{ per min}$ .

3. Upwelling IR window radiance (10.5 - 12.5  $\mu\text{m}$ )
  - complete global coverage at least two per day:  
one pass at local noon and one at midnight
  - horizontal resolution of 100 km
  - accuracy of 1°C (effective radiation temperature).
4. Total precipitable water vapor (cm)
  - complete global coverage at least two per day:  
one pass at local noon and one at midnight
  - horizontal resolution of 100 km
  - accuracy 0.2 cm.

Requirement 4 will be limited by clouds in the sensor's field of view. In those cases, a statistical estimate with higher resolution sensors (<100 km) should be made to determine clear sky total precipitable water.

Two observations of the upwelling broadband solar radiance are required during daylight. The hours suggested are 1200 and 1430 LST (local sun time). Polar orbiters are assumed at these hours.

The IR radiance, IR window, and total water vapor measurements are required at 0000 and 1200 LST. Thus, one polar orbiter is required.

## 2. GLOBAL OCEAN SEA-SURFACE TEMPERATURE

Kirby Hanson

### 2.1 Background

The "southern oscillation," a long-term sea-air interaction phenomenon, was first described by Sir Gilbert Walker in 1924. Following this, it received little attention until the 1960's when Austin (1960) examined mid-Pacific equatorial ocean temperatures, and Bjerknes (1966) suggested the importance of this tropical sea-air interaction phenomenon to the



predictability of the atmosphere in midlatitudes. Berlage (1966) has studied this phenomenon in relation to world weather for nearly 40 years.

The Eastern Pacific Ocean is the largest area of sub-normal temperatures observed anywhere in tropical oceans. As stated by Bjerknes (1969):

"The cause of the temperature deficiency is partly the cold water supplied by the Humbolt Current from southern sources, aided by upwelling along the Chilean and Peruvian coast. Even more important, though, is the upwelling along 10,000 km, more or less, of the Pacific equator.

"The upwelling in the open ocean along the equator is due to the prevailing easterly winds. In addition to the westward drift produced by these winds, a diverging Ekman drift is maintained, to the right north of the equator and to the left south of the equator, so as to pump upwelling water to the surface at the equator. As long as this process continues uninterruptedly, more and more upwelling water gathers at the surface and spreads sideways from the equator until a tongue of cold water establishes as wide as shown in figure 1."

Ocean temperature anomalies in this cold current can also lead to catastrophic conditions for some South American countries. The *El Niño* is an anomalously *warm* ocean temperature condition that occurs in the otherwise cold water along the west coast of South America. The occurrence of it and associated meteorological conditions can lead to torrential rains and flooding in the normally arid regions of Ecuador and Peru; red tide; invasion by tropical nekton; and mass mortality of various marine organisms including guano birds, sometimes with subsequent decomposition and release of hydrogen sulfide (Wooster, 1960) (cited by Quinn, 1970).

Ocean temperature anomalies also have a large effect on precipitation along the equatorial dry zone of the Pacific. A time plot of sea/air temperatures and precipitation at Canton Island (Bjerknes, 1969) is shown in figure 2. Many

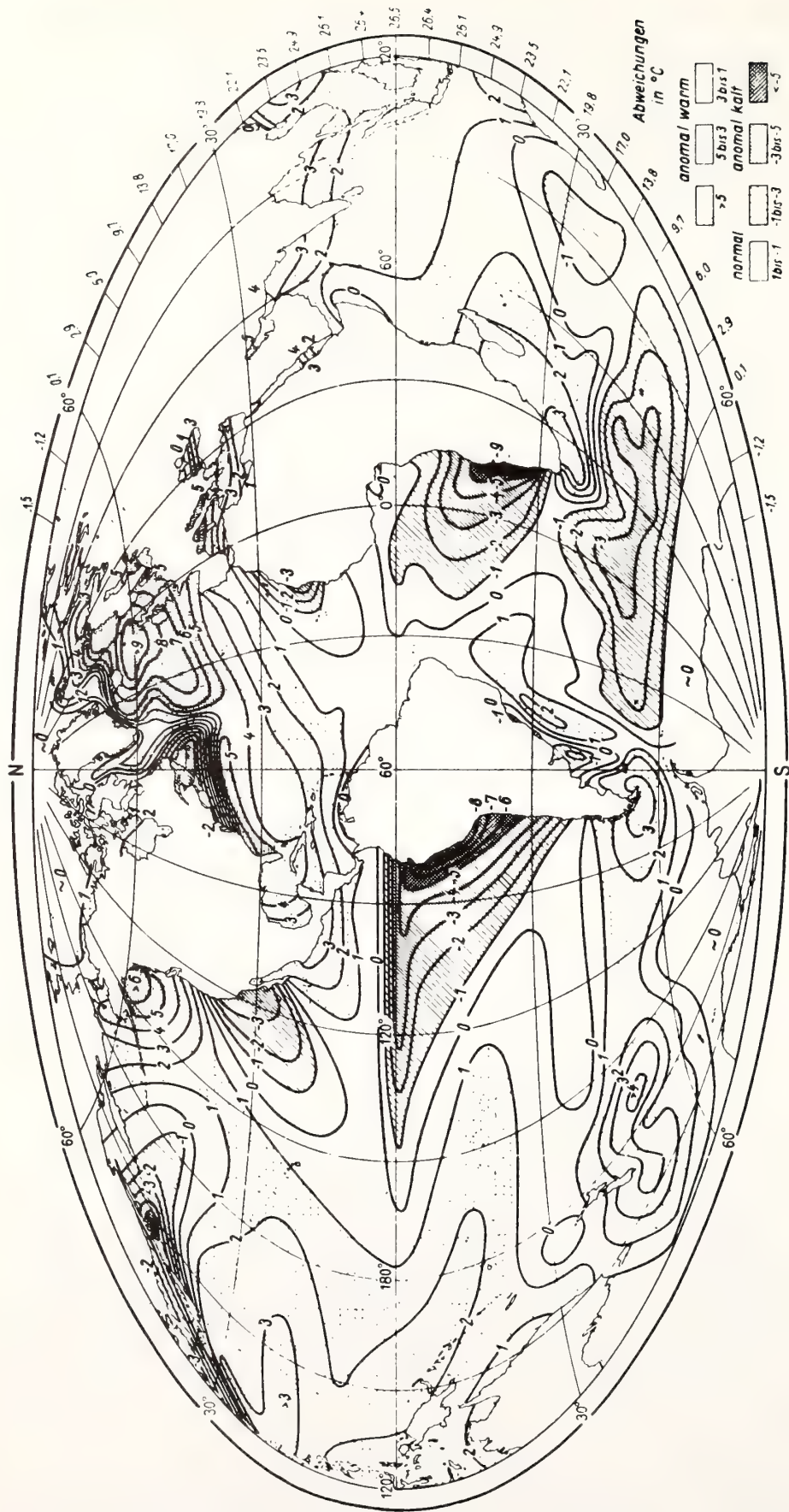


Figure 1. Sea-surface temperature represented as deviation from the average at each latitude (after Bjerknes, 1969; from Dietrich and Kalle, 1957).

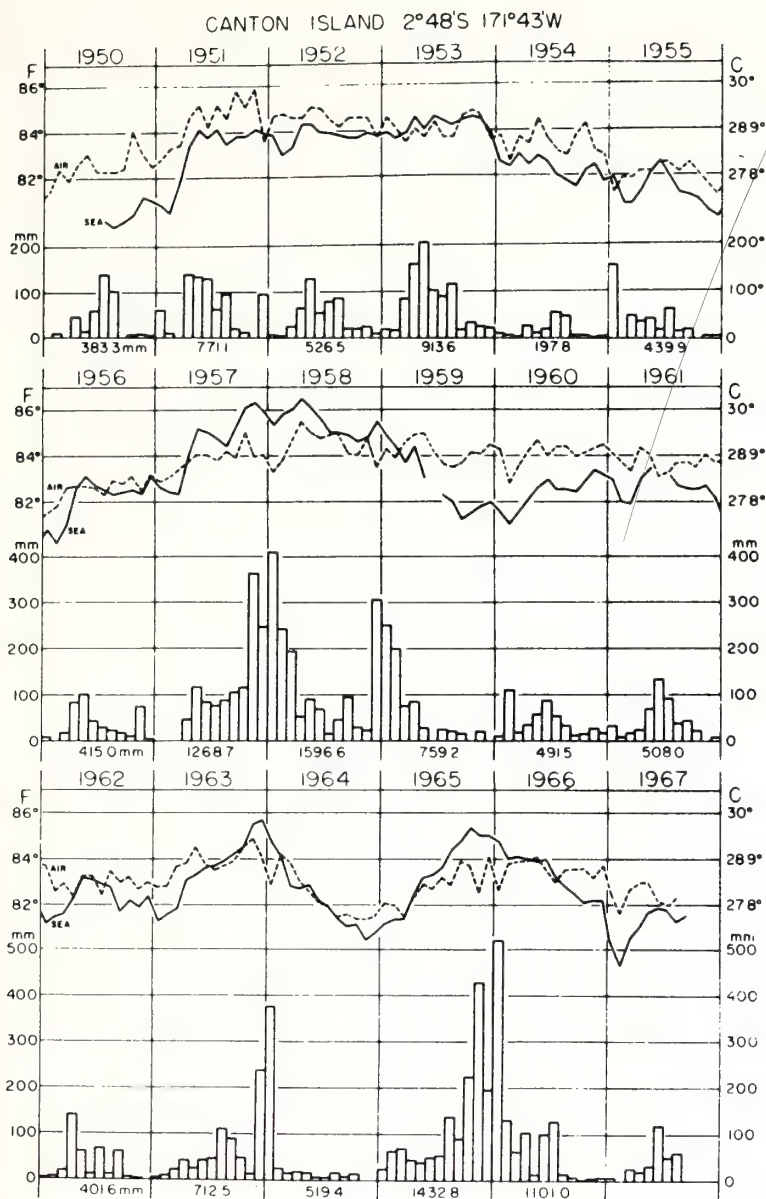


Figure 2. Time series of monthly air and sea temperatures and of monthly precipitation at Canton Island from 1950 to 1967 (from Bjercknes, 1969).

other investigators have examined this response of the tropical atmosphere (more precipitation) to warm surface waters and its self-amplification (Krueger and Gray, 1969; Quinn, 1970; and others). This increased precipitation has been suggested as an explanation for the midlatitude westerlies being stronger during periods of warm surface temperatures in the equatorial dry zone. The suggestion is that the greater heat supply



from the equatorial ocean is added to the atmospheric Hadley circulation by precipitation intensifying that circulation and producing more than the normal flux of angular momentum at the midlatitude belt of westerlies (Bjerknes, 1969).

The response of midlatitude circulation patterns to tropical (or extratropical) ocean temperature anomalies has obvious importance to the predictability of the atmosphere. Thus, the initial work by Berlage and Bjerknes has brought on a number of diagnostic studies during the past few years on teleconnections of the atmosphere and ocean (Krueger and Gray, 1969; Namias, 1969). These studies are very useful in establishing the global nature of this phenomena. Furthermore, they have shown the need for global satellite measurements to study these long-term, sea-air interaction phenomena.

Studies that should be undertaken when adequate satellite data are available are:

1. The Ekman divergence has been postulated as a response to the strength of the equatorial trade winds. The time development of sea surface temperature patterns in response to surface wind stress should be studied to verify this or offer another explanation.
2. The long-term sea surface temperature anomalies recorded at Canton Island need to be extended to all of the tropical and subtropical oceans. Unfortunately, only a few island stations record sea surface temperatures, and ships provide only limited data (time and space). Satellite sea surface temperature measurements (to required precision) are required on a global scale to provide the necessary sampling resolution and accuracy to study these anomalies. These will provide basic information for diagnostic studies of long-term sea surface temperature anomalies as a means for forcing (and interacting with) the circulation patterns in the atmosphere.
3. If there are large-scale teleconnections between the ocean and atmosphere, we can also expect to have large-scale teleconnections between the world's oceans (with the atmosphere as a link). Sea surface temperature data obtained by satellite will provide basic input for such studies.

## 2.2 Requirements

The requirement is for sea surface temperature, once a day at 0000 LST, a spatial resolution of 100 km, an accuracy of  $1^{\circ}\text{K}$ , and a precision of  $0.5^{\circ}\text{K}$ .

The satellite measurements required have not been specified in table 3 (only sea surface temperature has been specified). It is assumed that some organization with satellite data processing capability (such as NESS) will reduce the necessary measurements to sea surface temperature values. This requires eliminating the effect of the atmosphere and clouds on the measurement.

## 3. WATER MASS IDENTIFICATION

George Maul

Oceanic circulation is a fundamental geophysical phenomenon that affects every milligram of biota on this planet. The advection of heat and nutrients is the controlling influence in the primary biological production and hence the entire food web. Major weather systems, such as subtropical cyclones, are influenced (if not controlled) by the ability of the ocean to release thermal energy; regional climates are established because of this. Marine transportation, commercial fishing, deep-sea mining and drilling, national defense, and other such ocean-oriented activities of man are influenced by the surface and near-surface circulation.

If we are to use the ocean in an ecologically acceptable and commercially practical manner, the perturbations in the average surface flow are the meaningful properties that must be measured and eventually predicted. Fortunately, due to the intense baroclinicity of the important currents, there are several surface features that hold promise for detection by remote sensors.

Characteristically, the surface manifestation of major currents, such as the Gulf Stream, Kuroshio, Agulhas, Peru, and Somali, are (1) a high temperature gradient, (2) a high salinity gradient, (3) a high turbidity gradient, (4) a high velocity gradient, (5) a change in sea state, (6) a change in cloudiness or cloud patterns, and (7) a change in sea-surface slope. The possibility of remotely sensing these features and the requirements to do so are discussed in the following paragraphs. The goal is to make appropriate measurements of each of these features and by machine processing and decision, provide the maritime community with synoptic maps. The feasibility of machine processing and decision of multispectral scanner data has been demonstrated by Higer et al. (1970).

### 3.1 Thermal Gradient Detection

The surface thermal signature of the Gulf Stream has been documented as a reliable, year round, indication of the current (Hansen and Maul, 1970). Attempts to track routinely the thermal boundary by using Nimbus II data have led to the conclusion that the uncontaminated sea surface temperature must be known to  $\pm 1^\circ\text{K}$  (Maul, 1972). To accomplish this, we recommend that a high resolution infrared sensor (HRIR), response-limited to the range of oceanic surface temperatures with allowance for atmospheric attenuation (namely  $260^\circ\text{K} - 310^\circ\text{K}$ ), be flown. The subsatellite ground resolution should be about 2 km for meaningful location of the thermal field with respect to the velocity field, the attitude control requirements of the altimeter (discussed in sections 2.4 and 2.5) must keep the location of the HRIR ground spot in an area less than the spot size itself. A second channel that simultaneously measures the planetary albedo with the same resolution is required for cloud detection. The spectral range of the HRIR desired is 10.5 to 12.5  $\mu$ , because energy at earth temperatures is maximized, reflected energy is negligible, and atmospheric



attenuation due to  $H_2O$ ,  $CO_2$ , and  $O_3$  is small. The albedo channel specifications are less well-determined; however, 0.4 to 0.7  $\mu$  should be adequate. The multispectral approach (Anding and Kauth, 1970) seems to have the potential for very accurate measurements, but field tests have yet to be made.

### 3.2 Salinity Gradient Detection

Salinity changes across the Mississippi River outflow were measured by Droppleman et al. (1970) using a passive microwave radiometer operating on 1.4 GHz from a low-flying aircraft. Although this experiment is in its infancy, it is very promising for current boundary detection where changes of 2 ‰ may occur over several kilometers. It may prove especially valuable in the region of the ocean between 30°N and 30°S (about half the earth's surface), where surface thermal fronts are absent or seasonal.

The inclusion of a passive microwave radiometer on an oceanographic satellite is most desirable for applications in ice detection and sea state; one channel should operate on 1 to 1.5 GHz. The ground spot size and attitude control requirements discussed for temperature apply to the salinity discussion as well as the other observations discussed below.

### 3.3 Turbidity Gradient Detection

Clarke et al. (1969) showed that the differences in color of oceanic water masses could be detected from aircraft. These measurements have been linked to the chlorophyll content of the water and hence to its bioassay. Color change between water masses is independent of location, and thus is as valuable in the tropics as in midlatitude regions. The measurements of Clarke et al. (1969) suggest that two narrow (0.015  $\mu$ ) channels centered on 0.54 and 0.46  $\mu$  are necessary to perform these studies. Absolute accuracies needed correspond to the capability of measuring chlorophyll-A

concentrations of about  $0.2 \text{ mg m}^{-3}$  to precisions of  $\pm 0.1 \text{ mg m}^{-3}$ . This translates (Ramsey, 1968), to an accuracy of  $3.0 \text{ W m}^{-2} \text{ ster}^{-1} \mu\text{m}^{-1}$  and a precision of  $\pm 1.5 \text{ W m}^{-2} \text{ ster}^{-1} \mu\text{m}^{-1}$ .

### 3.4 High Velocity Gradients

The other features listed above are covered in sections 2.4 and 2.5 and come naturally out of those requirements, except for item (4), Velocity Gradients. McManus et al. (1968) have shown that a Doppler laser can give absolute current speeds. The adaptability of such a device enables an oceanographer to separate the barotropic flow from the baroclinic flow and, hence, obtain the entire current field from measurement of sea surface slope by an altimeter.

### 3.5 Other Applications

Being able to measure the thermal, salinity, and turbidity gradients in the open ocean to the required accuracies allows one to easily apply the techniques to estuarine and near-shore circulation problems. These areas are of immediate interest in problems of ocean waste disposal, pollution, and recreation. These capabilities also help geological interests solve such problems as longshore transport, and river plume sedimentation.

### 3.6 Platform Location and Interrogation

Finally, the basic need for Lagrangian drifters in ocean circulation studies must be promulgated. An oceanographic satellite system must be able to locate free drifting buoys and to telemeter basic measurements. Thus the system can also service moored buoys, which serve as operational ground

truth stations for the remote measurements. Without periodically comparing remotely sensed data with acceptable standards, we will not have the beginning of genuinely reliable synoptic oceanography.

### 3.7 Development Studies

Many of the items discussed in this section require further R&D before we attempt to integrate them into a satellite. We strongly recommended that a vigorous aircraft program be supported to determine, first, the optimum spectral bands needed for ocean sensing in order to simplify the satellite as much as possible, and second, to determine if these optimum bands can see through the atmosphere with adequate resolution to warrant integration at all.

## 4. SURFACE WIND AND WAVE CONDITIONS

Duncan Ross

### 4.1 Problems

The problem area here is in the general knowledge of surface wind and wave conditions as input to research programs studying the exchanges of heat, energy, and moisture at the sea-air interface. This study will also help the continued development of numerical forecasting of oceanic wind and wave conditions.

There are numerous organizations and programs that desire synoptic wind and wave observations over the oceans. These needs are documented in various reports of the World Meteorology Organization (WMO), World Weather Watch (WWW), etc.



Typical of these are the objectives stated by the WMO in Resolution 1721 (XVI) adopted at the United Nations General Assembly in December 1961:

- "1. To develop a deeper understanding of the global circulations of the atmosphere and the associated system of climates;
2. To place weather forecasting on a firmer scientific basis: to develop techniques for predictions on extended time scales and to provide knowledge needed to improve weather forecasts of small space-scales and time space;
3. To explore the extent to which weather and climate may be modified through artificial means."

These objectives have been addressed by numerous organizations, and current experimental programs gather data from ships, aircraft, and satellites. The system requirements stated here will provide additional input to these programs. Section 4 is concerned with the rationale behind the stated requirements; however, note that elements of those requirements are in the area of technology development.

## 4.2 Requirements

A multi-frequency scanning microwave radiometer system is needed to provide data from which the aforementioned parameters can be inferred. The system should contain the following features:

1. Frequencies - approximately 1-3, 5-8, 10, and 15-19 GHz
2. Polarization - dual
3. Spatial resolution - 20-100 km
4. Scan -  $\pm 30-50^\circ$  orthogonal to ground track and conical at  $50^\circ$
5. Accuracy - antenna temperatures  $\pm 1^\circ\text{K}$ .

We desire to remotely determine oceanic surface wind and wave conditions. Microwave sensitivity to these parameters also appears to be frequency dependent (Hollinger, 1971). Although the mechanism of this sensitivity and its relationship to surface wind and wave conditions are not well understood or quantified, for the sake of argument, we assume our current knowledge is adequate. It remains then to account for the atmosphere at some frequency where adequate sensitivity to sea state is evident.

The proposed approach — a multi-frequency, dual-polarization, passive microwave sensing system — is suggested for the following reasons:

1. By using currently available HRIR images, we can make assumptions about the atmosphere, and good sea state information can be obtained at the higher frequencies (10 and 19 GHz) during clear sky conditions.
2. By using visual and HRIR images to reveal moderate to heavy cloud conditions, we could use 1 or 10 GHz data with the attendant sacrifice in resolution and sensitivity.
3. By using a conical scan at, say, 37 GHz, and with dual polarization at an incidence angle of  $50^\circ$ , we might determine atmospheric moisture content well enough to correct measurements at 19.5 or 10 GHz in order to extend the available sea state "look" opportunities at these frequencies.

The above rationale is, of necessity, somewhat less positive than would be desired, since experimental data now available are sparse. Hopefully, current NASA Goddard Space Center (GSFC), Manned Spacecraft Center (MSC), Langley Research Center (LRC), and planned (NOAA/NRL) experimental programs will yield the desired information. Note that the oft quoted 50-km resolution for sea state determination is based on average conditions. Under the influence of a large extra-tropical storm, reasonably homogenous surface conditions usually extend over several hundred kilometers. Thus, while the availability of 50-km resolution is very appealing, it should not be the only consideration.

### 4.3 Intended Use of Data

The Atlantic Oceanographic and Meteorological Laboratories will use these data in connection with specific research objectives such as:

1. The effect of fetch and stability on the growth of ocean surface waves
2. The prediction of surf and of shallow and deep water wave conditions associated with hurricanes and extra tropical storms
3. The prediction of storm surge associated with tropical storms and hurricanes.

The desired data would be useful in both the short- and long-term aspects of the above research objectives.

### 4.4 Justification

The application of passive microwave techniques to marine meteorology is given excellent treatment by Paris (1969 and 1971). In these publications, numerous calculations have been carried out relating to the microwave signature of the ocean and atmosphere, such as, surface temperature, sea state, salinity, and atmospheric moisture. Hollinger (1971), Ross et al. (1970), and Nordberg et al. (1971) present extensive data on the effects of sea state on the microwave brightness temperature. To summarize the conclusions of these workers and others, it may be stated that no one frequency is ideally suited to observing remotely a specific environmental parameter, since all parameters are frequency dependent in their signature and to varying degrees. Thus 19.5 GHz is very sensitive to sea state, but even more so to atmospheric moisture. By choosing a lower frequency such as in the 1 to 3 GHz range, we find that atmospheric moisture sensitivity essentially disappears. Unfortunately, sea state sensitivity also appears to be greatly reduced, while at the same time salinity becomes important. Figures 3 to 11, from the publications by Paris (1969), do clearly show the frequency dependence of some of these parameters.



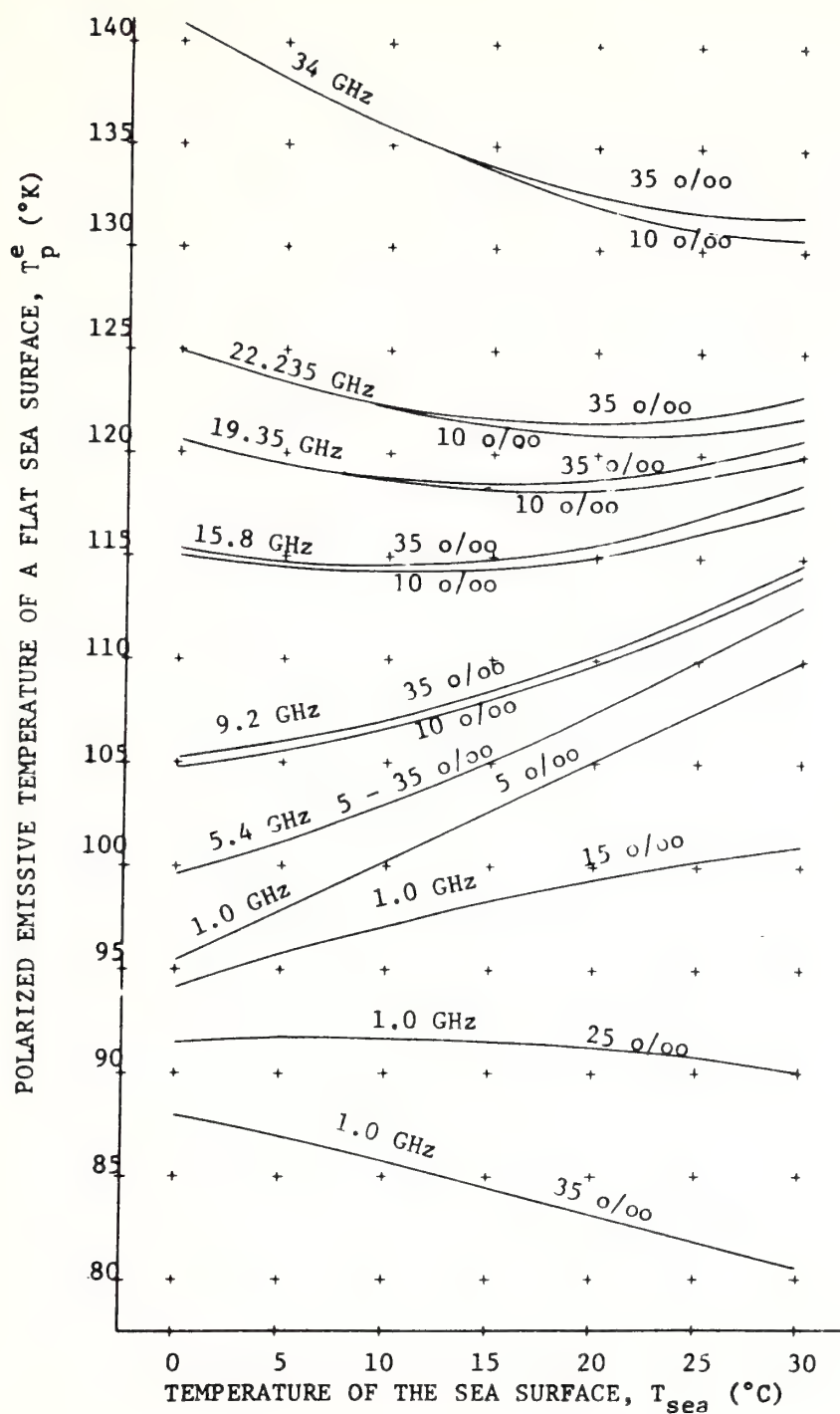


Figure 3. Polarized emissive temperature of a flat sea surface vs. thermometric temperature of the sea surface for 1, 5.4, 9.2, 15.8, 19.35, 22.235, and 34 GHz and for various salinities (Paris, 1969 and 1971).

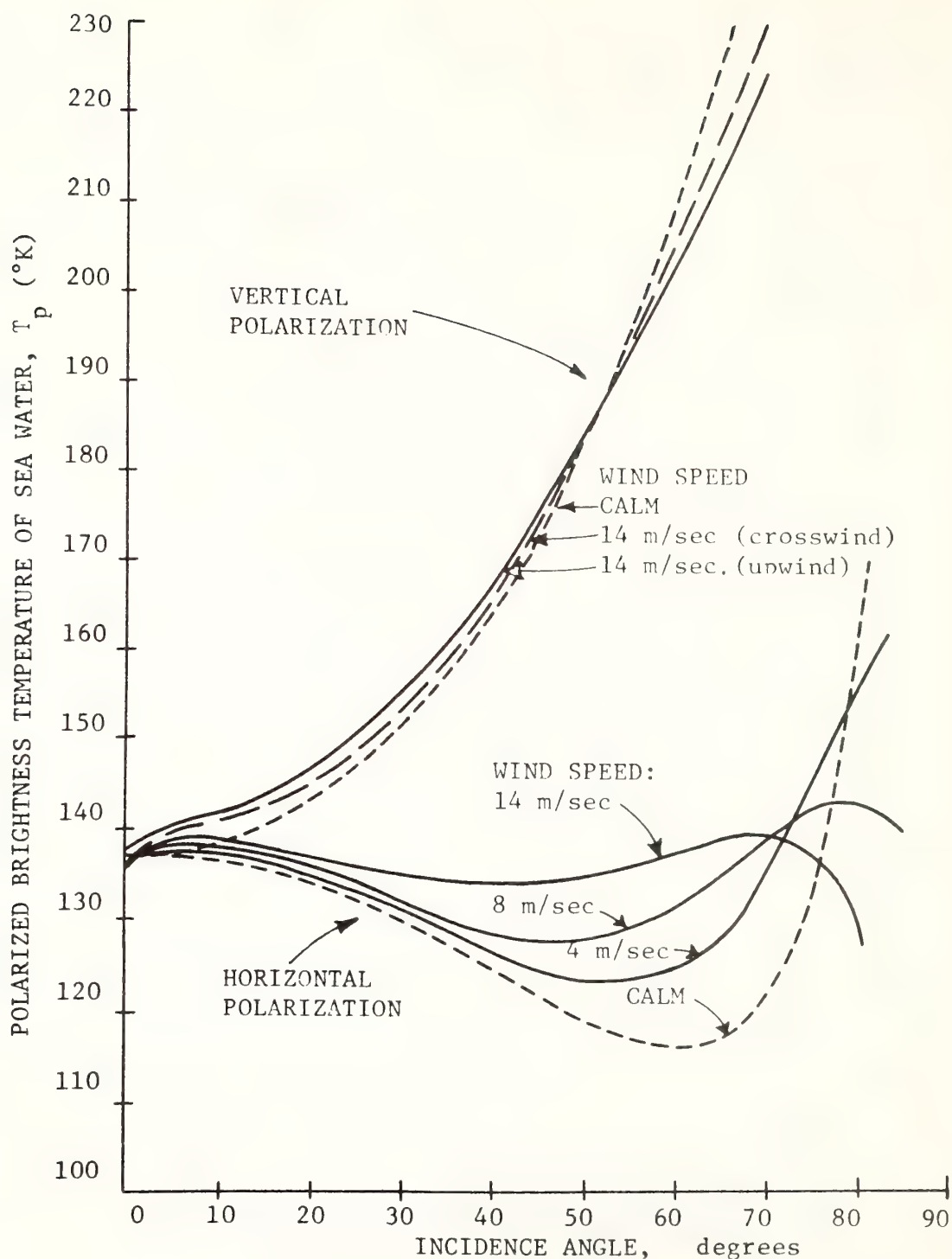


Figure 4. Polarized brightness temperatures of sea water vs. incidence angle for horizontal and vertical polarization, for fully developed sea driven by surface winds of 0, 4, and 14 m/sec; altitude is 1 km, and frequency is 19.4 GHz (from Paris, 1969 and 1971; after Stogryn, 1967).

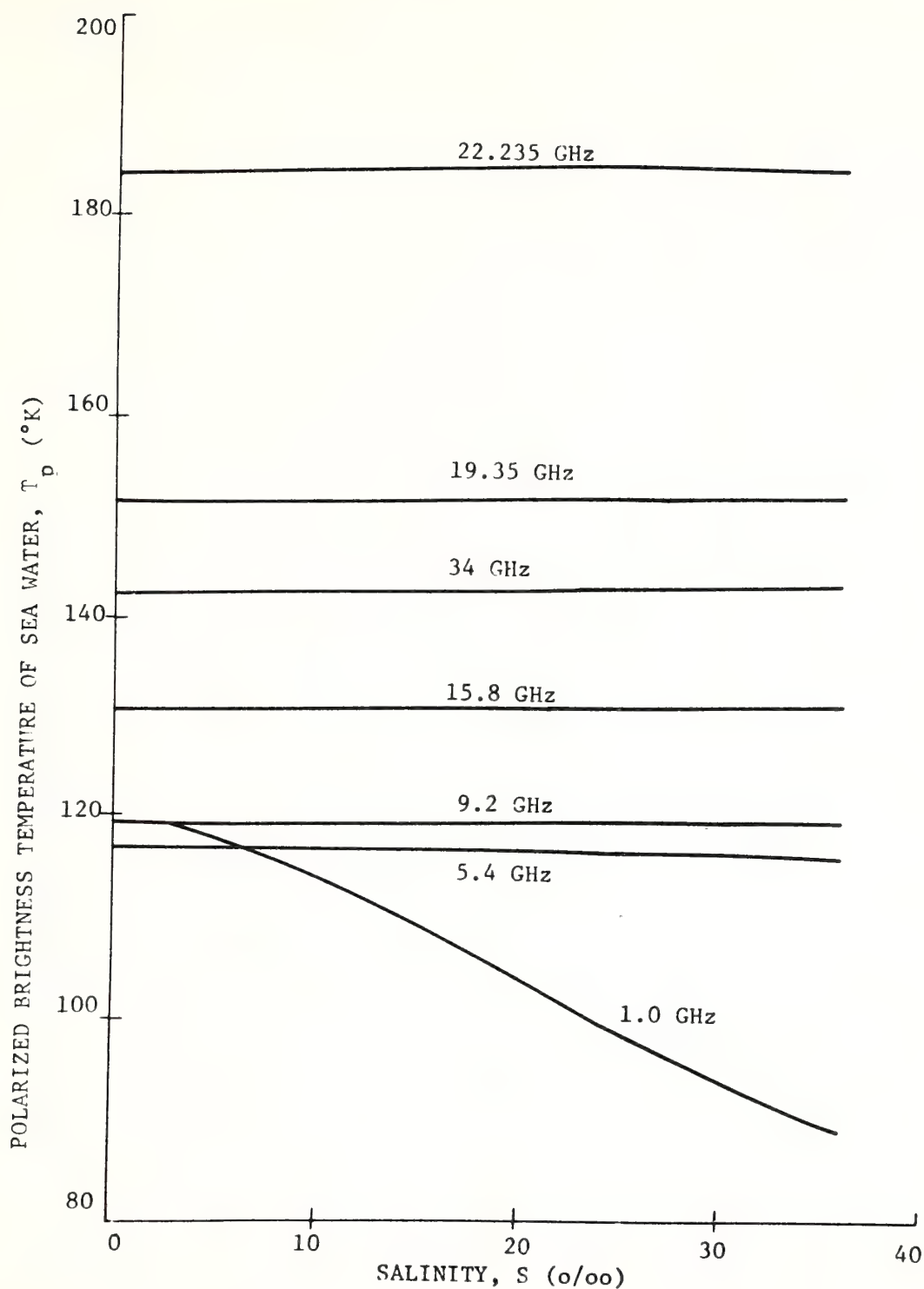


Figure 5. Polarized brightness temperature of sea water vs. salinity for a water temperature of  $303^{\circ}\text{K}$ , an incidence angle of  $0^{\circ}$ , frequencies of 1, 5.4, 9.2, 15.8, 19.35, 22.235, and 34 GHz, and an altitude of 1 km (Paris, 1969 and 1971).



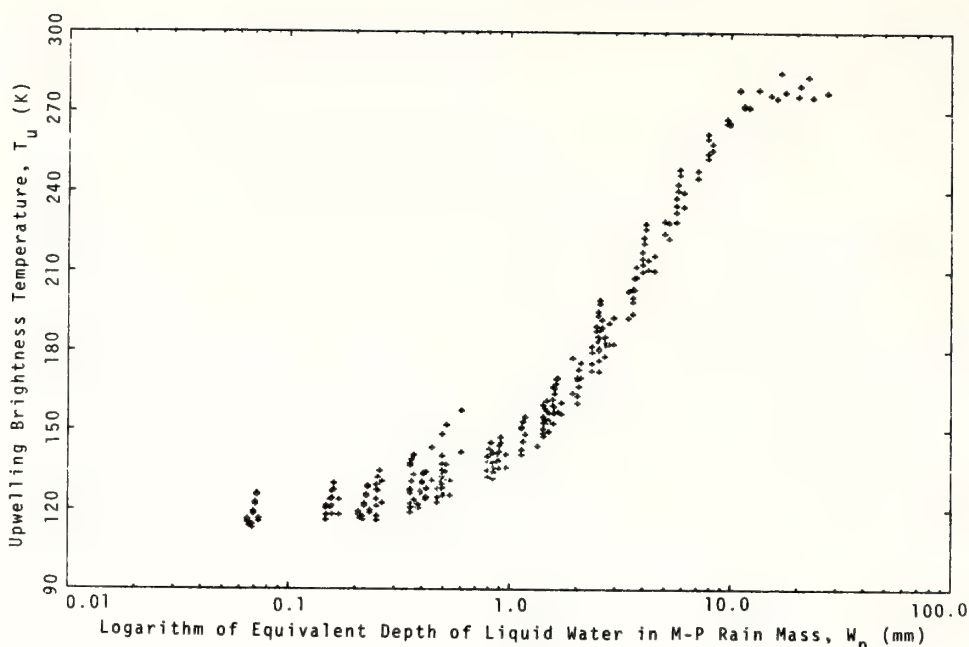


Figure 6. Scattergram of the upwelling radiation of 575 model atmospheres for normal incidence and for a calm ocean vs. their equivalent depths of liquid water in the M-P rain mass:  $\nu = 10.69$  GHz (Paris, 1969 and 1971).

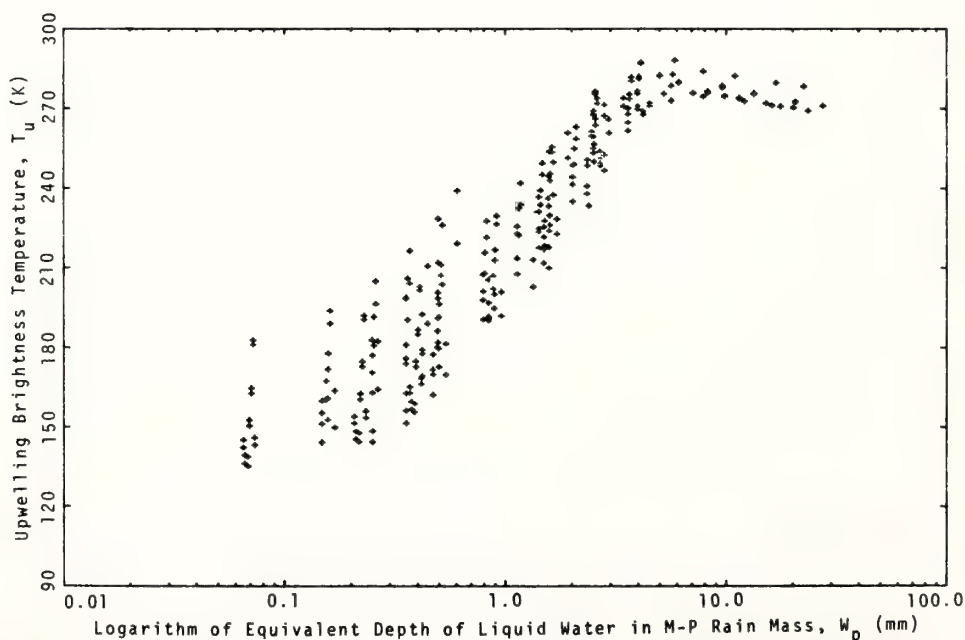


Figure 7. Scattergram of the upwelling radiation of 575 model atmospheres for normal incidence and for a calm ocean vs. their equivalent depths of liquid water in the M-P rain mass:  $\nu = 19.35$  GHz (Paris, 1969 and 1971).

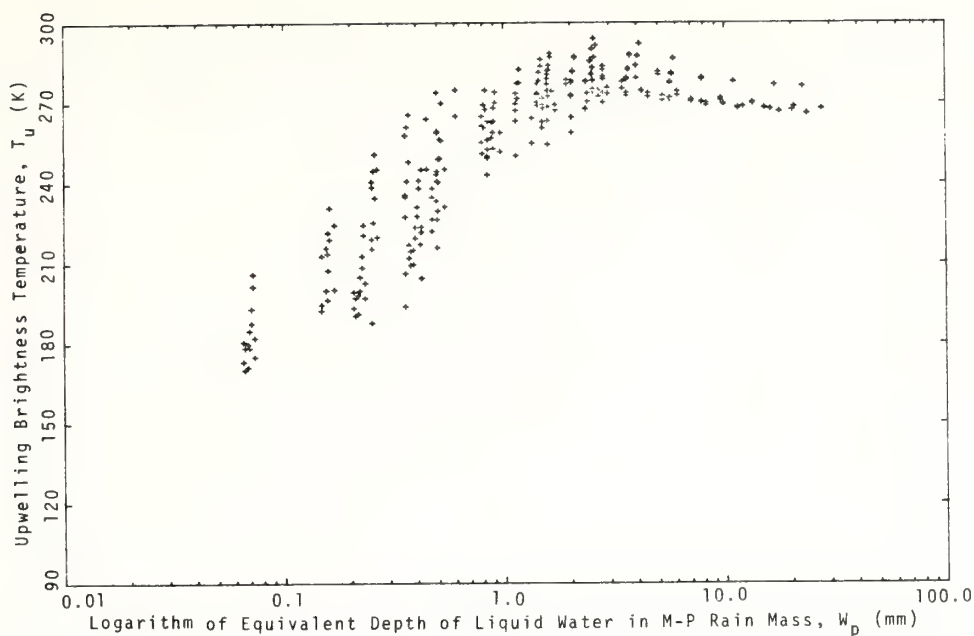


Figure 8. Scattergram of the upwelling radiation of 575 model atmospheres for normal incidence and for a calm ocean vs. their equivalent depths of liquid water in the M-P rain mass:  $\nu = 37.0$  GHz (Paris, 1969 and 1971).

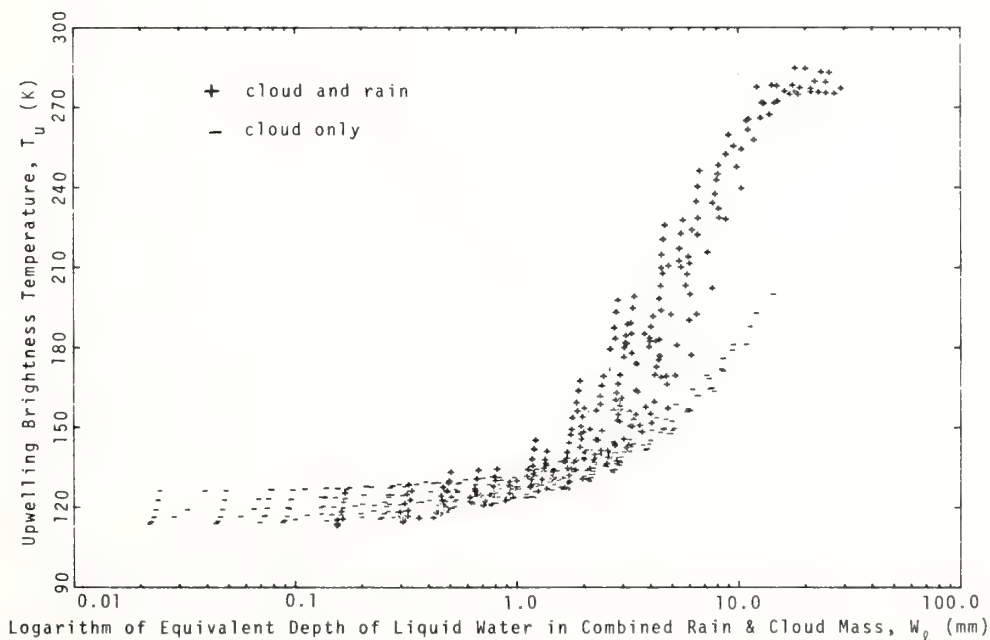


Figure 9. Scattergram of the upwelling radiation of 575 model atmospheres for normal incidence and for a calm ocean vs. their equivalent depth of liquid water in combined rain and cloud mass:  $\nu = 10.69$  GHz (Paris, 1969 and 1971).

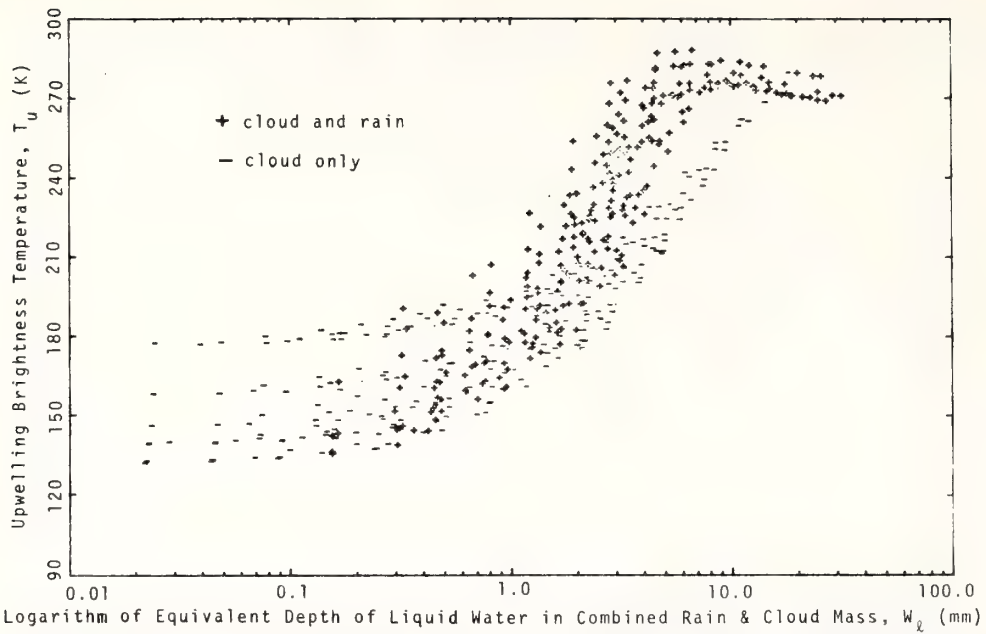


Figure 10. Scattergram of the upwelling radiation of 575 model atmospheres for normal incidence and for a calm ocean vs. their equivalent depth of liquid water in combined rain and cloud mass:  $\nu = 19.35$  GHz (Paris, 1969 and 1971).

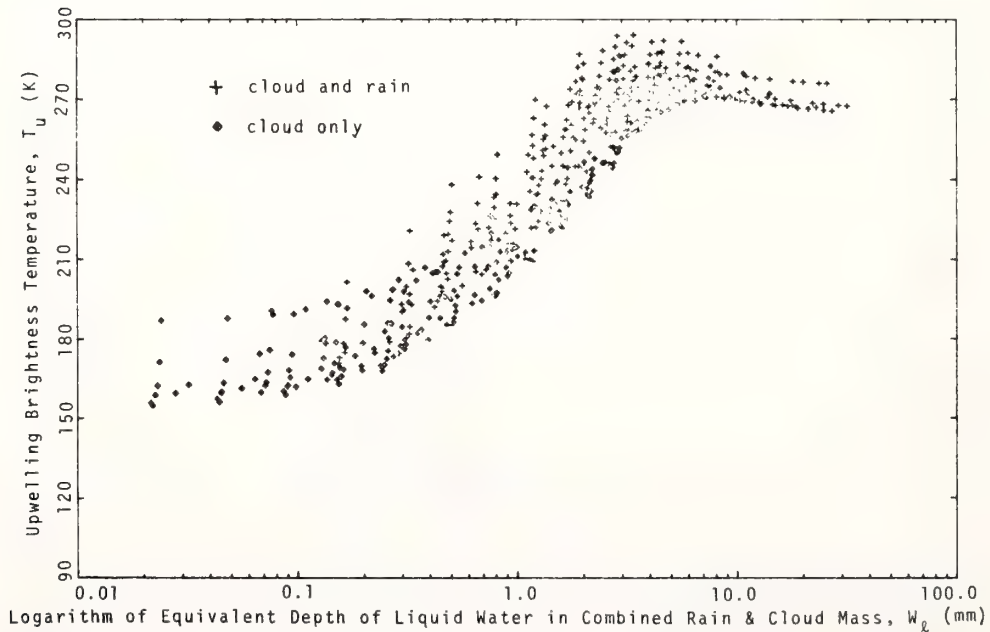


Figure 11. Scattergram of the upwelling radiation of 575 model atmospheres for normal incidence and for a calm ocean vs. their equivalent depth of liquid water in combined rain and cloud mass:  $\nu = 37.0$  GHz (Paris, 1969 and 1971).



## 5. SEA-STATE, TIDES, AND OCEAN SLOPES

John Apel, Bernard Zetler, and Donald Hansen

### 5.1 Problems

These problems fall into three general categories:

1. Determination of sea state on real-time, synoptic basis, both for research and for monitoring and predicting (NASA Report, 1969).
2. Worldwide determination of tides along coasts and in the midocean, with special emphasis on locating the amphidromic points (Munk et al., 1967; Zetler and Maul, 1971).
3. Measurement of absolute slopes of the sea surface as caused by intense current systems and by deep ocean trenches (NASA Report, 1969).

All three of these problems are, in principle, decipherable by microwave systems on board a spacecraft, e.g., a high precision, short pulse radar altimeter.

### 5.2 Requirements

1. If the altimeter pulse length is very short — approximately 3 to 10 nsec — the temporal distribution of the returned pulse is a convoluted measure of the distribution of heights of the reflecting surface, i.e., a measure of the state of waves over that part of the sea illuminated by the radar beam (a spot of about 8 km diameter). Recent experiments at NRL (Yaplee et al., 1971) show this technique gives accurate wave spectra for spots that are small compared with an ocean wavelength; in principle, it remains true for large spots, but in an integral form. The research problems are (a) to demonstrate the last assertion experimentally, (b) to develop high power ( $\sim 2$  kW), short pulse X-band sources that can function in a power-limited satellite, and (c) to devise techniques for sampling the instantaneous signal returned to the satellite at enough points to extract the sea state information from it.

These are difficult technological problems, but ones not insolvable. If handled satisfactorily, the altimeter could form the basis for a multi-satellite, worldwide sea state monitoring and prediction system (Apel, 1971).

2. If the altimeter is also very accurate (atmospheric fluctuations set the minimum altitude error at about 10 cm, while good electronic design can hold the instrument error below that), and if the satellite altitude can be consistently established to a relative precision of about 1 m (larger, constant biases are of no consequence), then ocean tide information with 10 percent error can be calculated by averaging data from a  $1^\circ$  square for a year, provided the tidal amplitudes there are equal to or greater than 1 m (Zetler and Maul, 1971). The technique holds some promise for synoptic studies of tides and a global monitoring and prediction system. It appears, however, considerably more difficult to implement than the sea state monitor. The 5 m precision quoted for current satellites probably could not meet these specifications even if extraordinary efforts are made (Vonbun, 1970). Note that until the sea state problem of item 1 is solved, there is little hope of approaching the required tidal accuracy, because the measured height of the reflecting surface will obviously depend upon the surface roughness as well as its mean elevation.
3. An altimeter having 5 m precision can measure ocean surface slopes such as exist over the deep ocean trenches (15 m depression over 200 km wide). If a 1 m noise figure is achieved, it may also be possible to determine surface slopes (1 m in 100 km) caused by oceanic current systems such as the Gulf Stream or the Kuroshio. It is possible that a combination of laser ranging and short-arc orbit prediction for the satellite would allow single-pass measurements over the Gulf Stream, thereby permitting time-resolved studies of the meanders in that current. The importance of this for a future monitoring and prediction service is apparent.

These three types of oceanographic studies all require a short-pulse, precision altimeter on a vertically stabilized, accurately tracked spacecraft. The orbit should not be synchronized with the major ocean tidal periods and their harmonics (in particular, sun-synchronous orbits are unacceptable);

in addition an inclination of near  $65^{\circ}$  and a low altitude — approximately 300 to 400 km — permits a view of tides at nearly all latitudes of interest with a minimum radar "foot-print" on the ocean surface. With a suitably designed radar altimeter and a significant effort on improved tracking, a mid-1970's satellite could meet the requirements. It is not until the altitude and pulse length figures approach those cited here that a spacecraft with an altimeter becomes seriously interesting for this type of oceanography (Townsend, 1971).



PART II: SOLID EARTH PROGRAMS

## 6. CHANGES IN SHORELINE AND SEAFLOOR FEATURES CAUSED BY STORMS

George Keller

### 6.1 Objective

The objective is to determine storm effects on shorelines and shallow water bottom topography in areas of carbonate deposits.

### 6.2 Problems

Effects of storms (of both minor and major proportions) on the alteration of shorelines and seafloor topography are not yet understood. Photographs taken during space flights indicate that it is feasible not only to record shorelines, but also to record shallow water bottom features (Ross and Jensen, 1969). Several studies have been made on the changes of shorelines by various means, in regard to both long-term changes (e.g., 20 to 40 years) and to rapid alterations resulting from severe storms. Photographic coverage for such studies has not been very complete, e.g., large gaps in the observation intervals. These studies have dealt primarily with shoreline changes and not the adjacent seafloor. The problem we wish to study is the long-term (1 to 2 years) and short-term (1 to 5 days) changes of island shorelines and the surrounding seafloor topography.

This study is proposed for the Bahama Islands, both because of their susceptibility to storm activity and because the clear waters are needed to photograph shallow water bottom features. The more or less continuous photographic coverage obtained by the Earth Resources Technology Satellite (ERTS) systems would provide, for the first time, adequate reference material for a study like this. The correlation of

wind and sea velocities and their respective forces with changes in shorelines and bottom topography is the goal of this study.

### 6.3 Approach

From satellite spectral imagery, the shoreline of a number of islands as well as the size and shape of prominent seafloor features (e.g., sand waves and sand dunes) in the area of the islands will be established. Measuring succeeding images, we can record changes in these features and attempt to correlate these changes with atmospheric and sea conditions. Ground truth measurements will consist of periodic beach surveys on the islands and a sampling program of the bottom features to determine characteristics and variations of sediment texture. Periodically bottom currents will be measured adjacent to the islands to provide additional data on the dynamics of the environment. To obtain greater resolution in photographic coverage of the study area, aircraft photographic surveys will be needed at least twice a year.

### 6.4 Benefits

The effect of "normal" atmospheric conditions, not to mention severe storms, on shorelines and the characteristics of the adjacent shallow seafloor are poorly known. We expect that the proposed study will provide data that can be used in predicting the effect severe storms will have on shore and near-shore features. Although the study is designed for the Bahamas, it is applicable to the Florida Keys. The study will also serve to evaluate the effectiveness of space observations for this type of problem.



## 6.5 Requirements

For determining shoreline changes a red spectral band ( $0.70 \mu$ ) is desirable for a clear delineation of the coastline. For determining seafloor changes, greater penetrating spectral bands ( $0.46$  to  $0.54 \mu$ ) are required for use in water depths up to 30 m. Use of the  $0.46 \mu$  and  $0.54 \mu$  bands would provide the necessary data.

## 7. TURBID WATER MASS MOVEMENT

George Keller

### 7.1 Objective

The objective is to determine the concentration and composition of suspended material in the ocean and to relate this to space photography.

### 7.2 Problem

Photography taken during space flights has shown that it is feasible to trace turbid water masses seaward from rivers, bays, and coastal lagoons. Although these photographs denote the presence of turbid water, the concentration of suspended material that can be detected is unknown. The problem we wish to pursue is to measure the concentration and composition of the suspended material extending from the Mississippi River into the Gulf of Mexico. We expect to trace the sediment mass and in turn relate this to appropriate photographs taken from space. This will provide the necessary ground control to evaluate the resolution of space photography in regard to turbid water masses. The composition analyses will identify exactly the sediment constituting the turbid mass.

### 7.3 Approach

Suspended material will be collected at prescribed locations out from the Mississippi River in a series of radial patterns. This will be accomplished by pumping 1 to 100 gallons of sea water from each study site through a series of filters. In addition to the surface waters, samples will be taken from various depths. The amount of organic vs. inorganic matter will be determined as will the composition of the inorganic fraction. A quantitative analysis and identification of the various inorganic constituents will be made by means of X-ray diffraction techniques.

The various concentration values will be compared with satellite photographs of the study area. Additional photography from aircraft (at 5000 ft) is essential to provide added resolution to the study.

The second phase of this study will be observations similar to those mentioned above in the vicinity of Pamlico Sound, North Carolina. Studies by Mairs (1970) clearly revealed that large concentrations of sediment-laden water enter the Atlantic through an inlet in the Hatteras barrier bar. This study, however, did not provide any data on sediment concentration or composition, and thus no ground truth has yet been provided for space photography of these turbid masses. The work will be conducted from NOAA vessels and in the laboratories of the Marine Geology and Geophysics Laboratory of the Atlantic Oceanographic and Meteorological Laboratories.

### 7.4 Benefits

Limited use has been made of tracing water movement by space photography. The tracing of turbid water masses would provide considerable information on local coastal circulation.

The presence of turbid water appears to correlate very well with the occurrence of marine life, e.g., fish, shrimp. We hope to learn how effective space photography can be for studying the movement of water masses from coastal areas into the sea.

### 7.5 Requirements

Three spectral bands will be required to delineate the transport of turbid water masses in the coastal zone. The red band ( $0.7\ \mu$ ) will detect surface concentrations of turbid masses; whereas, the green ( $0.46\ \mu$ ) and blue ( $0.54\ \mu$ ) spectral bands will enable the detection of turbid water masses at intermediate depths below the surface. The significance of making color separations in these regions of the spectrum has been discussed by Mairs (1970).



## 8. REFERENCES

- Apel, J. R. (January 5, 1971), Memo to H. B. Stewart, Jr., Status of GEOS-C Radar Altimeter and Its Use in Oceanography (Appendix A in this report).
- Anding, D., and R. Kauth (1970), Estimation of sea surface temperature from space, *Remote Sensing of Environment*, 1, 217-220.
- Ashbel, Dov. (1961), New world maps of global solar radiation, during I.G.Y. (1957-1958), Dept. of Climatology and Meteorology, The Hebrew University, Jerusalem, Israel.
- Austin, T. S. (1960), Summary, 1955-1957 ocean temperature, central equatorial Pacific, Marine Research Committee, California, Coop. Oceanic Fisheries Invest. Reports, 7, 52-55.
- Berlage, H. P. (1966), DeZuidelijke schommeling, en haar mondiale uitbreiding (The Southern Oscillation and World Weather) *Mededelingen eh Verhandeligen*, No. 88, Koninklijk Nederlands Meteol. Instit., 152 pp.
- Bernhardt, Fritz, and H. Phillipps (1958), Die raumliche und zeitliche verteilung der einstrahlung, der ausstrahlung und der strahlungsbilanz im meeresniveau, Teil I. Die einstrahlung (Spatial and temporal distribution of incoming and outgoing radiation and the radiation balance at sea level, Pt. 1. Incoming Radiation), *Adhandlungen Meteorologischer und Hydrologischer Dienst*, No. 45, Deutsche Demokratische Republik, Germany, 227 pp. plus numerous figures and tables.
- Bjerknes, J. (1966), A possible response of the atmospheric Hadley circulation to equatorial anomalies of ocean temperature, *Tellus*, 18, No. 4, 820-829.
- Bjerknes, J. (1969), Atmospheric teleconnections from the equatorial Pacific, *Monthly Weather Rev.*, 97, No. 3, 163-172.
- Black, J. N. (1956), The distribution of solar radiation over the earth's surface, *Arch. Meteorolo. Geophys. Bioclimatol.*, Ser. B, 7, 165.
- Budyko, M. I. (1963), Atlas Teplovogo Balansa Zemnogo Shara (Glavnaia Geofizicheskaya Observatoriya, Moscow).

- Budyko, M. I. (1955), Atlas Teplovogo Balansa (Gidrometeorologischeskoe Izdatel'stvo, Leningrad).
- Clarke, G. L., G. C. Ewing, and C. J. Lorenzen (1969), Remote measurement of ocean color as an index of biological productivity, Proc. of the Sixth International Symp. of Remote Sensing of the Environment (University of Michigan, Ann Arbor, Michigan), 2, 991-1001.
- Cox, Stephen K., and Stefan L. Hastenrath (1970), Radiation measurements over the equatorial central Pacific, *Monthly Weather Rev.*, 98, No. 11, 823-831.
- Dietrich, G., and K. Kalle (1957), Allgemeine Meeveskunde: eine Einführung in die Ozeanographie (General Science of the Sea: An Introduction to Oceanography), Gebrüder Borntraeger, Berlin, 492 pp.
- Droppleman, J. D., R. A. Mennella, and D. E. Evans (1970), An airborne measurement of the salinity variations of the Mississippi River outflow, *J. Geophysical Res.*, 75, No. 30, 5909-5913.
- Hansen, D. V., and G. A. Maul (1970), A note on the use of sea surface temperature for observing ocean current, *Remote Sensing of Environment*, 1, 161-164.
- Higer, A. L., H. S. Thomson, F. J. Thomson, and M. C. Kolo-pinski (1970), Application of multispectral remote sensing techniques to hydrobiological investigations in Everglades National Park, Technical Report 2528-5-T (U.S. Geological Survey, Washington, D. C.).
- Hollinger, James P. (1971), Passive microwave measurements of sea surface roughness, *IEEE Trans. on Geoscience Electronics*, GE-9, No. 3, 165-169.
- House, F. B. (1965), The radiation balance of the earth from a satellite, PhD thesis, Dept. of Meteorology (The Univ. of Wisconsin, Madison, Wisconsin).
- Kimball, H. H. (1928), Measurements of solar radiation intensity and determination of its depletion by the atmosphere, *Monthly Weather Rev.*, 56, 393.
- Krueger, A. F., and T. I. Gray (1969), Long-term variations in equatorial circulation and rainfall, *Monthly Weather Rev.*, 97, No. 10, 700-711.

- London, J. and T. Sasamori (1971), Radiative energy budget of the atmosphere, COSPAR Space Research XI, 1 (Akademie-Verlag, Berlin), 639-649.
- McManus, R. G., A. Chabot, and I. Goldstein (1968), CO<sub>2</sub> laser Doppler navigation proves feasible, *Laser Focus*, 29, 21-28.
- Mairs, R. (1970), Oceanographic interpretation of Apollo photographs, *Photogrammetric Engineering*, 36, No. 10, 1045-1058.
- Maul, G. A. (1972), A sequence of Gulf Stream trajectories measured by ship and satellite (in preparation).
- Munk, W. H., and B. D. Zetler (1967), Deep sea tides: A program, *Science*, 158, No. 3083, 884-886.
- Namias, J. (1969), Seasonal interactions between the north Pacific Ocean and the atmosphere during the 1960's, *Monthly Weather Rev.*, 97, No. 3, 173-192.
- NASA Report, Solid earth and ocean physics, Report of a study at Williamstown, Massachusetts, August 1969, Sponsored by NASA-Electronics Research Center MIT (Measurement Systems Laboratory, Cambridge, Massachusetts).
- Nordberg, W., J. W. Conaway, D. B. Ross, and T. Wilheit (1971), Measurement of microwave emission from a foam covered, wind driven sea, *J. Atmos. Sci.*, 28, No. 3, 429-435.
- Paris, Jack F. (1969), Microwave radiometry and its application to marine meteorology and oceanography, Ref. No. 69-IT, Dept. of Oceanography (Texas A&M University, College Station, Texas).
- Paris, Jack F. (1971), Transfer of thermal microwaves in the atmosphere, II, Dept. of Meteorology, Texas A&M University, College Station, Texas, Contract Final Report, NASA Grant NGR 44-001-098, NASA, GSFC, 211 pp.
- Quinn, W. H., and W. V. Burt (1968), Incoming solar radiation over the tropical Pacific, *Nature*, 217, No. 5124, 149-150.
- Quinn, W. H. (1970), Prediction of abnormally heavy precipitation over the equatorial Pacific dry zone, *J. Appl. Meteor.*, 9, No. 1, 20-28.

- Ramsey, R. C. (1968), Study of the remote measurement of ocean color, Final Report (Prepared by TRW for NASA Headquarters, Washington, D. C.).
- Ross, D. S., and R. C. Jensen (1969), Experiments in oceanographic aerospace photography: Ben Franklin special filter tests: NASA, 2nd Annual Earth Resources Aircraft Program Status Review V. 111, Houston, Texas, 51-1 to 51-32.
- Ross, D. B., V. J. Cardone, and J. W. Conaway (1970), Laser and microwave observations of sea surface condition for fetch-limited 17 to 25 m/sec winds, *IEEE Trans. on Geoscience Electronics*, GE-8, No. 4, 326-336.
- Townsend, J. W., Jr. (March 31, 1971), Letter to L Jaffe, NASA Headquarters, about NOAA's interest to altimetry (Appendix B in this report).
- Vonbun, F. O. (1970), Geodetic satellite mission and spacecraft (GEOS-C) NASA Identification a. 12 (Goddard Space Flight Center, Greenbelt, Maryland).
- Vonder Haar, T. H. (1968), Variation of the earth's radiation budget, PhD thesis, Dept. of Meteorology (The University of Wisconsin, Madison, Wisconsin).
- Vonder Haar, T. H., and K. Hanson (1969), Absorption of solar radiation in tropical regions, *J. of Atmos. Sci.*, 26, No. 4, 652-655.
- Walker, G. T. (1924), Correlation in seasonal varieties of weather: IX. A further study of world weather, *Memoirs of the Indian Meteorol. Dept.*, 24, Part 9, Calcutta, 275-332.
- Wooster, W. S. (1960), El Niño, California Coop. Fisheries Invest. Reports, 7, 43-45.
- Wyrtki, K. O. (1965), The average annual heat balance of the north Pacific Ocean and its relation to ocean circulation, *J. Geophys. Res.*, 70, 4547-4559.
- Yaplee, B. S., A. Shapiro, D. Hammond. B. D. Au, and E. A. Uliana (1971), Nanosecond radar observations of the ocean surface from a stable platform, *IEEE Trans. on Geoscience Electronics*, GE-9, No. 3, 170-174.
- Zetler, B. D., and G. A. Maul (1971), Precision requirements for a spacecraft tide program, *EOS Trans. of the American Geophysical Union*, 52, 250.



## APPENDIX A

March 31, 1971

Mr. Leonard Jaffe  
Deputy Associate Administrator  
for Space Science and Applications  
National Aeronautics & Space Administration  
Washington, D. C.

Dear Len:

The purpose of this letter is to state NOAA's interest in altimetry experiments on proposed NASA satellites such as GEOS-C. We believe these experiments are very important and offer much promise for the future in the field of oceanography and earth sciences.

From our analysis, it is clear that the matter of system accuracy is all important. Accuracies better than one meter will clearly excite the research community and make possible a number of unique and very meaningful experiments such as on ocean tides and dynamics, on ocean surface slopes, and on general sea state monitoring and predicting. If the system accuracy is poorer than one meter, there are still some valuable experiments that could be performed, and one could make use of the data for preparing for more accurate experimentation later on.

Hence, our position is that we urge the highest practical system accuracy. In a crude sense our interest goes up exponentially as system accuracies increase linearly.

Sincerely yours,

John W. Townsend, Jr.  
Associate Administrator

bcc: WNHess, Boulder, Colo.  
DAJones, Rm 1006, Bldg 1  
HBStewart, Miami, Fla.  
LWSwanson, Rm 1015, Bldg 1



**U.S. DEPARTMENT OF COMMERCE**  
**Environmental Science Services Administration**  
RESEARCH LABORATORIES  
Atlantic Oceanographic and  
Meteorological Laboratories  
901 South Miami Avenue  
Miami, Florida 33130

Date: January 5, 1971

Reply to  
Attention of: RF20x5

Subject: Status of GEOS-C Radar Altimeter and its use in Oceanography

To: Dr. Harris B. Stewart, Jr.

## 1. Background

The Geodetic satellite GEOS-C is scheduled for launch late in 1972; on board will be a number of position-determining instruments designed to refine measurements of the geoid to an accuracy of about 5m. These include radar and laser reflectors; doppler navigation; strobe lights; satellite-to-satellite tracking; and an X-band radar altimeter. The latter attracted my attention as a potentially useful tool for oceanography, and B. Zetler and I visited several Washington area laboratories during December 14-18, 1970, to gather further information on it.

The satellite will be in a low inclination orbit ( $i=22^\circ$ ) with its altitude ranging between 700 and 1500km, and will be gravity-gradient stabilized to within  $1-2^\circ$  of the local vertical. Under these conditions it will be observable overhead from the Caribbean and at slant angles from Key West. The radar will be a 3-cm, short pulse ( $\tau_p \approx 50\text{ns}$ ) device with a beam width of about  $3.5^\circ$  and an average power of 500W, available something like 50% of the time at best. The designed instrument precision in altitude is 1m rms; the overall system precision is intended to be 5m once the geodetic reference surface is further refined. Note that these numbers are apparently rms errors; there may well exist much larger biases; i.e., the absolute accuracy in position is considerably poorer than the precision, or the repeatability. Indeed, the radar altimeter may be the means by which this bias is reduced.

However, the advertised function of the radar is not to improve accuracy but simply to delineate some of the problems associated with a satellite altimeter; second-or third-generation altimeters based on GEOS-C experience could be expected ultimately to yield a 10-cm precision capability, whereupon the device becomes interesting for accurate measurements of sea surface slopes, tides and the like.

## 2. Uses of the Radar Altimeter

Even as it stands, the GEOS-C radar may nevertheless provide coarse information on slopes, tides and sea state. As implied in Zetler's memo (Ref. 1), the radar precision is probably too poor to make tidal measurements directly; however, when the radar height measurement is combined with a single, precise satellite range determination - 1.0m obtained from a laser rangefinder and an accurate, short-arc orbit prediction immediately thereafter (valid for track lengths of the order of 100km), it may be possible to observe the following in semiquantitative fashion:

- a.) The 15-m depression in sealevel associated with the Puerto Rico trench, which should be readily detectable during a single pass as a local variation in ocean-satellite separation (W. von Arx is pursuing this);
- b.) Local sea surface slopes such as arise from western oceanic boundary currents (assuming the satellite track to cross such areas);
- c.) With low (or zero) accuracy, deep sea tides.

By looking not at the altitude but instead at the detailed shape of the returned radar pulse in time, the average roughness of the sea surface may be obtained from the distortions which the ocean wave spectrum introduces into this shape. For example, a 10ns pulse occupies some 3m of space along the direction of propagation, and if the variations in the height of the reflecting sea surface are of this order or more, a significant smearing out of the return echo should occur. The research problem is then to discover the quantitative relationships between the actual state of the sea and the broadening of the echo, undoubtedly a project of several years' duration.

Assuming that the information hidden in the pulse can be ultimately deciphered, it is then possible to conceive of a system of several satellites that could provide shipping and weather services with world-wide monitoring of gross average, sea conditions. The data gathered from the altimeters could be processed and digested on the ground and read back into the satellites in a form suitable for relay to ships upon query, so that considerably more information than the instantaneous return under the vehicle would be available. Such a system is in the same spirit as the Satellite Navigation System and indeed its necessity is very nearly spelled out in NOAA's mission statement.

J. R. Apel

Reference 1: "Spacecraft Oceanography Proposal: Tidal measurements (Sampling and Accuracy Problems)", B. Zetler (1970).



## A Determination of Horizontal Divergence in the Gulf Stream off Cape Lookout

FRANK CHEW AND G. A. BERBERIAN

*Atlantic Oceanographic and Meteorological Labs., ESSA, Miami, Fla.*

(Manuscript received 4 May 1970)

### ABSTRACT

A horizontal divergence of  $2 \times 10^{-5} \text{ sec}^{-1}$  was determined by tracking three shallow drogues in the speed axis of the Gulf Stream. Concurrent bathythermograph soundings along a drogue track support this magnitude. The data also provide estimates of the strength of turbulence encountered. In terms of the neighbor diffusivity, they amount to  $2 \times 10^5 \text{ cm}^2 \text{ sec}^{-1}$  for a drogue separation scale of 4 km, and  $4 \times 10^4 \text{ cm}^2 \text{ sec}^{-1}$  for the 2-km scale.

### 1. Introduction

The three variables entering the theorem of potential vorticity conservation are the Coriolis parameter  $f$  and its latitudinal variation, the horizontal divergence  $D$ , and the vertical component of relative vorticity  $\zeta$ . Of these,  $D$  may have the least magnitude as in the discussion by Warren (1963) of topographic meandering where the magnitude of  $D$  is of the order of  $10^{-7} \text{ sec}^{-1}$ . However, in situations where the change in  $\zeta$  is rapid, we may expect a much larger  $D$ . For example, if the order of magnitude of relative vorticity change in one day is that of  $f$ , we have  $D \approx (1/f)(d\zeta/dt) \approx 10^{-5} \text{ sec}^{-1}$ . Such changes were envisaged by Newton (1961) and Chew and Berberian (1970). Although the latter represents a 100-fold increase, our ability to measure it directly remains marginal, unless conditions are optimal. This paper reports on a direct determination of local horizontal divergence in the Gulf Stream, together with a discussion of its implication.

### 2. The measurements

In conjunction with a Gulf Stream study by Richardson *et al.* (1969), four series of drogues were tracked by ESSA personnel on board the ESSA ship *Mt. Mitchell* in the offings of Onslow and Rayleigh Bays in June 1968. However, weather and sea conditions prevented simultaneous location by radar of all drifting drogues except for the final set, when the sea became smooth after the passage of a weather front. The light and variable winds also precluded the occurrence of Ekman divergence as discussed by Niiler (1969). This report is devoted to the last series only.

The 8.5 m diameter parachute drogue was of conventional design; it was attached by a 4 mm ( $\frac{5}{32}$  inch) diameter steel cable to a surface float of tire inner tube to which were lashed wooden cross arms supporting an aluminum pole that extended 2.5-3.0 m above the float.

In turn, the pole supported passive radar reflectors, an identifying blinking light, and marks.

The drogues were released in two groups of three each, and tracking was done by visiting and monitoring each drogue in turn for 1 hr while locating the others by radar. For each observation, the sighting of the drogues on radar was recorded manually with simultaneous plotting on the Decca Automatic Radar Plotter; as a further backup, 20 photographs of the radar scope display were taken over a 1-min interval for each observation. When on station, drogue positions were recorded once every 10 min; at the start and end of each drogue visit, a bathythermograph (BT) sounding was made and a surface water sample collected. A thermistor was used to continuously record the temperature of the water at  $\sim 2$  ft below the sea surface. The accuracy of the radar range reading is  $\pm 200$  m, and of azimuth  $\pm 2^\circ$ ; at the range of interest, the latter also amounted to  $\pm 200$  m. Navigation control was by Loran A with an accuracy of  $\pm 450$  m generally.

### 3. The data

Initially, two sets of three drogues each at two different depths were tracked. However, two drogues were later lost, presumably from leaks in the inner tubes serving as floatation units. For both original and re-

TABLE 1. Drogue releases and recovery times.

Drogue no.	Release (Date)	Release (GMT)	Recovery (Date)	Recovery (GMT)	Depth of parachute (ft)
10	29 June	1220	30 June	1222	150
11	29 June	1237	lost		150
12	29 June	1255	30 June	1324	150
13	29 June	1628	1 July	0230	65
14	29 June	1654	lost		65
15	29 June	1721	1 July	0330	65
14a	30 June	1806	lost		65



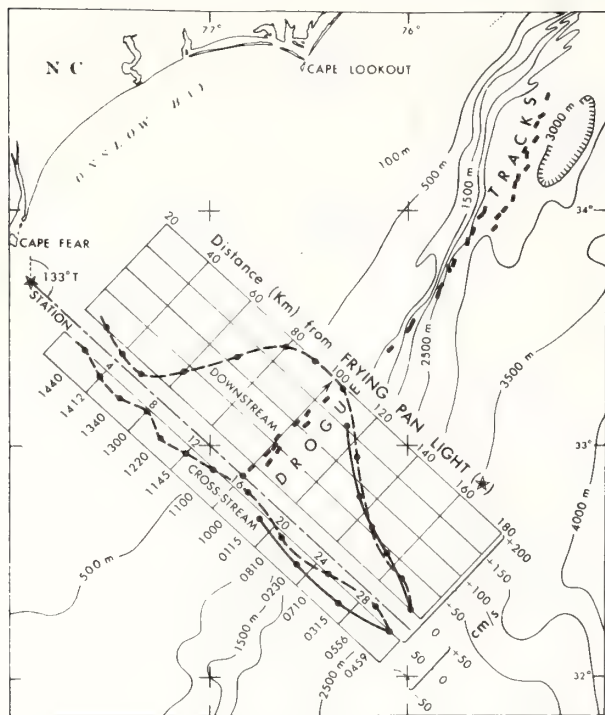


FIG. 1. Drogue tracks and cross-stream profile of surface current in the offings of Cape Fear and Cape Lookout. For drogues, each dash represents a 1-hr track. Surface currents are given in components along compass direction  $43^\circ$  true (downstream) and  $133^\circ$  true (cross stream). Universal time indicates when current was measured on 29 June 1968. Current data were supplied by W. S. Richardson.

placement drogues, Table 1 gives the depths and times of release and recovery.

For their transport measurement, Richardson *et al.* (1969) had selected a section across the stream that started from Frying Pan Light on a course of  $133^\circ$  true, and had, on the day of drogue releases, made the measurement of surface current shown in Fig. 1. All drogues were deployed at station 16 on this section. They are seen to follow nearly straight tracks more or less parallel to shallow bottom contours such as the 100 m isobath, but to cut across the deeper isobaths (1000–2000 m) at a considerable angle.

Fig. 2 presents a plot of the distance traversed by each drogue against time. The slopes of the curves, fitted by eye, give the speeds of the drogues. For all drogues, the initial velocity was  $200 \pm 5 \text{ cm sec}^{-1}$  on a weakly anticyclonic path. This compares favorably with Richardson's observation at Station 16 of a downstream speed of  $200 \text{ cm sec}^{-1}$  and a cross-stream speed of  $8 \text{ cm sec}^{-1}$  toward deeper water, although the time difference between the two independent sets varied from 2–7 hr. For drogues 13 and 15, in particular, the initial speed was  $200 \text{ cm sec}^{-1}$ ; they then slowed to  $160 \text{ cm sec}^{-1}$  after 25 hr, but later returned to a somewhat higher speed of  $170 \text{ cm sec}^{-1}$  toward the end of the observation period.

The beginning and end portions of the paths shown in Fig. 1 are enlarged and illustrated with a procession of triangles in Figs. 3 and 4. The vertices of the successive triangles represent the successive locations of the three drogues located simultaneously by radar. Positive identification, frequent monitoring, and two sets of backup data remove all doubts in the sequence of development shown in the figures, where for clarity of presentation, only about half the data are depicted. The salient features are: 1) the curvature of the paths; 2) the crossing of the paths of drogues 14a and 15; and 3) the rotation, deformation, and change in the size of the triangles. Some measures of these kinematic parameters for the whole series are shown in Fig. 5.

Fig. 6 shows the temperature sections along the paths of drogues 12 and 15, respectively, where all BT soundings were taken by the same instrument and are plotted without correction to facilitate detection of changes. Finally, in Fig. 7 we have plotted against time the natural logarithm of the area of the triangles formed with drogues 13, 14a and 15 as vertices.

#### 4. Turbulence

To help assess the accuracy of horizontal divergence measurements, we shall first consider the horizontal turbulence encountered, utilizing the theory of neighbor diffusivity which states that the neighbor diffusivity  $F$  is related to the neighbor separation  $L$  by

$$F = BL^{\frac{1}{2}}, \quad (1)$$

where  $B$  is a coefficient whose magnitude is poorly determined, but ranges from 0.001–0.01 when  $F$  is in  $\text{cm}^2 \text{ sec}^{-1}$  (Okubo, 1962). To avoid this uncertainty, we determined  $F$  directly by the method given by Stommel (1949), with the further assumption that the field of

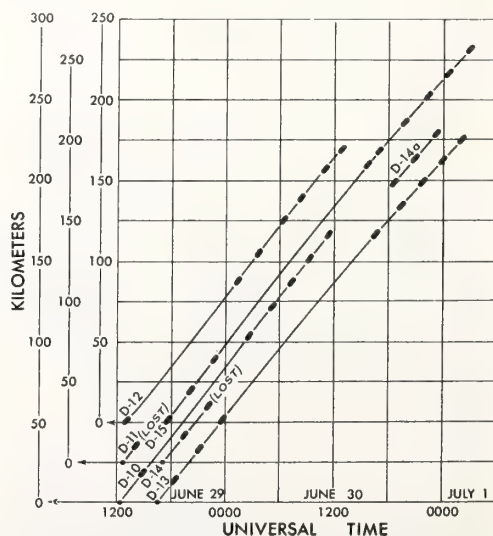
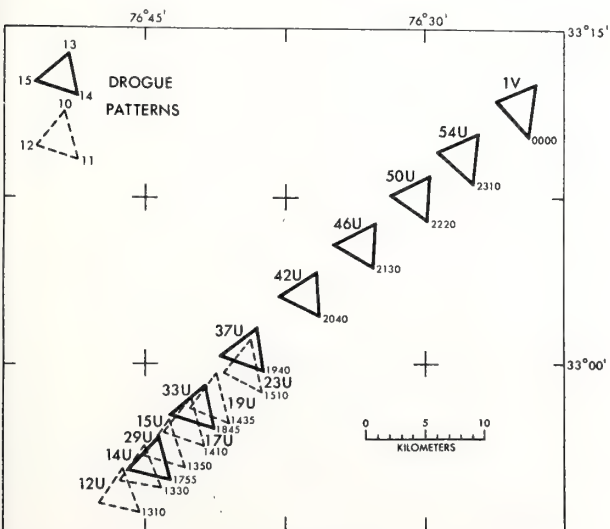


FIG. 2. Time-distance plot for all drogues. Initial slopes correspond to a drogue speed of  $200 \text{ cm sec}^{-1}$ , final slopes to 160 and  $170 \text{ cm sec}^{-1}$ .

Number of drogue pairs	$F$ ( $10^4 \text{ cm}^2 \text{ sec}^{-1}$ )	Degrees of freedom, $n^*$	95% Confidence level** ( $10^4 \text{ cm}^2 \text{ sec}^{-1}$ )
161	19.3	18	11.0-42.4
90	3.7	13	3.9- 9.6

\*\* 95%, for a Chi-square probability distribution.

In general,  $F$  contains contributions from many processes, some of which may not be stochastic and are



governed by other than probabilistic law. To detect the presence of a nonstochastic component, we apply the trend test to the data presented in Fig. 5. For  $N$  observations of a random variable, where the observations are denoted by  $x_i, i = 1, 2, 3, \dots, N$ , we count the number of times that  $x_i > x_j$ , for  $i < j$ . Each such inequality is called a reverse arrangement and the total number is denoted by  $A$ . The test is a relatively powerful one for detecting a monotonic trend. We confine the test to the distance between drogues with the results summarized in Table 3. During the first 10 hr, two out of three drogue pairs underwent separations that are compatible with stochastic processes, particularly the drogue pairs oriented closest to the downstream direction of the current. However, during the last 6 hr, all

Date	Time (GMT)	Drogue pair	<i>N</i>	<i>A</i>
29 June	1255-1510	10-11	12	8*
		12-10	12	27
		12-11	12	31
	1735-2350	13-14	31	151*
		14-15	31	220
30 June	0110-1210 1815-0010	13-15	31	241
		10-12	39	235*
		13-15	30	16*
		13-14a	30	77*
		14a-15	30	319*

\* Indicates rejection, at the 2% level of significance, of the hypothesis that the series were independent observations of a random variable (see, e.g., Bendat and Piersol, 1966).

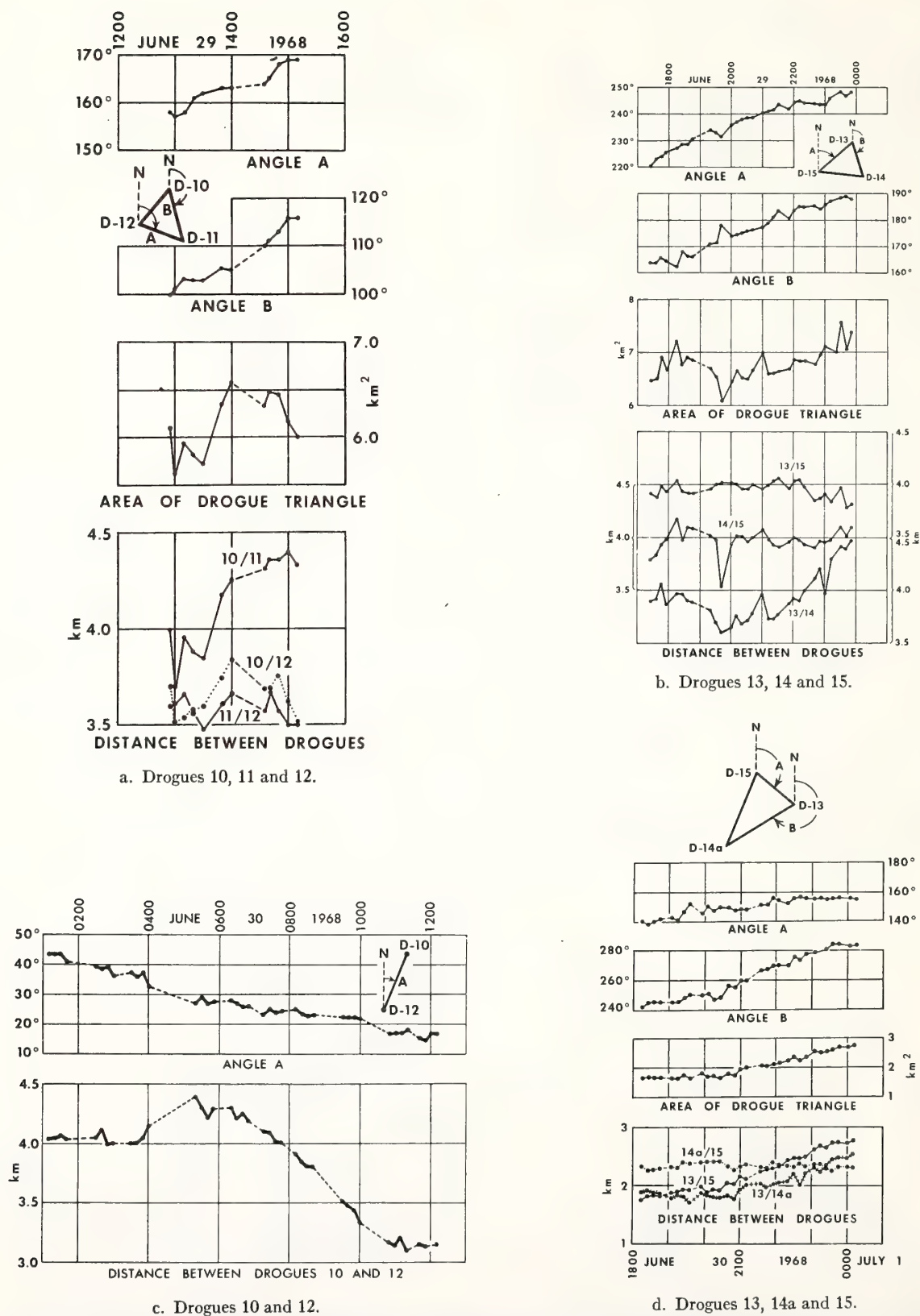


FIG. 5. Observed separation between drogue pairs, orientation of lines joining drogue pairs, and area of resulting triangles. An especially noteworthy feature is the large change in the orientation and length of the line joining drogue pair 13 and 15 between sequences b and d.



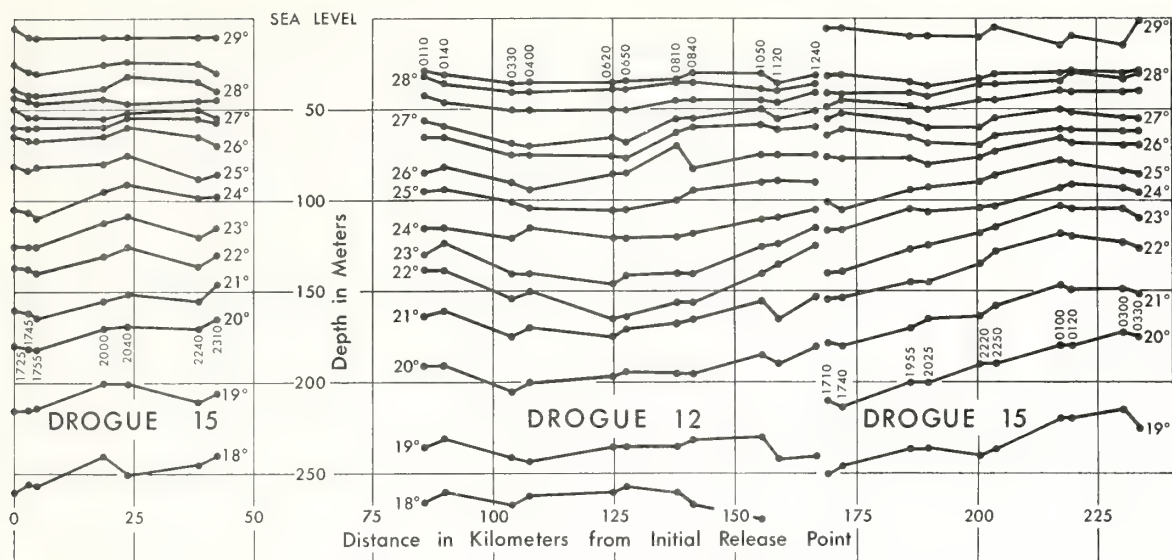


FIG. 6. Vertical temperature ( $^{\circ}\text{C}$ ) sections along paths of drogues 12 and 15. All soundings were made from same mechanical BT. Universal mean time began on 28 June and ended on 1 July 1968.

three drogue pairs underwent separations that are compatible only with non-stochastic processes. Generally, the overall situation was one of evolution toward a systematic trend.

### 5. Horizontal divergence

When there is no vertical shear in the horizontal velocity, the horizontal divergence  $D$  of a moving column is given by

$$D = (1/A)(dA/dt) = -(1/H)(dH/dt), \quad (2)$$

where  $A$  is the horizontal area of a column of height  $H$ . Vertical shear is usually present in the current, but that related to baroclinicity in the region of the current away from the cyclonic flank is generally weaker (see Richardson *et al.*, 1969). More pertinent to the present situation is the vertical shear associated with some of the many internal wave modes that are possible in a stratified fluid. The situation is simpler if a single inter-

nal wave mode predominates, as appears to have been the case during the last 6 hr. To see this, we view the temperature sections of Fig. 6 against the results of Table 3. The emergence of a definite trend in drogue separation implies a relative decline of stochastic processes and a concurrent rise of nonstochastic ones. Since the winds were light and the sea calm, the situation must be accompanied by a similar transition in the processes within the water. Turning to the temperature sequence in Fig. 6, we see undulations of the isotherms of many scales. But there is a tendency for a more readily recognizable pattern and a larger undulating amplitude in the lower isotherms as the tracking proceeded—a tendency matching the one for drogue separation. In the last temperature sequence, corresponding to the last set of three entries in Table 3, the field is dominated by the simultaneous and continuous rise of the 20–23°C isotherms. From their respective initial depths, they rose in near unison to depths 30–35 m shallower. The evidence is fragmentary and inconclusive, but it is not incompatible with the suggestion of the arrival of a progressive, large-amplitude internal wave. In the progression of the wave, horizontal divergence is involved with a magnitude given by the right member in (2) if the vertical shear of horizontal motion is small. Hence, from the last sequence in Fig. 6, we find

$$D = -(1/H)(dH/dt) \approx (1/120\text{m}) \times (35\text{m}/6\text{hr}) = 1.4 \times 10^{-5} \text{ sec}^{-1}. \quad (3)$$

While from Fig. 5d, with some smoothing of the time-area plot, we have

$$D = (1/A)(dA/dt) \approx (1/2.2\text{km}^2)(1\text{km}^2/6\text{hr}) \approx 2.1(\pm 0.5) \times 10^{-5} \text{ sec}^{-1}. \quad (4)$$

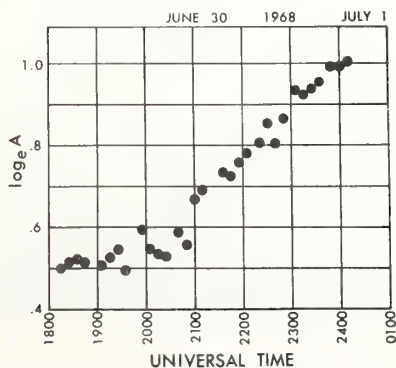


FIG. 7. Plot of the natural logarithm of the area of the triangles depicted in Fig. 4 vs time. The zero of the ordinate starts at 23.03 corresponding to the natural logarithm of  $1 \text{ km}^2$ .



These independent estimates are in agreement, for the difference may be reasonably ascribed to errors introduced when we extended horizontal divergence, actually a point property of the fluid, to situations covering areas and volumes.

## 6. Discussion

The horizontal divergence  $D$  affects the neighbor diffusivity  $F$ . An estimate of the order of magnitude of this effect is direct, if the square of the drogue separation  $L$  is proportional to the area  $A$ . For this purpose, we consider  $D$  a constant for the period in order to obtain from the left two members of (2) the expression

$$A = A_0 e^{Dt}, \quad (5)$$

a growth that is supported by the plot in Fig. 7 of the natural logarithm of the area against time. Thus, replacing  $A$  and  $A_0$  in (5) by  $L^2$  and  $L_0^2$ , we have from (1)

$$F = BL^3 \approx BL_0^3 (e^{Dt})^3 = 4 \times 10^4 \text{ cm}^2 \text{ sec}^{-1}, \quad (6)$$

for  $B = 1/400$ ,  $D$  as in (4),  $L_0 = 2$  km, and  $t = 6$  hr. Unless  $B$  is substantially smaller, we may conclude that the magnitude of  $F$  for the last 6 hr was due primarily to the process of horizontal divergence.

The progression of a wave is accompanied by horizontal divergence. If the divergence (4) is so related, the features of the responsible wave appear to share some of the characteristics of the Sverdrup wave, in the terminology of Veronis and Stommel (1955). On the basis of the 6 hr taken for the drogues to cover an apparent wavelength of 50 km, these features have a wavelength of the order of 200 km and a tidal or near-inertial frequency.

When long, internal waves of near-inertial frequency are present in the Gulf Stream, interaction between them appears likely. One aspect is the direct effect of the horizontal divergence of the wave on the relative vorticity of the current; we consider this briefly. Neglecting both the friction and solenoid terms, and writing  $f$  for the Coriolis parameter, the equation for time change in the vertical component of relative vorticity  $\zeta$  of a moving column is

$$d\zeta/dt = -(\zeta + f)D - \mathbf{V} \cdot \nabla f, \quad (7)$$

where all vectors are horizontal. We can evaluate  $\zeta$  from the observed data that went into the illustration in Fig. 4. Using natural coordinates, with the curvature and shear terms having opposite signs in the present case, we have

$$\begin{aligned} \zeta &= KV - (\partial V / \partial n) \approx (170 \text{ cm sec}^{-1} / 85 \text{ km}) \\ &\quad - (5 \text{ cm sec}^{-1} / 1.5 \text{ km}) \approx -1 \times 10^{-5} \text{ sec}^{-1}. \end{aligned} \quad (8)$$

Consequently, the first term in the second member of (7) is of the magnitude

$$\begin{aligned} -(f + \zeta)D &\approx -(7 \times 10^{-5})(1.7 \times 10^{-5}) \\ &\approx -120 \times 10^{-11} \text{ sec}^{-2} \end{aligned} \quad (9)$$

for  $f = 8 \times 10^{-5} \text{ sec}^{-1}$ , and  $D$  taken as the average of (3) and (4). The latitudinal change in the Coriolis parameter, important in the model of Warren (1963), is at most, in the present case, of the magnitude of  $(170 \text{ cm sec}^{-1})(2 \times 10^{-13} \text{ cm}^{-1} \text{ sec}^{-1}) = 3.4 \times 10^{-11} \text{ sec}^{-2}$ . Hence, in 6.5 hr, the amount of negative relative vorticity gained by the column is

$$(-120 + 3.4) \times 10^{-11} \times 2.35 \times 10^4 = -2.7 \times 10^{-6} \text{ sec}^{-1},$$

or one-third of the local magnitude of  $f$ . As the latitudinal change in  $f$  is small in comparison, Eq. (7) may be reduced to

$$(f_0 + \zeta)A = \text{constant}, \quad (10)$$

where  $f_0$  is a constant. The application of (10) to a portion of the Gulf Stream system was anticipated by Stommel (1953) who discussed the effect of the constriction of the Florida Channel on the relative vorticity of the Florida Current.

## 7. Conclusion

We have shown, on favorable occasions, that it is feasible to measure horizontal divergence on a scale relevant to potential vorticity conservation on an  $f$  plane. In this instance, the mechanism responsible for the divergence appears related to a large-amplitude, long internal wave of tidal or near-inertial frequency.

*Acknowledgments:* We are indebted to Capt. K. A. McDonald and his spirited officers and men for their zealous help on board the Coast and Geodetic survey ship *Mt. Mitchell*.

## REFERENCES

- Bendat, J. S., and A. G. Piersol, 1966: *Measurement and Analysis of Random Data*. New York, Wiley, 390 pp.
- Chew, Frank, and G. A. Berberian, 1970: Some measurements by shallow drogues in the Florida Current. *Limnol. Oceanogr.*, **15**, 88-99.
- Ichiye, R., and F. C. W. Olson, 1960: On neighbor diffusivity in the ocean. *Deut. Hydrol. Z.*, **13**, 13-23.
- Newton, C. W., 1961: Estimates of vertical motions and meridional heat exchange in Gulf Stream eddies, and a comparison with atmospheric disturbances. *J. Geophys. Res.*, **66**, 853-870.
- Niiler, P. P., 1969: On the Ekman divergence in an oceanic jet. *J. Geophys. Res.*, **74**, 7048-7052.
- Okubo, A., 1962: A review of theoretical models for turbulent diffusion in the sea. *J. Oceanogr. Soc. Japan*, 20th Anniv. Vol., 286-320.
- , 1968: A new set of oceanic diffusion diagrams. Chesapeake Bay Inst., Tech. Rept. 38, 35 pp.
- Richardson, W. S., W. J. Schmitz and P. P. Niiler, 1969: The velocity structure of the Florida Current from the Straits of Florida to Cape Fear. *Deep-Sea Res.*, **16**, 225-231.
- Stommel, 1949: Horizontal diffusion due to oceanic turbulence. *J. Marine Res.*, **8**, 199-225.
- , 1953: Examples of the possible role of inertia and stratification in the dynamics of the Gulf Stream system. *J. Marine Res.*, **12**, 184-195.
- Veronis, G., and H. Stommel, 1955: The action of variable wind stresses on a stratified ocean. *J. Marine Res.*, **15**, 43-75.
- Warren, B. A., 1963: Topographic influence on the path of the Gulf Stream. *Tellus*, **15**, 167-183.

*Dr. Hansen is director, Physical Oceanography Laboratory, Atlantic Oceanographic and Meteorological Laboratories, National Oceanic and Atmospheric Administration, Miami, Florida. This paper was presented at a Sunoco Science Seminar at the NSTA annual convention in Cincinnati, Ohio, March 14, 1970.*

**S**IGNS abound that the 1970s are to be a decade of concern for the environment. These are favorable signs for those interested in the scientific study of the oceans. As concern and displeasure grow over the unsightliness of environmental pollution, we are beginning to see that knowledge of the behavior of the water-covered portion of the earth is an essential ingredient to rational decisions on the local scale

and the key to avoiding potential planetary disasters.

Most oceanographic research has been and continues to be done by a few relatively affluent nations, notably, Canada, France, Germany, Japan, the United Kingdom, the United States, and Russia. The oceanographic capability of this country has grown most impressively in the last two decades, especially during the post-Sputnik scientific renaissance. About 1960, oceanography became a glamour field of science, and a considerable national effort was put into strengthening it. Due to the considerable investment required for facilities and equipment and due to the lack of immediate economic return, most oceanographic research has been sup-

ported by the federal government either in the name of basic research or national defense. In 1966, President Johnson announced a new focus on clearer objectives in marine affairs and asked for establishment of a commission to chart the new course. But in spite of initial high expectations and numerous studies of how the objectives were to be reached, the oceanographic community has grown increasingly frustrated. Debate over objectives and their implementation continues, and more recently there has been flagging support for oceanography, a condition shared with many other fields of science.

While the nation's investment in oceanography has been small relative to that for space technology and other

## OCEANOGRAPHY FOR THE 1970s Donald V. Hansen







NOAA

*Menhaden, a type of herring, is extremely abundant off the east coast of the U.S.*

major programs, progress has been good. Discoveries have been made which are at least as important as those in space. We have reached a point where progress in the 1970s will be determined more by what we choose to do than by what we are able to do. It is appropriate, therefore, to attempt to place our expectation of ocean benefits in perspective so that the slender resources may be used wisely.

### Ocean Resources— Present Perspective

The "wealth of the ocean" is doubtless commonly oversold. Man's major activity in the ocean—71 percent or so of the earth's surface—is still the simple matter of making his way about it. The world's ocean freight bill is around

\$15 billion annually. Shipping is not an exploitable resource in the sense of extracting useful substances from the ocean, but substantial benefits are to be gained by further improving and extending this most efficient means of transport to new regions. The 1970 cruise of the super-tanker *Manhattan* was an ambitious industrial experiment in this area.

The monetary value of the world fish and shellfish catch is on the order of half the world freight bill. One commonly hears expectations that the "limitless" stock of food from the sea will feed untold billions of future earth population. The great magnitude of standing stock of some unexploited species is indeed misleading; it is well to remember in this connection the bison herds that once populated the

Great Plains. But in more dispassionate moments we accept that the ocean and its contents are, like the rest of our planet, finite. Fishermen know that with modern technology and the size of modern fleets, even pelagic stocks are easily overfished. The history of a number of important fisheries shows that the catch increases with effort up to a point, after which the return begins to decline. Herring and cod of the North Atlantic and the global whale fishery are prime examples.

The solar energy requirement for photosynthesis certainly sets an upper limit on sustainable food yields, but conditions of life in the ocean, such as generally lower fertility in the photic zone, make the ocean less productive than comparable land areas. Due to the larger ocean area, the total biological production appears to be about equal to that on land. But conditions for life in the sea force much of the product to be microscopic and so dispersed that it is not likely to be harvestable directly. There are no pelagic trees or cereals, hence the product must be concentrated to harvestable packets by intermediate organisms. Evaluation of this complex process is difficult, but present estimates suggest that the harvest could be increased by from two to five times present levels.

The value of gas and petroleum from offshore wells is now perhaps three-quarters that of fisheries and is growing very rapidly. For example, approximately 20 percent of U.S. petroleum resources and 15 percent of our production is from offshore sources. Production of other minerals from oceanic sources is still relatively minor, but it is certain to increase tremendously as high-grade ores on land run out.

For the United States, the order of things is somewhat peculiar in that marine-oriented recreation ranks near transportation in dollar value; offshore petroleum production is flourishing; but our fisheries constitute a disaster area. Waste disposal probably would rank quite high if one could put a realistic dollar value on it, which we as a nation have been disinclined to do. The ability of the ocean to absorb large but finite amounts of waste material is



NOAA

**AREAS OF  
PROTEIN DEFICIENCY**

**FERTILE AREAS  
OF THE OCEANS**

certainly a major resource, whether we like to think about it or not.

Once resources are defined, the major impact of oceanography will be its contribution to efficiency of operations in the marine realm, including provision of guidelines to avoid ecological disasters. Decimation of exploited species is of immediate concern to fishermen, but more subtle problems can involve us all. It has been estimated that perhaps two-thirds of all the DDT ever produced still exists and is making its way to the oceans. Likewise, herbicides and lead and other heavy metal compounds may be accumulating to the detriment of primary biological productivity in the ocean.

Another subtle and complicated problem concerns the relationship between climate and the oceans. Most members of the scientific community are aware that the increasing amounts of carbon dioxide released by burning

fossil fuels could alter the atmosphere's radiation balance and result in global climate change. Less generally recognized, however, is the fact that the ocean is the planet's great reservoir of carbon dioxide, as well as water. Upon dissolving in the ocean, carbon dioxide becomes available for photosynthesis. It reacts with water to provide the carbonate ions used by calcareous organisms. In consequence, the ocean contains 50 times as much carbon dioxide as does the atmosphere, and more than 90 percent of a perturbation of atmospheric carbon dioxide will ultimately reside in the ocean. The question, then, is how rapidly atmospheric carbon dioxide is equilibrated with the ocean and distributed within the great mass of its waters. This rate will determine how much carbon dioxide can safely be released to the atmosphere.

I turn attention now to some recent activities and new insights which affect

our ability to understand the ocean and to use its resources wisely.

## Ocean Basins

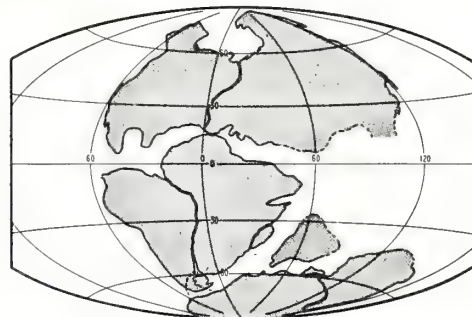
A revolution in geologic concepts is underway and that revolution is fired by oceanographic research. The concept of continental drift, advanced by the German geologist Alfred Lothar Wegener about a half century ago, long stood in poor repute, primarily because there were no apparent forces capable of pushing a continent. Geophysical surveys of the ocean basins are now providing strong support for this theory. Present interpretations indicate that new ocean floor material emerges from within the earth along the midocean ridges. The material is conveyed across the ocean basin and disappears beneath the continents, shifting the continents in the process.

A primary line of evidence for the continental drift concept is the pattern

*Robert S. Dietz and John C. Holden of the National Oceanic and Atmospheric Administration recently worked out this sequence of maps that for the first time identify the 200-million-year journey the continents have made across the face of the earth.*



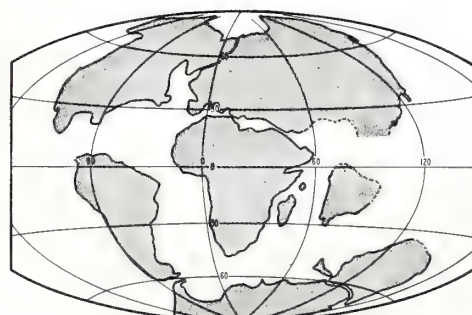
**PERMIAN** - 225 million years ago



**TRIASSIC** - 200 million years ago



**JURASSIC** - 135 million years ago



**CRETACEOUS** - 65 million years ago





It is being increasingly recognized that the behaviors of the two global fluids, ocean and atmosphere, are inseparable and must, therefore, be studied as a whole.

Solar radiation is the basic energy source for the circulation of both ocean and atmosphere. Studies like BOMEX (the Barbados Oceanographic and Meteorological Experiment) seek to analyze the various kinds of interactions.



of magnetic anomalies. It appears that the magnetic field of the earth has reversed polarity a number of times. As igneous rock emerges from within the earth it freezes-in the contemporary magnetic orientation, which is retained thereafter. As the sea floor moves away from the point of emergence, the record of magnetic reversals is preserved as though by a geophysical tape recorder. Events of the last few years are providing powerful new confirmation of these hypotheses.

The most exciting results have come from the investigations of the *Glomar Challenger*, a deep-ocean drilling ship operated by Scripps Institution of Oceanography under contract with the National Science Foundation. The first year's work of the *Glomar Challenger* resulted in discovery of oil and gas in the central Gulf of Mexico (the first such discovery in a deep-sea environment), and only small amounts of ferromanganese nodules in sediments at depth; these are both findings of immense practical value. This project has been extended until 1973 and is expected to produce further exciting results on the origin and nature of the ocean basins.

Short years ago we expected to find

a complete history of the earth locked in the ocean sediments, undisturbed by the erosion and turmoil through which the continental record of geologic history must be read. Now it appears that the ocean floor is in fact younger than the continents and younger than the ocean itself.

### Sea-Air Interaction

Another scientific endeavor that came into being in the last decade and will likely continue is large-scale study of sea-air interaction. At present, we are primarily interested in the influence of the oceans on weather, but it is generally accepted that the behaviors of the two fluids, ocean and atmosphere, are inseparable and must be studied as a whole. The basic energy source for the circulation of both mediums is solar radiation. This radiation is not efficiently absorbed by the atmosphere; rather, it penetrates to the earth's surface (predominantly the ocean) from which it is relayed to the atmosphere as longer wave radiation and latent heat of water vapor evaporated from the oceans. The ocean circulation in turn is driven by wind stress and exchanges of heat and water with the atmosphere. The ensuing circulations serve to transfer heat from low latitudes (where incoming radiation exceeds outgoing radiation at the top of the atmosphere) to high latitudes where there is a radiational deficit. The early studies are being done in the tropics where the energy flow is initiated.

Two such experiments were undertaken in 1969: the Atlantic Tradewind Experiment (ATEX), which involved four ships—two from the United Kingdom and one each from Germany and the United States—for a three-week period in March and April; and the Barbados Oceanographic and Meteorological Experiment (BOMEX), which used, in all, 12 ships, 28 airplanes, and 1,500 scientists. Preliminary results from BOMEX indicate that more solar radiation is absorbed in the atmosphere than has been thought and that the ocean currents are very different than indicated on charts.

The enormous number of environmental measurements made will require



*The sinking of the Titanic in 1912 renewed interest in ocean currents because of their importance in transporting icebergs into the North American shipping lanes.*

months or years for complete analysis. The results of these and larger projects to come will be appearing throughout the 1970s.

### Decade of Ocean Exploration

Presidents Johnson and Nixon both endorsed U.S. leadership in an International Decade of Ocean Exploration (IDOE) in the 1970s. It is unclear how vigorously IDOE will be pursued because of our current social, military, and economic commitments and because a substantial contribution from other countries is required. At least one project for IDOE, the Cooperative Investigation of the Caribbean and Adjacent Regions (CICAR) appears to be gaining momentum and may serve as a prototype for later projects in larger ocean basins. It also appears to be of considerable value for the U.S. interest in the Gulf of Mexico. The Gulf receives almost two-thirds of the waterborne natural, industrial, and agricultural pollutants of the United States, making it a likely candidate for pollution disaster. The flow of the Gulf Stream into and out of the Gulf is sufficient to completely renew Gulf waters in 30 months, but the extent to which the deep water and water of the western Gulf participate in this circulation is almost entirely unknown.

### Ocean Currents

One of the central problems of physical oceanography has been and remains that of transports—the movement of materials and energy by ocean

currents. During the birth of the industrial age and before the decline of the sailing ship in commerce, the transport of greatest interest was that of surface ships. (The speeds of ocean currents were not inconsiderable compared to those of the sailing vessels.) In the twentieth century the transports of greatest interest are much more subtle. The current favorites are transport of heat as it influences global weather and climate, transport of chemical nutrients as it influences fisheries, and transport of a variety of troublesome substances introduced by the activities of man.

Closure of the Suez Canal has also rekindled interest in the effects of currents on shipping. Experiments are in progress on optimizing use of the Gulf Stream to help tankers save a few hours between Gulf of Mexico oil fields and U.S. East Coast cities, but the real interest is in finding methods applicable for the run around Africa.

I will outline briefly some of the milestones in evolution of knowledge of currents in the North Atlantic Ocean, which, with the possible exception of the waters around Japan, is the best known major ocean region. I will focus on the Gulf Stream system as a familiar point of reference for North Americans and the most salient feature of the surface circulation of the North Atlantic.

### Early Charting of the Gulf Stream

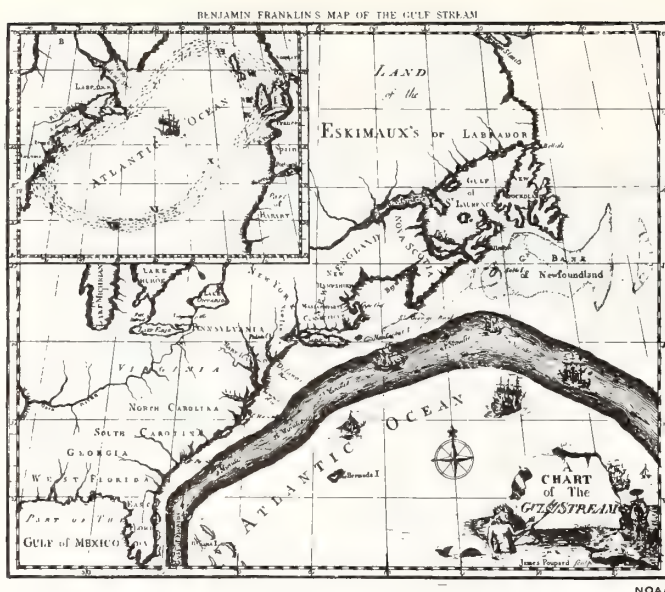
A general knowledge of the surface circulation and of the Gulf Stream was

used by the Spanish as early as 1519 in their annual voyages to and from the New World. Although a considerable body of practical knowledge was used by the great American whale fishery, the Stream was not charted for more systematic use until the 1780s. At that time, Benjamin Franklin, in his capacity as Postmaster General, had a chart of the Gulf Stream off New England drawn by Timothy Folger, a Nantucket whaler. The chart was printed by the General Post Office for use by the mail packets. This empirical approach was picked up and systematized by Matthew Fontaine Maury—now frequently cited as the father of American oceanography—who collated the information appearing in navigation logs of sailing ships, using the records of their drift to infer the ocean surface currents. In use of such data, averages of a large number of observations must be taken because of the imprecision of individual observations. Though many of the interesting and useful variations of the current are obscured by averaging, this technique is still the primary source of knowledge of the surface circulation in all published oceanic current charts.

During the same period the Coast and Geodetic Survey, directed by Alexander Bache, Franklin's grandson and an eminent scientist, among others, began a remarkable series of investigations of the Gulf Stream off the southeastern United States, from the Caribbean to Cape Hatteras. The Stream and its variations were metered directly from anchored ships—a feat not duplicated until very recent times—and some of the measurements are still the best available.

With the passing of the age of sail, interest in ocean currents declined for a number of years. The sinking of the steamship *Titanic* in 1912 provided new impetus for the observation of currents, because of their importance in transporting icebergs into the North Atlantic shipping lanes. These observations have been continued by the U.S. Coast Guard to the present. In such studies, average currents are of little value; week-to-week changes are all important.





Ben Franklin had this map of the Gulf Stream prepared when he was Postmaster General.

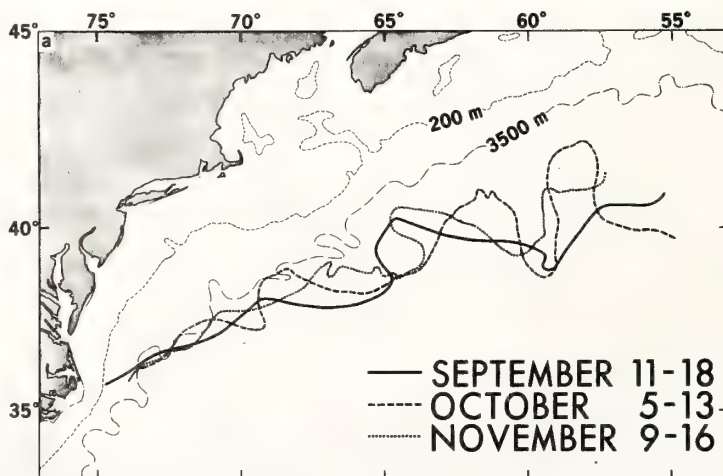
## Recent Analysis of Ocean Currents

The ice patrol work was made possible by development of a new technique—the geostrophic method—similar in principle to that by which winds are inferred from pressure patterns on a weather map. In application to the ocean, pressure cannot be directly measured, however. Instead, advantage is taken of the fact (not always true) that the surface currents are much more vigorous than the deeper waters, and the relative pressure is determined by integration of the density variations over the water column.

In the standard-temperature-and-pressure laboratory world we usually get by considering water as incompressible. Throughout the ocean, the density of water varies by approximately 7.5 percent, of which 5 percent is due to compression. The remaining 2.5 percent, the important part, is due to variation of temperature and salinity. To detect the variations of importance required development of special thermometers, special chemical methods, and special glassware.

The chemical method was based on the results of the British *Challenger* expedition of 1872-6 which showed that

the major ionic species dissolved in seawater occur in almost constant ratio and hence that determination of any one suffices. Determination of the chloride concentration by titration with silver nitrate was chosen as a practical method. Only in the last decade has the method been widely supplanted by modern electrical methods; the density tables of 1901 are still used.



Changing position of the Gulf Stream during three successive months in 1965. The lines show the month-by-month position of the core of the stream along the coast.

This method was applied in scientific investigations of the Gulf Stream soon following establishment of the Woods Hole Oceanographic Institution in 1931. The major goal was to monitor Gulf Stream transports as they might affect fisheries and climate in the North Atlantic and western Europe. To obtain sufficient measurements for a detailed description of the Gulf Stream was both tedious and expensive. The basic transport (of water) of the Stream could, however, be inferred from vertical soundings at just two stations. It was hoped to define standard stations that could be monitored for correlation with other events of interest. Because of confusing variations and indications of multiple streams, it was not possible to define the standard stations before the program was interrupted by World War II.

Following the war, scientific oceanographic research was pursued much more vigorously, particularly at the major centers such as Woods Hole. Synoptic surveys, accomplished by several ships working in coordination for two to several weeks, were done in 1950 and again in 1960. These projects showed the Stream to be coherent over hundreds of kilometers, but subject to wavelike meandering suggestive of that of the atmospheric jet stream. Theories based on hydrodynamic in-

stability, in which perturbations are able to extract energy from the basic current, or on effects of bottom topography, were advanced to explain this behavior; but the observations of Stream paths were too few to permit firm conclusions. A recent series of Stream path observations at monthly intervals by ESSA vessels<sup>1</sup> has shown that none of the present theories satisfactorily explains all features of the observations.

It appears that we do have a satisfactory explanation for the basic existence of the Gulf Stream. Details are still being debated, but the essential ingredients are the winds, which drive surface waters southward and westward over most of the North Atlantic; and the sphericity and rotation of the earth, which force a narrow return current on the western boundary of the ocean. Similar logic applied to the deeper waters (but with the flow driven by sinking of water in high latitudes and upward movement of deep water almost everywhere else) suggests that the deep circulation should be the exact opposite of that at the surface—its speed should be about 1 cm/sec; and it should be complete with a deep, opposite, counterpart to the Gulf Stream. It is now clear that this countercurrent exists, but attempts to demonstrate the existence of the general northward flow elsewhere have been thwarted by the discovery of variable currents on the order of 10 cm/sec which obscure the average flow. Because the effect of these transient currents on the average flow is unknown, it now appears that our understanding of ocean circulation may be as poor a representation of reality as the Hadley cell was of actual atmospheric winds.

One of the major problems in advancing knowledge of ocean currents has been the difficulty of obtaining use-

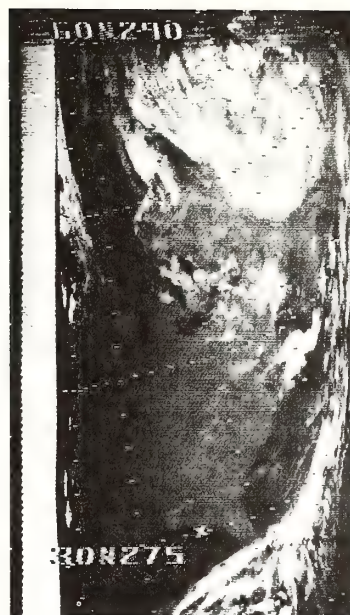
ful measurements. Current patterns can change too rapidly for a single ship to define more than their grossest features, and investigations involving several ships are expensive and difficult to organize. In the coming decade, however, there is the real possibility of observing oceanographic parameters related to ocean currents using satellite-mounted sensors. These sensors would provide observations of entire ocean basins in short times. Considerable work is being done at present on observations of sea surface temperatures using infrared sensors, but development of very precise satellite altimeters for observing variations of sea level can bring about a genuine revolution in observation of ocean currents by providing at last the badly needed measurement of absolute pressure gradient.

### The Coastal Zone

In the preceding pages, I have described developments in knowledge of the deep sea. By most measures other than national defense, however, the interest and emphasis of the nation, individually and collectively, will probably focus on what is described as the coastal zone. This zone is broadly defined as extending from the edge of the continental shelf, across the coastline, into the estuaries and the Great Lakes, and the land area affected by proximity to the ocean or the Great Lakes.

We are all aware of the growth of population generally. It is perhaps less well known to what extent this growth is occurring primarily in the coastal zone. Between 1860 and 1960 the fraction of the U.S. population living in counties bordering the sea or the Great Lakes increased from 25 percent to 45 percent. This is the region where man and the sea interact; and the interaction is becoming increasingly a two-sided proposition, as extensive modification becomes technologically possible. This is also the region where all marine economic activities have their greatest concentration, now and for the foreseeable future.

Traditionally, we have treated this margin of the sea, like other waterways, as property held in common, to be used by all according to their needs or de-



NOAA

*Infrared view of eastern U.S. was obtained in September 1966 by the research satellite Nimbus II. In processing, the usual arrangement of infrared photographs in which the warmest areas are the lightest has been reversed, so that the warm waters of the Great Lakes appear dark and the cold ice-crystal cirrus clouds over Florida (lower right) are light.*

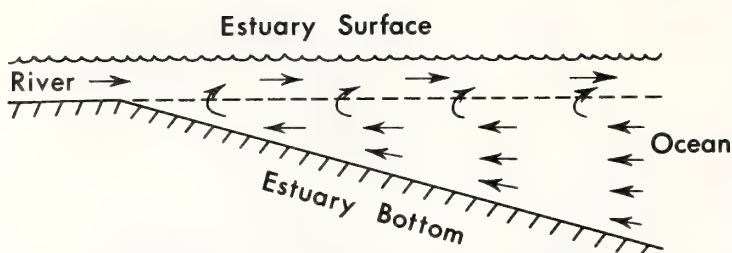
sires. With mounting population and economic pressures, this leads to a destructive procedure in which each sees a net personal gain in his personal contribution to overuse. Hence, this zone will be the scene not only of increasing activities and benefits during the 1970s, but also of increasing conflict and controversy. The general nature and importance of the biology and ecology of the region is currently receiving considerable exposure. For all these reasons, President Nixon in 1969 announced increased emphasis on the coastal zone as one of the major national programs in oceanography for the coming decade. By personal orientation and because the pressure is greatest there, I will focus primarily on physical behavior of estuaries.

### Estuaries

Originally the term estuary was used in reference to tidal portions of rivers, but usage has been broadened generally to include any semi-enclosed body of water having more or less free exchange

<sup>1</sup>The National Oceanic and Atmospheric Administration (NOAA) was created by President Nixon on October 3, 1970, by Executive Order and assigned to the Department of Commerce. The reorganization consolidated the efforts of 23 separate departments and agencies of government. Among these were: the Environmental Science Services Administration (ESSA); the Bureau of Commercial Fisheries; Marine Game Fish Research Program; Marine Minerals Technology Center; National Oceanographic Data Center; National Oceanographic Instrumentation Center; and the National Sea Grant Program.





*Schematic illustration of estuarine circulation. In its most basic form, this consists of seaward flow of fresh or brackish water near the surface and landward flow of salt or brackish water near the bottom, with turbulent mixing between the layers.*

with the ocean and in which ocean water is generally diluted by fresh water from rivers or other upland drainage. Extensive occurrence of estuarine areas, such as we have at present, appears to be an ephemeral state in geologic time, existing briefly following a change in sea level. The profusion of estuarine areas on our Gulf Coast, for example, is estimated to be only five to six thousand years old; it can be expected to last another four thousand years if the sea holds its present level and man does not interfere.

There are several reasons for the short life of estuaries. The most obvious is upland sediments deposited in the estuary by rivers and streams. More important, however, are reasons associated with the circulation of water. The estuary is a transition zone between fresh water of the river and salt-water of the sea. Because of its salt content, surface seawater is about 2.5 percent more dense than is fresh water. This density difference gives rise to a system of convection currents which is so common in estuaries as to be termed "estuarine circulation." In its most basic form, estuarine circulation consists of seaward flow of fresh or brackish water near the surface and landward flow of salt or brackish water near the bottom of the estuary, with turbulent mixing between the opposing layers. The landward flow near the bottom carries oceanic sediments into the estuary and impedes the movement of upland sediment through the estuary, thus forming a self-destroying trap for sediments from both sources.

Also, since deeper ocean waters tend

to be more fertile than are surface ocean waters, both the landward flow and the river flow tend to enrich the estuarine water, leading to much greater biological production than in the open sea and, hence, to much more rapid biological sedimentation.

On a much shorter time scale, this circulation pattern is of importance to the interests of man. It is a primary reason why Puget Sound is nearly as cold in the summer as in the winter. It is of obvious relevance to efficient disposal of wastes. The value of estuaries and wetlands as nursery areas for oceanic species is being well publicized; the larvae of these species have poor motility and ride this circulation system into the nursery areas. It is clear that knowledge of the dependence of the salinity stratification and circulation should be well established before the modifications that have been and will be made are begun. The general principles are in fact reasonably well known. The basic controlling features are geomorphology (primarily depth), volume of freshwater flow, and tidal regime of the estuary. An increase of depth, tidal current, or river flow can generally be expected to increase the circulation. It is difficult to give quantitative estimates, however, because the flow is turbulent, and turbulent processes have proved extraordinarily difficult to handle in all fields of science and engineering.

There are other very interesting variations on this basic pattern. It has been shown, for example, that because there is relatively little fresh water flowing into the Baltimore harbor, exchange of water between the harbor and the

larger Chesapeake Bay is three-layered: inward at surface and bottom, outward at mid-depth. Although this flow is weak, it provides flushing of the harbor five times as rapid as is estimated by standard engineering rules. In still other inlets, flushing takes place seasonally as water of different density, usually because of varying river flow, occurs at the entrance. Such a mechanism can be expected to be severely disturbed by river flow diversion or equalization projects.

There is also a growing body of evidence that these same general considerations apply in regard to movement of water between estuaries and open sea areas offshore, which is of quite obvious importance in regard to offshore waste disposal operations.

### Goals for Science Teaching

In conclusion, I wish to state three somewhat philosophical suggestions for science teaching as it touches on oceanography or, more generally, environmental problems. My thoughts here are strongly conditioned by a personal conviction that education for responsible citizenship is a higher goal than education for careers in science.

First, there is the necessity to impart to students the realization that value judgments must and will be made, consciously or unconsciously. Secondly, since the first law of thermodynamics is indeed irrevocable, students must be made cognizant of potential hidden costs in technological bargains.

Finally, students must be shown that it is science properly understood and used that gives us essential options. It is not until faced with really hard choices, like resolution of the thermal pollution problem, that we realize just how much research is still needed, particularly in environmental matters. Then we suddenly discover a great need to narrow the range of expert opinion on the effect of elevated temperature on biota and long for better knowledge of seasonal temperature and circulation patterns and more complex ecological puzzles in natural waterways. In the coming decade, it appears that these needs for environmental research can only become more acute. □

**Oceans from Space.** Edited by Peter C. Badgley, Leatha Miloy, and Leo Childs. Gulf Publishing Company, Houston, 1969. 234 pages—illustrations. \$13.95. Hardbound.

**Oceans from Space** contains the proceedings of a "Symposium on the status of knowledge, critical research needs, and potential research facilities relating to the study of the oceans from space," held in Houston in April 1967. Fifteen papers by a heterogeneous group of contributors are included. *In toto*, it has many of the same qualitative observations as, and little more depth than, those appearing in the several other studies of spacecraft applications to appear in recent years. It is useful, however, especially to those new to the field, to have several of the more promising applications contained in a single volume of this high quality. The dominant message is of the potential of satellite sensing for obtaining synoptic data for the vast expanses of ocean area on the planet. The illustrative material, including a considerable number of color photographs from the Gemini flights, is exceptionally good.

In the lead article, "Earth resources surveys from space," Peter C. Badgley and Leo F. Childs give an overview of the 1967 status of the potential application of passive and active remote sensing methods using a wide range of electromagnetic radiation frequencies. The orientation is that of the ERS (now ERTS) Program, and many of the examples given reflect the terrestrial aspects of this program. Don Walsh ("The Mississippi River Delta") presents some results from aircraft test flights over the Mississippi River distributary system obtained as part of the sensor evaluation studies for this program. In "The 200-mile fishline," Robert E. Stevenson uses Gemini photographs and a fair bit of conjecture to illustrate the potential value of large-scale coverage available from orbiting sensors to provide information on variation of oceanic conditions. Raymond M. Nelson describes some ESSA activities and aspirations in satellite remote sensing in "The potential application of remote sensing to selected ocean circulation problems." Here some striking pictures of oceanic eddies are marred by the lack of scale information. In a very short article, "The color of the sea," Gifford C.

Ewing points out the biological and fisheries significance of color difference in sea water. D. S. Ross contributed an article of considerably greater depth than those preceding, "Color enhancement for ocean cartography," in which the potential use of multispectral photography is explored by color separation and enhancement of a by-now-familiar Gemini color photograph of the Tongue of the Ocean. Poor editing is annoying but does not prevent passage of the message here. A concise description of the operating principles and general characteristics of the IRLS, OPLE, and EOLE systems is given in "Interrogation and position-fixing from spacecraft," by Marjorie R. Townsend. In "Apparent coastal water discolorations from space—oceanic and atmospheric," James E. Arnold and Aylmer H. Thompson point out the importance of adequate ground truth data for unambiguous interpretation of high altitude photographic materials. Although some of the color differences described as being evident in the original materials are not clearly rendered in the reproductions, the case is adequately made for how atmospheric smoke and haze can appear as differences in water color, depth, or other oceanic variations of interest. A sophisticated approach to selective remote sensing is presented by A. R. Barringer ("Remote sensing of marine effluvia"), who describes some experimental work on use of optical correlation spectrometry for remote sensing of iodine vapor and fish oil aerosols.

In "The sea surface," Willard J. Pierson, Jr., discusses thoughts on the use of orbiting radar for measuring a wide class of sea-surface perturbations. Radar scatterometry is suggested for determination of wind waves and winds over the open ocean as a technique for improved global sea-state predictions, with perhaps more optimism for early payoff than would be shown today. His description of the inter-related problems of determination of quasi-geostrophic ocean currents and large- and small-scale lumpiness of the geoid is well done. Paul M. Wolff, T. Laevastu and P. Patro, in

"Synoptic analyses and prediction of conditions and processes in the surface layers of the sea," describe procedures used at the Fleet Numerical Weather Facility for analysis and prediction of ocean thermal structure and surface waves, but without any explicit reference to the theme of the symposium or of the book. Numerous equations illustrative of the procedures are given, but with insufficient definition to serve any purpose other than show the general form and level of sophistication of the techniques. After their value in providing cloud pictures for use in weather forecasting, one of the most immediately useful of potential applications of satellite sensing techniques is likely to be for mapping snow and ice distribution. James H. McLerran provides a short overview of the registry of sea ice on photographic, infrared, radar, and microwave sensors by night and by day in "Remote sensing and interpretation of sea-ice features." E. D. McAlister ("Measurement of the total heat flow from the sea surface with an infrared two wavelength radiometer: Progress report") describes the principles and some results of his well-known work for sampling the temperature gradient in the half centimeter below water surfaces as a means of investigating surface heat transfer mechanisms, and of potential value for large-scale air-sea heat exchange measurement.

Wilbert M. Chapman, in "Implications of space research to fishery development," expertly summarizes post World War II trends in world-wide ocean fisheries, and indicates areas in which space and other sciences can aid in improving the efficiency of fisheries. An important point here is that the trend is toward exploitation of the smaller species

more dependent on environmental variations. After briefly outlining the various influences modulating catches, he points out that fishermen make operational decisions daily with very little guidance, and that even slight contributions of environmental science to improved efficiency will be of considerable value. John P. Craven's contribution, "Oceanography from inner space—the other side of the interface," deals exclusively with mostly recent developments in under-sea technology. It probably provided an interesting and useful counterpoint within the symposium, but will be of little value to most readers of this volume.

The book is of very high material quality, and, as indicated above, the illustrations are exceptional; it is therefore uncommonly unfortunate that it was not edited more carefully. Scarcely a contribution escapes structural errors and omissions, and seeming inclusion of contributors' marginal speaking notes. It appears that probably none of the contributors were afforded an opportunity to check proofs. The figures, although excellent, are in some cases unnecessarily duplicative from one article to another, as is some of the tabular information. With one exception, the order of the contributions is preserved in the preceding citations; simple rearrangement of the contributions along lines of concept development would have helped to make the book readable as a coherent entity rather than the disjoint collection in individual papers of varying value that it now is, and thereby would have added to the value of the individual contributions. Readers can accomplish this for themselves by reading the chapters in the order 14, 10, 2, 4, 5, 7, 3, 1, 12, 8, 11, 13, 9, 6, 15.—*Donald V. Hansen*



# PRECISE TWO-POINT STD CALIBRATIONS

*James K. Low*  
University of Miami  
Coral Gables, Florida

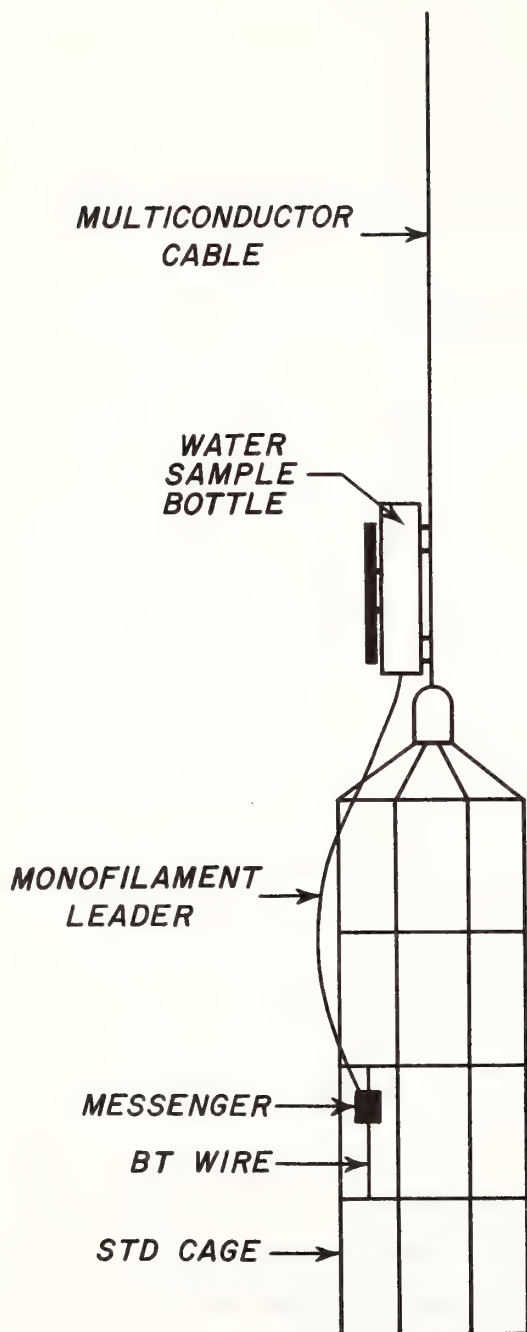
*George A. Maul*  
National Oceanic and Atmospheric Administration  
Atlantic Oceanographic and Meteorological Laboratories  
Miami, Florida

Periodic calibrations of the Bissett-Berman STD are advisable in order to maintain a quality check on the data collection. The usual two-point procedure is to obtain a water sample for standard analysis with a sampling bottle just below the surface and again at the bottom of a cast for comparison with the STD. In order to know when to read the STD output, it is necessary to know when the independent sample was obtained. This is easily accomplished at the surface visually. For the deep calibration point one has had to depend on estimating the travel time of a messenger down the multiconductor cable to the point where the deep sampler is attached a few meters above the STD.

Mr. Low at the University of Miami's Rosenstiel School of Marine and Atmospheric Sciences noticed that a slight impact on the frame of the Model 9006 will produce a one to two inch spike (toward low values) on the analog record of the salinity sensor. This slight jar, when coordi-

nated with the tripping time of the sampling bottle, provides a positive identification of the time of calibration. (In a vertical current shear the depth of the STD must be maintained by paying out or hauling in wire while waiting for the reversing thermometers to come to equilibrium). At the precise time of tripping, the analog record is annotated and the frequency output of each sensor's discriminator is read from frequency counters which monitor the data channels. Thus the temperature, salinity, and thermometric depth can be compared properly with the STD outputs.

The surface water sample bottle is soaking while the cast is being made. When the STD returns to the surface the second calibration is obtained immediately, in a similar fashion. Care must be exercised to insure that the sensor heads are at the same depth as the surface sample bottle. This precaution is usually unnecessary for the deep bottle where a small gradient correction may be applied.



The technique is to attach a piece of BT wire vertically to the STD (see figure) so that a messenger is free to fall a few inches and strike the frame. The messenger is connected in series to the water sampler with a long monofilament leader. When the water sampler trips, the messenger on the STD falls (about 4 inches is all that is required), strikes the frame, and causes the spike on the salinity trace. The impact is certainly less than that experienced by the STD in normal deck-side handling and should not affect the instrument; in two years of use aboard the University of Miami's research vessels there have been no ill effects to the STD noted in the application of this technique.

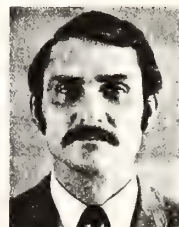
The procedures outlined have materially improved the static calibrations of this oceanographic instrument.

In the Florida Straits for example, in 250 meters of water, the average difference between the thermometric depth and the STD depth at calibration was  $\pm 16.2$  meters before application of the technique, and  $\pm 3.3$  meters afterwards. It should be recognized that the success of such a two-point calibration does not reflect the quality of the data acquisition which is a function of the dynamic response of the system. It does however offer the ocean scientist a higher degree of confidence in his data with the investment of little additional expense and time.



**JAMES K. LOW** is the marine technician supervisor of the Division of Physical Oceanography at the University of Miami's Rosenstiel School of Marine and Atmospheric Sciences, where he has been employed for eight years. He is currently working under the direction of Dr. Walter Duing on a new current profiling technique in the Straits of Florida.

**GEORGE A. MAUL** is a research oceanographer in the Physical Oceanography Laboratory of the National Oceanic and Atmospheric Administration's Atlantic Oceanographic and Meteorological Laboratories, Miami, Fla. Mr. Maul has worked in marine surveying, geodesy, and most recently the application of remote sensing to problems in physical oceanography.



## Earth tides

Progress in obtaining and analyzing longer, more accurate series of Earth tide observations has made clear that ocean tide effects, both loading and attraction, are significant and must be considered in the geophysical interpretation of the data. Therefore many recent research studies have used the available ocean cotidal and corange charts for estimating the deformation of the Earth due to tidal loading and for calculating the varying gravitational attraction of the nearby water mass at different stages of the tide. The effects of ocean tides on Earth tide observations can best be observed by a network of stations, varying in distance to the coast, which systematically monitor the ocean loading or attraction contributions to the observations.

**Western Europe tiltmeter networks.** Two tiltmeter networks in Western Europe have been established by the Institut de Physique du Globe de Paris and the Observatoire Royal de Belgique, in Normandy and in the Massif of the Ardennes, respectively. Both networks are aiming at the determination of (1) the deformation of the Earth's surface due to ocean tidal loads in the Atlantic Ocean, the English Channel, and the North Sea, and possibly (2) the regional variations due to heterogeneities in the crust or in the mantle, and even the anelastic properties of the mantle. That the effects of ocean tidal loading on the tilt of the Earth's surface are greater than those of the Earth's tidal tilt in Western Europe makes the separation of various effects on the tilt measurements, particularly the geological influences, very difficult, if not impossible. The data so far obtained still lack a general consistency.

**United States tidal gravity profile.** Most recent results, from a United States transcontinental tidal gravity profile established by the Solid Earth Tides Group of Columbia University, for the principal tidal constituents  $M_2$  and  $O_1$  have shed direct light on the long-standing problem of the influence of the ocean tides on solid Earth tides.

The network of the transcontinental profile consisted of nine semipermanent (6-month observation) stations around latitude 39–41°N, extending from New York City to Point Arena, Calif.

The observed relative values of the gravimetric factor and the phase do indeed follow a definite logarithmical pattern with respect to distance from the Atlantic and Pacific oceans. Figures 1 and 2 show the relative differences of gravimetric factor  $\Delta\delta$  in percent and of phase  $\kappa$  in degrees for  $M_2$  and  $O_1$  (solid circles). The maximum difference of gravimetric factors for  $M_2$  between New York City and Point Arena amounts to approximately 8%. There is a lag of about 4° for the phases of  $M_2$  in both New York City and Point Arena; these phases decay toward midcontinent, where the phase lag is less than 1°. The gravimetric factors for  $O_1$

are nearly equal for all stations east of Kansas, and the value of  $\Delta\delta$  increases at a rate of about 0.14% per 100 km toward the West Coast. The phases for  $O_1$  are equal, with a nearly constant lag of about 1° across the continental United States. They gradually begin to lead west of Ephraim, Utah, and the lead increases very rapidly to 5° in Point Arena. These results demonstrate the different tidal regimes in the nearby Atlantic and Pacific oceans. In the Pacific, both diurnal and semidiurnal tides are important, and therefore the ocean loading due to both  $O_1$  and  $M_2$  is important. In the Atlantic, only the semidiurnal tides are important. This is borne out by the small changes in gravimetric factor and phase due to  $O_1$  near the Atlantic end of the network.

Quantitative calculations were made for each station by taking into account the effects of ocean tides on tidal gravity, namely, a variation in the height of the point of observation, a distortion of the tidal potential, and an addition to the variation of the vertical component of acceleration of gravity due to the water mass of the ocean tide, making use of the cotidal and corange information for the  $M_2$  and  $O_1$  ocean tidal constituents. The observed values of  $\Delta\delta$  and  $\kappa$  as shown in Fig. 1 agree remarkably well with those calculated (triangles) for the  $M_2$  constituent. For the  $O_1$  constituent the agreement is not as good (Fig. 2), but the general trend for the values of  $\Delta\delta$  and  $\kappa$  indicates that, even though the cotidal and corange information for the  $O_1$  ocean tidal constituent is inferior to that of the  $M_2$  ocean tidal constituent, the  $O_1$  ocean constituent is a primary influence on the  $O_1$  Earth tidal constituent. Nevertheless, there is a considerable degree of uncertainty about the ocean tides on open oceans. The agreement between the observed deviations of the gravimetric factors and the phases and the calculated deviations due to the influence of ocean tides merely substantiates the fact that the influence of ocean tides on tidal gravity is of primary importance.

Although the question of the influence of geological structure on tidal gravity has drawn much attention in the past, the theoretically calculated gravimetric factors for several Earth models involving drastic differences in the crustal and upper mantle structures are nearly constant. The small residual deviations of both the gravimetric factors and the phases, after subtracting the effects of ocean tides on tidal gravity, do not seem to correlate with the major different geological provinces such as the Interior Plains and the Rocky Mountains.

The Earth models deduced from seismic body waves, for example, the Jeffreys-Bullen and the Gutenberg-Bullen models, have long been regarded as close approximations to the actual Earth. The observed areal strain of solid Earth tides with improvements of extensometer measurements at



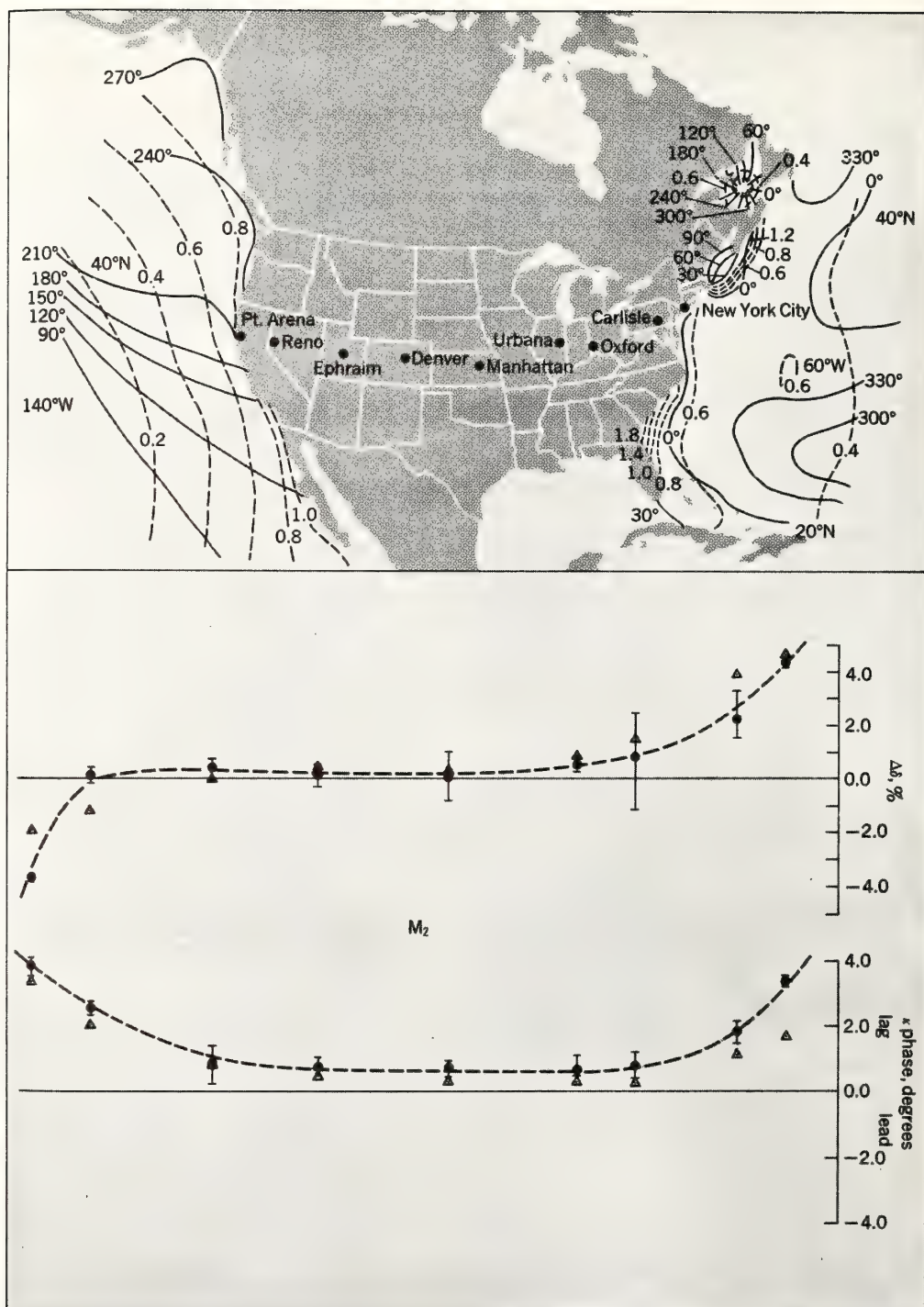


Fig. 1. Observed values of  $\Delta\delta$  (in percent) and  $\kappa$  (in degrees) for  $M_2$  tidal constituent (solid circles) compared with calculated values of  $\Delta\delta$  and  $\kappa$  (triangles).

Ogdensburg, N.J., which is nearly independent of the load strain caused by the ocean tidal loading off the Atlantic coast based on the Boussinesq solution, confirms the theoretical tidal strain based on

Cophase (in degrees) and coamplitude (in meters) of  $M_2$  ocean tidal constituent are also shown by solid and broken lines, respectively.

the Gutenberg-Bullen Earth model with a New York-Pennsylvania crustal structure, which has the characteristic Love numbers  $h=0.621$  and  $l=0.084$ . These Earth models have been further sup-

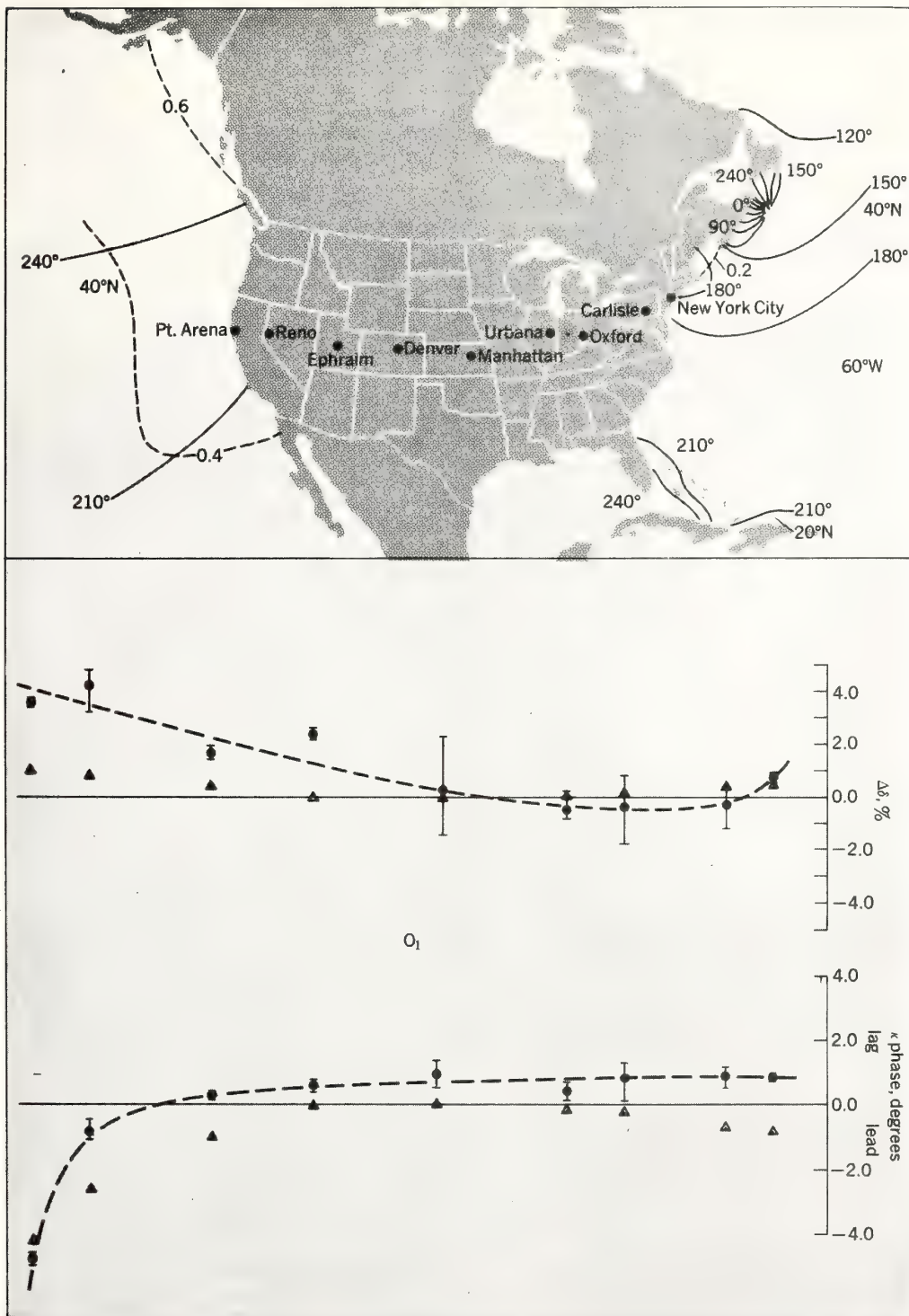


Fig. 2. Observed values of  $\Delta\delta$  (in percent) and  $\kappa$  (in degrees) for  $O_1$  tidal constituent (solid circles) compared with calculated values of  $\Delta\delta$  and  $\kappa$  (triangles). Cophas

(in degrees) and coamplitude (in meters) of  $O_1$  ocean tidal constituent are also shown by solid and broken lines, respectively.

ported by good agreement between the theoretical and experimental values of the periods of the free oscillations of the Earth, although refinements are still needed.

It is now evident that it is fruitless to try to verify the theory of Earth tides by using the inferred or theoretically calculated cotidal and corange charts to make corrections for the indirect effects of

ocean tides on solid Earth tides, as has been done in the past. If measurements can be made to an accuracy of 1% or better, it is more appropriate to consider the possibility of mapping ocean tides on the open oceans by means of extended Earth tidal gravity measurements on the adjacent lands supplemented by a few ocean-bottom stations of ocean tides measurements and by the tidal information of nearshore tidal stations.

**International Symposium on Earth Tides.** The Sixth International Symposium on Earth Tides was held in France at the University of Strasbourg, Sept. 15–20, 1969. It was organized by the Permanent Commission on Earth Tides, International Association of Geodesy, IUGG.

Many aspects of the meeting were comparable to those of previous Earth tide symposia in that the papers dealt primarily with instrumentation and data analysis. With regard to instrumentation, considerably greater emphasis is being placed on possible contributions by various potential sources of error, on calibration, on the interchange of instruments between stations, and on simultaneous observations using multiple sensors at the same site. With this increased sophistication has come an awareness that the geophysical interpretation of the observations may hinge on a high degree of accuracy.

A similar change has come about in data analysis in that there is now an active program to use longer series to achieve both more accurate results and a high degree of resolution. Thus the fixed 29-day analysis is no longer the ultimate end product, and least-squares analysis of data that may not be continuous and equally spaced in time is accepted as a basic tool. With this has come an interest in other frequency bands, not only the long-period tides but also high-frequency tides. There is considerable interest in  $M_3$ , and frequencies as high as 8 cycles per day are being investigated.

The various resolutions adopted at the symposium included (1) the recommendation that long-term observational series be planned as regular observatory-type programs in a number of different regions of the Earth; (2) the recommendation that complete Earth tide stations be established in the equatorial regions and in the Southern Hemisphere, particularly in Africa, South America, and Australia, and at Schiltach, Black Forest, Germany, to fill the gap in the net between France, Belgium, and Luxembourg on the one hand and the stations at Berchtesgaden (Germany), Czechoslovakia, and Austria on the other hand; and (3) the endorsement of efforts now under way in the oceanographic community to develop more accurate cotidal and corange charts by means of deep-sea observations and hydrodynamic model studies.

For background information see EARTH; EARTH TIDES; TERRESTRIAL GRAVITATION in the McGraw-Hill Encyclopedia of Science and Technology.

[BERNARD D. ZETLER; JOHN T. KUO]

*Bibliography:* J. T. Kuo, *J. Geophys. Res.*, 74: 1635–1644, 1969; J. T. Kuo et al., *Science*, in press; P. Melchior and A. Venedikov, *Phys. Earth Planet. Interiors*, 1:363–372, 1968; J. C. Usandivaras and B. Ducarme, *Bull. Acad. Roy. Belg. Cl. Sci.*, June 7, 1969.



## Precision Requirements for a Spacecraft Tide Program

BERNARD D. ZETLER AND GEORGE A. MAUL

*National Oceanic and Atmospheric Administration, Atlantic Oceanographic  
and Meteorological Laboratories, Physical Oceanography Laboratory  
Miami, Florida 33130*

A tidal analysis of sea-surface elevations from an orbiting altimeter will include errors due to the instrument and the orbital determinations. Furthermore, the results may be somewhat degraded by the small amount of data and their random distribution in time. These effects have been evaluated in a numerical feasibility investigation with the use of observed hourly heights at two tide stations and a hypothetical satellite orbit with a  $30^\circ$  inclination and a period of about 95 min. For a station at  $13^\circ\text{N}$  with a water elevation assumed to be obtained each time the altimeter transits a  $1^\circ$  square centered at the station, 86 observations are obtained in a year. For a station at  $22^\circ\text{N}$ , areas of  $1^\circ$  to  $5^\circ$  square were used and the number of observations in a year varied from 112 to 551. Degradation of the signal is studied by introducing sequentially increased levels of white noise to the observations. The harmonic constants for the smaller constituents deteriorate rather quickly as white noise is added, but the largest constituents appear to be reasonably determined even when random numbers with extreme absolute values as large as the amplitude are added to the data. These results indicate that previously stated minimum precision requirements for a spacecraft tide program can be relaxed by roughly an order of magnitude.

Observation of the tide is frequently mentioned in conjunction with the proposals to orbit a radar altimeter [*National Academy of Sciences*, 1969]. Essentially these proposals have been oriented toward geodetic applications, but oceanographers such as *von Arx* [1966] have recognized the inseparable coupling of geoid determinations and absolute sea-surface topography. Most recently, in the report of a study made at Williamstown, Massachusetts [*NASA*, 1969], oceanographers have assisted in specifying precision requirements for an orbiting altimeter on the Geos satellite that is useful in a broad spectrum of geophysical investigations.

Any attempts to obtain tidal measurements on space platforms should be considered within the constraints of EODP (Earth and Ocean Dynamics Program), presently under consideration at NASA. It seems fruitful then to numerically investigate if the tide is at all detectable in perfect measurements from the systems suggested for EODP, and if so, what noise levels are tolerable in the data. Details of error sources in radar altimetry are discussed by *Greenwood et al.* [1969] and will not be con-

sidered here except that reasonable values will be chosen.

The approach to the problem is to imagine a satellite-borne altimeter transiting a particular oceanic region and obtaining tidal elevations. The orbital characteristics will dictate how often and when the hypothetical instrument will obtain values. For the calculated transit times, tidal elevations from actual observations during one year are analyzed for the major constituents. These values are then compared with harmonic constants obtained by the standard methods of harmonic analysis [*Zetler and Lennon*, 1967]. Finally the observed tides are degraded by progressively adding levels of white noise and the data are reanalyzed at each noise level.

### ANALYSIS

The EODP satellites are likely to be in a low inclination, low altitude orbit, and will be gravity-gradient stabilized to within  $1^\circ$ - $2^\circ$  of the local vertical. Within these constraints it was decided to initially consider a  $1^\circ \times 1^\circ$  square in low latitudes and require that every time the satellite transited this area an elevation of the sea surface was to be obtained.

The first tide data used are the hourly heights

TABLE 1. La Union, El Salvador, 1964, Normalized Residuals and Standard Deviations

Noise	$M_2(3.89')$		$N_2(0.85')$		$S_2(0.88')$		$K_1(0.37')$		$O_1(0.18')$	
	$\langle R \rangle/A$	$\sigma(R/A)$	$\langle R \rangle/A$	$\sigma(R/A)$	$\langle R \rangle/A$	$\sigma(R/A)$	$\langle R \rangle/A$	$\sigma(R/A)$	$\langle R \rangle/A$	$\sigma(R/A)$
0.0	0.032	0.015	0.117	0.073	0.139	0.057	0.244	0.125	0.291	0.113
0.5	0.038	0.016	0.130	0.080	0.141	0.065	0.317	0.145	0.394	0.243
1.0	0.047	0.026	0.179	0.103	0.169	0.083	0.482	0.212	0.619	0.391
1.5	0.059	0.037	0.241	0.140	0.211	0.110	0.678	0.284	0.875	0.544
2.0	0.074	0.046	0.309	0.181	0.260	0.142	0.886	0.358	1.140	0.703
3.0	0.105	0.064	0.450	0.270	0.371	0.207	1.314	0.508	1.677	1.028
4.0	0.138	0.082	0.595	0.360	0.486	0.276	1.749	0.658	2.218	1.357
5.0	0.171	0.100	0.743	0.450	0.604	0.345	2.187	0.808	2.761	1.688

$1^\circ \times 1^\circ$  window (86 values).

$R$  is the amplitude of the residual.

$\langle R \rangle$  is the mean of  $R$ .

$A$  is the ground truth amplitude (from a year of hourly heights).

$\sigma$  is the standard deviation of  $R/A$ .

Noise is in feet.

observed at La Union, El Salvador ( $13^\circ 20'N$ ,  $87^\circ 49'W$ ) for the year 1964. The mean range of the tide here is 8.11 feet, which is typical for coastal regions but about four times larger than mid-ocean tides [Dietrich, 1963].

The orbital parameters used for this study were provided by W. S. von Arx (personal communication, 1970). The orbit, which is realistic

for altimeter applications, has a  $30^\circ$  inclination and a period of about 95 min. The regression (change in longitude per orbit) of the sub-orbital track at the latitude of the chosen tide station was carefully determined. From an arbitrary start time, this was used to calculate the cumulative times that the spacecraft would pass over any portion of the  $1^\circ$  square centered at the tide station during one year. There were 43 culminations on both ascending and descending transits, averaging about one observation every four days.

A power spectrum analysis of the hourly tidal heights for the year at La Union showed the dominant energy to be at two cycles per day with considerably smaller values at one cycle per day and near zero frequency and negligible values everywhere else in the spectrum up to the Nyquist frequency at 12 cycles per day. Ordinarily, geophysical phenomena at one and two cycles per day are not readily studied by observations obtained several days apart. However, tidal frequencies are well determined from astronomical considerations and the signal to noise ratio of the tides is quite high. Hence, we are able to use a procedure developed for the harmonic analysis of data randomly spaced in time [Zetler et al., 1965].

A least-square solution in tides solves for the mean level, the amplitude, and the phase of each constituent. A normal National Ocean Survey analysis of a year of data solves for 37 constituents and mean sea level (75 unknowns). It

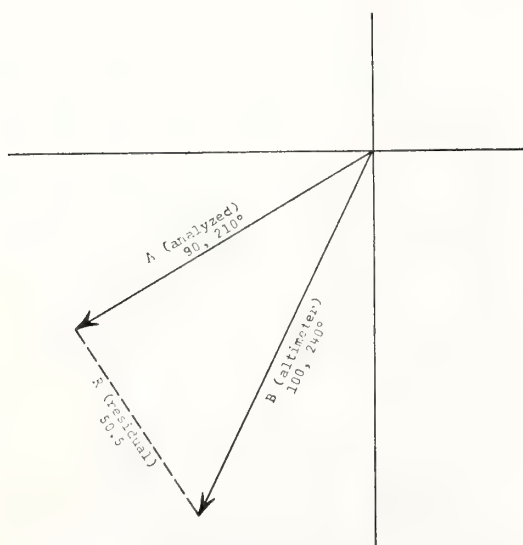


Fig. 1. Sample graphical determination of the residual amplitude ( $R$ ). If the accepted vector ( $A$ ) has an amplitude of 90 and a phase of  $210^\circ$ , and the altimetric determination ( $B$ ) has an amplitude of 100 and a phase of  $240^\circ$ , then the modulus of the residual vector is 50.5.

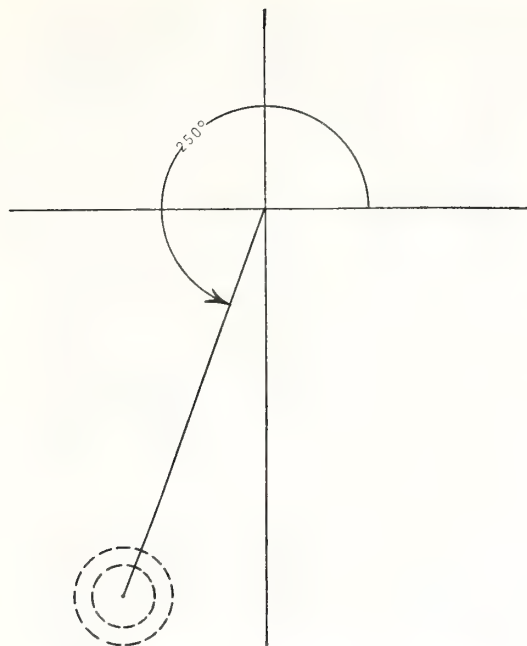


Fig. 2. Sample plot of residual distribution. Consider the normalized  $M_2$  vector at La Union with unit amplitude and phase of  $250^\circ$ . For the case where the noise is  $\leq 2.0$  feet,  $\langle R \rangle / A = 0.074$  and  $\sigma(R/A) = 0.046$ . Then 50% of all  $R/A$  lie within the inner circle (radius = 0.074) and 84% of all  $R/A$  lie within the outer circle (radius =  $0.074 + 0.046 = 0.120$ ).

would not be reasonable to do this with just 86 observation equations and, fortunately, there are 5 principal constituents that ordinarily provide more than 95% of the total tidal energy. These are  $M_2$ ,  $S_2$ , and  $N_2$  in the semidiurnal species and  $K_1$  and  $O_1$  in the diurnals. Solving for these in a year of data, the omitted constituents will not have significant sidebands and hence their contributions will be primarily noise rather than bias.

Spectra of geophysical data in general show a peak in the continuum near zero frequency, diminishing rapidly and monotonically in the higher frequencies; the continuum of sea level studied carefully by Munk and Bullard [1963], Munk *et al.* [1965], and Groves and Zetler [1964] shows this quite clearly. By using real data in our tests, we have a frequency spectrum of tidal lines superimposed on such a continuum. Then, by systematically adding controlled amounts of white noise (to simulate observation errors), we progressively increase

the level of the continuum in order to decrease the signal to noise ratio and thus degrade the quality of the analyzed results.

A University of Miami program generating random numbers was used to prepare the white noise. The program outputs integers ranging from zero to a preset maximum. Manipulation of these values produced a series with an average of zero and with an appropriate least count (a tenth of a foot, the same as the tidal data). A spectral analysis of the modified random numbers showed a reasonably uniform level of energy across the entire frequency range.

Our initial evaluation of the results of analysis compared separately the resolved amplitudes and phases for each constituent with the comparable values obtained from an analysis of all hourly heights for the year. However, tidal harmonic constants from the complete and the incomplete sets of data are more meaningfully compared when combined into vectors as follows:

Any given constituent (speed per solar hour =  $\omega$ ) can be expressed as  $A \cos(\omega t - a)$  where  $A$  is the amplitude,  $t$  is the time in hours cumulative from a start time, and  $a$  is the phase lag at that start time. Evaluations of  $A$  and  $a$  are the goals of conventional tidal analysis. If the analysis of the less-frequently sampled data provides the comparable harmonic constants  $B$  and  $b$ , then the difference between these two curves is a third cosine curve of the same fre-

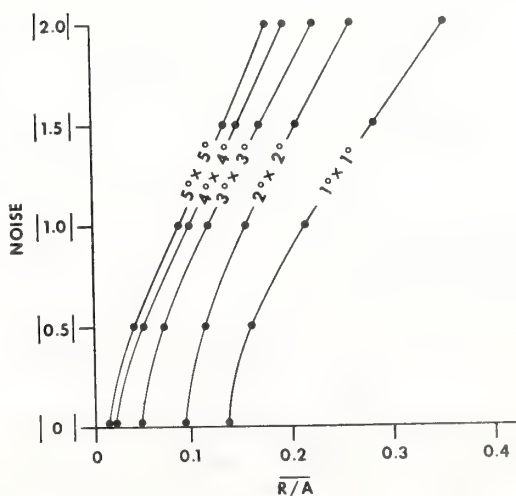


Fig. 3. Plot of noise versus  $\langle R \rangle / A$  for the five area sizes for  $M_2$  at Nawiliwili.



TABLE 2. Nawiliwili, Hawaii, 1965, Normalized Residuals and Standard Deviations

Noise	$M_2(0.480')$		$N_2(0.105')$		$S_2(0.166')$		$K_1(0.508')$		$O_1(0.297')$	
	$\langle R \rangle/A$	$\sigma(R/A)$	$\langle R \rangle/A$	$\sigma(R/A)$	$\langle R \rangle/A$	$\sigma(R/A)$	$\langle R \rangle/A$	$\sigma(R/A)$	$\langle R \rangle/A$	$\sigma(R/A)$
$1^\circ \times 1^\circ$ (112 Values)										
0.0	0.138	0.056	0.418	0.263	0.114	0.083	0.129	0.078	0.127	0.058
0.5	0.158	0.077	0.870	0.559	0.276	0.180	0.203	0.126	0.193	0.131
1.0	0.210	0.112	1.635	0.997	0.552	0.342	0.349	0.221	0.330	0.227
1.5	0.276	0.151	2.420	1.473	0.833	0.516	0.507	0.324	0.482	0.325
2.0	0.348	0.191	3.210	1.960	1.114	0.692	0.669	0.431	0.637	0.424
$2^\circ \times 2^\circ$ (222 Values)										
0.0	0.091	0.037	0.213	0.063	0.094	0.041	0.076	0.029	0.078	0.022
0.5	0.111	0.053	0.457	0.301	0.175	0.110	0.107	0.059	0.140	0.077
1.0	0.152	0.077	0.839	0.545	0.348	0.194	0.166	0.095	0.258	0.137
1.5	0.202	0.105	1.245	0.778	0.528	0.281	0.232	0.133	0.382	0.200
2.0	0.255	0.133	1.656	1.008	0.711	0.369	0.303	0.168	0.508	0.263
$3^\circ \times 3^\circ$ (331 Values)										
0.0	0.049	0.014	0.117	0.045	0.106	0.034	0.051	0.019	0.049	0.022
0.5	0.071	0.034	0.281	0.161	0.155	0.074	0.071	0.029	0.099	0.050
1.0	0.118	0.061	0.528	0.292	0.283	0.134	0.105	0.056	0.191	0.079
1.5	0.168	0.091	0.782	0.427	0.421	0.202	0.146	0.080	0.286	0.112
2.0	0.220	0.122	1.038	0.563	0.562	0.273	0.188	0.104	0.381	0.147
$4^\circ \times 4^\circ$ (441 Values)										
0.0	0.023	0.009	0.088	0.038	0.076	0.030	0.053	0.017	0.037	0.014
0.5	0.052	0.024	0.220	0.133	0.121	0.064	0.062	0.030	0.085	0.042
1.0	0.097	0.046	0.424	0.244	0.227	0.125	0.091	0.051	0.162	0.075
1.5	0.143	0.069	0.633	0.357	0.338	0.192	0.130	0.067	0.241	0.112
2.0	0.190	0.093	0.847	0.473	0.452	0.258	0.172	0.085	0.320	0.148
$5^\circ \times 5^\circ$ (551 Values)										
0.0	0.019	0.006	0.074	0.038	0.056	0.018	0.063	0.016	0.036	0.011
0.5	0.046	0.025	0.214	0.151	0.102	0.067	0.068	0.032	0.091	0.042
1.0	0.088	0.048	0.414	0.283	0.202	0.129	0.091	0.049	0.160	0.083
1.5	0.130	0.073	0.618	0.416	0.309	0.190	0.127	0.059	0.232	0.120
2.0	0.172	0.098	0.823	0.551	0.418	0.250	0.165	0.069	0.306	0.157

quency with amplitude and phase  $R$  and  $r$  respectively, such that

$$R \cos(\omega t - r) = A \cos(\omega t - a) - B \cos(\omega t - b)$$

Figure 1 shows a plot of a vector  $A$  and a vector  $B$ , with  $R$  calculated as the distance between the end points.

A single pass of the data through the program for least squares analysis provides a solution for an arbitrary start time. By shifting the orbital times an hour at a time, different sets of observed data can be sequentially sampled and a family of solutions obtained. For La Union, 23 such solutions at each level of noise were obtained for each constituent. The modulus of the residual vector was computed for each solution

and normalized by dividing by the amplitude obtained from the conventional analysis of the complete series. Means and standard deviations of the normalized residuals were computed and are presented in Table 1.

## RESULTS

Figure 2 shows a sample distribution of the normalized residuals for  $M_2$  at La Union when noise  $\leq |2|$  feet is added to the data. Half the residuals lie within the inner circle whose radius is  $\langle R \rangle/A$ . By the addition of one standard deviation to the mean, 84% of the residuals lie within the outer circle.

La Union was chosen as a test site because it is on a narrow continental shelf. Co-tidal and co-range charts in this region indicate that the tidal amplitudes and phases are reasonably uni-

form in a  $1^\circ$  square. Further offshore, depending on the proximity to amphidromic points, it appears that this areal constraint may be relaxed even further. This is important because the amplitude of the  $M_2$  tide at some mid-ocean stations is much smaller than at La Union. The decrease in signal to noise ratio may be somewhat compensated for by increased sampling.

Accordingly, a similar experiment has been conducted with a year of tide data at Nawiliwili, Hawaii, using a variety of areas varying from  $1^\circ$  to  $5^\circ$  squares. Because the slope of the  $30^\circ$  inclination orbit is smaller at the latitude of Nawiliwili, the number of culminations even for the  $1^\circ$  square is greater, 112. The number of transits is maximized when the inclination nearly equals the latitude of the station. Noise levels at 0.5-foot increments were added up to a maximum of 2 feet and 20 solutions were obtained for each size area at each noise level. The results are shown in Table 2.

The results show that the residual ratios and standard deviations for each constituent increase with increased noise and that the weaker signals degrade rapidly to the point where the results have little or no value. The largest constituent  $M_2$  appears to have useful values even with the largest amount of added noise.

Although reasonably useful values are obtained for  $M_2$  and  $K_1$  with a  $1^\circ$  square when the signal and the added noise level are about equal (0.5 foot), the reliability of the results improves significantly (Figure 3) with successively larger areas (increased number of observations). However, it will not always be justifiable to use so large a square since in some regions the cotidal and/or co-range lines may be spaced more closely than at Nawiliwili.

#### CONCLUSIONS

The Williamstown study indicated that a resolution of 2 or 10 cm was necessary for a spacecraft tide program, depending on the usage of the data. It would appear from the results obtained, particularly for Nawiliwili, which is more typical of ocean tides, that these minimum precision requirements can be relaxed by roughly an order of magnitude.

A further improvement in accuracy of results can be anticipated in the sense that similar results will be obtained for numerous adjacent or overlapping water areas (in this case, all

water areas between  $30^\circ\text{N}$  and  $30^\circ\text{S}$ ) and therefore a least square contouring program for each important tide frequency will produce cotidal and co-range charts presumably more accurate than the individual values for each particular area. The computing effort will be extensive but far from impossible.

**Acknowledgments.** The authors thank William von Arx for supplying the orbital data, Donald V. Hansen for numerous suggestions, in particular, the vectorial approach for statistical score-keeping, Alan Herman for his valuable programming assistance, and the Division of Oceanography, National Ocean Survey, for the tide data. This research was in part supported by the National Aeronautics and Space Administration's Earth Resources Survey Program through the National Environmental Satellite Service's Environmental Science Group.

#### REFERENCES

- Dietrich, G., *General Oceanography*, John Wiley, New York, 1963.
- Greenwood, J. R., A. Nathan, G. Neumann, W. Pierson, F. C. Jackson, and T. E. Pease, Radar altimetry from a spacecraft and its potential applications to geodesy, in *Remote Sensing of Environment*, 1, 59-70, Elsevier, New York, 1969.
- Groves, G. W., and B. D. Zetler, The cross spectrum of sea level at San Francisco and Honolulu, *J. Mar. Res.*, 22, 269-275, 1964.
- Munk, W. H., and E. C. Bullard, Patching the long-wave spectrum across the tide, *J. Geophys. Res.*, 68, 3627-3634, 1963.
- Munk, W. H., B. D. Zetler, and G. W. Groves, Tidal cusps, *Geophys. J. Royal Astron. Soc.*, 10, 211-219, 1965.
- National Academy of Sciences, *Useful Applications of Earth-Oriented Satellites*, pp. 55-63, Washington, D. C., 1969.
- National Aeronautics and Space Administration, The terrestrial environment, solid earth and ocean physics, application of space and astronomical techniques, report of a study at Williamstown, Mass., pp. 1-7, 1969.
- von Arx, W. S., Geophysical applications based on an orbiting microwave altimeter and gradiometer, Space Research/Directions for the Future, *Nat. Acad. Sci. Nat. Res. Council. Publ.* 1403, 330, 1966.
- Zetler, B. D., and G. W. Lennon, Some comparative tests of tidal analytical processes, *Int. Hydrogr. Rev.*, 44, 139-147, 1967.
- Zetler, B. D., M. D. Schuldt, R. W. Whipple, and S. D. Hicks, Harmonic analysis of tides from data randomly spaced in time, *J. Geophys. Res.*, 70, 2805-2811, 1965.

(Received June 22, 1971.)



## Radiational Ocean Tides Along the Coasts of the United States

BERNARD D. ZETLER

*Atlantic Oceanographic and Meteorological Labs., ESSA, Miami, Fla.*

(Manuscript received 4 May 1970)

### ABSTRACT

A procedure has been developed for separating an analyzed  $S_2$  ocean tide amplitude and phase into gravitational and radiational components. Values obtained by applying the method to 11 one-year sets of harmonic constants at San Francisco were found to be reasonably consistent. Results have been obtained for 15 outside or near-outside stations on each of the east and west coasts of the United States. For both coasts the mean amplitude ratio (radiational to gravitational) is 0.16; the mean phase differences (radiational minus gravitational) are  $133^\circ$  and  $185^\circ$  for west and east coasts, respectively. The observed  $S_1$  amplitude of 1 cm, consistent on the east, west and Gulf coasts, is larger than would be expected from equilibrium considerations, from the  $K_1$  cusp, or from the continuum; it is therefore considered to be primarily radiational.

### 1. Introduction

Although classical studies of tides deal almost exclusively with gravitational tide producing forces, some discussion of periodic meteorological forcing functions appears in Schureman (1941). He points out that although  $S_a$ ,  $S_{sa}$  and  $S_1$  (representing annual, semi-annual, and solar diurnal periods, respectively) appear in the development of the gravitational tide-producing forces, the tidal variations of these periods are primarily related to meteorological changes such as variations in temperature, barometric pressure and periodic land and sea breezes. Since most meteorological contributions to variations in sea level are random in phase, they are not predictable well in advance. However, since the physical mechanisms causing  $S_a$ ,  $S_{sa}$  and  $S_1$  remain fixed in phase, these constituents are treated as tides. Undoubtedly, the meteorological energy applied by these mechanisms varies in phase more than do the gravitational tides, probably causing a cusp<sup>1</sup> rather than a line in the spectrum. This reduces the value of the long-range predictions somewhat, but there is nevertheless some residual benefit and these constituents have long been included in classical tide predictions.

If the phases of the semidiurnal constituents obtained by a conventional tidal analysis are plotted as a function of frequency, usually an irregularity is found at  $30^\circ$  per solar hour ( $S_2$ ). A plot of semidiurnal amplitudes divided by the appropriate theoretical coefficients shows a similar behavior. Although this had been known to tidal mathematicians for some time, it had not been understood that the analyzed  $S_2$  harmonic constants consisted of a trigonometric combination of

gravitational and radiational contributions. From the practical point of view, it meant that some small errors were introduced into predictions by inferring additional constituents based on the assumption that the analyzed  $S_2$  was completely gravitational. Munk and Cartwright (1966) developed a response method of tidal analysis, relying on a "credo of smoothness" in the admittances of the species frequency bands to disentangle gravitational, radiational and nonlinear contributions to observed tides. Among the various advantages of the method is its more satisfactory delineation of the response of the ocean to the tide-producing forces, since it is unlikely that the oceans are so finely tuned as to show strong selectivity among nearby frequencies.

The Munk-Cartwright method of analysis requires considerable computation and has thus far been applied to relatively few places. Because the amplitudes and phases for the radiational  $S_2$  are available for so few places, it has been difficult to assess the importance of these tides in any general sense.

A simple method has been devised for inferring the radiational  $S_2$  from traditionally obtained tidal harmonic constants. The rationale and shortcomings of the method are discussed here and results are shown for various places along the coasts of the United States.

The  $S_1$  (solar diurnal) tide is flanked on either side in frequency—just one cycle per year away—by  $K_1$  and  $P_1$ , which are two of the three largest diurnal constituents. Harmonic constants for  $S_1$  are ordinarily obtained in analysis of data of a year's duration. Because the amplitude is always quite small, little consideration has been given to whether  $S_1$  is primarily gravitational or radiational. A study by Munk *et al.* (1965) demonstrated that at Honolulu the line stands above the continuum. Constants have been compiled from various analyses for  $S_1$  in the United States and it now seems clear that the values are primarily from a

<sup>1</sup> A rise in the continuum (spectral noise level associated largely with irregular oscillations due to wind and pressure) in the vicinity of a strong line.



TABLE 1. San Francisco tides.

Year	Total $K_2$		Total $S_2$		Gravitational $S_2$		Radiational $S_2$		Amplitude ratio†	Phase difference‡‡ (deg)
	Amplitude (cm)	Kappa (deg)	Amplitude (cm)	Kappa (deg)	Amplitude (cm)	Kappa (deg)	Amplitude (cm)	Kappa (deg)		
1904	3.7	328	12.2	339	14.9	331	3.4	120	0.23	149
1905	3.0	330	11.9	333	12.5	333	0.6	142	0.05	169
1906	3.7	335	12.5	334	14.6	337	2.1	171	0.14	194
1907	4.0	331	12.2	335	15.5	334	3.4	149	0.22	175
1908	4.0	323	12.2	335	15.5	326	4.0	115	0.26	149
1909	3.4	328	12.2	334	13.7	330	1.8	124	0.13	154
1910	4.0	335	12.5	334	15.8	337	3.4	167	0.22	190
1911	4.0	326	12.5	333	15.5	329	3.4	137	0.22	168
1912	4.0	322	12.5	333	15.5	325	3.7	115	0.24	150
1913	3.7	325	12.8	333	14.6	328	2.1	115	0.14	147
1935	4.0	321	12.5	333	15.5	324	4.0	115	0.26	151
Mean	3.8	328	12.4	334	14.9	330	2.9	134	0.19	163
Standard deviation	0.4	5	0.3	2	1.0	5	1.1	21	0.07	17

† Amplitude of radiational  $S_2$  divided by amplitude of gravitational  $S_2$ .‡‡ Phase of radiational  $S_2$  less phase of gravitational  $S_2$ .

radiational (not gravitational) source and that ordinarily the line stands significantly above the continuum.

## 2. Discussion

Inasmuch as the inference of the  $S_2$  radiational tide uses analyzed values for  $N_2$ ,  $M_2$ ,  $S_2$  and  $K_2$ , and  $S_2$  and  $K_2$  are separated in frequency by two cycles per year, analyses of at least one year of data are used in this study to achieve proper resolution. Furthermore, only places located on or near the coast are used in order to reduce as much as possible the complications implicit in generating additional contributions at the frequencies of the major constituents through nonlinear interaction (Zetler, 1969).

A parabolic function of frequency, fitted to the phases of  $N_2$ ,  $M_2$  and  $K_2$ , is used to interpolate the phase of the gravitational  $S_2$ . Similarly, a parabola is fitted to the ratios of each amplitude for these three constituents divided by the appropriate theoretical coefficient. The ratio at the frequency of  $S_2$  on this parabola, combined with the  $S_2$  theoretical coefficient, furnishes an amplitude for the gravitational  $S_2$ . The phase and amplitude of the gravitational  $S_2$  so determined are subtracted vectorially from the observed  $S_2$  to obtain a phase and amplitude for the radiational  $S_2$ . The computations for a station are readily done on a desk calculator in a few minutes.

There are two weaknesses in the above procedure. A strong line is being inferred largely from a weak line. Although  $N_2$ ,  $M_2$  and  $K_2$  are all used in the parabolic fit, the  $S_2$  frequency is very close to that of  $K_2$  and hence most strongly determined by it. The analyzed value for any tidal constituent is a vectorial sum of the signal and the noise in the continuum. Since the inference of gravitational  $S_2$  uses a factor of about 3 on the  $K_2$  amplitude, the effective noise content of the inferred  $S_2$  is greater than the continuum by a factor of 3. Furthermore, the procedure assumes that the  $K_2$  value is purely gravitational when, in fact, it is known that

there is a small radiational input. As with the  $K_2$  solar gravitational tide, a radiational  $K_2$  modulates the radiational  $S_2$  due to declinational splitting. However, the principal part of  $K_2$  comes from the development of the gravitational lunar tide-producing force which does not have an associated radiational component. Cartwright (personal communication) has estimated the amplitude of the radiational  $K_2$  to be 0.086 times<sup>2</sup> that of the radiational  $S_2$ , and the phases of the two to be equal. Therefore, in principle, the results can be improved by iterating the approximation, and since the method converges quickly, only one iteration is necessary. Although an iteration of this type appears to be theoretically sound, there is a question, in the light of the high noise level, whether the extra effort is warranted.

The consistency of the results was tested by applying the method to harmonic constants from 11 one-year analyses of San Francisco tides (Table 1). The standard deviation of the gravitational  $S_2$  amplitude is found to be about three times as large as the standard deviation for the analyzed (total)  $K_2$ , as is to be expected from the weights in the parabolic interpolating function. The standard deviation of the phase is equal to that of  $K_2$ . The standard deviation is smaller for the analyzed  $S_2$  phase than for the  $K_2$  phase because  $S_2$  is a stronger line.

Cartwright (1968) points out that if the radiational tide is mainly caused by the action of the atmospheric tide on the sea surface, the phase difference (radiational kappa<sup>3</sup> minus gravitational kappa) should be about 120° because the tidal atmospheric pressure is a minimum<sup>4</sup> 4 hr (120°) after the sun's meridional transit, both upper and lower. Cartwright also indicates: "The ratio of the amplitude of the atmospheric tide (in centimeters

<sup>2</sup> Ratio of the equilibrium coefficients of solar  $K_2$  and  $S_2$ .

<sup>3</sup> Phase difference between a tidal constituent and its local equilibrium argument.

<sup>4</sup> Cartwright's paper actually shows a phase difference of 240° but he uses phase leads of transit whereas this study uses kappas which are phase lags.

of water) to that of the solar equilibrium tide is of order 0.1," presumably in the tropics. Since the solar equilibrium tide decreases as  $\cos^2\phi$  and the atmospheric tide has been found to decrease as  $\cos^3\phi$  (Siebert, 1961), where  $\phi$  is the latitude, the ratio should vary as  $\cos\phi$ . Other atmospheric contributions to radiational tides include the horizontal transport of water onto and away from the coast by diurnal onshore-offshore winds and, to a much lesser extent, steric changes in water level due to thermal heating. A diurnal onshore-offshore wind regime can cause a semi-diurnal tide through significantly different maximum wind speeds or different durations (onshore and offshore). Furthermore, the diurnal modulation of a steady state wind can evolve as a semi-diurnal phenomenon in the wind stress equation through nonlinear interaction.

### 3. Results

Table 2 is a compilation of computed radiational  $S_2$  tides for a selection of places along the United States west coast chosen for their coastal or near-coastal positions. There is some degree of variation in the amplitude ratio (radiational over gravitational) with a definite trend for higher ratios at higher latitudes. Cartwright (1968) calculated comparable ratios and phase differences by the Munk-Cartwright response analysis method for seven places in the British Isles and for Honolulu. He found a mean ratio of 0.18, with values varying from 0.11 to 0.24, and phase differences averaging  $129^\circ$ , varying from  $63^\circ$  to  $206^\circ$ . The spread in ratios is somewhat larger in Table 2 but the spread in phase

angles is smaller. The means of both sets are remarkably close.

Table 3 is a comparable set of results for a selected group of east coast stations. The mean ratio is again 0.16 and the total spread in ratios is comparable to that of the west coast values. The spread in phase differences is roughly the same as the west coast but the mean difference is significantly higher,  $185^\circ$ . Once again there is a tendency, although not as well defined, for higher ratios at higher latitudes. In contrast to this, Cartwright has the highest ratio at Honolulu, his lowest latitude. The anomalous mean phase difference on the east coast may be related to the greater expanse of shallow shelf offshore or an indication of a greater contribution by diurnal onshore-offshore winds.

The  $S_1$  tide may be treated differently since the gravitational potential for this line is so weak that no calculation is necessary to separate the gravitational tide from the analyzed results. The principal question to be resolved is whether the analyzed value may be due to a  $K_1$  cusp or the continuum (Munk *et al.*, 1965). If not, it appears reasonable to conclude that it is primarily radiational.

The Coast and Geodetic Survey discontinued using the classical method of analysis (Schureman) for a year of data several years ago after Zetler and Lennon (1967) demonstrated that a least-squares solution provided slightly more accurate results. The data in this study of  $S_1$  on the coasts of the United States uses all available analyses completed subsequent to the change in procedure.

Although the theoretical coefficient of  $S_1$  (as given by Schureman) is zero, there is a nearby constituent,

TABLE 2. Radiational  $S_2$  tides for outside or near outside tide stations on the U. S. West Coast.

Place	Latitude (N)	Total $S_2$ Amplitude (cm)	Kappa (deg)	1 year series	Gravitational $S_2$ Amplitude (cm)	Kappa (deg)	Radiational $S_2$ Amplitude (cm)	Kappa (deg)	Amplitude ratio†	Phase difference‡ (deg)
Neah Bay	48 22	22.9	23	1939	21.9	13	4.3	94	0.20	81
Aberdeen	46 58	26.5	52	1934-35	29.6	40	6.7	163	0.23	123
Toke Point	46 42	24.7	36	1938	29.0	24	7.0	155	0.24	131
Astoria	46 13	21.3	51	1932	26.8	43	6.4	197	0.24	154
Newport, South Beach	44 38	22.9	14	1967	25.3	6	4.3	135	0.17	129
Marshfield, Coos Bay	43 23	16.5	56	1933	19.2	43	4.9	175	0.26	132
Crescent City	41 45	17.7	344	1939	17.4	331	4.0	61	0.23	90
Humboldt Bay	40 45	14.9	359	1911-12	16.2	352	2.1	120	0.13	128
San Francisco	37 48	12.5	333	1935	15.5	324	4.0	115	0.26	151
Santa Barbara	34 25	17.4	269	1961	19.2	266	2.1	56	0.11	150
Rincon Island	34 21	17.7	270	1966	19.8	270	2.1	90	0.11	180
Santa Monica	34 00	19.5	264	1938	20.7	260	1.8	33	0.09	133
Los Angeles outer harbor	33 43	20.1	264	1938	23.2	262	3.0	70	0.13	168
La Jolla pier gage	32 52	19.8	263	1933	22.0	260	0.3	*	0.01	*
bottom	32 52	21.3	263	418d.	19.8	262	1.4	23	0.07	121
				1961-63						
San Diego	32 43	21.9	270	1936	22.6	266	1.8	27	0.08	121
								Mean	0.16	133

\* Unreliable phase due to small amplitude.

† Amplitude of radiational  $S_2$  divided by amplitude of gravitational  $S_2$ .

‡‡ Phase of radiational  $S_2$  less phase of gravitational  $S_2$ .



TABLE 3. Radiational  $S_2$  tides for outside or near outside tide stations on the U. S. East Coast.

Place	Latitude (N)		Total $S_2$		1 year series	Gravitational $S_2$		Radiational $S_2$		Amplitude ratio†	Phase difference‡† (deg)
			Amplitude (cm)	Kappa (deg)		Amplitude (cm)	Kappa (deg)	Amplitude (cm)	Kappa (deg)		
Eastport	44	54	43.0	3	1938	58.8	352	18.6	145	0.32	153
Boston	42	22	22.6	4	1934	29.6	358	7.6	160	0.26	162
New York, The Battery	40	42	13.1	262	1961	15.2	260	2.4	67	0.16	167
Sandy Hook	40	28	13.4	246	1937	15.2	247	1.8	71	0.12	184
Atlantic City	39	21	12.2	229	1939	12.5	227	0.6	*	0.05	*
Cape May	38	58	13.1	264	1966	15.2	264	2.1	82	0.14	178
Breakwater Harbor	38	47	11.6	262	1936-37	14.0	268	2.7	114	0.19	206
Old Point Comfort	37	00	7.0	271	1938	9.8	262	2.7	59	0.28	157
Southport	33	55	10.4	236	1938	13.7	228	3.7	22	0.27	154
Myrtle Beach	33	41	13.1	223	1960	14.3	227	1.5	79	0.10	212
Charleston	32	47	12.8	239	1932	12.5	236	0.6	*	0.05	*
Daytona Beach	29	14	10.4	230	1938-39	9.8	231	0.6	*	0.06	*
Patrick AFB	28	14	8.5	224	1960	9.4	230	1.2	90	0.13	220
Miami	25	46	7.3	244	1933, 1940	7.6	253	1.2	153	0.16	260
Key West	24	34	5.2	289	1927, 1933 1939	6.1	287	0.9	90	0.15	163
Mean										0.16	185

\* Unreliable phase due to small amplitude.

† Amplitude of radiational  $S_2$  divided by amplitude of gravitational  $S_2$ .‡† Phase of radiational  $S_2$  less phase of gravitational  $S_2$ .

$B_{23}$ , that differs from  $S_1$  by only  $0.02^\circ$  per year and is therefore virtually inseparable from it. Its coefficient is 0.0042, less than half that of the smallest constituent ( $2Q_1$ , with coefficient 0.0097) ordinarily analyzed by the Coast and Geodetic Survey. Values for  $2Q_1$  are shown in Table 4 as an index of amplitudes equal to or greater than the continuum. Since the values for  $S_1$  consistently and significantly exceed the values for  $2Q_1$  at the same tide stations, it can be concluded that  $S_1$  values are greater than the continuum and also greater than what would be expected from the gravitational potential.

The possibility of the large  $S_1$  amplitudes resulting from the tidal cusp of  $K_1$  has also been considered. However, Munk *et al.* (1965) show that at Honolulu the cusp continuum near  $S_1$  is  $10^{-5}$  times the energy at  $K_1$  (an amplitude factor of  $\sim 1/300$ ). Since the analyzed  $S_1/K_1$  ratio on all three coasts is considerably greater, it seems reasonable to conclude that the  $S_1$  values are not due to the  $K_1$  cusp. The only alternative left seems to be to accept the  $S_1$  values as primarily related to radiational mechanisms.

TABLE 4. Mean amplitudes (cm) of diurnal tidal constituents.

		Tidal constituents			
		$P_1$	$S_1$	$K_1$	$2Q_1$
Theoretical coefficient		0.1755	0.0042*	0.5305	0.0097
Theoretical coefficient/ $K_1$		0.33	0.01	—	0.02
Number of Stations	U. S. Coast				
11	East	3.2	1.2	9.6	0.4
(Mean $\pm K_1$ )		0.33	0.13	—	0.04
15	Gulf	3.7	1.3	12.4	0.4
(Mean $\pm K_1$ )		0.30	0.10	—	0.03
3	West	11.8	0.9	37.9	0.5
(Mean $\pm K_1$ )		0.31	0.02	—	0.01

\* Schureman constituent No. B<sub>21</sub>. Theoretical coefficient of  $S_1$  is 0.0000.

The  $S_1$  phase angles (kappas) are not shown here but the distribution of values appears worthy of comment. For 11 stations on the east coast of the United States and 12 more in the Florida Keys and on the west coast of Florida, the phases for all but two are in the range from  $21^\circ$  to  $93^\circ$ . The two omitted have amplitudes much lower than the other 21 and therefore their phases are not considered reliable. The remaining six stations, three in Texas and three on the west coast of the United States, have  $S_1$  phases between  $189^\circ$  and  $259^\circ$ , roughly opposite to the first group. Some of the spread in phase within an area is attributable to the stations not being restricted to coastal or near-coastal locations; larger lags may be associated with the travel time of a progressive wave in shallow water. No attempt is made here to interpret the contrast in areal distribution of phase but some consideration of global distribution of  $S_1$  phase appears to be warranted.

#### 4. Summary

A simple method has been devised for estimating the amplitude and phase of the  $S_2$  radiational tide from harmonic constants. The values obtained appear to be reasonably consistent with comparable values obtained by the more elegant Munk-Cartwright response analysis method. Although the  $S_2$  radiational tide appears to be significantly related to the action of the atmospheric tide on the sea surface, it appears likely that cyclical (diurnal) offshore-onshore winds also contribute.

The  $S_1$  tide, obtained routinely in tidal analysis of a year of data, is not due to the gravitational potential, to the  $K_1$  cusp, or to the continuum, but is considered to be caused by radiational mechanisms.



*Acknowledgments.* I thank David Cartwright, Walter Munk, Don Hansen and Gordon Groves for their helpful suggestions in this study. However, this does not in any sense imply an endorsement of the final text by any of these. The Division of Oceanography, Coast and Geodetic Survey, furnished almost all of the data.

## REFERENCES

- Cartwright, D. E., 1968: A unified analysis of tides and surges round north and east Britain. *Phil. Trans. Roy. Soc. London*, **A1134**, 1-55.
- Munk, W. H., and D. E. Cartwright, 1966: Tidal spectroscopy and prediction. *Phil. Trans. Roy. Soc. London*, **A1105**, 533-581.
- , B. Zetler and G. W. Groves, 1965: Tidal cusps. *Geophys. J.*, **10**, 211-219.
- Schureman, P., 1941: Manual of harmonic analysis and prediction of tides. Special Publ. 98, U. S. Coast and Geodetic Survey, 317 pp.
- Siebert, Manfred, 1961: Atmospheric tides. *Advances in Geophysics*, Vol. 7, New York, Academic Press, 105-187.
- Zetler, B. D., 1969: Shallow-water tide predictions. *Proc. Symp. on Tides*, Monaco, 1967, UNESCO, 163-166.
- , and G. W. Lennon, 1967: Some comparative tests of tidal analytical processes. *Intern. Hydrogr. Rev.*, **44**, 139-147.

## TIDAL CONSTANTS DERIVED FROM RESPONSE ADMITTANCES

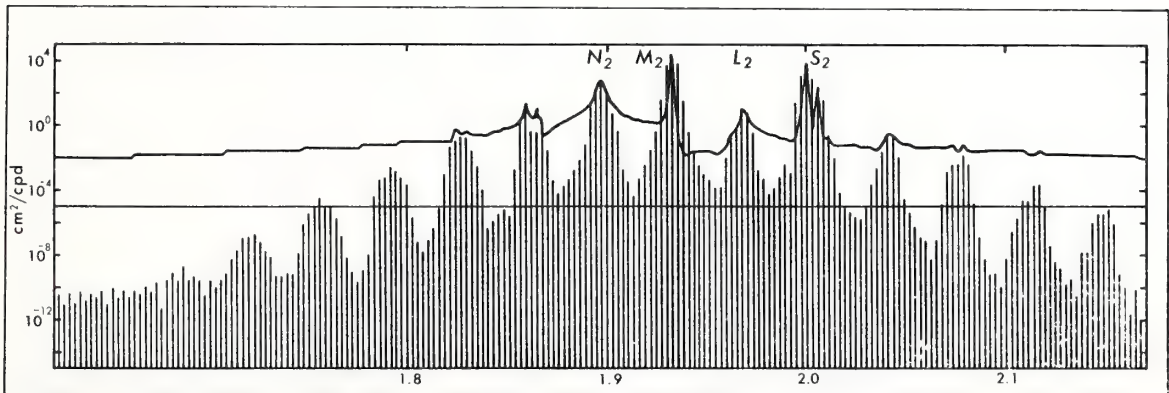
B. ZETLER<sup>1</sup>, D. CARTWRIGHT<sup>2</sup> and W. MUNK<sup>3</sup>

**ABSTRACT.** — The «response method» of tide prediction has previously been applied to various observed series to obtain frequency-dependent admittances that describe the tidal characteristics in a similar sense to what can be deduced from traditional harmonic constants. To bridge the gap between the two methods of presentation, procedures are described on how to derive harmonic constants from the response admittances and one method is applied to a set of observed data.

Munk and Cartwright (1966) have developed a «response method» of prediction in which the input functions are the time-variable spherical harmonics of the gravitational potential and of radiant flux on the Earth's surface. This is a major departure from the traditional solutions in which the tide oscillations are described by the amplitude and phase lags for a finite set of cosine curves of predetermined frequencies.

As an illustration of the result of dealing with the complete potential rather than a set of discrete frequencies, the vertical lines in figure 1 are from a high resolution Fourier analysis near 2 cycles per day of an equilibrium prediction that has been tapered to reduce the side bands of strong lines. The curving somewhat-horizontal line is the analyzed energy level for the same

series before it has been tapered. Doodson (1921) in his development of the tidal lines based on sums and differences of multiples of six frequencies, limited his compilation to amplitudes at least  $10^{-4}$  times the  $M_2$  amplitude. In figure 1, the vertical scale is energy rather than amplitude, so the comparable limit is  $10^{-8}$ . Some of the tidal groups from the tapered series show distinct peaks with energies lower than this limit and therefore could not have been predicted even if all of Doodson's constituents had been used. Although this indication of very small amplitudes being included is scientifically interesting, the principal advantage in the method lies in dealing with the known orbital constants and thereby using the complete potential rather than an arbitrarily determined finite set of frequencies.



High resolution analysis of one year of predictions of the gravitational potential near two cycles per day. The curving somewhat-horizontal line shows the energy level of the untapered series; the vertical lines are the energy levels for the same data, tapered to reduce side bands.

(1) ESSA Atlantic Oceanographic and Meteorological Laboratories, Miami, Florida, U.S.A.

(2) National Institute of Oceanography, U.K.

(3) Institute of Geophysics and Planetary Physics and Scripps Institution of Oceanography, University of California, San Diego, California, U.S.A.

The response method includes shallow water interaction and radiational inputs for ocean tides but these are not believed to be important to earth tides and do not receive further mention in this presentation.

In simplest terms, a responsive prediction,  $\zeta(t)$ , for time  $t$  can be a weighted sum of past and present values of the potential,  $V(t)$ ,

$$\zeta(t) = \sum_s w(s) V(t - \tau_s), \quad (1)$$

with the  $s$  weights,  $w$ , determined for a range of  $s$  lags,  $\tau$ , so that the prediction error is a minimum in the least square sense. The Munk-Cartwright response method expand  $V(t)$  in spherical harmonics\*

$$V(\theta, \lambda; t) = g \sum_{n=0}^{\infty} \sum_{m=0}^n a_n^m(t) U_n^m(\theta, \lambda) \quad (2)$$

where  $\theta$  is geographical colatitude,  $\lambda$  is east longitude,  $t$  is mean solar time and  $a(t)$  is the amplitude of the spherical harmonic  $U$  of order  $m$  and degree  $n$ . The  $m$ -values separate input functions according to species.

The convergence of the spherical harmonics is rapid and just a few terms  $m$ ,  $n$  will do. The prediction formalism is then

$$\zeta(t) = \sum_{m,n} \sum_s w_n^m(s) a_n^m(t - \tau_s), \quad (3)$$

with the prediction weights,  $w_n^m(s)$  determined by least-square methods for each port. For any given time, a prediction for the port is obtained by applying the weights,  $w_n^m(s)$ , to the global tide function for that period,  $a_n^m(t)$ .

Munk and Cartwright (1966) experimented with various lag intervals and finally selected an arithmetic series of lags with an increment of 2 days. If, in equation (3),  $s$  is taken as zero only (prediction based on present but no past or future values), the same weight,  $w_n^m(0)$ , applies to an entire species (for a particular degree  $n$ ) and therefore the prediction within any species will be found to be proportional to the equilibrium relationship. It is possible that this may be adequate for earth tides but clearly it is not generally so for ocean tides, and ocean loading may similarly effect earth tide analysis. In the calculation that is given in this paper, lags of 0,  $\pm 2$  and  $\pm 4$  days were used (i.e.  $\tau_s = 2s$  days,  $s = -2(1) + 2$ ). The table of results shows a changing but relatively smooth transition across the species.

In a sense, the amplitudes and phase lags of the traditional tidal constituents are replaced by the station weights,  $w_n^m(s)$ , of the response formalism but the two sets of numbers are closely related. In fact, the complex admittance,  $Z(f)$ , at a particular frequency  $f$  is the Fourier transform of the lagged weights

$$Z(f) = \int_{-\infty}^{\infty} w(\tau) e^{-i2\pi f\tau} d\tau \quad (4)$$

where  $|Z|$  is the amplitude response and  $\arg(Z)$  the

phase lead. Furthermore, the amplitude response,  $|Z|$ , when determined by the transform (4) rather than by spectral analysis, refers only to the coherent (or noise-free) part of the observations, as is in fact desirable.

## RESPONSE ANALYSIS

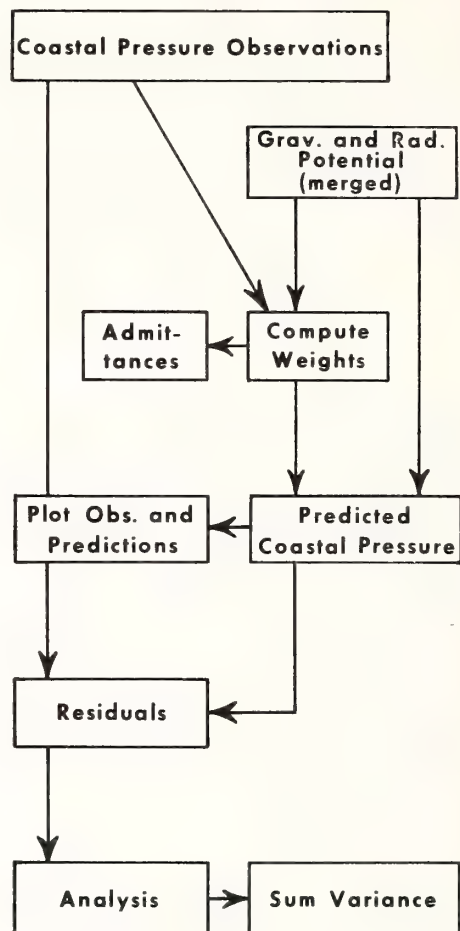


Fig. 2. — Flow diagram describing sequence of calculations.

The computer program to obtain the admittances permits the determination of any or all of the following:

1. Real part of  $Z(f)$
2. Imaginary part of  $Z(f)$
3.  $|Z(f)|$
4.  $\arg Z(f)$  in radians.

Thus far we have outlined the more-or-less standardized response analysis procedures that were available to the authors of this paper when they met in La Jolla earlier this year to discuss possible procedures for the analysis of pelagic tide measurements (Cartwright, Munk and Zetler, 1969). We decided that it would be useful and appropriate to present our results in two forms, admittances and harmonic constants.

\* In practice it is convenient to use complex harmonics,  $U_n^m + iV_n^m$ , that are  $90^\circ$  out of phase in longitude.



With reference to calculating the harmonic constants from the admittances, there were several possible methods considered for this procedure. These include: (a) Compute (once for all) the harmonic constants of the potential functions and then multiply by the calculated admittances to derive the harmonic constants for the observed tide series. This method would ultimately demand the least computing effort from the user, once the initial harmonic constants had been computed and presumably published. For each constituent, one would of course have to add vectorially the harmonic constants derived from the separate potentials. However, one would need an 18.61 year series of all the potentials to do this properly and we were not prepared to make so elaborate an effort at the time. Doodson's (1921) constants are based on slightly different astronomical values, and apply only to the gravitational potentials. (b) Since we were concerned with the eight principal constituents, a method was derived for the extraction of these constituents only. The series needs to be long

enough to extract by filtering the eight tidal groups without contamination by side bands. A 710-day series of 3-hourly heights was predicted by the response method, the series was multiplied by a symmetric cosine taper to make side-band effects negligible, and the following harmonics were determined:

634 ( $Q_1$ ), 660 ( $O_1$ ), 708 ( $P_1$ ), 712 ( $K_1$ ), 1346 ( $N_2$ ),  
1372 ( $M_2$ ), 1420 ( $S_2$ ), 1424 ( $K_2$ ).

The results needed to be corrected for the filter response as well as for equilibrium arguments and node factors. The corrections were by-passed simply by comparing the harmonics with corresponding harmonics derived from a tapered predicted series for the same epoch with  $H = 1$  and  $G = 0^\circ$  for the required constituents and  $H = 0$  for all others. The ratios of the harmonic amplitudes then give the required  $H$ 's and the differences in phase the required  $G$ 's.

TABLE 1.

Station Bottom pressure (La Jolla - 600 m from shore off Scripps pier). Water depth 18 m, sensor buried 3 m below bottom. 418 days. 1961 Dec 10 to 1963 Feb 1 (542953.9583 to 552985.9583).

Reference Gravitational and radiational potentials  $c_2^1 (0, \pm 1, \pm 2)$ ,  $c_3^1$ ,  $\chi_1^1$ ,  $\chi_2^1$ ,  $c_2^2 (0, \pm 1, \pm 2)$ ,  $c_3^2$ ,  $\chi_2^2$

CPD	Admittances (Station/Reference) Intervals 1 cpm (0.0366011 cpd)			STATION LEAD DEG.		Principal harmonic constituents G is Greenwich Epoch in degrees		
	REAL	IMAG.	R			CPD	STATION H (cm)	G
0.8929346	0.8454	—0.0986	0.8512	+173.34	( $Q_1$ )	0.8932441	4.18	186.63
0.9295357	0.8218	—0.1737	0.8399	+168.06	$O_1$	0.9295357	21.81	192.02
0.9661368	0.6689	—0.2492	0.7138	+159.57	( $P_1$ )	0.9972621	10.85	206.25
1.0027379	0.8332	—0.4205	0.9333	+153.22	$K_1$	1.0027379	34.40	206.80
1.0393390	0.8691	—0.5609	1.0343	+147.16				
Recorded variance	814.04 $\text{cm}^2$							
Residual variance	0.97 $\text{cm}^2$							
Ratio	0.0012							
1.8590714	—0.0322	—0.9968	0.9973	—91.85				
1.8956725	—0.5233	—0.8650	1.0110	—121.17	( $N_2$ )	1.8959820	12.21	122.92
1.9322736	—0.6433	—0.4903	0.8088	—142.69	$M_2$	1.9322736	51.02	142.66
1.9688747	—0.5416	—0.2001	0.5774	—159.72	( $S_2$ )	2.0000000	21.33	137.58
2.0054758	—0.4881	—0.5483	0.7341	—131.68	$K_2$	2.0054758	6.08	131.31
Recorded variance	1682.76 $\text{cm}^2$							
Residual variance	0.66 $\text{cm}^2$							
Ratio	0.0004							

In table 1 which shows species 1 and 2 admittances and harmonic constants, the elements of admittance are given at five evenly spaced frequencies, namely  $m$  cycles per lunar day +  $k$  cycles per month =  $(0.9651368 m + 0.0366011 k)$  cpd where  $m$  is the species number and  $k$  takes the value  $-2 -1 0 1 2$ . For these frequencies, there are listed the real and imaginary admittances and the ratio and station lead (in degrees) that are obtained from these. These admittances were derived from the complex coefficients of the spherical harmonic of order 2 only (for consistency in other aspects of the study) but the station harmonic constants shown on the right were derived

from the complete set of weights and potentials. The frequencies of the unbracketed constituents ( $O_1$ ,  $K_1$ ,  $M_2$ , and  $K_2$ ) match exactly those shown in the first column; for the bracketed constituents ( $Q_1$ ,  $P_1$ ,  $N_2$ , and  $S_2$ ), the admittances were evaluated from the response weights at the exact frequencies of the constituents.

Below the admittances for each species, there are listed the recorded variance within a band of frequencies from  $k = -4.5$  to  $k = +4.5$ , derived from a Fourier analysis of the entire series. Below this there is listed the corresponding variance of the residual series when the response convolution (prediction)

is subtracted from the recorded series. The ratios of the two, 0.0012 for species 1 and 0.0004 for species 2,

are indications of the reliability of the admittance figures.

TABLE 2.  
La Jolla Harmonic Constants

	Response Analysis		U.S. Coast & Geodetic Analysis	
	418 days from 10 Dec. 1961		369 days from 1 Jan. 1940	
	$H(\text{cm})$	$G$	$H(\text{cm})$	$G$
$Q_1$	4.18	187	3.75	183
$O_1$	21.81	192	21.03	192
$P_1$	10.85	206	10.82	204
$K_1$	34.40	207	33.04	206
$N_2$	12.21	123	11.67	121
$M_2$	51.02	143	49.74	143
$S_2$	21.33	138	20.03	137
$K_2$	6.08	131	5.15	133

Table 2 shows the harmonic constants derived in this study compared with a set of constants computed by the U.S. Coast and Geodetic Survey for a different series of observations for one year by conventional methods. The differences are not significant from a practical point of view and the comparison is made only to demonstrate that results from the classical and response methods of analysis are compatible.

The above analysis required about a year's data, as in conventional procedures. Where only about a month of data is recorded, the same harmonic constants can still be derived from the response formalism, provided a « reference station » exists whose constants have been computed from a year's or more data, and whose tidal characteristics are expected to be closely related to the short-term station. One simply multiplies the constants of the reference station by a special admittance or « transfer operator » describing the relationship of the tides at the two stations. This admittance can be determined quite adequately by comparing a month's data at the short-term station with simultaneous response-predictions for the reference station. The procedure is described in greater detail by Cartwright, Munk and Zetler (1969) with application to the analysis of tidal records from the deep ocean.

#### REFERENCES

- CARTWRIGHT, D., W. MUNK, and B. ZETLER. A suggested procedure for the analysis of pelagic tidal measurements. EOS, Trans., Amer. Geophys. Union, Vol. 50, No. 7, pp. 472-477, July 1969.
- DOODSON, A.T. The harmonic development of the tide-generating potential. Proc. R. Soc., (A) 100 : 305-329, 1921.
- MUNK, W. and D. CARTWRIGHT. Tidal spectroscopy and

prediction. Phil. Trans. Roy. Soc. London A, 259 : 533-581, 1966.

#### DISCUSSION

DEJAIFFE : What kind of method do you use to perform numerically your Fourier transform : Fast Fourier Transform, Fillon's quadrature formulas ?

ZETLER : We do not use Fast Fourier Transform because we need only a relatively small number of frequencies. Furthermore, some or all of the required frequencies are not likely to fall exactly on the harmonics of the series length.

BOZZI-ZADRO : How do you compute the radiational potential ?

ZETLER : We use an input function which is a half cycle of a sine curve ( $0^\circ$  to  $\pi$ ) in 12 hours, followed by 12 hours of zero, the sine curve again, etc. The period is solar diurnal but the sharp discontinuities make the series rich in higher harmonics,  $S_2$  etc.

As a further illustration of the need for a radiational input, consider the following : if one plots, for ocean tides, the phase as a function of frequency near 2 cpd, the plot is reasonably smooth until  $S_2$  where there is a sharp bend. Similarly, if one plots the ratio of analyzed amplitude to the Doodson coefficient, again there is a smooth curve abruptly terminated at  $S_2$ . Then, one must ask whether it is reasonable for the oceans to display such an abrupt change in response to the tide potential and the logical answer is « no ». When the radiational effects (diurnal heating, differential absorption by land and ocean causing diurnal onshore-offshore winds, barometric variations in tidal frequencies) are given consideration, the gravitational response becomes smooth across  $S_2$ .





NATIONAL FILM BOARD OF CANADA PHOTOS BY G. BLOUIN

Low and high tide at Parrsboro, Nova Scotia. Tides in the Bay of Fundy area are as high as 70 feet (21 meters).

**TIDE**, the periodic motion of the waters of the sea, caused by the attractive forces of the moon and the sun. Tidal motion is most readily noted along a beach that is periodically bared at low tide and then covered by the succeeding high tide.

Methods for tidal prediction were developed primarily as an aid to mariners. For example, a ship may ride too deep in the water to clear a sand bar except at high tide. Therefore, tables of predicted tides are needed to supplement the depth data on a nautical chart. Similarly, tidal currents may help or hinder the ship's progress, so that tables of predicted tidal currents may also be needed. In addition, tides are important in many engineering projects, such as pollution studies, harbor channel maintenance, and power generation.

If the earth were moonless, the tides would be caused by the sun alone and would be much simpler to predict. The tides would occur at about the same time each day, and the difference between high and low tide would be considerably smaller. The changes in tidal height from day to day would also be very much smaller, the principal variations being associated with the annual cycles of varying distance and declination of the sun.

#### TIDAL ACTIONS

Tides are caused primarily by the moon's gravitational attraction and tend to follow the lunar day of 24 hours and 50 minutes, which is the average time between the moon's transits over any given meridian of longitude on earth.

There are two tides a day at most places, marking the passing of the high-water crests below the moon and on the side of the earth opposite the moon. Thus the time between successive high waters averages 12 hours and 25 minutes. At a very few places in the world, such as Port Adelaide on the southern coast of Australia, the solar tide is dominant, and the average time between successive high waters is 12 hours. The range in height between high and low waters is less than a foot in some areas. In others, such as the Bay of Fundy in Nova Scotia, the tidal range may be as great as 50 feet (15 meters).

**Kinds of Tides.** Tides are ordinarily classified as semidiurnal, diurnal, or mixed.

When there are two high tides and two low tides each lunar day, and the differences in height between pairs of successive high waters

and successive low waters are relatively small, the tide is called *semidiurnal*. Tides on the Atlantic coast of the United States are representative semidiurnal tides.

In areas of *diurnal* tides there is only one high tide and one low tide each lunar day, except possibly for a few days during the month when the moon is near the equator. The tide at Pensacola, Fla., on the northern shore of the Gulf of Mexico, is a typical diurnal tide.

With a *mixed* tide, both diurnal and semidiurnal oscillations are important. There is a significant inequality in either the two high-water heights or the two low-water heights in a lunar day, or sometimes in both pairs of heights. The tides along the Pacific coast of the United States are mixed.

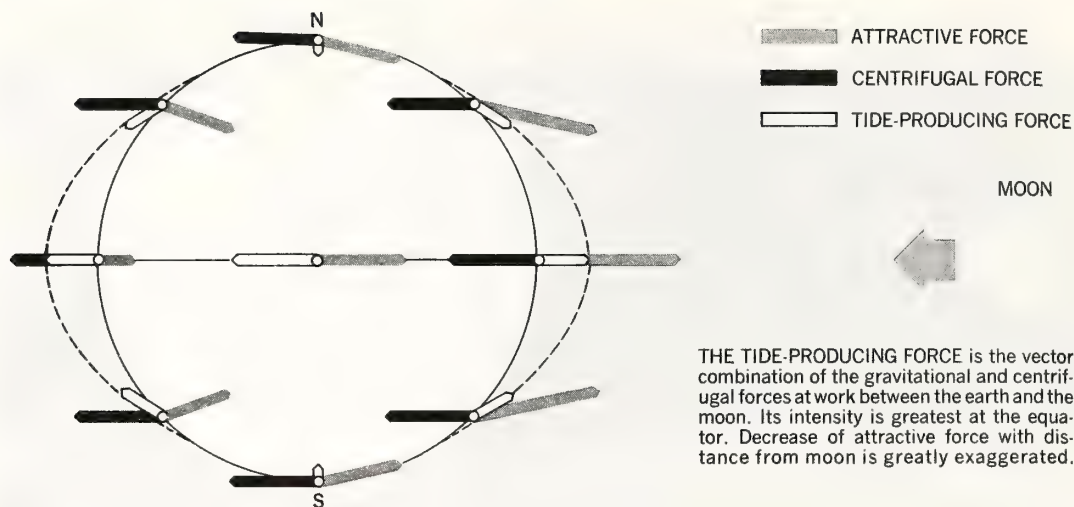
**Tidal Current.** The tide is a three-dimensional phenomenon, affecting water at depth as well as at the surface. Therefore there are horizontal changes, called *tidal currents*, that correspond to the rise and fall of tides.

In river mouths or in straits where the direction of flow is restricted, the tidal current reverses during the lunar day. That is, it flows alternately in opposite directions, with a short period of little or no current at each reversal that is called *slack water*. The tidal current flowing from the ocean into a river is called *flood current*, and the current flowing in the opposite direction is called *ebb current*.

In the ocean there are tidal currents offshore that flow continuously, changing in direction through all points of the compass during a tidal period. These are called *rotary currents*. A diagram showing a series of arrows from a common center, representing the speed and direction of the rotary current each hour, is called a *current rose*, and a curve connecting the ends of the arrows is called a *current ellipse*. Just as with tides, tidal currents may be semidiurnal, diurnal, or mixed.

**Bore.** The speed of progress of the crest of a tide varies directly as the square root of the water depth over which it is passing. Thus the speed is decreased when the wave enters shallow water. Since the water depth at the trough is more shallow than at the crest, the retardation is greater, and the slope of the wave front is steepened. This means that the time from low tide to high tide becomes less than the following time period from high tide to low tide. In a few estuaries with large tidal ranges and a sloping riverbed, the advance of the low-water





trough is so retarded that the crest of the rising tide virtually overtakes it. The crest then advances upstream as a turbulent wall of water, called a *bore*. On days when the tide range is large, there is a bore in the Petitcodiac River in the Bay of Fundy.

**Nontidal Phenomena.** Other phenomena that are sometimes noted on tide gauge records include tsunamis, storm surges, and seiches. A *tsunami*, or "tidal wave," is a series of long waves, usually caused by a seismic displacement of the sea floor. The waves travel across the ocean at speeds as great as 500 miles (800 km) per hour, sometimes building up to destructive heights as they move into the slopes of a coastal region. See also EARTHQUAKE—*Effects of Earthquakes*.

**Storm surges** are rises in sea level that are caused by hurricane winds piling water onto a coast. A *seiche* is a stationary or standing wave that is caused by strong winds or by changes in atmospheric pressure over closed basins. Seiches have periods ranging from a few minutes to possibly more than an hour.

#### THE FORMATION OF TIDES

In analyzing the ways in which tides form, it is convenient to study a theoretical "equilibrium tide" by developing a mathematical approach that uses a set of assumptions known to be fictitious. The assumptions specify that the earth is covered by a uniformly deep layer of water, and that these waters respond instantly to the tide-producing forces of the moon and sun to form a "surface of equilibrium," disregarding friction and inertia. Although the actual tides are quite different, this approach permits the determination of the astronomical periods that are important to tides. It thereby facilitates analysis of tide observations and the subsequent predictions based on empirical findings.

Calculation of the tide-producing force can also be simplified if the complex motions of the 3-body earth-moon-sun system are separated into the relatively simpler motions of the 2-body systems of earth-moon and earth-sun.

**Tides and the Moon.** The moon attracts every particle of matter in the earth, its ocean, and its atmosphere. The attractive force in effect is directed toward the center of the moon and is

inversely proportional to the square of the distance between the particle and the moon's center. If the distances of two points on the earth from the moon's center are unequal, the attractive forces at the two points are similarly unequal. The tide-producing force does not represent the attractive force itself. It represents the *difference* in attractive forces, and it varies approximately inversely as the cube of the distance to the center of the moon.

If no other force besides gravitational attraction acted on the earth-moon system, earth and moon would simply come together. However, there is also a centrifugal force at work that is equal and opposite to the gravitational force at the center of the earth. Thus the net force acting on any particle is the vector combination of these two forces. Furthermore, unlike the gravitational force, the centrifugal force is equal and in the same direction for every particle on earth. Whereas the gravitational force is directed toward the center of the moon, the centrifugal force is directed away from the moon in a direction that is always parallel to the imaginary line connecting the centers of the earth and the moon. Where this line intersects the crust of the earth on the moonward side, there is a net force directed toward the moon along the line. Where the line intersects the earth's crust on the side away from the moon, there is a net force directed away from the moon.

If the tide-producing forces at all points on the earth's surface are resolved into vertical and horizontal forces, it is readily demonstrated that the vertical forces in line with the gravitational field of the earth have little effect (see diagram). Instead it is the horizontal forces unopposed by the earth's gravity that draw particles of water over the earth's surface, thereby piling up high-water bulges under and opposite to the moon. That is, the high waters are not caused by any lifting of the water against the force of the earth's gravity, but rather by horizontal tractive forces unopposed by gravity.

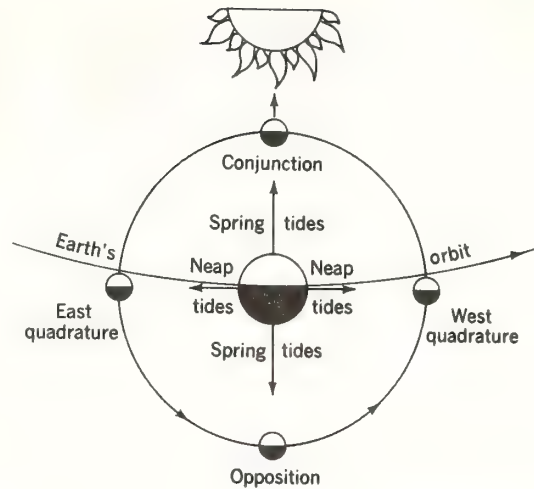
**Tidal Periods.** The simplest concept of the earth-moon system is that the moon revolves around the earth once each month in a circular orbit that is in the plane of the earth's equator. As the earth rotates on its axis once every 24 hours, there is a high-water bulge under the

moon, another bulge on the side away from the moon, and a low-water trough on either side of the earth between the bulges. The half lunar day of 12 hours and 25 minutes is the time interval between successive high tides or low tides, and it is the most important period in tidal studies.

In actuality the moon does not go around the earth in a circular orbit, but rather in an elliptical one. Two weeks after it is at *perigee*, the point in its orbit when it is closest to the earth, the moon is at *apogee*, the point farthest from the earth. Because the tide-producing force is inversely proportional to the cube of the distance to the center of the moon, the tidal range is greater than average by about 20% at perigee and smaller than average by about 20% at apogee. To account for this, the tidal mathematician introduces another semidaily tide whose period is such that it is in phase with, or reinforces, the lunar tide at perigee—"perigean tide"—and is out of phase with, or opposed to, the lunar tide at apogee—"apogean tide."

Another complicating factor is that the moon does not remain in the plane of the earth's equator. Instead it moves from an extreme northern declination across the equator to an extreme southern declination and back again, the cycle taking about 27 solar days. When the moon is at its extreme northern or southern declinations, the two tidal bulges are no longer centered on the equator. For example, if the high water under the moon has its maximum in the Northern Hemisphere, the maximum on the opposite side of the earth has its center in the Southern Hemisphere. Thus, as the earth rotates on its axis, a given point on the surface may experience two high- and two low-waters, but they are at different heights. The difference in height caused by the moon's change in declination is called the *diurnal high-water inequality*.

When the moon is at its extreme declination, the larger diurnal ranges—that is, the difference between the heights of the higher high tide and the lower low tide—are called *tropic tides*. The



COMBINED EFFECT OF SUN AND MOON on tidal ranges varies according to their positions relative to the earth. Small neap tides occur when the three bodies are aligned. Large spring tides occur when sun and moon are at right angles to the earth.

smaller diurnal ranges that occur when the moon is on the equator are called *equatorial tides*.

To simulate the declination period of the moon, the tidal mathematician uses two diurnal tides that are in phase when the moon is at either extreme northern or extreme southern declination and are opposed when the moon is on the equator. The two tides are also such that the sum of their speeds exactly equals the speed of the lunar semidaily tide.

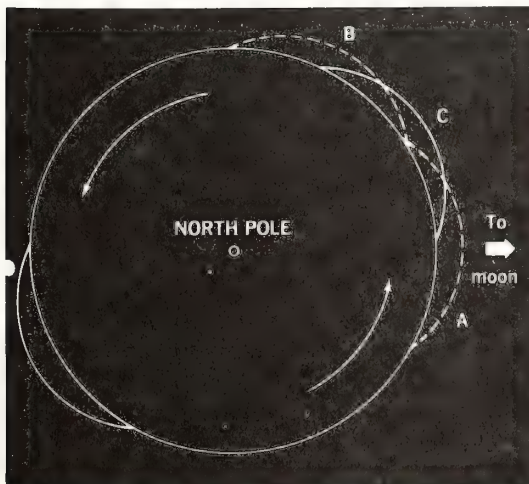
**Tides and the Sun.** As with the moon, the sun attracts every particle of the ocean and earth. In the earth-sun system there are solar tides under the sun and on the opposite side of the earth. They are smaller and occur at different times than lunar tides. The solar high waters are about 12 hours apart as the earth rotates on its axis. Although the sun's mass is nearly 27 million times the mass of the moon, the distance of its center from the earth is about 390 times that of the moon's distance. Therefore the solar semidaily tide is only 46% that of the lunar semidaily tide.

At new and full moon, both sun and moon are lined up so that the lunar and solar tides reinforce each other. The larger tidal ranges that result are called *spring tides*. In contrast, at first and last quarters of the moon the lunar and solar tides are opposed, and the smaller combined tides that result are called *neap tides*.

The range of the solar tide also varies annually between *perihelion* and *aphelion*, the points in the earth's orbit closest to and farthest from the sun, respectively. In addition a diurnal inequality is introduced because of the annual declinational cycle of the sun. These and other, smaller astronomical refinements are introduced in equilibrium theory by simulated tides of appropriate periods.

**Earth and Atmospheric Tides.** Unlike the familiar ocean tides, the occurrence of tides in the earth and in the atmosphere is not commonly known. The mechanisms causing these three kinds of tides are quite different.

A TIDAL BULGE of the oceans would occur directly below the moon if the earth were frictionless (A), but the friction of the ocean basins tends to drag the bulge forward as the earth rotates (B). The net result of gravitational pull and friction is that the tidal bulge moves slightly ahead of the moon (C).





Although the solid earth is subject to periodic deformations similar to those for ocean tides, the particles in the earth's crust cannot be moved freely by horizontal forces into high-tide bulges, as the particles in the oceans can. Therefore the vertical tide-producing forces are the effective mechanism for tides in the solid earth. The tides are usually measured by observation of the variations in the acceleration of gravity and by observation of the variations in the vertical—that is, in the direction in which a plumb line points.

Concerning the atmosphere, analyses of long series of barometric records indicate that there are small lunar tides and significantly larger semidaily solar tides. In low latitudes, atmospheric pressure tends to be high about 10 A. M. and 10 P. M. local time, and low about 4 A. M. and 4 P. M. Although some aspects of the causes of the solar atmospheric tide are unresolved, it is apparent that thermal factors are the principal mechanism causing these tides.

#### DEVELOPMENT OF TIDAL STUDIES

For centuries tides were measured by visual observations, such as of the level of water on a vertical graduated staff or plank. Automatic tide gauges that record the level of a float in a vertical well are believed to have been introduced about 1830. The float-type gauge is still in general use at most tide stations. Pressure-measuring devices placed on the sea floor have also been developed, but relatively few are yet in use.

**Tidal Theory.** A few references to tides appear in ancient Greek and Roman writings. Tidal theory essentially originated in the 17th century with Isaac Newton, who applied the laws of gravitation to develop a theoretical equilibrium tide. However, because the connection between the moon and tides was rather obvious, useful tide predictions were produced by rule-of-thumb methods independent of the development of tidal theory. The methods of calculations were considered a family secret to be passed on from father to son. The *Liverpool Tide Tables* by a clergyman named Moses Holden is an outstanding example.

In 1831, John Lubbock used then-existing tidal theory to develop a "nonharmonic" method of tide prediction, as contrasted to the harmonic method described below. He modified time and height predictions of high and low waters based on times of lunar transit by making corrections for the "age" of the moon in the cycle from one new moon to the next, and also by correcting for the declination and parallax of the moon and the sun.

In the late 18th century the French mathematician and astronomer Pierre Laplace formulated the equations of motion for tides on a rotating earth. Subsequent significant contributions were made by George Airy, Lord Kelvin, and George Darwin in Britain and by William Ferrel and Rollin A. Harris in the United States. By the beginning of the 20th century, the tide-prediction technique known as the harmonic method was in general use by the various government tidal agencies throughout the world.

**The Harmonic Method.** In the harmonic method an observed tide record is first broken down into a number of cosine curves, with each curve representing a significant astronomic period. The derived amplitude and the time lag of each cosine curve apply uniquely to the specific geographic location where the observations were obtained.

The individual cosine curves are adjusted in time according to the astronomic events prevailing at the time of the desired predictions. The cosine curves then are added together so that predicted times and heights of high and low waters can be read from the composite cosine curve.

The harmonic method is empirical. It uses equilibrium theory primarily to identify the significant tidal frequencies and to provide a phase reference for each of these frequencies at any time in the past or the future.

The U. S. Coast and Geodetic Survey used 37 tidal constituents—harmonic elements in the mathematical expression for the tide-producing force—on its mechanical tide-predicting machine built in 1910. The gearing on the machine included tidal frequencies ranging from 8 cycles per day to 1 cycle per year. The predicting machine at the Liverpool Tidal Institute included 60 constituents, the greater number being partly related to the nonlinear tides in shallow waters around the British Isles.

**Establishment of Datum Planes.** In general, tide tables were developed to supplement the depth information on nautical charts. To be able to add chart soundings and table predictions readily by algebraic means, so that depths could be ascertained at a particular time, it became necessary to relate the charts and tables to a particular *datum*, or base reference. There is an international agreement to the effect that the datum of a nautical chart should be so low that the tide seldom, if ever, falls below that level. The practical advantage of such a datum is that the navigator, without consulting a tide table, can count on at least the depth shown on the chart at all times.

However, for various legal and historical reasons, the U. S. Coast and Geodetic Survey does not use a chart datum that low. Instead it uses *mean low water*, the average height of low waters over a 19-year period, on the eastern coast of the United States. On the western coast it uses *mean lower low water*, the average height of the lower of the two low waters each day over a 19-year period—approximately the period required for the regression of the moon's nodes to complete a circuit of 360° in longitude.

Many European countries use *mean low water springs*, or the average low water near times of new and full moon, as their datum. Some countries that have large diurnal tides use *mean Indian spring low water*, which is the average of the lower low tides on days when the moon is new or full and is also near its maximum declination. The name derives from investigation of the tides of India.

#### TIDAL STUDY TODAY

Methods of tidal analysis and prediction had reached so high a level of achievement by the beginning of the 20th century that procedures remained relatively unchanged for more than 50 years, until the development of electronic computers. Thus, although in 1921 the British oceanographer Arthur Doodson published a greatly expanded study of the equilibrium tide that included about 400 constituents, these additional constituents were not used for practical tide predictions. The increased accuracy from the effort would have been small, and the increased friction in an enlarged mechanical predicting machine would have been too great.



**Computer Techniques.** In the 1960's changes brought about by the development of electronic computers were made in all aspects of tidal observation, analysis, and prediction. Digital recorders have been installed on automatic tide gauges, providing sequential, point-to-point values of the height of a given tide. These data are routinely processed on computers to calculate the times and heights of high and low waters, mean ranges and inequalities, various tidal planes and monthly extremes, and the lunital intervals—the intervals between the moon's transit over the local or Greenwich meridian and the following high or low water.

New analysis procedures have been developed for obtaining the amplitude and phase lag for each constituent of the tide. For example, a "least square" procedure has been programmed for large computers. This procedure solves for all constituents simultaneously, in contrast to the traditional Fourier analysis for one constituent at a time, which eliminates the effects of the other constituents from each result. (See HARMONIC ANALYSIS.) The newer procedure has been found to fit the recorded data somewhat more accurately. In addition, unlike Fourier analysis, it does not require an unbroken sequence of data equally spaced in time.

Electronic computers permit the specification of any frequencies in the prediction process, whereas the mechanical tide-predicting machines were limited to a finite set of frequencies for which appropriate gears were included in the basic design. In both Britain and the United States, studies of the prediction of shallow-water tides by harmonic methods exploited this newly found flexibility, using about 115 tidal constituents to permit more accurate analysis and prediction.

Research studies have used long series of data, for example, a list of 500,000 hourly readings of tidal heights taken over a 50-year period, to establish values of the *continuum*—the "noise," or nonpredictable variations in sea level—as a function of frequency. Determination of these values establishes the limits that may be achieved by even the best predicting procedures. Studies of this kind are also impossible without the use of electronic computers.

In addition, geophysicists Walter Munk of the United States and David Cartwright of Britain developed a "response" method of tide prediction. Weights are computed for a set of time-variable spherical harmonics of the gravitational potential and of radiant flux on the earth's surface to obtain an optimum fit to an observed series of tide heights. For predictions at another time, the same set of weights are then applied to a time series for the gravitational and radiational potentials for the required times.

**Study of Worldwide Tidal Patterns.** There are ordinarily about 1,000 tide gauges operating around the world at any given time. But for describing global patterns of the tide they could hardly be more poorly distributed. Most of them are at the mouths of harbors and on rivers, places for which tide predictions are a practical necessity. However, because the coastal features may severely modify both the amplitude and the phase of the ocean tide, the harbor and river observations have very limited use in attempts to depict tidal phenomena in the oceans.

Nevertheless, men have attempted for more than a century to use these data, together with

data gathered around islands, in preparing cotidal charts and co-range charts of the world. A *cotidal chart* is a set of lines on a chart, each line joining all points at which high water occurs at the same time. Similarly, a *co-range chart* has lines passing through places of equal tidal range. These charts are used in describing only a single harmonic constituent of the tide, so that in theory a chart would be needed for each constituent. In practice, however, charts have been attempted only for the major constituents: the lunar semidaily, solar semidaily, lunar-solar daily, and lunar daily. The principal effort has been applied to lunar semidaily charts, and the preparation of cotidal charts has received more attention than co-range charts.

The most critical aspect of cotidal charts is the location of *amphidromic points*. These are no-tide points from which the radiating cotidal lines progress through all hours of the tidal cycle. Even if there are some islands near these points for which tidal data are available, the "noise" to "signal," or significant data, ratio is large, and hence the data are less reliable when the range of tide is small.

An international program for measuring the tide in deep ocean was initiated in the mid-1960's. Free-fall gauges have been developed that record on the ocean floor and then are recalled to the surface by means of signals. Other bottom-mounted gauges, connected by cables to ships or to the shore, have also produced valuable data. The program to obtain a grid of tide stations covering the world's oceans will take a long time, but the data will be extremely useful for comparison with theoretical numerical studies of the world distribution of tides.

Although tidal characteristics change from place to place, tides in the Atlantic Ocean are basically semidaily, whereas Pacific Ocean tides tend to be mixed. There is some evidence that the tidal range observed on the east coast of the United States varies directly with the width of the continental shelf. Florida is in a somewhat unique tidal environment, having a semidiurnal tide at Miami, a mixed tide at Key West, and a diurnal tide at Pensacola.

**Publications.** The U. S. Coast and Geodetic Survey publishes annual tide tables for the entire world, in four volumes. Each volume contains daily predictions for key places and tables of time and height differences for secondary sites. There are also two annual volumes of tidal current tables, primarily for places in North America. In addition the survey publishes tidal current charts for a number of major harbors and estuaries. Most of the other important nautical countries publish their own tide tables in various formats.

BERNARD D. ZETLER, *ESSA Atlantic Oceanographic and Meteorological Laboratories, Miami*

#### Bibliography

- Defant, Albert, *Physical Oceanography*, vol. 2 (New York 1961).  
 Dietrich, Gunter, *General Oceanography: An Introduction* (New York 1963).  
 Doodson, Arthur T., and Warburg, H. D., *Admiralty Manual of Tides* (London 1941).  
 Dronkers, Jo J., *Tidal Computations in River and Coastal Waters* (Amsterdam, the Netherlands, 1964).  
 Macmillan, D. Henry, *Tides* (New York 1966).  
 Munk, Walter H., and Zetler, Bernard D., "Deep Sea Tides: A Program," *Science*, vol. 158, No. 3803, Nov. 17, 1967.  
 Schureman, Paul, *Manual of Harmonic Analysis and Prediction of Tides*, Coast and Geodetic Survey Special Publication No. 98 (Washington 1940).

Bernard D. Zetler:

50. TSUNAMIS AND THE SEISMIC SEA  
WAVE WARNING SYSTEM\*

Mariners, perhaps more than men of any other profession, distinguish themselves by their ability to utilize the elements. However, while sailing through favorable currents and fair winds, the mariner has learned to keep a weather eye cocked for the caprices of nature.

Nature does indeed like to play tricks on occasion and two of her favorite "Sunday punches" are the hurricane and the seismic sea wave. The latter is popularly known as a "tidal wave," a term scientists dislike because the wave results from an underwater earthquake and is completely unrelated to the tide. The mariner frequently seeks the shelter of a port during a hurricane whereas he heads for safety on the high seas when warned that a seismic sea wave is coming. The Japanese word for the seismic sea wave, tsunami, is very descriptive. "Tsu" means port and "nami" wave, the combination describing a wave that is dangerous only in port.

Long before meteorologists learned to track hurricanes, seasoned mariners developed a technique for anticipating their coming. Ground swells, increasing seas, falling barometer, and shifting winds telegraphed a stream of evidence, sometimes days in advance of the most destructive portion of the hurricane. When a port was inaccessible or threatened directly by a hurricane, they maneuvered for a favorable position relative to the "eye" and for additional sea room.

The seismic sea wave, however, does not telegraph its punch nor is there ordinarily a cushion of time for deliberation. Indeed, although seismic sea waves have been with us as long as recorded history, only within the past 18 yr. has a method of warning been developed. When there is a warning of an impending tsunami, ships

\* From *Mariners Weather Log*, Vol. 9, No. 5, September, 1965, pp. 149-152. "The Seismic Sea Wave Warning System, An Aid to Mariners" by Bernard D. Zetler. Reprinted by permission of the author.

Bernard D. Zetler is Acting Director of the Physical Oceanography Laboratory of the Environmental Science Services Administration.



leave port to go out to sea and those about to enter a port are instructed to wait outside the harbor. On the open sea the waves are very long, possibly 100 mi. or more, and are only about 1 ft. high. Consequently, not only are they no menace to ships, they are not even noticeable.

During a seismic sea wave alert, ships do not have to move far out to sea to avoid the destructive part of a tsunami. The master of a ship lying off Hilo during the destructive wave of April 1, 1946 reported he could see heavy waves breaking on shore while experiencing no extraordinary waves on the ship. The log of the S.S. *Lurline* on March 9, 1957 shows that she put to sea from Honolulu on receiving a warning of an impending tsunami. Despite the fact that the *Lurline* waited at a distance of only 2 mi. off the entrance to the harbor, she apparently experienced no difficulty. At the same time a submarine, the U.S.S. *Wahoo*, expecting small waves, left dockside to ride them out in the harbor of Nawiliwili, Kauai. Rapid water-level changes of 10 ft. and more caused the small funnel-shaped harbor to be alternately drained and refilled. A giant whirlpool action (about 300 yd. in diameter) was set up in the basin. The turbulence was so strong that in spite of a maximum twisting combination (by using right full rudder with the starboard engine at Back Emergency and the port engine at Ahead Flank), the ship's head changed at least 50 degrees in the opposite direction. With flank speed of 15 kt., the *Wahoo* at times had sternway (moved backwards). The commanding officer of the submarine, reporting on the maneuvering, said that in his opinion the worst possible place would have been alongside a dock as it was unlikely that mooring lines could be tended during a 10- to 12-ft. change in depth of water.

Ancient history contains numerous references to destructive waves that appear to have been seismic sea waves. Eyewitness accounts usually describe the seas receding suddenly, leaving vessels stranded on the newly exposed sea bottom. Then there follows a mighty wave roaring in from the sea, smashing upset ships before it and carrying surviving vessels thousands of feet onto the shore, and leaving them high and dry. Frequently there are a series of waves lasting over a period of hours. Particularly frustrating to the medieval seaman must have been the complete absence of advance notice, for this could occur in fair weather with the sea as calm as the proverbial millpond immediately before the first wave.

On April 1, 1946 the seas suddenly receded in Hilo Harbor in Hawaii and then returned, smashing the waterfront, claiming many lives, and causing millions of dollars of damage. Man had learned to identify this as a seismic sea wave and knew it was caused by an underwater earthquake somewhere in the Pacific. As photographic



seismograph records were developed many hours or days later, it became clear that the epicenter was located about 2,000 mi. to the north in the Aleutian Trench, a deep canyon running east and west immediately south of the Aleutian Islands.

Oceanographers had also learned by then that these waves move across the ocean at speeds up to 500 m.p.h. and that the speed increases with depth. As reports came in, it became clear that the wave had reached the Pacific coast of South America and had inflicted damage in various areas throughout the Pacific.

Shortly after the 1946 seismic sea wave, seismologists and oceanographers in the U. S. Coast and Geodetic Survey joined in an effort to formulate a warning system. There were many problems. A seismograph with a visible record and a warning signal to announce large earthquakes was invented. A technique for calculating wave speed was developed so that accurate arrival times of the tsunami could be computed. Although earthquakes occur frequently, destructive seismic sea waves are not always generated by them. A system of reporting tide stations was set up to establish the existence of a seismic sea wave. These are necessary as the seismological records are not sufficient to determine this condition. There are many earthquakes, few tsunamis. Therefore at least one report based on visual evidence from a tide station is necessary before a warning is disseminated. This required an umbrella of tide stations in all possible directions from the Hawaiian Islands to insure that one or more tide stations would lie in the path of a wave en route to the Islands. With seismic sea waves moving at such terrific speeds (the travel time of a wave from the Aleutian Trench to Hawaii requires only 4-½ hr.), high speed communication facilities between the Coast and Geodetic Survey's Honolulu Observatory (the center of the system during an alert) and the seismological and tide stations were an absolute necessity. The Defense Department and the Civil Aeronautics Administration (now FAA) cooperated to the fullest extent, assigning high priorities to the transmission of warning messages during an alert.

The available communication centers near some of our tide stations are manned only during certain scheduled hours, making these tide stations undependable sources of information as messages are not received at all hours. Oceanographers in the Coast Survey developed a seismic sea wave detector, (Figure 50-1) a mechanical device using pressure chambers in tide wells at these stations to filter out both short period wind waves and the gradual rise and fall of the tide. The detector sounds an alarm when sea level rises or falls rapidly during an intermediate period of from a few minutes to an hour, roughly the period of a seismic sea wave. When the alarm sounds, the tide observer can contact the communication facility

and initiate a message even though he has not heard from the Honolulu Observatory.

By 1948 the Coast and Geodetic Survey had an operating warning system designed to protect the Hawaiian Islands. Those who worked on it had their fingers crossed, for they knew that in announcing the service, they were accepting a fearful responsibility. Yet this warning system was built on a negligible budget with instrumentation developed internally and dependent on the devotion to service and good-will of men in various portions of the Pacific over whom they had little or no control.

The warning system has expanded greatly from its original design to protect the Hawaiian Islands. Many countries bordering the Pacific and various islands in the Pacific are now receiving the warning services. In April of this year, 12 countries (Canada, Chile, Republic of China, France, Japan, Mexico, New Zealand, Peru, Republic of the Philippines, United States of America, USSR, and

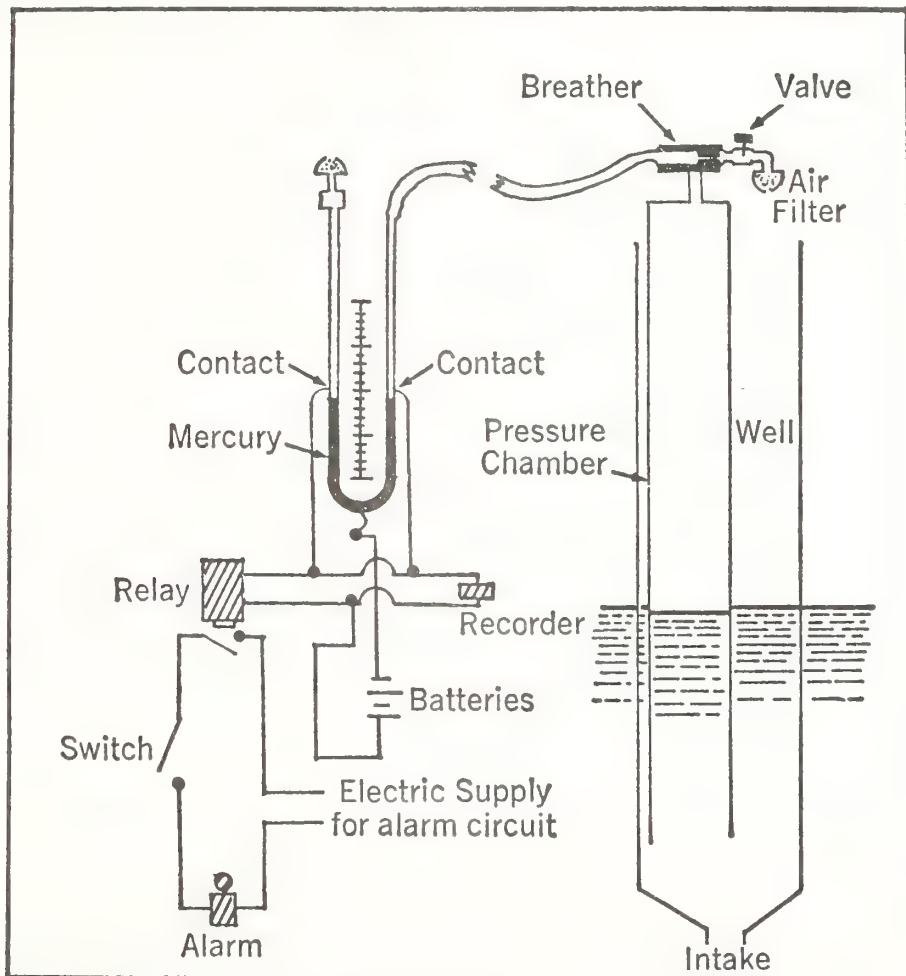


Fig. 50-1. Seismic sea wave detector.

Western Samoa) sent official delegations to a meeting in Honolulu on the international aspects of the tsunami warning system in the Pacific. Improved international cooperation stemming from this meeting is expected to considerably expand and strengthen the warning system.

There have been four destructive seismic waves since 1948, one in 1952 from Kamchatka, one in 1957 from the Aleutians, one on May 22, 1960 from Chile and one recently from Alaska on March 28, 1964. The warning system worked well in all four instances, giving a 6-hr. advance notice to the Hawaiian Islands in 1960.

However, the warning system did not protect the Alaskan area nearest the earthquake in 1964, nor did it protect Adak in 1957. The mechanisms for providing warnings were not designed to warn areas immediately adjacent to the tsunami source. In fact, to minimize the number of false alarms and thereby maintain public confidence in the warning system, it ordinarily relies on positive reports of observed tsunami before issuing warnings to places farther away from the epicenter. Although plans are underway for a tsunami warning system in Alaska based on seismological evidence only, even such a system requires some time to interpret the available data and to disseminate warnings. Consequently, the prudent person on shore heads for higher elevation when he feels a severe earthquake and the prudent captain of a ship immediately puts out to sea.

The Weather Bureau has assisted the Coast and Geodetic Survey in its operation of the warning system by maintaining tide gauges in isolated areas and furnishing communications, etc. On July 13, 1965 these two agencies were merged into the new Environmental Science Service Administration (ESSA). President Johnson's message of May 13, 1965 proposing the consolidation of these agencies said "The organizational improvements made possible by the reorganization plan will enhance our ability to develop an adequate warning system for the severe hazards of nature—for hurricanes, tornadoes, floods, earthquakes, and seismic sea waves, which have proved so disastrous to the Nation in recent years." The mariner is thereby assured that the government of the United States is determined to utilize its full scientific potential in maintaining and improving the seismic sea wave warning system.

*Bernard D. Zetler*



## A NUMERICAL MODEL OF THE SLOWLY VARYING TROPICAL CYCLONE IN ISENTROPIC COORDINATES

RICHARD A. ANTHERS

National Hurricane Research Laboratory, Environmental Research Laboratories, NOAA, Miami, Fla.

### ABSTRACT

A diagnostic axisymmetric model in isentropic coordinates is developed to study the effect of differential heating on the dynamics and energetics of the steady-state tropical cyclone. From the thermal forcing specified by various heating distributions, slowly varying solutions for the mass and momentum fields are obtained by an iterative technique.

The theory of available potential energy for open systems is utilized to study the energy budget for the hurricane. In the slowly varying state, the gain of available potential energy by diabatic heating and lateral boundary processes balances the conversion of potential to kinetic energy that, in turn, offsets frictional dissipation. For a domain of radius 500 km, the boundary flux of available potential energy is about 40 percent of the generation by diabatic heating. For a domain of radius 1000 km, however, the boundary flux is about 15 percent of the generation.

Horizontal and vertical mixing are studied through the use of constant exchange coefficients. As the horizontal mixing decreases, the maximum surface wind increases and moves closer to the center.

Several horizontal and two vertical distributions of latent heating are investigated. The maximum surface wind is dependent primarily on heating within 100 km. The transverse (radial) circulation is closely related to the heat release beyond 100 km. In experiments in which the vertical variation of heating is pseudoadiabatic, the temperature and outflow structures are unrealistic. A vertical distribution that releases a higher proportion of heat in the upper troposphere yields results that are more representative of the hurricane.

### CONTENTS

1. Introduction.....	617
2. Available potential energy of limited regions.....	618
A. Available potential energy equations for the model.....	618
B. Budget equations for volume.....	619
3. The diagnostic model.....	619
A. Steady state or slowly varying concept.....	620
B. Description of the model.....	620
C. Experimental parameters.....	622
4. Experimental results.....	623
A. Variation of internal mixing.....	624
B. Radial variation of latent heating.....	624
C. Vertical variation of latent heating, experiment 9.....	629
D. Variation of total heating, experiment 10.....	630
E. Experiments of a computational nature.....	630
F. High-resolution experiment with reduced horizontal mixing, experiment 14.....	631
G. Numerical and empirical pressure-wind relationship.....	633
5. Summary.....	633
Acknowledgments.....	634
References.....	634

### 1. INTRODUCTION

Within the last decade, numerical modeling has become a powerful tool for investigating the life cycle of tropical cyclones. With a realistic parameterization of latent heat release, the models of Yamasaki (1968a, 1968b), Ooyama (1969), and Rosenthal (1969) have been successful in duplicating many observed features of tropical storms. The practical limitations of computer size and speed, however, have so far restricted these models (and also the present model) to two dimensions.

In the parameterization of the heat imparted to the environment by the cumulus convection by Kuo (1965), Rosenthal (1969), and others, large-scale heating is a function of the cloud-environment temperature difference and the net moisture convergence in a column. These models release a much larger proportion of heat in the upper troposphere than the heat released by earlier models based on a pseudoadiabatic process.

The importance of latent heat release within the warm core for the production of kinetic energy was recognized by Palmén (1948) and re-emphasized by Yanai (1964). In simplest terms, the release of latent heat maintains the baroclinicity that drives the transverse radial circulation. The horizontal kinetic energy is produced in both the inward- and outward-flowing branches by accelerations toward lower pressure. This production of kinetic energy, in turn, offsets surface and internal frictional dissipation.

The conversion of potential to kinetic energy through cross-isobar flow has been examined in several diagnostic studies (e.g., Palmén and Jordan 1955, Palmén and Riehl 1957, Riehl and Malkus 1961, Miller 1958, and Hawkins and Rubsam 1968). Recently, Anthes and Johnson (1968) estimated the generation of available potential energy by diabatic heating in hurricane Hilda, 1964, and concluded that the generation within a 1000-km region was sufficient to balance the conversion to kinetic energy. Thus, on this scale, it was possible to consider that the hurricane was a self-sustaining system.

The importance of differential heating and cooling is emphasized in the theory of available potential energy. The sensitivity of the generation to different horizontal and vertical distributions of heating in Anthes and

Johnson's (1968) results suggests investigating the effect of differential heating on the dynamics as well as the energetics of tropical storms. In particular, the relation between generation of available energy and conversion to kinetic energy within the storm system should be studied to clarify the role of thermal versus mechanical forcing. This relationship has important implications in storm modification experiments in which the heating, generation, and possibly the conversion are altered in some manner.

Although interactions between temperature and momentum structure and large-scale heating certainly exist, the hurricane may be considered a direct consequence of thermal forcing. It makes sense, therefore, to study the response of the hurricane to differential heating by specifying steady heating distributions. The mass and momentum fields that develop in response to the steady forcing functions are useful in interpreting transient stages of hurricane forecast models as well as in testing various heating parameterizations.

The dynamics and energetics of the hurricane's response to thermal forcing are studied through a two-dimensional model in isentropic coordinates. An iterative technique is utilized to obtain slowly varying solutions of mass and momentum for different vertical and horizontal latent heating distributions and sensible heat addition at the earth's interface. The effects of vertical and horizontal mixing are also considered.

The present model differs from previous axisymmetric hurricane models in the following respects:

1. Only the slowly varying solutions for the mass and momentum fields that correspond to the mature hurricane are considered.
2. In contrast to previous steady-state models, the mass and momentum fields are investigated as functions of applied thermal forcing rather than vice versa. These experiments are numerical analogs to laboratory dishpan experiments that study fluid dynamics as a function of fixed heating (cooling) rates. The direct response of hurricane *dynamics* to variations in *heating* are relevant in view of the current interest in storm modification.
3. Isentropic coordinates are utilized for the first time in a system that includes diabatic effects. The results may therefore be of interest in areas outside the hurricane modeling problem.
4. The recent theory (exact in isentropic coordinates) of the available potential energy of open, isolated storm systems (Johnson 1970) is applied to the complete hurricane system.

## 2. AVAILABLE POTENTIAL ENERGY OF LIMITED REGIONS

The theory of available potential energy has historically been applied to the entire atmospheric system (Margules 1905, Lorenz 1955, and Dutton and Johnson 1967). Recently, however, Johnson (1970) has developed the theory for an open system to define the available potential energy of a storm and its time rate of change.

One appealing aspect of applying the theory of available potential energy to a tropical cyclone is the condition that, as a first approximation, the hurricane may be considered an isolated baroclinic disturbance superimposed on the nearly flat and horizontal barotropic Tropics. Thus one might reasonably expect the available potential

energy generated on the tropical cyclone scale to be converted to kinetic energy within the same scale. This may not be true in the middle latitudes where the flux of energy across the boundaries of systems will be large.

Symbols used frequently in this work are:

$A$	available potential energy,
$C_D$	drag coefficient,
$c_p$	specific heat at constant pressure,
$f$	Coriolis parameter,
$g$	acceleration of gravity,
$i, I$	vertical grid index, maximum index,
$j, J$	horizontal grid index, maximum index,
$k$	specific kinetic energy $= (1/2)(v_x^2 + v_r^2)$ ,
$K$	total kinetic energy,
$K_H$	horizontal coefficient of eddy viscosity,
$K_T$	horizontal coefficient of thermal diffusion,
$K_z$	vertical coefficient of eddy viscosity,
$p$	pressure,
$p_0$	reference pressure $= 1000$ mb,
$\dot{Q}$	heating rate per unit mass,
$q_s$	saturation specific humidity,
$R$	maximum radial distance of domain,
$R_d$	gas constant of dry air,
$r$	radial distance,
$\Delta r$	horizontal grid increment,
$T$	absolute temperature,
$T_s$	moist-adiabatic temperature,
$\Delta t$	time (iteration) step,
$\mathbf{V}$	horizontal wind vector,
$v_\lambda$	tangential wind component,
$v_r$	radial wind component,
$z$	height,
$\Delta z$	depth of boundary layer (assumed constant),
$\theta$	potential temperature,
$\theta_e$	equivalent potential temperature,
$\theta_0$	coldest $\theta$ in domain,
$\theta_t$	top isentropic surface in model,
$\Delta\theta$	vertical grid increment,
$\kappa$	$R_d/c_p$ ,
$\lambda$	tangential direction,
$\rho$	air density,
$\sigma$	area,
$\psi$	Montgomery potential $= c_p T + gz$ ,
$( )_r$	subscript $r$ denoting reference atmosphere,
$( )_s$	subscript $s$ denoting surface, $z=0$ ,
$(\overline{\quad})$	operator denoting area average,
$\nabla_\theta$	del operator on isentropic surface,
$\nabla^2$	operator $= \partial^2/\partial r^2 + (1/r)(\partial/\partial r)$ , and
$\theta_B$	vertical (upper or lower) boundary.

## A. AVAILABLE POTENTIAL ENERGY EQUATIONS FOR THE MODEL

When one follows Johnson (1970), the available potential energy,  $A$ , of any region in hydrostatic balance is

$$A = \frac{c_p}{p_0^{\kappa} g (1 + \kappa)} \int_{\sigma} \int_0^{\infty} (p^{1+\kappa} - p_r^{1+\kappa}) d\theta d\sigma. \quad (1)$$



When one divides the vertical integration into three parts, eq (1) becomes

$$A = \frac{c_p}{p_0^* g (1 + \kappa)} \int_{\sigma} \left[ \int_0^{\theta_0} (p^{1+\kappa} - p_r^{1+\kappa}) d\theta \right. \\ \left. + \int_{\theta_0}^{\theta_i} (p^{1+\kappa} - p_r^{1+\kappa}) d\theta + \int_{\theta_i}^{\infty} (p^{1+\kappa} - p_r^{1+\kappa}) d\theta \right] d\sigma. \quad (2)$$

In eq (2),  $\theta_0$  is the lowest potential temperature in the region; and  $\theta_i$  is the isentropic surface above which the atmosphere is assumed to be barotropic. The third integral vanishes by the barotropic assumption. When one follows Lorenz' convention that the pressure on isentropes which intersect the ground equals the surface pressure, the available potential energy for the model is

$$A = \frac{c_p}{p_0^* g (1 + \kappa)} \left[ \theta_0 \int_{\sigma} (p_s^{1+\kappa} - \bar{p}_s^{1+\kappa}) d\sigma \right. \\ \left. + \int_{\sigma} \int_{\theta_0}^{\theta_i} (p^{1+\kappa} - \bar{p}^{1+\kappa}) d\theta d\sigma \right]. \quad (3)$$

In eq (3), we have used the conditions that, for hydrostatic atmospheres,

$$p_r(\theta) = \bar{p}(\theta) \text{ and } p_s = \bar{p}_s.$$

In this model in which heating vanishes on the upper boundary, the time rate of change of  $A$  is

$$\frac{dA}{dt} = G + C + B \quad (4)$$

where

$$G = -\frac{1}{g} \int_{\sigma} \int_{\theta_0}^{\theta_i} [1 - (\bar{p}/p)^{\kappa}] \dot{Q} \frac{\partial p}{\partial \theta} d\theta d\sigma, \quad (5)$$

$$C = -\frac{1}{g} \int_{\sigma} \int_{\theta_0}^{\theta_i} (\mathbf{V} \cdot \nabla_{\theta}) \frac{\partial p}{\partial \theta} d\theta d\sigma, \quad (6)$$

and

$$B = \frac{1}{g} \int_{\sigma} \int_{\theta_0}^{\theta_i} \nabla_{\theta} \cdot \frac{\partial p}{\partial \theta} (\psi - \psi_r) V d\theta d\sigma. \quad (7)$$

The generation,  $G$ , by diabatic heating is positive for heating at high pressure and cooling at low pressure. The conversion,  $C$ , is the production of kinetic energy by cross-isobar flow. The last term,  $B$ , represents the change of  $A$  by mass flux across the lateral boundary. For the axisymmetric model,  $B$  simplifies to

$$B = \frac{2\pi R}{g} \int_{\theta_0}^{\theta_i} v_r (\psi - \psi_r) \frac{\partial p}{\partial \theta} d\theta. \quad (8)$$

For the hurricane, the surface pressure at the outer boundary will be greater than the mean surface pressure, so that  $\psi > \psi_r$ . From the low-level inflow, the covariance of  $(\partial p / \partial \theta)(v_r)$  and  $(\psi - \psi_r)$  will be positive. In the outflow region,  $(\psi - \psi_r)$  tends to vanish; thus the integral  $B$  usually provides a positive contribution to  $dA/dt$ .

### B. BUDGET EQUATIONS FOR VOLUME

In this subsection, the time-dependent budget equations are summarized for a stationary cylindrical volume. If  $f$  is

any specific quantity, such as water vapor per unit mass, the total amount of the property in the volume is

$$F = \int_0^{2\pi} \int_0^R \int_{\theta_0}^{\theta_i} r \rho \frac{\partial z}{\partial \theta} f d\theta dr d\lambda. \quad (9)$$

With the aid of Leibnitz' rule, the hydrostatic assumptions, and the continuity equation, the time rate of change of  $F$  (Johnson 1970) is

$$\frac{dF}{dt} = -\frac{1}{g} \int_0^{2\pi} \int_0^R \int_{\theta_0}^{\theta_i} \left[ \frac{\partial}{\partial t} \left( r f \frac{\partial p}{\partial \theta} \right) + \frac{\partial}{\partial \lambda} \left( r f \frac{\partial p}{\partial \theta} \frac{d\lambda_B}{dt} \right) \right. \\ \left. + \frac{\partial}{\partial r} \left( r f \frac{\partial p}{\partial \theta} \frac{dR}{dt} \right) + \frac{\partial}{\partial \theta} \left( r f \frac{\partial p}{\partial \theta} \frac{d\theta_B}{dt} \right) \right] d\theta dr d\lambda. \quad (10)$$

Equation (10) is greatly simplified for the stationary axisymmetric volume of this study in which all tangential derivatives vanish and  $dR/dt = 0$ . With these conditions and the use of the continuity equation,

$$\frac{dF}{dt} = -\frac{2\pi}{g} \int_0^R \int_{\theta_0}^{\theta_i} \left( -\frac{\partial}{\partial r} \left( r f v_r \frac{\partial p}{\partial \theta} \right) \right. \\ \left. - \frac{\partial}{\partial \theta} \left( r f \frac{\partial p}{\partial \theta} \left( \frac{d\theta}{dt} - \frac{d\theta_B}{dt} \right) \right) + r \frac{\partial p}{\partial \theta} \frac{df}{dt} \right) d\theta dr. \quad (11)$$

The upper and lower boundary conditions are

$$d\theta_B/dt = d\theta_s(r, \theta_s, t)/dt$$

and

$$d\theta_i/dt = d\theta_B/dt = 0.$$

With these conditions and after integration, the final budget equation becomes

$$\frac{dF}{dt} = \frac{2\pi R}{g} \int_{\theta_0}^{\theta_i} \left( f v_r \frac{\partial p}{\partial \theta} \right)_R d\theta - \frac{2\pi}{g} \int_0^R \int_{\theta_0}^{\theta_i} r \frac{\partial p}{\partial \theta} \frac{df}{dt} d\theta dr. \quad (12)$$

The first term is the change of  $F$  caused by transport of  $f$  across the lateral boundary while the second term is the change due to sources or sinks within the volume. The generalized budget and available potential energy equations provide integrated parameters for the hurricane volume, which are studied as the mass and momentum fields seek steady-state conditions for the applied thermal forcing.

### 3. THE DIAGNOSTIC MODEL

One of the appealing aspects of numerical modeling in isentropic coordinates is the absence of a "vertical velocity" in the equations of motion for isentropic flows. Such a model should have less truncation error than models in pressure or height coordinates that must include vertical advection terms. Even under diabatic conditions, it is probable that the vertical truncation is less in isentropic coordinates because the adiabatic part of the vertical motion should be free of error.

Besides the reduction in vertical truncation error, there are several other possible advantages of modeling in



isentropic coordinates:

1. The theory of available potential energy is exact in isentropic coordinates (Dutton and Johnson 1967).
2. Johnson and Dutton (1969) stress that mean energy and momentum transport processes of the general circulation are explicitly coupled with thermal forcing.
3. Horizontal resolution and vertical resolution are higher in the energetically active baroclinic zones.

Difficulties in using isentropic coordinates arise chiefly near the ground where superadiabatic lapse rates are found and isentropic surfaces intersect the ground. The first problem generally arises over small areas and may be solved by utilizing height coordinates in the boundary layer and isentropic coordinates above. The second has been reasonably well resolved by an interpolation scheme in some preliminary adiabatic experiments by Eliassen and Raustein (1968).

To the author's knowledge, there has been no previous work with numerical modeling in isentropic coordinates that includes diabatic processes. In this particular series of experiments in which the heating function is specified and the steady-state response determined, isentropic coordinates are especially attractive because the form of the thermodynamic equation is greatly simplified. In a broader sense, the experience gained by studying thermal forcing in this model should be useful in future work with more advanced numerical models.

#### A. STEADY STATE OR SLOWLY VARYING CONCEPT

The term "steady state," when applied to the tropical cyclone, usually refers to the storm's mature stage in which certain significant parameters, such as central pressure and maximum wind, remain relatively unchanged over a period of time. The axisymmetric assumption is usually best satisfied during this mature stage. It is difficult, if not impossible, for an entire axisymmetric hurricane system to reach a steady state, particularly in the outflow layer at radii greater than 400 km from the storm center (Anthes 1970b). However, steady-state solutions that compare favorably with observations are possible near the center of the storm, even under the axisymmetric assumption (Krishnamurti 1961 and Barrientos 1964).

In the iteration technique used in this model, mass and momentum are "forecast" using a constant specified heating function until the inner region reaches a slowly varying state. True steady-state conditions are never determined because of the large amount of time required to reach such a state. In typical experiments, changes from initial conditions in response to the constant heating function are very large during the first few iterations as the mass and momentum fields attempt to adjust to the new forcing function. Later, however, rates of change are less. When this "slowly varying" state is reached (usually after about 1,600 iterations), differences in the results

caused by experimental variation of physical processes or parameters are apparent.

#### B. DESCRIPTION OF THE MODEL

*Basic equations.* The tangential and radial equations of motion and the continuity equation in isentropic coordinates are

$$\frac{\partial r v_\lambda}{\partial t} = -v_r \frac{\partial r v_\lambda}{\partial r} + r \left[ -f v_r - \frac{d\theta}{dt} \frac{\partial v_\lambda}{\partial \theta} + K_H \left( \nabla^2 v_\lambda - \frac{v_\lambda}{r^2} \right) + \frac{\partial}{\partial z} \left( K_z \frac{\partial v_\lambda}{\partial z} \right) \right], \quad (13)$$

$$\frac{\partial v_r}{\partial t} = -v_r \frac{\partial v_r}{\partial r} + f v_\lambda + \frac{v_\lambda^2}{r} - \frac{\partial \psi}{\partial r} \frac{d\theta}{dt} \frac{\partial v_r}{\partial \theta} + K_H \left( \nabla^2 v_r - \frac{v_r}{r^2} \right) + \frac{\partial}{\partial z} \left( K_z \frac{\partial v_r}{\partial z} \right), \quad (14)$$

and

$$\frac{\partial}{\partial t} \left( \frac{\partial p}{\partial \theta} \right) = -\frac{1}{r} \frac{\partial}{\partial r} \left( r v_r \frac{\partial p}{\partial \theta} \right) - \frac{\partial}{\partial \theta} \left( \frac{d\theta}{dt} \frac{\partial p}{\partial \theta} \right) \quad (15)$$

where the horizontal and vertical mixing terms in eq (13) and (14) are expressed in height coordinates rather than the more complex transformed expressions for computational convenience. This approximation is justified from the relatively large uncertainty in the form of  $K_H$  and  $K_z$ .

The vertical velocity term in isentropic coordinates,  $d\theta/dt$ , is computed from

$$\begin{aligned} \frac{d\theta}{dt} = & -\frac{1}{c_p T} \dot{Q} + K_T \left\{ -\left( \frac{\partial p}{\partial \theta} \right)^{-1} \right. \\ & \times \left[ \frac{\partial^2 p}{\partial r^2} - \left( \frac{\partial p}{\partial \theta} \right)^{-1} \frac{\partial p}{\partial r} \left( 2 \frac{\partial^2 p}{\partial r \partial \theta} - \left( \frac{\partial p}{\partial \theta} \right)^{-1} \frac{\partial p}{\partial r} \frac{\partial^2 p}{\partial \theta^2} \right) \right. \\ & \left. \left. + \left( r \frac{\partial p}{\partial \theta} \right)^{-1} \frac{\partial p}{\partial r} \right\} + \frac{\partial}{\partial z} \left( K_z \frac{\partial \theta}{\partial z} \right) \right\} \quad (16) \end{aligned}$$

where  $\dot{Q}$  is the parameterized heating rate and is prescribed as a function of mass. The second term in eq (16) results from approximating the horizontal diffusion by  $K_T \nabla^2 \theta$  in pressure coordinates and transforming to isentropic coordinates. Again, the uncertainties in  $K_T$  outweigh the error in approximation.

The lowest prediction level for the velocity components corresponds to the center of a boundary layer of constant depth,  $\Delta z$ , in which a linear variation of stress with height is assumed and vertical advection is neglected. The surface stress is approximated by the quadratic stress law with the surface wind assumed equal to the wind at the center of the boundary layer. Similar one-level Ekman layers have been utilized in hurricane models (Ooyama 1969, Yamasaki 1968a, 1968b, and Rosenthal 1969). Under the above assumptions, the equations of motion for the lowest

Defined Variables	Level Number	Mean P
$Q = \frac{d\theta}{dt} = 0$		
	360	1 (140 mb)
$\frac{\partial p}{\partial \theta}, W, \psi$	350	2 (190 mb)
$p, Q, \frac{d\theta}{dt}$		
	340	3 (300 mb)
	330	4 (440 mb)
	320	5 (580 mb)
	310	6 (760 mb)
$V, p, \psi, Q, \theta_s, \frac{d\theta_s}{dt}$		
		$\frac{\Delta z}{z=0}$ 7

FIGURE 1.—Geometry of the isentropic model of the hurricane.

model level are

$$\frac{\partial v_\lambda}{\partial t} = -v_r \frac{\partial v_\lambda}{\partial r} + r \left[ -fv_r - \frac{C_D |V| v_\lambda}{\Delta z} + K_H \left( \nabla^2 v_\lambda - \frac{v_\lambda}{r^2} \right) \right] \quad (17)$$

and

$$\frac{\partial v_r}{\partial t} = -v_r \frac{\partial v_r}{\partial r} + fv_\lambda + \frac{v_\lambda^2}{r} - \frac{c_p \theta}{p_0} \frac{\partial p^*}{\partial r} - \frac{C_D |V| v_r}{\Delta z} + K_H \left( \nabla^2 v_r - \frac{v_r}{r^2} \right). \quad (18)$$

The local change of surface potential temperature computed from the thermodynamic equation is

$$\frac{\partial \theta_s}{\partial t} = -v_r \frac{\partial \theta_s}{\partial r} + \frac{d\theta_s}{dt} + K_T \nabla^2 \theta_s. \quad (19)$$

The remaining equations constituting the complete set are the hydrostatic equation

$$\frac{\partial \psi}{\partial \theta} = c_p \frac{T}{\theta} \quad (20)$$

and the definition of potential temperature

$$\theta = T(p/p_0)^{c_p}. \quad (21)$$

**Finite-difference equations.** The geometry of the model (fig. 1) consists of six equally spaced isentropic surfaces ( $\theta_i = 370^\circ\text{K} - i\Delta\theta$ ,  $\Delta\theta = 10^\circ\text{K}$ ,  $i=1,6$ ) and the sea-level surface. The approximate mean tropical pressures of the integer isentropic surfaces are given for reference (Jordan

1958). All variables are defined on the sea-level surface. On the isentropic surfaces, the variables are staggered for computational convenience with  $V$ ,  $\psi$ , and  $\partial p/\partial \theta$  defined on integer surfaces. The horizontal grid is also staggered with  $V$  defined at  $r=(j-1)\Delta r$  and the thermodynamic variables ( $\psi$ ,  $p$ ,  $\dot{Q}$ ,  $d\theta/dt$ ) defined at  $r=(j-1/2)\Delta r$  for  $j=1, 2, \dots, J$ . The horizontal domain extends to the radius  $R_j$ , which is either 500 or 1000 km.

In eq (13) through (19), all space derivatives are estimated by centered differences. The finite-difference form of eq (18) is given with the  $i$  index suppressed for simplicity:

$$\begin{aligned} \frac{\partial v_r}{\partial t} = & v_{r_j} \left( \frac{v_{r_{j+1}} - v_{r_{j-1}}}{r_{j+1} - r_{j-1}} \right) + fv_{\lambda_j} + \frac{v_{\lambda_j}^2}{r_j} \\ & \times \frac{c_p \theta}{p_0^*} \left[ \frac{p_{j+3/2}^* - p_{j+1/2}^*}{r_{j+3/2} - r_{j+1/2}} \right] - \frac{C_D [v_{\lambda_j}^2 + v_{r_j}^2]^{1/2} v_{r_j}}{\Delta z} \\ & + K_H \left\{ \frac{v_{r_{j+1}} - v_{r_j}}{r_{j+1} - r_j} - \frac{v_{r_j} - v_{r_{j-1}}}{r_j - r_{j-1}} - \frac{v_{r_{j+1}} - v_{r_{j-1}}}{r_j(r_{j+1} - r_{j-1})} - \frac{v_{r_j}}{r_j^2} \right\}. \quad (22) \end{aligned}$$

The finite-difference approximation of the vertical mixing term is

$$\frac{\partial}{\partial z} \left( K_z \frac{\partial v_r}{\partial z} \right)_i \approx \frac{K_{z_{i-1}} \left( \frac{v_{r_{i-1}} - v_{r_i}}{z_{i-1} - z_i} \right) - K_{z_i} \left( \frac{v_{r_i} - v_{r_{i+1}}}{z_i - z_{i+1}} \right)}{0.5(z_{i-1} - z_i)}. \quad (23)$$

The unwieldy expressions for the second derivative terms are greatly simplified for a constant grid interval. The general form is retained, however, in anticipation of the use of a variable grid in some experiments.

The pressure is obtained from  $\partial p/\partial \theta$  by integrating downward from a fixed value of  $p$  ( $365^\circ\text{K}$ ):

$$p_{i+1/2} = p_{i-1/2} - (\theta_{i-1/2} - \theta_{i+1/2}) \frac{\partial p}{\partial \theta_i} \quad i=1, 2, \dots, 5 \quad (24)$$

and

$$p_s = p_{11/2} - (\theta_{11/2} - \theta_s) \frac{\partial p}{\partial \theta_6}.$$

At the sea surface,  $\theta_s$  equals  $\theta_s(r)$ . From an integration of the hydrostatic equation upward from sea level,  $\psi$  is

$$\psi_6 = \psi_7 + (\theta_6 - \theta_s) c_p \left( \frac{p}{p_0} \right)^*$$

and

$$\psi_{i-1} = \psi_i + (\theta_{i-1} - \theta_i) c_p \left( \frac{p_{i-1/2}}{p_0} \right)^* \quad i=6, 5, \dots, 2 \quad (25)$$

where

$$\frac{\bar{p}}{p} = p_s + \frac{1}{2} (\theta_6 - \theta_s) \frac{\partial p}{\partial \theta_6}$$

and

$$\psi_7 = c_p T_7.$$

**Boundary conditions.** Those for the top isentropic surface are  $p=140$  mb,  $d\theta/dt=0$ , and  $\partial V/\partial z=0$ . At the lateral boundary, the pressure and temperature gradients, the horizontal divergence, and the relative vorticity are all assumed to vanish, which enables the calculation of the variables at  $R$  by

$$\begin{aligned} p_J &= p_{J-1}, \\ (rv_r)_J &= (rv_r)_{J-1}, \\ \psi_J &= \psi_{J-1}, \\ (rv_\lambda)_J &= (rv_\lambda)_{J-1}, \\ \text{and} \quad (\theta_s)_J &= (\theta_s)_{J-1}. \end{aligned} \quad (26)$$

**Computational procedure.** The iteration technique to determine the steady-state solutions utilizes a simulated backward-difference scheme (Matsuno 1966), which has the desirable property of damping high-frequency waves. One cycle of the scheme is summarized with the superscript referring to the iteration step number:

1. Given values of  $v_\lambda^n$ ,  $v_r^n$ ,  $\psi^n$ ,  $p^n$ ,  $(d\theta/dt)^n$ ,  $\theta_s^n$ .
2. Forecast tentative values  $v_\lambda^*$ ,  $v_r^*$ ,  $(\partial p/\partial\theta)^*$ ,  $\theta_s^*$  at step  $n+1$  (designated by an asterisk) using appropriate tendency eq (13) through (19) and values of variables at step  $n$ .
3. Calculate  $p^*$  and  $\psi^*$  using tentative estimates  $(\partial p/\partial\theta)^*$  and  $\theta_s^*$ .
4. Forecast final estimates of  $v_\lambda^{n+1}$ ,  $v_r^{n+1}$ ,  $(\partial p/\partial\theta)^{n+1}$ , and  $\theta_s^{n+1}$  using \* values of variables where they appear in tendency equations.
5. Calculate  $p^{n+1}$  and  $\psi^{n+1}$ .
6. Calculate  $(d\theta/dt)^{n+1}$  from eq (16).
7. Calculate variables at the lateral boundary from eq (26). This completes one iteration step.

For determining when the quasi-steady state has been reached, the following norm on any iterated variable,  $f$ , is defined by

$$L_2 \equiv \left[ \frac{1}{N} \sum_{j=1}^N (f_j^n - f_j^{n-20})^2 \right]^{1/2} \quad (27)$$

After each 20th iteration cycle,  $L_2$  is computed with  $f$  equal to the radial and tangential winds. The norm is computed for separate radial rings, 0–200, 200–400, 400–600 km, etc., and for each level to determine which parts of the domain reach a slowly varying state first.

**Computational stability.** The computational stability analysis of the complete set of equations is very complicated. Separate analyses were made for various combinations of the linearized prediction equations. The most stringent stability requirement from these results yields an estimate for the requirement for the complete set of nonlinear equations.

The most severe restriction on the size of the time increment,  $\Delta t$ , is governed by the speed of the external gravity wave (Anthes 1970a, appendix B). When one con-

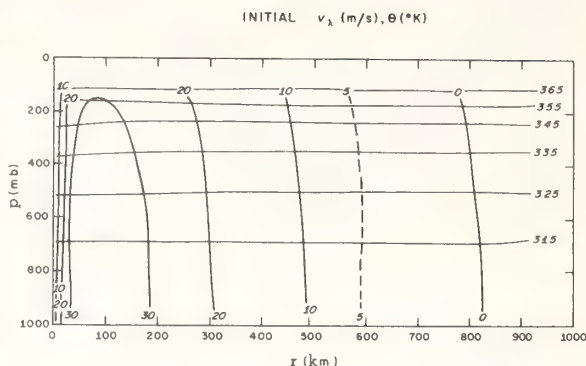


FIGURE 2.—Initial tangential wind and potential temperature cross section for all experiments.

siders the continuity equation and the radial equation of motion, the criterion for linear computational stability is  $(\Delta t/\Delta r)\sqrt{\bar{\rho}/\bar{p}} \leq 1$  where  $\bar{\rho}$  and  $\bar{p}$  are mean density and pressure, respectively, and  $\sqrt{\bar{\rho}/\bar{p}}$  is the approximate speed of the external gravity wave (about 330 m/s).

**Kinetic energy budget.** The kinetic energy budget for the volume obtained by equating  $f$  to the specific kinetic energy,  $k$ , in eq (12) is

$$\frac{dK}{dt} = \frac{2\pi R}{g} \int_{\theta_0}^{\theta_1} \left( \frac{\partial p}{\partial \theta} k v_r \right)_R d\theta - \frac{2\pi}{g} \int_0^R \int_{\theta_0}^{\theta_1} r \frac{dk}{dt} \frac{\partial p}{\partial \theta} d\theta dr. \quad (28)$$

The time rate of change of the specific kinetic energy obtained by multiplying the tangential and radial equations of motion by  $v_\lambda$  and  $v_r$ , respectively, and adding becomes

$$\begin{aligned} \frac{dk}{dt} &= -v_r \frac{\partial \psi}{\partial r} + K_H \left[ v_r \left( \nabla^2 v_r - \frac{v_r}{r^2} \right) + v_\lambda \left( \nabla^2 v_\lambda - \frac{v_\lambda}{r^2} \right) \right] \\ &+ \frac{C_D}{\Delta z} |\mathbf{V}| (v_r^2 + v_\lambda^2) \quad \text{surface only} \\ &+ v_r \frac{\partial}{\partial z} \left( K_z \frac{\partial v_r}{\partial z} \right) + v_\lambda \frac{\partial}{\partial z} \left( K_z \frac{\partial v_\lambda}{\partial z} \right) \quad \theta \text{ levels only.} \end{aligned} \quad (29)$$

**Initial conditions.** In all experiments, the initial conditions (or first guess) consist of a vortex having tangential winds in gradient balance with a surface maximum of 37 m/s at 80 km (fig. 2), a weak warm core with a temperature excess of 1°C in the center, and a central pressure of 970 mb. Through the thermal wind relation, there is a slight decrease of wind speed with height. The environmental pressure is 1011 mb. The radial winds are calculated to balance the vertical divergence term in the continuity equation so that the initial pressure tendency is zero.

### C. EXPERIMENTAL PARAMETERS

In the experiments presented in this paper, the constant parameters are the Coriolis parameter, the drag coefficient,



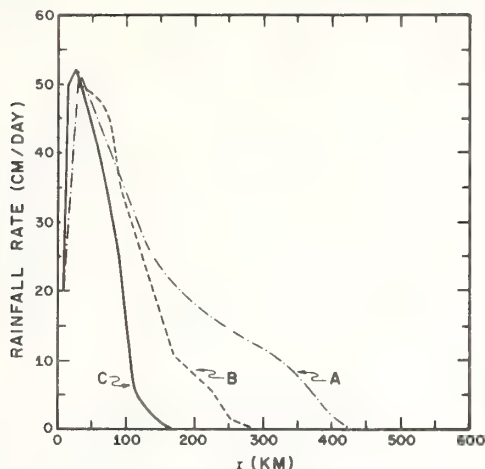


FIGURE 3.—Radial profiles of rainfall rates used to specify horizontal variations of latent heating.

and the depth of the boundary layer. The Coriolis parameter is  $5.0 \times 10^{-5} \text{ s}^{-1}$  and corresponds to  $20^\circ\text{N}$ . The drag coefficient, approximated by 0.003, is selected from empirical studies (Miller 1962). The depth of the boundary layer is assumed to be 1.0 km.

Very little is known about the variation of the vertical mixing coefficient,  $K_z$ . However, it seems qualitatively reasonable to assume that the vertical mixing decreases as the static stability increases. This effect is included in a crude fashion by decreasing  $K_z$  linearly with height from a value prescribed for the  $315^\circ\text{K}$  isentropic surface (about 700 mb) to one-half this value at the  $365^\circ$  surface. The value of  $K_z$  referred to in the experiments is the maximum value.

#### 4. EXPERIMENTAL RESULTS

In this section, results from some preliminary experiments are presented. First, the role of internal (vertical and horizontal) mixing for a fixed heating function is investigated. Then for constant mixing coefficients, the response of the mass and momentum structures to various horizontal and vertical distributions of latent heating is studied. Later, the computational aspects of the model, such as domain size, resolution, and variable grid spacing, are considered; and finally, fine horizontal resolution is utilized to study the effects of reduced horizontal mixing.

In all experiments, the latent heating function is computed by arbitrarily assuming a radial profile of rainfall rates and distributing the equivalent amount of heat vertically. In figure 3, the rainfall rates that determine the horizontal heating distributions in the various experiments are presented. The maximum rainfall rate of 50 cm/day at 30 km (corresponding roughly to the eye wall) is quite

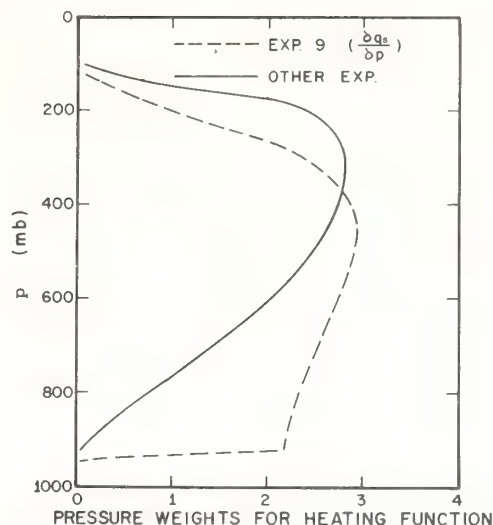


FIGURE 4.—Vertical profile of latent heat release for the experiments.

moderate for a mature hurricane. For example, Riehl and Malkus (1961) estimate a rainfall rate of 90 cm/day in hurricane Daisy, 1958.

The variation of the vertical distribution is one of the interesting aspects of the problem in view of our lack of knowledge concerning the effective heat release for the hurricane scale. The two vertical profiles of latent heat release studied in the experiments are shown in figure 4. The basis for these profiles is discussed in subsection 4C. All experiments, except experiment 9, utilize the distribution that releases the higher proportion of heat in the upper troposphere.

The importance of sensible heating at the sea-air interface to hurricane development and maintenance has been established from both empirical (Malkus and Riehl 1960) and numerical (Ooyama 1969) results. As air flows inward toward lower pressure in the boundary layer, the sensible heating increases its equivalent potential temperature. The higher equivalent potential temperature enhances the convection and increases the heating and generation of available potential energy. In this model, however, there is no feedback between sensible and latent heating, and the model is insensitive to this effect. In computing  $d\theta_s/dt$ , eq (19) is approximated by

$$\frac{d\theta_s}{dt} = \frac{\theta_s}{c_p T_s} \dot{Q}_s = \frac{\dot{Q}_s}{c_p} \quad (30)$$

The sensible heating,  $\dot{Q}_s$ , is modeled by assuming that the total sensible heating is  $0.11 \times 10^{14} \text{ W}$  (Malkus and Riehl 1960) and distributing the heat radially, as shown in figure 5.

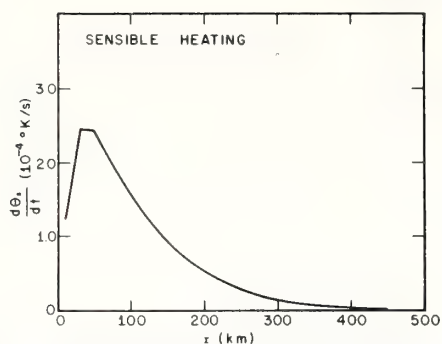


FIGURE 5.—Radial profiles of surface potential temperature change by sensible heating.

### A. VARIATION OF INTERNAL MIXING

The proper formulation of internal mixing (both horizontal and vertical) is an important, but unfortunately poorly understood, aspect of numerical modeling. Because of the difficulty in making direct measurements, the dissipation of kinetic energy by internal mixing is usually estimated as a residual in empirical energy budgets (e.g., Riehl and Malkus 1961 and Hawkins and Rubsam 1968). These studies indicate that the kinetic energy dissipation by internal mixing is about the same magnitude as the dissipation at the surface.

The horizontal diffusion of momentum in the hurricane has been modeled using constant mixing coefficients, but the values used by different investigators (table 1) vary over several orders of magnitude. A further complication is that the truncation errors of the finite-difference schemes produce large nonlinear damping. It is therefore of interest to investigate the magnitude of explicit horizontal and vertical diffusion with a model that does not contain a large computational damping.

The vertical mixing process is even more complex than horizontal mixing because the vertical eddies (cumulus clouds) have the same vertical scale as the hurricane. Gray (1967) has found that the momentum transport by cumulus convection is an important process in the steady-state dynamics of hurricanes. Constant vertical mixing coefficients seem particularly inadequate to describe this process correctly. Indeed, Gray finds a large variation of the vertical mixing coefficients with height ranging from  $10^6$  to  $10^9$   $\text{cm}^2/\text{s}$ .

Because of these uncertainties, the effects of horizontal and vertical mixing are investigated in experiments 1 through 6. The steady heating for these experiments is defined by the rainfall profile A (fig. 3) and the solid vertical profile in figure 4. The results from these preliminary experiments are discussed in some detail by Anthes (1970a), and only a brief summary is included here.

TABLE 1.—Exchange coefficients ( $\text{cm}^2/\text{s}$ ) in hurricanes

Investigator	$K_H$	$K_z$	Remarks
Estoque and Fernandez-Partagas (1968)	$10^8$ – $10^9$	—	Forecast model*
Gray (1967)	—	$10^6$ – $10^9$	Empirical study
Kasahara (1961)	$1.6 \times 10^8$	—	Forecast model*
Krishnamurti (1961)	$2.7 \times 10^8$	$1.2 \times 10^7$	Diagnostic study
Kuo (1965)	$10^8$	$10^4$ – $10^6$	Forecast model
Ooyama (1969)	$10^7$	$0$ – $10^5$	Forecast model
Riehl and Malkus (1961)	$10^8$	$10^6$	Empirical study
Rosenthal (1969)	$10^8$	$0$ – $10^5$	Forecast model*
Yamasaki (1968a, 1968b)	$10^7$	$10^6$	Forecast model*

\*Denotes additional nonlinear damping due to truncation error in finite-difference scheme

The results from experiments 1 through 6 establish ranges of the horizontal and vertical mixing coefficients that give results comparable to observations. Values of  $K_H \geq 10 \times 10^8$   $\text{cm}^2/\text{s}$  result in a large diffuse storm. Values of  $K_z \leq 1 \times 10^6$   $\text{cm}^2/\text{s}$  do not yield sufficient vertical mixing to produce the vertical momentum structure representative of hurricanes (Hawkins 1962, LaSeur and Hawkins 1963, Gray 1967, and Riehl and Malkus 1961). The strongest maximum wind and the results that compare most closely with the above empirical wind distributions (loc. cit.) are obtained for  $K_H = 5 \times 10^8$   $\text{cm}^2/\text{s}$  and  $K_z = 5 \times 10^6$   $\text{cm}^2/\text{s}$ ; the study of variable heating functions begins with these values. The energy budgets for experiments 3 through 6 are summarized in table 2 for comparison with later experiments.

### B. RADIAL VARIATION OF LATENT HEATING

From the premise of the thermal forcing of the hurricane, differences between size and intensity of individual storms are related to space and time variations of the heating distributions. However, the question of just how sensitive or responsive is the storm circulation to these variations remains unanswered. In this subsection and the following one, the results of the model attained from various combinations of horizontal and vertical heating distributions provide some insight into this relation between the hurricane circulation and thermal forcing.

The heating function in experiment 6 (Anthes 1970a) produced a rather large storm of only moderate intensity. The total heat release, generation of available energy, and conversion to kinetic energy were larger than empirical results by a factor of 2 or 3. These results suggest that the heating function overestimates the latent heat release at large distances from the center.

In experiments 7 and 8, the latent heat release beyond 100 km is progressively decreased with the result that the heating becomes more concentrated near the center (rainfall types B and C in table 3 and fig. 3). In these experiments, the vertical heating distribution is specified by the solid curve in figure 4.

TABLE 2.—Energy transformation rates ( $10^{11}$  W)

Experiment	3	4	5	6	7	8	9	10	11	14
Rainfall profile type	A	A	A	A	B	C	B	0.5B	B	B
Vertical profile (p, pseudoadiabatic; c, cloud environment)	c	c	c	c	c	c	p	c	c	c
$K_H$ ( $10^8$ cm <sup>2</sup> /s)	25.0	10.0	10.0	5.0	5.0	5.0	5.0	5.0	5.0	2.5
$K_v$ ( $10^6$ cm <sup>2</sup> /s)	0.5	1.0	5.0	5.0	5.0	5.0	5.0	5.0	5.0	5.0
Generation A	24.1	21.2	15.5	17.3	10.7	4.8	2.9	13.7	13.8	9.9
Boundary A	18.2	17.0	13.3	14.6	4.2	0.1	1.1	5.0	2.4	3.5
Conversion to K	42.0	39.2	30.3	32.9	16.5	6.2	5.3	18.8	18.6	15.1
Boundary K	- 5.0	- 4.3	- 2.2	- 2.2	0.0	0.0	0.0	0.0	- 0.1	- 0.2
Drag dissipation	-18.0	-22.0	-15.0	-14.0	- 9.2	-7.0	-5.0	-11.0	- 9.4	-12.0
Lateral mixing	-26.0	-16.0	-12.0	- 6.8	- 5.7	-5.0	-3.0	- 5.8	- 5.9	- 4.2
Vertical mixing	- 2.5	- 6.0	-18.0	-15.0	-11.0	-5.0	-5.0	-10.0	-13.0	-13.0

TABLE 3.—Summary of experiments investigating radial variation of heating

Experiment	Rainfall type	Total heating rate $10^{11}$ W
6	A	21.3
7	B	11.0
8	C	5.5

Before the discussion of the steady-state solutions, quantitative results illustrating the convergence to a steady state as shown by the decrease of the  $L_2$  norm are presented for a typical experiment. The behavior of  $L_2$  in the other experiments is quite similar. In figure 6, the convergence of the tangential winds is most rapid in the lower levels near the center. Inside 200 km, the tangential wind has reached a slowly varying state after 800 iterations. In the upper levels, however, at large distances from the center, convergence is much slower. In fact,  $L_2(v_\lambda)$  at 360°K does not begin to decrease until the inner region reaches a quasi-steady state (about 600 iterations). The tangential winds in the outer regions are primarily determined by the steady-state angular momentum distribution near the center. The slow convergence in this region reflects the time required for the angular momentum near the center to be advected to the edge of the domain.

The convergence of  $L_2(v_\lambda)$  indicates that the solutions (for the 500-km domain) may approach arbitrarily close to a steady state, the only limit being the time (and cost) required for each experiment. However, the point of diminishing returns has probably been reached long before 6,400 steps, since the tangential wind components at selected points (fig. 6) are qualitatively in near-steady state after 1,600 iterations. For experiments with 20-km resolution, therefore, a compromise of 1,600 steps is considered adequate for meaningful comparisons between experiments.

The convergence of the  $L_2$  norm on the radial winds for the surface and 360°K is shown in figure 7. The oscillations

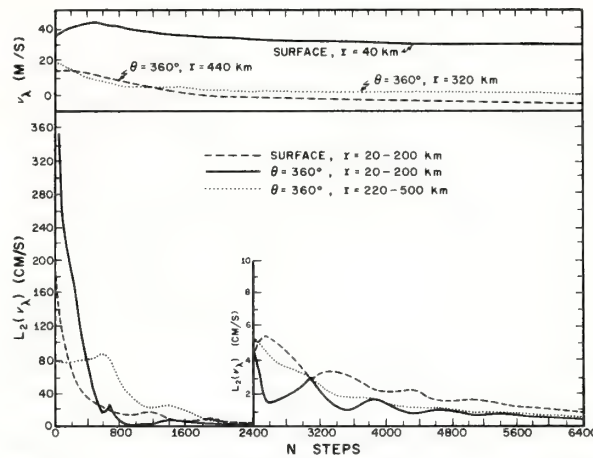


FIGURE 6.—Time (iteration step) variation of  $L_2$  norm on tangential wind for the surface and 360°K in a typical experiment. Also shown is the variation of  $v_\lambda$  at three model points.

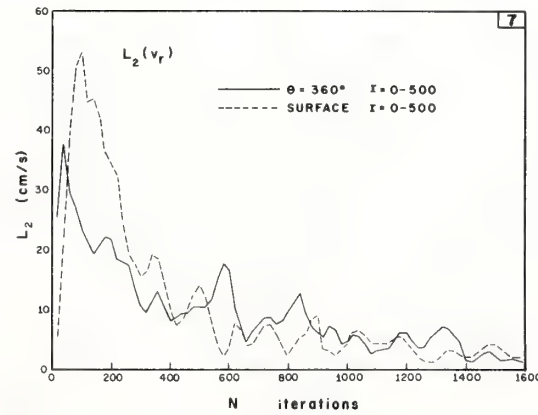


FIGURE 7.—Time (iteration step) variation of the  $L_2$  norm on radial wind for the surface and 360°K in experiment 7.



TABLE 4.—Empirical energy budgets

Investigation	Region of storm	Heating	Generation of $A$	Conversion to $K$	Advection of $K$	Surface dissipation	Internal dissipation
	(km.)	( $10^{14}$ W)	( $10^{12}$ W)	( $10^{12}$ W)	( $10^{12}$ W)	( $10^{12}$ W)	( $10^{12}$ W)
Anthes and Johnson (1968)	0-1000	3.2	10.3	—	—	—	—
Hawkins and Rubsam (1968)	0-150	2.2	—	2.3	3.9	-4.2	-2.0
Hughes (1962)	0-444	5.4	—	—	—	—	—
Miller (1962)	0-111	3.6	—	8.0	2.4	-5.1	-5.3
Palmén and Jordan (1955)	0-666	5.4	—	15.0	—	—	—
Palmén and Riehl (1957)	0-666	5.0	—	15.0	0.0	-13.0	0.0
Riehl and Malkus (1961)							
8/25	0-150	2.1	—	2.8	0.3	-1.6	-1.0
8/27	0-150	4.0	—	6.8	3.5	-3.2	-6.6

superimposed on the downward trend are evidence of inertial gravity waves.

*Concentrated heating near the center, experiment 7.* In this experiment (rainfall type B, fig. 3), the total heating rate is reduced from 21.3 to  $11.0 \times 10^{14}$  W, a rate closer to empirical results (table 4). The more concentrated heating function in this experiment generates a smaller warm core with nearly as intense a pressure gradient near the center as the one in experiment 6. The tangential and radial wind profiles are shown in figure 9 and may be compared with those from experiment 6 in figure 8. The effect of reducing the heating beyond 150 km on the tangential wind is to slightly decrease the maximum tangential wind from 34 to 33 m/s at 60 km. However, the winds beyond 150 km decrease significantly. The 3-percent decrease in the maximum tangential wind speed, despite a 50-percent reduction in total heating is somewhat paradoxical and emphasizes the importance of differential heating in establishing the temperature and pressure gradients and the angular momentum distribution.

The changes in the radial winds are greater than those in the tangential winds (figs. 8B and 9B). The inflow at the surface is reduced beyond 200 km (e.g., from 11 to 8 m/s at 250 km). The maximum outflow decreases from 19 to 14 m/s, and the radius of maximum outflow moves inward from 360 to 180 km.

The results from experiment 7 correspond to a minimal hurricane. The tangential winds show a region of maximum cyclonic winds near the center with little vertical wind shear below 300 mb. In the lower levels beyond the radius of maximum wind, positive vertical shear exists because of surface friction. A small region of anticyclonic winds occurs in the upper levels beyond 400 km.

The radial wind profiles show inflow from the surface to about 600 mb, although significant ( $|v_r| \geq 5$  m/s) inflow is limited to the region below 800 mb. The maximum inflow of 15 m/s is somewhat stronger than empirical observations (e.g., Miller 1962) but weaker than the inflow found in separate boundary-layer experiments (Anthes 1970a). Significant outflow occurs above 300 mb.

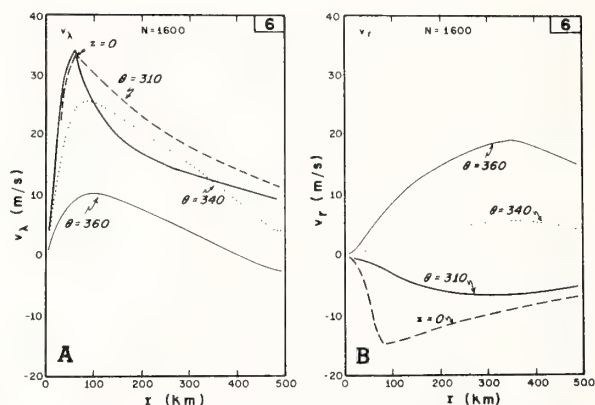


FIGURE 8.—Radial profiles of slowly varying (1,600 iterations) tangential (A) and radial (B) winds for various levels in experiment 6.

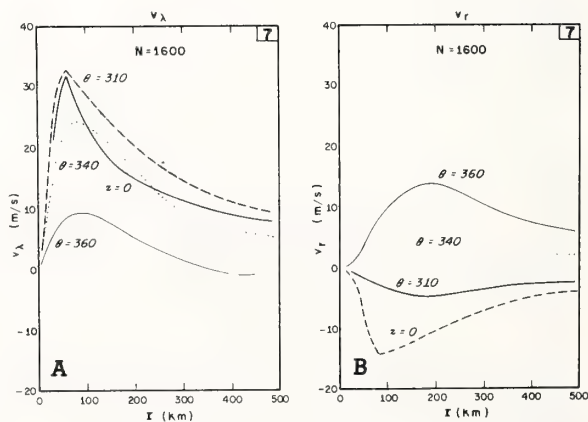


FIGURE 9.—Radial profiles of slowly varying (1,600 iterations) tangential (A) and radial (B) winds for various levels in experiment 7.

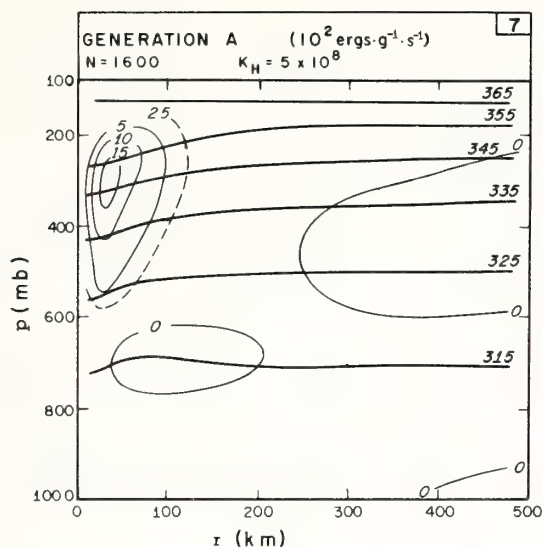


FIGURE 10.—Generation of available potential energy cross section for a slowly varying state (1,600 iterations) in experiment 7.

The vertical cross sections of the generation of available potential energy,  $A$ , are shown in figure 10. Most of the generation occurs in the middle and upper troposphere inside 150 km, a result that agrees well with the empirical estimate of Anthes and Johnson (1968). On the other hand, conversion of available to kinetic energy,  $C(A, K)$ , occurs mainly below 800 mb inside 300 km where the inflow and acceleration toward lower pressure are large.

The difference between observed rates of change in the total kinetic energy of the volume and the instantaneous tendencies computed from eq (29) is an estimate of the truncation error in the model. The tendencies as a function of iteration step and the observed changes evaluated over 100 steps (fig. 11A) show little systematic deviation. Maximum differences are about 10 percent, indicating that truncation error is small.

Figure 11B shows the evolution of the different components of the rates of change of available potential and kinetic energy. Initially, the dissipation by horizontal mixing is dominant, causing a large negative kinetic energy tendency. The internal mixing decreases slowly after 400 steps. Throughout the entire experiment, the dissipation from surface drag is smaller than that from internal mixing.

One of the most interesting features of the energy budget evolution is the relationship between changes in the generation  $G(A)$  and boundary flux  $B(A)$  of available potential energy and its conversion to kinetic energy. Although energetic consistency requires only that these changes be equal in the steady state, there is an extremely close correlation between the two at all stages of all the experiments. This suggests that the available energy gen-

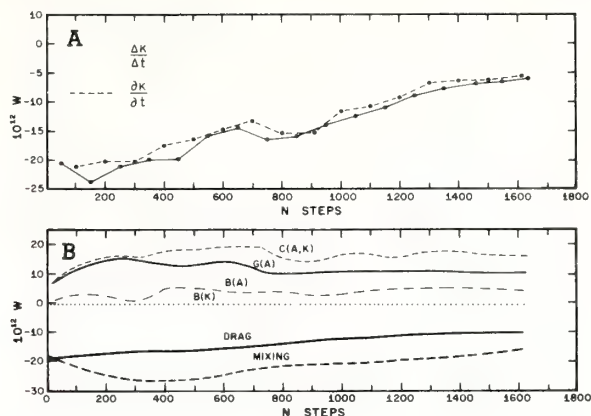


FIGURE 11.—(A) observed ( $\Delta K/\Delta t$ ) and analytic ( $\partial K/\partial t$ ) kinetic energy tendencies in experiment 7 and (B) time (iteration step) variation of energy budget components in experiment 7.

erated by the steady forcing is almost immediately converted to kinetic energy.

Initially, the kinetic energy conversion closely follows the generation. After 300 steps, however, the mass outflow is removing heat at 500 km that would otherwise reduce the radial temperature gradient. This process is reflected in an increase in the boundary term  $B$ , of the available energy change equation. The sum of the generation and boundary terms continues to almost exactly balance the conversion to kinetic energy, so that changes in the store of available potential energy are small.

Although the boundary term in the available energy budget is large, the boundary flux of kinetic energy  $B(K)$  is small compared to the conversion and dissipation processes within the volume. The contribution is relatively constant and is negative, indicating that the storm is exporting kinetic energy to the environment.

The contribution by the various energy transformation processes within 100-km radial rings is presented in figure 12. Most of the generation occurs inside 200 km while its conversion to kinetic energy occurs primarily between 100 and 300 km. The large contribution to the available energy budget by the boundary processes supports earlier studies which show that the hurricane cannot be considered a closed system on this scale. In the total energy budget (table 2), the generation of available potential energy and its conversion to kinetic energy are reduced to  $10.7$  and  $16.5 \times 10^{12}$  W, respectively—values that compare favorably with the empirical results in table 4. The kinetic energy sinks are  $9.2 \times 10^{12}$  W for surface drag,  $11.0 \times 10^{12}$  W for vertical (V) mixing, and  $5.7 \times 10^{12}$  W for horizontal (H) mixing. Comparison of these dissipation rates with empirical results is difficult. While the dissipation by drag friction is readily computed from hurricane wind data, dissipation by internal mixing is usually

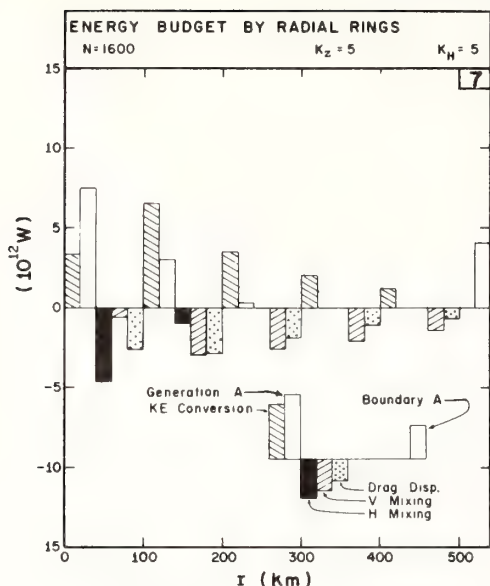


FIGURE 12.—Energy budget components within 100-km radial rings for a slowly varying state (1,600 iterations) in experiment 7.

computed as a residual in a kinetic energy budget. Also, the empirical results in table 4 were determined for only a small portion of the storm ( $r \leq 150$  km).

The ratio of internal mixing to surface friction in table 4 ranges from 0.48 to 2.06. The ratio in experiment 7 is 1.8 which is near the upper limit of the empirical estimates (the range of this ratio in all subsequent experiments is 1.02 to 2.01). Beyond 200 km, the vertical mixing may be overestimated for two reasons. First, the assumption that  $K_z$  is constant horizontally is very crude. The vertical turbulence, including cumulus convection, probably decreases with increasing radius; therefore,  $K_z$  in the model should decrease also. Second, the large vertical mixing dissipation is related to the fact that the middle-level winds in the outer region have not yet completely adjusted to the upper and lower level winds, a consequence of weak vertical coupling in the absence of heating. Thus, the vertical shear resulting from the initial conditions is still large.

In summary, the effect of reducing the heating beyond 200 km in experiment 7 is to significantly reduce the tangential and radial wind components at larger radii. For a reduction of the total heating by 50 percent, only a 3-percent decrease in maximum tangential wind is produced. The generation and conversion of available energy and dissipation of kinetic energy compare favorably with empirical evidence, even though the total heating is somewhat high.

*Very concentrated heating near center, experiment 8.* The thermal forcing by the extremely concentrated heating

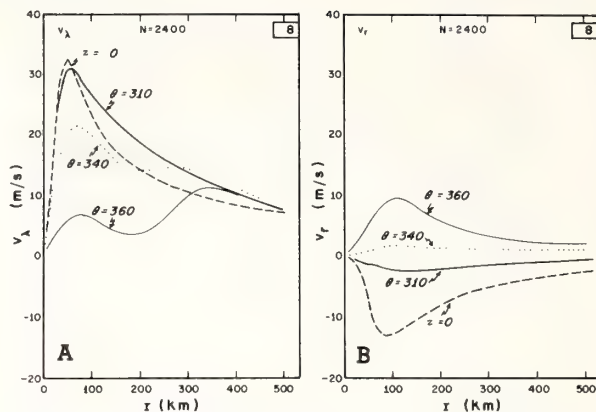


FIGURE 13.—Radial profiles of slowly varying (2,400 iterations) tangential (A) and radial (B) winds for various levels in experiment 8.

function, type C in figure 3, is studied in experiment 8. Inside 100 km, the horizontal distribution is essentially unchanged from that in experiments 6 and 7. The heating rate beyond 100 km is greatly reduced; and the total heating decreases to  $5.5 \times 10^{14}$  W, an amount comparable to observational evidence (table 4).

Because of the concentrated heating distribution, a variable grid was utilized in experiment 8. For  $r \leq 160$  km, the resolution is 10 km. For  $r > 160$  km, the resolution varies smoothly from 10 km to 25 km at the maximum radius of 500 km. The use of a variable grid is justified in a later experiment.

Within 100 km, the tangential and radial wind profiles for experiment 8 (fig. 13) are quite similar to the profiles for experiment 7 (fig. 9). The slight shift inward of the maximum wind from 60 km (exp. 7) to 50 km (exp. 8) is probably a consequence of the increased resolution rather than the heating reduction beyond 100 km.

Although changes inside 100 km are small, large differences are present at greater distances. Maximum outflow is reduced from 14 m/s at 180 km (exp. 7) to 10 m/s at 100 km (exp. 8). At 300 km, the outflow is reduced from 11 m/s to 3 m/s.

The decreased outflow produces a different tangential wind distribution at larger radii. Whereas the stronger outflow in experiments 6 and 7 produces anticyclonic winds at 500 km by an outward advection of low angular momentum from the center, there is little radial advection at this distance in experiment 8. Thus internal mixing dominates, and the tangential winds slowly decay.

The energy budget reflects the decrease in storm intensity compared with experiments 6 and 7. The generation of available energy occurs entirely within 100 km. The boundary term in the available energy budget decreases from  $4.2 \times 10^{12}$  to  $0.1 \times 10^{12}$  W. The total



energy budget (table 2) shows significantly smaller values for all processes, except horizontal mixing.

Experiments 6, 7, and 8 indicate that the reduction of heating at large distances has little effect on the inner region of the storm and suggests that the maximum winds are determined primarily by heating in the inner region. As the heating is reduced at larger distances, the storm decreases in horizontal extent; and the tangential and radial winds beyond 100 km are reduced. The size and intensity of the anticyclone aloft are closely related to the amount of heating at large distances from the center. This relationship suggests that the intensity of the thermal anticyclone associated with storms in nature should be closely correlated with the diameter of the active convective area.

### C. VERTICAL VARIATION OF LATENT HEATING, EXPERIMENT 9

The vertical distribution of latent heating is an important aspect of the tropical cyclone problem. Early attempts at hurricane modeling (e.g., Kasahara 1961 and Rosenthal 1964) related the heating to the variation of saturation specific humidity,  $q_s$ , along an appropriate moist adiabat. This pseudoadiabatic type of heating resulted in unrealistic circulations and showed that the hurricane could not be considered a huge cloud. Kuo (1965) attempted to relate the large-scale to the cloud scale heating by making the heat release at any level proportional to the cloud-environment temperature difference. Parameterization similar to this type of heating (hereafter called "cloud-environment" type) has given quite realistic results in hurricane models (Yamasaki 1968a, 1968b; and Rosenthal 1969).

In experiment 9, the vertical distribution of heating is proportional to  $\partial q_s / \partial p$  along the moist adiabat defined by an equivalent potential temperature of 365°K. The relative distribution is contrasted with the vertical heating distribution of the earlier experiments in figure 4. The horizontal heating distribution and all other parameters are identical to those in experiment 7.

Figure 14 shows the radial profiles of tangential and radial winds in experiment 9. The low-level tangential wind profiles are similar to those in experiment 7 (fig. 9). The reduced vertical transport of momentum in the upper levels, however, yields weaker winds. The radial wind profiles show a deep, weak outflow layer in experiment 9 in contrast to the shallow, strong outflow layer of experiment 7. This difference is related to the change in thermal structure shown in figure 15. In experiment 9, the level of maximum temperature departure drops from 300 to 500 mb, the pressure gradient decreases more rapidly with height, and the outflow begins at lower levels. Near 200 mb, the atmosphere is nearly undisturbed.

The upper level temperature structure and the radial winds of experiment 9 are not supported by empirical evidence. Observations show that the maximum tempera-

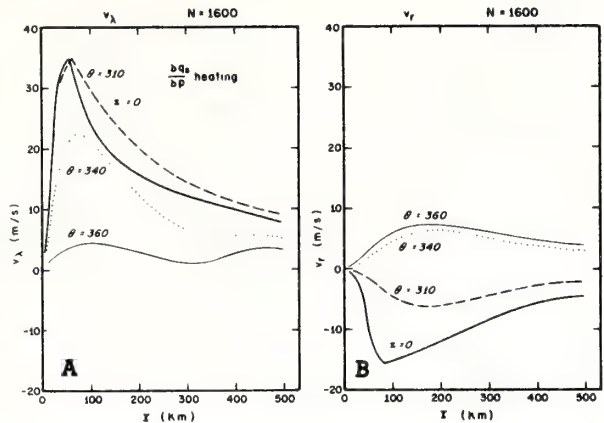


FIGURE 14.—Radial profiles of slowly varying (1,600 iterations) tangential (A) and radial (B) winds for various levels in experiment 9.

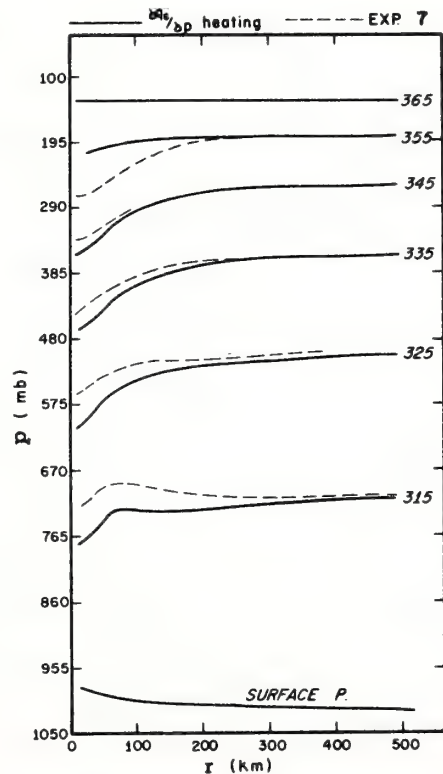


FIGURE 15.—Isentropic cross section for slowly varying state (1,600 iterations) in experiments 7 and 9.

ture departure occurs in the upper rather than middle troposphere (Hawkins and Rubsam 1968 and Malkus and Riehl 1961). They also support a thin, strong outflow

layer rather than a deep, sluggish layer (Miller 1958, 1964). These results confirm that the vertical heating distribution of experiment 9 is not appropriate to the hurricane scale in the mature, slowly varying state.

#### D. VARIATION OF TOTAL HEATING, EXPERIMENT 10

The results from the previous experiments emphasize the importance of variable heating distributions. In all the experiments, the heating maximum was defined by a rainfall rate of about 50 cm/day at 30 km, a moderate rate for a mature hurricane. In experiment 10, the heating function is one-half that of experiment 7, while the horizontal and vertical heating variation and all other parameters are identical.

As expected, the tangential and radial circulations are considerably less than those in experiment 7; and the thermal structure shows a weaker warm core. The maximum tangential wind is reduced from 33 to 25 m/s; maximum inflow is reduced from 15 to 9 m/s, while the outflow is decreased from 14 to 7 m/s. The maximum temperature departure is reduced from  $+10^\circ$  to  $+4^\circ\text{C}$ . The profiles are not shown. Thus, the thermal forcing given by the rainfall rates of experiment 10 produces maximum winds that are typical of a weak tropical storm.

#### E. EXPERIMENTS OF A COMPUTATIONAL NATURE

The experiments so far have emphasized primarily the role of physical processes such as variable mixing and heating in the determination of steady circulations. In numerical models, however, it is also important to ascertain the effect of the computational or artificial aspects of the model on the solutions. Ideally, the effects of domain size, boundary conditions, and resolution should be small in comparison to physical effects. The experiments in this section compare solutions with domains of 500 and 1000 km, with constant horizontal resolutions of 10 and 20 km, and with a variable horizontal grid.

*Domain size, experiment 11.* The effect of the arbitrary horizontal boundary conditions may be investigated by increasing the size of the horizontal domain. Experiments 7 and 11 are identical, except that the horizontal domain of 500 km is extended to 1000 km in the latter. Figure 16 shows the tangential wind profiles for both experiments. Differences for  $r < 200$  km are less than 30 cm/s at all levels. Between 300 and 500 km, however, the maximum difference is 1 m/s. The low-level tangential winds show greater anticyclonic shear in experiment 11, a result of the boundary condition of zero relative vorticity being shifted from 500 km in experiment 7 to 1000 km in experiment 11.

A small difference is also present in the low-level radial wind profile (not shown). The boundary condition of zero divergence at 500 km in experiment 7 is replaced by weak positive divergence in experiment 11, and the inflow is less by 0.4 m/s at this distance. The small differences between these two experiments, especially near the radius of maximum winds, justify the use of the 500-km domain.

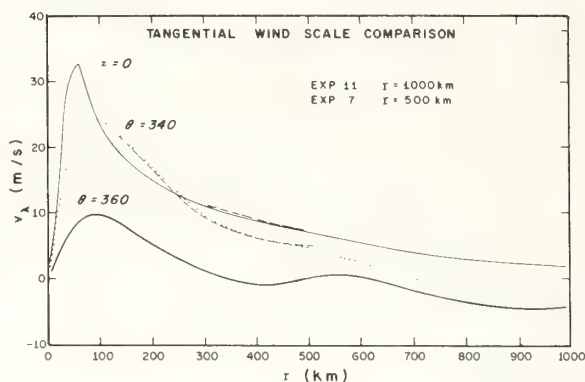


FIGURE 16.—Radial profile of slowly varying (1,600 iterations) tangential winds at various levels in experiments 7 and 11.

*Variable grid, experiment 12.* In numerical models of atmospheric convective phenomena such as cumulus clouds, squall lines, or hurricanes, a greater resolution for a portion of the domain is desirable. For the hurricane, a finer mesh is needed near the eye wall where horizontal gradients are larger than in the environment of the storm where gradients are weak. The variable grid for this model is defined by retaining a constant grid from the origin to  $R_0$  and introducing the transformation  $r = R_0 + x^2 + cx$  for  $r > R_0$ . This transformation, with proper choice of  $R_0$ ,  $c$ , and increment,  $\Delta x$ , increases computing efficiency with no significant reduction in accuracy.

Results from a variable and a fixed grid are compared, where the size of the domain is 1000 km and the horizontal resolution for  $r \leq 300$  km is 20 km in both experiments. For the variable grid (exp. 12), the parameters of the transformation are  $R_0 = 300$  km,  $c = 395.1 \text{ m}^{1/2}$ , and  $\Delta x = 43.6 \text{ m}^{1/2}$ . The resolution varies from 20 km at 300 km to 73.3 km at 1000 km. The number of grid points is reduced from 51 to 31, and a 40-percent saving in the computational time is achieved. Initial conditions for the grid points beyond 300 km are interpolated from the profiles of the fixed grid.

Figure 17 shows the radial wind profiles after 1,600 iterations. Differences are extremely small; for example, the difference in maximum inflow between the variable grid experiment and the fixed grid experiment is 0.09 m/s. The maximum tangential wind difference is 0.05 m/s. Exact comparisons beyond 300 km are difficult because the grid points in the two experiments do not coincide. Qualitatively, however, the results agree very well and suggest that a further reduction in grid points may be possible without generating unacceptable errors. The close agreement between experiments 11 and 12 justifies use of the variable grid as an economically useful substitute for the constant grid.

*High (10-km) resolution, experiment 13.* In the final experiment of a computational nature, experiment 7 is

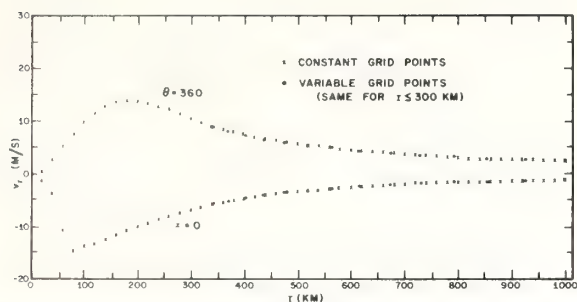


FIGURE 17.—Radial profile of radial winds after 1,600 iterations in experiments 11 and 12.

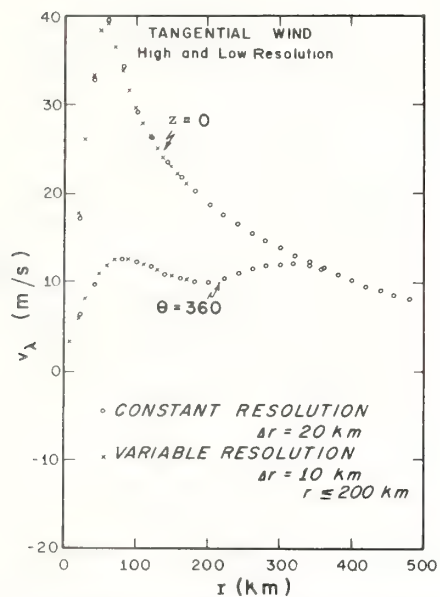


FIGURE 18.—Radial profile of tangential winds after 400 iterations in experiment 7 and 800 iterations in experiment 13.

repeated utilizing the variable grid. For  $R_0=150$  km,  $c=484.1$  m<sup>1/2</sup>, and  $\Delta x=19.85$  m<sup>1/2</sup>, the resolution varies from 10 km within 150 km of the center to 25 km at the outer boundary of 500 km. The number of grid points increases from 26 in experiment 7 to 36 in experiment 13. Because the time step must be halved to satisfy the linear computational stability requirement, an increase in computation time of 138 percent is required.

Figure 18 shows the tangential wind profiles for 400 and 800 iterations, respectively. The profiles for experiment 13 are somewhat smoother near the radius of maximum wind than for experiment 7. The maximum tangential wind is

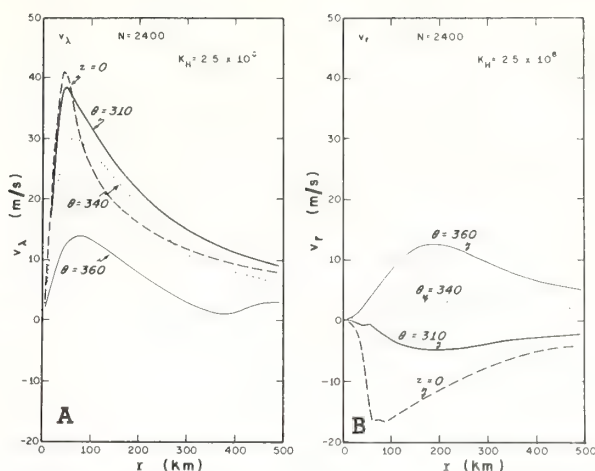


FIGURE 19.—Radial profile of slowly varying (2,400 iterations) tangential (A) and radial (B) winds for various levels in experiment 14.

reduced from 39.28 in experiment 7 to 38.65 m/s in experiment 13, while the maximum inflow decreases from 18.28 to 17.63 m/s. These differences, which are about 2 percent, appear insignificant in view of the 138-percent increase in computational time.

#### F. HIGH-RESOLUTION EXPERIMENT WITH REDUCED HORIZONTAL MIXING, EXPERIMENT 14

After the preliminary series of experiments, a value for  $K_H$  of  $5 \times 10^8$  cm<sup>2</sup>/s was used in subsequent experiments. For investigating the effect of decreasing this horizontal mixing coefficient to  $2.5 \times 10^8$  cm<sup>2</sup>/s, the variable grid of experiment 13 with 10-km resolution near the center and the heating function of experiment 7 is utilized.

**Momentum and temperature structures.** Figure 19 shows the slowly varying tangential and radial wind profiles for experiment 14 which should be compared to those for experiment 7 (fig. 9). The maximum tangential wind increases from 33 to 41 m/s in experiment 14, and the radius of maximum wind shifts inward from 60 to 40 km. Maximum inflow increases from 15 to 17 m/s. The irregularity in the radial wind profile at 70 km indicates that the resolution in this region is insufficient to adequately resolve the extremum. The temperature structure shows a more concentrated warm core in experiment 14 than in experiment 7, with a maximum temperature anomaly increase of 3°C.

The circulation in experiment 14 is the strongest of all the experiments. Figures 20 and 21 show cross sections of the tangential and radial wind. The tangential circulation is stronger and more concentrated near the center than in experiment 7. The weak upper level anticyclone at 500 km in experiment 7 is not present because the cyclonic circulation in the upper levels near the center is stronger



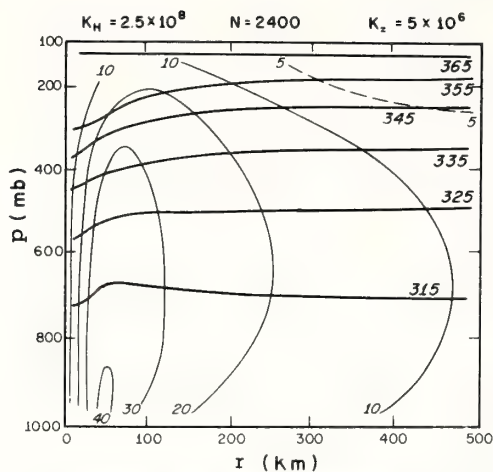


FIGURE 20.—Tangential wind (m/s) cross section for the slowly varying state (2,400 iterations) in experiment 14.

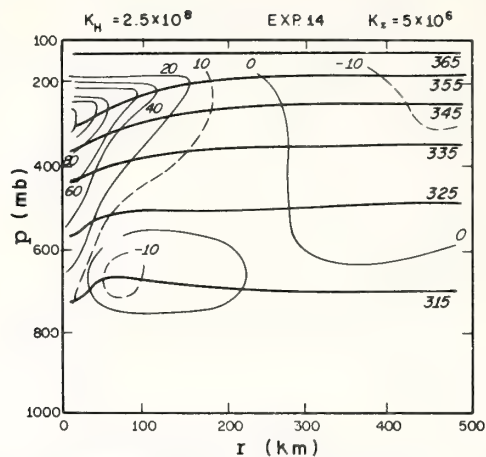


FIGURE 22.—Efficiency factor ( $10^{-3}$ ) cross section for the slowly varying state (2,400 iterations) in experiment 14.

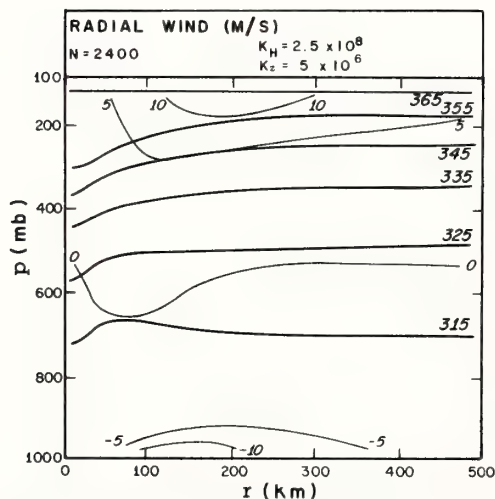


FIGURE 21.—Radial wind cross section for the slowly varying state (2,400 iterations) in experiment 14.

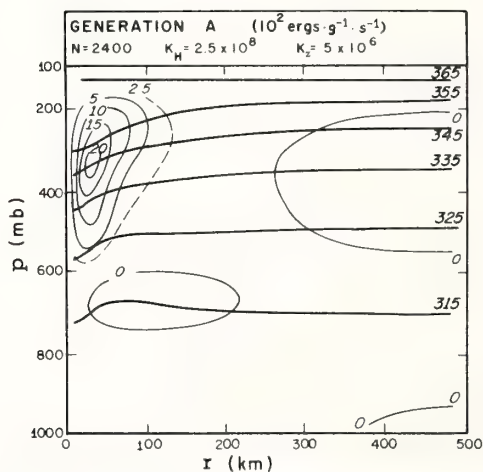


FIGURE 23.—Generation of available potential energy cross section for the slowly varying state (2,400 iterations) in experiment 14.

in experiment 14, so that the radius at which the relative circulation becomes anticyclonic is greater. This result and the strong dependency of the upper level outflow on the horizontal heating distribution found earlier suggest that relatively weak storms with large diameters should be accompanied by stronger upper level anticyclones than smaller more intense storms.

**Energy budget.** The efficiency factor cross section for experiment 14 (fig. 22) shows positive efficiency factors in the middle and upper troposphere extending from the center to 300 km. Negative efficiency factors occur in the

lower levels near the center and in the upper levels beyond 300 km. In figure 23, almost all the generation occurs inside 200 km and above 600 mb.

The energy budget shown in figure 24 and the total budget summarized in table 2 are quite similar to the results from experiment 7 (fig. 12). Although the dissipation of kinetic energy by horizontal mixing is reduced in experiment 14, the dissipation at the surface and through vertical mixing is increased. The latter increases are due to the greater low-level wind speed and the increased vertical wind shear.

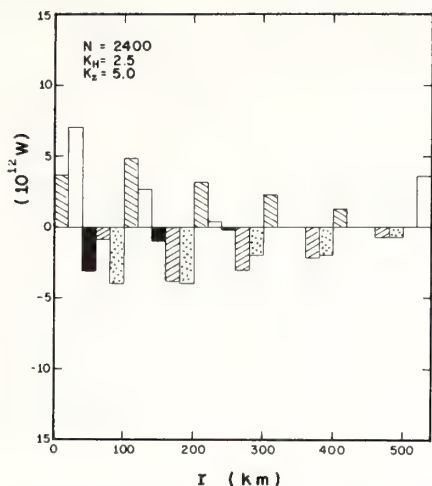


FIGURE 24.—Energy budget components within the 100-km radial rings for the slowly varying state (2,400 iterations) in experiment 14 (see fig. 12 for the key).

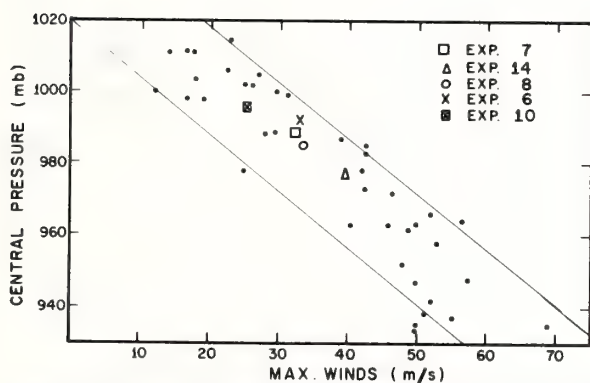


FIGURE 25.—Scatter diagram of maximum surface winds versus central pressure for empirical data (Colón 1963) and model experiments.

#### G. NUMERICAL AND EMPIRICAL PRESSURE-WIND RELATIONSHIP

Empirical evidence (Colón 1963) indicates a close relationship between central pressure and maximum wind speed. Figure 25 shows the model results from five experiments superimposed on Colón's data. Central pressure in the model is defined as the pressure at the first prediction point for pressure, which is either 5 or 10 km. All points from the model experiments lie within a region that bounds the empirical data.

The relationship between central pressure and radius of maximum wind is another aspect of the model to be

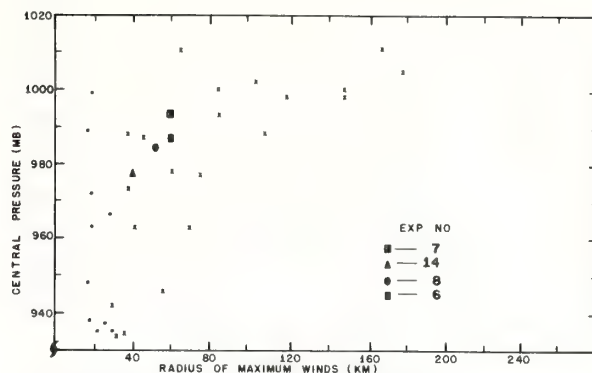


FIGURE 26.—Scatter diagram of radius of maximum surface winds versus central pressure for empirical data (Colón 1963) and model experiments.

compared with Colón's (1963) data (fig. 26). Colón discusses two types of storms. The "Daisy type," represented by dots in figure 26, is small and shows little relationship between central pressure and radius of maximum wind. The "Helene type" storm, represented by crosses in figure 26, is larger and shows an increasing radius of maximum wind with increasing central pressure. From figure 26, we see that storms produced by this model appear to fit the Helene type.

The degree of gradient balance throughout the storm system has received attention from investigators (e.g., Hawkins and Rubsam 1968). Their results show that the inner region is fairly close to gradient balance. In these experiments, except for the winds near the surface which are subgradient by 20 to 40 percent and in the outflow layer where radial advection is important, gradient balance is closely approximated. Models with low vertical resolution may have outflow layers closer to gradient balance because horizontal advection in a deeper outflow layer will be much weaker.

#### 5. SUMMARY

A diagnostic model in isentropic coordinates is developed to study the energetics and dynamics of the steady-state mature tropical cyclone. Slowly varying solutions for the mass and momentum fields are obtained by an iterative technique for the thermal forcing specified by several heating distributions. The principle conclusions from the preliminary experiments are:

1. The magnitude and distance of the maximum wind from the center is determined primarily by the heating inside 100 km. Large variations in heating beyond 100 km have little effect on the maximum wind but produce considerable changes in the outflow intensity. Because angular momentum tends to be conserved in the outflow layer, the size and intensity of the upper level anticyclone is also closely related to the heating at large distances from the center.

2. In experiments in which the vertical variation of heating is proportional to the condensation of water vapor along a moist adiabat, the temperature structure shows a low-level warm core and a deep, weak outflow layer. A vertical distribution that releases a higher proportion of heat in the upper troposphere gives more realistic results.

3. In experiments with a constant horizontal eddy coefficient and a vertical mixing coefficient that decreases linearly with height, values of  $K_H > 5 \times 10^8 \text{ cm}^2/\text{s}$  result in diffuse storms; and values of  $K_H < 1 \times 10^8 \text{ cm}^2/\text{s}$  produce storms with large vertical shear. Results most similar to observations are obtained for  $K_H = 2.5$  and  $5 \times 10^8 \text{ cm}^2/\text{s}$  and  $K_z = 5 \times 10^8 \text{ cm}^2/\text{s}$ .

4. In the slowly varying states, the generation and boundary flux of available potential energy, conversion to kinetic energy, and dissipation of kinetic energy by surface and internal friction are balanced. Paradoxically, therefore, experiments with the most internal friction contain the most kinetic energy. The relationship between low-level inflow, high-level outflow, and the warm core structure produce a positive boundary contribution to the available potential energy budget. On a scale of 500 km, this boundary term is nearly as large as the generation term in some experiments. On a scale of 1000 km, however, the generation is an order of magnitude greater.

5. In the computational experiments, it is established that a 500-km domain and 20-km resolution are satisfactory for the latent heating functions studied. A variable grid is utilized in some experiments to economically gain higher resolution near the center. For a 40-percent gain in computational time, differences in maximum wind are less than 0.1 percent using the variable grid.

6. Isentropic coordinates may be used effectively in numerical models and are particularly effective in studying adiabatic and diabatic effects.

Although the results presented have shown that the size and intensity of the tropical cyclone is directly linked to thermal forcing, the question of what determines the heating profiles has not been investigated. Large-scale synoptic features such as sea and environment temperatures and horizontal and vertical shears are all important in determining the distribution of convection that leads to the development and maintenance of the tropical storm. Theoretical investigation of these properties will require more sophisticated numerical models to describe the delicate balance in the early stages of hurricane development.

#### ACKNOWLEDGMENTS

This work is part of a doctorate thesis from The University of Wisconsin. The author extends his sincere thanks to his advisor, Dr. Donald R. Johnson, for his continuing interest, helpful suggestions, and many profitable discussions throughout the course of this research.

The author also wishes to thank Dr. Stanley L. Rosenthal, National Hurricane Research Laboratory (NHRL), for his many helpful ideas at various stages of this research and Dr. R. Cecil Gentry, Director of NHRL, for the opportunity to work at NHRL and use its computing facilities.

Thanks are also due the author's reading committee, Profs. Werner Schwerdtfeger and John Young, for their helpful suggestions.

#### REFERENCES

- Anthes, Richard A., "A Diagnostic Model of the Tropical Cyclone in Isentropic Coordinates," *ESSA Technical Memorandum ERLTM-NHRL 89*, U.S. Department of Commerce, National Hurricane Research Laboratory, Miami, Fla., Apr. 1970a, 147 pp.
- Anthes, Richard A., "The Role of Large-Scale Asymmetries and Internal Mixing in Computing Meridional Circulations Associated With the Steady-State Hurricane," *Monthly Weather Review*, Vol. 98, No. 7, July 1970b, pp. 521-528.
- Anthes, Richard A., and Johnson, Donald R., "Generation of Available Potential Energy in Hurricane Hilda (1964)," *Monthly Weather Review*, Vol. 96, No. 5, May 1968, pp. 291-302.
- Barrientos, Celso S., "Computations of Transverse Circulation in a Steady State, Symmetric Hurricane," *Journal of Applied Meteorology*, Vol. 3, No. 6, Dec. 1964, pp. 685-692.
- Colón, José A., "On the Evolution of the Wind Field During the Life Cycle of Tropical Cyclones," *National Hurricane Research Project Report No. 65*, U.S. Department of Commerce, Weather Bureau, Miami, Fla., Nov. 1963, 36 pp.
- Dutton, John A., and Johnson, Donald R., "The Theory of Available Potential Energy and a Variational Approach to Atmospheric Energetics," *Advances in Geophysics*, Vol. 12, 1967, pp. 333-436.
- Eliassen, Arnt, and Raustein, Elmer, "A Numerical Integration Experiment With a Model Atmosphere Based on Isentropic Surfaces," *Meteorologiske Annaler*, Vol. 5, No. 2, Oslo, Norway, 1968, pp. 45-63.
- Estoque, Mariano A., and Fernandez-Partagas, José J., "Hurricane Studies: Part II," *Institute of Atmospheric Science Paper No. 2*, University of Miami, Coral Gables, Fla., Mar. 1968, pp. 28-65.
- Gray, William M., "The Mutual Variation of Wind, Shear, and Baroclinicity in the Cumulus Convective Atmosphere of the Hurricane," *Monthly Weather Review*, Vol. 95, No. 2, Feb. 1967, pp. 55-73.
- Hawkins, Harry F., "Vertical Wind Profiles in Hurricanes," *National Hurricane Research Project Report No. 55*, U.S. Department of Commerce, Weather Bureau, Miami, Fla., June 1962, 16 pp.
- Hawkins, Harry F., and Rubsam, Daryl T., "Hurricane Hilda, 1964: I. Genesis, as Revealed by Satellite Photographs, Conventional and Aircraft Data," *Monthly Weather Review*, Vol. 93, No. 7, July 1968, pp. 428-452.
- Hughes, Lawrence A., "On the Low-Level Wind Structure of Tropical Storms," *Journal of Meteorology*, Vol. 9, No. 6, Dec. 1952, pp. 422-428.
- Johnson, Donald R., "The Available Potential Energy of Storms," *Journal of the Atmospheric Sciences*, Vol. 27, No. 5, Aug. 1970, pp. 727-741.
- Johnson, Donald R., and Dutton, John A., "Atmospheric Energetics and the General Circulation Viewed From Isentropic Coordinates," paper presented at the Conference on the Global Circulation of the Atmosphere, London, England, Aug. 25-29, 1969.
- Jordan, Charles L., "Mean Soundings for the West Indies Area," *Journal of Meteorology*, Vol. 15, No. 1, Feb. 1958, pp. 91-97.
- Kasahara, Akira, "A Numerical Experiment on the Development of a Tropical Cyclone," *Journal of Meteorology*, Vol. 18, No. 3, June 1961, pp. 259-282.
- Krishnamurti, T. N., "On the Vertical Velocity Field in a Steady, Symmetric Hurricane," *Tellus*, Vol. 13, No. 2, Stockholm, Sweden, May 1961, pp. 171-180.
- Kuo, Hsiao-Lan, "On Formation and Intensification of Tropical Cyclones Through Latent Heat Release by Cumulus Convection," *Journal of the Atmospheric Sciences*, Vol. 22, No. 1, Jan. 1965, pp. 40-63.
- LaSeur, Noel E., and Hawkins, Harry F., "An Analysis of Hurricane Cleo (1958) Based on Data From Research Reconnaissance Aircraft," *Monthly Weather Review*, Vol. 91, Nos. 10-12, Oct.-Dec. 1963, pp. 694-709.
- Lorenz, Edward N., "Available Potential Energy and the Maintenance of the General Circulation," *Tellus*, Vol. 7, No. 2, Stockholm, Sweden, May 1955, pp. 157-167.
- Malkus, Joanne S., and Riehl, Herbert, "On the Dynamics and Energy Transformations in Steady-State Hurricanes," *Tellus*, Vol. 12, No. 1, Stockholm, Sweden, Feb. 1960, pp. 1-20.



- Margules, Max, "Über die Energie der Stürme" (On the Energy of Storms), *Jahrbuch Zentralamt für Meteorologie und Geodynamik*, Vol. 40, Austria, 1905, 26 pp.
- Matsuno, Taroh, "Numerical Integrations of the Primitive Equations by a Simulated Backward Difference Method," *Journal of the Meteorological Society of Japan*, Ser. 2, Vol. 44, No. 1, Tokyo, Feb. 1966, pp. 76-84.
- Miller, Banner I., "On the Maximum Intensity of Hurricanes," *Journal of Meteorology*, Vol. 15, No. 2, Apr. 1958, pp. 184-195.
- Miller, Banner I., "On the Momentum and Energy Balance of Hurricane Helene (1958)," *National Hurricane Research Project Report No. 53*, U.S. Department of Commerce, Weather Bureau, Miami, Fla., Apr. 1962, 19 pp.
- Miller, Banner I., "A Study of the Filling of Hurricane Donna (1960) Over Land," *Monthly Weather Review*, Vol. 92, No. 9, Sept. 1964, pp. 389-406.
- Ooyama, Katsuyuki, "Numerical Simulation of the Life-Cycle of Tropical Cyclones," *Journal of the Atmospheric Sciences*, Vol. 26, No. 1, Jan. 1969, pp. 3-40.
- Palmén, Erik H., "On the Formation and Structure of Tropical Hurricanes," *Geophysica*, Vol. 3, Helsinki, Finland, 1948, pp. 26-38.
- Palmén, Erik H., and Jordan, Charles L., "Note on the Release of Kinetic Energy in Tropical Cyclones," *Tellus*, Vol. 7, No. 2, Stockholm, Sweden, May 1955, pp. 186-188.
- Palmén, Erik H., and Riehl, Herbert, "Budget of Angular Momentum and Kinetic Energy in Tropical Cyclones," *Journal of Meteorology*, Vol. 14, No. 2, Apr. 1957, pp. 150-159.
- Riehl, Herbert, and Malkus, Joanne S., "Some Aspects of Hurricane Daisy, 1958," *Tellus*, Vol. 13, No. 2, Stockholm, Sweden, May 1961, pp. 181-213.
- Rosenthal, Stanley L., "Some Attempts to Simulate the Development of Tropical Cyclones by Numerical Methods," *Monthly Weather Review*, Vol. 92, No. 1, Jan. 1964, pp. 1-21.
- Rosenthal, Stanley L., "Numerical Experiments With a Multilevel Primitive Equation Model Designed to Simulate the Development of Tropical Cyclones. Experiment I," *ESSA Technical Memorandum ERLTM-NHRL 82*, U.S. Department of Commerce, National Hurricane Research Laboratory, Miami, Fla., Jan. 1969, 36 pp.
- Yamasaki, Masanori, "A Tropical Cyclone Model With Parameterized Vertical Partition of Released Latent Heat," *Journal of the Meteorological Society of Japan*, Vol. 46, No. 3, Tokyo, June 1968a, pp. 202-214.
- Yamasaki, Masanori, "Detailed Analysis of a Tropical Cyclone Simulated With a 13-Layer Model," *Papers in Meteorology and Geophysics*, Vol. 19, No. 4, Tokyo, Japan, Dec. 1968b, pp. 559-585.
- Yanai, Michio, "Formation of Tropical Cyclones," *Reviews of Geophysics*, Vol. 2, No. 2, May 1964, pp. 367-414.

[Received August 19, 1970; revised January 22, 1971]

April 1971

261

UDC 551.509.313:551.509.327:551.515.21

# ITERATIVE SOLUTIONS TO THE STEADY-STATE AXISYMMETRIC BOUNDARY-LAYER EQUATIONS UNDER AN INTENSE PRESSURE GRADIENT

RICHARD A. ANTHERS

National Hurricane Research Laboratory, Environmental Research Laboratories, NOAA, Miami, Fla.

## ABSTRACT

Steady-state solutions to the complete axisymmetric Navier-Stokes equations are obtained by an iterative technique for an intense pressure-gradient force representative of the tropical cyclone. Solutions for the horizontal and vertical components of motion are compared for various horizontal and vertical mixing coefficients, drag coefficients, and Coriolis parameters. A multilevel model is used, and the results are compared with those from a simple one-level model.

## 1. INTRODUCTION

Because of the intense frictional convergence in the boundary layer and the rapid decrease of mixing ratio with height, the major water vapor convergence in tropical cyclones occurs in the lowest few kilometers. Thus, the frictionally induced vertical motion at the top of the planetary boundary layer becomes a close measure of this convergence (Miller 1962, Riehl and Malkus 1961). Approximate expressions relating this vertical motion to the mean steady-state tangential wind have been given by several investigators (e.g., Syono 1951, Charney and Eliassen 1949, Ogura 1964, and Smith 1968). Kuo (1971) utilized an iterative procedure to obtain exact solutions to the equations of motion in the boundary layer of a maintained vortex without the Coriolis term.

In a theoretical study of the hurricane boundary layer, Rosenthal (1962) neglected lateral mixing and vertical advection and obtained analytic solutions to the linearized equations. Rosenthal found a decreasing depth of inflow toward the center, with the consequence that the vertical velocities near the center appeared too small. Miller (1965) utilized a quasi-time-dependent numerical model to obtain steady solutions under various formulations of horizontal and vertical mixing and found that an inflow layer of constant depth could be obtained if the vertical mixing coefficient were made proportional to the pressure gradient.

In this paper, steady-state solutions to the axisymmetric boundary-layer equations are obtained by a numerical technique similar to Miller's (1965), with particular applicability to the boundary layer in hurricanes. The results are compared with those obtained by Kuo (1971) from a different approach. The results obtained from the equations of motion in primitive form are useful in interpreting results from more complex hurricane models, as well as providing lower boundary conditions on the mass transport required in diagnostic models such as Barrientos (1964) or Anthes (1970b).

In the experiments discussed here, the complete equations of motion are solved numerically for the horizontal and vertical velocity components under a steady, intense pressure-gradient force to study the effects of the variations of horizontal and vertical mixing, drag coefficients, and Coriolis parameter on the vertical motion at the top of the boundary layer. A multilevel model is used, and the results are compared with those obtained with a simple one-level model. This is a relevant comparison in view of the use of low vertical resolution boundary layers in hurricane models.

## 2. A MULTILEVEL BOUNDARY LAYER MODEL

### A. BASIC EQUATIONS

When assuming axisymmetry and a pressure-gradient force invariant with height, the equations of motion for the tangential,  $v$ , and radial,  $u$ , winds are

$$\frac{\partial v}{\partial t} = -u \frac{\partial v}{\partial r} + r \left\{ -w \frac{\partial v}{\partial z} - fu + \frac{\partial \mu}{\partial z} + \frac{1}{r^2} \frac{\partial}{\partial r} \left[ Kr^3 \frac{\partial v}{\partial r} \right] \right\} \quad (1)$$

and

$$\frac{\partial u}{\partial t} = -u \frac{\partial u}{\partial r} - w \frac{\partial u}{\partial z} + fv + \frac{v^2}{r} - \frac{1}{\rho} \frac{\partial p}{\partial r} + \frac{\partial \mu}{\partial z} + \frac{1}{r^2} \frac{\partial}{\partial r} \left[ Kr^3 \frac{\partial u}{\partial r} \right] \quad (2)$$

where  $w$  is vertical velocity,  $r$  is radial distance,  $z$  is height,  $f$  is the Coriolis parameter,  $\rho$  is mean density ( $1.1 \times 10^{-3} \text{ gm} \cdot \text{cm}^{-3}$ ),  $p$  is pressure, and  $K$  and  $\mu$  are the horizontal and vertical coefficients of eddy viscosity, respectively. The continuity equation, neglecting density variations, is

$$\frac{\partial w}{\partial z} = -\frac{1}{r} \frac{\partial(ru)}{\partial r} \quad (3)$$

### B. STRUCTURE OF MODEL

The model consists of nine levels in the vertical defined by

$$z_i = 50 \text{ m} + (9-i)\Delta z \quad (\Delta z = 100 \text{ m}, i = 1, 2, \dots, 9)$$

and 51 increments in the radial direction defined by

$$r_j = (j-1)\Delta r \quad (\Delta r = 10 \text{ km}, j = 1, 2, \dots, 51).$$

The horizontal boundary conditions are zero divergence and relative vorticity at 500 km. These conditions have given reasonable solutions for multilevel hurricane models (Rosenthal 1970, Anthes 1970a) and should be representative of the hurricane environment at this distance from the center. The vertical boundary conditions consist of the tangential flow in gradient balance at the upper level with zero radial velocity. These conditions for the top of the Ekman layer are reasonable for the hurricane, which is in near-gradient balance at this level (Hawkins and Rubsam 1968). At the lowest level (50 m), the vertical velocity is assumed equal to zero. Boundary conditions on the vertical mixing term at the surface are

$$\mu \frac{\partial v}{\partial z} = C_D |\mathbf{V}| v \quad (4)$$

and

$$\mu \frac{\partial u}{\partial z} = C_D |\mathbf{V}| u$$

where  $C_D$  is the drag coefficient and  $\mathbf{V}$  is the vector velocity. The eq (4) are the well-known quadratic stress law.

The choice of the vertical and horizontal resolutions and the top level of 850 m was made after a series of preliminary experiments in which these computational aspects of the model were investigated. These results showed that increasing the horizontal and vertical resolutions beyond 10 km and 100 m, respectively, did not substantially alter the steady-state solutions. They also showed that, under the upper level boundary condition of gradient balance, increasing the top level beyond 850 m had little effect on the solutions.

### C. COMPUTATIONAL PROCEDURE AND INITIAL CONDITIONS

Several finite-difference analogs to eq (1) and (2) are solved iteratively under a steady pressure-gradient force. The horizontal grid is staggered so that  $v$  and  $u$  are predicted at integer multiples of  $\Delta r$  with  $w$  computed diagnostically at points midway between  $u$  points according to

$$\frac{w_{i-1,j} - w_{i,j}}{\Delta z} = -\frac{r_{j+1}(u_{i,j+1} + u_{i-1,j+1}) - r_j(u_{i,j} + u_{i-1,j})}{2r_{j+1}\Delta r}. \quad (5)$$

The initial conditions, or first guess, are the tangential wind in gradient balance with zero radial and vertical

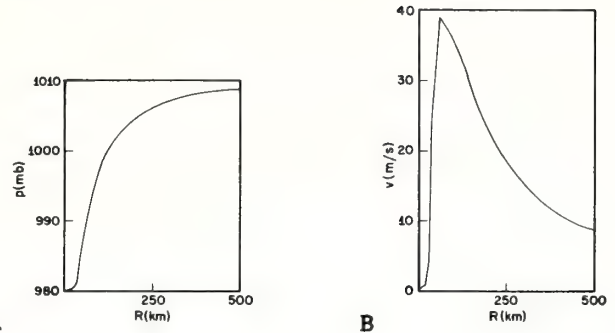


FIGURE 1.—(A) steady pressure profile and (B) the associated gradient wind at 20°N for the boundary-layer experiments.

velocity. The eq (1) and (2) are forecast<sup>1</sup> utilizing several finite-difference schemes (to be discussed later) until the difference between successive iterates becomes small (less than  $10^{-2} \text{ cm} \cdot \text{s}^{-1}$ ). This usually occurs after about 400 iteration steps. The gradient wind corresponding to the specified pressure-gradient force is shown in figure 1.

The first series of experiments are computed utilizing the Matsuno (1966) time-integration scheme which damps high-frequency waves. Centered differences are used to approximate the space differentials in eq (1) and (2). The time step,  $\Delta t$ , is 90 s.

## 3. RESULTS

### A. VARIATION OF HORIZONTAL AND VERTICAL EXCHANGE COEFFICIENTS

Values of  $K$  and  $\mu$  ranging over several orders of magnitude have been used by previous investigators for the hurricane problem (Anthes 1970a), and values that give realistic results (compared to observations) in a particular instance are functions of the type of model, the horizontal and vertical resolution, and finite-difference scheme utilized. Unfortunately, the results are strongly dependent on the poorly understood process of horizontal and vertical diffusion of momentum. The first set of experiments, therefore, considers various constant horizontal and vertical exchange coefficients.

Figure 2 shows the steady-state vertical motion cross-sections for  $\mu$  equal to 40 and three values of  $K$  ranging from 5 to 25 (units of  $\mu$  and  $K$  are  $10^4$  and  $10^8 \text{ cm}^2 \cdot \text{s}^{-1}$  throughout the paper). Although the vertical motion structures for the three values of  $K$  are quite similar beyond the radius of maximum wind ( $R_{\max} = 50 \text{ km}$ ), significant differences are present inside the 50-km radius. The maximum upward motion ranges from 70 cm/s for

<sup>1</sup> The term "forecast" is used here as in time-dependent forecast models in which the pressure field is free to interact with the momentum field. In these experiments, in which the pressure is steady, the transient solutions have little physical meaning, and the forecast steps are more properly called "iteration steps."



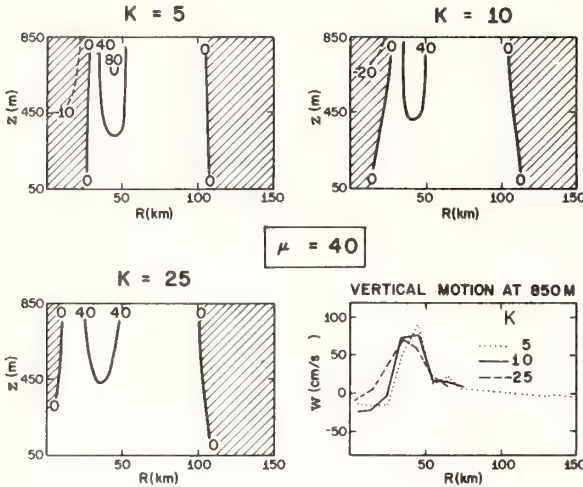


FIGURE 2.—Steady-state vertical motion for three horizontal mixing coefficients; units of  $K$ ,  $10^8 \text{ cm}^2 \cdot \text{s}^{-1}$ ; units of  $\mu$ ,  $10^4 \text{ cm}^2 \cdot \text{s}^{-1}$ ; units of vertical motion isolines,  $\text{cm/s}$ .

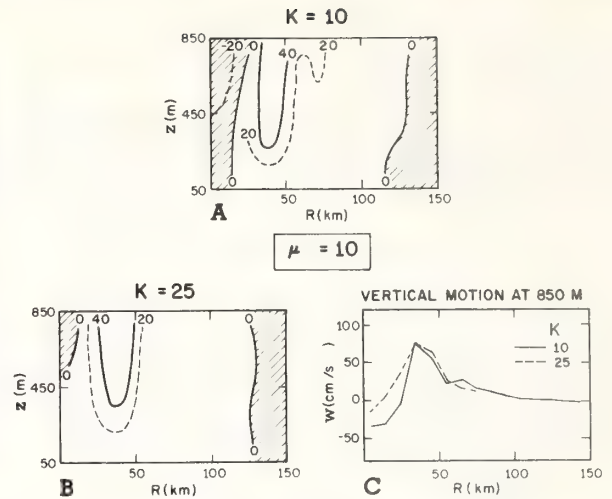


FIGURE 3.—Vertical motion for two horizontal mixing coefficients and a vertical mixing coefficient of  $10 \times 10^4 \text{ cm}^2 \cdot \text{s}^{-1}$ ; units of vertical motion isolines,  $\text{cm/s}$ .

$K=25$  to  $91 \text{ cm/s}$  for  $K=5$ . The subsidence near the center also shows strong dependence on horizontal mixing. For values of  $K < 25$ , this subsidence results from a mixing of tangential momentum into the "eye," causing an excess of centripetal over pressure-gradient force and an outward flow. For very large values of  $K$ , however, the tangential wind maximum is reduced, and the mixing of radial momentum is sufficient to allow inflow all the way to the center. The subsidence associated with the smaller values of  $K$  reaches all the way to the surface and appears somewhat too large. Observations inside hurricane eyes generally show some low-level clouds, indicating that subsidence probably does not extend to the surface. This consideration suggests that a value of  $K=25$  gives most realistic results for this model.

The values of  $K$  considered in the above experiments are higher than values used by previous investigators, a consequence perhaps of the differences in types of model, numerical scheme, and resolution noted above. If horizontal mixing is an important process in the vicinity of the radius of maximum wind, however, a simple scale analysis suggests values of this order of magnitude. For example, if the order of magnitude of the horizontal mixing term is equated to the magnitude of the centripetal term

$$K \frac{\Delta u}{\Delta r^2} \sim \frac{v^2}{r}$$

and

$v=30 \text{ m/s}$ ,  $r=50 \text{ km}$ ,  $\Delta r=10 \text{ km}$ , and  $\Delta u=10 \text{ m/s}$ ,

the magnitude of  $K$  is about  $20 \times 10^8 \text{ cm}^2 \cdot \text{s}^{-1}$ .

Figure 3 shows vertical motion cross-sections for  $\mu$  reduced from 40 to 10. The results show a more shallow layer of stronger radial velocities and more vertical shear. The subsidence inside  $R_{\max}$  is reduced as the stronger inflow reaches closer to the origin. The transition from upward to downward motion is shifted from 115 km to 135 km as  $\mu$  is reduced. The results also show more horizontal irregularities in vertical motion for small values of  $K$  (fig. 3C). These horizontal oscillations are apparently computational in nature and are related to nonlinear instability. Many experiments with a one-level model (Anthes 1970a) utilizing the same differencing scheme have shown these standing space oscillations of wavelength  $2\Delta r$ , which, for small values of  $K$ , may grow and prevent a steady-state solution. The computational nature of these oscillations is indicated by their strong dependence on time and space differencing and on horizontal resolution.

Figure 4 shows the boundary-layer structure for the tangential and radial winds for typical values of  $K$  and  $\mu$ . Figure 4A, when compared to figure 1B, shows a region of subgradient winds beyond the radius of maximum wind due to surface friction, and a region of supergradient winds near the radius of maximum wind due to the strong radial advection of angular momentum inward. The radial velocities show a maximum of over 20 m/s just above the surface. The radial and tangential components are thus the same order of magnitude in the lower levels. Rosenthal (1969) found inflow angles greater than  $45^\circ$  in a hurricane model. While this magnitude is larger than those generally observed, Rosenthal notes that aircraft observations are probably above the level of maximum inflow.

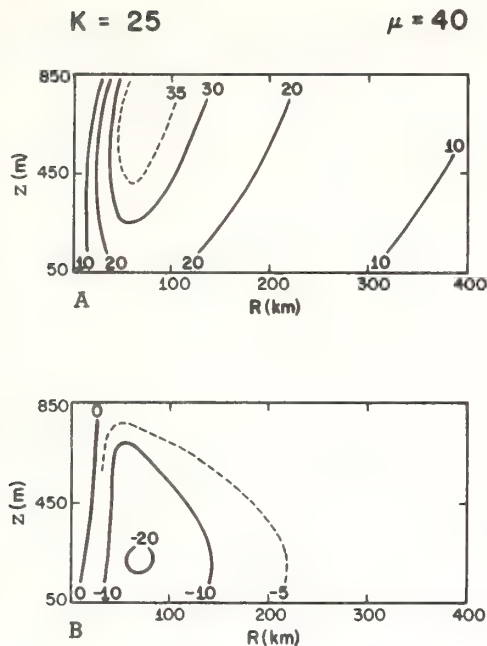


FIGURE 4.—Boundary-layer structures for (A) tangential and (B) radial wind components; units of  $K$ ,  $10^8 \text{ cm}^2 \text{ s}^{-1}$ ; units of  $\mu$ ,  $10^4 \text{ cm}^2 \text{ s}^{-1}$ ; units of velocity component isolines, m/s.

The trend for smaller vertical mixing toward stronger, more shallow inflow, weaker subsidence inside  $R_{max}$ , and larger transitional radius between upward and downward motion is investigated by a further reduction in  $\mu$  from 10 to 5. The results (not shown) confirm the above tendencies, as the inflow increases from 27.5 to 29.3 m/s, the subsidence inside  $R_{max}$  is reduced, and the transitional radius from upward to downward motion shifts outward from 135 to 145 km.

In summarizing the effects of horizontal and vertical mixing, the maximum upward motion near the radius of maximum wind and also the subsidence inside this radius increase with decreasing values of  $K$ . The results are less sensitive to variations in  $\mu$ , with higher values of  $\mu$  yielding less vertical shear, a deeper inflow layer, and slightly increased vertical motion.

#### B. VARIATION OF DRAG COEFFICIENT

Although empirical evidence suggests a linear increase of drag coefficient with wind speed (Miller 1964), many investigators have utilized a constant drag coefficient in hurricane studies (Yamasaki 1968, Rosenthal 1969, Anthes 1970a). Figure 5 shows vertical motion structures for constant values of  $C_D$  ranging from 0.001 to 0.003. The results beyond 50 km are insensitive to variations in  $C_D$ . Inside 50 km, the maximum upward motion increases,

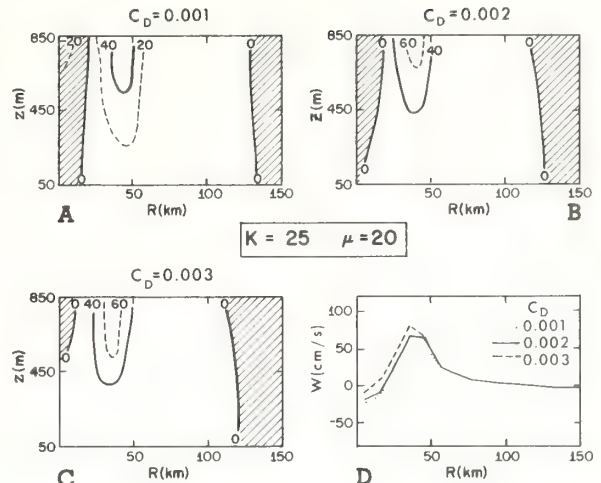


FIGURE 5.—Vertical motion for various drag coefficients; units of  $K$ ,  $10^8 \text{ cm}^2 \text{ s}^{-1}$ ; units of  $\mu$ ,  $10^4 \text{ cm}^2 \text{ s}^{-1}$ ; units of vertical motion isolines, cm/s.

and the subsidence decreases for increasing  $C_D$ , due to increased radial winds that penetrate closer to the axis. These results illustrate the paradox of the dual role of surface friction, with increased friction yielding more intense circulations for the range of drag coefficients considered.

#### C. VARIATION OF CORIOLIS PARAMETER

In this subsection, the Coriolis parameter is varied from  $12.6 \times 10^{-5} \text{ s}^{-1}$  (corresponding to  $60^\circ \text{N}$ ) to zero. For the constant pressure-gradient force, therefore, the gradient wind maximum varies from 36.9 m/s at 60 km (for  $60^\circ \text{N}$ ) to 40.5 m/s at 65 km ( $f=0$ ). The horizontal and vertical exchange coefficients are 25 and 5, respectively.

Figure 6 shows the vertical motion profiles for various values of  $f$ . As  $f$  decreases, the vertical motion maximum increases, the region of subsidence inside  $R_{max}$  disappears, and the area of rising motion expands outward. For the smaller values of  $f$ , the conversion of radial to tangential momentum decreases, and the inflow penetrates closer to the origin. For  $f=0$ , in fact, the tangential equation of motion becomes linearly uncoupled with the radial equation of motion, and no conversion from radial to tangential motion is possible. However, the radial equation is still strongly coupled to the tangential equation through the centripetal acceleration  $v^2/r$ . This strong coupling in one direction and weak coupling in the other makes the convergence to a steady state slower when  $f$  is small. Convergence is especially slow inside  $R_{max}$ , where the nonlinear coupling through vertical and horizontal advection is small and  $v^2/r$  is very large. In fact, the solutions do not converge to a steady state at all in this region when other

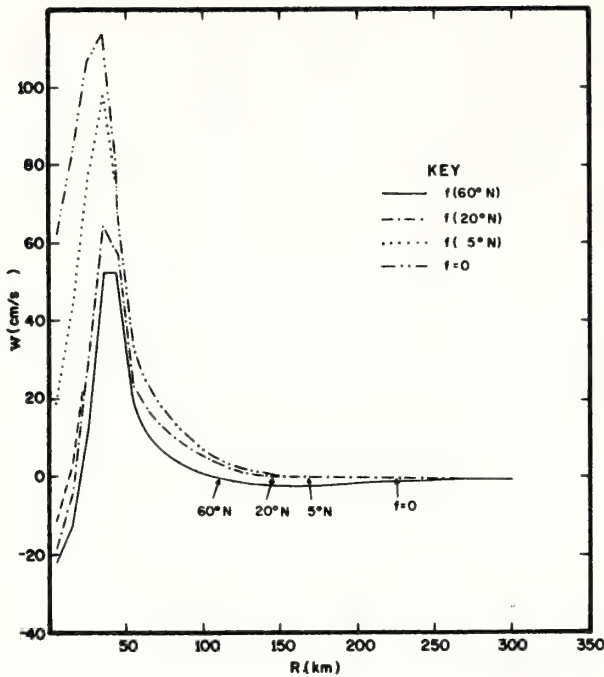


FIGURE 6.—Vertical motion at the top of the boundary layer for various latitudes.

integration schemes that do not damp the high frequencies are used (see appendix).

Further computational difficulties involving the non-linear vertical mixing term and the upper boundary condition of gradient balance appear for very small  $f$ . For certain values of  $\mu$ , vertical oscillations in  $u$  and  $v$  appear near the top of the boundary layer inside  $R_{max}$ . While the upper boundary condition of gradient balance appears realistic beyond  $R_{max}$  where horizontal mixing is unimportant, this condition yields unreasonable vertical shear inside  $R_{max}$  where horizontal mixing produces large cyclonic winds below the upper boundary. In the presence of the linear Coriolis coupling between the tangential and radial equations of motion, a balance is established in spite of this large shear. Without the Coriolis force, however, vertical oscillations develop near the upper boundary.

The experiment with  $f=0$  corresponds to the case treated by Kuo (1971); although in Kuo's work, the vertical and horizontal exchange coefficients are equal. Because of this fact and the different nature of the approaches, quantitative comparisons are difficult. Qualitatively, the results are in fairly good agreement, depending on which value of the parameter  $K$  in Kuo's paper is considered. Both results show weak descending motion in the outer region with strong rising motion with a sharp

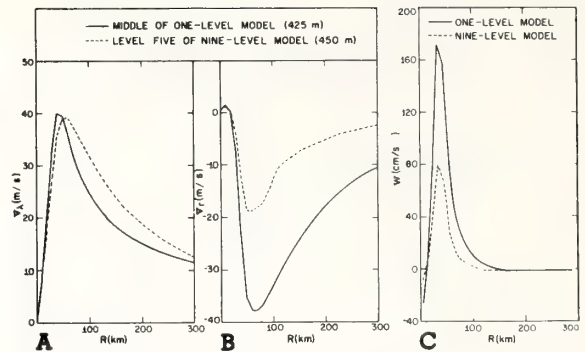


FIGURE 7.—Tangential and radial wind profiles in the middle of the nine-level and one-level models and the vertical motion profiles at the top of the nine-level and one-level models;  $V_\theta$  is tangential velocity.

maximum in the vicinity of  $R_{max}$ . The vertical oscillations of the  $v$  and  $u$  profiles inside  $R_{max}$ , which were found by Kuo for small values of  $K$ , are not observed in this experiment, due possibly to the large values of vertical and horizontal mixing coefficients.

#### D. COMPARISON OF NINE-LEVEL MODEL RESULTS WITH ONE-LEVEL MODEL RESULTS

Since hurricane models (Ooyama 1969, Yamasaki 1968, Rosenthal 1970) contain one-level boundary layers, it is interesting to compare the results from the multilevel boundary-layer model with results from a simple one-layer model used by Anthes (1970a) in a similar series of experiments. In this model,  $u$  and  $v$  are calculated at the center of a boundary layer of constant depth, a linear variation of stress with height is assumed, and vertical advection is neglected.

Figure 7 compares the tangential and radial wind profiles at the center of the multilevel and one-level models and the corresponding vertical motion profiles at the top of the boundary layer. In both models,  $K=25$ ; and in the multilevel model,  $\mu=20$ . It is evident from figure 7 that the effect of surface friction is overestimated by the one-level model. The tangential winds are less in the one-level model, and the radial velocities and vertical motion are larger by a factor of 2. This overestimation of the radial winds is probably a result of the assumption of linear stress over the boundary layer of constant depth. In the multilevel model, the stress varies strongly near the surface and less strongly throughout the upper part of the boundary layer.

#### E. BALANCE OF FORCES IN THE STEADY STATE

An estimate of the balance of forces in various regions of the domain may be made by comparing the various terms in eq (1) and (2) in the steady state. Table 1 shows



TABLE 1.—Ratio of terms in the radial equation of motion to the pressure-gradient force in the steady state;  $K=25 \times 10^8 \text{ cm}^2 \cdot \text{s}^{-1}$ ;  $\mu=20 \times 10^4$ ; and  $\epsilon < 0.1$ .

R	$\frac{1}{\rho} \frac{\partial p}{\partial r}$	Ratio of term to pressure-gradient force					
		$u \frac{\partial u}{\partial r}$	$w \frac{\partial u}{\partial z}$	$fv$	$v^2/r$	Vertical mixing	Horizontal mixing
(km)	(cm s <sup>-2</sup> )						
					$z=750 \text{ m}$		
10	0.0014	-17.6	-6.5	21.7	263.0	-193.0	-66.9
20	.0066	-0.5	44.2	11.6	176.0	-106.0	-124.0
30	.0733	1.0	-1.9	1.9	36.3	-11.4	-24.9
40	1.56	-.18	-1.7	.12	2.2	0.33	0.23
50	3.16	$\epsilon$	-.88	$\epsilon$	1.01	.41	.45
100	1.50	$\epsilon$	$\epsilon$	.12	.83	$\epsilon$	$\epsilon$
200	.37	$\epsilon$	$\epsilon$	.30	.65	$\epsilon$	$\epsilon$
400	.081	$\epsilon$	$\epsilon$	.63	.33	$\epsilon$	$\epsilon$
					$z=150 \text{ m}$		
10	0.0014	-10.5	-9.5	26.9	404.0	41.8	-452.0
20	.0066	-21.8	-6.0	11.4	169.0	21.8	-174.0
30	.0733	-9.4	-.5	1.5	21.1	3.9	-15.6
40	1.56	-0.9	$\epsilon$	$\epsilon$	1.1	.3	0.3
50	3.16	-.3	$\epsilon$	$\epsilon$	.5	.2	.5
100	1.50	.2	$\epsilon$	$\epsilon$	.3	.3	$\epsilon$
200	.37	.1	$\epsilon$	.2	.3	.4	$\epsilon$
400	.081	$\epsilon$	$\epsilon$	.5	.2	.4	$\epsilon$

the ratio of the terms in eq (2) to the pressure-gradient force for a typical experiment. From table 1, it is clear that no term, with the possible exception of the vertical advection term, may be neglected over the entire domain. Very close to the center, the centripetal acceleration nearly balances the horizontal and vertical mixing. The importance of horizontal mixing falls off rapidly with increasing distance and is relatively unimportant beyond 100 km. Vertical advection is important only near  $R_{max}$ . The relative importance of the Coriolis force increases with increasing distance. Horizontal advection and surface drag are important at all distances. The boundary layer, then, consists of an inner region where horizontal mixing and centripetal acceleration are dominant, an intermediate region in the vicinity of  $R_{max}$  where all terms are significant, and an outer region where vertical advection and horizontal mixing are unimportant.

#### 4. SUMMARY

The quantitative results from this series of experiments investigating the boundary-layer structure under a steady, intense pressure gradient are difficult to summarize, mainly because the numerical values are strongly dependent on the parameters  $K$ ,  $\mu$ ,  $f$ , and  $C_D$  as well as on vertical resolution and upper and lateral boundary conditions. The qualitative results are therefore summarized briefly in table 2. Thus, subsidence inside  $R_{max}$  is favored by small values of  $K$  and large values of  $f$ ; the vertical motion maximum increases as drag friction and vertical mixing increase, and the area of rising motion increases for small  $\mu$  and small  $f$ .

The results from the multilevel model are compared with the results from a one-level model. Although the conclu-

TABLE 2.—Qualitative effect of varying parameters on significant features of the vertical motion structure in the boundary layer

Parameter	Feature		
	Subsidence inside $R_{max}$	Vertical motion maximum	Transitional radius from upward to downward motion
$K$	Decreases	Decreases	-----
$\mu$	-----	Increases	Decreases
$C_D$	Decreases	Increases	-----
$f$	Increases	Decreases	Decreases

Increases in the above parameters are accompanied by the given effect on the features of the vertical motion structures; the dashed lines indicate no appreciable effect.

sions based on experiments using the one-level model (Anthes 1970a) are not changed, the one-level model appears to overestimate the radial and vertical motions in comparison to the multilevel results, due primarily to the assumption of a linear stress boundary layer of constant depth.

Most experiments are carried out with the Matsuno (1966) scheme that damps high frequencies. Comparative experiments with other schemes show similar results when the Coriolis term is large. However, for small values of  $f$ , the schemes without the high-frequency damping do not converge to a steady state.

## APPENDIX

### RESULTS FROM TWO ADDITIONAL FINITE-DIFFERENCE SCHEMES

For assessing some of the computational effects on the solutions, two additional finite-difference schemes are tested for the model. The two-step Lax-Wendroff (1960) time-integration scheme has second-order accuracy but contains some damping, especially for short wavelengths (Richtmyer 1963). One cycle of this scheme, which is twice as fast as the Matsuno scheme, is summarized for  $\partial\alpha/\partial t = F(\alpha)$ :

1. Given  $\alpha_{i,j}^n$ .
2. Compute the first step from

$$\alpha_{i,j}^{n+1} = \frac{1}{4} (\alpha_{i-1,j} + \alpha_{i+1,j} + \alpha_{i,j+1}^n + \alpha_{i,j-1}^n) + \Delta t F(\alpha^n).$$

3. Compute the final step from

$$\alpha_{i,j}^{n+2} = \alpha_{i,j}^n + 2\Delta t F(\alpha_{i,j}^{n+1}).$$

The space derivatives in eq (1) and (2) are evaluated with centered differences.

The other scheme tested is the popular forward-time upstream space-differencing scheme, which is also twice as fast as the Matsuno scheme. This scheme has only first-order accuracy and contains strong damping of short wavelengths, but nevertheless has given excellent results in hurricane modeling experiments (Rosenthal 1970).

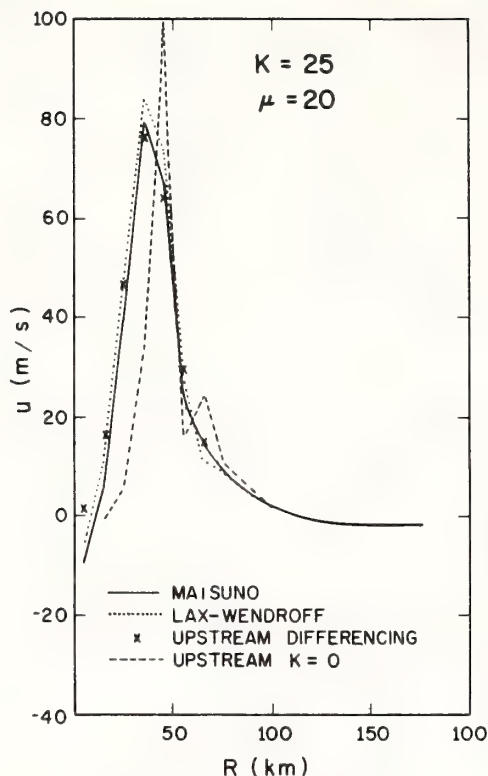


FIGURE 8.—Comparison of three integration schemes used to compute steady-state vertical velocity profiles at the top of the boundary layer for  $K=25 \times 10^8 \text{ cm}^2 \cdot \text{s}^{-1}$  and  $\mu=20 \times 10^4 \text{ cm}^2 \cdot \text{s}^{-1}$ . Also shown is the vertical velocity profile computed from forward-time upstream space-differencing with no explicit mixing ( $K=0$ ).

The steady-state solutions to the boundary-layer equations are computed for values of  $K=25$  and  $\mu=20$  for all three schemes. Figure 8 shows the vertical velocity profiles at the top of the boundary layer for the three experiments. The results are very nearly the same, indicating that the explicit damping is dominating the different damping properties of the three schemes. The only significant difference is the absence of subsidence near the origin in the upstream-differencing experiment. The large space truncation present in the upstream-differencing technique provides a pseudodiffusive effect (Molenkamp 1968, Rosenthal 1970, Orville and Sloan 1970) that allows steady-state solutions even with no explicit horizontal diffusion. With either the Matsuno or Lax-Wendroff schemes, however, steady-state solutions are not obtained for  $K=0$ . Figure 8 shows the vertical velocity profile for upstream differencing with  $K=0$ . The artificial damping yields reasonable solutions beyond the radius of maximum wind. However, this pseudodiffusion does not simulate the effect of horizontal mixing by eddy coefficients inside the

radius of maximum wind, as shown by the absence of subsidence. The pseudodiffusion depends on truncation in the advection terms. Inside the radius of maximum wind, the radial advection is small, so there is little implicit mixing, even though the curvatures of the tangential and radial wind profiles are large. The subsidence, which depends on mixing of cyclonic momentum inward from the radius of maximum wind, is not present in the upstream-differencing experiments with no explicit mixing. This difference is also present in experiments with a one-level boundary layer model (Anthes 1970a).

Although steady-state solutions that are not too different from each other are obtained from the three integration schemes tested for a value of the Coriolis parameter equal to  $5 \times 10^{-5} \text{ s}^{-1}$  ( $20^\circ \text{N}$ ), steady-state solutions for smaller values of  $f$  are not obtained from either the Lax-Wendroff or the forward-time integrations. For small values of  $f$  (see subsection C of section 2), the high-frequency damping in the Matsuno scheme is necessary for convergence to a steady state.

#### ACKNOWLEDGMENTS

The author expresses his appreciation to Drs. Banner I. Miller and Stanley L. Rosenthal for their helpful comments concerning this research and to Prof. H. L. Kuo for his careful review of the manuscript.

#### REFERENCES

- Anthes, Richard Allen, "A Diagnostic Model of the Tropical Cyclone in Isentropic Coordinates," *ESSA Technical Memorandum ERLTM-NHRL 89*, U.S. Department of Commerce, National Hurricane Research Laboratory, Miami, Fla., Apr. 1970a, 147 pp.
- Anthes, Richard Allen, "The Role of Large-Scale Asymmetries and Internal Mixing in Computing Meridional Circulations Associated With the Steady-State Hurricane," *Monthly Weather Review*, Vol. 98, No. 7, July 1970b, pp. 521-528.
- Barrientos, Celso S., "Computations of Transverse Circulation in a Steady State, Symmetric Hurricane," *Journal of Applied Meteorology*, Vol. 3, No. 6, Dec. 1964, pp. 685-692.
- Charney, Jule G., and Eliassen, Arnt, "A Numerical Method for Predicting the Perturbations in the Middle-Latitude Westerlies," *Tellus*, Vol. 1, No. 2, Stockholm, Sweden, May 1949, pp. 38-54.
- Hawkins, Harry F., and Rubsam, Daryl T., "Hurricane Hilda, 1964: II. Structure and Budgets of the Hurricane on October 1, 1964," *Monthly Weather Review*, Vol. 96, No. 9, Sept. 1968, pp. 617-636.
- Kuo, H. L., "Axisymmetric Flows in the Boundary Layer of a Maintained Vortex," *Journal of the Atmospheric Sciences*, Vol. 28, No. 1, Jan. 1971, pp. 20-41.
- Lax, Peter D., and Wendroff, Burton, "Systems of Conservation Laws," *Communications on Pure and Applied Mathematics*, Vol. 13, Interscience Publications, Inc., New York, N.Y., 1960, pp. 217-237 (see p. 217).
- Matsuno, Taroh, "Numerical Integrations of the Primitive Equations by a Simulated Backward Difference Method," *Journal of the Meteorological Society of Japan*, Ser. 2, Vol. 44, No. 1, Tokyo, Feb. 1966, pp. 76-84.
- Miller, Banner I., "On the Momentum and Energy Balance of Hurricane Helene (1958)," *National Hurricane Research Project Report No. 53*, U.S. Department of Commerce, Weather Bureau, Miami, Fla., Apr. 1962, 19 pp.

- Miller, Banner I., "A Study of the Filling of Hurricane Donna (1960) Over Land," *Monthly Weather Review*, Vol. 92, No. 9, Sept. 1964, pp. 389-406.
- Miller, Banner I., "A Simple Model of the Hurricane Inflow Layer," *Weather Bureau Technical Note 18—NHRL 75*, U.S. Department of Commerce, National Hurricane Research Laboratory, Miami, Fla., Nov. 1965, 16 pp.
- Molenkamp, Charles R., "Accuracy of Finite Difference Methods Applied to the Advection Equation," *Journal of Applied Meteorology*, Vol. 17, No. 2, Apr. 1968, pp. 160-167.
- Ogura, Yoshimitsu, "Frictionally Controlled, Thermally Driven Circulations in a Circular Vortex With Application to Tropical Cyclones," *Journal of the Atmospheric Sciences*, Vol. 21, No. 6, Nov. 1964, pp. 610-621.
- Ooyama, Katsuyuki, "Numerical Simulation of the Life-Cycle of Tropical Cyclones," *Journal of the Atmospheric Sciences*, Vol. 26, No. 1, Jan. 1969, pp. 3-40.
- Orville, H. D., and Sloan, L. J., "Effects of Higher Order Advection Techniques on a Numerical Cloud Model," *Monthly Weather Review*, Vol. 98, No. 1, Jan. 1970, pp. 7-13.
- Richtmyer, Robert D., "A Survey of Difference Methods for Non-Steady Fluid Dynamics," *NCAR Technical Notes 63-2*, National Center for Atmospheric Research, Boulder, Colo., 1963, 25 pp.
- Riehl, Herbert, and Malkus, Joanne S., "Some Aspects of Hurricane Daisy, 1958," *Tellus*, Vol. 13, No. 2, Stockholm, Sweden, May 1961, pp. 181-213.
- Rosenthal, Stanley L., "A Theoretical Analysis of the Field of Motion in the Hurricane Boundary Layer," *National Hurricane Research Project Report No. 56*, U.S. Department of Commerce, Weather Bureau, Miami, Fla., June 1962, 12 pp.
- Rosenthal, Stanley L., "Numerical Experiments With a Multilevel Primitive Equation Model Designed to Simulate the Development of Tropical Cyclones: Experiment I," *ESSA Technical Memorandum ERLTM-NHRL 82*, U.S. Department of Commerce, National Hurricane Research Laboratory, Miami, Fla., Jan. 1969, 36 pp.
- Rosenthal, Stanley L., "Experiments With a Numerical Model of Tropical Cyclone Development—Some Effects of Radial Resolution," *Monthly Weather Review*, Vol. 98, No. 2, Feb. 1970, pp. 106-120.
- Smith, R. K., "The Surface Boundary Layer of a Hurricane," *Tellus*, Vol. 20, No. 3, Stockholm, Sweden, 1968, pp. 473-484.
- Syoño, Sigekata, "On the Structure of Atmospheric Vortices," *Journal of Meteorology*, Vol. 8, No. 2, Apr. 1951, pp. 103-110.
- Yamasaki, Masanori, "Numerical Simulation of Tropical Cyclone Development With the Use of Primitive Equations," *Journal of the Meteorological Society of Japan*, Vol. 46, No. 3, Tokyo, June 1968, pp. 178-201.

[Received June 3, 1970; revised November 2, 1970]



## NUMERICAL EXPERIMENTS WITH A SLOWLY VARYING MODEL OF THE TROPICAL CYCLONE

RICHARD A. ANTHES

National Hurricane Research Laboratory, Environmental Research Laboratories, NOAA, Miami, Fla.

### ABSTRACT

Additional experiments with the slowly varying axisymmetric hurricane model described by Anthes are presented. Variable horizontal eddy viscosity coefficients are utilized to study circulations that result from an increased heating function and a heating function with a double maximum along the radial direction. Infrared radiative cooling is modeled for the clear tropical atmosphere following Sasamori. A representative cooling rate is used to study the effect of cooling in the hurricane environment on the dynamics and energetics of the slowly varying tropical cyclone.

### 1. INTRODUCTION

Preliminary results from a steady-state axisymmetric tropical cyclone model in isentropic coordinates have been presented in detail in paper I, a companion paper (Anthes 1971). These experiments showed that slowly varying states of the mass and momentum fields which were representative of tropical cyclones could be obtained as a direct result of steady thermal forcing. The experiments in paper I established values for horizontal and vertical momentum exchange coefficients, horizontal resolution, and domain size that yield realistic results for this model. The energetics of the slowly varying states were emphasized.

This paper (II) briefly summarizes the results of later experiments investigating additional heating distributions and a variable horizontal eddy viscosity coefficient. In particular, the latent heating function is increased to generate a more intense hurricane. A horizontal heating distribution with a double maximum is studied to simulate the effect of rainbands. Finally, cooling in the hurricane environment due to longwave radiation is modeled following Sasamori (1968); and the effect of cooling on the dynamics and energetics of the slowly varying hurricane is investigated.

### 2. SUMMARY OF THE MODEL

The numerical aspects of the steady-state model are summarized in this section for convenience. The model is axisymmetric and consists of six isentropic levels and the sea-level surface. Given arbitrary initial conditions, the mass and momentum fields are "forecast" for a steady heating function utilizing the Matsuno (1966) time integration scheme and centered space differences. The steady heating function is prescribed by assuming a horizontal profile of rainfall rates and distributing the equivalent latent heat vertically. Surface stress is parameterized using a constant drag coefficient of 0.003. Diffusion of momentum and heat is parameterized by constant horizontal exchange coefficients and a vertical eddy viscosity coefficient that decreases linearly upward. The forecast iterations continue until the mass and momentum fields reach a slowly varying state.

### 3. VARIABLE HORIZONTAL MIXING COEFFICIENTS

Although constant horizontal exchange coefficients for momentum and temperature were used in the previous experiments, the physical basis for the form and value of exchange coefficients is quite uncertain. Other numerical models contain a variable amount of horizontal diffusion, either through the use of exchange coefficients that are functions of the circulation or through horizontal truncation error which also yields a variable diffusion (pseudo-viscosity). The eddy viscosity coefficients of Smagorinsky et al. (1965) and Leith (1969) which are proportional to the local deformation of the velocity field and gradient of vorticity, respectively, belong to the first category. Orville's (1968) cloud model and Rosenthal's (1970) hurricane model which employ upstream differencing in the advection terms are examples belonging to the second category. Comparison of the relative merits of the various parameterizations is difficult and seems mainly to be a subjective judgment on which gives best results for the particular model.

Symbols used frequently in this work are:

$c_p$	specific heat at constant pressure,
$g$	acceleration of gravity,
$K_H$	horizontal coefficient of eddy viscosity,
$p$	pressure,
$q$	water vapor mixing ratio,
$r$	radial distance,
$\Delta r$	horizontal grid increment,
$R(u, T)$	absorptivity,
$T$	absolute temperature,
$u$	path length,
$z$	height,
$\Delta z$	vertical grid increment,
$\theta$	potential temperature,
$\rho$	air density, and
$\sigma$	Stefan-Boltzmann constant = $8.13 \times 10^{-11} \text{ cal} \cdot \text{cm}^{-2} \cdot \text{cm}^\circ \text{K}^{-4} \cdot \text{min}^{-1}$ .

For comparing the effects of variable and constant horizontal diffusion coefficients in this model, the experiments in sections 3 and 4 are computed following

Smagorinsky et al. (1965) in which the exchange coefficient for momentum is proportional to the local deformation. For cylindrical coordinates and circular symmetry, the expression for  $K_H$  is

$$K_H = k_0^2 \Delta r^2 |D| \quad (1)$$

where the deformation,  $D$ , is

$$|D| = r \left\{ \left[ \frac{\partial}{\partial r} \left( \frac{v_r}{r} \right) \right]^2 + \left[ \frac{\partial}{\partial r} \left( \frac{v_\theta}{r} \right) \right]^2 \right\}^{1/2} \quad (2)$$

The nondimensional parameter,  $k_0$ , is the Kármán constant. Smagorinsky et al. (1965) found that a value of  $k_0$  equal to 0.4 gave the best results in a general circulation model. In some trial experiments with the hurricane model, this value gave somewhat overdamped solutions; therefore, a value of 0.28 was selected for the following experiments.

The experiments in sections 3 and 4 utilize a domain size of 500 km and a variable grid with 10-km resolution from the origin to 200 km decreasing gradually to 25 km at the edge of the domain. This grid was shown to be an accurate substitution for a high-resolution constant grid in paper I. The time step is 15 s, and all results correspond to 3,200 iteration steps.

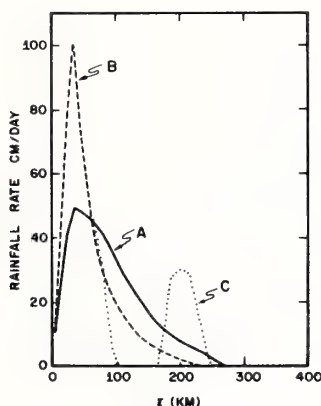


FIGURE 1.—Radial profiles of rainfall rates used to specify horizontal variations of the latent heating function.

#### A. UPPER LEVEL PRESSURE SURFACE OF 140 MILLIBARS, EXPERIMENT 1

For establishing continuity with previous experiments, experiment 1 utilizes the same heating function used in most of the experiments in paper I (see also rainfall type A in fig. 1 of paper II). The slowly varying momentum profiles for experiment 1 are shown in figure 2. The results using the variable coefficients are most similar to those with a constant coefficient,  $K_H$ , of  $2.5 \times 10^8$  cm<sup>2</sup>/s. The variable coefficient yields less mixing, however, as shown by an increase in maximum tangential wind from 41 in experiment 14 of paper I to 48 m/s. The energy budget, summarized in table 1, also shows a decrease in horizontal dissipation of kinetic energy. For the variable coefficient, the ratio of lateral dissipation to total dissipation is about 1/20; whereas for a constant coefficient of  $2.5 \times 10^8$  cm<sup>2</sup>/s, the ratio is about 3/20.

#### B. UPPER LEVEL PRESSURE SURFACE OF 110 MILLIBARS, EXPERIMENT 2

The experiments in which moderate storms are generated by a heating function maximum of 50 cm of rain per day have utilized the upper boundary condition of pressure equal to 140 mb. For intense storms, however, the undisturbed level occurs at a lower pressure (Koteswaram 1967). Therefore, in preparation for an increased heating

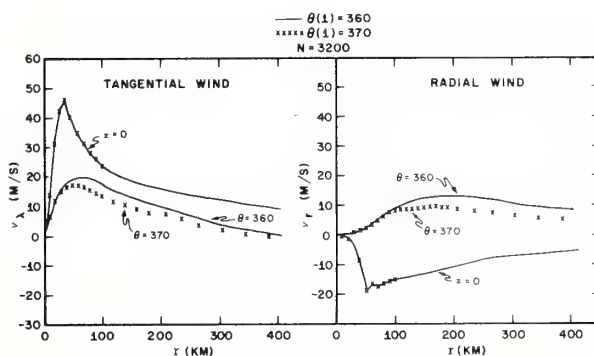


FIGURE 2.—Tangential and radial wind profiles for experiments 1 and 2.

TABLE 1.—Summary of experiments

Exp. no.	Rainfall type	$k_0$	Central pressure	Max. wind speed	Total heating	G(A)	B(A)	C(A)	Drag dissipation	Lateral mixing	Vertical mixing
			(mb)	(m/s)	( $10^{14}$ W)	( $10^{12}$ W)	( $10^{12}$ W)	( $10^{12}$ W)	( $10^{12}$ W)	( $10^{12}$ W)	( $10^{12}$ W)
1	A	0.28	970.1	52	11.2	8.0	4.2	14.8	—9.0	—1.0	—11.6
2	A	0.28	970.8	51	11.8	6.5	2.6	10.8	—8.9	—1.0	—9.6
3	A	0	963.8	61	11.8	5.9	2.5	10.2	—9.3	0	—9.6
4	B	0.28	962.6	55	8.7	6.7	1.1	9.7	—8.7	—1.7	—7.9
5	C	0.28	974.6	48	11.2	3.9	2.0	7.4	—7.8	—1.0	—7.0
6	A	$K_H = 5 \times 10^8$ cm <sup>2</sup> /s (constant)	984.9	38	7.6	14.6	2.4	19.0	—9.4	—5.9	—13.0

G(A) generation of available energy

B(A) boundary available energy

C(A) conversion of available energy to kinetic energy

TABLE 2.—Old and new isentropic levels and approximate mean pressures (Jordan 1958)

Level	Old		New	
	$\theta$ ( $^{\circ}\text{K}$ )	$p$ (mb)	$\theta$ ( $^{\circ}\text{K}$ )	$p$ (mb)
1	360	140	370	110
2	350	190	360	150
3	340	300	350	190
4	330	440	335	370
5	320	580	320	580
6	310	760	310	760

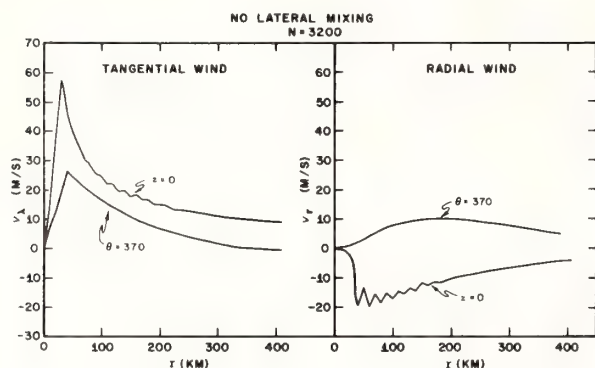


FIGURE 3.—Tangential and radial wind profiles for experiment 3.

function, experiment 1 is repeated with an upper boundary of 110 mb. The information levels are redefined so that the number (6) of isentropic levels remains the same (table 2).

The slowly varying solutions for experiment 2 with the higher upper surface are quite similar to those in experiment 1 (fig. 2). Although the low-level profiles are virtually identical, the upper levels show somewhat weaker outflow in experiment 2. This difference is probably related to the deeper outflow layer in experiment 2.

#### C. NO LATERAL DIFFUSION OF MOMENTUM, EXPERIMENT 3

All experiments with the steady-state hurricane model have contained some form of horizontal momentum diffusion. It is interesting, however, to run one experiment with no horizontal diffusion whatsoever, ( $K_H=0$ ). Because of the nonlinear terms in the equations of motion, difficulty may be expected from the accumulation of energy in the short wavelengths that may lead to nonlinear instability (Phillips 1959).

Figure 3 shows the momentum profiles for experiment 3 that contains no horizontal diffusion of momentum. In contrast to the smooth profiles of previous experiments, standing space oscillations of wavelength  $2\Delta r$  appear in the low-level profiles where horizontal advection is greatest. These oscillations do not amplify with time, but they remain as part of the slowly varying solutions

to the finite-difference equations. The nonamplification is apparently related to the steady heating function, the vertical mixing, and the high (time) frequency damping property of the Matsuno integration scheme. The increase in maximum wind speed from 51 to 61 m/s illustrates the sensitivity of the maximum wind to horizontal mixing.

Experiments 1, 2, and 3 have been discussed very briefly to establish continuity with the experiments in paper I. The experiments in section 4 utilize the variable horizontal mixing formulation defined by  $k_0=0.28$  and the upper boundary condition of  $p=110$  mb.

#### 4. HORIZONTAL VARIATION OF LATENT HEATING

The experiments in paper I considered latent heating functions defined by a single maximum in the rainfall rate profile of 50 cm/day. The strongest maximum wind speed produced by this heating function was only 44 m/s, typical of a weak hurricane. However, empirical (Riehl and Malkus 1961) and numerical (Rosenthal 1970) results indicate that rainfall rates near the center of the hurricane may be substantially greater than 50 cm/day. The first experiment in this section is computed with a rainfall maximum of 100 cm/day in an attempt to generate a stronger vortex. The second experiment considers a heating function with a secondary maximum about 200 km from the storm center, an attempt to investigate the cumulative effect of rainbands on the hurricane circulation.

##### A. RAINFALL MAXIMUM OF 100 CENTIMETERS PER DAY, EXPERIMENT 4

The experiments in paper I showed that, for given horizontal and vertical exchange coefficients, the maximum winds are determined primarily by the heat release within 100 km. The circulations generated by the heating functions associated with the 50 cm/day rainfall maximum correspond to a weak hurricane; however, the total heating is somewhat higher than empirical evidence. In experiment 4, therefore, the heating maximum at 45 km in experiment 2 is doubled while the heating beyond 100 km is substantially reduced (rainfall type B in fig. 1). The total heating is reduced from  $11.8$  to  $8.7 \times 10^{14}$  W. All other parameters are identical to those in experiment 2.

The momentum profiles (fig. 4) show an increase in maximum wind speed from 51 to 55 m/s, despite the reduction in total heating. The central pressure drops from 970.8 to 962.6 mb. The circulation at larger radii is slightly less, as indicated by the small reduction in outflow at 400 km and in the various components of the energy budget (table 1). The features of the circulation and the components of the energy budget for experiment 4 correspond to a moderate hurricane.

The results from experiment 4 with the increased heating maximum confirm that the maximum wind is determined primarily by the heat release inside 100 km



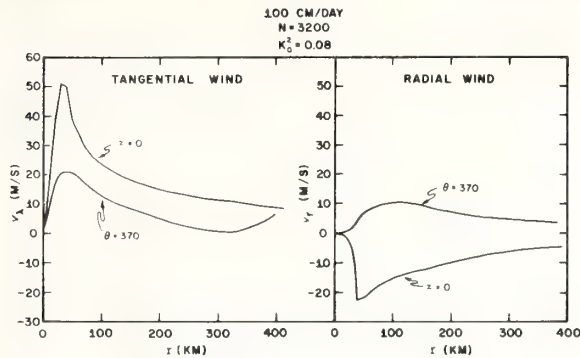


FIGURE 4.—Tangential and radial wind profiles for experiment 4.

and that variations in heating in the outer regions affect mainly the horizontal extent of the storm circulation.

#### B. SECONDARY HEATING MAXIMUM AT 200 KILOMETERS, EXPERIMENT 5

In the final experiment with the horizontal variation of heating, a secondary heating maximum is introduced at 200 km (rainfall type C in fig. 1). The introduction of a secondary heating maximum is an attempt to investigate the possible role of hurricane rainbands in which substantial precipitation occurs at some distance from the center (Gentry 1964). Although rainbands are generally asymmetric, the mean effect in an axisymmetric model appears as a ring of enhanced convection.

The results from experiment 5 show rather small changes from those in experiment 2. The secondary heating maximum reduces the maximum wind from 51 to 48 m/s and raises the central pressure 4 mb (fig. 5 and table 1). The radial wind profile shows a weaker circulation inside 200 km, and the single outflow maximum in experiment 2 is replaced by two weaker maxima in experiment 5. The rather small differences in the circulations inside 100 km again emphasize the insensitivity of the maximum wind to changes in heating at large (200 km) distances from the center in the steady-state model.

Experiment 5 may have some relevance to hurricane modification experiments (*PROJECT STORMFURY*, Annual Report, Staff, National Hurricane Research Laboratory 1969). One aspect of *PROJECT STORMFURY* involves seeding supercooled water in rainbands with silver iodide crystals. The additional heat of fusion might then stimulate additional convective heating at this distance and possibly reduce the amount of air reaching the center by deviating the inflow upward. This chain of events would then result in a decrease of the maximum winds near the center.

The changes in circulation in experiment 5 that result from an increase in heating at 200 km are small but

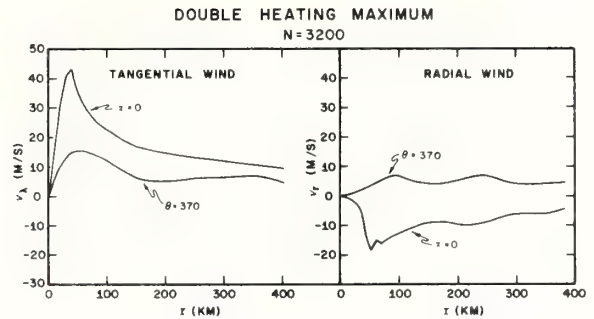


FIGURE 5.—Tangential and radial wind profiles for experiment 5.

qualitatively confirm the hypothesis of the rainband experiments in *PROJECT STORMFURY*. However, the results are inconclusive. From one point of view, it may be argued that the reduction in maximum winds is small in comparison to the changes in the heating distribution. On the other hand, if the hurricane vortex is unstable, a small change might produce interactions that cause greater differences with time. The steady-state model, of course, is not capable of studying such feedback.

The two experiments in section 4 have shown that a heating maximum defined by a rainfall rate of 100 cm/day is adequate to drive a moderate hurricane and indicate that the presence of a secondary heating maximum away from the storm center has a relatively small effect on the maximum wind near the center. Both experiments confirm the primary dependence of the maximum wind on the heat release inside 100 km. Section 5 shows the investigation of the role of infrared cooling on the steady-state hurricane.

#### 5. INFRARED RADIATIVE COOLING IN THE HURRICANE ENVIRONMENT

Because of the immense importance of latent and sensible heat as energy sources in the tropical cyclone system, little attention has been directed toward infrared cooling as a sink of energy. In numerical experiments to date, only Ooyama (1969) included the effect of radiative cooling. Ooyama experimented with a uniform cooling rate and found little change from the noncooling cases. He notes, however, that differential cooling may affect the development of tropical cyclones.

In a study of hurricane Hilda, 1964, Anthes and Johnson (1968) estimated that infrared cooling in the outer region of the storm could account for 15 to 20 percent of the total generation of available potential energy on the hurricane scale (1000 km). The total cooling nearly equaled the total latent heating on this scale. It is important, therefore, to ascertain whether radiative cooling represents a passive energy loss or contributes actively toward maintaining the baroclinicity in the hurricane.

If the 15- to 20-percent generation by infrared emission is representative, the effect of the cooling on the dynamics should be investigated, in view of the strong correlation between generation of available energy and conversion to kinetic energy in these experiments. The next section presents radiative cooling rates in the clear tropical atmosphere, which are computed using Sasamori's (1968) radiation model. Sasamori's model is quite suitable for use in numerical models of the tropical cyclone because of its relative simplicity and computational economy in terms of speed and storage.

Because of the small magnitude of the diabatic cooling by the divergence of infrared radiation and the uncertainties in the heating and mixing parameterization in the isentropic model, the estimation of an infrared cooling profile with high resolution is not required. However, profiles of infrared cooling from several temperature and moisture distributions are presented to illustrate ranges of cooling for various tropical conditions and to justify the use of a mean cooling rate. The basic temperature and moisture distribution is Jordan's (1958) mean hurricane season sounding, which will be considered representative of the nearly cloud-free region surrounding the storm.

#### A. COMPUTATIONAL PROCEDURE

In Sasamori's (1968) model, the absorptivities for water vapor ( $H_2O$ ), carbon dioxide ( $CO_2$ ), and ozone ( $O_3$ ) that are complicated functions of path length and temperature are approximated by empirical formulas. However, in these experiments where only the troposphere is considered, the effect of ozone is neglected. Sasamori's model is now summarized to study profiles of cooling in the tropical atmosphere.

The net flux of radiation through a unit area is a function of the amount of absorbing gas above and below the layer, as well as the vertical temperature profile. The mean absorptivity,  $R$ , is

$$R(u, T) = \int_0^\infty [1 - \tau(u)] \frac{dB_\nu}{dT} d\nu \quad (3)$$

where  $B_\nu$  is Planck's radiation function expressed in flux at frequency  $\nu$ ,  $T$  is temperature, and  $\tau$  represents the mean transmissivity. The effective path length,  $u$ , is approximately

$$u = g^{-1} \int_{p_1}^{p_2} q \left( \frac{p}{p_0} \right) dp \quad (4)$$

with  $q$  as the mixing ratio and  $p_0 = 1000$  mb.

At any level,  $z$ , the downward and upward fluxes are

$$F \downarrow(z) = \int_0^{T(z)} R\{u(T') - u[T(z)], T'\} dT' \quad (5)$$

and

$$F \uparrow(z) = \sigma T_0^4 + \int_{T_0}^{T(z)} R\{u[T(z)] - u(T'), T'\} dT' \quad (6)$$

with  $\sigma$  equal to the Stefan-Boltzmann constant ( $8.13 \times 10^{-11}$

cal·cm<sup>-2</sup>·°K<sup>-4</sup>·min<sup>-1</sup>);  $T_0$ , the surface temperature; and  $T'$ , the variable of integration corresponding to temperature.

The radiative temperature change calculated from the net vertical flux divergence is

$$\frac{\partial T}{\partial t_R} = -\frac{1}{\rho c_p} \frac{d(F \uparrow - F \downarrow)}{dz} \quad (7)$$

Sasamori transforms  $R(u, T)$  to a normalized absorptivity given by

$$\bar{A}(u, T) = \frac{R(u, T)}{4\sigma T^3} = \frac{\int_0^\infty [1 - \tau(u)] \frac{dB_\nu}{dT} d\nu}{\int_0^\infty \frac{dB_\nu}{dT} d\nu} \quad (8)$$

With this transformation, the downward and upward fluxes are

$$F \downarrow(z) = 4\sigma \int_0^{T(z)} \bar{A}\{u(T') - u[T(z)], T'\} T'^3 dT' \quad (9)$$

and

$$F \uparrow(z) = \sigma T_0^4 + 4\sigma \int_{T_0}^{T(z)} \bar{A}\{u[T(z)] - u(T'), T'\} T'^3 dT' \quad (10)$$

Sasamori notes that the mean absorptivity is nearly constant with temperature in the range  $+30^\circ$  to  $-50^\circ C$  but decreases with decreasing temperature at extremely low temperatures. For this reason, the integrals in eq (9) and (10) are separated into two parts. For example, eq (9) is written as

$$F \downarrow(z) = 4\sigma \int_{T(z_1)}^{T(z)} \bar{A}\{u(T') - u[T(z)], T'\} T'^3 dT' + 4\sigma \int_0^{T(z_1)} \bar{A}\{u[T(z_1)] - u[T(z)], T'\} T'^3 dT' \quad (11)$$

where  $z_1$  is the height of the level above which the path length changes very little. Disregarding the direct dependency of  $\bar{A}(u, T')$  on  $T'$  in the first integral and taking  $u[T(z_1)] - u[T(z)]$  as constant with  $T$  (by definition of  $z_1$ ) in the second integral, eq (11) becomes

$$F \downarrow(z) = 4\sigma \int_{T(z_1)}^{T(z)} \bar{A}_0\{u(T') - u[T(z)], T'\} T'^3 dT' + \sigma T^4(z_1) \bar{\bar{A}}\{u[T(z_1)] - u[T(z)], T(z_1)\} \quad (12)$$

$\bar{A}_0(u)$  is the average absorption for the temperature range  $+30^\circ$  to  $-50^\circ C$ , and  $\bar{\bar{A}}(u, T)$  is the mean absorptivity which varies with temperature.  $\bar{A}_0(\Delta u)$  and  $\bar{\bar{A}}(u, T)$ , approximated by empirical formulas, are

$$\bar{A}_0(\Delta u) = \begin{cases} 0.846(\Delta u + 3.59 \times 10^{-5})^{0.243} - 0.069 & \Delta u < 0.01 \text{ g} \\ 0.240 \log_{10}(\Delta u + 0.01) + 0.622 & 0.01 \text{ g} < \Delta u \end{cases} \quad (13)$$

and

$$\bar{\bar{A}}(u, T) = 8.34 T^{[0.353 \log_{10} u - 0.44]} u^{[-0.03455 \log_{10} u - 0.705]} \quad (14)$$

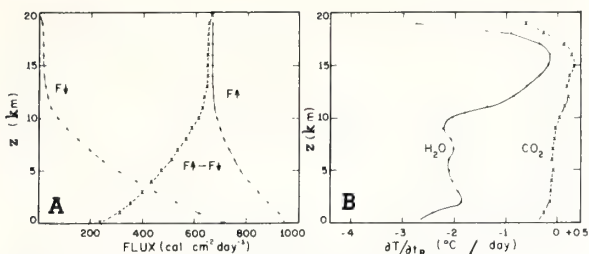


FIGURE 6.—(A) upward, downward, and net infrared flux for the mean tropical sounding and (B) rates of temperature change due to the infrared flux divergence.

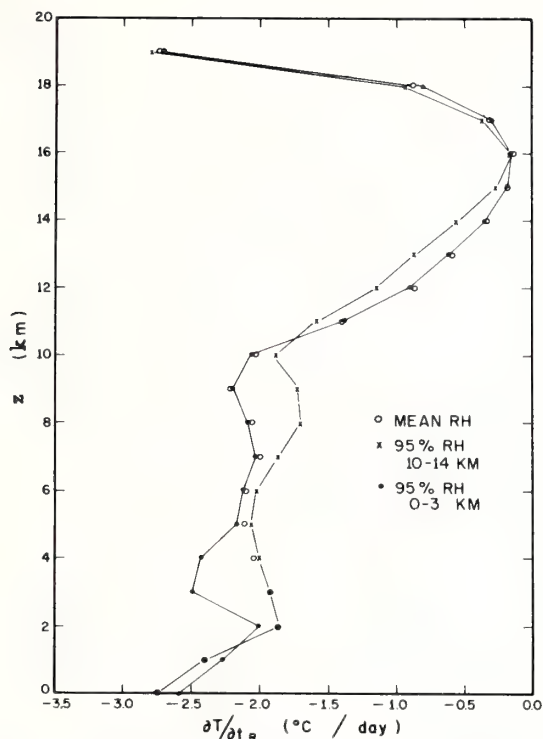


FIGURE 7.—Temperature change rates due to infrared flux divergence for various relative humidity distributions in the Tropics.

## B. EXPERIMENTAL COOLING RATES

Height coordinates with 21 levels are utilized to provide high resolution ( $\Delta z = 1$  km) for investigating the effects of different moisture distributions. In experiments with a resolution of 2 km, the mean cooling profiles are virtually unchanged. Thus, the vertical resolution needed to describe the essential features of cooling in a clear atmosphere is considerably less than 1 km. The vertical integrals are evaluated by the trapezoidal rule, and  $z_1$  is assumed to be 20 km.

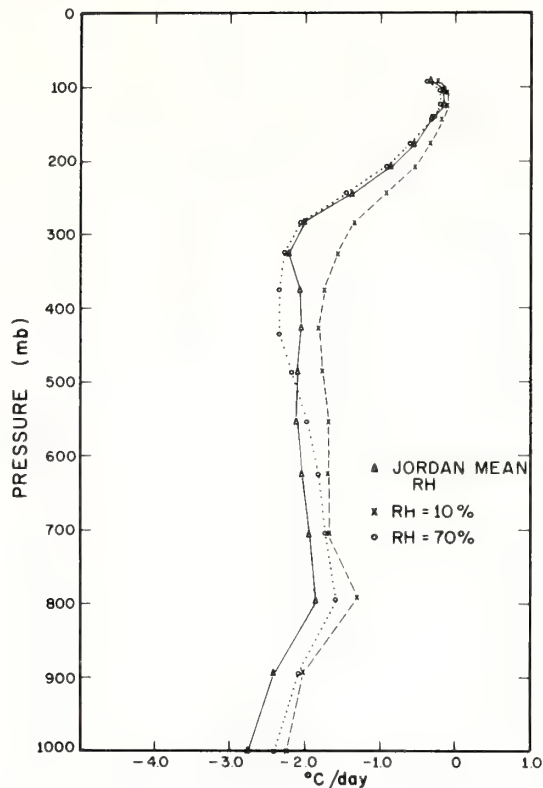


FIGURE 8.—Temperature change rates due to infrared flux divergence for various relative humidity distributions in the Tropics.

Figure 6 shows the upward, downward, and net fluxes from Jordan's (1958) mean hurricane sounding and the corresponding cooling rates caused by water vapor and carbon dioxide. The cooling effect from CO<sub>2</sub> is negligible compared to that from H<sub>2</sub>O. A nearly constant cooling rate of 2°C/day occurs from the surface to 10 km. From 10 km to the tropopause, the cooling rate decreases, reaching a minimum of 0.1°C/day near 16 km. Large cooling rates occur above the tropopause.

The next series of experiments is designed to investigate the dependency of the infrared cooling rates on the moisture distribution. The first two comparisons show the effect of nearly saturated layers, one close to the surface and the other high in the troposphere. Figure 7 shows the cooling profile that results from a 95-percent relative humidity in the layer from the surface to 3 km and another profile that results from a 95-percent relative humidity in the layer between 10 and 14 km. For the other layers, the temperature and moisture distributions are those of the mean hurricane sounding. Cooling is slightly increased above and decreased below the moist layers. Figure 8 shows the cooling rates that result from the mean hurricane season temperature sounding and two relative humidity profiles of 70 and 10 percent. Differences are again



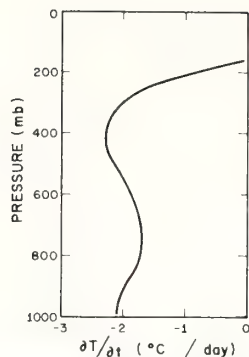


FIGURE 9.—Rate of temperature change due to infrared flux divergence used in the hurricane cooling experiment.

small with slightly lower cooling rates occurring in the drier air.

The relatively small dependency of the cooling rate on the moisture distributions justifies using the mean cooling rate in the hurricane model. Because the temperature in the hurricane environment is slowly varying, it is permissible to use the same cooling rate for several hours in numerical models of hurricanes. By such an approximation, the added storage and computational time are negligible. In this hurricane radiation experiment, the representative mean cooling profile (fig. 9) is nearly constant at 2°C/day below 400 mb and decreases to 0°C/day from 400 to 140 mb. It should be noted that the effect of clouds on infrared cooling is large; hence, this rate is valid only in the cloud-free region of the hurricane environment.

### C. RADIATIVE COOLING BEYOND 300 KILOMETERS, EXPERIMENT 6

Experiment 6 utilizes a 1000-km domain to study the effect of a uniform horizontal cooling from 300 km (assumed to be the edge of the cloud cover) to 1000 km. The control (no cooling) experiment is described in paper I as experiment 11.

**Momentum and temperature structures.** Figures 10, 11, and 12 show the tangential and radial wind profiles and the thermal structure for the cooling and noncooling experiments. The cooling results in an increase of 1.5 m/s in maximum tangential wind and an increase of 1 m/s in maximum inflow. As expected, the temperatures beyond 300 km are lower in experiment 6. A somewhat surprising result, however, is the cooling in the core of the storm, which is nearly as great as that in the outer regions. This cooling is apparently due to horizontal advection and mixing.

**Energy budget.** The difference in temperature structure (fig. 12) indicates that the radiative sink of energy is considerable. The total cooling of  $3.4 \times 10^{14}$  W is about a third of the total heating of  $11.0 \times 10^{14}$  W and confirms that the radiative heat loss is the same order of magnitude as the latent heat gain on the scale of 1000 km.

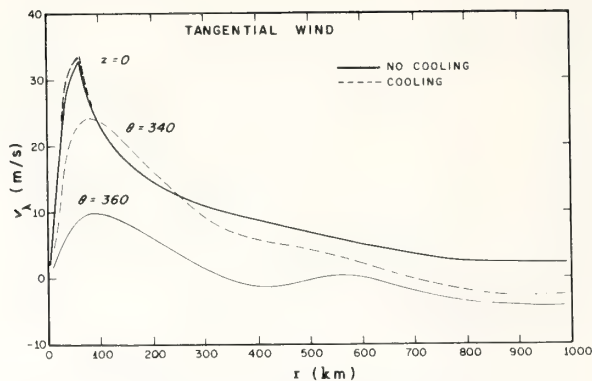


FIGURE 10.—Tangential wind profiles in experiment 11 (paper I) and experiment 6.

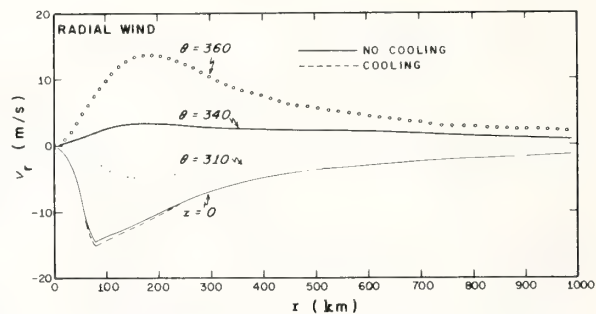


FIGURE 11.—Radial wind profiles in experiment 11 (paper I) and experiment 6.

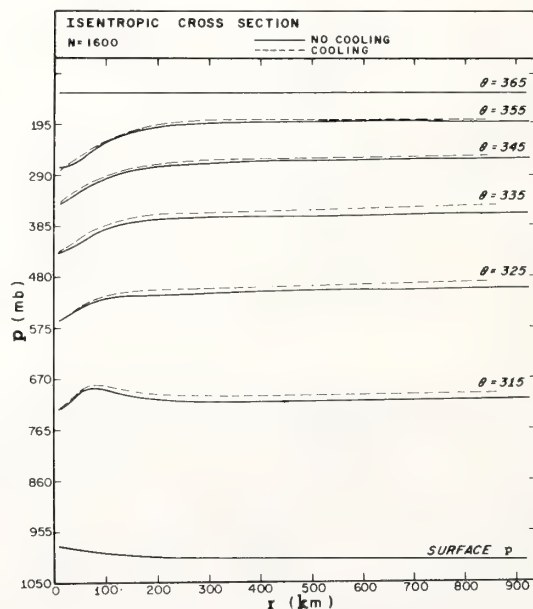


FIGURE 12.—Isentropic cross section for experiment 11 (paper I) and experiment 6.

The generation of available potential energy by the cooling is  $0.2 \times 10^{14}$  W or about 1.5 percent of the total generation. This is considerably less than the 17 percent estimated by Anthes and Johnson (1968). The difference is related to differences in temperature structures between hurricane Hilda and experiment 6. The Hilda environment contained greater large-scale baroclinicity beyond 500 km, resulting in larger negative efficiency factors. Thus cooling at 1000 km in the Hilda environment generates more available potential energy than in experiment 6. Another factor is the infrared emission in the region of positive efficiency factors. In Hilda, cooling was computed from 500 to 1000 km, a region of mostly negative efficiency factors. In experiment 6, cooling occurs from 300 to 1000 km. Because the 300- to 500-km region consists of positive efficiency factors, the infrared generation of available energy is negative in this region.

The total energy budget is summarized in table 1. Although the percentage of generation by radiation is less than 2 percent, the total generation is about 6 percent higher in the cooling experiment. Thus the slightly increased baroclinicity in the cooling experiment results in an increase in the generation by the latent heating.

Although the increase in maximum wind speed in the infrared experiment is only 1.5 m/s, the total cooling represents a significant energy sink. The infrared generation of available energy is considerably less than an earlier diagnostic estimate. Even though the cooling has a small effect on the dynamics of a mature storm in near-steady state, the possibility remains that it may play a more significant role in the earlier stages of tropical storm development. Because the formative stages frequently span several days, the cumulative effect of differential cooling between clear and cloudy regions may be significant. The gradual increase in baroclinicity could enhance the convective heating by accelerating the slow meridional circulation.

## 6. SUMMARY

This paper summarizes some additional experiments with an axisymmetric hurricane model in isentropic coordinates. A variable horizontal eddy viscosity coefficient of the type used by Smagorinsky et al. (1965) is used in these experiments. The results using variable exchange coefficients are similar to the previous results with constant coefficients.

Two additional latent heating functions are studied. Heating defined by a rainfall maximum of 100 cm/day near the center is sufficient to drive a moderate hurricane. A heating distribution with a secondary maximum at 200 km increases the radial extent of the storm but has a small effect on the maximum wind near the center.

Radiational cooling in the clear air is calculated for several moisture distributions in the Tropics using

Sasamori's (1968) model. Infrared cooling beyond 300 km causes a 1.5 m/s increase in maximum wind speed and a 6-percent increase in the generation of available potential energy. The total heat loss by radiation on a scale of 1000 km is about one-half the total heat gain.

## ACKNOWLEDGMENTS

The author wishes to thank Drs. Donald R. Johnson and Stanley L. Rosenthal for their helpful suggestions throughout this research. Mrs. Mary Jane Clarke typed the manuscript, and Mr. Robert Carrodus and staff prepared the figures.

## REFERENCES

- Anthes, Richard A., "A Numerical Model of the Slowly Varying Tropical Cyclone in Isentropic Coordinates," *Monthly Weather Review*, Vol. 99, No. 8, Aug. 1971, pp. 617-635.
- Anthes, Richard A., and Johnson, Donald R., "Generation of Available Potential Energy in Hurricane Hilda (1964)," *Monthly Weather Review*, Vol. 96, No. 5, May 1968, pp. 291-302.
- Gentry, R. Cecil, "A Study of Hurricane Rainbands," *National Hurricane Research Project Report No. 69*, U.S. Department of Commerce, Weather Bureau, Miami, Fla., Mar. 1964, 85 pp.
- Jordan, Charles L., "Mean Soundings for the West Indies Area," *Journal of Meteorology*, Vol. 15, No. 1, Feb. 1958, pp. 91-97.
- Koteswaram, P., "On the Structure of Hurricanes in the Upper Troposphere and Lower Stratosphere," *Monthly Weather Review*, Vol. 95, No. 8, Aug. 1967, pp. 541-564.
- Leith, Cecil E., "Two Dimensional Eddy Viscosity Coefficients," *Proceedings of the WMO/IUGG Symposium on Numerical Weather Prediction, Tokyo, Japan, November 28-December 4, 1968*, Japan Meteorological Agency, Tokyo, Mar. 1969, pp. 1-41-I-44.
- Matsuno, Taroh, "Numerical Integrations of the Primitive Equations by a Simulated Backward Difference Method," *Journal of the Meteorological Society of Japan*, Ser. 2, Vol. 44, No. 1, Tokyo, Feb. 1966, pp. 76-84.
- Ooyama, Katsuyuki, "Numerical Simulation of the Life-Cycle of Tropical Cyclones," *Journal of the Atmospheric Sciences*, Vol. 26, No. 1, Jan. 1969, pp. 3-40.
- Orville, Harold D., "Ambient Wind Effects on the Initiation and Development of Cumulus Clouds Over Mountains," *Journal of the Atmospheric Sciences*, Vol. 25, No. 3, May 1968, pp. 385-403.
- Phillips, Norman A., "An Example of Non-Linear Computational Instability," *The Atmosphere and the Sea in Motion*, Rockefeller Institute Press, New York, N.Y., 1959, pp. 501-504.
- Riehl, Herbert, and Malkus, Joanne S., "Some Aspects of Hurricane Daisy, 1958," *Tellus*, Vol. 13, No. 2, Stockholm, Sweden, May 1961, pp. 181-213.
- Rosenthal, Stanley L., "A Circularly Symmetric Primitive Equation Model of Tropical Cyclone Development Containing an Explicit Water Vapor Cycle," *Monthly Weather Review*, Vol. 98, No. 9, Sept. 1970, pp. 643-663.
- Sasamori, Takashi, "The Radiative Cooling Calculation for Application to General Circulation Experiments," *Journal of Applied Meteorology*, Vol. 7, No. 5, Oct. 1968, pp. 721-729.
- Smagorinsky, Joseph, Manabe, Syukuro, and Holloway, J. Leith, Jr., "Numerical Results From a Nine-Level General Circulation Model of the Atmosphere," *Monthly Weather Review*, Vol. 93, No. 12, Dec. 1965, pp. 727-768.
- Staff, National Hurricane Research Laboratory, *PROJECT STORMFURY, ANNUAL REPORT, 1968*, Miami, Fla., 1969, 40 pp.

[Received August 19, 1970; revised January 22, 1971]

U.S. DEPARTMENT OF COMMERCE  
National Oceanic and Atmospheric Administration  
Environmental Research Laboratories

NOAA Technical Memorandum ERL NHRL-94

THE DEVELOPMENT OF ASYMMETRIES  
IN A THREE-DIMENSIONAL NUMERICAL MODEL  
OF THE TROPICAL CYCLONE

Richard A. Anthes

National Hurricane Research Laboratory  
Coral Gables, Florida  
December 1971





# TABLE OF CONTENTS

	Page
1. INTRODUCTION	1
2. REVIEW OF MODEL	4
2.1 Basic Equations . . . . .	4
2.2 Structure of the Model. . . . .	4
2.3 Vertical Diffusion of Momentum. . . . .	6
2.4 Horizontal Diffusion of Heat and Momentum . . . . .	8
2.5 Time Integration. . . . .	9
2.6 Lateral Boundary Conditions . . . . .	9
2.7 Parameterization of Cumulus Convection. . . . .	10
2.8 Water Vapor Budget and Non-convective Latent Heat Release. . . . .	13
2.9 Air-sea Exchange of Sensible and Latent Heat. . . . .	15
2.10 Initial Conditions. . . . .	16
3. EXPERIMENTAL RESULTS	16
3.1 Addition of Explicit Water Vapor Cycle. . . . .	16
3.2 Increased Horizontal Resolution Utilizing Staggered Horizontal Grids . . . . .	20
3.3 Structure of Asymmetric Hurricane . . . . .	23
3.4 The Development of the Asymmetric Stage . . . . .	28
3.5 The Initial Perturbations . . . . .	30
3.6 Role of Dynamic Instability in the Development of the Asymmetries. . . . .	32
3.7 Eddy Kinetic Energy Budget. . . . .	39
3.8 Increase of Sea Temperature in One Quadrant . . . . .	43
4. SUMMARY AND CONCLUSIONS	45
ACKNOWLEDGMENTS	47
APPENDIX	48
REFERENCES	53

# THE DEVELOPMENT OF ASYMMETRIES IN A THREE-DIMENSIONAL NUMERICAL MODEL OF THE TROPICAL CYCLONE

Richard A. Anthes

Notable asymmetric features of an early experiment with a three-dimensional hurricane model (Anthes et al., 1971a) were spiral bands of convection and large scale asymmetries (eddies) in the outflow layer. Using an improved version of the model, the formation and maintenance of these features are described in greater detail in this paper. The spiral bands in the model are found to propagate cyclonically outward in agreement with bands in nature. The breakdown of symmetry into a chaotic pattern of eddies in the outflow region is shown to be the result of dynamic (inertial) instability, with the eddy kinetic energy derived from the kinetic energy of the azimuthal mean flow. This instability does not contribute to the overall intensification of the model storm, however.

A curious anticyclonic looping of the vortex center is observed in these experiments. This looping appears to be associated with asymmetries in the divergence pattern associated with the eddies in the outflow layer.

This paper also summarizes improvements made in the original version of the model. In contrast to the earlier model, the current version contains an explicit water vapor cycle. A staggered horizontal grid is utilized to provide for a higher resolution in evaluating the pressure gradient forces. Some of the pragmatic assumptions made in the earlier model, notably those involving horizontal diffusion of heat and momentum, have been eliminated in the current version.

## 1. INTRODUCTION

A preliminary version of an isolated, asymmetric hurricane model (Anthes et al., 1971a, hereafter referred to as paper A) reproduced at least two prominent asymmetric features associated with natural storms, i.e., spiral bands of upward motion and fairly large scale asymmetries in the outflow layer. However, detailed analysis and interpretation of these features were deferred until additional experiments with an improved version of the model could be carried out. Especially conspicuous

A curious feature of the later experiments, which was not present in the preliminary experiment (paper A), is an anticyclonic looping of the vortex center about the center of the grid. Figure 8 shows the path for Experiment 6, which approximates a circle of radius 75 km. The commencement of the looping is coincident with the formation of outflow asymmetries, suggesting that the eddies, which drift with the anticyclonic flow of the upper levels are controlling the looping of the vortex center. It is possible that the lateral boundary conditions are responsible for the tight, circular looping, and with a much larger domain the vortex center might meander in a much less organized pattern.

The time variation of the mass-integrated total kinetic energy budget for Experiment 6 is shown in figure 9. The kinetic energy equation for this model is presented in paper A. The difference between the observed kinetic energy rate of change and the tendency computed from the kinetic energy equation is small (see fig. 9, top). This close agreement indicates that truncation errors in the model, including those associated with the time integration, are small. The important components of the energy budget, are also shown in figure 9. The dissipation due to horizontal eddies is about half that due to vertical eddies, which includes dissipation at the surface. The values of the components are reasonable compared to observations and to symmetric model results (see Anthes, 1971 for a summary of empirical results). The following sections discuss the development of the asymmetric stage and investigate the energetics of the asymmetries.



among the deficiencies in the preliminary model were the low vertical (3 levels) and coarse horizontal (30 km) resolution, the absence of a water vapor cycle, and a very pragmatic treatment of the lateral mixing process for heat and momentum. At present, however, the model has been substantially improved with the exception of increasing the vertical resolution. In particular, improved horizontal resolution is attained through a staggering of the horizontal grid, an explicit water vapor cycle is added, and a formulation of the horizontal diffusion processes similar to that used by Smagorinsky et al. (1965) is adopted. In experiments with the improved version of the model, several relationships have emerged involving the development and interaction of the asymmetries. This paper examines, in detail, the development of the asymmetric features using the current version of the model. The asymmetries in the outflow arise from the dynamic instability of the mean flow, and the predominance of wave numbers one and two is unrelated to the form of the initial asymmetries. The changes in grid structure, treatment of water vapor, and horizontal mixing are also discussed.

A curious asymmetric feature not found in the preliminary experiment is an anticyclonic looping of the vortex center during the mature stage of the model storm. This looping seems to be associated with asymmetries in the upper level divergence pattern.

Well formed spiral bands are present in these experiments. These bands rotate cyclonically and propagate outward with a phase speed of about 24 knots.

Symmetric hurricane models (Ooyama, 1968) have shown a strong relationship between model storm intensity and the sea surface temperature. A symmetric model cannot, however, investigate the effect of sea surface temperature variations on the movement of the storm. A simple experiment is made to determine the effect of variations in sea temperature on the looping motion of the storm. As the looping storm passes over warmer water, an intensification occurs but there is no discernable effect on the motion of the storm.

## 2. REVIEW OF MODEL






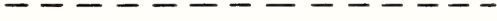

### 2.1 Basic Equations

The equations of motion are written in  $\sigma$ -coordinates (Phillips, 1957) on an  $f$ -plane, where  $f$ , the Coriolis parameter, is appropriate to approximately  $20^\circ\text{N}$  ( $5 \times 10^{-5} \text{ sec}^{-1}$ ). The equations of motion, the continuity equation, the thermodynamic equation, and the hydrostatic equation are identical to those employed by Smagorinsky et al. (1965) for general circulation studies. The basic equations are given in paper A and are not repeated here.

### 2.2 Structure of the Model

The vertical structure of the model is shown by figure 1a. The atmosphere is divided into upper and lower layers of equal pressure depth and a thinner Ekman boundary layer. The information levels for the dynamic and thermodynamic variables are staggered according to the scheme used by Kurihara and Holloway (1967).

## VERTICAL STRUCTURE

<u>VARIABLE</u>		K	P(mb)
$\dot{\sigma} = 0$		1	0
$\nabla, T$		1½	225
$\dot{\sigma}, \phi$		2	450
$\nabla, T$		2½	675
$\dot{\sigma}, \phi$		3	900
$\nabla, T$		3½	957.5
$\phi = \dot{\sigma} = 0$		4	1015

(a)

## HORIZONTAL STRUCTURE - Northwest Section

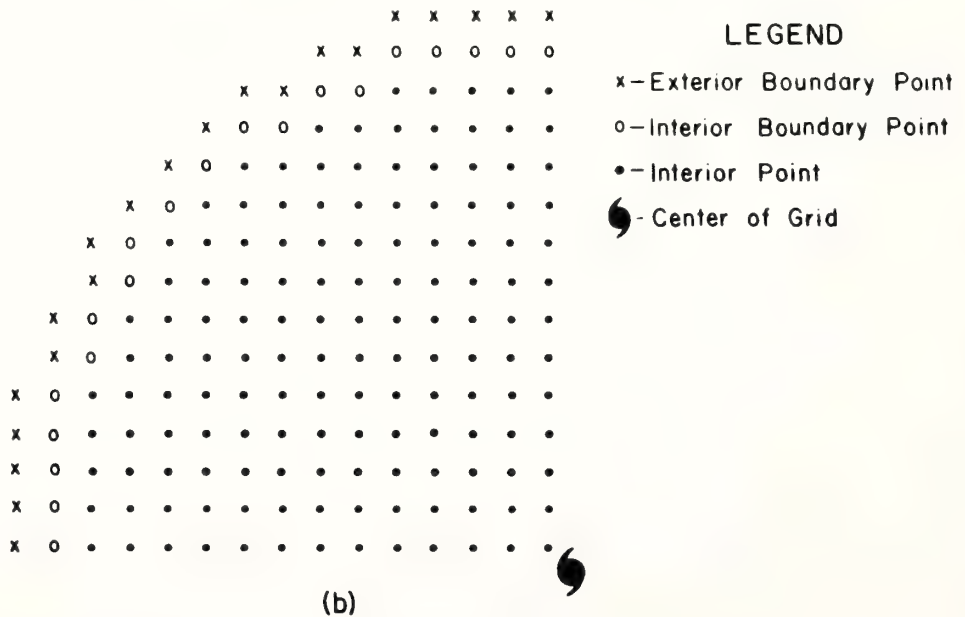


Figure 1(a). Vertical information levels.

(b). Northwest quadrant of horizontal grid (non-staggered).



In an effort to economically achieve an increase in the horizontal resolution, three horizontal grids are tested in the experiments discussed in this paper. The first is the grid utilized in paper A, in which all the variables are defined at all the grid points. Two staggered horizontal grids are tested and shown to provide for a better resolution of the pressure gradient forces. These grids, and their associated finite difference equations, are discussed in section 3.2.

### 2.3 Vertical Diffusion of Momentum

As in the preliminary version of the model, the vertical diffusive and "frictional" effects are due to the vertical transports of horizontal momentum by subgrid eddies smaller than the cumulus scale. The most important aspect of these effects is the surface drag which produces frictional convergence in the cyclone boundary layer and, therefore, a water vapor supply which controls the parameterized cumulus convection (Charney and Eliassen, 1964; Ooyama, 1969; Rosenthal, 1970b).

In vector notation, these terms are written for the  $\sigma$ -system as

$$\vec{F}_v = -g \frac{\partial \tau^z}{\partial \sigma} \quad (1)$$

where  $g$  is the acceleration of gravity and  $\tau^z$  is the vector Reynolds stress. The quadratic stress law, with the surface wind speed approximated by the speed at level 3, is employed for the stress at  $\sigma = 1$ ,

$$\tau_{k=4}^z = \rho * C_D |\vec{V}_3| \vec{V}_3, \quad (2)$$

where  $\vec{V}$  is the horizontal wind vector. A value of  $3 \times 10^{-3}$  is adopted for the drag coefficient,  $C_D$ , and a standard value of  $1.10 \times 10^{-3} \text{ ton-m}^{-3}$

is used for the surface density,  $\rho^*$ , in (2). As an upper boundary condition,

$$\tau_{k=1}^z = 0 . \quad (3)$$

For the remaining  $\sigma$ -levels,

$$\tau_{k=2,3}^z = \rho(z) \mu(z) \frac{\partial \vec{V}}{\partial z} . \quad (4)$$

Here,  $\rho(z)$  is density,  $z$  is height, and  $\mu(z)$  is the kinematic coefficient of eddy viscosity.

Following Smagorinsky et al. (1965),  $\mu(z) = \ell^2 \left| \frac{\partial \vec{V}}{\partial z} \right|$  where  $\ell$  is the mixing length. In this model,  $\ell$  need only be assigned at levels 2 and 3. In the preliminary report,  $\ell$  varied linearly from a maximum value of 35.5 at level 3 to 0 at level 1, yielding a value of 17.8 at level 2. In later experiments, the values of  $\mu(z)$  at levels 2 and 3 were increased by an order of magnitude to reduce what subjectively appeared to be excessive vertical shear. The form currently in use for  $\mu(z)$  is

$$\mu(z) = 25 + \alpha^2 \left| \frac{\partial \vec{V}}{\partial z} \right| \text{ m}^2 \text{ sec}^{-1}, \quad (5)$$

with  $\alpha^2 = 4 \times 10^4 \text{ m}^2$ .

The value of  $\mu(z)$  computed from (5) is about twenty times the value of  $\mu(z)$  computed in the original experiment at level 3 and about forty times the original value at level 2 during the mature stage of development.

It is recognized that the form of  $\mu(z)$  given by (5) is, at best, a temporary representation of the total effect of vertical mixing of momentum in the hurricane, since cumulus clouds having the same vertical scale as the hurricane itself play an important role in the vertical

transfer of momentum. However, this formulation yields an order of magnitude of  $\mu(z)$  ( $50-100 \text{ m}^2 \text{ sec}^{-1}$ ) found to give vertical shears representative of real hurricanes in symmetric models (Rosenthal, 1970a; Anthes, 1971). It is noteworthy that experiments with the symmetric analog (Anthes et al., 1971b) show that the exact form of  $\mu(z)$  above the boundary layer is relatively unimportant. Finally, the finite difference expression for the vertical "frictional" force is

$$\vec{F}_v = -g \frac{\delta \tau^z}{\delta \sigma}, \quad (6)$$

where the vertical differencing operator,  $\delta$ , is defined in appendix A.

#### 2.4 Horizontal Diffusion of Heat and Momentum

After Smagorinsky et al. (1965), the lateral exchange of horizontal momentum,  $F_H$ , by subgrid scale eddies is

$$F_H(\vec{V}) = \frac{\partial}{\partial x} K_H \frac{\partial \vec{p} \cdot \vec{V}}{\partial x} + \frac{\partial}{\partial y} K_H \frac{\partial \vec{p} \cdot \vec{V}}{\partial y}. \quad (7)$$

The formulation of  $K_H$  in paper A, based on early tests and on results from symmetric model experiments (Rosenthal, 1970a), was

$$K_H = C_1 |\vec{V}| + C_2 \quad (8)$$

where  $C_1 = 10^3 \text{ m}$  and  $C_2 = 5 \times 10^3 \text{ m}^2 \text{ sec}^{-1}$ . The current version of the model, however, utilizes a non-linear form similar to that used by Smagorinsky et al. (1965),

$$K_H = 5 \times 10^3 + \frac{k_o^2}{2} (\Delta S)^2 |D| \quad (9)$$

where  $\Delta S$  is the grid spacing (30 km),

$$D = \left\{ \left( \frac{\partial u}{\partial x} - \frac{\partial v}{\partial y} \right)^2 + \left( \frac{\partial v}{\partial x} + \frac{\partial u}{\partial y} \right)^2 \right\}^{\frac{1}{2}} \quad (10)$$

and  $k_o$ , the von Karman constant, equals 0.4.



In (9), the constant part is important only near the outer boundary where the kinetic energy and horizontal shear are small.

For simplicity, the diffusion of heat in the original version of the model was modelled using a constant thermal diffusivity,

$$F_H(T) = \rho^* \left( \frac{\partial K_T}{\partial x} \frac{\partial T}{\partial x} + \frac{\partial K_T}{\partial y} \frac{\partial T}{\partial y} \right) \quad (11)$$

with  $K_T = 5 \times 10^4 \text{ m}^2 \text{sec}^{-1}$ .

In the current version of the model, however, the diffusivities for heat, momentum, and water vapor are equal to  $K_H$  computed from (9).

## 2.5 Time Integration

As in paper A, the Matsuno (1966) simulated forward-backward scheme is utilized for the time integration. This scheme damps the very high frequency gravity waves, without significantly damping the low and medium frequencies.

## 2.6 Lateral Boundary Conditions

The small domain size and the irregular boundary make the choice of lateral boundary conditions very important. In paper A, the components of momentum were extrapolated outward from interior grid points regardless of the direction of the flow. A subsequent experiment, however, produced a more intense storm than the preliminary model storm, and the extrapolation outward of the momentum in areas of inflow led to an instability in which a rather intense jet formed near the boundary. The source of energy for this jet was apparently the unlimited supply of kinetic energy from the environment. In subsequent experiments,

therefore, the momentum components on the boundary are extrapolated only where the normal flow is outward. For inflow, the momentum on the boundary is set to zero.

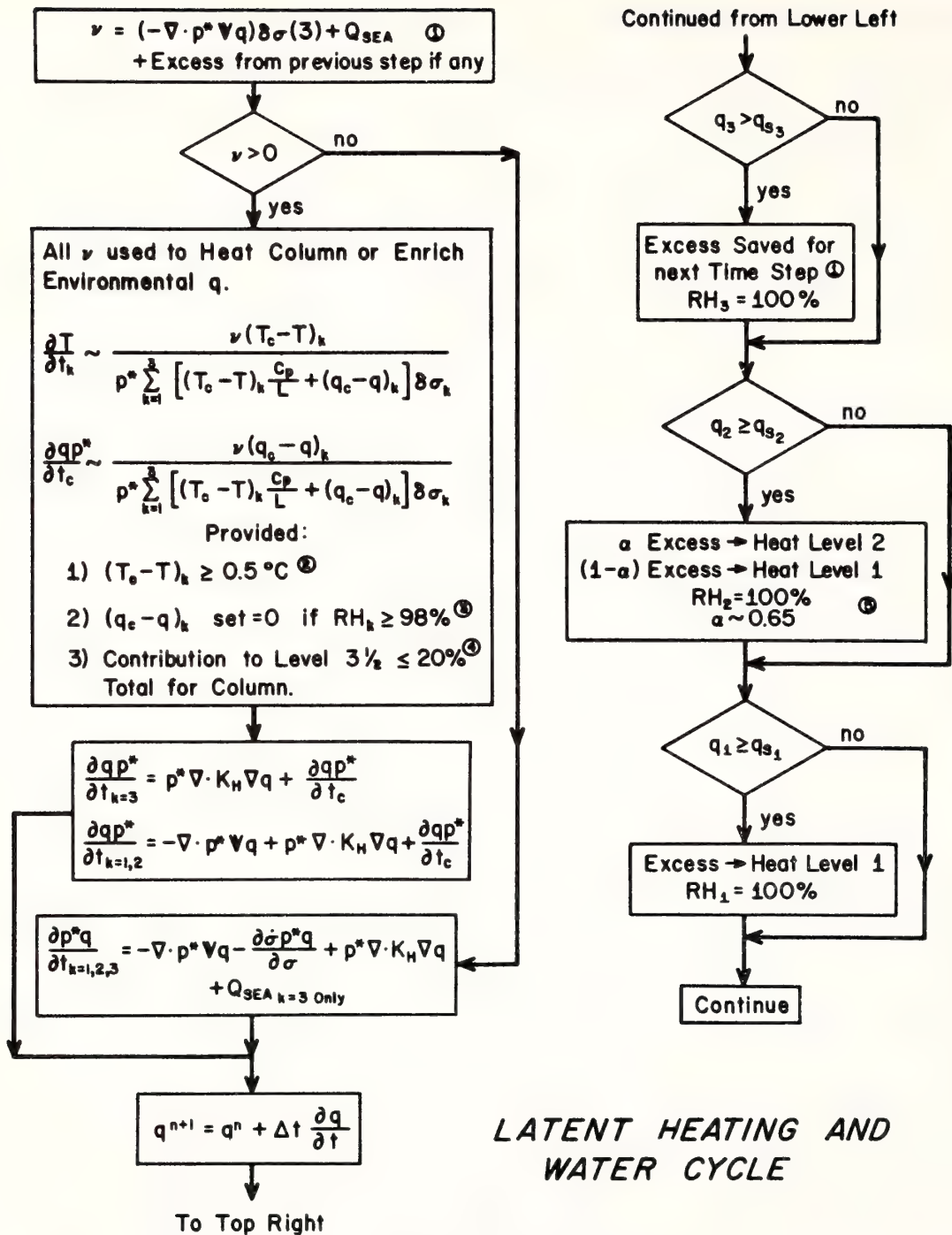
As in paper A, the boundary values for pressure and temperature are in uniform steady state. In experiments which include an explicit water vapor cycle, the relative humidity on the boundary is fixed at 90%.

## 2.7 Parameterization of Cumulus Convection

A major improvement in the model experiments discussed in this paper is the addition of an explicit water vapor cycle. This change eliminates the assumptions concerning boundary layer water vapor content that were necessary in paper A, and allows for simulation of non-convective release of latent heat. This section describes the parameterization of the feed-back between convection and the large-scale temperature and moisture fields. The following section describes the water vapor cycle and the non-convective release of latent heat. The flow chart for both schemes is summarized in figure 2.

The parameterization of the cumulus convection closely follows the scheme used successfully by Rosenthal (1970b), although some slight modifications are necessary because of the reduced vertical resolution. The basic characteristics of the scheme have been thoroughly discussed elsewhere (Rosenthal, 1969, 1970a) and will not be elaborated upon here. The two most important aspects of the scheme may be summarized, however:

- 1) In the convective parameterization, the vertical integral of latent energy is conserved.



## LATENT HEATING AND WATER CYCLE

Figure 2. Flow chart illustrating water vapor cycle and parametrization of convective and non-convective latent heat release. See sections 2.7 and 2.8 for details.



- 2) The heat and moisture made available to the environment are distributed vertically in such a way that the environment is driven toward an ultimate state in which the humidity and temperature are those defined by the equivalent potential temperature of the surface air.

The convective adjustment for the  $\sigma$ -system is

$$l = \frac{v}{\sum_{k=1}^3 (T_c - T)_k \frac{C_p}{L} + (q_c - q) \delta \sigma_k} \quad (12)$$

where  $T_c$  and  $q_c$  are the temperature and specific humidity, respectively, of the pseudo-adiabat with the equivalent potential temperature of the surface,  $q$  is the environmental specific humidity,  $L$  is the latent heat of vaporization, and  $C_p$  is the specific heat for dry air at constant pressure. The boundary layer convergence of water vapor and the latent heat addition from the sea ( $Q_{sea}$ ), is

$$v = -\nabla \cdot p^* \vec{V} q_3 \delta \sigma_3 + Q_{sea} \quad (13)$$

Then, if  $\dot{Q}_c$  is that part of the diabatic heating due to convection,

$$p^* \dot{Q}_c \begin{cases} = C_p l (T_c - T) & \text{if } (T_c - T) \geq 0.5^\circ\text{C} \\ & \text{and } l > 0 \\ = 0 & \text{otherwise.} \end{cases} \quad (14)$$

Letting  $\left(\frac{\partial p^* q}{\partial t}\right)_c$  represent the addition of moisture to the environment by cumulus convection,

$$\left(\frac{\partial p^* q}{\partial t}\right)_c \begin{cases} = l (q_c - q) & \text{if } l (q_c - q) > 0 \\ & \text{and } RH \leq 98\% \\ = 0 & \text{otherwise.} \end{cases} \quad (15)$$

Equations (12) through (15) are utilized only when the atmosphere is conditionally unstable, i.e.,  $(T_c - T)$  and  $(q_c - q)$  are positive for some value of  $k$ . In practice, convection occurs only if  $(T_c - T)$  equals or exceeds  $0.5^\circ\text{C}$  at either level  $1\frac{1}{2}$  or  $2\frac{1}{2}$ , in order to avoid numerical difficulties with small values of the denominator of (12). As an additional constraint on the vertical partitioning of latent heat, under nearly moist neutral conditions ( $T_c \approx T$  and  $q_c \approx q$ ), no more than 20% of the total latent heat in the column is assigned to the boundary layer (level  $3\frac{1}{2}$ ), and the remaining 80% is distributed equally between the middle and upper tropospheric layers.

An additional modification to the above scheme occurs under a nearly saturated environment, defined by a relative humidity (RH) equal to or greater than 98%. Under these conditions,  $(\frac{\partial p^* q}{\partial t})_c$  (which may be thought of as resulting from evaporating clouds) is set equal to zero, and all of the condensation heating is made available to the large scale flow.

The surface temperature,  $T^*$ , needed to establish the surface equivalent potential temperature, is computed by a downward extrapolation from level  $3\frac{1}{2}$ ,

$$T^* = T_{3\frac{1}{2}} + 3.636^\circ\text{K} \quad (16)$$

and the surface specific humidity is obtained by the assumption that the relative humidity at the surface equals the humidity at  $k = 3\frac{1}{2}$ .

## 2.8 Water Vapor Budget and Non-convective Latent Heat Release

The treatment of the water vapor cycle closely follows the scheme developed by Rosenthal (1970b) for the symmetric, 7-level model, again

with some modifications due to the limited vertical resolution. The scheme is outlined in figure 2.

Under unsaturated conditions in the presence of convection, all of the boundary layer water convergence and the evaporation from the sea is utilized in convection, and the forecast equation for specific humidity at level  $3\frac{1}{2}$  is simply,

$$\left(\frac{\partial p^* q}{\partial t}\right) \approx p^* \nabla \cdot K_H \nabla q + \left(\frac{\partial p^* q}{\partial t}\right)_c . \quad (17)$$

In the middle and upper layers, the forecast equation is

$$\frac{\partial p^* q}{\partial t} = -\nabla \cdot p^* \vec{V} q - p^* \frac{\partial \dot{\sigma} q}{\partial \sigma} + p^* \nabla \cdot K_H \nabla q + \left(\frac{\partial p^* q}{\partial t}\right)_c . \quad (18)$$

In columns which contain no convection, the forecast equation for level  $3\frac{1}{2}$  is identical to (18) with the additional term,  $Q_{\text{sea}}$ , representing evaporation from the sea surface (see section 2.9). The interpolation of  $q$  to the  $\dot{\sigma}$  levels, necessary for computing the vertical flux in (18), is obtained by assuming an exponential variation of  $q$  between the  $\sigma$ -levels,

$$q = q_o e^{\gamma(\sigma - \sigma_o)} ; \quad (19)$$

where the reference level is designated by the subscript  $o$ . Evaluating the constant,  $\gamma$ , we obtain for  $\bar{q}_k$ ,

$$\bar{q}_k = q_{k+\frac{1}{2}} \left( \frac{q_{k-\frac{1}{2}}}{q_{k+\frac{1}{2}}} \right)^{\left( \frac{\sigma_k - \sigma_{k+\frac{1}{2}}}{\sigma_{k-\frac{1}{2}} - \sigma_{k+\frac{1}{2}}} \right)} , \quad (20)$$

and,

$$\frac{\partial \dot{\sigma} q}{\partial \sigma} \sim \frac{\delta \dot{\sigma} q}{\delta \sigma} . \quad (21)$$

The release of non-convective latent heat is modeled in the following manner. After every forecast step, each grid point for specific



humidity is checked for supersaturation. If supersaturation occurs in the boundary layer, and conditional instability is still present, the excess water vapor over saturation is used to fuel additional convection according to the convective scheme given by (14) and (15). In the event (rare) that supersaturation occurs in the boundary layer and the atmosphere is conditionally stable, the excess moisture is condensed in situ.

For supersaturation at levels  $1\frac{1}{2}$  and  $2\frac{1}{2}$ , the excess vapor is assumed to condense as large scale precipitation rather than convection, since the atmosphere is conditionally stable above these levels. At level  $1\frac{1}{2}$ , all the excess is condensed and the latent heat is made available to the circulation at this level. For supersaturation at level  $2\frac{1}{2}$ , however, only part (65%) of the excess water vapor is condensed at this level, the remainder is assumed to condense at level  $1\frac{1}{2}$ . This partitioning follows from the assumption that the mechanism for the latent heat release is large scale ascent of saturated air. For typical hurricane soundings, a saturated parcel starting at level  $2\frac{1}{2}$  (about 675 mb) and rising to the tropopause, condenses about 65% of its total water vapor below 450 mb (level 2) and the rest above this level.

## 2.9 Air-sea Exchange of Sensible and Latent Heat

The sensible and latent heat fluxes at the air-sea interface obey the bulk aerodynamic relationships, and decrease linearly with  $\sigma$  until they reach zero at the  $k = 3$  level. This gives

$$p^* \dot{Q}_s = \begin{cases} \frac{g C_p C_E |\vec{V}| \rho^* (T_{sea} - T^*)}{\sigma_4 - \sigma_3}, & T_{sea} > T^* \\ 0 & T_{sea} \leq T^* \end{cases} \quad (22)$$

and

$$Q_{\text{sea}} = \begin{cases} \frac{g C_E |\vec{V}| \rho^* (q_{\text{sea}} - q^*)}{\sigma_4 - \sigma_3} & q_{\text{sea}} > q^* \\ 0 & q_{\text{sea}} \leq q^*, \end{cases} \quad (23)$$

where  $Q_s$  and  $Q_{\text{sea}}$  are the sensible and latent heat added per unit mass and time at level  $3\frac{1}{2}$ . The exchange coefficient  $C_E$  is taken equal to  $C_D$  (.003) and the value of  $T_{\text{sea}}$  is 302°K for most of the experiments.

## 2.10 Initial Conditions

The initial conditions consist of an axisymmetric vortex in gradient balance, with a maximum wind speed of  $18 \text{ m sec}^{-1}$  at a radius of 240 km. The details are presented in paper A. For initially symmetric conditions, the solutions to the differential equations remain symmetric for all time. However, asymmetries in the truncation and roundoff errors as well as in the lateral boundaries produce weak asymmetries (on the order of  $10^{-10}\%$ ) in the finite difference equations after the first time step. These perturbations may then grow with time and become a significant part of the total circulation. In a later section, the mechanism for this observed growth is investigated. It is also shown that the initial form of the perturbation is unimportant in determining the final form of the asymmetries.

## 3. EXPERIMENTAL RESULTS

### 3.1 Addition of Explicit Water Vapor Cycle

The next two sections briefly describe the effects of the major modifications to the original version of the model, specifically, the addition of the water vapor cycle and the horizontal staggering of the grid. The

details of the model storm structures associated with these intermediate stages of the model are not presented. Sections 3.3-3.7 present detailed analyses of the model storm's life history as computed from the current version of the model. These sections are primarily concerned with the development and structure of the asymmetric features including rainbands and outflow eddies.

Table 1 lists some of the properties of each experiment discussed in this paper. These properties, appropriate to the mature stage of each model storm, serve as an overall comparison of the experiments, and are discussed individually in later sections.

Figure 3 shows the time variation of the minimum surface pressure and the maximum surface wind speed for each experiment. The effect of adding the explicit water vapor cycle alone is illustrated by the curves labelled "non-staggered grid", and, as suggested by the close similarity to the corresponding profiles for Experiment 1, the water vapor cycle has a fairly small effect on the overall behavior of the model storm. The initial development is somewhat slower, since part of the water vapor convergence in the boundary layer is utilized to enrich the environmental water vapor content in the middle and upper troposphere (the initial relative humidity at all levels is 90%). In Experiment 1, which does not contain a water vapor cycle, all the water vapor convergence is condensed and made available as latent heat to the large scale flow.

Although the initial development in the experiment with the water cycle is slower, the ultimate state is equal to, or slightly greater than in Experiment 1. This difference is related to somewhat higher boundary



Table 1. Summary of Experiments

EXPERIMENT	GRID	MIN P (mb)	MAX S m sec <sup>-1</sup>	10 <sup>14</sup> Watts				10 <sup>12</sup> Watts		
				Total heating rate	Convective heating rate	Non-Conv heating rate	Sensible heating rate	C (K)	D <sub>H</sub>	D <sub>V</sub>
1. (Anthes et al., 1971a) (228 h)	Non-stag	965	66	13.9	13.9	-----	0.46	45	-11	-32
2. (H <sub>2</sub> O cycle added) (282 h)	Non-stag	962	66	11.8	11.4	0.4	0.24	43	-16	-28
3. (Initial asymmetries 10 <sup>-1</sup> %) (174 h)	S-1	976	60	10.0	8.6	1.4	0.19	31	-10	-19
4. (Initial asymmetries 10 <sup>-1</sup> %) (120 h)	S-1	976	60	11.2	9.9	1.3	0.21	36	-11	-23
5. (Aborted due to lateral boundary problems) (87 h)	S-2	980	57	7.2	6.8	0.4	0.11	17	-7	-9
6. Non-linear-type Hor. Mixing (156 h)	S-1	971	63	12.6	10.6	2.0	0.22	36	-11	-24
7. Symmetric analog (96 h)	1 Horizontal Dimension Staggered Grid	969	53	15.1	12.4	2.7	0.30	39	-11	-28

Time in ( ) is time at which components of energy budget are given.

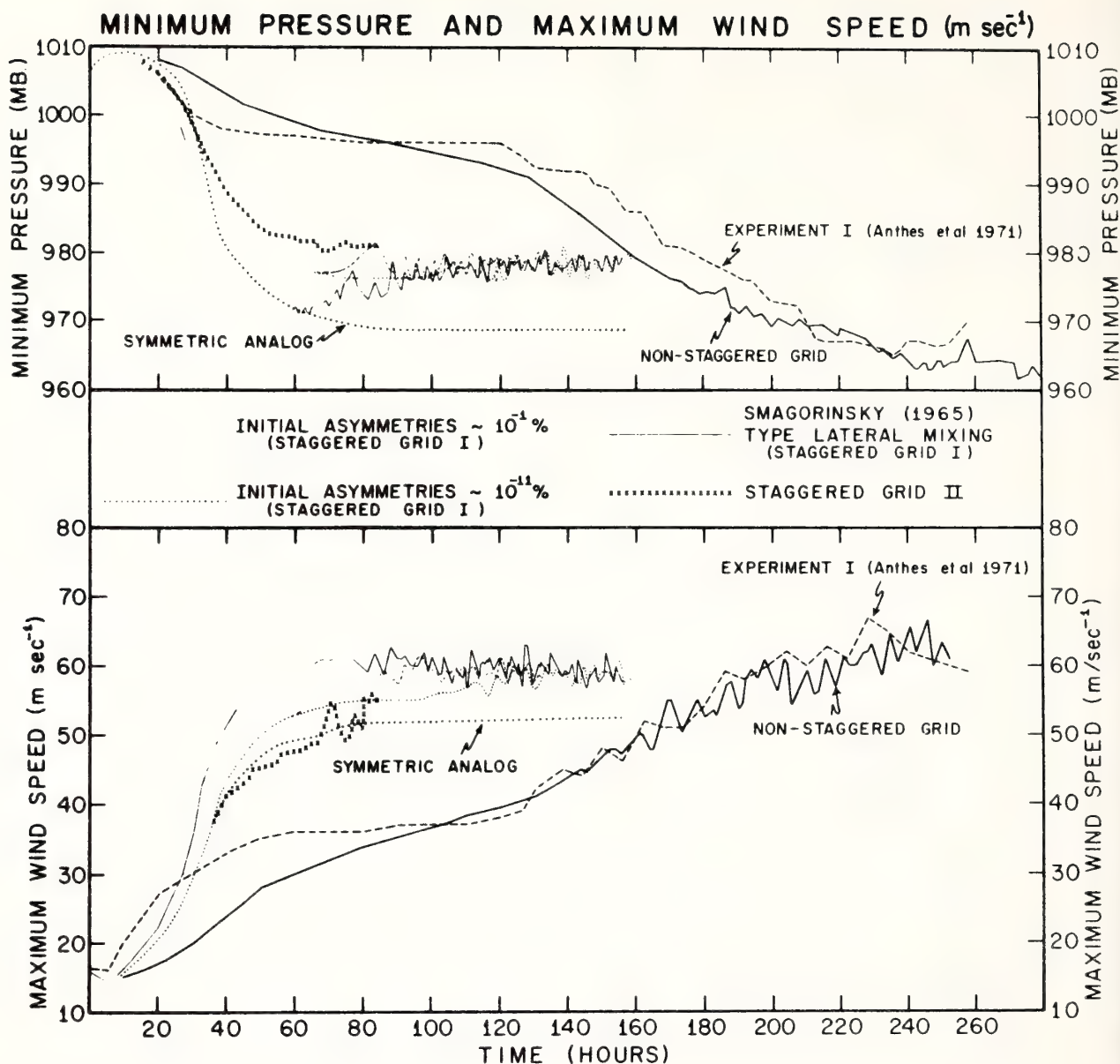


Figure 3. Time variation of (a) minimum pressure and (b) maximum surface wind speed for experiments discussed in this paper.

layer specific humidities in the later model. The structures of the two model experiments are quite similar and are not compared in detail.

Therefore, the primary advantages of adding the water vapor cycle are:

(1) the elimination of some arbitrary assumptions made in the first experiment, (2) the provision for a wider range of initial conditions (variations in initial humidity distributions), and (3) the provision for studying the hurricane water vapor budget.

### 3.2 Increased Horizontal Resolution Utilizing

#### Staggered Horizontal Grids

The behaviors of the two experiments utilizing the non-staggered grid are more similar to each other than to any of the other experiments shown in figure 3. More significantly, during the early stages of the storms, in which asymmetries are negligible, the behavior of the non-staggered grid storms varies markedly from the behavior of the symmetric analog (Anthes et al., 1971b). The differences during the early stages of the storm are related to greater truncation errors in evaluating the pressure gradient force in the asymmetric model. The symmetric analog, which utilized a staggered grid in the radial direction to avoid computational difficulties at the origin, evaluated the pressure gradient over 30 km rather than the 60 km interval used by the asymmetric model. The comparison suggested a staggering of the pressure and velocity variables in the asymmetric model as well.

The staggering of variables in two horizontal dimensions is somewhat more complicated than in one dimension. Two types of staggered grids, shown schematically in figure 4, were tested. The first



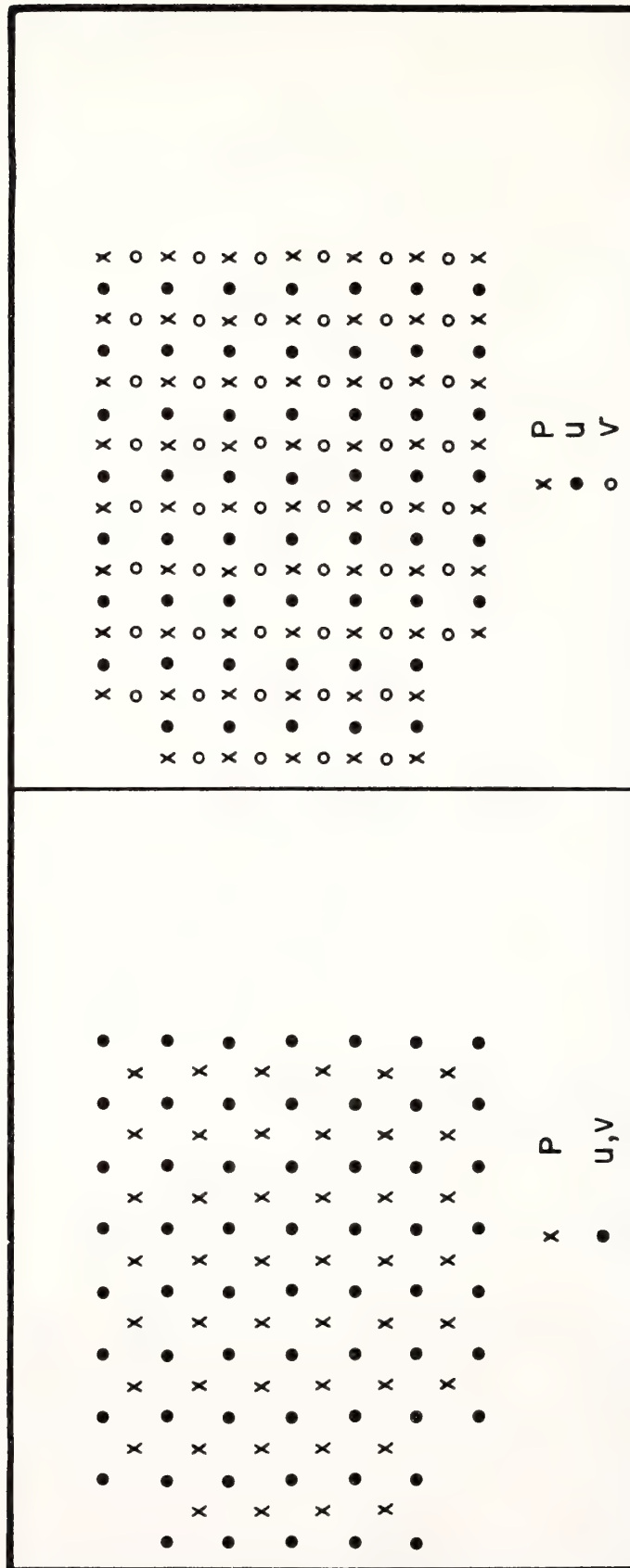


Figure 4. Schematic diagram for two staggered horizontal grids tested with hurricane model. S1 grid is shown on left, S2 grid is shown on right.

(designated by S1), consists of two sets of prediction points, one for the horizontal velocity components and one (offset by  $45^\circ$ ) for all the other variables. The second (designated by S2) consists of three sets of prediction points, one for each horizontal velocity component and a third for the remaining variables. The S2 grid has been used by Lilly (1965) and tested by Grammelvedt (1969). In both staggered grids, the evaluation of the pressure gradient and the horizontal divergence over smaller grid increments necessitates a reduction in the time step to maintain computational stability. Thus the time step of 60 s, which was adequate for the non-staggered grid, must be reduced to 45 s for S1 and to 30 s for S2. The alternate finite difference equations associated with each staggered grid are given in appendix A.

As seen in figure 3, both staggered grids yield very similar results during the first 48 hours of model time. Furthermore, both experiments are more similar to the symmetric analog than are the two experiments with the unstaggered grid. The solutions associated with the S1- and S2-grids diverge considerably after 48 hours, however, with the S2-storm reaching an asymmetric stage much earlier than the S1-storm. Furthermore, the solution associated with the S2-grid deteriorates after 72 hours and finally becomes unstable. The primary cause of this instability seems to be associated with the lateral boundary conditions, since the u and v components are not defined at the same points. This instability and the requirement for the small time step were the prime reasons for the choice of the S1-grid for the current version of the model. The S1-grid, then, provides for an economical increase in horizontal resolution, and

the behavior of the symmetric stage of the model storm utilizing this grid compares favorably with the behavior of the symmetric analog.

### 3.3 Structure of Asymmetric Hurricane

The structures of the storms generated in the later experiments are similar to the storm structure discussed in paper A. An overall view of the three-dimensional, time-dependent structure of a typical experiment (Experiment 2, Table 1) is shown in figure 5, which shows the tracks of particles released in the hurricane circulation over an eight day period. The computed velocities are interpolated in space and time for the computation of the trajectories. (See Anthes et al., 1971c for more details.) Figure 5 reveals a nearly steady state, axisymmetric boundary layer in which air accelerates as it flows inward to the center. Reaching the center, the particles are carried rapidly upward, reaching the outflow layer in about two hours. (Note, the large scale, mean vertical velocities are used to compute the vertical displacements; in reality, a particle would probably be carried upward in a cumulonimbus updraft in considerably less time.) After the particles reach the outflow layer, they decelerate and move outward in a highly asymmetric, unsteady flow.

Figure 5 also shows the path of one particle that is released in the middle troposphere (about 500 mb) rather than in the inflow layer. This particle experiences very little radial motion, and is carried slowly upward as it spirals around the storm center.

Figure 6 shows a typical streamline and isotach pattern in the upper level during the mature stage (156 hours) of Experiment 6. Noteworthy is



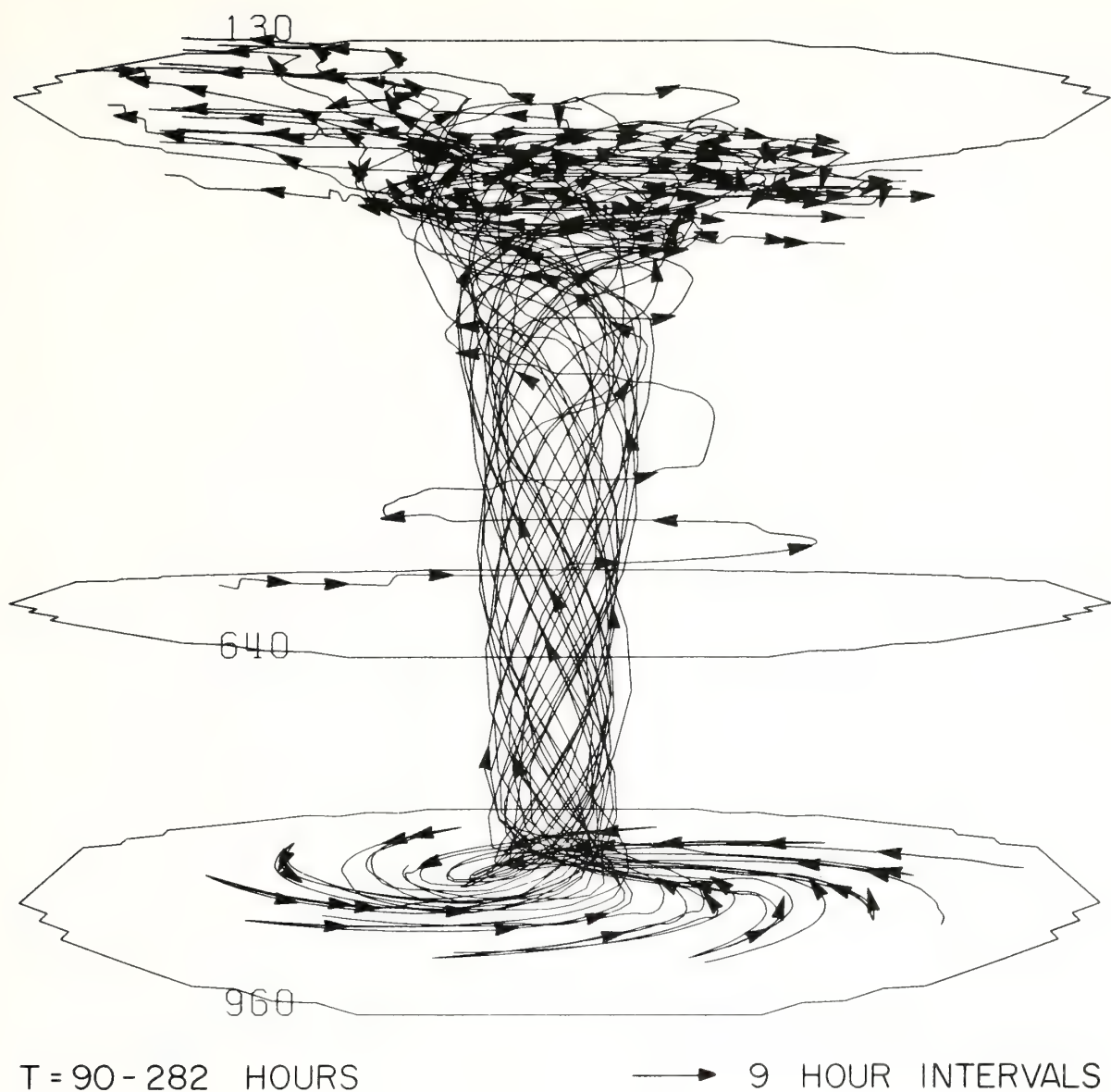


Figure 5. Particle trajectories calculated over a 9-day period in Experiment 2 (see Table 1). The three levels are labeled in mb (approximate). All particles start in boundary layer except one, which is started in the middle troposphere.

the anticyclonic eddy located to the "north" of the storm center. The outflow occurs mainly in two jets, in agreement with storms in nature (Black and Anthes, 1971).

Figure 7 shows the vertically integrated convective heat release, expressed as cm of rain per day. The semi-circle of rainfall rates over 200 cm/day corresponds well to the non-uniform eyewall convective region in real storms (see, for example, Hawkins and Rubsam, 1968). However, figure 7 shows that a rain-free "eye" is not present at this time, and only a region of relatively light rainfall occurs at the center of the storm. The absence of an eye is probably due to the coarse horizontal resolution. The notable spiral bands, with rainfall rates averaging about 2 cm/day, are approximately 90 km wide at large distances from the center, and somewhat wider closer to the center. These bands rotate cyclonically about the storm center and propagate outward at a speed of about 24 knots\*. Although the outer rain bands in nature apparently propagate outward (Gentry, 1964; Senn and Stevens, 1964), we feel that the model rate of 24 knots is somewhat too high. Since the bands are undoubtedly internal gravity waves, improved vertical resolution may give a more realistic phase speed. The band thickness of 90 km is considered fairly acceptable compared to observations, when the coarse resolution of the model is considered. The rainfall rate of 2 cm/day is also considered acceptable, although possibly on the low side, for an average over 90 km.

---

\*This speed is computed by measuring the normal displacement of the outer edge of the bands over a 6-hour period and hence includes the effect of rotation as well as outward propagation.

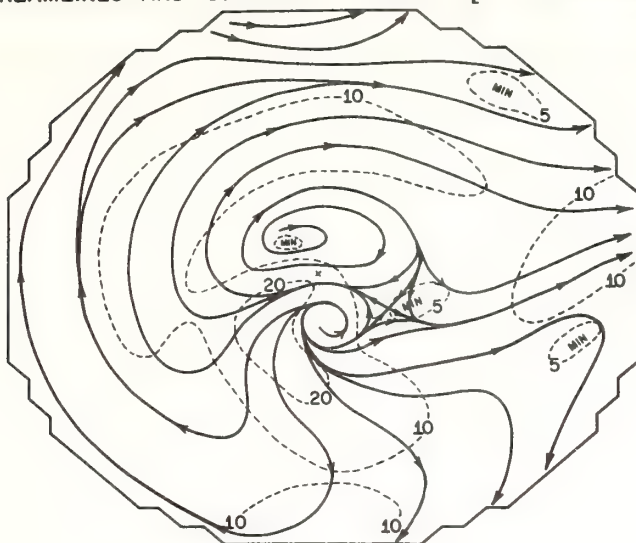
**156 HOURS**

Figure 6. Streamline and isotach ( $\text{m sec}^{-1}$ ) analysis for upper level in Experiment 6 (Table 1) during the mature asymmetric stage (156 hours).

**156 HOURS**

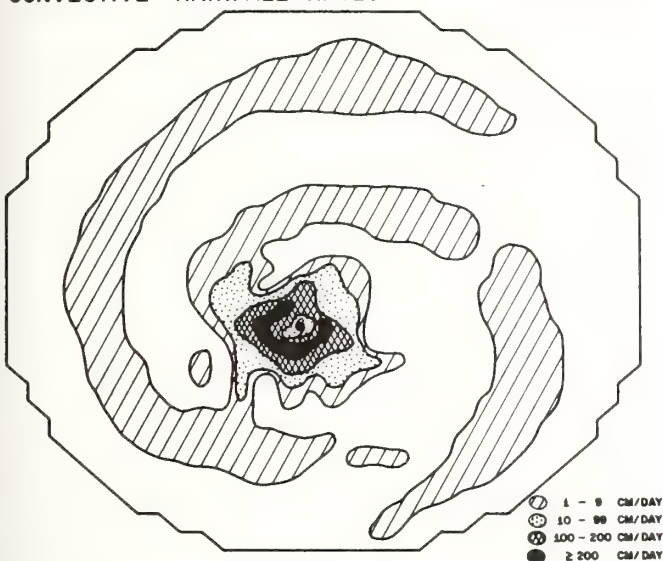


Figure 7. Vertically integrated convective heat release expressed as rainfall rates in cm/day at 156 hours of Experiment 6.

### LOOPING OF MINIMUM SURFACE PRESSURE

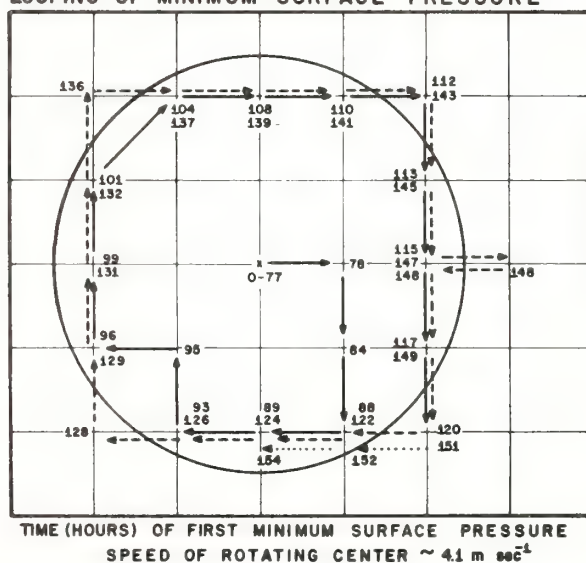


Figure 8. Positions of minimum pressure at selected times for Experiment 6 (Table 1), showing anticyclonic looping during asymmetric stage of storm.



The temperatures inside the bands are not appreciably different from the surrounding environment, in agreement with the mean thermal structure of outer bands in nature (Gentry, 1964). This uniformity in temperature may be related to the near compensation in the thermodynamic equation between the latent heat release and the adiabatic cooling in the region of upward motion, and the relatively short time (about 3 hours) required for the band to move past a particular point. It is noteworthy that, compared to earlier versions of the model, the current version yields spiral bands with the structure most like rain bands in nature.

Although the spiral bands in the model are undoubtedly internal gravity waves modified by latent heat release (Ogura and Charney, 1962), the mechanism for their generation is unknown. There does seem to be an interesting, although obscure, relationship between the bands, which are most pronounced at the top of the boundary layer, and the asymmetries in the outflow layer. In all experiments, the bands are conspicuously absent until the symmetric flow in the upper levels breaks down. Also, the number of bands (two) seems to be associated with the predominance of wave number two in the outflow layer.

The release of latent heat in the spiral bands is entirely convective. The non-convective latent heat release (not shown) occurs entirely within 180 km of the center in a roughly circular pattern. The total non-convective heat release of  $2.0 \times 10^{14}$  watts (Table 1), represents a significant contribution to the total latent heat release ( $12.6 \times 10^{14}$  watts), in agreement with observations (Hawkins and Rubsam, 1968) and symmetric model results (Rosenthal, 1970b).

### 3.4 The Development of the Asymmetric Stage

This section discusses the development and maintenance of the asymmetric features of the circulation using the current (Experiment 6) version of the model. A measure of the asymmetry is the standard deviation (from the circular mean) of any variable. Figure 10 shows the time variation of the standard deviations ( $\sigma$ ) of the tangential and radial wind components and of the temperature at 105 km in the upper level. The early part of the storm's history is quite symmetric, with maximum  $\sigma$  of the wind components about  $0.3 \text{ m sec}^{-1}$ , and for the temperature, about  $0.05^\circ\text{C}$ . The storm becomes quite asymmetric after 60 hours. Thereafter, the  $\sigma$  for the wind components are about equal in magnitude to the azimuthal means at this level. However, the temperature field remains relatively symmetric even during the later stages, with  $\sigma$  rarely exceeding  $1^\circ\text{C}$ . This relative symmetry may be, in part, due to the symmetric boundary conditions on temperature.

Detailed analysis of the development of the asymmetries (Trout, 1972) shows that during the symmetric stage, when the variance of any quantity is small, wave number four accounts for nearly all of the variance. Because of the orientation of wave number four with respect to the four irregular corners of the grid, this early symmetry is probably due solely to the artificial aspects of the irregular boundary. Subsequent to the rapid growth of the variance, however, wave numbers one and two become dominant and account for most of the variance, in agreement with observations (Black and Anthes, 1971). See Trout (1972) for further details.

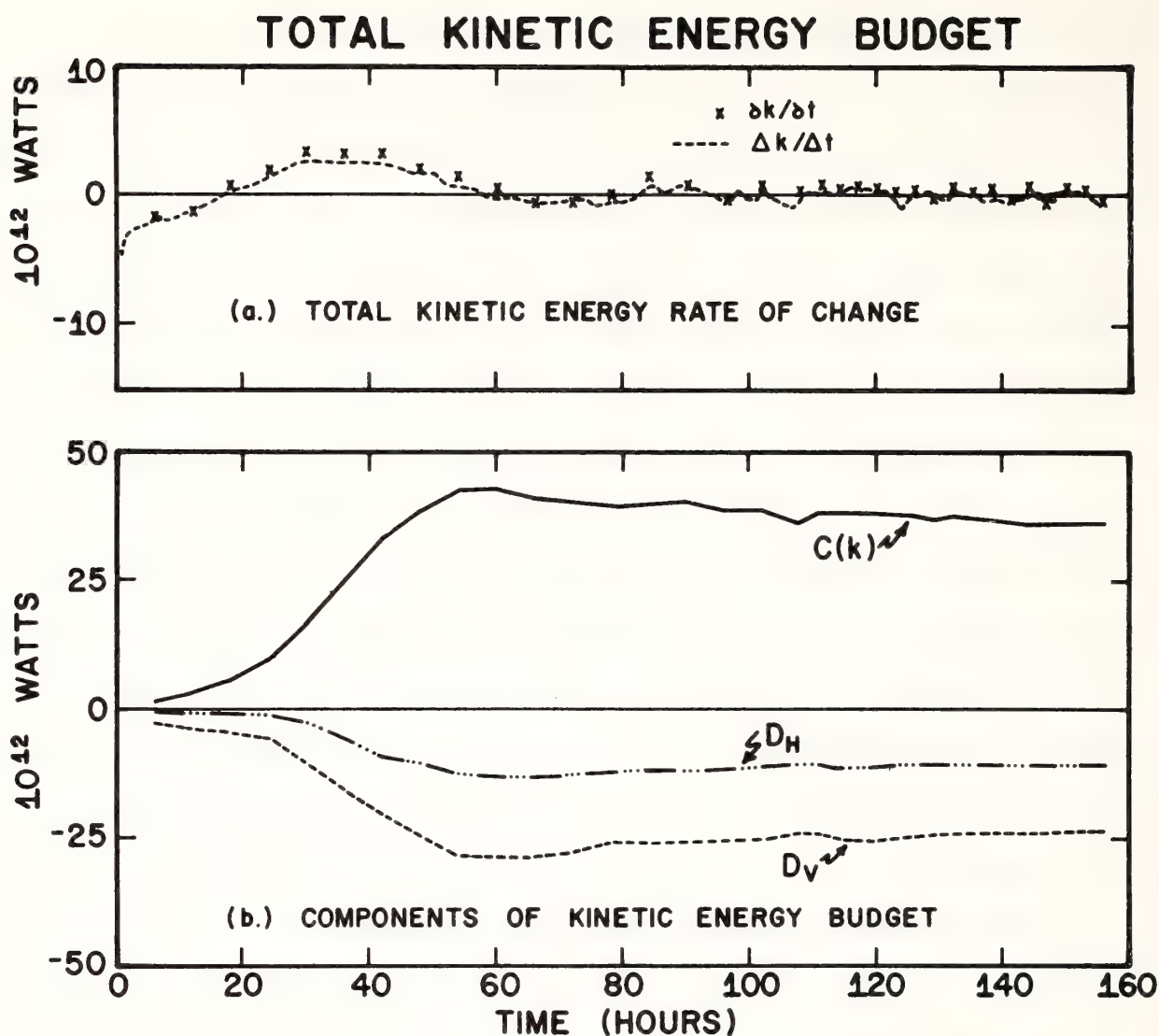


Figure 9(a). Time variation of the observed total kinetic energy change ( $\Delta K / \Delta t$ ) and the change computed from the kinetic energy equation ( $\partial K / \partial t$ ) for Experiment 6.

(b). Individual components of the kinetic energy tendency:  $C(K)$  is the conversion of potential to kinetic energy,  $D_H$  is the dissipation of kinetic energy through lateral eddy viscosity,  $D_V$  is the dissipation of kinetic energy through vertical eddy viscosity and includes the effect of surface drag friction. The flow of kinetic energy through the lateral boundary is negligible in this experiment.



The appearance of large scale asymmetries in the model storms which develop from initially axisymmetric conditions raises at least three questions: 1) What is the source of the initial perturbations? 2) Why do certain wavelengths become predominant? 3) What is the mechanism for growth of these disturbances? The next sections present results from two types of initial perturbations, and show that the initial form of the perturbations is unimportant in determining the dominant scale of the asymmetries. The growth of the initially small disturbances is shown to be a type of dynamic (or inertial) instability in which longer wavelengths are more unstable than the shorter wavelengths. The important mechanism for the growth of the eddies is the barotropic conversion of mean azimuthal kinetic energy to eddy kinetic energy.

### 3.5 The Initial Perturbations

The initial asymmetries in the preliminary experiment (I), and in the experiments discussed so far in this paper arise from non-symmetric truncation and roundoff errors in the finite difference schemes. These initial asymmetries (see fig. 11) after one time step are (in Experiment 1) on the order of  $10^{-10}\%$  on the interior of the grid and  $10^{-25}\%$  on the boundaries. Inspection of each term in the forecast equations showed these asymmetries to arise from the divergence terms in the continuity equation.

The magnitude and distribution of the initial perturbations, and consequently the time required for the disturbances to manifest themselves in the large scale flow, varies with the grid and finite difference scheme. The asymmetric stage begins at 120 hours for the non-staggered, grid, at 100 hours for the S1-grid and at 60 hours for the S2-grid.

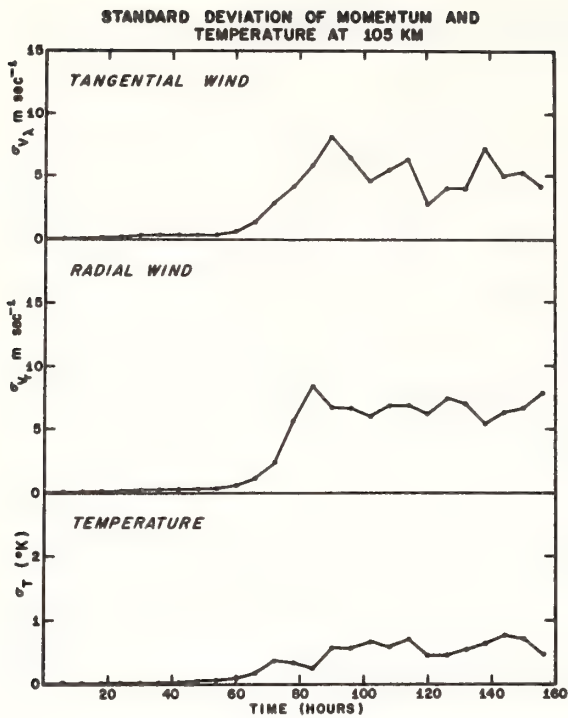


Figure 10. Time variation of standard deviations of tangential and radial wind components, and temperature for the upper level at a radius of 105 km in Experiment 6.

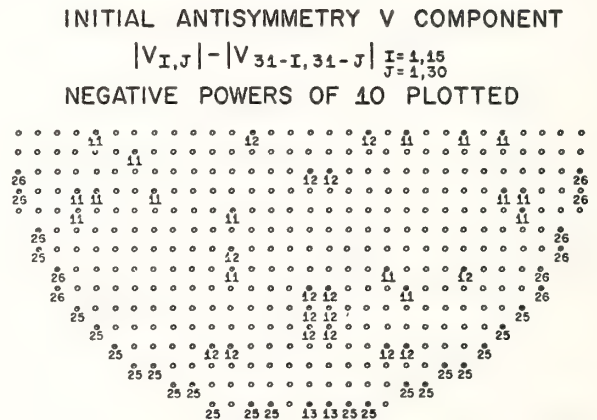


Figure 11. Asymmetries in the v-component after one time step in the preliminary experiment. These asymmetries are due to truncation and roundoff errors alone and are functions of the grid system and the finite difference scheme.

Although truncation errors produce perturbations which eventually grow to the interesting asymmetric features of the model, it is more appealing to deliberately introduce perturbations of known amplitude and variance. Therefore, initial asymmetries on the order of  $10^{-1}\%$  (ten orders of magnitude greater than the perturbations due to truncation errors) were introduced by adding random numbers to the initial  $u$  and  $v$  components. As shown in figure 3, the asymmetric stage is reached much earlier (60 hours rather than 100 hours) with the greater amplitude perturbations. (The onset of the asymmetric stage is marked in figure 3 by the rise in minimum pressure preceeding the oscillations in the pressure.) It is important to note, however, that during the asymmetric stage the structures of the model experiments are very similar (see also Table 1), indicating that the form of the initial asymmetries is unimportant in determining the ultimate structure of the asymmetric circulation.

### 3.6 Role of Dynamic Instability in the Development of the Asymmetries

The theory of dynamic instability has been investigated by many individuals over the years. The reader is referred to Kuo (1949), Godson (1950) and Van Mieghem (1951) for a review and discussion of the generalized concept of dynamic instability.

In the application of dynamic instability to the hurricane problem, meteorologists have generally referred to the growth of symmetric radial displacements in an axisymmetric vortex (Sawyer, 1947; Alaka, 1963; Yanai, 1964; Yanai and Tokioka, 1969). However, this instability, defined by the criterion



$$\left(\frac{\partial r \overline{v_\lambda}}{r \partial r} + f\right) \overline{Z} < 0, \quad Z = \left(\frac{2v_\lambda}{r} + f\right), \quad (24)$$

where  $v_\lambda$  is the tangential wind, and the  $\overline{(\quad)}$  operator refers to an azimuthal average, does not appear to play an important role in the intensification of symmetric model storms (Yamasaki, 1968; Ooyama, 1969; Rosenthal, 1969a).

A second type of dynamic instability which seems relevant in the asymmetric hurricane model is the instability represented by the growth of azimuthal perturbations at the expense of the axisymmetric flow. For purely horizontal, non-divergent flow, a necessary and sufficient criterion is

$$\frac{\partial}{\partial r} \left( \frac{r \partial r \overline{v_\lambda}}{\partial r} + f \right) = 0 \quad (25)$$

somewhere in the domain (Kuo, 1949). However, the derivation of (25) depends on the horizontal perturbations vanishing at the outer boundary, which is not strictly the case in the model in which the winds on the boundaries vary through the extrapolation procedure discussed earlier (see Section (2.6)).

It may also be shown that, for non-divergent, horizontal flow (24) is a sufficient criterion for the growth of azimuthal perturbations, regardless of the form of the perturbations on the boundary.

In Experiment 6 (the current version of the model), we have considered the criterion defined by (24) and (25). Figure 12 shows the time variation of the minimum azimuthal averages of  $\zeta_a$ ,  $Z$ , and the minimum value of the product,  $\overline{\zeta_a Z}$  for the upper (level 1½) and middle (level 2½)

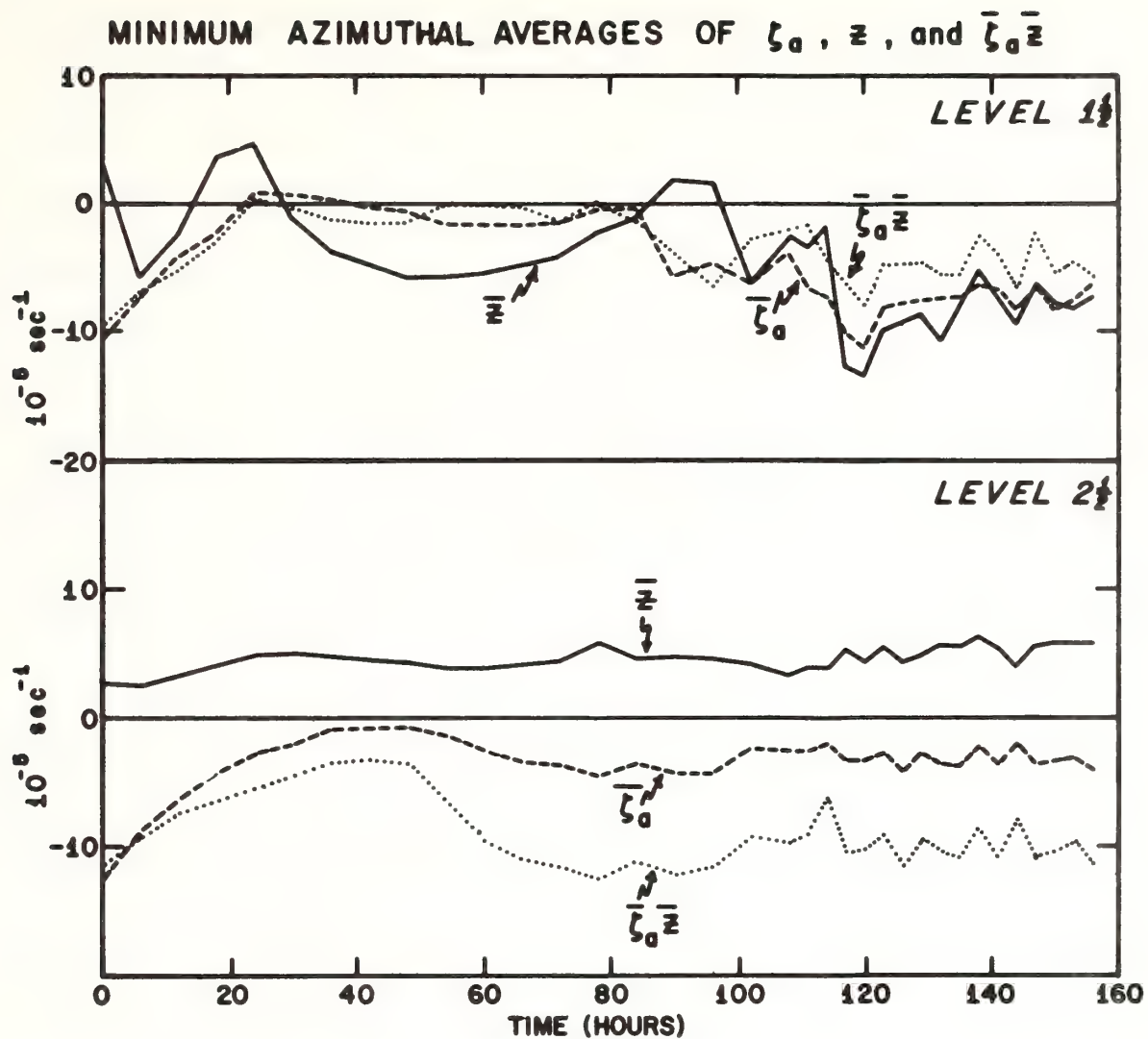


Figure 12. Time variation of minimum azimuthal averages of  $\bar{\zeta}_a$ ,  $\bar{z}$ , and  $\bar{\zeta}_a \bar{z}$  for levels  $1\frac{1}{2}$  and  $2\frac{1}{2}$  in Experiment 6.

tropospheric layers. Negative absolute vorticity is present in the initial conditions at both levels beyond 300 km radius. During the first 40 hours this outer area of negative  $\zeta_a$  decreases in intensity in both layers. After about 48 hours, a new region of negative  $\zeta_a$  appears close to the storm center, at a radius of about 150 km. This inner region persists for the remainder of the forecast.

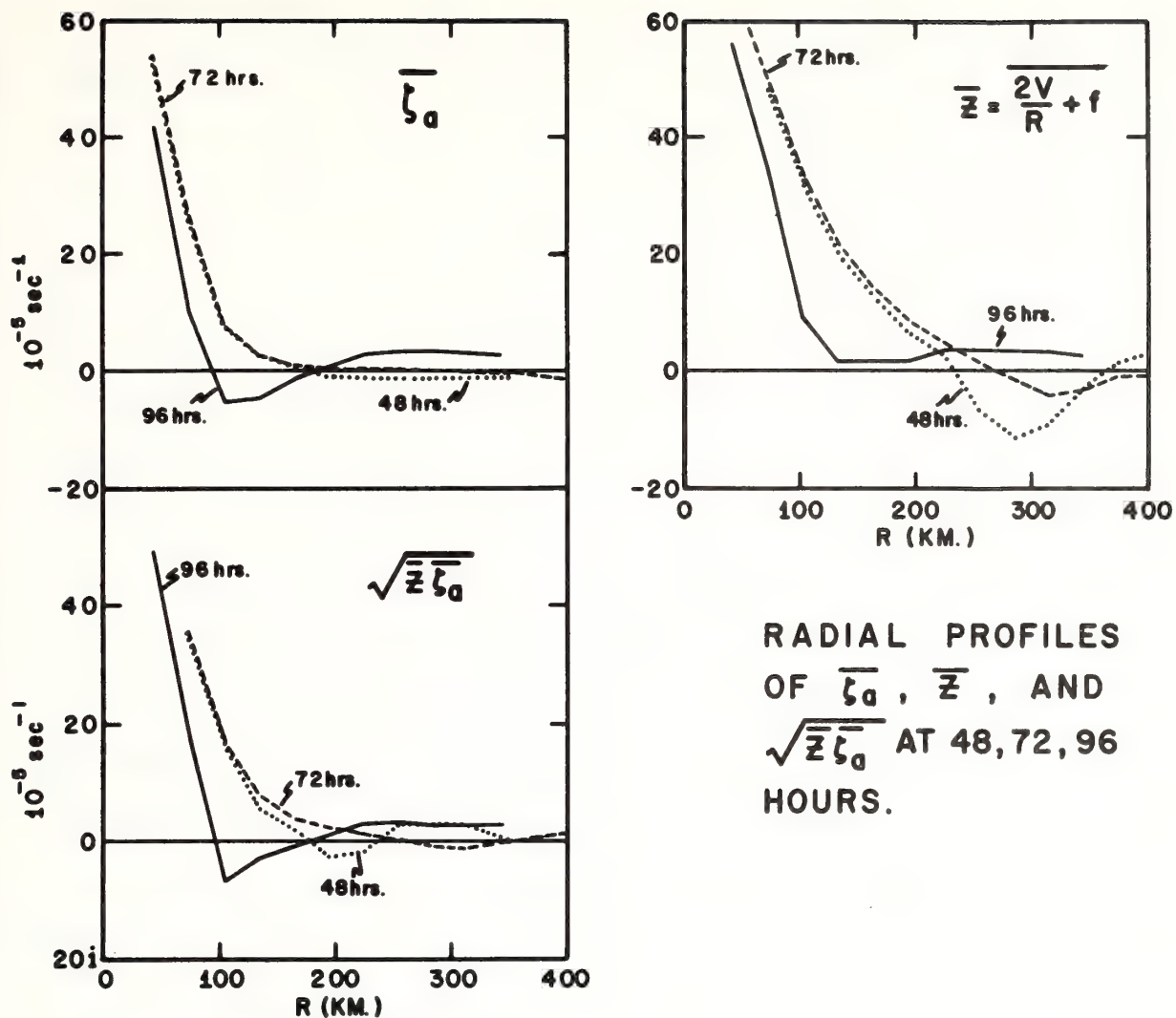
Figure 12 also shows that negative azimuthal averages of  $Z$  exist in level  $1\frac{1}{2}$ , but never at level  $2\frac{1}{2}$  where the flow is always cyclonic. There are regions in both levels where the product is negative, thus criterion (24) is satisfied in both levels over most of the forecast period.

Although the asymmetries at level  $1\frac{1}{2}$  have been emphasized, there is significant eddy kinetic energy present in the middle tropospheric layer as well. The mean radial pressure gradient and the mean tangential flow are much stronger at this level, however, so that the asymmetric portion of the flow is a smaller percentage of the mean flow. The strong, symmetric pressure gradient force at this level is undoubtedly resisting the development of the azimuthal perturbations to a greater extent than the weaker pressure field in the outflow layer.

Figure 13 shows radial profiles of  $\bar{Z}$ ,  $\bar{\zeta}_a$ , and  $\bar{\zeta}_a \bar{Z}$  for selected times at level  $1\frac{1}{2}$ . All the profiles have a minimum in absolute vorticity, so that criterion (25) is also satisfied during the forecast. We next investigate the generation of the negative vorticity near the center. The vorticity equation in  $\sigma$ -coordinates may be written

$$\frac{d\zeta_a}{dt} = D + T + F \quad (26)$$





RADIAL PROFILES  
OF  $\zeta_a$ ,  $\bar{Z}$ , AND  
 $\sqrt{\bar{Z} \zeta_a}$  AT 48, 72, 96  
HOURS.

Figure 13. Radial profiles of  $\zeta_a$ ,  $\bar{Z}$ , and  $\sqrt{\bar{Z} \zeta_a}$  at 48, 72, and 96 hours of Experiment 6.

where the divergence term,  $D$ , is

$$D = -\zeta_a \nabla \cdot \vec{V} \quad (27)$$

the tilting term,  $T$ , is

$$T = \frac{\partial \dot{\sigma}}{\partial y} \frac{\partial u}{\partial \sigma} - \frac{\partial \dot{\sigma}}{\partial x} \frac{\partial v}{\partial \sigma} \quad (28)$$

and the friction term,  $F$ , is

$$F = \frac{\partial F(v)}{\partial x} - \frac{\partial F(u)}{\partial y} \quad (29)$$

In (29)  $F(v)$  and  $F(u)$  represent the vertical and horizontal friction terms for the  $v$  and  $u$  components respectively. Given an initially positive absolute vorticity pattern, the divergence term by itself cannot produce negative  $\zeta_a$ . Production of negative  $\zeta_a$  must come from the tilting term,  $T$ . Figure 14 shows minimum azimuthal averages of  $D$ ,  $T$ , and the sum,  $(D + T)$ . The friction term,  $F$ , was also computed, and was much smaller in magnitude than either  $D$  or  $T$ . The terms in (27) through (29) were computed by interpolating the velocity components to the  $\sigma$ -levels and approximating the derivatives with centered differences. Figure 14 shows that both the divergence and tilting term contribute to the negative tendency. The spatial distributions of the minimums of  $T$  and  $D$  reveal the minimum divergence term to occur very close to the vortex center where the vorticity is large and positive and the divergence is maximum. The tilting term minimum occurs farther out, beyond the radius of maximum upward motion, where  $\frac{\partial \dot{\sigma}}{\partial r} > 0$ . (For a symmetric vortex,  $T = -\frac{\partial \dot{\sigma}}{\partial r} \frac{\partial v_\lambda}{\partial \sigma}$  and since  $\frac{\partial v_\lambda}{\partial \sigma}$  is positive in the hurricane, the negative contribution occurs with  $\frac{\partial \dot{\sigma}}{\partial r} > 0$ .)

The production of negative  $\zeta_a$  may be physically interpreted from angular momentum considerations, where the angular momentum,  $M$ , is defined by

$$M = rv_\lambda + \frac{1}{2}fr^2 \quad (30)$$

and 
$$\overline{\zeta_a} = \frac{\partial \overline{M}}{\partial r} . \quad (31)$$

In the early stages of cyclone development,  $M$  increases radially outward. The reversal of the radial gradient of  $M$  (production of negative  $\zeta_a$ ) may occur as air at large distances (high  $M$ ) is advected inward in the boundary layer. When this air is ultimately carried upward in the narrow ring of ascent near the center of the vortex, it may, in spite of some frictional loss to the sea surface, retain a higher value of  $M$  than air at the same level but at a larger radial distance. The air at larger distances, in the middle levels, experiences little radial or vertical motion as shown by the middle level trajectory in figure 5.

In summary, substantial regions of negative absolute vorticity are produced in the middle and upper tropospheric layers through the tilting term in the vorticity equation. Both criterion for the development of azimuthal perturbations (in horizontal, non-divergent flow) are satisfied throughout the integration. Preference for the growth of longer waves (wave numbers one and two) are probably the result of the selective effects of static stability in the presence of horizontal divergence (Houghton and Young, 1970). In the next section we investigate the eddy kinetic energy budget.



### 3.7 Eddy Kinetic Energy Budget

The eddy kinetic energy equation may be derived by forming the equation for the azimuthal mean kinetic energy and subtracting this equation from the total kinetic energy equation. The resulting equation is

$$\frac{\partial \overline{k_e}}{\partial t} = C_H + C_V + B + F \quad (32)$$

where the eddy kinetic energy is defined

$$\overline{k_e} \equiv \frac{\overline{u'^2} + \overline{v'^2}}{2} \quad (33)$$

and

$$C_H = -\overline{v'^2} \frac{\partial \overline{v_r}}{\partial r} + \overline{v'_r v'_\lambda} \left( \frac{2\overline{v_\lambda}}{r} - \frac{\partial r \overline{v_\lambda}}{r \partial r} \right) - \frac{\overline{v_r v_\lambda'^2}}{r} \quad (34)$$

$$C_V = -\overline{\sigma' v'_r} \frac{\partial \overline{v_r}}{\partial \sigma} - \overline{\sigma' v'_\lambda} \frac{\partial \overline{v_\lambda}}{\partial \sigma} \quad (35)$$

$$B = -\frac{\overline{v'_\lambda}}{r} \frac{\partial \overline{\phi'}}{\partial \lambda} - \overline{v'_r} \frac{\partial \overline{\phi'}}{\partial r} - \left( \frac{RT}{P} \right) \left( \overline{v'_r} \frac{\partial \overline{p'}}{\partial r} + \frac{\overline{v'_\lambda}}{r} \frac{\partial \overline{p'}}{\partial \lambda} \right) \\ - \left( \frac{RT}{P} \right)' \left( \overline{v'_r} \frac{\partial \overline{p'}}{\partial r} + \frac{\overline{v'_\lambda}}{r} \frac{\partial \overline{p'}}{\partial \lambda} \right) - \left( \frac{RT}{P} \right)' \overline{u'} \frac{\partial \overline{p}}{\partial r} \quad (36)$$

$$F = \overline{v'_r F'_r} + \overline{v'_\lambda F'_\lambda} \quad (37)$$

The term  $C_H$  represents the conversion of mean to eddy kinetic energy through horizontal, barotropic processes, and should be the predominant source of energy for the eddies if dynamic instability is the important mechanism in the eddy generation. The term  $C_V$  represents the effect of vertical eddies. The term  $B$  represents baroclinic effects and would be predominant if baroclinic instability were important. (The last two terms in  $B$  are several orders of magnitude smaller than the first three terms.) Finally,  $F$  represents the effects of asymmetries in the parameterization of the sub-grid scale eddy stresses.

Figure 15 shows the time variation of the volume integral of  $k_e$ , defined by

$$k_e = - \frac{2\pi}{g} \int_0^{R_m} r \int_1^0 \frac{\partial k_e}{\partial t} p^* d\sigma dr \quad (38)$$

where  $R_m$  is the edge of the domain (about 440 km). Because the computation of the various terms in (34) through (37) requires interpolation in the vertical, as well as from the cartesian grid to a polar coordinate grid, the values shown in figure 15 should be considered approximate.

Figure 15 shows that the significant positive contribution to the eddy kinetic energy is  $C_H$ , representing the barotropic conversion of mean to eddy kinetic energy, and provides strong support for the hypothesis that dynamic instability is present in the model. The vertical eddy term,  $C_V$ , is slightly positive at first, then slightly negative toward the end of the forecast. The baroclinic term (B) and the friction term (F) are negative throughout the forecast.

The eddy kinetic energy budget establishes dynamic, or inertial instability as the mechanism for the breakdown in symmetry and the development of large scale eddies in the outflow layer. These eddies continually extract kinetic energy from the mean circulation. The mean kinetic energy is maintained through the low-level cross isobar flow associated with the mean meridional circulation and the upward transport of kinetic energy by the rising motion near the center of the storm.

Figure 16 shows radial profiles of the various terms in the eddy kinetic energy equation at a typical time (138 hours) during the forecast. The terms are less reliable near the origin where the errors

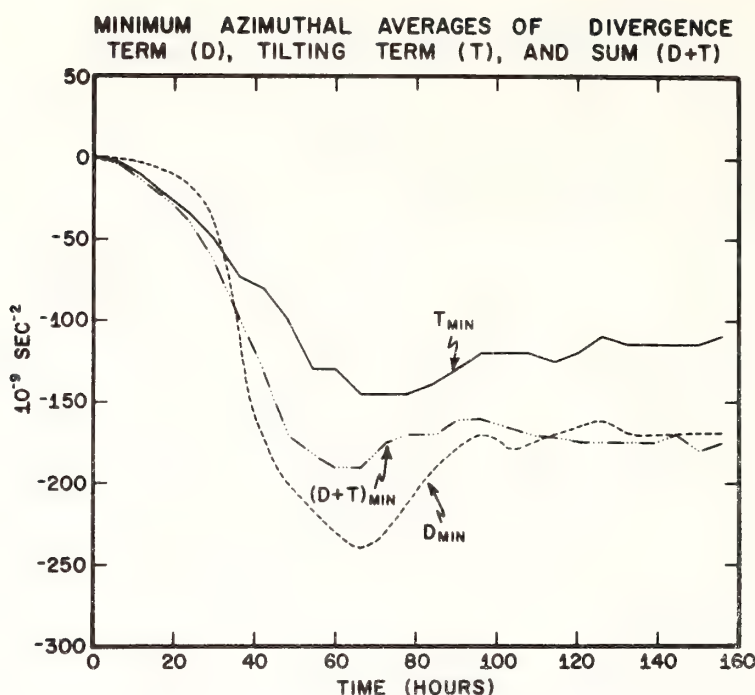


Figure 14. Time variation of minimum azimuthal averages of divergence term (d), tilting term (T), and sum (D+T) in the vorticity equation at level 2 for Experiment 6.

## EDDY KINETIC ENERGY BUDGET

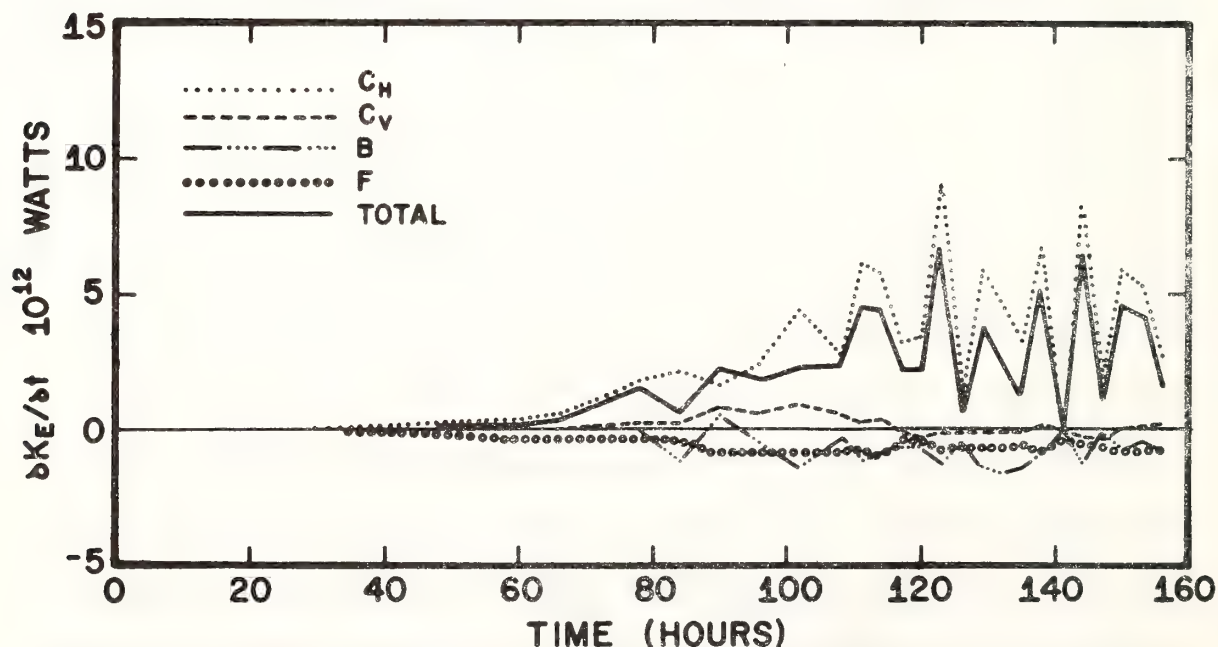


Figure 15. Time variation of total eddy kinetic energy budget. The term  $C_H$  represents the conversion of azimuthal mean to eddy kinetic energy through horizontal, barotropic processes;  $C_V$  represents the effects of vertical eddies;  $B$  represents baroclinic effects; and  $F$  represents frictional effects. See section 3.7 for discussion of these terms.



# RADIAL PROFILES of COMPONENTS of EDDY KINETIC ENERGY CONVERSION

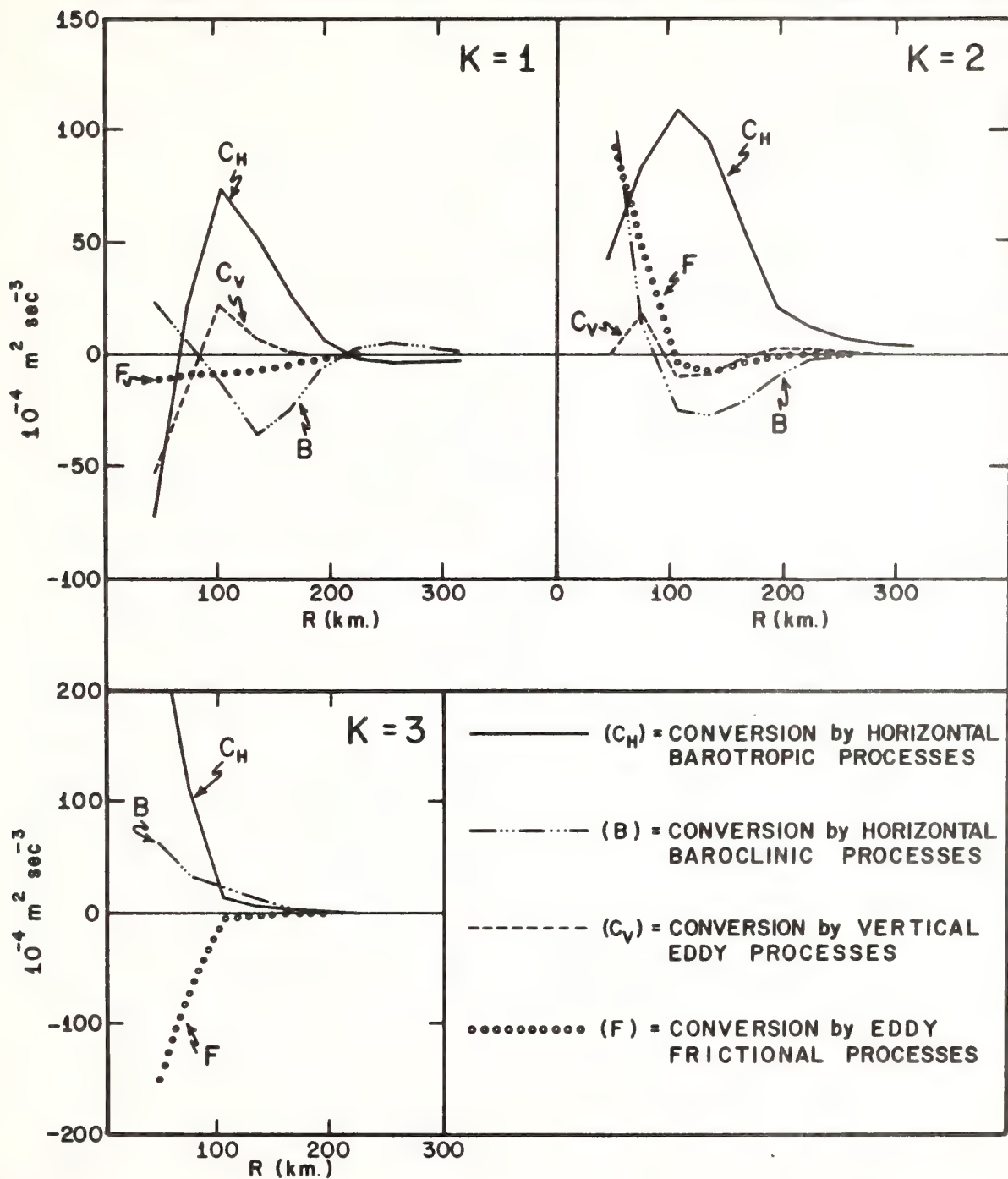


Figure 16. Radial profiles of terms in eddy kinetic energy budget at 138 hours in Experiment 6.

associated with the interpolation to the polar grid are maximum. From figure 16, the maximum conversion occurs around 100 km. The baroclinic processes consume eddy kinetic energy in the middle and upper troposphere. The slight positive contribution by baroclinic processes in the boundary layer may be associated with the generation of eddy kinetic energy on the scale of the spiral bands.

### 3.8 Increase of Sea Temperature in One Quadrant

Empirical results (Palmén, 1948; Miller, 1957; Perlroth, 1962) and symmetric hurricane model calculations (Ooyama, 1968) indicate a strong relationship between sea surface temperature and hurricane intensity. Figure 17 shows the effect of varying the sea surface temperature over a 2-degree range for 20 hours on the symmetric analog. The immediate response and the total range of  $26 \text{ m sec}^{-1}$  in the maximum wind speed confirms the sensitivity of the hurricane to small variations in sea surface temperature.

In addition to the recognized importance of the sea surface temperature to the intensity of the storm, it is sometimes suggested that horizontal sea-temperature gradients may also affect the storm's motion, perhaps through a differential enhancement of convective latent heat release. Although the looping motion of the asymmetric model storm is small, and poorly understood, it does afford the opportunity for at least a crude experiment to investigate the effect, if any, of sea surface temperature differences on the storm's motion.

Figure 18 shows the effect of raising the sea temperature from 302 to 303°K in the "northeast" quadrant of the grid over the last 30 hours

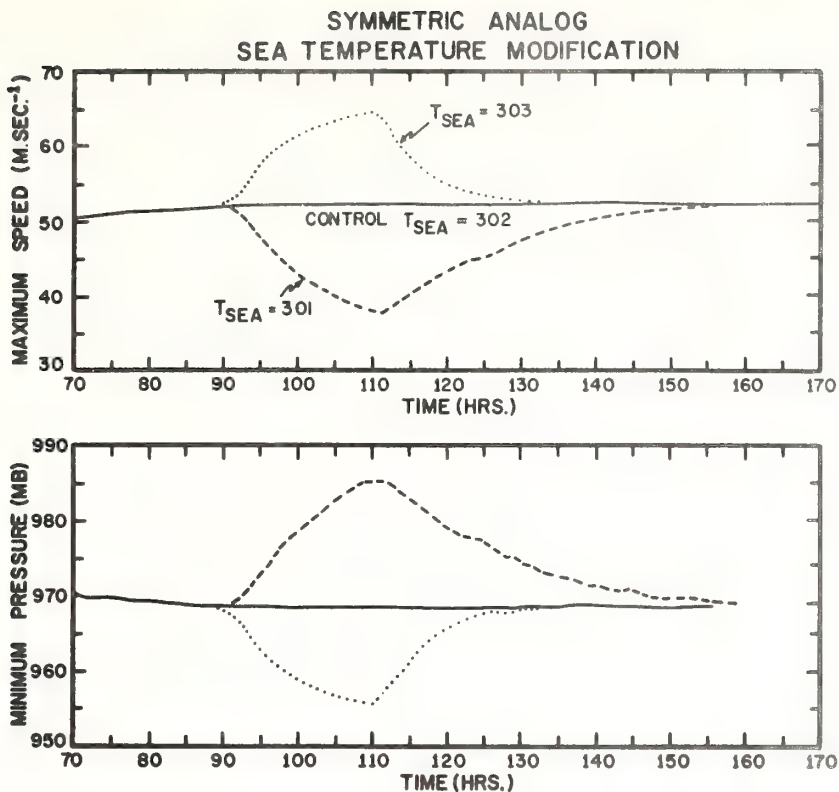


Figure 17. Effect of increasing and decreasing sea temperature by  $1^{\circ}\text{C}$  on maximum wind speed and minimum pressure.

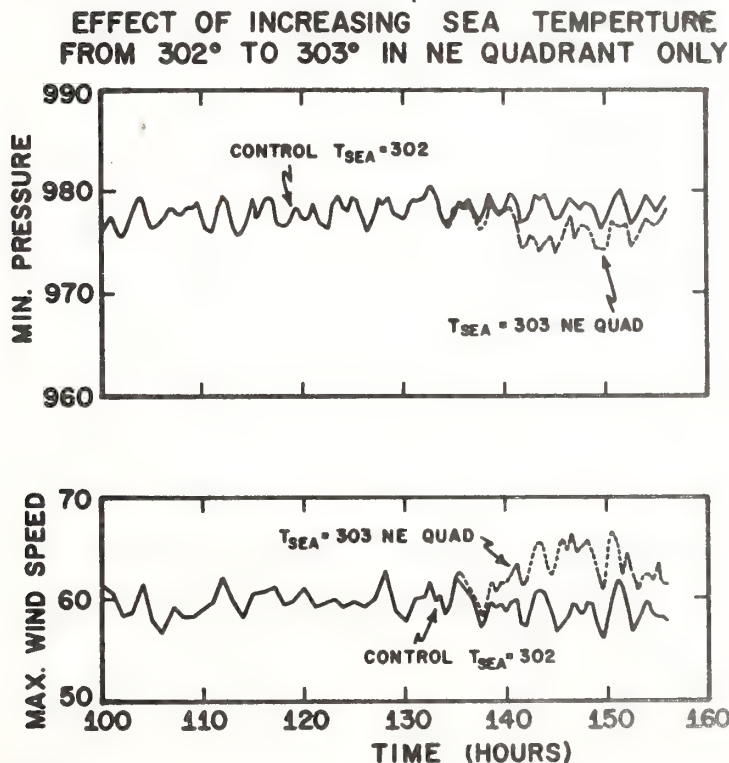


Figure 18. Effect of increasing sea temperature by  $1^{\circ}\text{C}$  in NE Quadrant alone for asymmetric model, Experiment 6.



of Experiment 6. The sea temperature over the rest of the grid remains unchanged. The position of the storm center at 136 hours, shown in figure 8, is in the 'northwest' quadrant where the temperature is constant. As the storm moves over the warmer water (at about 140 hours) an increase in intensity occurs, reaching a maximum at about 146 hours when the wind speed is about  $6 \text{ m sec}^{-1}$  greater than that of the control. As the storm moves back over colder water, the differences from the control become less.

If the differing sea temperature field affected the storm motion, one would expect at least a small change in speed or direction as the storm moved over the warmer water. There was, however, no discernable change in the motion of the storm, in spite of a considerable (10%) change in the storm's intensity. This result suggests, although by no means proves, that storm motion is not appreciably affected by horizontal temperature gradients in the sea temperature.

#### 4. SUMMARY AND CONCLUSIONS

Additional experiments with an improved version of an isolated, asymmetric model of the tropical cyclone are described. Increased horizontal resolution is achieved through the horizontal staggering of the variables. An explicit water vapor cycle is included which enables the study of the hurricane's water vapor budget and the simulation of non-convective heat release. The modeling of the horizontal diffusion of heat, water vapor, and momentum is considered more realistic in the current version of the model.

The development of the asymmetric structure of the model hurricane is examined in considerable detail. The asymmetries in the outflow layer are shown to result from dynamic instability, with the source of eddy kinetic energy being the mean azimuthal flow.

Well-defined spiral bands of convective heat release occur in these experiments. These bands propagate outward at a speed of about 24 knots, and compare favorably in structure with outer rain bands in nature.

An anticyclonic looping of the vortex center is observed during the later stages of these experiments. Although the mechanism for this motion is not clear, the looping seems to be closely associated with the asymmetries in the upper level circulation.

The intensity of the model is found to be sensitive to the sea surface temperature, in agreement with previous results. However, the looping motion of the storm is not noticeably affected as the storm passes over water of varying temperature.

The structure of the model storm, and the components of the energy budget agree quite well with empirical results and with previous symmetric model results, in spite of the coarse vertical and horizontal resolution.

## ACKNOWLEDGMENTS

Rapid progress with NHRL's asymmetric hurricane model would not have been possible without the firm background of work with the symmetric model by the head of the theoretical studies group, Dr. Stanley L. Rosenthal. His support and suggestions concerning this work are gratefully acknowledged.

Mr. James Trout aided substantially in the programming of various aspects of the current model. Mr. Robert Carrodus and Charles True were responsible for the figures, and Mrs. Mary Jane Moss typed the manuscript.



## APPENDIX A - FINITE DIFFERENCE EQUATIONS

### A.1: Finite Difference Equations for Staggered Grid S-1

In Appendix A, the following notation will be useful (Shuman and Stackpole, 1968):

$$\alpha_x \equiv \frac{\alpha_{i,j+\frac{1}{2}} - \alpha_{i,j-\frac{1}{2}}}{\Delta x}$$

$$\overline{\alpha}^x \equiv \frac{\alpha_{i,j+\frac{1}{2}} + \alpha_{i,j-\frac{1}{2}}}{2}$$

A.1.1

$$\alpha_y \equiv \frac{\alpha_{i+\frac{1}{2},j} - \alpha_{i-\frac{1}{2},j}}{\Delta y}$$

$$\overline{\alpha}^y \equiv \frac{\alpha_{i+\frac{1}{2},j} + \alpha_{i-\frac{1}{2},j}}{2}$$

We also introduce the following 4-point operators:

$$\overline{\alpha}^y \equiv \frac{\alpha_{i+1,j} + 2\alpha_{i,j} + \alpha_{i-1,j}}{4}$$

A.1.2

$$\overline{\alpha}^x \equiv \frac{\alpha_{i,j+1} + 2\alpha_{i,j} + \alpha_{i,j-1}}{4}$$

For vertical differences and averages, we define

$$\overline{\alpha}^\sigma \equiv (\alpha_{k+\frac{1}{2}} + \alpha_{k-\frac{1}{2}})/2$$

A.1.3

$$\delta\alpha \equiv (\alpha_{k+\frac{1}{2}} - \alpha_{k-\frac{1}{2}})$$

The finite difference equations associated with staggered grid S-1 for the u- and v-component equations of motion are:

$$\begin{aligned} \frac{\partial p^*u}{\partial t} \approx & -(\overline{u^x} \overline{p^*u^y})_x - (\overline{u^y} \overline{p^*v^x})_y - \frac{\overline{u^xy} \overline{p^*u}^\sigma}{\delta\sigma} \\ & - \overline{p^*xy} \overline{\phi_x^\sigma} - R\overline{T^xy} \overline{p_x^*y} + fp^*v \\ & + [K_H(p^*u)_x]_x + [K_H(p^*u)_y]_y + F_V(u), \end{aligned} \quad A.1.4$$

$$\begin{aligned} \frac{\partial p^*v}{\partial t} \approx & -(\overline{v^x} \overline{p^*u^y})_x - (\overline{v^y} \overline{p^*v^x})_y - \frac{\overline{v^xy} \overline{p^*v}^\sigma}{\delta\sigma} \\ & - \overline{p^*xy} \overline{\phi_y^\sigma} - R\overline{T^xy} \overline{p_y^*x} - fp^*u \\ & + [K_H(p^*v)_x]_x + [K_H(p^*v)_y]_y + F_V(v) \end{aligned} \quad A.1.5$$

where the finite difference analogs for the vertical friction terms,  $F_V(u)$  and  $F_V(v)$  have been presented earlier (6). In section A.1, the terms  $(p^*u)$  and  $(p^*v)$  represent  $(\overline{u^xy})$  and  $(\overline{v^xy})$  respectively.

The analogs for the continuity and thermodynamic equations are:

$$\frac{\partial p^*}{\partial t} \approx -(\overline{p^*u})_x^y - (\overline{p^*v})_y^x - p^* \frac{\delta\sigma}{\delta\sigma}, \quad A.1.6$$

and

$$\begin{aligned} \frac{\partial p^*T}{\partial t} \approx & -(\overline{p^*u} \overline{T^x})_x - (\overline{p^*v} \overline{T^y})_y - p^* \frac{\delta\sigma \overline{T}^\sigma}{\delta\sigma} \\ & + \frac{RT\omega}{c_p\sigma} + \frac{p^*}{c_p} \dot{Q} + p^* [K_T(T)_x]_x + p^* [K_T(T)_y]_y, \end{aligned} \quad A.1.7$$

with the finite difference form for  $\omega$  given by

$$\begin{aligned}\omega &= \frac{dp}{dt} = p^* \dot{\sigma} + \sigma \frac{dp^*}{dt} \\ &\approx p^* \dot{\sigma} + \bar{\sigma} \left( \frac{\partial p^*}{\partial t} + \bar{u}^{xy} \bar{p}_x^{*x} + \bar{v}^{xy} \bar{p}_y^{*y} \right).\end{aligned}\tag{A.1.8}$$

As in paper A, the notation  $\bar{T}^\sigma$  in (A.1.7) signifies that potential temperature is linearly interpolated between  $\sigma$ -levels rather than temperature itself.

The finite difference analogs for the horizontal derivatives in the water vapor forecast are analogous to the equation for temperature and are not given.

In (A.1.4) and (A.1.5), the use of the 4-point averaging operator is necessary if the finite difference equations are to conserve kinetic energy. The kinetic energy equation for this system may be written

$$\frac{\partial \bar{p}^{*xy} k}{\partial t} + k \left( \frac{\partial \bar{p}^{*xy}}{\partial t} + \nabla \cdot \bar{p}^{*xy} \vec{V} \right) + \nabla \cdot \bar{p}^{*xy} \vec{V} k + \frac{\vec{V}_i \cdot \bar{p}^{*xy} \delta \vec{\sigma} \vec{V}_i}{\delta_i \sigma} = 0.\tag{A.1.9}$$

For conservation of kinetic energy, the part of the finite difference analogs to the horizontal momentum flux terms that yield the  $\nabla \cdot \bar{p}^{*xy} \vec{V}$  term in (A.1.9) must cancel with  $\frac{\partial \bar{p}^{*xy}}{\partial t}$  as computed from the finite difference analog to the continuity equation. Consider the u-component equation (in one-dimension for simplicity)

$$\frac{\partial p^* u}{\partial t} = - \frac{\partial p^* u u}{\partial x},\tag{A.1.10}$$

which may be written, analytically,

$$p^* \frac{\partial u}{\partial t} + u \frac{\partial p^*}{\partial t} = - p^* u \frac{\partial u}{\partial x} - u \frac{\partial p^* u}{\partial x},\tag{A.1.11}$$



In the exact, differential equation, the cancellation of  $u \frac{\partial p^*}{\partial t}$  with  $-u \frac{\partial p^* u}{\partial x}$  by the continuity equation is necessary for the conservation of kinetic energy. Considering any finite difference analog to (A.1.10)

$$\frac{\delta \overline{p^{*xy}}}{\delta t} u = - \frac{\delta \overline{p^{*xy}}}{\delta x} uu, \quad A.1.12$$

it is also necessary that the part of  $\frac{\delta \overline{p^{*xy}}}{\delta x} uu$  corresponding to  $u \frac{\delta \overline{p^{*xy}}}{\delta x} u$  cancel with the part of  $\frac{\delta \overline{p^{*xy}}}{\delta t} u$  corresponding to  $u \frac{\delta \overline{p^{*xy}}}{\delta t}$  as computed from the continuity equation. It may be verified by substitution that the 4-point averaging operator yields this necessary cancellation with the continuity equation.

## A.2: Finite Difference Equations for Staggered Grid S-2

The finite difference analogs associated with staggered grid S-2 are derived by Lilly (1965) and tested as Scheme C by Grammeltevedt (1969).

For the equations of motion, the analogs are,

$$\begin{aligned} \frac{\partial p^* u}{\partial t} \approx & - [\overline{u^x} (\overline{p^* u})^x]_x - [\overline{u^y} (\overline{p^* v})^x]_y - p^* \frac{\delta \overline{u^x} \overline{u^x}}{\delta \sigma} \\ & - \overline{p^{*x}} \overline{\phi_x^\sigma} - R \overline{T^x} p_x^* + f(\overline{p^* v})^{xy}, \end{aligned} \quad A.2.1$$

$$\begin{aligned} \frac{\partial p^* v}{\partial t} \approx & - [\overline{v^x} (\overline{p^* u})^y]_x - [\overline{v^y} (\overline{p^* v})^y]_y - p^* \frac{\delta \overline{u^y} \overline{u^y}}{\delta \sigma} \\ & - \overline{p^{*y}} \overline{\phi_y^\sigma} - R \overline{T^y} p_y^* - f(\overline{p^* u})^{xy}. \end{aligned} \quad A.2.2$$

The friction terms are the same as those in (A.1.4) and (A.1.5) and are not repeated. In this section, the terms  $(p^* u)$  and  $(p^* v)$  represent  $\overline{p^{*x} u}$  and  $\overline{p^{*y} v}$  respectively.

The continuity and thermodynamic equations in this scheme are,

$$\frac{\partial p^*}{\partial t} \approx - (p^*u)_x - (p^*v)_y - p^* \frac{\delta \sigma}{\delta \sigma} \quad \text{A.2.3}$$

and

$$\begin{aligned} \frac{\partial p^*T}{\partial t} \approx & - [\bar{T}^x (p^*u)]_x - [\bar{T}^y (p^*v)]_y \\ & + \frac{RT\omega}{C_p \sigma} + \dots \end{aligned} \quad \text{A.2.4}$$

where

$$\omega \approx p^* \bar{\sigma}^\sigma + \bar{\sigma}^\sigma \left( \frac{\partial p^*}{\partial t} + \bar{u}^x \bar{p}^{*x}_x + \bar{v}^y \bar{p}^{*y}_y \right) . \quad \text{A.2.5}$$

The remaining terms in (A.2.4) are the same as those in (A.1.7). This scheme also conserves total energy (Lilly, 1965).

## REFERENCES

- Alaka, M. A. (1963), Instability aspects of hurricane genesis, National Hurricane Research Project Report No. 64, U. S. Weather Bureau, Washington, D. C., 23 pp.
- Anthes, R. A. (1971), A numerical model of the slowly varying tropical cyclone in isentropic coordinates, Monthly Weather Review, 99, No. 8, 617-635.
- Anthes, R. A., S. L. Rosenthal, and J. W. Trout (1971a), Preliminary results from an asymmetric model of the tropical cyclone, Monthly Weather Review, 99, No. 10, 744-758.
- Anthes, R. A., J. W. Trout, and S. L. Rosenthal (1971b), Comparisons of tropical cyclone simulations with and without the assumption of circular symmetry, Monthly Weather Review, 99, No. 10, 759-766.
- Anthes, R. A., J. W. Trout, and S. S. Ostlund (1971c), Three dimensional particle trajectories in a model hurricane, Weatherwise, 24, No. 4, 174-178.
- Black, P. G. and R. A. Anthes (1971), On the asymmetric structure of the tropical cyclone outflow layer, Journal of the Atmospheric Sciences, 28, No. 8, pp. 1348-1366.
- Charney, J. G. and A. Eliassen (1964), On the growth of the hurricane depression, Journal of the Atmospheric Sciences, 21, No. 1, 68-75.
- Gentry, R. C. (1964), A study of hurricane rainbands, National Hurricane Research Project Report No. 69, U. S. Weather Bureau, Washington, D. C., 85 pp.
- Godson, W. L. (1950), Generalized criteria for dynamic instability, Journal of Meteorology, 7, No. 4, 268-278.
- Grammelvedt, A. (1969), A survey of finite-difference schemes for the primitive equations, Monthly Weather Review, 97, No. 5, 384-404.
- Hawkins, H. F. and D. T. Rubsam (1968), Hurricane Hilda, 1964: II. Structure and budgets of the hurricane on October 1, 1964, Monthly Weather Review, 96, No. 9, 617-636.
- Houghton, D. D. and J. A. Young (1970), A note on inertial instability, Tellus, XXII, No. 5, 581-583.



## REFERENCES (continued)

- Kuo, H. L. (1949), Dynamic instability of two-dimensional nondivergent flow in a barotropic atmosphere, Journal of Meteorology, 6, No. 2, 105-122.
- Kurihara, Y. and J. L. Holloway, Jr. (1967), Numerical integration of a nine-level global primitive equation model formulated by the box method, Monthly Weather Review, 95, No. 8, 509-530.
- Lilly, D. K. (1965), On the computational stability of numerical solutions of time-dependent non-linear geophysical fluid dynamic problems, Monthly Weather Review, 93, No. 1, 11-26.
- Matsuno, T. (1966), Numerical integrations of the primitive equations by a simulated backward difference method, Journal of the Meteorological Society of Japan, Ser. 2, 44, No. 1, 76-84.
- Miller, B. I. (1957), On the maximum intensity of hurricanes, National Hurricane Research Project Report No. 14, U. S. Department of Commerce, National Hurricane Research Laboratory, Miami, Fla., 19 pp.
- Ogura, Y. and J. G. Charney (1962), A numerical model of thermal convection in the atmosphere, Proceedings of the International Symposium on Numerical Weather Prediction in Tokyo, Nov. 7-13, 1960, The Meteorological Society of Japan, 431-451.
- Ooyama, K. (1968), Numerical simulation of hurricanes, National Conference on Weather Modification, 1st, Albany, N. Y., April 28-May 1, Proceedings, 129-135.
- Ooyama, K. (1969), Numerical simulation of the life cycle of tropical cyclones, Journal of the Atmospheric Sciences, 26, No. 1, 3-40.
- Palmén, E. (1948), On the formation and structure of tropical hurricanes, Geophysica (Helsinki), 3, 26-38.
- Perlroth, I. (1962), Relationship of central pressure of Hurricane Esther (1961) and the sea surface temperature field, Tellus, XIV, No. 4, 404-408.
- Phillips, N. A. (1957), A coordinate system having some special advantages for numerical forecasting, Journal of Meteorology, 14, No. 2, 184-185.
- Rosenthal, S. L. (1969), Numerical experiments with a multilevel primitive equation model designed to simulate the development of tropical cyclones: Experiment I, ESSA Technical Memorandum ERLTM-NHRL 82, U. S. Department of Commerce, National Hurricane Research Laboratory, Miami, Fla., 36 pp.

## REFERENCES (continued)

- Rosenthal, S. L. (1970a), Experiments with a numerical model of tropical cyclone development--some effects of radial resolution, Monthly Weather Review, 98, No. 2, 106-120.
- Rosenthal, S. L. (1970b), A circularly symmetric, primitive equation model of tropical cyclone development containing an explicit water vapor cycle, Monthly Weather Review, 98, No. 9, 643-663.
- Rosenthal, S. L. (1971), The response of a tropical cyclone model to variations in boundary layer parameters, initial conditions, lateral boundary conditions, and domain size, Monthly Weather Review, 99, No. 10, 767-777.
- Sawyer, J. S. (1947), Notes on the theory of tropical cyclones, Quarterly Journal of the Royal Meteorological Society, 73, Nos. 315-316, 101-126.
- Senn, H. V. and J. A. Stevens (1964), Radar hurricane research 1 Sept. 1963 to 1 Aug. 1964, Final Report to U. S. Weather Bureau Contract No. Cwb-10755, Institute of Marine Science, University of Miami, Miami, Fla., 76 pp.
- Shuman, F. G. and J. D. Stackpole (1968), Note on the formulation of finite difference equations incorporating a map scale factor, Monthly Weather Review, 96, No. 3, 157-161.
- Smagorinsky, J., S. Manabe and J. L. Holloway, Jr. (1965), Numerical results from a nine-level general circulation model of the atmosphere, Monthly Weather Review, 93, No. 12, 727-768.
- Trout, J. W. (1972), Horizontal asymmetries in a numerical model of a hurricane, M. S. Thesis, Dept. of Atmospheric Sciences, University of Miami, Coral Gables, Fla.
- Van Mieghem, J. M. (1951), Hydrodynamic instability, Compendium of Meteorology, American Meteorological Society, Boston, Mass., 434-453.
- Yamasaki, M. (1963), Numerical simulations of tropical cyclone development with the use of primitive equations, Journal of the Meteorological Society of Japan, 46, No. 3, Tokyo, 178-201.
- Yanai, M. (1964), Formation of tropical cyclones, Reviews of Geophysics, 2, No. 2, 367-414.
- Yanai, M. and T. Tokioka (1969), Axially symmetric meridional motions in the baroclinic circular vortex: A numerical experiment, Journal of the Meteorological Society of Japan, 47, No. 3, 183-197.

U.S. DEPARTMENT OF COMMERCE  
National Oceanic and Atmospheric Administration  
Environmental Research Laboratories

NOAA Technical Memorandum ERL NHRL-92

THE RESPONSE OF A 3-LEVEL  
AXISYMMETRIC HURRICANE MODEL  
TO ARTIFICIAL REDISTRIBUTION  
OF CONVECTIVE HEAT RELEASE

Richard A. Anthes

National Hurricane Research Laboratory  
Miami, Florida  
June 1971





## TABLE OF CONTENTS

	Page
ABSTRACT	1
1. INTRODUCTION	1
2. REVIEW OF MODEL	2
3. THE ARTIFICIAL HEATING FUNCTION AND CORRESPONDING ADJUSTMENT TO WATER VAPOR BUDGET	3
4. RESULTS	6
5. STRUCTURE OF CONTROL AND MODIFIED STORMS	9
6. CONCLUSIONS	13
7. REFERENCES	14

# THE RESPONSE OF A 3-LEVEL AXISYMMETRIC HURRICANE MODEL TO ARTIFICIAL REDISTRIBUTION OF CONVECTIVE HEAT RELEASE

Richard A. Anthes

Numerical experiments with a 3-level, symmetric hurricane model have shown that the redistribution of water vapor associated with an artificial enhancement of convective heating beyond the radius of maximum wind can yield a large (about 40%) reduction in maximum surface wind speed generated by the model. The amount of reduction depends critically on the region of the storm which is assumed to supply the water vapor necessary to fuel the increased convection. The maximum effect occurs when the compensating water vapor is removed from the boundary layer. A much less effect is noted if all the compensating water vapor comes from the middle troposphere. The structures of the control model storm and several "modified" storms are presented.

## I. INTRODUCTION

In preparation for a "seeding" simulation experiment with our asymmetric hurricane model (Anthes et al., 1971a), some preliminary "seeding" experiments have been carried out with the two-dimensional (axially symmetric) analog model (Anthes et al., 1971b). These preliminary results are sufficiently interesting to warrant a brief summary at this time, in hopes of stimulating further thought and discussion on the possible effects of increasing convection beyond the radius of maximum wind in the hurricane.

Numerous discussions over the past years concerning hurricane modification by cloud seeding, have shown that more than one hypothesis can describe the chain of events, following seeding, in which the maximum wind speed is reduced. The original hypothesis (Simpson and Malkus, 1964) is an essentially hydrostatic argument based on the spreading out of the intense temperature gradient near the eye by the sudden freezing of supercooled water in the eye wall. Based primarily on numerical experiments with Rosenthal's (1970b) seven-level axisymmetric model, the most recent line of reasoning involves multiple seeding effort of clouds beyond the radius of maximum wind (Gentry, 1971). The increased convection hypothesized at distances beyond the eye wall would thereby divert a portion of the inflowing air upward at a larger radius. A reduction of surface wind speed then follows from angular momentum principles.

The above argument is essentially a mass circulation argument and is not directly concerned with changes in the essential water vapor budget associated with the increased heating. It is suggested in this note, that the utilization of existing water vapor by increased convection beyond the eye wall at the expense of the eye wall convection may be an extremely important effect (in addition to the mass circulation effect described above) in reducing the maximum wind speed. Depending on the assumptions concerning the actual redistribution of vapor, we find reductions in wind speed as large as 40%.

This note summarizes six experiments with the 3-level symmetric analog which tests various redistributions of the environmental water vapor that is required to support an artificially imposed heating at a prescribed radius and level. The essential feature, and constraint on the experiments, is that the water vapor budget is required to be satisfied during the application of the artificial heating function. The artificial heating function is envisioned to result primarily from an increase of water vapor condensation rather than from the latent heat of fusion liberated by the freezing of supercooled water. The physical mechanism of increasing convection, of course, depends on the presence of supercooled water. However, in this paper, cloud physics are not considered since we are only investigating the dynamical effect resulting from a hypothetical increase in convective heating. It is important to emphasize that these experiments study theoretical responses of a symmetric model only, and should not be compared to actual field experiments on any particular storm.

## 2. REVIEW OF MODEL

In spite of the low vertical (3 levels) and coarse (30 km) horizontal resolution, the so-called "symmetric analog" to the asymmetric model has yielded remarkably realistic results and has been a rather reliable predictor of the response of the asymmetric model to changes in computational methods and physical parameters. The numerical aspects of the model are designed to be as similar as possible to those of the asymmetric model. The details of the model are given by Anthes et al., (1971b) and will not be repeated here.

All experiments described in this note are carried out with 30-km resolution in order to be comparable with future simulations with the asymmetric model. However, a number of comparison experiments with 20-km resolution have been carried out. The important result was that the differences between the 30-km experiments and 20-km experiments were quantitatively minor and qualitatively similar to those discussed by Rosenthal (1970a). Thus, the results presented here are not expected to be qualitatively changed by increasing the resolution.



### 3. THE ARTIFICIAL HEATING FUNCTION AND CORRESPONDING ADJUSTMENT TO WATER VAPOR BUDGET

The "static" seeding hypothesis in which pre-existing supercooled water is suddenly induced to freeze, may be modelled by impulsively adding an equivalent amount of fusion heat at levels near the freezing level as was done by Rosenthal (1970b). A model of the effect of increasing convection (and, hence, water vapor condensation) covering a period of many hours, however, must include the implications of the increased heating on the latent energy budget of the hurricane system. Even a modest increase of convection over large depths and at large radii requires a substantial amount of water vapor which must come from the nearby hurricane environment and/or the sea. Since the transfer of water vapor from the sea to the air is not instantaneous, the first response of an increased convection at an arbitrary point would be the utilization of water vapor in adjacent columns to fuel the enhanced convection. Of course, the environmental air which supplies this additional moisture may then be enriched by evaporation from the sea through the model's air-sea interaction parameterization.

With the constraint that the latent energy budget must be satisfied during the artificial heating enhancement, there are an infinite number of possibilities concerning the redistribution of water vapor necessary to support the increased heating. We test six hypotheses which are designed to investigate some extreme possibilities and thereby give an indication of maximum and minimum effects. We may then rely on previous experimental and theoretical work concerning cloud seeding to determine the most probable redistribution pattern.

We next derive the expression for conservation of latent energy based on addition of an artificial heating rate and simultaneous removal of an equivalent amount of water vapor. If  $\frac{\Delta T}{\Delta t}$  is the individual rate of temperature change induced artificially, the corresponding change in moisture,  $\frac{\Delta q}{\Delta t}$  is

$$\frac{\Delta q}{\Delta t} = -\frac{c_p}{L} \frac{\Delta T}{\Delta t} \quad (1)$$

and, the amount of water vapor per unit mass condensed over a time step,  $\Delta t$ , is

$$\Delta q = \Delta t \frac{c_p}{L} \frac{\Delta T}{\Delta t} \quad (2)$$

Now, denote the reference volume to which the heat is added by the subscripts  $j_0$ ,  $k_0$ , so that the mass of this volume,  $M_0$ , is

$$M_0 = \pi \frac{\Delta P_{j_0 k_0}}{g} (r_{j_0 + \frac{1}{2}}^2 - r_{j_0 - \frac{1}{2}}^2) \quad (3)$$

where  $\Delta P_{j_0 k_0}$  is the pressure depth of the volume,  $g = 9.8 \text{ m sec}^{-2}$  and  $r$  is radial distance given by

$$r_j = (j - \frac{1}{2}) \Delta r \quad j = 1, 2, \dots \quad (4)$$

Then the total amount of water vapor required in time  $\Delta t$  for the additional heating is

$$q_0 = \Delta t \frac{C_p}{L} \frac{\Delta T}{\Delta t} M_0 \quad (5)$$

Now, denote the volumes "nearby" the reference volume by  $M_{jk}$ , and the percentage of total  $q_0$  removed from the various neighboring volumes by  $w_{jk}$ . The amount of water vapor per unit mass removed from each neighboring volume in time  $\Delta t$  is then

$$\Delta q_{jk} = \frac{w_{jk} q_0}{M_{jk}} \quad (6)$$

The percentage,  $w_{jk}$ , determines the relative contribution of neighboring volumes to the required total and may be assigned arbitrarily. To satisfy the latent energy budget, the amount of water vapor per unit mass given by (6) is subtracted from the appropriate volumes after each forecast time step during the period of artificial enhancement of the heating function.

The design of the six experiments may be clarified by referring to the schematic representation of the symmetric analog model in figure 1.

### MODIFICATION 3-LEVEL SYMMETRIC HURRICANE MODEL

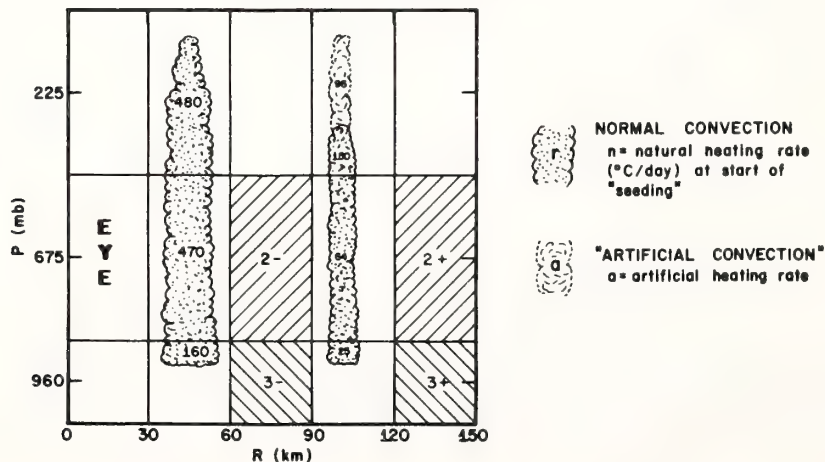


Figure 1. Schematic representation of modification experiments with three level symmetric hurricane model.

In the control experiment, the natural heating maximum (corresponding to the eye wall) occurs between 30 and 60 km. The artificial heating in all experiments consists of an additional  $4^{\circ}\text{C}/\text{hour}$  ( $96^{\circ}\text{C}/\text{day}$ ) added continuously over a 20-hour period in the upper tropospheric level in the radial ring between 90 and 120 km. (See Gentry, 1971, for discussion of the actual radial ring to be seeded in field experiments.)

Before describing the six experiments, we note that the compensating water vapor (corresponding to about 25 cm rain/day) cannot come from the adjacent upper tropospheric layer, where the saturation mixing ratio is only 0.2 gm/kg. If we then assume that the instantaneous effect of additional water vapor condensation in the ring centered at 105 km is a depletion of water vapor in the adjacent rings either interior (designated by -) or exterior (designated by +) to the reference ring, we need only assign the relative contributions from each of the four adjacent "boxes" which are hatched in figure 1. To test an extreme range of possibilities, we run the following experiments:

- 1) No water vapor removed from system. Latent energy of hurricane system is increased by the amount of the artificial heating function.
- 2) All of  $q_0$  is removed from the boundary layer of the inner ring (box 3-).
- 3) All of  $q_0$  is removed from the boundary layer of the outer adjacent ring (box 3+).
- 4) 50% of  $q_0$  is removed from the boundary layer on both sides of the column (50%  $q_0$  from box 3+; 50% of  $q_0$  from box 3-).
- 5) 50% of  $q_0$  is removed from the middle tropospheric layer on both sides of the column (50%  $q_0$  from box 2+; 50%  $q_0$  from box 2-).
- 6) 25% of  $q_0$  is removed from the boundary layer and middle tropospheric layer on each side of the column (25%  $q_0$  from boxes 3-, 3+, 2-, 2+).

We do not speculate on which of the possibilities is most likely, as this is a question that requires additional investigation utilizing cloud models.



#### 4. RESULTS

Figure 2 shows the maximum surface wind speed as a function of time for the control experiment and the six modification experiments. Note that the control experiment is in a near steady state from 90 to 170 hours with a maximum speed of about  $52 \text{ m sec}^{-1}$ .

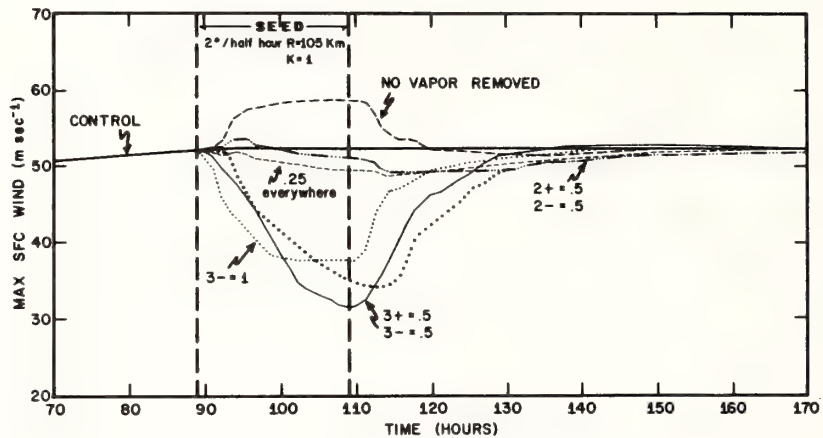


Figure 2. Time variation of maximum surface wind speed in control and six modified storms.

The artificial heating function of  $96^{\circ}\text{C}/\text{day}$  is applied at  $r = 105 \text{ km}$  in the upper tropospheric level during the 20 hour period beginning at 89 hours. The first major result is that in all experiments in which total latent energy is conserved, the maximum wind ultimately decreases in magnitudes ranging from  $3 \text{ m sec}^{-1}$  to  $21 \text{ m sec}^{-1}$ , depending on the particular adjustment of water vapor. However, in the experiment in which no water vapor is removed, so that the total energy of the system is increased, the maximum wind speed increases from  $52$  to  $58 \text{ m sec}^{-1}$ . It is also noteworthy that the circulations of all experiments return to that of the control experiment in about 20 hours after the artificial heating is terminated.

Of considerable interest in figure 2 is the large magnitude of wind decrease for experiments in which the compensating water vapor is removed from the boundary layer. The maximum reduction of  $21 \text{ m sec}^{-1}$  occurs when the vapor is removed from the interior and exterior rings in equal amounts. When all the vapor is removed from the interior ring (3-) the response is faster since the moisture reaching the eye wall is depleted sooner. However, the ultimate reduction is somewhat less. When all the vapor is removed from the exterior ring, the response is slower but the ultimate effect is greater than removing all the vapor from the interior ring. The reduction in wind speeds of  $14$ ,  $17$ , and  $21 \text{ m sec}^{-1}$  in these three experiments is greater than the reductions found in previous model experiments and shows the extreme sensitivity of the maximum wind to changes in boundary layer water vapor content. This very close relationship between storm intensity and water vapor supply was found by Rosenthal (1971) and Ooyama (1969) who noted a dramatic reduction in wind speed if the latent heat addition from the sea was suppressed.<sup>1</sup>

The differences between the three experiments in which water vapor is removed in varying proportions from the boundary layer are difficult to interpret because of the feed-backs between the continuity equation for water vapor, the thermodynamic equation, the equations of motion, and the parameterization of the air-sea interchange of latent heat. For example, the first response of the model to the removal of water vapor from the exterior ring is the reduction of the fuel for the natural convection in this ring. The amount of vapor flowing inward to the interior rings is also reduced although a finite time is required to advect the drier air inward. The increased evaporation from the sea caused by the greater difference between the air specific humidity and the saturation

---

<sup>1</sup>A similar experiment was carried out with the present 3-level model. When the latent heat transfer was suppressed for a 20-hour period beginning at 89 hours, the storm decayed rapidly to an intensity represented by a maximum wind speed of  $31 \text{ m sec}^{-1}$  and a minimum pressure of  $994 \text{ mb}$ .

specific humidity at the sea-air interface tends to compensate for the drying out of the boundary layer. (Indeed, the total energy of the system is increased because of the increased evaporation rate from the sea.) In any event, the net effect of all the interactions is to eventually cause a slight (less than 5%) reduction in water vapor reaching the eye wall. The slight decrease in heating then feeds back to a reduction in the vertical and radial circulation which further reduces the water vapor convergence in the boundary layer.

The experiments in which a substantial amount of water vapor is removed from the middle tropospheric layer yield a much smaller decrease of maximum wind speed. The decrease of 3-4 m/sec is the same order of magnitude found in some of Rosenthal's (1970b) experiments.

Figure 3 shows the minimum pressures for the control and six experiments. The minimum pressures are highly correlated with maximum wind speeds. In the experiment in which no water vapor is removed, the minimum pressure decreases by 7 mb. In all other experiments, the pressure rises from 4 to 26 mb depending on the redistribution of water vapor. The extreme effect of raising the pressure from 968 to 994 mb occurs when the water vapor is removed from the boundary layer in equal amounts from the interior and exterior rings.

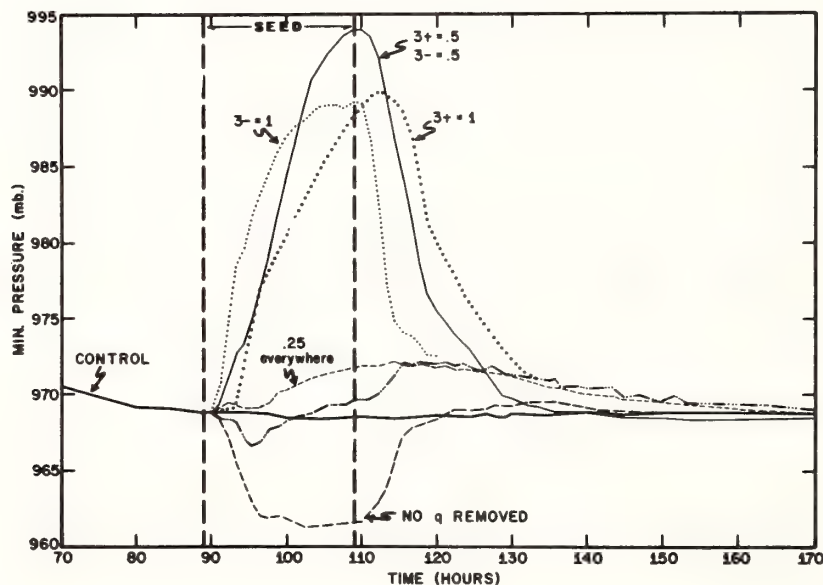


Figure 3. Time variation of minimum surface pressure in control and six modified storms.



## 5. STRUCTURE OF CONTROL AND MODIFIED STORMS

Figure 4 shows the vertical structure of the control experiment at 111 hours. Allowing for the coarse horizontal resolution, the wind speed, temperature departure, vertical motion, and relative humidity structures are considered reasonable compared to observations (Hawkins and Rubsam, 1968) and more sophisticated model results (Rosenthal, 1971).

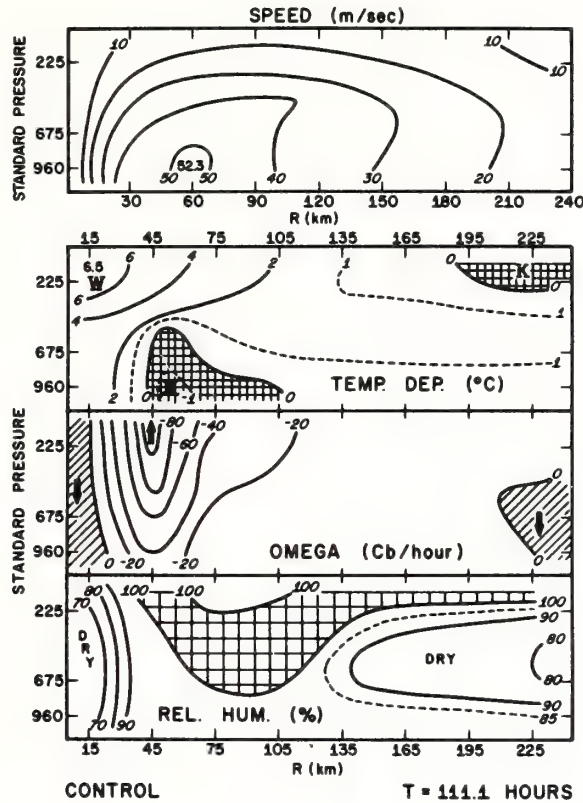


Figure 4. Vertical cross sections of wind speed, temperature departure, vertical p-velocity, and relative humidity for control experiment.

Figure 5 shows the structure of the modified storm in which no water vapor is removed. The over-all increase in intensity may be noted by comparison with figure 4. In particular, the wind speed has increased from 52.3 to 58.5 m sec<sup>-1</sup>, the temperature departure from 6.5 to 7.0°C, and the vertical motion from -100 to -120 cb/hour.

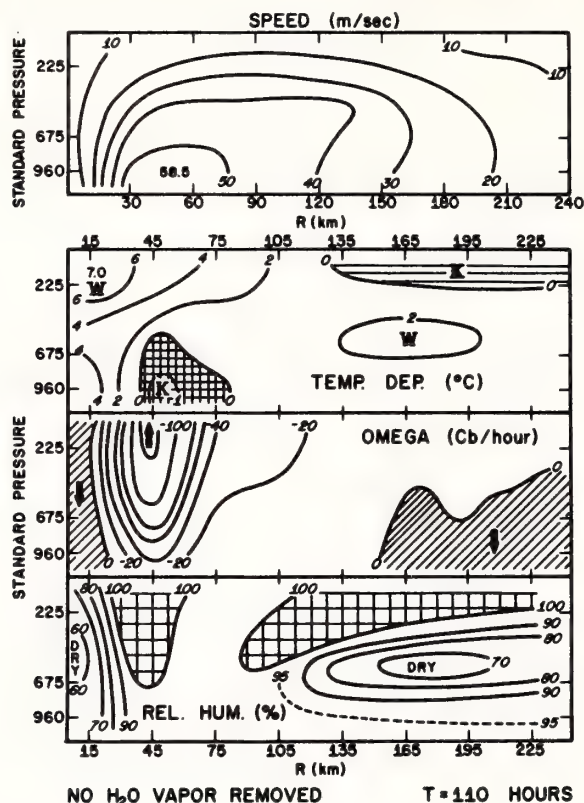


Figure 5. Structure of modified storm in which no compensating water vapor is removed from environment.

Figure 6 shows the modified storm structure in which the equivalent amount of water vapor is removed from the boundary layer in equal amounts from the interior and exterior rings. The change in structure over the control is dramatic. The wind speed maximum has spread from 60 to 150 km and is reduced by 35%. The temperature structure of the modified storm shows an increased cold-core structure near the center and a spreading

out of the middle and upper tropospheric warm core. The maximum rising motion has decreased in magnitude from 100 cb/hour to 40 cb/hour and has moved outward from 45 to 105 km. The circulation associated with the "eye" has become poorly defined and is much weaker as shown by the increase in relative humidity from about 70% to 90%. The total kinetic energy is reduced by 15 percent in the modified storm. However, the total heating rate is nearly the same;  $13.21 \times 10^{14}$  watts for the modified storm compared to  $13.14 \times 10^{14}$  watts for the unmodified storm.

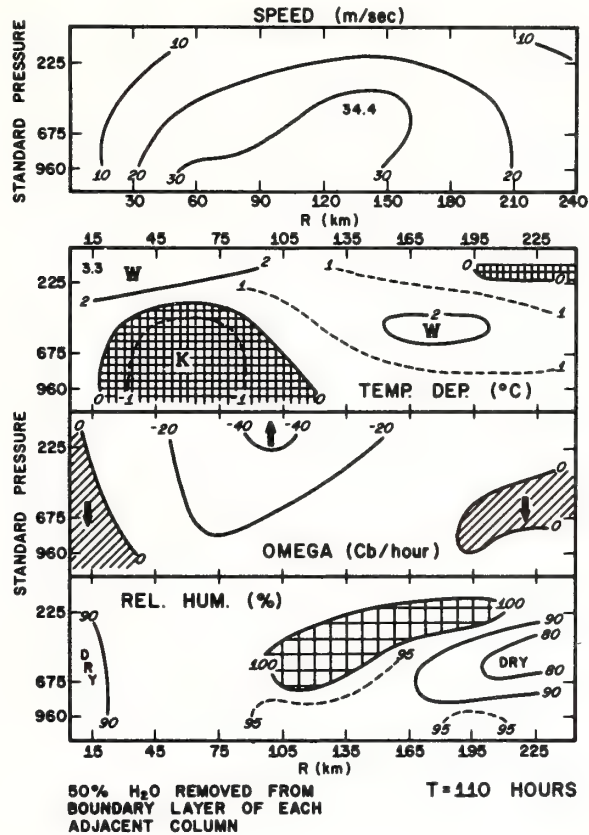
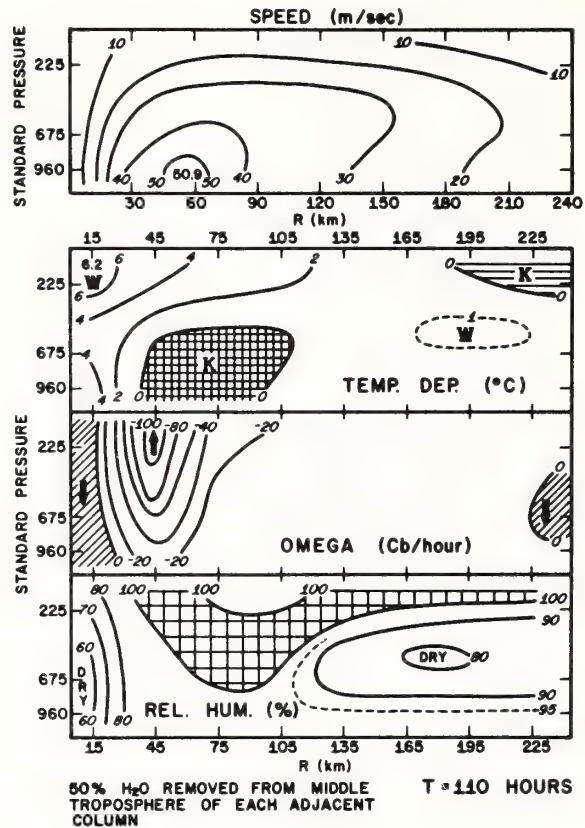


Figure 6. Structure of modified storm in which 50% of water vapor is removed from boundary layer of each adjacent column.



Although the changes in circulation are very large, the drying out of the boundary layer is not extreme, amounting to a reduction of about 5% in relative humidity. This illustrates that relatively minor changes in water vapor content in the boundary layer can cause major changes in hurricane structure.



course, that the water vapor in the middle troposphere is much less important in supporting the convective heating than the water vapor in the boundary layer.

## 6. CONCLUSIONS

Numerical experiments with a 3-level, symmetric hurricane model have shown that the redistribution of water vapor associated with an artificial enhancement of convective heating beyond the radius of maximum wind can yield a large (about 40%) reduction in maximum surface wind speed generated by the model. The amount of reduction depends critically on the region of the storm which is assumed to supply the water vapor necessary to fuel the increased convection. The maximum effect occurs when the compensating water vapor is removed from the boundary layer. Much less of an effect is noted if all the compensating water vapor comes from the middle troposphere. More knowledge of the response of cloud groups to massive seeding is needed to determine which redistribution of moisture is most likely in the hurricane environment.

## 7. REFERENCES

- Anthes, R. A., S. L. Rosenthal, and J. W. Trout (1971a), Preliminary results from an asymmetric model of the tropical cyclone, to be published in the Monthly Weather Review, 99.
- Anthes, R. A., J. W. Trout, and S. L. Rosenthal (1971b), Comparisons of tropical cyclone simulations with and without the assumption of circular symmetry, to be published in the Monthly Weather Review, 99.
- Gentry, R. Cecil (1971), A hypothesis for the hurricane modification experiments, Project STORMFURY Annual Report, 1970, U. S. Department of the Navy and U. S. Department of Commerce, (In press).
- Hawkins, H. F. and D. T. Rubsam (1968), Hurricane Hilda, 1964 - Part II. Structure and budgets of the hurricane on October 1, 1964, Monthly Weather Review, 96, No. 9, 617-636.
- Ooyama, K. (1969), Numerical simulation of the life cycle of tropical cyclones, Journal of the Atmospheric Sciences, 26, No. 1, 3-40.
- Rosenthal, S. L. (1970a), Experiments with a numerical model of tropical cyclone development, Monthly Weather Review, 98, No. 2, 106-120.
- Rosenthal, S. L. (1970b), A circularly symmetric, primitive equation model of tropical cyclones and its response to artificial enhancement of the convective heating functions, Project STORMFURY Annual Report, 1969, Appendix C, C-1-C-25.
- Rosenthal, S. L. (1971), The response of a tropical cyclone model to variations in boundary layer parameters, initial conditions, lateral boundary conditions, and domain size, to be published in the Monthly Weather Review, 99.
- Simpson, R. H. and J. S. Malkus (1964), Experiments in hurricane modification, Scientific American, 211, No. 1, 27-37.



# PRELIMINARY RESULTS FROM AN ASYMMETRIC MODEL OF THE TROPICAL CYCLONE

RICHARD A. ANTHES, STANLEY L. ROSENTHAL, and JAMES W. TROUT

National Hurricane Research Laboratory, Environmental Research Laboratories, NOAA, Miami, Fla.

## ABSTRACT

A three-layer primitive equation model of an isolated stationary tropical cyclone is constructed. The major difference between this and previously published models is the elimination of the assumption of circular symmetry. The release of latent heat by organized cumulus convection is parameterized by use of techniques previously shown to give realistic results in symmetrical models. In particular, the total release of heat in a vertical column is given by the horizontal convergence of water vapor in the Ekman layer and the vertical distribution of the heating follows the proposals made by Kuo. In the preliminary calculation reported on here, water vapor content is not forecast but, rather, is treated implicitly as was the case for the earlier circularly symmetric models.

The results show that the model reproduces many observed features of the three-dimensional tropical cyclone. Realistic portrayals of spiral rainbands and the strongly asymmetric structure of the outflow layer are obtained. The kinetic energy budget of the model compares favorably with empirical estimates and also shows the loss of kinetic energy due to truncation errors to be very small.

Large-scale horizontal asymmetries in the outflow are found to play a significant role in the radial transport of vorticity during the mature stage and are of the same magnitude as the transport by the mean circulation.

In agreement with empirical studies, the outflow layer of the model storm shows substantial areas of negative absolute vorticity and anomalous winds.

## 1. INTRODUCTION

Axisymmetric numerical models have simulated the life cycle of tropical cyclones with a large degree of realism (Ooyama 1969; Yamasaki 1968a, 1968b; Rosenthal 1970b). They have also yielded valuable insight into hurricane dynamics, energetics, and the important problem of parameterizing the latent heat released in organized cumulus convection. With this background, and with ever increasing computer capability, it is not premature to begin the study of the asymmetric features of the hurricane. Among the more notable of these are the upper tropospheric outflow layer, the rainbands, hurricane motion, and interactions between the hurricane and nearby synoptic systems.

Incorporation of all of these features into a single numerical model is an extremely ambitious goal that will require much further investigation. The model developed here represents an isolated stationary vortex and appears to be the logical first step beyond the axisymmetric models. For computational economy, we have limited the model to three vertical levels, a coarse horizontal resolution of 30 km, and a relatively small domain of 435-km radius. The results, nevertheless, are encouraging and appear to justify further effort.

Parallel investigations of our group are concerned with the design of grids with variable horizontal resolution (Anthes 1970c, Koss 1971). These will allow us to achieve increases in resolution near the hurricane center as well as in the size of the computational domain, with only moderate increase in the cost of computation. The very difficult problem of linking a large-scale forecast model with a moving high-resolution hurricane model will be investigated in the near future.

## 2. DESIGN OF THE MODEL

### A. BASIC EQUATION

The equations of motion in the  $\sigma$ -coordinate system (Phillips 1957) are

$$\frac{\partial p^*u}{\partial t} = -\frac{\partial p^*u^2}{\partial x} - \frac{\partial p^*uv}{\partial y} - p^* \frac{\partial \sigma u}{\partial \sigma} + fvp^* - p^* \frac{\partial \phi}{\partial x} - RT \frac{\partial p^*}{\partial x} + F_H(u) + F_V(u) \quad (1)$$

and

$$\frac{\partial p^*v}{\partial t} = -\frac{\partial p^*vu}{\partial x} - \frac{\partial p^*v^2}{\partial y} - p^* \frac{\partial \sigma v}{\partial \sigma} - fup^* - p^* \frac{\partial \phi}{\partial y} - RT \frac{\partial p^*}{\partial y} + F_H(v) + F_V(v). \quad (2)$$

Here,  $x$  and  $y$  are east-west and north-south Cartesian coordinates on an  $f$ -plane. The symbols  $u$  and  $v$  denote velocity components in the  $x$ - and  $y$ -directions, respectively;  $p^*$  is surface pressure;  $\sigma = p/p^*$  where  $p$  is the pressure; and  $\sigma$  is the vertical velocity in the  $\sigma$ -system. The symbol  $\phi$  denotes the geopotential of a  $\sigma$ -surface,  $T$  is temperature, and  $R$  is the gas constant for dry air. The Coriolis parameter,  $f$ , is assigned a value appropriate to approximately 20°N ( $5 \times 10^{-5} \text{ s}^{-1}$ ). The terms  $F_H$  and  $F_V$  represent effects produced by horizontal and vertical eddy diffusivity of horizontal momentum, respectively, and are discussed later.

The continuity and thermodynamic equations are given by

$$\frac{\partial p^*}{\partial t} = -\frac{\partial p^*u}{\partial x} - \frac{\partial p^*v}{\partial y} - \frac{\partial p^*\sigma}{\partial \sigma} \quad (3)$$

and

$$\frac{\partial p^* T}{\partial t} = -\frac{\partial p^* u T}{\partial x} - \frac{\partial p^* v T}{\partial y} - \frac{p^* \partial \sigma T}{\partial \sigma} + \frac{RT\omega}{c_p \sigma} + \frac{p^*}{c_p} \dot{Q} + F_H(T) \quad (4)$$

where  $\dot{Q}$  is the diabatic heating per unit mass,  $c_p$  is the specific heat at constant pressure, and  $\omega = dp/dt$  is related to  $\dot{\sigma}$  by

$$\omega = p^* \dot{\sigma} + \sigma \frac{dp^*}{dt} \quad (5)$$

$F_H(T)$  represents the lateral diffusion of heat due to the presence of subgrid-scale eddies. In the  $\sigma$ -system, the hydrostatic equation may be written

$$\frac{\partial \phi}{\partial \sigma} = -\frac{RT}{\sigma} \quad (6)$$

Equations (1) through (6) are identical to those employed by Smagorinsky et al. (1965) for general circulation studies. Since this preliminary calculation does not contain an explicit water vapor cycle, there are seven dependent variables ( $u, v, p^*, T, \phi, \omega$ , and  $\dot{\sigma}$ ). The vertical sum of eq (3) is used to compute  $\partial p^*/\partial t$  and provides the seventh equation needed to complete the set. Water vapor is treated implicitly in a fashion similar to that used in some symmetric models (Yamasaki 1968a, 1968b; Rosenthal 1969). The details are given later.

## B. STRUCTURE OF THE MODEL

The vertical structure of the model is shown by figure 1A. The atmosphere is divided into upper and lower layers of equal pressure depth and a thinner Ekman boundary layer. The information levels,  $k$ , for the dynamic and thermodynamic variables (fig. 1A) are staggered according to the scheme used by Kurihara and Holloway (1967).

The horizontal mesh (fig. 1B) is rectangular with a uniform spacing of 30 km. The lateral boundary points approximate a circle, and all boundary points are contained between radii of 450 and 435 km. All variables are defined at all grid points on the  $\sigma$ -surfaces.

## C. THE FINITE-DIFFERENCE EQUATIONS

We adopt Shuman and Stackpole's (1968) finite-difference notation and write

$$\alpha_x \equiv \frac{\alpha_{i,j+1/2} - \alpha_{i,j-1/2}}{\Delta x}$$

$$\alpha_y \equiv \frac{\alpha_{i+1/2,j} - \alpha_{i-1/2,j}}{\Delta y}$$

$$\bar{\alpha}^x \equiv (\alpha_{i,j+1/2} + \alpha_{i,j-1/2})/2,$$

and

$$\bar{\alpha}^y \equiv (\alpha_{i+1/2,j} + \alpha_{i-1/2,j})/2$$

where  $j$  is the east-west index and  $i$  is the north-south

## VERTICAL STRUCTURE

VARIABLE	k	p (mb)
$\dot{\sigma} = 0$	1	0
$\Psi, T$	1 1/2	225
$\sigma, \phi$	2	450
$\Psi, T$	2 1/2	675
$\sigma, \phi$	3	900
$\Psi, T$	3 1/2	957.5
$\phi = \sigma = 0$	4	1015

A

## HORIZONTAL STRUCTURE - Northwest Section

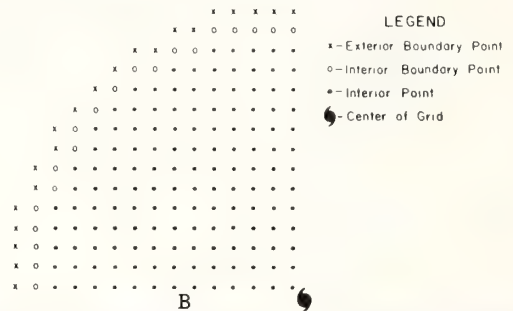


FIGURE 1.—(A) vertical information levels and (B) northwest quadrant of the horizontal grid.

index. For vertical differences and averages, we define

$$\bar{\alpha}^{\sigma} \equiv (\alpha_{k+1/2} + \alpha_{k-1/2})/2 \quad (8)$$

and

$$\delta \alpha \equiv (\alpha_{k+1/2} - \alpha_{k-1/2}).$$

The horizontal portion of the difference scheme is similar to Granneltvedt's (1969) scheme B and has been used extensively by the Geophysical Fluid Dynamics Laboratory, National Oceanic and Atmospheric Administration, in general circulation studies. With one exception, to be cited below, the vertical portion of the difference scheme has been discussed by Kurihara and Holloway (1967).

By use of the operators eq (7) and (8), the equations of motion can be expressed in the form

$$\frac{\partial p^* u}{\partial t} \approx -(\overline{u p^* u})_x - (\overline{v p^* u})_y - p^* \frac{\delta(\bar{\sigma} u)}{\delta \sigma} - p^* \bar{\phi}_x - RT \bar{p}_x^* \quad (9)$$

and

$$\frac{\partial p^* v}{\partial t} \approx -(\overline{u p^* v})_x - (\overline{v p^* v})_y - p^* \frac{\delta(\bar{\sigma} v)}{\delta \sigma} - p^* \bar{\phi}_y - RT \bar{p}_y^* \quad (10)$$

which are applied at the half levels. The continuity equation in the form

$$\frac{\partial p^*}{\partial t} = -[(\bar{u}^x \bar{p}^x)_x + (\bar{v}^y \bar{p}^y)_y] - p^* \frac{\delta \dot{\sigma}}{\delta \sigma} \quad (11)$$

is also applied at the half levels. The vertical sum of eq (11), subject to the boundary conditions  $\dot{\sigma}=0$  at  $\sigma=0$  and  $\sigma=1$ , is used to compute  $\partial p^*/\partial t$ . Equation (11) is then used to compute  $\dot{\sigma}$  at the integral levels. The thermodynamic equation, also applied at the half levels, is written

$$\frac{\partial p^* T}{\partial t} = -[(\bar{p}^* \bar{u}^x \bar{T}^x)_x + (\bar{p}^* \bar{v}^y \bar{T}^y)_y] - p^* \frac{\delta \dot{\sigma} \bar{T}^\sigma}{\delta \sigma} + \frac{RT\omega}{c_p \sigma} + \frac{p^*}{c_p} \dot{Q} + F_H(T). \quad (12)$$

The symbol,  $\bar{T}^\sigma$ , denotes a temperature at the integral levels computed by linear interpolation of potential temperature over  $\sigma$  between adjacent half levels. This provides for a substantial improvement in the calculation of static stability since potential temperature is much more nearly linear in  $\sigma$  than is temperature. Mintz and Arakawa (see Langlois and Kwok 1969) have adopted a similar procedure for their general circulation model.

The quantity  $\omega = dp/dt$  is defined at the half levels and computed from

$$\omega = p^* \bar{\sigma}^\sigma + \bar{\sigma}^\sigma \left( \frac{\partial p^*}{\partial t} + u \bar{p}^* \bar{\sigma}^x + v \bar{p}^* \bar{\sigma}^y \right). \quad (13)$$

The hydrostatic equation in the form

$$\frac{\delta \phi}{\delta \sigma} = - \frac{RT}{\sigma} \quad (14)$$

is also applied at the half levels.

With the exception of the use of  $\bar{T}^\sigma$  in place of  $\bar{T}$  in the vertical flux terms of eq (12), the differencing and staggering of variables in the vertical is identical to that of Kurihara and Holloway (1967). For adiabatic inviscid flow in a laterally closed domain with  $\dot{\sigma}=0$  at  $\sigma=0$  and 1, Kurihara and Holloway showed their system to conserve the finite-difference analog to

$$\int_z \int_y \int_0^1 p^* \left( c_p T + \frac{u^2 + v^2}{2} \right) d\sigma dy dx. \quad (15)$$

It is clear that replacement of  $\delta(\dot{\sigma} \bar{T}^\sigma)/\delta \sigma$  in the thermodynamic equation by  $\delta(\dot{\sigma} \bar{T})/\delta \sigma$  will not alter the conservation of the integral eq (15) since either term will sum to zero given the boundary conditions on  $\dot{\sigma}$  described above.

#### D. VERTICAL DIFFUSION OF MOMENTUM

Although vertical transport of horizontal momentum by the cumulus-scale motions has been shown to be an important element in maintaining the observed structure of hurricanes (Gray 1967, Rosenthal 1970b), this effect

is not included in the preliminary calculations reported on here. Therefore, the terms  $F_V(u)$  and  $F_V(v)$  which appear in eq (1) and (2) represent, for this calculation, diffusive and "frictional" effects due to the vertical transports of horizontal momentum by subgrid eddies smaller than the cumulus scale. The most important aspect of these terms is the surface drag which produces frictional convergence in the cyclone boundary layer and, therefore, a water vapor supply which controls the parameterized cumulus convection (Charney and Eliassen 1964, Ooyama 1969, Rosenthal 1970b).

By use of vector notation, these terms may be written for the  $\sigma$ -system in the form

$$\mathbf{F}_V = -g \frac{\partial \boldsymbol{\tau}^z}{\partial \sigma} \quad (16)$$

where  $g$  is the acceleration of gravity and  $\boldsymbol{\tau}^z$  is the vector Reynolds stress appropriate to the subcumulus eddies. To incorporate surface drag friction, we invoke the boundary condition

$$\boldsymbol{\tau}_{k=4}^z = \rho^* C_D |\mathbf{V}^*| \mathbf{V}^* \quad (17)$$

where  $\rho^*$  is the density at the surface,  $C_D$  is a drag coefficient, and  $\mathbf{V}^*$  is the surface wind.

Equation (17) is the well-known quadratic stress law. However, since winds are not defined at  $\sigma=1$ , eq (17) is approximated by

$$\boldsymbol{\tau}_{k=4}^z = \rho^* C_D |\mathbf{V}_3| \mathbf{V}_3. \quad (18)$$

A value of  $3 \times 10^{-3}$  is adopted for  $C_D$ , and a standard value of  $1.10 \text{ kg m}^{-3}$  is used for  $\rho^*$  in eq (18). As an upper boundary condition, we require

$$\boldsymbol{\tau}_{k=1}^z = 0. \quad (19)$$

For the remaining  $\sigma$ -levels, we use the Austausch formulation

$$\boldsymbol{\tau}_{k=2,3}^z = \rho K(z) \frac{\partial \mathbf{V}}{\partial z}. \quad (20)$$

Here,  $\rho$  is density,  $z$  is height, and  $K(z)$  is the kinematic coefficient of eddy viscosity. Following Smagorinsky et al. (1965), the Rossby-Montgomery formulation is adopted for  $K(z)$ ,

$$K(z) = l^2 \left| \frac{\partial \mathbf{V}}{\partial z} \right|, \quad (21)$$

where  $l$  is a mixing length given by

$$l = \begin{cases} k_0 h \left( \frac{H-z}{H-h} \right), & h < z < H \\ 0, & z > H \end{cases} \quad (22)$$

In these relationships,  $k_0$  is the Kármán constant,  $h$  is the depth of the Prandtl layer, and  $H$  is the level at which the stress vanishes. We take  $k_0=0.4$  and  $h=100 \text{ m}$ .



If we consider the boundary condition eq (19),  $H$  should be identified with the  $\sigma=0$  surface. To simplify matters, we allow  $l$  to vary linearly with  $\sigma$ . Thus,

$$l_k = k_0 h \sigma_k, \quad k=1, 2, 3. \quad (23)$$

Finally, the finite-difference approximations for eq (20) and (21) are written

$$\tau^z = \bar{\rho} K(z) \frac{\delta \mathbf{V}}{\delta \bar{z}^\sigma} \quad (24)$$

and

$$K(z) = l^2 \left| \frac{\delta \mathbf{V}}{\delta \bar{z}^\sigma} \right| \quad (25)$$

where  $\bar{\rho}$  is an appropriate standard density for the given  $\sigma$ -surface. Both equations are applied at integral levels. The finite-difference expression for eq (16) then takes the simple form

$$\mathbf{F}_V = -g \frac{\delta \tau^z}{\delta \sigma}. \quad (26)$$

#### E. LATERAL MIXING TERMS

Following Smagorinsky et al. (1965), the lateral exchange of horizontal momentum by subgrid-scale eddies is written

$$F_H(\mathbf{V}) = \frac{\partial}{\partial x} \left( K_H \frac{\partial p^* \mathbf{V}}{\partial x} \right) + \frac{\partial}{\partial y} \left( K_H \frac{\partial p^* \mathbf{V}}{\partial y} \right). \quad (27)$$

Preliminary tests, as well as calculations with a symmetrical analog to this model, revealed that neither a constant value of  $K_H$  nor Smagorinsky's (1965) variable  $K_H$  (proportional to the magnitude of the total deformation of the horizontal motion) provided acceptable results.

The formulation ultimately adopted was

$$K_H = C_1 |\mathbf{V}| + C_2 \quad (28)$$

where  $C_1 = 10^3$  m and  $C_2 = 5 \times 10^3$  m<sup>2</sup> s<sup>-1</sup>.

While this selection was based primarily on the results of numerical tests, the form was suggested by the encouraging results obtained from symmetrical models (Rosenthal 1970b, Yamasaki 1968b) which employed upstream differencing of advection terms with forward time steps. This scheme introduces a computational viscosity (Molenkamp 1968) which is similar to the variable portion of eq (28).

Although eq (28) is not very satisfying from a physical point of view, it does afford a useful interim representation of the statistical effect of horizontal interactions between the momentum fields of the cumuli and the macroscale. More satisfying formulations are dependent on the success of the future theoretical and observational studies of these interactions.

The preliminary tests also indicated that adequate results can be obtained if the lateral diffusion of heat is computed with a constant thermal diffusivity ( $K_T$ ) of

$5 \times 10^4$  m<sup>2</sup> s<sup>-1</sup>. The lateral mixing term in the thermodynamic equation was, therefore, expressed in the form

$$F_H(T) = p^* K_T \left( \frac{\partial^2 T}{\partial x^2} + \frac{\partial^2 T}{\partial y^2} \right). \quad (29)$$

#### F. TIME INTEGRATION

A number of experiments were conducted for the purpose of selecting a method of time integration. Comparisons were made between the usual leapfrog method, the two-step Lax-Wendroff scheme (Richtmyer and Morton 1967), and the Matsuno (1966) simulated forward-backward scheme. With the diabatic and viscous terms suppressed, the Lax-Wendroff technique provided the best results from the point of view of preserving the finite-difference analog to the energy integral eq (15). The Matsuno method was almost as good (but at the cost of twice the computational time). The leapfrog method gave errors in the energy integral more than an order of magnitude greater than those encountered with the other methods.

On the other hand, with viscous and diabatic effects included, the Matsuno technique was clearly superior to the Lax-Wendroff technique. This conclusion was based on intuitive meteorological inspection of the test results. Presumably, the superiority of the Matsuno scheme is due to its severe damping of high temporal frequencies. Since this model has very limited vertical resolution, the high-frequency inertial gravity waves (particularly the external gravity wave) are probably overly excited by the diabatic heating. The Matsuno damping may, then, compensate for this effect.

Except for friction and heating, the scheme is summarized for the equation  $\partial \alpha / \partial t = F(\alpha)$  as follows:

1. Given  $\alpha^n$ .
2.  $\alpha^* = \alpha^n + \Delta t F(\alpha^n)$ .
3. Compute lateral boundary points from  $\alpha^*$  data.
4.  $\alpha^{n+1} = \alpha^n + \Delta t F(\alpha^*)$ .
5. Compute lateral boundary points from  $\alpha^{n+1}$  data.
6. Return to 1.

The superscript  $n$  refers to the time-step number, and  $\Delta t$  is 60 s. The friction and heating terms are computed using the  $\alpha^n$  data in both steps 2 and 4. The extra time required by the two-step Matsuno scheme is only about 1.5 times that required by the other schemes tested.

#### G. LATERAL BOUNDARY CONDITIONS

The small domain size and the irregular boundary make the choice of lateral boundary conditions extremely important. Preliminary experimentation showed that realistic results could be obtained for steady-state pressure and temperature on the boundary and a variable momentum based on boundary conditions similar to those employed in symmetric models (Anthes 1970a; Rosenthal 1970a, 1970b).





Finally, the surface humidity and temperature are required in order to establish the pseudoadiabatic appropriate to parcel ascent from the surface. The surface temperature,  $T^*$ , is computed by a downward extrapolation from the temperature at level  $k=7/2$ ,

$$T^* = T_{k=7/2} + 3.636^\circ\text{K}. \quad (36)$$

This corresponds to a lapse rate between the dry and moist adiabatic rates. The surface specific humidity,  $q^*$ , is obtained from  $q_{k=7/2}$  through the assumption that the relative humidity is constant between the levels  $k=7/2$  and  $k=4$ .

### I. AIR-SEA EXCHANGE OF SENSIBLE HEAT

The sensible heat flux at the air-sea interface is assumed to obey the bulk aerodynamic relationship. It is further assumed that the heat flux decreases linearly with  $\sigma$  until it reaches a value of zero at the  $k=3$  level. This gives

$$p^* \dot{Q}_{k=7/2}^s = \begin{cases} \frac{g c_p C_E |V| \rho^* (T_{sea} - T^*)}{\sigma_4 - \sigma_3}, & T_{sea} > T^* \\ 0, & T_{sea} \leq T^* \end{cases} \quad (37)$$

where  $\dot{Q}_{k=7/2}^s$  is the sensible heat added per unit mass and time at  $k=7/2$ . The exchange coefficient  $C_E$  is taken equal to  $C_D$  (0.003);  $T_{sea}=302^\circ\text{K}$  is used for the experiment discussed below.

### J. INITIAL CONDITIONS

The initial conditions consist of an axisymmetric vortex in gradient balance. These conditions are established as follows. The temperatures at the levels  $k=3/2$ ,  $5/2$ , and  $7/2$  are taken from a mean tropical atmosphere (Hebert and Jordan 1959). The initial surface pressure (in mb) is then defined by

$$p^* = 1011.0 - 4.0 \cos\left(\frac{\pi}{375} r\right), \quad r < 375 \text{ km}$$

and

$$p^* = 1015.0, \quad r \geq 375 \text{ km}$$

where  $r$  is given in kilometers.

The initial geopotentials of the  $\sigma$ -surfaces are calculated by an upward integration of the hydrostatic equation.

To obtain the initial wind field, we write the gradient wind equation for the  $\sigma$ -system

$$\frac{v_\lambda^2}{r} + f v_\lambda = \frac{RT}{p^*} \frac{\partial p^*}{\partial r} + \frac{\partial \phi}{\partial r} \quad (38)$$

where  $v_\lambda$  is the tangential wind component in cylindrical coordinates. Since the initial temperatures have no gradients on  $\sigma$ -surfaces, the second term on the right side of eq (38) gives no contribution. Thus, the only vertical variation present in the initial  $v_\lambda$  is due to the vertical variation of  $T$  in the  $(RT/p^*) (\partial p^*/\partial r)$  term.

The pressure field eq (37) together with the specified temperature field yields a maximum gradient wind at the  $k=7/2$  level of 18 m/s at a radius of 240 km. Although these conditions represent a rather strong vortex, experiments with the symmetric analog showed the mature state of the storm to depend very little on the strength of the initial vortex. The time of development, on the other hand, varied from 6 days to 1 day depending on the strength of the initial circulation. Therefore, a computational economy is realized by increasing the strength of the initial vortex.

To obtain initial values of  $u$  and  $v$ , the usual trigonometric relationships between velocity components in cylindrical and Cartesian coordinates were employed. In the absence of truncation and roundoff errors, the resulting  $u$  and  $v$  fields should be nondivergent and circularly symmetric. The truncation and roundoff errors as well as lack of complete circular symmetry in the boundary conditions do, however, produce weak asymmetries and divergences. Without these effects, the solution would remain circularly symmetric for all time.

## 3. EXPERIMENTAL RESULTS

The history of the cyclone is summarized by figure 3, which shows the evolution of the minimum surface pressure and the maximum wind speed in the boundary layer ( $k=7/2$ ). Due to the substantial strength of the initial vortex, a short "organizational phase" of only 12 hr is needed before steady intensification begins. Hurricane-force winds appear at about 40 hr, and, thereafter, the relatively weak storm remains in a quasi-steady state until about 120 hr. At this point, a second period of intensification begins and the maximum wind eventually exceeds 60 m/s. The unsteady nature of the storm during this period seems to be related to the development of pronounced asymmetries (especially in the outflow region). The asymmetries are discussed in detail later.

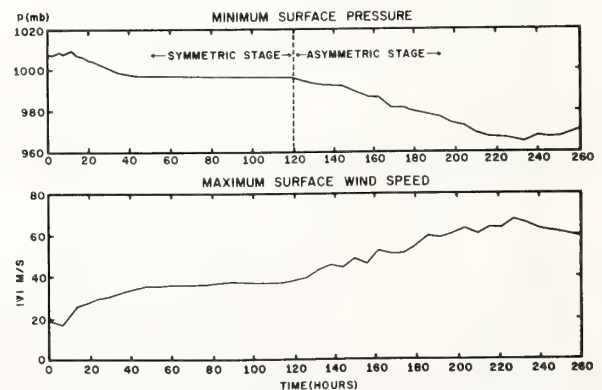


FIGURE 3.—Time variation of the minimum surface pressure and the maximum surface wind speed.



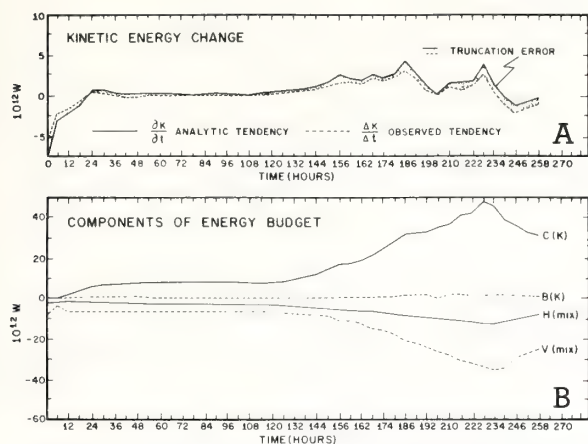


FIGURE 4.—(A) time variation of the observed kinetic energy change ( $\Delta K/\Delta t$ ) and the change computed from the kinetic energy equation ( $\partial K/\partial t$ ) and (B) time variation of individual components of the kinetic energy tendency.  $C(K)$  is the conversion of potential to kinetic energy,  $B(K)$  is the flow of kinetic energy through the lateral boundary,  $H(mix)$  is the loss of kinetic energy through lateral eddy viscosity and  $V(mix)$  is the loss of kinetic energy through vertical eddy viscosity including the effect of surface drag friction.

Figure 4B shows the temporal variations of the components of the kinetic energy budget. The sum of (1) the conversion of potential to kinetic energy [ $C(K)$ ], (2) the flux of kinetic energy across the lateral boundary [ $B(K)$ ], (3) the dissipation due to lateral mixing [ $H(mix)$ ], and (4) the dissipation due to vertical mixing [ $V(mix)$ ] equals the "analytic" kinetic energy tendency ( $\partial K/\partial t$ ). Figure 4A shows the observed rates of change of kinetic energy ( $\Delta K/\Delta t$ ). The difference between  $\partial K/\partial t$  and  $\Delta K/\Delta t$  is a measure of the truncation error and, as figure 4 shows, this difference is quite small. Furthermore, the individual components of the budget are reasonable when compared to empirical estimates (Hawkins and Rubsam 1968, Miller 1962, Palmén and Riehl 1957, Riehl and Malkus 1961).

For purposes of discussion, it is convenient to divide the history of the storm into two stages. From the initial instant until about 120 hr, all features are quite symmetric with respect to the storm center. During this period, there is neither evidence of a banded structure in the rainfall (analogous to rainbands in real hurricanes) nor does the upper tropospheric outflow show any preference for particular quadrants. We refer to this interval as the "early symmetric stage." After 120 hr, the upper outflow is quite asymmetric while the rainfall and vertical motions show distinct patterns analogous to the spiral rainbands found in real storms. We refer to this period as the "asymmetric stage." It is, however, important to keep in mind that these terms refer to the mesoscale features imbedded in the cyclone-scale vortex.

The life cycle of a tropical cyclone in the real atmosphere usually consists of three distinct phases. The first of these

is commonly some type of wavelike disturbance in the easterlies or in the equatorial convergence zone. This "seedling" has a characteristic wavelength of 1000 km or so and, of course, is highly asymmetric when viewed from the synoptic scale. The model, in its present simple form, is unable to represent this early wave stage.

In the second phase of the life cycle of real storms, pressures decrease in some portion of the wave perturbation and a closed depression with a distinct, but weak, cyclonic circulation is formed. When viewed from the synoptic scale, this stage shows a much greater degree of circular symmetry than does the wave stage. While initial conditions for the model (a balanced symmetric vortex) are highly arbitrary, these are intended to be some sort of counterpart to this second stage of real storms. However, the first day or so of the calculation should really be thought of as an initialization rather than as a prediction. During this time, the initial conditions of gradient balance are modified toward a new slowly varying state in which divergence, friction, and diabatic heating are important elements.

As already noted, the term *early symmetric stage* as applied to the first 120 hr of the calculation refers to the symmetry of the imbedded mesoscale structure. This structure is in reasonable agreement with the mesostructure of the second stage of the life cycle of real storms as described above.

Finally, the real depression undergoes intensification to the mature stage. It is during this time that distinct rainbands are most likely to appear, thus producing pronounced asymmetries on the mesoscale. However, when viewed on the cyclone or synoptic scale, the mature stage may appear to be highly symmetric. There is, however, one major exception: The upper tropospheric outflow layer of the mature storm tends to be highly asymmetric even when viewed from the synoptic scale. The asymmetric stage of the model calculation is felt to be analogous to this mature stage of the real hurricane.

#### A. EARLY SYMMETRIC STAGE OF THE MODEL STORM

A representative view of the structure during this period is provided by the data at 84 hr. Figures 5 and 6 show the flow in the boundary layer (level 7/2) for this time. The region of hurricane-force winds is very small, extending only about 75 km from the center. Gale-force winds extend outward to 150 km. The maximum tangential and radial winds are 34.0 and  $-19.4$  m/s, respectively, yielding an inflow angle of about  $29^\circ$ .

The circulation in the upper troposphere (level 3/2) shows a fairly symmetric outflow pattern (figs. 7 and 8). Cyclonic outflow occurs inside a radius of about 200 km. Beyond 200 km, the circulation is anticyclonic, reaching a maximum velocity of about 6 m/s around the outer boundary.

Dynamic (or inertial) instability of the upper tropospheric outflow has been suggested by Alaka (1961, 1962, 1963) and others as a contributory factor in the intensifica-

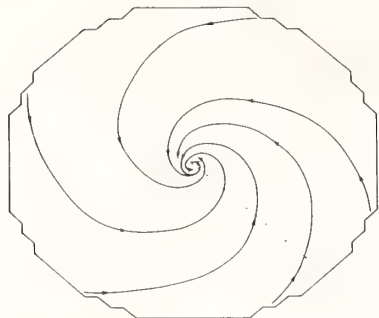


FIGURE 5.—Streamline analysis for the boundary layer (level 7/2) at 84 hr. Marks on the radial line from center of the grid to the lateral boundary represent 60-km intervals.

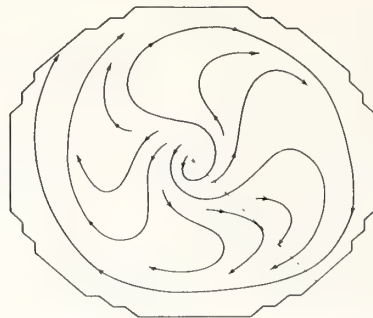


FIGURE 7.—Streamline analysis for the upper troposphere (level 3/2) at 84 hr.

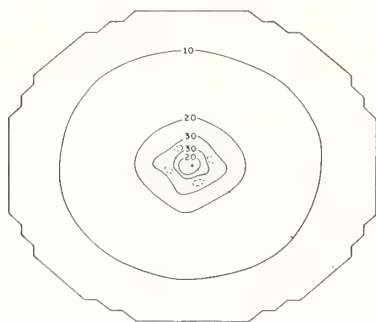


FIGURE 6.—Isotach analysis for the boundary layer (level 7/2) at 84 hr. Dashed contours near grid center represent 35-m/s isotachs. Isoleths are labeled in m/s.

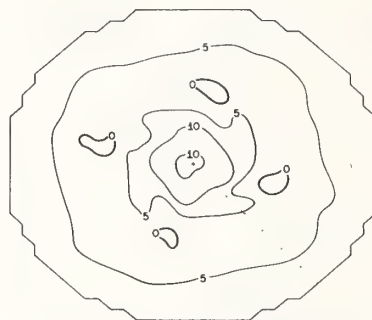


FIGURE 8.—Isotach analysis for the upper troposphere (level 3/2) at 84 hr. Contours labeled 0 contain wind speeds less than 0.5 m/s. Isoleths are labeled in m/s.

tion of tropical cyclones. An approximate necessary condition for this instability is given by

$$\zeta_a \left( \frac{2|V|}{R} + f \right) < 0 \quad (39)$$

where  $|V|$  is the wind speed,  $R$  is the radius of curvature of the streamlines, and  $\zeta_a$  is the absolute vorticity. Condition (39) may be satisfied if either  $\zeta_a$  or  $[(2|V|/R) + f]$  is negative. The second alternative corresponds to the occurrence of "anomalous" winds.

Great care must be taken in the application and interpretation of condition (39). Strictly speaking, this criterion for instability refers to horizontal parcel displacements normal to a streamline and is derived under the assumption that the velocity and pressure fields are invariant along the streamline. A necessary criterion for a closely related instability is

$$\left( \frac{\partial v_\lambda}{\partial r} + \frac{v_\lambda}{r} + f \right) \left( \frac{2v_\lambda}{r} + f \right) < 0. \quad (40)$$

Criterion (40) concerns the instability of horizontal symmetric fluid-ring displacement in a symmetric vortex.

A third type of dynamic instability is governed by the necessary condition that the radial gradient of the absolute vorticity of the tangential flow have at least one zero. That is, the condition

$$\frac{\partial}{\partial r} \left( \frac{\partial v_\lambda}{\partial r} + \frac{v_\lambda}{r} + f \right) = 0 \quad (41)$$

is satisfied somewhere in the fluid system. This is a necessary condition for asymmetric (azimuthally varying) horizontal perturbations to be unstable. The condition [eq (41)] can be derived in a straightforward manner by utilization of the techniques employed by Kuo (1949).

At the initial instant, when the flow is nearly symmetric and tangential, conditions (39) and (40) become equivalent. Since the initial data satisfy neither condition, these instabilities do not contribute to the very early intensification. On the other hand, eq (41) is satisfied even in the initial data since there is a maximum of cyclonic vorticity close to the center of the storm and a vorticity minimum (maximum of anticyclonic relative vorticity) at a radius of approximately 345 km. This should favor the growth of wavelike perturbations in the azimuthal direction. Since weak waves of this type are



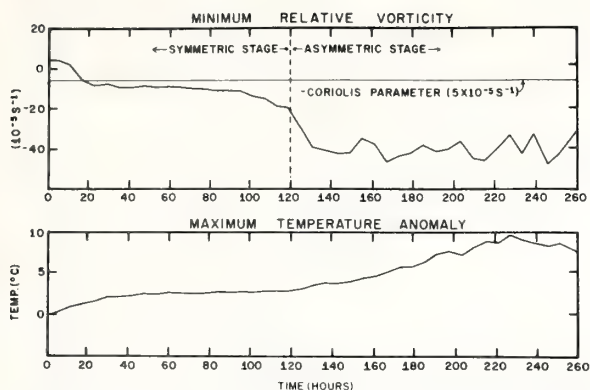


FIGURE 9.—(Top) time variation of the minimum relative vorticity in the upper troposphere (level 3/2) and (bottom) time variation of the maximum temperature anomaly (departure of temperature from the steady-state value at the lateral boundary) in the upper troposphere (level 3/2).

already present in the initial data (see subsection 2J), and since, as already noted, substantial symmetry is retained for the first 120 hr, it is clear that the instability is either quite weak or that it is being counteracted by other effects such as those due to eddy viscosity.

Figure 9(top) shows the time evolution of the minimum value of relative vorticity in the upper level within 350 km of the storm center. During the initial deepening stage, the minimum value of absolute vorticity becomes slightly negative. However, this occurs after the intensification and only over a small region.

Figure 10 shows the upper tropospheric relative vorticity at 84 hr, which is representative of the early symmetric stage. In view of the fact that the Coriolis parameter for this calculation is  $5 \times 10^{-5} \text{ s}^{-1}$ , it is clear that only small patches of negative absolute vorticity are present. The term  $[(2|V|/R) + f]$  was also evaluated for several times during the first 120 hr. These calculations revealed only small patches of anomalous winds. We, therefore, also feel that the instabilities represented by conditions (39) and (40) played no significant role in the early symmetric stage of the model storm.

Azimuthally averaged vertical cross sections provide an adequate description of the storm structure during the early symmetric stage. Mean cross sections<sup>2</sup> of this type for the tangential wind, radial wind, and the temperature departure at 84 hr are shown in figure 11. These cross sections reveal a structure very typical of that of a weak hurricane (Hawkins and Rubsam 1968).

The pattern of temperature anomaly (departure from the steady-state temperature on the lateral boundary) shows a maximum positive anomaly of  $2.8^\circ\text{C}$  in the upper troposphere. This value is small compared to those found

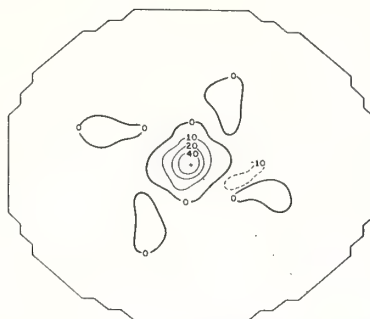


FIGURE 10.—Relative vorticity in the upper troposphere (level 3/2) at 84 hr. Isopleths are labeled in units of  $10^{-5} \text{ s}^{-1}$ .

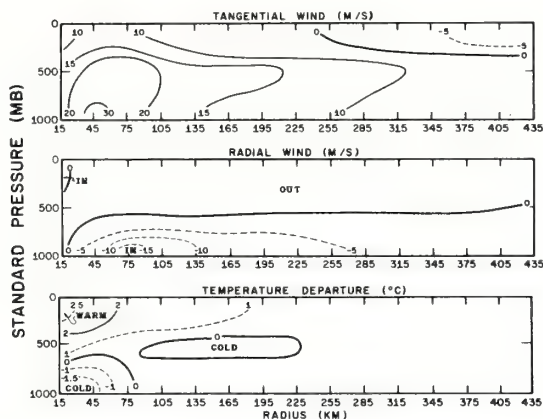


FIGURE 11.—Azimuthal mean vertical cross sections for the tangential wind, the radial wind, and the temperature anomaly at 84 hr. Isotherms are labeled in  $^\circ\text{C}$ ; isotachs are labeled in m/s.

in mature hurricanes. For a weak hurricane, however,  $2.8^\circ\text{C}$  does not seem unreasonable for the average temperature of a deep upper tropospheric layer. The cold core at level 7/2 (due primarily to an excess of adiabatic cooling over sensible and latent heating) contributes significantly to the low tropospheric inward pressure-gradient force through the hydrostatic equation. Some preliminary experiments, in which the cold core did not appear, showed only slight intensification. It is noted that observations frequently show a cold lower troposphere in the early stages of storm development (Yanai 1961). There is also evidence for a low-level cold region in the mature stage (Hawkins and Rubsam 1968, Colón et al. 1961).

The vertical motion at the top of the boundary layer at 84 hr shows a nearly circular region of upward motion that extends from the center to about 180 km. Maximum velocities of about  $-140 \text{ mb/hr}$  (about  $0.4 \text{ m/s}$ ) occur in a ring near the center. Weak subsidence occurs in the

<sup>2</sup> The circular averages were computed by linear interpolation of grid point values to a polar grid with a radial increment of 30 km and an angular increment of  $22.5^\circ$ .

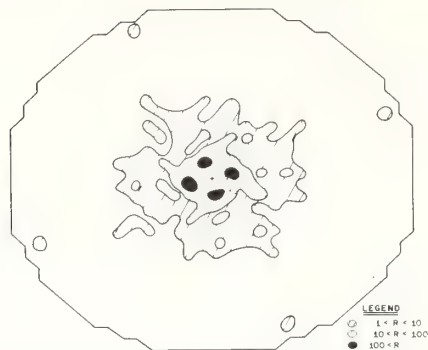


FIGURE 12.—Rainfall rates (cm/day) computed from the total latent heat release at 84 hr.

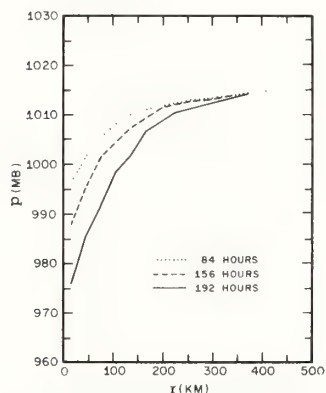


FIGURE 13.—Radial profiles of surface pressure along an east-west axis at 84, 156, and 192 hr.

environment beyond 180 km. The strongest upward velocities occur in the middle troposphere (level 5/2) and reach  $-230$  mb/hr (about  $0.7$  m/s). These values appear reasonable for averages over a 30-km interval of a weak hurricane (Carlson and Sheets 1971).

Figure 12 shows the rainfall rates at 84 hr. These are computed by conversion of the total release of latent heat in a column to the equivalent liquid water depth. Values of over 100 cm/day occur locally near the center and decrease rapidly outward. The average rainfall over the inner 100 km is 65 cm/day which is comparable with the estimates made by Riehl and Malkus (1961) for hurricane Daisy (1958). The total release of latent heat at this time is  $5.0 \times 10^{14}$  W. This also compares favorably with empirical estimates (Anthes and Johnson 1968). Finally, the rainfall pattern at 84 hr shows no evidence of spiral bands.

Figure 13 shows surface pressure profiles for various times along one radius from the center of the grid. Since the surface isobars are very nearly circular, these profiles

provide an adequate description of the surface pressure field. The minimum value at 84 hr (995 mb) is quite realistic for a maximum wind of 32 m/s (Colón 1963). The general shapes of the profiles agree well with observations (Fletcher 1955, Miller 1963).

The early symmetric period may be summarized as follows. After a short period of development (about 24 hr), a quasi-steady state is reached in which the model storm closely resembles a weak hurricane. The circulation is nearly axisymmetric. Air spirals inward in the low levels, ascends in a narrow ring, and flows outward in the upper levels. The outflow becomes anticyclonic beyond 200 km. However, the absolute vorticity in the outflow layer is positive except in small areas. The central pressure, temperature anomalies, rainfall rates, and the components of the kinetic energy budget correspond to a weak hurricane.

## B. ASYMMETRIC STAGE OF THE MODEL

As shown by the central pressure, maximum wind speed, and maximum temperature anomaly (figs. 3 and 9), the storm begins a second period of intensification at about 120 hr. Figures 14 and 15 show the low-level streamline and isotach analyses at 156 hr. The inflow is still fairly symmetric, but shows an increased intensity over that at 84 hr. The maximum wind speed is now 46 m/s; hurricane-force winds extend outward to 80 km and gale-force winds to 210 km. The average angle of inflow has increased to  $38^\circ$ .

In contrast to the symmetric inflow, the outflow occurs in a highly asymmetric fashion (figs. 16 and 17). Outflow occurs in two quadrants, and several small eddies are located about the main center. This asymmetric nature of the outflow is typical of many hurricanes (e.g., Alaka 1961, 1962; Miller 1963).

The vorticity at level 3/2 shows large regions of negative absolute vorticity (fig. 18). This is in contrast with the vorticity pattern at 84 hr (fig. 10). These regions are transient. They form and re-form in various sectors of the outflow level. This unsteady behavior of the outflow is probably related closely to the oscillations in the central pressure and maximum surface wind during the latter portions of the computation (fig. 3). It is noted that negative absolute vorticity is an observed feature of hurricane outflow (Alaka 1962) and even appears as a feature of composite mean storms (Izawa 1964).

The presence of large values of negative absolute vorticity suggests the presence of one or more of the types of dynamic instability discussed in the previous subsection. Since condition (40) refers to symmetric instability and since eq (41) is satisfied in the initial data without noticeable effect, attention was focused on condition (39). The quantity,  $2|V|/R$ , was computed for level 3/2 at 156 hr. In contrast to the early stages, anomalous winds are found to cover substantial areas of the domain and negative values of  $2|V|/R$  exceed  $40 \times 10^{-5} \text{ s}^{-1}$  (fig. 19). The presence of anomalous winds in hurricane outflow

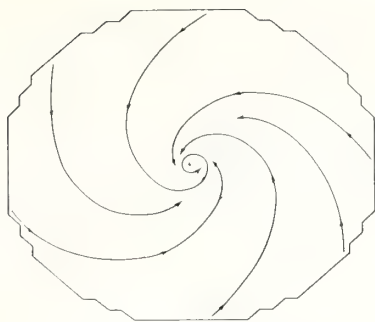


FIGURE 14.—Streamline analysis for the boundary layer (level 7/2) at 156 hr.

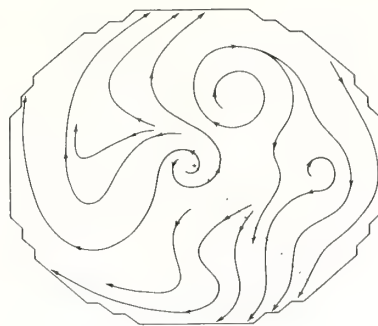


FIGURE 16.—Streamline analysis for the upper troposphere (level 3/2) at 156 hr.

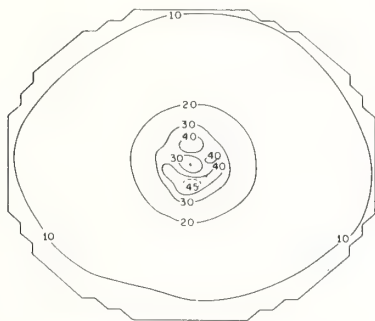


FIGURE 15.—Isotach analysis for the boundary layer (level 7/2) at 156 hr. Isopleths are labeled in m/s.

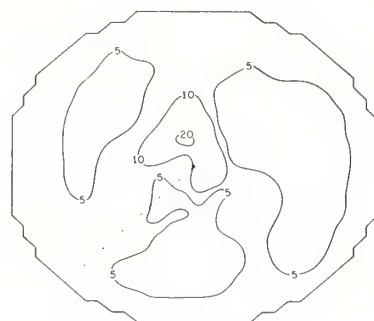


FIGURE 17.—Isotach analysis for the upper troposphere (level 3/2) at 156 hr. Isopleths are labeled in m/s.

has been documented by Alaka (1961). Indeed, the distribution and magnitude of  $2|V|/R$ , as shown by figure 19, is in remarkable agreement with Alaka's calculation for the 35,000-ft level of hurricane Daisy (1958).

On the other hand, figure 19 also shows that the regions of anomalous winds are closely related to the regions of negative absolute vorticity. As a result, condition (39) is satisfied only in the stippled region shown on the figure. This result is also similar to Alaka's (1963) findings. The stippled region on figure 19 shows a great deal of similarity to the corresponding region in the outflow layer of 1958 hurricane Daisy [see fig. 3 in Alaka (1963)].

The role of dynamic instability in the development of tropical cyclones has been subjected to prolonged debate. The work of Alaka (1961, 1962, 1963) clearly demonstrates that condition (39) is satisfied in the outflow layers of hurricanes; Sawyer (1947) and Alaka (1963) have further suggested that dynamic instability must already be present before significant development can take place. The pre-existence of dynamic instability in these hypotheses is accounted for by the presence of an upper tropospheric anticyclone. However, axisymmetric model calculations (Ooyama 1969, Rosenthal 1969) as well as the present asymmetric calculation indicate that dynamic instability

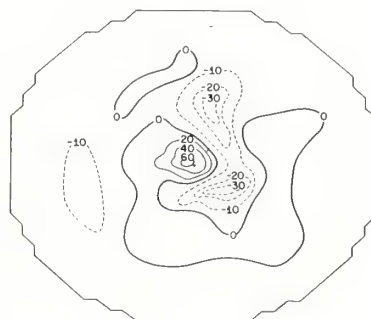


FIGURE 18.—Relative vorticity for the upper troposphere (level 3/2) at 156 hr. Isopleths are labeled in units of  $10^{-3} \text{ s}^{-1}$ .

is not a necessary condition for cyclone development, and instead can be generated as a consequence of cyclone intensification.

The numerical models, however, are probably not yet sufficiently sophisticated to give the final answer on this subject. In particular, all models available at this time consider only isolated vortices and make no provision for interactions with surrounding synoptic systems. Further-



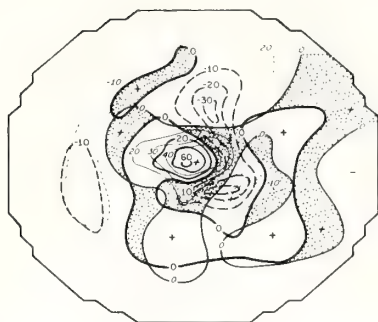


FIGURE 19.—Relative vorticity (heavy solid and dashed lines) and curvature term,  $2|V|/R$  (light solid and dashed lines), at 156 hr in the upper troposphere (level 3/2). The dotted area represents regions where the product of absolute vorticity and  $2|V|/R$  is negative. Isopleths are labeled in units of  $10^{-5} \text{ s}^{-1}$ .

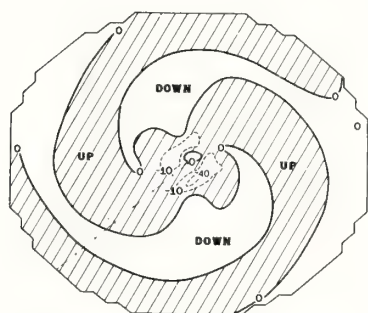


FIGURE 20.—Individual rate of change of pressure ( $\omega = dp/dt$ ) for level 7/2 at 156 hr. Isopleths are labeled in units of cb/hr.

more, none of the models has, as yet, reached the stage where testing with real data is justifiable. Regardless of the situation in the real atmosphere, the second period of intensification in this model calculation appears to be related to the development of areas of dynamic instability. If we refer to figure 9, we note that the minimum vorticity in the outflow layer becomes suddenly more negative at about 100 hr. The second period of deepening (as measured by central pressure and maximum winds) follows this increase in negative absolute vorticity by about 20 hr (fig. 3). As we have already pointed out, this second period of deepening is accompanied by a breakdown of the symmetry which had prevailed during the first 120 hr of the calculation. Since it is well known that the release of dynamic instability does not directly provide new kinetic energy but transforms azimuthal mean kinetic energy into perturbation kinetic energy (Yanai 1964, Kuo 1962, Kasahara 1961), the change in structure of the model storm is consistent with the release of dynamic instability. The change in intensity may, in an indirect fashion, also be related to dynamic in-

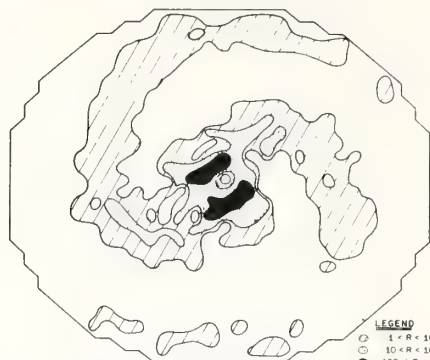


FIGURE 21.—Rainfall rates computed from the total release of latent heat at 156 hr. Isopleths are labeled in units of cm/day.

stability. The release of the dynamic instability provides for an increased upper level mass divergence and, therefore, increased low-level convergence. This, in turn, leads to a direct enhancement of the parameterized cumulus convection through eq (31) and (32). Coincident with the formation of asymmetries in the outflow is the appearance of spiral bands of rising motion which closely resemble hurricane rainbands. The vertical-motion pattern at level 7/2 (fig. 20) shows two bands of upward motion which begin at the edge of the domain and spiral inward toward the primary ring of upward motion near the center. The maximum vertical velocity near the center is  $-440 \text{ mb/hr}$  (about  $1.5 \text{ m/s}$ ).

In agreement with observations (Gentry 1964), the spiral bands are broken at a distance from the center (see the rainfall pattern, fig. 21) and become more solid as they spiral inward. The life span of a band is about 2.5 days.

The precipitation pattern, shown in figure 21, resembles a radar picture of a mature hurricane (e.g., Colón 1962, Colón et al. 1961, Donaldson and Atlas 1964). Strong convection occurs near the center in an irregular circle corresponding to an eye wall. Maximum rainfall rates in this region are over  $100 \text{ cm/day}$ . Two bands of weaker convection spiral in toward the center. The rainfall rates in the spiral bands are much less than those near the center of the storm, averaging only about  $3 \text{ cm/day}$ .

Tepper (1958) and Abdullah (1966) have suggested that hurricane rainbands are gravity waves similar to pressure jumps and, hence, to middle latitude squall lines. However, the rate of propagation and life span of these gravity waves (Abdullah 1966) are not at all consistent with the long life span of the observed bands (Gentry 1964) or those generated by the model. Faller (1962, 1965) has proposed that the rainbands may be explicable by Ekman-layer instability. The latter phenomenon has been reproduced in laboratory experiments with dishpans and results in spiral bands whose kinetic energy is derived from the kinetic energy of the mean tangential flow. This Ekman-

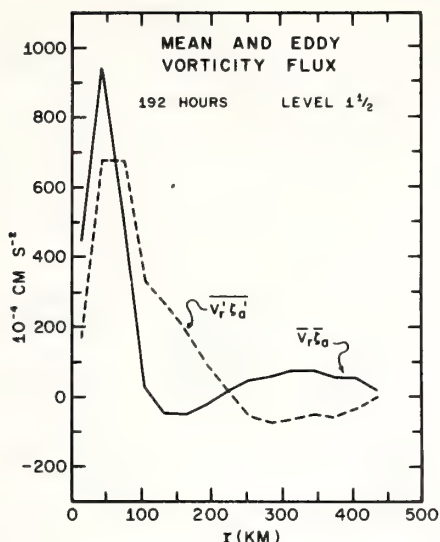


FIGURE 22.—Azimuthal mean ( $\overline{v_r \xi_a}$ ) and eddy ( $\overline{v_r' \xi_a'}$ ) horizontal vorticity flux in the upper troposphere (level 3/2) at 192 hr.

layer instability may well contribute to the development of spiral bands in the real atmosphere as well as in the model calculation. However, the fact that the spiral bands do not appear in the model calculation until the symmetry of the outflow pattern has been destroyed suggests that the generation of the bands and the breakdown of the outflow pattern may be related. As we have noted above, the loss of symmetry in the outflow appears to be associated with dynamic instability. It should be emphasized, however, that this linkage is merely speculation at this time and will be pursued further when we have had the opportunity to perform experiments with greater horizontal resolution. Such experiments will allow meaningful budget calculations on the scale of the rainband.

In a recent paper, Anthes (1970b) hypothesized that large-scale asymmetries between radii of 400 and 1000 km from the hurricane center may play an important role in satisfying the angular momentum budget of the mature hurricane. The mean radial flux of vorticity may be written

$$A \equiv \overline{v_r' \xi_a'} + \overline{v_r \xi_a} \quad (42)$$

where the  $\overline{(\quad)}$  operator refers to the azimuthal mean at a given radius and  $(\quad)'$  refers to departures from this mean.

For a hypothetical mean tangential velocity distribution which was typical of a hurricane, Anthes (1970b) calculated a minimum value of  $-150 \times 10^{-4} \text{ cm} \cdot \text{s}^{-2}$  for the eddy term,  $\overline{v_r' \xi_a'}$ , in the upper troposphere at a radius of

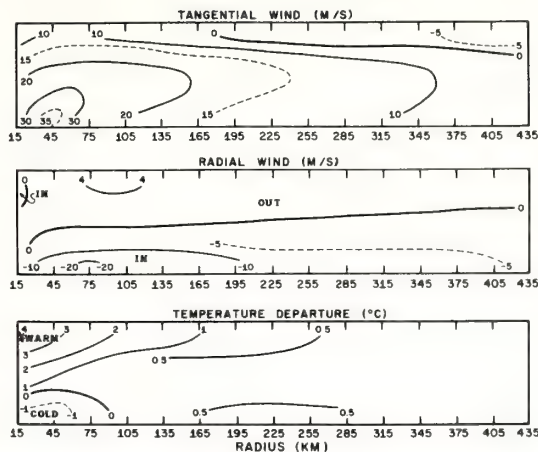


FIGURE 23.—Azimuthal mean vertical cross sections for the tangential wind, the radial wind, and the temperature anomaly at 156 hr. Isotherms are labeled in °C; isotachs are labeled in m/s.

400 km. This indicates that the outflow should be inversely correlated with absolute vorticity to satisfy the angular momentum budget in the slowly varying outflow region. Figure 22 shows the radial profiles of  $\overline{v_r' \xi_a'}$  and  $\overline{v_r \xi_a}$  computed for the model storm at 192 hr. Both mean and eddy transports of vorticity are positive inside 100 km. Beyond 100 km, however, where the vertical motion is small, there is indeed a negative correlation between outflow and absolute vorticity, and the eddy flux very nearly balances the mean flux from there to the limit of the domain.

Although the minimum value of  $\overline{v_r' \xi_a'}$  in figure 22 is  $-70 \times 10^{-4} \text{ cm} \cdot \text{s}^{-2}$  which is about half the minimum value found by Anthes (1970b), the qualitative agreement is good.

Figure 23 shows the azimuthally averaged vertical cross sections at 156 hr. The mean tangential and radial circulations are more intense than at 84 hr (fig. 11). The temperature section shows an increase in mean temperature anomaly from 2.5° to 4.1°C and a reduction in the low-level cold core maximum from  $-1.5^\circ$  to  $-1.0^\circ\text{C}$ . The weak middle-level cold region located between 105 and 225 km at 84 hr has disappeared by 156 hr.

In summary, beginning at about 100 hr, substantial areas of negative absolute vorticity appear in the upper level and the outflow pattern becomes asymmetric. Rainbands appear during this asymmetric stage. The storm is considerably less steady than during the earlier, symmetric stage, and the central pressure and maximum winds oscillate with a period of about 6 hr. This unsteady behavior appears to be related to the transient behavior of the regions of negative vorticity in the outflow layer.

From the time of appearance of the asymmetries at 120 hr, more or less continuous deepening occurs until



the storm reaches a maximum intensity at about 230 hr (fig. 3). At this time, the storm corresponds to a strong hurricane with a central pressure of 963 mb and a maximum wind speed of 65 m/s. The lapse rate in the inner region is very nearly pseudoadiabatic. After 230 hr, the storm begins to slowly fill and the calculation is terminated at 260 hr.

#### 4. SUMMARY AND CONCLUSIONS

Preliminary results show that the model is capable of reproducing many observed features of the three-dimensional tropical cyclone. Rather realistic simulations of spiral rainbands and the strongly asymmetric structure of the outflow are obtained.

Despite a relatively coarse horizontal resolution of 30 km, the model produces a storm with maximum winds exceeding 65 m/s and a kinetic energy budget that compares favorably with empirical estimates.

In the mature asymmetric stage of the storm, substantial regions of negative absolute vorticity, anomalous winds, and dynamic instability are present in the upper troposphere. There is a suggestion that the breakdown of the early symmetry of the flow, as well as the deepening which takes place during the asymmetric stage, are related to the dynamic instability. Large-scale horizontal asymmetries in the outflow are found to play a significant role in the transport of vorticity during the mature stage. Beyond 200 km, the eddy transport of vorticity is opposite in sign and nearly equal in magnitude to the mean transport. This agrees well with earlier estimates.

Obvious deficiencies of the present model include the absence of a continuity equation for water vapor, the lack of a representation of the vertical transport of momentum by cumulus, a coarse horizontal resolution, and a small computational domain. Work toward the elimination of these shortcomings is in progress.

#### ACKNOWLEDGMENTS

The authors thank Mr. Billy M. Lewis for his cooperation in obtaining computer facilities for this experiment. We also thank the operators of the User 200 facility, Miss Shirley Parris, Mrs. Barbara Creech, Miss Deborah Goray, and Messrs. Karl Kellar and William Foltz for their time and effort that was necessary for the progress of the model.

We acknowledge Mr. Robert Carrodus, Mr. John Lundblad, and Mr. Glenn Frye for the drafting of the figures; and Mr. Charles True for the photography. We also thank Mrs. Mary Jane Clarke for typing the manuscript.

#### REFERENCES

- Abdullah, Abdul Jabbar, "The Spiral Bands of a Hurricane: A Possible Dynamic Explanation," *Journal of the Atmospheric Sciences*, Vol. 23, No. 4, July 1966, pp. 367-375.
- Alaka, M. A., "The Occurrence of Anomalous Winds and Their Significance," *National Hurricane Research Project Report No. 45*, U.S. Department of Commerce, Weather Bureau, Miami, Fla., June 1961, 26 pp.
- Alaka, M. A., "On the Occurrence of Dynamic Instability in Incipient and Developing Hurricanes," *National Hurricane Research Project Report No. 50*, U.S. Department of Commerce, Weather Bureau, Miami, Fla., Mar. 1962, pp. 51-56.
- Alaka, M. A., "Instability Aspects of Hurricane Genesis," *National Hurricane Research Project Report No. 64*, U.S. Department of Commerce, Weather Bureau, Miami, Fla., June 1963, 23 pp.
- Anthes, Richard Allen, "A Diagnostic Model of the Tropical Cyclone in Isentropic Coordinates," *ESSA Technical Memorandum ERLTM-NHRL 89*, U.S. Department of Commerce, National Hurricane Research Laboratory, Miami, Fla., Apr. 1970a, 147 pp.
- Anthes, Richard Allen, "The Role of Large-Scale Asymmetries and Internal Mixing in Computing Meridional Circulations Associated With the Steady-State Hurricane," *Monthly Weather Review*, Vol. 98, No. 7, July 1970b, pp. 521-528.
- Anthes, Richard Allen, "Numerical Experiments With a Two-Dimensional Horizontal Variable Grid," *Monthly Weather Review*, Vol. 98, No. 11, Nov. 1970c, pp. 810-822.
- Anthes, Richard Allen, and Johnson, Donald R., "Generation of Available Potential Energy in Hurricane Hilda (1964)," *Monthly Weather Review*, Vol. 96, No. 5, May 1968, pp. 291-302.
- Carlson, Toby N., and Sheets, Robert C., "Comparison of Draft Scale Vertical Velocities Computed From Gust Probe and Conventional Data Collected by a DC-6 Aircraft," *ESSA Technical Memorandum ERLTM-NHRL 91*, U.S. Department of Commerce, National Hurricane Research Laboratory, Miami, Fla., June 1971, 39 pp.
- Charney, Jule G., and Eliassen, Arnt, "On the Growth of the Hurricane Depression," *Journal of the Atmospheric Sciences*, Vol. 21, No. 1, Jan. 1964, pp. 68-75.
- Colón, José A., "Changes in the Eye Properties During the Life Cycle of Tropical Hurricanes," *National Hurricane Research Project Report No. 50*, U.S. Department of Commerce, Weather Bureau, Miami, Fla., Mar. 1962, pp. 341-354.
- Colón, José A., "On the Evolution of the Wind Field During the Life Cycle of Tropical Cyclones," *National Hurricane Research Project Report No. 65*, U.S. Department of Commerce, Weather Bureau, Miami, Fla., Nov. 1963, 36 pp.
- Colón, José A., and Staff, "On the Structure of Hurricane Daisy," *National Hurricane Research Project Report No. 48*, U.S. Department of Commerce, Weather Bureau, Miami, Fla., Oct. 1961, 102 pp.
- Donaldson, Ralph J., Jr., and Atlas, David, "Radar in Tropical Meteorology: A Survey Paper," *Proceedings of the Symposium on Tropical Meteorology, Rotorua, New Zealand, November 5-13, 1963*, New Zealand Meteorological Service, Wellington, 1964, pp. 423-473.
- Faller, Alan J., "An Experimental Analogy to and Proposed Explanation of Hurricane Spiral Bands," *National Hurricane Research Project Report No. 50*, U.S. Department of Commerce, Weather Bureau, Miami, Fla., Mar. 1962, pp. 307-313.
- Faller, Alan J., "Large Eddies in the Atmospheric Boundary Layer and Their Possible Role in the Formation of Cloud Rows," *Journal of the Atmospheric Sciences*, Vol. 22, No. 2, Mar. 1965, pp. 176-184.
- Fletcher, Robert Dawson, "Computation of Maximum Surface Winds in Hurricanes," *Bulletin of the American Meteorological Society*, Vol. 36, No. 6, June 1955, pp. 247-250.
- Gentry, R. Cecil, "A Study of Hurricane Rainbands," *National Hurricane Research Project Report No. 69*, U.S. Department of Commerce, Weather Bureau, Miami, Fla., Mar. 1964, 85 pp.
- Grammeltvedt, Arne, "A Survey of Finite-Difference Schemes for the Primitive Equations for a Barotropic Fluid," *Monthly Weather Review*, Vol. 97, No. 5, May 1969, pp. 384-404.
- Gray, William M., "The Mutual Variation of Wind, Shear, and Baroclinicity in the Cumulus Convective Atmosphere of the Hurricane," *Monthly Weather Review*, Vol. 95, No. 2, Feb. 1967, pp. 55-73.



- Hawkins, Harry F., and Rubsam, Daryl T., "Hurricane Hilda, 1964: II. Structure and Budgets of the Hurricane on October 1, 1964," *Monthly Weather Review*, Vol. 96, No. 9, Sept. 1968, pp. 617-636.
- Hebert, Paul J., and Jordan, Charles L., "Mean Soundings for the Gulf of Mexico Area," *National Hurricane Research Project Report No. 30*, U.S. Department of Commerce, Weather Bureau, Miami, Fla., Apr. 1959, 10 pp.
- Izawa, Tatsuo, "On the Mean Wind Structure of Typhoon," *Typhoon Research Laboratory Technical Note No. 2*, Meteorological Research Institute, Tokyo, Japan, Mar. 1964, 19 pp.
- Kasahara, Akira, "A Study of the Stability of Thermally Driven and Frictionally Controlled Symmetric Motions With Application to the Mechanism for the Development of Tropical Cyclones," *Technical Report No. 16*, Contract No. Cwb-9941, Department of Meteorology, University of Chicago, Ill., Aug. 1961, 63 pp.
- Koss, Walter J., "Numerical Integration Experiments With Variable Resolution Two-Dimensional Cartesian Grids Using the Box Method," *Monthly Weather Review*, Vol. 99, No. 10, Oct. 1971, pp. 725-738.
- Kuo, Hsiao-Lan, "Dynamic Instability of Two-Dimensional Non-divergent Flow in a Barotropic Atmosphere," *Journal of Meteorology*, Vol. 6, No. 2, Apr. 1949, pp. 105-122.
- Kuo, Hsiao-Lan, "Mechanism Leading to Hurricane Formation," *National Hurricane Research Project Report No. 50*, U.S. Department of Commerce, Weather Bureau, Miami, Fla., Mar. 1962, pp. 277-283.
- Kuo, Hsiao-Lan, "On Formation and Intensification of Tropical Cyclones Through Latent Heat Release by Cumulus Convection," *Journal of the Atmospheric Sciences*, Vol. 22, No. 1, Jan. 1965, pp. 40-63.
- Kurihara, Yoshio, and Holloway, J. Leith, Jr., "Numerical Integration of a Nine-Level Global Primitive Equations Model Formulated by the Box Method," *Monthly Weather Review*, Vol. 95, No. 8, Aug. 1967, pp. 509-530.
- Langlois, W. E., and Kwok, H. C. W., "Description of the Mintz-Arakawa Numerical General Circulation Model," *Numerical Simulation of Weather and Climate, Technical Report No. 3*, Department of Meteorology, University of California, Los Angeles, Feb. 1969, 95 pp.
- Matsuno, Taroh, "Numerical Integrations of the Primitive Equations by a Simulated Backward Difference Method," *Journal of the Meteorological Society of Japan*, Ser. 2, Vol. 44, No. 1, Tokyo, Feb. 1966, pp. 76-84.
- Miller, Banner I., "On the Momentum and Energy Balance of Hurricane Helene (1958)," *National Hurricane Research Project Report No. 53*, U.S. Department of Commerce, Weather Bureau, Miami, Fla., Apr. 1962, 19 pp.
- Miller, Banner I., "On the Filling of Tropical Cyclones Over Land," *National Hurricane Research Project Report No. 66*, U.S. Department of Commerce, Weather Bureau, Miami, Fla., Dec. 1963, 82 pp.
- Molenkamp, Charles R., "Accuracy of Finite-Difference Methods Applied to the Advection Equation," *Journal of Applied Meteorology*, Vol. 7, No. 2, Apr. 1968, pp. 160-167.
- Ogura, Yoshimitsu, "Frictionally Controlled, Thermally Driven Circulations in a Circular Vortex With Application to Tropical Cyclones," *Journal of the Atmospheric Sciences*, Vol. 21, No. 6, Nov. 1964, pp. 610-621.
- Ooyama, Katsuyuki, "Numerical Simulation of the Life-Cycle of Tropical Cyclones," *Journal of the Atmospheric Sciences*, Vol. 26, No. 1, Jan. 1969, pp. 3-40.
- Palmén, Erik H., and Riehl, Herbert, "Budget of Angular Momentum and Kinetic Energy in Tropical Cyclones," *Journal of Meteorology*, Vol. 14, No. 2, Apr. 1957, pp. 150-159.
- Phillips, Norman A., "A Coordinate System Having Some Special Advantages for Numerical Forecasting," *Journal of Meteorology*, Vol. 14, No. 2, Apr. 1957, pp. 184-185.
- Richtmyer, Robert D., and Morton, K. W., *Difference Methods for Initial Value Problems*, 2d Edition, Interscience Publishers, New York, N.Y., 1967, 405 pp.
- Riehl, Herbert, and Malkus, Joanne S., "Some Aspects of Hurricane Daisy, 1958," *Tellus*, Vol. 13, No. 2, Stockholm, Sweden, May 1961, pp. 181-213.
- Rosenthal, Stanley L., "Numerical Experiments With a Multilevel Primitive Equation Model Designed to Simulate the Development of Tropical Cyclones: Experiment I," *ESSA Technical Memorandum ERLTM-NHRL 82*, U.S. Department of Commerce, National Hurricane Research Laboratory, Miami, Fla., Jan. 1969, 36 pp.
- Rosenthal, Stanley L., "A Survey of Experimental Results Obtained From a Numerical Model Designed to Simulate Tropical Cyclone Development," *ESSA Technical Memorandum ERLTM-NHRL 88*, U.S. Department of Commerce, National Hurricane Research Laboratory, Miami, Fla., Jan. 1970a, 78 pp.
- Rosenthal, Stanley L., "A Circularly Symmetric Primitive Equation Model of Tropical Cyclone Development Containing an Explicit Water Vapor Cycle," *Monthly Weather Review*, Vol. 98, No. 9, Sept. 1970b, pp. 643-663.
- Sawyer, John Stanley, "Notes on the Theory of Tropical Cyclones," *Quarterly Journal of the Royal Meteorological Society*, Vol. 73, Nos. 315-316, London, England, Jan.-Apr. 1947, pp. 101-126.
- Sheets, Robert C., "Some Mean Hurricane Soundings," *Journal of Applied Meteorology*, Vol. 8, No. 1, Feb. 1969, pp. 134-146.
- Shuman, Frederick G., and Stackpole, John D., "Note on the Formulation of Finite Difference Equations Incorporating a Map Scale Factor," *Monthly Weather Review*, Vol. 96, No. 3, Mar. 1968, pp. 157-161.
- Smagorinsky, Joseph, Manabe, Syukuro, and Holloway, J. Leith, Jr., "Numerical Results From a Nine-Level General Circulation Model of the Atmosphere," *Monthly Weather Review*, Vol. 93, No. 12, Dec. 1965, pp. 727-768.
- Syōno, Sigekata, and Yamasaki, Masanori, "Stability of Symmetrical Motions Driven by Latent Heat Release by Cumulus Convection Under the Existence of Surface Friction," *Journal of the Meteorological Society of Japan*, Ser. 2, Vol. 44, No. 6, Tokyo, Dec. 1966, pp. 353-375.
- Tepper, Morris, "A Theoretical Model for Hurricane Radar Bands," *Proceedings of the Seventh Weather Radar Conference, Miami Beach, Florida, November 17-20, 1958*, American Meteorological Society, Boston, Mass., Dec. 1958, pp. K-56-K-65.
- Yamasaki, Masanori, "A Tropical Cyclone Model With Parameterized Vertical Partition of Released Latent Heat," *Journal of the Meteorological Society of Japan*, Vol. 46, No. 3, Tokyo, June 1968a, pp. 202-214.
- Yamasaki, Masanori, "Detailed Analysis of a Tropical Cyclone Simulated With a 13-Layer Model," *Papers in Meteorology and Geophysics*, Vol. 19, No. 4, Meteorological Research Institute, Tokyo, Japan, Dec. 1968b, pp. 559-585.
- Yanai, Michio, "A Detailed Analysis of Typhoon Formation," *Journal of the Meteorological Society of Japan*, Ser. 2, Vol. 39, No. 4, Tokyo, Aug. 1961, pp. 187-214.
- Yanai, Michio, "Formation of Tropical Cyclones," *Reviews of Geophysics*, Vol. 2, No. 2, May 1964, pp. 367-414.

[Received September 20, 1970; revised January 20, 1971]

## Three Dimensional Particle Trajectories in a Model Hurricane

RICHARD A. ANTHERS AND JAMES W. TROUT, *National Hurricane  
Research Laboratory, NOAA, and* STELLAN S. OSTLUND,  
*Coral Gables Senior High School*

WHAT paths would small particles (or balloons) follow if released near the surface of a stationary hurricane? This paper presents several views of some theoretical trajectories of particles released in the low levels of a three-dimensional hurricane model. The tracks of the particles illustrate the three-dimensional structure of a model hurricane circulation during an eight-day period of the storm's life cycle. These results may prove useful in the development of balloon monitoring systems that are designed to investigate the hurricane circulation.

### Discussion of Model

The asymmetric hurricane model utilized to compute the trajectories is quite similar to the model described by Anthes et al. (1971). The model consists of three levels in the vertical and covers a horizontal domain of approximately 900 km. The model simulates the physical processes that are currently considered to be crucial to hurricane formation and maintenance; i.e., release of latent heat of condensation through cumulus convection, surface friction, and the addition of sensible and latent heat to the air from the ocean. The model storm starts from a nearly symmetric (above the vertical axis of rotation) vortex with a maximum wind speed of about 35 knots. After a short "organizational period," the model storm intensifies and reaches a relatively steady state in which the maximum wind speed is about 75 knots. During this stage the storm remains nearly symmetric about the axis of rotation. After several days, the storm enters a new stage in which horizontal asymmetries (azimuthal variations about the vertical axis) become large. The storm continues to intensify and maximum winds eventually exceed 110 knots.

Notable asymmetric features of the storm circulation during the more intense stage are

weak bands of upward motion which spiral into the center of the storm, and large, horizontal eddies in the upper-level outflow region. These eddies, which are cyclonic or anticyclonic vortices with radii of about 100 miles, continuously form near the center and drift slowly outward. Because of the small domain and absence of any environmental "steering flow," the storm remains nearly stationary during its life cycle.

### Computation of Particle Trajectories

To compute the three-dimensional trajectories, it is necessary to know the horizontal and vertical motions as a function of time. The velocity components at each point in the model are saved at 4-hour intervals during the model forecast. These data are interpolated in time to provide values at more frequent intervals (15 minutes) for the calculation of the trajectories. Since the model has very coarse horizontal and vertical resolution, it is also necessary to interpolate the velocity components in space. If  $\bar{f}$  denotes the interpolated value of any variable  $f$ , the successive positions of each particle are computed from the following equations:

$$x^{t+15 \text{ min}} = x^t + \bar{u}\Delta t \quad (1)$$

$$y^{t+15 \text{ min}} = y^t + \bar{v}\Delta t \quad (2)$$

$$z^{t+15 \text{ min}} = z^t + \bar{w}\Delta t \quad (3)$$

where  $x^t$ ,  $y^t$  and  $z^t$  are the 3-dimensional coordinates of a particle at a time,  $t$ ,  $\Delta t$  is 15 minutes;  $u$ ,  $v$ , and  $w$  are the east-west, north-south, and vertical velocity components, respectively. (Although the vertical coordinate system in the model is the  $\sigma$ -coordinate system (Phillips, 1957), the more familiar geometric height,  $Z$ , is employed in this paper.)

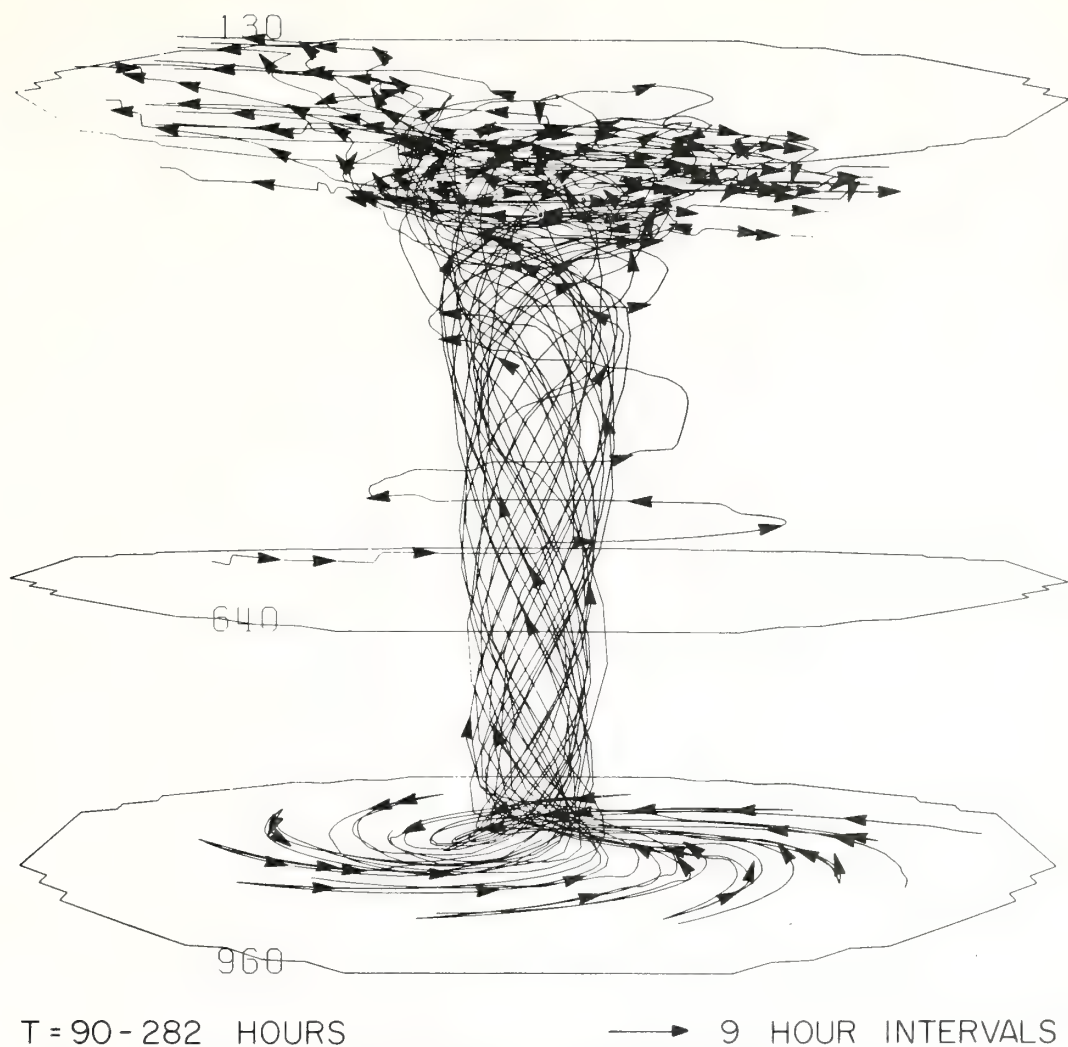


Fig. 1. Particle trajectories calculated from a numerical model of an asymmetrical hurricane. Labels of three levels in millibars.

The computation procedure consists of following ten particles moving through the hurricane system during an eight-day period. The eight-day period begins at 90 hours following the beginning of the model forecast and continues until 282 hours. The initial positions of the ten particles are scattered throughout the inflow layer of the hurricane at an elevation of about 3,000 ft above sea level. If any particle is carried outside the model's domain, a new particle is started in the inflow layer at a distance of about 200 nautical miles from the storm center. The starting position of each successive particle is rotated  $36^\circ$  to provide uniform coverage of the inflow layer.

#### Particle Trajectories Viewed from Four Perspectives

Figure 1 shows the tracks made by the particles during the eight-day period. (The paths of the particles are plotted automatically by a CalComp pen plotter.) The arrows denote the position and direction of motion for each particle at 9-hour intervals. In interpreting the figures, it must be remembered that the vertical dimension is greatly exaggerated. The vertical scale of the hurricane is only about 10 miles compared to the horizontal scale of about 500 miles.

In figure 1, the particles spiral inward, reaching the intense updraft region (cor-

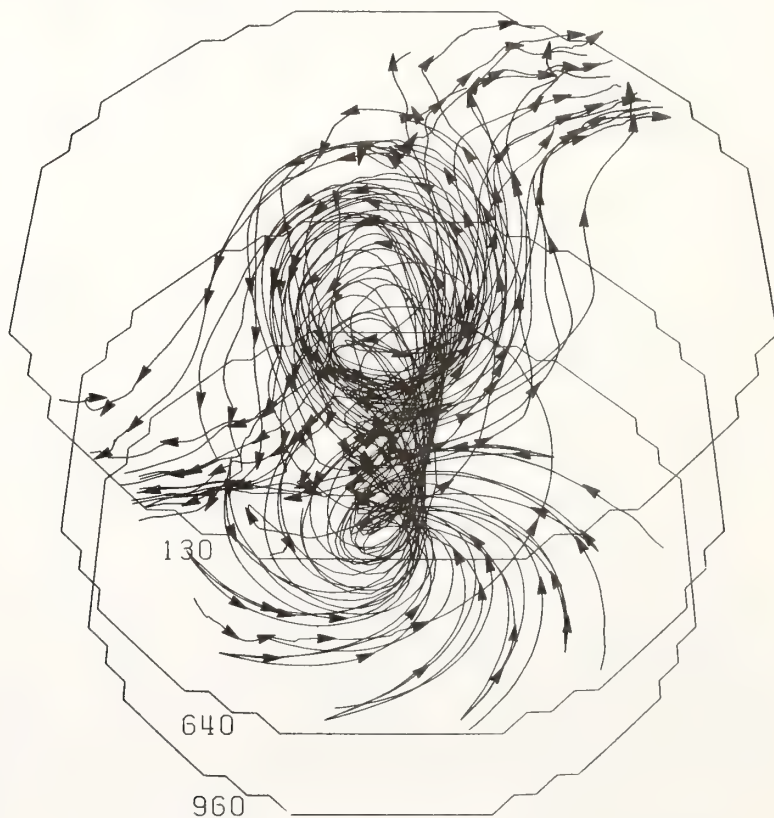




T = 90 - 282 HOURS

→ 9 HOUR INTERVALS

Fig. 2. View of same trajectories (see Fig. 1) from a higher elevation angle.



T = 90 - 282 HOURS

→ 9 HOUR INTERVALS

Fig. 3. Another view of trajectories from a still higher elevation angle.

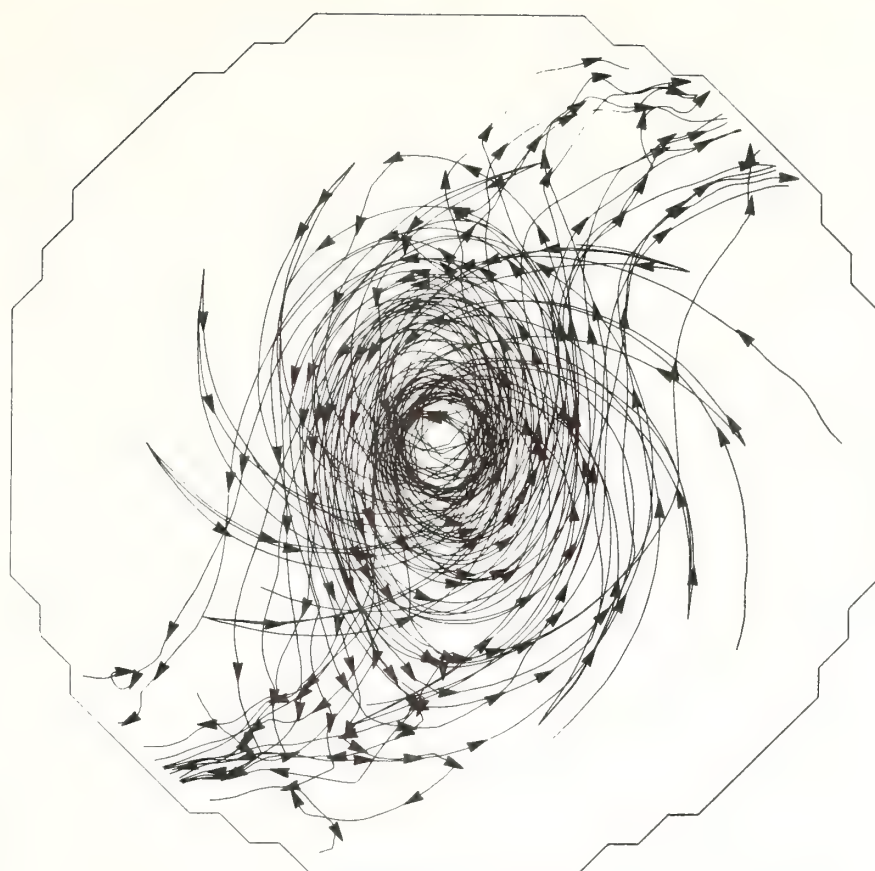


Fig. 4. Projection of particle trajectories onto a horizontal.

T = 90 - 282 HOURS

→ 9 HOUR INTERVALS

responding to the eye-wall) near the center of the storm after about 10 hours. The particles are quickly carried upward in a spiral ascent, circling the storm center once during the approximately three hours required to reach the top. It should be noted at this point that the *large-scale* vertical velocity rather than the *cloud-scale* vertical velocity is used to compute the vertical displacement of the particles, since clouds are not forecast explicitly in the model. In reality a specific particle would probably be carried up in a cloud updraft at a much faster rate than that calculated using the average vertical velocity.

Upon reaching the upper levels of the model, the particles are carried away from the storm center. In contrast to the nearly symmetric inflow, it may be noted that during the 8 days the outflow occurs mainly in two quadrants. The two preferred quadrants of outflow reflect the asymmetric circulation around the horizontal eddies which are present during this period.

Figure 1 also shows the path of one particle which was started in the middle levels rather than in the inflow layer. Since the inflow is very weak at this level, the particle spirals slowly upward around the center of the storm. The particle does not enter the eyewall before reaching the outflow layer.

Figures 2-4 illustrate several views of the same trajectories from higher (more vertical) zenith angles. Figure 4 shows the trajectories projected on a horizontal plane in which the vertical dimension is not distinguishable.

The views which emphasize the horizontal motions show that relatively few particles are trapped in the slow-moving air at the center of the horizontal eddies in the outflow region. Occasionally, however, a particle approaches the center of an eddy and makes a complete loop. Figure 5 shows one such particle which makes a clockwise loop during a 15-hour time period. (Note that the arrows are drawn at 3-hour intervals in figure 5.)

In summary, particle trajectories over an 8-day period of a model hurricane illustrate

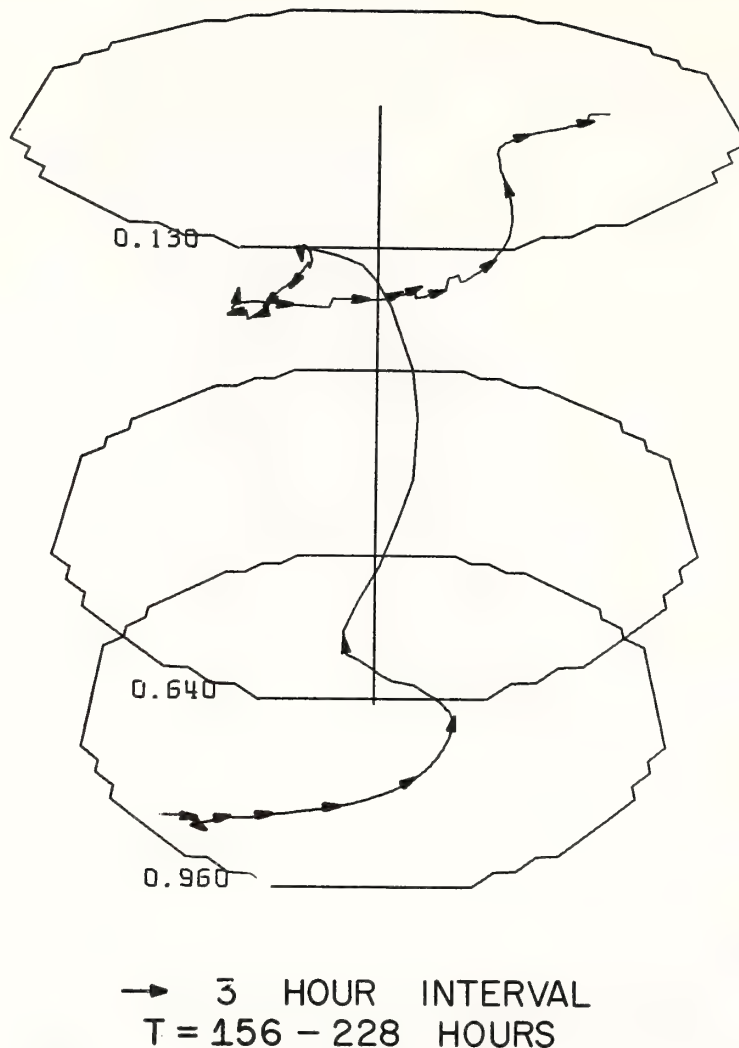


Fig. 5. Trajectory of a single particle showing complete anticyclonic (clockwise) loop in the upper level outflow layer.

a nearly symmetric, steady, inflow layer, a small ring of rapidly rising air near the center, and a relatively asymmetric, unsteady outflow region where the paths of the particles are governed by the position of one or two horizontal eddies. Based on the large-scale, average velocities in the hurricane, it takes a typical particle about 10 hours to reach the eyewall from a distance of 200 miles, and about 3 hours to rise from the low level to the upper level. After reaching the outflow region the particles decelerate and follow widely differing paths. Most particles are carried out of the hurricane environment in

2 to 4 days by relatively fast-moving air streams which are controlled by the position of eddies in the outflow layer. Occasionally, a particle may approach the center of one of these eddies and make a complete loop. Such particles may reside in the outflow layer for more than 5 days.

#### References

- Anthes, Richard A., Stanley L. Rosenthal and James W. Trout, 1971: Preliminary results from an asymmetric model of the tropical cyclone. *Mon. Wea. Rev.* **99** (in press).
- Phillips, Norman A., 1957: A coordinate system having some special advantages for numerical forecasting. *J. Meteor.* **14-2**, 184-85.



October 1971

759

UDC 551.515.21

## COMPARISONS OF TROPICAL CYCLONE SIMULATIONS WITH AND WITHOUT THE ASSUMPTION OF CIRCULAR SYMMETRY

RICHARD A. ANTHERS, JAMES W. TROUT, and STANLEY L. ROSENTHAL

National Hurricane Research Laboratory, Environmental Research Laboratories, NOAA, Miami, Fla.

### ABSTRACT

Results from a three-layer asymmetric hurricane model previously described by the authors are compared with results from an axially symmetric analog to investigate the effect of the symmetry assumption on the internal dynamics of model cyclones. The symmetric model storm initially develops more rapidly than the asymmetric storm. The differences in intensity during the first 100 hr are related to differences in horizontal resolution produced by the staggered grid used with the symmetric model. The symmetric model, on the other hand, does not produce the second period of intensification that starts at 120 hr in the asymmetric model. This fact supports the conclusion reached in the earlier paper that the development of large-scale asymmetries at 100 hr is closely related to the subsequent intensification.

Although the life cycles of the two storms are different, the azimuthally averaged structure of the asymmetric storm at maximum intensity is similar to the corresponding structure of the symmetric model storm and supports the adequacy of symmetric models in investigating many aspects of tropical cyclone structure.

### 1. INTRODUCTION

Preliminary results from an asymmetric model have simulated the characteristic features of the tropical cyclone with a surprising degree of realism in spite of the coarse horizontal (30 km) and vertical (three layers) resolution (Anthes et al. 1971, hereafter designated ART). In particular, this model reproduced spiral rainbands and the strongly asymmetric structure of the outflow layer. Although realistic results with axisymmetric models have been obtained by a number of authors (Yamasaki 1968, Ooyama 1969, Rosenthal 1970, Sundqvist 1970), the symmetry assumption, at first glance, appears to be rather severe. An important area of investigation is, therefore, the effect of the symmetry assumption on the internal dynamics of the model cyclone. Comparison between results obtained from symmetric and asymmetric models which are otherwise similar is a potential tool in this area of investigation.

The primary purpose of this paper is to compare results of the asymmetric model (ART) with results from an axially symmetric analog model which is nearly identical. A secondary objective is to briefly summarize experiments with this symmetric model which were helpful in the design of the asymmetric model. The next section describes the numerical framework of the symmetric analog with particular emphasis on the differences between it and the asymmetric model. The major differences are the use of polar rather than Cartesian coordinates and the horizontal staggering of variables, which is a feature of the symmetric model but not of the asymmetric model.

### 2. DESIGN OF THE SYMMETRIC MODEL

#### A. BASIC EQUATIONS

The equations of motion in the  $\sigma$ -coordinate system (Phillips 1957) under the assumption of axial symmetry

may be written

$$\frac{\partial p^* u}{\partial t} = -\frac{1}{r} \frac{\partial}{\partial r} (r p^* u^2) + \frac{p^* v^2}{r} - p^* \frac{\partial \dot{\sigma}}{\partial \sigma} + f v p^* - p^* \frac{\partial \phi}{\partial r} - R T \frac{\partial p^*}{\partial r} + \frac{1}{r^2} \frac{\partial}{\partial r} \left[ K_H r^3 \frac{\partial}{\partial r} \left( p^* \frac{u}{r} \right) \right] + F_v(u) \quad (1)$$

and

$$\frac{\partial p^* v}{\partial t} = -\frac{1}{r} \frac{\partial}{\partial r} (r p^* u v) - \frac{p^* u v}{r} - p^* \frac{\partial \dot{\sigma}}{\partial \sigma} - f u p^* + \frac{1}{r^2} \frac{\partial}{\partial r} \left[ K_H r^3 \frac{\partial}{\partial r} \left( p^* \frac{v}{r} \right) \right] + F_v(v). \quad (2)$$

The symbols  $u$  and  $v$  are the velocity components in the radial ( $r$ ) and tangential ( $\lambda$ ) directions respectively,  $p^*$  is the surface pressure,  $\sigma = p/p^*$ , where  $p$  is pressure and  $\dot{\sigma}$  is the vertical velocity in the  $\sigma$ -system. The symbol  $\phi$  denotes the geopotential of a  $\sigma$ -surface,  $T$  is temperature, and  $R$  is the gas constant for dry air. The Coriolis parameter,  $f$ , is  $5 \times 10^{-5} \text{ s}^{-1}$  and is appropriate to approximately  $20^\circ \text{N}$ . Terms involving  $K_H$  (the horizontal eddy viscosity coefficient) represent the horizontal diffusion of momentum, and the terms involving  $F_v$  represent vertical eddy diffusivity of momentum. These are discussed later.

The continuity and thermodynamic equations are

$$\frac{\partial p^*}{\partial t} = -\frac{1}{r} \frac{\partial}{\partial r} (r p^* u) - \frac{\partial p^* \dot{\sigma}}{\partial \sigma} \quad (3)$$

and

$$\frac{\partial p^* T}{\partial t} = -\frac{1}{r} \frac{\partial}{\partial r} (r p^* u T) - p^* \frac{\partial \dot{\sigma} T}{\partial \sigma} + \frac{R T \omega}{c_p \sigma} + \frac{p^*}{c_p} \dot{Q} + \frac{p^* K_r}{r} \frac{\partial}{\partial r} \left( r \frac{\partial T}{\partial r} \right) \quad (4)$$

where  $\dot{Q}$  is the diabatic heating per unit mass,  $c_p$  is the specific heat at constant pressure, and  $\omega = dp/dt$  is related

VERTICAL STRUCTURE			
VARIABLE		K	p(mb)
$\sigma = 0$	////////////////////	1	0
$\nabla, T$	-----	1 1/2	225
$\sigma, \phi$	-----	2	450
$\nabla, T$	-----	2 1/2	675
$\sigma, \phi$	-----	3	900
$\nabla, T$	-----	3 1/2	957.5
$\phi = \sigma = 0$	-----	4	1015

FIGURE 1.—Vertical information-levels for symmetric and asymmetric models.

to  $\dot{\sigma}$  by

$$\omega = p^* \dot{\sigma} + \sigma \frac{dp^*}{dt}. \quad (5)$$

The term involving the thermal diffusivity for heat,  $K_\tau$ , represents the lateral diffusion of heat due to the presence of subgrid-scale eddies. The hydrostatic equation in the  $\sigma$ -system is

$$\frac{\partial \phi}{\partial \sigma} = -\frac{RT}{\sigma}. \quad (6)$$

Except for the assumption of symmetry and the use of polar coordinates, these are the equations used by Smagorinsky et al. (1965) for general circulation studies and those used in ART for the asymmetric hurricane model.

## B. STRUCTURE OF THE SYMMETRIC MODEL

The vertical structure of the model (fig. 1) is identical to that of the asymmetric model and features upper and lower tropospheric layers of equal pressure depth and a thinner Ekman boundary layer. The information levels for the dynamic and thermodynamic variables are staggered according to the scheme used by Kurihara and Holloway (1967). The horizontal mesh, however, differs significantly from that for the asymmetric model. To avoid the singularity at the origin of the polar coordinate system, the thermodynamic variables, including  $p^*$ ,  $T$ ,  $\dot{Q}$ ,  $\dot{\sigma}$ , and  $\omega$ , are forecast at grid points halfway between the prediction points for the momentum variables, as in previous symmetric models (Yamasaki 1968, Ooyama 1969, Rosenthal 1970). While identical horizontal grids in the symmetric and asymmetric models would be desirable for purposes of comparison, the alternative of defining the thermodynamic and momentum variables at the same points in the symmetric analog would yield additional computational differences at the singularity,  $r=0$ . Difference in results due to this effect would make comparisons with the asymmetric model as difficult as is presently the case. Finally, it is important to isolate and explain differences due to the horizontal grid systems since the vast majority of previous symmetric hurricane experiments have utilized the staggered grid system. Since the motion vanishes at  $r=0$  because of the symmetry condition, no computations are required at the pole. The pressure-weighted horizontal velocity components,  $up^*$  and  $vp^*$  are thus forecast at the radii

$$r_j = (j-1)\Delta r, \quad j=2, 3, \dots, \quad (7)$$

while the remaining variables are calculated at the radii

$$r_j = (j - \frac{1}{2})\Delta r, \quad j=1, 2, \dots \quad (8)$$

This grid staggering is the major numerical difference between the two models and results in a smaller truncation error when horizontal derivatives are estimated. As we will see below, differences in truncation error are a major factor in determining the differences in the behavior of the two models.

## C. THE FINITE-DIFFERENCE EQUATIONS

The finite-difference equations for the symmetric model are summarized very briefly in this section; in most cases, the equations are straightforward analogs to those described in ART. We adopt Shuman and Stackpole's (1968) finite-difference notation and write

$$\alpha_r = \frac{\alpha_{j+1/2} - \alpha_{j-1/2}}{\Delta r} \quad (9)$$

and

$$\bar{\alpha}^r = (\alpha_{j+1/2} + \alpha_{j-1/2})/2$$

where  $j$  is the radial index.

For vertical differences and averages, we define

$$\bar{\alpha}^\sigma = (\alpha_{k+1/2} + \alpha_{k-1/2})/2 \quad (10)$$

and

$$\delta\alpha = (\alpha_{k+1/2} - \alpha_{k-1/2})$$

where  $k$  is the vertical index.

The horizontal portion of the difference scheme is similar to the scheme utilized for the asymmetric model with allowance made for the horizontal staggering of the variables. The vertical differencing is identical to that in the asymmetric model.

By use of the operators [eq (9) and (10)], the equations of motion can be expressed in the form

$$\frac{\partial p^* u}{\partial t} = -\frac{1}{r} (\overline{ru p^* u^r})_r - p^* \frac{\delta \bar{r} \bar{u}^\sigma}{\delta \sigma} - \bar{p}^* \bar{\phi}_r - R \bar{T} \bar{p}_r^* + \frac{1}{r^2} \left[ K_H r^2 \left( \frac{p^* u}{r} \right)_r \right], \quad (11)$$

and

$$\frac{\partial p^* v}{\partial t} = -\frac{1}{r} (\overline{ru p^* v^r})_r - p^* \frac{\delta \bar{r} \bar{v}^\sigma}{\delta \sigma} + \frac{1}{r^2} \left[ K_H r^2 \left( \frac{p^* v}{r} \right)_r \right], \quad (12)$$

which are applied at the half levels. The continuity equation takes the form

$$\frac{\partial p^*}{\partial t} = -\frac{1}{r} (\overline{ru p^*})_r - p^* \frac{\delta \dot{\sigma}}{\delta \sigma} \quad (13)$$

and is also applied at the half levels. The vertical sum of eq (13), subject to the boundary conditions  $\dot{\sigma}=0$  at  $\sigma=0$  and  $\sigma=1$ , is used to compute  $\partial p^*/\partial t$ . Equation (13) is then used to compute  $\dot{\sigma}$  at the integral levels. The thermodynamic equation, also applied at the half levels, is

written

$$\frac{\partial p^* T}{\partial t} = -\frac{1}{r}(p^* u \bar{T})_r - p^* \frac{\delta \bar{\sigma} \bar{T}^\sigma}{\delta \sigma} + \frac{RT\omega}{c_p \sigma} + \frac{p^*}{c_p} \dot{Q} + \frac{p^* K_T}{r} (r T_r)_r. \quad (14)$$

The symbol  $\bar{T}^\sigma$  denotes a temperature at the integral levels computed by linear interpolation of *potential* temperature over  $\sigma$  between adjacent half levels.

The quantity  $\omega = dp/dt$  is defined at the half levels and computed from

$$\omega = p^* \bar{\sigma}^\sigma + \bar{\sigma} \left[ \frac{\partial p^*}{\partial t} + \overline{u(p^*)}_r \right]. \quad (15)$$

The hydrostatic equation in the form

$$\frac{\delta \phi}{\delta \sigma} = -\frac{RT}{\sigma} \quad (16)$$

is also applied at the half levels. The horizontal velocity components are computed from

$$u = \frac{p^* u}{p^*}, \quad v = \frac{p^* v}{p^*}. \quad (17)$$

#### D. COMPARISON OF HORIZONTAL TRUNCATION ERROR IN THE SYMMETRIC AND ASYMMETRIC MODELS

As already noted, a significant difference in the computational aspects of the asymmetric model and its two-dimensional analog is the difference in truncation errors caused by the staggering of variables in the symmetric model. This appears to be especially important in the computation of the pressure gradient terms.

The finite-difference analog to the east-west component of pressure gradient force (PGF) for the asymmetric model is

$$(\text{PGF})_{\text{ASYM}} \approx -p^* \bar{\phi}_r^\sigma - RT(\bar{p}^*)_r \quad (18)$$

while the corresponding term for the symmetric model is

$$(\text{PGF})_{\text{SYM}} \approx -\bar{p}^* \bar{\phi}_r^\sigma - RT \bar{p}^*_r. \quad (19)$$

The pressure differences are evaluated over 60-km intervals in the asymmetric model, compared to 30-km intervals in the symmetric analog; thus, the symmetric model will resolve the intense pressure gradients that are typical of hurricanes with greater accuracy than will the asymmetric model.

The importance of this effect may be shown by a simple example. Consider the evaluation of the pressure gradient for a symmetric pressure field utilizing the finite-difference schemes for the asymmetric and symmetric models.<sup>1</sup> For this example, consider the following function that is similar to the shape of pressure profiles in hurricanes:

$$p(r) = -(1+ar)e^{-ar} \quad (20)$$

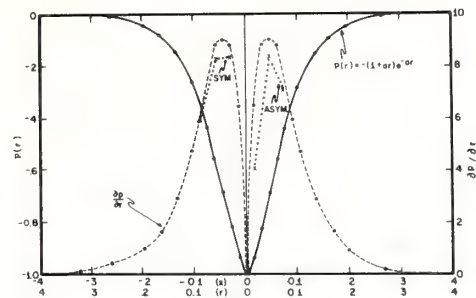


FIGURE 2.—Hurricane-like pressure profile through the symmetric-vortex center and finite-difference estimates of pressure gradient corresponding to symmetric and asymmetric model evaluations. Note that the maximum pressure gradient estimate for the asymmetric model occurs at a larger distance from the vortex center than does the estimate for the symmetric model.

and

$$\frac{\partial p}{\partial r} = a^2 r e^{-ar}. \quad (21)$$

The graphs of  $p(r)$  and its radial derivative are shown in figure 2 for  $a=25$  and a nondimensional  $r$  ranging from 0 to 0.4. (For a rough comparison with the hurricane scale,  $r$  may be multiplied by 1000 km.) Figure 2 also shows the finite-difference estimates for  $\partial p/\partial r$  computed over 0.060 units of  $r$  at points 0.015, 0.045, and 0.075 (corresponding to the evaluation for the asymmetric model); and the estimates computed over 0.030 units of  $r$  at points 0.030, 0.060, and 0.090 (corresponding to the evaluation for the symmetric model). Large differences between the estimates occur at the first grid point from the center. While the maximum gradient for the symmetric model occurs at  $r=0.030$  (the grid point closest to the center), the maximum gradient in the asymmetric model is displaced to the second grid point from the center ( $r=0.045$ ) and is underestimated by a factor of 2 at  $r=0.015$ . This is due to the large grid increment which requires pressure values on the opposite side of the pressure minimum. Thus, for a hurricane-like pressure field, the asymmetric model, in comparison with the symmetric model, significantly underestimates the pressure gradient close to the center. As we shall see, this results in a considerably weaker storm during the earlier portions of the asymmetric integration.

#### E. VERTICAL DIFFUSION OF MOMENTUM

The terms  $F_v(v)$  and  $F_v(u)$ , which appear in eq (1) and (2), represent diffusive and "frictional" effects due to vertical transports of horizontal momentum by subgrid eddies smaller than the cumulus scale and include the important surface drag. These terms are identical in form to those in the asymmetric model (ART) and, hence, are not presented here.

#### F. TIME INTEGRATION

As in the asymmetric model, the Matsuno (1966)

<sup>1</sup> This analysis is directly pertinent for comparison of the symmetric model results and the results from the first 120 hr of the asymmetric model when the model storm is quite symmetric (see ART).



simulated forward-backward scheme is used for time integration. The criteria for linear computational stability is primarily determined by the external gravity wave. While a time step of 60 s was adequate for the asymmetric model, the evaluation of horizontal divergence in eq (13) over intervals of 30 km in the symmetric version necessitated a smaller time step of 40 s.

### G. LATERAL BOUNDARY CONDITIONS

The small domain size (450 km radius) makes the choice of lateral boundary conditions extremely important. Preliminary experimentation showed that realistic results could be obtained for boundary conditions similar to those employed in other symmetric models (Anthes 1970, Rosenthal 1970). These boundary conditions require the pressure and temperature gradients, the horizontal divergence, and the relative vorticity to vanish. The zero divergence assumption and the finite-difference formulation [eq (13)] for the continuity equation imply that the pressure at the lateral boundary is steady state, as is also the case for the asymmetric model. The boundary condition on temperature for the symmetric model, however, allows the temperature on the boundary to change, unlike the steady-state temperatures on the boundary of the asymmetric model. This second difference is probably less important than that due to the horizontal grids since temperatures at the boundary of the symmetric analog change by no more than 1°C during experiments.

### H. DIABATIC EFFECTS

As in ART, this preliminary experiment does not contain an explicit water cycle and the convective adjustments of macroscale temperature are parameterized as they were in the original version of Rosenthal's (1969) symmetric model. The basic characteristics of this convective adjustment, summarized in ART, are not repeated here.

The heating function, previously written for the  $z$ -system (Rosenthal 1969), may be expressed in the  $\sigma$ -system as follows. Let

$$I = \frac{-L[(\nabla \cdot p^* \nabla q) \delta \sigma]_{k=7/2}}{\sum_{k=1}^3 (T_c - T) \delta \sigma} \quad (22)$$

where  $T_c$  is the temperature along the pseudoadiabatic with the equivalent potential temperature of the  $\sigma=1$  surface;  $q$  is the specific humidity;  $L$  is the latent heat of vaporization. Then,

$$p^* \dot{Q} = I(T_c - T) \quad (23)$$

if  $I > 0$  and  $(\nabla \cdot p^* \nabla q)_{k=7/2} < 0$ .

Otherwise,

$$p^* \dot{Q} = 0. \quad (24)$$

In finite-difference form,

$$(\nabla \cdot p^* \nabla q)_{k=7/2} = [(u p^* \tilde{q})_r]_{k=7/2}. \quad (25)$$

The parameterization of nonconvective latent heat release under nearly moist adiabatic conditions, under

which  $T_c \approx T$ , proceeds as follows. Whenever  $(T_c - T) \leq 0.5^\circ\text{C}$  at  $k=3/2$  or  $7/2$ , this quantity is arbitrarily set to  $0.5^\circ\text{C}$ . Under a nearly moist adiabatic lapse rate, therefore,  $T_c - T = 0.5^\circ\text{C}$  at both levels, and the latent heat is partitioned equally between the upper and lower troposphere. From eq (23), therefore, latent heat is released in the column as long as a water vapor supply from the boundary layer is present.

The value of  $q_{k=7/2}$ , needed for the evaluation of eq (22), is assumed to be given by

$$q_{7/2} = \min \left\{ \begin{array}{l} 0.90 q_s \\ 0.020 \end{array} \right\} \quad (26)$$

where  $q_s$  is the saturation specific humidity.

The surface temperature,  $T^*$ , and specific humidity,  $q^*$ , required to establish the pseudoadiabatic appropriate to parcel ascent from the surface are computed, as in the asymmetric model, by downward extrapolation from the  $k=7/2$  level,

$$T^* = T_{k=7/2} + 3.636^\circ\text{K} \quad (27)$$

and

$$q^* = 0.90 q_s(T^*, p^*). \quad (28)$$

The formulation of the air-sea exchange of sensible heat is identical to that used in ART.

### I. INITIAL CONDITIONS

The initial conditions consist of a vortex in gradient balance. The temperatures at the levels  $k=3/2$ ,  $5/2$ , and  $7/2$  are taken from a mean tropical atmosphere (Hebert and Jordan 1959). The initial surface pressure (in mb) is then defined by

$$p^* = 1011.0 - 4.0 \cos\left(\frac{\pi}{375} r\right), \quad r < 375 \text{ km} \quad (29)$$

and

$$p^* = 1015.0 \quad r \geq 375 \text{ km}$$

where  $r$  is given in kilometers.

The initial geopotentials of the  $\sigma$ -surfaces are calculated by an upward integration of the hydrostatic equation. To obtain the initial wind field, we write the gradient wind equation for the  $\sigma$ -system as

$$\frac{v^2}{r} + f v = \frac{RT}{p^*} \frac{\partial p^*}{\partial r} + \frac{\partial \phi}{\partial r}. \quad (30)$$

The pressure field [eq (29)], together with the specified temperature field, yields a maximum gradient wind at the  $k=7/2$  level of 18 m/s at a radius of 240 km. Although these conditions represent a rather strong vortex, two experiments, to be briefly discussed later, showed the mature state of the storm to depend very little on the strength of the initial vortex. The time of development, on the other hand, varied from 6 days to 1 day depending on the strength of the initial circulation. Therefore, a computational economy is realized by increasing the strength of the initial vortex.

## 3. EXPERIMENTAL RESULTS

### A. VARIATIONS IN INITIAL CONDITIONS AND LATERAL MIXING TERMS

One of the objectives of this paper is to present results

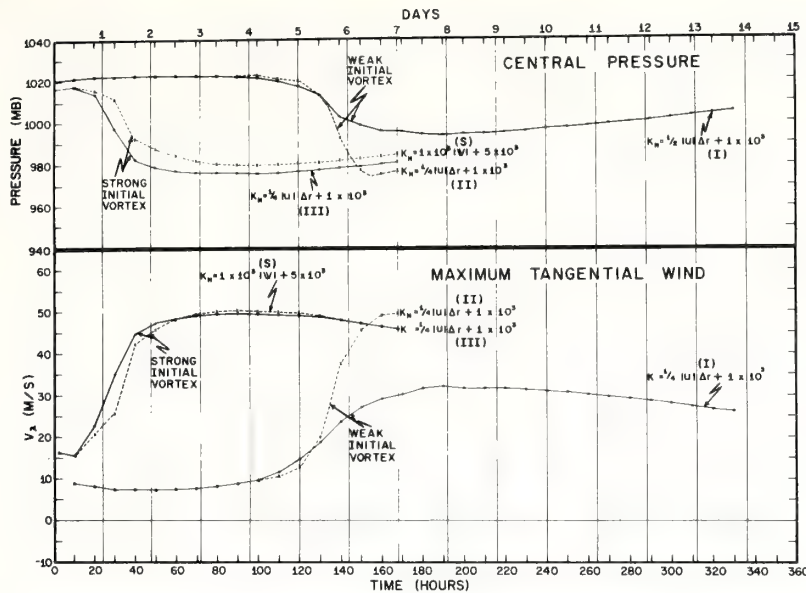


FIGURE 3.—Summary of four experiments with the symmetric analog model. Experiments I and II start with a weak initial vortex and compare two formulations of the horizontal eddy viscosity coefficient. Experiments labeled III and S start with a stronger initial vortex. The experiment labeled S is most nearly similar to the asymmetric model experiment and serves as the basis for comparison.

from the symmetric model that were useful in the design of the asymmetric model. The first series of experiments provided useful information regarding the formulation of the horizontal eddy diffusivity for momentum ( $K_H$ ) and the effect of the strength of the initial vortex on the life cycle of the model storm.

Figure 3 contains the time variation of minimum pressure and maximum wind speeds for four of the more significant symmetric model experiments. The profiles marked "S" denote the symmetric experiment that is most similar to the asymmetric experiment described in ART and will serve as the basis for a detailed comparison in the next section.

These experiments suggested the form for the variable horizontal eddy diffusivity of momentum that was ultimately adopted for the asymmetric model and which may be written

$$K_H = c_1 |V| + c_2 \quad (31)$$

where  $c_1 = 1.0 \times 10^3 \text{ m}^2 \cdot \text{s}^{-1}$  and  $c_2 = 5 \times 10^3 \text{ m}^2 \cdot \text{s}^{-1}$ . A number of experiments showed that constant values of  $K_H$  were unacceptable because values small enough to allow the initial vortex to intensify provided too little diffusion in the more intense mature stage. Conversely, values large enough for an intense circulation yielded an overdamping in the early stages to the extent that intensification was unable to take place. Experiments with Smagorinsky's (1965) variable  $K_H$  (proportional to the magnitude of the total deformation of the horizontal motion) gave unrealistic velocity fields near the storm center.

Encouraged by results obtained from symmetric models (Rosenthal 1970, Yamasaki 1968) in which upstream dif-

ferencing provided an implicit diffusion coefficient proportional to the advecting velocity, a coefficient of the form

$$K_H = c_3 |u| \Delta r + c_4 \quad (32)$$

was tested with the symmetric analog. This formulation yields the required compromise between values small enough to allow storm development and large enough to provide realistic structures in the intense mature state. Equation (31) which was utilized in the asymmetric model represents a generalization of eq (32) to two horizontal dimensions in which both horizontal velocity components are advecting components.

Figure 3 shows three experiments with the  $K_H$  formulation given by eq (32). The curves labeled I and II represent experiments which are identical except for the value of the proportionality constant  $c_3$ . For  $c_3 = \frac{1}{2}$  (case I) the lowest pressure and maximum tangential wind speed of the storm are 994 mb and 33 m/s, respectively, typical of a weak hurricane. For  $c_3 = \frac{1}{4}$  (case II) the minimum central pressure is 975 mb and the maximum tangential wind is 50 m/s, representative of a moderate hurricane. The evolution of both experiments is similar, with both storms beginning a very slow filling process shortly after reaching maximum intensity.

The "organization phase" of 6 days in experiments I and II is typical of hurricane models that start with a weak vortex. It is computationally uneconomical, however, especially with three-dimensional models, to devote 6 days to the relatively uninteresting stage of gradual intensification. Experiment III represents an effort to shorten this phase, and is identical to experiment II except that the initial pressure perturbation in experiment III is twice the



amplitude of that in experiment II. These conditions, given by eq (29), are identical to those used for the asymmetric calculation. A comparison of curves II and III reveals that the mature stages of both experiments have nearly the same intensity. The structures (not shown) are also quite similar, indicating that the major effect of the strength of the initial vortex is on the early growth rate rather than on the final stage of the storm.

The structures of the experiments utilizing a  $K_H$  of the form given in eq (32) were all quite reasonable compared to empirical data. As already noted, the generalization of eq (32) to two horizontal dimensions suggests the utilization of the total wind rather than the inflow component alone. Thus, in eq (31), the variable part of  $K_H$  is made proportional to the wind speed. This formulation, with  $c_1 = 1 \times 10^3 \text{ m}$  and  $c_2 = 5 \times 10^3 \text{ m}^2 \cdot \text{s}^{-1}$ , gave results which were comparable to those obtained by eq (32). This experiment, designated S in figure 3, is the basis for comparison of the symmetric and asymmetric models in the next section.

#### B. COMPARISON OF SYMMETRIC AND ASYMMETRIC MODEL RESULTS

Figure 4 compares the maximum wind speed in the boundary layer with the minimum surface pressure for the symmetric and asymmetric experiments. Results for the first 24 hr are nearly identical. After this time, however, significant differences develop. At about 40 hr, the asymmetric model reaches a near steady state that closely resembles a weak hurricane. The symmetric model storm, however, intensifies at a faster rate and deepens until a considerably stronger steady state is reached at about 100 hr.

Thereafter, the symmetric storm fills and the computation is terminated at 165 hr. The asymmetric model, on the other hand, remains in a weak quasi-steady state until 120 hr when a second period of intensification begins. This second deepening phase, as discussed in ART, seems to be related to the appearance at this time of large-scale asymmetries, notably in the outflow layer.

During the first 120 hr the differences between the symmetric and asymmetric model storms are striking. They are not, however, directly attributable to differences in storm symmetry, since the asymmetric model storm remains very nearly circularly symmetric for the first 100 hr or so. The differences appear to be related to the differences in horizontal grid structure and truncation error discussed in section 2D. Apparently, the better resolution of the pressure gradient force that results from the grid staggering in the symmetric model produces a stronger pressure gradient, increased inflow, and consequently increased tangential winds. This indicates that the nonstaggered 30-km resolution of the asymmetric model severely limits the early development of the storm.

In ART, it was shown that the second period of intensification in the asymmetric experiment was related to the development of a form of inertial (or dynamic) instability that leads to the growth of asymmetric perturbations. This type of instability cannot be released in the sym-

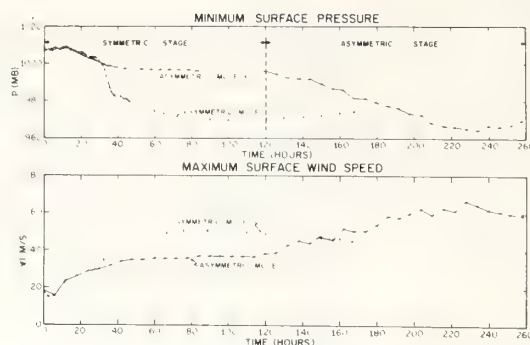


FIGURE 4.—Time variation of the minimum surface pressure and the maximum surface wind speed for the symmetric and asymmetric model experiments.

metric model and possibly explains why the symmetric model does not exhibit two stages of deepening. On the other hand, a symmetric vortex can exhibit an inertial instability for horizontal symmetric ring displacements if

$$\left(\frac{\partial v}{\partial r} + \frac{v}{r} + f\right)\left(\frac{2v}{r} + f\right) < 0. \quad (33)$$

The tentative conclusion reached in ART was that this instability played no significant role in either phase of the deepening since it was not present during the first phase and since the second phase was highly asymmetric. In previous studies with symmetric models, similar conclusions have been reached by Ooyama (1969) and Rosenthal (1969). The behavior of the symmetric analog discussed here appears to directly support this conclusion, and it indirectly supports the conclusions reached in ART regarding the importance of asymmetric inertial instabilities during the second period of deepening in the asymmetric model.

Figure 5 shows the time variation of minimum upper tropospheric relative vorticity for the symmetric and asymmetric models. The relative vorticity in the symmetric model reaches a minimum value of  $-6 \times 10^{-5} \text{ s}^{-1}$  after the intensification has occurred. Since  $f = 5 \times 10^{-5} \text{ s}^{-1}$ , the absolute vorticity is positive until the intensification is nearly complete, and remains nearly zero thereafter. For the symmetric model, the second factor in eq (33),  $[(2v/r) + f]$ , is always positive. It would appear, therefore, that this instability is *not* a factor in the development of the symmetric model storm. For the asymmetric model, the vorticity shown by figure 5 contains the asymmetric component of the wind as well as the symmetric component. These values, therefore, are not applicable to the type of instability represented by eq (33); rather they must be applied to the type of instability discussed in ART that leads to the growth of asymmetric perturbations.

Figure 6 shows the temporal variations of the components of the kinetic energy budget. The sum of (1) the conversion of potential to kinetic energy,  $[C(K)]$ , (2) the flux of kinetic energy across the lateral boundary,  $[B(K)]$ ,



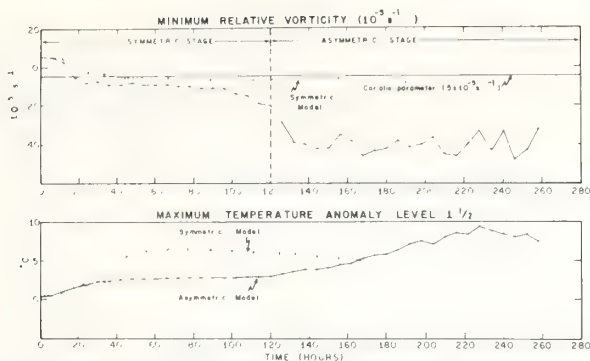


FIGURE 5.—Time variation of (A) the minimum relative vorticity in the upper troposphere and (B) the maximum temperature anomaly in the upper troposphere, for the symmetric and asymmetric model experiments.

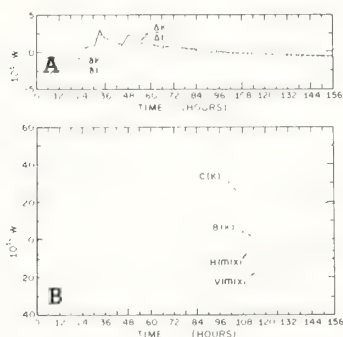


FIGURE 6.—(A) time variation of the observed kinetic energy change and of the change computed from the kinetic energy equation, (B) time variation of individual components of the kinetic energy tendency:  $C(K)$  is the conversion of potential to kinetic energy,  $B(K)$  is the flow of kinetic energy through the lateral boundary,  $H(mix)$  is the loss of kinetic energy through lateral eddy viscosity,  $V(mix)$  is the loss of kinetic energy through vertical eddy viscosity and includes the effect of surface drag friction. Both (A) and (B) are for the symmetric model.

(3) the dissipation due to lateral mixing,  $[H(mix)]$ , and (4) the dissipation due to vertical mixing,  $[V(mix)]$  equals the "analytic" kinetic energy tendency  $(\partial K/\partial t)$ . Also shown by figure 6 are the observed rates of change of kinetic energy,  $(\Delta K/\Delta t)$ . The difference between  $\partial K/\partial t$  and  $\Delta K/\Delta t$  is a measure of the truncation error and, as figure 6 shows, this difference is quite small. Furthermore, the individual components of the budget are reasonable when compared to empirical estimates (Hawkins and Rubsam 1968, Miller 1962, Palmén and Riehl 1957, Riehl and Malkus 1961).

Comparison of the energy budgets for the symmetric and asymmetric model storms for the same intensity (as measured by minimum pressure) shows that the individual components of the energy budgets are quite similar in magnitude. The ratio of the components to each other are nearly the same; for example, the dissipation

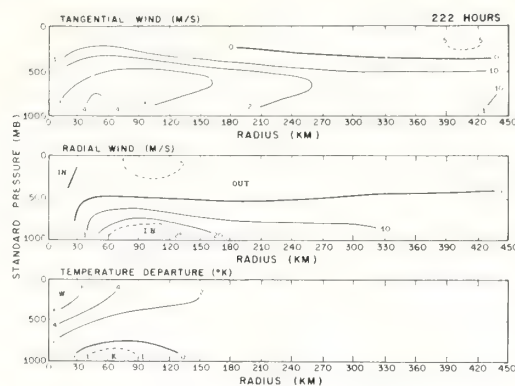


FIGURE 7.—Azimuthal mean vertical cross sections for the tangential wind, the radial wind, and the temperature anomaly at 222 hr for the asymmetric model experiment.

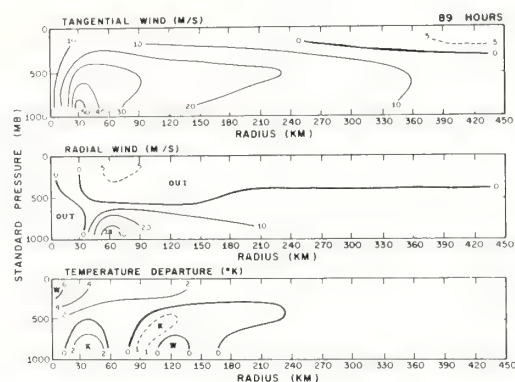


FIGURE 8.—Vertical cross sections for the tangential wind, the radial wind, and the temperature anomaly at 89 hr for the symmetric model experiment.

pation by vertical mixing is about 2.5 times that due to horizontal mixing in both models. Thus, for a given intensity, the models are energetically quite similar.

It is interesting to compare the circular mean vertical cross sections of the asymmetric model with the corresponding vertical sections of the symmetric model at a time when the storms are approximately of the same intensity. Mean cross sections for the tangential wind, radial wind, and temperature departure at 222 hr of the asymmetric model storm are shown in figure 7, and may be compared with the analogous sections at 89 hr for the symmetric model shown in figure 8. These times correspond to the maximum intensity in both models.

The symmetric model shows a somewhat more intense circulation that is concentrated nearer to the origin. The maximum wind of about 50 m/s occurs at 30 km. The mean cross sections for the asymmetric storm show a larger circulation with mean maximum winds of about 45 m/s occurring at 45 km. These differences are probably related to the differences in effective horizontal resolution which result from the different horizontal grids

The better resolution of the pressure gradient force by the staggered grid in the symmetric model produces the maximum inflow at a smaller radius (60 compared to 105 km). Through the conservation of angular momentum, this increased inflow at a smaller radius produces a higher maximum wind speed.

Aside from the differences caused by different resolutions near the center, the symmetric storm structure is very similar to the azimuthal mean asymmetric storm structure. Both storms show an eye with sinking motion at the center, both show nearly identical outflow patterns, and both have a maximum temperature anomaly of 6°C in the upper troposphere and a weak cold core in the lower troposphere. These similarities tend to support the validity of utilizing symmetric models to study many of the essential features of tropical cyclones.

#### 4. SUMMARY AND CONCLUSIONS

This paper compares the asymmetric model hurricane (described by ART) with an axially symmetric analog. Significant differences in the sequence of events in the histories of the two model storms are found. The symmetric model quickly reaches a maximum intensity corresponding to a moderate hurricane, and then begins to slowly decrease in intensity. The asymmetric system, on the other hand, initially reaches a much weaker intensity, remains in a nearly steady state for a time, and then shows a second period of intensification. The differences in intensity during the first 100 hr are related to differences in horizontal resolution produced by the staggered grid used with the symmetric model. The staggered grid provides for a better resolution of the intense pressure gradient near the center of the storm than does the unstaggered grid of the asymmetric model, and confirms that increased resolution near the center of the asymmetric grid is necessary. These facts suggest that the asymmetric model should be recoded in a staggered grid similar to that used for the symmetric model.

The second period of intensification that starts at 120 hr in the asymmetric model does not occur in the symmetric analog. This fact supports the conclusion reached in ART that the development of large-scale asymmetries at about 100 hr is closely associated with the subsequent intensification.

Although the life cycles of the two model storms were quite different, the azimuthally averaged structure of the asymmetric storm at maximum intensity appeared to differ from the structure obtained with the symmetric analog mainly in details attributable to the differences in resolution produced by the staggering of horizontal grid points in the symmetric analog. This similarity tends to support the adequacy of symmetric models in investigating many important aspects of tropical cyclone structure.

#### ACKNOWLEDGMENTS

The authors thank Messrs. Robert Carrodus, John Lundblad, and Glenn Frye for the drafting of the figures; Mr. Charles True for the photography; and Mrs. Mary Jane Clarke for typing the manuscript.

#### REFERENCES

- Anthes, Richard Allen, "A Diagnostic Model of the Tropical Cyclone in Isentropic Coordinates," *ESSA Technical Memorandum ERLTM-NHRL 89*, U.S. Department of Commerce, National Hurricane Research Laboratory, Miami, Fla., Apr. 1970, 147 pp.
- Anthes, Richard Allen, Rosenthal, Stanley L., and Trout, James W., "Preliminary Results From an Asymmetric Model of the Tropical Cyclone," *Monthly Weather Review*, Vol. 99, No. 10, Oct. 1971, pp. 744-758.
- Hawkins, Harry F., and Rubsam, Daryl T., "Hurricane Hilda, 1964: II. Structure and Budgets of the Hurricane on October 1, 1964," *Monthly Weather Review*, Vol. 96, No. 9, Sept. 1968, pp. 617-636.
- Hebert, Paul J., and Jordan, Charles L., "Mean Soundings for the Gulf of Mexico Area," *National Hurricane Research Project Report No. 30*, U.S. Department of Commerce, Weather Bureau, Miami, Fla., Apr. 1959, 10 pp.
- Kurihara, Yoshio, and Holloway, J. Leith, Jr., "Numerical Integration of a Nine-Level Global Primitive Equations Model Formulated by the Box Method," *Monthly Weather Review*, Vol. 95, No. 8, Aug. 1967, pp. 509-530.
- Matsuno, Taroh, "Numerical Integrations of the Primitive Equations by a Simulated Backward Difference Method," *Journal of the Meteorological Society of Japan*, Ser. 2, Vol. 44, No. 1, Tokyo, Feb. 1966, pp. 76-84.
- Miller, Banner L., "On the Momentum and Energy Balance of Hurricane Helene (1958)," *National Hurricane Research Project Report No. 53*, U.S. Department of Commerce, Weather Bureau, Miami, Fla., Apr. 1962, 19 pp.
- Ooyama, Katsuyuki, "Numerical Simulation of the Life-Cycle of Tropical Cyclones," *Journal of the Atmospheric Sciences*, Vol. 26, No. 1, Jan. 1969, pp. 3-40.
- Pamlén, Erik H., and Riehl, Herbert, "Budget of Angular Momentum and Kinetic Energy in Tropical Cyclones," *Journal of Meteorology*, Vol. 14, No. 2, Apr. 1957, pp. 150-159.
- Phillips, Norman A., "A Coordinate System Having Some Special Advantages for Numerical Forecasting," *Journal of Meteorology*, Vol. 14, No. 2, Apr. 1957, pp. 184-185.
- Riehl, Herbert, and Malkus, Joanne S., "Some Aspects of Hurricane Daisy, 1958," *Tellus*, Vol. 13, No. 2, Stockholm, Sweden, May 1961, pp. 181-213.
- Rosenthal, Stanley L., "Numerical Experiments With a Multilevel Primitive Equation Model Designed to Simulate the Development of Tropical Cyclones: Experiment I," *ESSA Technical Memorandum ERLTM-NHRL 82*, U.S. Department of Commerce, National Hurricane Research Laboratory, Miami, Fla., Jan. 1969, 36 pp.
- Rosenthal, Stanley L., "A Circularly Symmetric Primitive Equation Model of Tropical Cyclone Development Containing an Explicit Water Vapor Cycle," *Monthly Weather Review*, Vol. 98, No. 9, Sept. 1970, pp. 643-663.
- Shuman, Frederick G., and Stackpole, John D., "Note on the Formulation of Finite Difference Equations Incorporating a Map Scale Factor," *Monthly Weather Review*, Vol. 96, No. 3, Mar. 1968, pp. 157-161.
- Smagorinsky, Joseph, Manabe, Syukuro, and Holloway, J. Leith, Jr., "Numerical Results From a Nine-Level General Circulation Model of the Atmosphere," *Monthly Weather Review*, Vol. 93, No. 12, Dec. 1965, pp. 727-768.
- Sundqvist, Hilding, "Numerical Simulation of the Development of Tropical Cyclones With a Ten-Level Model, Part I," *Tellus*, Vol. 22, No. 4, Stockholm, Sweden, 1970, pp. 359-390.
- Yamasaki, Masanori, "A Tropical Cyclone Model With Parameterized Vertical Partition of Released Latent Heat," *Journal of the Meteorological Society of Japan*, Vol. 46, No. 3, Tokyo, June 1968, pp. 202-214.

[Received November 17, 1970; revised February 5, 1971]



## conference summary

Peter G. Black

Atlantic Oceanographic and Meteorological Laboratories

Environmental Research Laboratories

National Hurricane Research Laboratory, NOAA

Miami, Fla.

### cumulonimbus modification of tropical nature

During the week of 15-19 February 1971, the first United States-Japan conference on modification of cumulus clouds and cloud systems including the tropical cyclone was held at the Columbus Hotel in Miami, Fla. The title of this first conference was "Cumulonimbus Modification of Tropical Nature." Sponsored by the National Science Foundation and the Japan Society for the Promotion of Science under the auspices of the U. S.-Japan Science Program, the purpose of the conference was to discuss the present state of the art of cumulus cloud and tropical cyclone modification in both countries as well as future cooperation in this field. The meeting was organized through the efforts of Dr. N. Fukuta, Denver Research Institute, and Dr. R. C. Gentry, Director, National Hurricane Research Laboratory, NOAA, in the U. S. and by Dr. K. Terada, Director, National Research Center for Disaster Prevention, in Japan. H. Hawkins, Assistant Director, National Hurricane Research Laboratory, NOAA, was acting chairman of the conference and W. D. Mallinger, National Hurricane Research Laboratory, NOAA, handled the necessary arrangements.

The conference was carried on in a relaxed and informal atmosphere, which helped to encourage the free exchange of ideas, comments and criticisms. Liberal time allowances were given for the presentation of papers and discussion afterward.

The Americans present felt that the biggest single factor that contributed to the success of the conference was the excellent command of the English language by the Japanese participants. Because of this, mutual understanding and exchange of ideas were extremely easy.

Several informal social events were held during the week in order to provide time for the U. S. and Japanese participants to get to know one another personally and to discuss each other's work in more detail than was possible during the sessions. A tour of the Atlantic Oceanographic and Meteorological Laboratories and the Miami Seaquarium was conducted on Wednesday morning. On Wednesday afternoon the participants were given a tour of the Experimental Meteorology Laboratory, the National Hurricane Research Laboratory and the National Hurricane Center. Short talks concerning the basic research conducted by each organization were presented.

An interesting chain of events became apparent to the author by the time the conference drew to a close. This

chain of events interestingly had a parallel in both the U. S. and Japan. An interest in "making rain" from clouds led to early experiments in the late 1940's in both countries. Experience gained in these modification attempts during the 1950's led to intensified basic research on the mechanisms of precipitation formation and basic microphysical processes during the 1960's. In this decade, an interest in tropical storm modification developed in the U. S. Several experiments led to the conclusion that a better understanding of cloud microphysics, tropical storm dynamics, and their interaction was necessary before a more effective modification of the tropical storm could be carried out. Furthermore, for the purposes of evaluating the effects of tropical storm modification it has become apparent that a better understanding of the damages caused by tropical storm winds is necessary. These early cumulonimbus and tropical cyclone modification experiments in the U. S. and Japan have raised questions and suggested fruitful avenues of research such as that reported during the conference on "Cumulonimbus Modification of Tropical Nature." The papers presented, which are summarized below, suggest four main areas of cooperative study between the U. S. and Japan in the years ahead. These are:

- 1) A greater understanding of the microphysical processes in clouds.
- 2) The relationships between the microphysical and dynamical processes in clouds.
- 3) The interaction between the cloud scale and tropical cyclone scale of motion.
- 4) The relationship between tropical cyclone winds and the damage caused by these storms.

Examples of recent cumulus cloud modification experiments in Japan were reported by Prof. K. Takeda, Kyushu University, and by Dr. Y. Omoto, National Research Center for Disaster Prevention. For a comprehensive review of weather modification activities in Japan the reader is referred to a recent article in the *BULLETIN* by Fukuta.<sup>1</sup> Prof. Takeda described a warm cloud seeding experiment that was carried out in middle Kyushu during the summers of 1961 to 1966. The method involved spraying shallow cumulus clouds (those with a thickness of 50-2400 m) with a fine water spray discharged from a small aircraft flying over the cloud

<sup>1</sup> Fukuta, N., 1971: Weather modification activities in Japan. *Bull. Amer. Meteor. Soc.*, **52**, 4-14.



top. Evaluation of the experimental results proved to be difficult since the artificial changes in the cloud caused by spraying were of the same order of magnitude as the natural changes.

Dr. Omoto described an ingenious rocket system, developed during the past two years, which was designed for use in hail suppression experiments in Japan. The rocket has two stages, is only 785 mm long and is designed to completely burn up before falling back to the ground. The rocket is launched from a mobile rocket launcher and is designed to reach altitudes above 7000 m. The second stage contains an AgI mixture that disperses a large number of relatively large AgI particles near the top of the rocket trajectory. The exact number and size of particles have not yet been determined due to limited facilities. Even so, the rocket system is a remarkable achievement. The first rocket seeding experiment was carried out in October 1970 at a Japanese Self Defense Force site northwest of Tokyo. An RHI, 3.2-cm radar was used for evaluation and was oriented along the direction of the rocket trajectory. Some echo formation was noted after the rocket firings. Further tests and seeding evaluations are planned.

Cumulus cloud modification activities in the U. S. were reported by Dr. W. Woodley, Experimental Meteorology Laboratory, NOAA, and Dr. A. Weinstein, Meteorology Research, Inc. Dr. Woodley reported on cumulus cloud seeding experiments over South Florida in 1968 and 1970. The clouds were seeded by AgI pyrotechnics which were dropped into the clouds at about the  $-5^{\circ}\text{C}$  level. The experiments were carried out in conjunction with a one-dimensional cloud model that was used to predict days on which cumulus clouds could be expected to grow following seeding. The results showed that seeded clouds grew 7000 ft taller than control clouds and produced 270 acre-ft more precipitation on the average. Dr. Woodley also reported an interesting case of extreme rainfall enhancement associated with the merger of two seeded clouds. An increase of 8750 acre-ft of precipitation was reported over that of the control clouds.

A similar case was reported by Dr. Weinstein in his experiments in Flagstaff. He suggested that stimulation of such cloud mergers was the key to creating significant rainfall increases. He went on to present the results of the Flagstaff seeding program and presented the interesting result that glaciation occurred during the active phase of the seeded cloud lifetime whereas in natural clouds glaciation occurred during the dissipating stages. He suggested that the primary microphysical reason for the added precipitation in seeded clouds is the increased vertical motion leading to a second surge of moisture into the cloud.

It was evident during the course of the conference that cumulus cloud modification programs such as those discussed above have helped a great deal in the understanding of the physical processes in clouds. They have also helped to point out the pertinent questions that

have to be answered before a complete knowledge of the precipitation process is obtained. One such area where many questions remain unanswered and where active research is presently underway in both the U. S. and Japan is the area of the microphysics of cloud glaciation. Prof. C. Magono, Hokkaido University, reported on studies of the vertical structure of snow clouds carried out during the winter of 1970 in Hokkaido using "snow crystal sondes" designed by Magono and Tazawa,<sup>2</sup> and sampling in the region from  $-10^{\circ}\text{C}$  to  $-20^{\circ}\text{C}$ . Due to a lack of aircraft with which to investigate the upper portions of cumulonimbus, the study of the microphysics of easily accessible snow clouds in winter was considered as a first step in learning more about the ice phase in cumulonimbus clouds and more about modification of such clouds. Prof. Magono reported the interesting observation that the concentration of ice crystals in the snow clouds always exceeded the concentration of ice nuclei by one to three orders of magnitude.

This same observation was reported by Dr. A. Ono, Meteorological Research Institute, who described his observations of relatively warm ( $-10^{\circ}\text{C}$  and warmer) supercooled maritime clouds by aircraft near Tasmania during May 1968. Dr. Ono found many very small regular ice crystals that could not have originated from natural ice nuclei. These observations suggested that some ice crystal enhancement mechanism was operating, an understanding of which is of great importance for cloud seeding. If a cloud is capable of complete glaciation with only natural ice nuclei present, it is possible that additional ice nuclei injected artificially could inhibit precipitation rather than stimulate it. Dr. Ono suggested that the most plausible explanation for ice crystal multiplication, based on his observations of size, concentration and microphysical conditions of occurrence, was that they were formed when ice fragments were thrown off from water drops freezing after accretion on ice crystals.

Dr. M. Fujiwara, Meteorological Research Institute, discussed the relationship between the stage of glaciation of snow clouds topping at  $-18^{\circ}\text{C}$  and the cloud dynamics. He used a vertically pointing Doppler radar and a ground based snowflake sampling network in a study conducted on the coast of the Japan Sea in February 1966. Based on these observations Dr. Fujiwara constructed a model showing the dependence of the ice crystal habit on vertical air velocities. He also showed the amounts of artificial ice nuclei needed for complete glaciation and the altitude above the melting level where the seeding material should be injected under assumptions of different natural ice nuclei concentrations and vertical velocities. For example, a concentration of  $50\text{ l}^{-1}$  at 1.6 km above the  $0^{\circ}\text{C}$  level was needed for complete glaciation when  $5\text{ l}^{-1}$  natural ice nuclei were present in an updraft of  $1\text{ m sec}^{-1}$ .

<sup>2</sup> Magono, C., and S. Tazawa, 1966: Design of "snow crystal sondes." *J. Atmos. Sci.*, **23**, 618-625.

Dr. R. Koenig, Rand Corporation, presented the results of recent experiments to model the ice phase microphysics in the U. S. He discussed his model, which predicts the growth rate of ice crystals by deposition in the temperature range from  $-1^{\circ}\text{C}$  to  $-35^{\circ}\text{C}$ . Agreement with observations, where available, was good. Maximum growth rates were shown to occur at temperatures near  $-5^{\circ}\text{C}$  and  $-15^{\circ}\text{C}$ .

Dr. N. Fukuta, Denver Research Institute, reported on recent experiments in the U. S. using different seeding agents in a burner developed by Meteorology Research, Inc. He discussed the current status of ice technology for ice nuclei and ice crystal generation.

Attempts to model the microphysical cloud processes and their relationship to the cloud dynamics have been carried on primarily in the U. S. and were discussed by Dr. H. Orville, South Dakota School of Mines and Technology, Dr. W. Cotton, Experimental Meteorology Laboratory, NOAA, and Dr. D. Lilly, National Center for Atmospheric Research. Dr. Orville's model is a two-dimensional model of the life cycle of a cumulonimbus cloud initiated over a simulated mountain ridge. He has recently incorporated cloud-ice and hail processes into the model. In spite of the underdamped nature of the model (vertical motion is too great), it may be useful, with improved ice phase microphysics, in determining the dynamic response of the environment (on the meso-scale) to seeding. A point brought out by several of the participants, in this connection, was that cloud physicists should try to estimate the increase in the low-level convergence of moisture into a cloud due to high-level seeding.

Dr. Cotton's model is a one-dimensional model but incorporates more sophisticated microphysics. Two recent experiments were described, one which developed high amounts of supercooled water and was very sensitive to moderate amounts of seeding material and another which developed relatively little supercooled water and was relatively insensitive to large amounts of seeding material. Dr. Cotton went on to suggest that overseeding could produce an overabundance of ice crystals, increase the middle level horizontal convergence, and thus kill the cloud. Such an effect is strongly a function of the humidity structure of the environment and the size of the tower.

Dr. Lilly outlined the cloud modelling activities at NCAR. This included development of numerical methods that would be necessary for a three-dimensional cloud model that is under development. This model is designed to study the influence of turbulence in the boundary layer on cumulus cloud development.

Dr. E. Berry, Desert Research Institute, reported on observations of the echo-free vault being present in Alberta hailstorms for periods up to one hour. He suggested that dry air entered the side of the intense up-draft above the cloud base producing a cloud free region in some instances as well as an echo free region.

Dr. Berry also outlined a new data acquisition system that was being flight tested for possible use on the C-130 aircraft during tropical storm reconnaissance missions. The system provides for display of meteorological and navigational information simultaneously with a recently acquired radar display.

Recent numerical modelling work on hurricanes was discussed in some detail at the conference. Dr. S. Rosenthal, National Hurricane Research Laboratory, NOAA, described several recent experiments with his two-dimensional, seven-level hurricane model in which he found that there is a crucial drag coefficient above which the frictional convergence of water vapor dominates over frictional dissipation. He also showed that the sensible heat exchange from the sea is less important than latent heat addition from the sea in determining the storm intensity.

This same conclusion was arrived at by Dr. K. Terada, Director, National Research Center for Disaster Prevention, who modelled the effects on a typhoon's energy supply by increased evaporation from the sea surface as the model typhoon moved over warmer waters. He found, by a detailed trajectory analysis technique, that the energy supply increased by 30% as the typhoon moved over a belt of water 400 km wide that was one degree warmer than the surroundings.

Dr. R. Anthes, National Hurricane Research Laboratory, NOAA, described recent experiments with a three-dimensional, three-level hurricane model. He showed how the use of a staggered grid system helped overcome certain problems encountered with the coarse grid system that had to be used. He also showed how the model produced spiral convective bands in the lowest layer and several transient horizontal eddies in the outflow layer.

Dr. K. Ooyama, New York University, described a linearized model to investigate the effects of various vertical heating distributions on wave disturbances in easterly zonal flow with variable vertical shear. Depending on the vertical profiles of zonal flow and distribution of released heat, various types of tropical disturbances were possible.

Considerable discussion was devoted to the effects on the hurricane dynamics that should occur by altering the microphysics of the imbedded cumulonimbus clouds by artificial seeding. It was apparent during the conference that considerable progress has been made recently in Japan and the U. S. in understanding cumulus cloud microphysics and in understanding hurricane dynamics. One of the main points the various discussions brought out was the gap that exists in our knowledge concerning the interaction between the two. Perhaps the program of hurricane modification will supply the impetus for closing this gap.

The results of the first multiple seeding of a hurricane by Project STORMFURY were presented by Dr. R. C. Gentry, Director, National Hurricane Research



Laboratory and Project STORMFURY. He showed the reductions in the maximum wind that were observed following the five seedings of hurricane Debbie on both 18 August and 20 August 1969. The reduction amounted to 31% on the 18th and 15% on the 20th. He went on to explain the new seeding hypothesis that has been developed during the past year. In this case, the energy needed for modification comes primarily from the latent heat of condensation as clouds just beyond the eyewall are made to grow. Of course, latent heat of fusion will still be important as a trigger to promote deeper moist convection.

Dr. N. Fukuta added to the discussion on hurricane modification by proposing another mechanism that may be active in modifying the hurricane after seeding. He suggested that enhancement of precipitation would cause additional cooling as a greater number of frozen particles melt and evaporate while falling. It was further suggested that cooling of the environmental air brought downward with the precipitation would reduce the cloud buoyancy and help cut off updrafts in the boundary layer.

Considerable discussion centered on the relative importance of the various heat exchange mechanisms in cumulus clouds as they applied to the hurricane. The general feeling was that the additional latent heat release by condensation stimulated by cloud growth following seeding, and further augmented by frictional convergence of water vapor beneath the cloud, was the dominant heat exchange mechanism.

The economic benefits of tropical storm modification were discussed by Dr. Gentry who showed that only a 10% reduction in a storm's maximum wind would result in a multimillion dollar savings in terms of damage prevented. He stressed that much work is needed in establishing a relation between the wind speed and damage. He quoted work presently being carried out at Stanford Research Institute which suggested that wind damage should be proportional to the wind speed raised to the power of from three to six. This would make a small reduction in wind speed extremely beneficial.

Prof. T. T. Fujita, University of Chicago, presented a semiquantitative scheme of assessing storm damage by categorizing storms according to areal extent of damage of a certain magnitude. To establish the magnitude of damage he proposed using his F-scale which related damage of a certain type to sustained winds and fastest 1/4-

mile winds. His F-scale connects the upper end of the Beaufort scale with the lower end of the Mach scale.

Future cooperation between the U. S. and Japan in the area of tropical cyclone modification was discussed on the last day of the conference. It has been proposed that Project STORMFURY move its operation to the Pacific during some part of the 1972 season. This would provide an excellent opportunity for cooperation between the U. S. and Japan. With this in mind, Dr. T. Kitaoka, Director, Meteorological Research Institute, presented a climatological study of killer typhoons in the western Pacific that would have been suitable for seeding during the period 1965-1969. Dr. Kitaoka imposed stricter seeding regulations in his study than are presently in use in the Caribbean area in order to avoid any possibility of a political problem. Therefore, he eliminated any storm from his study that struck land during its lifetime. With this criteria, he concluded that a STORMFURY operation could be carried out on from one to three typhoons during a 45-day period from mid-September through the end of October using Guam as a staging base and Wake and Yokota (or Atsugi) as secondary bases. It is planned to extend the study to include a ten-year period.

Results from a similar study made by W. D. Mallinger, National Hurricane Research Laboratory, NOAA, were presented by Dr. Gentry. This study used slightly less stringent rules, but still eliminated any storm that 1) was within 50 n mi of land 24 hr after seeding would have ended, 2) was recurving, or 3) was rapidly accelerating. Guam was suggested as the primary operating base with the possibility of terminating an operation in Okinawa. Using typhoon data from 1961 to 1969, an average of six typhoons would be eligible for seeding during the three-month period from August through October.

It was decided to hold future discussions concerning exact seeding eligibility in the western Pacific. In general, close cooperation between the U. S. and Japan on the planning, execution and evaluation of such an experiment would be carried out.

It was thought that a good time for the next meeting on the modification of cumulus clouds and cloud systems including tropical cyclones, sponsored by the U. S.-Japan Science Program, would be sometime early in 1973. By that time, much new information should be forthcoming from both countries concerning the various problem areas discussed during this conference.



## On the Asymmetric Structure of the Tropical Cyclone Outflow Layer

PETER G. BLACK AND RICHARD A. ANTHES

*National Hurricane Research Laboratory, NOAA, Miami, Fla.*

(Manuscript received 18 March 1971, in revised form 26 July 1971)

### ABSTRACT

ATS-III satellite data and conventional aerological data are used to construct detailed wind analyses of the outflow layer for four hurricanes and one tropical storm. Harmonic analysis of these data, and of the data for a mean Atlantic hurricane and a mean Pacific typhoon, shows that wave numbers 1 and 2 around the circumference of the storm account for most of the variance of momentum and kinetic energy. Subtraction of the symmetric part of the vortex circulation from the total flow to yield the "asymmetric wind" reveals two eddies located in preferred quadrants of the storm. An anticyclonic eddy is found to the right and a cyclonic eddy to the left of the storm motion. These eddies transport absolute vorticity inward, opposing the outward transport by the mean circulation. They also transport a significant amount of negative relative angular momentum outward.

The presence of inertial (or dynamic) instability is investigated. Although substantial areas of negative absolute vorticity and anomalous anticyclonic winds exist in all cases, these areas are correlated so well that the regions of dynamic instability are small.

### 1. Introduction

The outflow layer of tropical storms is considerably more asymmetric (azimuthally varying about the axis of rotation) than the middle and lower layers (Alaka, 1961, 1962; Miller, 1963). However, lack of data has hampered work that quantitatively describes the outflow structure for individual storms and ascertains the significance of the horizontal asymmetries. Previous analyses of the upper tropospheric structure of tropical storms have relied on 1) averaging rawinsonde data from a number of storms, 2) using scattered rawinsonde data from the periphery of individual storms, or 3) using high-level aircraft over a small area near the storm center. For example, Jordan (1952) and Miller (1958) constructed average upper tropospheric structures with data from primarily six Atlantic hurricanes and Izawa (1964) constructed an average typhoon with data from fourteen Pacific typhoons. Koteswaram (1967) studied several individual hurricanes, but his data were limited by the density of rawinsonde stations along the U. S. Gulf and Atlantic coasts, with the consequence that several quadrants were data void. Hawkins and Rubsam (1968), LaSeur and Hawkins (1963) and Gentry (1967) studied the inner region of individual storms using aircraft data, but these analyses were restricted to within 200 km of the center by the limited aircraft coverage.

Each of the above methods has disadvantages when making quantitative studies of the outflow layer. The averaging of several storms eliminates individual asymmetries that do not have a preferred location with

respect to the center of the storm. The sparse rawinsonde network over the oceans limits the use of the conventional aerological data. Finally, aircraft data are normally restricted by the range of the aircraft to within a few hundred kilometers of the storm center. Thus, there is a data gap between roughly 300 and 1000 km from the hurricane center. The importance of this region on hurricane dynamics, including the processes of inertial instability and interactions with the synoptic-scale environmental flow, therefore, is not well understood. Recently, however, it has been possible to utilize ATS-III satellite photographs to construct flow fields at levels which contain traceable cloud elements. These data have made it possible to construct nearly instantaneous, detailed flow patterns in the hurricane outflow layer beyond 300 km (Fujita and Black, 1970).

This paper investigates the structure of the outflow layer of five individual tropical cyclones and of two mean storms (Miller, 1958; Izawa, 1964). Quantitative estimates are made of the magnitude of large-scale horizontal asymmetries. In particular, harmonic analysis of the radial and tangential wind components and the specific kinetic energy determines quantitatively the predominant scale of the asymmetries. Subtraction of the axisymmetric portion of the flow from the total flow isolates the asymmetric part of the circulation and reveals horizontal eddies located in preferred quadrants of the tropical cyclone. The production and maintenance of these eddies are discussed. The role of the asymmetries in transporting vorticity and momentum is computed. Finally, the presence of negative absolute vorticity, anomalous

TABLE 1. Tropical cyclones selected for analyses.

Storm	Time period studied [time (GMT), date]	Storm motion		Direction of motion (deg)
		$u$ (m sec <sup>-1</sup> )	$v$ (m sec <sup>-1</sup> )	
Carla	1200, 10 September to 0000, 12 September 1961	-2.3	2.1	312
Candy	2110-2230, 22 June 1968	0.0	5.7	360
Debbie	1435-1625, 20 August 1969	-2.8	4.1	325
Camille	1630-1735, 17 August 1969	-1.8	5.9	343
Celia	1530-1700, 3 August 1970	-6.7	3.5	298
Mean Atlantic hurricane	1954-56	*		5.6
Mean Pacific typhoon	1950-61	*		5.5

\* Mean storms were composited relative to a single arbitrary direction of motion.

anticyclonic winds, and the related inertial instability are investigated.

## 2. Discussion of data

The tropical cyclones selected for this study are listed in Table 1. Table 2, compiled from the Fleet Weather Facility *Tropical Storm Reports* (1962, 1969, 1970) and the hurricane season reports (Dunn *et al.*, 1962; Sugg and Hebert, 1969; Simpson *et al.*, 1970) shows the central pressures and maximum wind speeds for each storm bracketing the time period used in this study. This table shows that the individual storms were nearly steady state over the period of study, except for hurricane Celia which was rapidly intensifying.

To obtain sufficient data for quantitative analysis of hurricane Carla, rawinsonde data were composited relative to the storm center for four synoptic times as the storm approached the Texas coast. This time-to-space conversion is considered valid since the storm was nearly steady state during the period.

For the remaining cases, the major source of data was the cirrus cloud motions derived from ATS-III satellite data, with supplemental rawinsonde and aircraft observations included where available. Cirrus cloud velocities for Debbie and Camille were provided by Fujita<sup>1</sup> and for Celia by Smith,<sup>2</sup> and were analyzed by the authors. The exact height of the cirrus clouds is difficult to determine, but best estimates (Waco, 1970) indicate that cirrus cloud heights near the center of an intense hurricane are between 150-100 mb. For less intense storms, the tops are probably somewhat lower, in the vicinity of 200 mb. Although the cirrus is definitely in the outflow layer, the cirrus motions may not occur at the level of *maximum* outflow. Thus, the calculations presented later possibly *underestimate* the maximum values found in the outflow layer.

Considerable care was taken to select cirrus cloud elements that were clearly persistent during the 2-hr period of observation. Wave motion effects, dissipation

of clouds, and thunderstorm anvils were avoided as unrepresentative of the large-scale flow. Cirrus cloud dissipation is not thought to be a serious problem since Merritt and Wexler (1967) have shown that cirrus bands in the hurricane outflow layer have an average lifetime of 12 hr. The accuracy of the satellite winds may be estimated by comparison of the 200-mb rawinsonde winds with the cirrus cloud motions for tropical storm Candy, shown in Fig. 1. Comparable agreement to that shown in Fig. 1 was also found for the Camille and Celia cases, while no comparison was possible in hurricane Debbie. From Fig. 1, the accuracy of the satellite wind speeds and directions appear to be within  $\pm 3$  m sec<sup>-1</sup> and  $\pm 15^\circ$ , respectively. This magnitude of error is close to that found by Serebreny *et al.* (1969) for ATS-III cirrus cloud motion observations in the tropics.

TABLE 2. Storm intensities.

Storm	Date	Day	Time (GMT)	Central pressure (mb)	maximum wind (kt)
Carla	September 1961	10	0000	942	115
		10	1200	935	120
		11	0000	935	130
		11	1200	931	140
		12	0000	940	130
Candy	June 1968	22	0000	1006	25
		22	1200	1004	25
		23	0000	1004	30
		23	1200	1001	35
Debbie	August 1969	20	0000	954	100
		20	1200	954	110
		21	0000	956	110
		21	1200	959	100
Camille	August 1969	16	1200	908	155
		17	0000	905	160
		17	1200	...	170
		18	0000	901	170
Celia	August 1970	02	1200	986	80
		03	0000	986	80
		03	1200	971	105
		04	0000	949	140

<sup>1</sup> T. Fujita, 1970: Personal communication.

<sup>2</sup> C. L. Smith 1970: Personal communication.

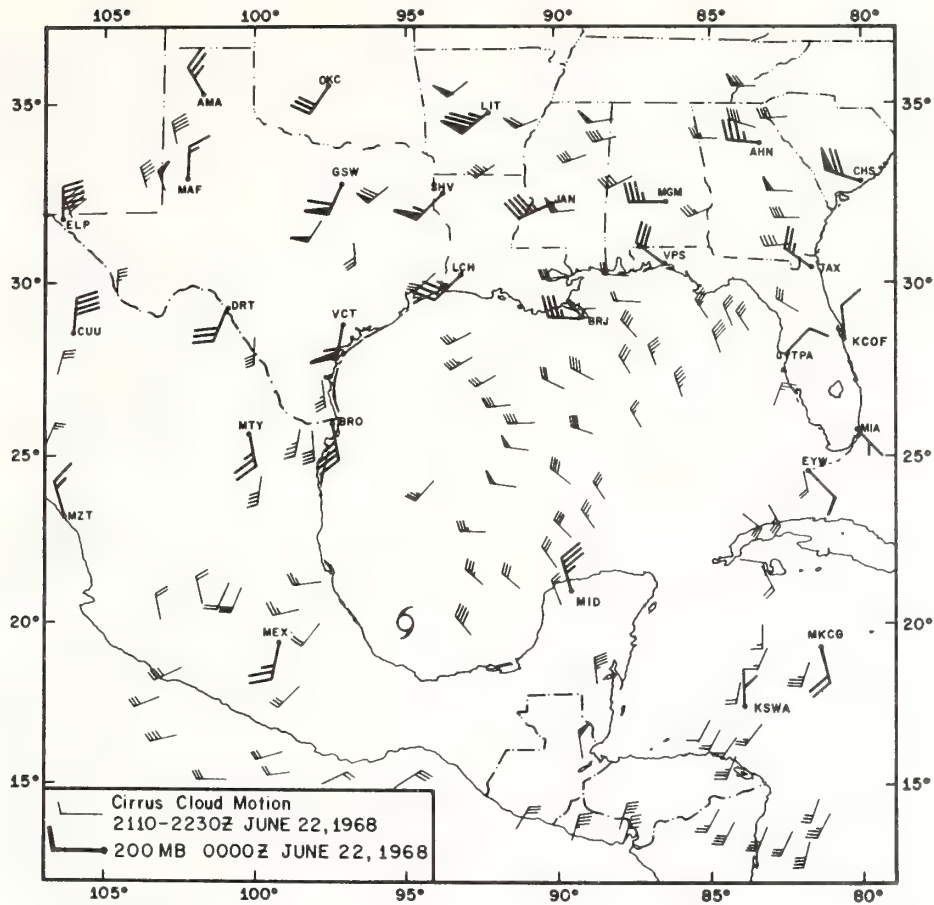


FIG. 1. Comparison of ATS-III cirrus cloud motions with 200-mb rawinsonde winds for tropical storm Candy.

### 3. Qualitative description of outflow structures

Historically, descriptions of the flow structure of tropical cyclones have differentiated between the total flow (storm circulation plus vortex translation) and flow relative to the moving storm center (total flow minus storm motion). This comparison is of primary interest close to the center of the storm in which the symmetric vortex circulation is dominant. At large distances, however, the physical meaning of relative motion is less clear as the intensity of the storm diminishes and environmental synoptic scales increase in importance. Since the primary region of interest in this paper links the hurricane scale with the larger synoptic scale, it is probably desirable to consider both total and relative flow. However, in the cases considered here, the storm motion is small compared to the total flow and differences in quantitative results due to this effect are minor.

The total streamline and isotach analysis for each individual storm is shown in the left hand column of Figs. 2 and 3. Hurricane Carla shows a huge outflow circulation with the most intense branch of the circu-

lation spiralling anticyclonically outward in the northeast quadrant. The corresponding analysis for weak tropical storm Candy shows a pronounced trough in the northwest quadrant, only a weak cyclonic circulation at the center, and a broad band of anticyclonic winds in the eastern semi-circle. Hurricane Debbie presents still another upper level pattern, with a small but intense cyclonic circulation at the center surrounded by anticyclonic winds. Outflow occurs mainly in the northeast and southwest quadrants. Hurricane Camille shows a large region of cyclonic flow near the center with cyclonic inflow in the left quadrant and massive outflow in the north and east quadrants. The outflow from hurricane Celia occurs almost entirely in the west quadrant. Inflowing air from the east penetrates to within  $1^\circ$  latitude of the center.

The upper level total flow patterns for the mean Atlantic (Miller, 1958) and Pacific storms (Izawa, 1964) are shown in the left-hand portions of Fig. 4. Both storms show strong anticyclonic outflow in the right quadrant. In other respects, however, they are quite different. The mean typhoon shows a large region of

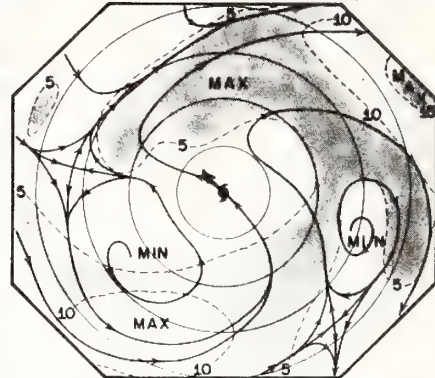
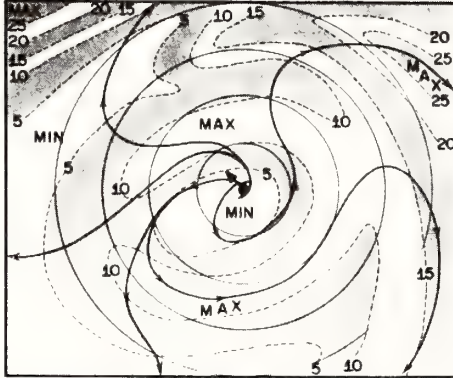


cyclonic motion near the center whereas the mean hurricane shows practically none. This difference is probably due to the greater intensity of the typhoons as shown by Table 3, but may also reflect a lack of data near the hurricane center. Considerable cyclonic inflow is evident in the left-rear quadrant of the mean

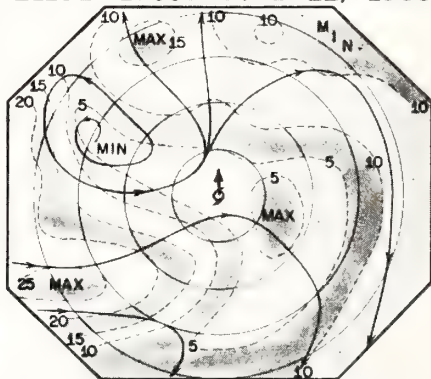
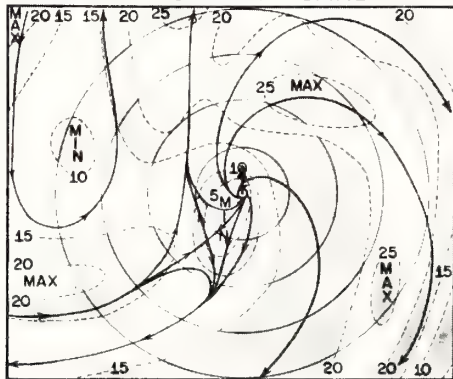
typhoon, whereas a smooth anticyclonic outflow is present for the mean hurricane.

Both mean storms show a surprising degree of asymmetry in spite of the smoothing inherent in the averaging process. Both Miller and Izawa note high values of persistence, defined as the ratio of vector mean velocity

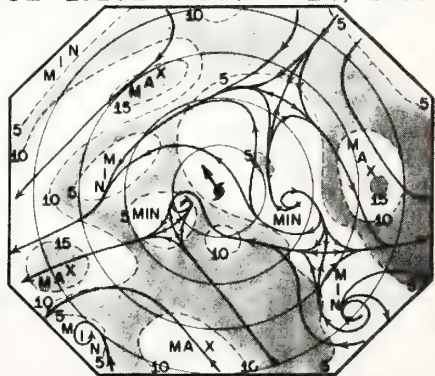
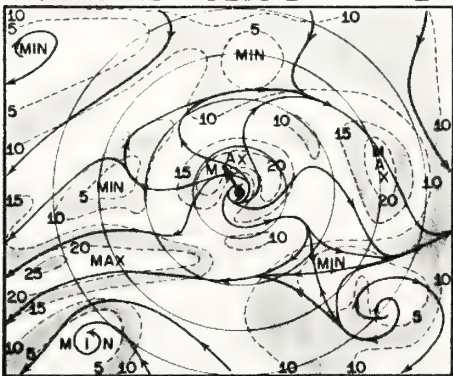
### HURRICANE "CARLA" 1200Z, SEPT. 10 — 00Z SEPT. 12, 1961



### TROPICAL STORM "CANDY" 2110Z - 1735Z JUNE 22, 1968



### HURRICANE "DEBBIE" 1435Z - 1625Z AUGUST 20, 1969



TOTAL STREAMLINES AND ISOTACHS

TOTAL ASYMMETRIC STREAMLINES AND ISOTACHS

FIG. 2. Total streamlines and isotachs ( $\text{m sec}^{-1}$ ), left, compared with total asymmetric streamlines and isotachs ( $\text{m sec}^{-1}$ ), right, for hurricane Carla, tropical storm Candy and hurricane Debbie. The range circles are at  $2^\circ$  latitude radius intervals. The arrow indicates the direction of storm motion.

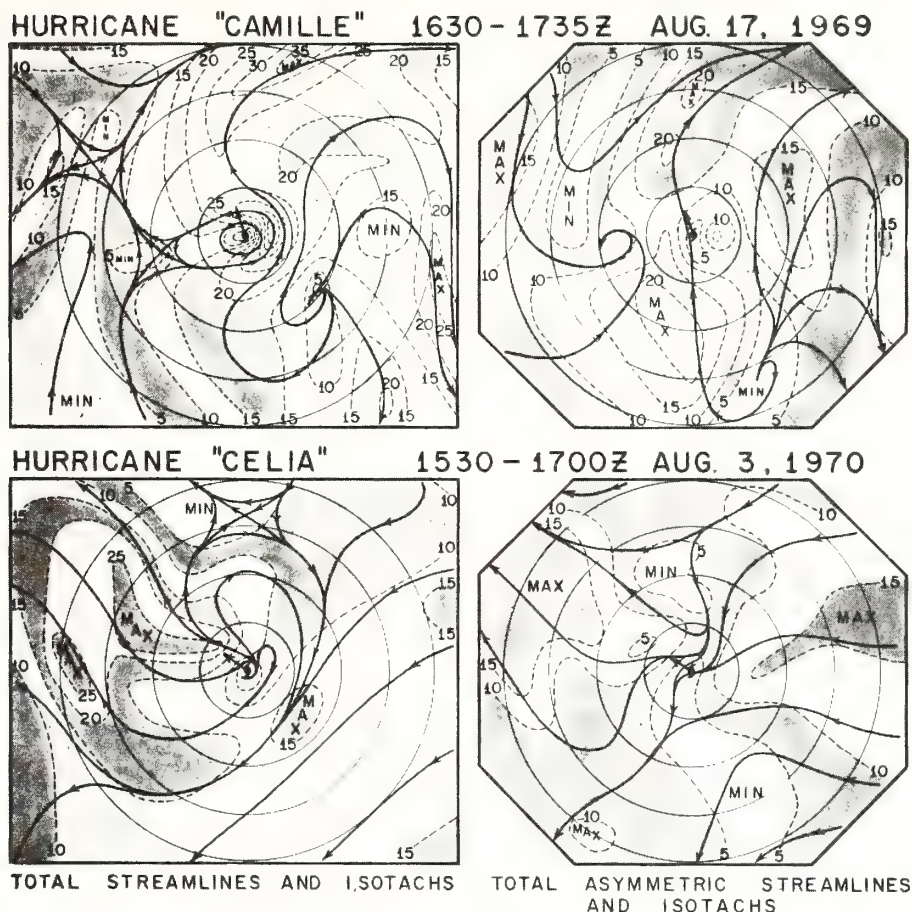


FIG. 3. Same as Fig. 2 except for hurricanes Camille and Celia.

to scalar mean speed. This preference of asymmetric features for certain quadrants, implied by the high persistence values, is discussed later.

Although the individual and mean tropical storms show a wide variety of structures, the streamline and isotach analyses suggest that the semi-circle to the left of the storm center tends to be cyclonic while the greatest anticyclonic circulation occurs to the right of the storm center.

#### 4. Quantitative description of outflow asymmetries

##### *a. Harmonic analysis of momentum and kinetic energy*

The scale of the asymmetries in the outflow layer of each storm may be determined by harmonic analysis of the tangential and radial wind components and specific kinetic energy. The east-west ( $u$ ) and the north-south ( $v$ ) components of the wind were linearly interpolated from a  $20 \times 20$  rectangular grid with 111-km resolution to a polar grid with 111-km radial and  $22\frac{1}{2}^\circ$  azimuthal resolution. The radial and tangential wind components were then calculated and the harmonic

analysis performed at radii from  $2-8^\circ$  of latitude in  $1^\circ$  increments. Computation of the total variance and percent variance by each harmonic is straightforward (e.g., Panofsky and Brier, 1958).

Figs. 5 and 6 show the radial and tangential wind components for the individual storms. These figures show that there are generally one or two maxima and minima around the storm's circumference. The corresponding fields for mean storms are presented by Izawa (1964) and Miller (1958) and are not repeated here.

Figs. 7 and 8 show the results from the harmonic analysis together with the azimuthal means and standard deviations of the radial and tangential winds for the individual storms. Fig. 9 shows the corresponding calculations for the mean storms. In interpreting the horizontal scales of the asymmetries from these figures, it should be noted that the wavelengths for a given wavenumber increase by a factor of 4 from the  $2^\circ$  latitude radius to the  $8^\circ$  radius.

The harmonic analysis emphasizes the strong asymmetric nature of the outflow structure. In nearly every



case the standard deviation is greater than the mean for each component beyond 400 km, indicating that the horizontal eddies dominate the circulation far from the center. The higher ratio of mean to standard deviation near the center indicates a more symmetric flow in this region.

The mean radial profiles of tangential velocities for hurricanes Carla, Debbie and Camille show a strong cyclonic circulation near the center ranging in intensity from roughly 8 (Carla) to 25  $\text{m sec}^{-1}$  (Camille). The radius of cyclonic winds varies from 250 km in Debbie to 650 km in Carla. Beyond the region of cyclonic winds the anticyclonic component reaches a peak intensity of about 10  $\text{m sec}^{-1}$  at 900 km for Carla and Camille, and at 450 km for Debbie, a smaller storm.

Weak tropical storm Candy, and hurricane Celia, which was undergoing rapid intensification, do not show the cyclonic flow near the center that is present in the other cases. This difference seems to be related to differences in the intensity and maturity of the storms, with greater cyclonic outflow associated with the mature

TABLE 3. Average intensities of mean storms.

Storm	Minimum pressure (mb)	Maximum wind (kt)
Mean Atlantic hurricane	944	125
Mean Pacific typhoon	925	155

intense storms. In these cases, the cyclonic winds result from prolonged upward transport of cyclonic momentum by the mean vertical motion and the organized cumulus convection (Gray, 1967).

Figs. 7 and 8 show the percent of total variance accounted for by wavenumbers 1–3. Wavenumber 4 is shown whenever it is significant ( $>5\%$ ). Higher wavenumbers account for a very small percent of the variance and are not shown. In most cases, wavenumbers 1 and 2 explain over 90% of the variance. Furthermore, the percent of variance accounted for by wavenumbers 1 and 2 is nearly constant with radial distance, in-

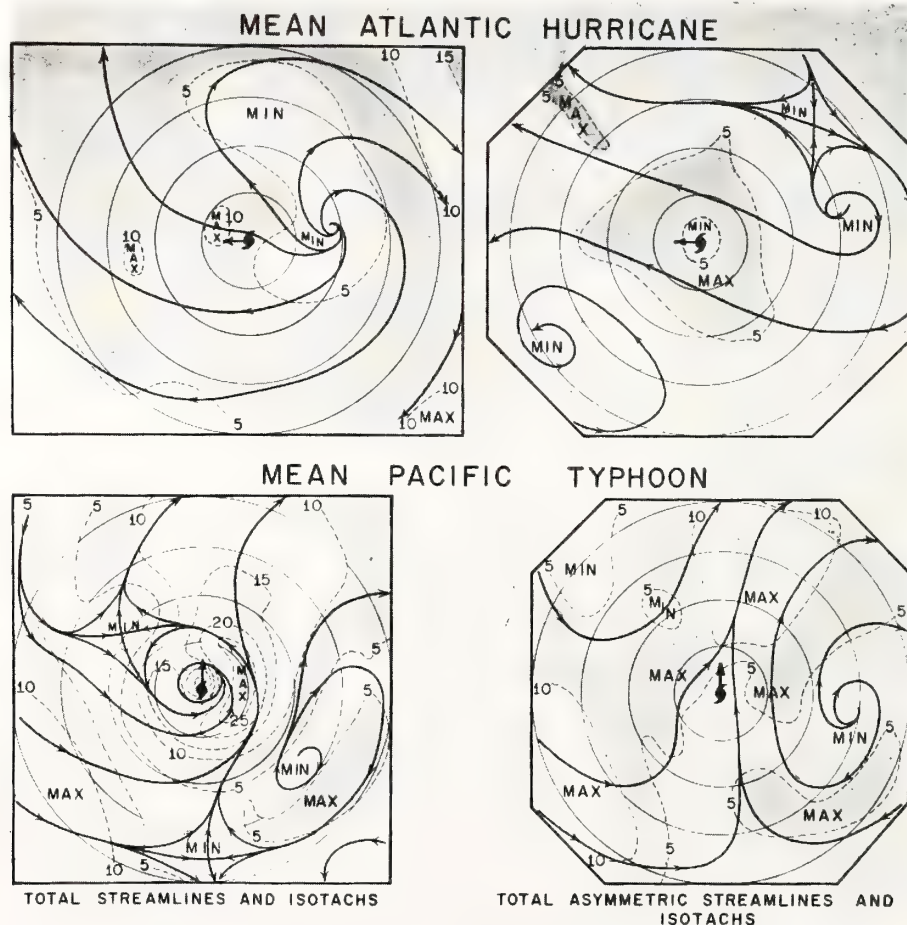


FIG. 4. Same as Fig. 2 except for the mean Atlantic hurricane and the mean Pacific typhoon.



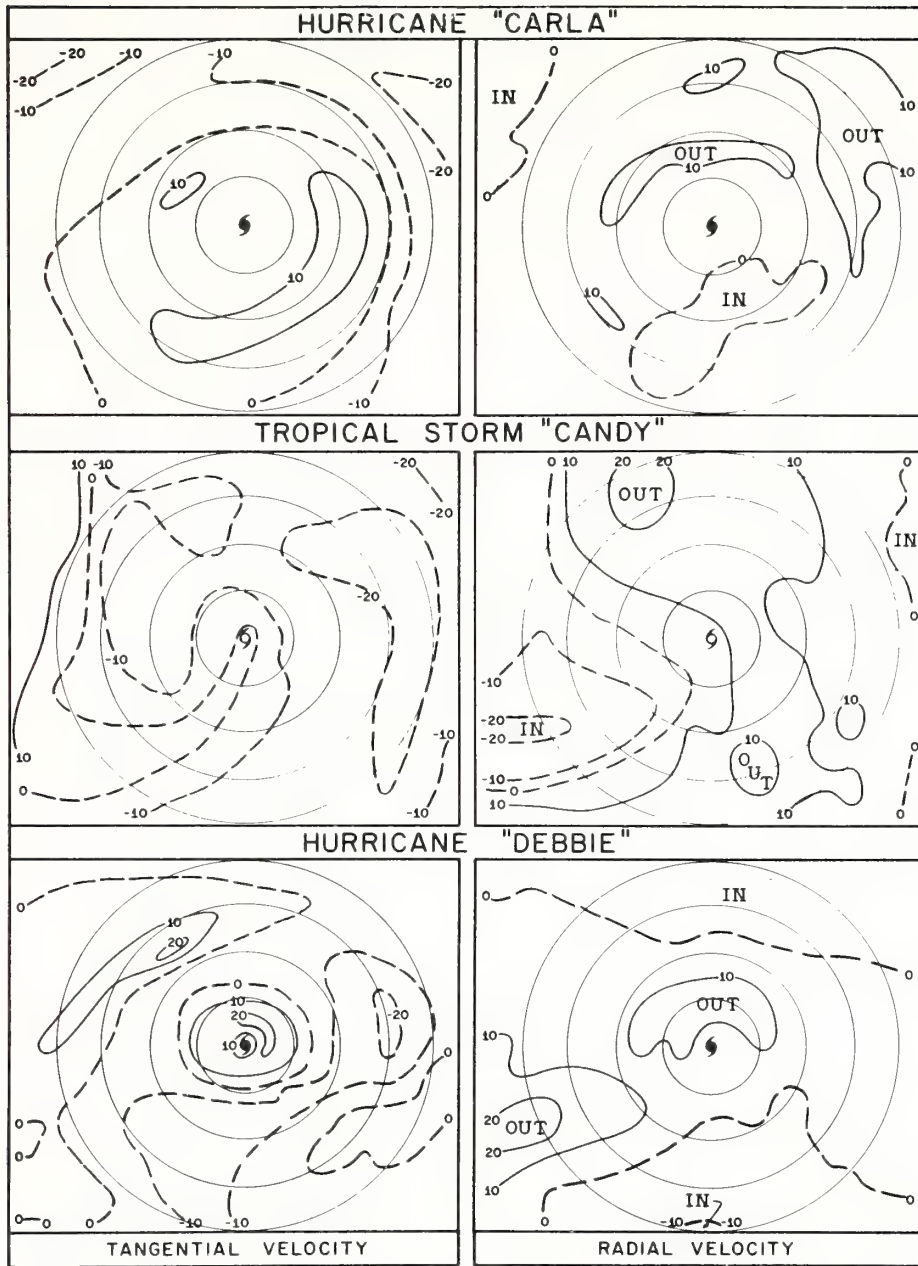


FIG. 5. Relative tangential and radial wind components ( $\text{m sec}^{-1}$ ) for Carla, Candy and Debbie.

dicating that the horizontal scale of the asymmetries *increases* outward.

Since the storm motion is usually different from the flow at any one level, the predominance of wavenumber 1 in the tangential and radial wind components is partially due to the geometric effect of the storm moving through an upper level current of different velocity. It should also be noted that the harmonic analysis is biased toward smaller wavenumbers since the averaging

and smoothing which is present in varying degrees in all cases will suppress higher spatial frequencies.

For the individual and mean storms, Figs. 10, 11 and 12 show the harmonic analysis of specific kinetic energy  $k$ , where

$$k = (u^2 + v^2)/2. \quad (1)$$

The analysis of kinetic energy shows somewhat less energy in wavenumber 1 than does the analysis of the

tangential and radial winds, possibly because the asymmetric distribution of kinetic energy is not directly related to the motion of the vortex through the atmosphere, as is the case for the tangential and radial wind components. Figs. 10–12 show that the standard deviation of kinetic energy increases outward, and that nearly all of the variance is accounted for by wave-numbers 1, 2 and 3. There is a slight tendency for the higher harmonics to increase in importance beyond 400 km.

In summary, the harmonic analysis of tangential and radial components and specific kinetic energy indicates the presence of one or two large-scale eddies which are most prominent beyond 400 km. The production and maintenance of these eddies, and their role in the vorticity and angular momentum budgets of the hurricane, are discussed in the following sections.

#### b. The asymmetric wind

To isolate the asymmetric structure of the outflow layer, the “asymmetric wind”  $\mathbf{V}'$  is defined by subtract-

ing the azimuthal mean tangential and radial wind components from the observed components, i.e.,

$$\left. \begin{aligned} v_{\lambda}' &= v_{\lambda} - \overline{v_{\lambda}} \\ v_r' &= v_r - \overline{v_r} \end{aligned} \right\} \quad (2)$$

where

$$\mathbf{V}' = v_{\lambda}' \boldsymbol{\lambda} + v_r' \mathbf{r},$$

where  $\boldsymbol{\lambda}$  and  $\mathbf{r}$  are unit vectors in the tangential and radial directions, respectively, and the overbar denotes the azimuthal average. The  $\mathbf{V}'$  field represents the environmental flow after the symmetric part of the vortex is removed. The asymmetric streamlines and isotachs for the individual storms are shown in the right-hand column of Figs. 2 and 3, and for the mean cases in Fig. 4.

The asymmetric flow field reveals that for three of the five storms (Carla, Camille and Debbie), two eddies are present in the outflow layer as was suggested by the harmonic analysis. In each case, there is a cyclonic eddy to the left of the storm motion vector (given in Table 1), and an anticyclonic eddy to the right. Furthermore, in the case of hurricane Debbie, two more eddies are present downstream from the hurricane, a cyclonic

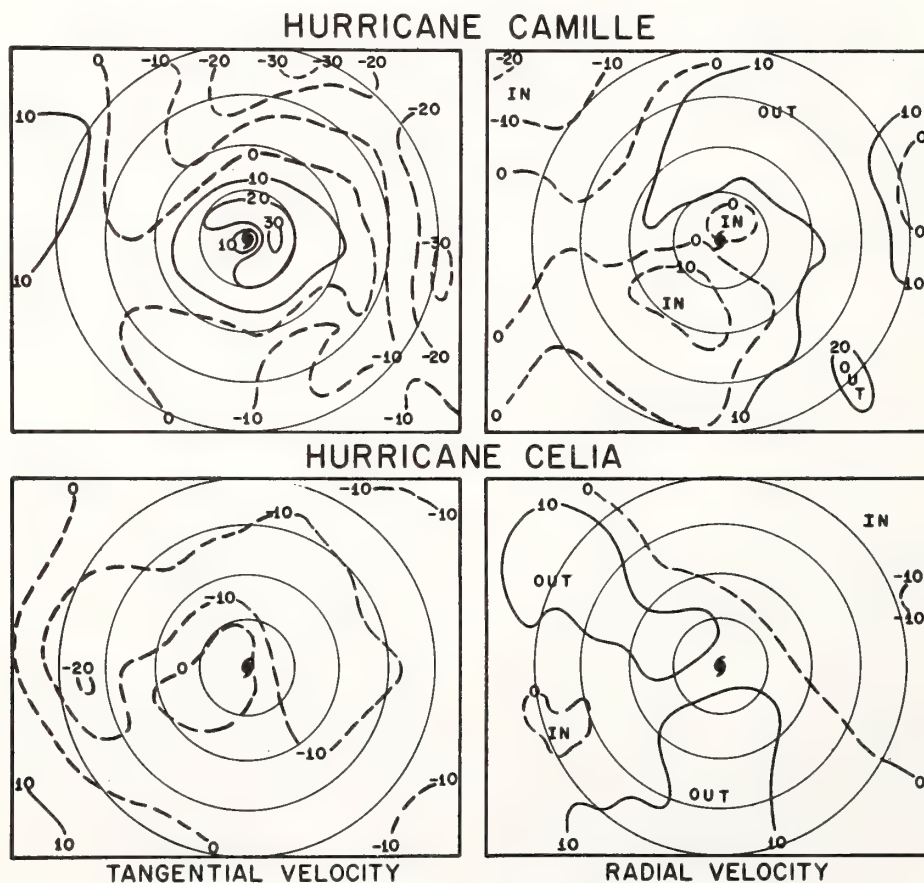


FIG. 6. Relative tangential and radial wind components ( $\text{m sec}^{-1}$ ) for Camille and Celia.

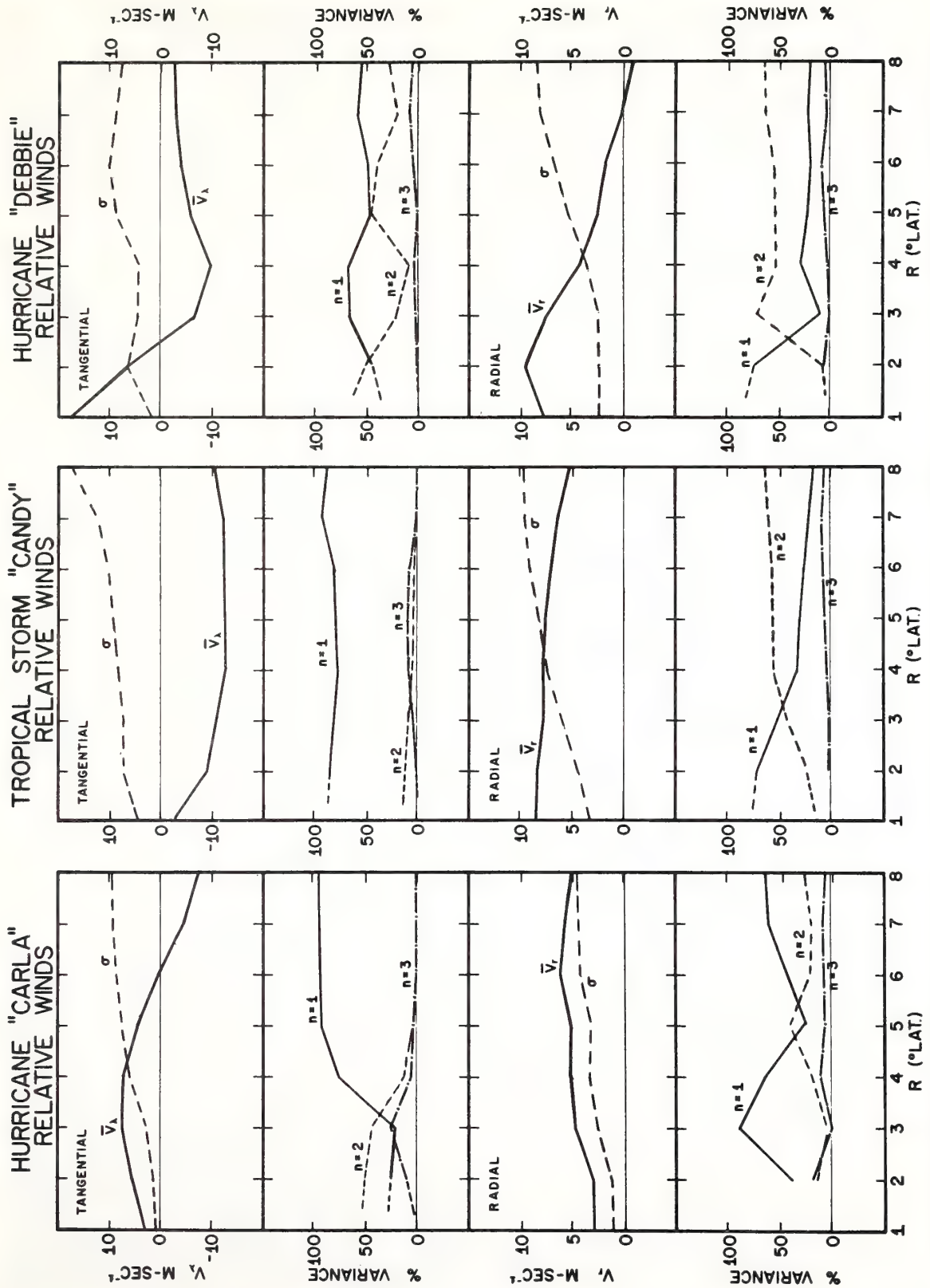


FIG. 7. Harmonic analysis of the relative radial and tangential wind components for storms Carla, Candy and Debbie together with the azimuthal means and standard deviations.



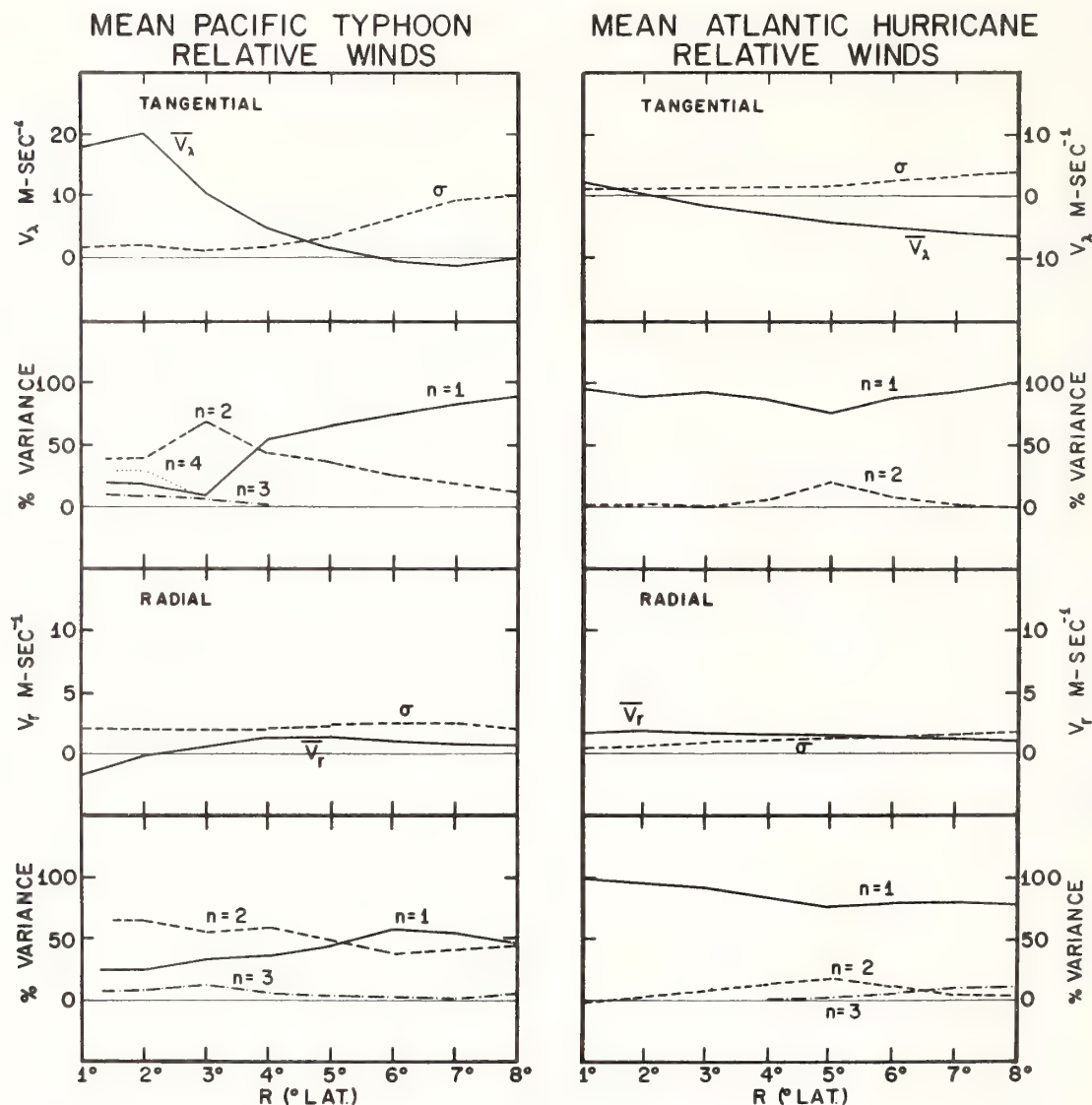


FIG. 9. Same as Fig. 7 except for the mean Pacific typhoon and the mean Atlantic hurricane.

vortices observed on several scales in the atmosphere. Hubert and Krueger (1962) analyzed vortex streets to the lee of Madeira Island. Lyons and Fujita (1968) showed that stratus dissipation to the lee of the Aleutians was caused by standing eddies and vortex streets. Fujita and Grandoso (1968) have shown from Doppler wind data that a wake region at 500 mb existed to the lee of a large cumulonimbus located near Topeka, Kan., on 21 April 1961.

The hurricane outflow circulation, of course, is not a solid barrier and the analogy to vortex formation caused by flow around solid obstacles must not be carried too far. Indeed, the phenomena of boundary layer separation in the vicinity of a solid obstacle is very important in the formation of vortices (Schlichting,

1968, p. 29). Nevertheless, it is reasonable to assume that a strong divergent outflow will partially deflect oncoming air around the storm circulation and result in an organized rather than random distribution of eddies.

Some simple qualitative arguments may help explain the organization of the eddies that are found in the outflow layer of hurricanes. For a stationary barrier located in a mean horizontal flow with zero relative vorticity, viscous stresses in the vicinity of the obstacle retard the fluid and produce velocity maxima at some distance away from the obstacle. This produces a vorticity maximum (cyclonic) on the left side (facing upstream) of the obstacle and a vorticity minimum (anticyclonic) on the right side of the obstacle. The

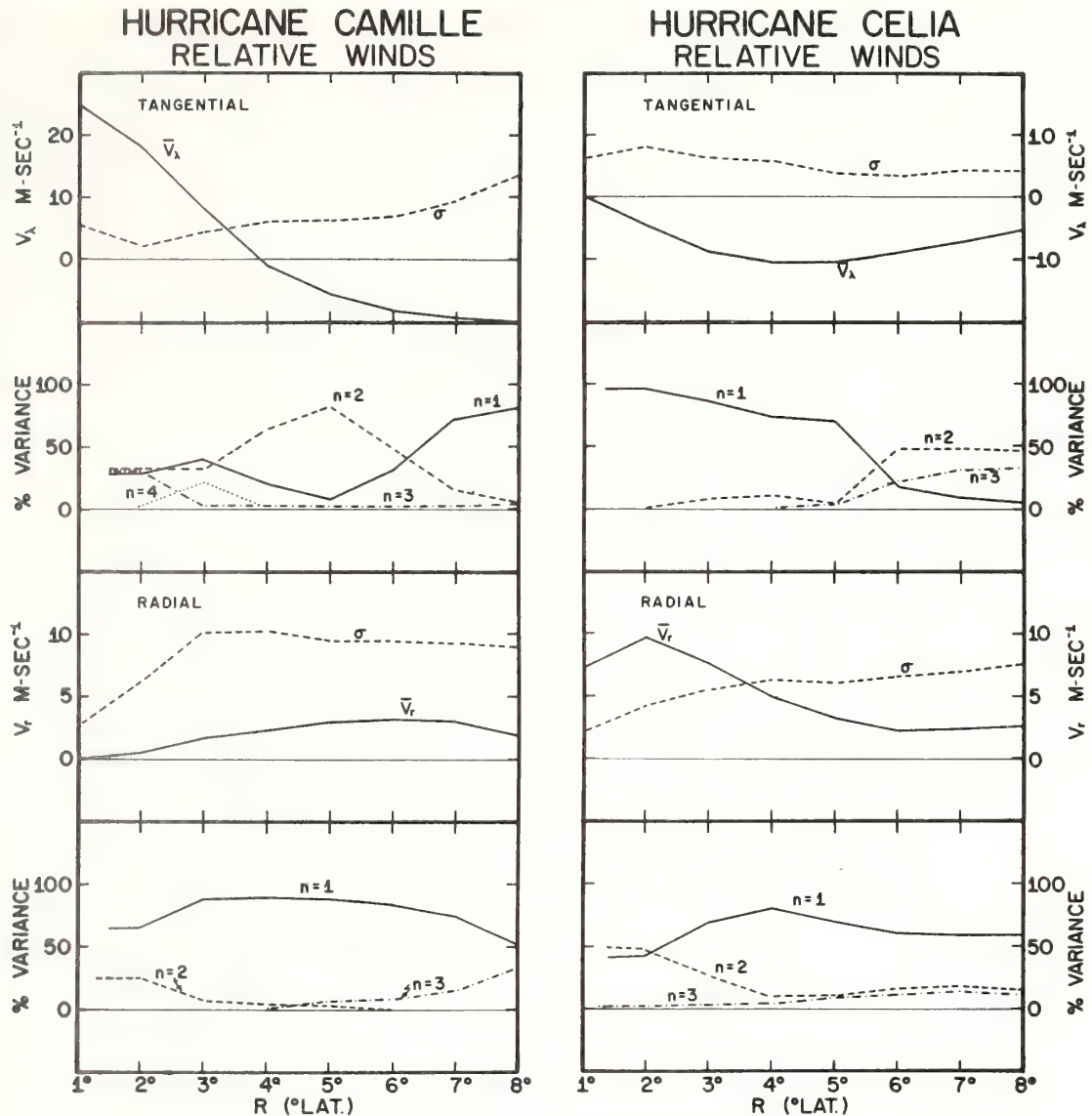


FIG. 8. Same as Fig. 7 except for storms Camille and Celia.

eddy southwest of the center and an anticyclonic eddy to the southeast. The scale of the eddies seems to be dependent on the size of the storm. For example, the eddies associated with the huge outflow area of Carla are much larger than those associated with the smaller storm Debbie.

Although there are no closed eddy circulations for Candy and Celia, there are sharp regions of cyclonic flow to the left and anticyclonic flow to the right of the storms' direction of motion. This difference may be related to the immature stage of these storms.

It is significant that an eddy pair is present in both of the mean storms, although for the Pacific typhoon only strong cyclonic turning is evident. The asym-

metries in the mean data imply a preferred location in the outflow for the eddies. Both the Atlantic and Pacific storms show an anticyclonic eddy to the right of the storm motion vector and a cyclonic eddy to the left of the storm motion vector.

The presence of a cyclonic and anticyclonic eddy pair associated with each individual and mean storm suggests the possibility that these eddies are organized by the high tropospheric flow streaming around the outflow layer of the storm which acts as an obstacle to the flow. The total flow may be considered as a superposition of a vortex and source in a basic current. After subtracting the symmetric source-vortex flow, the circulations in the right-hand columns of Figs. 2-4 resemble wake

vortex pair is symmetric, and the total vorticity of the mean flow is unchanged. A more complex situation results if a symmetric, anticyclonic vortex with outflow replaces the solid barrier. On the left side of the vortex, the vortex flow opposes the mean flow, while on the right side the vortex flow increases the mean flow. Because the symmetric vortex is adding negative relative vorticity, the net result will be a decrease in vorticity of the mean flow downstream. Therefore, relatively straight flow is deflected around the storm, with a cyclonic eddy to the left of the storm center and a larger anticyclonic eddy to the right.

The above discussion is not meant to imply that flow around an obstacle is the only mechanism to produce eddies in the outflow layer of hurricanes. For example, recent work with an asymmetric hurricane model

(Anthes *et al.*, 1971) has shown that eddies are generated in the hurricane outflow layer by the internal dynamics of the hurricane alone. These eddies vary in size and sense of rotation and have no preferred location with respect to the storm center. We suggest, therefore, that the flow around the hurricane outflow plays the role of organizing the otherwise random eddy pattern in the outflow layer by producing preferred regions of anticyclonic and cyclonic vorticity.

### c. Eddy flux of vorticity and angular momentum

Although Riehl and Malkus (1961) have shown that asymmetries are unimportant in the transport of angular momentum within 200 km of the cyclone center, various investigators have found large contributions

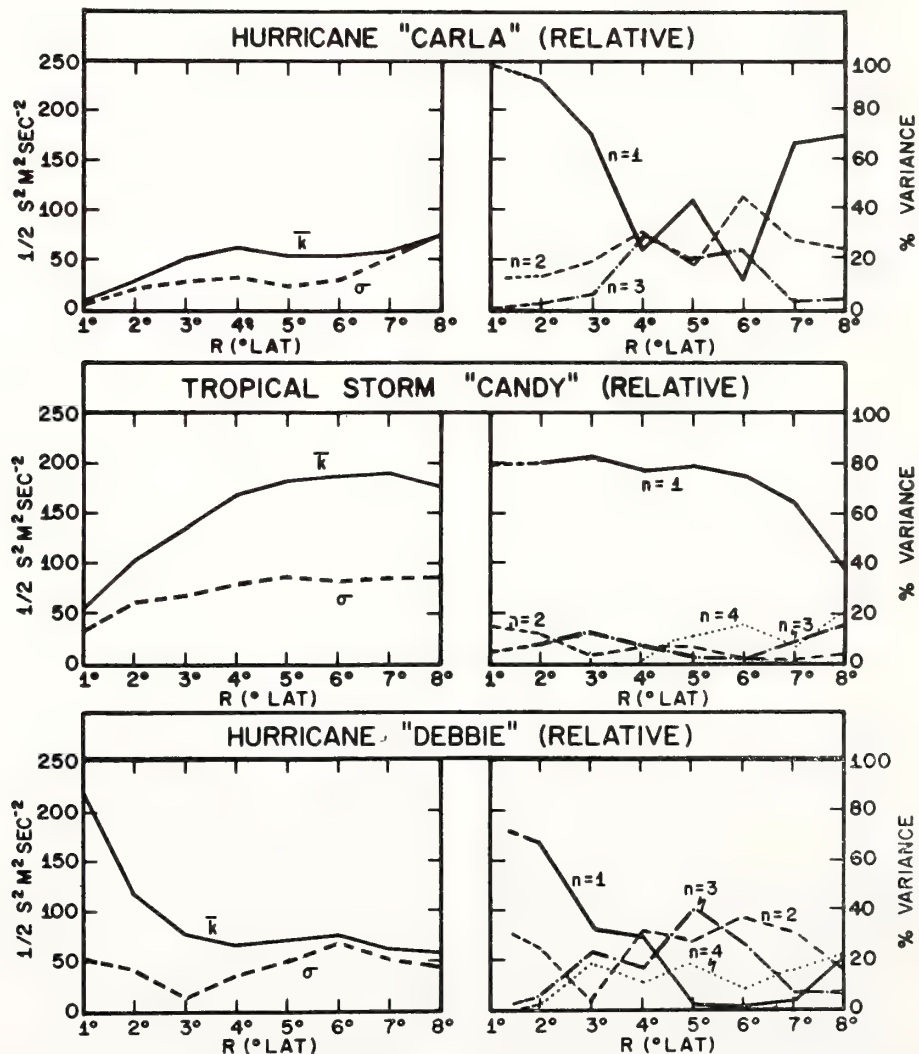


FIG. 10. Harmonic analysis of specific kinetic energy (right) together with the azimuthal mean and standard deviation (left) for Carla, Candy and Debbie.



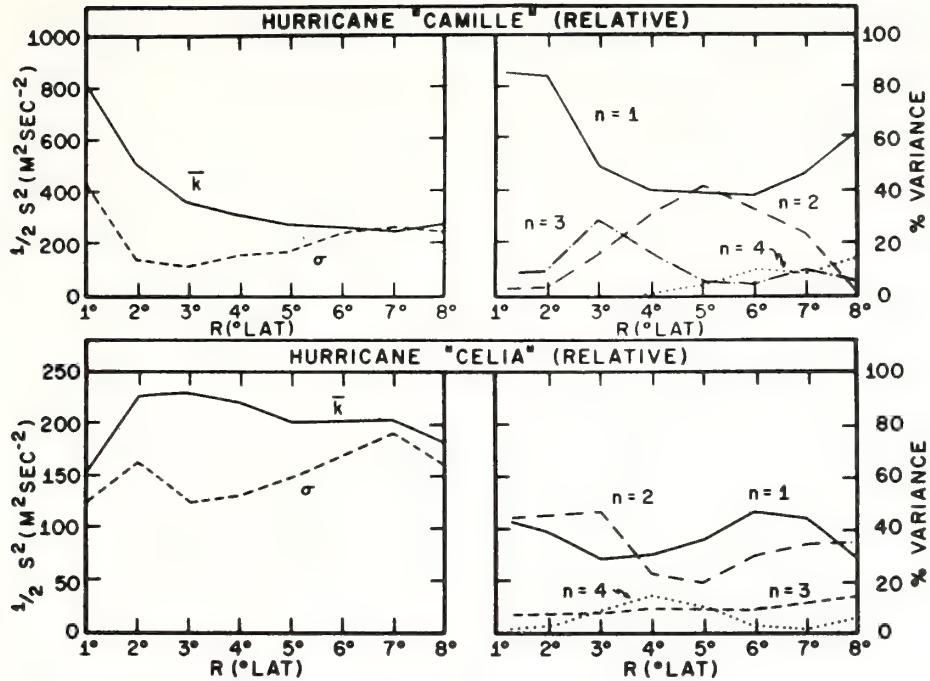


FIG. 11. Same as Fig. 10 except for Camille and Celia.

to the angular momentum budget from large-scale horizontal eddies at greater distances from the center. Pfeffer (1958) used the mean data of Jordan (1952) and Hughes (1952) and found a vertically integrated

inward flux of angular momentum by horizontal eddies. The eddy flux increased outward to  $6^{\circ}$  latitude radius (666 km) from the center, the edge of Pfeffer's computational domain. Palmén and Riehl (1957) also utilized

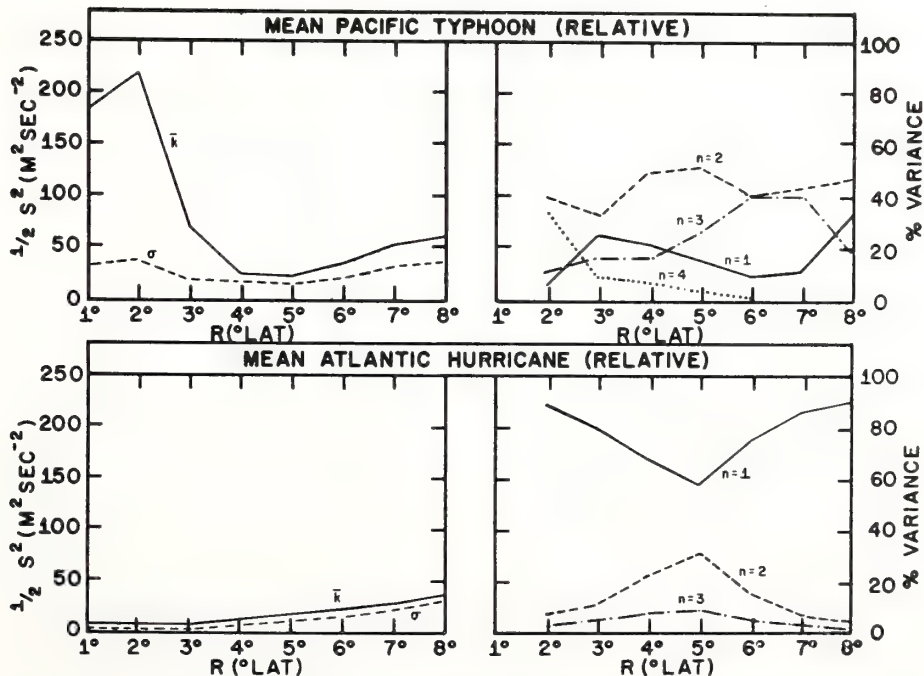


FIG. 12. Same as Fig. 10 except for the mean Pacific typhoon and the mean Atlantic hurricane.

Jordan's mean data and found a negative correlation between radial and tangential velocities and a significant inward transport of angular momentum in the layer between 500 and 100 mb.

Recently, Anthes (1970) hypothesized that large scale asymmetries between radii of 400 and 1000 km from the hurricane center may play an important role in satisfying the angular momentum budget of the steady-state hurricane. Neglecting vertical eddies, the circularly averaged, steady-state equation of motion for the tangential wind component may be written as

$$\overline{v_r \zeta_a} + \overline{v_r' \zeta_a'} + w \frac{\partial \overline{v_\lambda}}{\partial Z} = \overline{F_\lambda}, \quad (3)$$

where the absolute vorticity  $\zeta_a$  is

$$\zeta_a = \frac{\partial v_\lambda}{r \partial r} + f, \quad (4)$$

$w$  is the vertical velocity component,  $Z$  height,  $f$  the Coriolis parameter, and  $\overline{F_\lambda}$  the net effect of all "fric-

tional" forces. The  $(\overline{\quad})$  operator refers to the azimuthal mean at a given radius and  $(\quad)'$  to departures from this mean. The relationship between absolute vorticity flux and angular momentum advection is given by

$$\frac{1}{r} \frac{\partial M}{\partial r} = v_r \left( f + \frac{1}{r} \frac{\partial v_\lambda}{\partial r} \right) = v_r \zeta_a, \quad (5)$$

where the absolute angular momentum  $M$  is

$$M = \frac{f r^2}{2} + r v_\lambda. \quad (6)$$

Thus, in terms of angular momentum, (3) becomes

$$\frac{\partial \overline{M}}{\partial r} + \overline{v_r' \frac{\partial M'}{\partial r}} + w \frac{\partial \overline{M}}{\partial Z} = r \overline{F_\lambda}. \quad (7)$$

In the outflow layer at moderate distances from the storm center, angular momentum is approximately conserved (if the frictional force  $\overline{F_\lambda}$  is small and the

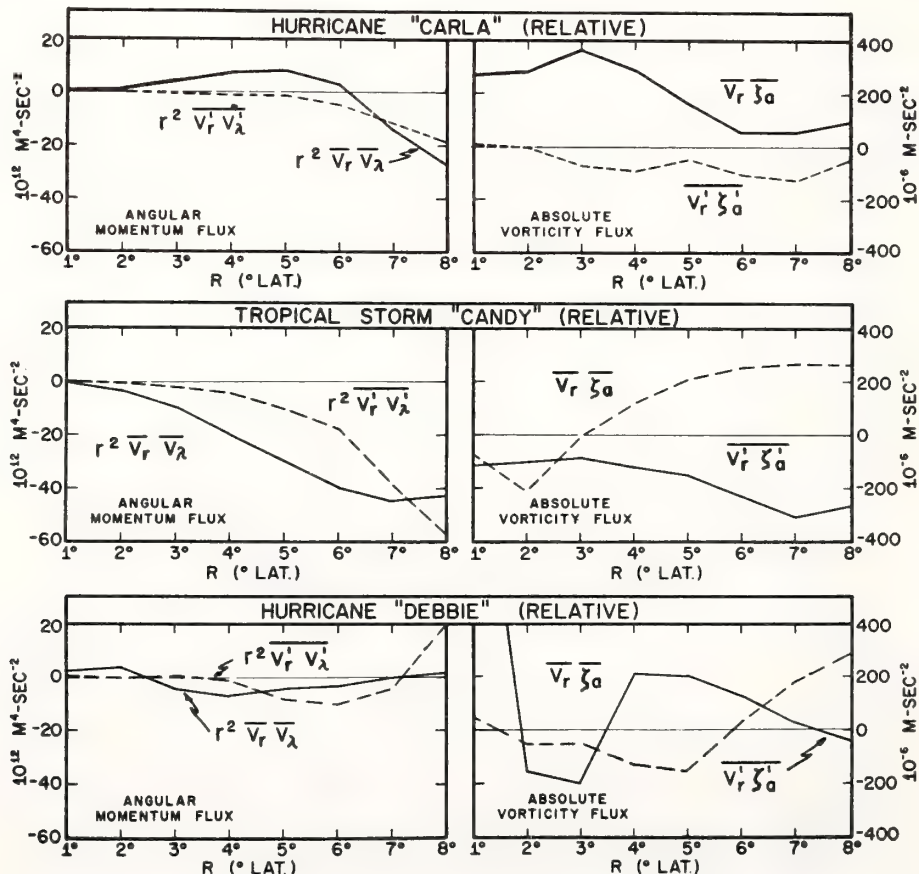


FIG. 13. Profiles of mean and eddy transport of relative angular momentum (left) and absolute vorticity (right) for Carla, Candy and Debbie.

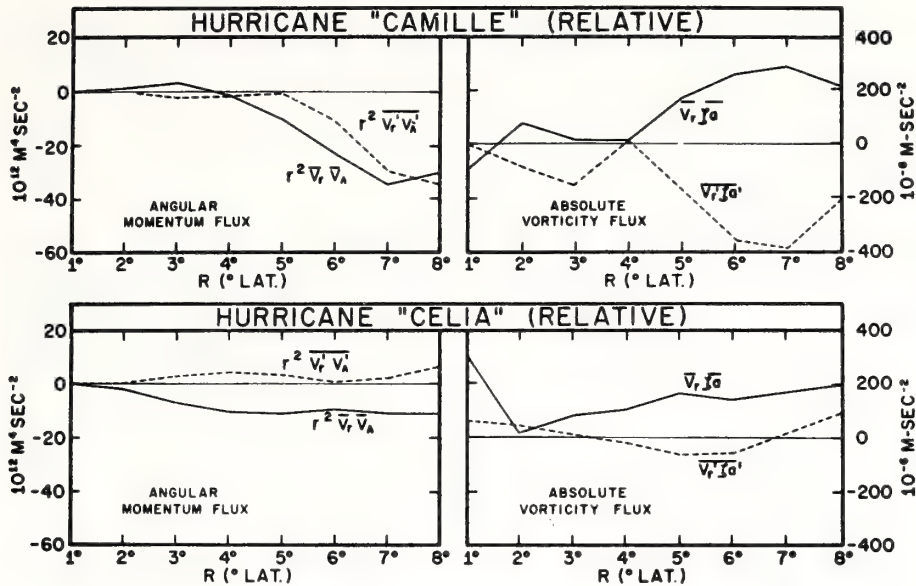


FIG. 14. Same as Fig. 13 except for Camille and Celia.

vertical velocity is negligible). Under these conditions, the horizontal eddies must oppose the mean flow in transporting vorticity, i.e.,

$$\overline{v_r \zeta_a} + \overline{v_r' \zeta_a'} \approx 0. \quad (8)$$

For a hypothetical mean tangential velocity distribution which was typical of a hurricane, Anthes (1970) calculated a maximum value of  $-150 \times 10^{-6} \text{ m sec}^{-2}$  for

the eddy term  $\overline{v_r' \zeta_a'}$  in the upper troposphere at a radius of 400 km.

Figs. 13 and 14 show the radial profiles of  $\overline{v_r \zeta_a}$  and  $\overline{v_r' \zeta_a'}$  computed for the individual storms. Fig. 15 shows these profiles for the mean storms. It should be noted that the data resolution for computing azimuthal means is minimal within  $3^\circ$  of the center and the results are less reliable in this region. In all storms the eddy transport of vorticity is negative and opposes the mean flux

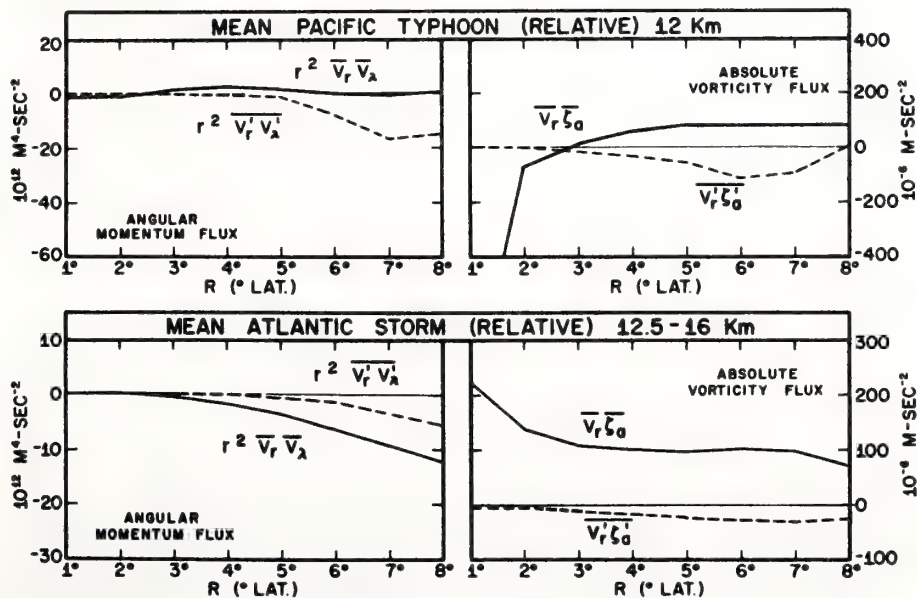


FIG. 15. Same as Fig. 13 except for the mean Pacific typhoon and the mean Atlantic hurricane.



beyond about 300 km. The magnitude of the eddy flux is comparable to the magnitude of the mean flux, although the mean flux is somewhat larger. The closest balance between the mean and eddy flux is found in hurricane Camille, where the eddy flux reaches a value of  $-400 \times 10^{-6} \text{ m sec}^{-2}$ .

Another measure of the importance of horizontal eddies is the eddy transport of angular momentum (Palmén and Riehl, 1957; Pfeffer, 1958). The mean and eddy transports of relative angular momentum,  $r^2 \bar{v}_r \bar{v}_\lambda$  and  $r^2 \bar{v}_r' \bar{v}_\lambda'$ , for the individual and mean storms are compared in Figs. 13–15. Both components show a net outward transport of negative relative angular momentum. The magnitude of the eddy flux is very small within  $5^\circ$  of the center for all cases, but increases outward from there to the edge of the outflow region. The mean transport is generally larger than the eddy transport except near the edge of the outflow region where the two terms are nearly equal.

The profiles of angular momentum transport for the mean Atlantic hurricane and mean Pacific typhoon are in general agreement with the profiles for the individual storms. The Pacific storm, however, shows a much larger eddy transport, suggesting that the eddies play a larger role in the angular momentum budget of more intense storms. The transport of negative angular momentum outward by the eddies is in agreement with the earlier results of Palmén and Riehl (1957) and Pfeffer (1958).

### 5. The occurrence of dynamic instability in the hurricane outflow layer

Dynamic (or inertial) instability of the upper tropospheric outflow has been suggested by Alaka (1961, 1962, 1963) and others as a contributory factor in the intensification of tropical cyclones. An approximate condition for this instability is

$$\zeta_a \left( \frac{2V}{R} + f \right) < 0, \quad (9)$$

where  $V$  is the wind speed,  $R$  the radius of curvature of the streamline, and  $\zeta_a$  the absolute vorticity given by

$$\zeta_a = \frac{\partial u}{\partial y} - \frac{\partial v}{\partial x} + f. \quad (10)$$

Condition (9) may be satisfied with either positive absolute vorticity and anomalous winds  $[(2V/R) + f < 0]$  or for normal winds and negative absolute vorticity. This type of instability was closely associated with the development of asymmetries in a three-level asymmetric model of the tropical cyclone (Anthes *et al.*, 1971). It is conceivable that dynamic instability plays a role in maintaining the eddies in the outflow region.

The criterion given by Eq. (9) refers to horizontal parcel displacements normal to a streamline, and should not be confused with a related instability governed by

$$\left( \frac{\partial r v_\lambda}{r \partial r} + f \right) \left( \frac{2v_\lambda}{r} + f \right) < 0, \quad (11)$$

which refers to the instability of horizontal symmetric ring displacements in a symmetric vortex.

The instability represented by the condition in Eq. (9) was investigated utilizing the total wind fields for the cases in this study. The radius of curvature  $R$  was evaluated (Alaka, 1961), according to

$$\left. \begin{aligned} \frac{1}{R} &= \frac{1}{V^3} \left( u \frac{dv}{dt} - v \frac{du}{dt} \right) \\ \frac{1}{R} &= \frac{1}{V^3} \left[ u \left( \frac{\partial v}{\partial x} + v \frac{\partial v}{\partial y} \right) - v \left( \frac{\partial u}{\partial x} + v \frac{\partial u}{\partial y} \right) \right] \end{aligned} \right\}, \quad (12)$$

which assumes the local time derivatives are negligible compared to the advective terms. The differentials in (10) and (12) were evaluated over 222-km intervals.

The left-hand column of Figs. 16 and 17 show the absolute vorticity and  $[(2V/R) + f]$  analyses for Carla, Candy, Debbie, Camille and Celia. It is extremely interesting that, although large regions of negative absolute vorticity and anomalous winds are present, the two terms are so well correlated that only small regions exist where the product is negative. The negative values are very small in magnitude compared to the positive values.

By comparison of Figs. 16 and 17 with Figs. 2 and 3, the regions of inertial instability seem to be most commonly associated with the combination of strong cyclonic shear and anticyclonic curvature. Note, for example, the regions  $4^\circ$  north of Carla,  $6^\circ$  northeast of Candy, and  $6^\circ$  north of Camille. Dynamic instability is also possible for uncurved flow under strong anticyclonic shear. However, this combination appears less frequently than the combination of cyclonic shear and anticyclonic curvature. An example of the second condition may be found in the extreme northwest quadrant of Carla.

Alaka (1961, 1962) has reported larger regions of dynamic instability in the upper level of hurricanes than we have found in these cases. This is perhaps not surprising since four of the five storms studied in this report were in relatively steady state.

### 6. Summary and conclusions

ATS-III satellite data, supplemented by conventional rawinsonde data, are utilized to study the asymmetric structure of the outflow layer of five tropical cyclones. In addition to these individual cases, the out-

flow structure of Miller's (1958) mean Atlantic storm and Izawa's (1964) mean Pacific storm are studied.

The outflow circulation is highly asymmetric, especially beyond 400 km from the storm center where the standard deviation of the radial and tangential wind components and the specific kinetic energy exceed the mean values.

The asymmetric part of the circulation is emphasized by subtracting the axisymmetric part of the circulation from the total flow. The resultant circulation, defined as the asymmetric wind, reveals that two eddies dominate the outflow structure in each *mature* storm as well as the two mean cases. An anticyclonic eddy is located to the right of the storm's direction of motion and a

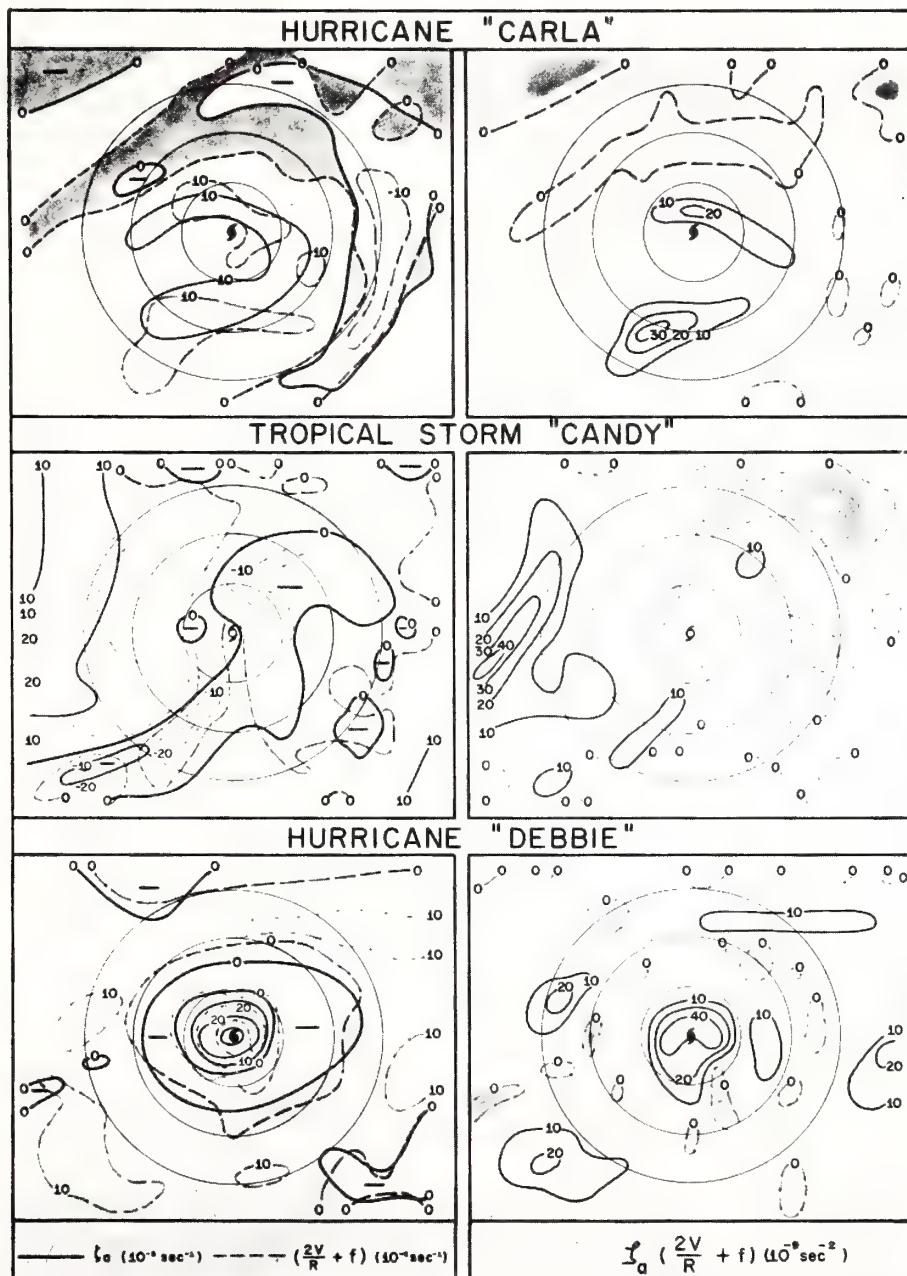


FIG. 16. Absolute vorticity,  $\zeta_a$ , and anomalous wind term,  $[(2V/R) + f]$ , for Carla, Candy and Debbie, left. The shading represents the areas where the product of the two terms is negative. Right, horizontal analysis of the product,  $\zeta_a[(2V/R) + f]$ . The shading represents the areas where this product is less than  $-1 \times 10^{-9} \text{ sec}^{-2}$ .

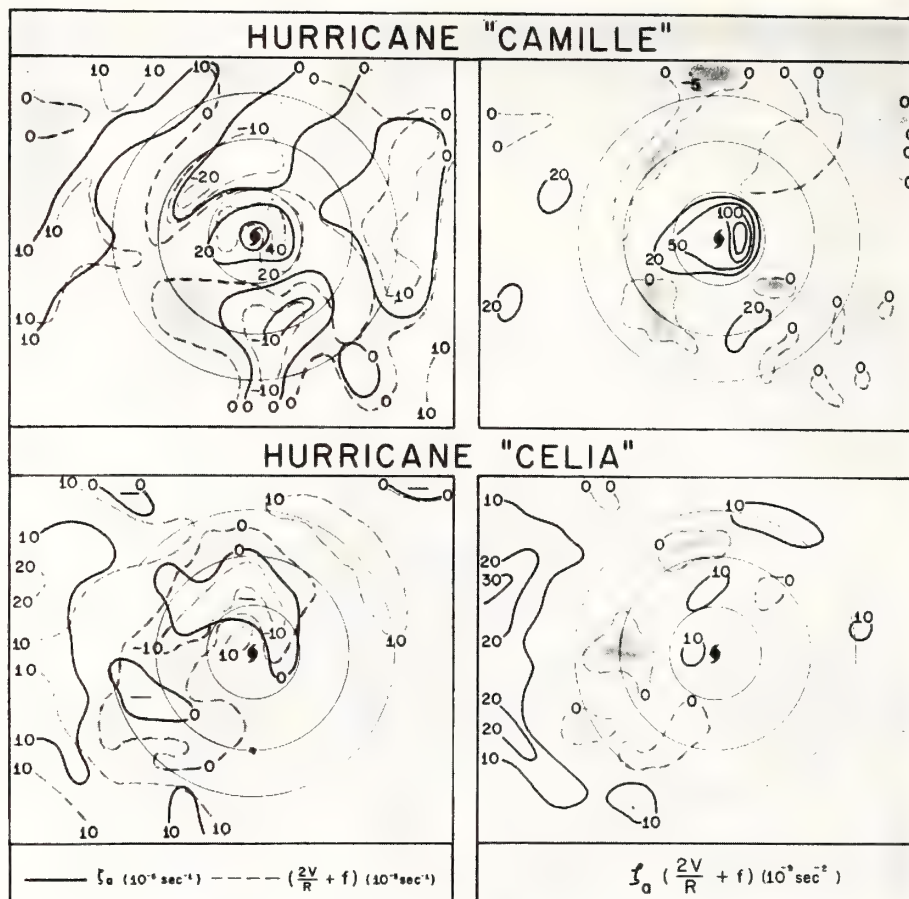


FIG. 17. Same as Fig. 16 except for Camille and Celia.

cyclonic eddy occurs to left. It is suggested that these eddies are organized by the environmental flow streaming around the divergent outflow field, generating anticyclonic vorticity to the right of the storm center and cyclonic vorticity to the left.

The eddies transport absolute vorticity inward, opposing the outward transport by the mean flow. They also transport negative relative angular momentum outward, reaching a magnitude nearly equal to the mean transport near the edge of the outflow region.

Large areas of positive and negative absolute vorticity are closely correlated with normal and anomalous winds, so that only very small areas of weak dynamic instability are present.

*Acknowledgments.* Mr. Nickolas Berry assisted in writing the programs to compute the various quantities and provided substantial aid in the data reduction.

We are indebted to Prof. Tetsuya Fujita, University of Chicago, for making the cloud motion data for hurricanes Camille and Debbie available to us. Mr. Clark Smith provided the cloud motion data for hurricane

Celia and Dr. Banner Miller kindly provided the punch card data for the mean Atlantic storm.

We wish to thank Prof. Heinz Lettau, University of Wisconsin, for his careful review of the manuscript.

Mr. Robert Carrodus and Mr. Charles True were responsible for the figures and Mrs. Mary Jane Clarke typed the manuscript.

#### REFERENCES

- Alaka, M. A., 1961: The occurrence of anomalous winds and their significance. *Mon. Wea. Rev.*, **89**, 482-494.
- , 1962: On the occurrence of dynamic instability in incipient and developing hurricanes. National Hurricane Research Project, Rept. No. 50, U. S. Weather Bureau, Washington, D. C., 51-56.
- , 1963: Instability aspects of hurricane genesis. National Hurricane Research Project, Rept. No. 64, U. S. Weather Bureau, Washington, D. C., 23 pp.
- Anters, R. A., 1970: The role of large-scale asymmetries and internal mixing in computing meridional circulations associated with the steady state hurricane. *Mon. Wea. Rev.*, **98**, 521-528.



- , S. L. Rosenthal and J. W. Trout, 1971: Preliminary results from an asymmetric model of the tropical cyclone. *Mon. Wea. Rev.*, **99** (in press).
- Dunn, G. E., et al., 1962: The hurricane season of 1961. *Mon. Wea. Rev.*, **90**, 107–119.
- Fleet Weather Facility, 1962: Annual tropical storm report—1961. Miami, Fla., 33.
- , 1969: Annual tropical storm report—1968. Jacksonville, Fla., 11–28.
- , 1970: Annual hurricane summary—1969. Jacksonville, Fla., 9–16.
- Fujita, T. T., and P. G. Black, 1970: In- and outflow field of hurricane Debbie as revealed by echo and cloud velocities from airborne radar and ATS-III pictures. *Preprints of Papers, 14th Conf. Radar Meteor.*, Tucson, Amer. Meteor. Soc., 353–358.
- , and H. Grandoso, 1968: Split of a thunderstorm into anticyclonic and cyclonic storms and their motions as determined from numerical model experiments. *J. Atmos. Sci.*, **25**, 416–439.
- Gentry, R. C., 1967: Structure of the upper troposphere and lower stratosphere in the vicinity of hurricane Isbell, 1964. *Papers Meteor. Geophys.*, **18**, 293–310.
- Gray, W. M., 1967: The mutual variation of wind, shear and baroclinicity in the cumulus convective atmosphere of the hurricane. *Mon. Wea. Rev.*, **95**, 617–636.
- Hawkins, H. F., and D. T. Rubsam, 1968: Hurricane Hilda, 1964: II. Structure and budgets of the hurricane on October 1, 1964. *Mon. Wea. Rev.*, **96**, 617–636.
- Hubert, L. F., and A. F. Krueger, 1962: Satellite pictures of mesoscale eddies. *Mon. Wea. Rev.*, **90**, 457–463.
- Hughes, L. A., 1952: On the low-level wind structure of tropical storms. *J. Meteor.*, **9**, 422–428.
- Izawa, T., 1964: On the mean wind structure of typhoon. Typhoon Research Laboratory, Tech. Note No. 2, Meteor. Res. Inst., Tokyo, 19 pp.
- Jordan, E. S., 1952: An observational study for the upper wind circulation around tropical storms. *J. Meteor.*, **9**, 340–346.
- Koteswaram, P., 1967: On the structure of hurricanes in the upper troposphere and lower stratosphere, *Mon. Wea. Rev.*, **95**, 541–564.
- LaSeur, N. E., and H. F. Hawkins, 1963: An analysis of hurricane Cleo (1958) based on data from research reconnaissance aircraft. *Mon. Wea. Rev.*, **91**, 694–709.
- Lyons, W. A., and T. T. Fujita, 1968: Mesoscale motions in oceanic stratus as revealed by satellite data. *Mon. Wea. Rev.*, **96**, 304–314.
- Merritt, E. S., and R. Wexler, 1967: Cirrus canopies in tropical storms. *Mon. Wea. Rev.*, **95**, 111–120.
- Miller, B. L., 1958: The three-dimensional wind structure around a tropical cyclone. National Hurricane Research Project, Rept. No. 15, 41 pp.
- , 1963: On the filling of tropical cyclones over land. National Hurricane Research Project, Rept. No. 66, 82 pp.
- Palmén, E., and H. Riehl, 1957: Budget of angular momentum and energy in tropical cyclones. *J. Meteor.*, **14**, 150–159.
- Panofsky, H. A., and G. W. Brier, 1958: *Some Applications of Statistics to Meteorology*. Pennsylvania State University Press, 224 pp. (see pp. 128–134).
- Pfeffer, R. L., 1958: Concerning the mechanics of hurricanes. *J. Meteor.*, **15**, 113–119.
- Riehl, H., and J. S. Malkus, 1961: Some aspects of hurricane Daisy, 1958. *Tellus*, **13**, 181–213.
- Schlichting, H., 1968: *Boundary Layer Theory*. New York, McGraw-Hill, 747 pp.
- Serebreny, S. M., R. G. Hadfield, A. M. Trudeau and E. J. Wiegman, 1969: Comparison of cloud motion vectors and rawinsonde data. Stanford Research Institute, Final Rept., Contract E-193-68, 53 pp.
- Simpson, R. H., A. L. Sugg and staff, 1970: The Atlantic hurricane season of 1969. *Mon. Wea. Rev.*, **98**, 293–306.
- Sugg, A. L., and P. J. Hebert, 1969: The Atlantic hurricane season of 1968. *Mon. Wea. Rev.*, **97**, 225–239.
- Waco, D. E., 1970: Temperature and turbulence at tropopause levels over hurricane Beulah (1967). *Mon. Wea. Rev.*, **98**, 749–755.

U.S. DEPARTMENT OF COMMERCE  
National Oceanic and Atmospheric Administration  
Environmental Research Laboratories

NOAA Technical Memorandum ERL NHRL-90

A DETAILED ANALYSIS OF SOME AFRICAN DISTURBANCES

Toby N. Carlson

National Hurricane Research Laboratory  
Miami, Florida  
April 1971



## Errata Sheet

- P. 4. 2nd line: 840 mb should read 850 mb.
- P. 8. equation (2):  $\partial J$  should read  $2J$ .
- P. 9. equation (3):  $\lambda_y, \lambda_x$  should read  $\tau_y, \tau_x$ .
- P. 11. bottom line:  $c(q)$  should read  $c(q_0)$ .
- P. 13. line 6, second paragraph: 7 cycles should read 8 cycles.
- P. 24. line 9: fig. 5a and 4a should read 5b and 4b.



## TABLE OF CONTENTS

	Page
LIST OF FIGURES	iv
LIST OF SYMBOLS	viii
ABSTRACT	x
1. INTRODUCTION	1
2. DATA REDUCTION AND ANALYSIS	3
3. THE DIAGNOSTIC EQUATIONS	7
4. CASE STUDIES OF AFRICAN DISTURBANCES	17
4.1 Wave 7/23 (0000 GMT July 22)	17
4.2 Wave 8/14 (0000 GMT August 13)	30
4.3 Wave 9/11 (0000 GMT September 11)	38
5. DISCUSSION	50
6. SUMMARY	54
ACKNOWLEDGMENTS	56
REFERENCES	57

## LIST OF FIGURES

- Figure 1 Average number of wind observations plotted at 1000, 700 and 250 mb within 18 area boxes. The four cases consist of the three in this study plus one other not presented. Figure shows degeneration of data coverage with increasing height.
- Figure 2a ESSA V satellite photograph.
- Figure 2b Nephanalysis based on 0000 GMT ground-based cloud observations. (See text for expansion of legend.) The dashed contours show regions with latent heat release in the model greater than the equivalent of 2.5 degrees C/day. The dot-dashed contour shows the area where the potential to kinetic energy conversion in the model ( $-\alpha'\omega'$ ) exceeded 0.5 ergs/g/sec at 400 mb. The symbols H, W. and G signify local maxima of latent heat release, relative warmth and kinetic energy generation, respectively, at 400 mb.
- Figure 3a Streamline and isotach analysis at 1000 mb for 0000 GMT July 22, 1968. The heavy dashed line labelled trough signifies the prominent wind shift at that level. The letters C or A denote cyclonic and anticyclonic centers of motion. Stippled areas correspond to the convective regimes outlined in the nephanalysis (fig. 2b).
- Figure 3b Same as figure 3a, except for 850 mb. (Arrows indicate centers of maximum wind speed.)
- Figure 3c Same as figure 3b, except for 700 mb.
- Figure 3d Same as figure 3b, except for 550 mb.
- Figure 3e Same as figure 3b, except for 400 mb.
- Figure 3f Same as figure 3b, except for 250 mb.
- Figure 4a Contours of relative vorticity (thick lines in units of  $10^{-5} \text{ sec}^{-1}$ ) and divergence (thin dashed lines in units of  $10^{-5} \text{ sec}^{-1}$ ) at 1000 mb; 0000 GMT July 22, 1968.

- Figure 4b Streamlines and relative vorticity (heavy solid line in units of  $10^{-5} \text{ sec}^{-1}$ ) for 550 mb (the level of maximum cyclonic vorticity in the wave) at 0000 GMT July 22, 1968. Stippled areas correspond to those in previous figures.
- Figure 5a Observed geopotential height contours (solid lines in meters) and frictionally-induced vertical motion (dashed lines in cm/sec) at 0000 GMT July 22, 1968. Stippled areas correspond to those in previous figures.
- Figure 5b Streamlines and vertical motion (cm/sec) at 700 mb 0000 GMT July 22, 1968. Stippled areas correspond to those in previous figures.
- Figure 5c Same as figure 5b, except for 400 mb. The letters H, W, and G refer to centers of latent heat release generation at 400 mb. (See also figure 2b for these symbols.) Omega values determined with time-dependent terms.
- Figure 5d Same as figure 5b but derived from omega equation with time-dependent terms included.
- Figure 6a Mixing ratios (dashed lines in g/kg) and potential temperature (solid lines in degrees C) for 1000 mb, July 22, 1968. Areas of greatest convective instability (surface wet-bulb potential temperature) are indicated by the symbol  $\theta_w$  labelled accordingly in degrees C. Stippled areas correspond to those in previous figures.
- Figure 6b Potential temperature (dashed lines in g/kg) and geopotential heights (solid lines in m) for 0000 GMT July 22, 1968. (All quantities are derived from model.) Stippled areas correspond to those in previous figures.
- Figure 6c Same as figure 6b, but for 400 mb. The symbol W denotes warm center referred to in figures 5c and 2b.



- Figure 7 Vertical cross section along latitude  $12.5^{\circ}\text{N}$  (the latitude of maximum cyclonic vorticity in the disturbance) showing contours of relative vorticity (solid lines in units of  $10^{-5} \text{ sec}^{-1}$ .) Arrows indicate direction and magnitude of the vertical motion and broken lines the axis of wind shift. The letters H, W, and G refer to centers of latent heat release, relative warmth and kinetic energy generation as shown in previous figures. Omega values refer to time-dependent solution.
- Figure 8a Same as figure 2a, but for 0000 GMT August 13, 1968.
- Figure 8b Same as figure 2b, but for August 13, 1968
- Figure 9a Same as figure 3a, but for August 13, 1968.
- Figure 9b Same as figure 3c, but for August 13, 1968.
- Figure 9c Same as figure 3e, but for August 13, 1968.
- Figure 9d Same as figure 3f, but for August 13, 1968.
- Figure 10a Same as figure 4a, but for August 13, 1968.
- Figure 10b Same as figure 4b, but for August 13, 1968.
- Figure 11a Same as figure 5a, but for August 13, 1968.
- Figure 11b Same as figure 5b, but for August 13, 1968.  
Solution with time-dependent terms.
- Figure 11c Same as figure 5c, but for August 13, 1968.  
Values pertain to first estimate solutions.
- Figure 12a Same as figure 6a, but for August 13, 1968.
- Figure 12b Same as figure 6b, but for August 13, 1968.
- Figure 12c Same as figure 6c, but for August 13, 1968.
- Figure 13 Same as figure 7, but for August 13, 1968.  
Cross section taken along latitude  $14.5^{\circ}\text{N}$ .  
Solution with time dependent terms.
- Figure 14a Same as figure 2a, but for September 11, 1968.

- Figure 14b Same as figure 2b, but for September 11, 1968. Note that the solid black represents the convective areas in this case.
- Figure 15a Same as figure 3a, but for September 11, 1968.
- Figure 15b Same as figure 3b, but for September 11, 1968.
- Figure 15c Same as figure 3c, but for September 11, 1968.
- Figure 16a Same as figure 4a, but for September 11, 1968.
- Figure 16b Same as figure 4b, but for 700 mb on September 11, 1968.
- Figure 17a Same as figure 5a, but for September 11, 1968.
- Figure 17b Same as figure 5b, but for September 11, 1968.
- Figure 17c Same as figure 5c, but for September 11, 1968. First estimate solution. Stippled areas refer to legend in figure 14b.
- Figure 18a Same as figure 6a, but for September 11, 1968.
- Figure 18b Same as figure 6b, but for September 11, 1968.
- Figure 18c Same as figure 6c, but for September 11, 1968.
- Figure 19 Same as figure 7, but for September 11, 1968. The cross section is taken along latitude  $15.5^{\circ}\text{N}$ . First estimate solution.

## LIST OF SYMBOLS

$C_D$	Drag coefficient
$C_p$	Specific heat of air at constant pressure
$f$	Coriolis parameter
$f_o$	Mean value of coriolis parameter
$g$	Acceleration of gravity
$H$	Total heating function (= $H$ (surface flux) + $H$ (latent heat release))
$J$	Jacobian operator
$K_h$	A coefficient for lateral mixing
$K_m$	A coefficient for vertical mixing
$A$	Area of analysis
$p$	Pressure
$q$	Mixing ratio
$R$	Gas Constant
$t$	Time
$\bar{T}^*$	Mean virtual temperature between 850 and 1000 mb
$u$	Zonal component of the wind
$v$	Meridional component of the wind
$V_o$	Wind speed at the surface
$V$	Horizontal velocity vector
$x$	Distance in east-west direction
$y$	Distance in north-south direction



$\alpha$	Specific volume
$\beta$	$= df/dy$
$\zeta$	Relative vorticity
$\eta$	Absolute vorticity
$\theta$	Potential temperature
$\pi$	$= \frac{RT}{p}$
$\rho$	Density
$\sigma$	Static stability - $\frac{\alpha \partial \theta}{\theta \partial p}$
$\tau_x, \tau_y$	Horizontal shearing stresses
$\Phi$	Geopotential
$\chi$	Velocity potential
$\psi$	Stream function
$\omega$	$dp/dt$ vertical $p$ velocity
$\nabla^2$	Horizontal Laplacian operator
$\omega_0$	Frictionally-induced vertical velocity at 1000 mb
$\theta_0$	Potential temperature at 1000 mb
$q_0$	Mixing ratio at 1000 mb
$C(q_0)$	Arbitrary function of the 1000 mb mixing ratio
$a, b$	Constants
$D$	Divergence ( $\equiv \frac{\partial u}{\partial x} + \frac{\partial v}{\partial y}$ )
$F_s$	Surface heat flux
$G$	Potential to kinetic energy conversion rate ( $= A \int_p \frac{\alpha' \omega'}{g} dp$ ) (primed quantities denote departures from area average)

## ABSTRACT

Three disturbances observed over Africa during the summer of 1968 have been analyzed at seven pressure levels from 1000 mb to 100 mb. Using a diagnostic set of equations adapted from a model by Miller (1969) and previously employed in the study of a cold low in the Caribbean, the analysis of wind and moisture data yielded compatible analyses of geopotential height, temperature values, vertical wind velocities, and areal distribution of latent heat release.

The results show that the disturbances were most intense at middle levels and were undetectable in the flow pattern above 400 mb. Widespread ascending atmospheric motion accompanied the disturbances; the core of upward vertical motion at high levels was located near the wave axis. Principal areas of convection were associated with ascending motion at high levels and were generally confined, as was the release of latent heat aloft in the model, to the latitude belt between 10 and 15°N. At low levels, the strongest upward motion and cyclonic vorticity were located in a relatively arid sector of the disturbance near 18 to 20°N, west of the mean position of the wave axis. Descending motion was much weaker than ascent in the belt of convection due to the importance of latent heat release in convection. In the absence of latent heat release in the model, the derived vertical motions were extremely weak above 550 mb, although they were largely unaffected by latent heat below this level.

Indications are that the disturbances generate kinetic energy at high levels as the result of rising motion in the presence of an upper warm core centered not far from the axis of the wave. The warm core is felt to be maintained by the sensible warming produced by the release of latent heat at high levels. The disturbances were relatively cold with respect to their surroundings at middle and low levels where, in contrast to upper levels, rising motion may have resulted in kinetic energy destruction. Experiments done with the inclusion of surface heat flux over land suggest that the large-scale pattern of heating and cooling, in which air tends to rise in the Saharan heat low and descend elsewhere (in the absence of perturbations in the flow), serves to generate kinetic energy and maintain the strong easterly current at mid-levels.



# A DETAILED ANALYSIS OF SOME AFRICAN DISTURBANCES

Toby N. Carlson

## 1. INTRODUCTION

An increasing awareness of African disturbances as initiators of tropical storms and hurricanes over the Atlantic Ocean has been brought about by recent articles on the subject by Carlson (1969a, 1969b), by Simpson et. al. (1969) and by Frank (1969, 1970). Except for the first authors the detection, classification, and analyses of disturbances of African origin have depended almost exclusively on the use of satellite photographs and on the examination of individual soundings along the African coast and over the Antilles. This author has previously made use of the abundant wind observations over West Africa to analyze and track disturbances over the continent and subsequently, with the sole aid of continuity of motion and satellite photographs, across the Atlantic Ocean. The analyses, which were confined to two levels in the atmosphere, 2- and 10-thousand feet, show that African disturbances are wave-like perturbations in the easterly current.

The concept of an African disturbance which emerges from these analyses is similar to that of the classical easterly wave of Riehl (1954). To date three years of analyses show that the characteristic wave length of African disturbances is close to 2200 km with a westward phase speed of about 15 kts (a frequency of about one every three days along the coast

of Africa). This wavelength is somewhat less than the 3000 to 6000 km value and the frequency rather more than the 4 to 5 day interval deduced from statistical analyses for data for the Tropical Pacific: (see Wallace and Chang (1969) and Yanai et. al. (1968), for example.). In view of their early history over Africa it would not be surprising to find that Caribbean easterly waves are highly similar to their African counterpart, not only in scale and frequency, but also in their overall structure. Detailed synoptic investigations into the structure of various Caribbean easterly waves have been reported by Riehl (1954), Krishnamurti and Baumhefner (1966), Lateef (1967), Lateef and Smith (1967), Yanai and Nitta (1967), Saito (1968), Hawkins (1971). What emerges from these studies is some understanding of the dynamics and energetics of Caribbean easterly waves, a picture not unlike that for Pacific waves (Yanai, 1961). It is our objective to analyze, in detail, three African disturbances from the summer of 1968 which had particularly abundant coverage of upper air data over West Africa and to reconstruct as best possible, using the still limited upper wind data, the geopotential, temperature, and vertical motion patterns associated with this important class of waves. We also hope to be able to shed some light on the energetics of African disturbances.

## 2. DATA REDUCTION AND ANALYSIS

A brief account of the data coverage over West Africa and a description of the analysis techniques which were used in this paper have been set forth by the author in the earlier papers. The data coverage was maximized (at the time of observation, 0000 GMT) by taking a composite over a 24-hour interval beginning 12 hours prior to analysis time. It was assumed that scales of motion associated with the center of attention, the wave disturbance, are moving westward with the speed of the wave; such reports are therefore plotted a short distance east or west of the station circle. Use was also made of observations which were slightly off-level in situations where the on-level information was missing. Thus, an acceptable density of data can be assembled for a number of levels in the atmosphere on some days when the data happens to be particularly abundant.

Mixing ratios present a different analysis problem from that of winds, since the latter are obtainable by pilot balloon observations while humidity and temperature are available only at the very few stations which have radiosondes. However, reasonable patterns of humidity and temperature can be drawn at 1000 mb because of the abundant network of stations which report conventional surface data. Surface data, in fact, were used to augment the 1000 mb wind analyses over the ocean and along the coast of Africa. For purposes of computing the release of latent heat aloft, however, (see section 3) a crude analysis of mixing ratios was carried out



for levels above the surface by using both vertical continuity from below (beginning with the 840 mb level) and the observed cloud patterns to delineate moist and dry areas. At the same time, the patterns were required to conform to the few available observations of mixing ratio. In formulating the release of latent heat aloft the mixing ratios need not be as accurate except at the surface where they are highly important in determining the vertical flux through the boundary layer.

A cloud cover analysis has also been drawn for each of the three cases, its purpose being to bridge the gap between the satellite photograph taken approximately 6 hours prior to map time and the ground-based observations at 0000 GMT. The cloud diagram is somewhat schematic in its representation of three basic weather patterns. These patterns are: (1) cumulonimbus activity and heavy showers (possibly accompanied by lightning or thunder) taking place near or at station with dense and chaotic cover at middle and upper levels, (2) dense middle and high cloud, with or without lower cloud, and with intermittent light showers or drizzle, and (3) dense stratocumulus with or without upper cloudiness but with little or no appreciable rainfall. All three cloud types may be simultaneously present at one point, in which case the most prominent category is drawn; type (1) taking precedence over the other two and type (2) taking precedence over type (3).

Of all the African disturbances catalogued during the summer of 1968 by this author, a total of three disturbances were selected for intensive analysis on the basis of their being both reasonably intense in the vicinity of 10°W longitude and accompanied by the greatest possible coverage of data at high levels according to a survey made of all the waves. Following the nomenclature used by this author the three waves under study here are wave 7/23 (analyzed at 0000 GMT, July 22), wave 8/14 (analyzed at 0000 GMT, August 13), and wave 9/11 (analyzed at 0000 GMT, September 11). Even in these cases<sup>1</sup> there is a characteristic rapid deterioration of the data coverage with height as indicated in figure 1. Some additional aircraft winds were available at 250 mb, but generally, there were only 5 or 6 observations plotted over the area at 250 and 400 mb and about 3 or 4 at 100 mb. Altogether, detailed analyses were made for streamlines, isotachs, and (for the lowest level only) mixing ratios at 1000, 850, 700, 550, 400, 250, and 100 mb; rough analyses of mixing ratio were also constructed for levels 2 through 4.

---

<sup>1</sup>A fourth case, not presented in this paper, is included in the statistics of figure 1.

# **MEAN FREQUENCY OF PLOTTED WIND OBSERVATIONS ( 4 CASES )**

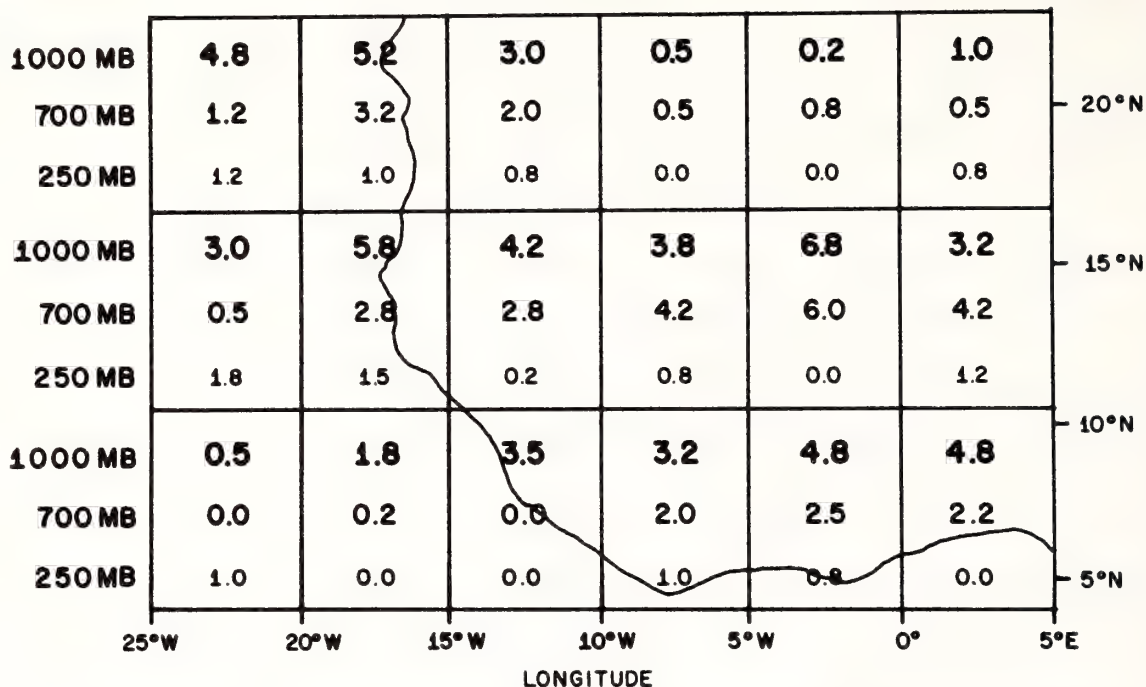


Figure 1. Average number of wind observations plotted at 1000, 700, and 250 mb within 18 area boxes. The four cases co-sist of the three in this study plus one other not presented. Figure shows degeneration of data coverage with increasing height.



### 3. THE DIAGNOSTIC EQUATIONS

A set of equations based on a forecast model of Miller (1969) was used to refine the wind fields and to generate additional fields of temperature, geopotential height and vertical motions. Sets of equations which define a diagnostic model are now appearing frequently in the literature (Krishnamurti and Baumhefner (1966), Krishnamurti (1968) and Hawkins (1971)). The set used in this study closely resembles those used by Krishnamurti (1968) and by Miller and Carlson (1970) in their analysis of a cold low in the Caribbean. In this study, a complete version of Miller's forecast model was employed to deal with motions at rather low latitudes. It was the success of this model in its application to the energetics of a cold low which promoted its further application to African data; full discussion of the model is contained in the report by Miller (1969). Some modifications have been made in the equations: These changes are implicit in the following summary of the diagnostic procedure:

- 1) Streamlines (isogons) and isotachs were analyzed and tabulated over an area encompassed by a  $19 \times 23$  grid spacing  $1.05^\circ$  of longitude (63 n mi). Row 1 corresponded to a latitude of  $4^\circ\text{N}$  and Row 19 to about  $23^\circ\text{N}$  while column 1 lay along  $21^\circ\text{W}$  in the July and August cases and  $26^\circ\text{W}$  in the September analysis. Initially, the raw fields were examined for unreasonable patterns and particularly for negative absolute vorticity. In areas where the latter was computed over more

than a few isolated points successive smoothing of the data was applied over the area where the data were felt to be unrealistic. This involved smoothing the  $u$  component of the winds with its neighboring points in the  $y$ -direction and the  $v$  component with the nearest points along the  $x$ -direction until the absolute vorticity became virtually zero in the area; on the average such smoothing affected about 10 percent of the analysis area. In the main body of the program the tempered fields were again smoothed in the horizontal using a conventional 9-point operator. (Vorticity values were also smoothed prior to their explicit use in any of the equations and a number of additional smoothing routines were used in computing time derivatives and boundary terms.)

2) Next, the stream function ( $\psi$ ) was computed, where

$$\nabla^2 \psi = \frac{\partial v}{\partial x} - \frac{\partial u}{\partial y} . \quad (1)$$

From the stream function was obtained the nondivergent wind components and the vorticity.

3) The divergence equation was evaluated to obtain the derived height and temperature fields where

$$\begin{aligned} \nabla^2 \Phi = & \partial J(u,v) + f\eta - \beta u + g \frac{\partial}{\partial p} \left( \frac{\partial \tau_x}{\partial x} + \frac{\partial \tau_y}{\partial y} \right) - \left( \frac{\partial \omega}{\partial x} \frac{\partial u}{\partial p} + \frac{\partial \omega}{\partial y} \frac{\partial v}{\partial p} \right) \\ & + K \nabla^2 D - \left( \frac{\partial D}{\partial t} + \mathbf{V} \cdot \nabla D + \omega \frac{\partial D}{\partial p} + D^2 \right) . \end{aligned} \quad (2)$$

As a first approximation in solving (2) it was assumed that  $D=\omega=0$  everywhere and that the winds were purely rotational and given by the

stream function. The initial patterns of  $\Phi$ , which we shall henceforth refer to as the first estimate solution, are therefore similar to a balanced height but with a friction term included. Test runs with the data showed that the balanced heights differed very little from the first estimate values which contain a frictional component. The geopotential height, temperature, vorticity, and the total wind field (so far non-divergent) were used explicitly in the omega equation to arrive at a first guess for vertical motion.

4) The diabatic, viscous omega equation is expressed as

$$\begin{aligned} & \nabla^2 \sigma \omega + f_o \eta \frac{\partial^2 \omega}{\partial p^2} - f_o \omega \frac{\partial^2 \eta}{\partial p^2} - f_o \frac{\partial}{\partial p} \left( \frac{\partial \omega}{\partial p} \frac{\partial v}{\partial p} - \frac{\partial \omega}{\partial y} \frac{\partial u}{\partial p} \right) \\ & = f_o \frac{\partial}{\partial p} (V \cdot \nabla \eta) - f_o K_H \nabla^2 \frac{\partial u}{\partial p} - f_o g \frac{\partial^2}{\partial p^2} \left( \frac{\partial \lambda}{\partial x} y - \frac{\partial \lambda}{\partial y} x \right) \\ & + \pi \nabla^2 (V \cdot \nabla \theta) - \nabla^2 \left[ \frac{R}{P} \frac{\partial}{\partial p} (\rho^2 g^2 K_M \frac{\partial \theta}{\partial p}) \right] \\ & - \nabla^2 \frac{R}{P} (K_H \nabla^2 \theta) - \nabla^2 \frac{R}{PC_P} \cdot H + \pi \nabla^2 \frac{\partial \theta}{\partial t} + f \frac{\partial}{\partial t} \left( \frac{\partial \eta}{\partial p} \right) \end{aligned} \quad (3)$$

Initially, the time derivatives are set to zero to permit a first estimate of  $\omega$  to be made using a convergence criteria of 1.5 mm/sec.<sup>2</sup>

5) A first estimate of the total derived wind field is then produced by adding the non-divergent component of the wind obtained from (1) to the irrotational component of the wind derived from the computed vertical velocity through use of the velocity potential equation

$$\nabla^2 \chi = - \frac{\partial \omega}{\partial p} \quad (4)$$

<sup>2</sup>Henceforth, omega, the vertical velocity in pressure coordinates (dp/dt), will be used interchangeably with W, the vertical velocity in length coordinates (dz/dt).



The total heating (H) was considered to be the sum of latent plus sensible heating in the system. Except over the ocean where heat exchange was determined from conventional formulae, the sensible heating was assumed to be zero at the surface, since it would be difficult to model the variable heat exchange over the African continent.<sup>3</sup> Aloft, the Kuo (1965) heating parameterization was used to determine the distribution of heat release in the cumulonimbus. The total water vapor flux into the convective elements was given by the frictional convergence in the boundary layer as represented by the relationship for  $\omega$  at 1000 mb where

$$\omega_o \approx \frac{\rho g}{f} \left[ \frac{\partial}{\partial y} c_D u V_o - \frac{\partial}{\partial x} c_D v V_o \right] \quad (5)$$

is the lower boundary condition in (4). The flux of water vapor through the hypothetical boundary layer is then partitioned aloft into sensible heat release and water vapor accumulation according to the cloud-environment differences in temperature and water vapor as the parcel is lifted moist adiabatically from the cloud base (lifting condensation level at 1000 mb).<sup>4</sup> Latent heat release was also permitted by large-scale ascent of saturated air.

<sup>3</sup>Some additional experiments were performed using an arbitrary but realistic surface heating function for expressing sensible heat flux at the surface. These are not presented in this paper but will be reported on briefly in a later section.

<sup>4</sup>Convection was permitted in the model only where there was frictional convergence in the boundary layer, and the ascending parcel remained warmer than the environment from 700 to 250 mb. Otherwise heating was assumed to be zero at that point.

The drag coefficient ( $C_D$ ) was taken to be 0.005 over land and between 1 and  $2 \times 10^{-3}$  over water according to the wind speed at 1000 mb. At upper levels the stress terms were defined in terms of an eddy viscosity for vertical and horizontal mixing. The former, ( $K_M$ ), was essentially a constant value of  $5 \times 10^5$  cm<sup>2</sup>/sec with a slight dependence on vertical wind shear. Although this is a fairly large value for the free atmosphere, its effect will depreciate rapidly with height in (3) due to the rapid decrease with height of the modifier  $\rho^2$ .

In order to compute the temperature from the quasi-balanced height field determined from (2) the mean (or some reference) geopotential must be known at each height and a lapse rate must be assumed in the bottom layer. Usually, the mean Caribbean sounding is used as a standard in determining a basic temperature field at low latitudes. Over Africa, however, it is evident that the thermal patterns are vastly different from those over the Western Atlantic Ocean especially in the lower levels. For example, the lapse rate in the bottom few hundred millibars is markedly steeper over arid terrain (being almost dry adiabatic) than it is where conditions are moist. Under normal conditions in the tropics, where the surface mixing ratio ( $q_0$ ) is large ( $\geq 16$ g/kg), the model expresses the 1000 mb temperature ( $\theta_0$ ) in terms of the mean virtual temperature in the layer from 1000 to 850 mb ( $\bar{T}^*$ ) and a parameter  $C(q)$  where

$$\theta_0 = \bar{T}^* + C(q_0) \quad (6a)$$

Over arid regions ( $q_0 < 16 \text{ g/kg}$ ) the empirical relationship between lapse rate and the terrain factor  $C(q_0)$  is modelled simply by the expression

$$C(q_0) = \begin{cases} \sim 3 & (q_0 \geq 16 \text{ g/kg}) \\ a + bq_0 & (q_0 < 16 \text{ g/kg}) \end{cases} \quad (6b)$$

where  $a$  and  $b$  are empirically determined constants, the maximum value of  $C(q_0)$  being about 6 and the minimum 3. The mean geopotential at the two lowest levels was adjusted for each case to permit the calculated temperature over the desert (the northern fringes of the grid) to agree with the known values of  $40\text{--}42^\circ\text{C}$  which are found at the surface in that region and to decrease in such a fashion with height that the lapse rate remains slightly less than dry adiabatic in the lowest three layers over the desert. The mean temperature at each successive level was accordingly adjusted to permit it to approach that of the mean tropical atmosphere at 550 mb, the approximate top of the Saharan mixing layer.

Starting with the first estimate of  $\omega$ ,  $\theta$ , and  $\Phi$  and the total wind, the first estimate of the time-dependent terms in (2) and (3) can be arrived at through application of the forecast equations for  $u$ ,  $v$ , and  $\theta$  which are written:

$$\partial u / \partial t = -V \cdot \nabla U - \frac{\partial \Phi}{\partial x} + K_H \nabla^2 u + fv + g \frac{\partial \tau_x}{\partial p} \quad (7a)$$

$$\partial v / \partial t = -V \cdot \nabla V - \frac{\partial \Phi}{\partial y} + K_H \nabla^2 v - fu + g \frac{\partial \tau_y}{\partial p} \quad (7b)$$

$$\partial \theta / \partial t = -V \cdot \nabla \theta + \frac{\theta}{T} K_H \nabla^2 \theta + \frac{\theta}{C_p T} H \quad (7c)$$



The first two equations (7a and 7b) were combined to form the time-dependent terms  $\frac{\partial D}{\partial t}$  and  $\frac{\partial}{\partial t}(\frac{\partial \eta}{\partial p})$ . These terms, along with  $\partial/\partial t$  were smoothed prior to use in (2) and (3) during a second cycle in the diagnostic routine.<sup>5</sup> The cycles were repeated until successive estimates of  $\omega$  began to differ by no more than 2-3 mm/sec from the previous estimate. Allowing for a few points to exceed this amount, convergence between successively generated fields of omega was accomplished after about 8 cycles. The entire procedure closely parallels that of Krishnamurti (1968) in the solution of his primitive equation model.

Miller and Carlson (1970) showed that the time dependent terms contributed insignificantly to the overall patterns of  $\omega$  and to the kinetic energy balance in the Caribbean cold low. At the start of these calculations it was thought that the time dependent terms, as defined above, would be unimportant over Africa, an assumption which was influenced by the tremendous increase in computer time<sup>6</sup> necessary to run 7 cycles of the model rather than a single cycle. Later, after some figures had been drafted, a full model was run in order to clear up lingering doubts on this point. It was indeed found that there were substantial changes in the vertical motions at some of the lower levels, although the height and

---

<sup>5</sup>In this and subsequent cycles the u and v components contained the total (irrotational plus non-divergent) wind.

<sup>6</sup>A single cycle required about 100 seconds on the CDC-6600 computer.

temperature patterns were not greatly altered. Subsequent diagrams will refer only to the first estimate values except in a few instances where important differences were visible between first estimate fields and the complete solution. In such instances, the diagrams provided are explicitly labelled in the captions as containing time dependent terms.

Initial output from the diagnostic equations showed very poor agreement between the observed 1000 mb heights and those obtained from the surface isobars and, consequently, between the observed temperatures and the calculated ones. The derived height fields were not only dissimilar to the observed ones at 1000 mb (as determined from the surface pressure analysis) but gradients were decidedly weaker, although the upper surfaces look quite reasonable, if also a bit weak. Admittedly, there is no way of knowing for sure what the isotherm configuration should be above 1000 mb since there is very little data on which to base judgement. Although the wind data at the surface and 850 mb are certainly abundant enough to define a field of motion, the prime weakness in the model lies in how it reacts to the highly unusual effects found near the ground over the African continent. In particular, the dramatic reversal of wind direction which occurs in the lowest 1.5 km, coupled with the strong vertical wind shear and horizontal temperature gradient and complicated by the peculiar irregularities of heating and vertical mixing over the land, are deep sources of uncertainty when calculations are involved. It may also be

that the vertical derivatives seriously truncate the physics near the ground since the surface height (pressure) pattern is representative of only a thin layer near the surface; at 850 mb the height field is completely changed in character and reversed in overall meridional gradient from its counterpart below. At 1000 mb the large angle at which the wind field crosses the isobars toward lower pressure is probably representative of a very shallow layer, in view of the unreasonably large values of convergence that would otherwise be found near the ground. Even with a relatively large vertical mixing the model is unable to reproduce this effect.

Recognizing that the analyzed surface temperature fields are probably superior to the calculated ones we have chosen to make an additional restriction binding on the model. This restriction was to omit the calculation of  $\Phi$  at 1000 mb and to substitute in its place the observed height fields drawn from the surface pressure chart. The only direct effect of this substitution on (3) is to change  $\theta$  in the bottom layer and therefore, to a lesser degree to change terms involving  $\theta$  at 850 mb, the lowest level at which the omega equation is applied. One might argue that since the surface lapse rate is somewhat arbitrary, it could be tailored to produce the desired temperature field. However, it is felt that this would be equivalent to using the observed temperatures in a less forthright manner.



The temperature patterns at 1000 mb which were generated through use of the observed 1000 mb heights were found to be quite reasonable in their representation of the large scale temperature gradients in the area, an indirect confirmation that the 850 mb heights (which are used in determining  $\theta$  at the surface) are also not entirely unreasonable. The effect on the  $\omega$  pattern of restricting the surface  $\theta$  by substitution of the observed heights for the calculated ones can not be accurately assessed. It should be noted that the vertical motions above 850 mb were not drastically affected by this alteration of the model.

It is our primary desire to present a coherent picture of an African disturbance, consistent with the observations, but with no more detail in the analyses than is permitted by the inherent uncertainties in the data and method of analysis. In the derived fields of height and motion, the final product is felt to be largely free of gross inconsistencies even though some of the original detail is missing, while the smoothness of the patterns helps focus attention on the salient aspects of the disturbances. On the other hand, it is evident that the vertical motions are more highly suspect than the other fields, being susceptible to large uncertainties. Particular features of the  $\omega$  patterns will be emphasized in later sections only insofar as they appear to be consistent with the weather or are supportable by findings from other researchers.

#### 4. CASE STUDIES OF AFRICAN DISTURBANCES

##### 4.1 Wave 7/23 (0000 GMT July 22)

This disturbance was first recognized when it entered the West African data network at 19°E longitude on July 18. It was a rather well-developed system when it arrived at the west coast of Africa on the 23rd, where it was accompanied by 2-3 mb pressure falls at the surface and a weak surface vortex which formed near 12°N on the 22nd. The disturbance reached the Antilles on the 29th where it continued to be fairly active.<sup>7</sup>

The satellite picture (fig. 2a) shows two main areas of convective activity, one near 5°W and the other near 14°W, the latter having reached the coast by 0000 GMT (fig. 2b). By far the most important convection was associated with the cloud area near 5°W; close inspection of the satellite photo shows that it is composed of a number of circular blobs, each probably representing an individual cumulonimbus cluster. The streamline and isotach charts (figs. 3a-f) show the primary wave disturbance between 5 and 10°W and a very weak (and rather poorly defined) wind shift near the coast. The dramatic reversal of the winds from a mainly southwesterly direction at 1000 mb to a basic easterly current at 850 mb and above is typical of tropical West Africa in summer. Between 850 and 400 mb, the wave resembles the classical easterly wave but with a rather

---

<sup>7</sup>This disturbance has been discussed in brief by Simpson et. al. (1969).

1700 G.M.T

JULY 21, 1968

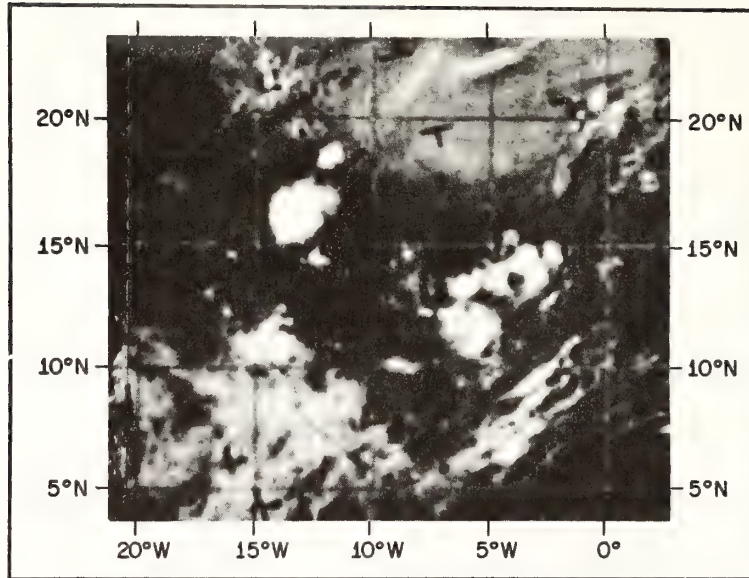


Figure 2a. ESSA V satellite photograph

JULY 22, 1968

0000 Z

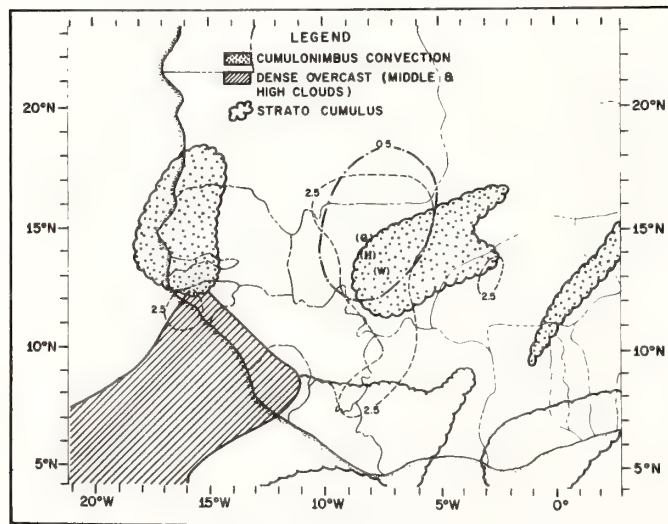


Figure 2b. Nephanalysis based on 0000 GMT ground-based cloud observations. (See text for expansion of legend.) The dashed contours show regions with latent heat release in the model greater than the equivalent of 2.5° C/day. The dot-dashed contour shows the area where the potential to kinetic energy conversion in the model ( $-\alpha'\omega'$ ) exceeded 0.5 ergs/g/sec at 400 mb. The symbols H, W, and G signify local maxima of latent heat release, relative warmth and kinetic energy generation, respectively, at 400 mb.



1000 MB STREAMLINES AND ISOTACHS (KTS.)  
JULY 22, 1968 0000 Z

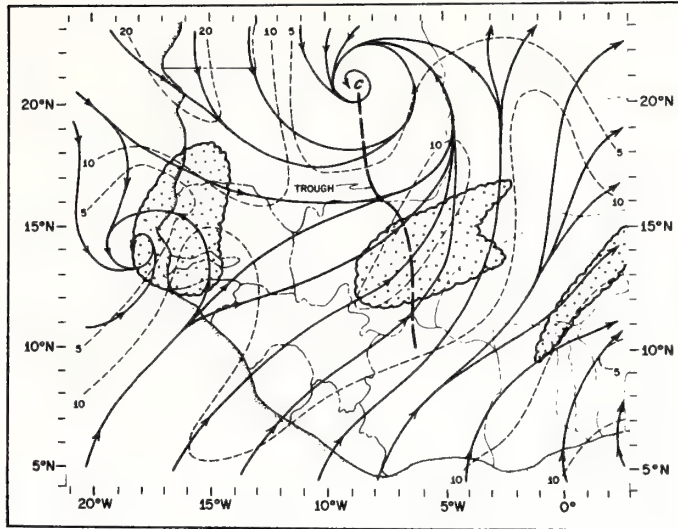


Figure 3a. Streamline and isotach analysis at 1000 mb for 0000 GMT July 22, 1968. The heavy dashed line labelled 'trough' signifies the prominent wind shift at that level. The letters C or A denote cyclonic and anticyclonic centers of motion. Stippled areas correspond to the convective regimes outlined in the nephanalysis (fig. 2b).

850 MB STREAMLINES AND ISOTACHS (KTS.)  
JULY 22, 1968 0000 Z

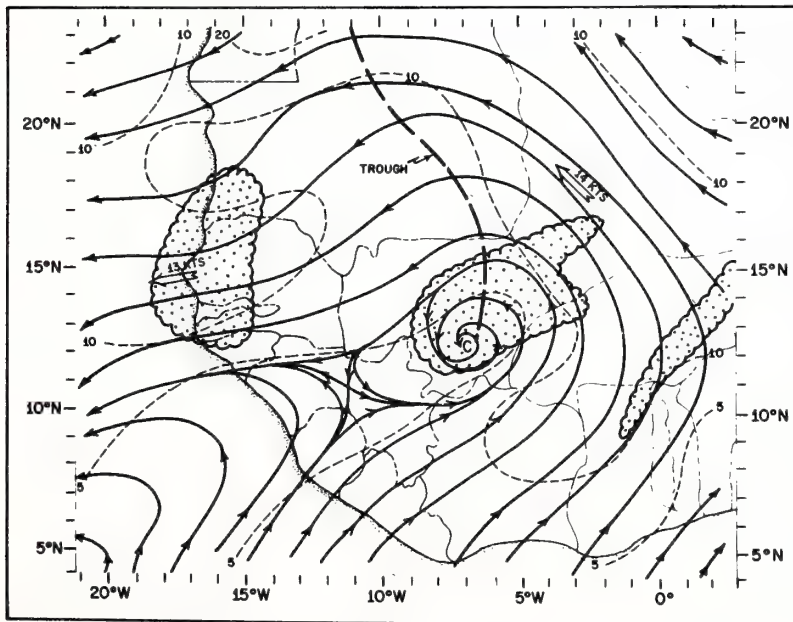


Figure 3b. Same as figure 3a, except for 850 mb. (Arrows indicate centers of maximum wind speed.)

700 MB STREAMLINES AND ISOTACHS (KTS.)

JULY 22, 1968

0000 Z

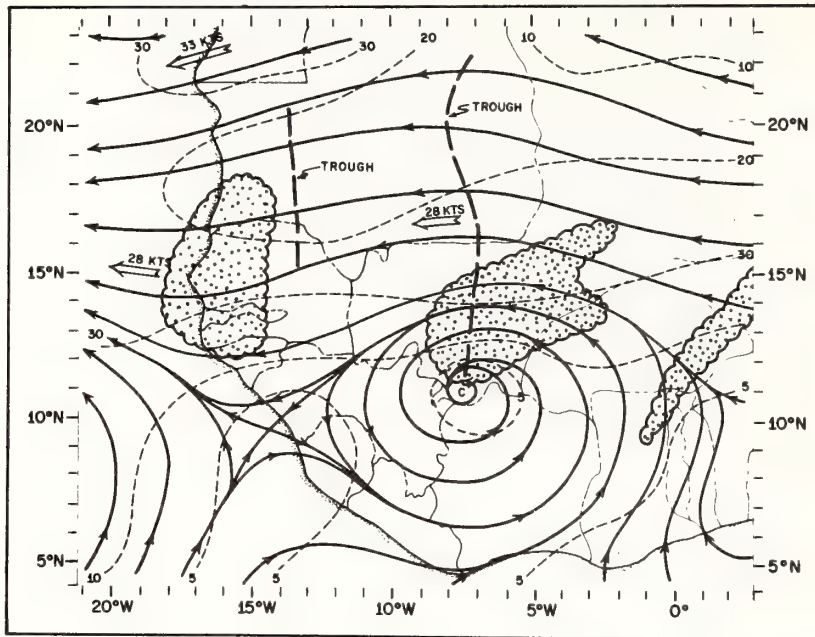


Figure 3c. Same as figure 3b, except for 700 mb

550 MB STREAMLINES AND ISOTACHS (KTS.)

JULY 22, 1968

0000 Z

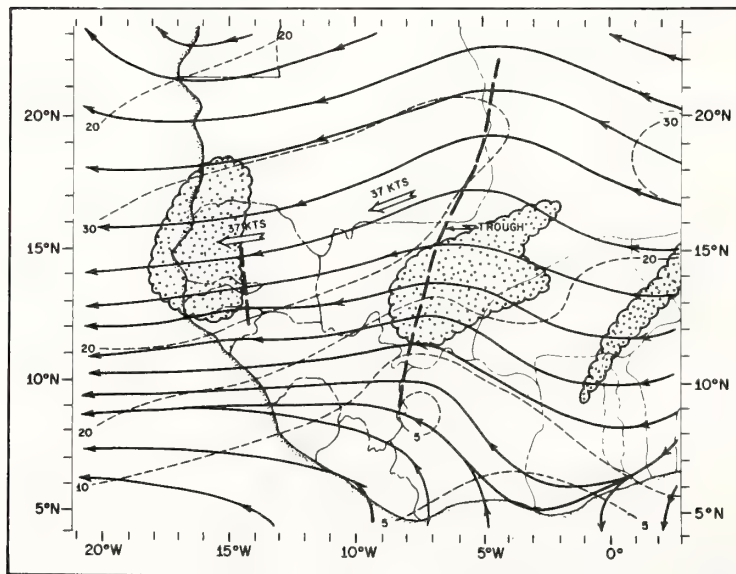


Figure 3d. Same as figure 3b, except for 550 mb

# 400 MB STREAMLINES AND ISOTACHS (KTS.)

JULY 22, 1968

0000 Z

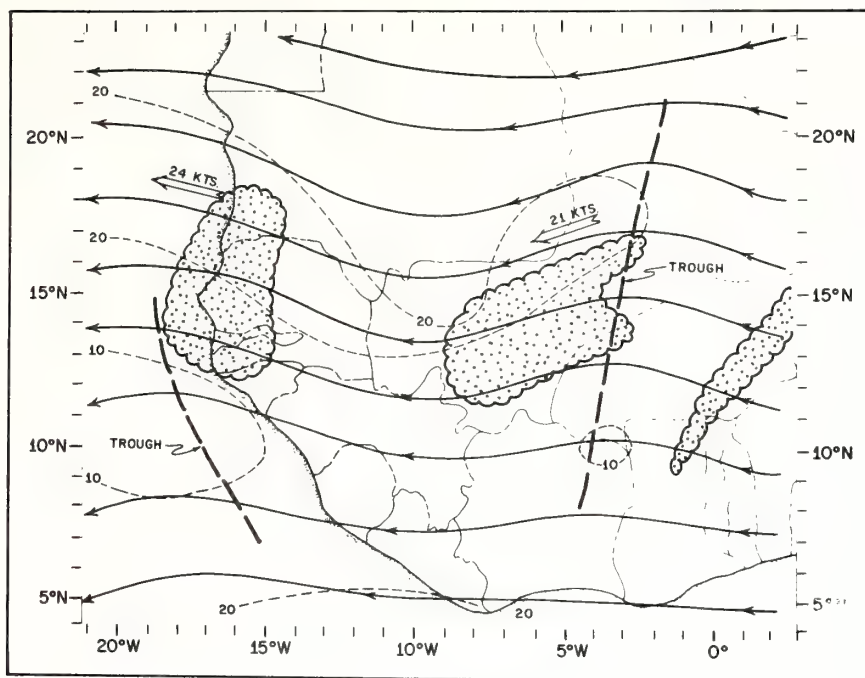


Figure 3e. Same as figure 3b, except for 400 mb

# 250 MB STREAMLINES AND ISOTACHS (KTS.)

JULY 22, 1968

0000 Z

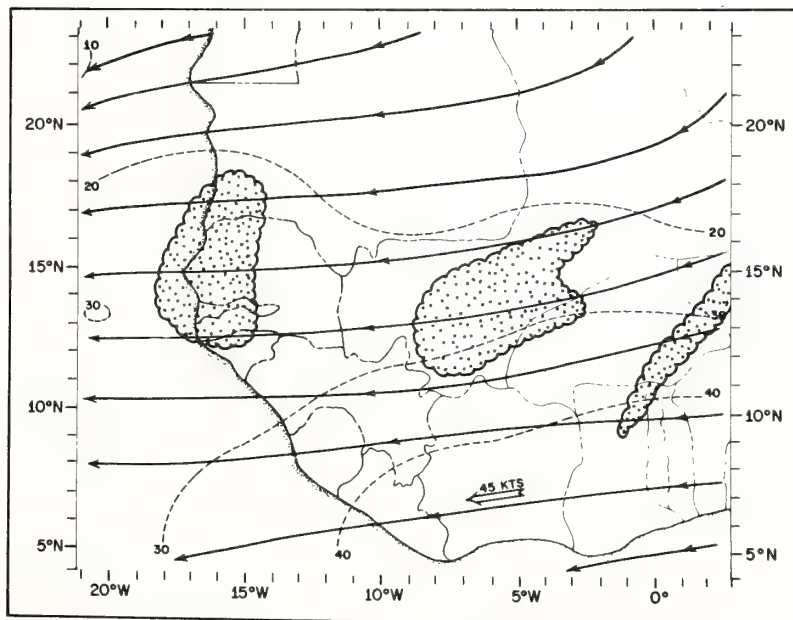


Figure 3f. Same as figure 3b, except for 250 mb



strong easterly jet of almost 40 kts located near the 550 mb level and between 15 and 20°N latitude. The easterly jet, a semipermanent feature over West Africa in summer, has been discussed by this author and is also mentioned by Reiter (1963). Significant weather is largely confined south of the jet axis, and within the region of strong cyclonic vorticity formed by a combination of shear of the basic current and curvature along the wave axis. Here, the absence of a closed center in the streamline patterns, as occurs at 550 and 400 mb, may be due as much to the irregular data distribution as to fluctuations in the strength of the basic current with respect to the degree of curvature vorticity. The disturbance generally appears to be most intense just south of 15°N latitude and near the 550 mb level. Above 400 mb the wave is no longer recognizable in the flow pattern.

Reflecting the south to southeastward displacement of the vorticity pattern with height (figs. 4a, b), the primary ascending region shifts from the vicinity of the major vortex, located northwest of the wave axis near 20°N at 1000 mb (fig. 4b), toward the southeast where it can be found near the wave axis at 13°N on the 400 mb chart (fig. 5c). Inclusion of the time dependent terms in the model caused a reversal in the vertical motion pattern at 700 mb, with upward motion in the east instead of the western side of the wave (fig. 5d). At 400 mb (fig. 5c) the upward motions are reduced, both in magnitude and areal coverage,

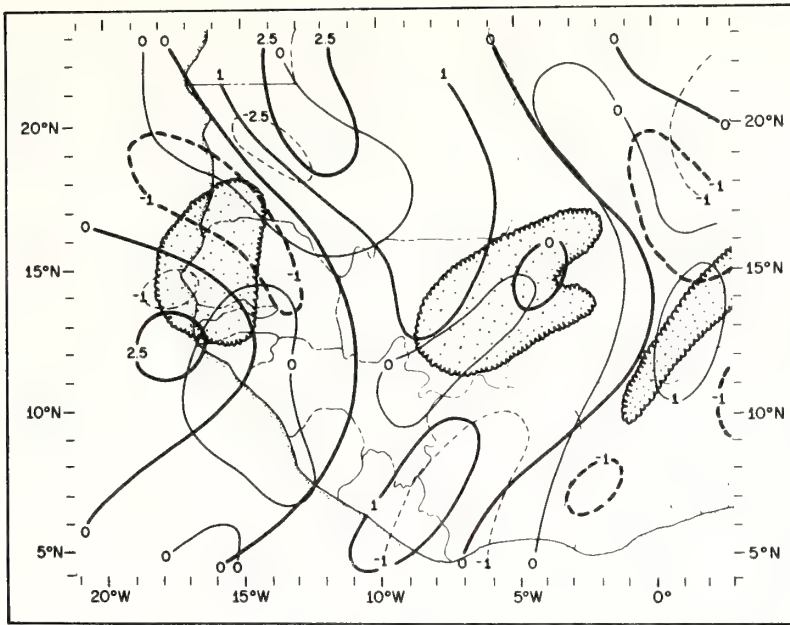


Figure 4a. Contours of relative vorticity (thick lines in units of  $10^{-5}\text{sec}^{-1}$ ) and divergence (thin dashed lines in units of  $10^{-5}\text{sec}^{-1}$ ) at 1000 mb; 0000 GMT July 22, 1968.

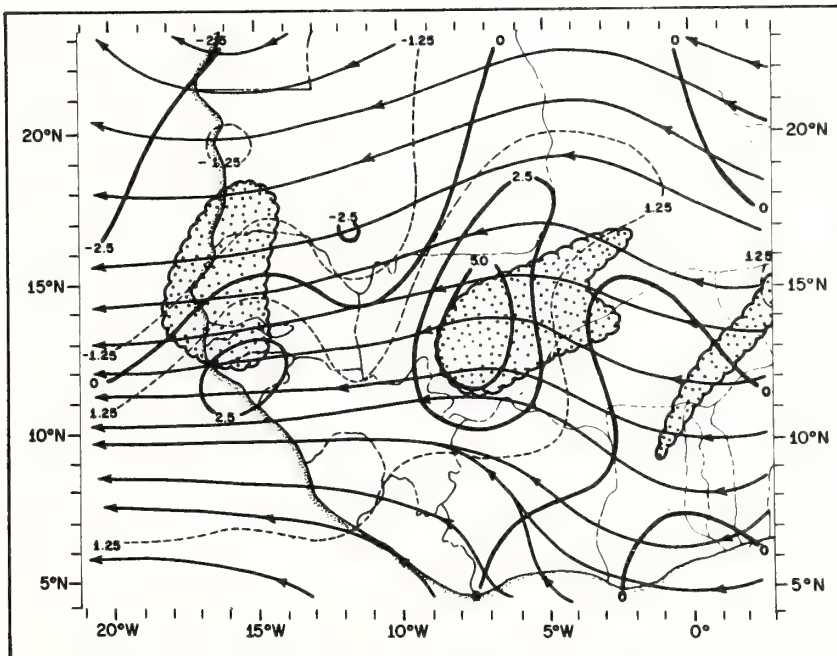


Figure 4b. Streamlines and relative vorticity (heavy solid line in units of  $10^{-5}\text{sec}^{-1}$ ) for 550 mb (the level of maximum cyclonic vorticity in the wave) at 0000 GMT July 22, 1968. Stippled areas correspond to those in previous figures.

with the inclusion of the time dependent terms; otherwise figure 5c is similar to that of the first estimate solution (not shown) inasmuch as the principle area of ascent remains centered near the main convective area. It is interesting that the indices of wave strength at 1000 mb, such as the vorticity, convergence, and surface pressure falls, are found to be centered in the northwest quadrant of the upper wave axis and along the lower fringe of the desert (fig. 5a and 4a) whereas the vorticity and upward vertical motion centers shift closer to the central portion of the wave axis at upper middle levels (fig. 5a and 4a) where they are in better agreement with the disturbed weather. For the most part, this shift takes place in the lowest layer.

One reason for the shift in vertical motion patterns toward the south with height lies in the fact that the mixing ratios at 1000 mb (fig. 6a) are not sufficiently high to support convection north of about  $16^{\circ}\text{N}$ . Because the Gulf of Guinea is rather cool in summer and the southwesterly current is initially anticyclonic and divergent, the air is also stable with respect to deep cumulonimbus convection south of about  $10^{\circ}\text{N}$ ; consequently the greatest release of latent heat occurs in a narrow latitudinal belt centered near  $13^{\circ}\text{N}$ . Within this belt the primary release of latent heat is shown to be occurring near the wave axis. The maximum latent heat release, signified by the letter H in figure 2b (the



1000 MB GEOPOTENTIAL HEIGHT AND VERTICAL  
VELOCITY (cm/sec)

JULY 22, 1968

0000 Z

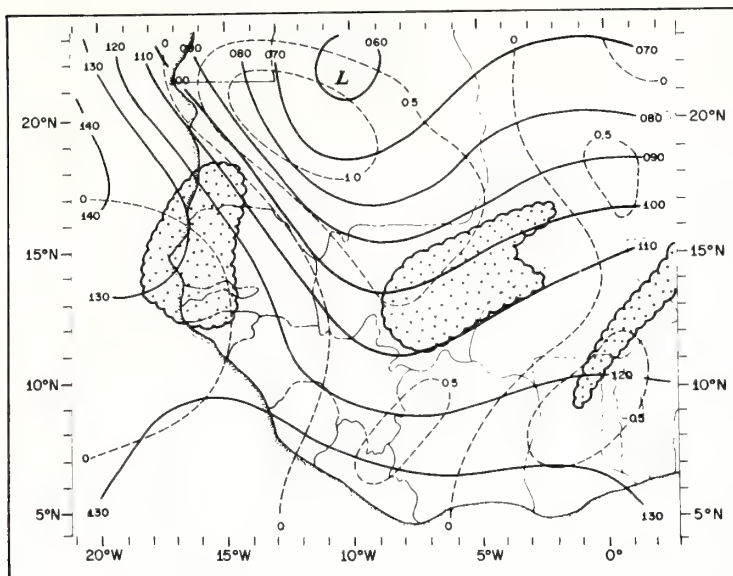


Figure 5a. Observed geopotential height contours (solid lines in meters) and frictionally-induced vertical motion (dashed lines in cm/sec) at 0000 GMT July 22, 1968. Stippled areas correspond to those in previous figures.

700 MB STREAMLINES AND VERTICAL VELOCITY  
(cm/sec)

JULY 22, 1968

0000 Z

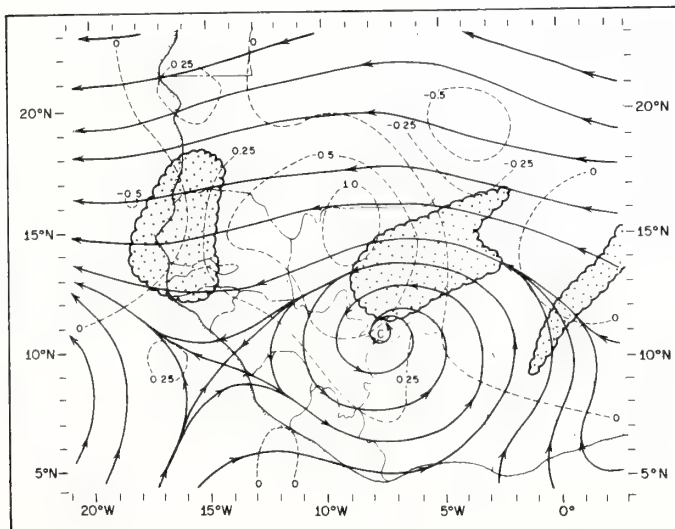


Figure 5b. Steamlines and vertical motion (cm/sec) at 700 mb 0000 GMT July 22, 1968. Stippled areas correspond to those in previous figures.

equivalent of about  $3^{\circ}\text{C}/\text{day}$  in sensible heating)<sup>8</sup>, was almost entirely responsible for the updrafts in the wave axis at 400 mb. When latent heat was omitted from the calculations the model produced very weak (less than a few mm/sec) and substantially different patterns of vertical motion above 700 mb in which a relatively greater amount of descent occurred at  $10\text{--}15^{\circ}\text{N}$ .

The disturbance appears to be relatively cold at 700 mb (fig. 6b) and warm at 400 mb (fig. 6c). The warm center at 400 mb, designated by the letter W in figures 6c, 5c, and 2b, strikingly coincides both with the general area of latent heating at that level and with the observed convection. Consequently, the maximum kinetic energy generation at 400 mb, denoted by the letter G in the various diagrams, is in the region near the wave axis.

Figure 7 is a vertical cross section along  $12.5^{\circ}\text{N}$  intersecting the disturbance at the latitude of the upper level vorticity maximum. Centers of heat release, warmth, and energy generation at 400 mb, denoted by the letters H, W, and G, respectively, lie close to the wave axis in the region of strongest upward motion. In view of the convection maximum at this latitude it is not surprising to find this preponderance of ascent.

---

<sup>8</sup>The actual sensible heating due to latent heat release will be less than the equivalent latent heat release because of adiabatic cooling in the ascending air. Calculations show, however, that the two are highly correlated.

400 MB STREAMLINES AND VERTICAL VELOCITY CM/SEC  
JULY 22, 1968 0000 Z

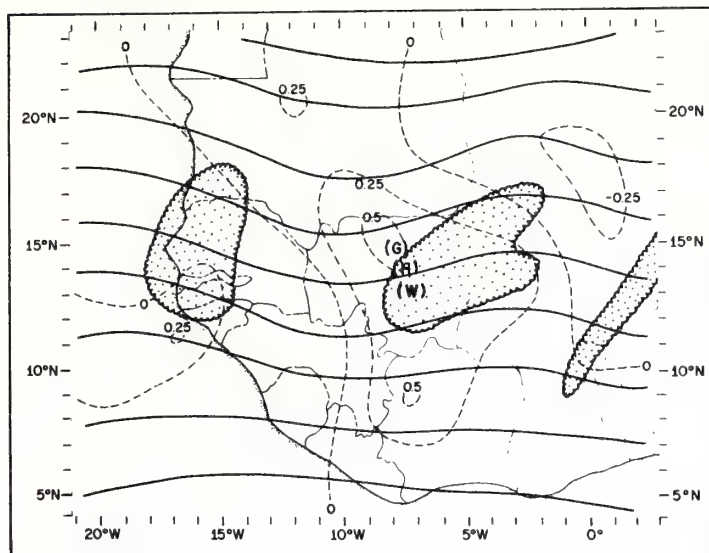


Figure 5c. Same as figure 5b, except for 400 mb. The letters H, W, and G refer to centers of latent heat release generation at 400 mb. (See also figure 2b for these symbols.) Omega values determined with time-dependent terms.

700 MB STREAMLINES AND VERTICAL VELOCITY  
(cm/sec)  
JULY 22, 1968 0000 Z

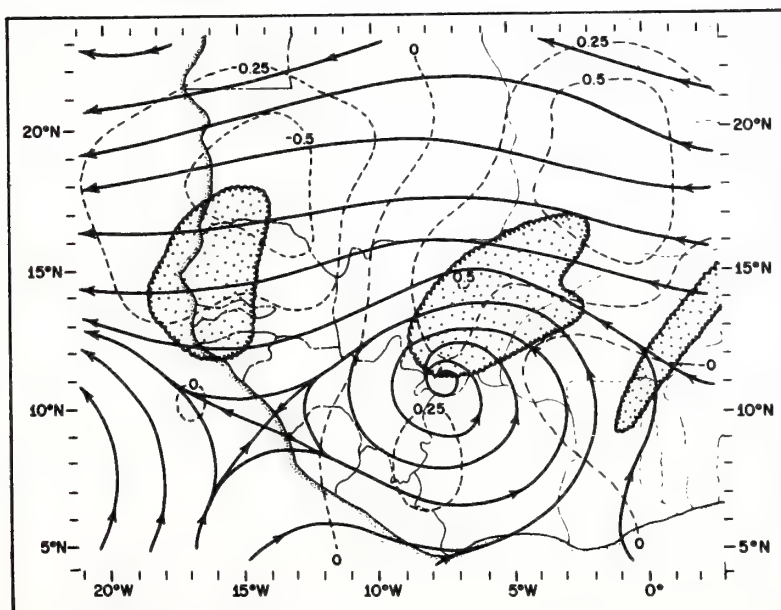


Figure 5d. Same as figure 5b but derived from omega equation with time-dependent terms included.



# 1000 MB MIXING RATIO AND POTENTIAL TEMPERATURE

JULY 22, 1968

0000 Z

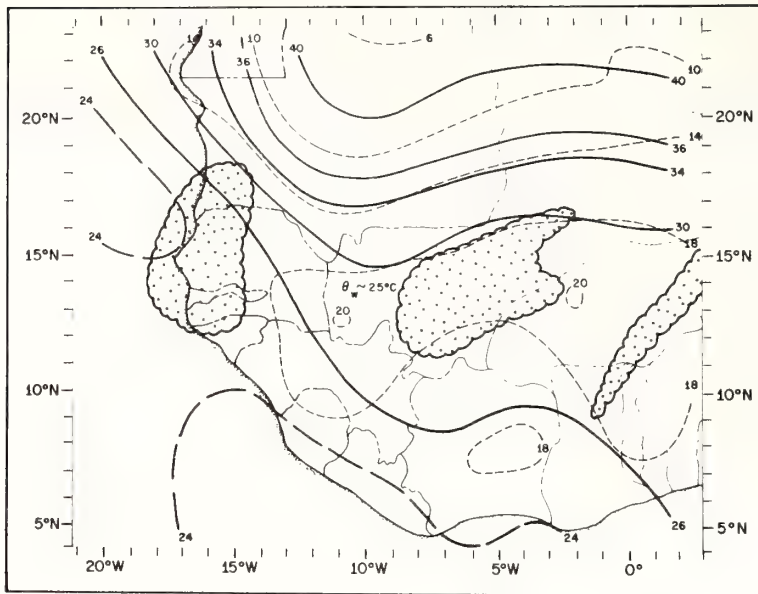


Figure 6a. Mixing ratios (dashed lines in g/kg) and potential temperature (solid lines in degrees C) for 1000 mb, July 22, 1968. Areas of greatest convective instability (surface wet-bulb potential temperature) are indicated by the symbol  $\theta_w$  labelled accordingly in degrees C. Stippled areas correspond to those in previous figures.

# 700 MB GEOPOTENTIAL HEIGHT AND POTENTIAL TEMPERATURE

JULY 22, 1968

0000 Z

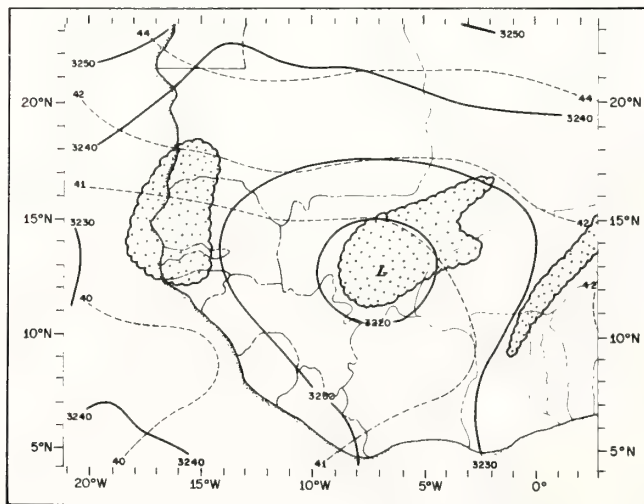


Figure 6b. Potential temperature (dashed lines in g/kg) and potential heights (solid lines in m) for 0000 GMT July 22, 1968. (All quantities are derived from model.) Stippled areas correspond to those in previous figures.

# 400 MB GEOPOTENTIAL HEIGHT AND POTENTIAL TEMP

JULY 22, 1968

0000 Z

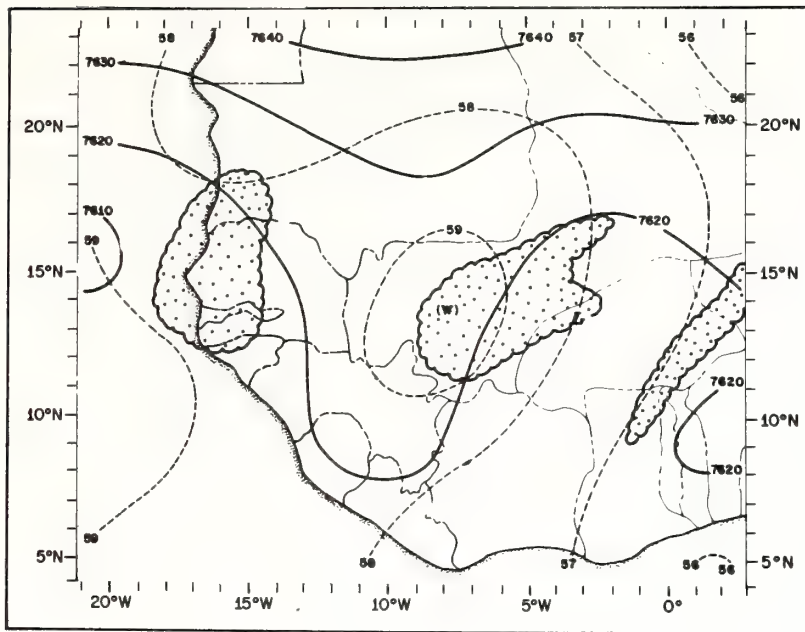


Figure 6c. Same as figure 6b, but for 400 mb. The symbol W denotes warm center referred to in figures 5c and 2b.

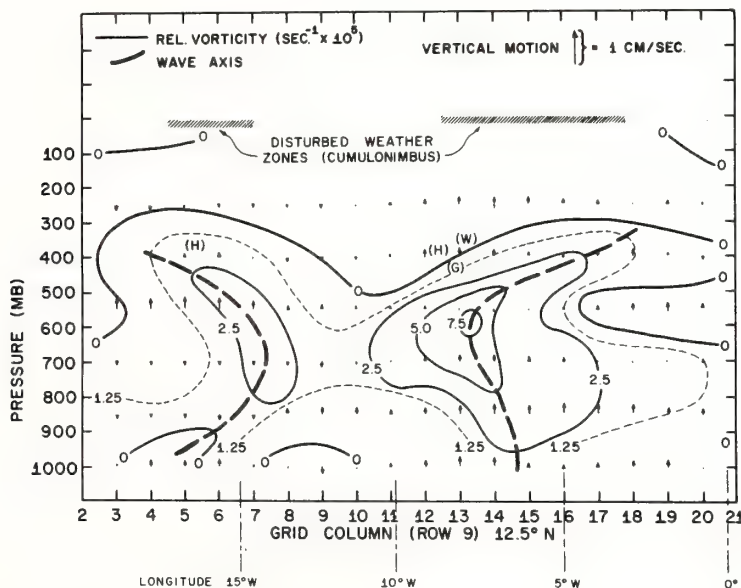


Figure 7. Vertical cross section along latitude 12.5°N (the latitude of maximum cyclonic vorticity in the disturbance) showing contours of relative vorticity (solid lines in units of  $10^{-5} \text{sec}^{-1}$ ). Arrows indicate direction and magnitude of the vertical motion and broken lines the axis of the wind shift. The letters H, W, and G refer to centers of latent heat release, relative warmth and kinetic energy generation as shown in previous figures. Omega values refer to time-dependent solution.

With the time dependent terms included in (2) and (3), the amount of motion in the wave is considerably reduced (and the amount of descent increased) at lower levels as compared to that of the first estimate solution. Vertical coherence is also reduced but the overall appearance of the updrafts is similar to that of the first estimate solution and the strongest ascent at high levels continues to favor the area near (and a little to the west of) the wave axis.

#### 4.2 Wave 8/14 (0000 GMT August 13)

This disturbance was first observed by this author near  $21^{\circ}\text{E}$  on August 8; it reached the central portion of the African bulge by the 12th, where it was accompanied by a tremendous increase in cloudiness. On the following day the wave reached the west coast of Africa causing a 2-3 mb sea-level pressure fluctuation in that area. A week later Barbados experienced showers as the same disturbance passed into the Caribbean.

The satellite photograph (fig. 8a) and the corresponding nephanalysis (fig. 8b) show a dense cloud system near  $10^{\circ}\text{W}$ , which consisted of two areas of deep convection imbedded in dense layer-type of cloud. The streamline charts for the six levels resemble the July case (figs. 9a-d). The dry, Saharan vortex is visible at  $17^{\circ}\text{N}$  near the coast. A trough extends a little to the east of due south from the vortex center within which can be found the two main convective areas. Centers of convergence and relative cyclonic vorticity at 1000 mb are found in the northern



ESSA V SATELLITE PHOTO  
1700 G.M.T AUG. 13, 1968

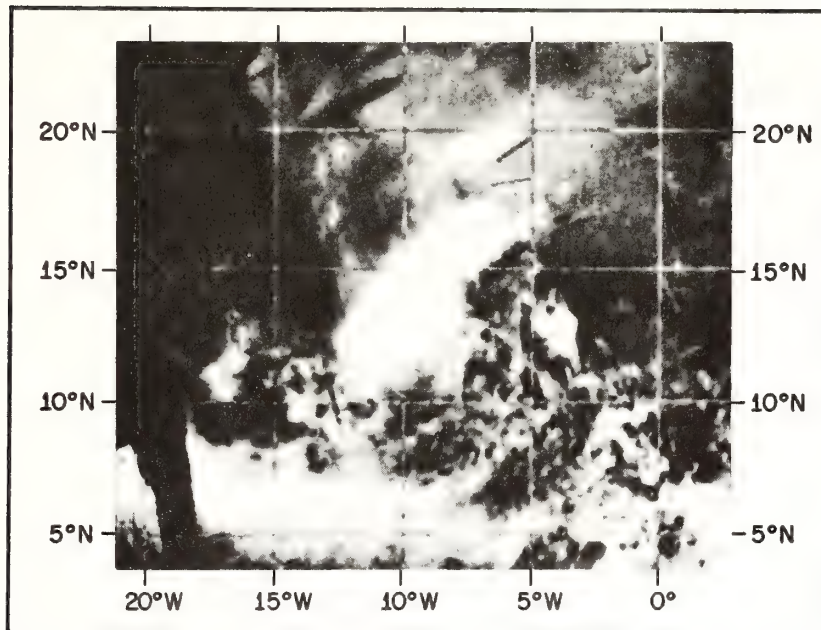


Figure 8a. Same as figure 2a, but for 0000 GMT August 13, 1968

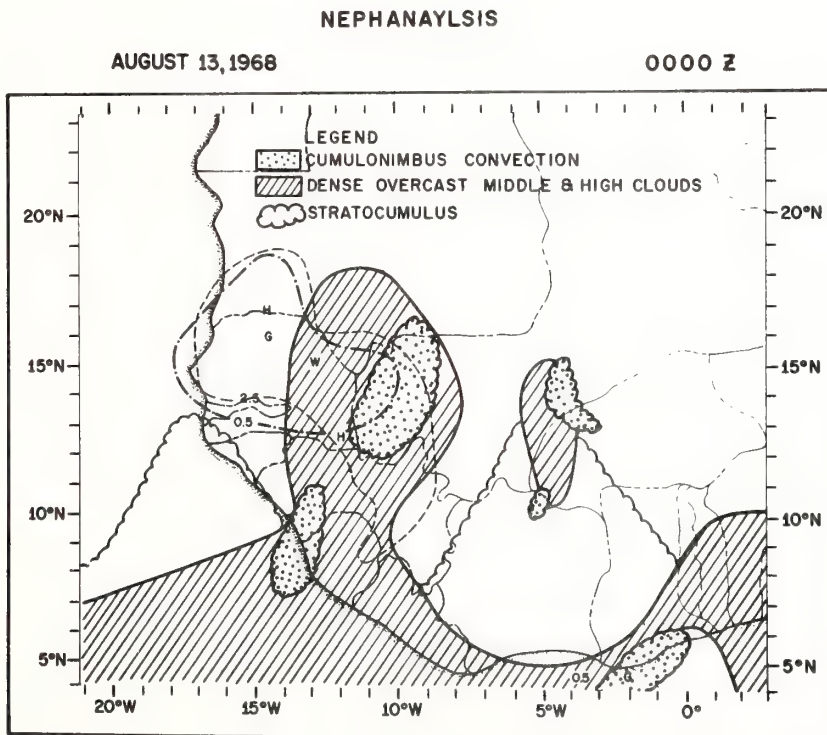


Figure 8b. Same as figure 2b, but for August 13, 1968

1000 MB STREAMLINES AND ISOTACHS (KTS.)

AUGUST 13, 1968

0000 Z

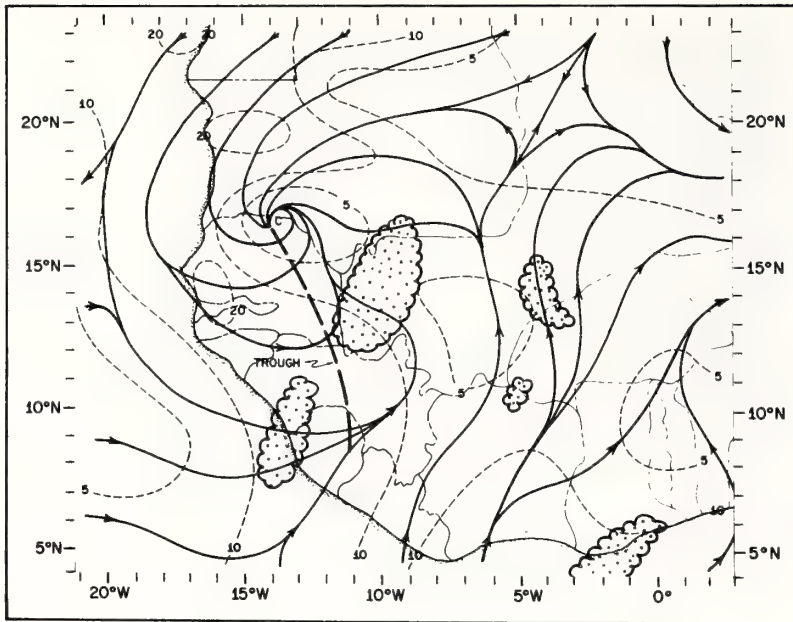


Figure 9a. Same as figure 3a, but for August 13, 1968

700 MB STREAMLINES AND ISOTACHS (KTS.)

AUGUST 13, 1968

0000 Z

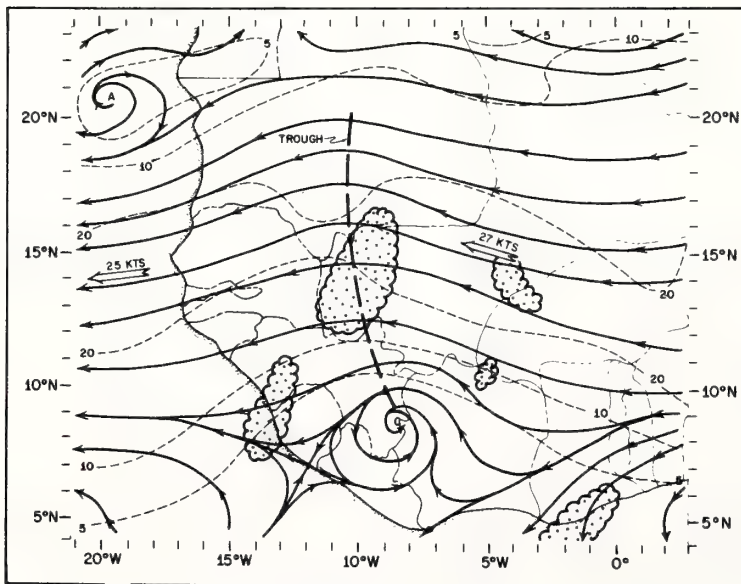


Figure 9b. Same as figure 3c, but for August 13, 1968

portion of the wave near  $18^{\circ}\text{N}$  (fig. 10a). At 850 mb and above the perturbation resembles the classical easterly wave; the easterly jet and vorticity pattern (fig. 10b) attain their maximum strength at 550 mb, above which the wave weakens rapidly with height and becomes no longer visible at 250 mb (fig. 9d). The next major disturbance to pass through the area is partly visible along the eastern border.

At 1000 mb an area of upward vertical motion extends from a center near the dry vortex across the area of disturbed weather (fig. 11a). The vertical motion and vorticity centers shift south to southeastward between 1000 and 400 mb, but the 400 mb pattern does not coincide as closely with the weather as it did in the previous case, the main convective center lying a little to the east of the rising core.<sup>9</sup> Inclusion of the time-dependent terms in (2) and (3) failed to improve the agreement between vertical motion and disturbed weather and even resulted in some deterioration of the vertical coherence in the omega pattern due to suppression of ascent on the west side of the wave (fig. 11b) which was prominent in the lowest estimate solution. The 400 mb chart shows a center of motion just west of the wave axis near the upper warm core

---

<sup>9</sup>The cloud analysis in fig. 8b is based strongly upon surface observations made 12 hours prior to the standard map time of 0000 GMT, July 22. Since these reports were not displaced as were the wind data, the disturbed weather is probably about two degrees of longitude farther to the west at 0000 GMT.

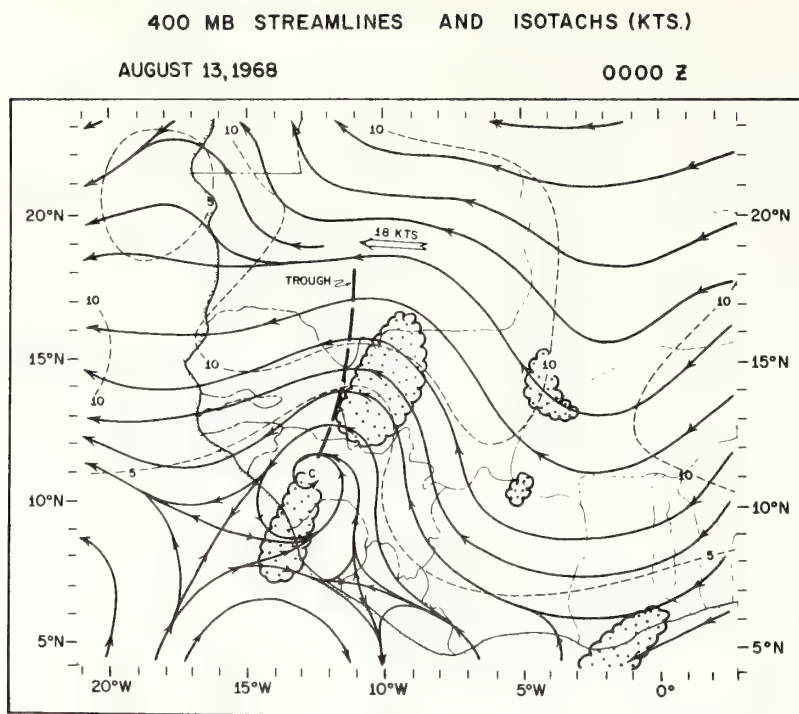


Figure 9c. Same as figure 3e, but for August 13, 1968

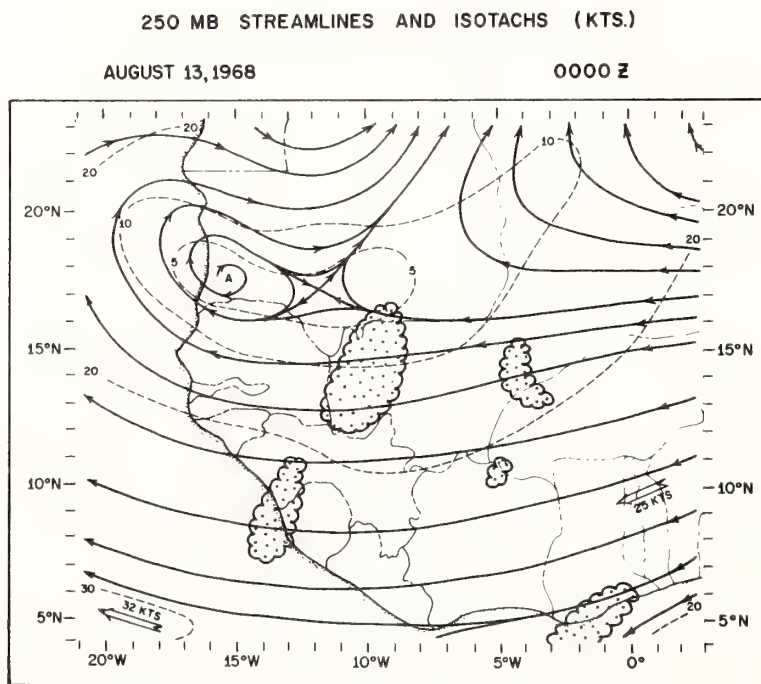


Figure 9d. Same as figure 3f, but for August 13, 1968



1000 MB DIVERGENCE AND VORTICITY ( $10^5 \text{ SEC}^{-1}$ )

AUGUST 13, 1968

0000 Z

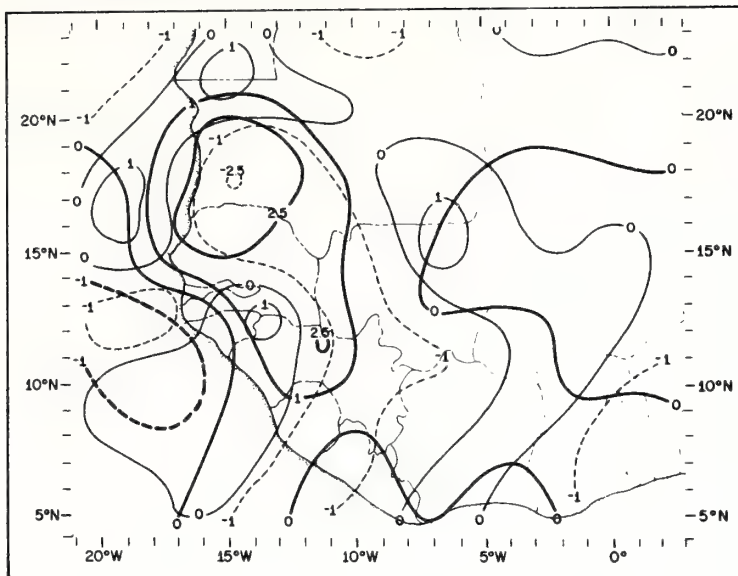


Figure 10a. Same as figure 4a, but for August 13, 1968

550 MB RELATIVE VORTICITY ( $\times 10^5$ )  $\text{SEC}^{-1}$   
& STREAMLINES

AUGUST 13, 1968

0000 Z

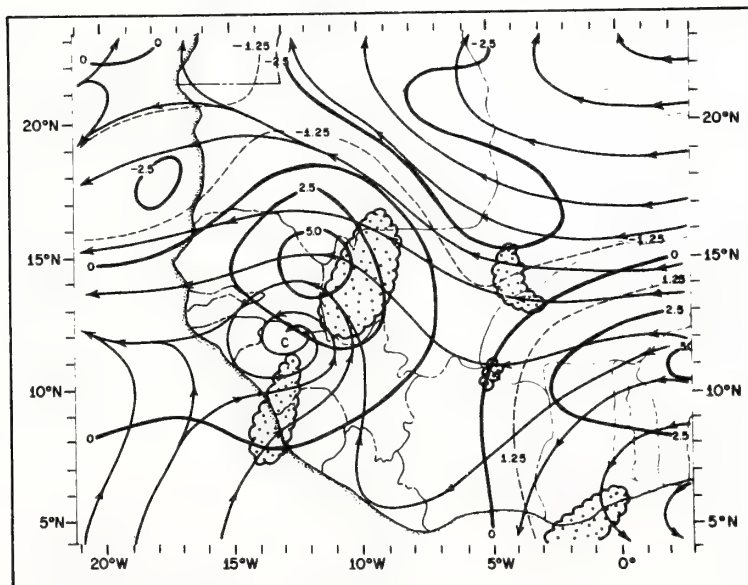


Figure 10b. Same as figure 4b, but for August 13, 1968

1000 MB GEOPOTENTIAL HEIGHT AND VERTICAL  
VELOCITY (cm/sec)

AUGUST 13, 1968

0000 Z

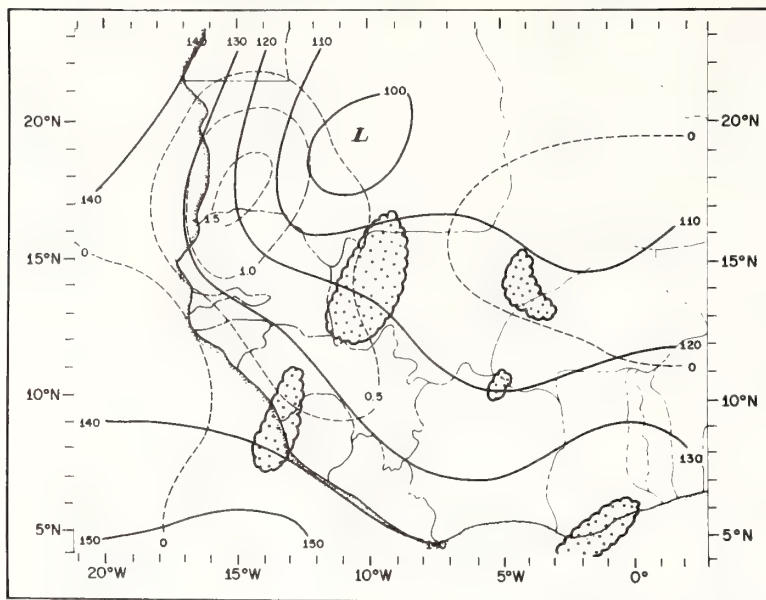


Figure 11a. Same as figure 5a, but for August 13, 1968

700 MB STREAMLINES AND VERTICAL VELOCITY CM/SEC

AUGUST 13, 1968

0000 Z

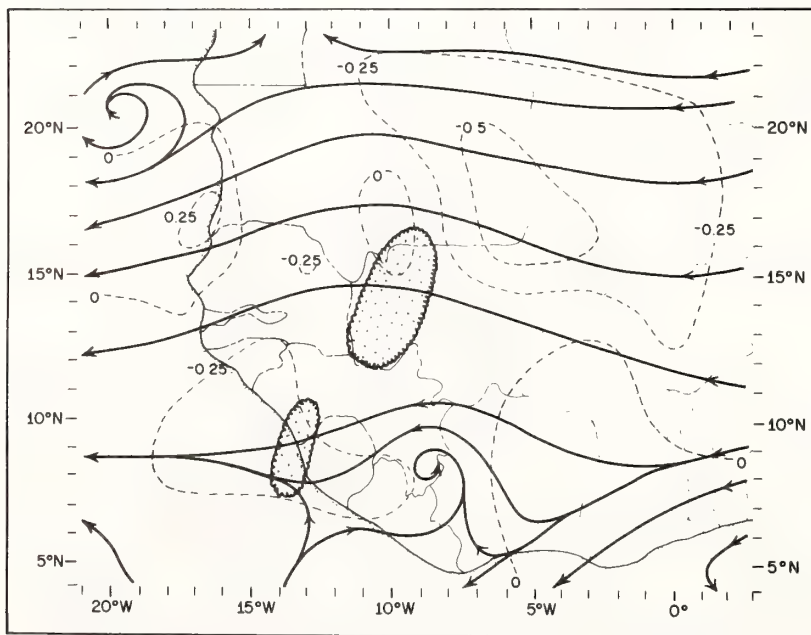


Figure 11b. Same as figure 5b, but for August 13, 1968.  
Solution with time-dependent terms.

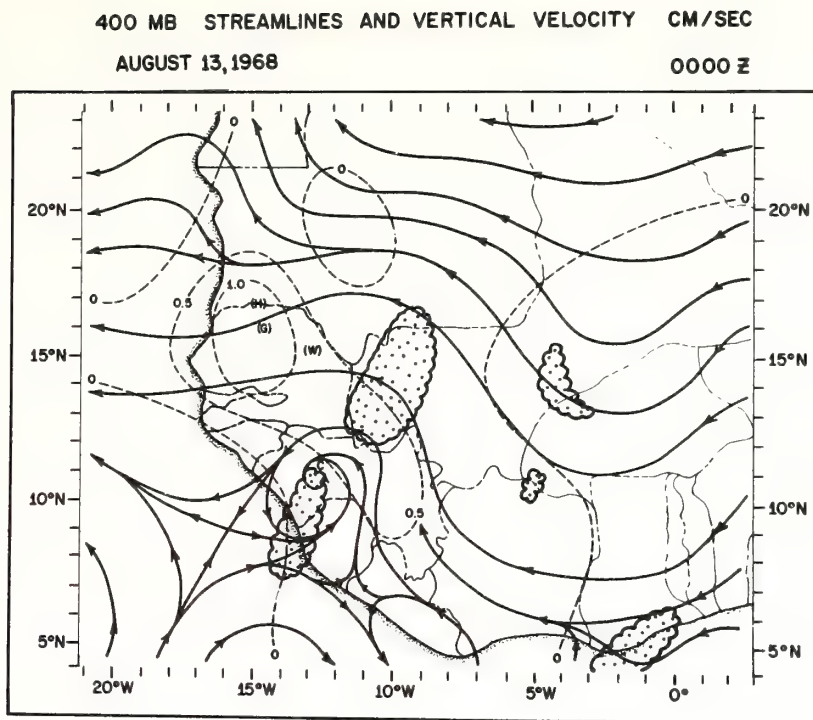


Figure 11c. Same as figure 5c, but for August 13, 1968.  
Solution with time-dependent terms.

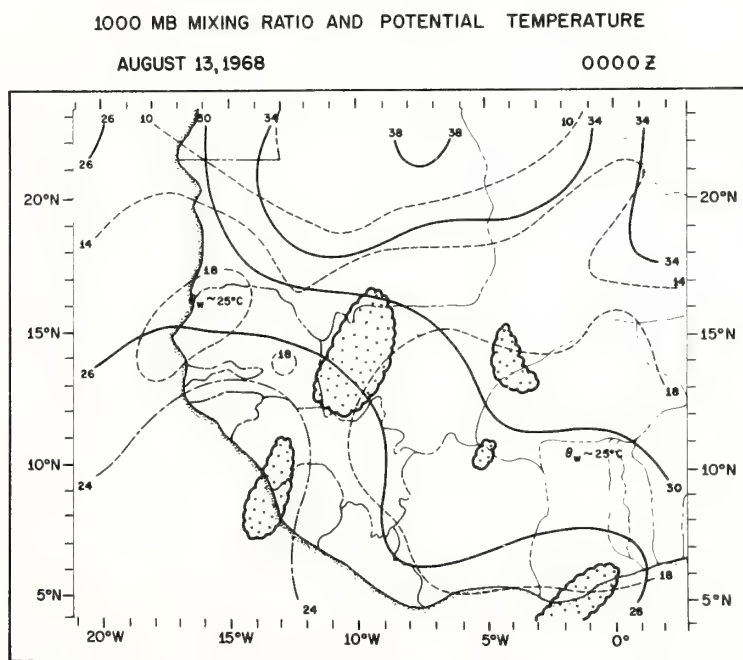


Figure 12a. Same as figure 6a, but for August 13, 1968

(fig. 12c). Near the warm core can be found a center of latent heat release denoted by the letter H in figure 8b which has a value of about  $7^{\circ}\text{C}/\text{day}$  of equivalent warming at 400 mb. (The sensible warming at this point is somewhat less.) Kinetic energy generation is also strongest in this same area. At lower and middle levels, however, the wave is somewhat colder than its environment. Removal of latent heat in the model resulted in very weak fields of vertical motion at all levels but with the upward motion distinctly favoring the eastern sector of the wave at middle and high levels. With heating, the upward motions remained strongest in the western and central portions of the wave (fig. 13).

#### 4.3 Wave 9/11 (0000 GMT September 11)

This disturbance was the most notable one of the 1968 season because of its rapid development into tropical storm Edna shortly after leaving the African coast. First observed by this author on the 4th of September near  $20^{\circ}\text{E}$ , the wave reached the coast by the 11th and became a tropical storm at  $37^{\circ}\text{W}$  on the 15th. The wave appeared particularly well-developed from the start of its passage across West Africa and upon reaching  $5^{\circ}\text{W}$  it had developed a distinct circular cloud system in association with a weak vortex at the surface near  $12^{\circ}\text{N}$ . The circular cloud pattern with numerous small curved bands of stratocumulus, can be seen in figures 14a and 14b but, oddly enough, the surface vortex was not to be found at this time (fig. 15a). Moreover, the circular bands do not appear to fit the



700 MB GEOPOTENTIAL HEIGHT AND POTENTIAL TEMPERATURE  
AUGUST 13, 1968 0000 Z

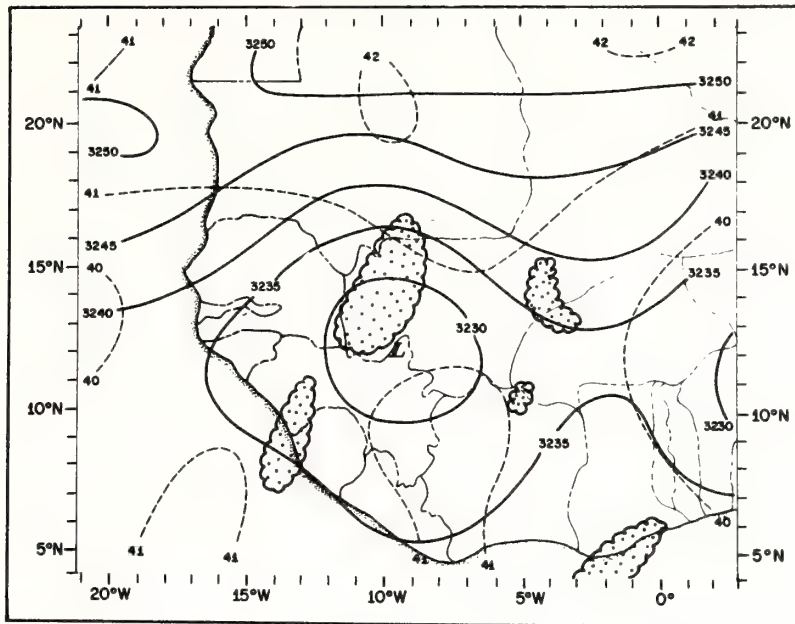


Figure 12b. Same as figure 6b, but for August 13, 1968

400 MB GEOPOTENTIAL HEIGHT AND POTENTIAL TEMP.  
AUGUST 13, 1968 0000 Z

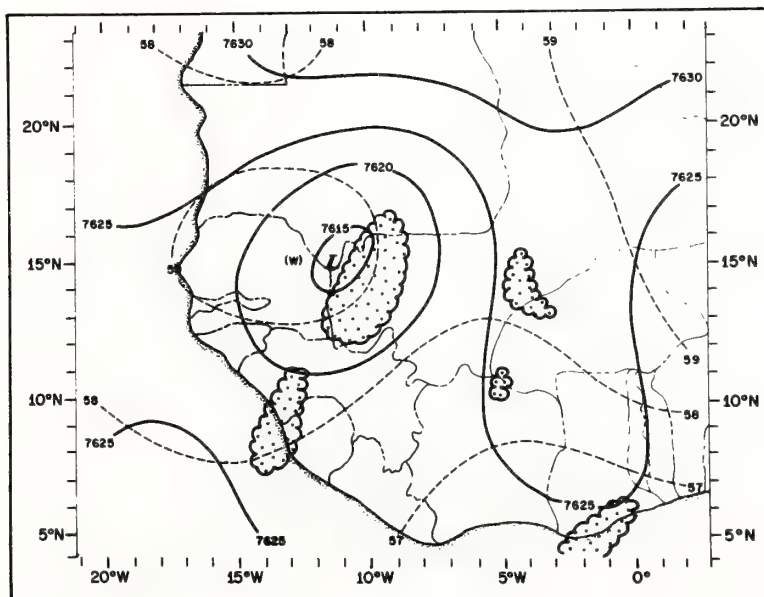


Figure 12c. Same as figure 6c, but for August 13, 1968

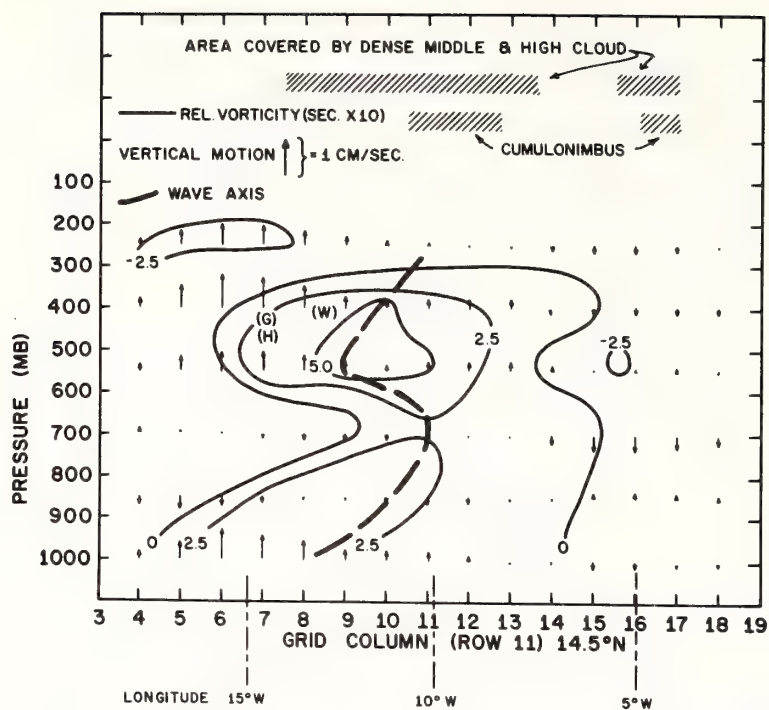


Figure 13. Same as figure 7, but for August 13, 1968. Cross section taken along latitude 14.5°N. Solution with time-dependent terms.

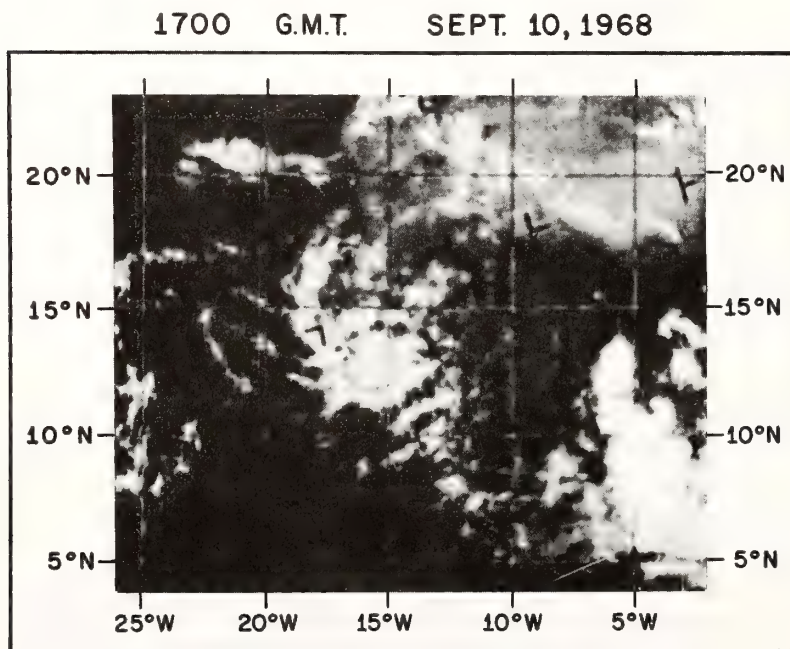


Figure 14a. Same as figure 2a, but for September 11, 1968

# 1000 MB STREAMLINES AND ISOTACHS (KTS.)

SEPT. 11, 1968

0000 Z

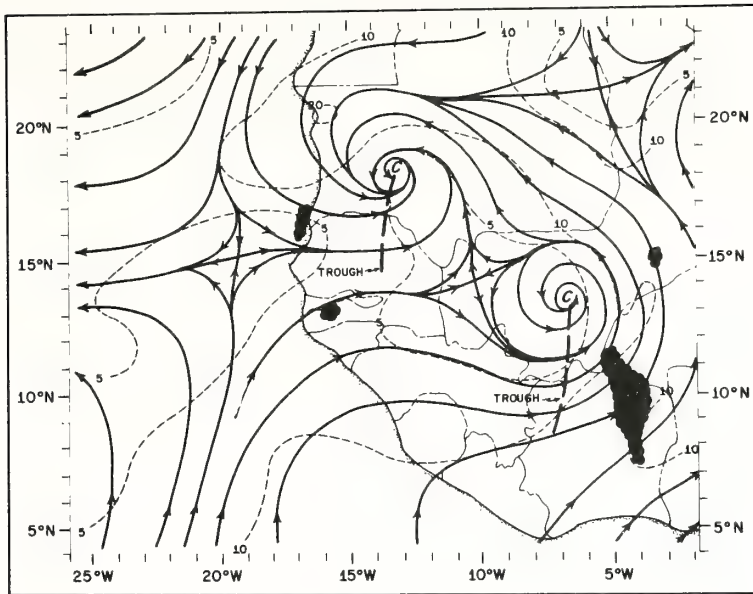


Figure 14b. Same as figure 2b, but for September 11, 1968.  
Note that the solid black represents the convective areas in this case.

SEPT. 11, 1968

0000 Z

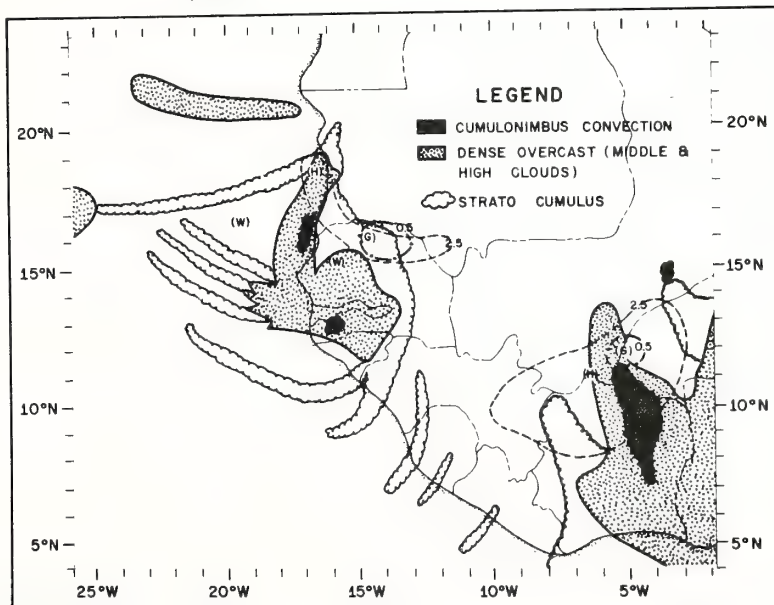


Figure 15a. Same as figure 3a, but for September 11, 1968

streamlines at either 850 or 1000 mb and thus their orientation may reflect an intermediate flow lying between the two disparate regimes of motion. Pressure falls of 2-3 mb accompanied the passage of the wave across the coast of Africa. A very active disturbance, but one which later failed to develop, is visible near the eastern edge of the charts. Streamlines and isotachs for the three levels are shown in figures 15a-c.

There was a slight southward shift in the centers of maximum updraft between the 1000 mb level (fig. 17a) and 400 mb (fig. 17c), although this was not as pronounced as in the two previous cases. A similar movement of the primary vorticity center with height can be noted in a comparison of figs. 16a and 16b. One reason for the relatively weak ascending motion in the center of the wave at 400 mb (fig. 17c) was the limited amount of latent heat released in the model, a facet of the calculations which is supported by the apparent lack of convection at this time. Because of this lack of diabatic heating, the derived vertical motions associated with the disturbance differ little from the case where latent heat release was omitted entirely from the calculations. Inclusion of the time-dependent terms appears also to make little change in the vertical motions, even at low levels. Kinetic energy generation was confined to a small area near the wave axis (fig. 14b), not far from the location of the warm core at 400 mb (fig. 18c). At middle levels, the wave is distinctly cold



700 MB STREAMLINES AND ISOTACHS (KTS.)

SEPT. 11, 1968

0000 Z

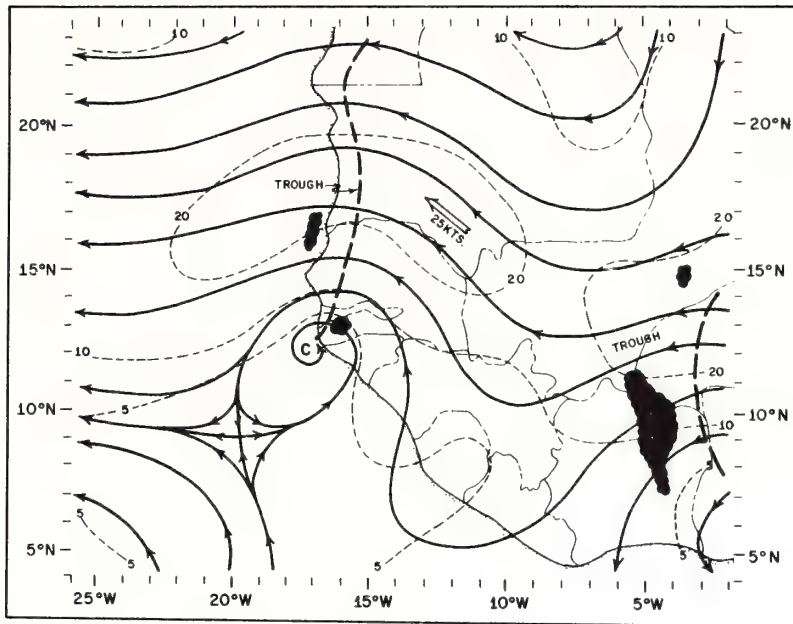


Figure 15b. Same as figure 3b, but for September 11, 1968

400 MB STREAMLINES AND ISOTACHS (KTS.)

SEPT. 11, 1968

0000 Z

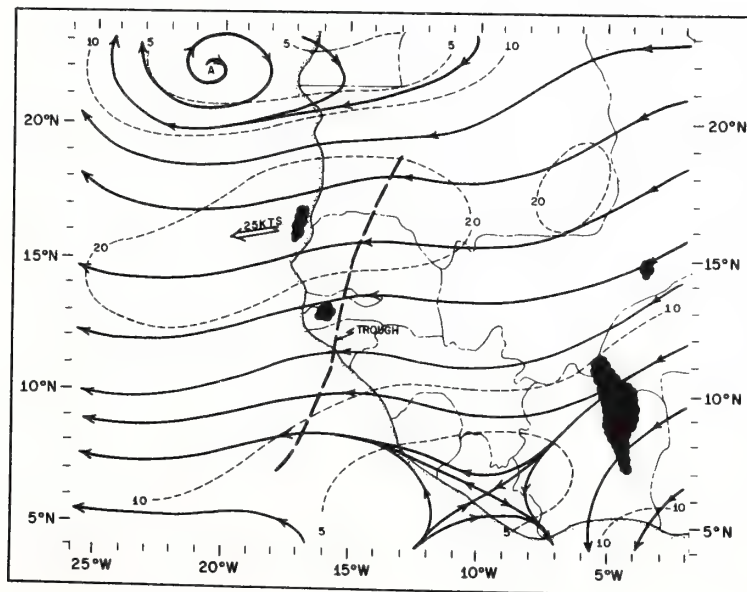


Figure 15c. Same as figure 3c, but for September 11, 1968

1000 MB DIVERGENCE AND VORTICITY ( $10^5 \text{ SEC}^{-1}$ )

SEPT. 11, 1968

0000 Z

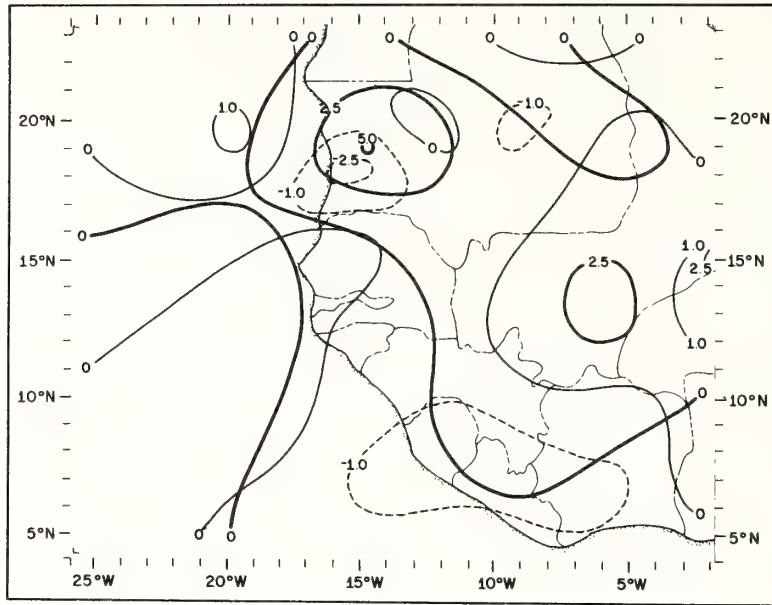


Figure 16a. Same as figure 4a, but for September 11, 1968

700 MB RELATIVE VORTICITY ( $\times 10^5$ )  $\text{SEC}^{-1}$  & STREAMLINES

SEPT. 11, 1968

0000 Z

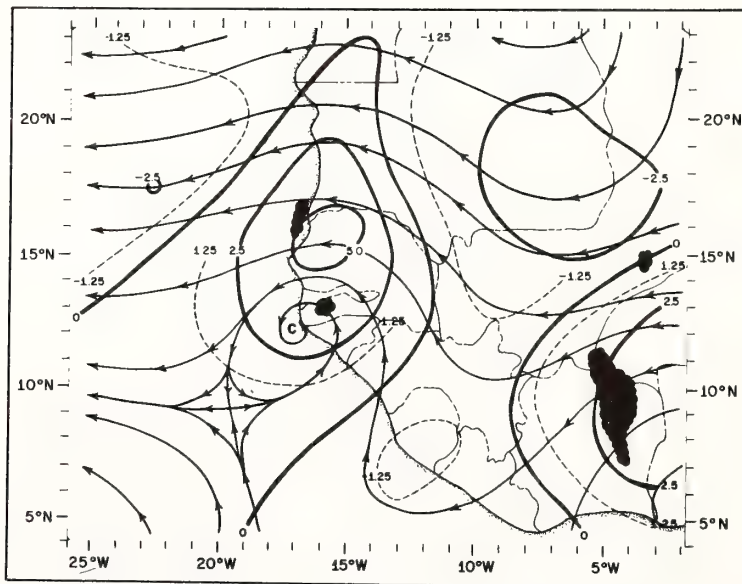


Figure 16b. Same as figure 4b, but for 700 mb on Sept. 11, 1968

1000 MB GEOPOTENTIAL HEIGHT AND VERTICAL  
VELOCITY (cm/sec)

SEPT. 11, 1968

0000Z

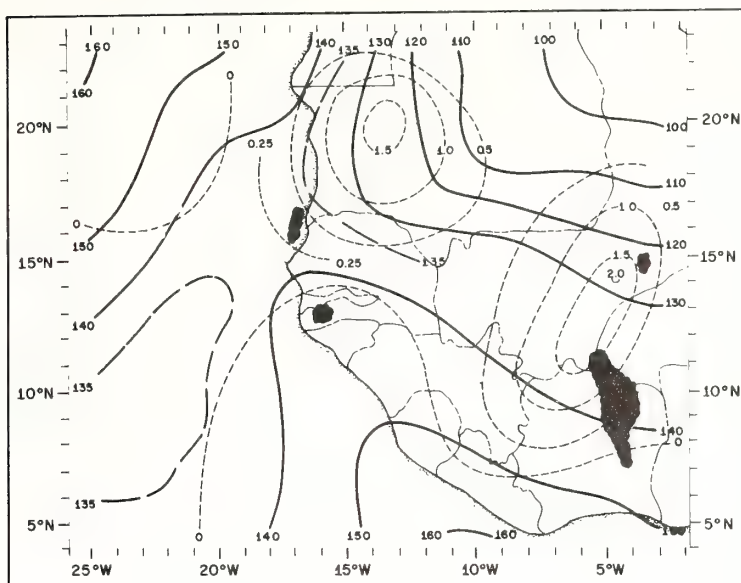


Figure 17a. Same as figure 5a, but for September 11, 1968

700 MB STREAMLINES AND VERTICAL VELOCITY  
(cm/sec)

SEPT. 11, 1968

0000Z

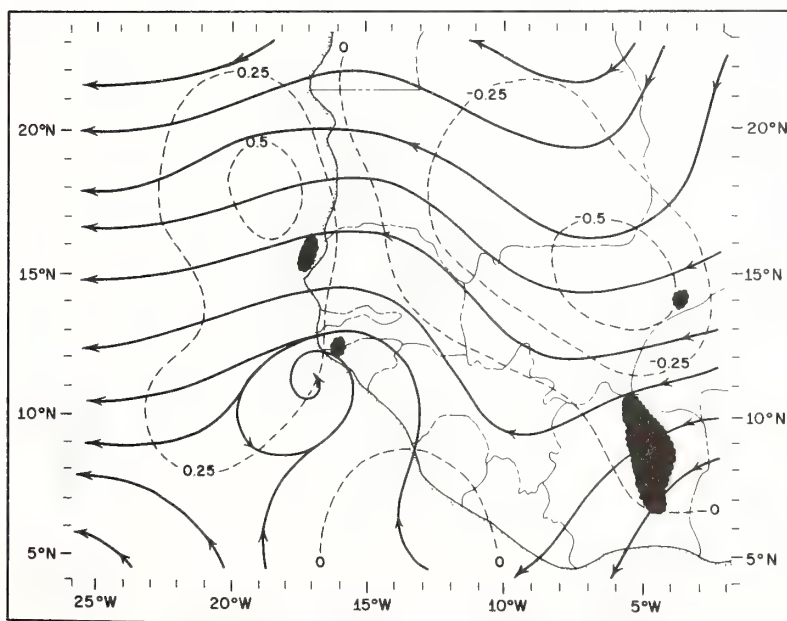


Figure 17b. Same as figure 5b, but for September 11, 1968

400 MB STREAMLINES AND VERTICAL VELOCITY CM/SEC  
SEPT 11, 1968 0000 Z

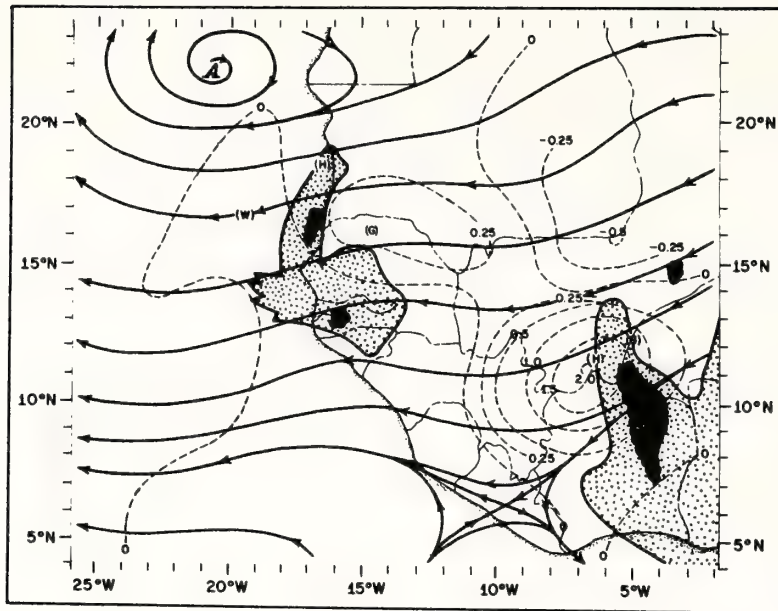


Figure 17c. Same as figure 5c, but for September 11, 1968  
First estimate solution. Stippled areas refer to legend  
in figure 14b.

1000 MB MIXING RATIO AND POTENTIAL TEMPERATURE  
SEPT. 11, 1968 0000 Z

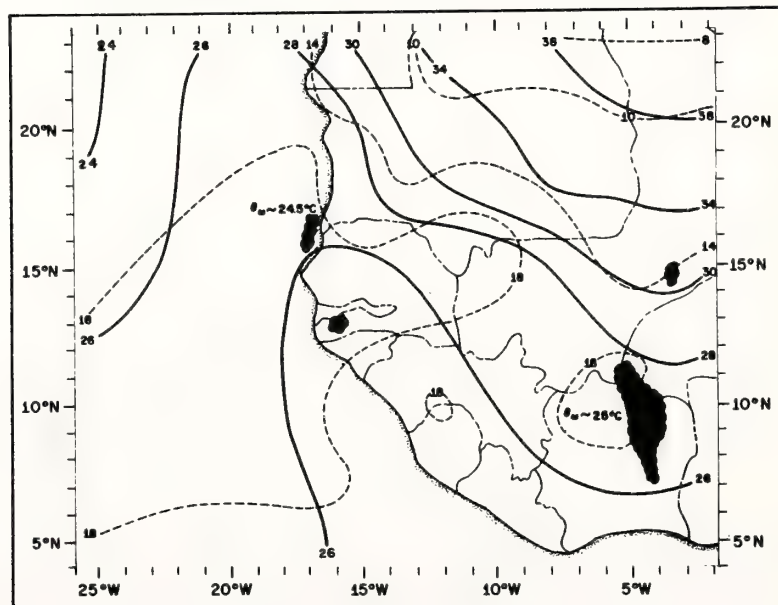


Figure 18a. Same as figure 6a, but for September 11, 1968



with respect to its surroundings (fig. 18b). The vertical motion and vorticity profile through the disturbance at the latitude where vorticity pattern shows the wave to be strongest is presented in figure 19. Strongest updrafts are found in the disturbance with some weak descent, occurring well away from the wave axis. Upward motions are weaker in this instance than in the two previous cases. It seems paradoxical that this disturbance lacked the widespread amount of convection and strong core of rising motion at upper levels which characterized the two previous cases even though the overall cloud pattern possesses the typical common shape of the developing tropical storm.

0000 Z

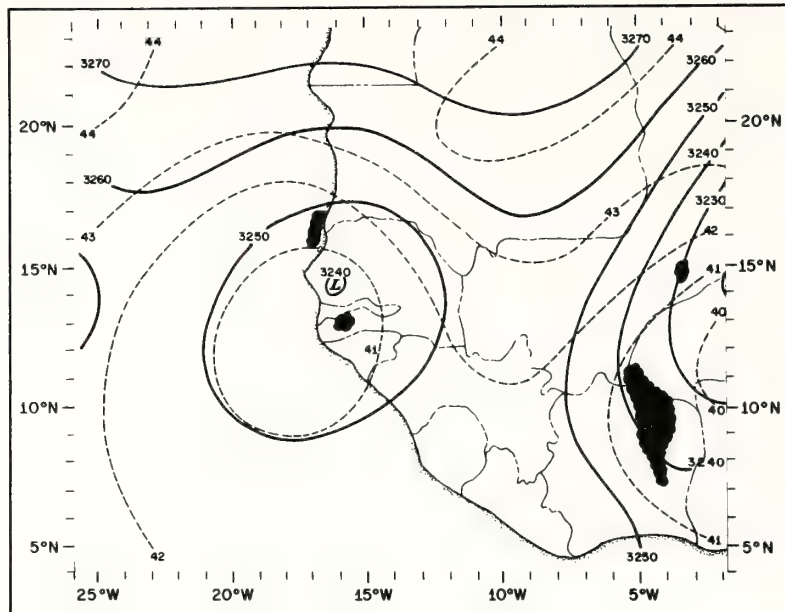


Figure 18b. Same as figure 6b, but for September 11, 1968

0000 Z

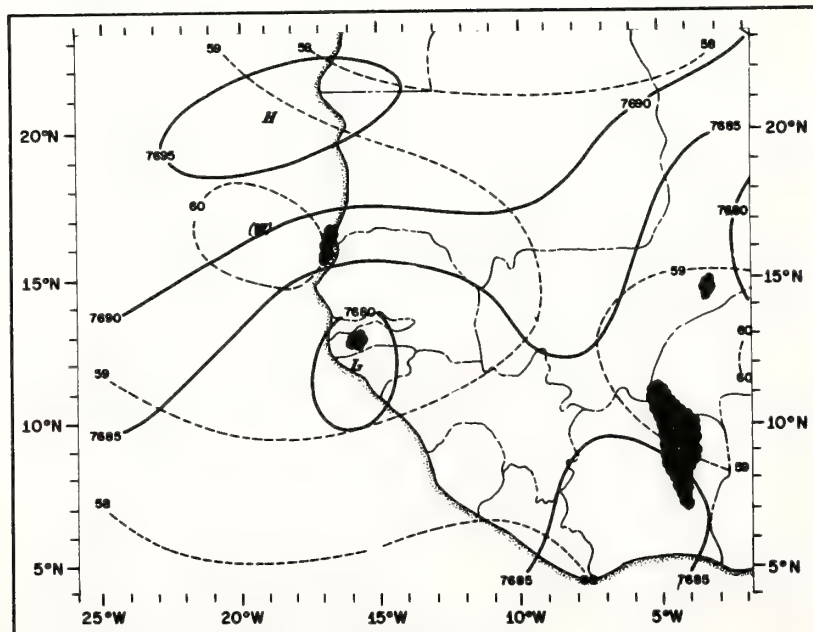


Figure 18c. Same as figure 6c, but for September 11, 1968

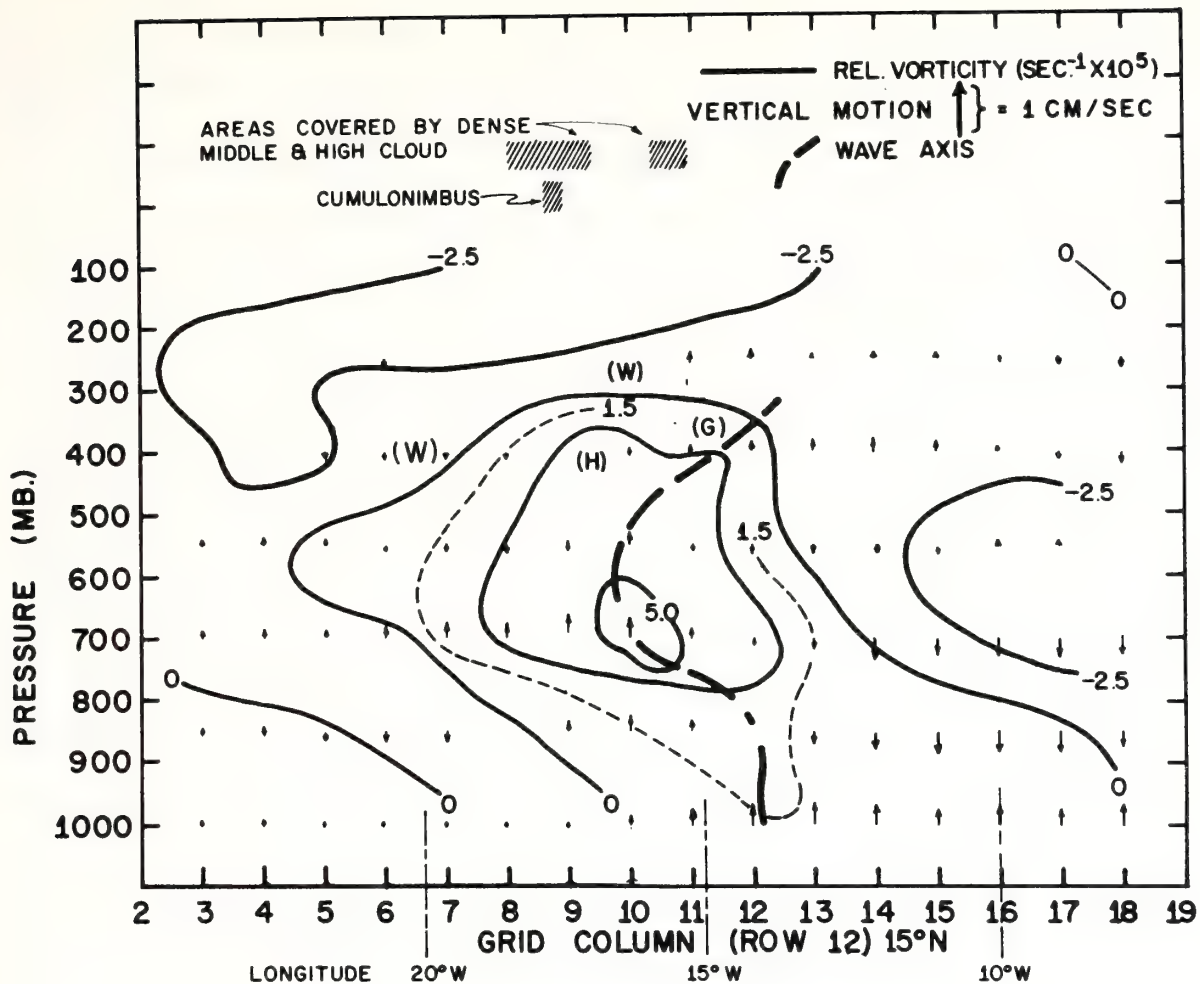


Figure 19. Same as figure 7, but for September 11, 1968. The cross section is taken along latitude 15.5°N. First estimate solution.

## 5. DISCUSSION

This paper sheds little light on the origin of African disturbances. Most of them are formed some distance east of the West African data network by causes yet unknown or travel westward in the prevailing easterlies from more distant sources. Initiating circumstances may result from the presence of mountain waves and their interaction with the convective processes or by the presence of barotropic (horizontal shear) instability. The latter is a definite possibility in view of the very strong horizontal wind shears which exist in connection with the mid-level easterly jet (10-12 m/sec over  $5^{\circ}$  of latitude near  $15^{\circ}\text{N}$ ). Lipps (1970) follows Yanai (1961) in suggesting that disturbances form and grow by barotropic instability of the tropical easterlies. The same mechanism has been proposed by Bates (1970) whose model of low latitude disturbances contains many features exhibited by African disturbances. In addition, Yanai and Nitta (1969) have demonstrated, in their theoretical models, that horizontal shears weaker than those observed over Africa can lead to growth of a perturbation whose wavelength is slightly in excess of 2000 km and whose phase speed of propagation lies between 4 and 9 m/sec. Bates found that with convection included in his model, the wave first intensified by barotropic instability, doubling in amplitude every three days, and finally approached a steady state in which the energy was maintained more by direct conversion of potential to kinetic energy through the convective



processes than by barotropic conversion. In his model the maximum up-drafts in the disturbance (2.5 cm/sec) were found about 13°N.

Following Miller and Carlson (1970) an attempt was made to construct a kinetic energy balance of African disturbances based on the generated patterns of wind, temperature and vertical motions. Three different sets of conditions were used in evaluating the energy balance for each of the three cases. These conditions were (1) no latent heat release or surface heating over land, (2) latent heat release but no surface heating over land, and (3) latent heat release and surface heating everywhere. The last category was performed using a realistic but modestly large heating function over the land, which distributed the vertical flux of sensible heat in a progressively diminishing fashion with height to a value of zero at 625 mb. Over land, the heating function was made inversely dependent on the surface mixing ratio, in order to permit the heating to be a maximum over the desert while varying continuously in the horizontal. All the diagrams presented in this paper refer to the second set of conditions.

Because of the extreme sensitivity of the boundary terms in the energy balance to slight changes in the initial conditions and the uncertainty of these initial conditions, only the most important aspect of the energy balance, the energy generation term, will be discussed here. The energy generation term ( $G=A \int_p \frac{\overline{\alpha' \omega'}}{g} dp$ ) expresses the rate of conversion of

potential to kinetic energy in a given layer expressed by the integral bounds. The values of G are shown in table 2 for two 150 mb deep layers in the atmosphere, one in the lower and one in the upper troposphere, and for the three sets of basic heating conditions. These figures remained relatively unchanged throughout all the progressive alterations made in the model, and they represent with some confidence the energy conversion centered at the levels appropriate to the high tropospheric warm core (325 mb) and the mid tropospheric cold core of the disturbance (775 mb). All figures refer to the model in its time dependent state.

Table 2

Eddy Conversion of Potential to Kinetic Energy in 150 mb layers centered at 775 and 325 mb for heating conditions (1), (2) and (3). (See text.)

Units -  $10^{19}$  ergs/sec.

	22 July 1968			13 August 1968			11 Sept 1968		
heating conditions	(1)	(2)	(3)	(1)	(2)	(3)	(1)	(2)	(3)
G (775 mb)	-0.07	-0.09	+0.20	-0.34	-0.36	-0.24	-0.29	-0.31	-0.24
G (325 mb)	-0.04	0.00	-0.01	0.00	+0.06	+0.06	0.00	+0.03	+0.03

At 325 mb the small increases in kinetic energy generation, which

are found when latent heat is added and result in a net positive generation in two out of three cases, are attributable to latent heat release at high levels in the disturbance. The preference for energy generation in the wave is illustrated in the nephanalyses which show in a rough sense the areal distribution of  $G$ . At middle levels kinetic energy destruction is indicated by the negative values, which become less negative or positive when surface heating is applied. Yanai (1961) and Bates (1970) noted the destruction of kinetic energy in the cold core of easterly disturbances and have postulated the growth of disturbances at the expense of the zonal flow. Table 2 indicates that the strong zonal flow, characteristic of middle levels between 15 and 20°N, is maintained by the large-scale heating distribution in which air tends to rise in the hotter areas (the desert heat low) and sink elsewhere. Conversely, it seems quite likely that the waves provide a source of kinetic energy for the high level easterly jet, called the Tropical Easterly Jet by Reiter (1963), which can be found at 250 mb on some of the analyses (fig. 3f, for example). This high level easterly jet is thought to be produced by the monsoonal circulation and is therefore strongest over India, Africa and Central America, areas which are known for their intense convection in summer. Examination of the computations for  $\partial\theta/\partial t$  showed that the release of latent heat aloft was accompanied by a net sensible warming in the vicinity of the wave axis, although this warming was of smaller magnitude than the equivalent latent heat release ( $H$ ) portrayed in the nephanalysis diagrams.

## 5. SUMMARY

Examined from a broad vantage, African disturbances exhibit a number of important features, beyond the more superficial aspects of scale and phase speed, which are common to easterly waves in other parts of the world. The following statements are felt to be realistic and supportable by the observations.

(1). No facile model can be made with respect to the distribution of cloudiness and vertical motion except insofar as both tend to be centered near the wave axis and in a region of strong cyclonic vorticity at middle levels. The disturbances appear to slope a little eastward with height in the northern sector. Although upward motion can be found on both sides of the wave axis, the strongest updrafts at high levels (1-2 cm/sec) are found a little to the west of the wave axis. There was rough agreement between the computed release of latent heat at high levels (and sensible warming derived thereof) and the convection. Almost all of the important convection was concentrated in the latitude interval between 10 and 15°N. At these latitudes ascent dominated descent, the latter being very weak.

(2). According to the vorticity patterns the disturbances were most intense at middle levels (700-550 mb). Between 250 and 400 mb they were strongly warm core, the maximum difference between thermal trough and ridge being about 1-2° in the vicinity of 15°N. The disturbances were



cold core in the lower troposphere.

(3). Primary centers of convergence and cyclonic vorticity were closely associated at 1000 mb, the strongest values being located near  $18^{\circ}\text{N}$  in a relatively cloud free portion of the disturbance. At upper levels, however, the maximum vorticity was found near  $14^{\circ}\text{N}$ , the shift being reflected in the vertical motion patterns as well.

(4). Calculations showed that neglect of latent heat release in the model led to very weak vertical motions at high levels, which were diffuse and in poor agreement with the observed cloudiness. Conversely, the latent heat release was the dominant term in producing the vertical velocity pattern at high levels, although it had little effect on the patterns below 550 mb.

(5). In view of the mutual proximity of the main ascending region, the warm core, and the observed convection, it is reasonable to conclude that the convection contributes to the thermally direct circulation. By producing eddy potential energy which is converted to kinetic energy the disturbances serve to maintain the high tropospheric easterly jet. At low levels, however, the disturbances may be functioning indirectly.

## ACKNOWLEDGMENTS

I would like to thank Banner I. Miller of this laboratory for his permission to use his diagnostic model and for his constant encouragement and advice during the course of the work. Thanks are also due Harry Hawkins, Stanley Rosenthal, and Cecil Gentry for their comments and criticisms. Robert Carrodus and his staff were responsible for the drafting and Charles True did the photography and reductions. Mary Jane Clarke did the typing.

## REFERENCES

- Bates, J.R. "Dynamics of Disturbances in the Intertropical Convergence Zone," Symposium on Tropical Meteorology, June 2-11, 1970, Extended Abstracts, University of Hawaii, Honolulu, Hawaii. pp (FVII) 1-4.
- Carlson, T.N. "Synoptic Histories of three African disturbances that developed into Atlantic hurricanes," Monthly Weather Review, vol. 97, no. 3, Mar.1969, pp 256-276.
- Carlson, T.N. "Some Remarks on African disturbances and their Progress over the tropical Atlantic," Monthly Weather Review, vol. 97, no. 10, Oct. 1969, pp 716-726.
- Frank, N.L. "The 'Inverted V' cloud pattern - an easterly wave?," Monthly Weather Review, vol. 97, no. 2, Feb.1969, pp 124-129.
- Frank, N.L. "Atlantic tropical disturbances of 1969," Monthly Weather Review, vol. 98, no. 4, April 1970, pp 307-314.
- Hawkins, H.F. "Development of a seven-level Balanced, Diagnostic model and its application to three Disparate Tropical Disturbances," Ph.D. Thesis, Florida State University, 1971.
- Krishnamurti, T.N. and D. Baumhefner "Structure of a tropical disturbance based on solutions of a multi-level baroclinic model," J. Applied Meteorol., vol. 5, Aug. 1966, pp 396-406.
- Krishnamurti, T.N. "An Experiment in Numerical Prediction in Equatorial Latitudes," Scientific Report #4, Dept. of Meteorology and Oceanography, Naval Postgraduate School, October 1968, 47 pp.
- Kuo, H.L. "On the formation and intensification of tropical cyclones through the release of latent heat release by cumulus convection," Jour. Atm. Sci., vol. 22, Jan. 1965, pp 40-63.
- Lateef, M.A. "A case study concerning vertical motion, divergence, and vorticity in the troposphere over the Caribbean," Monthly Weather Review, vol. 95, no. 11, Nov. 1967, pp 778-790.
- Lateef, M.A. and C.L. Smith "A synoptic study of two tropical disturbances in the Caribbean," ESSA Tech. Memo. IERTM-NHRL 78, 1967, 33 pp.

- Lipps, F.B. "Barotropic Stability and Tropical Disturbances," Monthly Weather Review, vol. 98, no. 2, Feb. 1970, pp 122-131.
- Miller, B.I. "Experiment in forecasting hurricane development with real data," ESSA Tech. Memo. 85, April 1969, 28 pp.
- Miller, B.I. and T.N. Carlson "Vertical motions and the kinetic energy balance of a cold low," Monthly Weather Review, vol. 98, no. 5, May 1970, pp 363-374.
- Reiter, E. Jet Stream Meteorology, University of Chicago Press, 1963, 515 pp.
- Riehl, H. Tropical Meteorology, McGraw-Hill Book Company, Inc., New York, 1954, 392 pp.
- Saito, N. "On the large-scale structure of a disturbance in the easterlies over the Caribbean Sea," ESSA Tech. Memo. IELTM-NHRL 81, June 1968, 35 pp.
- Simpson, R.H., Frank, N., Shideler, D., and Johnson, H.M. "Atlantic tropical disturbances of 1968," Monthly Weather Review, vol. 97, no. 3, Mar.1969, pp 240-255.
- Wallace, J.M., and Chang, C-P. "Spectrum Analysis of Large-Scale Wave Disturbances in the tropical lower troposphere," Journal of Atmospheric Sciences, vol. 26, Sept. 1969, pp 1010-1025.
- Yanai, M. "A detailed analysis of typhoon formation," J. Meteorol. Soc. Japan, vol. 39, 1961, pp 187-214.
- Yanai, M., and Nitta, T. "Computation of Vertical Motion and Vorticity Budget in a Caribbean Easterly Wave," J. Meteor. Soc. Japan, vol. 5, 1967, pp 444-466.
- Yanai, M., Maruyama, T., Nitta, T., and Hayashi, Y. "Power Spectra of Large-Scale Disturbances over the Tropical Pacific," J. Meteor. Soc. Japan, vol. 46, no. 4, August 1968, pp 308-323.
- Yanai, M. and Nitta, T. "A note on the Barotropic Instability of the Tropical Easterly Current," J. Meteor. Soc. Japan, vol. 47, no. 1, Feb. 1969, pp 127-130.



April 1971

309

UDC 551.526.6:551.515.23(263)''1966.08+1968.08''

## WEATHER NOTE

### An Apparent Relationship Between the Sea-Surface Temperature of the Tropical Atlantic and the Development of African Disturbances Into Tropical Storms

TOBY N. CARLSON

National Hurricane Research Laboratory, Environmental Research Laboratories, NOAA, Miami, Fla.

#### ABSTRACT

An analysis of sea-surface temperatures over the tropical Atlantic for the past 5 yr shows a correlation between the number of tropical storms formed between July 10 and September 20 and the ocean temperatures over a wide area centered near 10°N and 35°W.

In a recent article by Carlson (1969) it was suggested that the frequency of tropical storm formation from African disturbances is dependent upon the sea-surface temperatures over the tropical Atlantic west of the African Continent. Evidence in support of this included a comparison of the August 1968 sea-surface temperatures over the tropical North Atlantic with those of August 1966. The earlier year was one in which several African disturbances developed into tropical storms, whereas 1968 was a notably inactive hurricane season. In the more active season, the August sea temperatures were 1° to 2°F higher than those of August 1968 in the area between longitude 30° and 40°W and latitude 5° and 20°N.

The hurricane season of 1969 was noted for being one of the most active in recent years, especially with respect to the number of African disturbances that became tropical storms or hurricanes, a total of seven between July 10 and September 20. We have obtained the machine-analyzed mean sea temperature data from the U.S. Fleet Numerical Weather Facility at Monterey, Calif., for the month of August 1969. Our own hand analyses of sea-temperature data have indicated that these machine analyses may be quite useful in examining relative temperature variations in the Tropics provided that the analyses represent an average over an extended period of time. Although the Tropics contain relatively few ship reports, a minimum of one or two reports are likely to be found within each 10° longitude square at any given observation period, while the composite analyses consist of about 60 such observation periods (Wolff 1969). Of course, such analyses are comparable from year to year only if the data density and method of analyses remain the same.

Figure 1 contains sea-temperature analyses for the 3 mo, August 1969, August 1968, and August 1966. The departure isotherm patterns show that August 1969 was clearly warmer than August 1966 over the tropical Atlantic Ocean; in the vicinity of 35°W, the tropical Atlantic was 2° to 3°F higher in August 1969 than the same area during August of the inactive season of 1968. For focusing attention on this area of maximum departure,

subsequent tabulations will refer primarily to an area box located between 10° and 20°N and between 30° and 40°W.

Table 1 is a version of the sea-temperature data for the past five Augusts (1965-1969), showing the area average and area maximum values over this box. The years of data are listed from bottom to top in the table, in order of the increasing number of African disturbances to develop into tropical storms or hurricanes in the interval between July 10 and September 20 of that year.<sup>1</sup> It is evident that there is some degree of correlation between storm growth and sea temperature for these 5 yr. Were it not for a narrow intrusion of relatively cool water that extended into the northern part of the box, August 1969 would have yielded the warmest average of the past 5 yr (as the values in the third column of table 1 suggest) rather than taking second place to August 1967 when only four disturbances grew into tropical storms. The two most inactive seasons were also the coldest of the five.<sup>2</sup>

Recent studies such as those of Namias (1969) and Perlroth (1969) have also been concerned with the effects of sea temperatures on the development of Atlantic hurricanes. However, this note attempts only to relate the sea-surface temperature field lying in the path of (African) tropical disturbances to the propensity for growth of these disturbances beyond the wave stage into tropical storms. Examination of monthly mean circulation maps for the past 5 yr, as furnished to us by the Extended Forecast Division of the U.S. Weather Bureau, showed very little consistency between the behavior of the general circulation at low levels in the Tropics and the development of tropical storms. For illustrating this, the last five columns of table 1 include respectively the monthly mean 1000-mb geopotential height in the afore-mentioned area box, the

<sup>1</sup> The vast majority of tropical storms that form during this period develop from disturbances with origins appearing to be over the continent of Africa. These storms can be identified on the basis of their tracks as given by the U.S. Weather Bureau (now the National Weather Service) in its yearly summary of hurricanes in the *Monthly Weather Review*.

<sup>2</sup> Figures for August 1970 show 78.6 average temperature and 80.2 maximum temperature for the area box. The number of developing disturbances was 3.

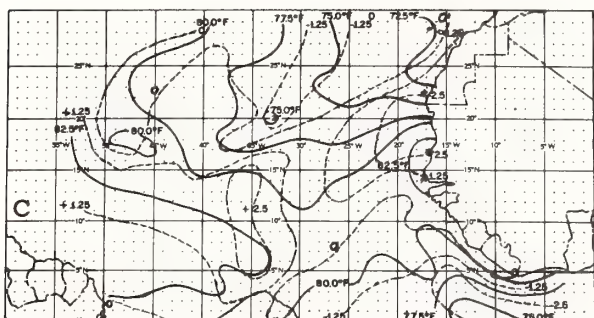
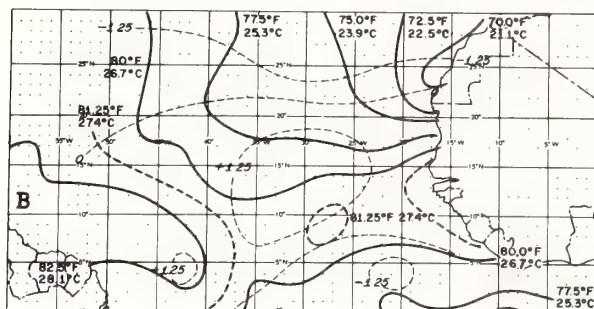
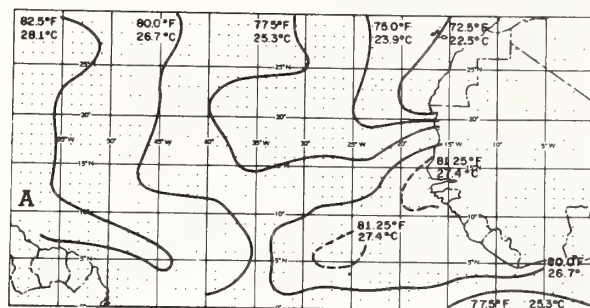


FIGURE 1.—Mean sea surface temperature field ( $^{\circ}\text{C}$  and  $^{\circ}\text{F}$ ) for (A) August 1968, (B) August 1966, and (C) August 1969 (labeled  $^{\circ}\text{F}$  only). The light dashed lines (labeled in  $^{\circ}\text{F}$ ) in (B) and (C) represent departure isotherms of that month from August 1968.

700-mb height averaged over the same area, the mean thickness in this area, the 1000-mb zonal height gradient along latitude  $20^{\circ}\text{N}$  between  $20^{\circ}$  and  $30^{\circ}\text{W}$  (a measure of the strength of the northeasterlies along the African coast), and the 1000-mb meridional height

TABLE 1.—Version of the sea-temperature data for five Augusts (1965–1969) in the area box  $10^{\circ}$  to  $20^{\circ}\text{N}$  and  $30^{\circ}$  to  $40^{\circ}\text{W}$

Year	Average sea temperature	Maximum sea temperature	No. of storms July 10–Sept. 20	Average 1000-mb height (m) in box	Average 700-mb height (m) in box	Average 700-to 1000-mb thickness (m) in box	Zonal height gradient (m) at 1000 mb along $20^{\circ}\text{N}$ between $20^{\circ}$ and $30^{\circ}\text{W}$	Meridional height gradient (m) at 1000 mb along $45^{\circ}\text{W}$ between $20^{\circ}$ and $30^{\circ}\text{N}$
1969	79.0	81.7	7	146	3195	3049	27	53
1966	78.9	80.8	5	158	3206	3048	31	56
1967	79.4	81.0	4	148	3198	3050	29	55
1965	78.7	80.0	3	156	3194	3038	30	44
1968	78.1	79.9	2	157	3199	3042	26	43

gradient along longitude  $45^{\circ}\text{W}$  between  $20^{\circ}$  and  $30^{\circ}\text{N}$  (a measure of the strength of the trades). Except for the 1000- and 700-mb thickness being somewhat less in the 2 coldest months, the only relationship worthy of mention is that the strength of the trades was somewhat reduced in the two inactive seasons. Oddly enough, the strength of the northeast trades along the coast of Africa does not appear to be greater in the years when the southward intrusion of cold water west of Africa was more pronounced. As suggested by Namias (1969), seasonal variations of sea-surface temperature in the Tropics may be influenced by anomalies in the circulation at higher latitudes which can affect the amount of cloudiness and insolation over a considerable area. Indeed, a comparison of the monthly composite satellite cloud pattern (prepared by the Walter A. Bohan Co., Parkridge, Ill.) for August 1967 with that of August 1968 shows a notably greater amount of cloud over the eastern tropical Atlantic in the latter (inactive) year.

If the sea-temperature anomaly in the tropical Atlantic proves to be persistent for periods of several months, it may become useful as a predictor of hurricane activity for that season.

#### REFERENCES

- Carlson, Toby N., "Some Remarks on African Disturbances and Their Progress Over the Tropical Atlantic," *Monthly Weather Review*, Vol. 97, No. 10, Oct. 1969, pp. 716–726.
- Namias, Jerome, "On the Causes of the Small Number of Atlantic Hurricanes in 1968," *Monthly Weather Review*, Vol. 97, No. 4, Apr. 1969, pp. 346–348.
- Perloth, I., "Effects of Oceanographic Media on Equatorial Atlantic Hurricanes," *Tellus*, Vol. 21, No. 2, Stockholm, Sweden, 1969, pp. 230–244.
- Wolff, Paul M., "Numerical Synoptic Analysis of Sea Surface Temperature," *International Journal of Oceanography and Limnology*, Vol. 1, No. 4, Omnipress, Cherry Hills, N.J., Oct. 1969, pp. 277–290.

[Received May 5, 1970; revised July 17, 1970]

U.S. DEPARTMENT OF COMMERCE  
National Oceanic and Atmospheric Administration  
Environmental Research Laboratories

NOAA Technical Memorandum ERL NHRL-91

COMPARISON OF DRAFT SCALE VERTICAL VELOCITIES  
COMPUTED FROM GUST PROBE AND CONVENTIONAL DATA  
COLLECTED BY A DC-6 AIRCRAFT

Toby N. Carlson  
Robert C. Sheets

National Hurricane Research Laboratory  
Miami, Florida  
June 1971



## TABLE OF CONTENTS

	Page
ABSTRACT	1
1. INTRODUCTION	1
2. COMPUTATIONS	6
3. STATISTICAL EVALUATION OF CONVENTIONAL DRAFTSCALE MEASUREMENTS	12
3.1 A Total Comparison	12
3.2 Agreement As A Function Of Wavelength	22
4. COMPUTATION OF DRAFT-SCALE VERTICAL MOTIONS IN A HURRICANE	27
5. CONCLUDING REMARKS	35
6. ACKNOWLEDGEMENTS	36
7. REFERENCES	37



COMPARISON OF DRAFT SCALE<sup>1</sup> VERTICAL VELOCITIES  
COMPUTED FROM GUST PROBE AND CONVENTIONAL DATA  
COLLECTED BY A DC-6 AIRCRAFT

Toby N. Carlson and Robert C. Sheets

In an experiment involving six passes through cumulus clouds on October 27, 1969, the draft scale vertical motions determined from the RFF inertial platform gust probe were compared with those computed from the conventional DC-6 output of pitch angle, true air speed, and radio altimeter. The results showed a high correlation between the two records of vertical motion particularly where no power setting changes were made during straight line flights through six cumulus clouds over the Florida Everglades. Indications are that the conventional method of measuring vertical motions provides useful accuracy in the study of individual cumulus clouds. An analysis of vertical draft velocity in Hurricane Debbie (1969) yielded reasonable profiles of vertical motions across the eye and wall cloud of the hurricane.

## 1. INTRODUCTION

Various investigators have spent considerable time and energy in attempts to measure selected scales of vertical motion in the atmosphere based on aircraft displacement. A properly instrumented aircraft is thought to be capable of providing information on the vertical motions associated with horizontal scales of motion ranging from about 10 meters to 10 meters in length where the magnitude of the vertical motions range from 10 to 10 cm/sec. This part of the vertical motion spectrum encompasses cumulus motions as well as lee waves and clear air turbulence. A leading investigator in the field of aircraft measurement of turbulent motions in the lower atmosphere is Bunker (1955; 1960; 1968; 1969). Others such as Jones (1954), Malkus (1954), Carlson and Glass (1962), Telford and Warner (1962), Cunningham, Glass, and Carlson (1963)

---

<sup>1</sup>The draft scale is that scale of motion in the atmosphere which lies roughly between 0.1 and 10 km in length.

Ross (1966), and Axford (1968) have attempted to measure the draft scale motions in cumulus clouds and thunderstorms while Vergeiner and Lilly (1969) have used aircraft measurements in a study of mountain waves. Gray (1965) computed vertical velocities along radial legs in hurricanes using data from the NHRL files which were gathered on board a B-50 aircraft. One of the earliest attempts to measure draft scale motions by aircraft was in the Thunderstorm Project (Byers, 1949).

The basic approach for computing vertical motion with aircraft data is to measure the vertical motion of the aircraft relative to the ground and to calculate the vertical motion of the air relative to the aircraft as determined from the pitch, roll, and angle of attack of the aircraft. The sum of these two components is equal to the vertical motion of the air relative to a fixed horizontal plane. In two dimensions (roll neglected) the angular component of the vertical velocity is represented simply in figure 1 which shows the pitch angle  $\theta$ , defined as the inclination of the longitudinal axis of the plane to the horizontal, and the angle of attack  $\alpha$ , the latter being the inclination of the longitudinal axis to the relative wind. In calm air, with no vertical component of air motion, the aircraft will assume an equilibrium position to maintain constant altitude. This equilibrium position will differ somewhat from the horizontal and may change with time as fuel is consumed. Following Gray (1965), the deviational quantities of pitch angle of attack  $\alpha$  and true air speed  $V_t$  are each defined with respect to an equilibrium value of that quantity or that

$$\theta_d \equiv \theta - \theta_e \quad (1)$$

$$\alpha_d \equiv \alpha - \alpha_e \quad (2)$$

$$V_{td} \equiv V_t - V_{te} \quad (3)$$

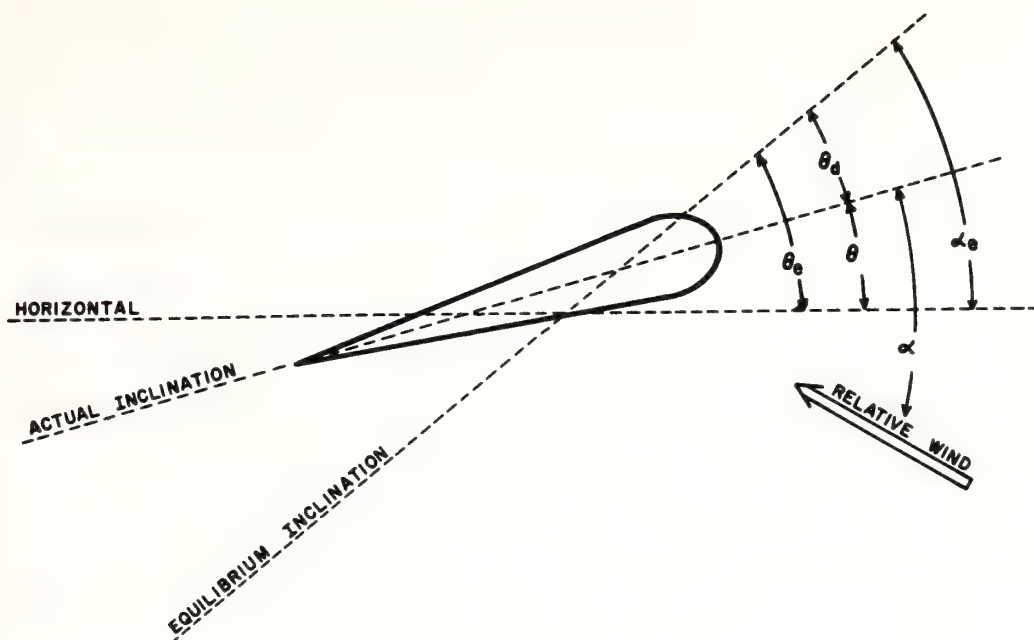


Figure 1. Airfoil in an updraft.

where the subscripts d and e refer to deviational and equilibrium values, respectively.

For small angles, the vertical gust velocity,  $W$ , can be expressed as

$$W = V_t (\alpha_d - \theta_d) + W_p \quad (4)$$

where  $W_p$  is the vertical velocity of the aircraft. (Note that since  $\theta_e \approx \alpha_d$ ,  $\alpha_e - \theta_d \approx \alpha - \theta$ ) On the RFF DC-6 aircraft the true air speed, pitch angle, and radio altitude are measured respectively by the aircraft sensors and recorded digitally on tape at one second intervals. The pitch angle measurement comes from an APN-81 pitch gyro located near the center of gravity of the plane and the radio altitude determined from a Stewart-Warner APN-159 instrument. The angle of attack is not directly measured on the aircraft but a rough estimate can be made from the aircraft equation of motion (see next section). The lag times of the pitch and radar altitude are probably less than one second but the

rapid pulses received by the radio altimeter are not electronically integrated and therefore the one second values of altitude are subject to some spurious fluctuations.

A lot of controversy has surrounded vertical velocity computations derived from the conventional aircraft instrumentation. As the result of numerous uncertainties in measuring the vertical wind there has been a widespread desire among meteorologists to see a more reliable system developed, one which would be as independent of the aircraft response as possible. Recently, various measurements in inertial Platform Gust Probe systems have been developed in England (Ross, 1966; Axford, 1968) and in the United States by the Air Force (Dutton, 1967) for its project HICAT. A modification of the latter system was adapted by the Research Flight Facility (RFF) of NOAA for use during BOMEX and is described by Lappe (McFadden et al., 1970). According to Axford (1968) the maximum error in vertical velocities determined by data from such a gust probe will be less than 1 m/sec. The average uncertainty inherent in the measurements should be much less than this figure, possibly no more than 10 or 20 cm/sec. In the investigation of turbulent conditions associated with cumulus clouds or clear air thermals, an uncertainty in  $W$  of at least 20 to 40 cm/sec can be tolerated without serious harm being done to the flux and energy calculations. Accepting the uncertainty, it becomes permissible in dealing with Axford's gust equations to permit the cosines of angles to be zero and the sine (or tangent) to be equal to the angle itself. Thus Axford's equation for  $W$  can be reduced to

$$W_g = V_{tg} (\alpha_g - \theta_g) + W_p + \ell(d\theta/dt)_g \quad (5)$$



where  $l$  is the distance between the center of gravity of the aircraft to the tip of the boom and the subscript  $g$  refers to the measurements made with the RFF gust probe package.

On October 27, 1969, the ESSA DC-6 (39C) aircraft made a series of six passes through individual cumulus clouds at 11,000 ft over the Florida Everglades. Mounted on board the aircraft was the gust probe package which provided a separate but parallel set of measurements to those obtained from the conventional system. It is our objective in this paper to compare, both visually and statistically, gust probe and "conventionally-determined" draft scale vertical motion and to assess the usefulness of the conventional system in terms of its ability to duplicate the profiles of vertical motion which were obtained from the more reliable gust probe system.

## 2. COMPUTATIONS

Vertical motions derived from the gust probe system were processed by Turbulence Consultants, Inc. and Rinaldi Consultants, Inc. A low frequency band pass filter was designed to sharply remove all scales of motion in the gust probe data which were less than 1 second duration (about 100 meters), the rate at which data pieces are digitally recorded in the conventional RFF system. No filtering was done on scales of motion larger than one second other than the averaging which was taken over the total length of each pass. In the processing of gust probe data the individual components were treated as deviations from their respective means over the 4 or 5 minute duration of the pass.

In the gust probe system, the vertical velocity of the aircraft was measured from an accelerometer located on the boom structure and evaluated using the customary relationship  $W_{pg} = \int_{t_1}^{t_2} a_z dt$ , where  $a_z$  is the vertical acceleration of the aircraft. Scale analysis suggests that the torque term,  $(ld \theta/dt)_g$ , is negligibly small, a fact confirmed by the processed gust probe data. Neglecting the torque term, (5) is quite similar to (4). In the conventional system, however, the angle of attack is computed indirectly and the aircraft displacement is measured by a radio altimeter instead of being determined by integrating the acceleration. Because of spurious high frequency fluctuations contained in the data the basic one second values of  $\theta$  and  $V_t$  were smoothed using a 4-second running mean. Aircraft displacement was computed from the difference in radio altitude between the beginning and end of the 4-second period using a centered 3-second running mean to compute both the initial and

final altitude along the segment. (For hurricane work, a straight 6-second average, instead of the 4-second running mean, is used in making the vertical velocity computations.) Vertical velocity measurements were still generated at one-second intervals.

Except for Gray's (1965) work, the radio altimeter has not recently been used aboard aircraft to measure air motions. The radio altimeter is obviously useless for this purpose over hilly or irregular terrain. Both the Everglades and the ocean, however, are exceedingly flat. Gray has stated that the term  $\alpha_d$  is usually less than  $0.2^\circ$  when averaged over several seconds or more. Examination of the data for October 27 showed that  $\alpha_d$  was considerably smaller than  $\theta_d$  most of the time although the former occasionally attained values of a degree or more for a period of 2 or 3 seconds. An attempt was made to reduce spurious fluctuations in the altimeter data. Prior to determining each value of  $W_p$ , the basic unsmoothed height measurements were subjected to a least squares fit of the data taken over a 6-second running interval which overlapped the basic 4-second interval used to form the vertical displacements of the aircraft. Height values which differed from the linear trend by an amount which was considered to be excessive were rejected in favor of the least squares value, the latter being subsequently used in determining  $W_p$ . Less than one value in 20 was rejected in this way.

A serious difficulty arises in the use of (4) with respect to the evaluation of  $\theta_e$ . Because of fuel consumption and changes in power setting,  $\theta_e$  will vary gradually during the course of an extended flight though not appreciably so in short cumulus passes. On longer

flights, however,  $\theta_e$  may suffer a considerable variation with time. A direct measurement of  $\alpha_d$  would circumvent this problem in view of the equivalence of  $\theta_e$  and  $\alpha_e$  but this is not yet possible on the RFF aircraft. It should also be pointed out that  $\theta_e$  can be seriously affected by turns or changes in power setting.

For straight (radial, in the case of hurricanes) passes we make use of (4) to determine  $\theta_e$  by assuming that the calculated value of  $W$  is negligibly small when averaged over a sufficiently large interval or that

$$\tilde{W} \equiv \frac{1}{T} \int^T W dt \approx 0. \quad (6)$$

Here  $W$  refers to a running average vertical motion over the interval  $T$  and applies to the mid point of that interval.

Equation (4) becomes in view of (6)

$$0 + \overbrace{[V_t \theta - V_t \alpha_d - W_p]} = \tilde{V}_t \theta_e \equiv \tilde{V}_t \theta_e \quad (7)$$

The equilibrium value of  $\theta$ , solved for in (7) refers to the mid point of the sliding scale of length  $T$  which may be less than the total pass duration. At that point the calculated vertical motion is computed using an equilibrium value of  $\theta$  which requires that the mean vertical motion over the interval  $-T/2$  to  $+T/2$  be zero. Alternatively,  $\theta_e$  could be computed by simply forming an average of  $\theta$  as in (6). However, conditions which would result in  $\tilde{W}$  differing appreciably from zero would also result in  $\tilde{\theta}$  differing appreciably from  $\theta_e$ ; thus the predicament remains.

In hurricane flights of a half hour or more the value of  $T$  was chosen to be 15 or 20 minutes (50-70 miles). Obviously, the computations are unable to be determined by this method at times closer than  $T/2$  from



the end points of the passes. In practice the original equilibrium interval of  $T$  was allowed to compress progressively to a value of  $T/2$  between times  $T/2$  and  $T/4$  from the end points, allowing the equilibrium pitch angle to be continuously measured in that interval. Between  $T/4$  and 0 seconds from the end points  $\theta_e$  was fixed at its value at  $T/4$ . In short cumulus passes, such as the ones made on October 27, 1969, the value of  $T$  was set equal to the duration of the pass and the single value of  $\theta_e$  derived thereof was used as a constant for that pass. It is evident, therefore, that scales of motion of length greater than  $T$  can not be accounted for by these calculations. For passes which are large compared to the scale of the vertical motions the residual error between the true vertical velocity and the measured  $W$  will be rather small, i.e. it will be below the resolution of which the system is capable. In hurricanes, however, and in flights along the axis of a cloud band the residual may be rather large. Adjustment of the zero line may be necessary in such instances provided that a reasonable physical basis for determining this displacement can be established. One criterion for this is to assume that the vertical motion profile approaches zero at a great distance from the cloud or, in the case of hurricanes, near the center of the eye.

Gray (1965) was unable to measure  $\theta$  or  $\alpha$  directly but he calculated the former using the lifting equation for aircraft motion. Our procedure makes use of the normal equation for aircraft motion to calculate  $\alpha_d$ .

This equation is written

$$\Delta N = \frac{1}{2} \frac{\rho S}{m} (V^2 \frac{dC_L}{d\alpha} \alpha_d + 2V_t C_L V_{td}) - V_t d\theta_d/dt, \quad (8)$$

where  $\Delta N$  is the normal acceleration,  $\rho$  the air density,  $S$  the wind area,  $C_L$  the coefficient of lift and  $m$  the aircraft mass. The various constants were obtained from RFF and, to the best of our knowledge, are appropriate to the DC-6. These are  $m = 4.5 \times 10^7$  g ( $\pm 10$  percent),  $S = 1.36 \times 10^6$  cm<sup>2</sup>, and  $C_L = 0.092 + 0.368 (\alpha \text{ in degrees})$ . If one assumes that the normal acceleration is approximated by the second derivative of the RA,  $d\theta/dt \approx d\theta_d/dt$ , and  $\alpha \approx \theta_e$  in the expression for  $C_L$  then (8) can be solved for  $\alpha_d$  in terms of known quantities. The expression we obtain is

$$\alpha_d \text{ (degrees)} = \frac{720}{\rho V_t} \left( \frac{\Delta N}{V_t} - \rho V_{td} [0.00278 \theta_e + 0.0112] + d\theta/dt \right) \quad (9)$$

where the components are in cgs units and the angles in degrees. The deviational air speed was approximated by taking the departure of the true air speed from a 20-40 second least square fit of  $V_t$ . The other terms were determined from a least squares fit of the data taken over the small (4 seconds for cumulus passes) smoothing interval for  $\theta$  and altitude of flight.

Table I. Statistical summary of cloud run data showing a comparison between gust probe data (subscript g) and conventional data (subscript c) for the vertical motion ( $W$ ) and for the components of the gust equation, pitch angle ( $Vt \theta_d$ ), vertical aircraft velocity ( $W_p$ ) and angle of attack ( $Vt \alpha_d$ ).\*

PASS NO.	VERTICAL GUST VELOCITY ( $W$ )							PITCH ANGLE ( $Vt \theta_d$ )				
	$\sigma_c$	$\sigma_g$	$\sigma_{g*}$	$(\sigma_g/\sigma_c)$	R	$F_c$	$F_g$	$\sigma_c$	$\sigma_g$	$\sigma_{g*}$	$(\sigma_g/\sigma_c)$	R
90 SEC. + PASS #1	90	59	58	1.06	0.70	-0.1	-0.2	44	44	18	0.45	0.87
131 SEC. + POWER SET CHANGE PASS #2	92	37	68	2.05	0.73	-0.6	0.0	48	42	25	0.61	0.83
78 SEC. PASS #3	82	45	72	1.60	0.48	-0.4	-0.2	63	55	33	0.60	0.85
60 SEC. POWER SET CHANGE PASS #4	75	64	114	1.78	-0.33	-3.6	3.8	29	31	19	0.61	0.80
55 SEC. PASS #5	44	56	51	0.91	0.50	-0.3	-0.4	32	26	9	0.35	0.97
84 SEC. + POWER SET CHANGE PASS #6	70	42	56	1.46	0.48	-0.4	0.0	27	23	16	0.66	0.84

PASS NO.	VERTICAL AIRCRAFT VELOCITY ( $W_p$ )							COMPUTED/MEASURED ATTACK ANGLE ( $Vt \alpha_d$ )				
	$\sigma_c$	$\sigma_g$	$\sigma_{g*}$	$(\sigma_g/\sigma_c)$	R	—	—	$\sigma_c$	$\sigma_g$	$\sigma_{g*}$	$(\sigma_g/\sigma_c)$	R
90 SEC. + PASS #1	57	49	44	0.90	0.64	—	—	** (40 SECONDS) 34 24		41	1.73	0.04
131 SEC. + POWER SET CHANGE PASS #2	74	44	53	1.32	0.71	—	—	** (81 SECONDS) 44 23		40	1.75	0.40
78 SEC. PASS #3	67	57	52	0.91	0.66	—	—	52	21	47	2.24	0.44
60 SEC. POWER SET CHANGE PASS #4	56	71	90	1.27	0.02	—	—	49	25	49	1.96	0.28
55 SEC. PASS #5	50	61	46	0.75	0.67	—	—	36	12	32	2.65	0.43
84 SEC. + POWER SET CHANGE PASS #6	64	38	46	1.29	0.77	—	—	** (44 SECONDS) 37 17		30	1.76	0.59

+ AVERAGE OF TWO SEGMENTS

\*\* TWO SEGMENTS MADE, COMPUTED OVER ONE SEGMENT

\* Parameters listed in the table are for the standard deviation ( $\sigma$ ) of the respective samples and the adjusted error deviation ( $\sigma_{g*}$ ) which is defined in the text. R is the linear correlation coefficient between the two records and F the water vapor flux in m cal/cm/sec. Small figures in parenthesis listed under R are the linear correlation coefficients in the case where the derived angle of attack was omitted from the conventional calculations. The duration of the flight segment and other pertinent information is listed under the column labelled Pass No.

Table II. Same as Table I but for clear air segments.

PASS NO.	VERTICAL GUST VELOCITY ( $W$ )							PITCH ANGLE ( $Vt \theta_d$ )				
	$\sigma_c$	$\sigma_g$	$\sigma_{g*}$	$(\sigma_g/\sigma_c)$	R	$F_c$	$F_g$	$\sigma_c$	$\sigma_g$	$\sigma_{g*}$	$(\sigma_g/\sigma_c)$	R
70 SEC. PASS #1	278	251	142	(0.73) 0.57	(0.80) 0.86	149	156	174	173	39	0.23	0.98
92 SEC. POWER SET CHANGE PASS #2	124	104	86	(0.72) 0.83	(0.74) 0.73	6	-13	71	77	50	0.65	0.78
112 SEC. PASS #3	156	154	98	(0.98) 0.64	(0.86) 0.80	51	76	109	105	47	0.45	0.90
85 SEC. POWER SET CHANGE PASS #4	124	195	213	(1.21) 1.09	(0.02) 0.16	-33	-12	126	112	59	0.53	0.88
126 SEC. PASS #5	137	296	238	(0.81) 0.80	(0.61) 0.61	34	79	117	103	75	0.73	0.78
125 SEC. POWER SET CHANGE PASS #6	89	62	77	(1.17) 1.24	(0.37) 0.53	3	-4	55	50	33	0.46	0.81

PASS NO.	VERTICAL AIRCRAFT VELOCITY ( $W_p$ )							COMPUTED/MEASURED ATTACK ANGLE ( $Vt \alpha_d$ )				
	$\sigma_c$	$\sigma_g$	$\sigma_{g*}$	$(\sigma_g/\sigma_c)$	R	—	—	$\sigma_c$	$\sigma_g$	$\sigma_{g*}$	$(\sigma_g/\sigma_c)$	R
70 SEC. PASS #1	208	182	155	0.85	0.69	—	—	82	89	90	1.01	0.44
92 SEC. POWER SET CHANGE PASS #2	98	102	53	0.52	0.86	—	—	75	59	66	1.12	0.54
112 SEC. PASS #3	137	141	57	0.40	0.92	—	—	81	61	86	1.41	0.30
85 SEC. POWER SET CHANGE PASS #4	150	196	165	0.84	0.58	—	—	92	87	90	1.03	0.50
126 SEC. PASS #5	130	238	235	0.99	0.29	—	—	67	37	82	2.22	-0.17
125 SEC. POWER SET CHANGE PASS #6	81	62	51	0.82	0.78	—	—	58	44	59	1.34	0.35

### 3. STATISTICAL EVALUATION OF CONVENTIONAL DRAFT SCALE MEASUREMENTS

#### 3.1 A Total Comparison

Superimposed records of the gust probe and conventional vertical motion data are shown in figures 2 (a-f). As an aid in outlining the cloud dimensions, a graph of the absolute humidity is presented above each pair of vertical motion traces. Significant departures of the vapor content of the air from the ambient value of absolute humidity ( $3\sim\text{g}/\text{m}^3$ ) denotes the presence of cloud or evaporated cloud material; total saturation occurs at about  $7\text{ g}/\text{m}^3$ . Passes 1, 3, and 5 were made through cumulus clouds with the pilot attempting to maintain constant power setting and altitude; in passes 2, 4, and 6 the pilot was instructed to change the power setting at will. The purpose in doing this was to assess the effects of such power set changes on the calculations. Inadvertent or procedural augmentation and reductions in power are made in hurricanes when the aircraft penetrates the eye wall or enters a particularly intense band of cumulonimbus. It was unfortunate that the three passes chosen to make power setting changes were associated with the three weakest clouds, thus making it more difficult to assess the effect of changing power on the updraft profile.

Tables 1 and 2 statistically summarize the degree of match between the conventional and gust probe calculations for cloud and clear air regimes, respectively. The 'cloud runs' correspond approximately to the turbulent conditions in and around the cloud; the end points of the cloud runs are delineated in figures 2 (a-f) by the (dotted) vertical lines which are labelled accordingly. The clear air statistics are composed of an average of the two (approximately equal) data segments which lie on either side



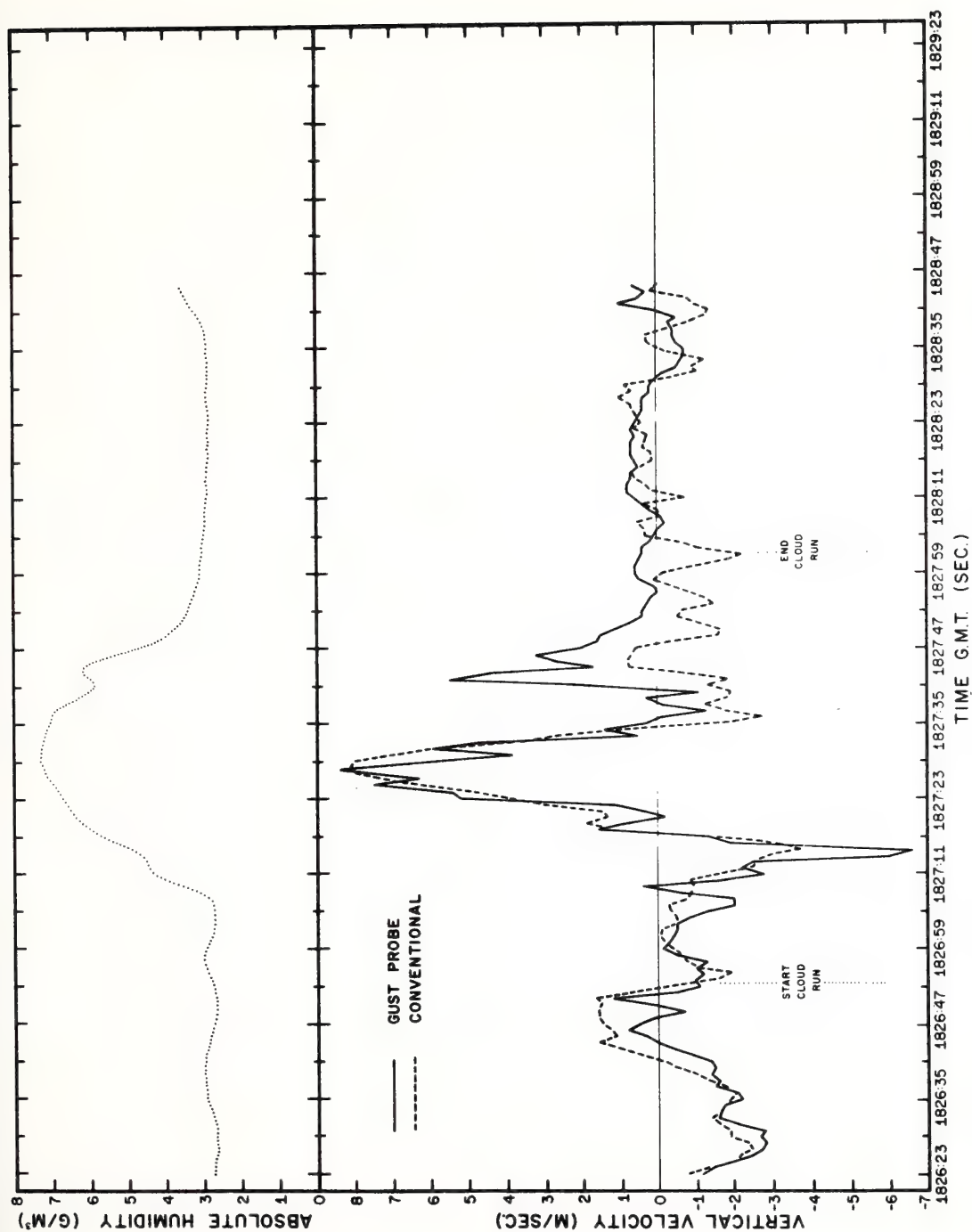


Figure 2(a). Profiles of draft-scale vertical motion and absolute humidity in pass 1. Statistics compiled in table 1 refer to segment of flight which lies between vertical pecked lines labelled start and end cloud run.

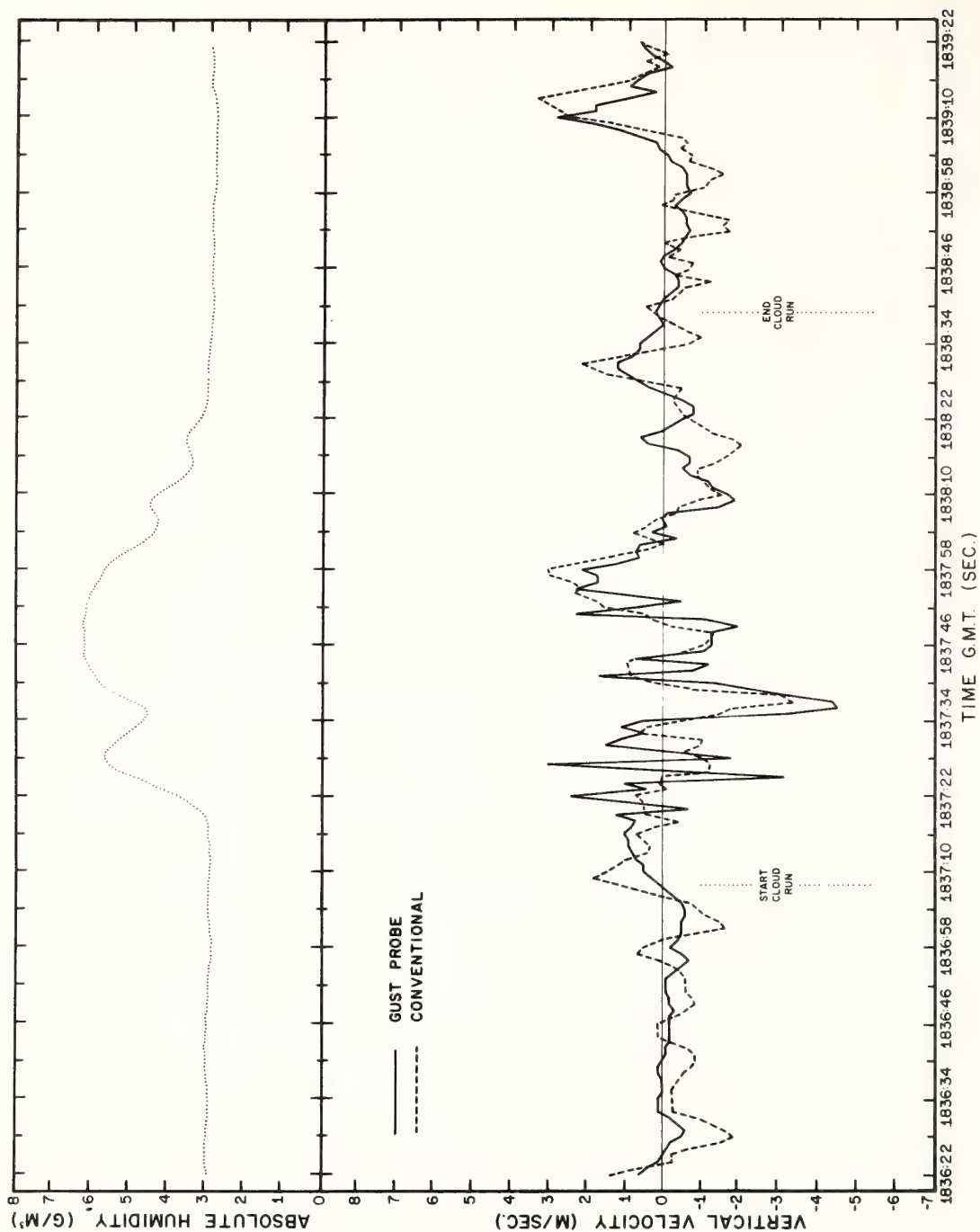


Figure 2(b). Same as figure 2a but for pass 2.

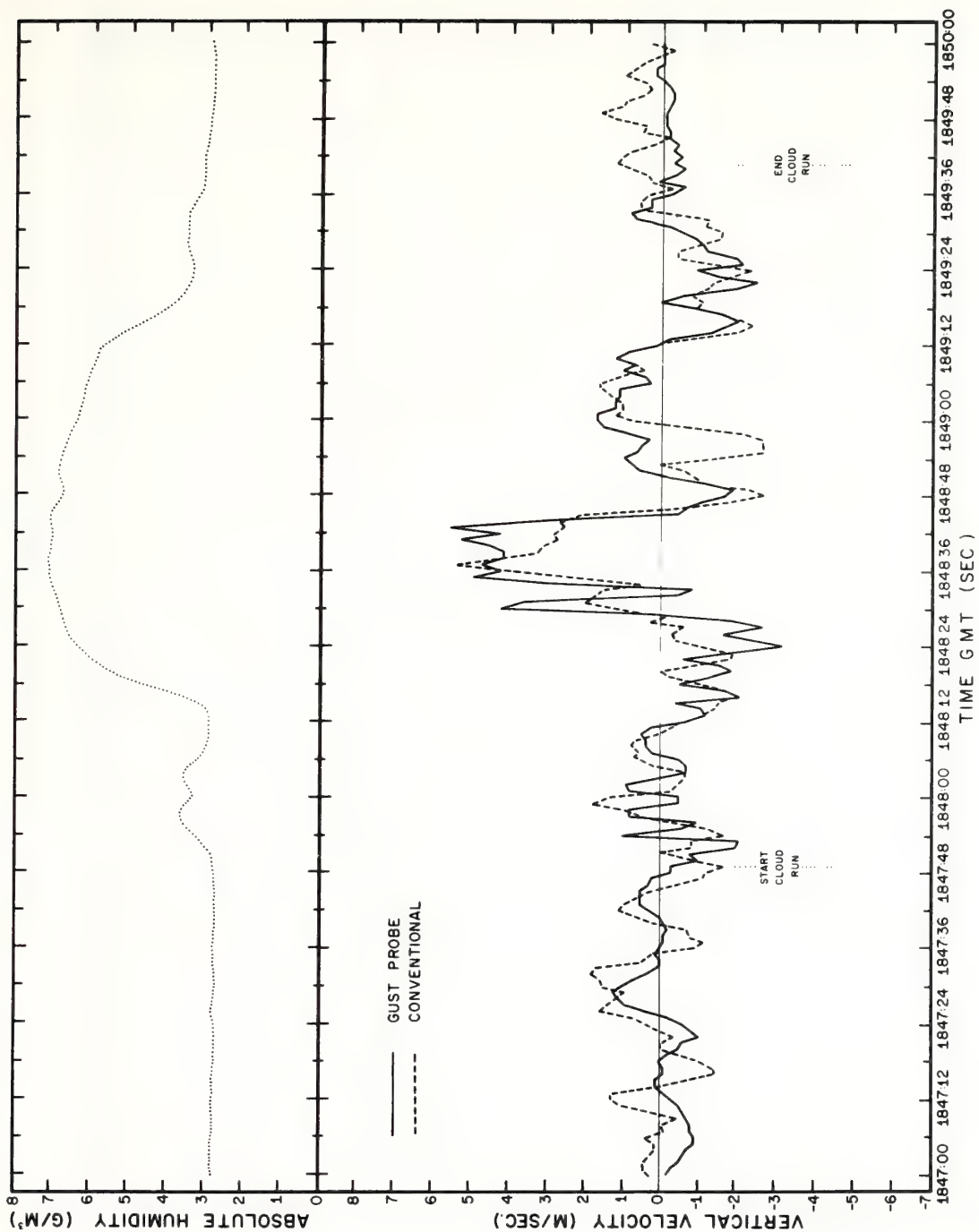


Figure 2(c). Same as figure 2a but for pass 3.

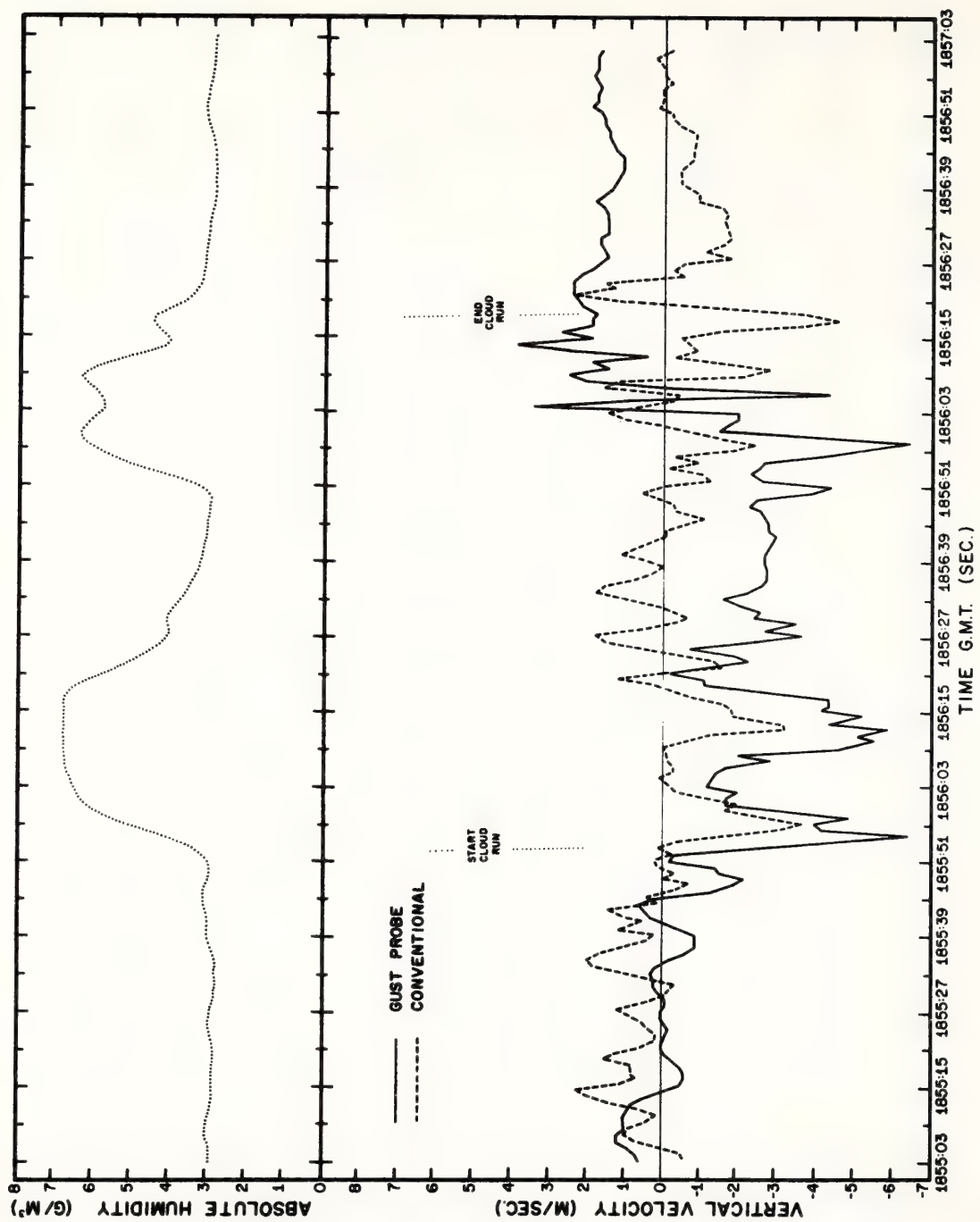


Figure 2(d). Same as figure 2a but for pass 4.



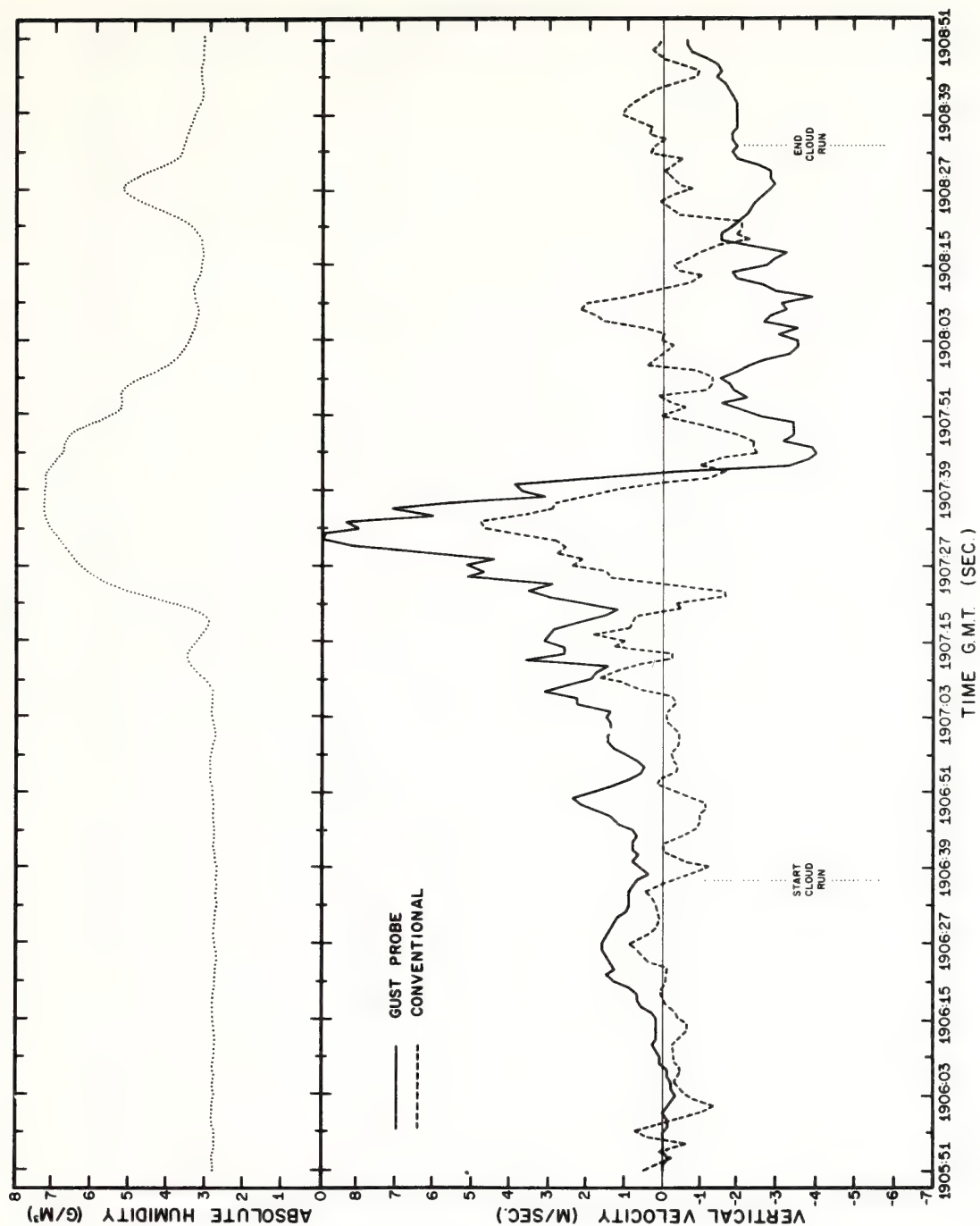


Figure 2(e). Same as figure 2a but for pass 5.

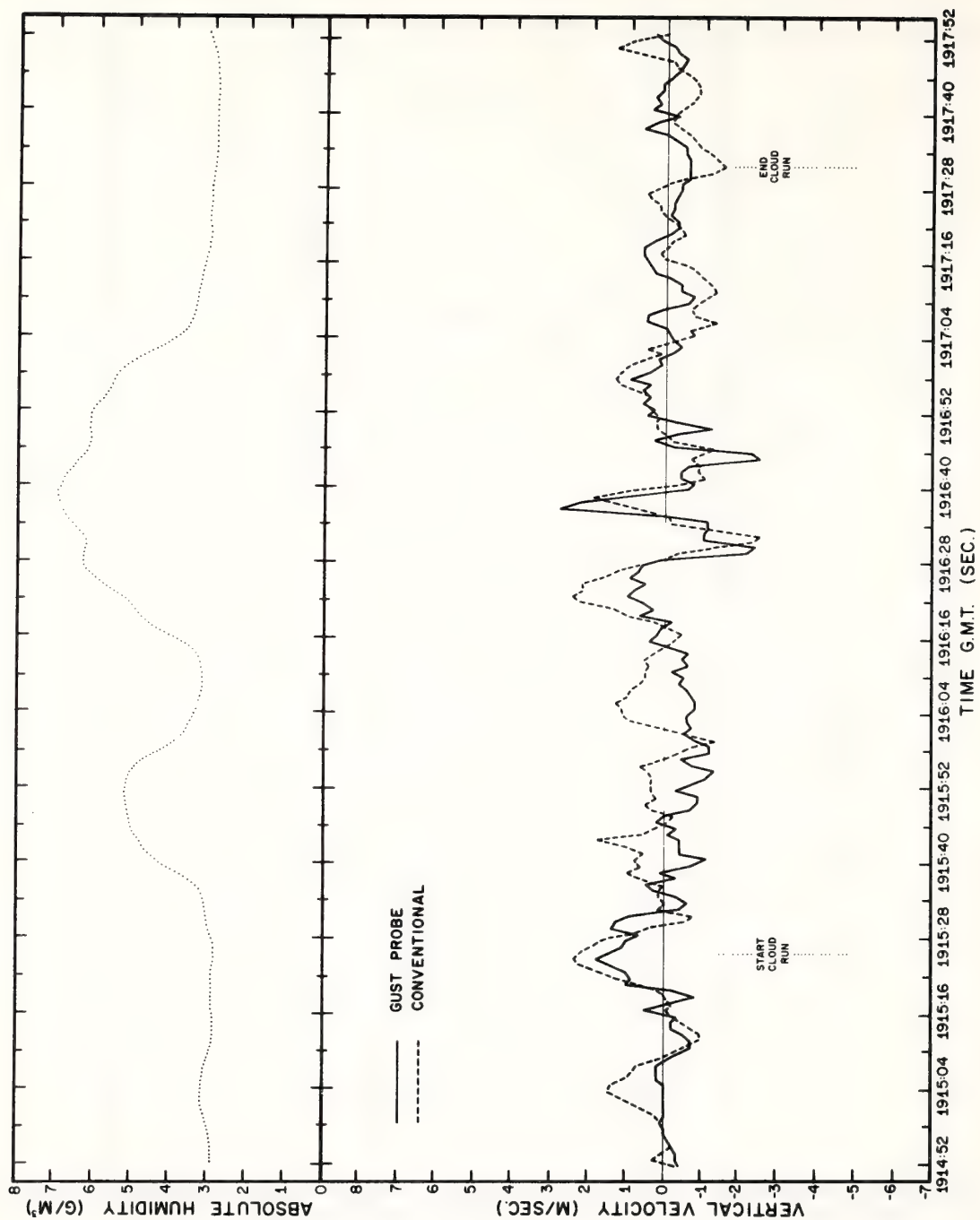


Figure 2(f). Same as figure 2a but for pass 6.

of the cloud run segment. In tables 1 and 2, statistics for each of the four components in the gust velocity (4) are presented separately, showing the standard deviation of the record  $\sigma$  (the square root of the variance), the adjusted standard deviation of the error  $\sigma_e^*$ , and the linear correlation coefficient R between the gust probe (subscript g) and the conventional system (subscript c). The error sigma,  $\sigma_e^*$ , is defined as the standard deviation of the point by point differences between the two records after the means have been subtracted out of both the records or that

$$\sigma_e^{*2} = \sigma_e^2 - (\bar{X}_c - \bar{X}_g)^2 \quad (10)$$

where the bar operator represents the record average over the particular segment. It should be noted again that the records are composed of data taken at one-second intervals. In determining tables 1 and 2 the original gust probe records, shown in figures 2 (a-f), have been smoothed by taking a 4-second running average in order to conform to the smoothing used in making the conventional calculations. In addition to the linear correlation coefficient R, a measure of record similarity is the error to signal ratio ( $\sigma_e^*/\sigma_g$ ), a concept which contains the implication that the gust probe data are essentially perfect. In actuality the gust probe will not yield perfect information and therefore the statistics will generally underestimate the reliability of the conventional system.

A comparison of the water vapor fluxes (F) for both records is also shown in tables 1 and 2. The fluxes (m-cal/cm<sup>2</sup>/sec) were computed using the formula  $F = \overline{Lw^1q^1}$ , where L is the latent heat of condensation for water, q is the mixing ratio in g/m<sup>3</sup>, and the bar operator refers to an average over the segment of the pass (clear or cloudy) in question.

Additional cloud physics information concerning maximum droplet size and liquid water content of the six cumuli are presented in figure 3. The liquid water content was computed from cloud particle samples collected by a continuous hydrometeor sampler which consists of a moving strip of soft aluminum foil exposed to the ambient airflow through a small slot. Cloud particles larger than 200 microns in diameter leave impressions when they impact on the foil, the liquid water content of the large (raindrop) sized hydrometeors is computed using a method similar to that used by Tacheuchi (1969). Maximum drop diameters were obtained at approximately 1.35-second intervals and liquid water contents were computed over each 5.4-second interval. Terminal velocities corresponding to the largest drop sizes were obtained from a relationship experimentally obtained by Gunn and Kinzer (Byers, 1965). Figure 3 therefore contains a qualitative but independent assessment of cloud activity and updraft strength based on the maximum fall velocity of the drops.

On the whole, passes 1, 3, and 5, show the better agreement between the gust probe and conventional data than passes 2, 4, and 6 both visibly, in terms of the location and strength of the maximum up- and downdrafts, and with respect to the statistical parameters of tables 1 and 2. In pass 1, the records are remarkably similar except that the secondary updraft at 1827:45 failed to be captured in the conventional record. Cloud pass 5 exhibits the strongest updrafts (9.2 m/sec) according to the gust probe data but is clearly less substantial than cloud 1 which contained a considerably higher liquid water content and much larger droplets. Although the gust probe is undoubtedly superior to the conventional system



# FLIGHT 691027-A

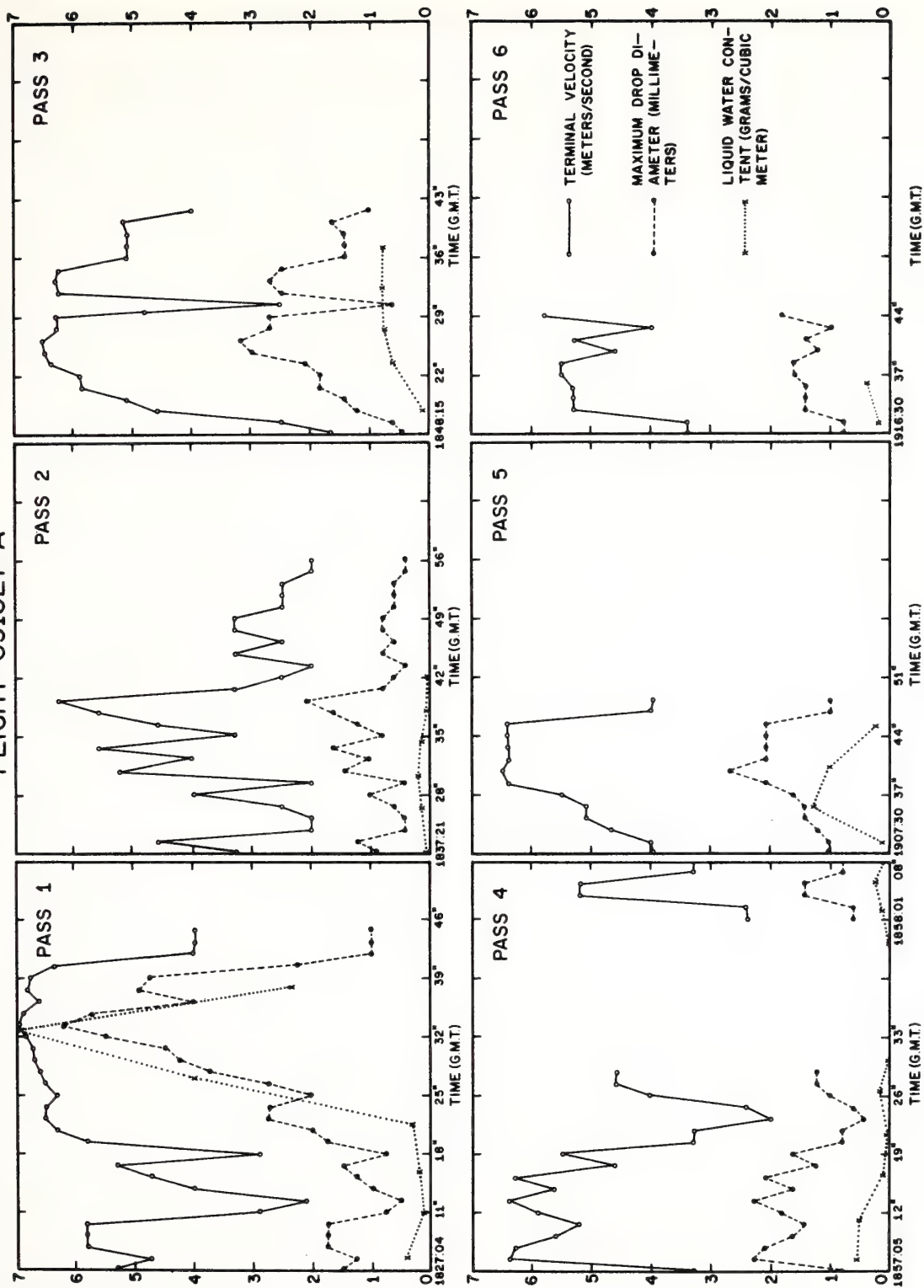


Figure 3. Selected hydrometeor data for passes one through six.

### 3.2 Agreement As A Function Of Wavelength

In an attempt to assess the dependency of  $\sigma_e$  and  $\sigma_e^*/\sigma_g$  on the wavelengths, the harmonic analysis (power spectra distribution) was computed for each of the six passes over the entire length of the pass using the generalized E-M method described by Evans et al. (1963). This method determines the autocorrelation coefficients in one step and then transforms them into power spectral density using Fourier techniques. Numerical uncertainties, probably resulting from the shortness of the records and the singularity of having a discrete cumulus cloud in the middle, made it necessary to average the power over discrete wave bands for each pass and then combine the averages for all six passes in order to arrive at a representative value for that wave band. In figure 4 the power density (variance) spectrum versus wavelength is presented for the gust probe measurements on a log-log scale. The mean variance in each wave band is shown by a series of horizontal line segments through which a smooth curve has been drawn. The figure shows the decrease in power with decreasing wavelength that customarily occurs in cumulus spectra (see Rhyne and Steiner, 1964).

The semi-log plot at the top of figure 4 shows the ratio  $(\sigma_e^*/\sigma_g)$  as a function of wavelength. Here  $\sigma_e^*$  was obtained from a power spectral analysis of the error variance  $\sigma_e^*$  comparable to the one done for  $\sigma_g$ . The ratio of the two was formed for each wave band and plotted as a series of single points. The pair of smooth curves drawn through the points represent values for all six passes combined and for just the three passes in which no power setting changes were made.

in measuring draft scale vertical motions the former may have suffered from a pronounced zero drift in passes 4 and 5. In that case, the major ascending plume at 1907:33 may have been overestimated by at least a couple meters per second in  $W_g$ ; after 1907:39 the zero shift seems to have been in the opposite direction. The same problem may also be afflicting pass 4 which yielded the worst comparison with conventional data in both clear and cloud runs. Pass 2, despite power set changes, is in better mutual agreement than pass 5 with respect to the correlations although  $(\sigma_e^*/\sigma_g)$  and the fluxes are slightly poorer for this run.

In clear air passes 1, 3, and 5 are generally superior to the other three runs even though the variance of the records are about the same. However, statistical agreement is notably poorer in the clear air runs than it is in cloud, signifying the improvement gained in the statistics with increasingly turbulent conditions. In the non-constant-power set runs the fluxes agree in sign and in magnitude to within a factor of about 2 in either regime. Even with power setting changes a certain amount of useful information is contained in the conventional data; for example, the agreement between the primary up- and downdraft profiles in passes 2 and 6 (figures 2b and 2e). Under constant power setting and in turbulent conditions ( $\sigma_c > 100$  cm/sec) the draft scale vertical motions computed conventionally and those which represent the true values are felt to be in reasonable agreement.

Agreement between the individual components in the gust probe (4) is by far the best with respect to the pitch angle term,  $(V_t \theta_d)$  as compared to the other terms. Unfortunately, most of the variance in  $W$  comes from the aircraft vertical velocity ( $W_g$ ), a component which has a poorer correspondence between conventional and gust probe values than does the pitch angle. It appears that the inability of the conventional system to attain more than about 5 m/sec in pass 5, as compared with 9 m/sec for  $W_g$  at the point of maximum updraft, is entirely attributable to the much smaller aircraft vertical motions determined from the radio-altimeter. Since the pitch angle variance was not particularly large in pass 5 there is additional reason to suspect the accuracy of the gust probe accelerometer in this run. By far the worst correspondence in the gust equation lies in the angle of attack values  $(V_t \alpha_d)$ , a fact not surprising in view of the vastly differing ways in which they are determined for each system. Nevertheless, there appears to be some information contained in the computed angle of attack. Draft velocities computed from (4), using the computed value of  $\alpha_d$  determined from (7), are found to be slightly superior to those generated with  $\alpha_d$  set to zero (see parenthesized figures located above the bold-faced numbers in table 1). Although the variance of  $\alpha_d$  is small compared to that of  $W$ , there is obviously no substitute for measuring this term directly.



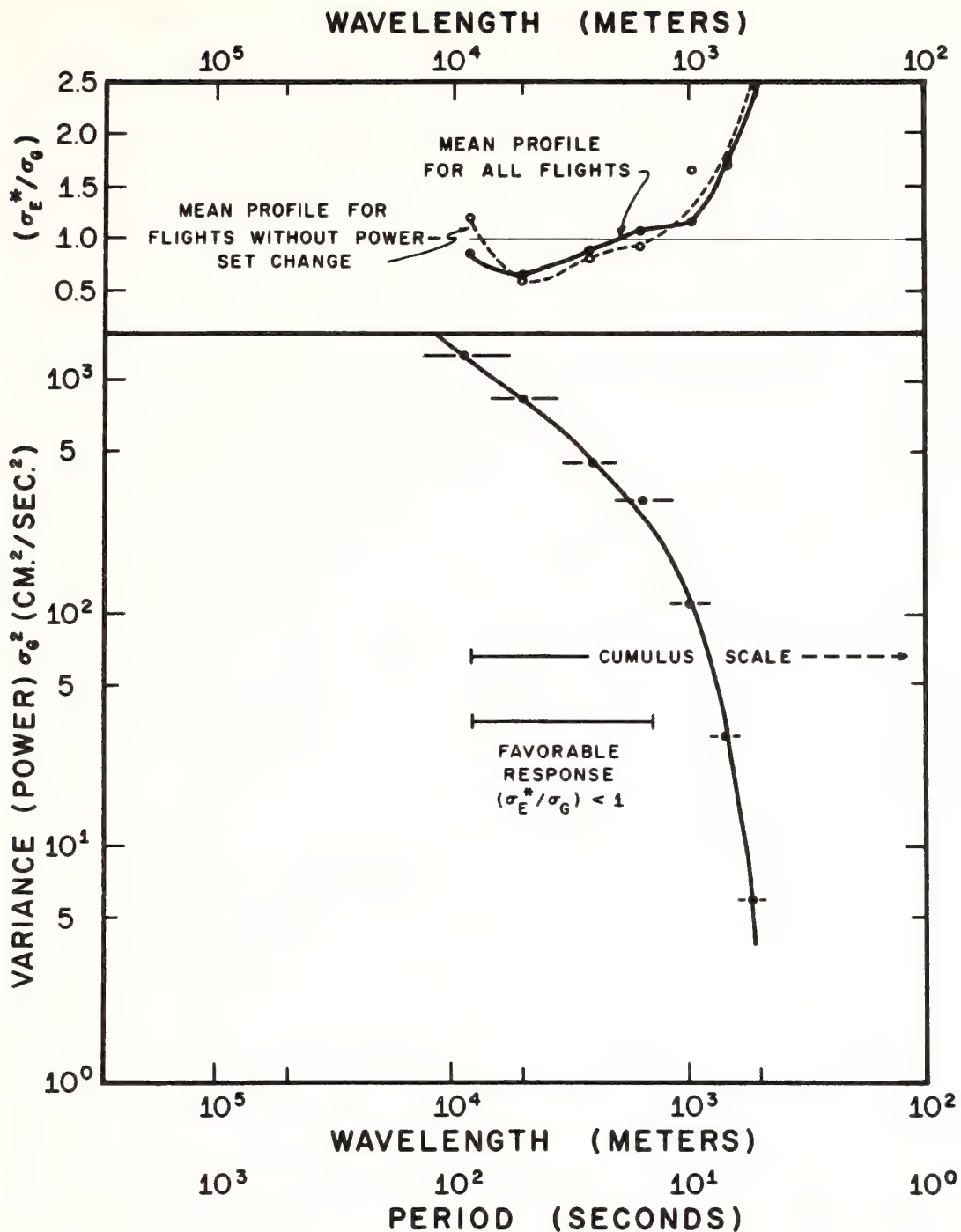


Figure 4. Variance (Power spectrum density) of the gust probe vertical motions versus wavelength (period) for the six cumulus passes (lower part of figure). Horizontal line segments indicate width of spectrum over which the average power (signified by the solid dot) was computed. The top pair of curves show the ratio  $(\sigma_E^*/\sigma_g)$  as a function of wavelength for all six passes (solid curve and filled dots) and for the three passes made without power setting changes (dashed curve and open dots).

Lowest values ( $\sim 0.6$ ) are found near 4000 meters, the approximate width of the cumulus cloud and its surrounding perturbation in the clear air. Between 1000 and 4000 meters wavelength this ratio remains below 1.0, a value considered by this author to be a reasonable criteria for a favorable comparison between gust probe and conventional motions. Below 1000 meters the ratio rises sharply with decreasing wavelength. Thus, on the scale comparable to the width of a cumulus cloud the conventional system provides a favorable response to the pattern of updrafts and downdrafts particularly when power setting changes on the aircraft are reduced to a minimum. Although it is not possible to assess with any reliability the dependency of the forementioned ratio on the intensity of the turbulent motions it seems quite likely that the system responds more favorably when there is a greater amount of energy in the longer wave lengths.

Part of the difficulty in measuring the smaller scale of vertical motions lies in the inability of the conventional system to properly determine  $\alpha_d$ . Tables 1 and 2 show that the magnitude of  $\alpha_d$  is grossly overestimated in the conventional system during passes in clear air but is comparable to that obtained from the gust probe in cloudy regimes. Another factor in the poor agreement at short wavelengths may be the use of a running mean which acts as an imperfect filter and therefore distorts wavelengths near or below 400 meters (in the case of a 4 second running mean).<sup>2</sup>

---

<sup>2</sup>At present a running binomial smoother is being used which is thought to be an improvement on the straight running mean.

#### 4. COMPUTATION OF DRAFT-SCALE VERTICAL MOTIONS IN A HURRICANE

Gray (1965) has attempted to measure draft scale vertical motions in hurricanes, arriving at some radial profiles of vertical motion from which he compiled a set of statistics on draft strength and width. With an improved system on board the DC-6, capable of making more accurate measurements than were available to Gray, and with some confidence gained in the validity of the data as the result of the gust probe comparison, we find it desirable to reopen the question of measuring hurricane vertical motions with an aircraft. In this section vertical motions associated with Hurricane Debbie (1969) will be discussed.

As stated in section 2, the vertical velocity is determined at the center point of a sliding time scale of length,  $T$ , over which the mean vertical motion is assumed to be zero. In cumulus work the basic data sub-unit was a 4 point running average of the one-second interval observations; the interval  $T$  is regarded as the length of the straight line pass--usually a few minutes duration. In hurricanes, the data are manifestly less steady. The smaller scales of motion investigated in cumulus passes are felt to be of even less general importance and have less reliability in the hurricane flights. Radial legs are typically 15 to 45 minutes in duration and a single pass may intersect rainbands, both eye walls, and the eye itself.

It was decided in hurricane work to use a 6-second (~600 meter) block average (not a running mean) for the basic data sub-unit and a 12-minute (~72 km) interval for  $T$ . As stated in a previous section, the value of  $\theta_e$  is determined by assuming that the mean vertical motion is

zero when averaged over the 72 km interval except for the interval centered between  $T/2$  and  $T/4$  from the end points. Here the original value of  $T$  is gradually reduced from  $T$  to  $T/2$  at  $\pm T/4$  from the end points; closer than  $\pm T/4$  from the end points  $\theta_e$  is held constant. This procedure permits  $\theta_e$  to vary slowly in response to a drift or to slow oscillations in the actual equilibrium pitch angle. The results of section III suggest that the effects of infrequent power setting changes by the pilot may not seriously compromise the results although it should be noted that power setting changes simulated in the October 27 passes were not likely representative of the actual power setting changes that take place in an eye wall penetration.

On August 20, 1969, ten passes were made through Hurricane Debbie by the RFF 39C aircraft during Project STORMFURY.<sup>3</sup> Figure 5 shows an example of the vertical motions, along with wind speed, temperature, and a composite of the vertical profile of the radar presentation, on a northeast to southwest traverse at 12,000 ft. In this figure the 6-second block values of vertical motion have been additionally smoothed using a centered 36-second running mean. Southwest of the eye center the tallest and widest isoecho contour coincides closely with the largest updraft ( $\sim 5$  m/sec). Elsewhere the principal updrafts tend to coincide with isoechoes and the stronger downdrafts with gaps between the cells. In the eye itself the computed vertical motions behave erratically, in contrast to one's expectations. Strongest winds recorded were located

---

<sup>3</sup>See Project STORMFURY, Annual Report 1969.



HURRICANE "DEBBIE" AUGUST 19, 1969 FLIGHT 690820A1  
 NORTHEAST — SOUTHWEST CROSS SECTION ALTITUDE ≈ 12,000 FT.

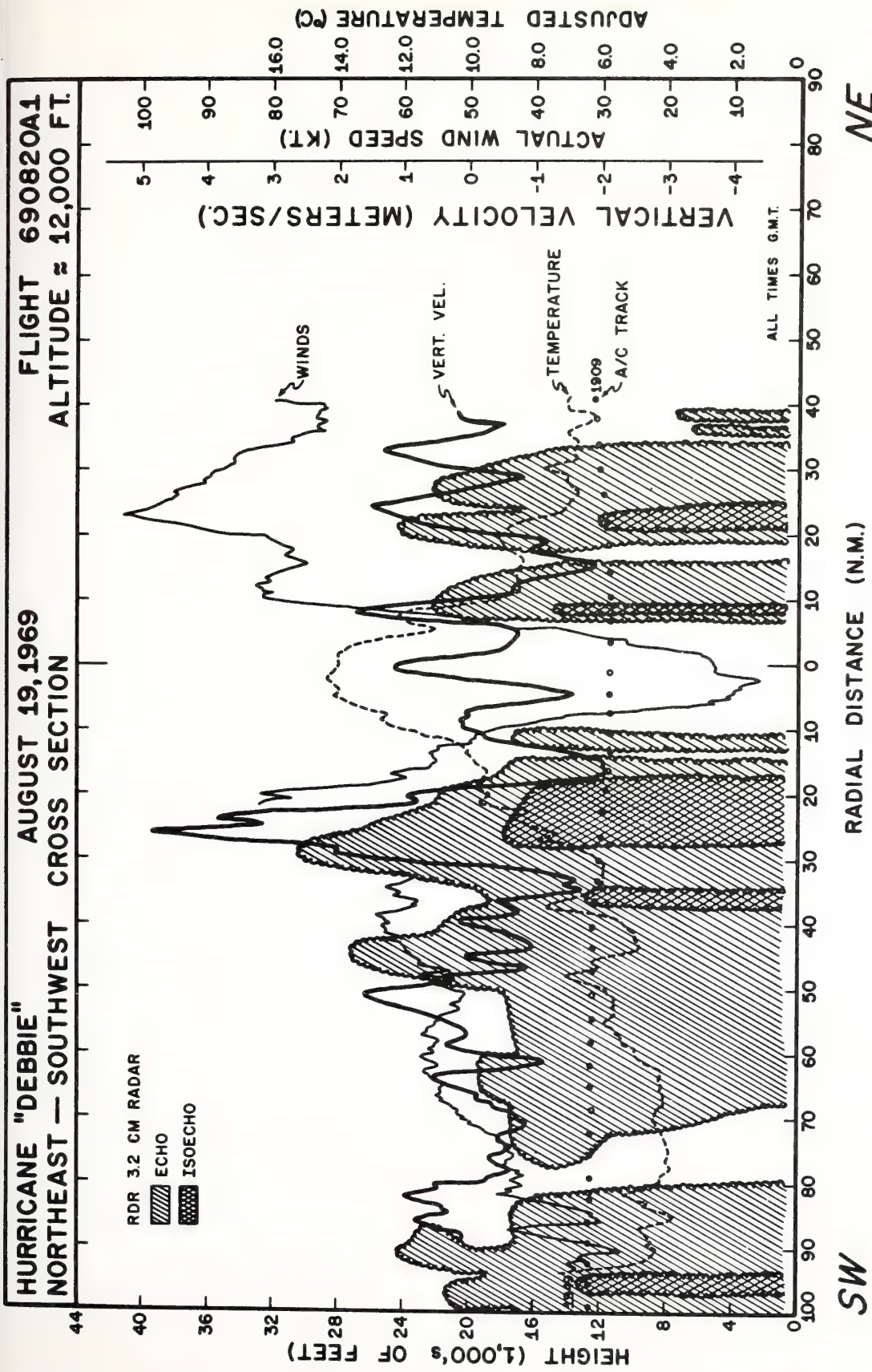


Figure 5. Profiles of vertical velocity (heavy solid line), wind speed (thin solid line), temperature (dashed line) along a northeast to southwest pass through Hurricane Debbie at approximately 12,500 ft. Range-height contours of low and high gain (iosecho) radar echoes are indicated by hatched and cross hatched lines, respectively. The aircraft track, starting at 1909 GMT and ending at 1940 GMT, is indicated by the row of closed circles spaced at one minute intervals.

on the northeast side of the storm; however, the wind speeds computed relative to the moving storm were about equal on both sides of the eye wall.

Altogether eight passes were made along the same azimuth, four approaching the eye from the northeast and four from the southwest. An arithmetic composite of the eight passes was made by first aligning the data for each radial segment such that the point of entry or exit through the physical eye wall was mutually in common and then averaging the vertical motions for all passes. Examination of the initial data, however, revealed that the eye of Hurricane Debbie consisted of an inner 'undisturbed region,' over which temperature, humidity and tangential wind varied slowly in the horizontal, and a transition region, across which the wind speed and dewpoint decreased rapidly (inward) and the temperature increased at a rate comparable to that found near the edge of the eye wall cloud. Since the eye itself varied in size from one pass to another the inner eye was composited separately and then linked together with the vertical velocity profile averaged relative to the eye wall in order to produce a mean profile of vertical motion across Hurricane Debbie. In figure 6 the solid curve is the composite vertical velocity profile with respect to the azimuth from the eye center. In order to examine the directional bias in the computations the vertical velocity profile was also formed without regard to azimuth, the starting and finishing points of the flight being on the left and right, respectively, of figure 6 (dotted curve). Ideally, the latter profile should be symmetric, unlike the former which would show real aximuthal variations.

HURRICANE "DEBBIE"  
AUGUST 20, 1969  
FLIGHT 690820A  
MEAN VERTICAL VELOCITY (CM./SEC.)

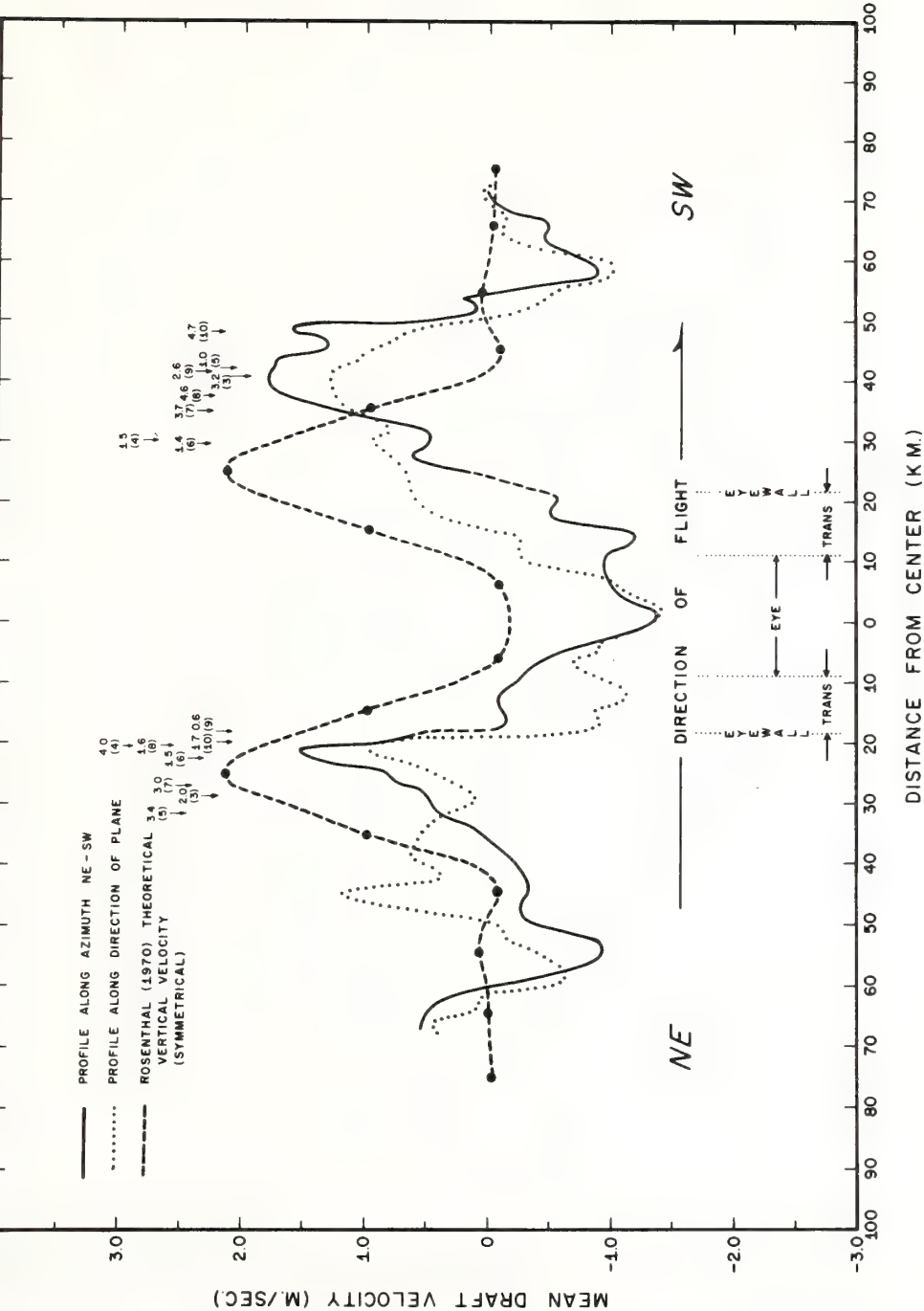


Figure 6. Composite profiles of vertical motion through Hurricane Debbie averaged from eight separate passes through the storm at approximately 12,000 ft. (For meaning of profile legends, see test.) Figures shown above profiles (with arrow showing location of point along azimuthal profile) give maximum strength of updraft (meters per second) within eye wall band for passes three through ten (pass number in parentheses). Dashed curve is for Rosenthal's (1970) symmetric hurricane model.

According to figure 6 the southwest portion of the hurricane appears to have been stronger than the northeastern sector in terms of the maximum value of  $W$  ( $\sim 2$  m/sec). The overall draft profile, however, resembles Rosenthal's (1970) symmetric model. Individual updrafts are shown to vary considerably in strength and location from pass to pass, figure 5 being representative of one of the strongest updrafts. Sinking motion of about 1 m/sec is found in the eye and on the outside edges of the eye wall cloud. This amount of subsidence in the eye seems excessive and may be attributed to the effects of power setting changes. Alternatively, it could be explained by the fact that the residual vertical motion on scales larger than  $T$  are not captured by the method of calculating  $W$  due to an incorrect value of  $\theta_e$ . The existence of scales of vertical motion having dimensions greater than  $T$  (as well as the presence of systematic fluctuations in power setting near the eye wall) can result in an underestimate of  $W$ , not only in the eye wall cloud but across the eye itself. In this event, a correction in the form of an undetermined amount of ascending motion may have to be added to the updraft profiles in figure 6 to make them more realistic. According to Miller (1963) the mean upward vertical motion at 700 mb in Hurricane Donna, 1960, averaged between 20 and 80 km, was slightly greater than 0.6 m/sec. An upward shift of the vertical motion profiles in figure 6 by this magnitude would evidently result in better degree of fit with the Rosenthal (1970) curve, thereby encouraging one to believe that such a correction to the computed values should be made.



Following Bunker (1968) the vertical transport of sensible heat

H and water vapor E can be written

$$\begin{aligned} H &= c_p \rho (\overline{W'T'} + \overline{W^*T^*}) \\ E &= L (\overline{W'q'} + \overline{W^*q^*}) \end{aligned} \quad (11)$$

where  $c_p$  is the specific heat of air at constant pressure,  $\rho$  the air density,  $L$  the latent heat of condensation for water,  $q$  the water vapor content of the air,  $W$  the vertical velocity, and  $T$  the temperature. The fluxes are represented as energy per unit area per unit time and consist of two components, a small (cumulus) scale eddy term (signified by the primed quantities) and a hurricane-scale eddy term (signified by the product of the two starred quantities). The latter term represents the deviations in the mean of  $T$  and  $q$  in the eye wall cloud region from that in the mean tropical environment. In this case the bar signifies a linear mean taken between the eye wall and the outer edge of the wall cloud region, a distance of about 50 km. The above equations were evaluated for the individual passes and the quantities of  $E$  and  $H$  multiplied by the appropriate area, and averaged over all passes to arrive at a rough estimate for the total energy and moisture flux across the level of flight (640 mb). The values for the southwest and north-eastern portions of the storm are shown in table 3.<sup>4</sup>

---

<sup>4</sup>Since the figures refer to a linear rather than a cylindrical average in the table the values are likely to be overestimated slightly. Recalculation of the fluxes in cylindrical coordinates showed little change in the figures, however.

Table 3. Small and Large (hurricane) scale sensible heat and moisture fluxes across the 640 mb surface for the portion of Hurricane Debbie lying between the edge of the eye wall (radius 20 km) and the outer edge of the principal hurricane clouds (radius 70 km).\*

	H (small scale)	H (hurricane scale)	H (total)	E (small scale)	E (hurricane scale)	E (total)
( $\bar{\sigma} = 161$ )						
Southwest	0.3	1.2	1.5	3.7	31.5	35.2
( $\bar{\sigma} = 152$ )						
Northeast	0.7	0.1	0.8	5.6	1.6	7.2
Average eye wall band	1.0	1.3	2.3	4.6	16.6	21.2

\* Units are in joules/sec  $\times 10^{13}$  for H and cm/day of rainfall for E (see (11) and (12) in text).

Surprisingly, the small-scale eddy fluxes are smaller than the band-scale fluxes. This could indicate that processes associated with the mean hurricane circulation and with the very large clusters of cumulonimbus are the dominant ones in the eye wall band. It is probably also true that the smaller scales of motion are less adequately represented in the calculations as has been suggested in a previous section. Nevertheless, the total values in table 3 are quite reasonable when compared to the results of Hurricane Hilda (Hawkins and Rubsam, 1969). In that storm the production of kinetic energy within the inner 80 km radius was about  $0.2 \times 10^{13}$  j/sec and the rainfall in the same annular ring about 25 cm/day.

## 5. CONCLUDING REMARKS

Based on a small sample of six passes through cumulus, it seems reasonable to conclude that the conventional method of computing draft scale vertical motion can yield values which are not only meaningful but are relatively quick and inexpensive to obtain. According to the results shown in this paper one can tentatively conclude that on a straight line flight through an individual cumulus cloud, the linear correlation between the vertical velocities computed by the conventional method and those which actually exist may be 0.7 to 0.9. Alternatively, the degree of fit between computed and actual vertical motion profiles as expressed by the ratio of error variance to the actual variance of the motions will be substantially less than 1.0 over the whole spectrum of wavelengths and lowest (less than 0.5) in the longer wavelengths that are comparable in scale to the width of a cumulus cloud. There is also some indication that the relative accuracy of the conventional measurements improves with increasing intensity of the vertical motions.

Power setting changes on the aircraft are shown to be detrimental to the conventional results, though less so in active cumulus clouds than in clear air where agreement between gust probe and conventional measurements was poor. It is anticipated that a direct measurement of angle of attack, using an angle of attack vane mounted on the aircraft, will be incorporated into the conventional system in the near future. This improvement would reduce the uncertainties caused by power setting changes on the aircraft and enable a better estimate of vertical velocity to be made at shorter wavelengths. Despite power setting changes and their adverse affects on the results, it was shown that reasonable profiles of vertical motions can be obtained across the principal cloud band outside the eye wall of a hurricane.

## 6. ACKNOWLEDGEMENTS

We are especially grateful to Dr. Joanne Simpson of NOAA's Experimental Meteorology Laboratory whose support made possible the comparison flight with the gust probe package and the later reduction of the gust probe data. The cooperation and support of the Research Flight Facility was also a critical factor in carrying out the project. A number of helpful suggestions and comments have been contributed by O. Lappe of Turbulence Consultants, Inc. and by Harry Hawkins of this laboratory. Mr. Robert Carrodus did the drafting and Mrs. Mary Jane Clarke typed the manuscript.



## 7. REFERENCES

- Axford, D.N., "On the Accuracy of Wind Measurements Using an Inertial Platform in an Aircraft, with an Example of a Measurement of the Vertical Mesostructure of the Atmosphere," J. App. Met., Vol. 7, No. 4, August 1968, pp. 645-666.
- Bunker, A.F., "Turbulence and Shearing Stresses measured over the North Atlantic Ocean by an airplane--acceleration technique," J. Meteor., Vol. 12, No. 5, October 1955, pp. 445-455.
- Bunker, A.F., "Heat and Water Vapor Fluxes in and flowing southward over the Western Atlantic Ocean," J. Meteor., Vol. 17, 1960, pp. 52-63.
- Bunker, A.F., "Turbulence and Turbulent Fluxes over the Indian Ocean," WHOI Technical Report: Reference no. 68-62, Unpublished Manuscript, Sept. 1968, 31 pp.
- Bunker, A.F., "Turbulence and Turbulent Fluxes over the Pacific Ocean in the Line Islands Region," WHOI Technical Report: Reference no. 69-2, Unpublished Manuscript, Jan. 1969, 17 pp.
- Byers, H.B., Elements of Cloud Physics, University of Chicago Press, Chicago and London, 1965.
- Byers, H.R., The Thunderstorm, U.S. Weather Bureau, Washington, D.C., June 1949, 287 pp.
- Carlson, T.N. and Glass, M., "Vertical Velocities obtained from aircraft accelerometer measurements in a Severe Thunderstorm," U.S. Air Force, GRD Research Note, May 1962, 11 pp.

- Cunningham, R.M., Glass, M. and Carlson, T.N., "Properties of active Cumulus Clouds Determined from Coordinated Ground Photography and Aircraft Penetrations," National Conference on the Physics and Dynamics of Clouds, Chicago, draft copy, March 1964.
- Dutton, J.A., "Belling the CAT in the Sky," Bull. Am. Met. Soc., Vol. 48, No. 11, November 1967, pp. 813-820.
- Evans, G.W., Sutherland, G.L., McCarty, R.C. and Omlor, P.H., "Comparison of Power Spectral Density Techniques as applied to Digitalized Data Records of Nonstationary Processes, Part I," Technical Report 14, prepared by Stanford Research Institute for the Pentagon. Contract SD-103, Sept. 1963, 139 pp.
- Gray, W.M., "Calculations of Cumulus Vertical Draft Velocities in Hurricanes from Aircraft Observations," Vol. 4, No. 4, August, 1965, pp. 463-474.
- Hawkins, H.F. and Rubsam, D.T., "Hurricane Hilda, 1964: II, Structure and Budgets of the Hurricane on October 1, 1964," MWR, Vol. 96, No. 9, September 1968, pp. 617-636.
- Jones, R.F., "Flights through a Thunderstorm Belt," QJRMS, Vol. 80, No. 345, July 1954, pp. 377-387.
- Malkus, J.S., "Some Results of a Trade-Cumulus Cloud Investigation," J. Meteor., Vol. 11, No. 3, June 1954, pp. 220-237.
- McFadden, J.D., Travis, C.W., Gilmer, R.O. and McGaven, R.G., "Water Vapor Flux Measurements from ESSA Aircraft," Symposium on Tropical Meteorology, June 2-11, 1970, University of Honolulu, Hawaii. Extended abstracts (AMS-WMO), pp. BIII 1-6.

- Miller, B.I., "On the Filling of Tropical Cyclones over Land," NHRP Report No. 66, U.S. Weather Bureau, December 1963, 82 pp.
- Project STORMFURY, Annual Report 1969, U.S. Dept. of Commerce, May, 1970.
- Rhyne, R.H. and Steiner, R., "Power Spectral measurement of atmospheric turbulence in Severe Storms and Cumulus Clouds," Technical Note D-2469 NASA-Langley Field, Oct. 1964, 48 pp.
- Rosenthal, S.L., "A Survey of Experimental Results obtained from a Numerical Model Designed to Simulate Tropical Cyclone Development," ESSA Technical Memorandum ERLTM-NHRL 88, U.S. Dept. of Commerce, Jan. 1970, 78 pp.
- Ross, I., "Inertial Navigation and Gust Measurements from Meteorological Research Flight Aircraft," Meteor Mag, Vol. 95, 1966, pp. 370-375.
- Takeuchi, D.M., "Analysis of Hydrometeor Sampler Data for ESSA Cumulus Experiments, Miami, Florida, May 1968," MRI FR-849, Meteorology Research, Inc., 1969, 44 pp.
- Telford, J.W. and Warner, J., "On the measurement from an aircraft of buoyancy and vertical air velocity in cloud," J. Atmos. Sci., Vol. 19, 1962, pp. 415-423.
- Veigeiner, I. and Lilly, D.K., "The Dynamic Structure of the Wave Flow as Obtained from Balloon and Airplane Observation," Monthly Weather Review, Vol. 95, No. 3, March 1970, pp. 220-232.

R. Cecil Gentry

## To tame a hurricane

The recent devastation of East Pakistan has tragically highlighted man's urgent need for means of averting hurricanes. If the successful results of Project Stormfury in the US could now be translated into routine practice, the damage caused by future hurricanes might well be halved.

HURRICANES, the most destructive of nature's phenomena, may soon have part of their own power turned against them to blunt their punches. Until recent years no hope was offered that man could reduce the increasingly heavy destruction caused by these storms which originate in the tropics and lay waste to any coast obstructing their path. The research conducted by 'Project Stormfury' since 1961 and the experiments on Hurricane Debbie in August 1969 give promise that something may yet be done.

Project Stormfury is sponsored by the United States Government and was organized to explore the structure and energy processes of hurricanes and to test the possibility of moderating their intensity. The present experiments are not aimed at 'killing' hurricanes, nor of diverting them from one area to another, nor of affecting their contributions to the general weather circulations of the world. They do, however, try to blunt the power of the killer forces in hurricanes and make the storms more acceptable to man.

Between 1915 and 1924 hurricanes

caused an average annual damage in the United States of \$13 million. By the period 1960 to 1969, this figure had soared to \$432 million. Even after adjusting these values for the inflated cost of construction in recent years (at 1957-59 costs) these statistics represent a 650 per cent increase in the average annual cost of hurricane damage in less than 50 years. Since more and more valuable buildings are being constructed in areas vulnerable to hurricanes, these damage costs should continue to increase. Hurricane Betsy of 1965 and Hurricane Camille of 1969 each caused more than \$1400 million in damage. In many other countries of the world the loss due to tropical cyclones, when expressed as a percentage of the gross national product, is even more severe than in the United States.

In the experiments on Hurricane Debbie during August 1969 the maximum wind speeds decreased in intensity by about 30 and 15 per cent on the two experimental days. We are still trying to determine whether these changes were caused by the experiment or if they were consequences of natural changes in the storm. The data are highly suggestive that some degree of beneficial modification was achieved. If later experiments confirm these indications, man may at last be able to reduce the

power exerted by the tropical cyclones.

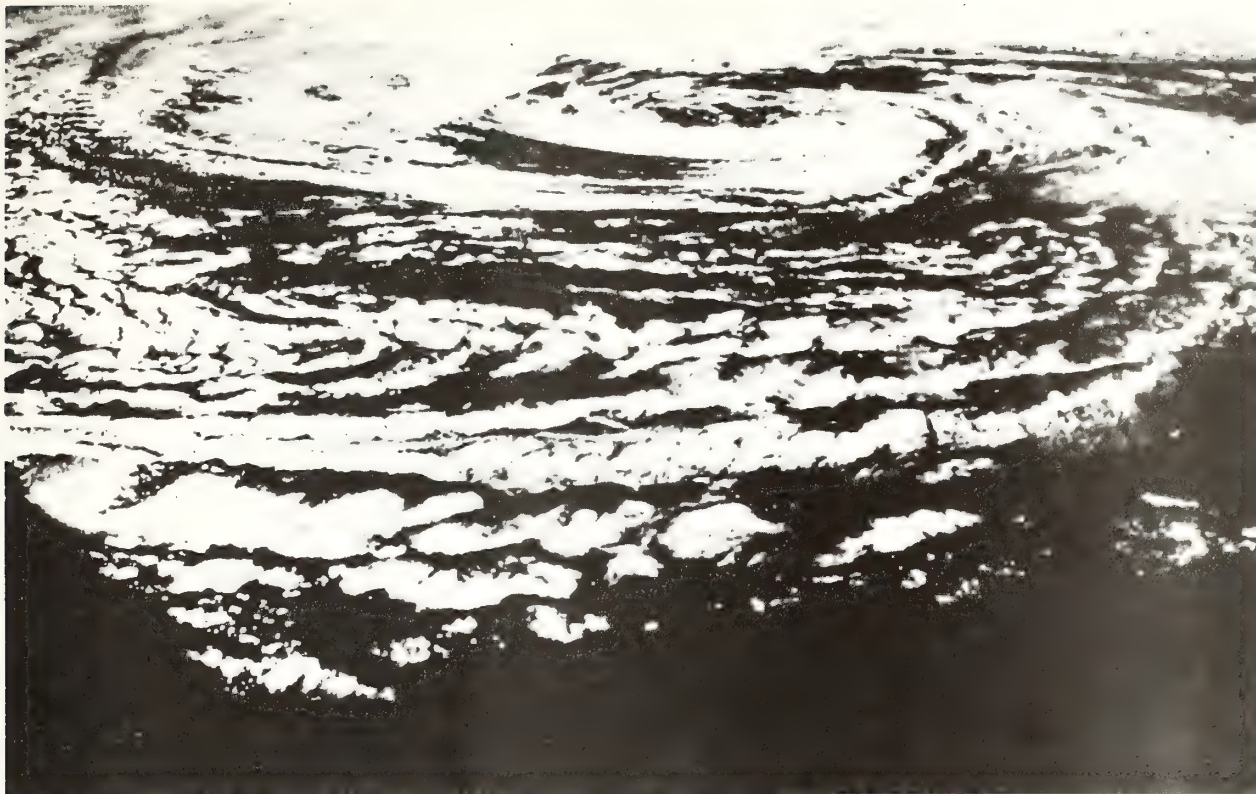
Two general considerations justify Project Stormfury. They are, first, that recent improvements in our understanding of the physical processes fundamental to hurricanes suggest promising avenues of experimentation, and, second, that enormous rewards can be derived from even a slight degree of beneficial modification. The latter may be illustrated by a rough cost-benefit analysis of hurricane research.

If the United States continues supporting hurricane modification research at the present rate for the next 10 years and if by that time we modify just one severe hurricane, such as Betsy or Camille, enough to reduce the damage by only 10 per cent, the nation will obtain more than a 10-fold return on its investment. Similarly, if within 10 years we can reduce the damage caused by such a storm by only one per cent, the nation will get its money back. The benefits in terms of prevention to human suffering are, of course, incalculable. I should emphasize that we are trying for a much higher percentage of reduction in damages, and if we learn to tame one storm partially, there is no reason why we cannot do it to others. The cost of the treatment is relatively minor; the major cost is learning how to modify the storms and in demonstrating that we can do so.

---

Dr R. Cecil Gentry is Director of Project Stormfury and Director of the National Hurricane Research Laboratory in Miami, Florida. His research has covered the prediction of hurricane motion and the structure and energetics of hurricanes.





THE FIRST DOCUMENTED effort at modifying a hurricane occurred 13 October 1947. Project Cirrus of the US Air Force, using ideas suggested by Irving Langmuir, tried a small experiment on a weak hurricane near the northeast Florida coast. Approximately 35 kilograms of dry ice were dropped into the hurricane clouds some distance removed from the storm centre. The exact results of this act could not be determined because insufficient facilities were available to monitor changes in the storm.

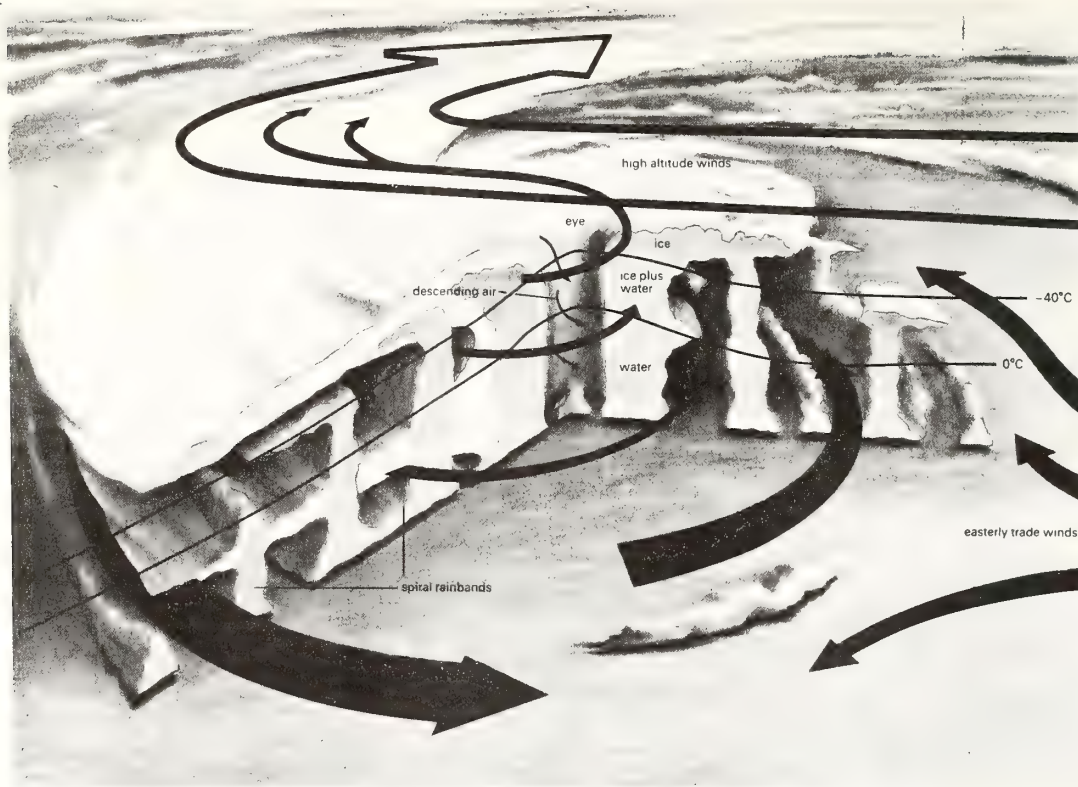
In 1961, Dr R. H. Simpson of the US Weather Bureau proposed that hurricanes might be modified by introducing freezing nuclei into the massive clouds surrounding the centre of the storm. At about the same time, Dr Pierre St Amand and his associates at the Navy Weapons Center, China Lake, California, developed pyrotechnic generators which made it practicable to introduce within a few minutes very large quantities of silver iodide into clouds. Groups from the Weather Bureau and the Navy, under the leadership of the first and second directors of Stormfury, Drs R. H. and Joanne Simpson, experimented on Hurricane Esther and Hurricane Beulah

respectively, with single seedings on two days each in September 1961 and August 1963. The results of these earlier experiments were encouraging but inconclusive, because the changes in the hurricanes were about the same magnitude as many natural changes.

The latest modification hypothesis is still being developed and is based on five assumptions. The first is that large quantities of water substance exist in the liquid state in hurricane clouds at temperatures of  $-4^{\circ}\text{C}$  to  $-30^{\circ}\text{C}$  and possibly to even lower temperatures; such cloud droplets are referred to as supercooled. The second assumption is that the droplets do not freeze because there is a scarcity of ice crystals or other natural freezing nuclei in many of the hurricane clouds. The third assumes that the introduction of silver iodide crystals or other types of artificial freezing nuclei into the supercooled clouds will cause the droplets to freeze; these frozen particles then serve as natural freezing nuclei, causing any remaining supercooled droplets to freeze. The fourth assumes that when the supercooled water freezes, it releases latent heat stored within it equal in amount to that

required to melt an equivalent mass of ice. It further assumes that this heat will increase the buoyancy of the rising air plumes; cause the ones in the clouds radially outward from the wall clouds to ascend to greater heights and thus cause the condensation of extra amounts of water vapour and release of additional latent heat. Finally, we assume that there are in fact rings or sectors in the hurricane where addition of heat will result in a reduction of the maximum wind speed.

In the 1961 experiment, eight large canisters, each containing four kilograms of silver iodide, estimated to produce  $2.4 \times 10^{15}$  silver iodide crystals, were dropped into the main clouds in the eyewall clouds surrounding the centre of Hurricane Esther. On 16 September 1961 the maximum winds decreased by about 10 per cent for a two hour period. The radar pictures of the hurricane showed some dramatic changes in the structure of the eyewall clouds, which could be explained by assuming that the water in the clouds changed to ice following the seeding. On 17 September the experiment was repeated with no significant changes observed in the storm structure. After a pilot of one of the



**TROPICAL STORM** (above left) was photographed by US astronauts on board *Apollo 9*. Hurricanes are usually less than 15 km high but may have a diameter of several hundred kilometres. Air at low levels spirals around and towards the centre of the hurricane, ascending in the massive clouds around the 'eye' of the storm, or in the rainband clouds further removed from the centre (above). As the air ascends, it expands and cools, forcing much of the water vapour present to condense. Unless there are freezing nuclei in the clouds, the water droplets may not freeze in the temperature range 0° to -40°C

monitoring aircraft reported he saw a seeding canister fall in the clear area of the eye it was assumed that the seeding agent was not properly placed.

In the 1963 experiments on Hurricane Beulah 240 kg of silver iodide were dropped into the eyewall of the storm on 24 August along a track from 25 to 65 kilometres from the centre. Following the seeding the maximum wind migrated farther outward from the storm centre—from 6.5 to 16 kilometres—and decreased by about 14 per cent. On 23

August the storm had been similarly seeded and R. H. Simpson, the Project Director, wrote: "A sudden shift in the storm track occurred just before seeding with the result that the silver iodide was dropped in an open, almost cloud free, portion and probably could not have entered the tall [cloud] towers during the 2½ hour monitoring period after seeding."

Thus, up until 1963, there were four seedings of hurricanes. On one day in 1961 and one day in 1963 results had been apparently favourable, but the changes in the hurricanes were well within the limits of changes that frequently occur in hurricanes from natural causes. On the other days, in 1961 and 1963, either the silver iodide was improperly placed, or the monitoring aircraft did not remain in the storm long enough to observe any changes that might have eventually resulted from the seeding.

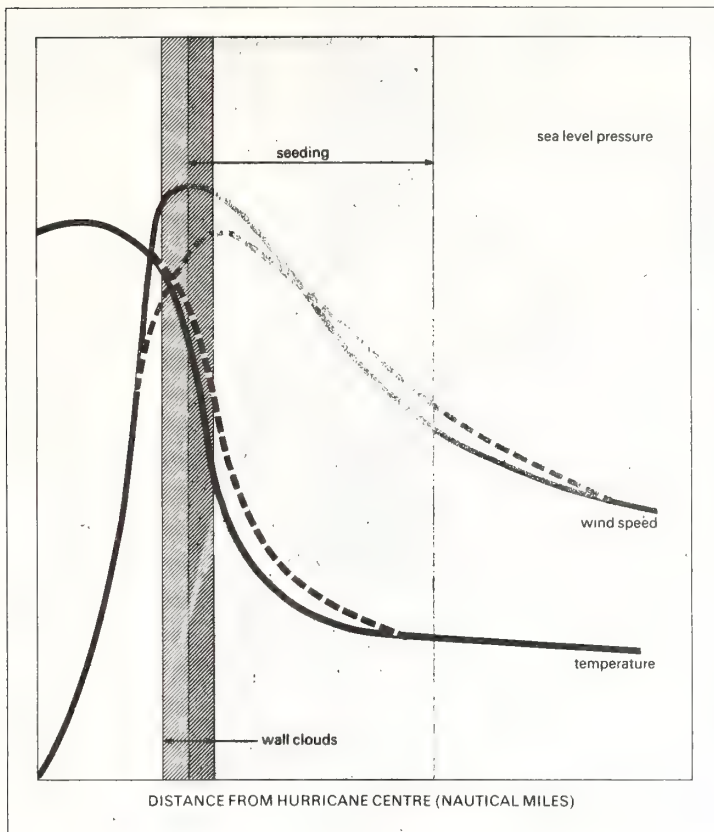
Because of the difficulty of interpreting results from the single seeding experiments, a multiple seeding experiment was planned. By seeding at two hourly intervals over a period of eight hours, one might determine if small effects from single seedings would be

either cumulative or periodic and be identified more easily by analysis of the data. The time for monitoring the clouds and hurricane structure was also greatly extended. In the single seeding experiments the monitoring aircraft stayed in the hurricane for two to three hours after the seeding. In the multiple seeding experiment, relatively complete coverage of the storm was furnished from five hours before the first seeding, through the eight hours of the five seedings, until six hours after the last seeding.

No operations were conducted in 1964 while aircraft instrumentation was improved, and no hurricane considered a suitable subject for the experiment passed through the experimental area in the years 1965 or 1966. In the earlier years of the project, experiments were restricted to a comparatively small area in the Atlantic between Puerto Rico and Bermuda from which no recorded hurricane had reached a populated land area within 36 hours.

Improvements in objective techniques for forecasting hurricane motion prior to 1967 suggested a change in the concept of selecting areas for experiments by the project. During that and later years, the





**VARIATION** in a hurricane of temperature at upper levels, pressure at sea level and wind speed at low levels are shown in the graph (left). The dashed lines indicate typical changes which could possibly be caused by seeding of supercooled clouds along a radial band outwards from the hurricane's main wall clouds

was never a severe hurricane, and on this date it had not yet gained even hurricane force. The crew flew through hurricane rainbands on three passes for a total of 20 minutes. These are areas normally characterized by heavy turbulence and heavy icing—the worst kind of flying. This portion of the flight was completed with no great difficulty. The crew then proceeded to the reforming centre of the hurricane to get information needed by forecasters of the hurricane warning centre. These data were also obtained without any problems. With the work done, the crew relaxed and started for home. They then flew through a cloud that was small compared to the ones in which they had collected the data but which, in retrospect, must have been the reforming eyewall cloud. Here they encountered the worst turbulence the Research Flight Facility had experienced in nine years of severe weather flying. All the crew were severely shaken and one had to spend several weeks in hospital. (In jest, the Research Flight Facility later sent Harry Hawkins, Assistant Director of the National Hurricane Research Laboratory, a bill for damage done to the aircraft by his hard head.)

Was it worth it? The crew did get the needed information. By contrast to what had been found in ordinary tropical clouds, the water substance in the hurricane clouds at the flight level where temperatures were  $-5^{\circ}\text{C}$  to  $-8^{\circ}\text{C}$  was nearly all in liquid drops—there being very few ice crystals. These measurements have since been repeated in other hurricanes with less drastic flight reactions, and the answer has continued to be the same. At temperatures down to at least  $-8^{\circ}\text{C}$ , there is very little ice in many of the hurricane clouds. This confirmed that there was a deficiency of natural freezing nuclei in the clouds. The insertion of artificial nuclei, therefore, might modify the clouds.

**NUMERICAL MODELS** capable of simulating the life history of hurricanes have been developed by a number of researchers at universities and in the National Hurricane Research Laboratory. While the models are not perfect, they do reproduce many features of a hurricane quite well. We have used the one developed by Dr Stanley Rosenthal at the

selection of eligible storms was based on the Environmental Science Service Administration's Weather Bureau forecasts instead of the climatological study previously used.

The new seeding eligibility 'area' was not bounded by definite co-ordinates. Under the new guidelines, a tropical cyclone in the southwestern North Atlantic (Caribbean Sea and Gulf of Mexico areas were added in 1969) was considered eligible for seeding as long as there was only a small probability (10 per cent or less) of the hurricane centre coming within 80 kilometres of a populated land area within 24 hours after the first seeding.

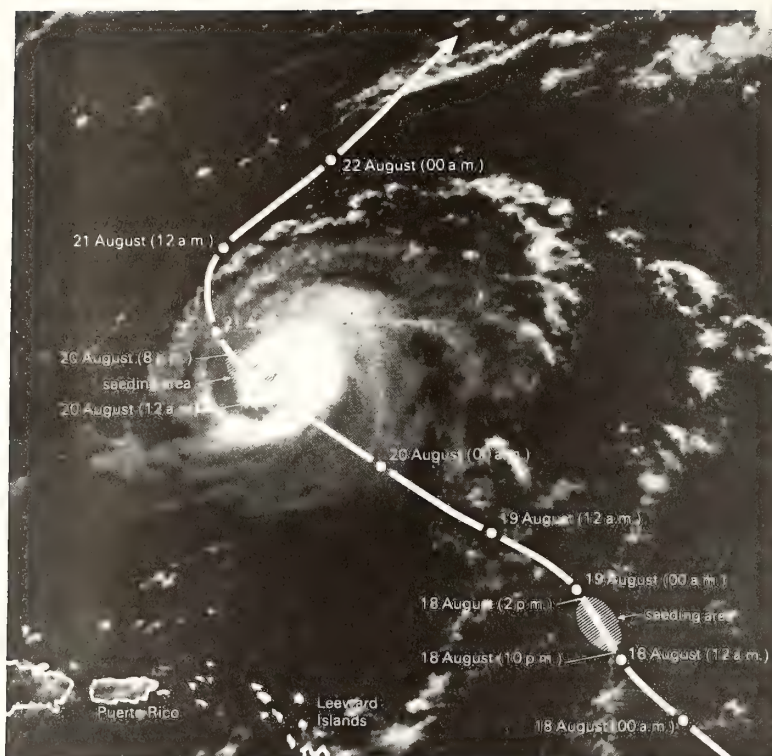
There are two primary reasons for not seeding storms near land while we are still trying to learn how to modify them. First, by seeding further out at sea, the artificially induced effects (good or bad) will have subsided before the storm can affect a land mass or cause extensive damage. Second, marked changes in the structure of a hurricane occur when it passes over land or even approaches close to land. These land-induced

modifications would obscure the short period effects produced by the seeding experiments and greatly complicate the scientific evaluation of the results.

Even though no operations were conducted on hurricanes during the period 1965-68, research continued, both on hurricanes and on development of improved pyrotechnics for distributing the silver iodide into the hurricane clouds. We tried to verify some of the statements listed among the hypotheses. The first two relate to amounts of supercooled water and number of natural freezing nuclei occurring in hurricanes.

**WE ENCOUNTERED** our roughest and most dangerous flying while making measurements in hurricane clouds of relative amounts of liquid and ice forms of water. ESSA's Research Flight Facility has been flying in hurricanes since 1960 and has been in some of the worst hurricanes—Donna, Carla, Beulah and Betsy—with no serious accident.

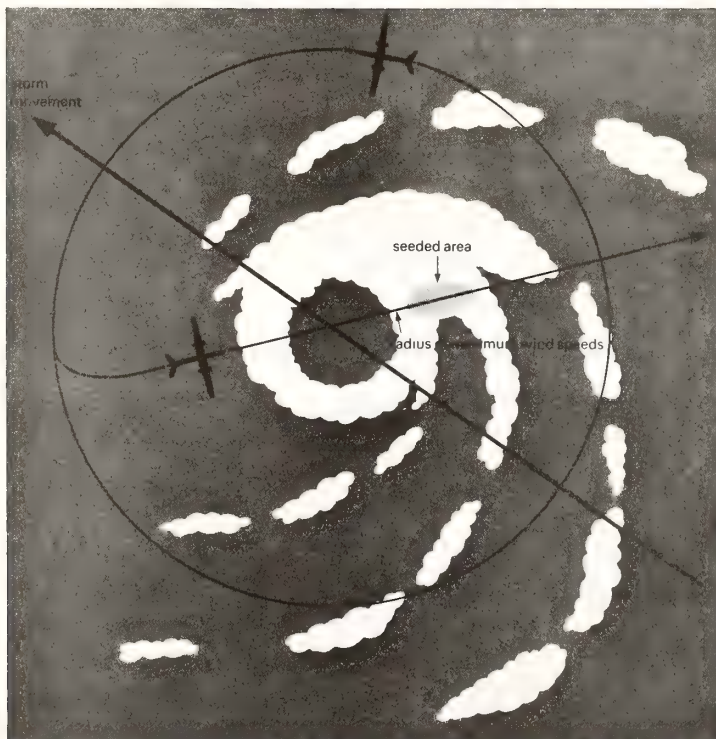
In October 1968 we sent a research flight into Tropical Storm Gladys, as it was reforming north of Cuba. Gladys



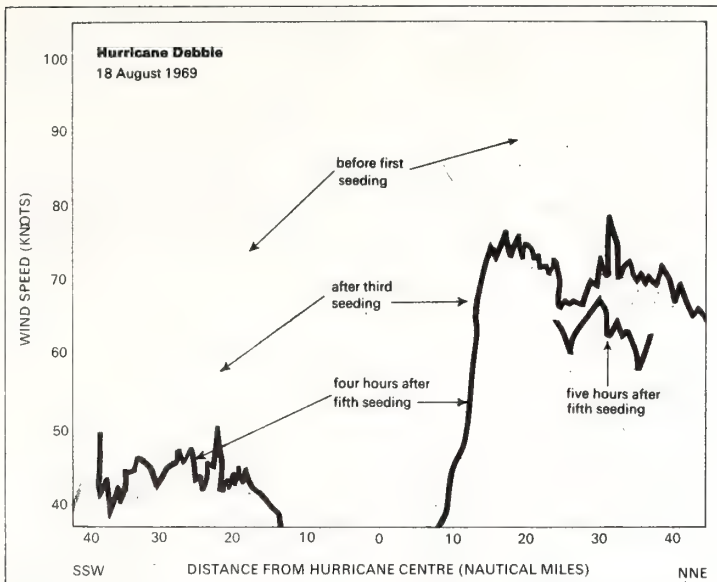
**HURRICANE DEBBIE** was seeded twice in August 1969 as it moved west-northwest towards the Caribbean (left). In these experiments, the aircraft flew at 10,000 metres altitude, discharging their pyrotechnic canisters along the radius of maximum wind speed (below left)

Hurricane Research Laboratory in Miami to answer the question concerning where in the hurricane will the addition of heat most likely result in a reduction of maximum internal wind speed. It is convenient to run the modification experiment with this model in a high speed computer. There is no waiting for nature to send a hurricane, no risking of lives, and it is much cheaper than the field experiments.

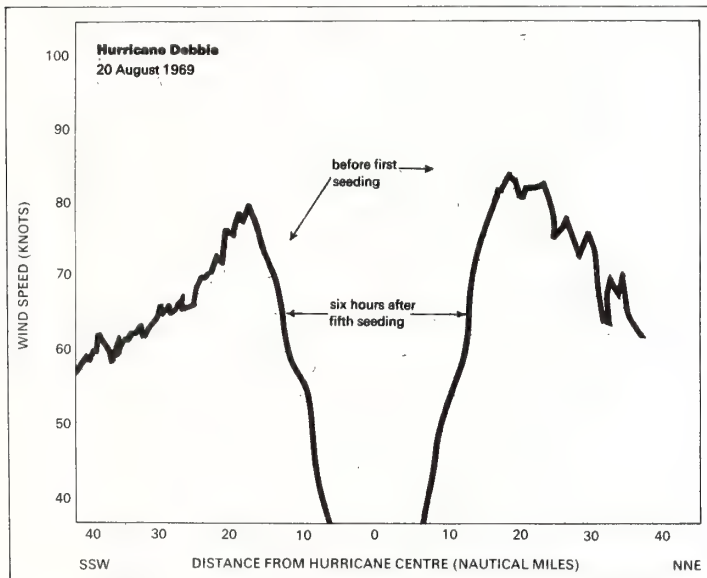
With the computer model, we simulated seeding the storm in several different bands at different distances from the centre. In particular, we tried the simulated seeding between the belt of maximum winds and the centre of the storm, across the band of maximum winds, and at radial distances greater than that of the maximum winds. We found the greatest reduction in storm intensity when we worked on the outside of the maximum winds. Incidentally this is also at the outer edge of the mass of warm air occupying the central portion of the hurricane. This location is illustrated in the diagram on page 52, which shows schematically the distribution along a radius of temperatures in the middle and upper layers of the storm, pressure at sea level and winds near the surface. Note that the air is warmest near the hurricane centre. If heat is added in the band marked seeding, the temperature distribution should change so that the difference between the temperatures in the core of the storm and those at the same elevation a few kilometres farther away should become less (see the dashed line). Pressure at sea level represents the weight of the air above. Changing the temperatures should therefore result in changes of the pressure distribution (again, see dashed line). The wind speeds vary with the rate the pressure changes across the storm. Thus, changing the temperatures changes the pressure distribution and eventually the wind speeds. Another factor is also working to reduce the maximum wind speeds. Recent research results suggest it may be the main one. In the fourth assumption listed on page 50 it was mentioned that the seeding should cause an increase of buoyancy in the clouds located radially outward from the wall cloud. Under favourable circumstances this process can cause a new wall cloud to develop at a greater radius than the old one. Much of the air spiralling inward at







**WIND SPEED** variations at 3600 metres altitude in Hurricane Debbie on 18 August 1969 are shown (left). In the second seeding experiment (below left), on 20 August 1969, the subsequent reduction in maximum wind speeds was only about half that achieved two days earlier. (1 knot = 1.852 km/h)



developing compounds for special purposes and for specific temperature ranges in the clouds.

The second concern has been with the manner of delivering the silver iodide. In tests performed in laboratory cold boxes the silver iodide crystals coagulate when too many are released per unit volume. Dr Pierre St Amand's Navy group has also concluded from tests made in cumulus clouds that more effective nuclei per gramme of material are produced when delivered by smaller units. In the 1969 experiments we therefore used many small units each having 190 g of silver iodide rather than eight units each containing 4000 g of silver iodide as in the 1961 experiment. Results strongly suggest that the smaller units give much better results per gramme of material used.

In the Debbie experiment we used a unit called Stormfury-1. The compound was compressed into a cylinder measuring 3.5 cm in diameter, 10.2 cm long and weighing 290 g and capable of producing 190 g of silver iodide. It was loaded into a standard photoflash cartridge case. The formulation of the compound used was: silver iodate 78 per cent by weight, aluminium 12 per cent, magnesium four per cent and binder six per cent. The output of silver iodide was calculated to be 65 per cent (190 g per unit). One gramme of the silver iodide produces between  $10^{12}$  and  $10^{14}$  crystals, each an effective freezing nuclei at temperatures encountered in the hurricane supercooled layer.

**HURRICANE DEBBIE** was a mature storm with winds stronger than 185 km/h. On 18 August 1969 it was about 1200 km east-northeast of Roosevelt Roads, Puerto Rico, the primary operating base of Project Stormfury. This was an extreme range for the experiment, but other conditions were favourable, and the storm was moving west-northwestward on a course that would bring it closer to the base as the day progressed. Thirteen aircraft were available (nine from the US Navy, two from ESSA and two from the US Air Force). Fourteen flights were made with these aircraft. Five carried the pyrotechnics for seeding the hurricane

low levels would therefore ascend at a greater radius before it had reached such a strong velocity. That is to say, from absolute angular momentum consideration the sooner the air coming from the outside stops its inflow the less the rotational wind will be.

The preceding is an over-simplified explanation of what actually takes place, but the simulated modification experiment with the theoretical model does indicate that a reduction of maximum winds of

about 15 per cent might be achieved if the extra heat is added in the correct portion of the hurricanes.

**THE DEVELOPMENT WORK** on new pyrotechnic generators for delivering the silver iodide crystals has been influenced by two concerns. First, much research has been done to develop compounds that produce more effective freezing nuclei per gramme of silver iodide. In this case, special emphasis has been given to

and the other nine monitored the storm for changes in structure and intensity, beginning about four hours before the first seeding and continuing until six hours after the last one.

The Navy seeder aircraft approached the storm from the south-southwest at an altitude of 10,000 metres, penetrated and crossed the eye, and entered the wall cloud on the north-northeast side. Shortly after entering the wall cloud at a spot where past experience suggested that the aircraft would pass the radius of maximum winds as well as the most intense temperature gradients, the crew started dropping the pyrotechnic generators that produced the silver iodide. Each aircraft carried 208 of these generators and dropped them along a line leading radially away from the centre.

Each seeding run lasted from two to three minutes and covered between 26 and 40 km. The 208 units dropped along this track burned as they fell and produced a curtain of silver iodide crystals extending down to slightly below the freezing level. The idea was that the winds in the layer would sweep the crystals around the storm and the turbulence distribute them through a ring around the storm several kilometres deep. (Of course many crystals precipitated in raindrops, or blew out of the top in the up and out drafts.) After the first few minutes of dispersion there was probably a concentration of about 1000 nuclei per litre of space. After the nuclei were more completely dispersed—after one or two hours—this concentration was probably reduced to less than one nucleus per litre.

The seeding was repeated at approximately two hour intervals for five seedings. Many data were collected during the nine monitoring flights and some by the five seeder aircraft. The most detailed were collected at 3660 metres elevation by the two DC-6 aircraft of ESSA's Research Flight Facility. They have similar instrumentation which has been cross-calibrated and have crews trained in using the same techniques. Data from the two aircraft are as nearly comparable as planning and calibration procedures can make them. These aircraft were assigned to relieve each other in making repetitive passes across the storm and to provide almost continuous coverage of the hurricane by one of them from three hours before the first seeding until five or six hours after the fifth one. Only on 18 August were there appreciable time gaps when the storm was at such great range that the first aircraft could not make the round trip to base for refuelling during the time that the second aircraft could remain in Debbie. In previous mature hurricanes such as Debbie where there were measurements at several levels, winds at

3660 metres have been about 95 per cent as strong as those near the surface.

The flight patterns called for each aircraft to make a round trip across the storm from a point about 90 km west-northwest of the hurricane centre to 90 km east-southeast of it, or to a point beyond the belt of the strongest winds. Each aircraft then flew similar traverses from the south-southwest quadrant to the north-northeast quadrant until fuel shortage dictated departure from the storm. Since there were more data on the latter passes, they are the ones presented in the graphs on page 54. In a storm moving towards the west-northwest, the strongest winds are usually found a short distance north-northeast of the centre.

Between successive passes on both 18 and 20 August, the winds sometimes increased and sometimes decreased. In the mean, however, the wind speeds dropped from shortly after the second seeding until at least five or six hours after the fifth seeding. This decrease was most marked on 18 August.

Before the first seeding on 18 August, maximum wind speeds at 3660 metres were 182 km/h. By five hours after the fifth seedings, they had decreased to 126 km/h—a decrease of 31 per cent. On 20 August the maximum wind speed before the first seeding was 183 km/h. Within six hours after the final seeding, the maximum had dropped to 156 km/h—a decrease of 15 per cent.

Variations in the force of the wind are closely related to variation of the *square* of the wind speed or the kinetic energy of the air particles. These decreases in maximum winds represent a reduction in kinetic energy in the belt of maximum winds of 52 and 28 per cent respectively on 18 and 20 August 1969.

THAT HURRICANE DEBBIE decreased in intensity following multiple seedings on 18 and 20 August 1969 is well established. What is not known for certain is whether the decreases were caused by the seeding or by natural forces. From analyses of past storms, however, we can conclude that the changes of wind speeds like those in Debbie have not occurred more often than 1 in 40 cases for non-modified hurricanes. This is based on consideration of the reduction of 31 per cent on the 18th, no seeding and a regaining of intensity on the 19th and a reduction of 15 per cent on the 20th of August.

Some further support for concluding that the seeding affected the hurricane is provided by analyses of the radar pictures taken of the hurricanes by the Navy and ESSA aircraft. These analyses show there were changes in the size of the eye of the hurricane on 18 August and changes in the rate of rotation of the major axis of

the elliptical eye of the hurricane on 20 August. On both days the period of the changes was approximately two hours, which was the same period as the seedings.

The results of the Debbie experiments strongly suggest that some degree of beneficial modification was attained. The changes that occurred, however, might just have been due to natural causes rather than the seeding experiment. We must therefore wait for a repetition of the experiments before saying categorically that man has at last found the means of making a hurricane work against itself and moderate its own intensity.

#### FURTHER READING

ATLANTIC HURRICANES by Gordon E. Dunn and Banner I. Miller (*Louisiana State University Press*)

HARVESTING THE CLOUDS by L. J. Battan (*Doubleday and Company*)

PROJECT STORMFURY by R. Cecil Gentry (*in Bulletin of the American Meteorological Society*, 50, 404)

EXPERIMENTS WITH A NUMERICAL MODEL OF TROPICAL CYCLONE DEVELOPMENT by Stanley L. Rosenthal (*in Monthly Weather Review*, 98, 106)

EXPERIMENTS IN HURRICANE MODIFICATION by R. H. Simpson and J. S. Malkus (*in Scientific American*, 211, 27)

October 1971

725

UDC 651.509.313

## NUMERICAL INTEGRATION EXPERIMENTS WITH VARIABLE-RESOLUTION TWO-DIMENSIONAL CARTESIAN GRIDS USING THE BOX METHOD

WALTER JAMES KOSS

National Hurricane Research Laboratory, Environmental Research Laboratories, NOAA, Miami, Fla.

### ABSTRACT

Numerical experiments were performed with variable resolution two-dimensional rectangular Cartesian grids. The shallow-water equations were integrated on several variable-mesh grids and on a constant increment fine-resolution grid; the method of integration used the "box" technique for spatial representation. The grids were designed to be used in numerical experiments that examine vortex-type motions that may be embedded in a fairly uniform basic current. With this in mind, two systems were investigated: (1) a closed system containing a balanced vortex and (2) a semiopen system with east-west cyclic continuity containing a moderately strong easterly jet. The results indicate that, for a weak vortex embedded in a zonal current, a 2-step "telescope"-type grid can be used in numerical integrations with success; that is, the incurred error is relatively small and the computation time and computer memory requirements are not excessive. For an intense vortex, a graded-type grid yields a relatively better numerical integration at the expense of an increase in computation time.

### 1. INTRODUCTION

Considerable interest has been shown in the use of variable horizontal resolution grids for numerically integrating the equations that govern the behavior of meteorological phenomena. Variable increment-space meshes have been used with some success in studies of models possessing one horizontal space dimension. For two horizontal space-dimensioned models, the interest has been in the embedding of a fine-resolution mesh in a relatively coarse grid to resolve interesting small-scale features that are present in a large-scale environment. In this paper, we are concerned with the characteristics of fine-to-coarse resolution two-dimensional grids which are rectangular Cartesian in nature. These grids are of a type that would be useful in the study of vortex-type motions embedded in a large-scale flow. The integrations make use of a technique that originally appeared in fluid dynamics applications, and that has been given the name "box" method. The method has the desirable property that the momentum and mass of the system are preserved under the finite-difference formulation to within time-differencing errors because the equations are expressed in flux form.

The grid systems described here effect a reduction in the amount of internal storage needed on a computer when compared to a fixed fine-resolution mesh for the same region of integration. Also, computing time is reduced by the elimination of calculation points; but parts of these savings are at the expense of more sophisticated computer programming effort.

One of the advantages of Cartesian systems is the simplicity of the derivatives in both analytic and finite-difference form. This is in comparison with variable grids that are generated by transforming a desired grid structure into a rectangular Cartesian system such as was done by Anthes (1970). Methods of the latter type

increase computation time at each grid point because of the added terms in the tendency equations and introduce transformation factors in the equations that can result in computational difficulties such as those described by Shuman and Stackpole (1968). A further problem with transformation systems is the definition of the boundary when meshing the transformed grid with a large-scale coarse grid. The graded systems described here have a smooth transition into the large-scale system with no additional computations being needed to merge the systems, whereas the non-Cartesian-type grids often incur added computations (and perhaps approximations) where the grids join together. One experiment (No. 18) simulated, to a certain degree, the incorrect handling of the boundary; there, different frequency gravity waves were generated by reflections at the boundary and the effect of their interaction at the center of the vortex was observed.

Truncation error propagation can also be a serious problem. In variable-grid computations (as with computations done on a map-oriented grid), an upper bound on the truncation error is initially given locally by the evaluation of the appropriate series expansion remainder term using the local value of space increment and derivative maximum in this region. If the physical system is principally contained in the fine mesh and does not interact with the environment, the local truncation estimate should hold for the forecast period. Otherwise, system interactions will admit the large-scale truncation into the finer mesh computations; this error will dominate throughout the remainder of the forecast period.

### 2. GRID STRUCTURE

Three variable-resolution grids and one fixed-resolution grid were used in the numerical integrations. The variable resolution grids were of two basic types: (1) a constant



fine mesh embedded in a constant coarse mesh and (2) a fixed fine mesh embedded in a grid system that becomes progressively coarser with distance from the central region. Both types are members of a generalized family of grids, the construction and characteristics of which are described in the following discussion.<sup>1</sup>

The basic construction element of the variable-resolution grids is a square having side length  $\delta$ . Each graded grid has the following properties:

1. The area elements (boxes) of the grid structure are squares with side lengths that are integral multiples of the basic side length  $\delta$ .
2. The boxes increase in area outward from the center in a systematic manner.
3. The geometry of contiguous boxes having equal area is that of a "square annulus" (except for the central region).

As will be shown, the square annulus is not necessarily composed of a single ring of boxes.

The above properties set a requirement that contiguous annuli having different area elements must satisfy at their common interface. For definition, consider an inner annulus composed of elements having equal area  $A_1^2$  that is enclosed by an outer annulus with elements having area  $A_2^2$ . Then, if  $A_1 = n\delta$  and  $A_2 = n'\delta$ , where  $n$  and  $n'$  are arbitrary positive integers ( $n < n'$ ), the length of a common side, when expressed in terms of the number of boxes in each annulus at the interface, must be an integral relationship. That is,

$$A_1 m = (n\delta)m = (n'\delta)m' = A_2 m' \quad (1)$$

must hold, where  $m$  and  $m'$  are positive integers. We will exclude from consideration those cases where  $n'$  is an integral multiple of  $n$ ; in those cases there is a rapid variation in grid structure that is not acceptable. We wish to construct grids that have a less pronounced variation. The minimal increase in box size is given when  $n' = n + 1$ . If we begin the construction by having the central "core" region composed of basic area elements only, then the minimal variation requirement allows core regions the sides of which are made up of only even numbers of basic elements. Hence, for  $i$  a positive integer, there are  $(2i \times 2i)$  elements in the core. Now let  $n = 1, 2, \dots$  also represent the count (increasing outward) of the interface between the annuli as defined above. Then the only positive integer solutions at the  $n$ th interface for eq (1) above are  $m_n = i(n+1)$  and  $m'_n = i(n)$ . At the  $(n+1)$ st interface  $m_{n+1} = m'_n + 2i$ ; from this we see that the index  $i$  also represents the number of rings of equal-area boxes which make a square annulus.

The construction for  $i=1$ ,  $i=2$ , and  $i=3$  is shown in figure 1. Here we note how the index  $i$  is the controlling factor in the degree of variation possessed by the graded

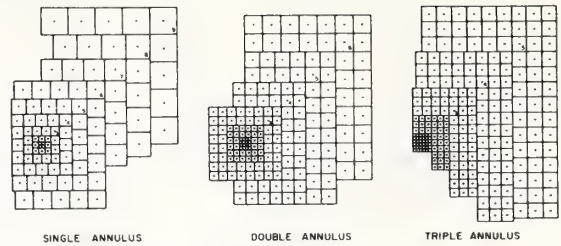


FIGURE 1.—Graded mesh constructions for  $i=1$  (single annulus),  $i=2$  (double annulus), and  $i=3$  (triple annulus). The smallest box in each case has area  $=\delta^2$ . The number in the box is the value of  $n$  [where box area  $= (n\delta)^2$ ] for the "square" annulus which contains the box.

TABLE 1.—Percent increase in box area as a function of  $n$  where box area  $= (n\delta)^2$

$n$	1	2	3	4	5	6	7	8	9	10	11	12	13	14
% Increase	300	125	77	56	44	36	31	27	23	21	19	17	16	15

mesh and that the grid variation can be reduced by choosing larger values of  $i$ , since this essentially introduces regions of constant mesh length throughout the structure. However, for any value of  $i$ , the percent increase in box area as a function of  $n$  (table 1) is largest for small values of  $n$ , which corresponds to the central region of the construction. Since this may not be a desirable feature, modifications to these grids can be made based on the following considerations: (1) the overall scale of the physical system, (2) the scale of the interesting variations within the system, and (3) numerical stability criterion with regard to computational time needed for the integration. All three of these will determine the specification of the magnitude of  $\delta$ .

The use of a grid devised by the above rules with small values of  $\delta$  will force the use of small time increments in the numerical integration, which can be economically unfeasible. Also, one desires a variable grid on which the major variations in the physical parameters take place in the fine-resolution portions of the mesh. Hence, item (2) places a restriction on the choice of  $\delta$ . This, along with item (1), helps determine the grid index  $i$ .

Since the percent changes of box area are largest for small values of  $n$  and this may be undesirable even in conjunction with large values of the grid variation index  $i$ , the central region can be modified by deleting the annuli for small values of  $n = 1, 2, \dots, (k-1)$  and replacing the deleted inner region with a fixed-resolution mesh, the boxes of which have side length  $k\delta$ . This yields a graded grid structure that has a fine resolution inner region and that gradually increases in "mesh length" toward the periphery of the region of interest. The graded grids used here were constructed in this manner. Table 2 gives the

<sup>1</sup> A clarification of nomenclature should be made at this point. Although the words "grid" and "mesh" denote a systematically arranged array of points, we shall use them to denote the "box" structure which is used in the integration technique. In reality a grid or mesh point is a point within a box, that figuratively will be taken as the center of the box.



TABLE 2.—Characteristics of the grid structures used in the numerical experiments. Here,  $\delta^2$  is the area of the basic construction element,  $i$  is the grid variation index, and  $\Delta$  is a box side length.

Grid type	$i$	$\delta$ (km)	$\min \Delta = n\delta$	$\max \Delta = n\delta$	Total area (km <sup>2</sup> )	Area of fine resolution (km <sup>2</sup> )
Constant:15	—	15.0	15 km, $n=1$	—	(900) <sup>2</sup>	all
2-Step:15	10	15.0	15 km, $n=1$	30.0 km, $n=2$	(900) <sup>2</sup>	(300) <sup>2</sup>
Graded:10	2	2.5	10 km, $n=4$	32.5 km, $n=13$	(910) <sup>2</sup>	(100) <sup>2</sup>
Graded:15	2	2.5	15 km, $n=6$	32.5 km, $n=13$	(910) <sup>2</sup>	(210) <sup>2</sup>

Grid type	Total number of boxes (points)	Percent of the Constant:15 total	Number of boxes in the central (210 km) <sup>2</sup> region
Constant:15	3,600	100	196
2-Step:15	1,200	33	198
Graded:10	1,396	39	276
Graded:15	1,316	37	196

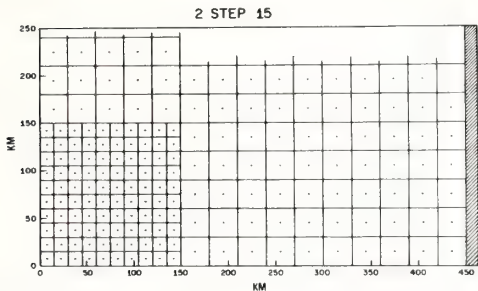


FIGURE 2.—A section of the northeast quadrant of the 2-Step:15 grid. The hatched area represents the boundary which encloses the entire (900 km)<sup>2</sup> region.

characteristics of the four grids used in the integrations. The constant-resolution mesh was used to generate comparison control cases for the variable-resolution cases. The 2-Step:15 “telescope”-type grid has a  $20 \times 20$  fine-resolution interior mesh surrounded by a coarse mesh; a portion of the northeast quadrant of the grid is shown in figure 2. Figure 3 shows a similar section of the Graded:15 mesh, which has an interior  $14 \times 14$  fine mesh with a (15 km)<sup>2</sup> box area. The central region of the Graded:10 mesh is depicted in figure 4. Here, the interior mesh is  $10 \times 10$  and has a box area of (10 km)<sup>2</sup>. The Graded:10 and Graded:15 grids differ in structure only within the (75 km)<sup>2</sup> central region; the grids are identical otherwise. From table 2, we also note the large percent-reduction of total number of grid points in going from the constant-resolution mesh to the variable-resolution grids. A summary of the graded grid construction follows:

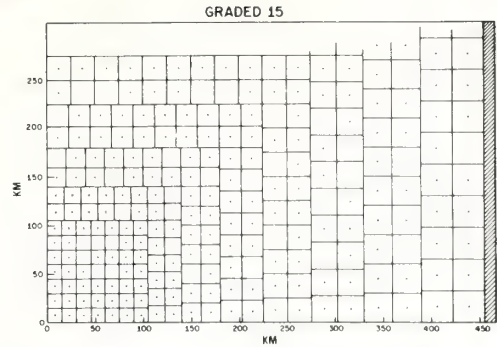


FIGURE 3.—A section of the northeast quadrant of the Graded:15 grid. The hatched area represents the boundary which encloses the entire (910 km)<sup>2</sup> region.

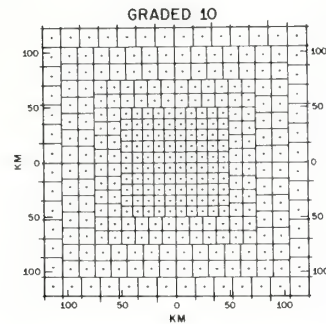


FIGURE 4.—The central region of the Graded:10 grid.

1. A basic side length  $\delta$  is selected. This is the amount that box side length will increase in going outward from one annulus to the next.
2. The grid variation index  $i$  (a positive integer) is chosen. The initial core region will contain  $(2i \times 2i)$  basic elements, and a square annulus will have  $i$  rings of equal-area boxes.
3. Let  $n=1, 2, 3, \dots$  represent the count of the annuli interfaces. At the  $n$ th interface, the inner annulus is composed of boxes having side length  $n\delta$ , and the outer annulus of those with side length  $(n+1)\delta$ . There are  $i(n+1)$  inner annulus boxes at the interface; adjacent to these are  $i(n)$  outer annulus boxes.
4. The positive integer  $k$  is determined such that  $k\delta = \Delta S_{\min}$ , where  $\Delta S_{\min}$  is the desired mesh length for the fine inner region grid. The annuli for  $n=1, 2, \dots, (k-1)$  are deleted and replaced with a fixed-resolution mesh which has box side length  $k\delta$ .

### 3. THE PHYSICAL MODEL AND BOUNDARY CONDITIONS

The physical model adopted for the experiments was governed by the free-surface (shallow water) equations written in flux form on an  $f$ -plane in  $x, y$  rectangular Cartesian coordinates ( $x$  positive eastward,  $y$  positive

northward). The equations are

$$\frac{\partial h}{\partial t} = -\frac{\partial}{\partial x}(hu) - \frac{\partial}{\partial y}(hv), \quad (2a)$$

$$\frac{\partial hu}{\partial t} = -\frac{\partial}{\partial x}(huv) - \frac{\partial}{\partial y}(huv) + hf v - gh \frac{\partial h}{\partial x}, \quad (2b)$$

and

$$\frac{\partial hv}{\partial t} = -\frac{\partial}{\partial x}(huv) - \frac{\partial}{\partial y}(hvv) - hf u - gh \frac{\partial h}{\partial y}. \quad (2c)$$

Here,  $h$  is the height of the free surface,  $u$  is the eastward component of the horizontal velocity,  $v$  is the northward component of velocity,  $g$  is a constant gravitational acceleration,  $f$  is the constant Coriolis parameter, and  $t$  is time. The fluid is contained in a square basin which has a plane level bottom.

Two sets of boundary conditions were used in the experiments. In one set the physical system is closed; that is, the fluid is bounded by fixed vertical walls. Here, the no-normal transport, free-slip conditions hold and the height of the free surface is allowed to change with time. In the second set, the east and west boundaries are open and the fluid is assumed to have cyclic continuity. The north and south boundary conditions are as before.

The mean total available energy (henceforth called total energy) of the fluid system at a time  $t$  is given by

$$\overline{TE} = \frac{1}{2\sigma} \int_{\sigma} [h(u^2 + v^2) + g(h - \bar{h})^2] d\sigma \quad (3)$$

where  $\bar{h}$  is the areal mean height of the fluid, and  $\sigma$  is the total area of the region under consideration. The percent change in total energy from that at the initial time  $t=t_0$  is defined by

$$\Delta \overline{TE} = (\overline{TE} - \overline{TE}_0) / \overline{TE}_0. \quad (4)$$

$\Delta \overline{TE}$  was computed at every time step in all of the experiments. In the absence of numerical truncation and round-off error,  $\Delta \overline{TE}$  is zero with either of the above sets of boundary conditions.

#### 4. INITIAL CONDITIONS

Two sets of initial conditions were used in the numerical integrations:

1. An easterly jet under geostrophic balance, with the height and speed fields specified by

$$H(y) = \bar{H} - H \cos(\pi y / Y_N) \quad (5)$$

and

$$U(y) = -\frac{g}{f} \frac{\pi H}{Y_N} \sin(\pi y / Y_N). \quad (6)$$

There is no  $x$  variation;  $y$  ranges in value from  $y=0$  at the southern boundary to  $y=Y_N$  at the northern boundary.  $H$  is a constant with the dimensions of height. Profiles of  $H(y)$  and  $U(y)$  are shown in figure 5. With the condition

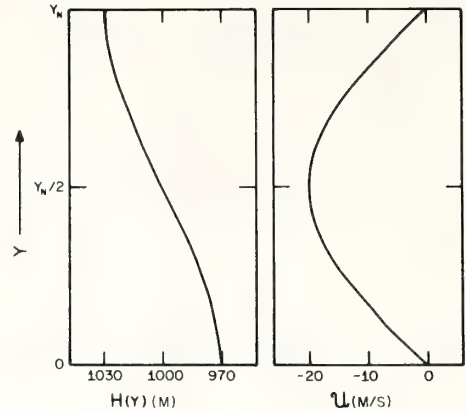


FIGURE 5.—Meridional profiles of the height and speed fields for the easterly jet initial condition.

that  $U_{max} = -20.0$  m/s we have  $H \approx 30.0$  m, which is the maximum departure of the fluid from the mean height  $\bar{H}$ .

2. A circular vortex in gradient balance, with the height field specified by

$$H(R) = \bar{H} + h \quad (7)$$

where

$$h = \begin{cases} -\hat{H} \cos^m \left[ \frac{\pi}{2} (R/R_{max})^Q \right], & \text{for } R \leq R_{max} \\ 0, & \text{for } R > R_{max}. \end{cases}$$

In eq (7),  $\bar{H}$  is the height of the undisturbed fluid at distances far from the vortex center,  $\hat{H}$  is a constant with the dimensions of height,  $R$  is the radial distance from the geometric center of the vortex ( $R^2 = x^2 + y^2$ ),  $R_{max}$  is the radial distance from the center of the system at which the vortex motion vanishes,  $m$  is a positive integer, and  $Q$  is a rational number.  $Q=1/3$  and  $R_{max}=405$  km were used in all of the experiments. Under the gradient balance assumption, the magnitude  $c$  of the fluid velocity is given by

$$c = -\frac{fR}{2} + \sqrt{\left(\frac{fR}{2}\right)^2 + gR \frac{\partial h}{\partial R}} \quad (8)$$

The east-west and north-south velocity components are then given by

$$u = -c \sin \phi$$

and

$$v = c \cos \phi \quad (9)$$

where  $\phi = \tan^{-1}(y/x)$ . Figure 6 shows radial profiles of  $h$  and  $c$  for various values of the parameters  $\hat{H}$  and  $m$  which were used in the computations.

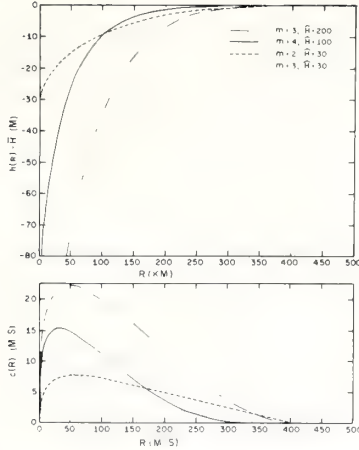


FIGURE 6.—Radial profiles of the height departure and magnitude of the fluid velocity for the balanced-vortex initial condition.

The numerical values of the functions were computed for the first (northeast) quadrant only, and assigned to the remaining three quadrants under the symmetry conditions of the system.

### 5. FINITE-DIFFERENCE EQUATIONS

Equations (2a, 2b, 2c) are transformed to the discrete form of area-integral equations by methods described in detail by Noh (1964). This technique was used by Kurihara and Holloway (1967) in a global primitive equation model, with some success. A brief description of the method follows. If  $\sigma$  is an arbitrary element of area, then for any scalar  $\alpha$  we can write the integral equation

$$\int_{\sigma} \left( \frac{\partial \alpha}{\partial t} + \nabla_H \cdot \alpha \mathbf{V}_H + B \right) dS = 0 \quad (10)$$

as

$$\frac{\partial \bar{\alpha}}{\partial t} \Delta S_{\sigma} + \oint_C v_n \alpha dl + \bar{B} \Delta S_{\sigma} = 0 \quad (11)$$

where  $(\bar{\phantom{x}})$  is the mean value over the element  $\sigma$  and  $\Delta S_{\sigma}$  is the area of  $\sigma$ .  $B$  is either a source term for  $\alpha$  or an external force.  $\nabla_H \cdot$  is the horizontal divergence operator,  $v_n$  is the outward normal component of the horizontal velocity vector  $\mathbf{V}_H$ , and  $C$  is the boundary contour of the area element  $\sigma$ . In our experiments all elements are rectangles, hence the line integral in eq (11) can be written as

$$\oint_C v_n \alpha dl = \int_{x_1}^{x_2} [(-\alpha v)_{v=v_1} - (-\alpha v)_{v=v_2}] dx + \int_{y_1}^{y_2} [(\alpha u)_{u=u_2} - (\alpha u)_{u=u_1}] dy \quad (12)$$

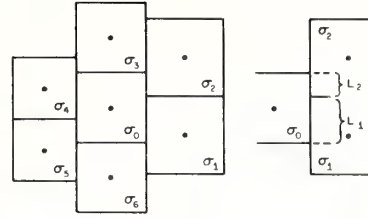


FIGURE 7.—A typical box configuration. In the text, the area integral is being evaluated over the box  $\sigma_0$ .  $L_1$  is the length of the line segment common to the boxes  $\sigma_0$  and  $\sigma_1$ , and  $L_2$  is the length of the segment common to  $\sigma_0$  and  $\sigma_2$ .

where the  $x_i$  and  $y_j$  are the  $x, y$  coordinates of the vertices of the rectangle. These integrals are evaluated by assuming that the integrands are given on the line segments (box sides) by the mean values of the variables from adjoining boxes which have a common side. In the following, we will use operator notation similar to that of Kurihara and Holloway (1967). See section 2 of their paper for a complete discussion of the operators' characteristics. In their notation,

$$\oint_C v_n \alpha dl \approx N(Z) \Delta S_{\sigma} \quad (13)$$

where  $\alpha$  is given by  $\alpha = hZ$ , with  $Z$  an arbitrary scalar, and

$$N(Z) = \left( \sum_E - \sum_W \right) \left[ \frac{(hu)_0 + (hu)_i}{2} Z w_i \right] + \left( \sum_N - \sum_S \right) \left[ \frac{(hv)_0 + (hv)_i}{2} Z w_i \right] \quad (14)$$

Here, the summations are over the  $l$  boxes which are contiguous to the box  $\sigma = \sigma_0$ ; E, W, N, and S represent the east, west, north, and south sides of the boxes which all have their sides oriented in the cardinal directions, and  $w_i = L_i / \Delta S_{\sigma_0}$  where  $L_i$  is the length of the line segment common to  $\sigma_0$  and  $\sigma_i$ . Figure 7 shows a typical box configuration.

In the momentum equations, the Coriolis terms are given by

$$f(\bar{h}v) \Delta S_{\sigma} \quad (15a)$$

and

$$f(\bar{h}u) \Delta S_{\sigma} \quad (15b)$$

since  $f$  is a constant in the experiments.

Of final concern are the integral forms of the pressure gradient terms

$$g \int_{\sigma} h \frac{\partial h}{\partial x} dS \quad (16a)$$

and

$$g \int_{\sigma} h \frac{\partial h}{\partial y} dS. \quad (16b)$$

Two distinct numerical forms arise from the application of simple cubature rules in evaluating the integrals



(16a, 16b) over rectangular regions. One method of evaluation yields

$$g \int_{\sigma} h \frac{\partial h}{\partial x} dS \approx \frac{g \Delta S_{\sigma}}{4} \left[ \left( \sum_E - \sum_W \right) w_i (h_i^2 - h_0^2) \right] \\ = g \Delta S_{\sigma} L_x(h, h) \quad (17a)$$

and

$$g \int_{\sigma} h \frac{\partial h}{\partial y} dS \approx \frac{g \Delta S_{\sigma}}{4} \left[ \left( \sum_N - \sum_S \right) w_i (h_i^2 - h_0^2) \right] \\ = g \Delta S_{\sigma} L_y(h, h). \quad (17b)$$

A second method gives

$$\frac{g}{2} \int_{\sigma} \frac{\partial h^2}{\partial x} dS \approx \frac{g}{2} \frac{\Delta S_{\sigma}}{4} \left[ \left( \sum_E - \sum_W \right) w_i (h_i + h_0)^2 \right] \\ = \frac{g}{2} \Delta S_{\sigma} G_x(hh) \quad (18a)$$

and

$$\frac{g}{2} \int_{\sigma} \frac{\partial h^2}{\partial y} dS \approx \frac{g}{2} \frac{\Delta S_{\sigma}}{4} \left[ \left( \sum_N - \sum_S \right) w_i (h_i + h_0)^2 \right] \\ = \frac{g}{2} \Delta S_{\sigma} G_y(hh). \quad (18b)$$

$G_s(\ )$  and  $L_s(\ )$  (where  $S$  is either  $x$  or  $y$ ) are the operator notations of Kurihara and Holloway (1967). In these expressions the summation convention is the same as that for eq (14).

The equations for the time changes of the areal averages (over  $\sigma_0$ ) of the dependent variables, which are the analogs of eq (2a, 2b, 2c) are (at time  $t = n\Delta t$ ,  $n$  a positive integer):

$$\frac{\partial h_0}{\partial t} = -N^n(1), \quad (19a)$$

$$\frac{\partial (hu)_0}{\partial t} = -N^n \left( \frac{u_0 + u_i}{2} \right) + f(hv)_0^n - g \left\{ \frac{1}{2} G_x^n(hh) \right. \\ \left. L_x^n(h, h) \right\}, \quad (19b)$$

and

$$\frac{\partial (hv)_0}{\partial t} = -N^n \left( \frac{v_0 + v_i}{2} \right) - f(hu)_0^n - g \left\{ \frac{1}{2} G_y^n(hh) \right. \\ \left. L_y^n(h, h) \right\}. \quad (19c)$$

Here, either the  $G_s(\ )$  or  $L_s(\ )$  operator is to be used as the representation of the pressure gradient terms, and the box index subscript replaces the overbar notation for the mean value.

It can be shown that this system of equations conserves mass and quadratically conserves momentum. The total energy [eq (3)] of the system is not conserved because of the design of the  $G_s(\ )$  and  $L_s(\ )$  operators.

The time differences are written in the familiar centered-difference "leapfrog" form. All integrations were initiated with a forward time-difference set of equations.

For a constant (equal area) box subdivision of the integration domain, eq (19a, 19b, 19c) reduce to equations

which can be written in terms of the mean and difference operators

$$\bar{\alpha} = \frac{1}{2} \left[ \alpha \left( x + \frac{\Delta}{2} \right) + \alpha \left( x - \frac{\Delta}{2} \right) \right] \quad (20a)$$

and

$$\alpha_x = \frac{1}{\Delta} \left[ \alpha \left( x + \frac{\Delta}{2} \right) - \alpha \left( x - \frac{\Delta}{2} \right) \right]. \quad (20b)$$

With this notation, the equations for a fixed-resolution mesh are

$$\bar{h}_i' + (\overline{hu})_x^z + (\overline{hv})_y^v = 0, \quad (21a)$$

$$(\overline{hv})_i' + (\overline{hu})_x^{z-z} + (\overline{hv})_y^{v-v} - f\bar{h}v + g \left\{ \frac{1}{2} \left[ \frac{1}{2} (\overline{h^2})_x^z + \bar{h} \bar{h}_x^z \right] \right. \\ \left. \frac{1}{2} (\overline{h^2})_x^z \right\} = 0, \quad (21b)$$

and

$$(\overline{hv})_i' + (\overline{hu})_x^{z-z} + (\overline{hv})_y^{v-v} - f\bar{h}u + g \left\{ \frac{1}{2} \left[ \frac{1}{2} (\overline{h^2})_y^v + \bar{h} \bar{h}_y^v \right] \right. \\ \left. \frac{1}{2} (\overline{h^2})_y^v \right\} = 0. \quad (21c)$$

Here, we note that the equations are very nearly in total energy conservation form (see Grammelvedt 1969, scheme B) except for the height gradient terms. The term  $\frac{1}{2} (\overline{h^2})_s^s = L_s(h, h)$  which appears in both formulations of the momentum equations prevents the energy conservation property.

The no-normal transport boundary condition is numerically applied by making appropriate modifications to the operator  $N(Z)$  [eq (14)] for the boxes adjacent to the walls. Here, the arithmetic mean which represents the normal transport at the wall is set equal to zero. The free-slip condition is computationally unnecessary in this formulation; in fact, viscous effects would have to be explicitly represented by a source term in the numerical equation if they were present at the wall, which is not the case here.

Although a physical boundary condition for the height of the free surface is not necessary, the difference equations require this knowledge for the numerical evaluation of the  $G_s(\ )$  and  $L_s(\ )$  operators. Here, the height of the surface at the wall (which is allowed to vary with time) is assumed to have the value of  $h$  for the box adjacent to the wall. This is equivalent to numerical evaluation by the method of images of the boundary condition  $\bar{n} \cdot \nabla h = 0$ . The above assumption allows us to avoid extrapolations in evaluating the height field at the fixed wall.

The finite summation analog of eq (3) is given by

$$\overline{TE} = \sum_k \sum_j TE_{j,k} \Delta S_{j,k} / \sigma \quad (22)$$

where

$$TE_{j,k} = \frac{1}{2} (u_{j,k}^2 + v_{j,k}^2) h_{j,k} + \frac{g}{2} (h_{j,k} - \bar{h})^2 \quad (23)$$



TABLE 3.—List of the numerical integration experiments. EJ is the easterly jet initial state; BV( $m, \hat{H}$ ) is the balanced vortex initial state for the parameters  $m$  and  $\hat{H}$ ;  $L$  and  $G$  are the operators  $L_S(\ )$  and  $G_S(\ )$  respectively; CB represents the closed boundary condition, and CC represents the east-west cyclic continuity boundary condition.

Experiment group	Experiment number	Initial state	Grid type	$\Delta t$ (s)	Number of iterations	Gradient operator	Initial data	Boundary condition
A	1	EJ	2-Step:15	90	100	$L$	$\overline{hu}$	CC
	2	EJ	2-Step:15	90	100	$L$	$\overline{hu}$	CC
	3	EJ	2-Step:15	90	100	$G$	$\overline{hu}$	CC
	4	EJ	2-Step:15	90	960	$G$	$\overline{hu}$	CC
	5	EJ	2-Step:15	90	960	$G$	$hu$	CC
	6	EJ	Graded:15	90	960	$G$	$hu$	CC
	7	BV(2,30)	2-Step:15	90	960	$G$	$hu$	CC
	8	BV(2,30)	Graded:15	90	960	$G$	$hu$	CC
	9	BV(2,30)	2-Step:15	90	1,920	$G$	$hu$	CB
B	10	BV(3,30)	Constant:15	90	1,920	$G$	$hu$	CB
	11	BV(3,30)	2-Step:15	90	3,112	$G$	$hu$	CB
	12	BV(3,30)	Graded:10	60	2,880	$G$	$hu$	CB
	13	BV(3,30)	Graded:15	90	1,920	$G$	$hu$	CB
C	14	BV(4,100)	Constant:15	90	1,920	$G$	$hu$	CB
	15	BV(4,100)	2-Step:15	90	1,920	$G$	$hu$	CB
	16	BV(4,100)	Graded:10	60	2,880	$G$	$hu$	CB
	17	BV(4,100)	Graded:15	90	1,920	$G$	$hu$	CB
Off-center	18	BV(4,100)	Constant:15	90	1,920	$G$	$hu$	CB
D	19	BV(3,200)	Constant:15	90	4,993	$G$	$hu$	CB
	20	BV(3,200)	2-Step:15	90	3,404	$G$	$hu$	CB
	21	BV(3,200)	Graded:15	90	4,551	$G$	$hu$	CB

is taken as the average value of the total energy of the fluid in the  $j$ th box of the  $k$ th annulus.  $\Delta S_{j,k}$  is the area of the box,  $\sigma$  is the total area of the region under consideration, and  $\bar{h}$  is the mean height of the free surface over  $\sigma$ .<sup>2</sup>

For the Graded:15 grid experiments, eq (22) was written as

$$\overline{TE} = \frac{1}{132,496} \sum_{k=6}^{13} k^2 \sum_{j=1}^{N_k} TE_{j,k} \quad (24)$$

where  $TE_{j,k}$  has the definition given by eq (23). In this case,  $\Delta S_{j,k} = (k\delta)^2 \text{ km}^2$ , the number of boxes,  $N_k$ , in the  $k$ th annulus is  $N_k = 16k$  for  $k \geq 7$ , and  $N_6 = 196$  (since  $k=6$  represents the  $14 \times 14$  interior fine mesh). The Graded:10 grid formula for  $\overline{TE}$  is analogous to eq (24). Equation (22) reduces to simple summation formulas for the Constant:15 and 2-Step:15 experiments.

Similar formulas for computing the mean value of the square of the  $v$ -component,  $v^2$ , were used in several of the experiments.

## 6. THE EXPERIMENTS AND RESULTS

Table 3 lists the experiments that are discussed in this paper. Of these, we present detailed results for the groups A, B, C, and D, since they provide the main basis for determining the relative merits of the various grid systems.<sup>3</sup>

<sup>2</sup> After 2,000 iterations,  $\bar{h}$  decreases by approximately two parts in  $10^3$ , which indicates that the leapfrog time-integration scheme is slightly dissipative.

<sup>3</sup> The remaining experiments are discussed in the appendix. All computations were performed on a Control Data Corporation 6600 computing system.

Experiments 10 through 13 were computed using four different grids with the same weak vortex as the initial state. Experiments 14 through 17 repeated those above except that the initial state was a more intense vortex (fig. 6). In all these cases, the initial vortex was specified so that its center coincided with the geometric center of the grid. On the other hand, experiment 18, which is comparable to experiment 14, had the center of the initial vortex displaced  $7.5\sqrt{2} \text{ km}$  to the northeast of the geometric center of the grid.

A very intense vortex (fig. 6) was specified as the initial condition for experiments 19, 20, and 21. Here, the three grids with a  $(15 \text{ km})^2$  interior box were used, and the integrations were continued out in time until the calculations showed that the system was computationally unstable (the criterion was that the total energy increase by 50 percent over the initial value).

The following values of parameters were used in all the experiments:

$$f = 5 \times 10^{-5} \text{ s}^{-1},$$

$$\bar{H} = 1000 \text{ m},$$

and

$$g = 9.8 \text{ m/s}^2.$$

### THE EASTERLY JET EXPERIMENTS

*Group A.* Since the analytic system of equations with the specification of easterly jet initial conditions and appropriate boundary conditions yields a steady-state solution, the behavior of the errors introduced by the finite-difference approximation to the initial conditions

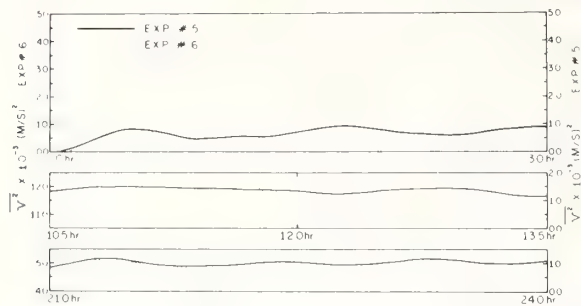


FIGURE 8.—Time variation of  $\bar{v}^2$  for the experiments in group A. Note the change in ordinate scales.

is a measure of the error induced by the mesh. These approximations are not in geostrophic balance since both the height and fluid velocity fields were analytically specified. Figure 8 shows the temporal variation of  $\bar{v}^2$ , which is zero analytically but finite nonzero in the integrations because of the above-mentioned errors. Three 3-hr periods are depicted from the 24-hr forecast period for both experiment 5 and experiment 6. In experiment 5 we note that after an initial growth of  $\bar{v}^2$ , by 12 hr the computations become stable (bounded), and  $\bar{v}^2$  exhibits a slow ( $\sim 1$  hr) oscillation with time. In contrast, experiment 6 shows a growth of  $\bar{v}^2$  to values which are an order of magnitude larger than that of experiment 5. Here,  $\bar{v}^2$  reaches a maximum ( $12.7 \times 10^{-3} \text{ m}^2 \text{ s}^{-2}$ ) at about 10 hr and begins to decrease with time. After 22 hr, the graph exhibits a slow, bounded oscillation with values approximately five times larger than those of experiment 5. The traces of  $\Delta \bar{T}E$  (not shown) exhibit a similar behavior, with the experiment 6 trace having larger amplitude than that for experiment 5.

After 24 hr, the  $v$ -component fields (not shown) in both experiments show a two-space increment ( $2\Delta S$ ) noise pattern evenly distributed over the entire region of integration. (This is also true for the height fields, with the maximum variation being less than 1 m.) Of interest is the fact that over the  $12 \times 12$  equal-interval fine mesh which is common to both grids,  $\bar{v}^2 = 0.00462$  for experiment 5 and  $\bar{v}^2 = 0.00205$  for experiment 6. This is opposite to the result for the entire regime and indicates that, for fluid motions with moderate shear in the mass and momentum fields, the graded grid structure induces relatively large errors of alternate sign throughout the annuli structure. However, the central region yields a state of less error as the computations stabilize.

A detailed examination of the initial tendency patterns for both experiments revealed that the errors in the tendencies computed at the inner interface boxes in the 2-Step:15 case were at times two orders of magnitude larger than those for the Graded:15 case. This helps explain the paradoxical behavior of the  $\bar{v}^2$  statistics previously mentioned. Although the errors forced by the interface of the 2-Step:15 grid are relatively large, the cumulative effect of the errors induced by the graded grid over a much larger portion of the integration region is a larger value of  $\bar{v}^2$ . This is also true of the  $\Delta \bar{T}E$  computa-

tions. After 960 iterations, the innermost region ( $12 \times 12$  central mesh) of the graded grid had less error than the equivalent portion of the 2-Step grid; that is, the amplitude of the induced gravity wave structure was larger in the latter case. This can be attributed to the abrupt change in grid size at the interface of the coarse- and fine-mesh regions. In general, though, the 2-Step type structure gives a better overall representation of the variable states than a graded structure in cases where there are non-negligible shears in the velocity and height fields in the nonuniform portions of the grid.

#### THE BALANCED-VORTEX EXPERIMENTS

In the following discussion, the root-mean-square error of the height field (denoted by  $\text{RMSE:h}$ ) is used as a comparative statistic. The data are taken from the  $(210)^2$  km<sup>2</sup> central square region which is common to the four grids and contains the most active portion of the vortex. The comparison is with the data from the initial time  $t_0$ .

After the initial time step, the error in the height and velocity component fields results from a combination of

1. space-differencing truncation,
2. forward time-extrapolation,
3. approximation of the areal mean values of the dependent variables by point values, and
4. imbalance of the discrete system caused by specifying both the height and velocity component fields analytically.

*Group B.* The initial state for these experiments was a centered balanced vortex having a height deficit of 30 m at the center and a speed maximum of about 8 m/s near 40 km from the center.

Within the first 100 iterations, the computations for all four experiments reached quasi-equilibrium (slowly varying) balanced states as they recovered from the imbalances induced by the initial finite-difference representations. Figure 9 shows the percent change in total energy and  $\text{RMSE:h}$  for the 3-hr period ending at 48 hr. The traces for the preceding hours of the forecast are not presented because of their similarity to those shown.

Of all the profiles of  $\Delta \bar{T}E$ , the Graded:15 case shows the most active variation, with a pronounced two time-increment ( $2\Delta t$ ) oscillation. Otherwise, all four profiles are remarkably similar in that the traces show no apparent trend and are upper bounded by the 0.01 percent change isoline. The  $\text{RMSE:h}$  profiles have the same trend and boundedness character as the  $\Delta \bar{T}E$  profiles except that here we do see the effect of the variable-resolution mesh on the computations. The control computation (exp. 10) has an average height error which is generally less than 0.5 m, whereas the other experiments have average height errors between 0.75 and 1.25 m. Each of the curves exhibits a  $4\Delta t$ - $6\Delta t$  oscillation which is probably directly related to the gravity wave motion on the free surface. Considering the energy and mean height changes together for each case, we note that the Graded:10 results are slightly better than the comparable 2-Step:15 results and both of these are only slightly better than the Graded:15 results. In terms of computational expediency, the 2-Step grid would be preferred. Experiment 11 was continued out to 77.8 hr.

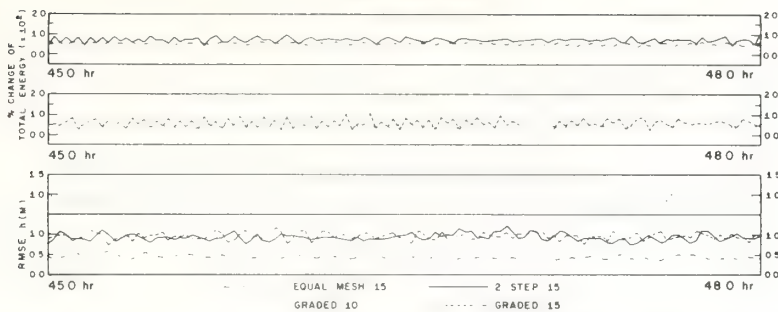


FIGURE 9.—Percent change in total energy,  $\Delta\overline{TE}$ , and root-mean-square error of the height field,  $RMSE:h$ , for the experiments in group B (Equal Mesh:15  $\equiv$  Constant:15).

The profiles are similar to those shown; the percent change in total energy remains less than 0.01 percent.

*Group C.* The initial state for these experiments was a more intense vortex than that used for group B. The central height deficit was 100 m (10 percent of the undisturbed fluid height) and the maximum tangential speed was 15.5 m/s near 30 km from the center (fig. 6). Figure 10 shows  $RMSE:h$  for five 3-hr intervals during the 48-hr forecast period. We note that the large error during the initial iterations diminishes (stabilizes) rapidly in the equal-mesh case (exp. 14). For this case, throughout most of the forecast,  $RMSE:h$  remains in the range 1.0–1.25 m and oscillates with a period of about 9 min. In the other cases, the error is about twice that magnitude and the oscillations have larger amplitudes with variable periods of from 4 to 9 min. Of the three variable grids, the Graded:10 (exp. 16) gives a slightly better height field for the first 24 hr, but the three profiles are comparable at 36 hr, with the Graded:15 and 2-Step:15 experiments having slightly better results at 48 hr. The profiles of  $\Delta\overline{TE}$  (fig. 11) for the 3-hr periods corresponding to those

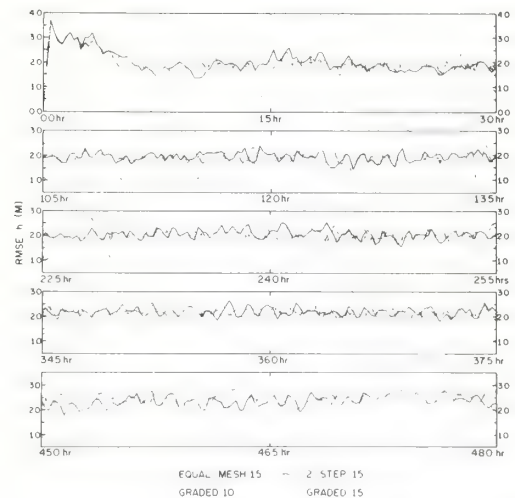


FIGURE 10.—Root-mean-square error of the height field,  $RMSE:h$ , for the experiments in group C (Equal Mesh:15  $\equiv$  Constant:15).

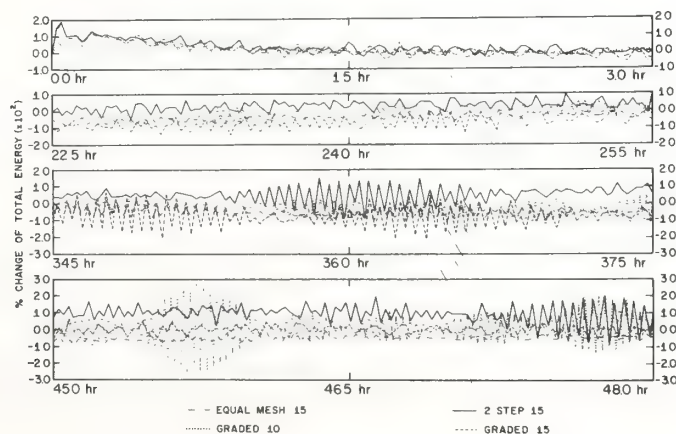


FIGURE 11.—Percent change of total energy  $\Delta\overline{TE}$  for the experiments in group C (Equal Mesh:15  $\equiv$  Constant:15).



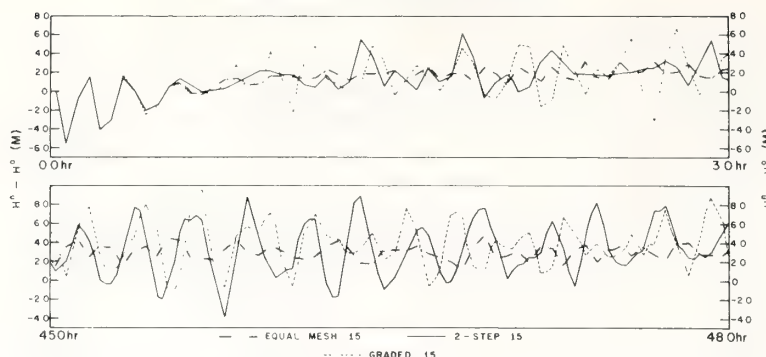


FIGURE 12.—Departures from the initial height  $H^0$  of the fluid in one of the four central boxes for experiments 14, 15, and 17.  $H^h$  is the height of the fluid at time  $n\Delta t$  (Equal Mesh:15=Constant:15).

of  $\text{RMSE}/h$  give further insight into the behavior of the computations. Initially, all four profiles of  $\Delta\overline{TE}$  have the same character except that the 2-Step:15 and Graded:15 curves exhibit slightly larger amplitudes. The profiles for experiments 15, 16, and 17 have trends which indicate very slow increases in total energy. In the 3-hr period centered at 24 hr, all experiments show a tendency for a  $2\Delta t$  oscillation in the profiles which is most pronounced in the Graded:10 and Graded:15 cases. The Graded:10 amplitudes are modulated, with maximum amplitude occurring at about 50-min intervals. The 2-Step:15 and Graded:15 cases exhibit the largest percentage changes.

The next period shown (centered at 36 hr) has profiles which have a pronounced  $2\Delta t$  oscillation for all the experiments in this group. Again, the amplitudes are largest in the Graded:15 and 2-Step:15 cases. The amplitudes for the variable grid cases are modulated, the 2-Step:15 with a period of approximately 120 min, the Graded:15 of about 90 min, and the Graded:10 of about 35 min. The Graded:10 profile is beginning to show changes which indicate that the computations are becoming less stable.

At 45–48 hr, the control experiment has a relatively steady profile with an average percentage change of about  $-0.005$ . Of the three variable-grid experiments, the Graded:15 computations give energy changes which most nearly resemble the control case in both magnitude and variation; the amplitude of the oscillations is less than that of the later periods previously examined, and the profile displays little change from the initial values. In contrast, the 2-Step:15 and Graded:10 experiments both exhibit total energy changes of variable amplitudes which are from four to six times larger than that for experiment 17. The Graded:10 profile continues to show a marked variable modulation of the  $2\Delta t$  oscillation with an average period of about 35 min. The variation in amplitude has changed considerably from the earlier periods, the changes being by a factor of two to four. In the above experiments, the pronounced  $2\Delta t$  oscillation in  $\Delta\overline{TE}$  can

be directly related to the behavior of the kinetic energy changes. The changes of mean available potential energy have relatively smooth oscillations of a longer period. Also, the final periods of the 2-Step:15 and Graded:10 forecasts have velocity component RMSE's (not shown) which have a slight  $2\Delta t$  oscillation. The above symptoms strongly suggest that the computational noise is predominant in the velocity component fields.

Figure 12 shows the departure from initial height of the fluid in one of the four central boxes of the grid for the initial and last 3-hr period of the forecast. In all cases, these four boxes have equal height values throughout the forecast period. Only the experiments which used a  $(15 \text{ km})^2$  interior box are shown. The initial displacements in all cases are a result of the initialization (finite differencing) errors and can be thought of as an impulse which initiates free oscillations in the systems. The effects of grid variation become apparent after about 20 min with gravity wave interactions causing changes in amplitudes and periods of the oscillation. In all cases the period was about  $6\Delta t$  initially; the equal-mesh profile retains this period throughout the forecast but the profiles are modified in the other cases to those with somewhat longer and variable periods. These modifications are undoubtedly due to the differences in the behavior of the computational gravity waves which are generated by the variable-mesh differencing. The amplitude of the control case profile remains steady after the system reaches an equilibrium state but the other amplitudes show increases which probably result from the superposition of the additional gravity waves mentioned above. The Graded:15 and 2-Step:15 profiles are very similar, both having an average variation about four times that of the control case. Plan views of the velocity component and height fields (not shown) display symmetries throughout the entire forecast period. The  $u$ ,  $v$  fields have radial (rotational  $180^\circ$ ) anti-symmetry, and the  $h$  field has rotational ( $90^\circ$ ) symmetry. Detailed time-step examinations of the fields showed that there was apparently no time splitting of the fields; but



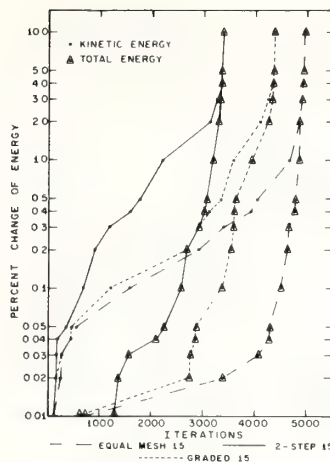


FIGURE 13.—Time iteration number of the first occurrence of certain percent changes of kinetic and total energy for the experiments in group D (Equal Mesh:15=Constant:15).

that the computations did produce  $2\Delta S$  waves of small amplitude which were more evident in the control-case computations.

The effects of nonsymmetry are apparent in the results (not shown) for experiment 18 where the symmetric initial state was prescribed off-center in the grid system. Here, the gravity waves reflected at the boundaries at different times and the wave interaction pattern quickly destroyed the symmetry of the various fields. The center of the system remained in the box where it was initially prescribed, but its position is not stationary as evidenced by the oscillations in the mean velocity component values for this box. After 42 hr, a  $2\Delta t$  oscillation became evident in both the percentage changes in kinetic energy and available potential energy, with the percentage changes in total energy increasing to an order of magnitude larger than those in the comparable centered-vortex experiment (exp. 14). The RMSE profile for the height field (not shown) has the same character as that of experiment 14.

**Group D.** The very intense vortex specified for this group of experiments gave a central height deficit of 200 m and a speed maximum of 22.1 m/s at 50 km from the center (fig. 6). With this specification the initialization errors are of much larger amplitude than those for groups B and C, and amplification of the computational errors through nonlinear interactions proceeds at a more rapid rate than for those experiments.

The profiles of  $\Delta TE$  and  $RMSE/h$  (not shown) have relatively the same character as those for the group C experiments (figs. 10 and 11) except that increases in amplitudes are in evidence earlier in the forecast period. In the later periods of the integrations, there is a pro-

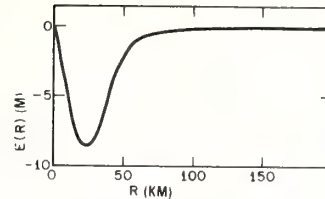


FIGURE 14.—The approximate form of the amplitude of the initial height error pattern for experiments 14 through 18.

nounced  $2\Delta t$  oscillation in the  $\overline{\Delta TE}$  and kinetic energy profiles for each experiment.

Figure 13 gives the iteration count of the first occurrence of selected percentage changes (from the initial values) of kinetic and total energy. The 2-Step:15 grid computations reached all percentage change levels (greater than 0.02 percent) in the least number of iterations, the Constant:15 computations in the largest number, and the Graded:15 somewhat half-way between the two. All three experiments showed changes of up to 0.05 percent in kinetic energy during the initial 550 iterations, followed by moderate increases in the 2-Step:15 computations and relatively slow increases in the other two cases.

In these experiments, the velocity component and height fields showed symmetries similar to those described for the group C experiments throughout most of the forecast period. During the later iterations, noticeable asymmetries appeared in these fields, and as the computations approached instability, the symmetry in the fields was totally destroyed.

**Discussion of the group B, C, and D results.** The initial error pattern in the height field has a wave form given approximately by

$$E(R) \sin 4\theta, \quad 0 \leq \theta \leq 2\pi$$

where  $\theta$  is the usual horizontal azimuth displacement.  $E(R)$  is given schematically in figure 14, for experiments 14 through 18. This initial fluid displacement from the balanced state excites gravity wave propagation which is both radial and tangential; the tangential propagation being due, in part, to advection by the vortex fluid motion.<sup>4</sup>

The total height-field contour pattern is altered from the initial concentric circles to concentric elliptical shapes, and the contours retain this characteristic throughout the forecast periods regardless of the mesh on which the integration is performed. Wave reflection at the boundaries and subsequent wave interaction give rise to further error components because of the nonlinearity of the system.

In the variable-grid experiments, the mesh variation adds its error contribution through the advection of large grid-scale truncation by the gravity waves which reflect

<sup>4</sup> In the equal-mesh computations (exp. 14) the initial impulse traveled radially to the boundary in 45 min ( $30\Delta t$ ), which gives an average wave speed  $c=165$  m/s.

from the boundaries. The truncation error is local in nature and initially dominates in the center of the grid system where the vortex is relatively intense. But here  $\Delta S$  is minimum; hence, the maximum truncation error is equivalent to that for an equal-mesh system having the minimal grid increment. Within several tens of iterations, the excited truncation error of the coarser grid contaminates the computations on the fine sections of the grid; and all subsequent error analysis must use the largest mesh increment in an error estimate.

The above phenomenon is manifested in the profiles of  $RMSE:h$  for the experiments, and therefore aids in a valid comparison of the integrations on the various grid systems. Certain aspects of the grid systems must be considered in the analysis. Referring to figures 2 and 3 and table 2, we note that the 2-Step:15 system has fixed fine resolution in the  $(300 \text{ km})^2$  central region whereas that for the Graded:15 is in the  $(210 \text{ km})^2$  central region. For the experiments in group B, this is relatively unimportant since the variations in the initial vortex height field and velocity components are small in the region from 105 km to 150 km from the center (fig. 6). The group C vortex (fig. 6) has a greater variation in this region. The Graded:10 system (fig. 4) improves the resolution of the vortex centers since the velocity component maxima are contained within the  $(100 \text{ km})^2$  central region that has 10-km resolution. As was pointed out previously in the group B experiments, although the Graded:10 results were best relative to the control case, the comparable 2-Step:15 results indicate that the 2-Step:15 mesh would give sufficient resolution for weak vortex-type motions. The utility of the Graded:15 system was not realized here because of the weak character of the physical system in regions of grid variation; whereas the grid variation given by the Graded:10 system enhanced the representation of the vortex near its center. The truncation error generated in the coarse-mesh regions of the latter case was undoubtedly small because of the small amplitude of the gravity waves generated by the processes described previously.

The vortex prescribed in the group C experiments proved to be a more crucial test of the mesh systems. Clearly, for the first 24 hr of the forecast period, the Graded:10 variable grid yielded integrations which were superior to the other variable grid results; but by 36 hr the integrations on that grid gave results which were comparable to the 2-Step:15 and Graded:15 results. By 48 hr, this integration appeared to be degenerating under some form of computational instability. Detailed time-step examination of the height and velocity component fields revealed no time splitting of the fields as is usually observed in linear models which use the leapfrog time-integration scheme. But the large amplitude  $2\Delta t$  oscillations of the  $\Delta TE$  profile, when considered together with increasing values of  $RMSE:h$ , strongly suggest the presence of aliasing errors common to nonlinear systems that do not damp the large wave-number space oscillations. The

fact that the system remains stable may be a result of the inherent smoothing which is built into the "box" method of integration, but it appears that the computations are yielding to an accumulation of energy in the short wavelengths, and the physical system is deteriorating from a quasi-balanced state.

The  $2\Delta t$  oscillation is evident in the  $\Delta TE$  profiles for all the integrations in this group, including the control case. Hence, we might interpret this as a manifestation of an iteration-by-iteration "return to balance" phenomenon.<sup>5</sup> The increase in amplitude of the  $\Delta TE$  profiles for the variable-grid cases reflects the ability of the system to restore a balance under the influence of the errors generated at each time step.

Although the fine-resolution region of the 2-Step:15 grid contains a larger section of the vortex than does the analogous region of the Graded:15 grid, the results of the integration clearly demonstrate the advantage of a gradual change in mesh increment over an abrupt one. On each mesh there is essentially an increase in box area of 4 to 1 (table 2) going from the center of the system to the boundary. Figure 10 shows that there is no large difference in the  $RMSE:h$  profiles for either case although there is an indication that the height field for the Graded:15 integration may be slightly better than that for the 2-Step:15 at the end of the 48-hr period. Table 4 lists the 3-hr time average of the  $RMSE:h$  for the periods centered at 1.5, 24, and 46.5 hr. We note the obvious deterioration of the Graded:10 computations and the relative improvement of the Graded:15 computations over the 2-Step:15. The profiles of  $\Delta TE$  for these cases show that there is indeed a difference in the character of the forecasts which is grid dependent.

The phenomena discussed above for the group C experiments are observed in the group D experiments except that they occur on a much shorter time scale. Here, the computational mode interacts nonlinearly with a large-amplitude physical mode and the computational noise grows at a rapid rate. The graph of energy changes versus iteration count for the control experiment 19 (fig. 13) shows the typical energy increases which are associated with the nonlinear computational instability of integrations done on a constant-resolution mesh. The additional

TABLE 4.—Three-hr time averages of  $RMSE:h$  (m) for experiments 15, 16, and 17

Experiment number	Time periods (hr)		
	0-3	22.5-25.5	45-48
15	2.07	2.05	2.41
16	1.92	1.83	2.57
17	2.22	2.12	2.29

<sup>5</sup> In the Graded:10 experiment (exp. 16), the modulated  $2\Delta t$  oscillation in the  $\Delta TE$  profile could possibly be interpreted as a "folding" of a temporal 2.1-2.2 increment oscillation in the manner described by Robert et al. (1970). The computational and/or physical significance of this frequency in the temporal variation of an areal average is not readily apparent.



computational noise introduced into the calculations by the use of a variable grid structure stimulates the growth of computational errors. This is evidenced by the graphs of energy changes for the 2-Step:15 and Graded:15 grid experiments (fig. 13).

In these experiments, kinetic energy is the principal component of the total energy; the available potential energy of the system is smaller by an order of magnitude. From the graphs (fig. 13) we note that the kinetic energy quickly undergoes relatively large percentage changes, but these are compensated for in the total energy change by very large percentage changes in available potential energy (not shown). Comparison of the results of the 2-Step:15 and Graded:15 grid computations against those for the Constant:15 grid shows that computational trends exhibited in the group C experiments were correctly interpreted. Here, the kinetic energy changes in the Graded:15 experiment closely resemble those of the control computation up to the 0.5 percent change level, whereas those for the 2-Step:15 case differ noticeably. In the interval 0.05–0.5 percent, a percent change level was reached in the Graded:15 grid computations, on the average, in 85 percent of the number of iterations taken by the control case; whereas the average was 44 percent in the 2-Step:15 case.

A comparison of the percent changes of total energy shows that the number of iterations taken to reach a particular percent change level (in the interval 0.2–10.0 percent) was on the average 79 percent of the control case value for the Graded:15 grid case, whereas in the 2-Step:15 case the number was, on the average, 59 percent. These statistics certainly indicate that the error growth rate for computations done on the graded-type variable grid is substantially less than that for the comparable computations on a telescope-type grid.

## 7. SUMMARY AND CONCLUSIONS

Three variable Cartesian grids were used in the numerical integration of the shallow-water equations over a square two-dimensional domain. The grids were selected from a family of Cartesian grid structures which possesses many degrees of variation. The 2-step formulation has the advantage of having only one interface at which there is an abrupt change in mesh length, whereas the Graded:10 and Graded:15 systems of the double annulus group effect a gradual change. The single and triple annulus configurations (fig. 1) were not used since they gave variations which are either too pronounced or too gradual. For the experiments considered here, we restricted the inner to outer ring mesh ratios to be either 3:1 or 2:1.

Integrations on fixed fine-resolution mesh were done in three of the cases (groups B, C, D). These computations offer criteria against which the variable grid experiments can be compared. The differences in the results are due to the variation in mesh structure which (1) alters the

forms of the second order finite-difference equations in the regions of grid variations because of the box-method formulation and (2) introduces further approximation errors through an averaging process along the line segments which form the boundaries of the individual boxes. This essentially introduces spatial smoothing into the integration formulas. The equations do not conserve total energy, but the computations for the control (constant mesh) cases showed no apparent trend toward an increase or decrease of total energy throughout the forecast periods for experiments 10 and 14, and for most of the experiment 19 forecast. Hence, we can consider the finite-difference equations to be "nearly" total energy conserving. The weak vortex computations (group B) yielded total energy changes which closely approximated those of the control case.

In the computations with a more intense vortex (group C), the departures from the control case are pronounced in some instances but remain less than 0.03 percent in magnitude. The behavior of the height field is more striking; the control case  $RMSE/h$  shows a bounded  $6\Delta t$  oscillation (fig. 10) which is strongly correlated with the free oscillation at the vortex center (fig. 12), and which has a temporal mean of approximately 1.25 m. The variable-grid profiles of  $RMSE/h$  have temporal means from two to three times larger with more pronounced variations. The group D experiments purposely used a very intense vortex as the initial state in order to observe the behavior of error growth and nonlinear computational instabilities. The results prior to the onset of instability replicate, on a shorter time scale, those of the group C experiments.

Although the differences in the results are due entirely to the grid structures, the amplification of some error is due to the nondamping characteristic of the time integration scheme. No effort was made to suppress the high-frequency temporal and/or spatial oscillations as might be done, say, with a Lax-Wendroff (1960) type integration rule; this is evident in the results for experiment 17.

Considering the experiments in toto, the results indicate that, for a *weak* vortex-type motion embedded in a zonal current, the 2-step type telescope grid might be adequate since the integrations have relatively small error. The computational times and computer memory requirements are minimal when compared to the comparable equal-mesh computations. On the other hand, for an *intense* vortex a graded-type grid yields relatively better numerical integrations at the expense of an increase in computational time (compared to that for the 2-step type grid). Clearly, though, relative to the constant resolution grid integrations, the graded-type variable grid yields integrations that are more satisfactory than the telescope-type grid in terms of both the error induced by the grid structure in the differencing schemes and the error growth rate.

The application of these horizontal grid structures to numerical integrations of primitive equation multilevel models of atmospheric systems can result in considerable

savings in computer memory requirements and running times. The graded annulus-type grids are systematically constructed and allow a large range of variation and resolution. For systems which are active in these central regions and quiescent in the peripheral regions, the central mesh can be specified to give resolutions that would permit definitions of small-scale phenomena. In these cases, the small time-increment needed to maintain computational stability would be a major consideration. For long-term integrations, such as in the study of hurricane dynamics, the growth of any computational mode (as evidenced in exp. 17) must be controlled since variable-type horizontal grid structures obviously generate error components that can become unstable if not damped. This instability is primarily due to nonlinear interaction. In these cases, a time integration scheme can be used that minimizes, or eliminates entirely, the computational mode. For model investigations of very short time-scale phenomena, such as cumulus dynamics, the damping of high-frequency oscillations might be unnecessary.

## APPENDIX

Experiments 1, 2, 3, and 4 were designed to compare the height gradient operators  $L_s(\ )$  and  $G_s(\ )$ . These experiments showed that the momentum tendencies and the  $v$ -component field had less error when the  $G_s(\ )$  operator was used. Hence, the  $G_s(\ )$  operator was used in all of the remaining experiments. Experiments 3, 4, and 5 differ only in the manner of specifying the initial values for the box-means of the dependent variables. In experiment 5, the point values of the functions [eq (5) and (6)] at the box centers were selected as the initial means. In experiments 3 and 4, initial values were specified through analytical integration of eq (5) and (6). A comparison of the results for these experiments showed that the correct mean values  $\overline{hu}$ ,  $\overline{hv}$ , and  $\overline{h}$  gave slightly better results initially, but after several hundred iterations there were no significant differences in the  $\overline{v^2}$  and  $\Delta\overline{TE}$  statistics for these experiments. This indicated that the computational (finite difference) errors soon dominated the initialization errors in the calculations, and the point values  $hu$ ,  $hv$ , and  $h$  were sufficient for beginning the integrations. The point values were used in the initialization of all subsequent experiments.

Experiments 7, 8, and 9 had a weak, flat profile vortex (fig. 6) for the initial state. East-west cyclic continuity was used in experiments 7 and 8; experiment 9 used a closed system. Comparisons of the experiments showed that, after an initial adjustment, the changes in mean total energy from the initial value for each experiment exhibited a smooth oscillation with time; but the amplitude of this oscillation in experiments 7 and 8 was  $\sim 10^2$  kJ m $^{-2}$  whereas for experiment 9 it was  $\sim 10^{-1}$  kJ m $^{-2}$  (the mean total energy  $\overline{TE}$  is on the order of  $10^4$  kJ m $^{-2}$  in these experiments). This behavior is related to the gravity wave interactions and the symmetry of the calculations. In the closed system, the initial perturbations on the prescribed height field (which are due to the differencing of the analytically specified initial fields) are symmetric and remain so throughout the entire integration. By removing the east and west walls and thereby allowing wave propagation through the system (instead of wave reflections at the walls), the symmetry patterns are altered; a strong beat pattern is induced and the north-south symmetry is strongly modified. The remaining experiments (10 through 18) were performed with the closed system to avoid this effect.

## REFERENCES

- Anthes, Richard Allen, "Numerical Experiments With a Two-Dimensional Horizontal Variable Grid," *Monthly Weather Review*, Vol. 98, No. 11, Nov. 1970, pp. 810-822.
- Grammelvedt, Arne, "A Survey of Finite-Difference Schemes for the Primitive Equations for a Barotropic Fluid," *Monthly Weather Review*, Vol. 97, No. 5, May 1969, pp. 384-404.
- Kuribara, Yoshio, and Holloway, J. Leith, Jr., "Numerical Integration of a Nine-Level Global Primitive Equations Model Formulated by the Box Method," *Monthly Weather Review*, Vol. 95, No. 8, Aug. 1967, pp. 509-530.
- Lax, Peter D., and Wendroff, Burton, "Systems of Conservation Laws," *Communications on Pure and Applied Mathematics*, Vol. 13, Interscience Publications, Inc., New York, N.Y., 1960, pp. 217-237.
- Noh, W. F., "CEL: A Time-Dependent Two-Space-Dimensional Coupled Eulerian-Lagrange Code," *Methods in Computational Physics*, Vol. 3, Academic Press, New York, N.Y., 1964, pp. 117-179.
- Robert, André J., Shuman, Frederick G., and Gerrity, Joseph P., Jr., "On Partial Difference Equations in Mathematical Physics," *Monthly Weather Review*, Vol. 98, No. 1, Jan. 1970, pp. 1-6.
- Shuman, Frederick G., and Stackpole, John D., "Note on the Formulation of Finite Difference Equations Incorporating a Map Scale Factor," *Monthly Weather Review*, Vol. 96, No. 3, Mar. 1968, pp. 157-161.

[Received November 30, 1970; revised February 8, 1971]



October 1971

767

UDC 551.515.21:551.509.313

# THE RESPONSE OF A TROPICAL CYCLONE MODEL TO VARIATIONS IN BOUNDARY LAYER PARAMETERS, INITIAL CONDITIONS, LATERAL BOUNDARY CONDITIONS, AND DOMAIN SIZE

STANLEY L. ROSENTHAL

National Hurricane Research Laboratory, Environmental Research Laboratories, NOAA, Miami, Fla.

## ABSTRACT

Tropical cyclone model experiments are summarized in which the drag coefficient and the analogous exchange coefficients for sensible and latent heat are varied. During the early portions of the immature stage, the response of the model storm follows linear theory and growth is more rapid with larger drag coefficients. However, the ultimate intensity reached by model storms varies inversely with the drag coefficient. The experiments indicate that air-sea exchanges of latent heat are crucial for the development and maintenance of the model storm. The air-sea exchange of sensible heat appears to be far less important.

Experiments conducted with open lateral boundary conditions revealed that the structure and intensity of the mature stage of the model cyclone is relatively insensitive to the initial perturbation and to the size of the computational domain. The time required to reach the mature stage is, however, quite sensitive to these influences.

Comparisons between experiments with open and mechanically closed lateral boundaries show the lateral boundary conditions to be extremely important. For computational domains of 2000 km or less, model cyclones with closed lateral boundaries are less intense than their counterparts with open lateral boundaries. However, the intensity of the closed systems increases markedly with domain size and the experiments suggest that differences due to boundary conditions might be minimized if the domain size exceeded 2000 km.

## 1. INTRODUCTION

This paper summarizes a new series of experiments conducted with the circularly symmetric tropical cyclone model described by Rosenthal (1970b). Recent studies with a three-dimensional model (Anthes et al. 1971a, 1971b) indicate that many symmetric results can be extrapolated to the asymmetric case and, therefore, justify continued experimentation with symmetric models.

The new experiments are based on a version of the symmetric model which differs from that described by Rosenthal (1970b) only in one important aspect. Whereas air-sea exchanges of sensible and latent heat were previously simulated by some rather pragmatic constraints on the Ekman layer humidities and temperatures, these energy fluxes are now computed explicitly by the bulk aerodynamic method. Details are given in section 2.

Comparisons of the physical and numerical characteristics of this model and those of Ooyama (1969) and Yamasaki (1968) were presented earlier (Rosenthal 1970b) and need not be repeated here. More recently, a new symmetric model (Sundqvist 1970) has appeared in the literature. There are a number of differences between Sundqvist's model and ours; the most prominent of which is his use of the gradient wind assumption. In our system, the primitive equations govern the horizontal motion. Sundqvist works in the  $p$ -system in contrast to our  $z$ -system, but he has better vertical resolution (10 levels spaced at 100-mb intervals in contrast to our seven irregularly spaced levels). Radial resolution is 25 km in Sundqvist's model, while most of our calculations are performed with a radial increment of 10 km.

Section 2 of this paper gives a verbal description of the model and also presents the formulations of the air-sea exchanges of sensible and latent heat that have now been adopted. Section 3 describes a basic (control) experiment that serves as a comparison for the later experiments.

Section 4 is concerned with the interesting dual role played by surface drag friction in hurricane dynamics; frictional convergence of water vapor in the Ekman layer drives the organized cumulus convection but, on the other hand, drag friction at the air-sea interface is the prime dissipater of kinetic energy for mature tropical cyclones.

The still controversial problem (Dergarabedian and Fendell 1970) of the significance of air-sea exchanges of sensible and latent heat is the topic of section 5. In general, the experiments discussed in sections 4 and 5 qualitatively confirm conclusions reached by Ooyama (1969). In view of substantial differences in the physical and numerical details of the two models, their qualitative agreement is an important matter which lends credence to both models.

Section 6 is concerned with some of the more arbitrary aspects of the model such as lateral boundary conditions, initial conditions, and radial extent of the computational domain. Finally, section 7 reviews the main conclusions of the paper.

## 2. REVIEW OF THE MODEL

A brief description of the main features of the model is given below. The reader concerned with mathematical details should refer to Rosenthal (1970b). The vertical structure of the atmosphere is represented by seven levels and geometric height is the vertical coordinate. The levels correspond to pressures of 1015, 900, 700, 500, 300, 200, and 100 mb in the mean tropical atmosphere. All variables are defined at all levels. The primitive equations govern the horizontal motion. The hydrostatic assumption is employed.

The continuity equation is simplified as follows. The local rate of change of density is neglected and a climatological density (a function of height alone) is used to evaluate the vertical and horizontal mass flux terms. We then eliminate the external gravity wave by demanding

that the vertical integral of the horizontal mass divergence vanish.

In the control experiment, the radial limit of the computational domain is 440 km. The system is open at the lateral boundary. The lateral boundary conditions require the relative vorticity and horizontal divergence to vanish. In addition, the radial derivatives of potential temperature and specific humidity are also required to vanish.

Through a generalization of the procedure suggested by Kuo (1965), the model simulates convective precipitation (and the macroscale heating due to this latent heat release) as well as the enrichment of the macroscale humidity due to the presence of the cumuli. Convection may originate in any layer, provided that the layer has a water vapor supply from horizontal convergence and that conditional instability exists for parcels lifted from the layer. Nonconvective precipitation is also simulated. Details are given by Rosenthal (1970b).

Time derivatives are estimated by forward differences except in the case of specific humidity, where a Matsuno (1966)-type integration is employed. Advective derivatives are calculated by the upstream method except for the case of humidity, where a conservation form of the equations is used. All nonadvective space derivatives are calculated as centered differences.

Grid points in the radial direction are staggered. Horizontal velocity is defined at the radii

$$r_j = (j-1)\Delta r, \quad j=1, 2, \dots \quad (1)$$

Temperature, pressure, vertical motion, and humidity are carried at the radii

$$r_j = (j-\frac{1}{2})\Delta r, \quad j=1, 2, \dots \quad (2)$$

The constant drag coefficient ( $C_D$ ) of  $3 \times 10^{-3}$  used in previous experiments (Rosenthal 1969, 1970a, 1970b) has been replaced with Deacon's empirical relationship (Roll 1965, p. 160). The latter may be written

$$C_D = 1.1 \times 10^{-3} + 4.0 \times 10^{-5} |V_{10}|. \quad (3)$$

The symbol  $|V_{10}|$  denotes the wind speed 10 m above the sea surface. In the model, the sea-level wind is used to evaluate  $C_D$ .

The sensible and latent heat fluxes at sea level are calculated, respectively, from

$$F_s = [\bar{\rho} C_p C_S |V_{10}| (T_{sea} - T)]_{z=0} \quad (4)$$

and

$$F_l = [\bar{\rho}_L C_L |V_{10}| (q_{sea} - q)]_{z=0}. \quad (5)$$

Here,  $C_S$  and  $C_L$  are exchange coefficients for sensible and latent heat analogous to  $C_D$ ,  $T_{sea}$  is the sea surface temperature,  $q_{sea}$  is the saturation specific humidity at the temperature and pressure of the sea. The remainder of the symbols are standard. Equation (4) is used only when  $(T_{sea} - T)_{z=0} > 0$ . In other circumstances the flux is zero. When  $(q_{sea} - q)_{z=0} < 0$ , the latent heat flux is zero.

In the basic experiment,  $C_S = C_L = C_D$ . The flux convergences that appear in the thermodynamic and water

TABLE 1.—Standard values of thermodynamic variables

Level	Height (m)	$\theta$ (°K)	$\bar{T}$ (°K)	$\bar{p}$ (mb)
1	0	300	301.3	1015.0
2	1,054	303	294.1	900.4
3	3,187	313	282.6	699.4
4	5,898	325	266.5	499.2
5	9,697	340	240.8	299.2
6	12,423	347	218.9	199.5
7	16,621	391	203.1	101.1

vapor continuity equations are evaluated through the assumption that the fluxes have a linear variation over height and are zero at and above the height of the 900-mb level. This is based on the assumption that at 900 mb and above, fluxes produced by small-scale turbulence are insignificant in comparison to those produced by cumulus-scale motions.

The sea temperature is an external parameter and, for experiments discussed here, is taken 2°K greater than the initial sea-level air temperature (the latter is initially horizontally uniform for all experiments). Since the sea-level air temperature varies with time according to the thermodynamic equation, the air-sea temperature difference varies both with radius and time as the model hurricane evolves. In our basic experiment (section 3), the sea-level air temperature approaches the sea temperature before rapid development begins. Subsequent experiments, as well as a recent linear analysis by Rodenhuis (1971), have indicated that an important aspect of the boundary layer is its static stability. The model yields a somewhat more rapid development (in comparison to the basic experiment, section 3) when the initial sea-level air temperature is taken 2°K warmer than in the basic experiment but with the same sea temperature.

### 3. THE BASIC EXPERIMENT (EXP. S35)

The initial conditions for this experiment are those used for our previous (Rosenthal 1970b) calculations. They are established as follows. A field of standard potential temperatures [a function of height alone and almost identical to those of the Hebert and Jordan (1959) mean hurricane season sounding] is specified. With a lower boundary condition of 1015 mb, hydrostatic standard pressures and temperatures (table 1) are computed for the levels above the surface.

The initial temperature field is then specified by

$$T_{i,j} = \bar{T}_i + T_* \left( \cos \frac{\pi}{\hat{r}} r_j + 1 \right) \sin \frac{\pi}{z_7} z_i \quad (6)$$

where  $i$  and  $j$  are, respectively, height and radial indices,  $\bar{T}_i$  is the standard temperature,  $T_* = 0.16^\circ\text{K}$ ,  $\hat{r} = 440$  km, and  $z_7$  is the height of level 7. These are given in table 1. The initial pressure at level 7 is then taken to be the standard value and the hydrostatic equation is integrated downward to obtain the remainder of the initial pressure field. Finally, the gradient wind equation is solved for the initial tangential wind while the initial radial and



TABLE 2.—Initial values of relative humidity at the information levels

Level	Height	Relative humidity
	(m)	(%)
1	0	90
2	1,054	90
3	3,187	54
4	5,898	44
5	9,697	30
6	12,423	30
7	16,621	30

vertical motions are taken to be zero. A base state relative humidity is specified as a function of height (table 2). By use of the data given in table 1, a base state specific humidity is calculated. The initial specific humidity is then assumed horizontally homogeneous and equal to this base state value.

The initial surface wind reaches a maximum of 7 m/s at a radius of 250 km. The central pressure of the vortex is 1013 mb. Since the initial conditions are clearly arbitrary, the early portions of the time integration are not particularly significant. This matter will be reconsidered later.

Radial resolution for the basic experiment is 10 km and the time step is 2 min. A lateral mixing coefficient of  $2.5 \times 10^3 \text{ m}^2 \cdot \text{s}^{-1}$  is used for momentum, heat, and water vapor.

Figure 1 summarizes the control storm's evolution at sea level.<sup>1</sup> The "organizational" period is about twice as long as that found in our previously published results (Rosenthal 1970b). This is primarily a result of replacing the constant drag coefficient ( $3 \times 10^{-3}$ ) with the variable  $C_D$  given by eq (3). Linear analysis (Ooyama 1969, Rosenthal and Koss 1968) shows growth rates for models of this general type to be directly proportional to the drag coefficient. From eq (3), the largest  $C_D$  at the initial instant is about  $1.38 \times 10^{-3}$  and this is less than half the constant  $3 \times 10^{-3}$  used in the previous calculations. Equation (3) does not yield a  $C_D$  of  $3 \times 10^{-3}$  until a wind of 47.5 m/s is reached.

The time needed for the model cyclone to become organized is also highly sensitive to the arbitrary initial conditions. Rosenthal (1970b) showed that enrichment of the initial humidity field could shorten the organizational period by several days. Ooyama (1969) showed that variations of the scale of the initial perturbation strongly affected the length of this period while Anthes et al. (1971b) showed a relationship between the intensity of the initial perturbation and the length of the organizational period. The latter is revealed by figure 2 where we show the result of an experiment (Q2) in which  $T_*$  [eq (6)] was three times the value used for the control experiment. This provided a maximum initial wind approximately twice that of the control. The organizational period for Q2 is only 24 hr and peak intensity is reached at 120 hr.

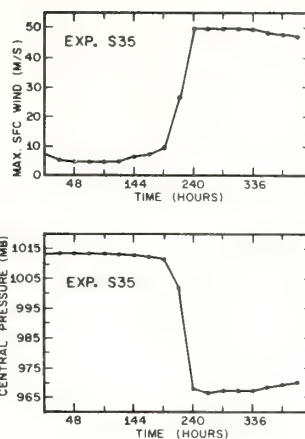


FIGURE 1.—Results from experiment S35. (Top) maximum surface wind as a function of time and (bottom) central pressure as a function of time.

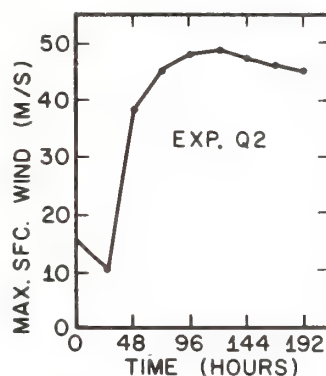


FIGURE 2.—Maximum surface wind as a function of time for experiment Q2. The initial maximum surface wind for this experiment is twice as strong as for the control.

Despite differences in the histories, the peak intensities for S35 and Q2 differ only by 1.5 m/s.

The material presented in the last few paragraphs indicates that the length of the organizational period, as given by model calculations, is only of significance when experiments are compared against each other. Ramage's (1970) comments concerning the unrealistic length of the organizational period of some of Ooyama's (1969) experiments would, therefore, appear to be irrelevant since Ooyama's calculations are based on hypothetical initial data. Ramage's point, of course, will become highly pertinent when models reach a level of sophistication that justifies their application to real data.

Figures 3, 4, 5, 6, and 7 illustrate structural features of the basic experiment (at 312 hr) that are representative of the period between 240 and 336 hr. The wind field (fig. 3), while similar to those obtained previously, is somewhat smoother and the thermal structure (fig. 4) is substantially improved (cf. fig. 7, Rosenthal 1970b). The weak warm center at low elevations and large radii is produced by sub-

<sup>1</sup> Pressure is not defined at zero radius because of the grid staggering [eq (1) and (2)]. Central pressure values presented in this paper are pressure values at  $z=0$ ,  $r=\Delta r/2$ .

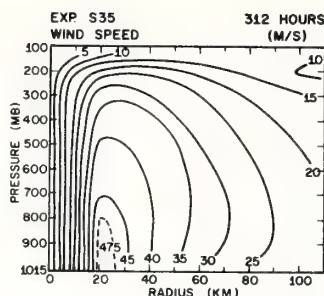


FIGURE 3.—Cross section of wind speed at hour 312 of experiment S35. Isotachs are labeled in m/s.

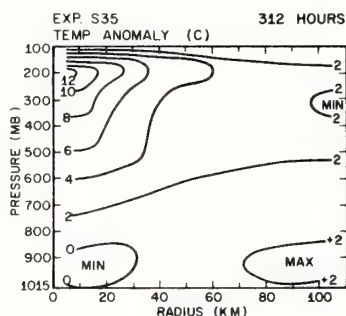


FIGURE 4.—Cross section of temperature anomalies at hour 312 of experiment S35. Isotherms are labeled in °C.

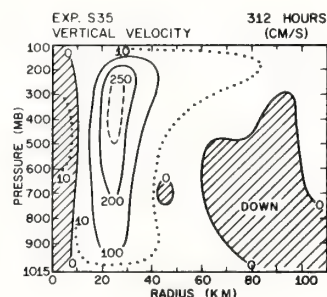


FIGURE 5.—Cross section of vertical velocity at hour 312 of experiment S35. Isotachs are labeled in cm/s. Hatched areas indicate negative values (subsidence).

sidence (fig. 5) while the low-level cool pocket near the storm center is a result of a slight excess of adiabatic cooling over the sum of the convective heating and the air-sea exchange of sensible heat. We note that empirical evidence in support of low-level cold pockets near the storm center exists (Hawkins and Rubsam 1968, Colón et al. 1961). The vertical motions (fig. 5) show a more distinct region of subsidence ("eye") at the storm center than found in our previous experiments.

The relative humidity (fig. 6) shows saturation in the region of major upward motion. This region is an analog to the eye wall. An upper tropospheric tongue of saturation extends outward to large radii and appears to be analogous to the cirrus canopy. The humidity pattern is highly

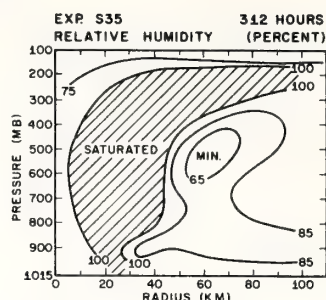


FIGURE 6.—Cross section of relative humidity (percent) at hour 312 of experiment S35. Saturated areas are hatched.

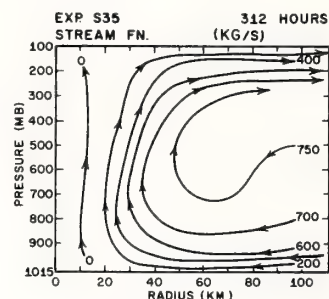


FIGURE 7.—Cross section of the mass transport Stokes' stream function at hour 312 of experiment S35. Streamlines are labeled in kg/s. No streamlines are drawn inside the 10-km radius.

correlated to the meridional circulation as revealed by the Stokes' stream function for mass transport (fig. 7).

The midtropospheric humidity minimum near 60-km radius is very nearly coincident with the circulation center revealed by figure 7. Relative humidity values in this region are only 20 percent or so greater than the initial values. The dry tongue extending to large radii at low elevations is associated with the subsidence already noted.

Detailed histories of various integral properties are not presented since these are similar to those previously published (Rosenthal 1970b). Tables 3 and 4 do, however, make some comparisons between the mature stage of the model and that of hurricane Daisy (1958). The data for hurricane Daisy are taken from Riehl and Malkus (1961). In view of the observational uncertainties in the empirical estimates and the natural storm-to-storm variability [cf. estimates by Riehl and Malkus (1961) with Hawkins and Rubsam (1968) and Miller (1962)], the agreement between the model values and those for hurricane Daisy is as good as can be expected.

#### 4. DUAL ROLE OF THE DRAG COEFFICIENT

Linear analysis shows growth rates to be directly proportional to the drag coefficient, as already noted, and to the boundary layer humidity (Ooyama 1969, Rosenthal and Koss 1968). From the point of view of water vapor supply, this result is entirely logical since the primary



TABLE 3.—Sensible heat flux and evaporation rates for 1958 hurricane Daisy and experiment S35 at 312 hr. Rainfall rates for experiment S35 are also shown.

	Average model values for radial interval 0-100 km at 312 hr	Average values for hurricane Daisy for radial interval 0-80 n.mi. on Aug. 27, 1958
Sensible heat flux ( $\text{cal} \cdot \text{cm}^{-2} \cdot \text{s}^{-1}$ )	$1.5 \times 10^{-3}$	$2.9 \times 10^{-3}$
Evaporation ( $\text{cm/day}$ )	1.8	2.3
Rainfall ( $\text{cm/day}$ )	22	

TABLE 4.—Kinetic energy generation and dissipation by surface drag friction for 1958 hurricane Daisy and experiment S35 at 312 hr

	Integrated values from model for radial inter- val 0-100 km at 312 hr	Integrated values for hurricane Daisy for radial interval 0-60 n.mi. on Aug. 27, 1958
Kinetic energy production ( $10^{14}$ kJ/day)	5.8	4.6
Kinetic energy dissipation by surface friction ( $10^{14}$ kJ/day)	2.9	2.1

TABLE 5.—Experiments in which the drag coefficient is varied during the immature stage of the model cyclone. The initial data for these experiments are from hour 168 of experiment S35.

Experiment	$C_D$	$C_S = C_L = C_E$	$C_D/C_E$
S35	eq (3)	eq (3)	1
Q3	$2 \times \text{eq (3)}$	do.	2
Q5	$5 \times \text{eq (3)}$	do.	5
Q17	$0.75 \times \text{eq (3)}$	do.	$3/4$
Q20	$0.20 \times \text{eq (3)}$	do.	$1/5$

source of water vapor for the organized cumulus convection is frictional convergence in the Ekman boundary layer. On the other hand, increased surface drag also leads to an increased dissipation of kinetic energy.

Apparently, in the earlier stages of development where linear theory is valid, increased water vapor convergence dominates increased dissipation (provided that the static stability is not too large) and growth rates increase with increasing drag coefficients.

However, as growth rates are increased through increases of the drag coefficient, the nonlinear effects should become significant earlier in the life cycle and linear theory should fail at an earlier point in the evolution of the cyclone. As a result, linear theory in itself is not sufficient for determining whether the ultimate intensity of the model cyclone will vary directly or indirectly with the drag coefficient. For this answer, we must resort to numerical experimentation. Ooyama's (1969) experiments indicate that the ultimate intensity decreases as the drag coefficient increases and the results of our experiments provide a similar conclusion.

In the first group of these experiments,  $C_D$  was varied during the linear phase of the system. The initial data for these experiments are taken from hour 168 of the control. The calculations were continued from this point with the modifications in drag coefficient shown by table 5 and do not differ from S35 in any other way. In particular, the exchange coefficients for latent and sensible heat are evaluated as they were in the control [eq (3)].

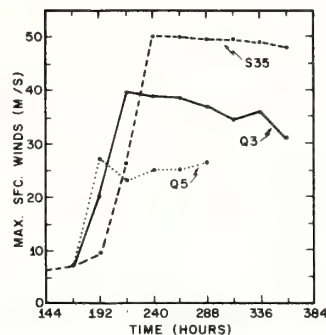


FIGURE 8.—Comparison of the maximum surface wind for experiment S35 with those for experiment Q3 [ $C_D$  twice the value given by eq (3)] and Q5 [ $C_D$  five times the value given by eq (3)]. See table 5 for details. Initial data for Q3 and Q5 are taken from hour 168 of S35.

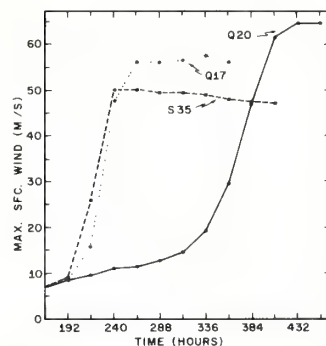


FIGURE 9.—Comparison of maximum surface wind for experiment S35 with those for experiments Q17 [ $C_D = 0.75$  of the value given by eq (3)] and Q20 [ $C_D = 0.20$  of value given by eq (3)]. See table 5 for details. Initial data for Q17 and Q20 are taken from hour 168 of S35.

Figure 8 shows the result of increasing<sup>2</sup>  $C_D$  (exp. Q3 and Q5) and, clearly, the early portions of these calculations behave as predicted by linear theory. On the other hand, as suggested by the arguments earlier in this section, linear theory becomes invalid sooner with increasing  $C_D$  and peak intensities are inversely related to the drag coefficient. Figure 9 verifies that decreased drag coefficients (exp. Q17 and Q20) lead to smaller growth rates but greater peak intensities. However, we should expect no growth at all when  $C_D$  is decreased to zero.

A similar series of experiments for the mature stage of the storm is summarized by table 6. Here, the initial data are from hour 288 of the basic experiment. Increasing the drag coefficient (fig. 10) results in a weakening of the storm which appears to vary directly with the amount by which  $C_D$  is raised (exp. Q4 and Q6). It is noted that the latent heat release (rainfall) and the kinetic energy generation are larger in Q4 and Q6 than in the control.

<sup>2</sup> For ease of expression, we will use terms such as "increase  $C_D$ ," "double  $C_D$ ," etc. Since  $C_D$  is wind dependent [eq (3)], these terms may not be quite accurate. What we, in fact, mean is that the constants in eq (3) are increased, doubled, etc.

TABLE 6.—Experiments in which the drag coefficient is varied during the mature stage of the model cyclone. The initial data are from hour 288 of experiment S35.

Experiment	$C_D$	$C_S=C_L=C_B$	$C_D/C_B$
S35	eq (3)	eq (3)	1
Q4	$2 \times \text{eq (3)}$	do.	2
Q6	$5 \times \text{eq (3)}$	do.	5
Q15	0	do.	0
Q19	$0.75 \times \text{eq (3)}$	do.	3/4

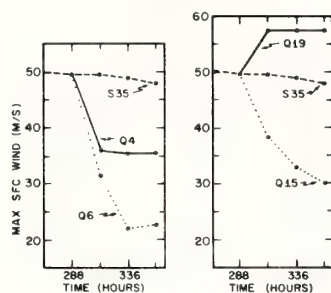


FIGURE 10.—Comparison of maximum surface wind for experiment S35 with those for experiment Q4 [ $C_D$  twice the value given by eq (3)], Q6 [ $C_D$  five times the value given by eq (3)], Q15 ( $C_D=0$ ), and Q19 [ $C_D=0.75$  of value given by eq (3)]. See table 6 for details. Initial data taken from hour 288 of S35.

When the drag coefficient is reduced by 25 percent (exp. Q19, fig. 10), the maximum surface winds rise by about 7 m/s. However, experiment Q15 ( $C_D=0$ ) indicates that a continued decrease in  $C_D$  will not result in ever stronger peak winds.

The response of the mature model storm to changes of  $C_D$  is then fairly complex. Increased drag coefficients lead to greater rainfall and latent heat release but to weaker peak winds due to increased dissipation. If the drag coefficient is decreased, the maximum winds increase unless  $C_D$  is made so small that the water vapor convergence at low levels becomes the dominant factor. In this case, reductions in drag coefficient result in reductions in the maximum winds.

### 5. AIR-SEA EXCHANGE OF SENSIBLE AND LATENT HEAT

Air-sea exchanges of sensible and latent heat have long been considered important ingredients in the development and maintenance of tropical storms. Palmén (1948) showed, on a climatological basis, that tropical storms form primarily over warm ocean waters ( $T_{sea} > 26^\circ\text{C}$ ). Malkus and Riehl (1960) showed that the deep central pressures associated with hurricanes could not be explained hydrostatically unless the equivalent potential temperature,  $\theta_e$ , in the boundary layer was  $10^\circ$  to  $15^\circ\text{K}$  greater than that of the mean tropical atmosphere. Byers (1944) pointed out that the observed near-isothermal conditions for inward spiraling air in the hurricane

boundary layer required a source of sensible heat to compensate for the cooling due to adiabatic expansion. Ooyama (1969) argued that if the  $\theta_e$  of the boundary layer remained constant, the conditional instability near the storm center would soon be decreased as the storm's warm core developed and that the vertical mean temperatures of atmospheric columns would be unlikely to increase further once the lapse rate became moist neutral.

Despite these arguments and observations, the evaporation rates for hurricanes are very small compared to the lateral inflows of water vapor and, furthermore, the air-sea exchange of sensible heat is only a few percent of the latent heat release (Riehl and Malkus 1961, Malkus and Riehl 1960). As a result, controversy over the importance of these boundary layer processes continues (Dergarabedian and Fendell 1970).

Ooyama (1969) found drastic reductions in the strength of his model storm when the air-sea exchanges of sensible and latent heat were suppressed. He pointed out that at sufficiently large radii, the boundary layer is divergent (the so-called Ekman layer "sucking"). Examples of this feature from our model are illustrated by figures 5 and 7. This subsidence tends to decrease the boundary layer  $\theta_e$ , since  $\partial\theta_e/\partial z < 0$  in the lower troposphere. Ooyama argued that unless the energy supply from the ocean can again raise the  $\theta_e$  of the boundary layer air to sufficiently large values before the inflowing air reaches the inner region, the convective activity will diminish in those regions and, hence, the storm will begin to weaken.

Ooyama's line of reasoning can be extended to show that evaporation is far more important than sensible heat flux. The air sucked into the boundary layer has a higher potential temperature than the original boundary layer air. The subsiding air has a smaller  $\theta_e$  only because it is relatively dry.

Experiments appropriate to the immature stage of the model storm are summarized by table 7. Results are given by figure 11. During the first 48 hr, the only experiments in this group that depart significantly from the control are those for which  $C_D$  was altered (Q10 and Q18). This is consistent with the linear theory described in the previous section and again verifies that frictional convergence of water vapor is the most crucial factor during the early stages of development. The small growth shown by experiment Q10 ( $C_D=0$ ) is a result of the meridional circulation already established in experiment S35 and which, therefore, is present in the initial data for Q10. Experiment Q18 is nearly identical to Q3 (table 5 and fig. 8) in which only  $C_D$  was doubled. In experiment Q11 where  $C_S$  and  $C_L$  are doubled while  $C_D$  is left as in the control, significant departures from the control are noted only after the mature stage is reached.

Experiments Q8 ( $C_S=0$ ) and Q9 ( $C_L=0$ ) support the extension of Ooyama's argument offered earlier. When the sensible heat flux is suppressed, the model storm develops a peak intensity of 45 m/s in comparison to 50 m/s for the control. When evaporation is suppressed, the peak intensity is only 22 m/s.

Experiments for the mature stage are listed in table 8 and results are summarized by figure 12. Suppression of

TABLE 7.—Experiments that examine the relative importance of air-sea exchanges of sensible heat, latent heat, and momentum during the immature stage of the model cyclone. The initial data are from hour 168 of experiment S35.

Experiment	$C_D$	$C_S$	$C_L$
S35	eq (3)	eq (3)	eq (3)
Q8	do.	0	do.
Q9	do.	eq (3)	0
Q10	0	do.	eq (3)
Q11	eq (3)	$2 \times \text{eq (3)}$	$2 \times \text{eq (3)}$
Q18	$2 \times \text{eq (3)}$	do.	do.

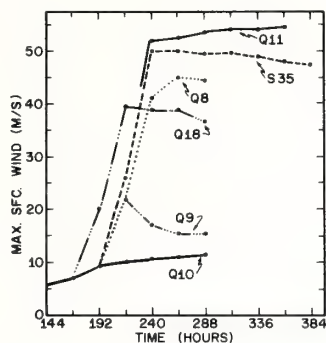


FIGURE 11.—Comparison of maximum surface winds for experiments that study the relative importance of air-sea exchanges of sensible heat, latent heat, and momentum during the immature stage of the model cyclone. Initial data are taken from hour 168 of experiment S35. The experiments compared with the control are Q8 ( $C_S=0$ ), Q9 ( $C_L=0$ ), Q10 ( $C_D=0$ ), Q11 ( $C_S=C_L=2C_D$ ), and Q18 ( $C_S=C_L=0.5C_D$ ). See table 7 for details.

the evaporation (exp. Q14) again leads to a more dramatic response than does cutting off the sensible heat supply (Q13). In contrast to the immature stage, a greater departure from the control occurs in Q14 ( $C_L=0$ ) than in Q15 ( $C_D=0$ ). This is due to the presence of a well-marked Ekman layer convergence in the initial data. The latter is able to maintain itself for some time after  $C_D$  is set to zero. Indeed, as noted in section 4, *small* reductions in the drag coefficient during the mature stage lead to an *intensification* of the system (exp. Q19, fig. 10, table 6).

Experiment Q16 ( $C_S=C_L=2C_D$ ) shows the type of response to be expected of a mature hurricane moving over warmer waters.

Despite the qualitative similarity of the wind maxima curves for Q14 and Q15 (fig. 12), the structural changes of the model storms are very different. In experiment Q14 where evaporation is suppressed, winds decrease everywhere and the area covered by strong winds decreases in size. This is illustrated by figure 13 where the outer radial limit of gale-force winds (approx. 17 m/s) is plotted as a function of time. In contrast, when the surface drag is suppressed (Q15), the area covered by strong winds expands (fig. 13) as the peak wind decreases. This, of course, is due to the fact that air spiraling inward does not lose momentum to the sea and, hence, reaches a particular

TABLE 8.—Experiments that examine the relative importance of air-sea exchanges of sensible heat, latent heat, and momentum during the mature stage of the model cyclone. The initial data are from hour 288 of experiment S35.

Experiment	$C_D$	$C_S$	$C_L$
S35	eq (3)	eq (3)	eq (3)
Q13	do.	0	do.
Q14	do.	eq (3)	0
Q15	0	do.	eq (3)
Q16	eq (3)	$2 \times \text{eq (3)}$	$2 \times \text{eq (3)}$

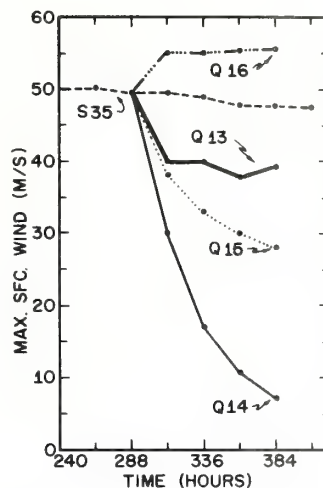


FIGURE 12.—Comparison of maximum surface winds for experiments that study the relative importance of air-sea exchanges of sensible heat, latent heat, and momentum during the mature stage of the model cyclone. Initial data are taken from hour 288 of experiment S35. The experiments compared with the control are Q13 ( $C_S=0$ ), Q14 ( $C_L=0$ ), Q15 ( $C_D=0$ ), and Q16 ( $C_S=C_L=2C_D$ ). See table 8 for details.

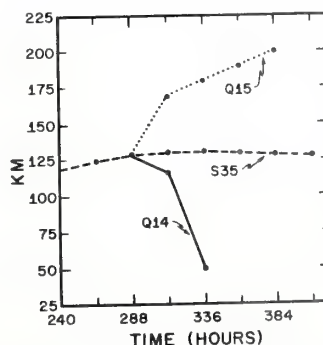


FIGURE 13.—Histories of the outer radial limit of gale-force winds for experiment Q15 ( $C_D=0$ ), Q14 ( $C_L=0$ ), and S35 (control). See table 8 for details.

radius with tangential winds greater than those found in the control.

The last two experiments to be discussed in this section are intended to simulate the passage of a mature hurricane



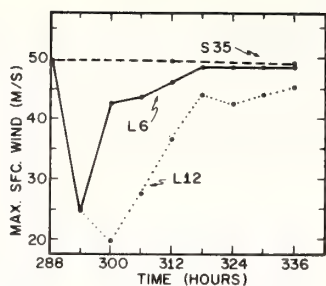


FIGURE 14.—Maximum surface winds as a function of time for experiment L6 and L12. These experiments are intended to simulate a hurricane that makes landfall at hour 288. In L6, the storm is over land for 6 hr and returns to water at hour 294. In L12, the storm is over land for 12 hr and returns to water at hour 300.

over an island. The initial data are again from hour 288 of experiment S35. In experiment L6, we set  $C_s = C_L = 0$  and  $C_D = 10^{-2}$  for 6 hr and then restore the original evaluations for these quantities. Experiment L12 differs only in that the modified exchange coefficients are retained for 12 hr before the original formulations are restored. Experiment L6 is then intended to represent a hurricane which spends 6 hr over land before returning to the sea while L12 is intended to simulate a 12-hr stay over land with a subsequent return to water.

The results, summarized by figure 14, show rapid filling upon "land fall." Comparisons of L6 and L12 show the filling to be most rapid during the earlier portion of the storm's land fall. Reintensification is rapid when the storm returns to "water." In experiment L6, the storm recovers its original intensity and structure (not shown) within 24 hr of its return to water. In experiment L12, the recovery is somewhat slower but the intensity appears to be approaching that of the control when the calculation is terminated. The storm structure for L12 at hour 336 (not shown) is very much like that of the control.

## 6. SOME ARBITRARY ASPECTS OF THE MODEL

Earlier, we pointed out that the length of the organizational period was extremely sensitive to variations in the initial conditions. This point will receive further attention below. We will also discuss two other arbitrary aspects of the model, the radial extent of the computational domain and the lateral boundary conditions.

In the first group of experiments (table 9), the computational domain is enlarged (exp. C16) and the scale of the initial perturbation is decreased (exp. Q1). To initialize C16, eq (6) is used for the inner 440 km. Beyond this radius, the initial temperatures are the standard values (table 1). As a result, the initial conditions for the inner 440 km are identical to the control. Beyond 440 km, the initial conditions are those of a stagnant mean tropical atmosphere. For experiment Q1, eq (6) with  $\hat{r} = 220$  km is used for the inner 220 km and  $T_{i,j} = \bar{T}_i$

TABLE 9.—Experiments in which the size of the computational domain (C16) and the horizontal scale of the initial perturbation (Q1) are varied

Experiment	Domain size	Perturbation size	Initial maximum wind
	(km)	(km)	(m/s)
S35	440	440	7
C16	1000	440	7
Q1	440	220	6

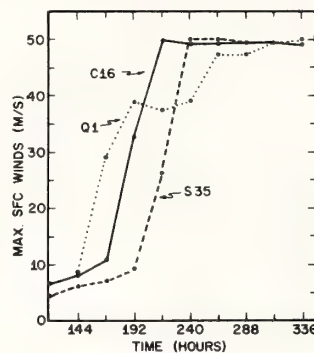


FIGURE 15.—Maximum surface winds for experiment C16 (computational domain 1000 km in comparison to 440 km for S35) and experiment Q1 (initial perturbation half as large in horizontal extent as that for S35). See table 9 for details.

is used for the outer 220 km. This leads to a stagnant mean tropical atmosphere at radii greater than 220 km.

The maximum surface winds for these experiments (fig. 15) approach those of the control. The evolution of experiment C16 indicates that moving the lateral boundary outward relative to the initial perturbation allows the storm to reach the mature stage more rapidly. Experiment Q1 introduces two conflicting effects. By reducing the scale of the initial perturbation, the active perturbation is removed from the lateral boundary in a fashion somewhat analogous to C16. However, this reduction in scale also increases the importance of the lateral mixing terms (Ooyama 1969). The calculations show Q1 to have a period in which growth is more rapid than the control, followed by a longer period in which growth is slow and uncertain. This model storm does not reach a mature steady state until well after the control does. Qualitatively similar results were obtained by Ooyama (1969).

Despite the evolutionary differences, table 10 shows the mature stages of the three model cyclones to be remarkably similar. We tentatively conclude that the structure and intensity of the mature stage is relatively insensitive to the size of the computational domain and the scale of the initial perturbation<sup>3</sup> with the boundary conditions used here. The time required to reach the mature stage, however, is highly sensitive to these parameters. In section 3, similar results were obtained when the intensity of the initial perturbation was varied (exp. Q2, fig. 2).

<sup>3</sup> It must, however, be kept in mind that, if the initial perturbation is made sufficiently small in scale, the lateral mixing terms will become dominant and, according to linear theory, the system will decay rather than grow.



TABLE 10.—Summary of surface structure at hour 336 of experiments S35, Q1, and C16

Experiment	Radius of maximum wind	Outer limit of hurricane-force winds	Outer limit of gale-force winds
	(km)	(km)	(km)
S35	20	55	130
Q1	20	55	125
C16	20	55	130

The 440-km computational domain, used extensively in our experiments (Rosenthal 1969, 1970a, 1970b), was selected at a very early stage in the design of the model (Rosenthal 1969), based on a need for computational economy. With the selection of this rather limited domain, it was realized that lateral boundary conditions would be extremely important. It was clear that the model hurricane could not be treated as a mechanically closed system since this would force the outflow air to sink relatively close to the storm center and the attendant adiabatic warming would inhibit the development of a warm core system. Empirically, it is well known (Riehl 1954) that upper tropospheric flow patterns that inhibit the escape of outflow air from the near vicinity of tropical disturbances generally are unfavorable for further storm development. The lateral boundary conditions of zeros for the vertical component of relative vorticity, horizontal divergence, and radial gradient of potential temperature were introduced at the very beginning of our experimental program (Rosenthal 1969). The lateral boundary condition of zero radial gradient of specific humidity was added at a later date (Rosenthal 1970b) when the explicit water vapor cycle was added. One would hope that it would be possible to reduce the impact of the exact form of the lateral boundary conditions by making the computational domain larger. The material presented below indicates that, if such a domain size exists, it is well in excess of 2000 km. To establish this, comparisons were made between experiments with the original boundary conditions and experiments in which the lateral boundary conditions were approximately those of a smooth, insulated wall. The mathematical expressions are identical to the original ones with the exception that the zero for horizontal convergence is replaced by a zero for the radial wind.

A first experiment with the new (closed) boundary conditions (exp. CC1), otherwise identical to the control, was carried to 504 hr and showed continuous decay from the initial state. In a second experiment (C10), the computational domain was increased to 1000 km but the intensity and scale of the initial perturbation were the same as for the control. With the exception of the lateral boundary conditions, this experiment is identical to C16 (fig. 15, table 9). The results showed a peak intensity of 21 m/s at 384 hr followed by rapid decay.

Since extensions of the computational domain beyond 1000 km with a 10-km radial resolution would have required substantial modifications of the computer program, a new series of experiments (table 11) with 20-km

TABLE 11.—Experiments (20-km radial resolution) which compare the effects of domain size and lateral boundary conditions

Experiment	Domain size	Lateral boundary condition	Initial perturbation
	(km)		
C17	440	open	S35
C18	440	closed	Do.
C19	1000	open	Do.
C20	1000	closed	Do.
C21	2000	open	Do.
C22	2000	closed	Do.

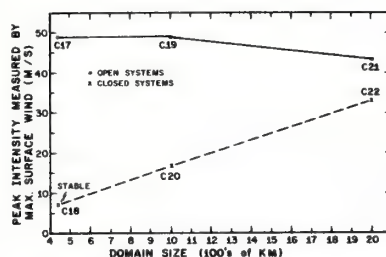


FIGURE 16.—Comparisons of the ultimate intensity attained by model cyclones with open lateral boundaries (C17, C19, and C21) and model cyclones with closed lateral boundaries (C18, C20, and C22) as a function of the radial extent of the computational domain. See table 11 for details.

radial resolution was carried out.<sup>4</sup> Figure 16 summarizes the results of these experiments.

Experiment C18 (closed, 440-km domain), identical to CC1 except for radial resolution, also showed monotonic decay (for 504 hr) from the initial conditions. With open boundary conditions, an increase in domain size from 440 to 1000 km produced virtually no change in peak intensity. This is similar to the result obtained above with 10 km resolution. However, a further increase in domain size from 1000 to 2000 km produced a reduction in peak wind of 6 m/s.

The experiments with closed boundaries showed a marked linear increase of peak winds with domain size (if we are allowed to include exp. C18 where peak wind occurs at the initial instant) of about 16 m/s per 1000 km. Linear extrapolation of the two curves on figure 16 (there is, of course, no guarantee that this is valid) shows a crossing point at a domain size of 2500 km. If the curve for closed systems is extrapolated to a peak wind of 50 m/s (that given by the open boundary exp. S35, C17, and C19), this occurs with a domain of about 3000 km.

With 1000-km domains, the open system (C19) reaches its greatest intensity at hour 264 whereas the closed system (C20) does not attain maximum intensity until hour 408. With the 2000-km domain, peak surface winds occur at hour 264 for both sets of boundary conditions (exp. C21 and C22).

Aside from those described above, several other experiments with the closed boundary conditions were run. The

<sup>4</sup> It is not our purpose here to study errors due to radial resolution (see Rosenthal 1970a, 1970b) and we will not compare the members of the 20-km series with the analogous 10-km experiments.

results of these may be summarized as follows. With a computational domain of 1000 km, peak intensity is strongly dependent on the scale of the initial perturbation (this conflicts with the results obtained with open boundaries). As the scale of the initial perturbation decreases, peak intensity increases until the scale becomes sufficiently small for lateral mixing to dominate. Thereafter, further reduction in scale results in decreases of peak intensity. When the domain size is increased to 2000 km, however, the ultimate intensity is relatively insensitive to the scale of the initial perturbation provided that the latter is not sufficiently small to allow the lateral mixing terms to become dominant.

In agreement with the results obtained with open boundaries, the ultimate intensity of model storms with closed boundaries is relatively insensitive to the strength of the initial perturbation.

## 7. SUMMARY AND CONCLUSIONS

The experiments can be placed in two broad categories. Those discussed in sections 4 and 5 are mainly concerned with responses to variations in *physical* parameters and attempt to gain deeper insight into the dynamics of tropical cyclones. The experiments discussed in section 6 are mainly concerned with *computational* aspects. These are intended to reveal the biases introduced by some of the arbitrary decisions which were necessary in the design of the model.

The physical parameters examined were those that control the air-sea exchanges of momentum, sensible heat, and latent heat. Many of these experiments yield results in qualitative agreement with experiments performed by Ooyama (1969). In view of the differences between the physical and numerical details of the two models, this is an important result that lends credence to both models.

Perhaps the most striking aspect of the experimental results is the overwhelming dominance, in the immature stage, of the drag coefficient in comparison to the analogous exchange coefficients for sensible and latent heat. This was most vividly portrayed by figure 11. Here, the only significant departures from the control, during the first 48 hr of integration, are in the calculations where the drag coefficient was altered (exp. Q10 and Q18).

The air-sea exchange of latent heat was shown to be a crucial ingredient for development and maintenance of the model storm. It was also found to be far more important than the analogous exchange of sensible heat. A simple extension of Ooyama's (1969) discussion of boundary layer processes (see section 5) provides a plausible explanation for this result.

Experiments in the immature stage showed that linear theory can be somewhat misleading. While, as predicted by linear analysis, the rate of growth during the early periods increased with increasing drag coefficient, the ultimate intensity reached by the model storm varied inversely with the drag coefficient (figs. 8 and 9). In the mature stage, small decreases of drag coefficient lead to stronger peak winds but when the drag coefficient was reduced to zero the peak winds diminished (fig. 10). In the latter situation, it appears that there is insufficient

low-level convergence of water vapor to sustain the required convection in the storm core.

The computational experiments revealed a number of interesting points that will be useful in the design of future experiments with tropical cyclone models. With open lateral boundaries and the standard 440-km computational domain, the intensity and structure of model cyclones, when they reached the mature stage, were relatively insensitive to the scale and intensity of the initial vortex (provided that the scale was not so small as to allow lateral mixing terms to become dominant). The time required to reach the mature stage was, however, highly sensitive to initial conditions.

When the size of the computational domain was increased to 1000 km (open lateral boundary) while retaining the initial vortex used for the control, the structure and intensity of the mature model cyclone was again virtually the same as for the control. A further increase in domain size to 2000 km resulted in a 6 m/s reduction of the mature stage peak winds. The structure of the mature cyclone was, however, quite similar to that of the control.

As was to be expected, the lateral boundary conditions proved to be extremely important in determining the life cycle of the model storm. When the zero for horizontal divergence was replaced by a zero for the radial wind, thus converting the open system to one that was mechanically closed, an experiment, otherwise identical to the control, showed monotonic decay from the initial conditions. By increasing the size of the computational domain, it was possible to generate developing model cyclones (closed boundaries). These systems (fig. 16) showed a strong relationship between peak intensity and domain size.

The results summarized by figure 16 suggest that differences due to boundary conditions might be minimized if the domain size were enlarged to something between 2000 and 3000 km. This, however, cannot be guaranteed since no experiments were run with domains larger than 2000 km.

## ACKNOWLEDGMENTS

Mr. Robert Carrodus was responsible for drafting and reproducing the figures. Mrs. Mary Jane Clarke typed the manuscript. Computations were performed on the NOAA Control Data Corporation (CDC) 6600 at Suitland, Md., with access made possible through a CDC User 200 remote terminal at the National Hurricane Research Laboratory. Mr. Billy M. Lewis was responsible for the liaison work between Miami and Suitland.

## REFERENCES

- Anthes, Richard Allen, Rosenthal, Stanley L., and Trout, James W., "Preliminary Results From an Asymmetric Model of the Tropical Cyclone," *Monthly Weather Review*, Vol. 99, No. 10, Oct. 1971a, pp. 744-758.
- Anthes, Richard Allen, Trout, James W., and Rosenthal, Stanley L., "Comparisons of Tropical Cyclone Simulations With and Without the Assumption of Circular Symmetry," *Monthly Weather Review*, Vol. 99, No. 10, Oct. 1971b, pp. 759-766.
- Byers, Horace Robert, *General Meteorology*, McGraw-Hill Book Co., Inc., New York, N.Y., 1944, 645 pp.
- Colón, José A., and Staff, "On the Structure of Hurricane Daisy (1958)," *National Hurricane Research Project Report No. 48*, U.S. Department of Commerce, Weather Bureau, Miami, Fla., Oct. 1961, 102 pp.



- Dergarabedian, Paul, and Fendell, Francis, "On Estimation of Maximum Wind Speeds in Tornadoes and Hurricanes," *The Journal of the Astronautical Sciences*, Vol. 17, No. 1, Jan.-Feb. 1970, pp. 218-236.
- Hawkins, Harry F., and Rubsam, Daryl T., "Hurricane Hilda, 1964; II. Structure and Budgets of the Hurricane on October 1, 1964," *Monthly Weather Review*, Vol. 96, No. 9, Sept. 1968, pp. 617-636.
- Hebert, Paul J., and Jordan, Charles L., "Mean Soundings for the Gulf of Mexico Area," *National Hurricane Research Project Report* No. 30, U.S. Department of Commerce, Weather Bureau, Miami, Fla., Apr. 1959, 10 pp.
- Kuo, H.-L., "On Formation and Intensification of Tropical Cyclones Through Latent Heat Release by Cumulus Convection," *Journal of the Atmospheric Sciences*, Vol. 22, No. 1, Jan. 1965, pp. 40-63.
- Malkus, Joanne S., and Riehl, Herbert, "On the Dynamics and Energy Transformations in Steady-State Hurricanes," *Tellus*, Vol. 12, No. 1, Stockholm, Sweden, Feb. 1960, pp. 1-20.
- Matsuno, Taroh, "Numerical Integrations of the Primitive Equations by a Simulated Backward Difference Method," *Journal of the Meteorological Society of Japan*, Ser. 2, Vol. 44, No. 1, Tokyo, Feb. 1966, pp. 76-84.
- Miller, Banner I., "On the Momentum and Energy Balance of Hurricane Helene (1958)," *National Hurricane Research Project Report* No. 53, U.S. Department of Commerce, Weather Bureau, Miami, Fla., Apr. 1962, 19 pp.
- Ooyama, Katsuyuki, "Numerical Simulation of the Life-Cycle of Tropical Cyclones," *Journal of the Atmospheric Sciences*, Vol. 26, No. 1, Jan. 1969, pp. 3-40.
- Palmén, Erik Herbert, "On the Formation and Structure of Tropical Hurricanes," *Geophysica*, Vol. 3, No. 26, Helsinki, Finland, 1948, pp. 26-38.
- Ramage, Colin S., "Comments on 'Numerical Simulation of the Life-Cycle of Tropical Cyclones,'" *Journal of the Atmospheric Sciences*, Vol. 27, No. 3, May 1970, pp. 506-507.
- Riehl, Herbert, *Tropical Meteorology*, McGraw-Hill Book Co., Inc., New York, N.Y., 1954, 392 pp.
- Riehl, Herbert, and Malkus, Joanne S., "Some Aspects of Hurricane Daisy, 1958," *Tellus*, Vol. 13, No. 2, Stockholm, Sweden, May 1961, pp. 181-213.
- Rodenhuis, David, "A Note Concerning the Effect of Gravitational Stability on the CISK Model of Tropical Disturbances," *Journal of the Atmospheric Sciences*, Vol. 28, No. 1, Jan. 1971, pp. 126-129.
- Roll, Hans Ulrich, *Physics of the Marine Atmosphere*, Academic Press, New York, N.Y., 1965, 426 pp.
- Rosenthal, Stanley L., "Numerical Experiments With a Multilevel Primitive Equation Model Designed to Simulate the Development of Tropical Cyclones: Experiment I," *ESSA Technical Memorandum ERLTM-NHRL 82*, U.S. Department of Commerce, National Hurricane Research Laboratory, Miami, Fla., Jan. 1969, 36 pp.
- Rosenthal, Stanley L., "Experiments With a Numerical Model of Tropical Cyclone Development—Some Effects of Radial Resolution," *Monthly Weather Review*, Vol. 98, No. 2, Feb. 1970a, pp. 106-120.
- Rosenthal, Stanley L., "A Circularly Symmetric Primitive Equation Model of Tropical Cyclone Development Containing an Explicit Water Vapor Cycle," *Monthly Weather Review*, Vol. 98, No. 9, Sept. 1970b, pp. 643-663.
- Rosenthal, Stanley L., and Koss, Walter J., "Linear Analysis of a Tropical Cyclone Model With Increased Vertical Resolution," *Monthly Weather Review*, Vol. 96, No. 12, Dec. 1968, pp. 858-866.
- Sundqvist, Hilding, "Numerical Simulation of the Development of Tropical Cyclones With a Ten-Level Model, Part I," *Tellus*, Vol. 22, No. 4, Stockholm, Sweden, July 1970, pp. 359-390.
- Yamasaki, Masanori, "Detailed Analysis of a Tropical Cyclone Simulated With a 13-Layer Model," *Papers in Meteorology and Geophysics*, Vol. 19, No. 4, Tokyo, Japan, Dec. 1968, pp. 559-585.

[Received December 2, 1970; revised March 9, 1971]

U.S. DEPARTMENT OF COMMERCE  
National Oceanic and Atmospheric Administration  
Environmental Research Laboratories

NOAA Technical Memorandum ERL NHRL-95

NUMERICAL EXPERIMENTS OF RELEVANCE  
TO PROJECT STORMFURY

Stanley L. Rosenthal  
Michael S. Moss

National Hurricane Research Laboratory  
Coral Gables, Florida  
December 1971





## TABLE OF CONTENTS

	Page
ABSTRACT	1
1. INTRODUCTION	1
2. REVIEW OF THE MODEL	2
3. THE CONTROL EXPERIMENT	5
4. SUGGESTED TACTICS FOR HURRICANE MODIFICATION	15
5. PROCEDURES FOR THE SEEDING SIMULATIONS	17
6. CALCULATIONS RELEVANT TO HYPOTHESIS I	25
7. CALCULATIONS RELEVANT TO HYPOTHESIS II	28
8. SUMMARY AND CONCLUSIONS	45
9. ACKNOWLEDGMENTS	47
REFERENCES	48
APPENDIX	52

# NUMERICAL EXPERIMENTS OF RELEVANCE TO PROJECT STORMFURY

Stanley L. Rosenthal and Michael S. Moss

A number of new experiments which provide theoretical guidance for Project STORMFURY are summarized. The results indicate that artificial heating just radially outward from the eyewall produces the most rapid reduction of the maximum winds at sea level. Older model storms are found to react more rapidly to artificial heating than younger storms. If a substantial reduction of the maximum wind is to be obtained, the artificial heating must be allowed to remain in effect until a new eyewall is formed at a radius greater than that of the original eyewall.

## 1. INTRODUCTION

This report describes numerical experiments that provide theoretical guidance for Project STORMFURY. The numerical model employed (Rosenthal, 1970a, 1970b, 1971c) is clearly representative of the current state of the art as may be verified by comparison with models developed by Ooyama (1969), Sundqvist (1970) and Yamasaki (1968).<sup>1</sup> It should be made clear, however, that these models are highly idealized theoretical tools. While gross qualitative comparisons can be made with certain aspects of real hurricanes, model results are representative only of some sort of "average" or "typical" hurricane. Skillful prediction from real initial data for a specific hurricane is still a thing of the future.

---

<sup>1</sup>The National Hurricane Research Laboratory has recently developed a hurricane model (Anthes et al., 1971) which eliminates the assumption of circular symmetry and, therefore, is more advanced than those cited in the text.

In addition, a fair amount of uncertainty arises in simulations of hurricane modification experiments since the diabatic effects due to latent heat release are highly parameterized with no explicit representation of the cloud physics.<sup>2</sup> Hence, techniques for representing the seeding of supercooled clouds through silver iodide seeding are quite arbitrary.

Despite these difficulties, it is our opinion that helpful information may be obtained through controlled numerical experimentation. Some preliminary results based on this approach have already been published (Rosenthal, 1971a). Later sections of this paper present a number of new experiments as well as a reassessment of some of the older calculations.

## 2. REVIEW OF THE MODEL

A brief description of the main features of the model is given below. (The reader concerned with mathematical details should refer to Rosenthal (1970a).) The model storm is an isolated, stationary, circularly symmetric vortex. The vertical structure of the atmosphere is represented by seven levels and geometric height is the vertical coordinate. The levels correspond to pressures of 1015, 900, 700, 500, 300, 200 and 100 mb in the mean tropical atmosphere. All variables are defined at all levels. The primitive equations govern the horizontal motion. The hydrostatic assumption is employed.

---

<sup>2</sup>Estoque (1971) has recently attempted simulations of hurricane seeding experiments with a model incorporating Kessler's cloud physics. Unfortunately, Estoque's equations appear to be more representative of layer clouds than convective clouds.

The continuity equation is simplified as follows. The local rate of change of density is neglected and a climatological density (a function of height alone) is used to evaluate the vertical and horizontal mass flux terms. We then eliminate the external gravity wave by demanding that the vertical integral of the horizontal mass divergence vanish.

In the experiments discussed here, the radial limit of the computational domain is 440 km. The system is open at the lateral boundary. The lateral boundary conditions require that the relative vorticity and horizontal divergence vanish. In addition, the radial derivatives of potential temperature and specific humidity are also required to vanish.

Through a generalization of the procedure suggested by Kuo (1965), the model simulates convective precipitation (and the macroscale heating due to this latent heat release) as well as the enrichment of the macroscale humidity due to the presence of the cumuli. Convection may originate in any layer provided that the layer has a water vapor supply from horizontal convergence and that conditional instability exists for parcels lifted from the layer. Non-convective precipitation is also simulated. Details are given by Rosenthal (1970a).

Time derivatives are estimated by forward differences except in the case of specific humidity where a Matsuno (1966) type integration is employed. Advective derivatives are calculated by the upstream method except for the case of humidity where a conservation form of the equations is used. All nonadvective space derivatives are calculated as centered differences.



The drag coefficient is represented by Deacon's empirical relationship (Roll, 1965, p. 160) which is a linear function of surface-wind speed. The sensible and latent heat fluxes at the sea surface are calculated by the bulk aerodynamic equations and the surface drag is represented by the usual quadratic stress law. The exchange coefficients for sensible and latent heat are equal to the drag coefficient. The turbulent flux convergences that appear in the thermodynamic and water vapor continuity equations are evaluated through the assumption that the fluxes have a linear variation over height and are zero at and above the height of the 900-mb level. This is based on the assumption that at 900 mb and above, fluxes produced by small scale turbulence are insignificant in comparison to those produced by cumulus-scale motions.

The sea temperature is an external parameter and, for experiments discussed here, is taken 2°C greater than the initial sea-level air temperature (initially, the latter is horizontally uniform for all experiments). Since the sea-level air temperature varies with time according to the thermodynamic equation, the air-sea temperature difference varies both with radius and time as the model hurricane evolves.

Radial resolution is 10 km and the time step is 2 minutes. A lateral mixing coefficient of  $2.5 \times 10^3 \text{ m}^2 \text{ sec}^{-1}$  is used for all prognostic variables.

### 3. THE CONTROL EXPERIMENT

The model is initialized with hypothetical data representative of a weak vortex (Rosenthal, 1970a). With judicious choices of static stability, humidity, sea temperature, etc., a hurricane-like vortex ultimately is developed.<sup>3</sup> The structure of the mature storm is, in general, highly realistic.

For the control experiment (Experiment S-35) employed in this report, initial conditions are established as follows. Climatological potential temperatures (a function of height alone and very nearly those of the Hebert and Jordan (1959) mean hurricane season sounding) are specified. With a lower boundary condition of 1015 mb, hydrostatic base-state pressures and temperatures (table 1) are computed for the levels above the surface.

The initial temperature field is then specified by

$$T_{i,j} = \bar{T}_i + T_* \left\{ \cos \left( \frac{\pi}{\hat{r}} r_j + 1 \right) \right\} \sin \left( \frac{\pi}{z_7} z_i \right)$$

where  $i$  and  $j$  are, respectively, height and radial indices,  $\bar{T}_i$  is the standard temperature (table 1),  $T_* = 0.16^\circ\text{K}$ ,  $\hat{r} = 440$  km, and  $z_7$  is the height (table 1) of level 7. The initial pressure at level 7 is then taken to be the standard value (table 1) and the hydrostatic equation is integrated downward to obtain the remainder of the initial pressure field. Finally, the gradient wind equation is solved for the initial

---

<sup>3</sup>For discussions of the circumstances under which models of this type do not produce hurricanes, see Rosenthal (1971c) and Anthes (1971).

tangential wind while the initial radial and vertical motions are taken to be zero. The initial surface wind reaches a maximum of  $7 \text{ m sec}^{-1}$  at a radius of 250 km. The central pressure of the vortex is 1013 mb. A base state relative humidity is specified as a function of height (table 2). By use of the data given by table 1, a base state specific humidity is calculated. The initial specific humidity is then assumed horizontally homogeneous and equal to this base state value.

Table 1. Standard values of thermodynamic variables

Level	Height	$\bar{\theta}$	$\bar{T}$	$\bar{p}$
	(m)	(°K)	(°K)	(mb)
1	0	300	301.3	1015.0
2	1054	303	294.1	900.4
3	3187	313	282.6	699.4
4	5898	325	266.5	499.2
5	9697	340	240.8	299.2
6	12423	347	218.9	199.5
7	16621	391	203.1	101.1

Table 2. Initial values of relative humidity at the  
information levels

Level	Height	Relative Humidity
	(meters)	(percent)
1	0	90
2	1054	90
3	3187	54
4	5898	44
5	9697	30
6	12423	30
7	16621	30

Although Experiment S-35 has been discussed elsewhere (Rosenthal, 1971c), a detailed summary is presented here since we wish to emphasize different points.

Figure 1 summarizes the control's life cycle in terms of central pressure<sup>4</sup> and maximum sea-level wind. The initial conditions are clearly arbitrary and, therefore, the early portions of the integration are not especially significant. In particular, the rather long "organizational"

<sup>4</sup>Pressure is not defined at zero radius because of a horizontal staggering of variables. As a consequence, central pressure values are taken from a grid point 5 km from the storm center at sea-level.



period (168 hours) required for the vortex to begin intensification is easily altered by changing such arbitrary parameters as the scale and/or intensity of the initial vortex, the size of the computational domain and the lateral boundary conditions (Rosenthal, 1971c). The values of some rather poorly defined physical parameters also strongly effect the organizational period (Rosenthal and Koss, 1968; Rosenthal, 1970a; Rosenthal, 1971c).

The rapid intensification of the storm to the mature stage (see 192 to 240 hours, fig. 1) is fairly typical of real hurricanes. Indeed cases exist where deepening of this magnitude has occurred in as little as 12 to 24 hours. The long, quasi-steady, mature stage is fairly typical of hurricanes which remain over the ocean without encountering cold surface waters or unfavorable surrounding flow patterns.

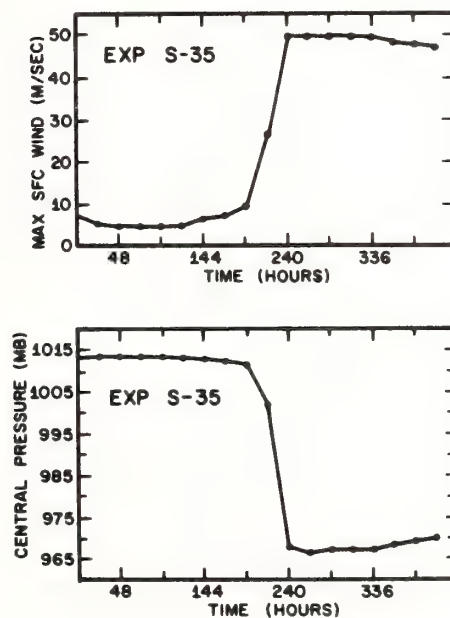


Figure 1. Results from experiment S-35. Top, maximum surface wind as a function of time. Bottom, central pressure as a function of time. Taken from Rosenthal (1971c).

Figures 2, 3, 4, 5 and 6 illustrate structural features fairly representative of the mature stage between 240 and 336 hours. The strongest winds (fig. 2) are concentrated in a narrow zone near the storm center. The strongest vertical motions (fig. 3) and condensation heating as represented by the rainfall rate, (analogous to the hurricane eye wall, fig. 4) are also concentrated in an extremely narrow zone which extends from slightly outside to slightly inside the wind maximum. The radial motions (fig. 5) show that virtually all of the storm's inflow occurs in the lower kilometer of the atmosphere while significant outflow occurs only in the high troposphere. The transverse circulation is then characterized by inflowing air very close to the surface, ascent in the vicinity of the wind maximum and outflow at high levels.

Close to the sea surface, the tangential wind is controlled by the opposing effects of angular momentum conservation as air spirals inward and loss of angular momentum to the ocean through surface drag. This then explains the close association of the eyewall and the wind maximum since it is in the eyewall region that large centrifugal and coriolis effects prevent further inward penetration of the air and hence force ascent to take place. Inflow is concentrated close to the sea surface because the rotational stability of the mature vortex does not allow inward penetration unless absolute angular momentum (following a parcel) is rapidly dissipated (Rosenthal, 1971c) and surface drag provides the only sink sufficient to allow significant penetration. The outflowing branch of the circulation in the high troposphere is largely controlled by conservation of absolute angular momentum since frictional forces are small at these levels.

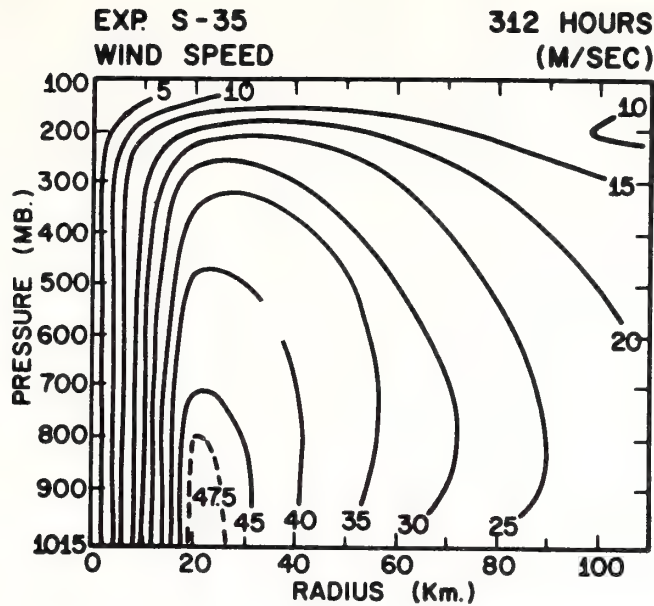


Figure 2. Cross section of wind speed at 312 hours of experiment S-35. Isotachs are labelled in  $\text{m sec}^{-1}$ . Taken from Rosenthal (1971c).

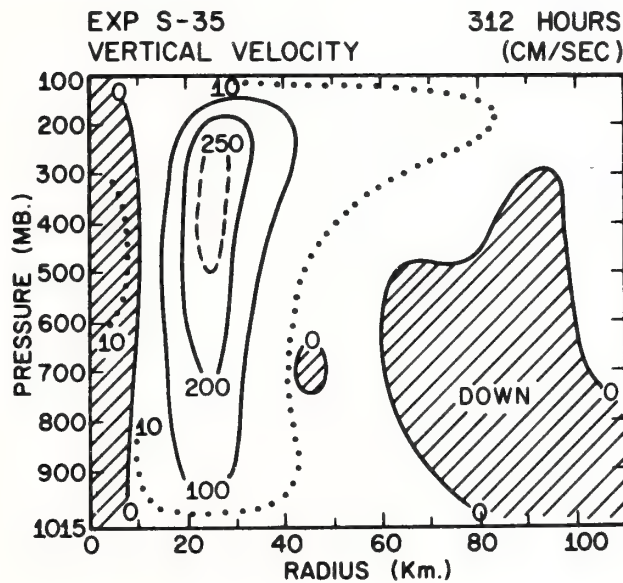


Figure 3. Cross section of vertical velocity at 312 hours of experiment S-35. Isotachs are labelled in  $\text{cm sec}^{-1}$ . Hatched areas indicate negative values (subsidence). Taken from Rosenthal (1971c).

The fact that the wind maximum (fig. 2) and the isotachs inward of the maximum are essentially vertical is a consequence of the control of the midtropospheric wind field by vertical transports of absolute angular momentum (Rosenthal, 1970b).

The model very nicely provides a subsiding eye (fig. 3) at the storm center. The region of weaker subsidence at larger radii reflects the well known "sucking" effect of rotational boundary layers and has been noted by previous hurricane modelers (Ooyama, 1969). This subsidence is an extremely important feature of the hurricane (Ooyama, 1969; Rosenthal, 1971c). Air parcels entering the inflow layer from midtropospheric levels are relatively dry and have lower equivalent potential temperature than the boundary-layer air. If this air does not gain sufficient water vapor by evaporation from the ocean as it spirals inward, its potential buoyancy upon reaching the eyewall will be small and the cumulus convection required to drive the hurricane will diminish. Numerical experiments (Ooyama, 1969; Rosenthal, 1971c) have verified that model hurricanes rapidly dissipate when oceanic evaporation is suppressed. Observationally, it is well known that cold surface waters suppress hurricane development and lead to filling of existing storms.



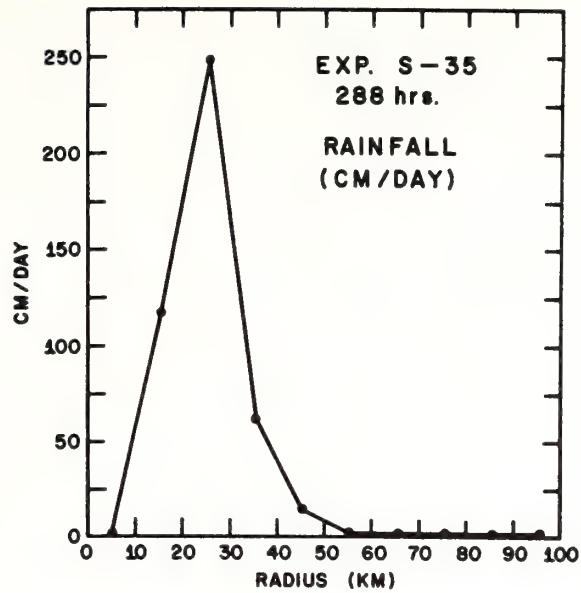


Figure 4. Radial profile of rainfall rates at 288 hours of experiment S-35.

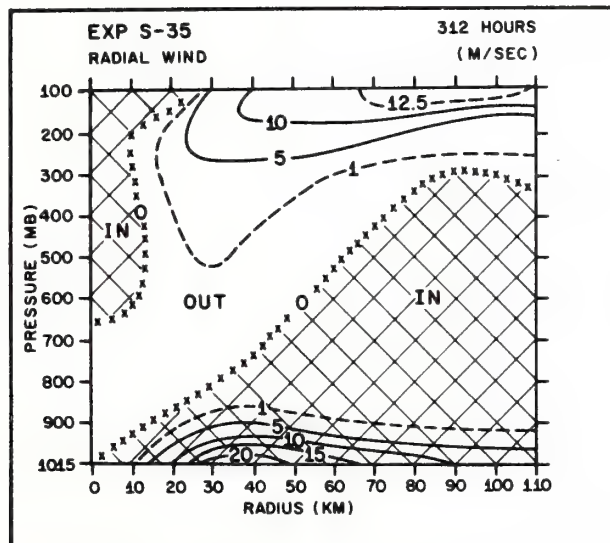


Figure 5. Cross section of radial velocity at 312 hours of experiment S-35. Hatched areas depict inflow.

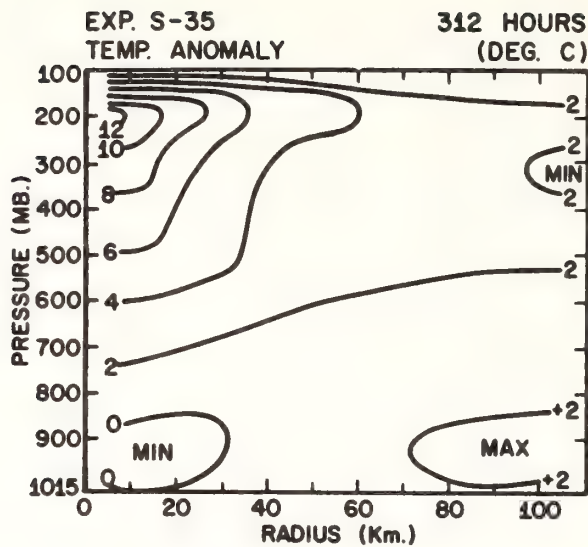


Figure 6. Cross section of temperature anomalies at 312 hours of experiment S-35. Isotherms are labelled in degrees K. Taken from Rosenthal (1971c).

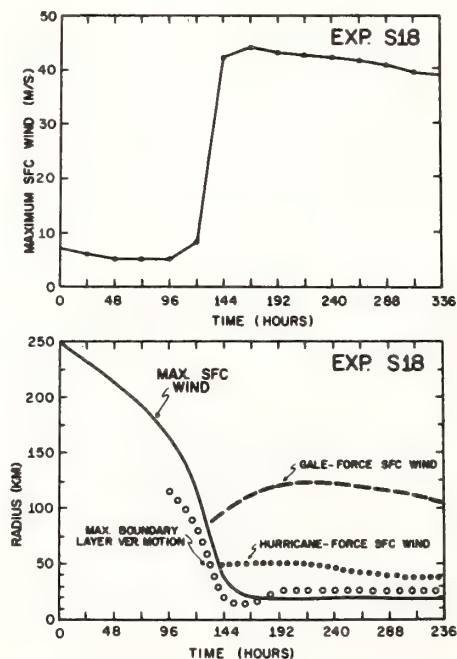


Figure 7. Results from experiment S-18. Top, maximum wind at sea level as a function of time. Bottom, radii of maximum wind at sea level, outer limits of hurricane and gale force winds, radius of maximum 900-mb vertical velocity. Taken from Rosenthal (1971a).

Table 3. Sensible heat flux and evaporation rates for Hurricane Daisy (1958) and experiment S-35 at 312 hours. Rainfall rates for experiment S-35 also shown.

	Average values from model for radial interval 0-100 km at 312 hours	Average values for Hurricane Daisy for radial inter- val 0-80 n mi on 27 Aug. 1958
Sensible Heat Flux ( $\text{cal-cm}^{-2}\text{-sec}^{-1}$ )	$1.5 \times 10^{-3}$	$2.9 \times 10^{-3}$
Evaporation ( $\text{cm-day}^{-1}$ )	1.8	2.3
Rainfall ( $\text{cm-day}^{-1}$ )	22	

Table 4. Kinetic energy generation and dissipation by surface drag friction for Hurricane Daisy (1958) and experiment S-35 at 312 hours.

	Integrated values from model for radial inter- val 0-100 km at 312 hours	Integrated values for Hurricane Daisy for radial interval 0-60 n mi on 27 Aug. 1958
Kinetic Energy Production ( $10^{14} \text{ KJ-day}^{-1}$ )	5.8	4.6
Kinetic Energy Dissipation by Surface Friction ( $10^{14} \text{ KJ-day}^{-1}$ )	2.9	2.1

Tables 3 and 4 make some comparisons between the mature stage of the model and that of Hurricane Daisy (1958). The data for Hurricane Daisy are taken from Riehl and Malkus (1961). In view of the observational uncertainties in the empirical estimates and the natural storm to storm variability (compare estimates by Riehl and Malkus (1961) with Hawkins and Rubsam (1968) and Miller (1962)), the agreement between the model values and those for Hurricane Daisy is certainly satisfactory.

#### 4. SUGGESTED TACTICS FOR HURRICANE MODIFICATION

What we will refer to as 'Hypothesis I' was first put forth by Simpson et al. (1963) and later published in more polished form by Simpson and Malkus (1964). Simpson and Malkus recognized that the hurricane wall cloud is located quite close to the region of maximum low-level pressure gradient and further contended that the wall cloud contains significant quantities of supercooled water. According to the hypothesis, if this supercooled water were frozen through nucleation by silver iodide crystals, the released heat of fusion would produce temperature increases; and therefore, hydrostatically, pressure decreases near the region of the strongest pressure gradient. If the central pressure did not concomitantly decrease, a reduction in maximum pressure gradient and, in turn, a reduction in wind speed should be the net result. Temperature increases of  $2^{\circ}\text{C}$  were estimated on the assumption of freezing  $1\text{ gm m}^{-3}$  of supercooled water in the layer 500 to 150 mb. With the further assumption that the 150-mb surface remains unaltered, hydrostatic arguments were invoked to estimate reductions at the seeded radii of as much as 200 ft



in the heights of the pressure surfaces at and below 500 mb. This, in turn, was expected to reduce the maximum pressure gradient force by 10 to 15 percent.

Questions which are difficult to answer can be raised concerning both the actual supercooled liquid water content of eyewall clouds and the efficiency of the seeding operation in freezing this supercooled water (see Section 5 and Gentry and Hawkins, 1971). However, Hypothesis 1 is also questionable from other points of view. The estimates of temperature increase to be realized from the released heat of fusion assume a constant pressure process. It is, however, not unlikely that the air would follow an ice pseudoadiabat with substantial amounts of the heat of fusion being converted to potential rather than internal energy.

An even more critical consideration is the fact that the eyewall drives the storm's transverse circulation and seeding this region alone would very likely accelerate this circulation thus providing a more rapid inflow of both angular momentum and water vapor to the eyewall region.

Diagnosis of the results of a number of numerical experiments led to a proposed strategy which is a slight tactical variant of Hypothesis 1 (Rosenthal, 1971a). Typically, the organizational period for a developing model storm does not terminate until a concentrated vertical-velocity maximum (eyewall) develops at a radius smaller than that of the low tropospheric wind maximum. Once this feature appears, the storm deepens rapidly and, at the same time, the eyewall and wind maximum migrate inward. The wind maximum, however, moves more rapidly than the eyewall. Invariably development ceases when the eyewall and wind maximum become

nearly coincident. (An example taken from a previous paper is shown by fig. 7.) The sequence is clearly consistent with the angular momentum considerations of the previous section.

Hypothesis II differs from Hypothesis I in that the latter calls for seeding the eyewall alone whereas the former suggests seeding either from the eyewall outward or entirely outward from the eyewall. While the logistics of these hypotheses differ only slightly, the physical arguments are substantially different. In Hypothesis II, the basic idea is to stimulate convection and ascent at radii greater than that of the eyewall. The region of stimulated convection is intended to compete with the eyewall for the inflowing air at low levels. If significant portions of the inflow can be diverted upward at the seeded radii, the angular momentum and water vapor supplies to the original eyewall and wind maximum will be reduced. As a consequence, one would expect the original wind maximum to be reduced and the eyewall convection to be diminished.<sup>5</sup>

## 5. PROCEDURES FOR THE SEEDING SIMULATIONS

Since the hurricane model contains no cloud physics, simulation of silver-iodide seeding through the application of basic physical laws, as has been done in cloud models (e.g. Cotton, 1970), is not yet possible. The techniques employed are, therefore, highly pragmatic and presuppose the occurrence of certain cloud physical processes. They have evolved from extensive discussion with those involved in the field program

---

<sup>5</sup>A similar proposal has been put forth by Sundqvist (1970). He, however, suggested seeding experiments at extremely large radii.

(Gentry, 1969; Gentry and Hawkins, 1971; Rosenthal, 1971a). An early and extremely crude version of the model (Rosenthal, 1969) was used in 1968 to simulate seeding of the hurricane by silver iodide. These calculations were intended to simulate "single seeding" field experiments in which the seeder aircraft discharges its material once in a pass of 2-3 min covering a radial interval of about 30 km. The feeling of those involved in the field program (Gentry, 1969) was that a single-seeding experiment could release heat of fusion over the 500- to 300-mb layer equivalent to a heating rate of  $2^{\circ}\text{C}/30 \text{ min}$  and lasting for a period of 30 min. At 300 mb, this amounts to freezing about  $2.5 \text{ g water} \cdot \text{m}^{-3} \cdot (30 \text{ min})^{-1}$ . At 500 mb, the figure is approximately  $4 \text{ g water} \cdot \text{m}^{-3} \cdot (30 \text{ min})^{-1}$ . While the release of silver iodide is made along a particular azimuth, those involved in the field program felt that the circulation of the storm sweeps the material in a more or less circular path, thus providing the heating rates cited above in a circular fashion. To simulate this process, the heating function that represents the cumulus feedback on the macroscale (Rosenthal, 1969) was simply increased by the amount and for the period cited above at selected radii.

By August 1969, the design of the field experiment (Gentry, 1970) had been altered such that single seedings (as previously defined) were repeated five times at 2-hr intervals. Since the model had been substantially improved by this time and since no simulations of multiple-seeding experiments had as yet been carried out, a new series of calculations (Rosenthal, 1971a) were performed. The heating rates for these seeding simulations were established after discussion with Dr. Gentry (NHRL).

These consultations revealed that he continued in his belief that  $2^{\circ}\text{C}/30$  min was the correct heating rate for a single seeding. However, he was now of the opinion that the effect would be felt for at least 1 hr (in contrast to the 0.5 hr cited at the time of the 1968 calculations). It was also Dr. Gentry's feeling that the enhanced heating might be more or less continuous over the 10-hr period spanned by the multiple-seeding operation.

The heating functions were enhanced at 300 and 500 mb which are the model levels corresponding to the layer seeded in the field experiment. Calculations were performed where the enhanced heating was applied continuously for ten hours and intermittently at 2-hr intervals for 30 minutes. Differences between calculations with continuous and intermittent enhanced heating were relatively minor. Consequently, because of conceptual simplicity, the continuous heating was adopted as a basic procedure.

Generally speaking, the earlier calculations (Rosenthal, 1971a) favored Hypothesis II over Hypothesis I. They also appeared to provide a response time to the simulated seeding which compared favorably to that observed in the Hurricane Debbie (1969) field experiment (Gentry, 1970; Hawkins, 1971) if one assumes the changes in Debbie were indeed produced by the seeding. As we will see later, this may have been a fortuitous result produced by choice of initial conditions. Unfortunately, this was not suspected during 1969 and 1970 when extensive empirical investigations pertinent to hurricane seeding were under progress at NHRL.



In the meantime, new studies of cloud-physics data obtained in unseeded hurricanes (Sheets, 1969; Gentry and Hawkins, 1971) led to the tentative conclusion that the supercooled water content of the major eye-wall clouds was similar to that already suggested by Simpson et al. (1963) and Gentry (1969). At this time, however, Gentry and Hawkins (1971) did a more careful analysis of the rate of release of heat of fusion which might be expected under optimal field conditions. For such a calculation, the supercooled water content of clouds is only one of the important parameters. Other crucial factors include, at the very least; (1) the time scale for freezing supercooled water by silver-iodide nucleation, (2) the time scale over which silver iodide is active and effective as freezing nuclei in a given cloud updraft, (3) the time scale for the regeneration of an equivalent amount of supercooled water in the updraft, (4) the effectiveness and time scale of nucleation of supercooled water by the ice crystals formed from the silver-iodide seeding, (5) the number of clouds available for seeding, (6) the number of clouds which reasonably can be expected to be seeded by a field operation of the type previously described.

Observational data for establishing all of these parameters in the hurricane context do not exist. Gentry and Hawkins (1971) made the reasonable (and implicit) assumption that time scales (1) and (2) were on the order of 1-2 minutes while time scale (3) was much larger. (Simple calculations on a pseudoadiabatic chart indicate time scale (3) to be 500 to 1000 secs for a  $5 \text{ m sec}^{-1}$  updraft.) With these assumptions for time scales (1), (2) and (3) and with 100 percent freezing efficiency, we

deduce a pulse-like heating function (in a cloud) 15 to 30 times the normal heating rate used in the previous simulations (Rosenthal, 1971a) but existing only for a few minutes. In view of time scale (3), substantial freezing by ice nucleation of newly generated supercooled water does not appear likely. If we average the heating pulse over two hours (the time between seedings) we obtain a heating function per seeded eyewall cloud of .25 to .50 of the normal rate used in the simulations.

However, we must also take into account that the heating functions applied to the model are averages over 10 km (distance between grid points) of radial distance and 360 degrees of azimuth angle. In view of the fact that even in the eyewall the areal coverage of active updrafts is less than 10% (Malkus, 1960) and that the areal coverage decreases rapidly with radius and considering the rate of azimuthal transport of silver iodide by the tangential wind, Gentry and Hawkins (1971) concluded that the rate of release of heat of fusion in Hurricane Debbie was probably 1 to 2 orders of magnitude less than the normal rate used for the model simulations.

As a consequence, the authors were asked to conduct calculations under Hypothesis II with successively smaller heating until a ten hour operation failed to provide responses similar to those obtained previously. The first of these calculations was made with half the normal rate and already showed no significant response. (At this time, we were still not aware of the dependence of model response on initial conditions.)

Soon after this, however, a new and highly attractive view of the cloud-physical response to silver-iodide seeding emerged. The members of

the Project STORMFURY Advisory Panel (1971) wrote, "The augmented heating rates used to simulate seeding probably cannot be realized in nature solely from release of latent heat of fusion. The most reasonable analog in nature is the possibility that convective clouds in the region just outside the existing eyewall could be stimulated by seeding to more active growth and intensity thus replacing the previous eyewall with a new one at a greater radius. Augmented heating from enhanced condensation, plus freezing in such circumstances, probably exceeds the augmented heating rates used in the seeding simulations."

The macroscale dynamical aspects are here identical to Hypothesis II in that the strategy is to divert inflowing air to rise at radii greater than that of the eyewall. The field tactics are also identical and call for seeding radially outward from the eyewall. In addition to the augmented heating expected under this approach, there is an interesting and beneficial side effect. Radar data (Senn, 1971) indicate that more than 50 percent of the cumuli within 30 nm of the hurricane center have tops within the 20,000- to 30,000-ft range. Since, in most hurricanes, very little macroscale inflow or outflow occurs at middle tropospheric levels (Riehl and Malkus, 1961; Miller, 1962; Hawkins and Rubsam, 1968), the mass transported upward in clouds whose tops are at these levels must subside relatively close to the cloud and thus reduce the net upward mass transport. If through silver-iodide seeding these clouds can be induced to grow vertically into the outflow layer not only would the additional latent heat postulated by the STORMFURY Advisory Panel be realized but also, the mass transported upward would be caught in the macroscale

outflow and evacuated from the storm core. Consequently, this so-called "New Hypothesis" provides not only a larger heat source but also a more efficient mechanism for evacuating the air diverted from the inflow layer.<sup>6</sup> Calculations by Sheets (1969) indicate that individual clouds just beyond the eyewall can be induced to grow to outflow levels by silver-iodide seeding.

While the postulated mechanisms of the new hypothesis appear capable of providing heat at rates which approach the values used in the model calculations (see also Gentry and Hawkins, 1971), some conceptual problems arise with the model simulations. The major source of energy is now to be obtained from clouds which are induced to grow from mid- to upper-tropospheric levels. However, the model parameterization of cumulus activity is essentially a generalization of the technique introduced by Kuo (1965) in which model clouds are comprised of undilute ascent. Consequently, all model clouds whose bases are in the boundary layer reach upper tropospheric levels by natural processes. The model eyewall differs from other regions of the storm in cloud concentration but not in cloud depth. This is a distinct discrepancy between model and real hurricanes (Senn, 1971; Malkus, 1960).

Simulations relevant to the new hypothesis are not easily visualized unless one adopts a highly philosophical attitude. The basic feature, it may be argued, is the stimulation of tall convection at radii beyond the

---

<sup>6</sup>Despite differences between hypotheses, all flight tracks for hurricanes seeded to date have been more or less the same (Gentry and Hawkins, 1971).



eyewall. In the field program, this is to be accomplished by causing relatively short clouds to become tall. The ultimate effect, however, is to increase the concentration of tall clouds in the seeded region. While the current version of the model cannot simulate the intermediate stages in which short clouds grow to tall clouds, the techniques previously employed (Rosenthal, 1971a) do indeed provide for increased tall cloud concentrations in the "seeded" regions.

Consequently, we have retained the original technique for seeding simulation. Aside from the virtue of simplicity, this also allows direct comparisons between the new calculations and those previously published. The technique consists simply of increasing the heating function that represents the cumulus feedback on the macroscale by fixed amounts for certain periods of time. This artificial enhancement of the heating functions is always applied at only the 300- and 500-mb levels.<sup>7</sup> The radial interval and duration of seeding varies from experiment to experiment and is clearly stated in each case. The "normal" enhancement rate is retained as the equivalent of a 2°C per 30 min temperature change at constant pressure (Rosenthal, 1971a). In the meter-ton-second system of units employed in the model, this is approximately 1 kilojoule per ton per second (approximately  $4.2 \times 10^{-3}$  calories per gram per second). For the reader's convenience, the Appendix provides a table which summarizes the essential features of new experiments not discussed in previous publications.

---

<sup>7</sup>For ease of expression, artificial enhancement of the heating function will be referred to as "seeding". We fully realize the looseness of this expression.

## 6. CALCULATIONS RELEVANT TO HYPOTHESIS I

A previous calculation in which the normal enhanced heating rate was applied for ten hours at the eyewall center (25-km radius) and the next grid point inward (15 km) resulted in a slight intensification of the model storm (see fig. 8, taken from Rosenthal, 1971a) with a rapid recovery to a state close to the control after the seeding was terminated. Examination of the 900-mb vertical motions (fig. 9) clearly showed that boundary-layer convergence was increased at the seeded radii but rather little at other radii.

Two new calculations provide somewhat similar results. The initial data are hour 288 of Experiment S-35. To exaggerate the effect, enhanced heating is applied at twice the normal rate ( $2 \text{ KJ Ton}^{-1} \text{ sec}^{-1}$ ) for 20 hours at 15 and 25 km (Experiment N-12) and 25-km radius (see figs. 3 and 4 for radius of maximum vertical motion). The behavior of maximum sea-level wind (MSLW) for these experiments, summarized by figure 10, is much the same as that obtained from the previous experiment. No further experiments relevant to Hypothesis I have been conducted.

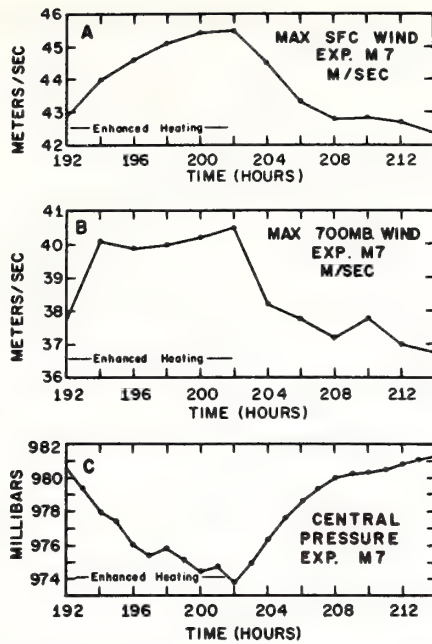


Figure 8. Results from an experiment with seeding at radii of 15 and 25 km from 192 to 202 hours. The rate of artificial seeding is  $1 \text{ KJ ton}^{-1} \text{ sec}^{-1}$ . The eyewall is at 25-km radius. The control is experiment S-18 (fig. 7) and is very nearly in steady state during the interval shown. Taken from Rosenthal (1971a).

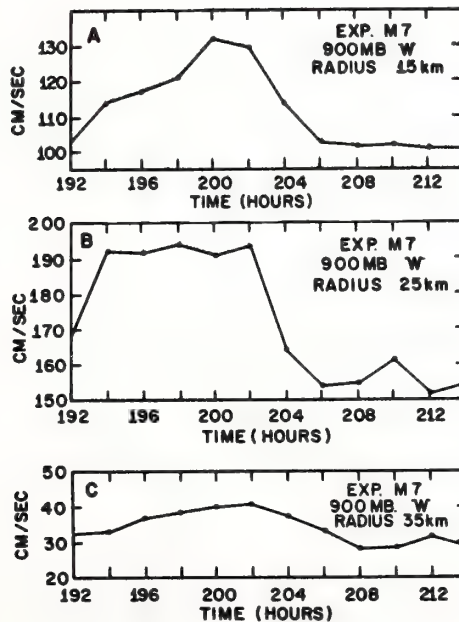


Figure 9. Vertical motions at 900 mb during and after the seeding operation shown by figure 8. Seeding is at radius of 15 and 25 km.

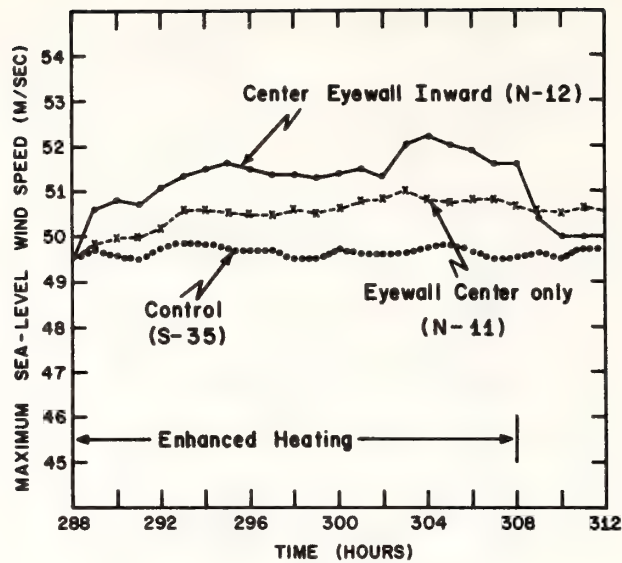


Figure 10. Results from two seeding experiments. Artificial heating is applied from 288 to 308 hours. The initial conditions are hour 288 of experiment S-35. The rate of artificial heating is  $2 \text{ KJ ton}^{-1} \text{ sec}^{-1}$ . The eyewall is at 25-km radius. For experiment N-11, artificial heating is applied at 25-km radius. For experiment N-12, artificial heating is applied at 15- and 25-km radius.

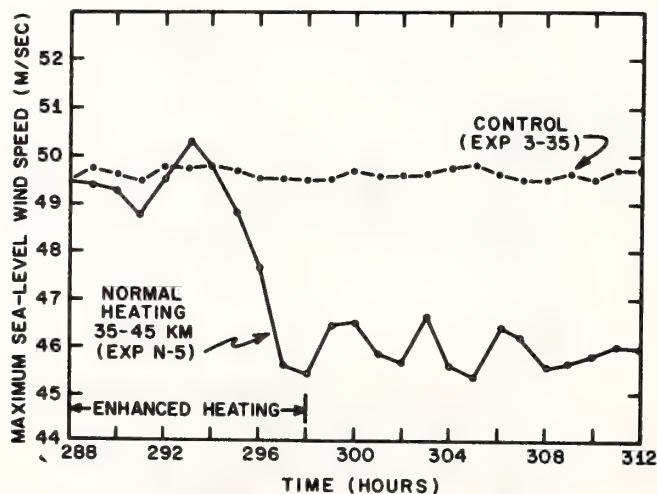


Figure 11. Results from a seeding experiment (N-5) where artificial heating is applied from 288 to 298 hours at radii of 35, 45 and 55 km. The initial conditions are hour 288 of experiment S-35. The eyewall is at 25-km radius.



## 7. CALCULATIONS RELEVANT TO HYPOTHESIS II

Figure 11 summarizes an experiment (N-5) in which the normal ( $1 \text{ KJ ton}^{-1} \text{ sec}^{-1}$ ) enhanced heating rate was applied for ten hours over a 30 km radial interval just beyond the eyewall center (35, 45 and 55 km). Initial conditions are again 288 hours of S-35. Figures 12 and 13 vividly portray the diversion of boundary-layer inflow and the formation of a new eyewall 10 km radially outward from the original. When the seeding is terminated, the system attempts to restore the original eyewall. Significant changes in MSLW do not occur until the new eyewall has become established which is about eight hours after the start of seeding. Important changes in the wind profile (fig. 14) occur earlier. In response to the increased transverse circulation that is produced by the seeding, angular momentum is carried inward more rapidly than is the case for the control. Consequently, low-level winds increase at all radii larger than that of the MSLW. A later experiment will verify that the increased centrifugal and coriolis forces associated with these low-level wind increases play a vital role in cutting off the supplies of mass and angular momentum to the original eyewall.

Winds at 700 mb (fig. 15) behave quantitatively in a fashion similar to those at sea level. Here, however, the response to seeding is more rapid and extreme. Peak winds exceed those of the control until after seeding is terminated. The rapid response of 700-mb winds in the seeded zone results from lack of the moderating effects of drag friction as well as the increased vertical advection associated with increased vertical

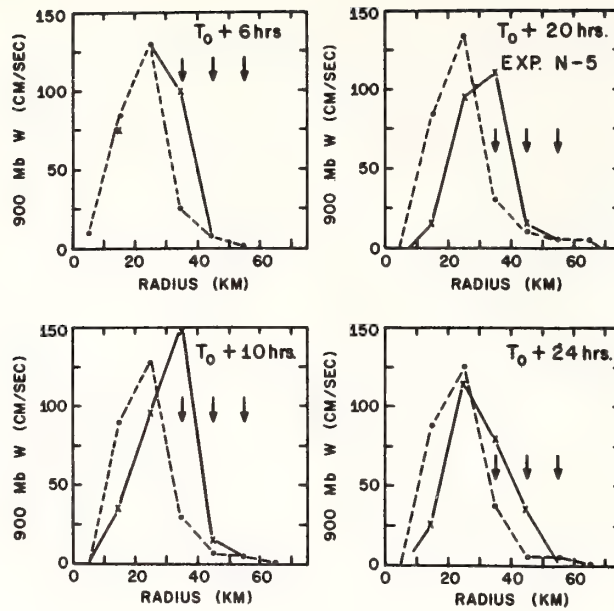


Figure 12. Radial profiles of 900-mb vertical motion at selected times during experiment N-5. The control (S-35) data are shown by dashed lines. The arrows indicate the seeded radii. Initial conditions ( $T_0$ ) are hour 288 of experiment S-35. Seeding terminates at  $T_0 + 10$  hours.

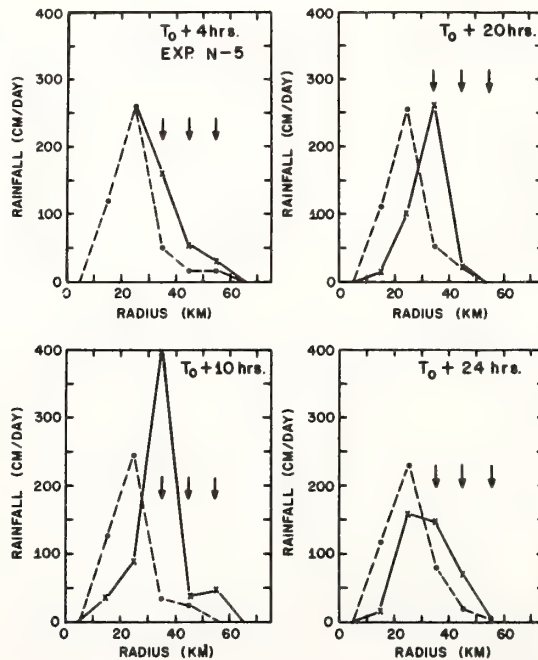


Figure 13. Same as figure 11 but rainfall rates are shown.

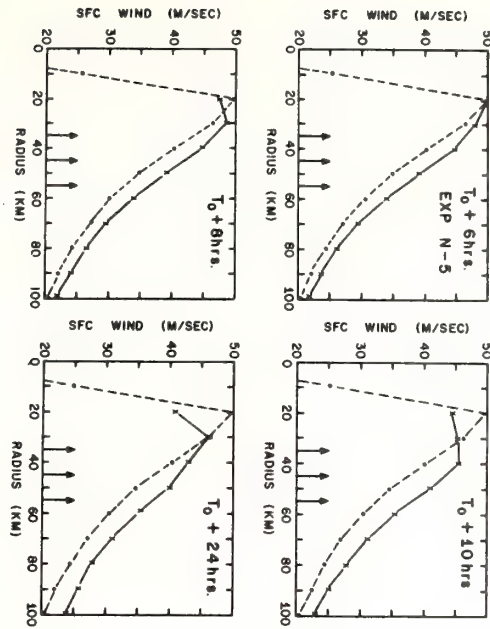


Figure 14. Same as figure 11 but wind speed profiles at sea level are shown.

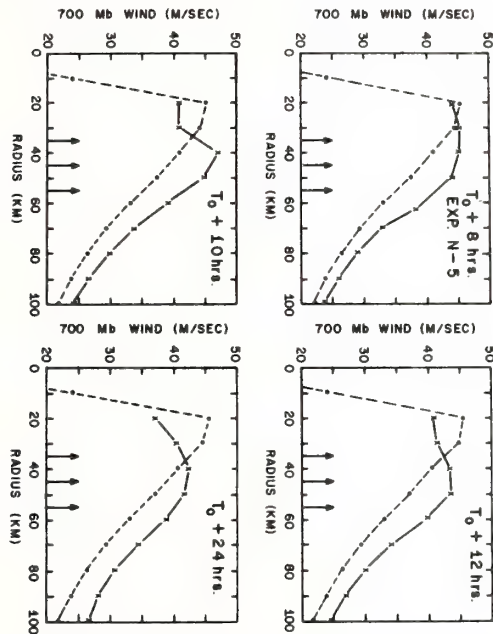


Figure 15. Same as figure 11 but 700-mb wind speed profiles are shown.

motions. These 700-mb results are similar to those previously obtained (Rosenthal, 1971a) and have raised some concern. This stems from the fact that Hurricane Debbie was monitored near 700 mb and showed wind variations more nearly like the model results at sea level. It is the authors' opinion that little information can be drawn from these differences because of the idealized nature of the model. As pointed out earlier, computational results can only validly be compared in detail with other computational results.

The central pressure in Experiment N-5 (not shown) drops 4 mb during the first 8 hours of seeding. As soon as the new eyewall is formed, the central pressure rises and approaches that of the control.

Previous calculations (Rosenthal, 1971a) found only minor differences between experiments in which the seeding was conducted entirely beyond the original eyewall (such as N-5) and those in which seeding was conducted from the original eyewall outward. This appears to be a result of fortuitous initial conditions and not in general true. Experiment N-4 (fig. 16) is identical to N-5 with the sole exception that the seeding is performed at radii of 25, 35 and 45 km and, hence, includes the eyewall center. The MSLW exceeds that of the control during the entire calculation. The behavior of the winds at 700 mb (not shown) is similar to that of the surface winds. The vertical-motion and precipitation patterns (also not shown) show only minor increases at the seeded radii with no tendency for outward displacement of the eyewall.

If, however, the seeding is extended for another ten hours (Experiment N-4D), the ultimate effect is similar to that obtained in N-5



(compare figs. 11 and 16). Thus seeding from the eyewall center outward appears to be a potentially successful tactic but a less desirable one than seeding that entirely avoids the eyewall center.

The major difference in the results of Experiments N-4 and N-4D is that in the former case seeding is terminated just before any important diversions of boundary-layer inflow take place. We are, therefore, left with an increased transverse circulation that is more or less congruent with that of the control. When the seeding is extended in time (Experiment N-4D), the heating beyond the eyewall ultimately becomes effective in stimulating convection and significant diversions of inflow are noted at 300 hours (fig. 17). By 302 hours, the new eyewall is established. Decreases in MSLW do not become significant until 300 hours when the diversion of inflow first becomes apparent.

Two additional experiments, with tactics between those of N-4 and N-4D, yielded interesting results. One of these (N-45) continued seeding just two hours longer than N-4, that is from 288-300 hours. The result, of course, is identical to N-4D until 300 hours. Thereafter, the model storm quickly adjusted in structure and intensity to a state nearly identical to that of N-4. This again indicates that seeding must be continued at least until a new eyewall is established if reductions in MSLW are to be achieved. To further examine this point, the seeding was continued for still another two hours and terminated at 302 hours (N-46). Since this experiment is identical to N-4D from 288 to 302 hours, the eyewall (fig. 17) has already reformed at a radius of 35 km when the seeding is terminated. The result of this experiment (N-46) was very similar to

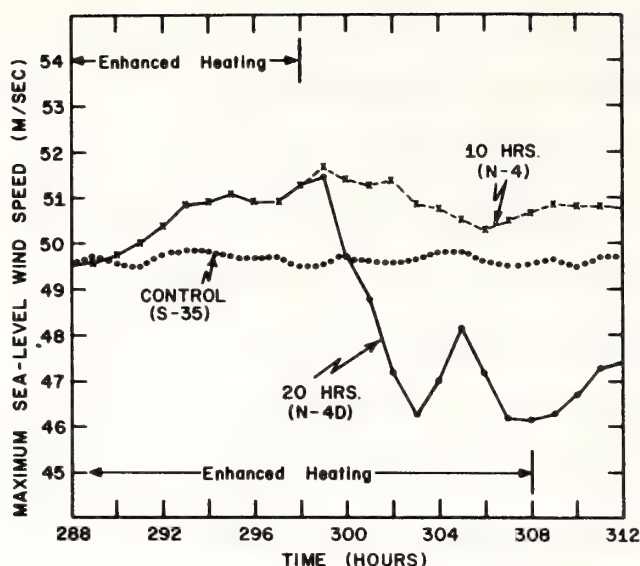


Figure 16. Results from two seeding experiments. The initial conditions are hour 288 of experiment S-35. The artificial heating rate is  $1 \text{ KJ ton}^{-1} \text{ sec}^{-1}$  and is applied at radii of 25, 35 and 45 km. For experiment N-4, artificial heating is in effect from 288 to 298 hours. For experiment N-4D, artificial heating is in effect from 288 to 308 hours.

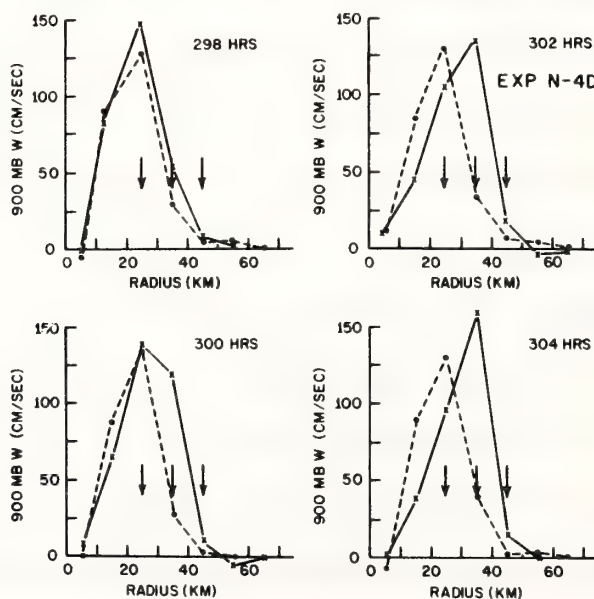


Figure 17. Radial profiles of 900-mb vertical motion at selected times during experiment N-4D. The control (S-35) data are shown by dashed lines. The arrows indicate seeded radii. Initial conditions are hour 288 of experiment S-35. Seeding terminates at 308 hours.

that of N-4D. It appears, therefore, that continued seeding at the same radii after the formation of the new eyewall has no significant effect in further reductions of the MSLW.

An experiment (N-21) was then conducted in which at hour 304 of N-4D the seeded radii were shifted from 25, 35 and 45 km to 35, 45 and 55 km. The heating rate was the normal value and the operation was continued for 16 hours. No consistent deviations from N-4D were observed. An eyewall temporarily appeared at 45-km radius after 6 hours (310 hours) but within two more hours receded to a radius of 35 km. The MSLW for this experiment oscillated around that of N-4D. At 310 hours, when the eyewall was at 45 km, the MSLW was  $2.5 \text{ m sec}^{-1}$  less than that of N-4D. But by 312 hours, the MSLW was only  $1 \text{ m sec}^{-1}$  less than that of N-4D. Earlier, at 305 hours, N-21 showed MSLW  $1 \text{ m sec}^{-1}$  greater than N-4D.

Experiment N-6 (fig. 18) was conducted to determine if increased seeding rates would lead to more rapid responses and/or greater decrease in MSLW. It is identical to N-4 except that the artificial heating is twice ( $2 \text{ KJ ton}^{-1} \text{ sec}^{-1}$ ) the normal value. The response here is much more rapid. The vertical-motion and precipitation patterns (not shown) indicate a new eyewall at 35-km radius by 294 hours. However, despite the more rapid response, the reduction in MSLW is not significantly greater than that observed in N-4D.

In our discussion of Experiment N-5, we stated that an important factor in the formation of a new eyewall at a larger radius is an increase of wind at radii from the seeded zone outward (figs. 14 and 15) during the early portions of the operation. Experimental results in

support of this contention have been deferred to this point. Experiment N-15 (fig. 19) was identical to N-4D with the sole exception that the coriolis and centrifugal terms in the radial equation of motion were held constant at the value given by the initial conditions. The MSLW oscillates about the control (S-35) with no consistent departure. The storm structure yielded by N-15 (not shown) shows no significant differences from S-35. There is absolutely no tendency to form a new eyewall. Therefore, by comparison of N-4D and N-15, we conclude that increased coriolis and centrifugal forces at larger radii are vital if the inflow is to be prevented from reaching the original eyewall and if a new eyewall is to be formed at a larger radius.

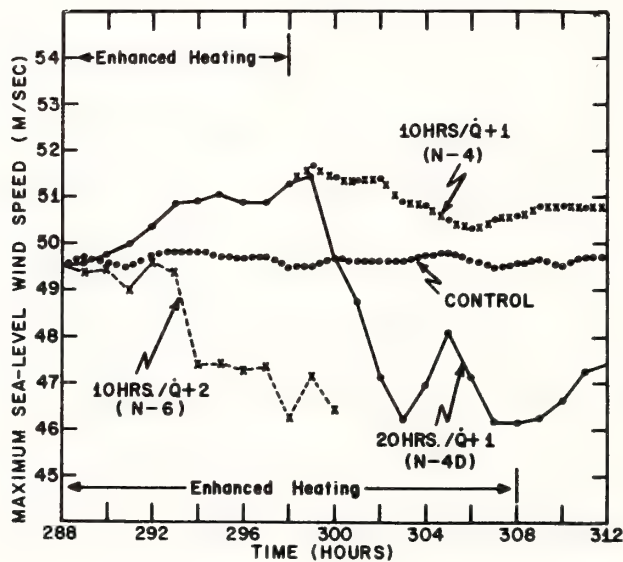


Figure 18. Results from three seeding experiments. The initial conditions are hour 288 of experiment S-35. For experiment N-6, the artificial heating rate is  $2 \text{ KJ ton}^{-1} \text{ sec}^{-1}$ . For experiments N-4 and N-4D, the rate is  $1 \text{ KJ ton}^{-1} \text{ sec}^{-1}$ . Artificial heating is in effect from 288 to 298 hours in experiments N-6 and N-4. For experiment N-4D, the artificial heating is in effect until 308 hours. The seeded radii are 25, 35 and 45 km for all three experiments.



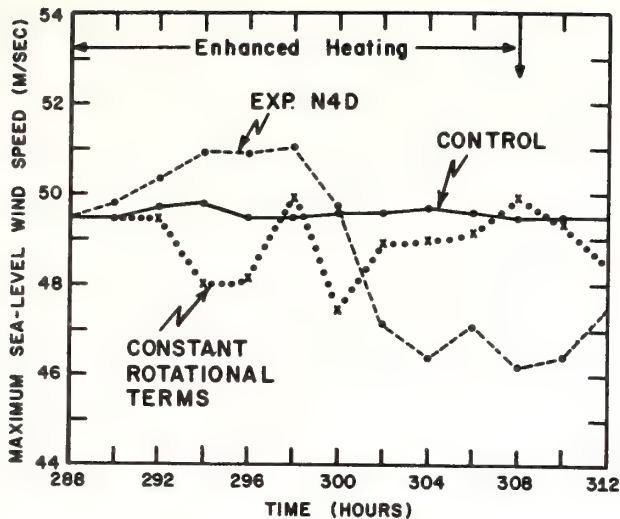


Figure 19. Results from two seeding experiments. The initial conditions are hour 288 of experiment S-35. The artificial heating rate is  $1 \text{ KJ ton}^{-1} \text{ sec}^{-1}$  and is applied at radii of 25, 35 and 45 km and is in effect from 288 to 308 hours. The experiment labeled "constant rotational terms" evaluates the coriolis and centrifugal terms in the radial equation of motion from the initial winds. This experiment is referred to as N-15 in the text and appendix.

We have already seen, other conditions being equal, that seeding entirely beyond the eyewall produces a more rapid, but no greater, reduction in MSLW than seeding from the eyewall center outward. In both cases, however, the new eyewall forms only one grid point (10 km) radially outward from the original eyewall. With this in mind, it is of interest to compare the results of seeding at still larger radii. The following questions motivate these experiments: (1) Will the reduction of MSLW occur even more rapidly as the artificial heating is applied at even larger radii? (2) Can larger reductions in MSLW be achieved by seeding at still larger radii? (3) Can we induce eyewall formation with the model at larger radii than observed in the experiments already discussed?

Experiments N-4F, N-13 and N-27 are addressed to these questions. The common aspects of these experiments are the normal heating rate ( $1 \text{ KJ ton}^{-1} \text{ sec}^{-1}$ ) for 20 hours with 288 hours of S-35 constituting the initial conditions. The radial intervals seeded are: 35, 45 and 55 km (N-4F); 45, 55 and 65 km (N-13); 75, 85 and 95 km (N-27). Note that the first 10 hours of N-4F are identical to N-5. Figure 20 gives the MSLW histories for these calculations. The ultimate results of the three experiments are much the same. Furthermore, the variation in response time is opposite in sense from what might have been expected from the results of N-5 and N-4D. It thus appears that the answers to questions (1) and (2) of the previous paragraph are no. The structural evolution of N-13, though lagging in time, is similar to that of N-4F which in turn is similar to N-5 (figs. 12 to 15). In each case, the new eyewall is formed at a radius of 35 km.

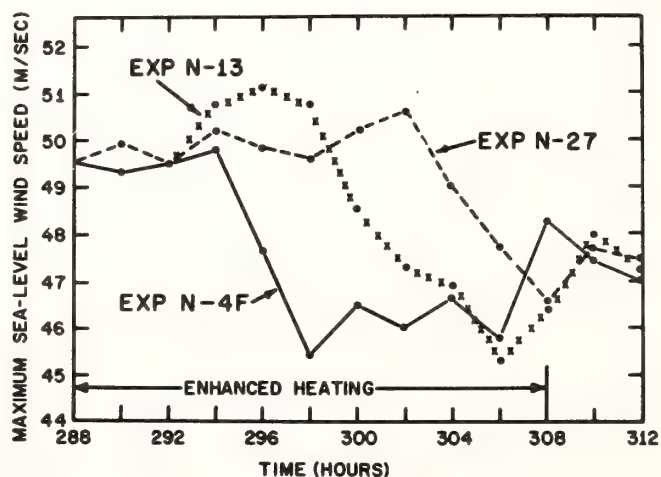


Figure 20. Results from three seeding experiments. The initial conditions are hour 288 of experiment S-35. The artificial heating rate is  $1 \text{ KJ ton}^{-1} \text{ sec}^{-1}$  and is in effect from 288 to 308 hours. The seeded radii are: 35, 45 and 55 km (Experiment N-4F); 45, 55 and 65 km (Experiment N-13); 75, 85 and 95 km (Experiment N-27).

Even in experiment N-27, where the seeded zone is 75, 85 and 95 km, the new eyewall is formed at a radius of 35 km. In this case, however, there are some interesting differences in the structural evolution (figs. 21 and 22). At 296 hours, 8 hours after the start of seeding, the only significant response of the 900-mb vertical motions (fig. 21) is a small increase centered at the inner edge of the seeded zone. Between 302 and 304 hours (14 to 16 hours after the start of seeding) significant increases of vertical motion (in comparison to the control) begin to occur at a radius of 35 km. It is at this time that the MSLW (fig. 20) begins to fall. It is not until 308 hours (a full 20 hours after the start of seeding) that the eyewall becomes established at the larger radius. It is also at this time that the MSLW reaches its minimum value (fig. 20). It is interesting that the 900-mb vertical motions at 308 hours in the seeded zone are downward (fig. 21).

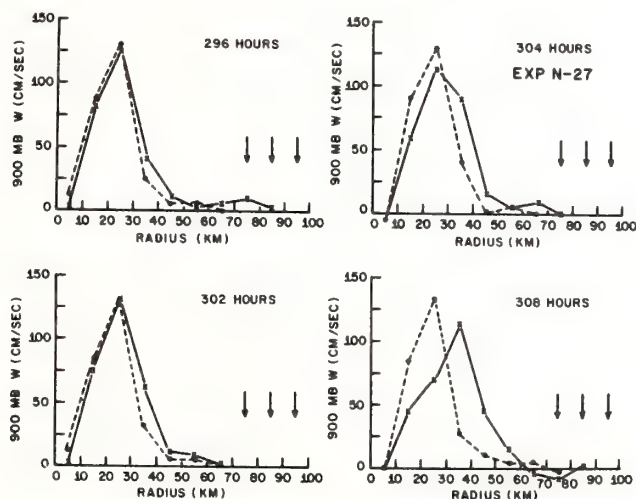


Figure 21. Radial profiles of 900-mb vertical motion at selected times during experiment N-27. The control (S-35) data are shown by dashed lines. The arrows indicate seeded radii. Initial conditions are hour 288 of S-35. Seeding terminates at 308 hours.

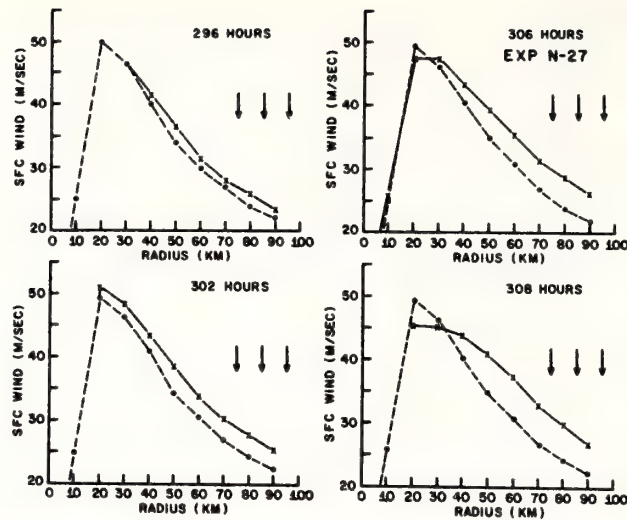


Figure 22. Same as figure 21 except that profiles of sea-level wind speed are shown.

The wind structure at sea level (fig. 22) also shows some differences from the experiments already discussed. In particular, the reduction of MSLW is accomplished without radial displacement. Here, essentially, we observe a flattening of the original sharp maximum and the formation of a plateau-like wind profile with a poorly delineated maximum.

The results thus far show one major discrepancy in comparison to those presented earlier (Rosenthal, 1971a). Experiments with the normal seeding rate applied at radii of 25, 35 and 45 km (Experiments N-4 and N-4D) show a substantially longer response time than those with the same heating rate at radii of 35, 45 and 55 km (Experiments N-5 and N-4F). Similar experiments summarized by Rosenthal (1971a) did not show this difference as may be verified by examination of figure 23.



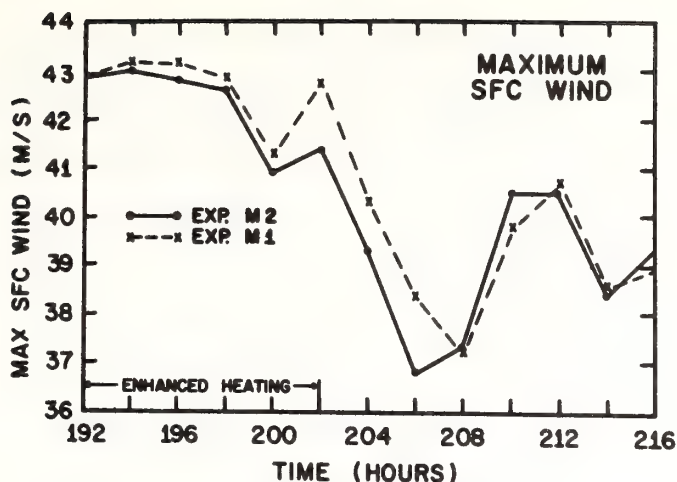


Figure 23. Results from two seeding experiments. The rate of artificial heating is  $1 \text{ KJ ton}^{-1} \text{ sec}^{-1}$  and is in effect from 192 to 202 hours. The control is very nearly in steady state during the interval shown and has its eyewall at 25-km radius. In experiment M-1, seeding is at radii of 25, 35 and 45 km. For experiment M-2, the seeding is at radii of 35, 45 and 55 km. Taken from Rosenthal (1971a).

It was originally thought that this discrepancy was attributable to a change in the treatment of the drag coefficient<sup>8</sup> introduced in the interim between the two sets of calculations. However, the calculations discussed below indicate that a more likely explanation may be found in differences in initial conditions.

Figure 24 summarizes departures from the control MSLW obtained from four experiments with the normal heating rate applied for 20 hours at 25, 35 and 45 km. The initial conditions for these experiments are the control (S-35) at 264 hours (N-22), 288 hours (N-4D), 312 hours (N-23) and

<sup>8</sup>A constant drag coefficient of  $3 \times 10^{-3}$  was used in the old calculations. The present calculations use a drag coefficient which is a linear function of wind speed. See Rosenthal (1971c) for details.

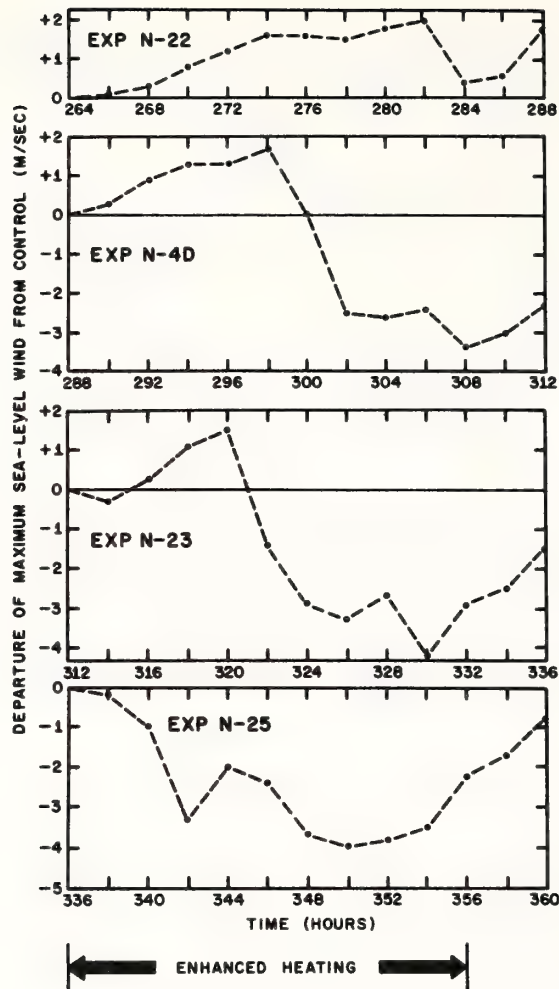


Figure 24. Results from four seeding experiments. The rate of artificial heating is  $1 \text{ KJ ton}^{-1} \text{ sec}^{-1}$  and is in effect for 20 hours at radii of 25, 35 and 45 km. The initial conditions are: hour 264 of S-35 (Experiment N-22); hour 288 of S-35 (Experiment N-4D); hour 312 of S-35 (Experiment N-23) and 336 hours of S-35 (Experiment N-25).

336 hours (N-25). Clearly the response time decreases with storm age. This strongly suggests that seeding operations are more likely to be successful with older storms. As we shall shortly see, the static stability of the eyewall region is increasing over the time span of the calculation. This further suggests that the changes of success in a seeding operation are greater the greater the static stability of the eyewall region.

The response times of the experiments which begin at 312 and 336 hours (N-23 and N-25) are comparable to those previously obtained (fig. 23). The experiment (N-22) which begins at 264 hours never shows MSLW less than that of the control. However, the curve indicates that a decrease in intensity would likely have occurred if the seeding had been extended over a longer period of time. This is verified by figure 25 which shows the result of an additional eight hours of seeding.

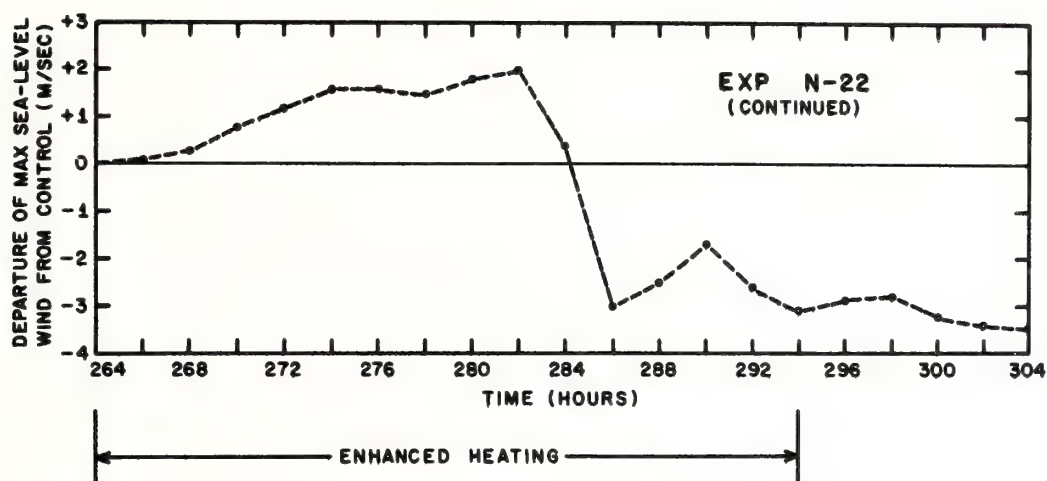


Figure 25. Same as experiment N-22 of figure 24 except that the seeding is continued for a total of 30 hours (264 to 294 hours).

Figure 26 is a time-cross section of temperature departures from values at 240 hours at the eyewall center (25-km radius) of the control (S-35). The warming is clearly concentrated in the upper troposphere and thus distributed such that static stability is increasing with time. Figure 27 shows the time dependence of precipitation at radii of 25, 35 and 45 km. In the eyewall, precipitation is decreasing by natural processes as the storm ages. At the two larger radii shown, natural processes are tending to increase the precipitation.

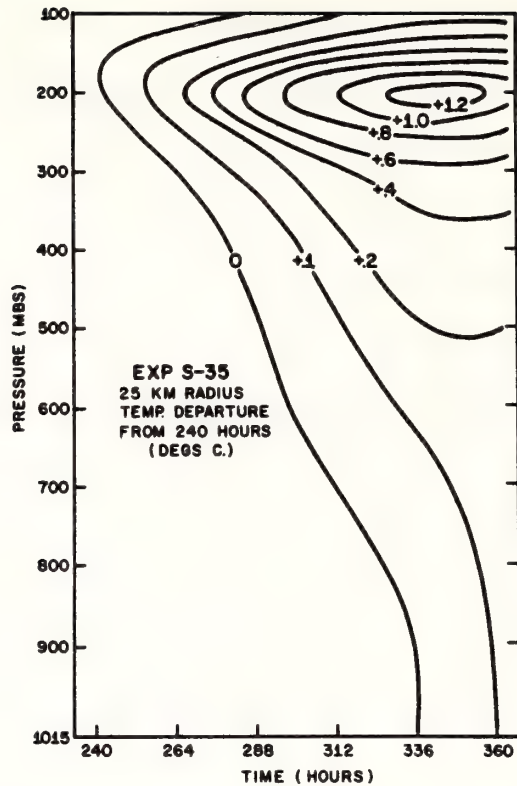


Figure 26. Time-cross section of temperature departures from their values at 240 hours at a radius of 25 km for experiment S-35.

Intuitively, increasing static stability of the eyewall, decreasing eyewall rainfall, and lateral spreading of the rain area would all seem to favor a seeding operation under the tactics of Hypothesis II.



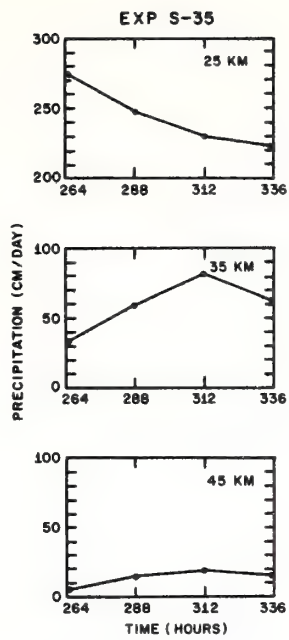


Figure 27. Rainfall rates as a function of time for selected radii for experiment S-35.

## 8. SUMMARY AND CONCLUSIONS

While only a small number of experiments are described here, consistent features emerge that, taken together with previous results (Rosenthal, 1971a), appear to allow certain generalizations. Clearly neither these calculations nor those of Rosenthal (1971a) provide support for Hypothesis I. It is our feeling that this strategy should not be employed in future field experiments.

The calculations indicate that of the potential tactics under Hypothesis II, a seeding operation just radially outward from the eyewall center is optimum. This is primarily reflected in the rapidity of response to the artificial heating rather than in ultimate reductions of the maximum winds. The latter were more or less the same for all calculations which succeeded in building a new eyewall at a larger radius. The experiments in which the artificial heating was applied at fairly large radii (beyond, say, 55 km) are probably pushing a point since in real hurricanes seedable clouds may be rather scarce in these locations. Despite this, the response times (all other factors being equal) were clearly greater with heating from the eyewall center outward and with heating at relatively large radii. The latter result may well reflect opposition to ascent due to the boundary layer "sucking" phenomenon discussed in Section 3.

The experiments clearly indicate that seeding must be continued until a new eyewall is formed at a larger radius if significant reductions of the maximum winds at sea level are to be achieved. On the other hand,

continued seeding, at the same radii, beyond the time that the new eyewall is established does not appear to be desirable. Comparison of Experiment N-5 (fig. 11) with Experiment N-4F (fig. 20) seems to indicate that this tactic may well reduce the effect of the earlier seeding. In all probability, the upward trend of the peak winds near the end of Experiments N-4D, N-23 and N-25 (fig. 24) represent this same effect.

In all successful calculations, the ultimate effect was to displace the eyewall 10 km (one grid point) radially outward from the original eyewall and to reduce the wind maximum at sea level by 3 to 4 m sec<sup>-1</sup>. Variations in the radius of seeding and the rate of artificial heating altered only the time required for these changes to take place.

Response times decreased markedly with storm age. Intuitively, this appears to be related to an increase of the static stability of the control storm's eyewall as the model storm ages. In addition, aging of the control storm was accompanied by a natural tendency for eyewall rainfall to diminish and for rainfall to increase at radii just beyond the eyewall.

The increased transverse circulation which results from application of the artificial heating tends to increase winds at relatively large radii as inward transports of absolute angular momentum are increased. This is not a particularly desirable feature of a modification experiment since it may well produce adverse storm-surge effects. It also results in an increase of 20 percent in the modified storm's kinetic energy (Rosenthal, 1971a). On the other hand, we were able to show that these increased winds are vital if the eyewall is to be reformed at a larger radius and the maximum wind is to be reduced. It is the increased

centrifugal and coriolis forces arising from these larger winds that prevents the inflow from reaching the original eyewall and thus forces ascent at a larger radius.

While virtually all of the tactical variations of Hypothesis II ultimately resulted in similar modifications of the model hurricane, those with larger response times are clearly less likely to be effective in a real hurricane. It thus appears that field programs conducted with older storms, seeded just beyond the eyewall are most amenable to beneficial modification. It also appears that the seeding operation should be massive since larger heating rates clearly lead to more rapid responses of the model storm.

Since many of the numerical experiments show temporary increases of the maximum wind during the early phases of the operation, it would appear that the policy of not seeding storms whose early landfall is predicted should be continued.

## 9. ACKNOWLEDGMENTS

Members of the Advisory Panel of Project STORMFURY suggested several of these experiments. Frequent discussions with Drs. R. C. Gentry and H. F. Hawkins were of value in planning and interpreting the calculations.



## REFERENCES

- Anthes, R. A. (1971), Non-developing experiments with a three-level axisymmetric hurricane model, NOAA Technical Memorandum ERLTM-NHRL, (In press).
- Anthes, R. A., S. L. Rosenthal, and J. W. Trout (1971), Preliminary results from an asymmetric model of the tropical cyclone, Monthly Weather Review, (In press).
- Cotton, W. R. (1970), A numerical simulation of precipitation development in supercooled cumuli, NSF Grant No. GA-13818, (Dept. Meteorol., Pennsylvania State Univ., University Park, Pennsylvania), 178 pp.
- Estoque, M. A. (1971), A hurricane model for simulating cloud seeding, NOAA Grant No. E-22-47-68(G), (Division of Atmospheric Sciences, Rosenstiel School of Marine and Atmospheric Science, University of Miami, Coral Gables, Florida), 16 pp.
- Gentry, R. C. (1969), Project STORMFURY, Bulletin of the American Meteorological Society, 50, No. 6, 404-409.
- Gentry, R. C. (1970), Hurricane Debbie modification experiments, August 1969, Science, 168, No. 3930, Apr. 24, 473-475.
- Gentry, R. C. and H. F. Hawkins (1971), A hypothesis for modification of hurricanes, Project STORMFURY Annual Report 1970, U. S. Department of Navy and U. S. Department of Commerce, Appendix B, B-1 - B-15.
- Hawkins, H. F. (1971), Comparison of results of the hurricane Debbie (1969) modification experiments with those from Rosenthal's numerical model simulation experiments, Monthly Weather Review, 99, No. 5, 427-434.
- Hawkins, H. F. and D. T. Rubsam (1968), Hurricane Hilda, 1964: II. Structure and budgets of the hurricane on October 1, 1964, Monthly Weather Review, 96, No. 9, 617-636.
- Hebert, P. J. and C. L. Jordan (1959), Mean soundings for the Gulf of Mexico area, National Hurricane Research Project Report No. 30, U. S. Department of Commerce, National Hurricane Research Laboratory, Miami, Florida, 10 pp.
- Kuo, H. L. (1965), On formation and intensification of tropical cyclones through latent heat release by cumulus convection, Journal of the Atmospheric Sciences, 22, No. 1, 40-63.

## REFERENCES (continued)

- Malkus, J. S. (1960), Recent developments in studies of penetrative convection and an application to hurricane cumulonimbus towers, Cumulus Dynamics, Pergamon Press, New York, 65-84.
- Matsuno, T. (1966), Numerical integrations of the primitive equations by a simulated backward difference method, Journal of the Meteorological Society of Japan, Ser. 2, 44, 76-84.
- Members, Advisory Panel to Project STORMFURY (1971), Report on meeting of Project STORMFURY Advisory Panel, Miami, Florida, 29-30 September 1970, Project STORMFURY Annual Report 1970, U. S. Department of Navy and U. S. Department of Commerce, Appendix A, A-1 - A-4.
- Miller, B. I., (1962), On the momentum and energy balance of hurricane Helene (1958), National Hurricane Research Project Report No. 53, U. S. Department of Commerce, National Hurricane Research Laboratory, Miami, Florida, 19 pp.
- Ooyama, K. (1969), Numerical simulation of the life cycle of tropical cyclones, Journal of the Atmospheric Sciences, 26, No. 1, 3-40.
- Riehl, H. and J. S. Malkus (1961), Some aspects of hurricane Daisy, 1958, Tellus, 13, No. 2, 181-213.
- Roll, H. U. (1965), Physics of the Marine Atmosphere, Academic Press, New York & London, 426 pp.
- Rosenthal, S. L. (1969), Numerical experiments with a multilevel primitive model designed to simulate the development of tropical cyclones: Experiment I, ESSA Technical Memorandum, ERLTM-NHRL 82, U. S. Department of Commerce, National Hurricane Research Laboratory, Miami, Florida, 36 pp.
- Rosenthal, S. L. (1970a), A survey of experimental results obtained from a numerical model designed to simulate tropical cyclone development, ESSA Technical Memorandum, ERLTM-NHRL 88, U. S. Department of Commerce, National Hurricane Research Laboratory, Miami, Florida, 78 pp.
- Rosenthal, S. L. (1970b), A circularly symmetric primitive equation model of tropical cyclone development containing an explicit water vapor cycle, Monthly Weather Review, 98, No. 9, 643-663.

## REFERENCES (continued)

- Rosenthal, S. L. (1971a), A circularly symmetric primitive-equation model of tropical cyclones and its response to artificial enhancement of the convective heating functions, *Monthly Weather Review*, 99, No. 5, 414-426.
- Rosenthal, S. L. (1971b), Hurricane modeling at the National Hurricane Research Laboratory (1970), Project STORMFURY Annual Report 1970, U. S. Department of Navy and U. S. Department of Commerce, Appendix C, C-1 - C-13.
- Rosenthal, S. L. (1971c), The response of a tropical cyclone model to variations in boundary layer parameters, initial conditions, lateral boundary conditions and domain size, *Monthly Weather Review*, (In press).
- Rosenthal, S. L. and W. J. Koss (1968), Linear analysis of a tropical cyclone model with increased vertical resolution, *Monthly Weather Review*, 96, No. 12, 858-866.
- Senn, H. V. (1971), A summary of radar precipitation echo heights in hurricanes, Project STORMFURY Annual Report 1970, U. S. Department of Navy and U. S. Department of Commerce, Appendix K, K-1 - K-18.
- Sheets, R. C. (1969), Preliminary analysis of cloud physics data collected in hurricane Gladys, 1968, Project STORMFURY Annual Report 1968, U. S. Department of Navy and U. S. Department of Commerce, Appendix D, D-1 - D-11.
- Sheets, R. C. (1969), Computations of the seedability of clouds in a hurricane environment, Project STORMFURY Annual Report 1968, U. S. Department of Navy and U. S. Department of Commerce, Appendix E, E-1 - E-4.
- Simpson, R. H., M. R. Ahrens, and R. D. Decker (1963), A cloud seeding experiment in hurricane Esther, National Hurricane Research Project Report No. 60, 30 pp.
- Simpson, R. H. and J. S. Malkus (1964), Experiments in hurricane modification, *Scientific American*, 211, No. 6, 27-37.
- Sundqvist, H. (1970), Numerical simulation of the development of tropical cyclones with a ten-level model. Part I, *Tellus*, 22, No. 4, 359-390.

## REFERENCES (continued)

- Yamasaki, M. (1968), Detailed analysis of a tropical cyclone simulated with a 13-layer model, *Papers in Meteorology and Geophysics*, 19, No. 4, 559-585.



# APPENDIX

Table A.1. Characteristic parameters of the seeding simulations

Exp. No.	Initial Conditions	Seeding Rate (KJ Ton <sup>-1</sup> sec <sup>-1</sup> )	Seeded Radii (km)	Duration of Seeding (hours)
N-4	288 hrs (S-35)	1	25, 35, 45	10
N-4D	Do.	Do.	Do.	20
N-4F	Do.	Do.	35, 45, 55	Do.
N-5	Do.	Do.	Do.	10
N-6	Do.	2	25, 35, 45	Do.
N-11	Do.	Do.	25	20
N-12	Do.	Do.	15, 25	Do.
N-13	Do.	1	45, 55, 65	Do.
N-15*	Do.	Do.	25, 35, 45	Do.
N-21	304 hrs (N-4D)	Do.	35, 45, 55	16
N-22	264 hrs (S-35)	Do.	25, 35, 45	20
N-23	312 hrs (S-35)	Do.	Do.	Do.
N-25	336 hrs (S-35)	Do.	Do.	Do.
N-27	288 hrs (S-35)	Do.	75, 85, 95	Do.
N-45	Do.	Do.	25, 35, 45	12
N-46	Do.	Do.	Do.	14

\*Experiment N-15 is conducted with temporally constant values of the coriolis and centrifugal terms in the radial equation of motion.

U.S. DEPARTMENT OF COMMERCE  
National Oceanic and Atmospheric Administration  
Environmental Research Laboratories

NOAA Technical Memorandum ERL NHRL-96

THE RESPONSE OF A TROPICAL CYCLONE MODEL  
TO RADICAL CHANGES IN DATA FIELDS  
DURING THE MATURE STAGE

Stanley L. Rosenthal  
Michael S. Moss

National Hurricane Research Laboratory  
Coral Gables, Florida  
December 1971



## TABLE OF CONTENTS

	Page
1. INTRODUCTION	1
2. REVIEW OF THE MODEL	2
3. RESULTS AND DISCUSSION	6
4. SUMMARY	17
5. ACKNOWLEDGMENTS	17
REFERENCES	18

# THE RESPONSE OF A TROPICAL CYCLONE MODEL TO RADICAL CHANGES IN DATA FIELDS DURING THE MATURE STAGE

Stanley L. Rosenthal and Michael S. Moss

A long-range goal of the National Hurricane Research Laboratory is the development of numerical models capable of skillful prediction of the track and intensity of tropical storms. Initial data for such models will need to define the large-scale features of the tropical atmosphere. It will also be necessary to have data at several levels with about 10-km horizontal resolution in the core of the storm.

In this paper, the NHRL seven-level, circularly symmetric hurricane model is used in an attempt to define those meteorological variables that are basic and must be measured with such resolution and those that are secondary and could be diagnosed through application of a skillful numerical model. The validity of the results is dependent on the assumption that the existing model behaves in a manner at least qualitatively, similar to real hurricanes.

The computations are pertinent to short-range (24 hr) prediction of the intensity of mature storms and indicate that the tangential component of the wind as measured, or as estimated from the gradient wind equation, is basic. For forecasts in excess of 24 hrs, the computations tend to indicate that the humidity field is also basic.

## 1. INTRODUCTION

Despite substantial progress in the design of theoretical models of hurricanes, skillful numerical prediction for real hurricanes remains beyond the state of the art. A major deterrent to research on this problem is the lack of meteorological observations over the tropical oceans. Aside from the definition of the large-scale features of the atmosphere, the hurricane problem will require data at several levels with about 10-km horizontal resolution within the storm core.

In view of the costs involved in the development and production of systems to gather such data, it is of value to attempt to define those meteorological variables that are basic and must be measured and those that are secondary and could be diagnosed through application of skillful numerical models. Some insight may be obtained if one is willing to assume that the behavior of existing hurricane models is qualitatively similar to real hurricanes.



The computations reported here are pertinent to short-range prediction (24 hrs) of the intensity of mature storms. The numerical vehicle is the NHRL seven-level, circularly symmetric hurricane model (Rosenthal, 1970a, 1970b, 1971). After a model storm reaches the mature stage, drastic changes of temperature, humidity, tangential wind, radial wind, vertical motion, and pressure are introduced in various combinations, and the calculations are continued for another 24 hrs.

In experiments where the tangential wind component is retained (or estimated by means of the gradient wind equation), the altered data fields are restored to configurations reasonably close to the control well within the 24-hr period. If the purpose of the calculations is stated to be a skillful 24-hr prediction of maximum wind at sea level, these experiments can be considered highly successful. On the other hand, two experiments that contained zero guesses for the initial tangential wind were, by this definition, complete failures.

## 2. REVIEW OF THE MODEL

The equations that govern the model have been presented elsewhere (Rosenthal, 1970a, 1970b). Because certain mathematical aspects are important in the interpretation of the experiments discussed below, some equations are reproduced in this section.

The model storm is an isolated, stationary, circularly symmetric vortex. The vertical structure of the atmosphere is represented by seven levels, and geometric height is the vertical coordinate. The levels correspond to pressures of 1015, 900, 700, 500, 300, 200, and 100 mb in the mean-tropical atmosphere. All variables are defined at all levels. The primitive equations govern the horizontal motion. The hydrostatic assumption is employed.

The continuity equation is simplified in the following manner. The local rate of change of density is neglected and a climatological density (a function of height alone) is used to evaluate the vertical and horizontal mass flux terms. We then eliminate the external gravity wave by demanding that the vertical integral of the horizontal mass divergence vanish. This constraint forces the vertical integral of the radial equation of motion to become a diagnostic equation that defines the pressure field at sea level, given the wind and potential temperature as a function of height and radius, consequently, the model does not allow independent specification of the initial wind and pressure fields.

We may, therefore, write

$$\frac{\partial M}{\partial t} = -u \frac{\partial M}{\partial r} - w \frac{\partial M}{\partial z} - f r u + \frac{1}{\bar{\rho}} \frac{\partial}{\partial z} (\bar{\rho} K_z \frac{\partial M}{\partial z}) + \frac{K_H}{r} \frac{\partial}{\partial r} \left\{ r^3 \frac{\partial}{\partial r} \left( \frac{v}{r} \right) \right\}, \quad (1)$$

$$\begin{aligned} \frac{\partial u}{\partial t} = & -u \frac{\partial u}{\partial r} - w \frac{\partial u}{\partial z} + \frac{M}{r} \left( f + \frac{M}{r^2} \right) - \theta \frac{\partial \phi}{\partial r} + \frac{1}{\bar{\rho}} \frac{\partial}{\partial z} (\bar{\rho} K_z \frac{\partial u}{\partial z}) \\ & + \frac{K_H}{r^2} \frac{\partial}{\partial r} \left\{ r^3 \frac{\partial}{\partial r} \left( \frac{u}{r} \right) \right\}, \end{aligned} \quad (2)$$

$$\frac{\partial \phi}{\partial z} = - \frac{g}{\theta}, \quad (3)$$

$$\frac{\partial \bar{\rho} w}{\partial z} = - \frac{1}{r} \frac{\partial \bar{\rho} r u}{\partial r}, \quad (4)$$

$$\phi = c_p \left( \frac{p}{p_0} \right)^{R/c_p}, \quad (5)$$

$$\theta \phi = c_p T, \quad (6)$$

and

$$M = r v. \quad (7)$$

The symbols are defined as:

$r$	radius,
$z$	height,
$t$	time,
$M$	relative angular momentum,
$u$	radial velocity,
$v$	tangential velocity,
$w$	vertical velocity,
$f$	Coriolis parameter,
$\bar{\rho} = \bar{\rho}(z)$	density of a reference-tropical atmosphere,
$K_z$	kinematic coefficient of eddy viscosity for vertical mixing,

$K_H$	kinematic coefficient of eddy viscosity and conductivity for lateral mixing,
$\theta$	potential temperature,
$c_p$	specific heat capacity at constant pressure for dry air,
$g$	acceleration of gravity,
$p_0$	1000 mb,
$p$	pressure,
$T$	air temperature, and
$R$	specific gas constant for air.

To eliminate the external gravity wave, we take

$$\int_0^H \bar{\rho} u dz = 0, \quad (8)$$

where  $H$  is the height (16,621 m) of the highest information level of the model. From equations (2) and (8),

$$\begin{aligned} \int_0^H \bar{\rho} \theta \frac{\partial \phi}{\partial r} dz &= \int_0^H \bar{\rho} \left\{ \frac{M}{r} \left( f + \frac{M}{r^2} \right) - u \frac{\partial u}{\partial r} - w \frac{\partial u}{\partial z} \right\} dz \\ &+ \int_0^H \bar{\rho} \left\{ \frac{K_H}{r^2} \frac{\partial}{\partial r} \left[ r^3 \frac{\partial (u)}{\partial r} \right] + \frac{1}{\bar{\rho}} \frac{\partial}{\partial z} \left( \bar{\rho} K \frac{\partial u}{\partial z} \right) \right\} dz \equiv B. \end{aligned} \quad (9)$$

By use of the hydrostatic equation (3), we obtain

$$\int_0^H \bar{\rho} \theta \frac{\partial \phi}{\partial r} dz = \frac{\partial \phi_0}{\partial r} \int_0^H \bar{\rho} \theta dz - \int_0^H \bar{\rho} \theta \frac{\partial H}{\partial r} dz, \quad (10)$$

where

$$H = \int_0^z \frac{g}{\theta} dz'; \quad (11)$$

$z'$  is a dummy variable, and the subscript on  $\phi$  denotes a sea-level value.

From equations (9), (10), and (11) we see that

$$\frac{\partial \phi_0}{\partial r} = \frac{B + \int_0^H \bar{\rho} \theta \frac{\partial H}{\partial r} dz}{\int_0^H \bar{\rho} \theta dz}.$$

In the computational process,  $\phi_0$  is calculated by numerical integration of (12) over radius, given the boundary condition that the sea-level pressure at the outer limit of the computational domain is 1015 mb. The remaining values of  $\phi$  are then obtained through vertical integration of the hydrostatic equation (3).

The thermodynamic equation is written,

$$\frac{\partial \theta}{\partial t} = -u \frac{\partial \theta}{\partial r} - w \frac{\partial \theta}{\partial z} + \frac{c_p}{r} \frac{K_H}{\phi} \frac{\partial}{\partial r} \left( r \frac{\partial \theta}{\partial r} \right) + \frac{\dot{Q}}{\phi}, \quad (13)$$

where  $\dot{Q}$  is the diabatic heating per unit time and mass produced by latent heat of condensation.

Through a generalization of the procedure suggested by Kuo (1965), the model simulates convective precipitation (and the macroscale heating caused by this latent heat release) and the enrichment of the macroscale humidity caused by the presence of the cumuli. Convection may originate in any layer, provided that the layer has a water-vapor supply from horizontal convergence and that conditional instability exists for parcels lifted from the layer. Nonconvective precipitation is also simulated. Details are given by Rosenthal (1970a).

The prediction of specific humidity is fairly complex and will not be discussed here. Again, the reader concerned with details should consult Rosenthal (1970a).

Time derivatives are estimated by forward differences, except in the case of specific humidity where a Matsuno (1966) type integration is employed. Advective derivatives are calculated by the upstream method, except for the case of humidity where a conservation form of the equations is used. All nonadvective space derivatives are calculated as centered differences.

The drag coefficient is represented by Deacon's empirical relationship (Roll, 1965, p. 160) and is a linear function of surface wind speed. The sensible and latent heat fluxes at the sea surface are calculated by the bulk aerodynamic equations, and the surface drag is represented by the usual quadratic stress law. The exchange coefficients for sensible and latent heat are equal to the drag coefficient. The turbulent flux convergences that appear in the thermodynamic and water-vapor continuity



equations are evaluated through the assumption that the fluxes have a linear variation over height and are zero at and above the height of the 900-mb level. This is based on the assumption that at 900 mb and above, fluxes produced by small-scale turbulence are insignificant in comparison to those produced by cumulus-scale motions.

The sea temperature is an external parameter and is taken  $2^{\circ}\text{C}$  greater than the initial sea-level air temperature (the latter is initially horizontally uniform). Since the sea-level air temperature varies with time according to the thermodynamic equation, the air-sea temperature difference varies both with radius and time as the model hurricane evolves.

Radial resolution is 10 km, and the time step is 2 minutes. A lateral mixing coefficient of  $2.5 \times 10^3 \text{ m}^2 \text{ sec}^{-1}$  is used for all prognostic variables.

In the experiments discussed here, the radial limit of the computational domain is 440 km. The system is open at the lateral boundary. The lateral boundary conditions require the relative vorticity and horizontal divergence to vanish. In addition, the radial derivatives of potential temperature and specific humidity are also required to vanish.

### 3. RESULTS AND DISCUSSION

The control experiment (denoted by S-35) has been discussed in previous publications (Rosenthal, 1971; Rosenthal and Moss, 1971); a history of its intensity is shown by figure 1. Table 1 provides a list of the new experiments and describes their essential characteristics. These calculations begin at 288 hrs of S-35 and continue for 24 hrs.

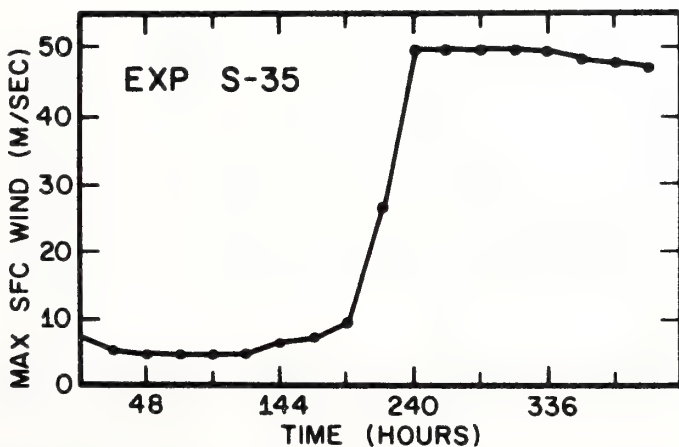


Figure 1. Summary of the control experiment (S-35). Maximum wind at sea level as a function of time.

Table 1. List of Experiments and Changes in Data Fields.\*

Exp No.	Tan Wind	Radial Wind	Vert Motion	Potential Temperature	Relative Humidity	Dependent variables retained from control
1	set to zero	set to zero	set to zero	none	set to mean tropical	$\theta$
2	none	Do.	Do.	Do.	Do.	$\theta, v$
3	gradient wind	Do.	Do.	Do.	Do.	$\theta, \phi$
3A	Do.	Do.	Do.	Do.	none	$\theta, \phi, q^1$
4	none	none	none	Do.	set to mean tropical	$\theta, \phi, v, u, w$
5	set to zero	Do.	Do.	Do.	none	$u, w, \theta, q$
6	none	set to zero	set to zero	set to mean tropical	set to mean tropical	$v$

<sup>1</sup>The symbol "q" is the specific humidity.

\*Introduced at 288 hr of the control experiment. The last column of the table lists those dependent variables that at 288 hr are same as in the control. Symbols are defined in section 2 of the text.

Experiments 1 and 5, where the tangential winds were initially zero, were unable to generate tangential winds greater than a few  $\text{m sec}^{-1}$ . In both cases, the characteristic-thermal structure of the hurricane was destroyed during the first few hours of calculation. The remaining experiments provided model storms that adjusted fairly rapidly to configurations reasonably close to the control. This is partially illustrated by figure 2, where the maximum winds at sea level are shown for experiments 2, 3, 3A, 4, and 6.

Interpretation of experiments 1, 5, and 6 in terms of a classical wind-pressure adjustment problem is probably not valid. The drag coefficient and the analogous coefficients that control the air-sea exchanges of latent and sensible heat are represented by a linear function of wind speed at sea level (Rosenthal, 1971). In the core of the storm, the coefficients for experiments 1 and 5 are initially less than

## MAXIMUM SEA - LEVEL WIND

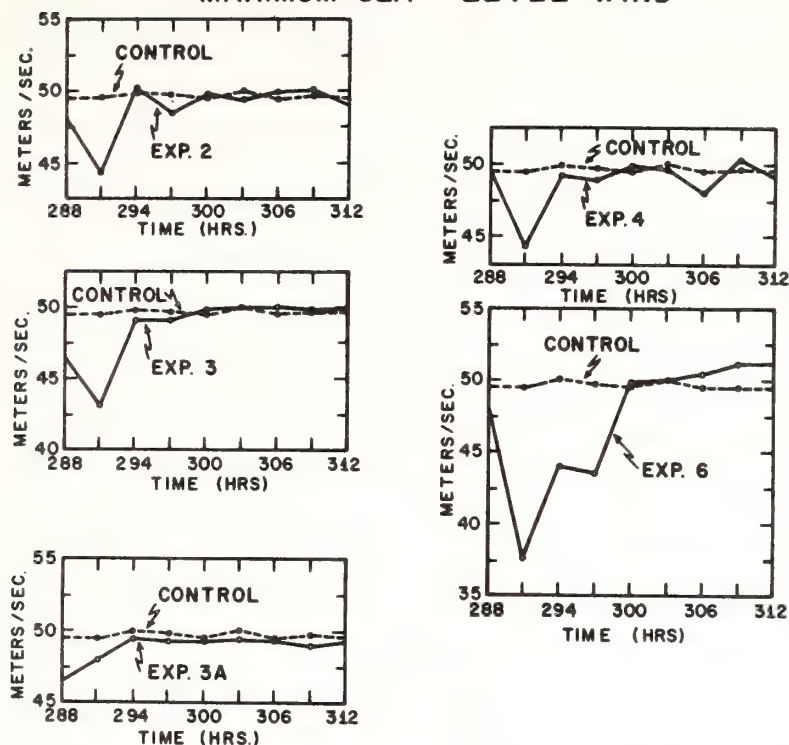


Figure 2. Comparisons of maximum wind at sea level for experiments 2, 3, 3A, 4 and 6 with the control experiment (S-35).

50 percent of the values found for the control experiment. Surface drag, evaporation, and air-sea exchange of sensible heat consequently are all much smaller at 288 hrs than in either the control or the other experiments listed by table 1. Previous experiments with physical explanations of these results (Rosenthal, 1971) have shown that reductions of this magnitude in these exchange processes during the mature state of the model storm lead to rapid decay.

The initial-pressure fields for experiments 1 and 5 are also strongly modified when the tangential wind is set to zero. The vertical shear of the pressure gradient ( $\frac{\partial}{\partial z} \frac{\partial \phi}{\partial r}$ ) is unaltered, since the field of  $\theta$  is retained; see (3). The term B (defined by equation (9)) that appears in the numerator of equation (12) is initially zero for experiment 1 and is extremely small for experiment 5. Consequently, the overall pressure drop (at sea level) between the storm periphery and the storm center is initially less than two thirds of that for the control.

In experiment 1, despite the reduced pressure-gradient force at low levels, the absence of centrifugal and coriolis effects allows a deep (extending upward to 500 mb) inflow layer to develop very rapidly and to penetrate the vortex center. At the center, vertical motions of  $3 \text{ m sec}^{-1}$

are present after only one time step, and the attendant adiabatic cooling produces temperature drops of up to 6°C. The characteristic thermal structure of the hurricane is completely destroyed within 3 hrs.

In experiment 5, where the transverse circulation of the control is retained, the strongest radial winds are accelerated during the first few time steps despite the reduction of pressure gradient force. This, again, is a reflection of the absence of centrifugal and coriolis forces. In a fashion similar to experiment 1, the inflow layer becomes quite deep, and inflow reaches the storm center. After the first-time step,  $7 \text{ m sec}^{-1}$  vertical motions are present at the storm center. The decay of the thermal pattern is similar to that of experiment 1.

The development of deep inflow layers in these two experiments is in contrast to the shallow inflow layer associated with the control storm (see Rosenthal and Moss, 1971) and is also attributable to centrifugal and coriolis effects. In the control, the strong tangential winds provide a rotationally stable system in such a way that inflow with approximate conservation of absolute angular momentum is not possible. Consequently, strong inflow occurs only near the ocean surface where frictional loss of angular momentum is large. In experiments 1 and 5, however, the absence of this rotational stability allows inflow without significant friction and thus allows the development of deeper inflow layers.

Since, in experiment 5, the transverse circulation of the control was retained in the initial conditions, it is of interest to inquire why inward transport of absolute angular momentum did not restore the tangential wind field quickly enough to prevent the destruction of the system by the mechanisms described in the previous paragraphs. The local effect produced by inward transport of absolute angular momentum, in the absence of a tangential wind, is, from equation (1),

$$\frac{\partial v}{\partial t} = -fu. \quad (14)$$

The time scale ( $\tau_1$ ) to produce  $v \approx 50 \text{ m sec}^{-1}$  with  $u \approx 20 \text{ m sec}^{-1}$  and  $f = 5 \times 10^{-5} \text{ sec}^{-1}$  is then

$$\tau_1 \sim \frac{50 \text{ m sec}^{-1}}{5 \times 10^{-5} \text{ sec}^{-1} \times 20 \text{ m sec}^{-1}} = 5 \times 10^4 \text{ sec} \sim 10 \text{ hrs.} \quad (15)$$

As we have already seen, the storm's thermal structure was destroyed within 3 hrs, and, in turn, the pressure field required to sustain the transverse circulation was destroyed in a period of time substantially smaller than  $\tau_1$ .



Experiments 3 and 3A discard the transverse circulation of the control and estimate the initial-tangential wind from a gradient balance. The potential temperature of the control storm is retained. Examination of equations (2), (9), (12), and (3) reveals that the pressure field at the initial instant (288 hr) is identical to that of the control. Indeed, these two experiments are the only ones of the group listed by table 1 that initially have the same pressure field as the control.

In both of these experiments, inflow velocities of about  $2 \text{ m sec}^{-1}$  develop in the boundary layer after only two time steps (4 min), and these inflow components exceed  $18 \text{ m sec}^{-1}$  after 3 hr of calculation. The transverse circulation is able to develop so rapidly because of the efficiency of surface drag in reducing boundary-layer winds to subgradient values. The calculations presented in the next few paragraphs verify this.

A typical hurricane produced by our model shows the pressure-gradient force in the boundary layer to be 10 to 15 percent stronger than the sum of the centrifugal and coriolis forces (Rosenthal, 1969). Near the wind maximum (20-km radius), a  $50 \text{ m sec}^{-1}$  gradient wind would have to be reduced by  $\Delta v \approx -2.5 \text{ m sec}^{-1}$  to provide a 10-percent imbalance of the type cited above. Now, the response of the boundary layer tangential wind to surface drag may be approximated by

$$\frac{\partial v}{\partial t} \approx - \frac{C |\vec{V}| v}{\Delta z} \quad (16)$$

where  $C$  is the drag coefficient and  $\Delta z \approx 1000 \text{ m}$ . The time scale ( $\tau_2$ ) for surface drag to provide  $\Delta v = -2.5 \text{ m sec}^{-1}$  is

$$\tau_2 \sim \frac{|\Delta v| \Delta z}{C |\vec{V}| v} \quad (17)$$

With  $C = 3 \times 10^{-3}$  and  $|\vec{V}| = v = 50 \text{ m sec}^{-1}$ ,

$$\tau_2 \sim 300 \text{ sec}; \quad (18)$$

hence, a 10-percent imbalance can be produced in two to three time steps.

Next, we seek the time scale ( $\tau_4$ ) required to produce  $u \approx -20 \text{ m sec}^{-1}$  at  $r = 20 \text{ km}$  provided that a 10-percent imbalance exists between pressure

gradient forces and the sum of centrifugal and coriolis forces. Since at this radius with  $v \approx 50 \text{ m sec}^{-1}$ , the coriolis term is negligible,

$$\frac{\partial u}{\partial t} \approx -\frac{1}{10} \left( \frac{v^2}{r} \right) . \quad (19)$$

Then,

$$\tau_4 \sim \frac{10 |\Delta u| r}{v^2} \approx 1000 - 2000 \text{ sec.} \quad (20)$$

Finally, we will show that  $\tau_4$  is small compared to the time scale ( $\tau_3$ ) for complete destruction of the  $v$ -field by surface drag. From (16),

$$\tau_3 \sim \frac{v \Delta z}{C |\vec{V}| v} . \quad (21)$$

With  $v = |\vec{V}| = 50 \text{ m sec}^{-1}$  and the same values for  $C$  and  $\Delta z$  as those used above,

$$\tau_3 \sim 6000 - 7000 \text{ sec.} \quad (22)$$

These calculations not only explain the rapid development of transverse circulation but, also, by comparison of  $\tau_4$  and  $\tau_1$  provide further understanding of the success of experiments 3 and 3A and failure of experiments 1 and 5.

The decrease in maximum wind (fig. 2) observed during the first 3 hr of experiments 2, 3, 4, and 6 is attributable not only to the elimination of the transverse circulation but also to the drier atmosphere that results from setting the initial relative humidity to values appropriate to the mean tropical atmosphere. This may be verified by comparison of experiment 4 with the control and by comparison of experiments 3 and 3A.

Figure 2 also shows that of the five successful experiments, experiment 6 (where the least initial information was retained) required the longest time to return to a state close to that of the control.

The root-mean-square-differences (RMSD) between the tangential and radial wind components of experiments 2, 3, 3A, 4, and 6 and those of the control are shown by figures 3, 4, 5, 6, and 7. These are calculated over the entire computational domain and are presented as functions of time.

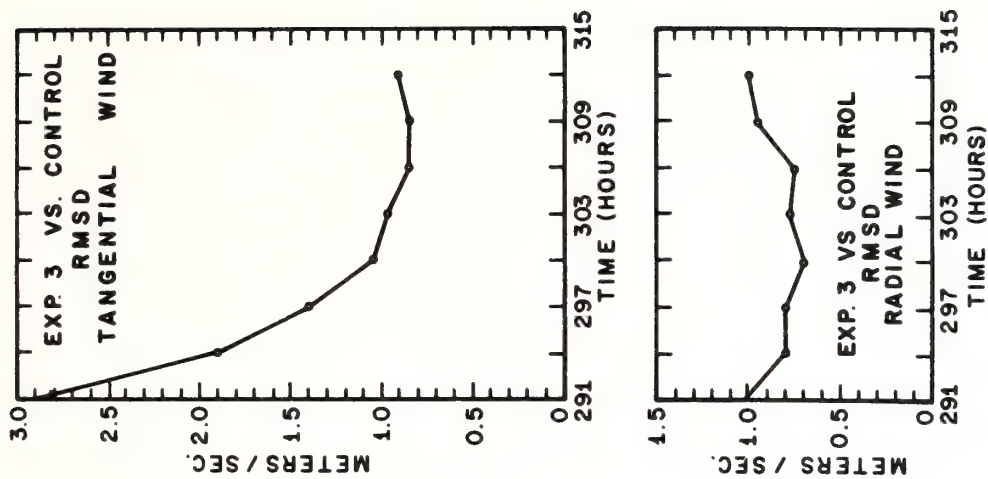


Figure 4. Same as figure 3 but for experiment 3.

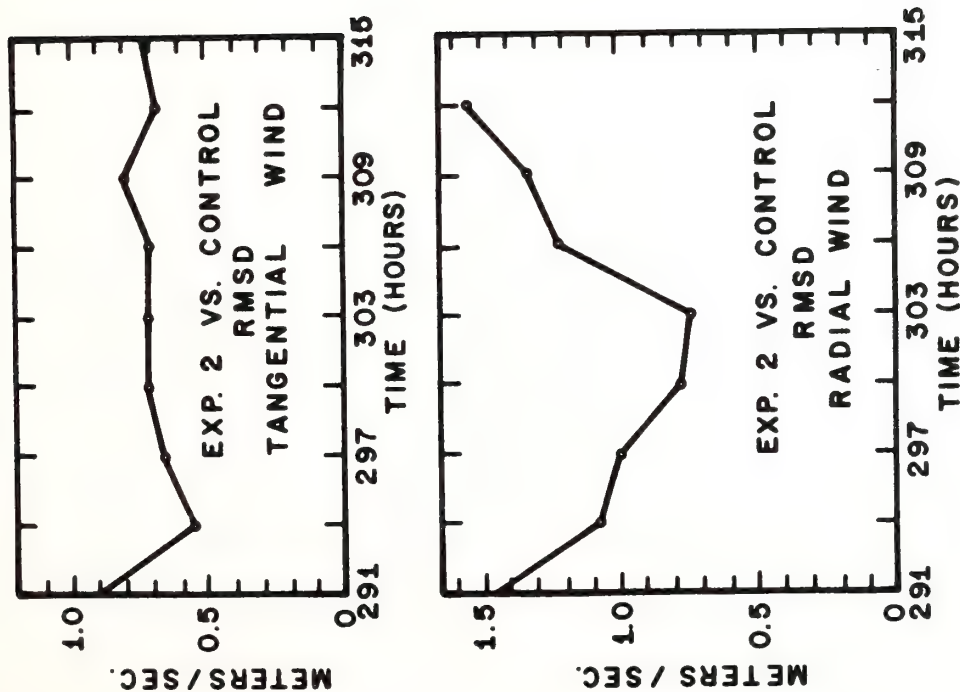


Figure 3. Root-mean-square-difference-between the tangential and radial wind components of experiment 2 and those of the control experiment (S-35).

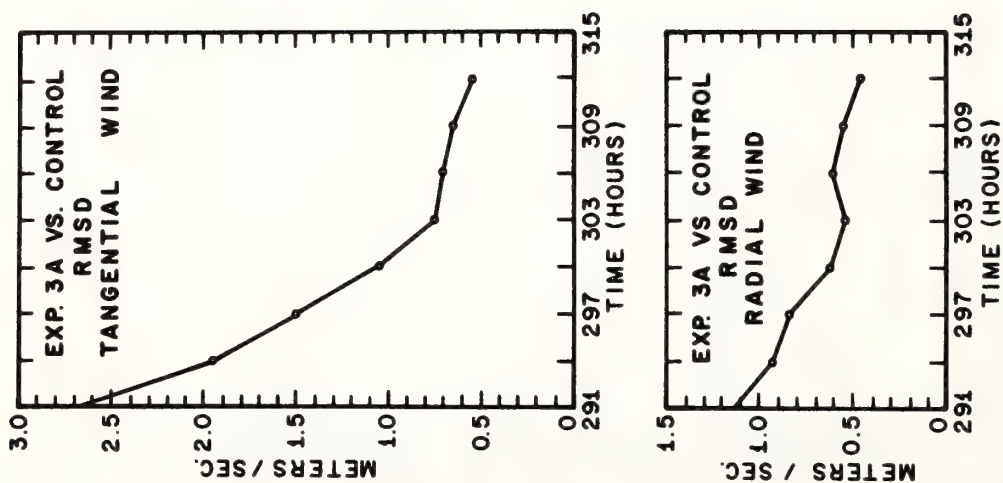


Figure 5. Same as figure 3 but for experiment 3A.

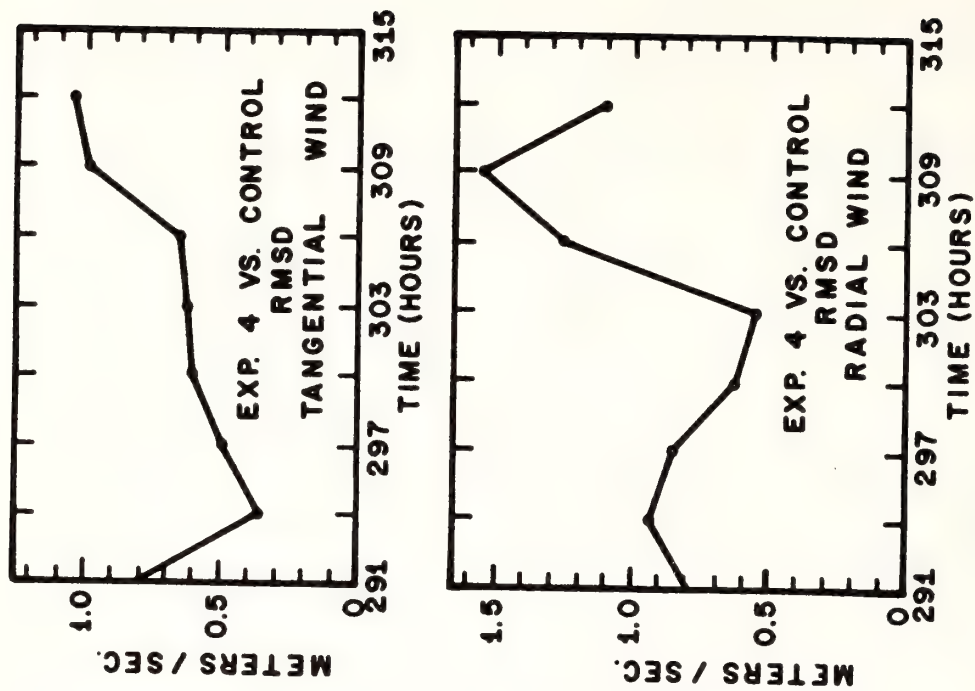


Figure 6. Same as figure 3 but for experiment 4.



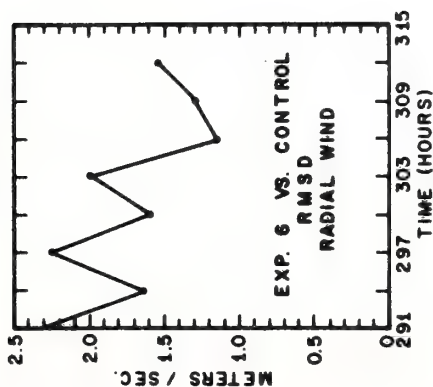
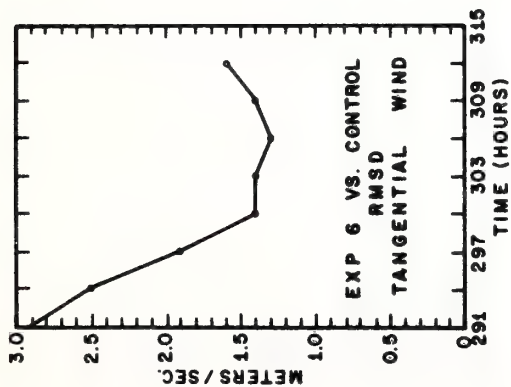


Figure 7. Same as figure 3 but for experiment 6.

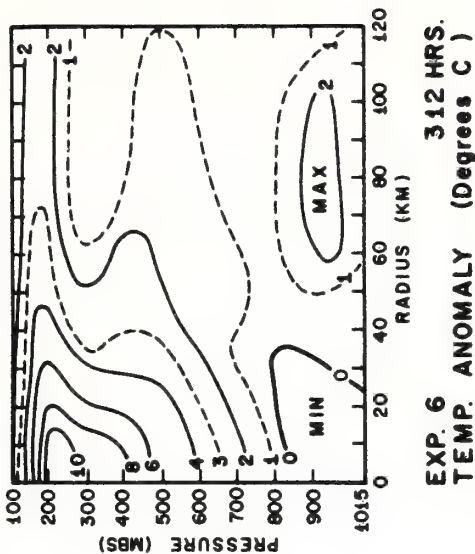
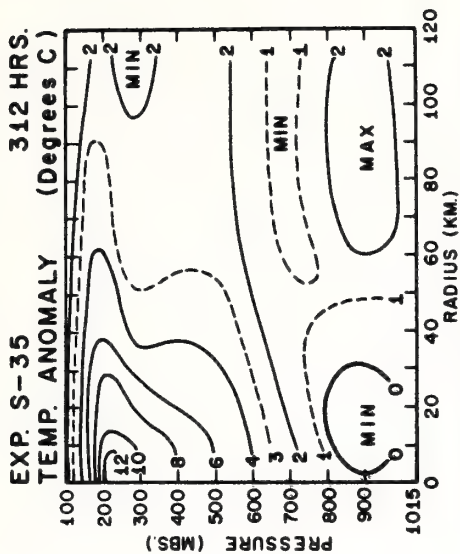


Figure 8. Cross section of temperature departures from the mean-tropical atmosphere at 312 hrs for experiment S-35 (top) and experiment 6 (bottom).

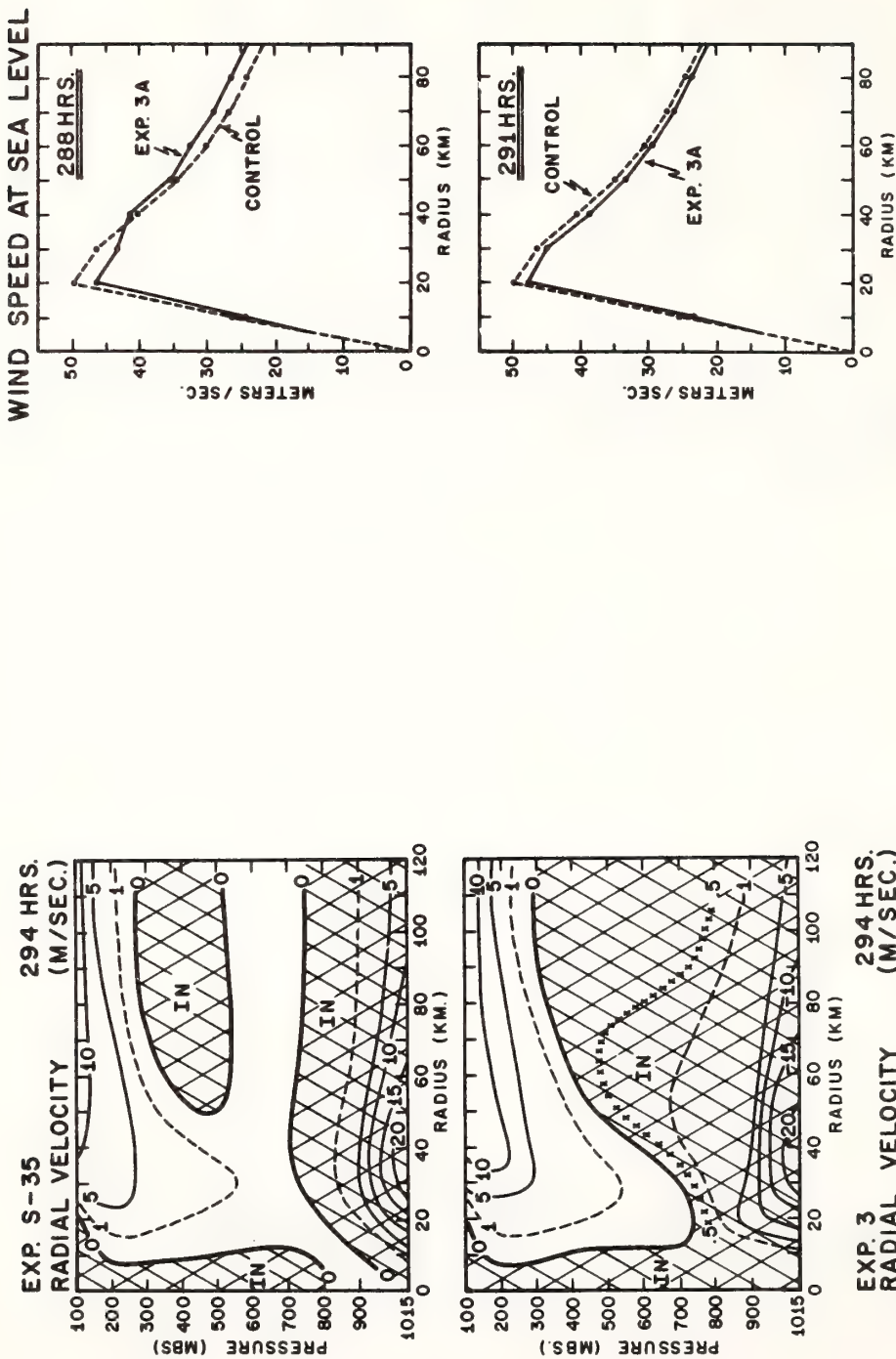


Figure 9. Cross section of radial component of wind at 294 hrs for experiment S-35 (top) and experiment 3 (bottom).

Figure 10. Radial profiles of total wind speed at sea level for 288 hrs (top) and 291 hrs (bottom). Dashed profile is the control experiment (S-35). Solid profile is for experiment 3A.

While figure 2 presents, perhaps, an overly optimistic picture of the results, the RMSD appear to give an overly pessimistic view. This is particularly true with regard to experiments 2, 4, and 6, where the structural features are fairly similar to those of the control even at 312 hr.

On the other hand, the RMSD indicate that longer term integrations with experiments 2, 4, and 6 probably would have shown substantial departures from the control. It should be noted that experiment 3A shows the smallest RMSD at 312 hr and is the only calculation where RMSD are still decreasing at the end of the experiment.

Figure 8 compares the thermal structure of the control with that of experiment 6 at 312 hr. As pointed out earlier, of the five successful experiments, experiment 6 provides the poorest results. Also, as indicated by figures 2 and 7, 312 hr is well after the closest approach of experiment 6 to the control. In view of these circumstances and because experiment 6 was initialized with the thermal structure of the mean tropical atmosphere, the resemblance of the two patterns shown by figure 8 is rather remarkable.

The radial velocities from experiment 3 and the control at 294 hr are compared in figure 9. Since experiment 3 was initialized with a zero transverse circulation at 288 hr, the resemblance to the control at 294 hr is also quite impressive.

Figure 10 shows the sea-level wind profile for experiment 3A and the control at 288 and 291 hr. At 294 hr (not shown), these profiles cannot be distinguished from each other on the scale used to plot figure 10. At 288 hr, the winds for 3A exceed those of the control at the larger radii. This is a reflection of the subgradient status of the boundary-layer tangential winds in the control. Near the wind maximum, the control winds exceed those of experiment 3A. This is caused by the contribution of relatively large radial wind components to the total wind. Had the tangential wind been plotted rather than the total wind, experiment 3A would have shown larger winds at all radii at 288 hr.

#### 4. SUMMARY

We do not plan to draw any firm conclusions from this limited set of experiments. Aside from the highly idealized nature of the model, the fact that all computations utilize the same control and that the latter was, for all practical purposes, in a steady state during the experimental period precludes such conclusions.

It does, however, appear that the tangential component of the wind, either as observed or as estimated from the pressure field, must be known from observations for skillful short-range prediction of hurricane intensity. While the gradient wind seemed to provide a better initial condition than the actual tangential wind in these computations, we are certainly not sure that such would even be the case with another model much less than with the real atmosphere.

Accurate determination of the field of specific humidity is indicated to be of importance for very short range forecasts (3 to 6 hr) and for longer range forecasts (in excess of 24 hr). This is indicated by comparisons between experiment 4 and the control and by comparison of experiments 3 and 3A.

#### 5. ACKNOWLEDGMENTS

Computations were performed at the NOAA CDC 6600 complex, Suitland, Maryland. Access to the computer facility is via a remote terminal located at NHRL, Miami, Florida. Mr. Billy M. Lewis was responsible for the computer liaison between Miami and Suitland.



## REFERENCES

- Kuo, H. L. (1965), On formation and intensification of tropical cyclones through latent heat release by cumulus convection, Jour. Atmospheric Sciences, 22, No. 1, 40-63.
- Matsuno, T. (1966), Numerical integrations of the primitive equations by a simulated backward difference method, Jour. Meteorol. Soc. Japan, Ser. 2, 44, 76-84.
- Roll, H. U. (1965), Physics of the Marine Atmosphere, Academic Press, New York & London, 426 pp.
- Rosenthal, S. L. (1969), Numerical experiments with a multilevel primitive model designed to simulate the development of tropical cyclones: Experiment I, ESSA Tech. Memo., ERLTM-NHRL 82, U. S. Department of Commerce, National Hurricane Research Laboratory, Miami, Florida, 36 pp.
- Rosenthal, S. L. (1970a), A survey of experimental results obtained from a numerical model designed to simulate tropical cyclone development, ESSA Tech. Memo., ERLTM-NHRL 88, U. S. Department of Commerce, National Hurricane Research Laboratory, Miami, Florida, 78 pp.
- Rosenthal, S. L. (1970b), A circularly symmetric primitive equation model of tropical cyclone development containing an explicit water vapor cycle, Monthly Weather Review, 98, No. 9, 643-663.
- Rosenthal, S. L. (1971), The response of a tropical cyclone model to variations in boundary layer parameters, initial conditions, lateral boundary conditions and domain size, Monthly Weather Review, 99, No. 10, 767-777.
- Rosenthal, S. L. and M. S. Moss (1971), Numerical experiments of relevance to Project STORMFURY, NOAA Tech. Memo., ERLTM-NHRL, U. S. Department of Commerce, National Hurricane Research Laboratory, Miami, Florida, 52 pp.

AEROSOL SAMPLING AND DATA ANALYSIS  
WITH THE NCAR COUNTER

by

William D. Scott  
Cloud Physicist  
National Hurricane Research Laboratory  
ESSA Adjunct Professor  
University of Miami



INTRODUCTION

In the latter part of 1968, B.F. Ryan and I found that the counts from the NCAR Counter increased markedly with the onset of rainfall (Ryan and Scott, 1969). The tentative explanation for this was that ice nuclei were concentrated near the rain envelope. It is possible that they were scavenged by the rainfall. Alternately, perhaps, the Bergeron precipitation mechanism was operating and we measured the particles responsible for the precipitation growth. The smaller raindrops presumably had evaporated and left the observed large concentration of particles.

In any case, it was desirable to continue the measurements and try to obtain an estimate of the number of ice nuclei in the raindrops. For this purpose, a differential sampling technique was devised. The raindrops were nebulized and evaporated; then the counts obtained from air containing the residual solid particles were compared with the counts from the air alone. Before long it was apparent that there was an increase in count due to the rainfall. But, surprisingly, this increase sometimes occurred without rainfall (see Scott et al., 1969).

An explanation for this effect is difficult but it was probably associated with the orientation of the sampling systems and the containment of the outside air in the drop dispersing chamber. It may indicate that ice nuclei are occasionally large particles or that their activity is altered while in a closed chamber.

My object in coming to the Workshop is to look in detail at the effects of the sampling system on the count from an NCAR Counter. In support of this objective, an electronic analyzing system has been developed to analyze the output of the acoustical sensor and gain a maximum of information from the counter. Of course, these data may add to our knowledge of ice nuclei.

In particular, I hope to answer these questions:

1) Are a substantial number of natural ice nuclei large particles? Are nuclei deactivated during sampling? If so, the Workshop participants measuring natural ice nuclei should take care in their sampling procedures and in applying their results to the natural aerosol.

2) Does a multiplication of ice crystals or a recycling of particles occur in the NCAR Counter?

It may be possible to answer these questions by close examination of the pulse height spectra and time lag spectra of the acoustical pulses.

#### SAMPLING

Samples of the natural aerosol in Fort Collins (designated "outside") will be taken directly from a vertical, 1½ inch aluminum tube 20 feet long which sticks approximately 12 feet above the roof of the Atmospheric Simulation Laboratory. As time permits, samples will be taken from the sampling duct (designated "duct").

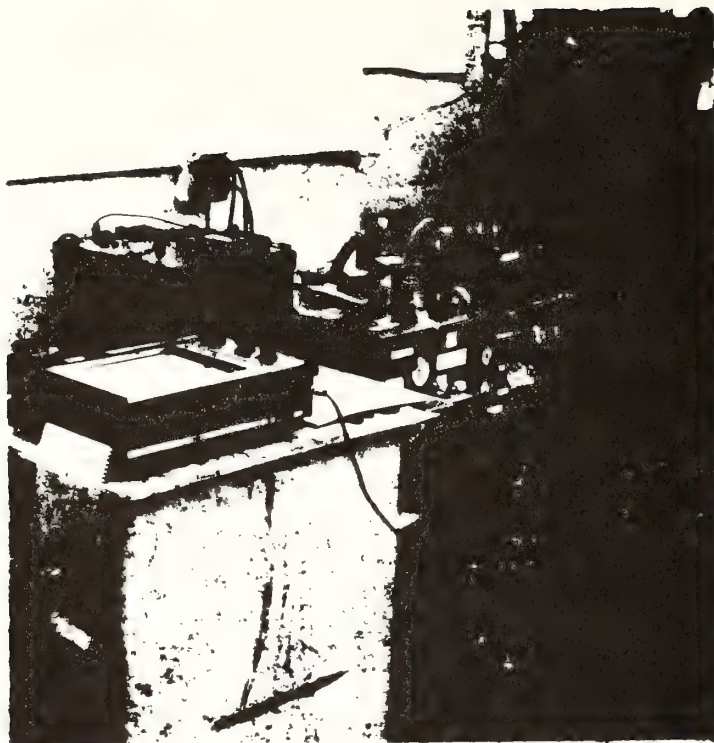


Fig. 1. Apparatus.

A photograph of the apparatus is shown in Fig. 1.

The entire sampling system is shown in Fig. 2. Both tubes enter directly into the top of the cold chamber of the NCAR Counter. The sampling rate is 10 l/min. Humid air with a salt aerosol is added to the sample air at a rate of 5 l/min. The air is humidified by bubbling in water at a temperature of approximately 86°F. Valves b, c, and d are pinch clamps; valve a is a sleeve and rubber cork. Alternately either a and b are opened (c and d are closed) or a and b are closed (c and d are opened).

#### ANALYZING THE ACOUSTICAL PULSES

The pulses are recorded individually on a strip chart recorder using a peak sample and hold amplifier. The schematic diagram of the amplifier is shown in Fig. 3. Figure 4 is a picture of the amplifier. It is contained entirely within a small aluminum box attached directly to a 110 V.A.C. power plug.



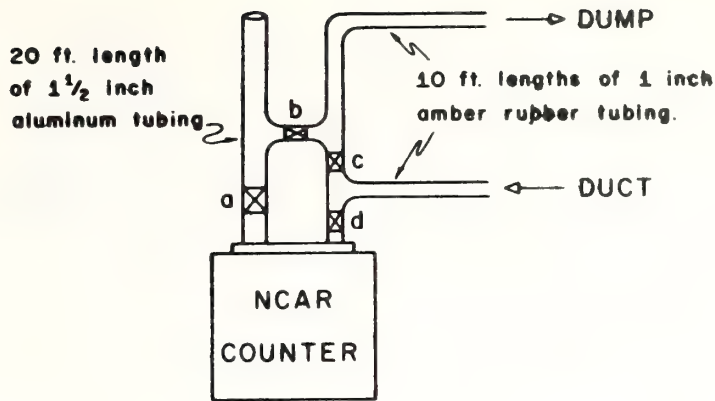


Fig. 2. Diagram of the sampling system.

The amplifier is tuned to a frequency of 2500 Hz and has a voltage gain of 250 at that frequency. The output of the microphone sensor on the NCAR Counter is a damped harmonic signal of approximately 2500 Hz. The final stage is coupled to a peak-sample-and-hold circuit that automatically holds pulses of amplitude greater than 0.5 volts. The circuit is designed so that high frequency electronic noise merely raises the voltage threshold and hence has a minimum effect on the recording of the pulses.

An example of the readout of the amplifier is shown in Fig. 5. Bunching of the pulses as shown creates errors and small signals are not recorded immediately following larger ones. Also, the circuit is not entirely linear. Nevertheless, for counts less than 10 per minute, the amplitudes of the pulses are reproduced to better than 20%.

#### TYPICAL RESULTS

The pulse heights and the times between pulses are measured, tallied and plotted as a function of their relative frequency of occurrence. Figures 6a and 6b show some results.

It is interesting that the histogram of Fig. 6a is bimodal. As a result, the average time between pulses is not the most frequent.

#### ACKNOWLEDGMENTS

Thanks are due to Gerhard Langer for his willing help and the loan of an NCAR Counter during the period of the Workshop.

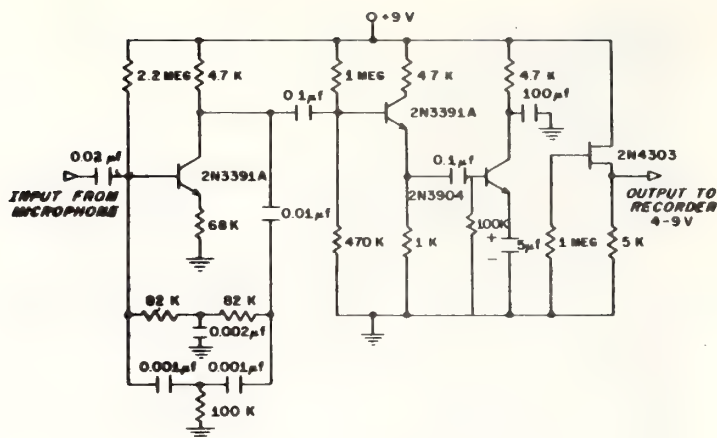


Fig. 3. Ice nuclei pulse holding amplifier. All resistors are 10%,  $\frac{1}{4}$  watt; capacitors 10%, except components in the twin "T" filter which are matched to 1%. Gain =  $250 \pm 20\%$  at the tuned frequency of 2500 Hz.



Fig. 4. Picture of the amplifier.

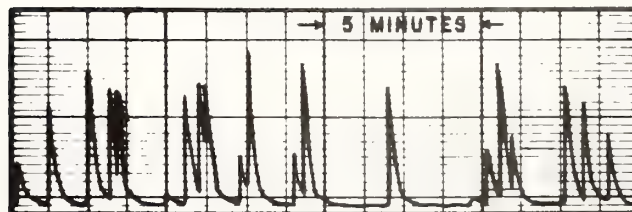
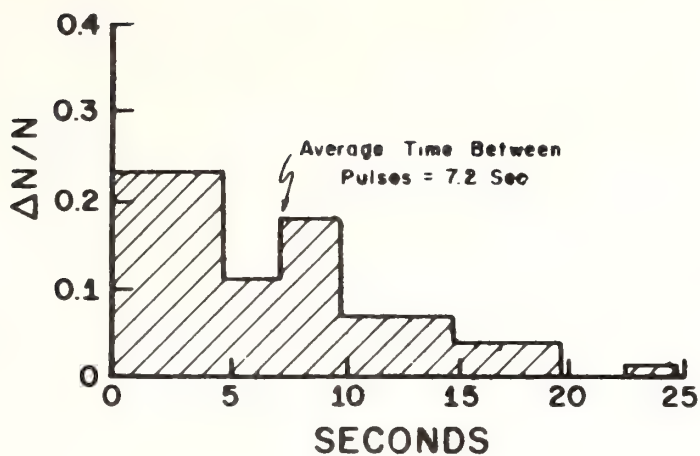
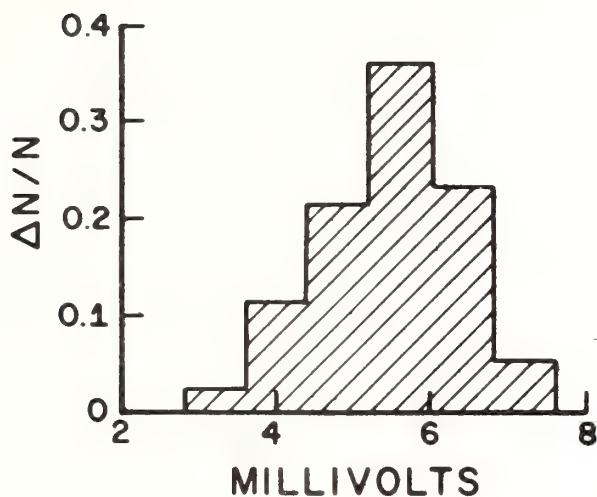


Fig. 5. Output pulses from the amplifier.



(a)



(b)

Fig. 6. Histograms of the time between pulses (a) and Pulse heights (b). August 10, 1970, 1653-1703 hrs., chamber at  $-20^{\circ}\text{C}$ ; natural aerosol at Ft. Collins.

#### REFERENCES

- Ryan, B.F., and W.D. Scott: 1969: Ice Nuclei and the Onset of Rainfall. *J. Atmos. Sci.*, 26, 611-612.
- Scott, W.D., J.D. Locatelli and J.H. Pinnons, 1969: Some Characteristics of the NCAR Counter. *Proceedings of the 7th International Conference on Condensation and Ice Nuclei*, Prague-Vienna.

## conference summary

### symposium on the measurements of cloud elements

William D. Scott

National Hurricane Research Laboratory,  
NOAA, Miami, Fla.

Robert M. Cunningham

Air Force Cambridge Research Laboratories,  
Bedford, Mass.

Robert G. Knollenberg

University of Chicago, Ill.

and William R. Cotton

Experimental ~~Research~~ Laboratory, NOAA,  
Meteorology Miami, Fla.

The Symposium on the Measurement of Cloud Elements was held 10-11 June at the Department of Geophysical Sciences, University of Chicago. Prof. Robert G. Knollenberg of the University of Chicago hosted the meeting, while Dr. William D. Scott of the National Hurricane Research Laboratory, NOAA, and the University of Miami, was the program chairman. The meeting was entirely informal and held with the objectives of improving our measurements of cloud elements and, perhaps, the planning of a workshop to accomplish this. Approximately 24 persons were in attendance.

The program started at 9:00 a.m. Thursday, 10 June, with a session "The need for measuring cloud elements" in which Dr. E. Danielsen of NCAR presented a paper "Simulated hail growth and radar observations in a cloud model." Following his paper, Dr. William R. Cotton of the Experimental Meteorology Laboratory, NOAA, and the University of Miami presented a paper "The need for broad spectrum, multiphase cloud particle samples for verification of numerical models."

The papers emphasized the need for close correspondence in time and space between measured quantities, the need for complete thermodynamic soundings in near time and space, as well as detailed case studies. Progress in our cloud measurement capability in the past 17 years has been minimal and is certainly limiting the development of improved cloud models. Of major importance at this time are instruments with appropriate sampling characteristics in the intermediate range, (50-250 $\mu$ ) in the raindrop sizes, and for measuring ice crystals.

The next session was entitled "Instruments in use,

their characteristics, reliability and faults." Prof. Roscoe R. Braham of the Department of Geophysical Sciences, University of Chicago, spoke on "A summary of particle measuring techniques at the University of Chicago." Then Robert E. Ruskin of the Naval Research Laboratory discussed "Our experiences in the measurements of cloud elements"; Don Takeuchi, Meteorology Research Inc., Altadena, Calif., "MRI experience in the measurement of cloud hydrometeors"; Dr. Robert M. Cunningham, AFCRL, Bedford, Mass., "CRL experience in airborne instrumentation."

It appears that all the instruments in current use have grave failings: one of the worst of these being the data reduction problem. Nevertheless, in our operational programs we would do well to accept them as they are and attempt to utilize the limited information that they supply. Assorted comparisons between instruments on different aircraft in flight, and aircraft in flight with ground-based instruments indicate that although such comparisons can be made, the small scale variability in the atmosphere puts a limit on such comparisons and requires that the measurements be made in near time and space.

The session lasted on into the afternoon of 10 June and was followed by a session "Instruments in development." In this session Dr. Thomas Kyle of NCAR spoke on "Extinction measurements of single particles"; Dr. Robert T. Ryan of A. D. Little, Inc., Cambridge, Mass., "Cloud microstructure as determined by an optical cloud particle spectrometer"; Dr. James E. Dye of NCAR, "Some in-cloud measurements with an electrostatic cloud droplet probe"; Joe Sutherland of Weather



Science, Inc., Norman, Okla., "An impact transducer method of measuring raindrop spectra"; Prof. Robert G. Knollenberg of the Department of Geophysical Sciences, University of Chicago, "The measurement of cloud and precipitation particles spectra using an optical array and extinction instrument." The session ended late (about 8:00 p.m.) with Prof. Knollenberg demonstrating his instruments.

At 9:00 a.m. Friday the session continued with Richard Nelson of SUNY at Albany, N. Y., speaking on "The design, construction, and testing of a raindrop recording dropsonde"; Prof. Warren Ketcham of the Meteorology Department, University of Utah, "Optical character recognition techniques for measuring cloud droplets"; Dr. James E. Dye spoke for Dr. Theodore Cannon of NCAR on "A camera for photographing airborne atmospheric particles"; Dr. William D. Scott of the NHRL, NOAA, and the University of Miami "The measurement of ice with the Mee Industries Ice Particle Counter"; Robert Ruskin of the Naval Research Laboratory spoke on "Use of a transmissometer in conjunction with measurements of liquid water to determine average drop size and number" and "Forward-to-back scattering ratios as a method of ice detection." Then Loren Nelson of AFCRL spoke on "Holographic distrometer for cloud particulates." Just after lunch Dave Culnan of the Bureau of Reclamation, Denver, spoke on "Remote sensing of cloud elements."

Instruments for the real time measurement of the sizes of cloud droplets are available, have undergone preliminary calibration, and are operational. Similar operational instruments are not yet available, however, for the measurement of either raindrops or ice crystals although prototype units are under development. Only one of these instruments (a device being tested by Dr. R. Cunningham) currently has the capability of gathering a large enough sample of raindrops to have resolution over a 100 m path. No instruments are presently available that gather a sufficient quantity of hydrometeors and at the same time have sufficient resolution in the intermediate range 50–250 $\mu$ . The limited ranges of both the older and newer aircraft instruments suggests that three instruments will probably be required to sample the entire cloud droplet-raindrop range. However, Prof. Knollenberg has developed a device for use on a Venus probe that is a combination of three instruments which may be capable of operation over a large portion of the entire range.

As instruments with real time measuring capabilities become operational, it will probably be necessary to have devices which have little or no operational capability to be used for the calibration of instruments as intermediate calibration standards. The current instrumentation may be able to operate partially in this capacity. It may be required, however, that all direct measurements of particles be relegated to the role of standardization and used to calibrate remote sensors which can accommodate the enormous sampling requirements.

After the discussion of the instruments being developed was a brief session to summarize our sampling and instrument needs in the various size ranges. The group then decided that there was both a sufficient need and a sufficient number of operational instruments to hold a minimal workshop to compare instruments for measuring cloud droplets with due consideration for the comments made by the members of the Cloud Physics Committee (read by Dr. R. Cunningham). A discussion of the support facilities followed by Dr. W. D. Scott representing E. Zelezny in a discussion of the possible use of the Army Natick Laboratories as a test facility. This was followed by a talk by Richard Smith of Eglin AFB entitled "The Climatic Laboratories' facilities test capabilities at Eglin AFB"; Howard A. Friedman of RFF, NOAA, Miami, "RFF airborne platform capabilities for cloud physics measurements"; Dr. R. Cunningham discussed "The pros and cons of using AFCRL's C-130 as a test platform"; Dr. Ulrich Katz of Cornell Aeronautical Laboratory, Inc., Choohtowago, N. Y., spoke on "The CAL environmental chamber." Following this, a list of available facilities for testing was prepared.

In closing, the group as a whole recommended:

- 1) A workshop to test three of the promising instruments for the measurement of cloud droplets be held, perhaps, early next year at Cornell Aeronautical Laboratory. The instruments and the test facilities should be extended to cover droplets of as large a size as possible. At least one instrument should be capable of airborne operation for future aircraft testing.
- 2) A plan for the testing of three of four instruments for operation on aircraft during the NOAA Experimental Meteorology Laboratory-Naval Research Laboratory Cloud Physics Program in May 1972, should be considered. This would include on-ground testing of the instruments on board the RFF DC-6 and the NRL/Environmental Chamber. Pods would be acquired and supplied to the scientists for installation of their instruments. The pods would then be shipped to Miami and fitted to the aircraft.
- 3) A program for high-speed testing of the instruments should be initiated in the near future. Perhaps testing at the Air Force Arnold Test Center will be possible. There is a real need at the present time for a facility capable of testing the instruments and, specifically, supplying the sample detail and aircraft effects appropriate to real in-cloud measurements.
- 4) Adequate comparisons of instruments for the measurement of raindrops and ice crystals cannot be made at present. There are too few instruments and they cannot be considered operational because of data handling problems.

The meeting adjourned at about 5:00 p.m., 11 June.

U. S. DEPARTMENT OF COMMERCE  
NATIONAL OCEANIC AND ATMOSPHERIC ADMINISTRATION  
NATIONAL WEATHER SERVICE

NOAA Technical Memorandum NWS SR 56\*

MEMORABLE HURRICANES OF THE UNITED STATES SINCE 1873

SOUTHERN REGION HEADQUARTERS  
SCIENTIFIC SERVICES DIVISION  
FORT WORTH, TEXAS  
April 1971

\* Revision of ESSA WBTM SR 42

## MEMORABLE HURRICANES OF THE UNITED STATES SINCE 1873

Arnold L. Sugg and Leonard G. Pardue  
National Hurricane Center  
National Weather Service, NOAA  
Miami, Florida

and

Robert L. Carrodus  
National Hurricane Research Laboratory  
Environmental Research Laboratories, NOAA  
Miami, Florida

Whether a hurricane is notable and should be remembered depends upon many things. The selections in this publication are limited to those which have made landfall in the United States or have been near misses. Also, most of them were major, extreme, or great hurricanes; these adjectives usually refer to intensity as determined by the maximum wind or the sea-level pressure within the eye. Some hurricanes were "Great" while at sea but reached land with considerably diminished intensity. Connie was classified as "Great" at sea but is classified here as "Major" because of its diminished intensity as it reached the coast. On the other hand, some which did not have particularly low pressures or high winds were devastating because of flooding. Most notable in this category was Diane 1955. For these reasons the criteria used to determine the memorable hurricanes of this century were not rigid and have been omitted here.

The data on each map should be considered extremes. Needless to say, some are subject to contradiction depending upon what source or reference one consults. For the most part, the data were drawn from the Monthly Weather Review articles; from the Publication "Hurricanes and Tropical Storms in the Gulf of Mexico," Weather Service Forecast Office, New Orleans; Atlantic Hurricanes by Dunn and Miller; and Hurricanes by Tannehill. Tracks through 1963 are from Weather Bureau Technical Paper No. 55, by Cry, and from Monthly Weather Review thereafter, but the varying intensities along the tracks have been omitted. Revision of the track and data of the hurricane of September 22-October 4, 1929, was made possible through a study by Mr. Pierce S. Rosenberg, Atlantic Underseas Test and Evaluation Center, West Palm Beach, Florida. Additional information on tides in the Great Atlantic Hurricane of 1944 was supplied by Mr. R. E. Lynde, Weather Service Forecast Office, Boston, Massachusetts, and Mr. George Moore, National Ocean Survey, Rockville, Maryland.

Table 1, listing the greatest United States hurricanes of all times, has been revised in this edition in accordance with figures supplied by NOAA's National Climatic Center. Dollar estimates have not been adjusted for inflation. It is also quite obvious that damage figures have increased and will continue to do so as the population and industry increase, especially along the coastal areas.

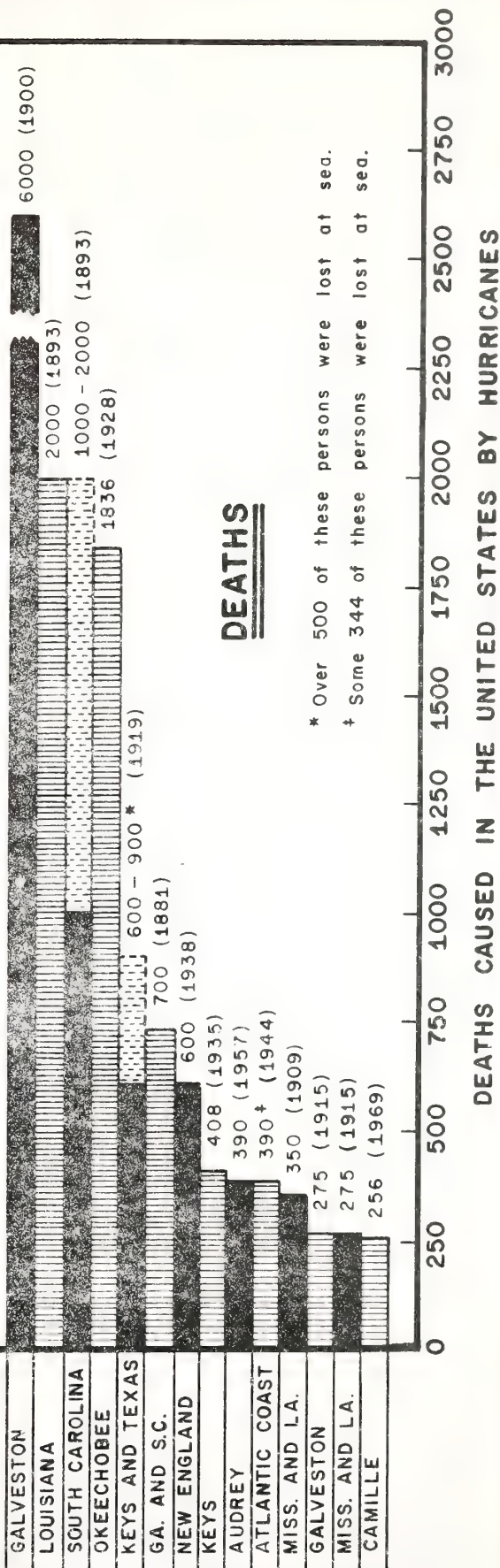
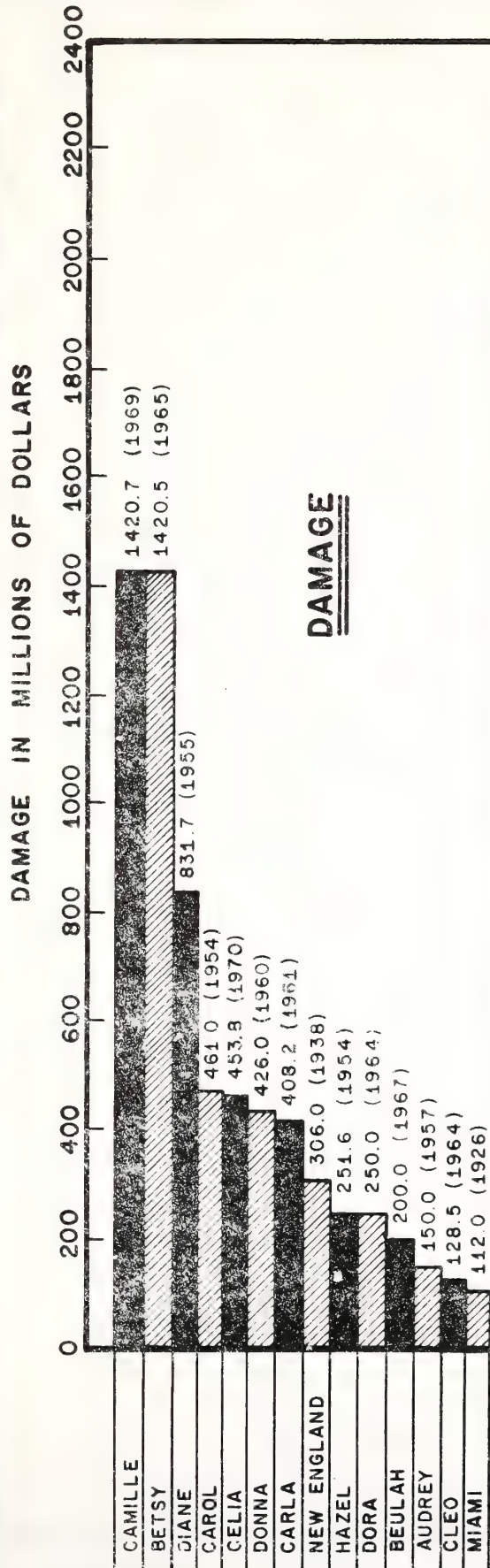
It is hoped that this paper will serve as a ready reference, as a climatological aid in forecasting, for speeches, and for preparedness conferences.

---

We are grateful to Mrs. Liliias Wilson, Miss Wendy Searle, and Ashby Andrews, National Hurricane Center, for the typing and clerical help, and to John Lundblad and Glenn Frye, University of Miami student trainees at the National Hurricane Research Laboratory, for assistance with drafting.



# EFFECTS OF MEMORABLE HURRICANES IN THE UNITED STATES



# AREAS AND YEARS WHERE MEMORABLE HURRICANES MADE LANDFALL; 1873 - 1970

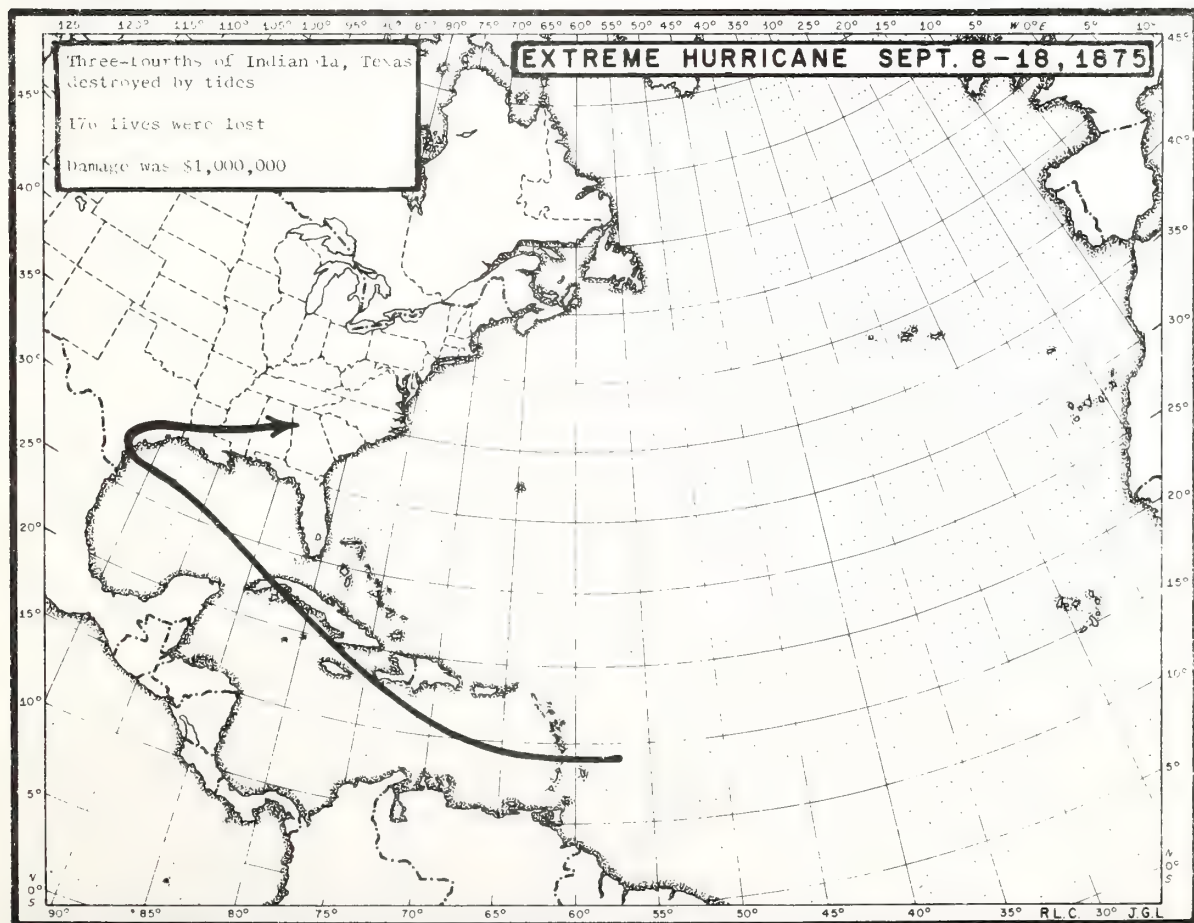
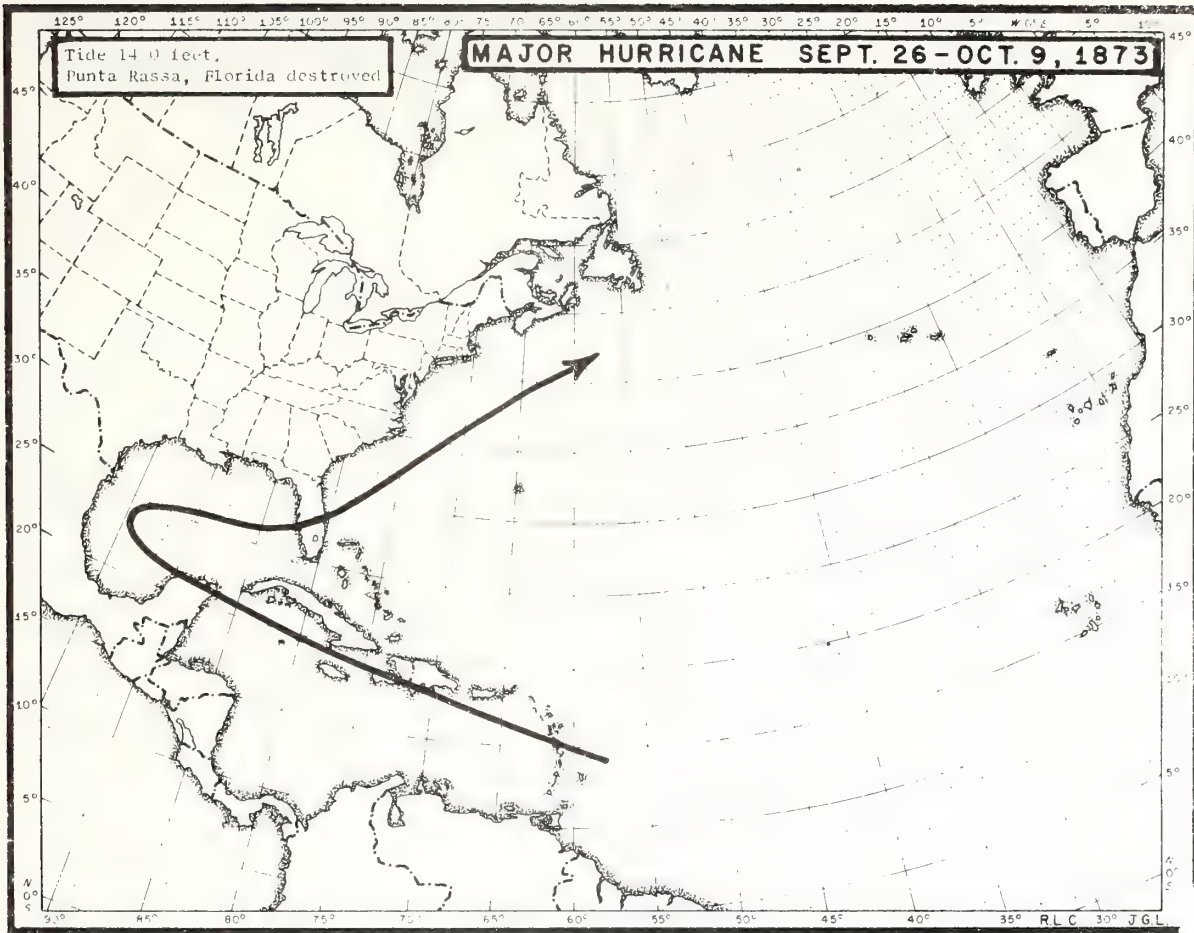
**I** - 1875, '77, '80, '86, '86, '93, 1900, '06, '09, '09, '15, '15, '16, '16, '18, '19, '26, '26, '32, '33, '40, '41, '42, '45, '47, '49, '56, '57, '61, '64, '65, '67, '69, '70

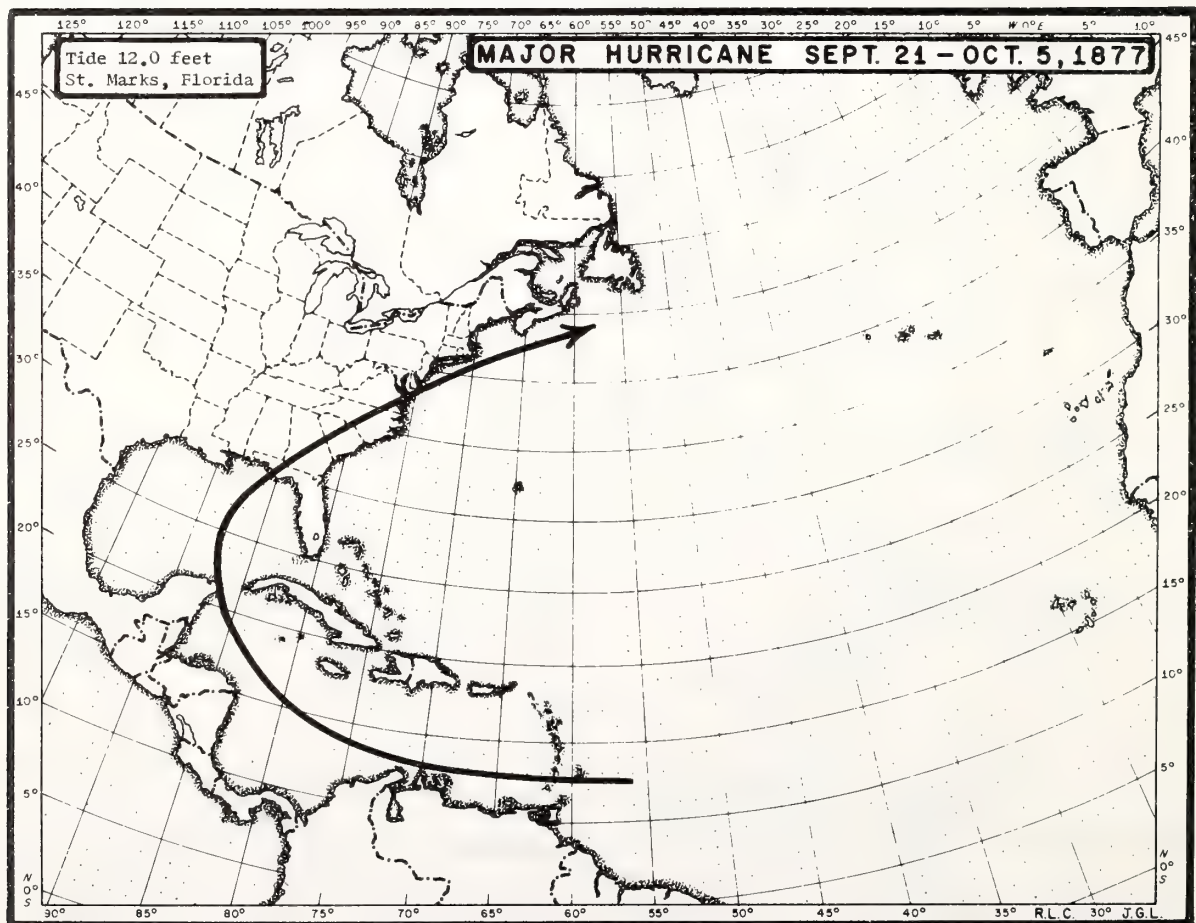
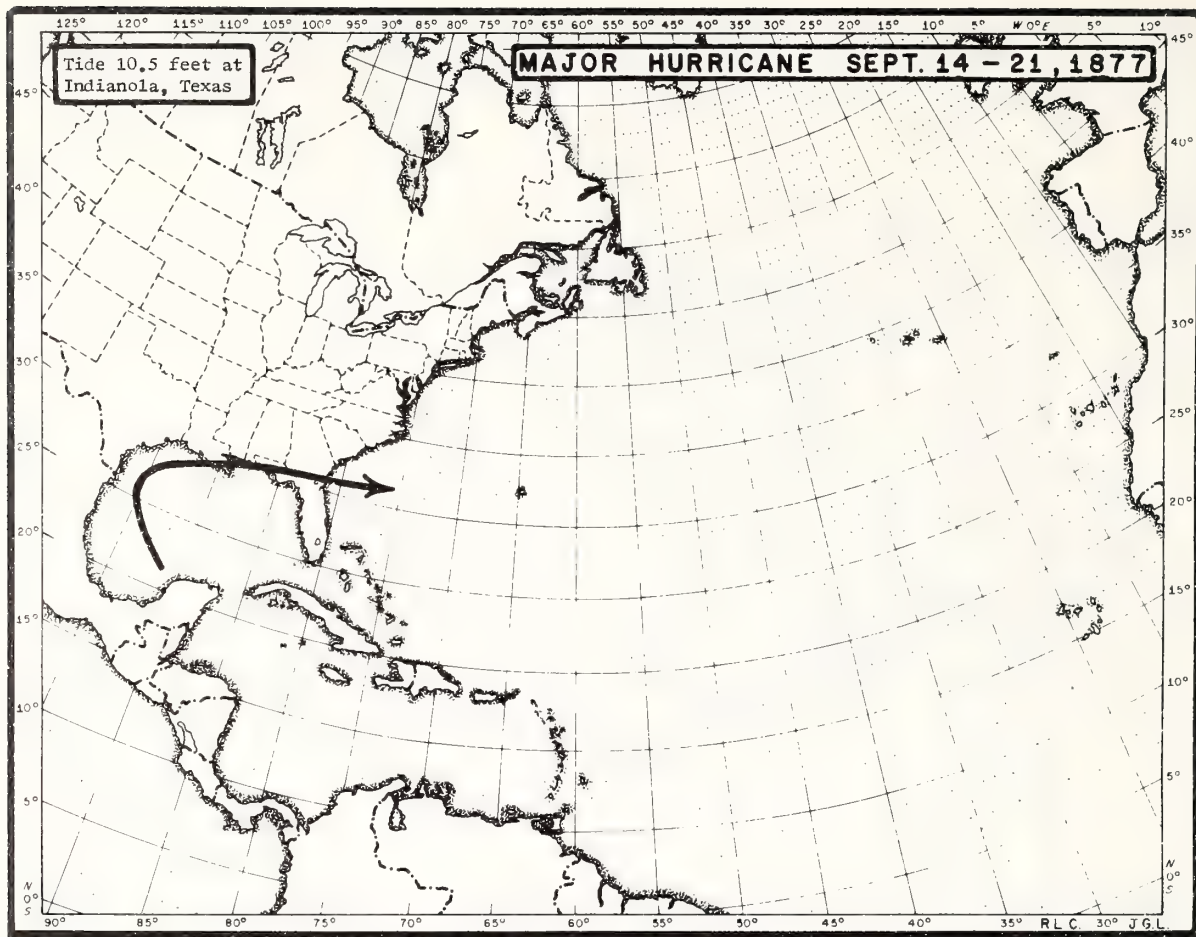
**II** - 1873, '77, '77, '78, '80, '81, '82, '85, '86, '86, '93, '93, '93, '94, '96, '96, '98, '99, '99, 1906, '06, '06, '09, '10, '11, '16, '17, '19, '21, '26, '28, '29, '29, '33, '33, '35, '35, '40, '40, '41, '41, '44, '45, '46, '47, '47, '47, '48, '48, '49, '50, '50, '56, '59, '60, '64, '64, '65, '66, '66

**III** - 1878, '79, '82, '82, '83, '99, 1910, '33, '33, '36, '44, '44, '49, '54, '54, '54, '55, '55, '55, '58, '60, '66

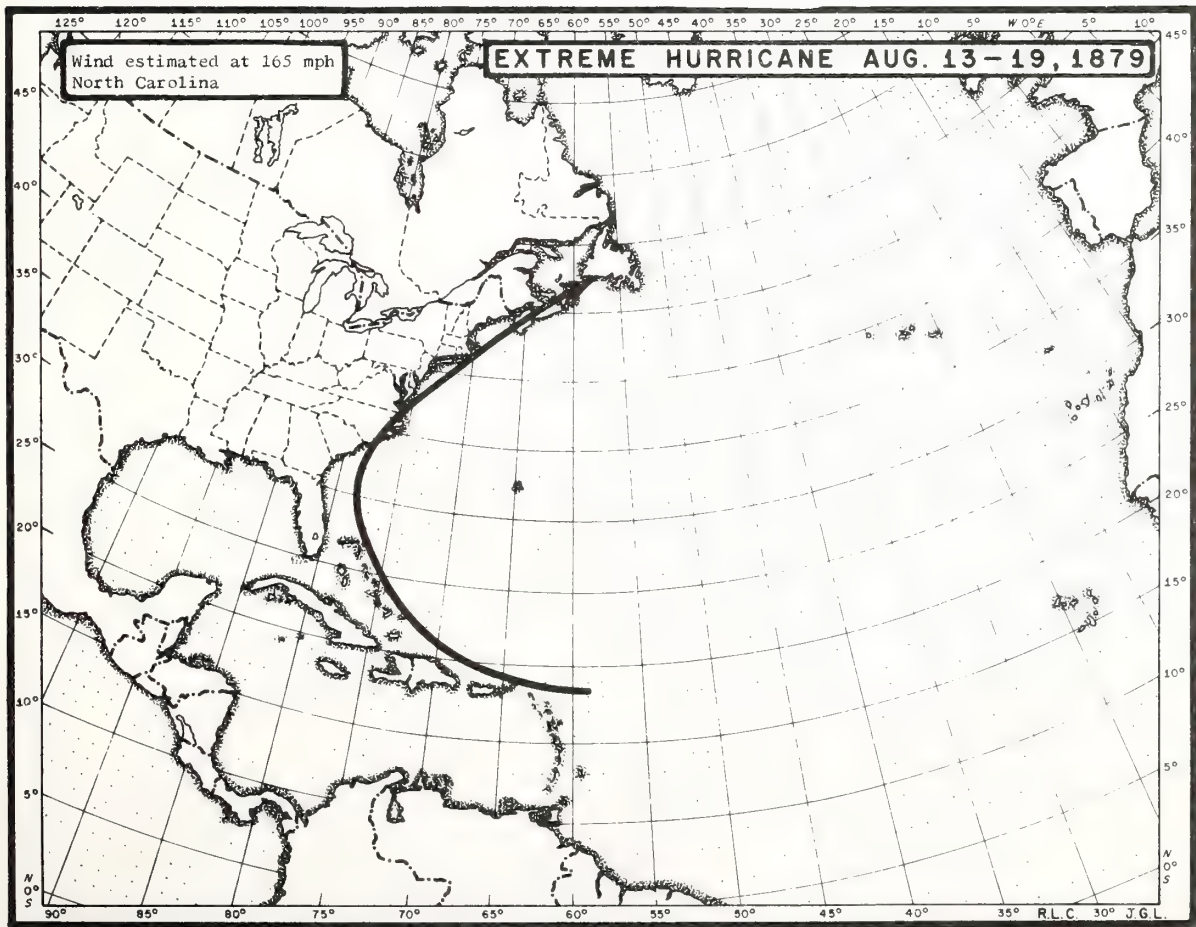
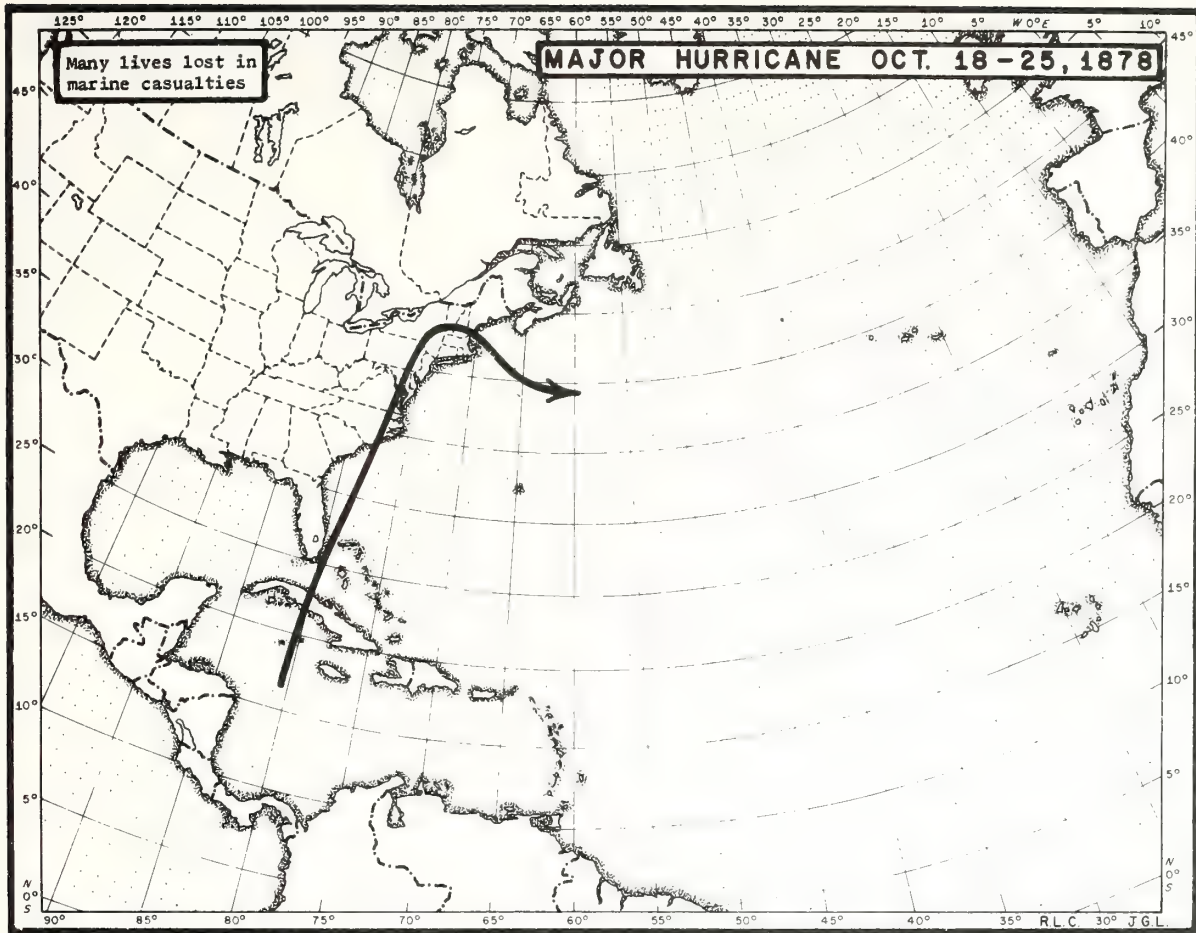
**IV** - 1877, '79, '82, 1933, '36, '38, '44, '44, '45, '54, '54, '55, '59, '60, '64, '66

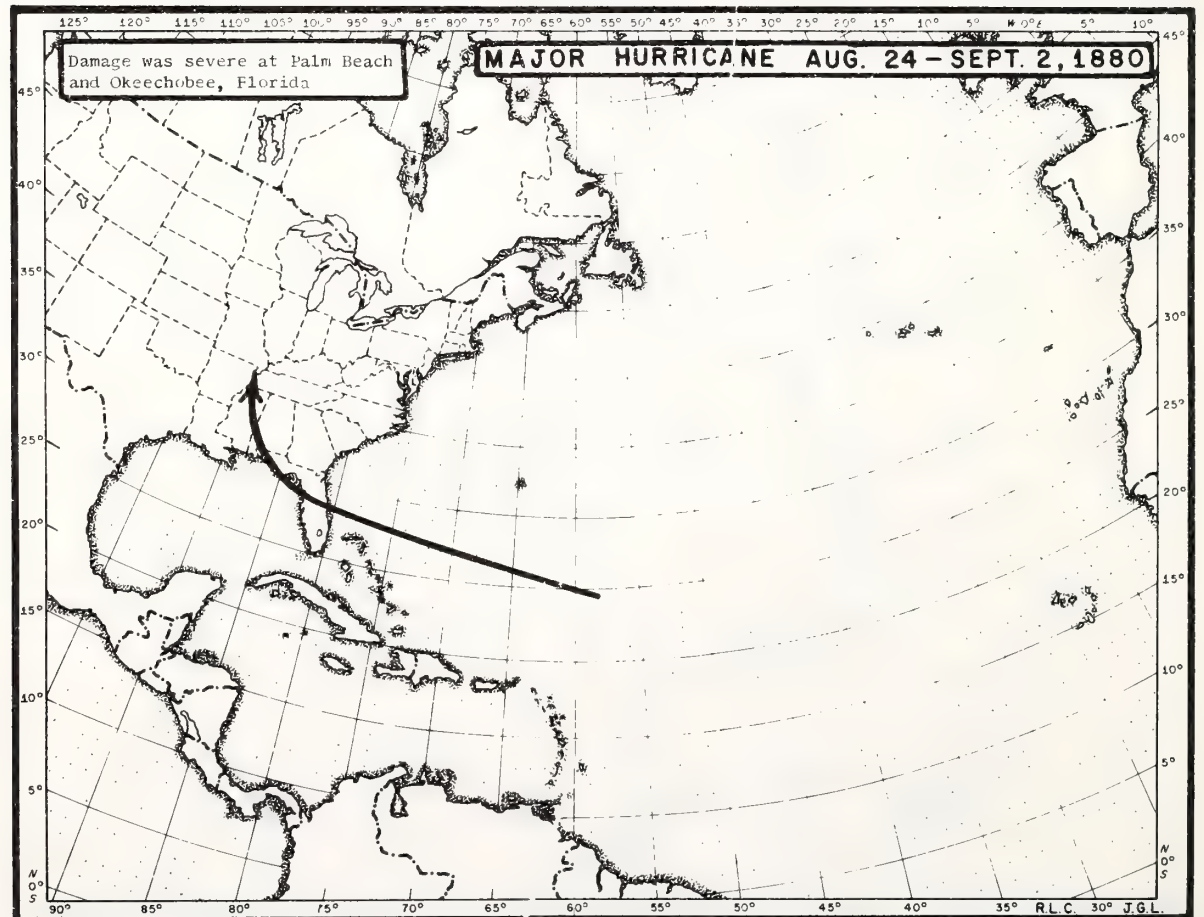
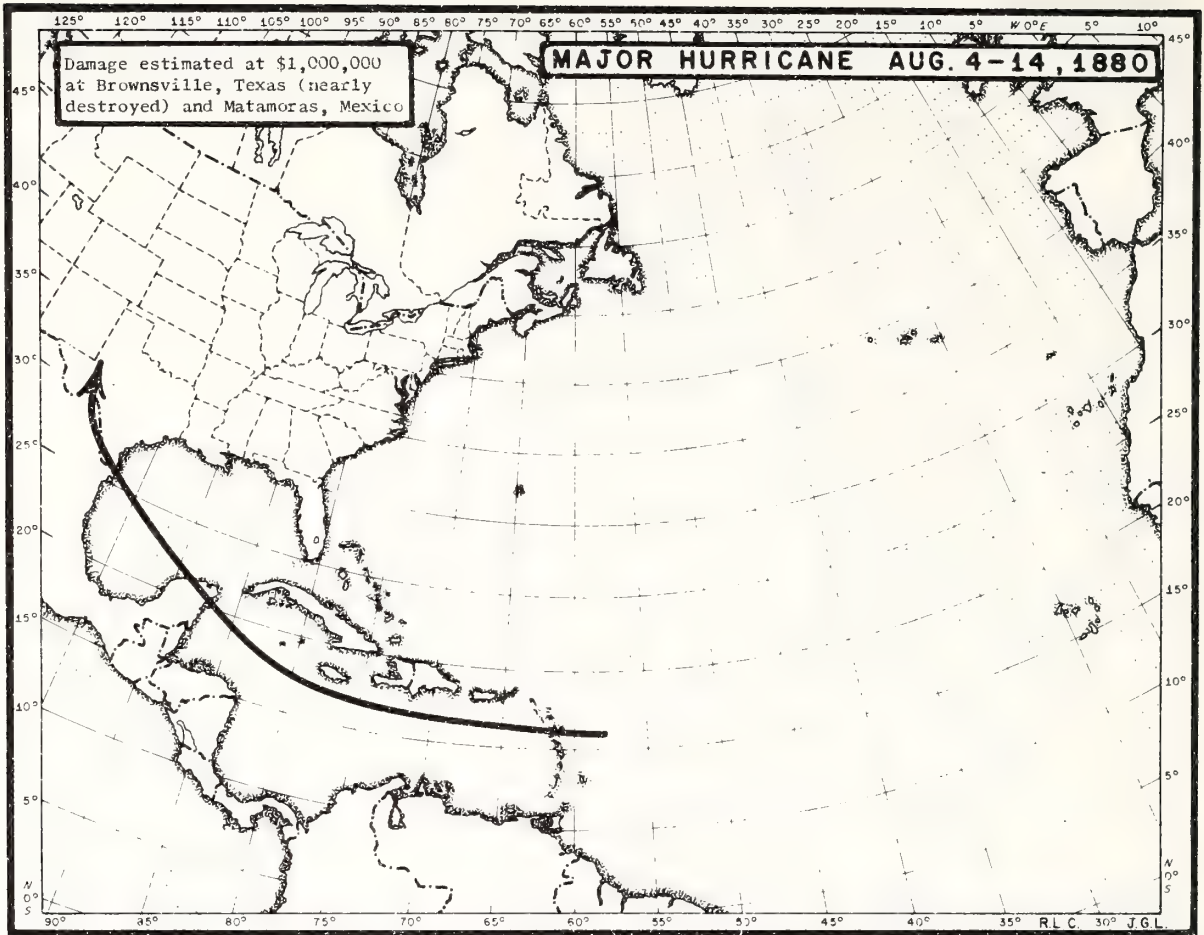




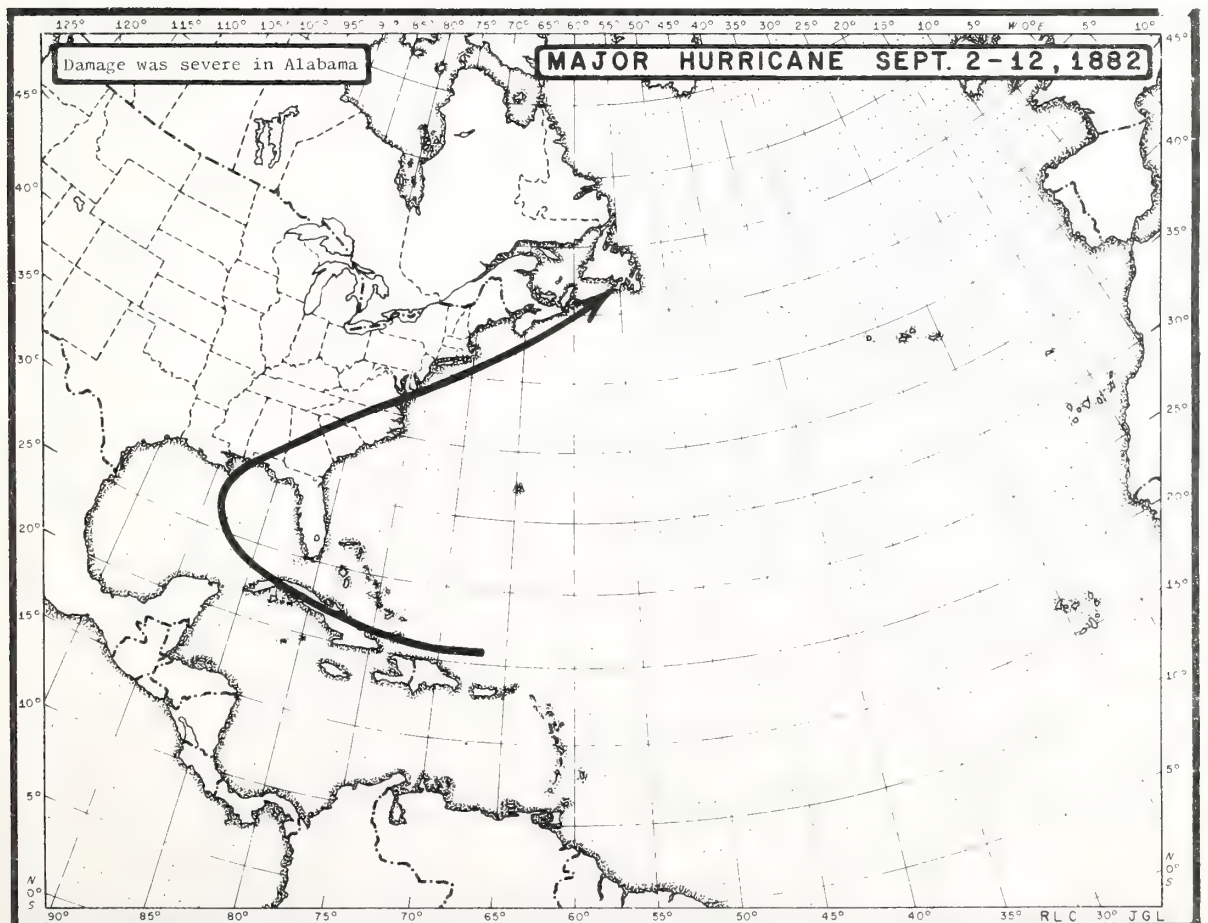
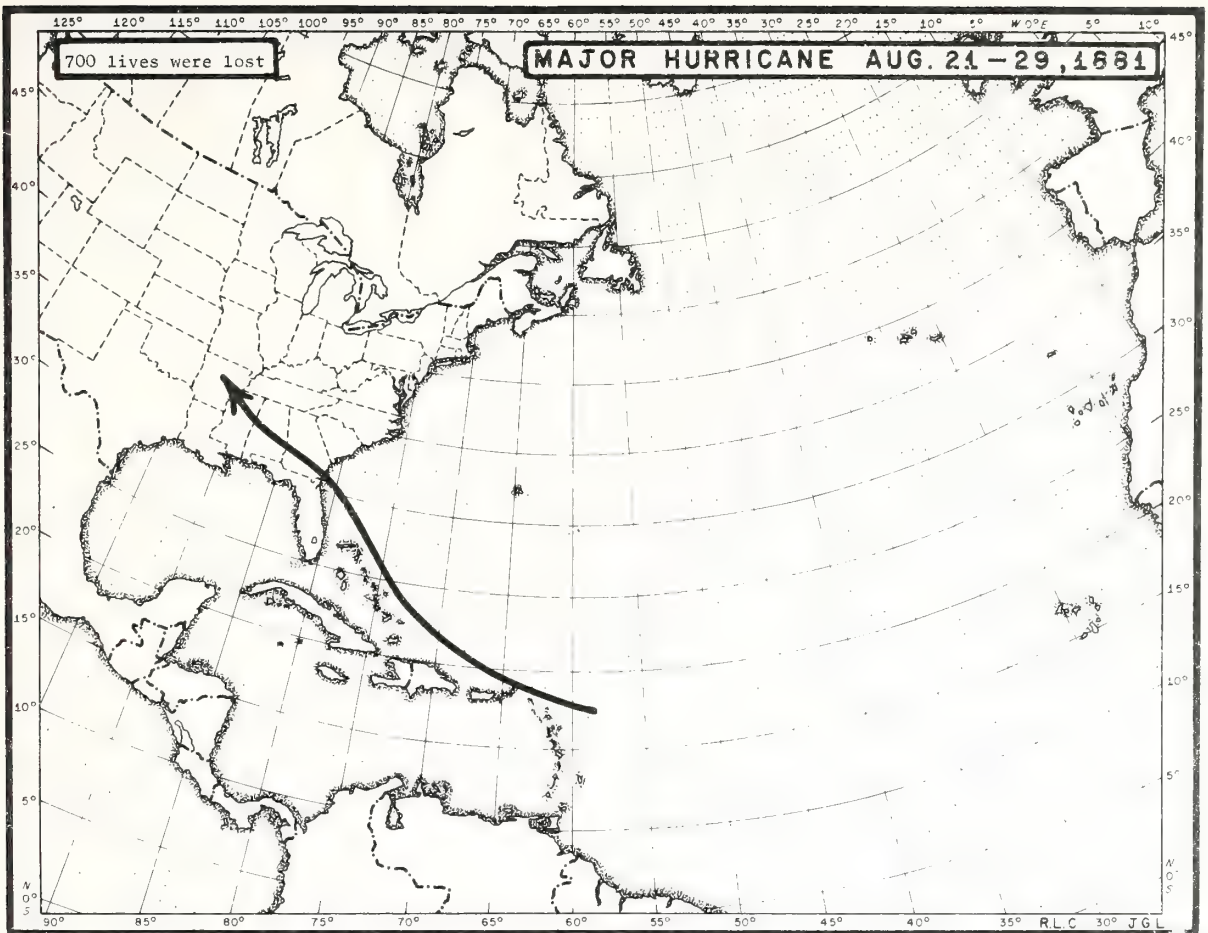


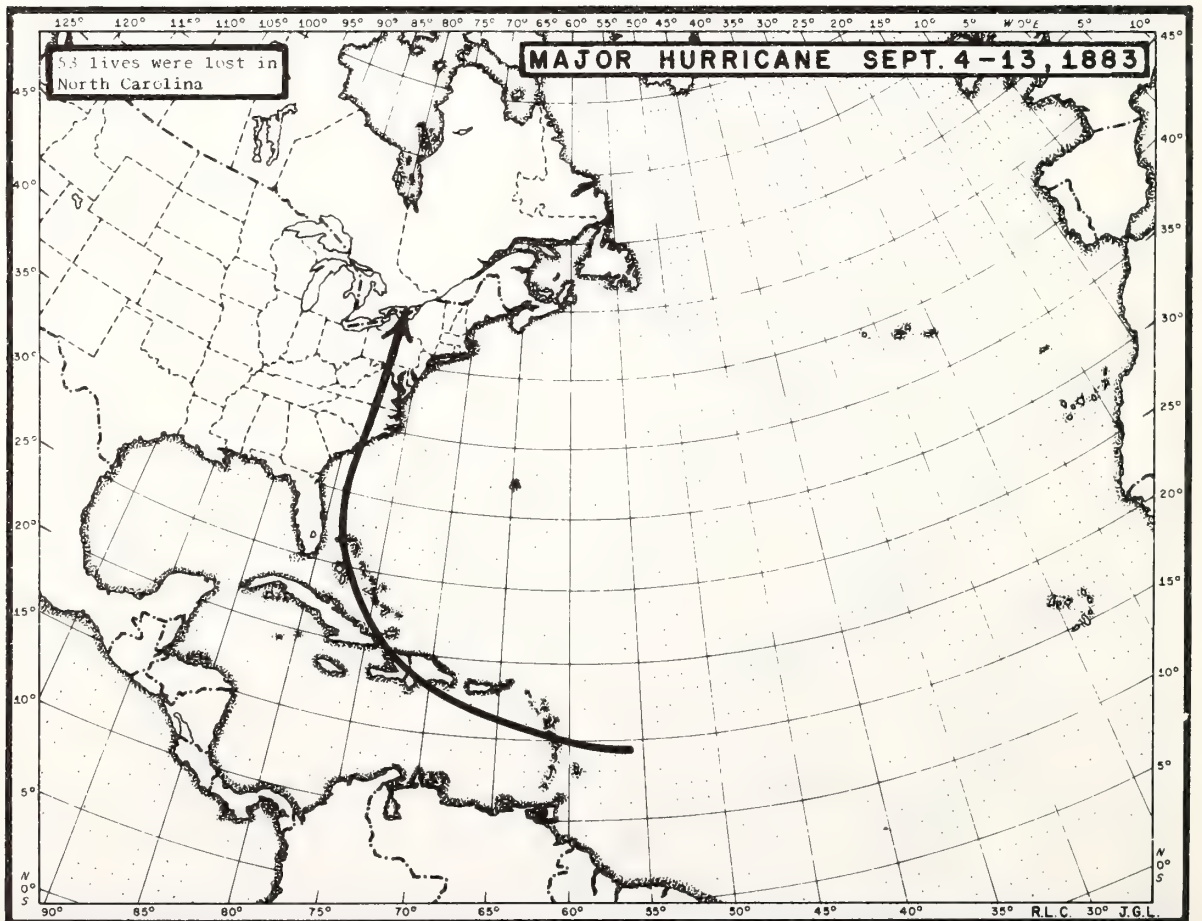
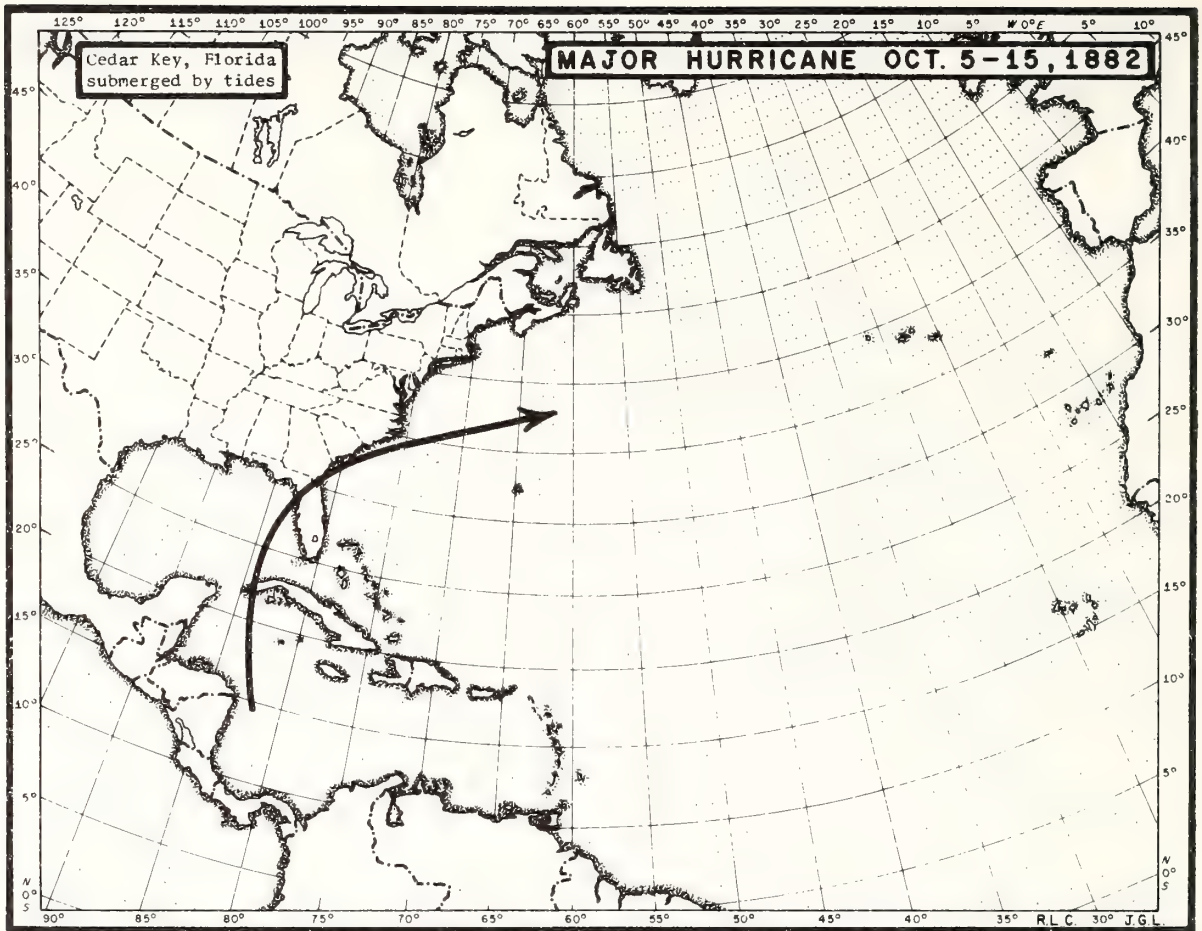




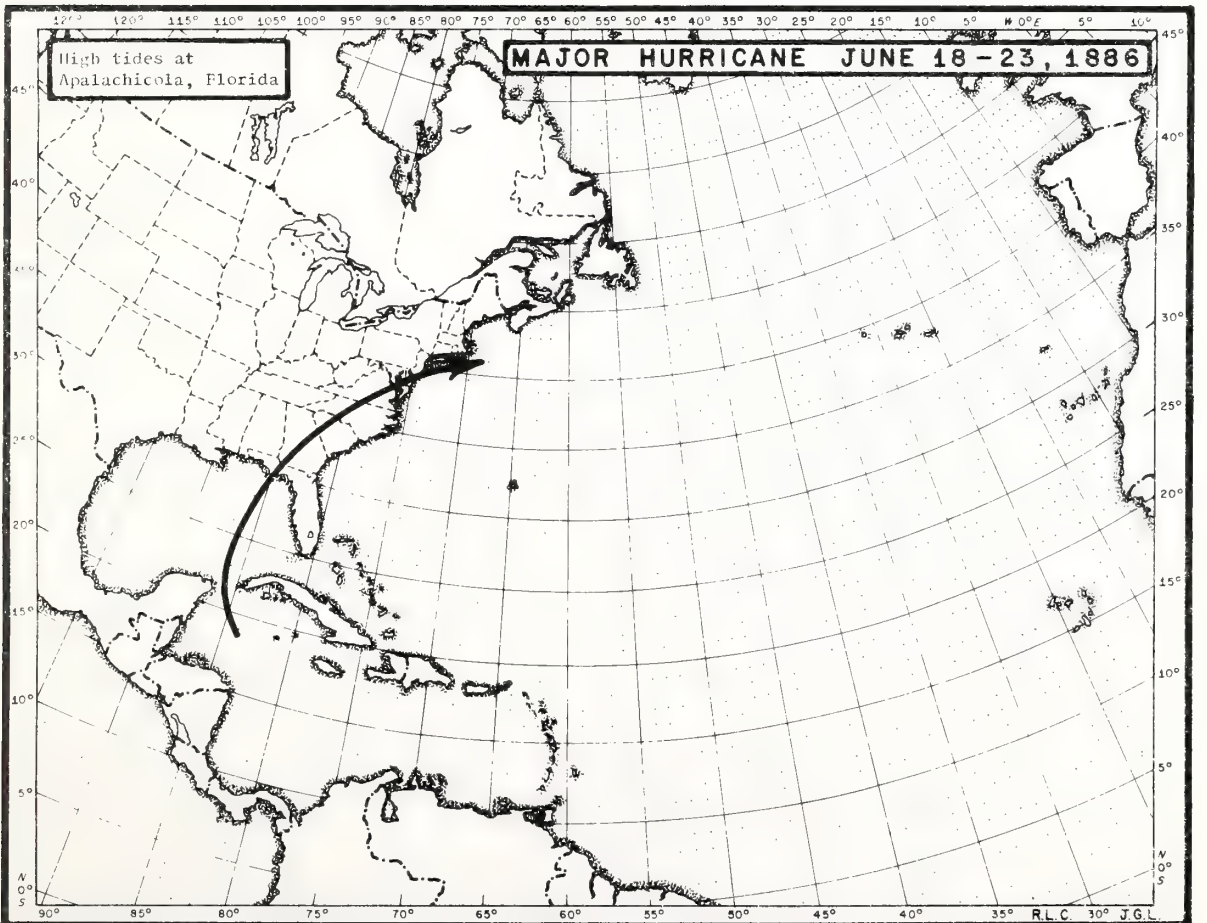
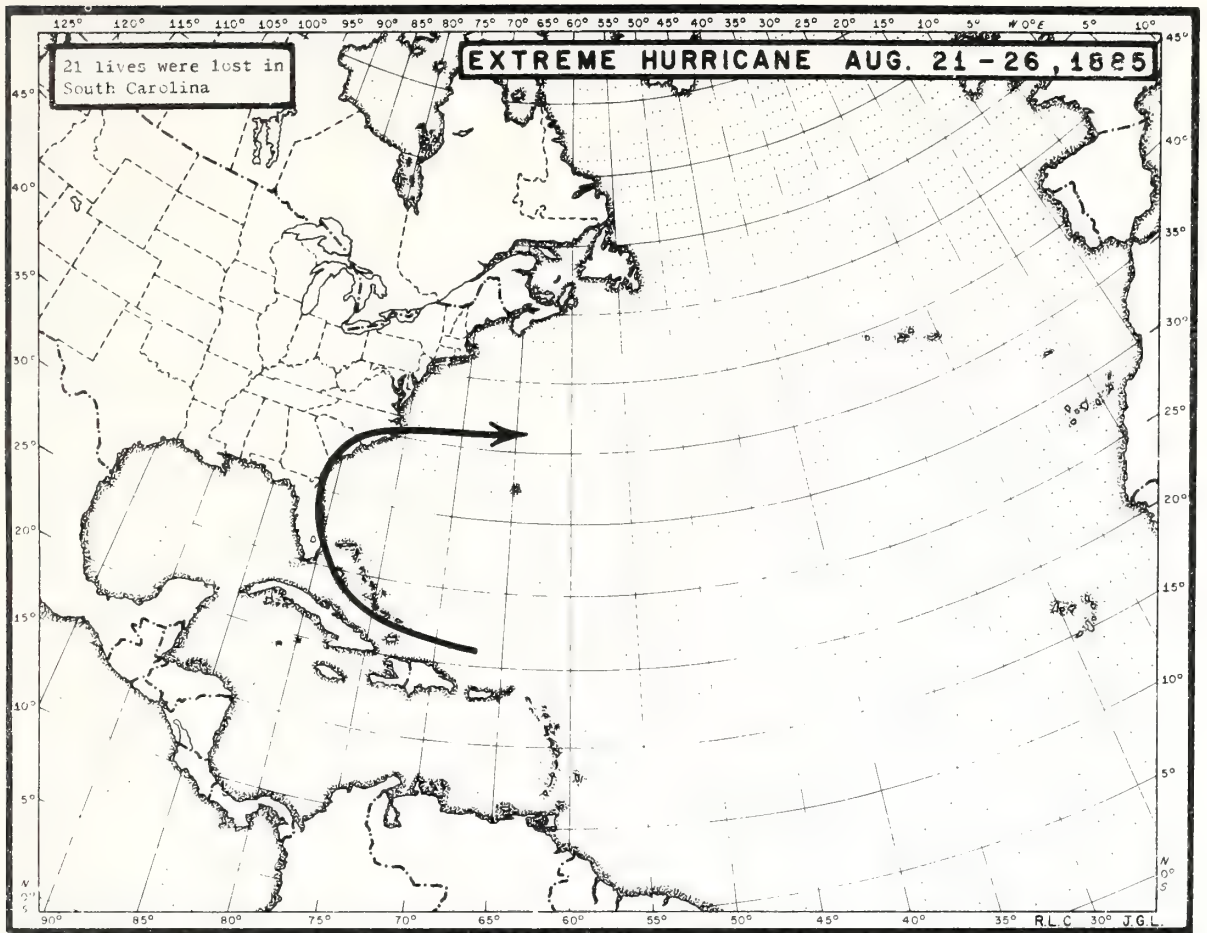


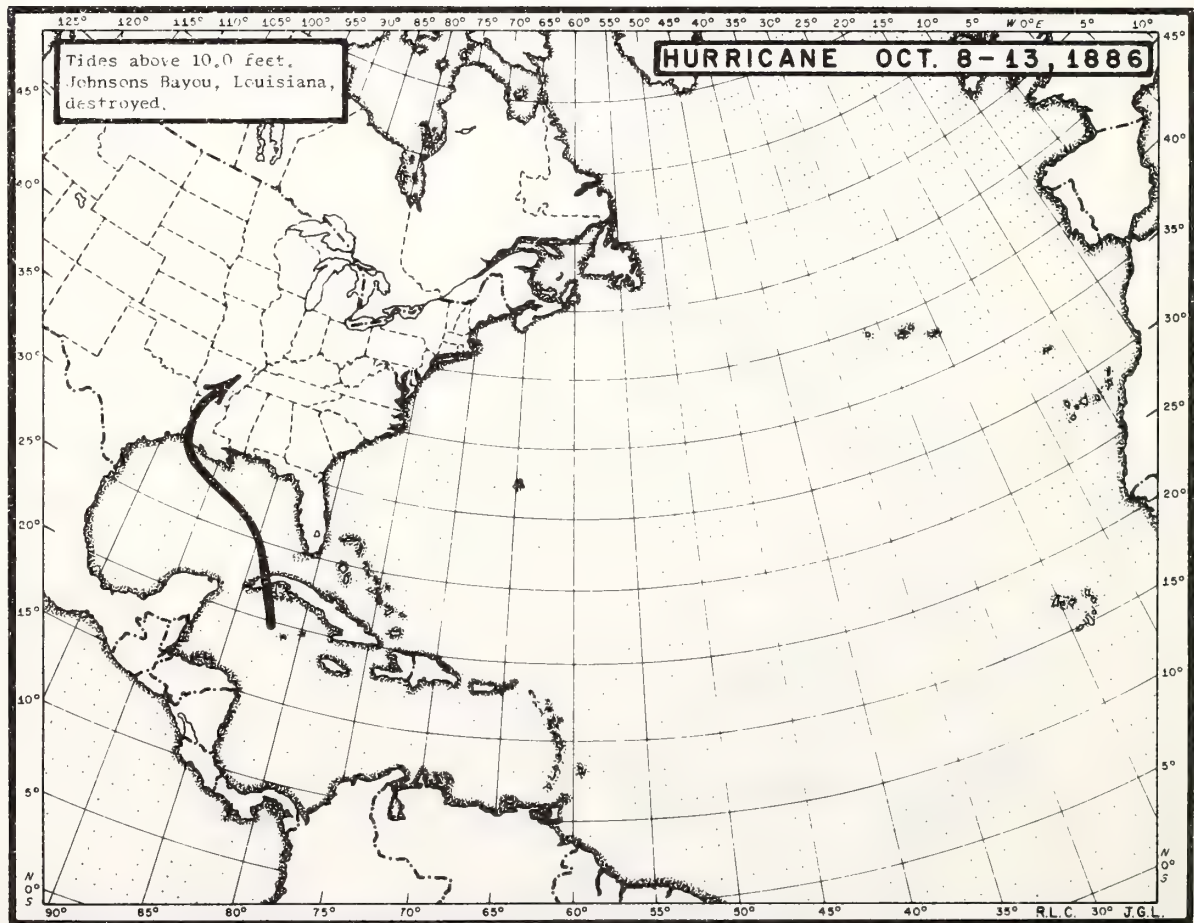
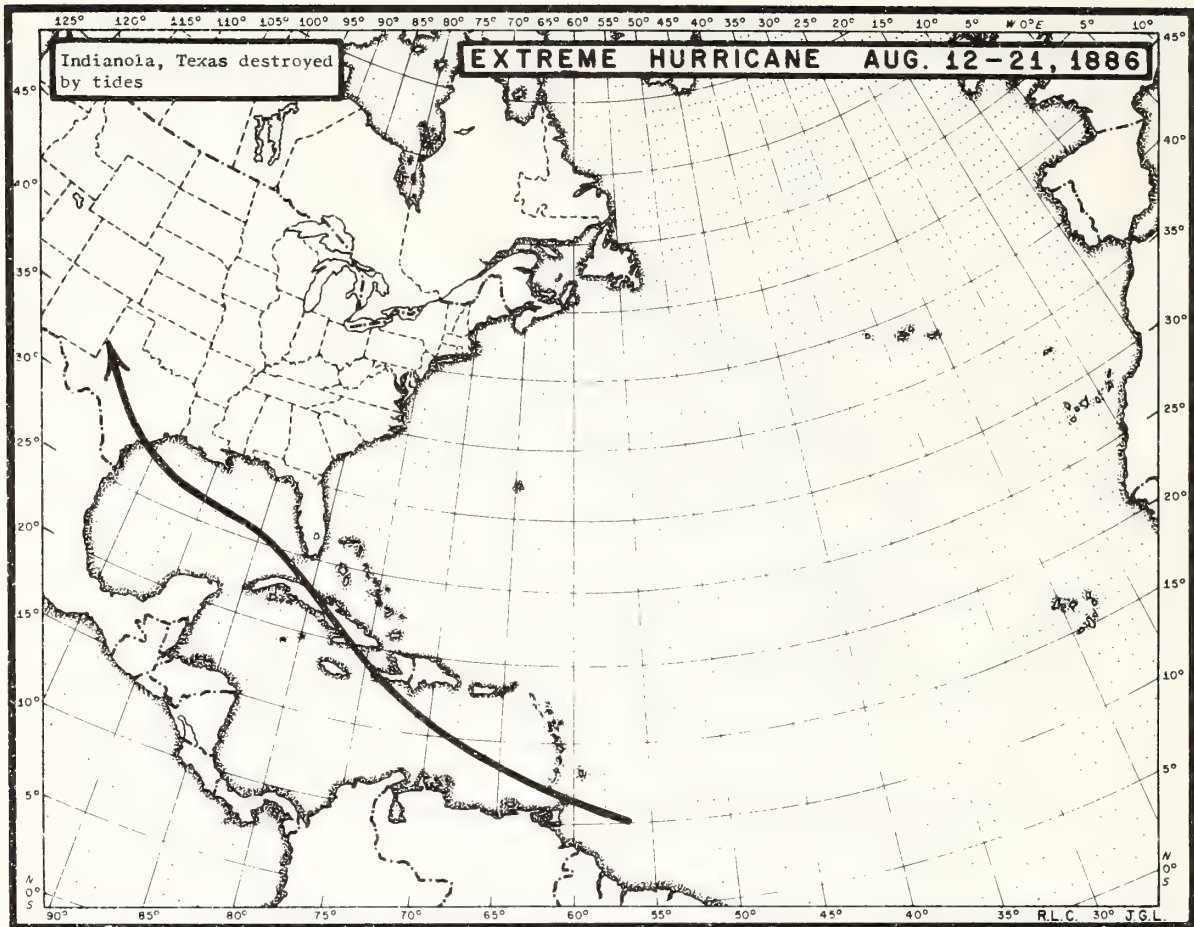




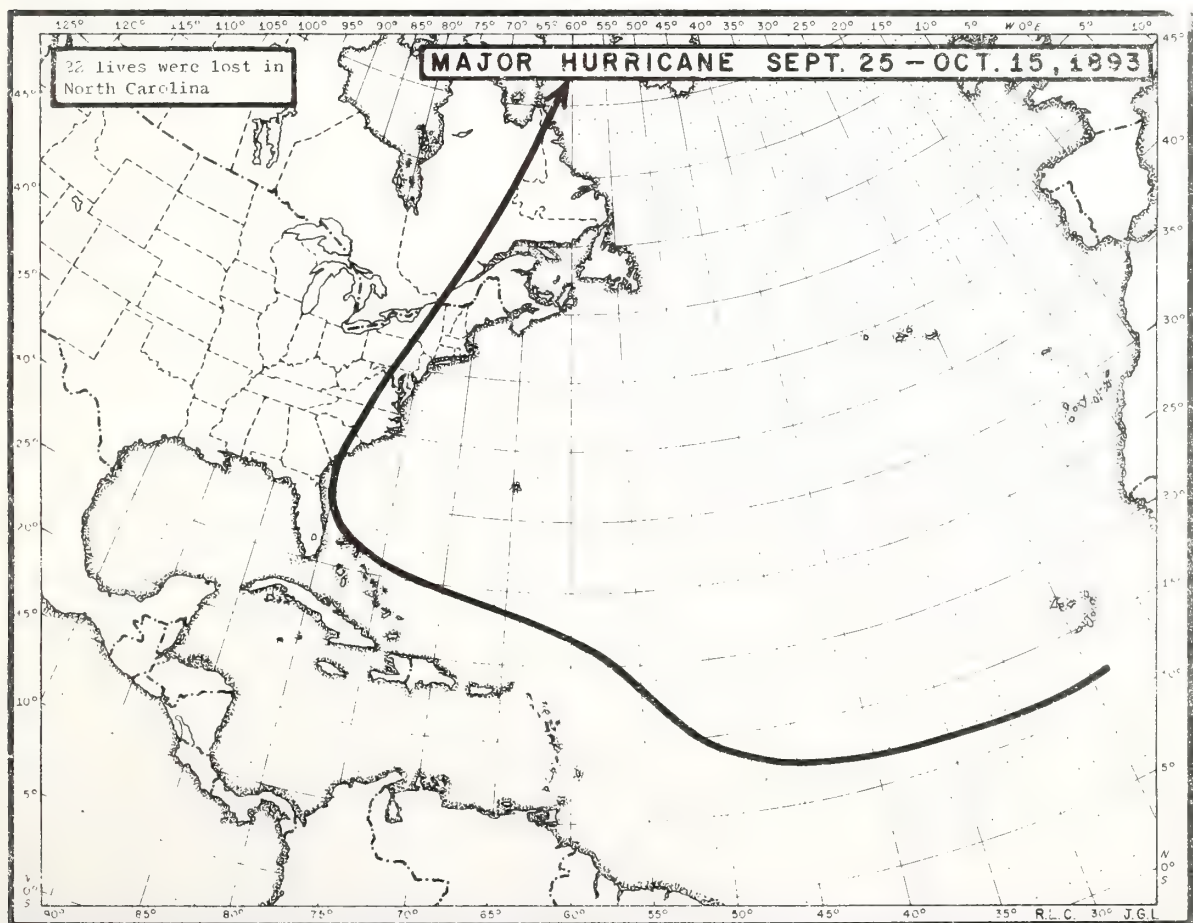
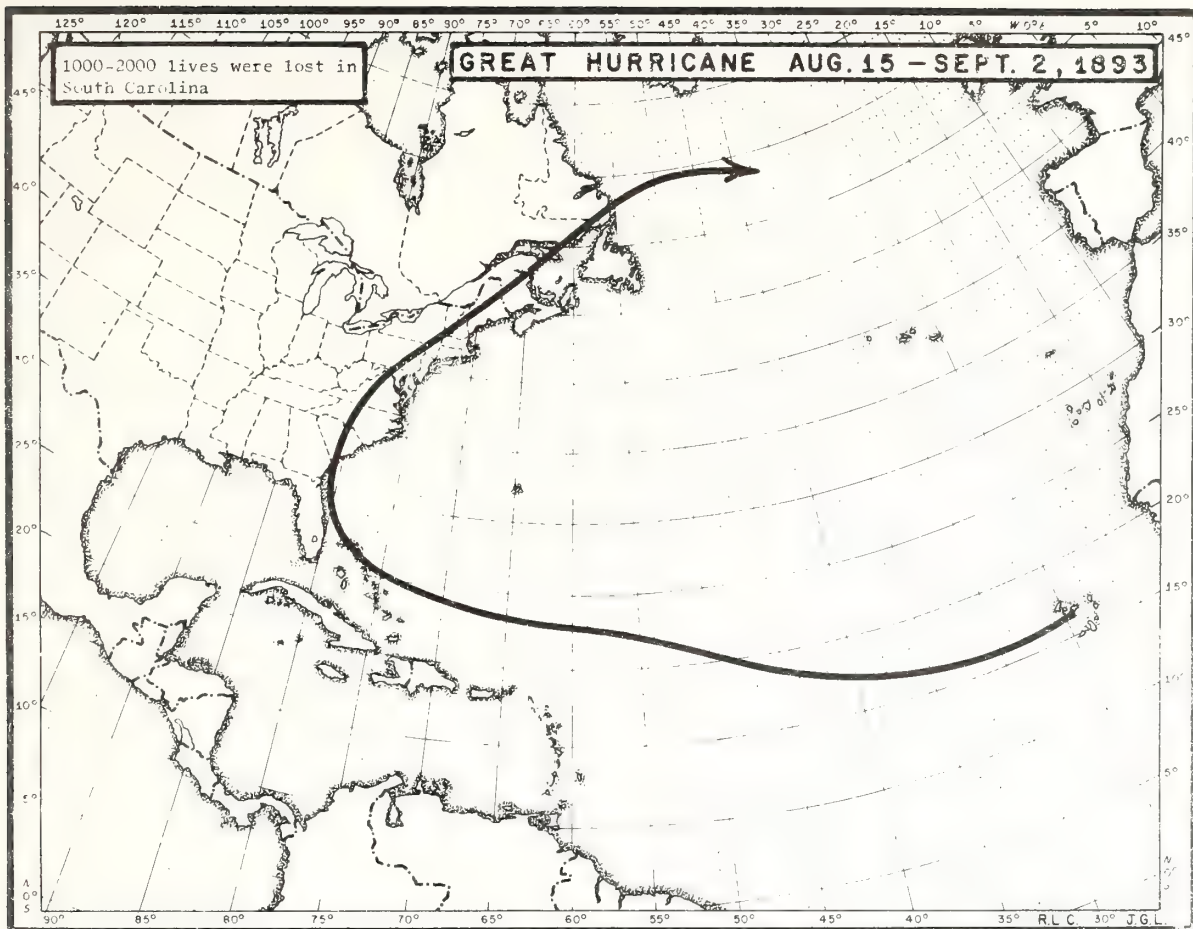


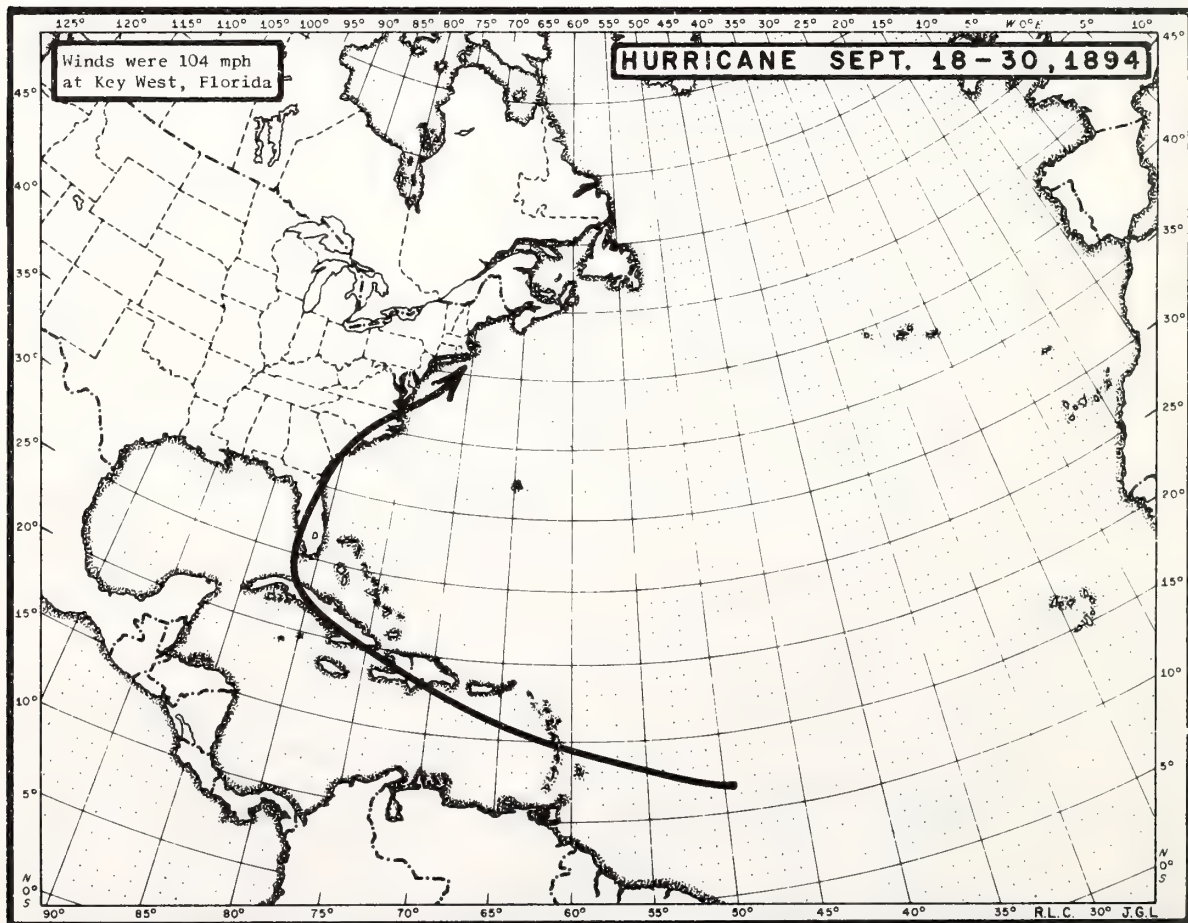
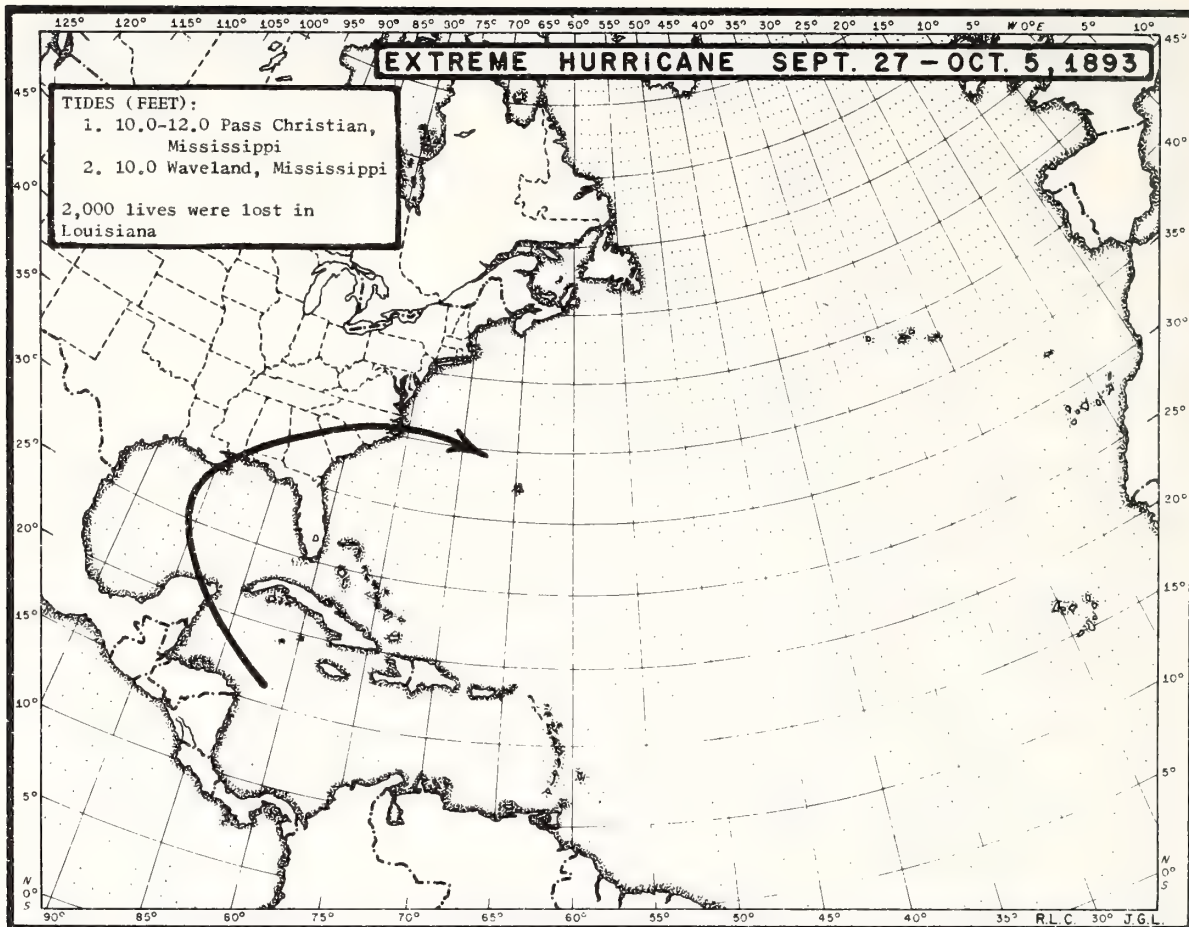




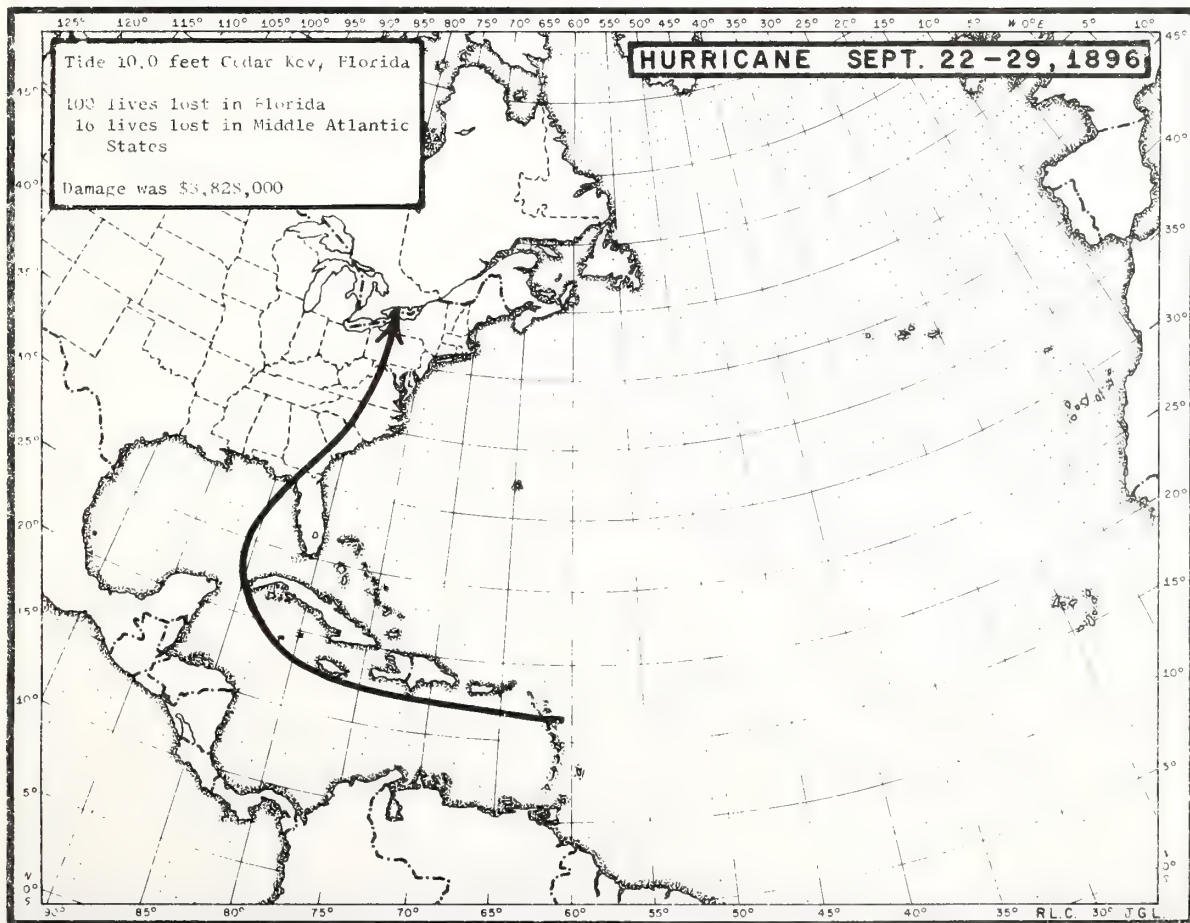
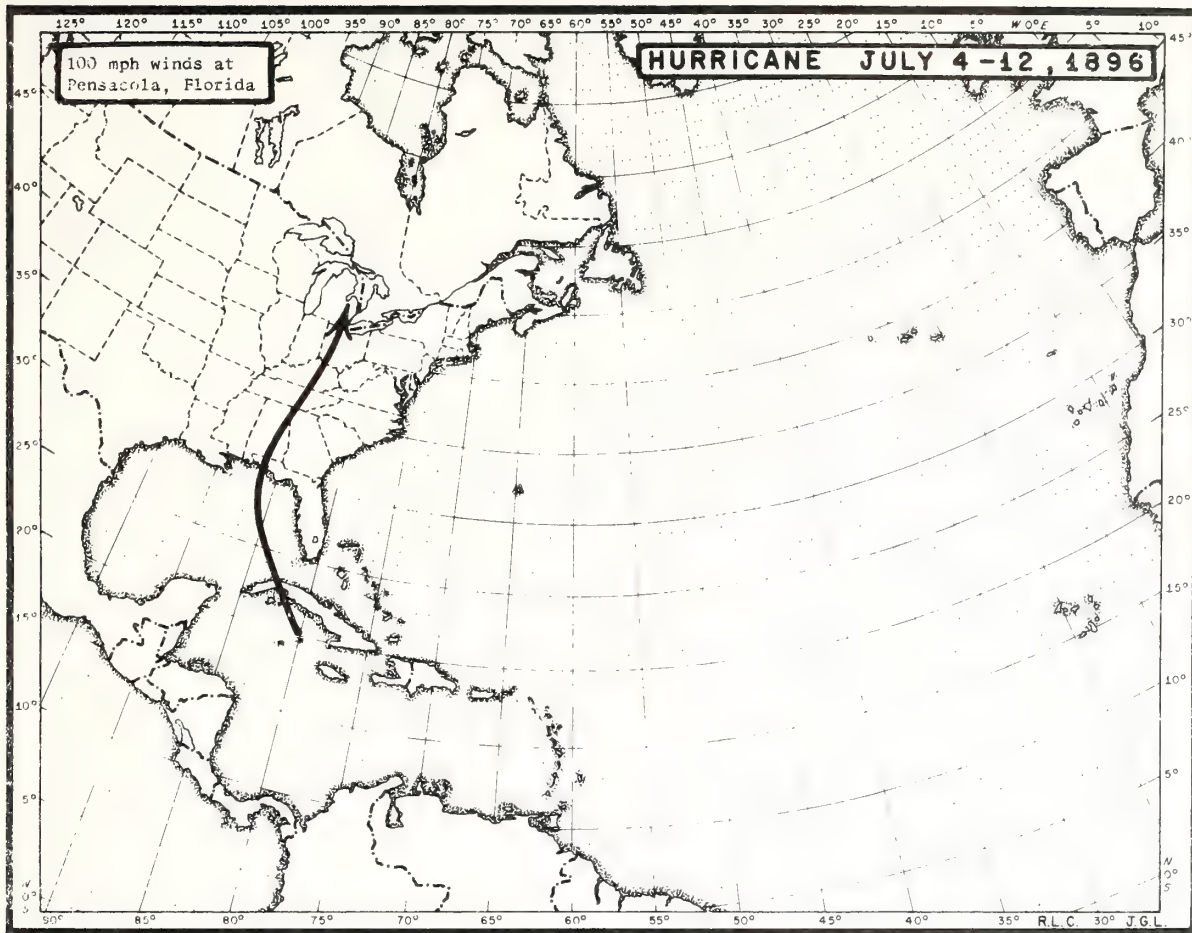


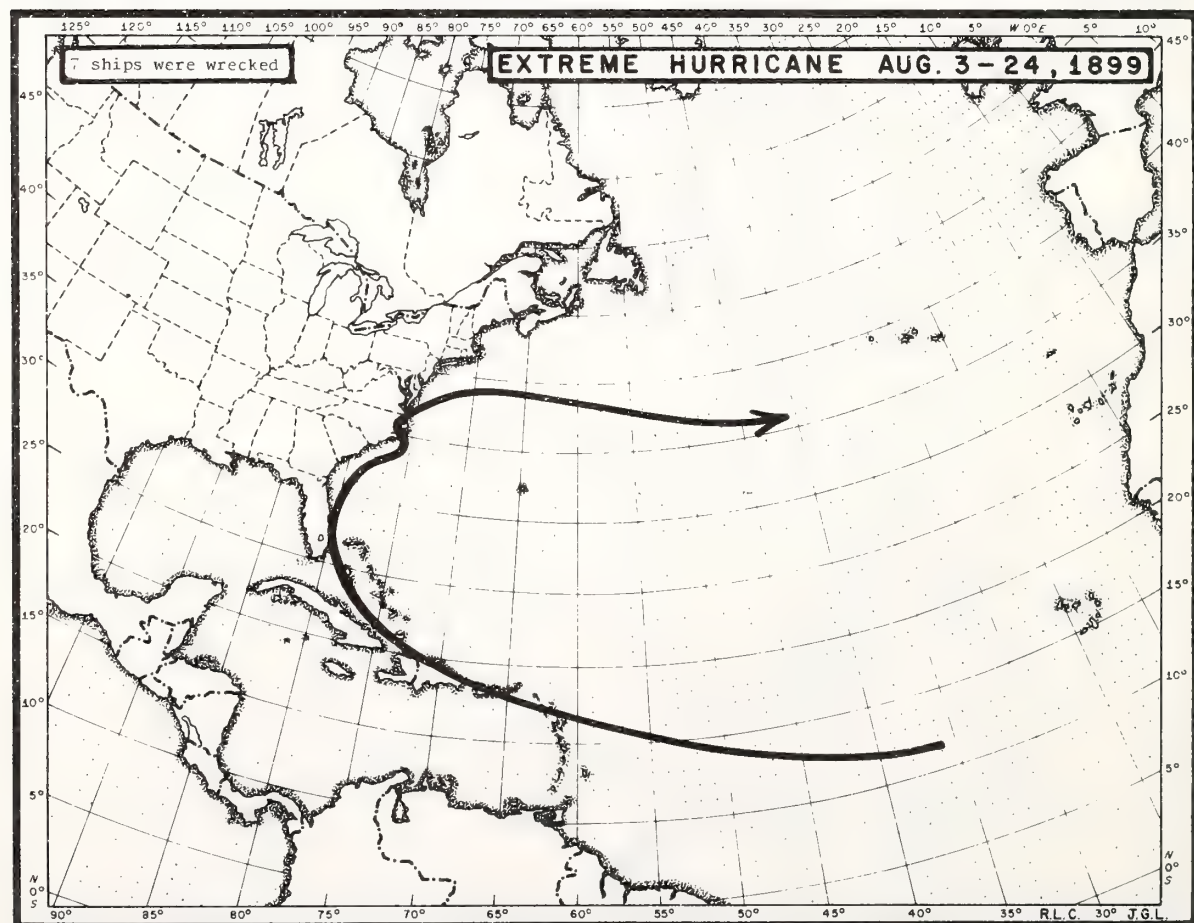
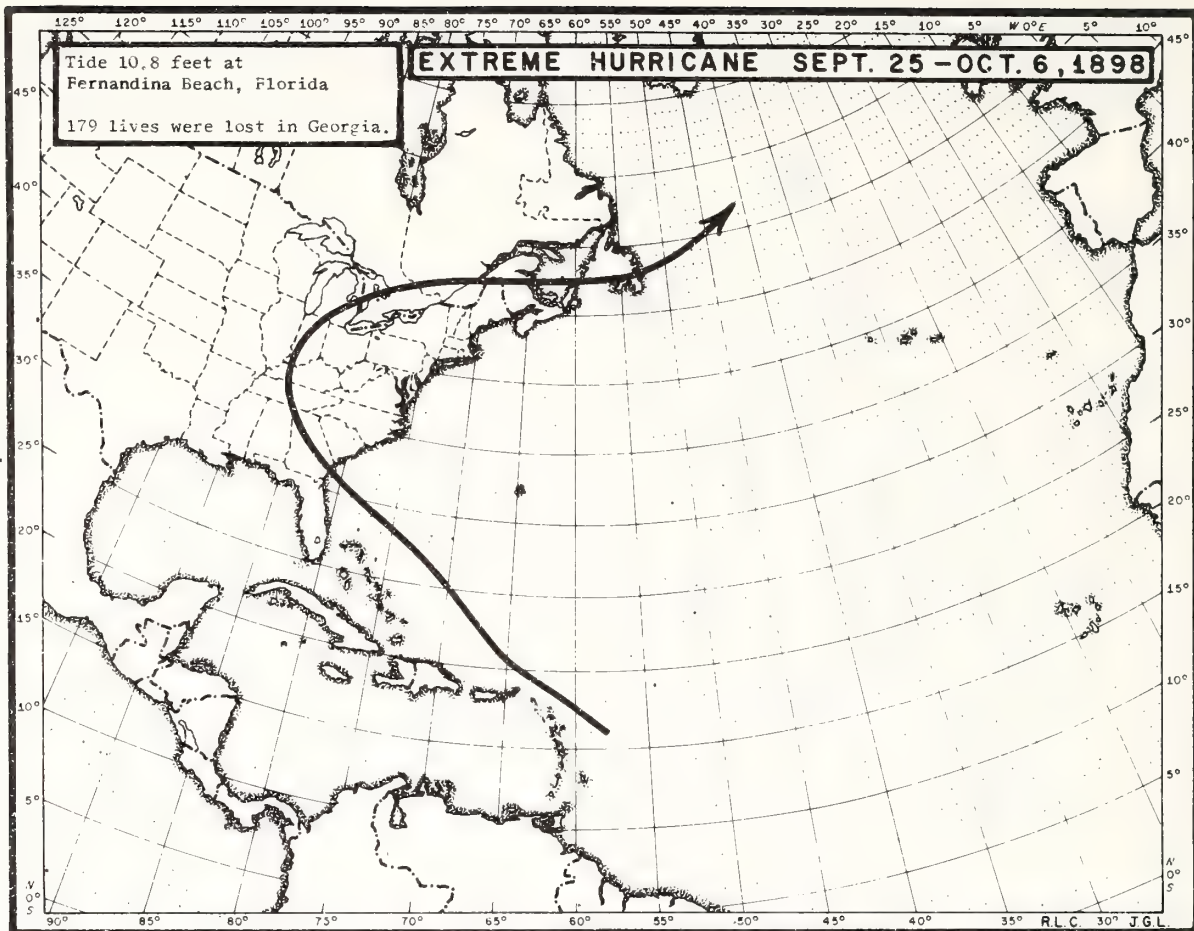




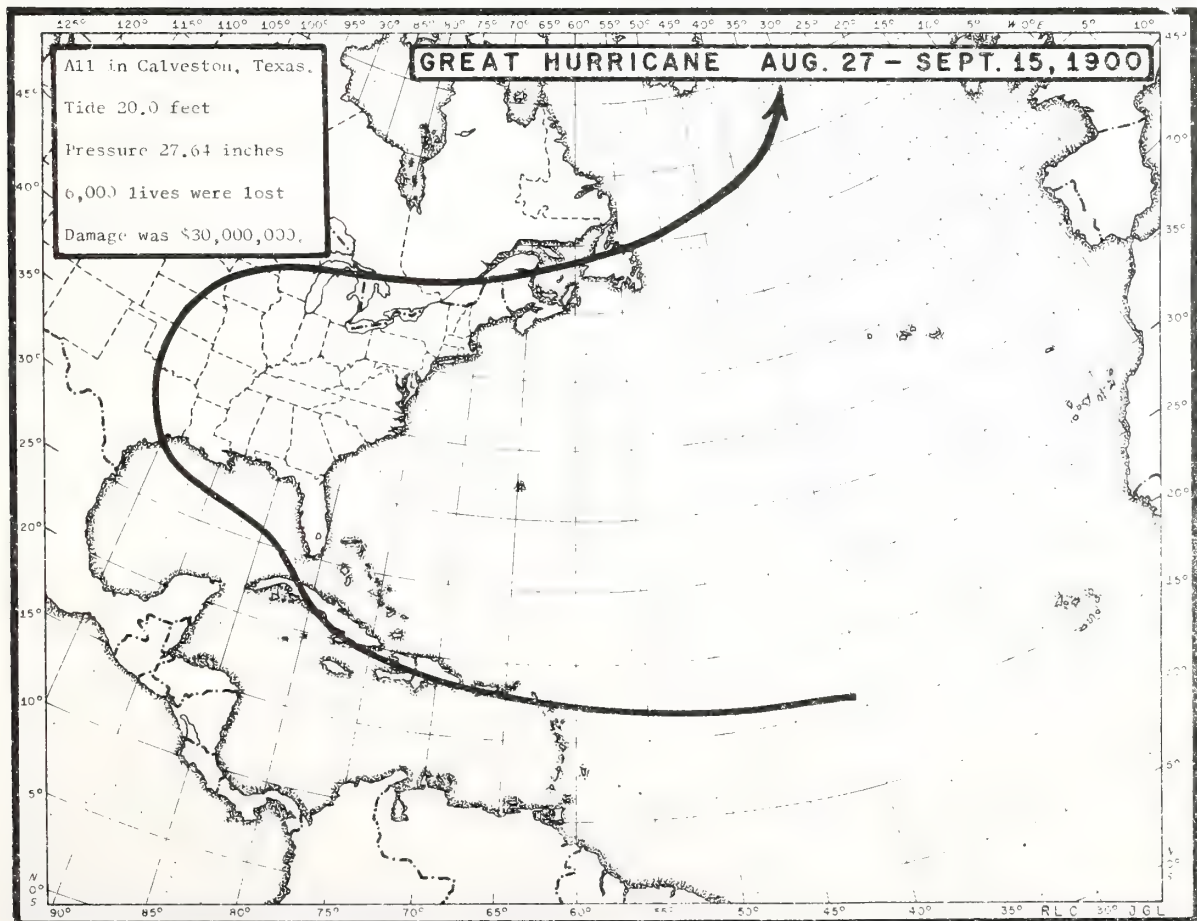
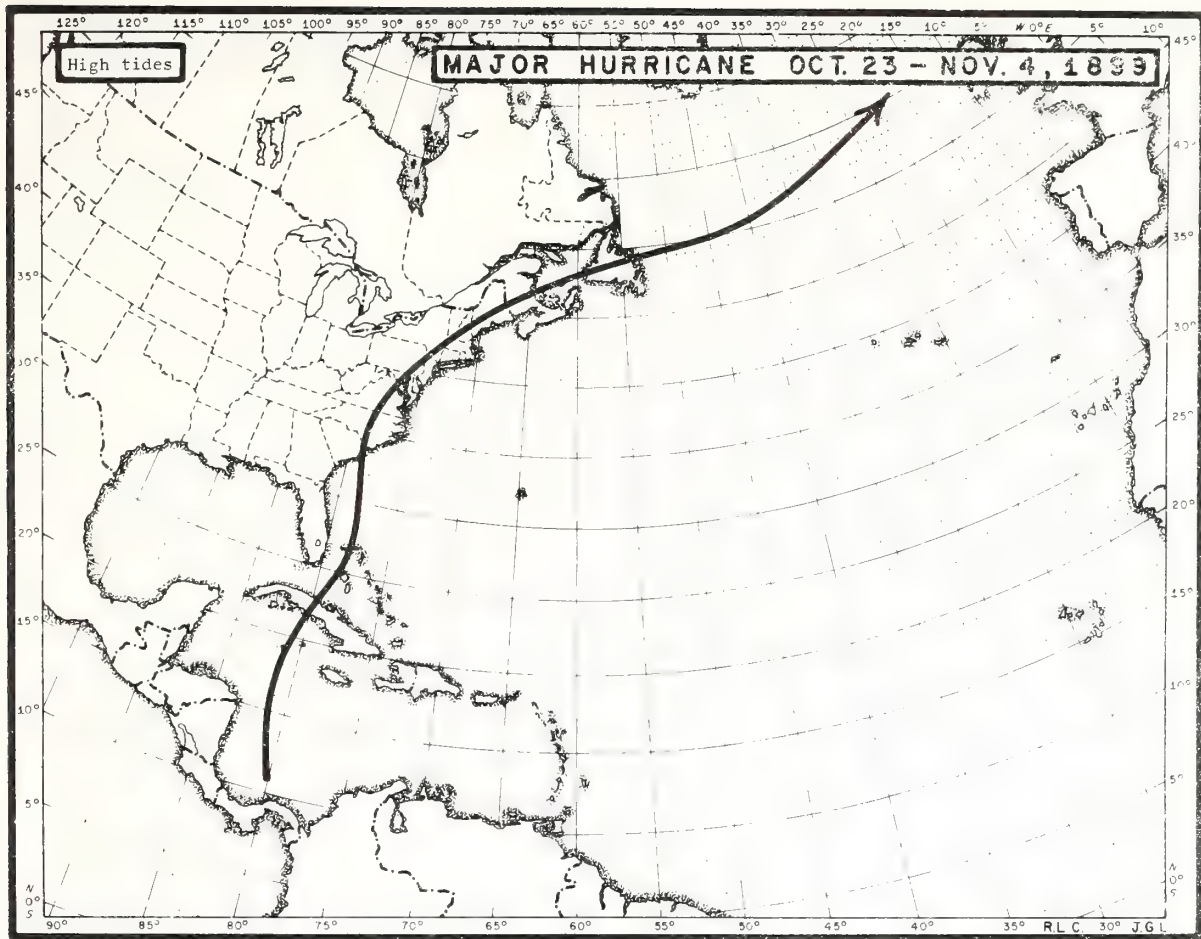


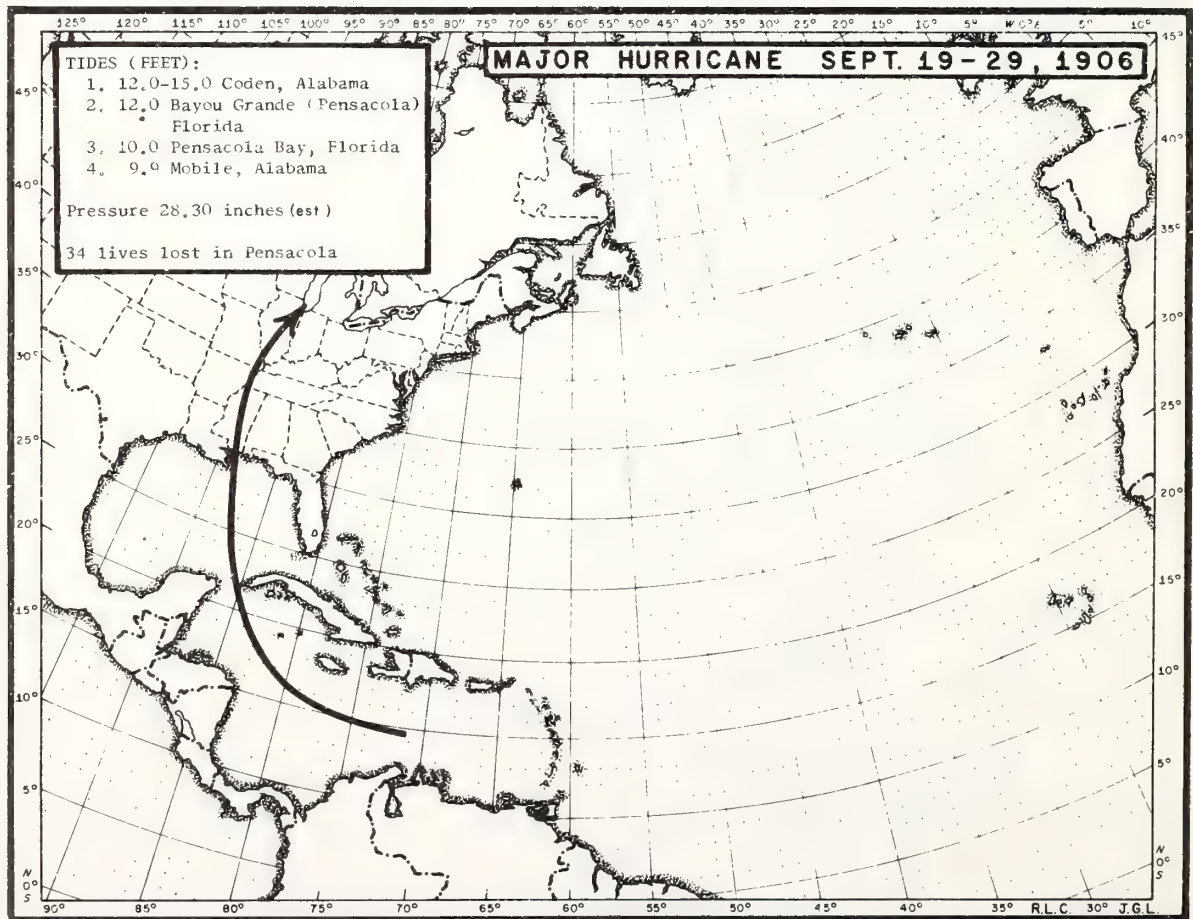
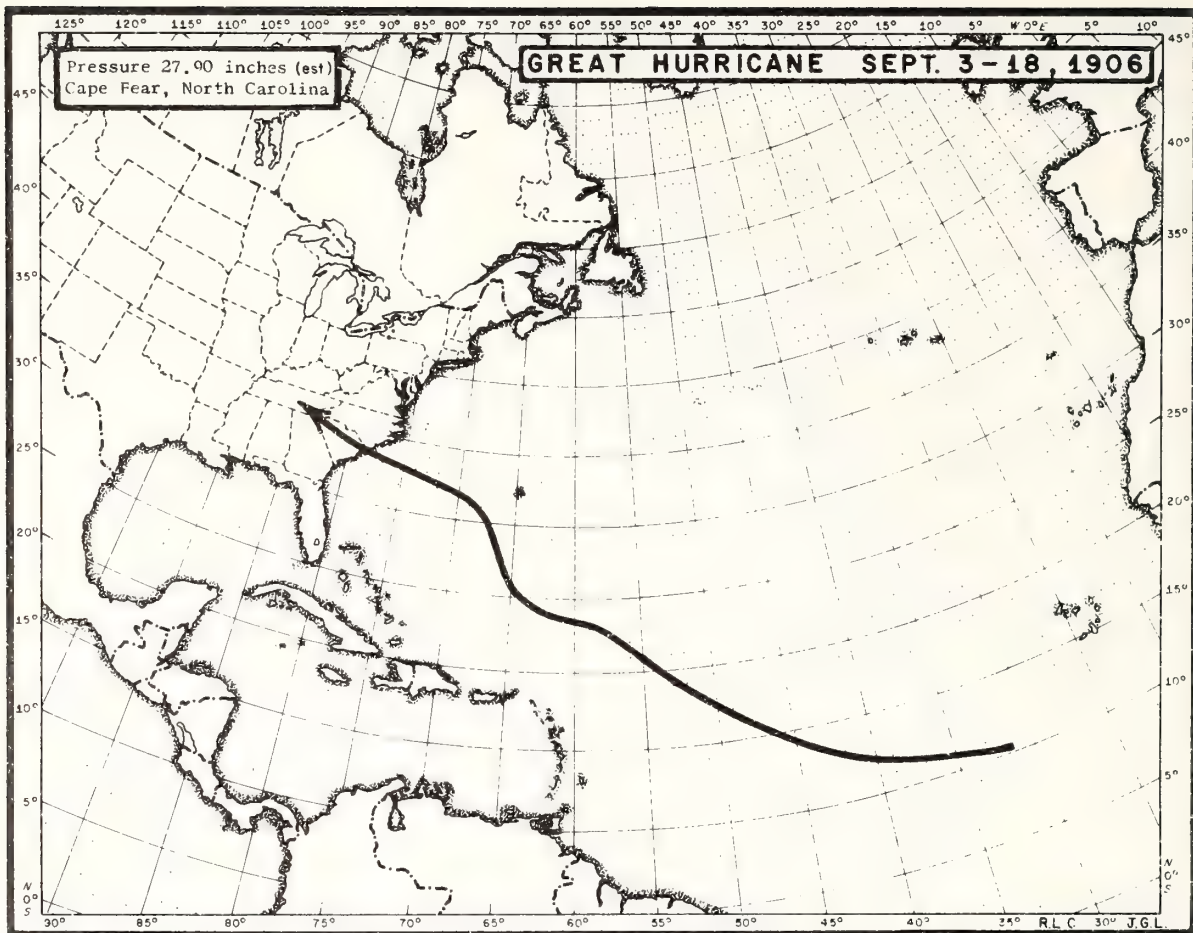




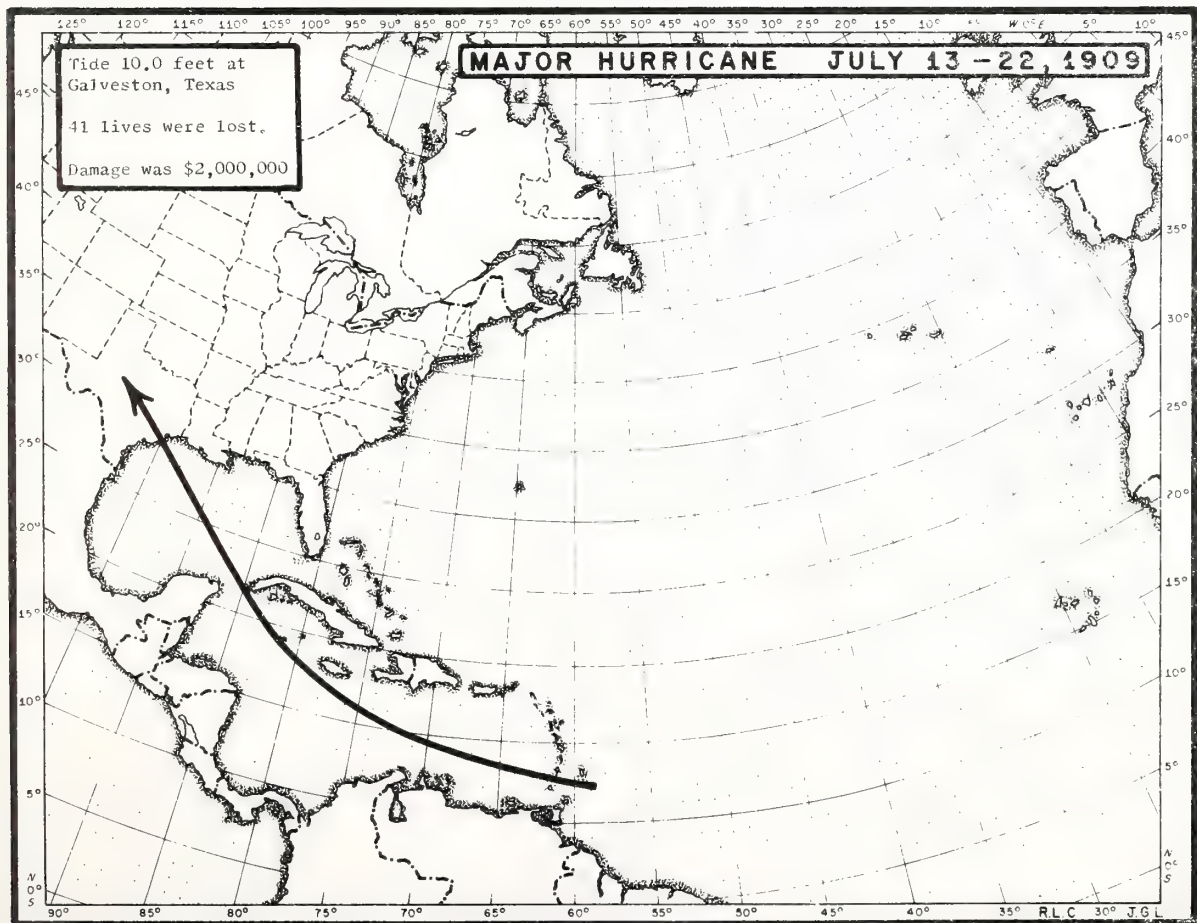
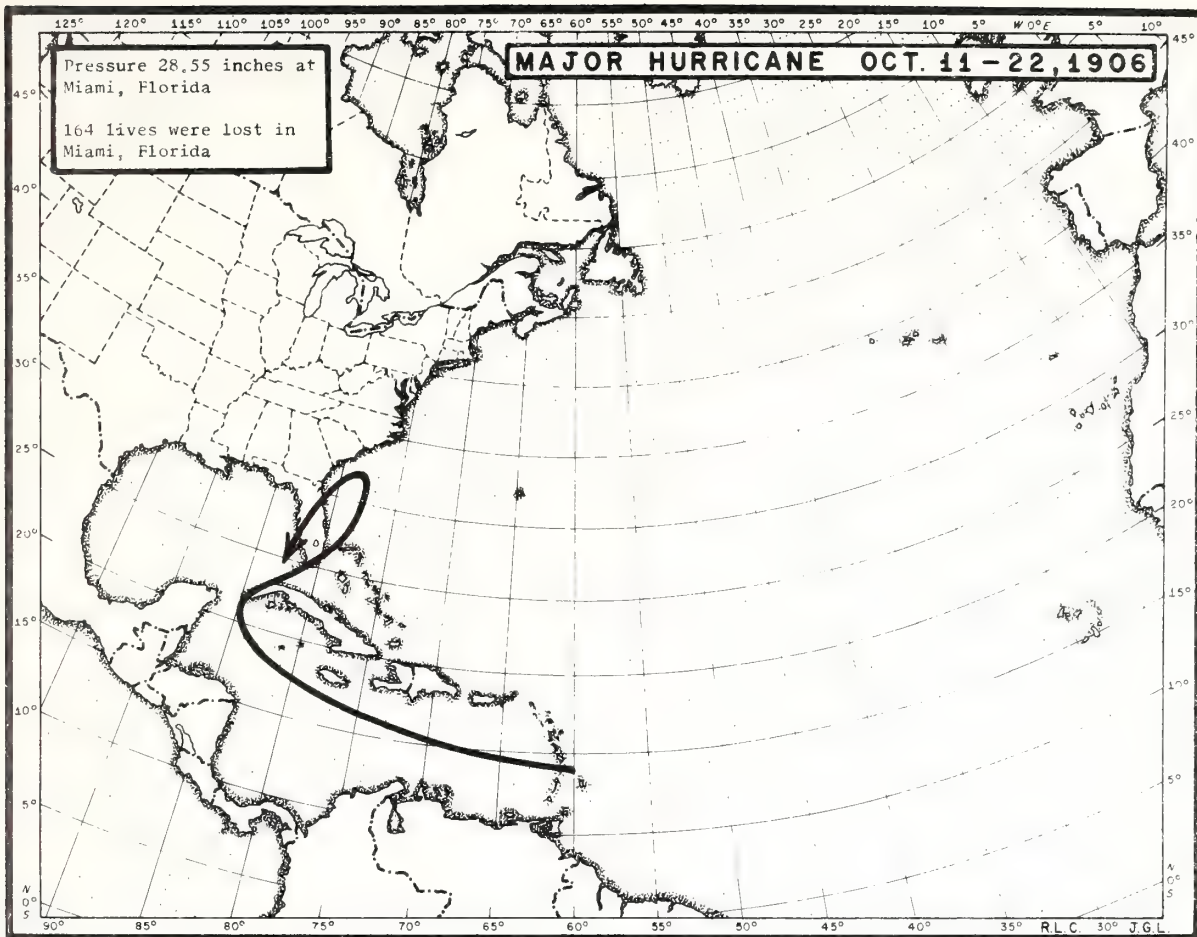


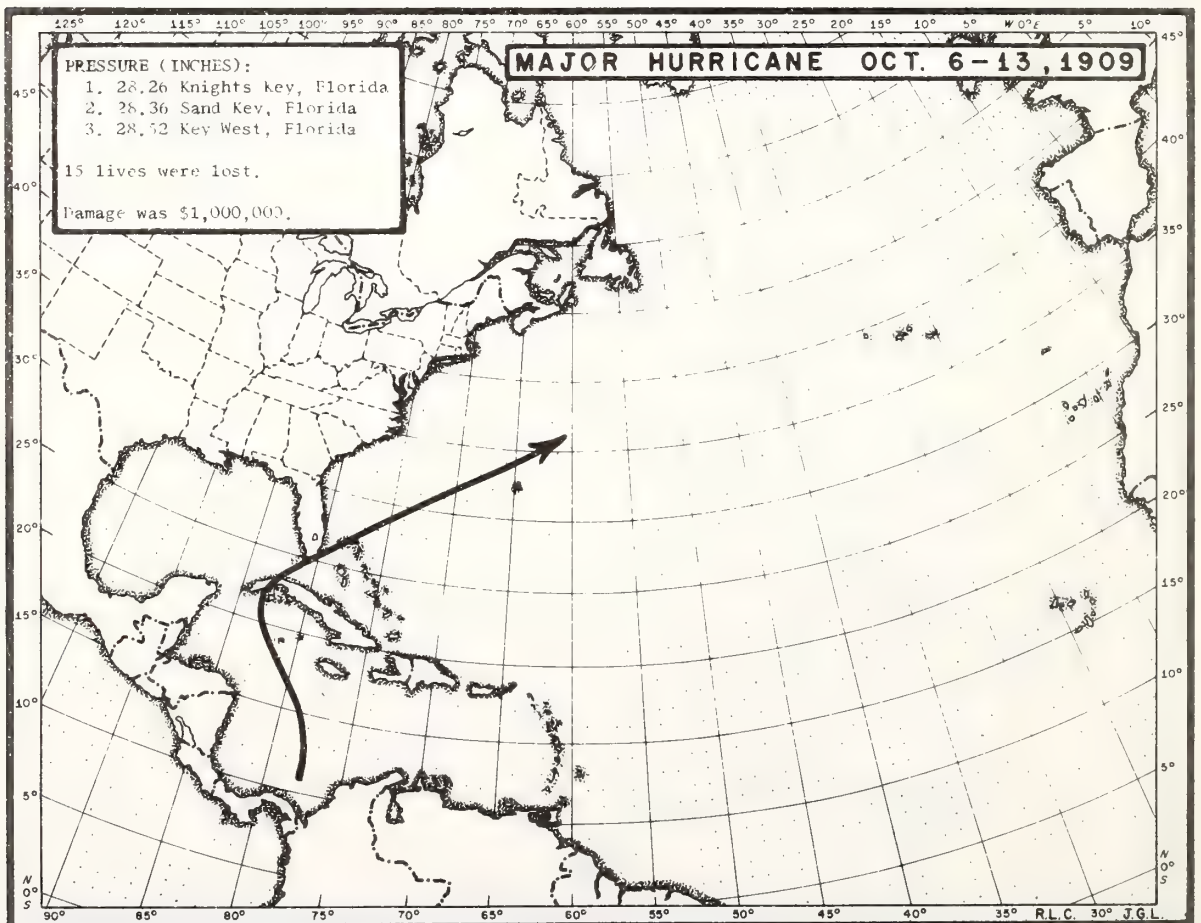
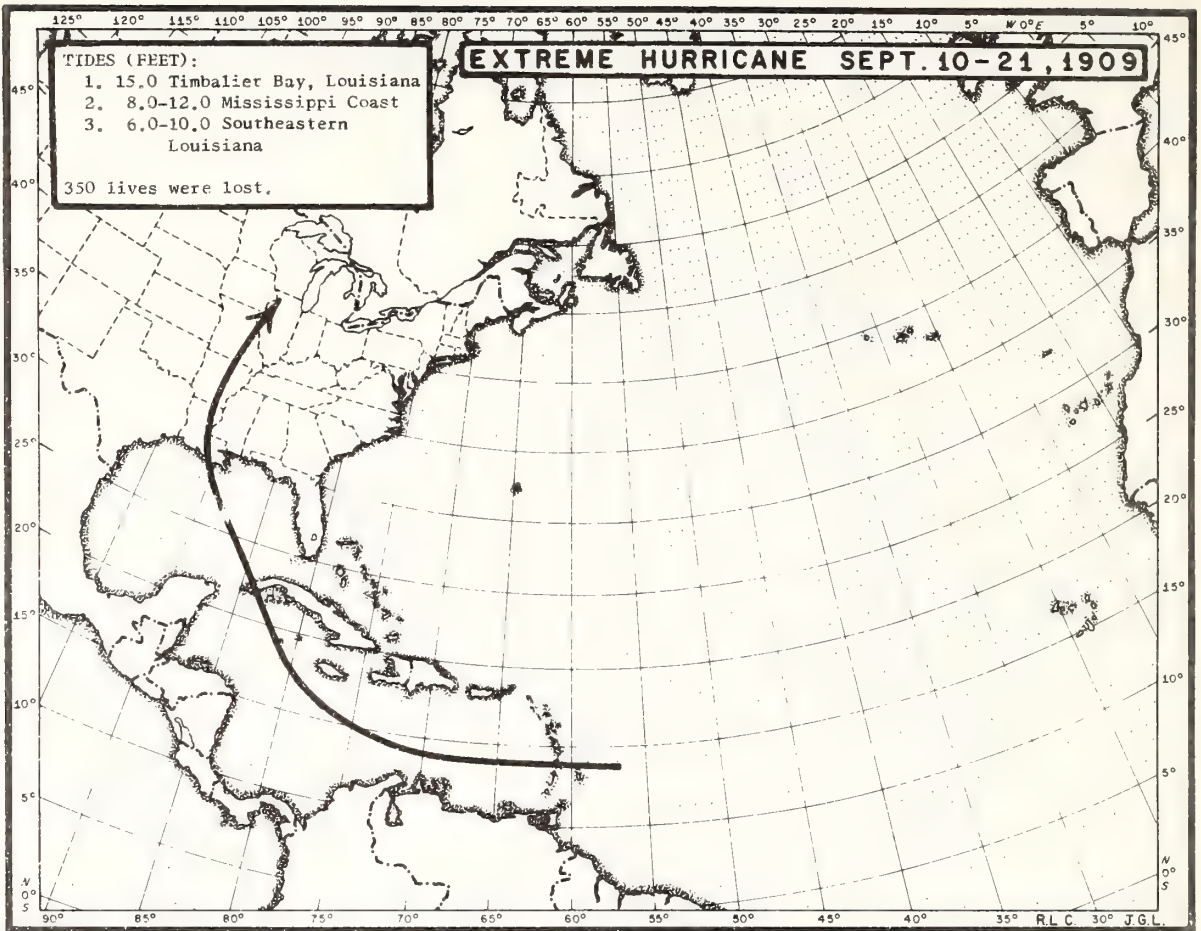




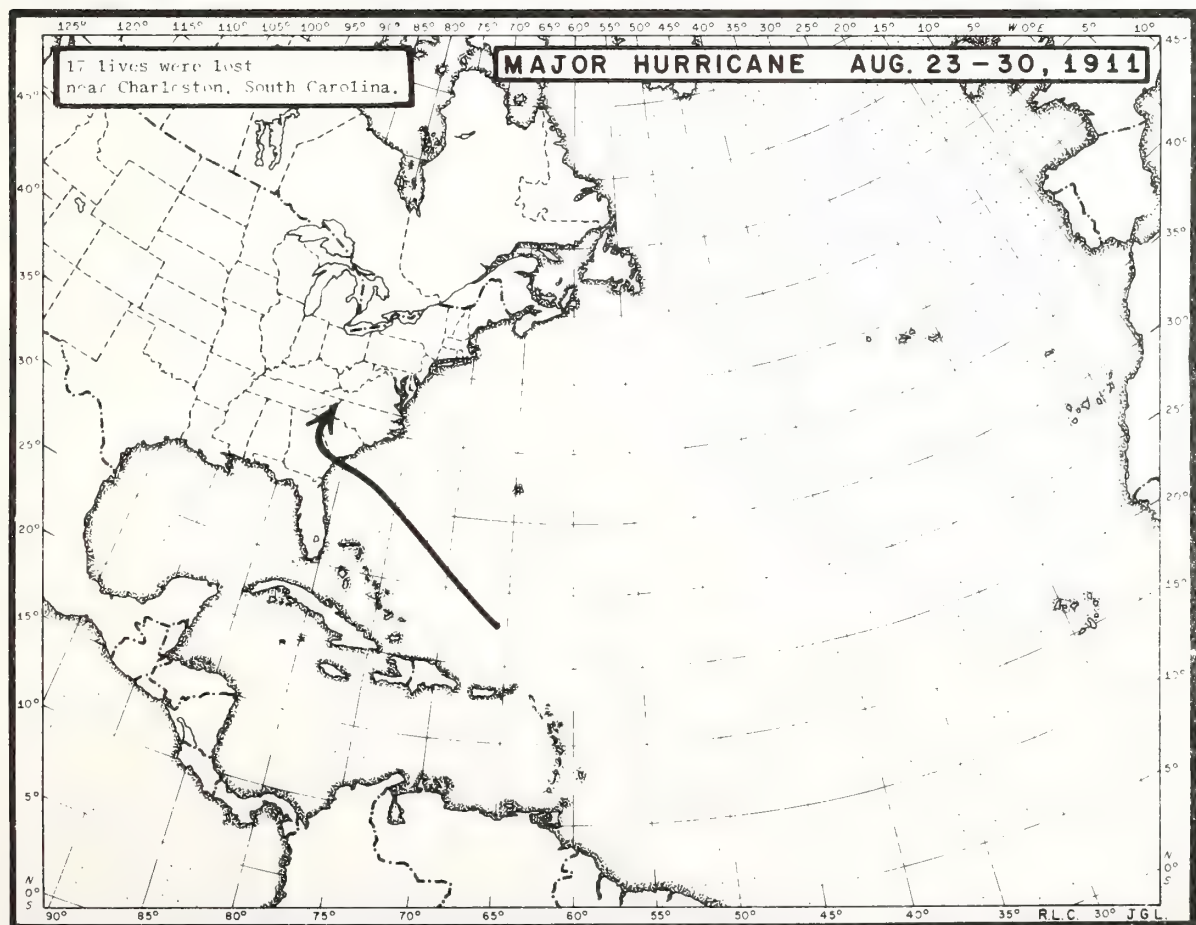
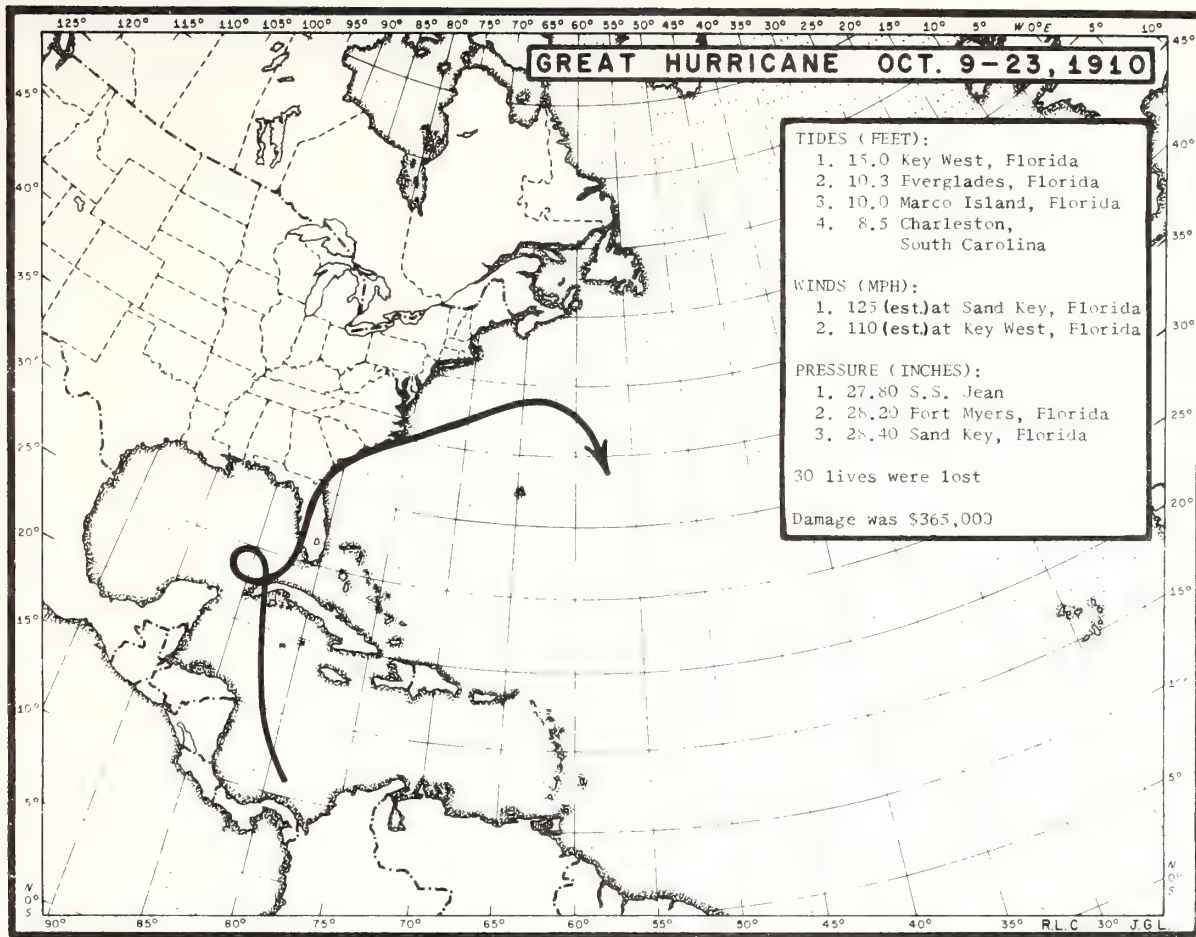


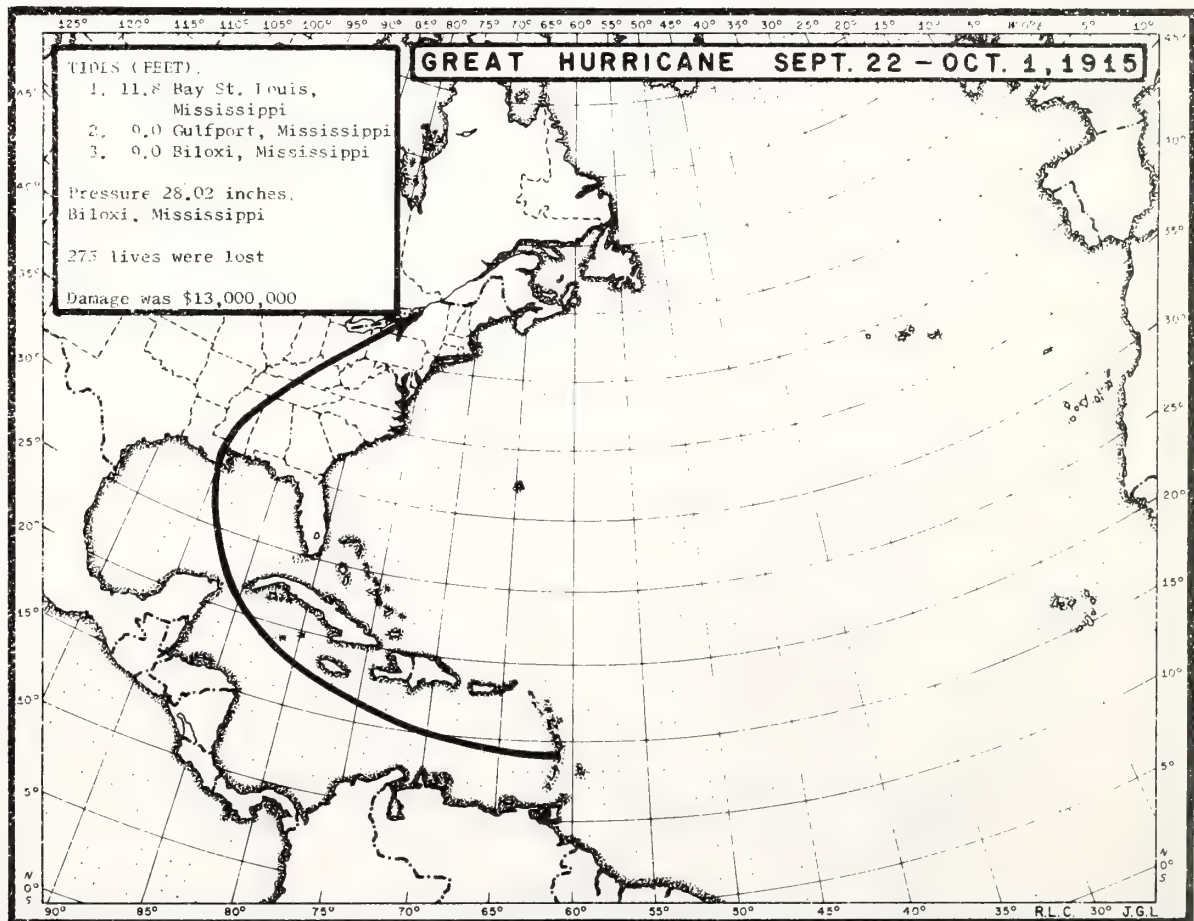
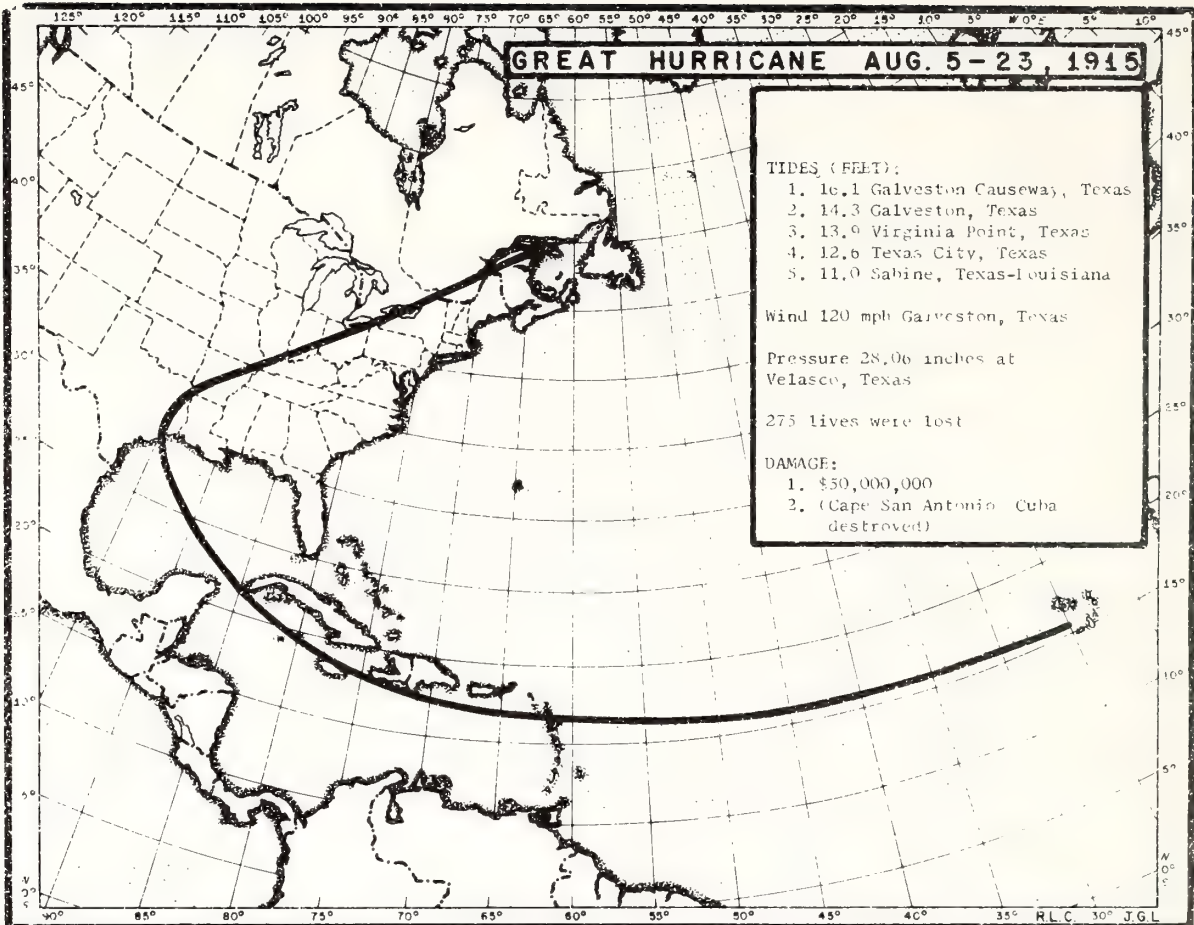




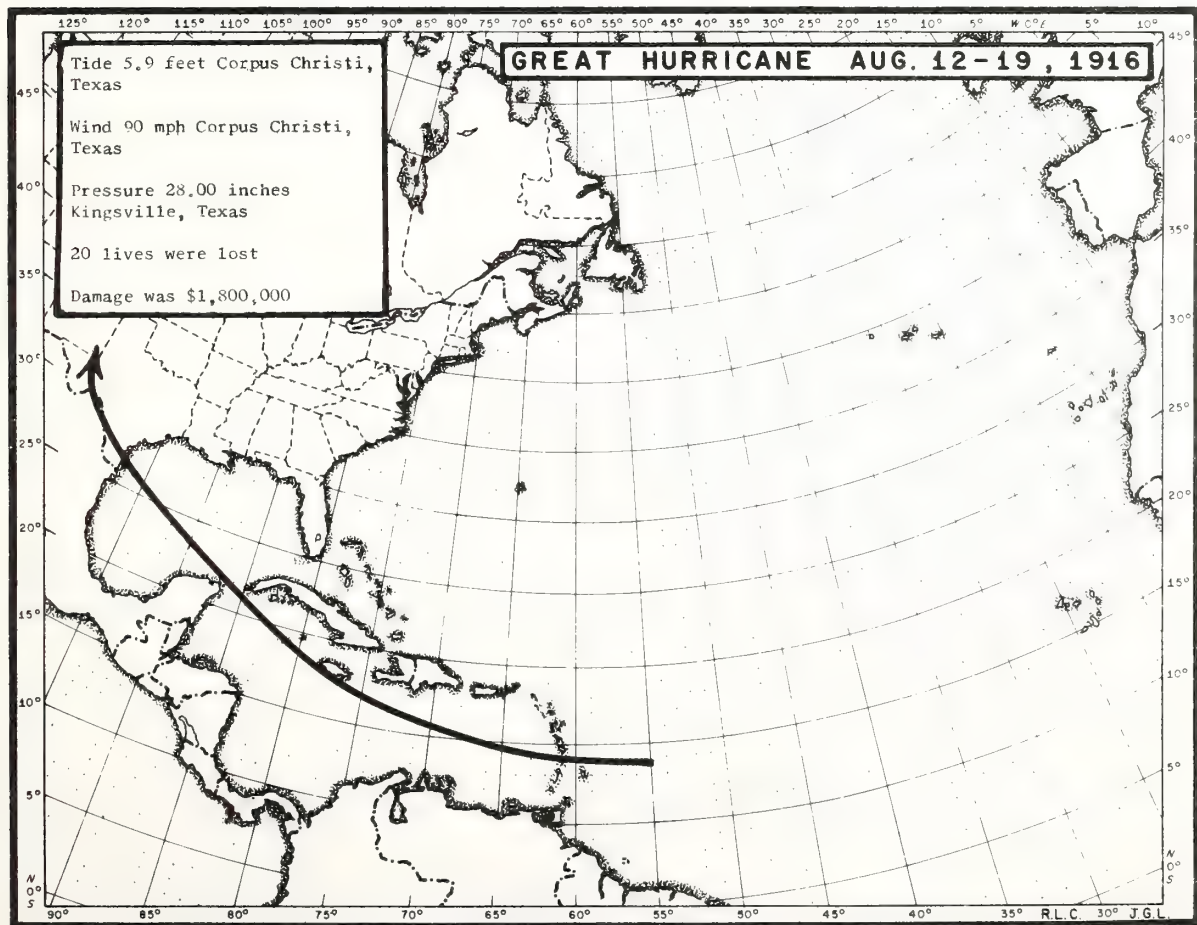
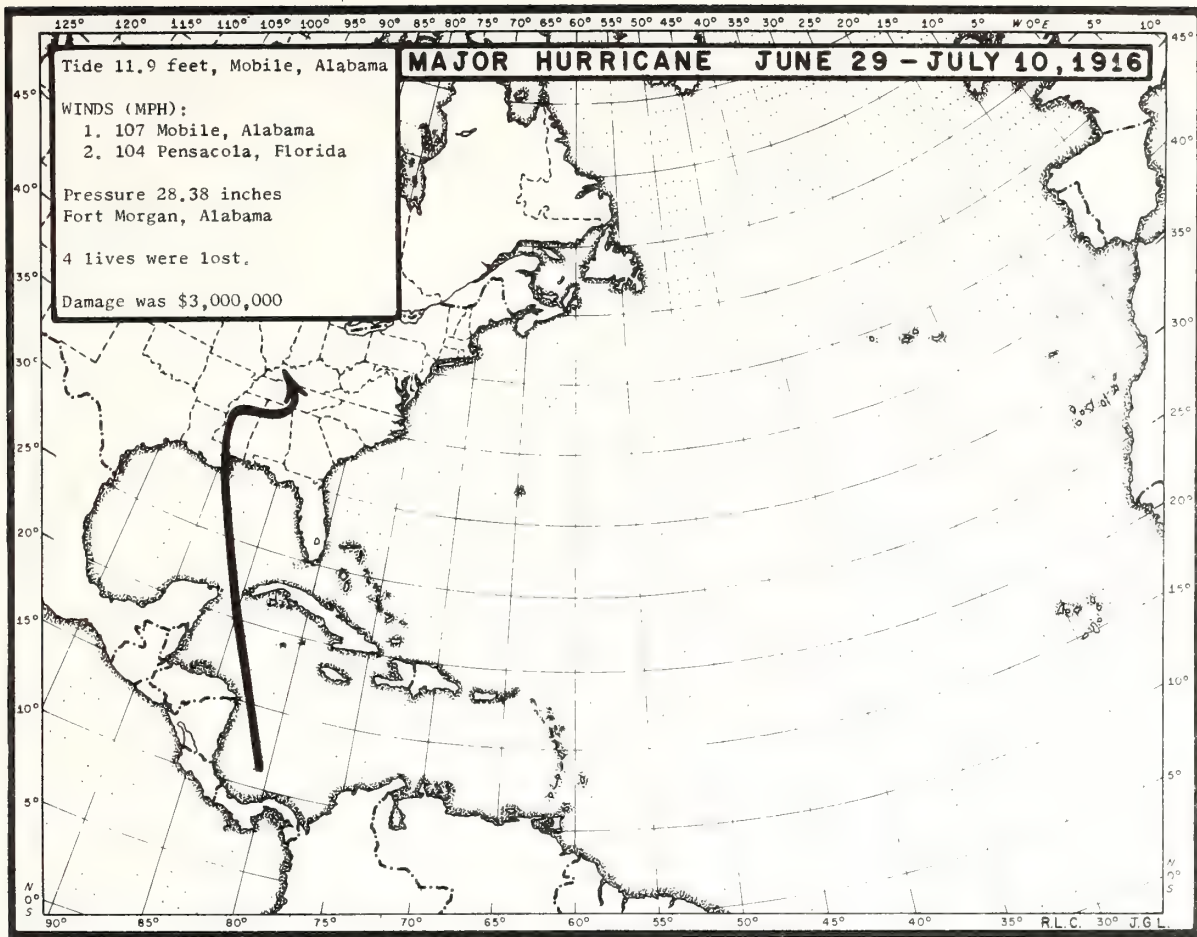


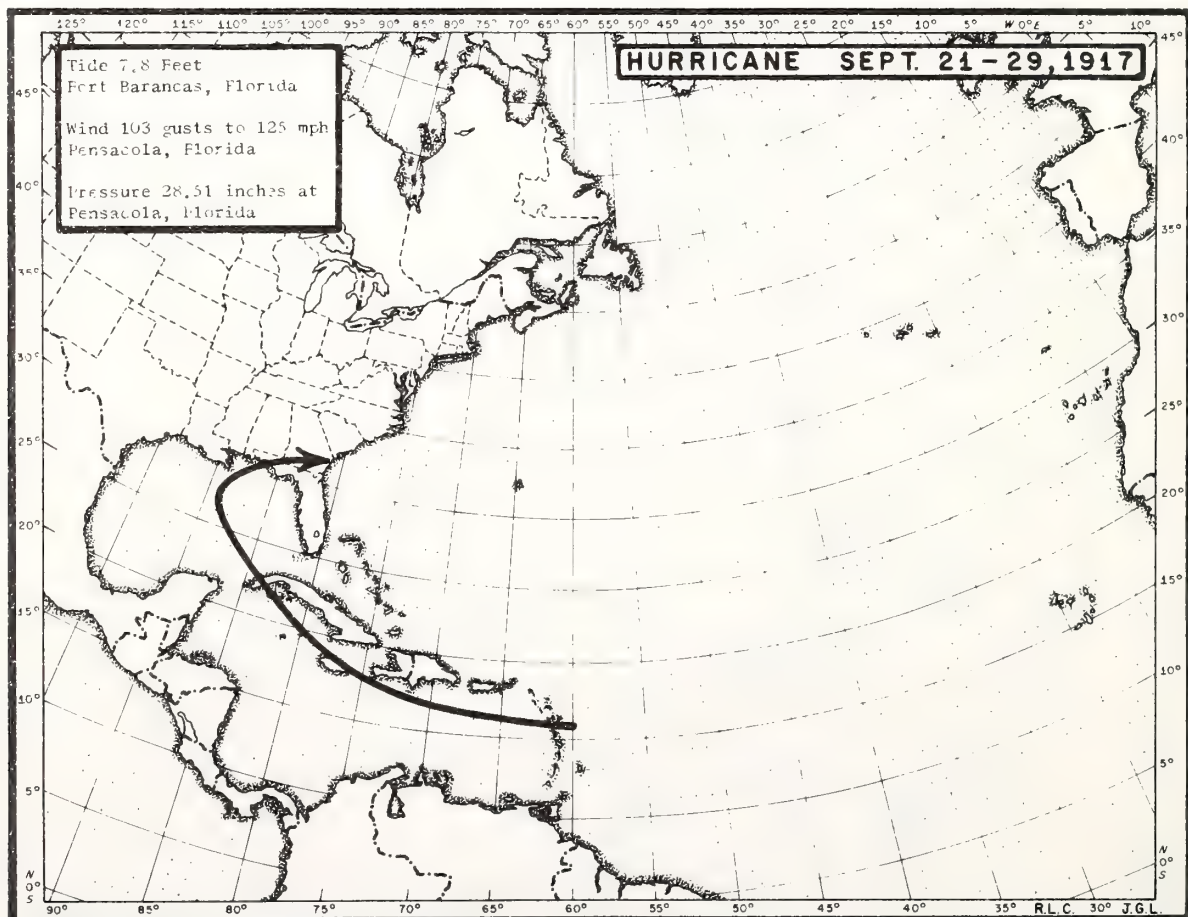
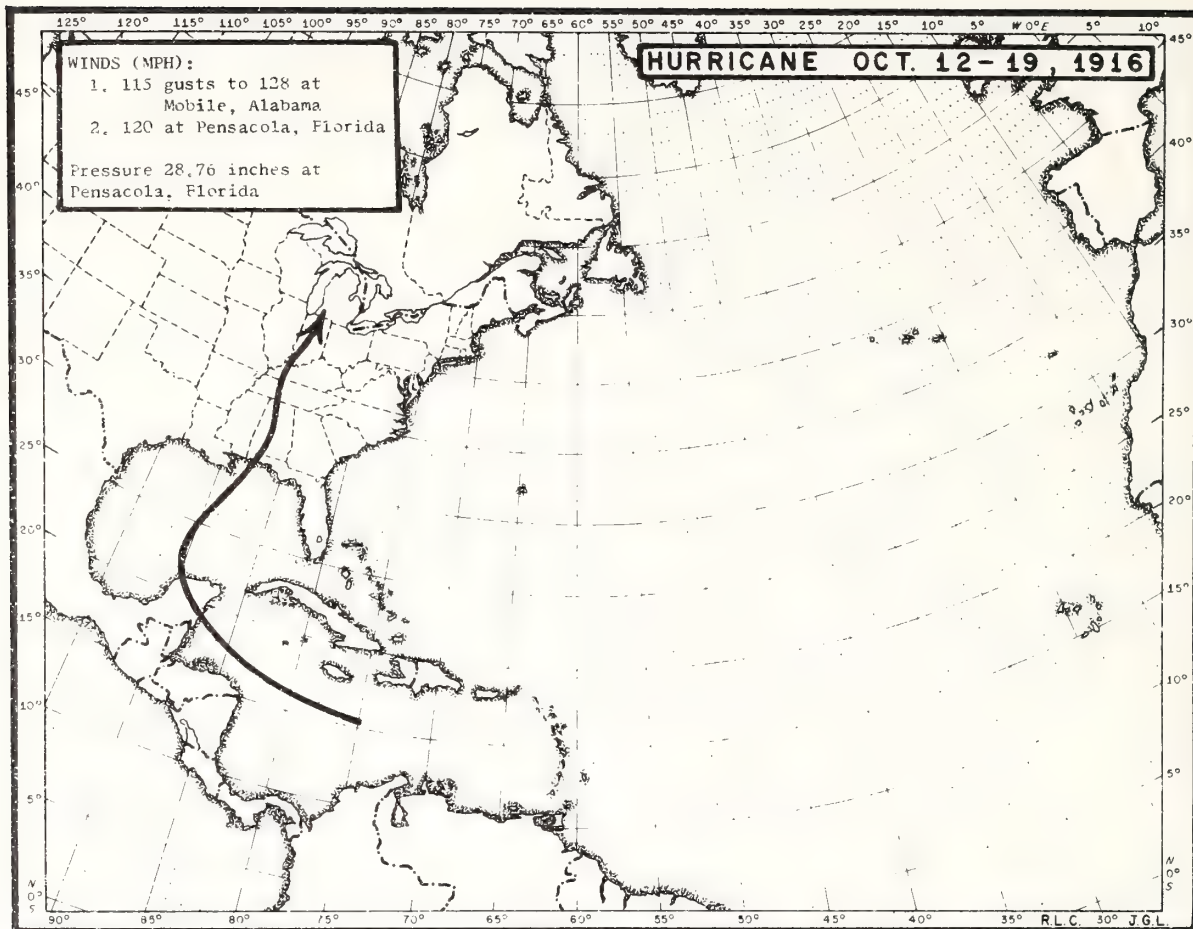




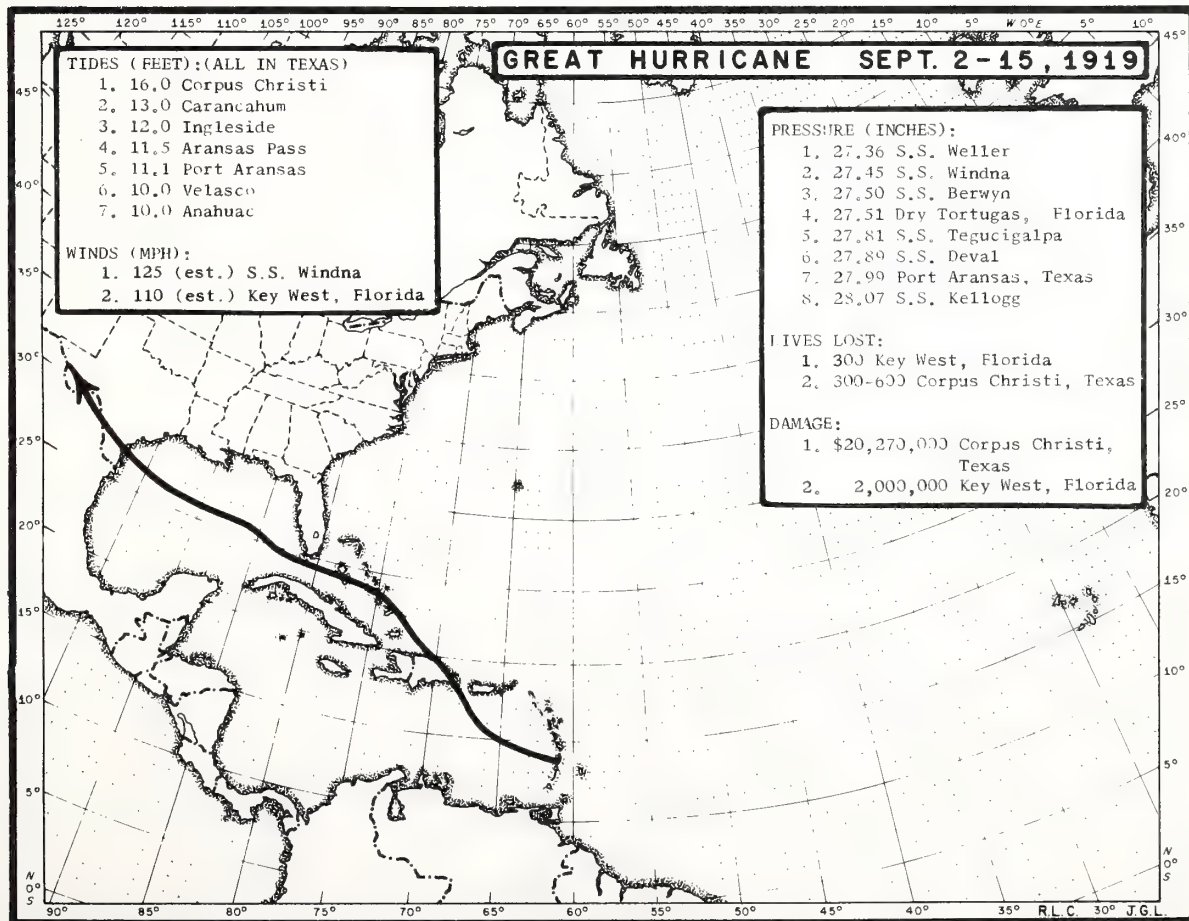
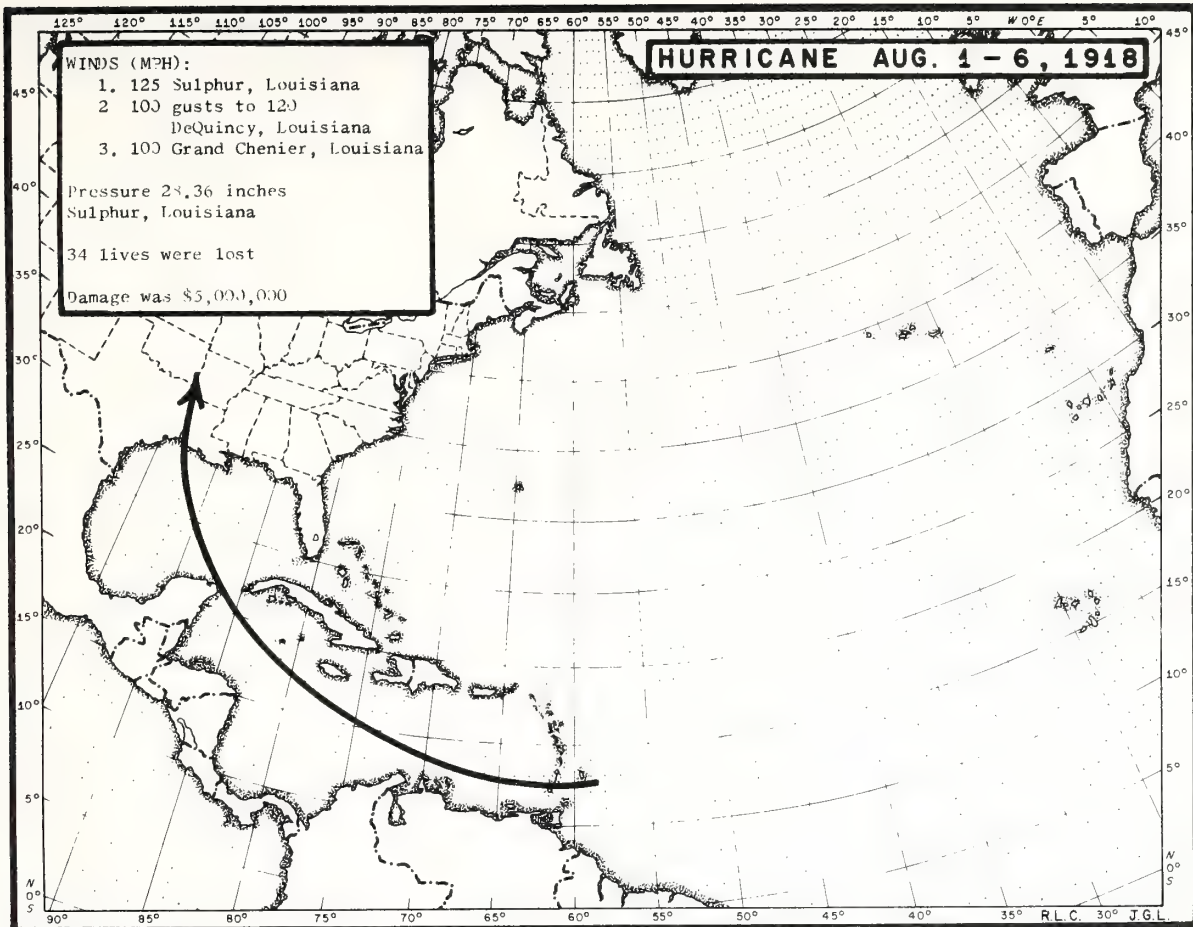


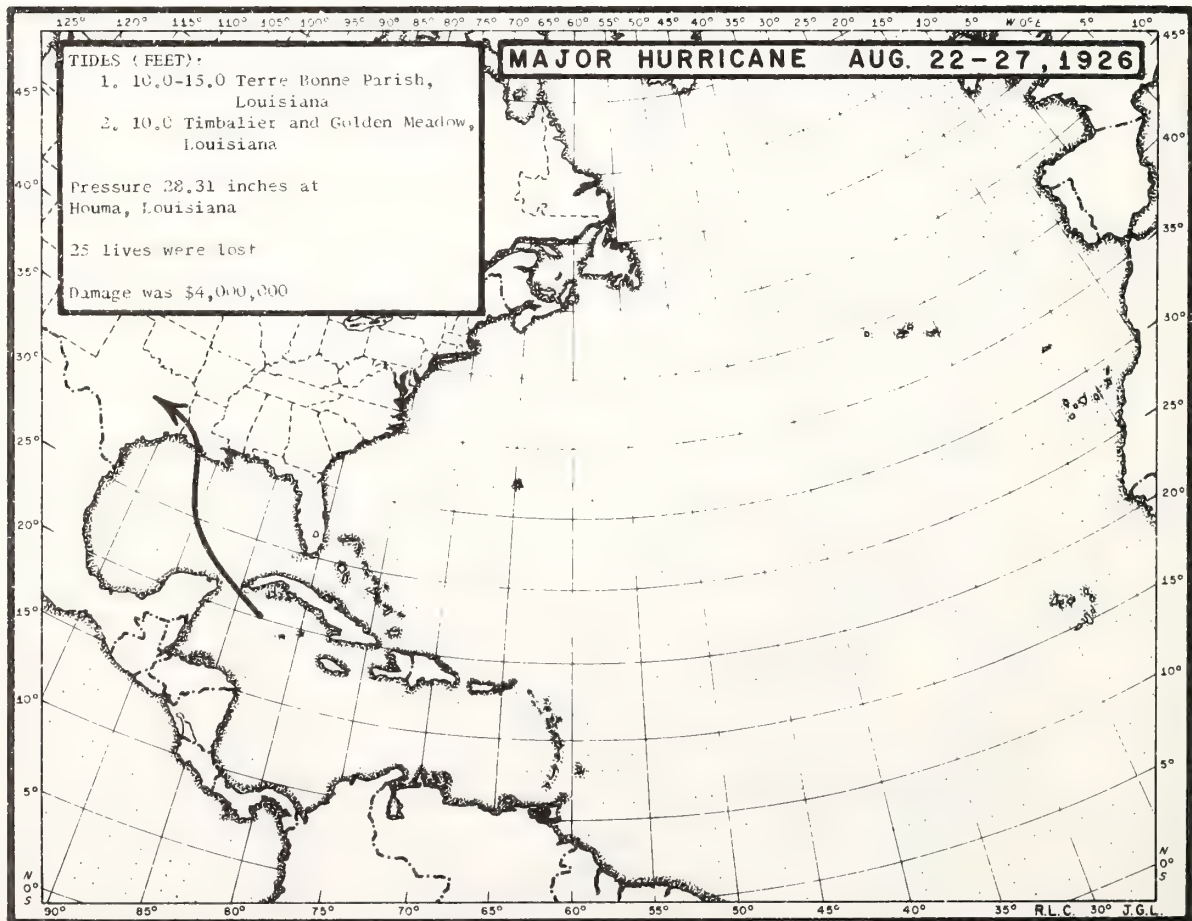
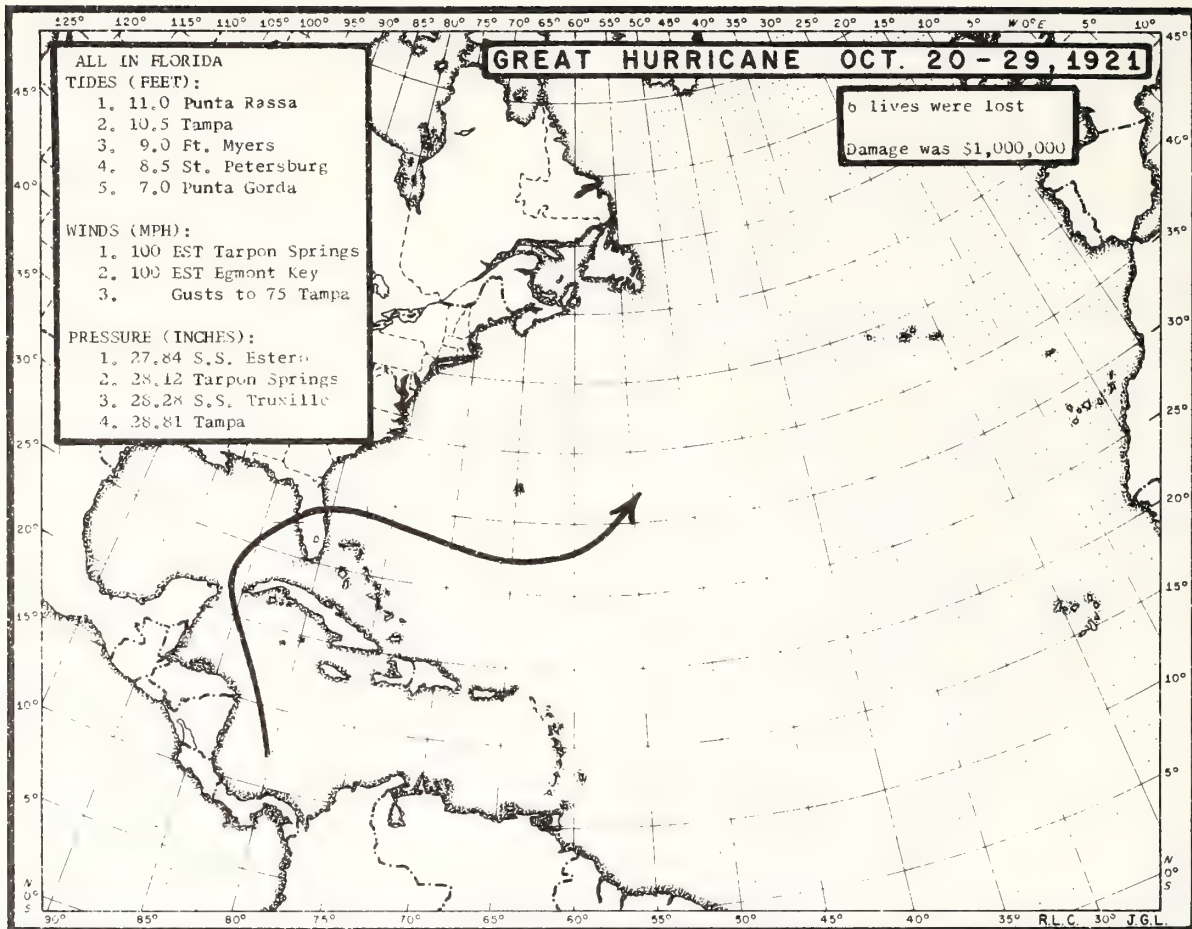




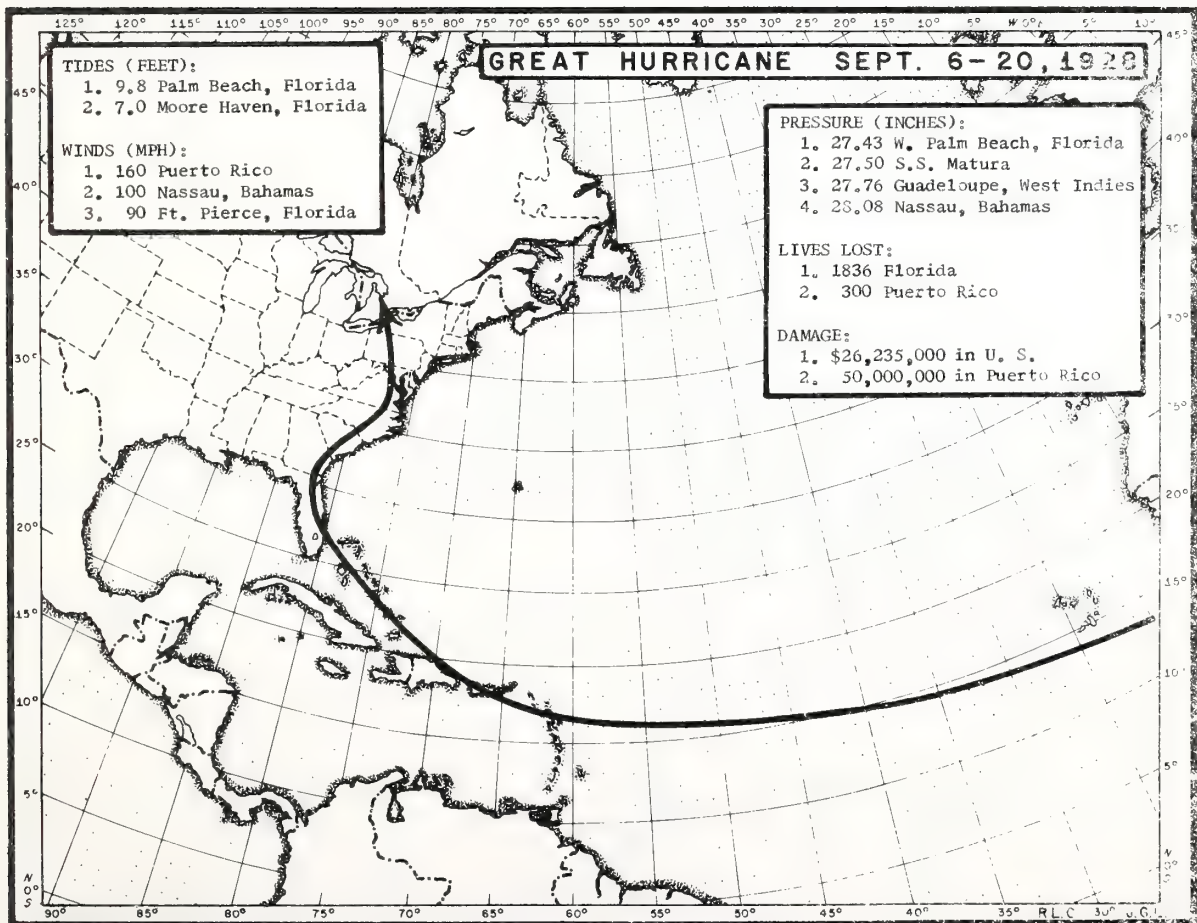
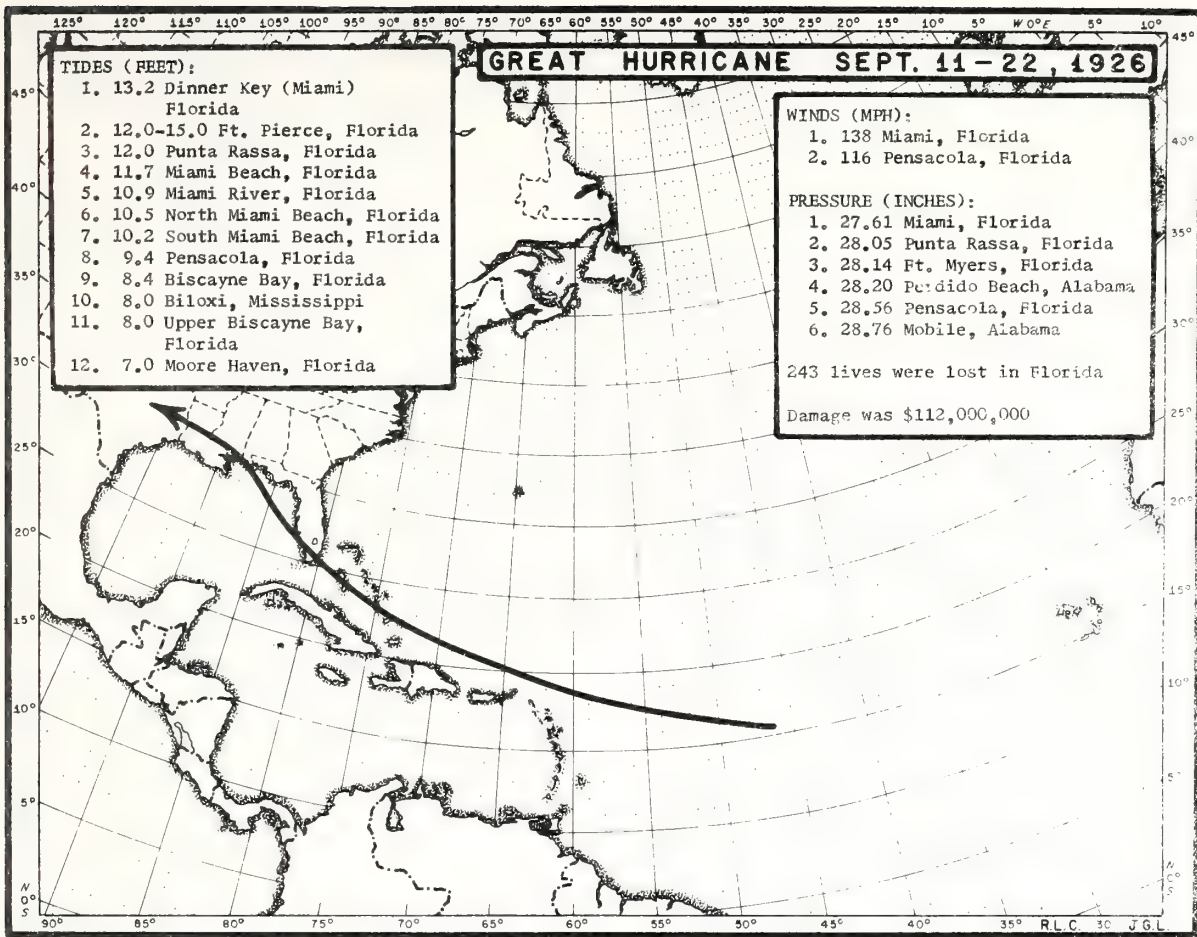


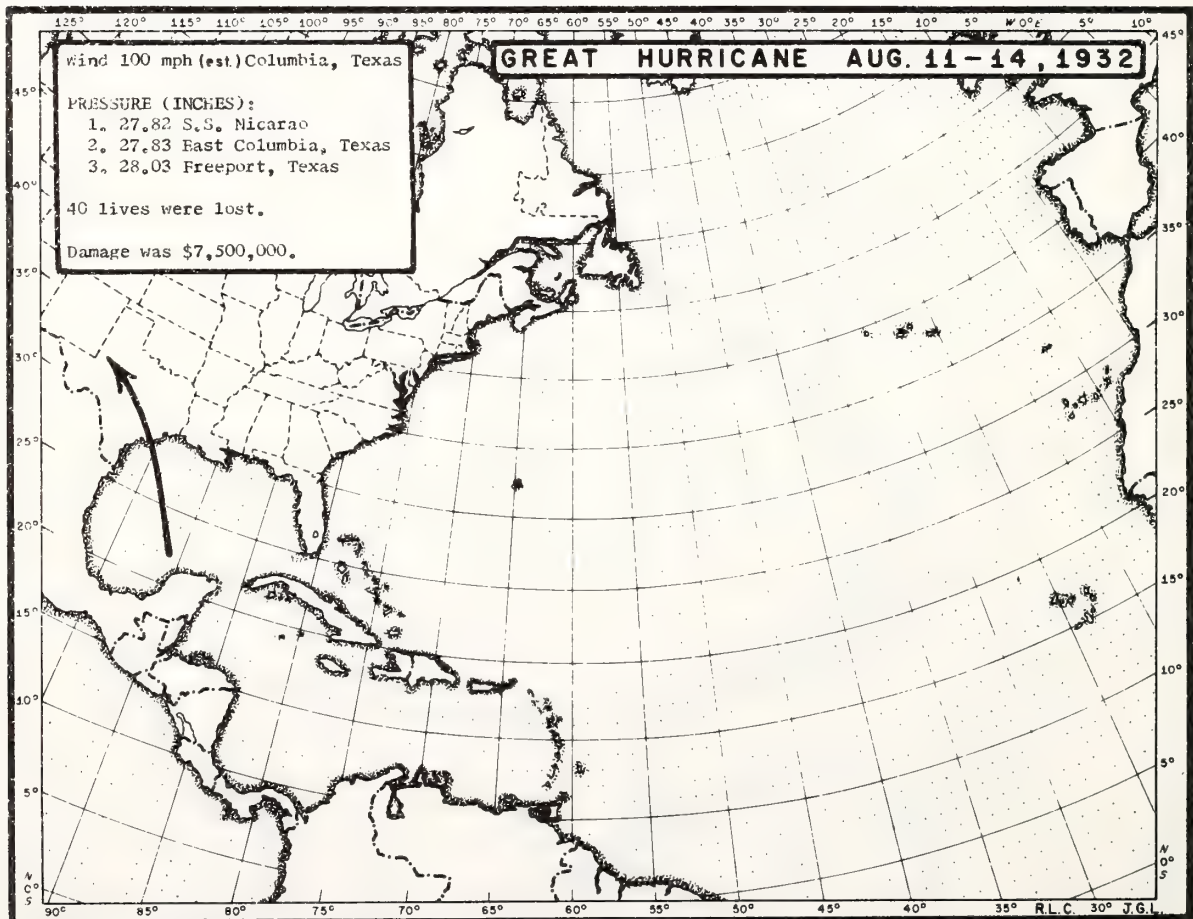
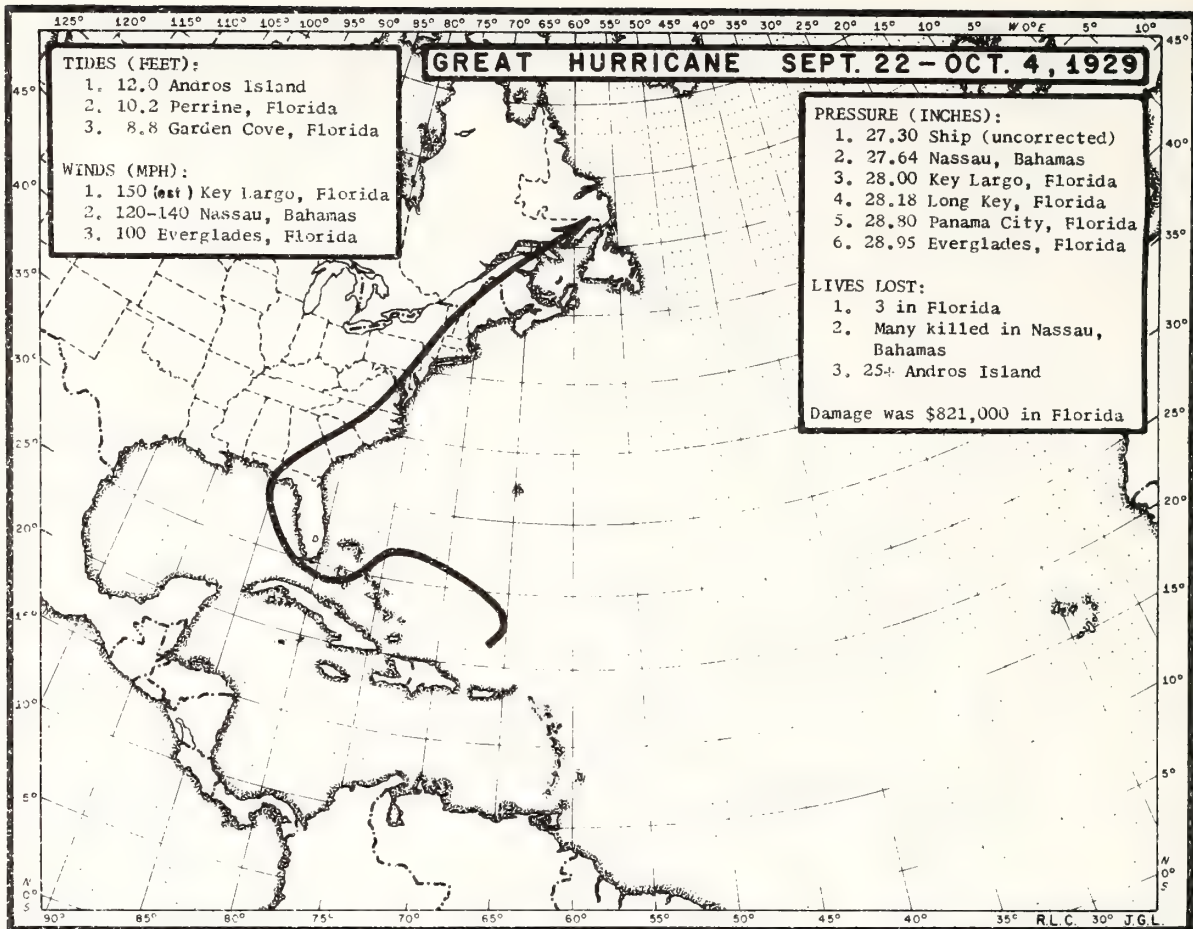




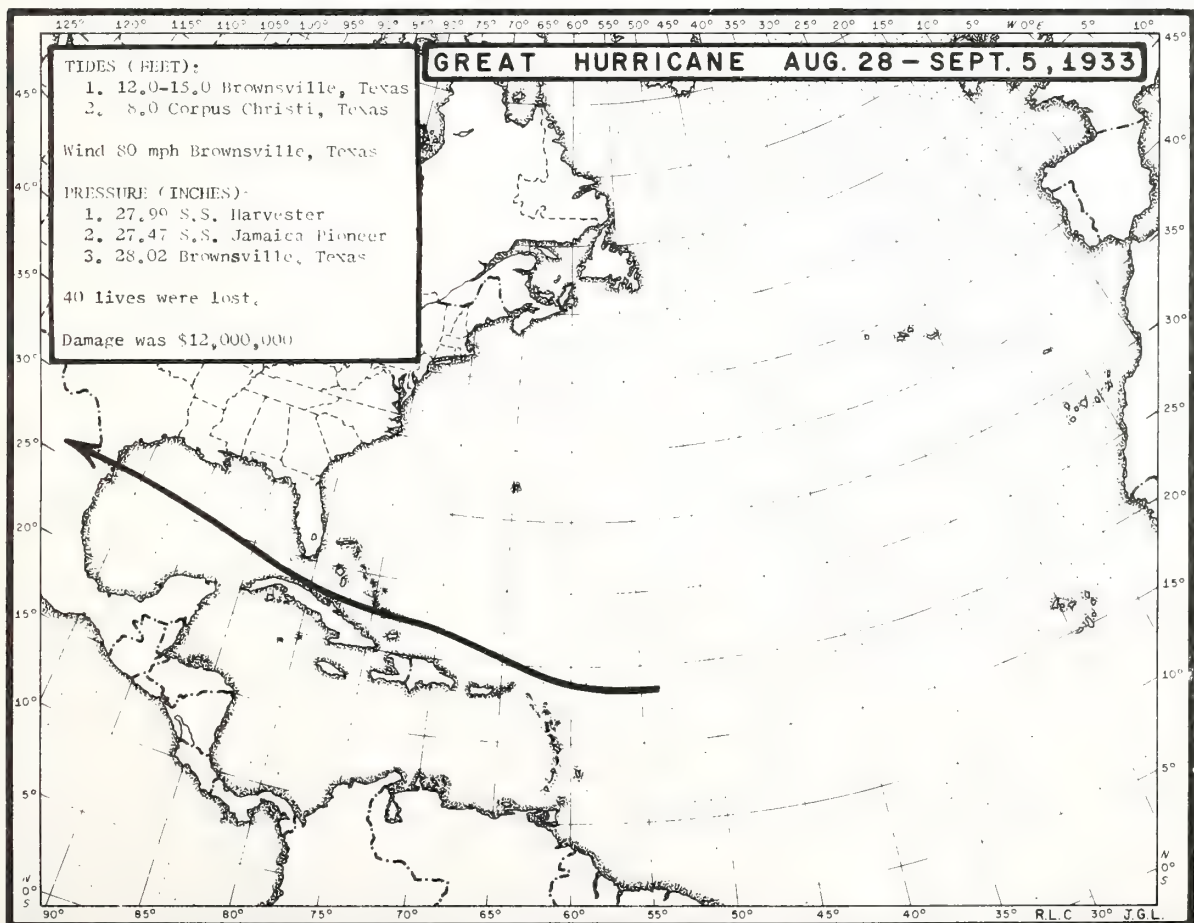
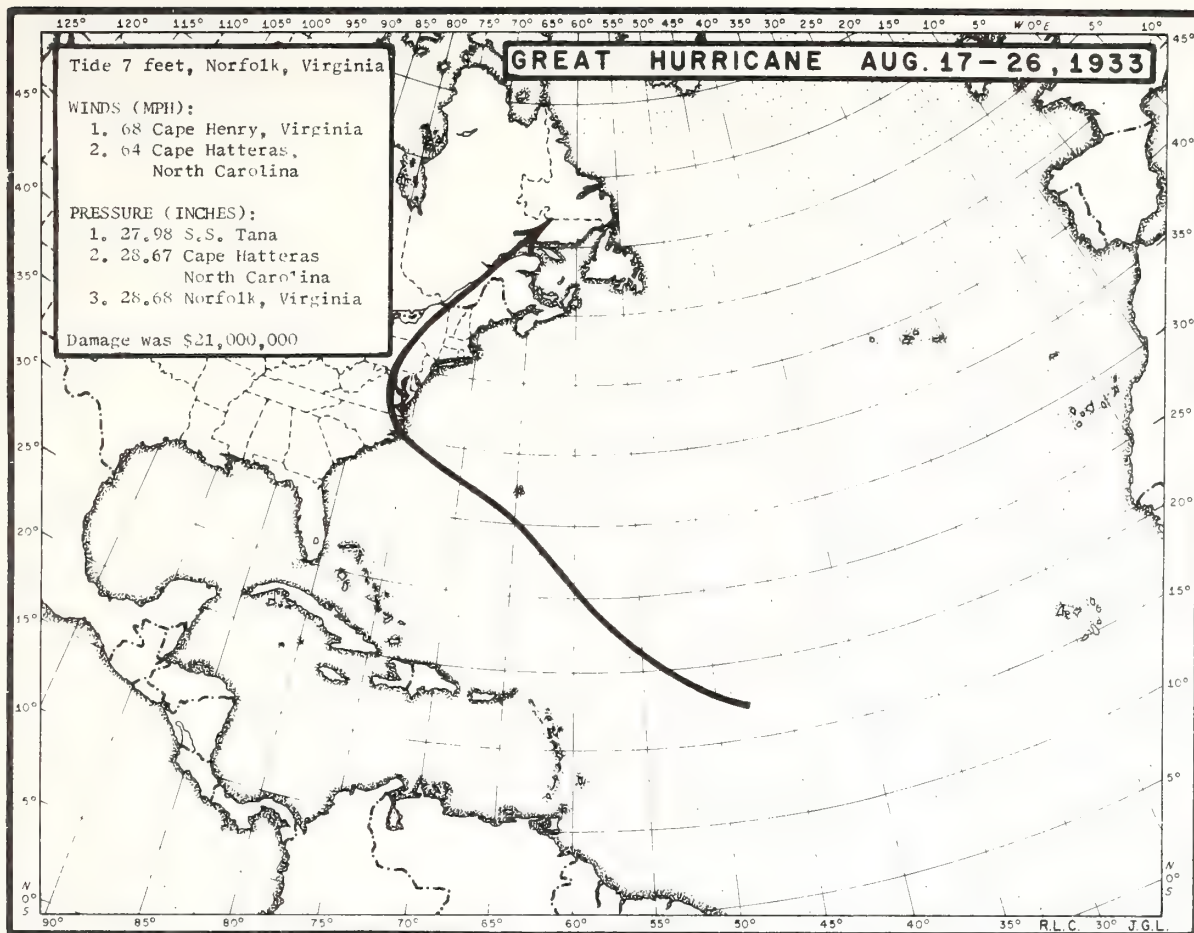


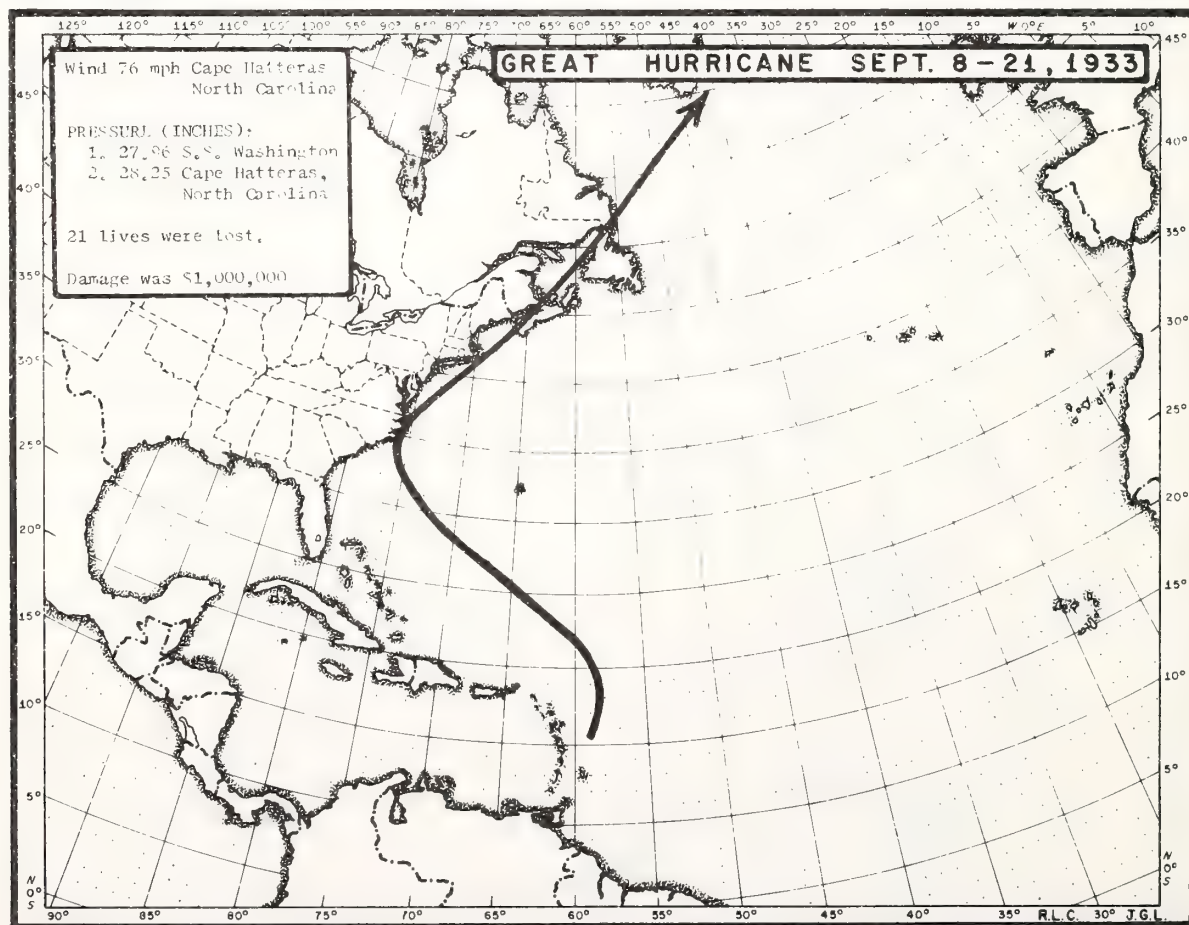
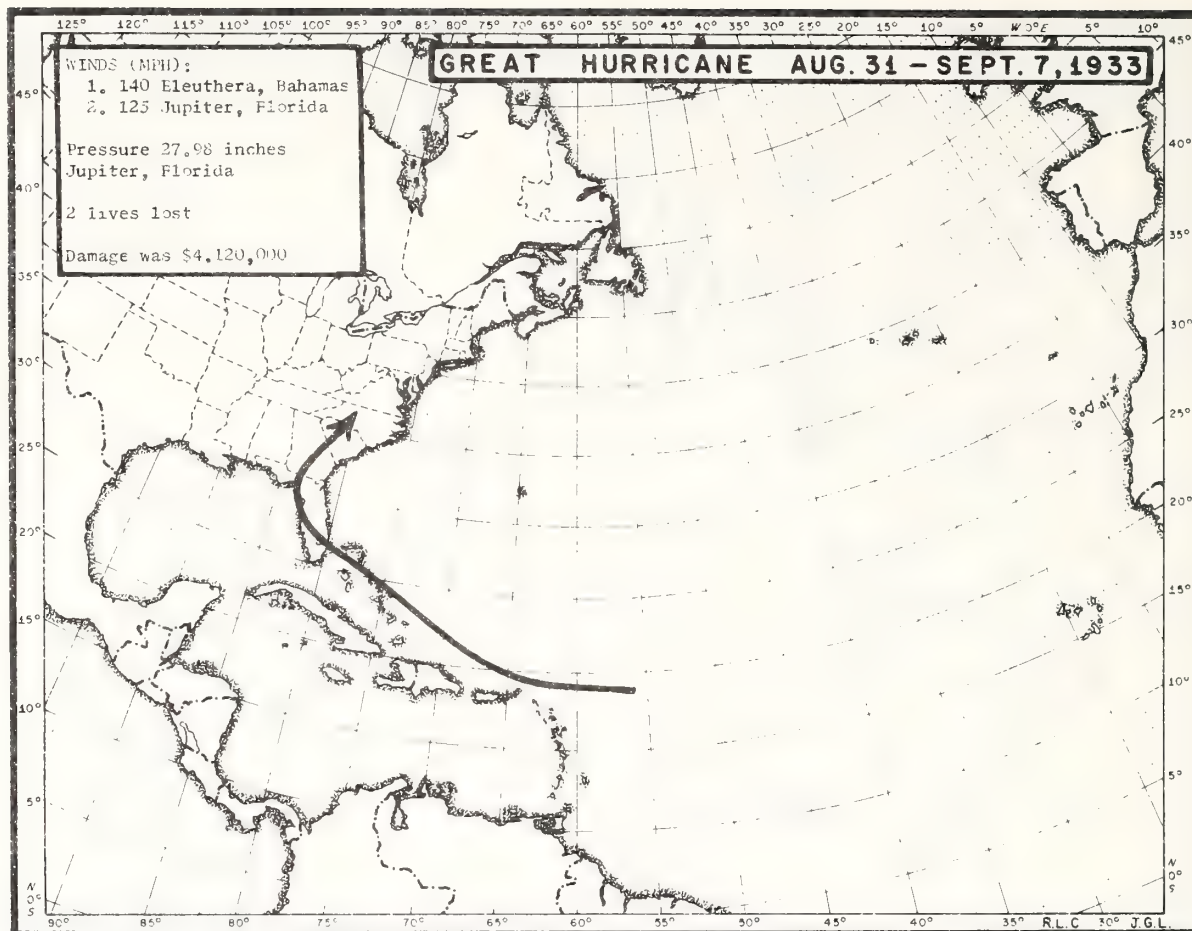




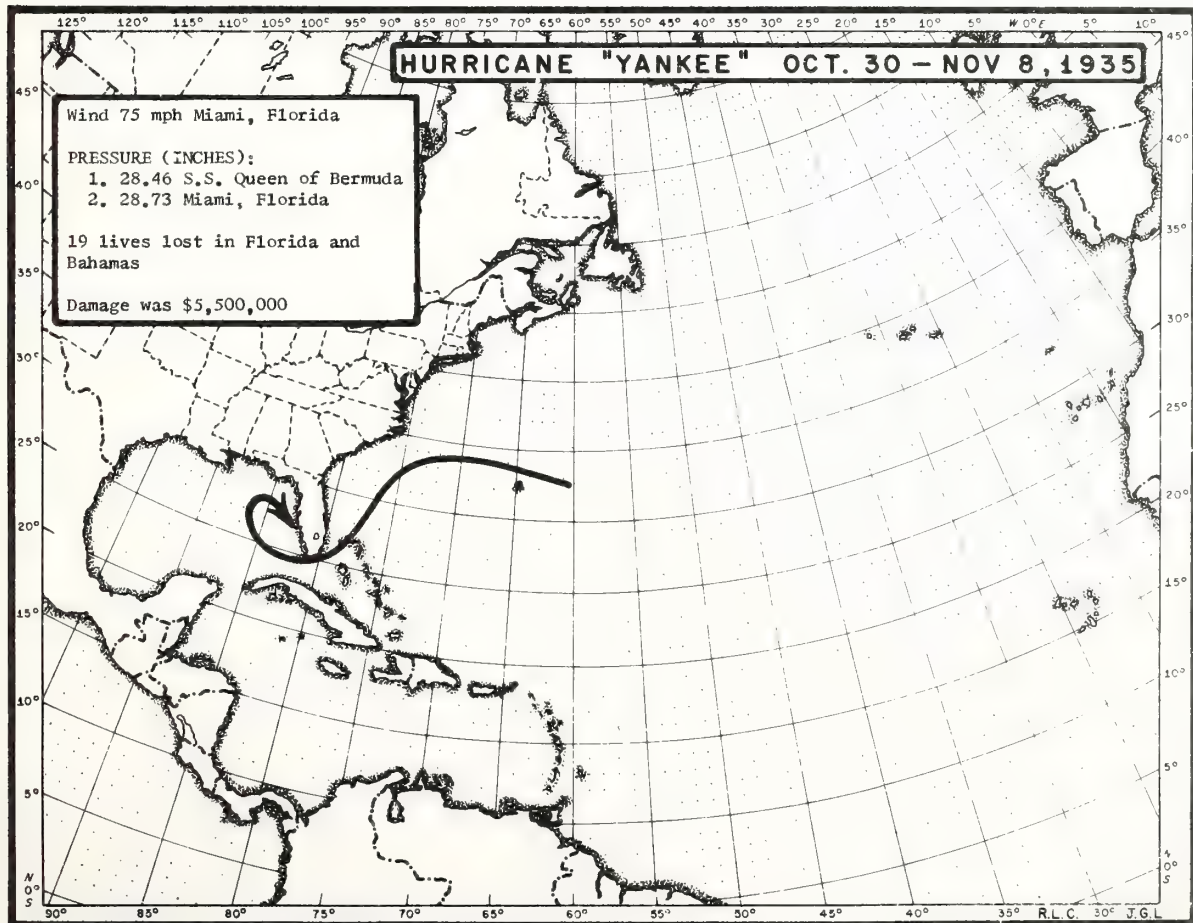
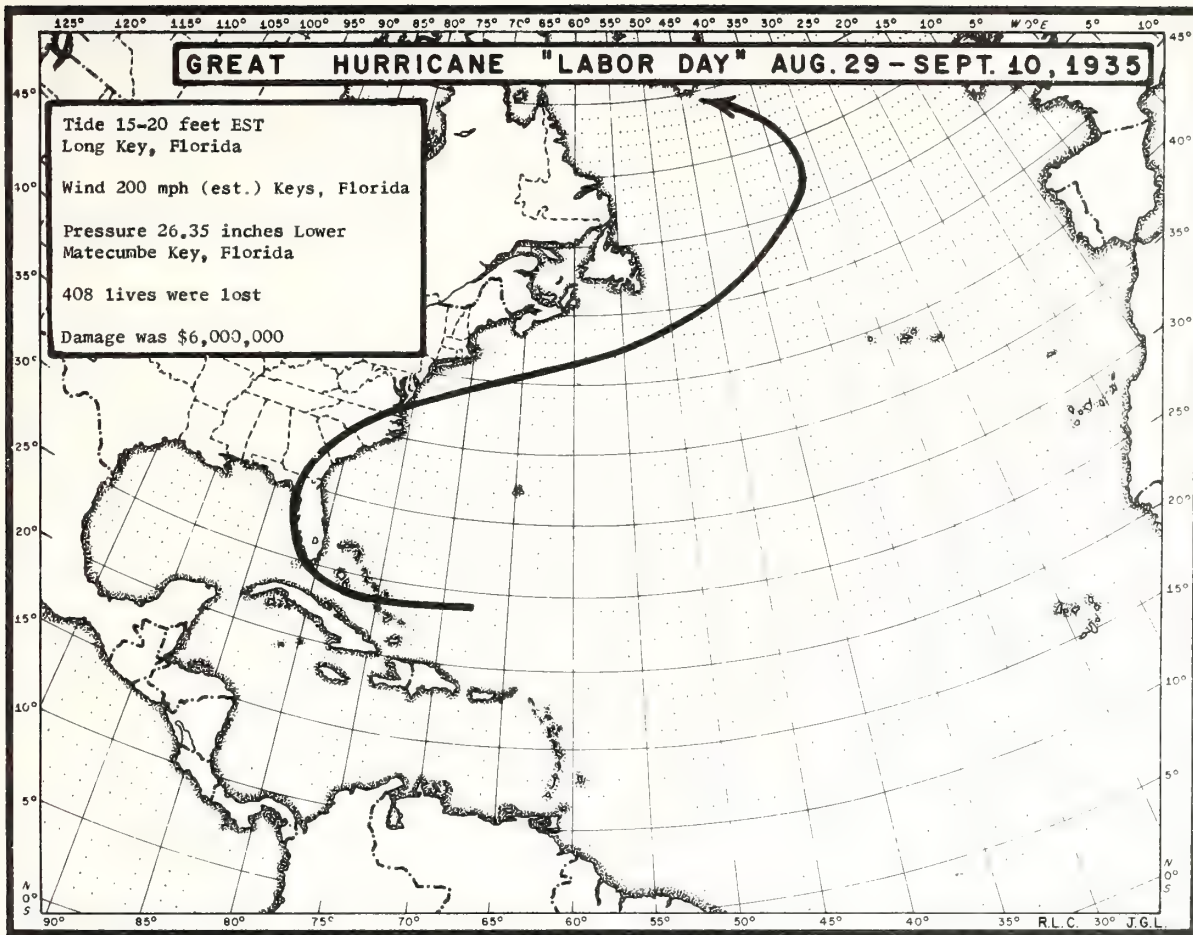


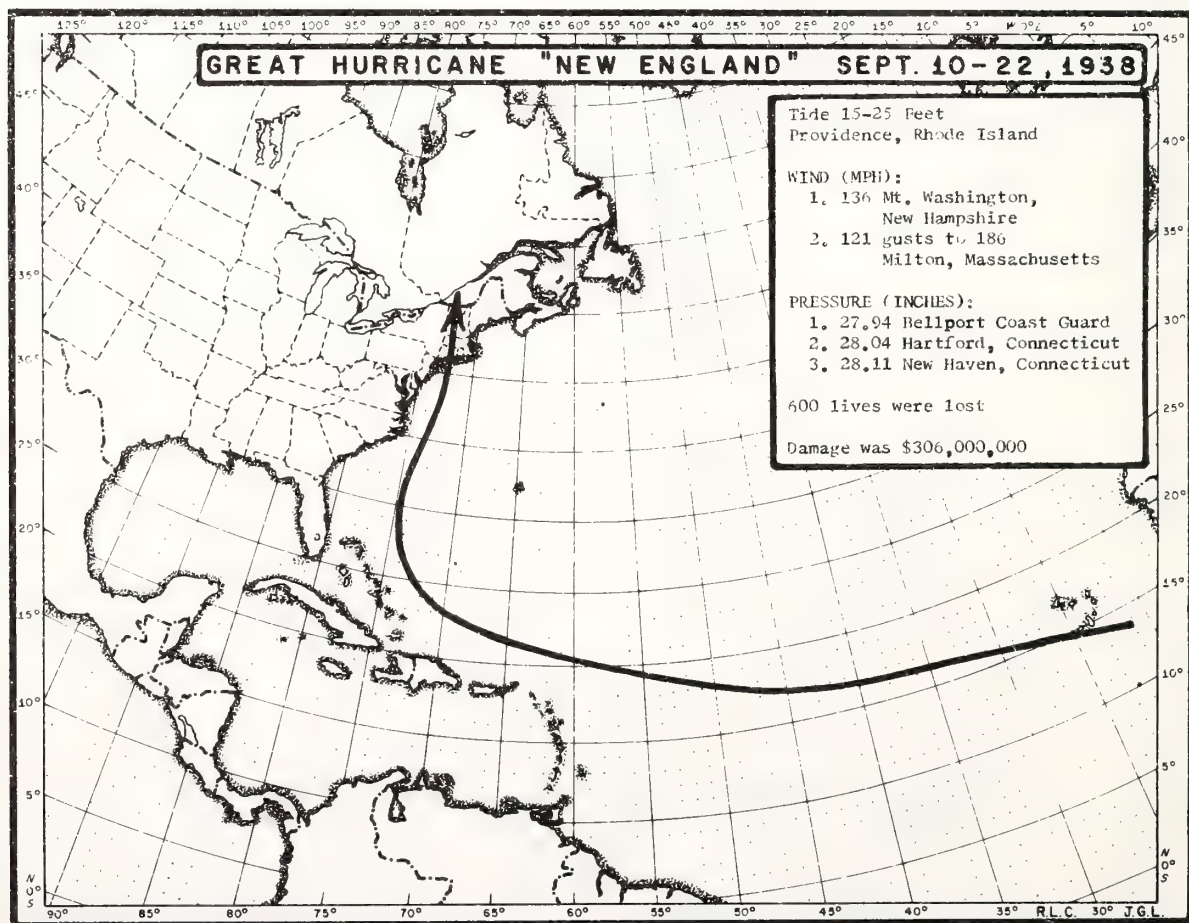
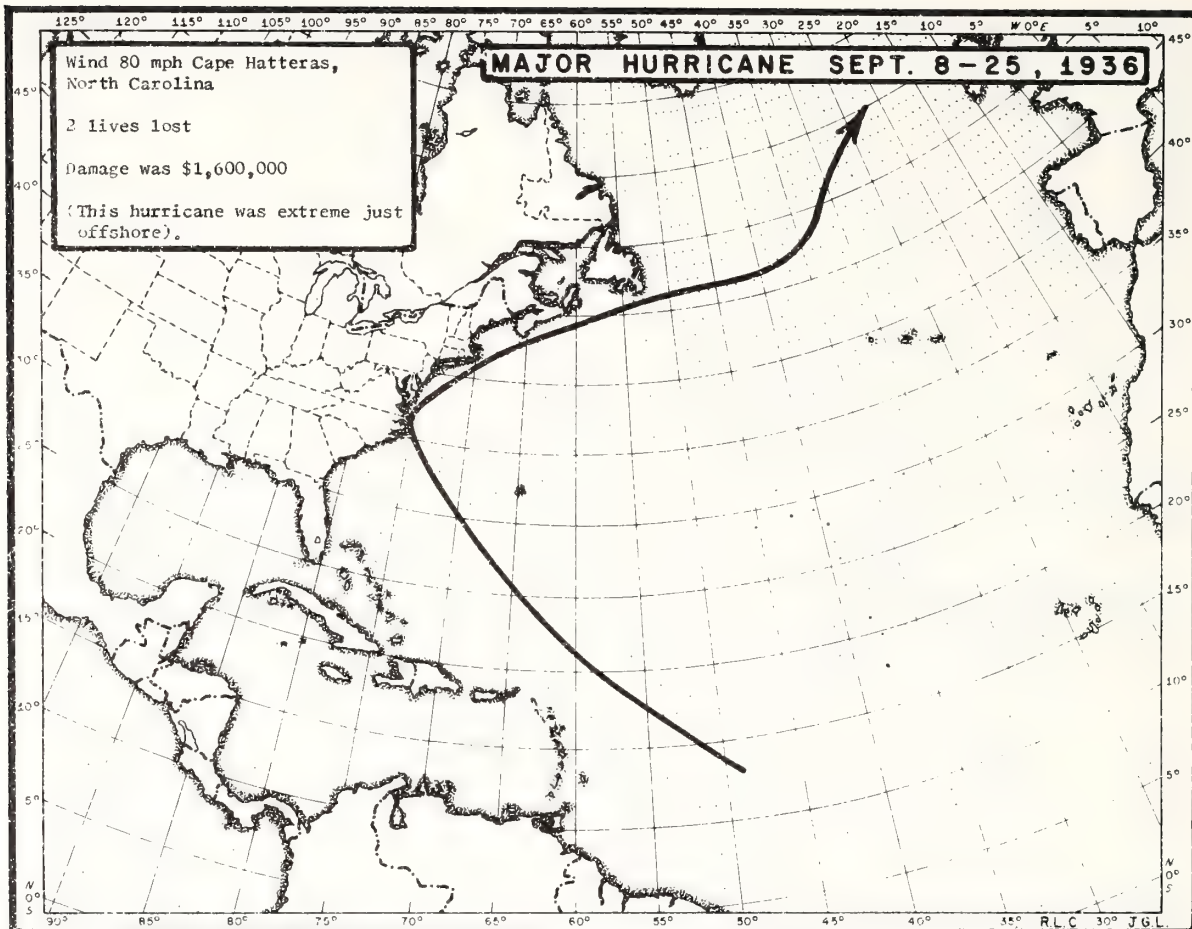




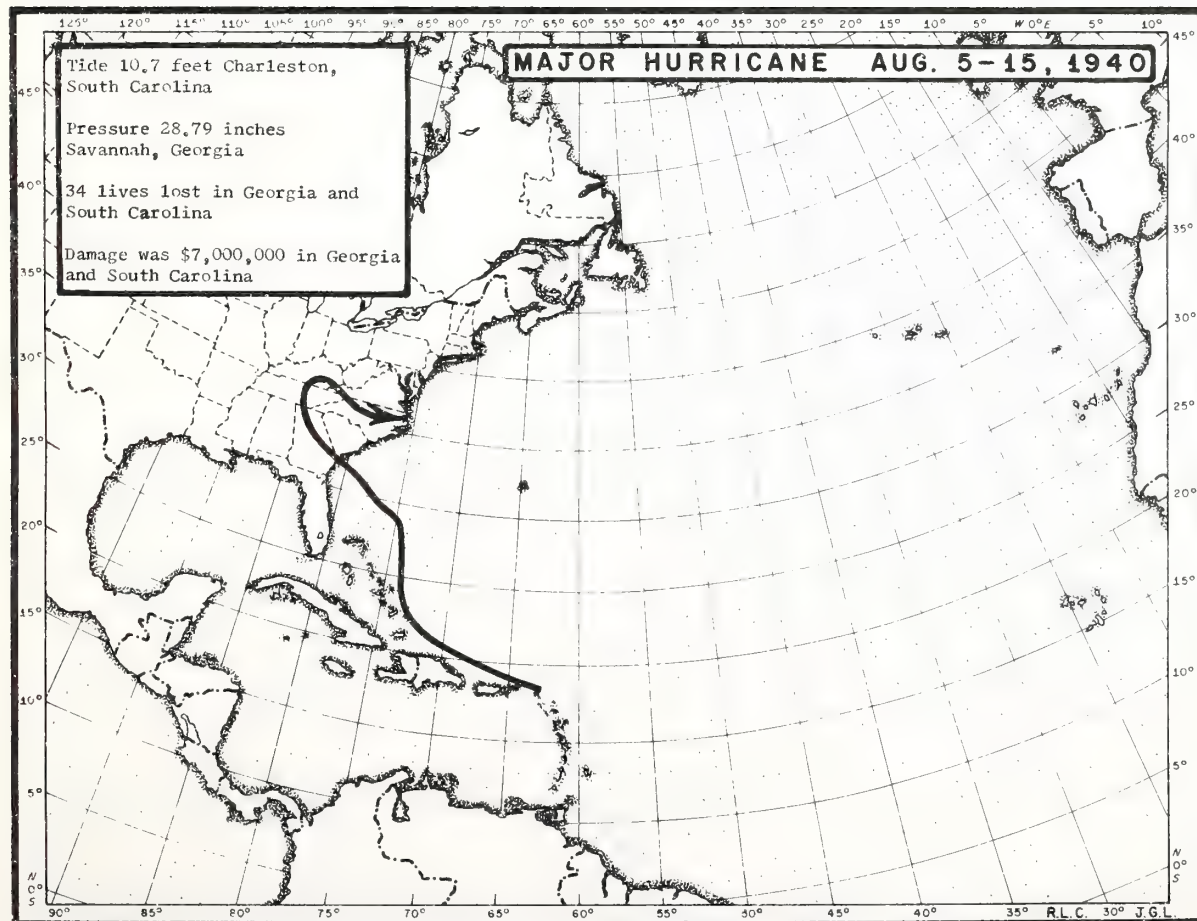
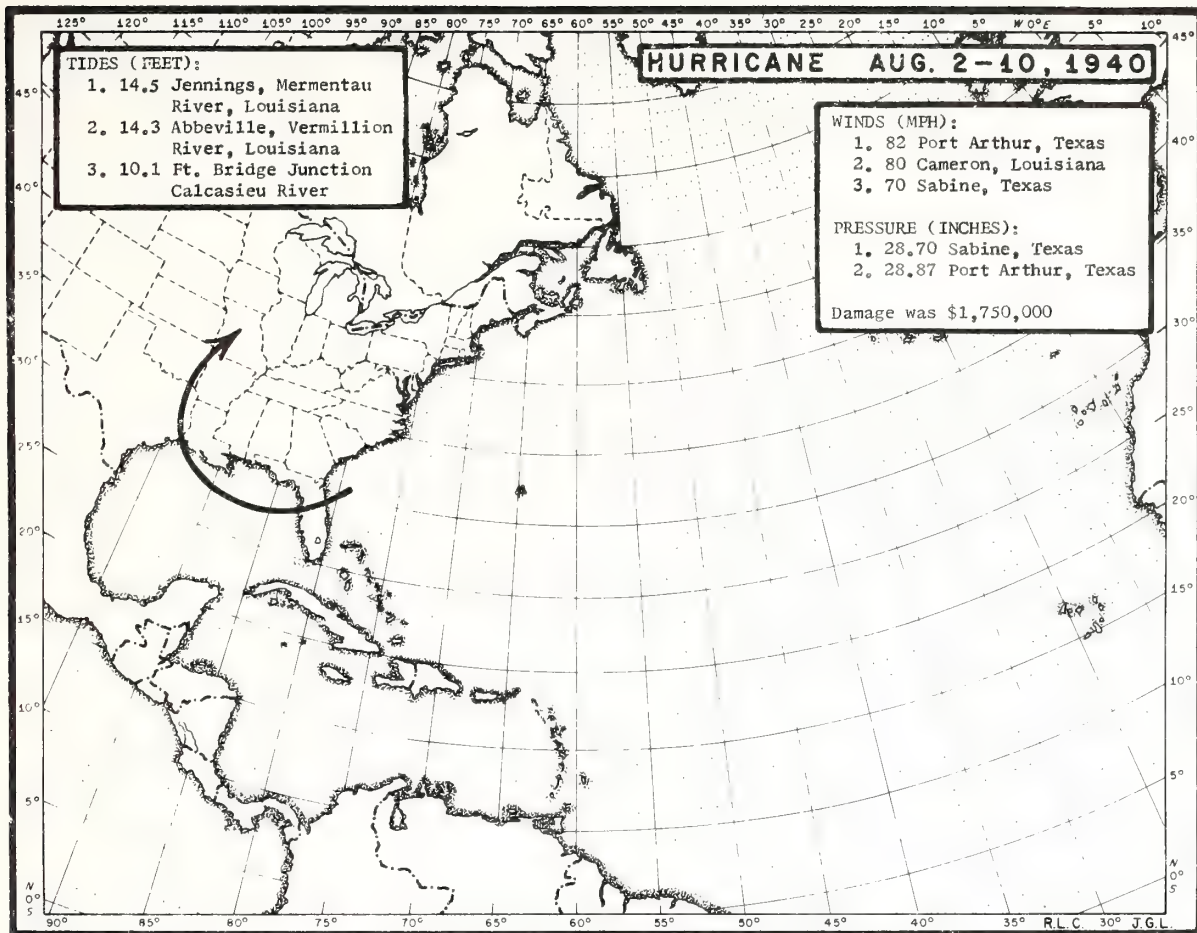


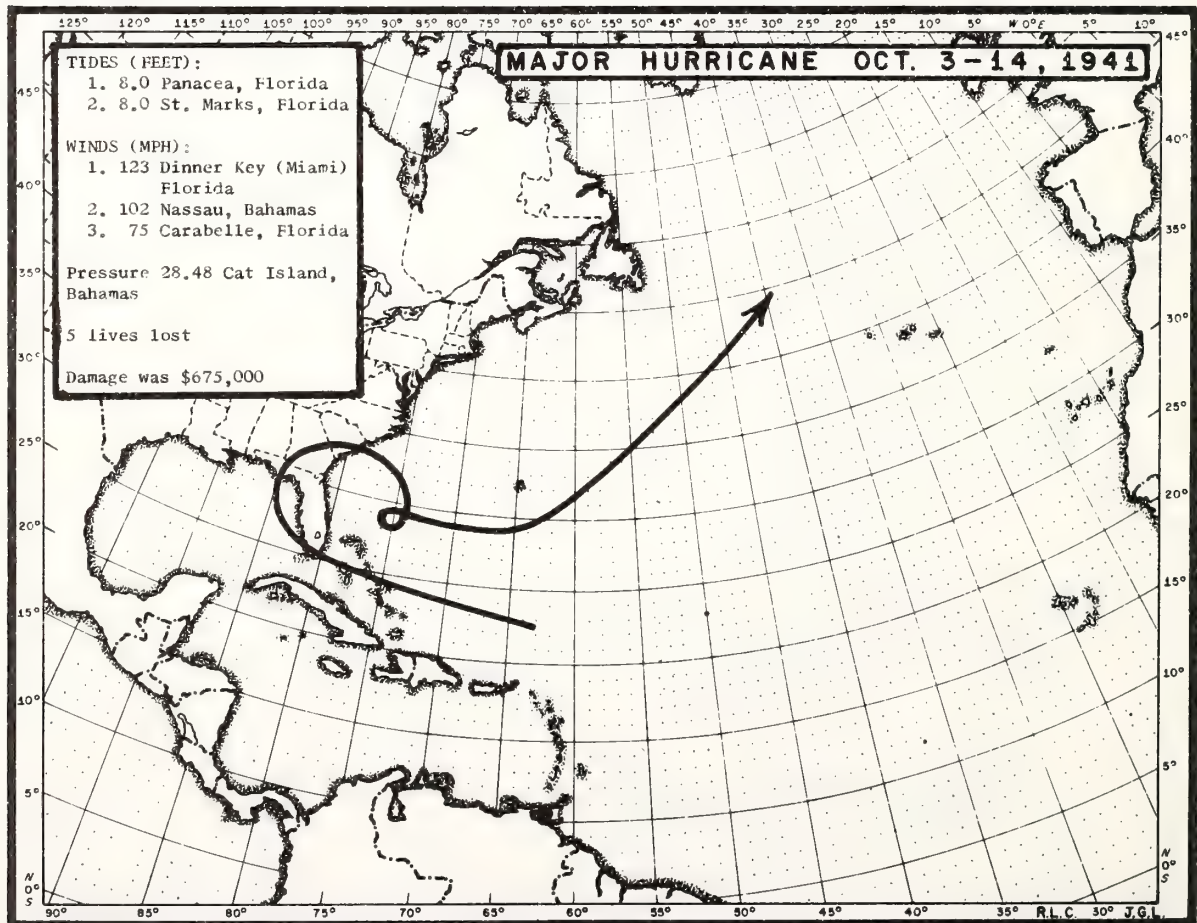
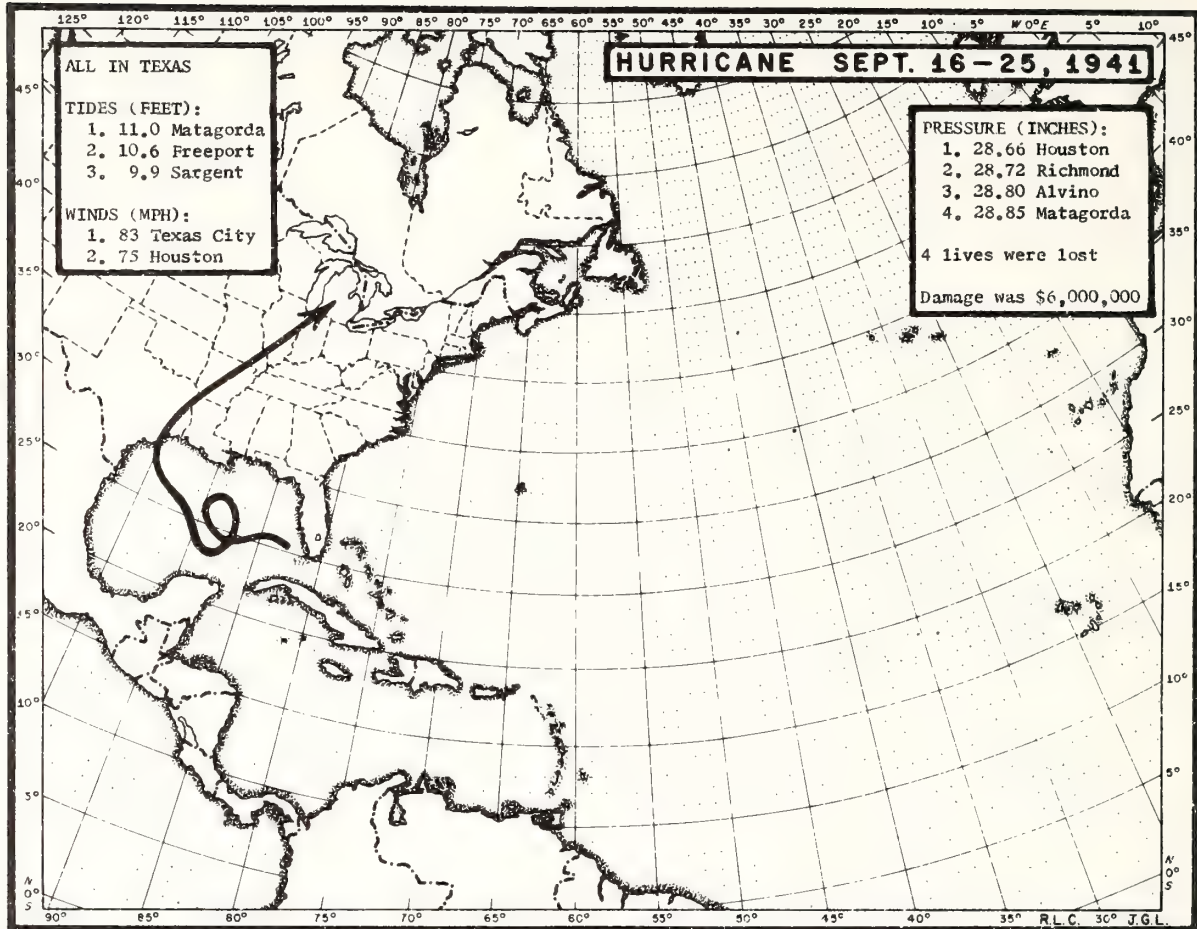




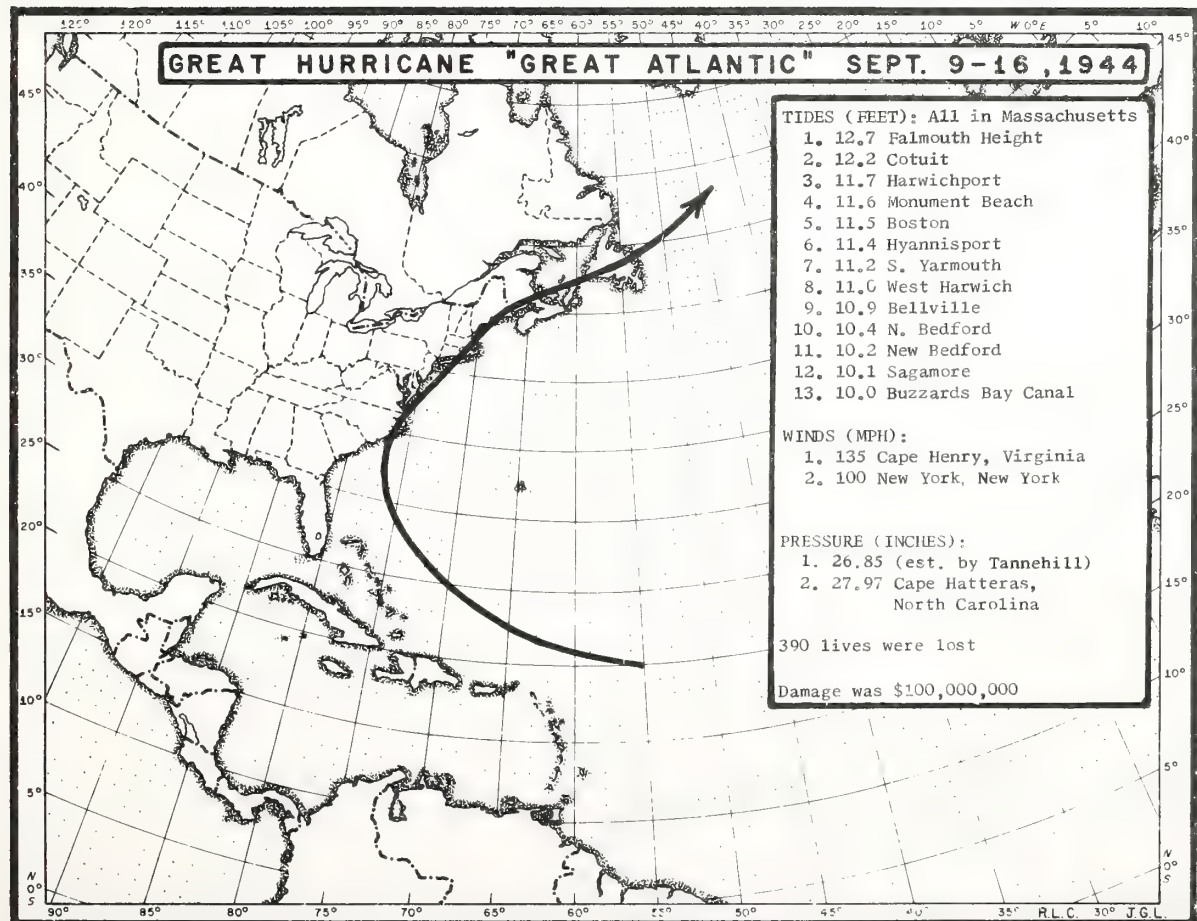
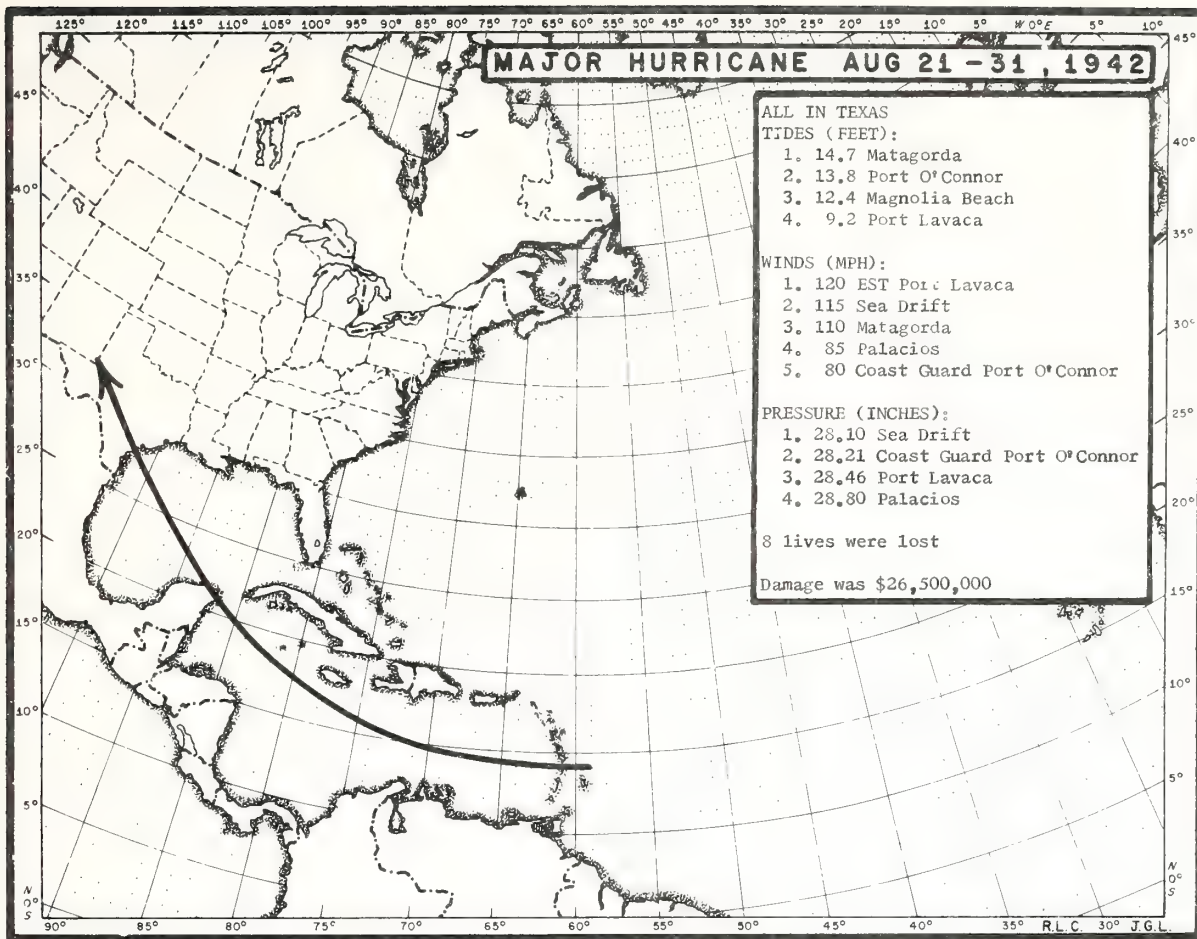


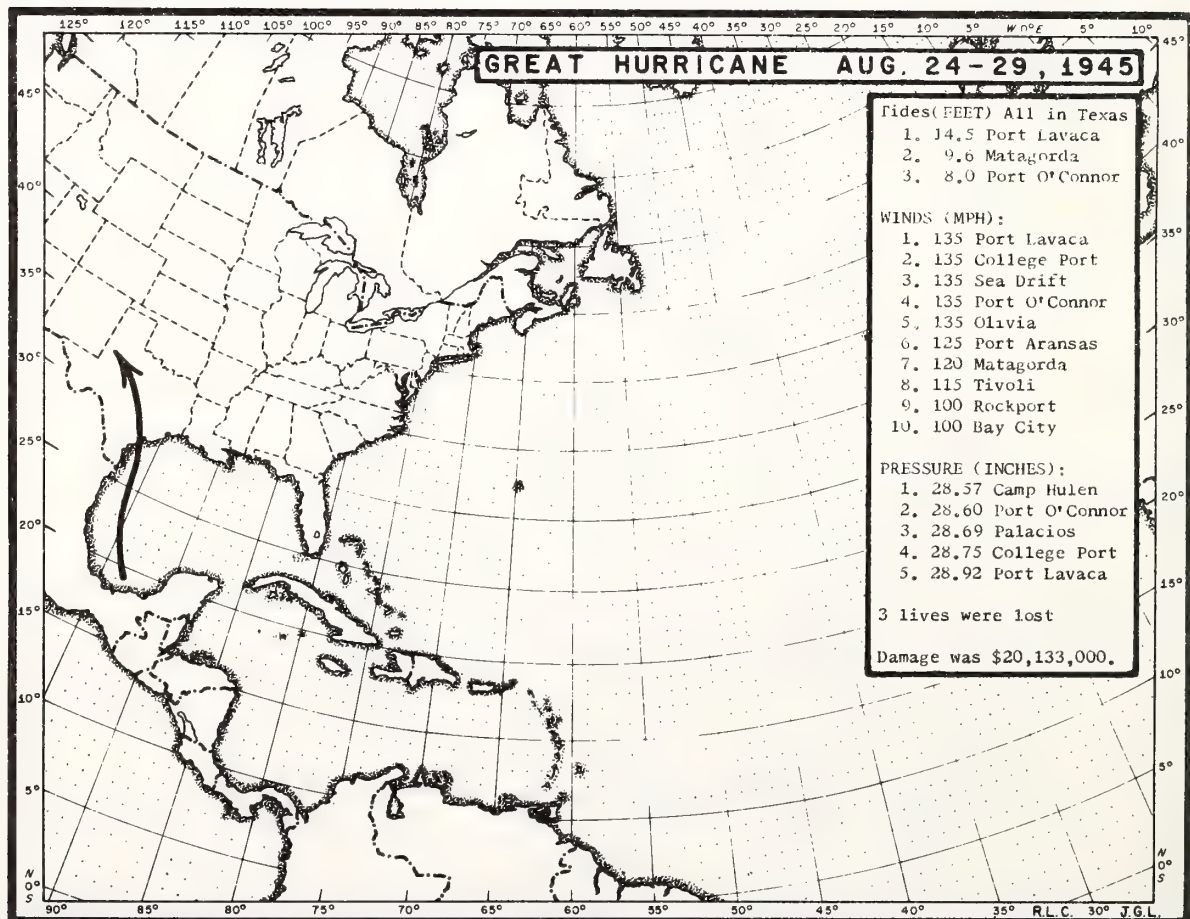
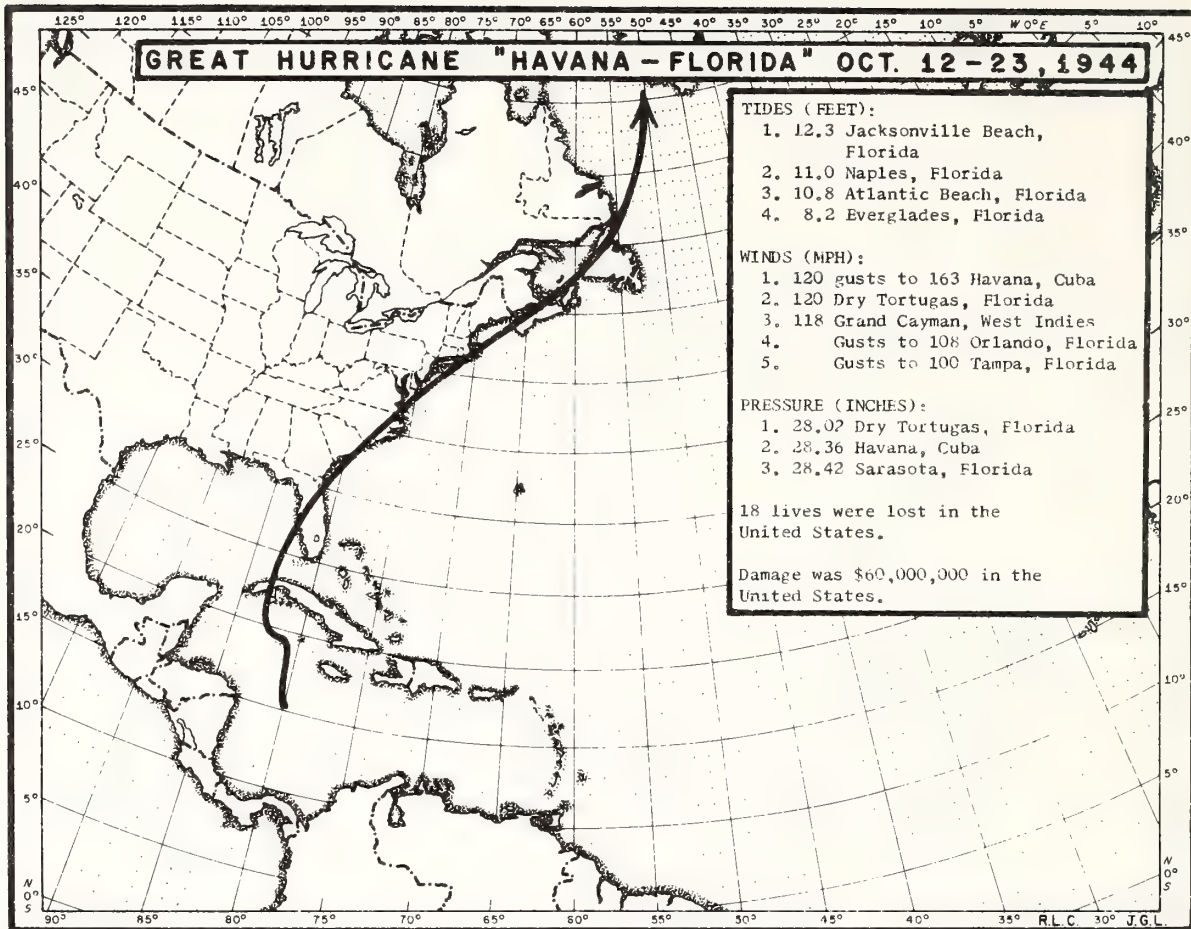




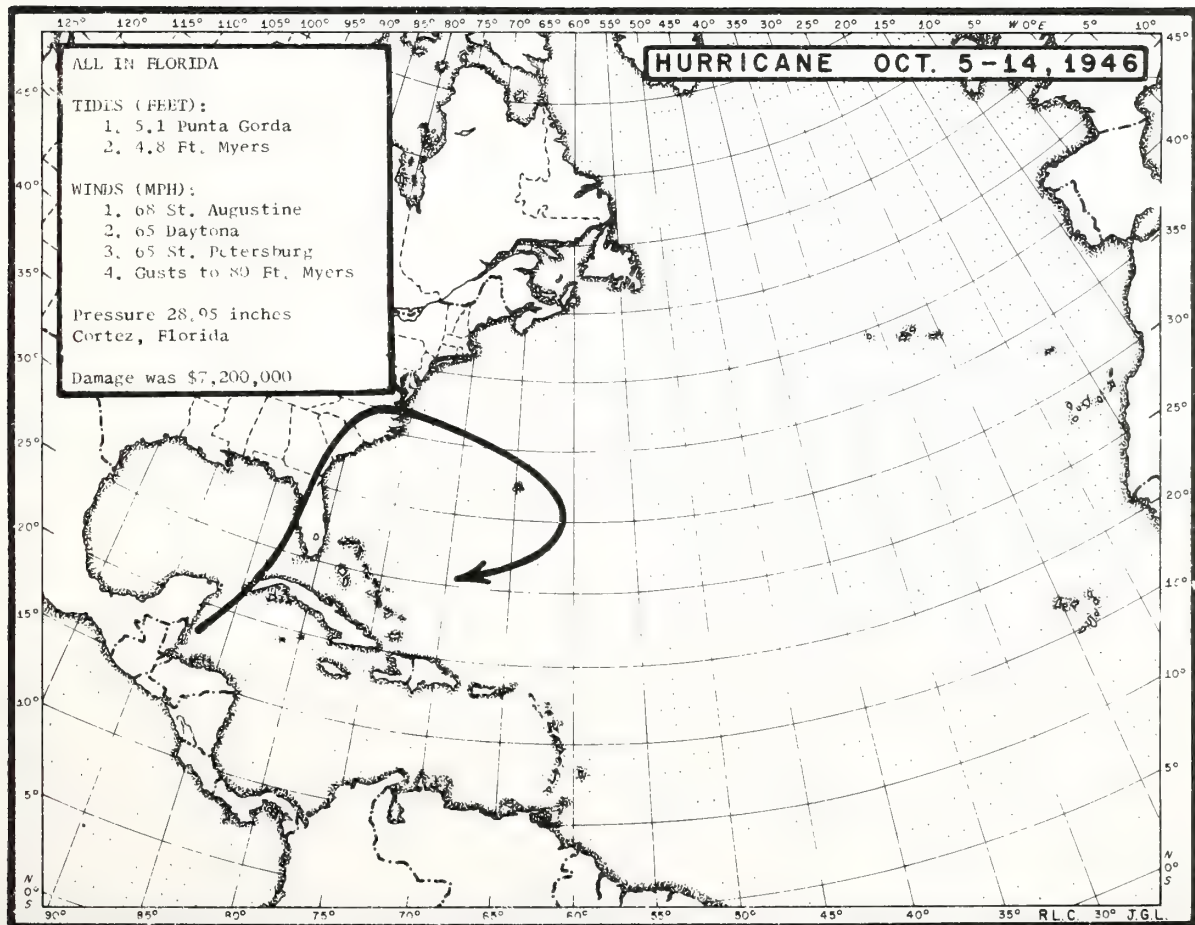
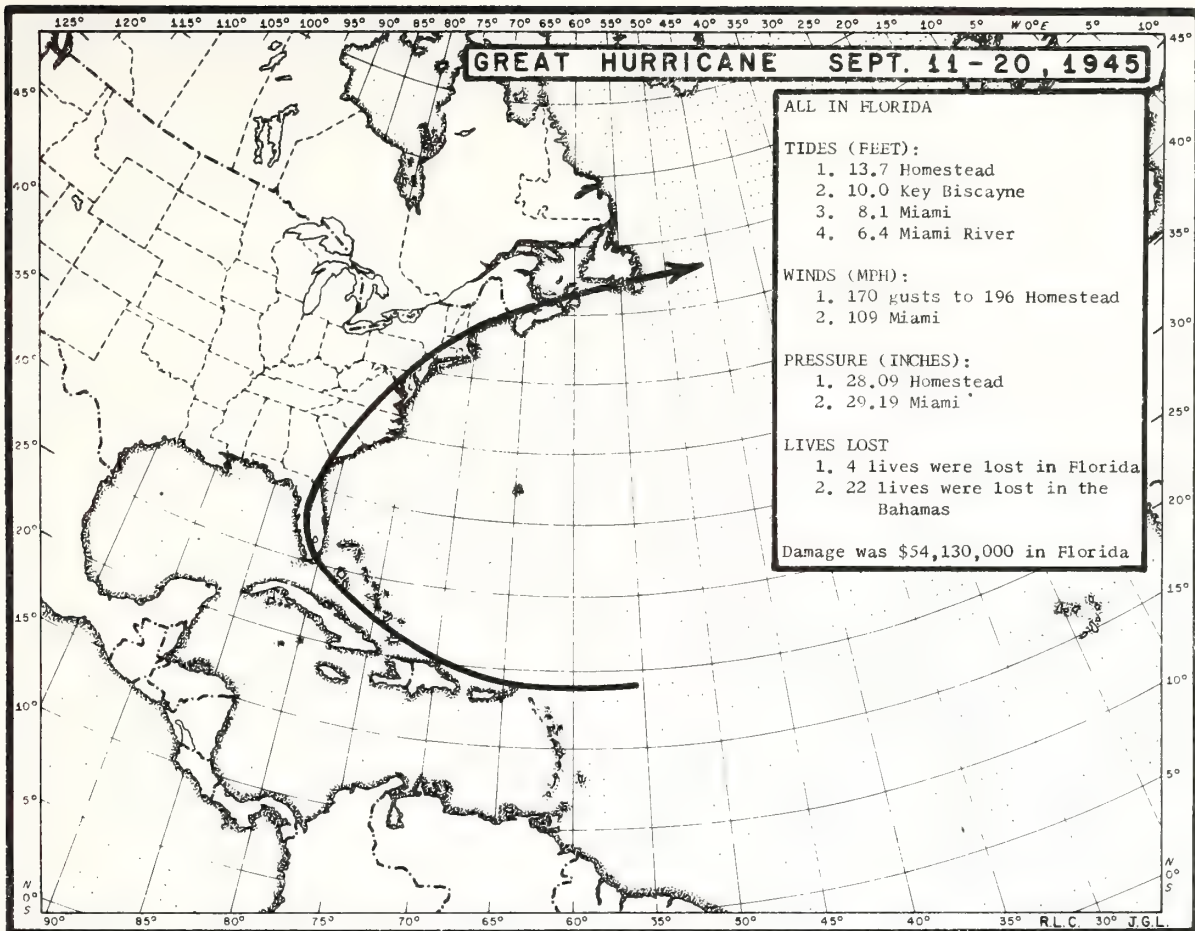


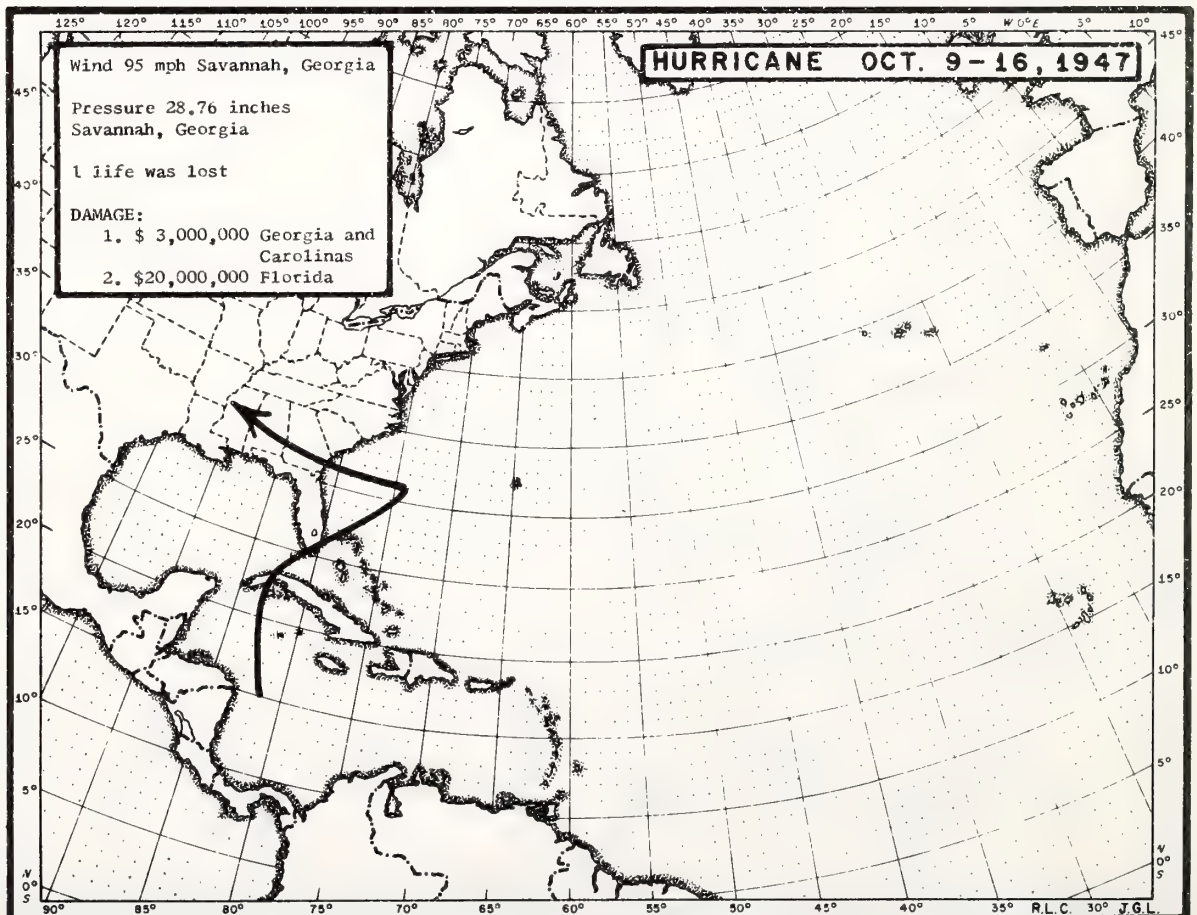
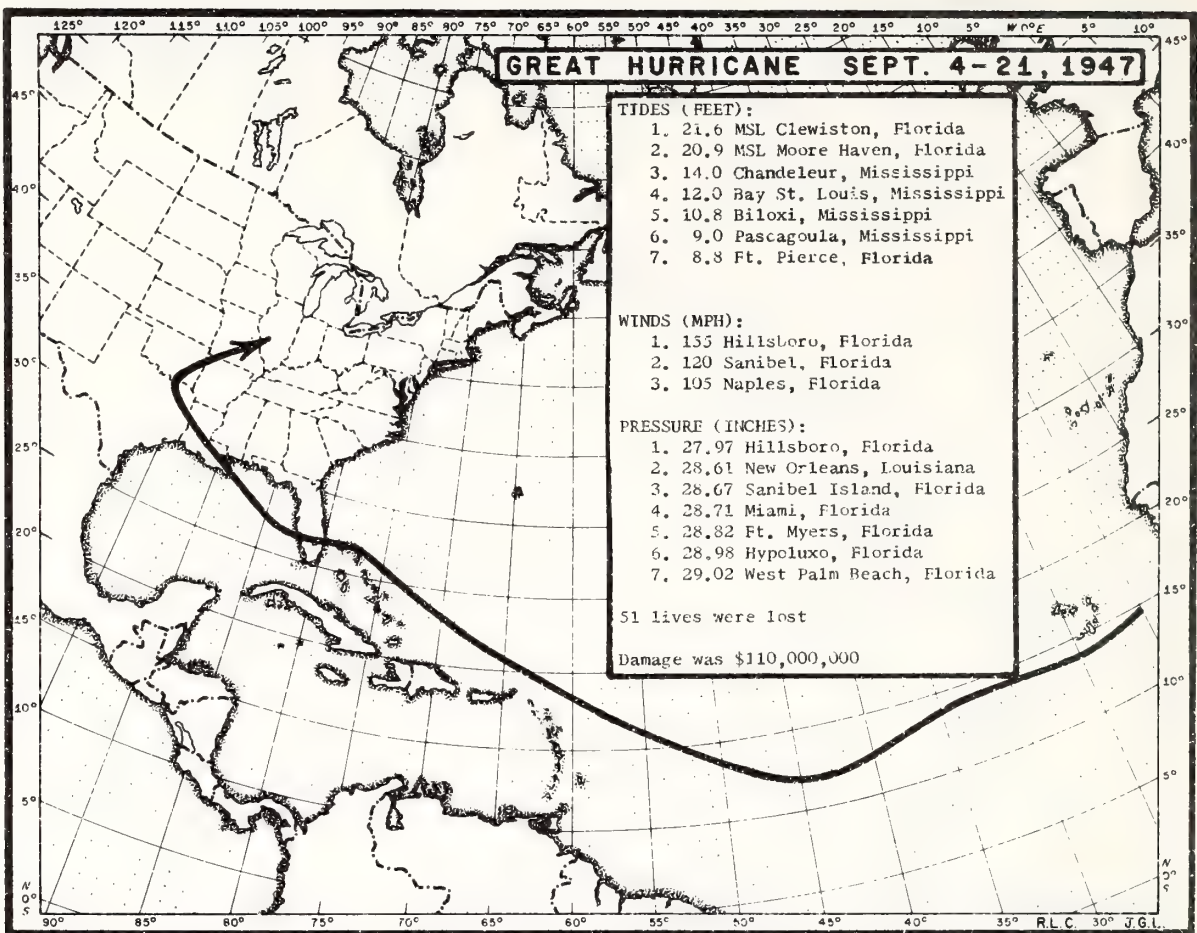




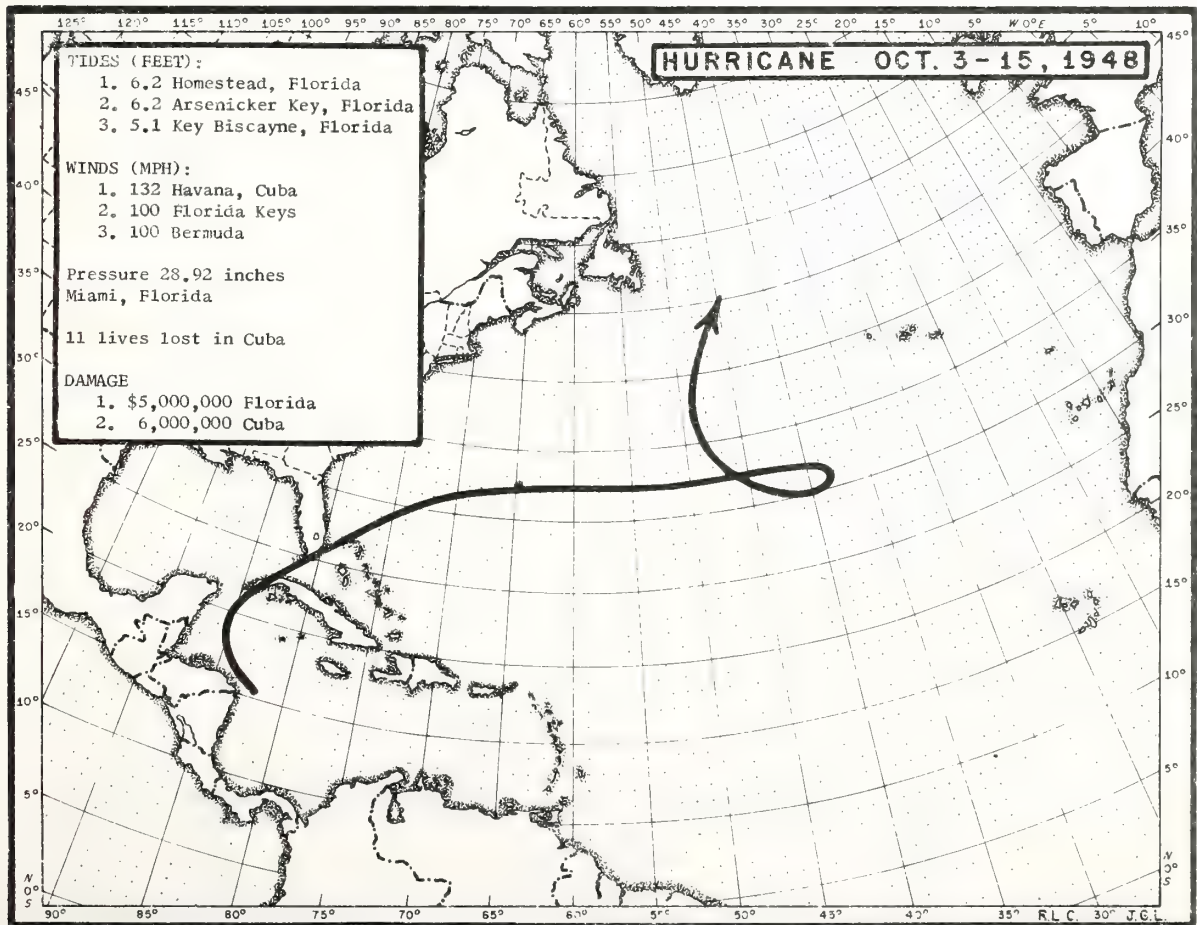
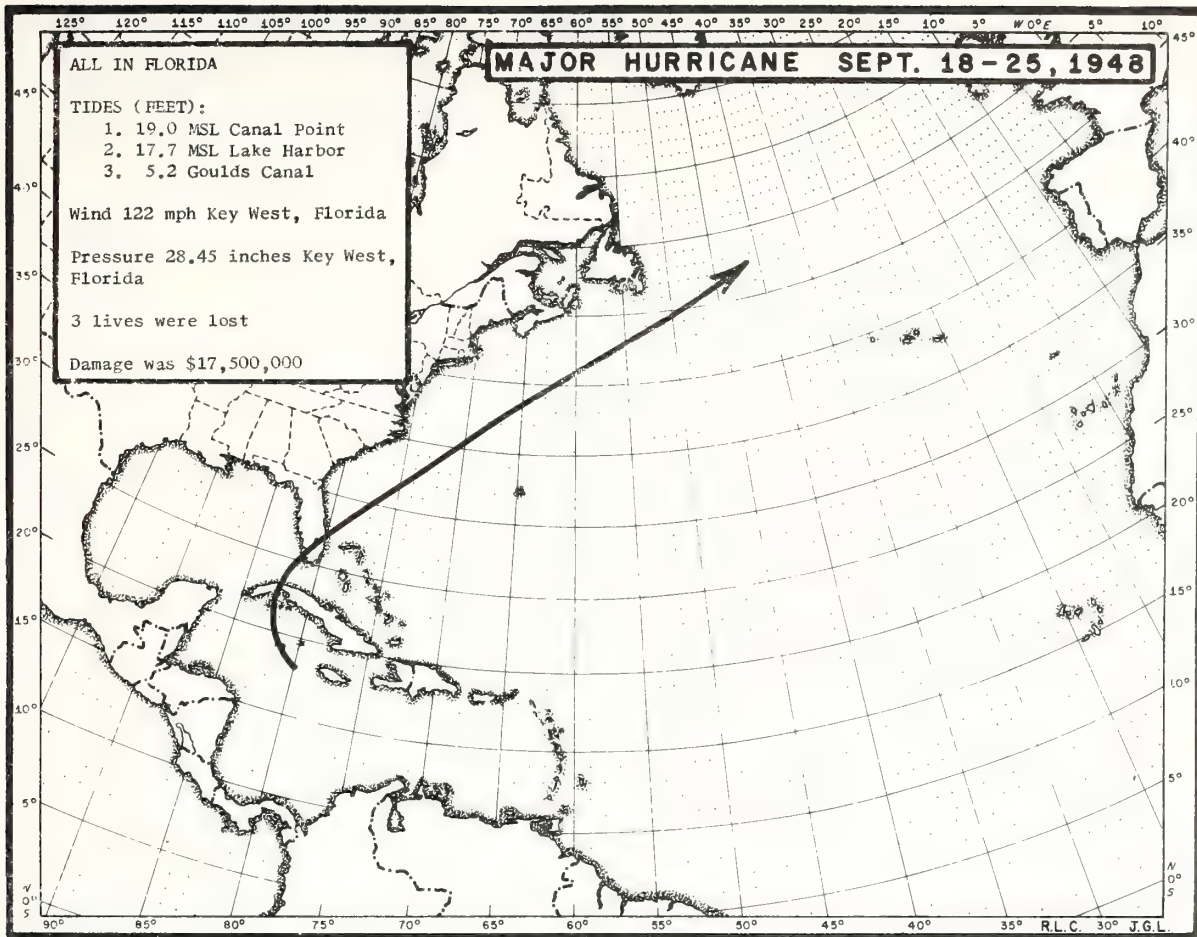


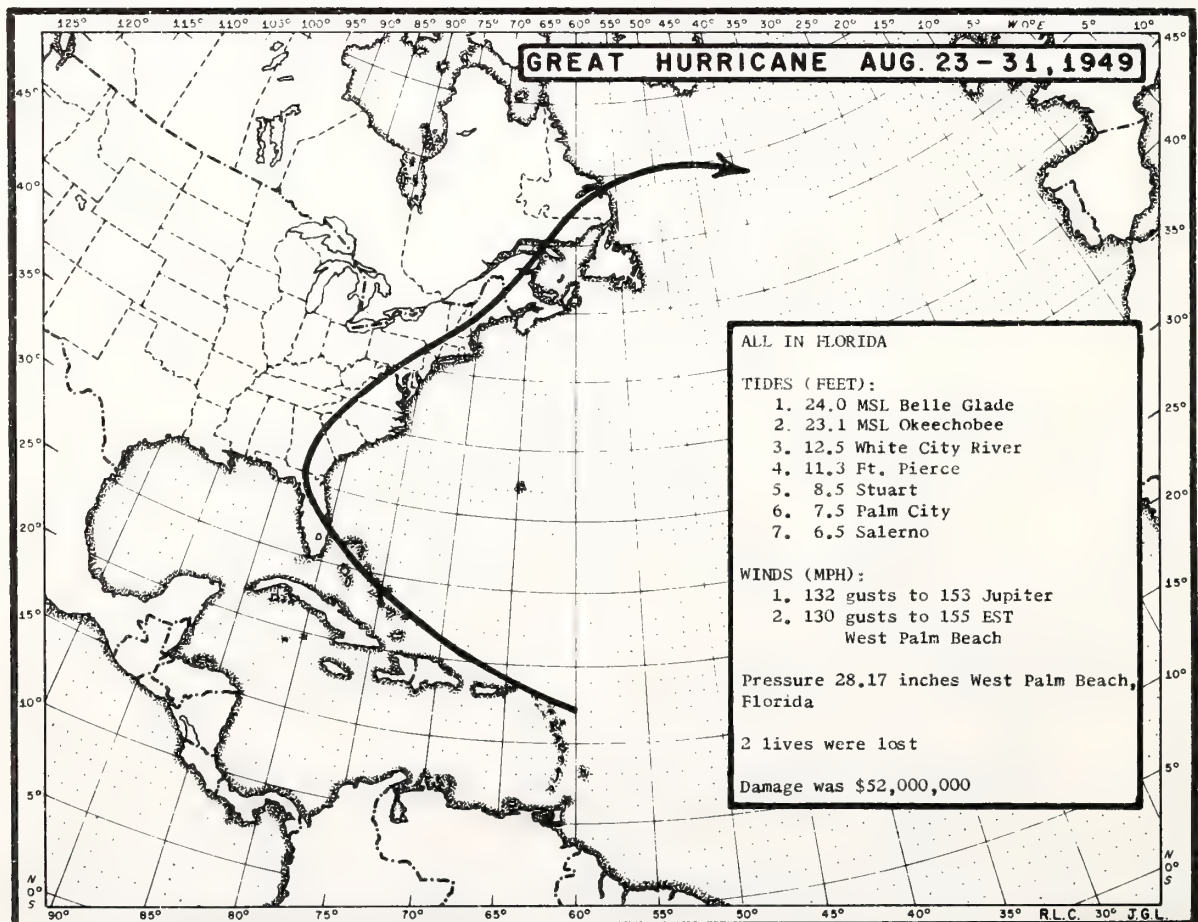
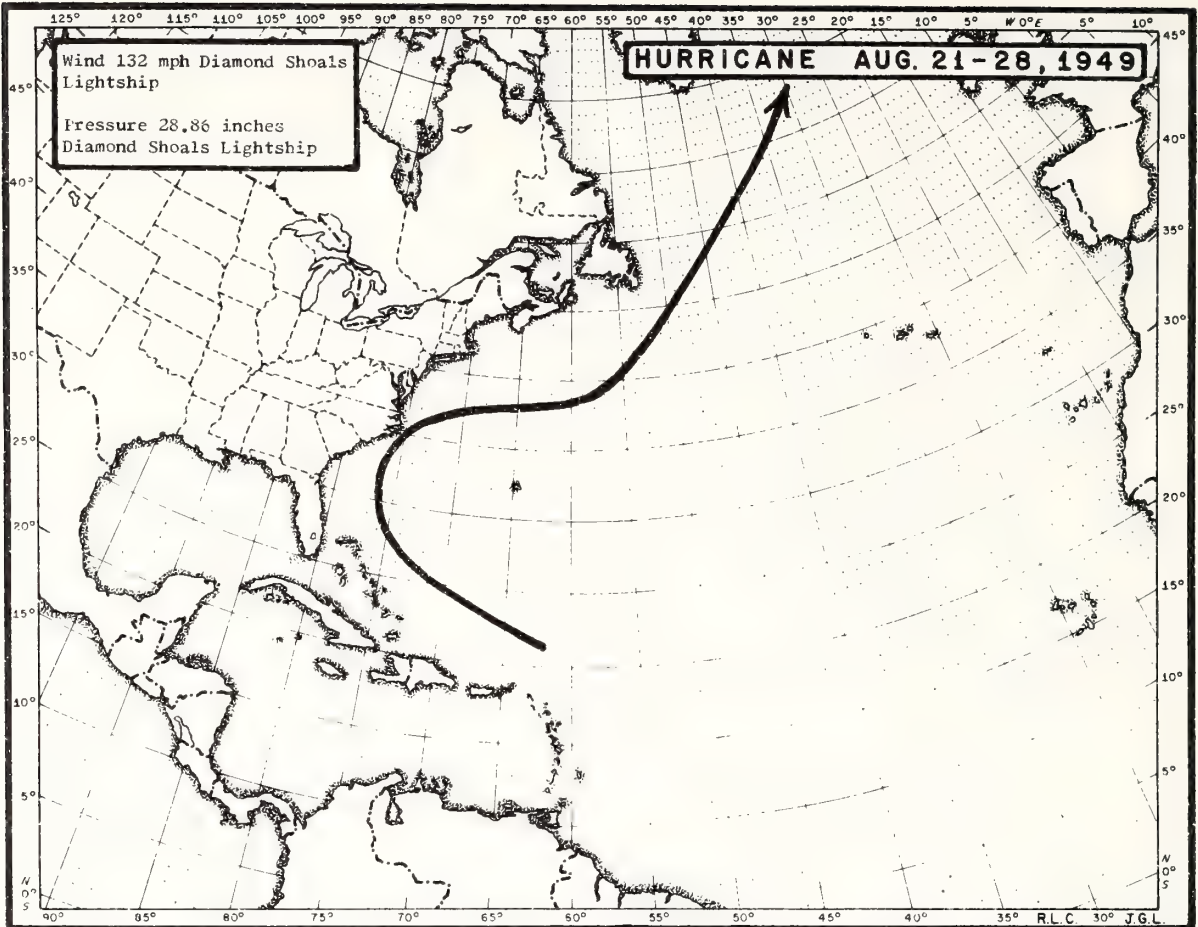




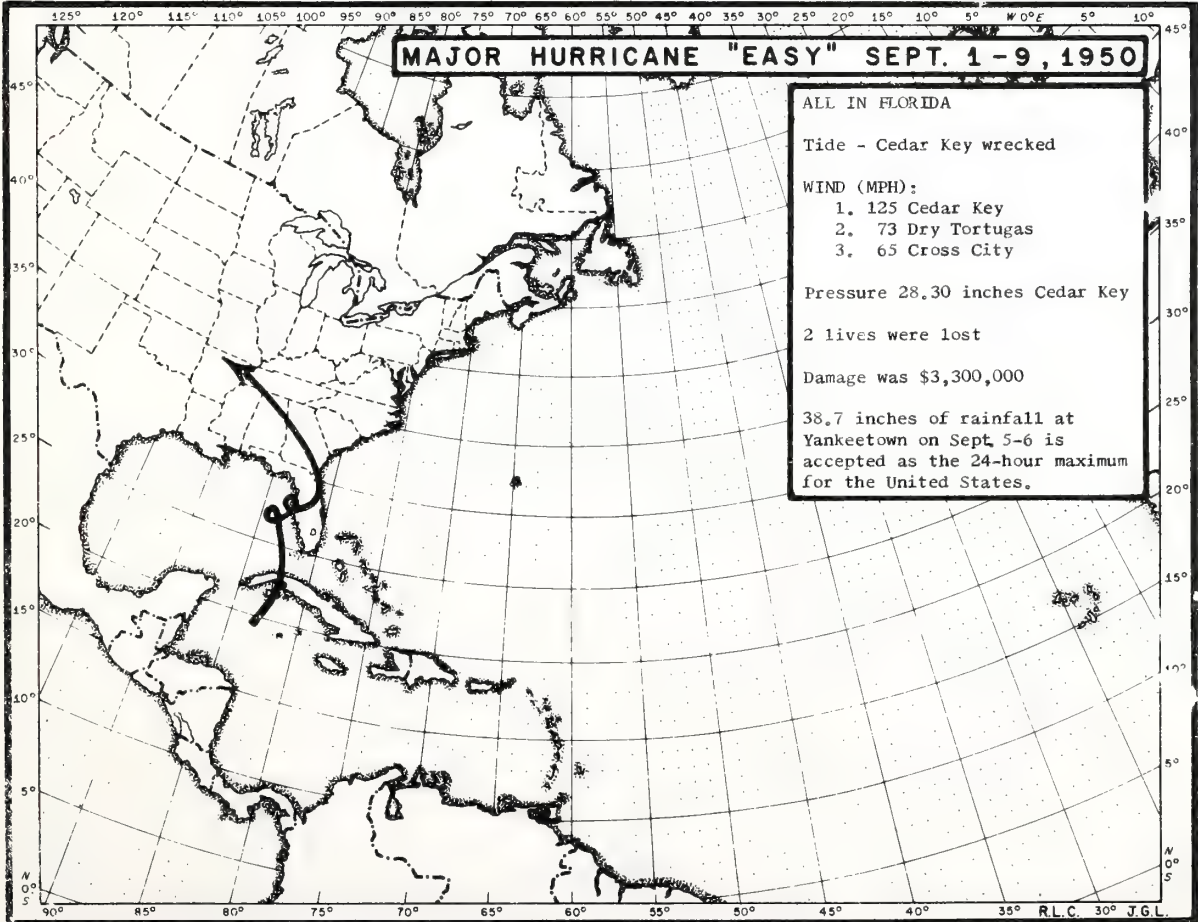
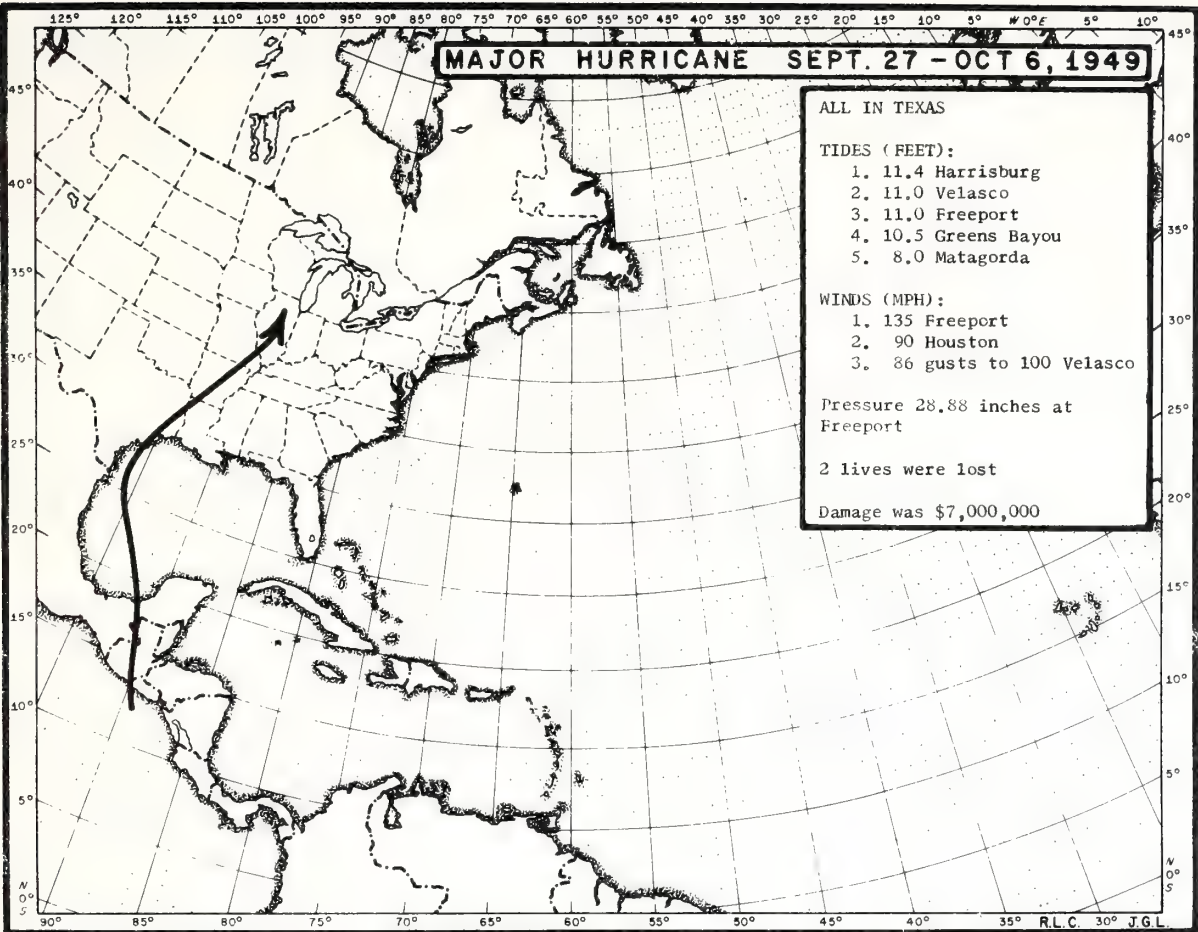


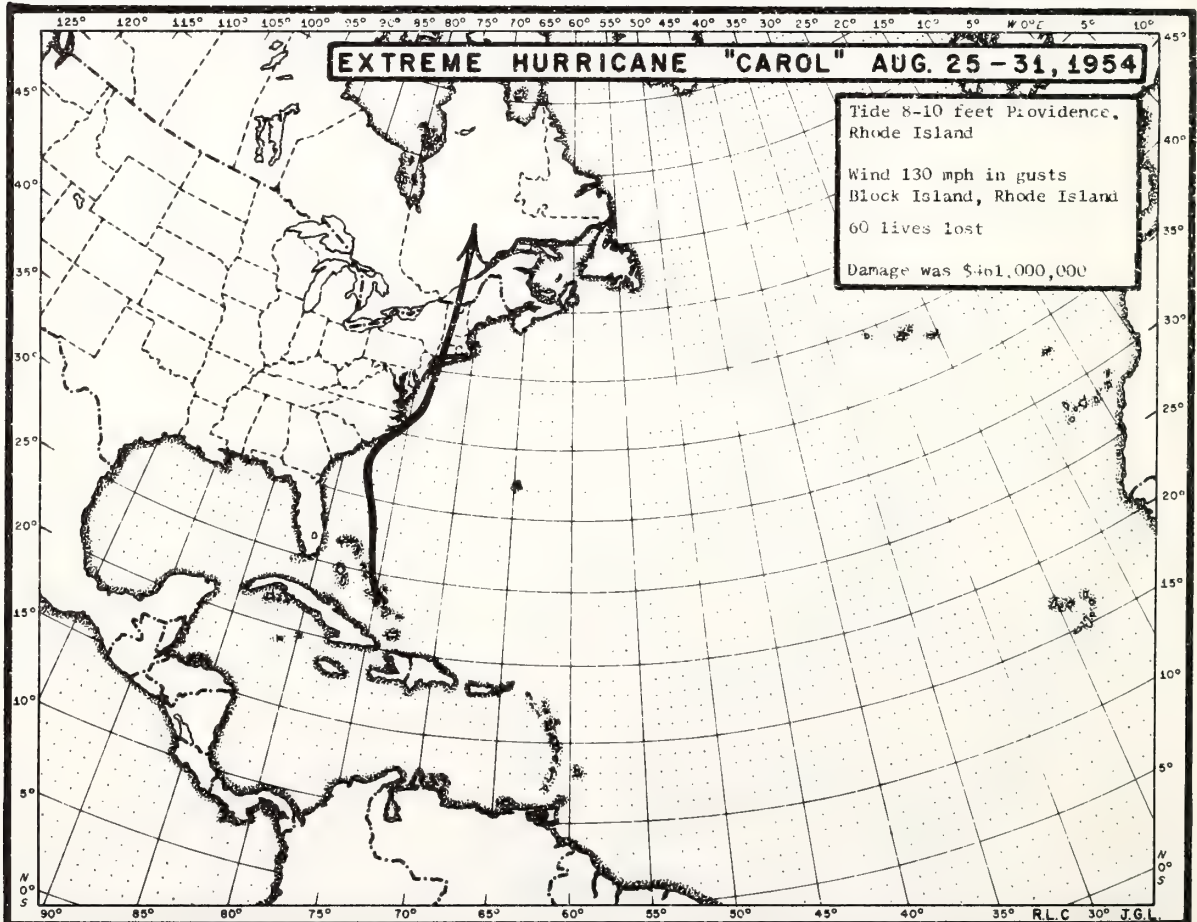
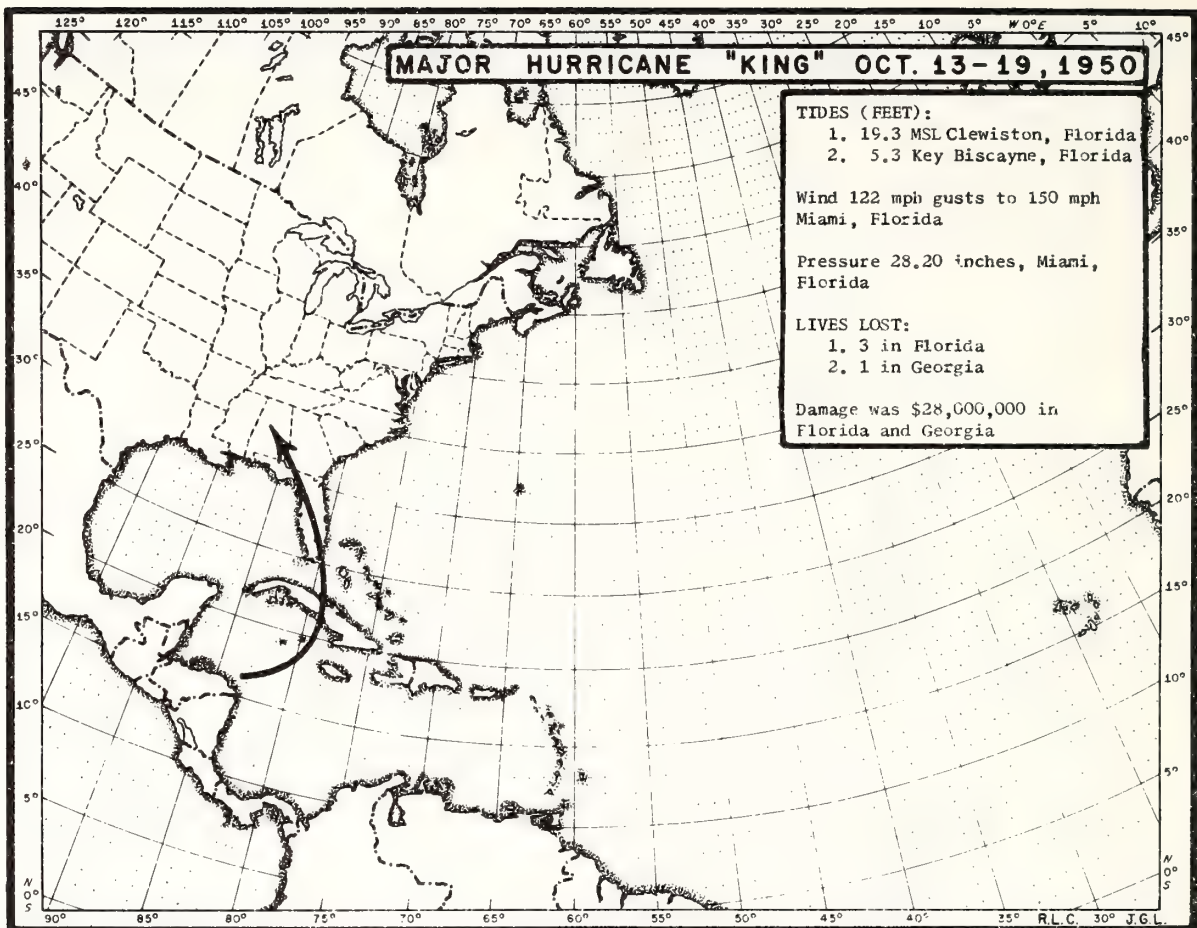




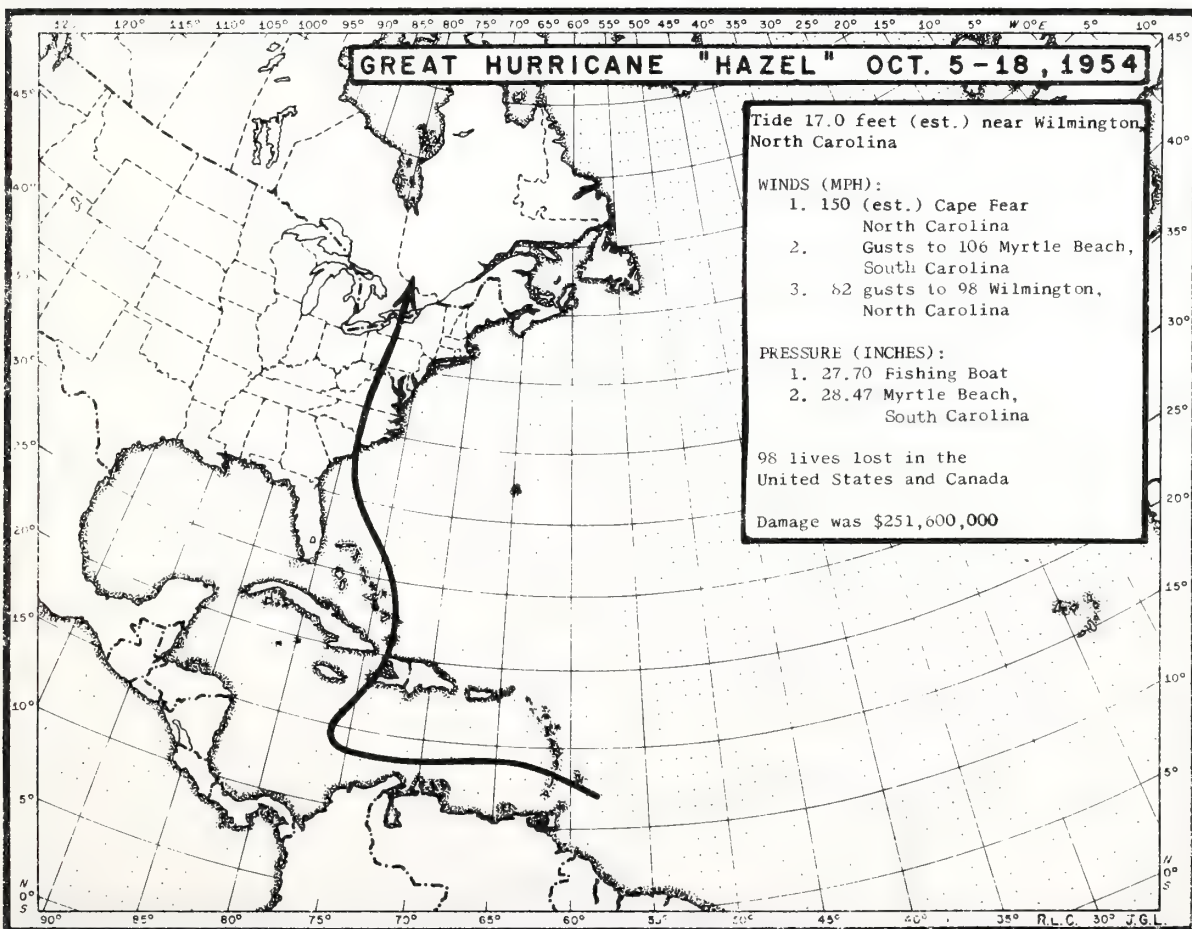
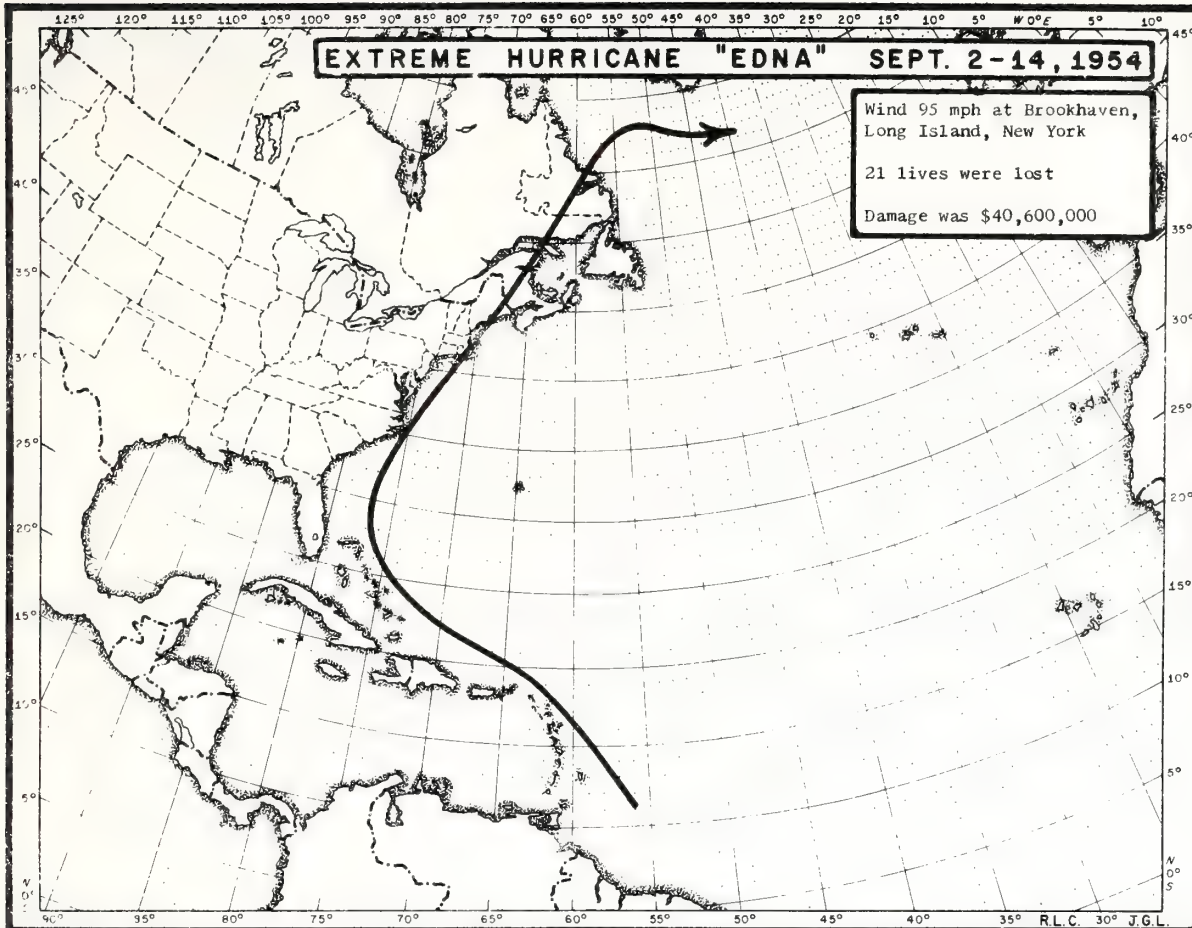


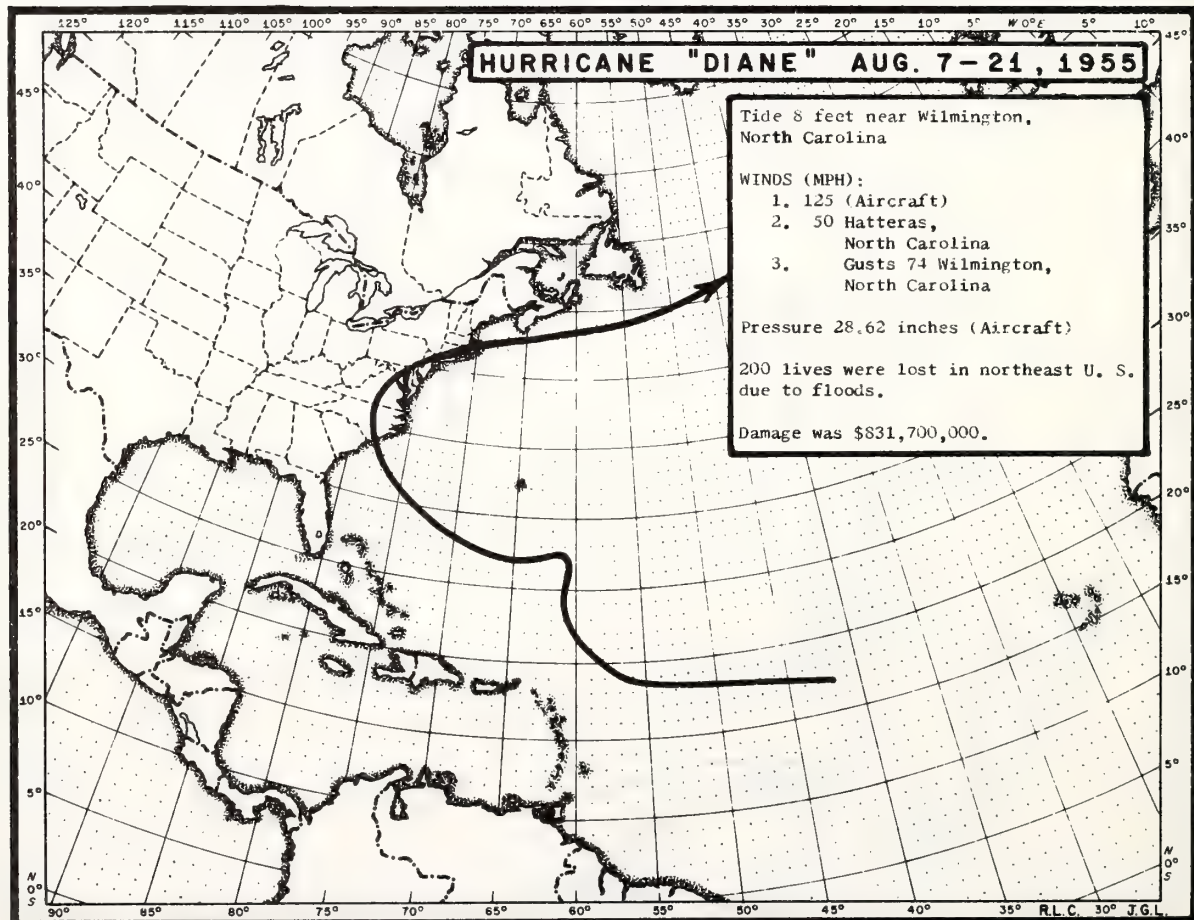
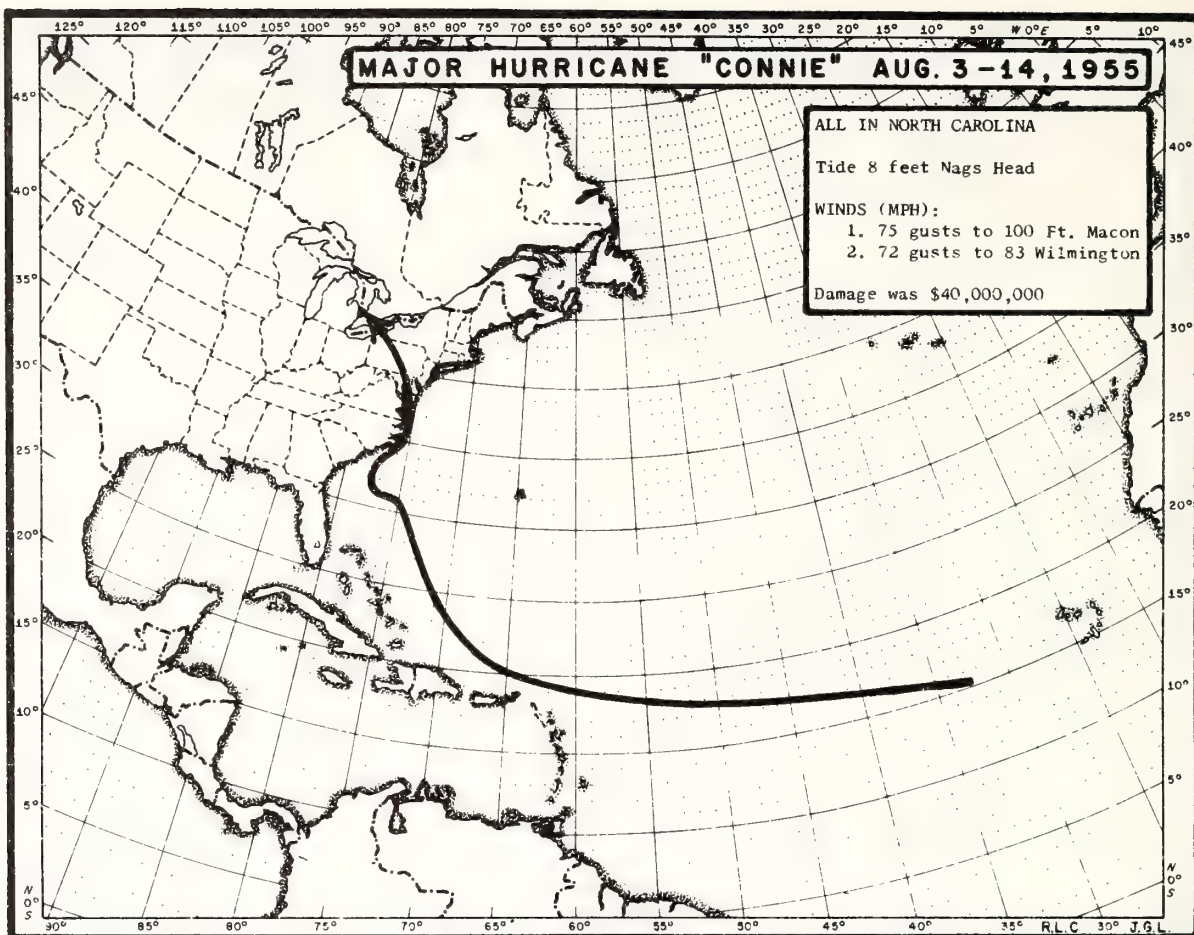




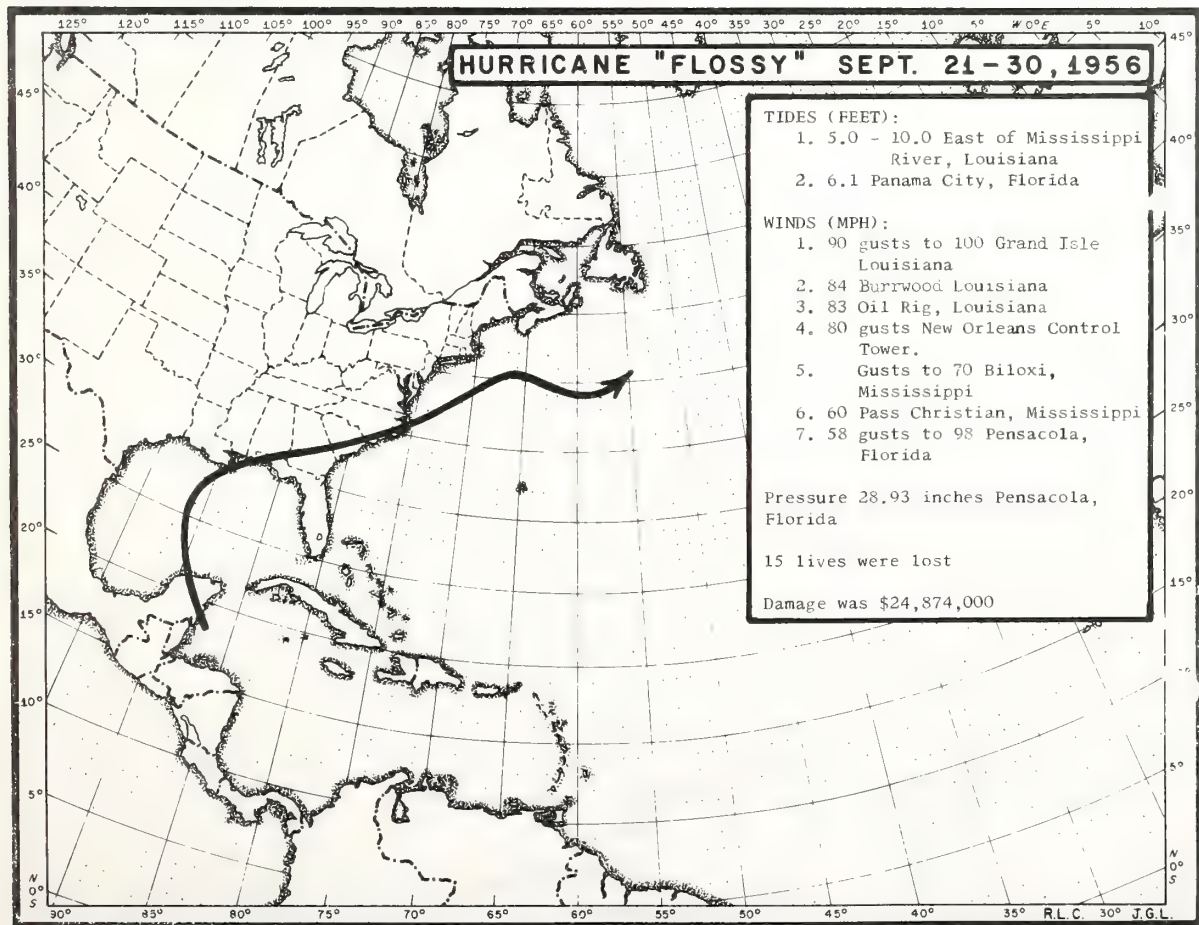
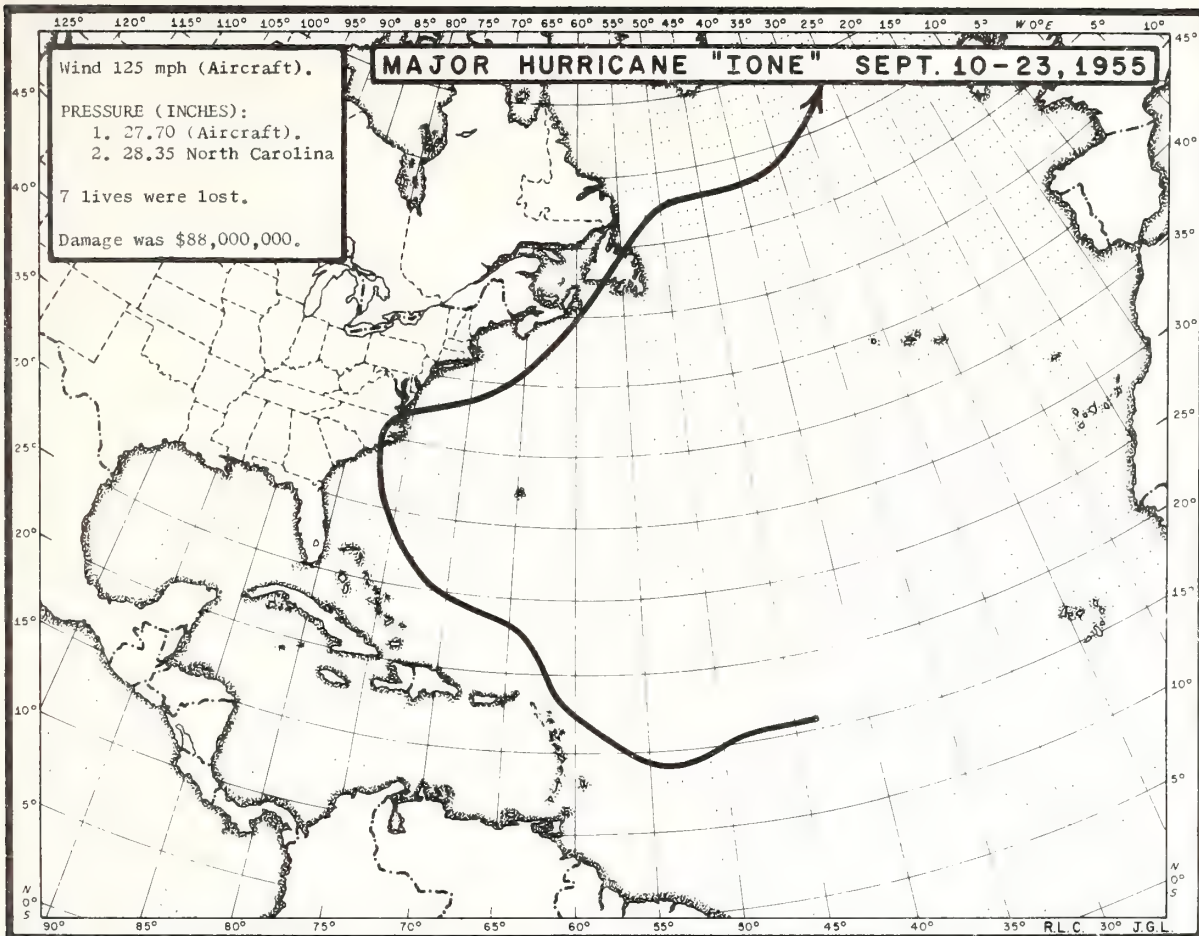


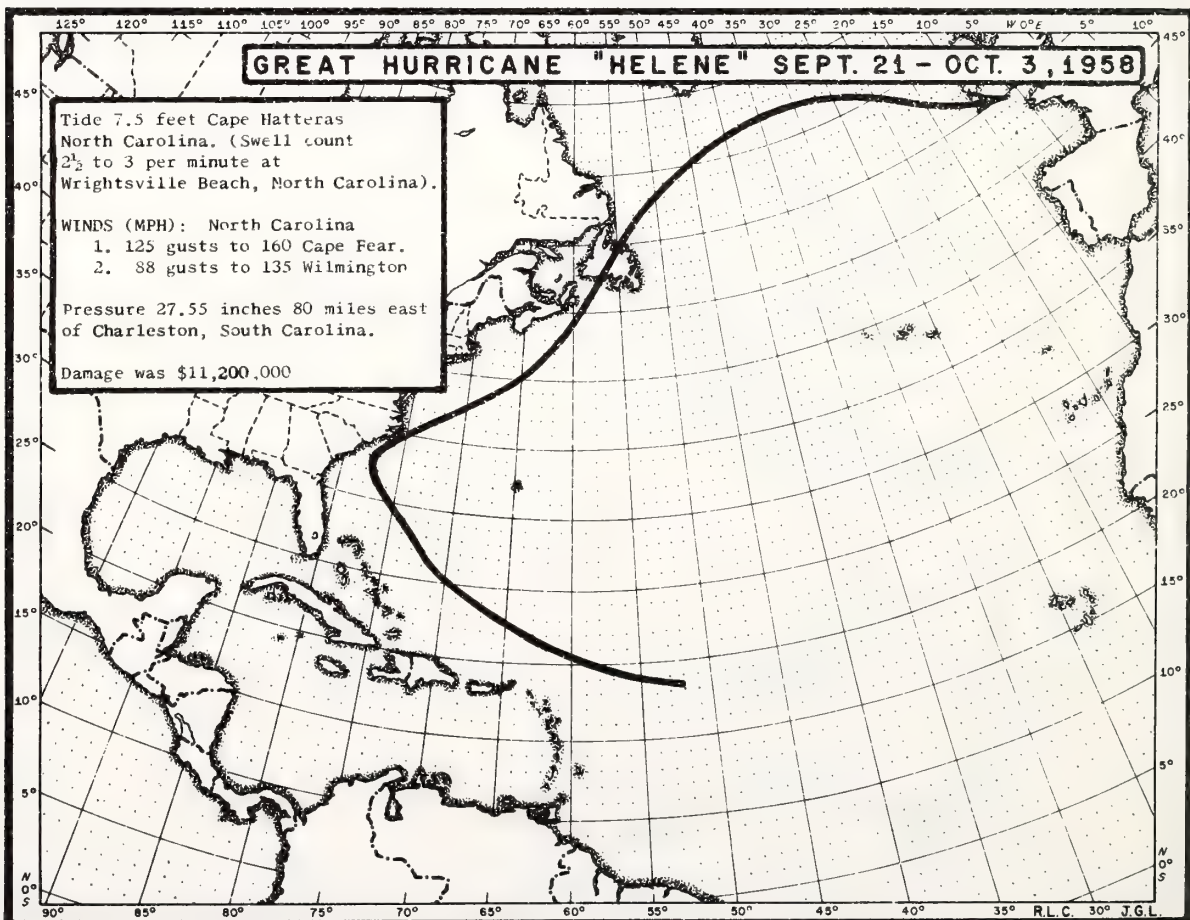
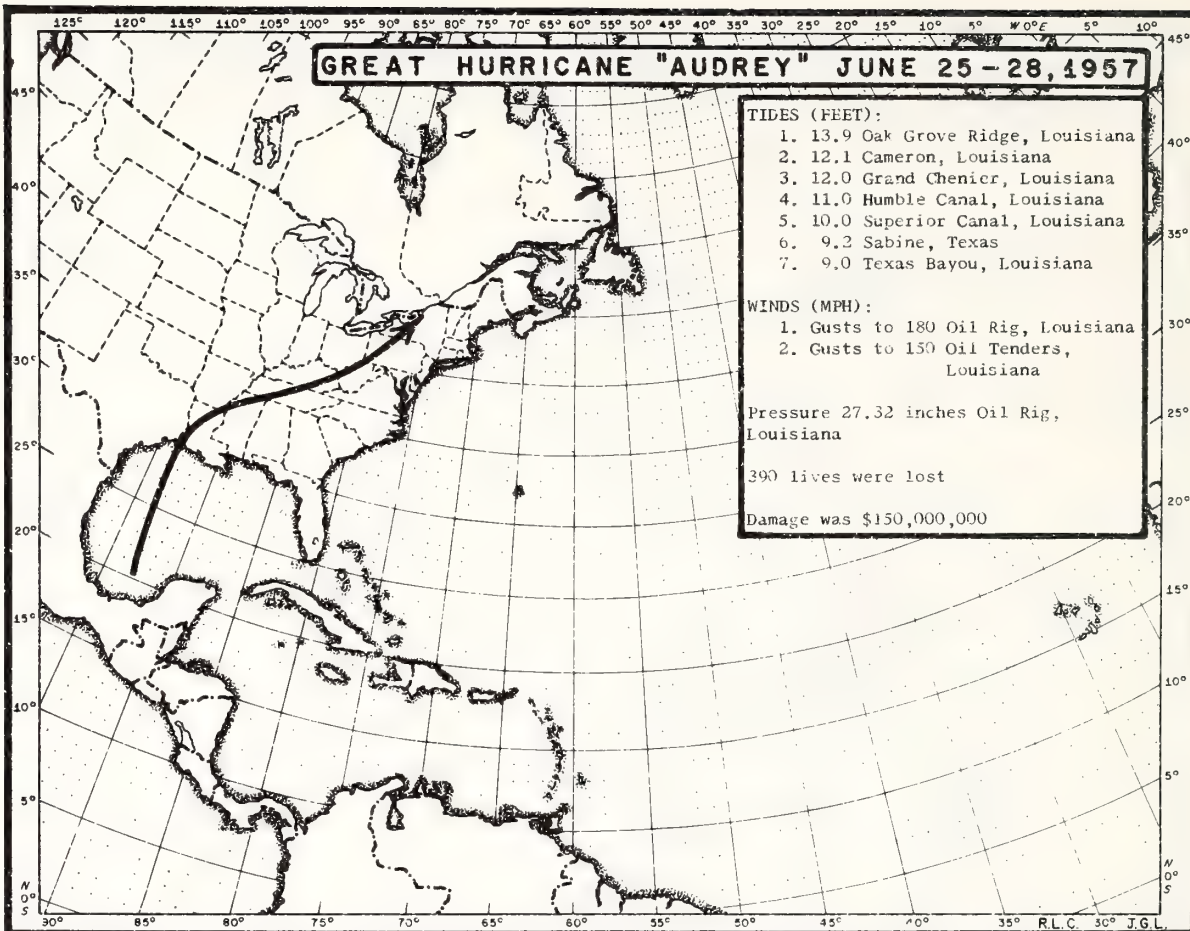




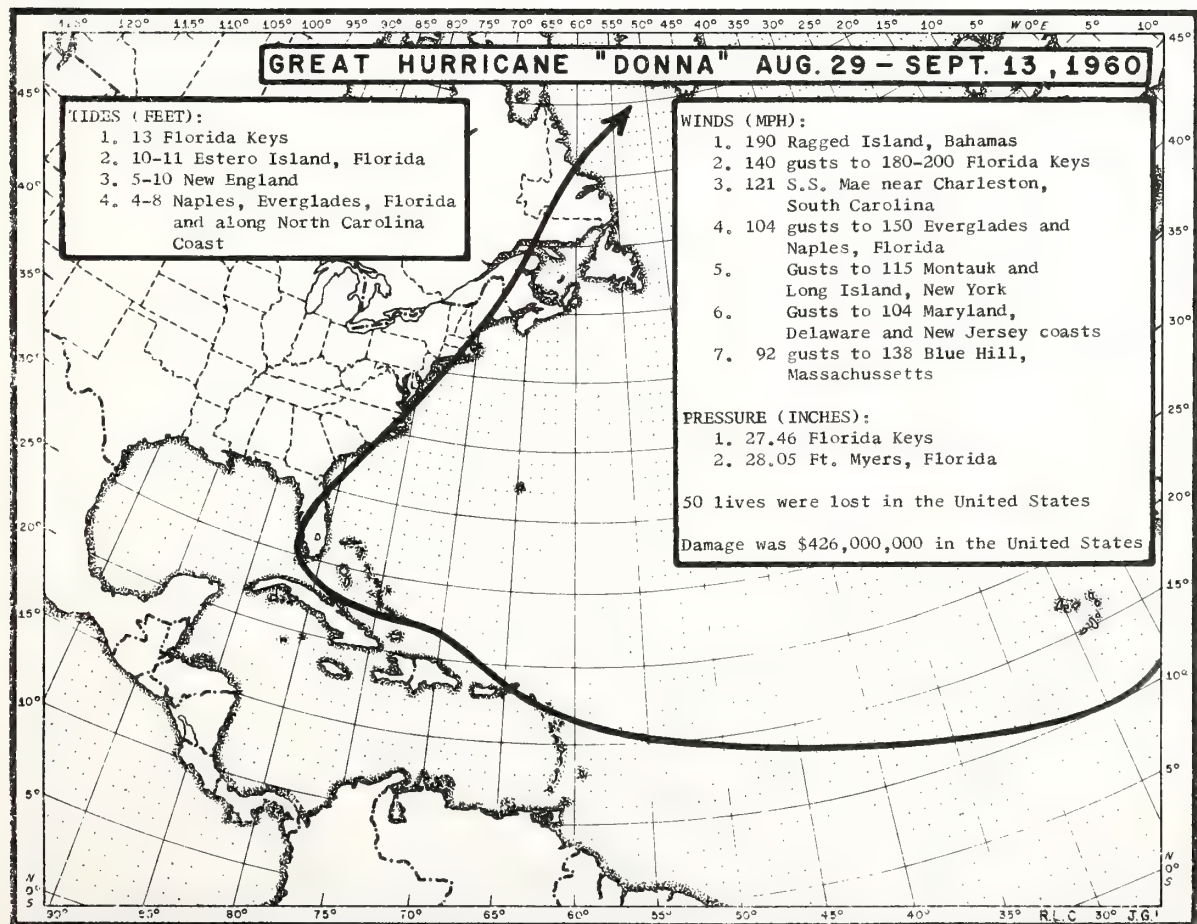
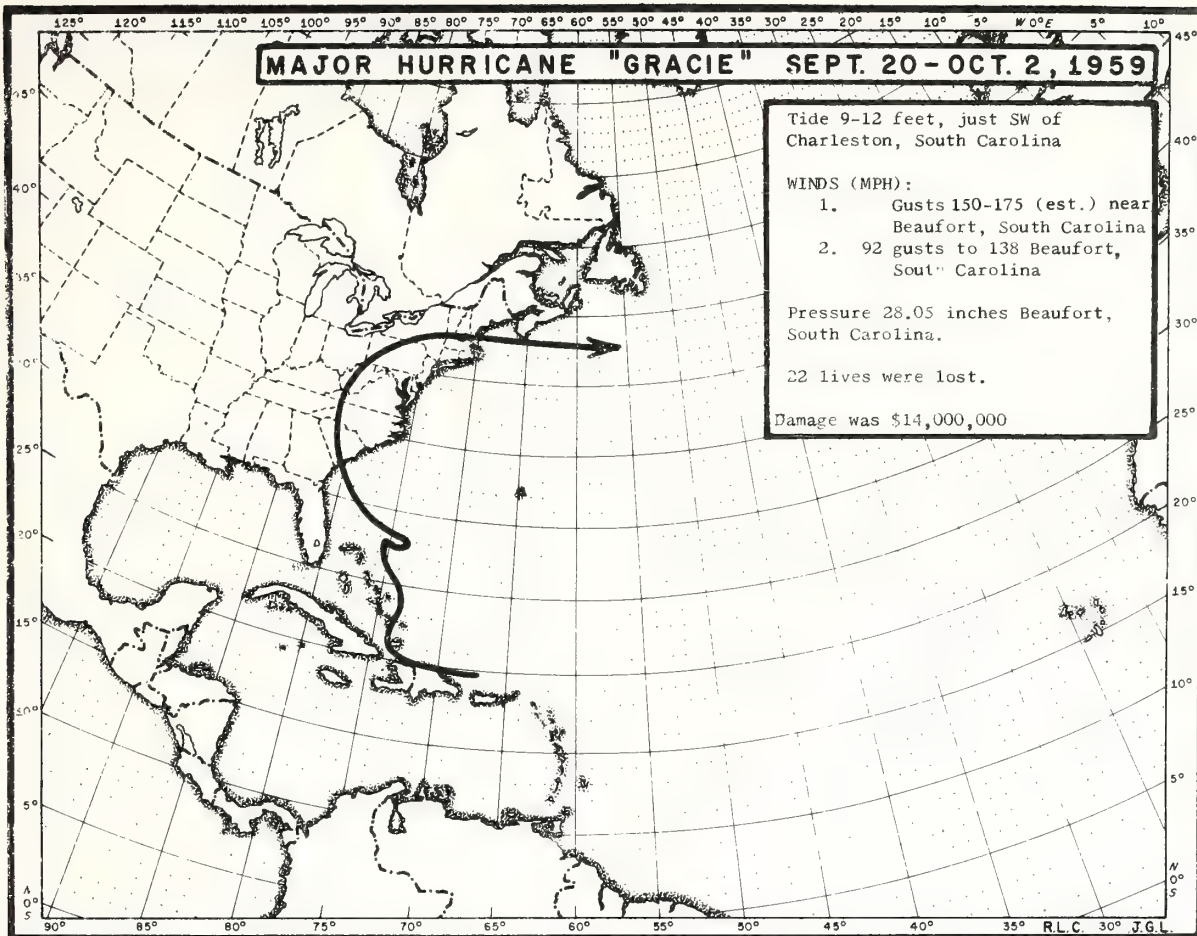


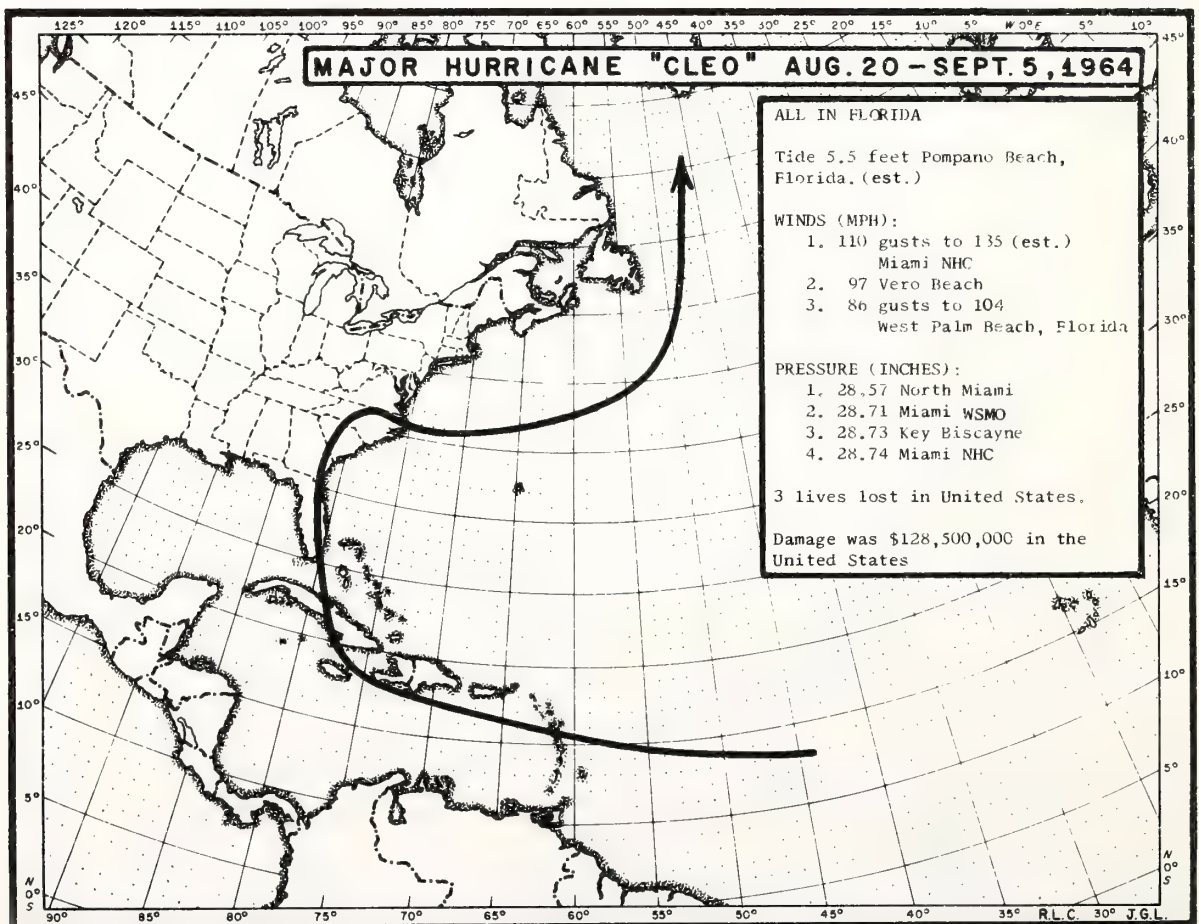
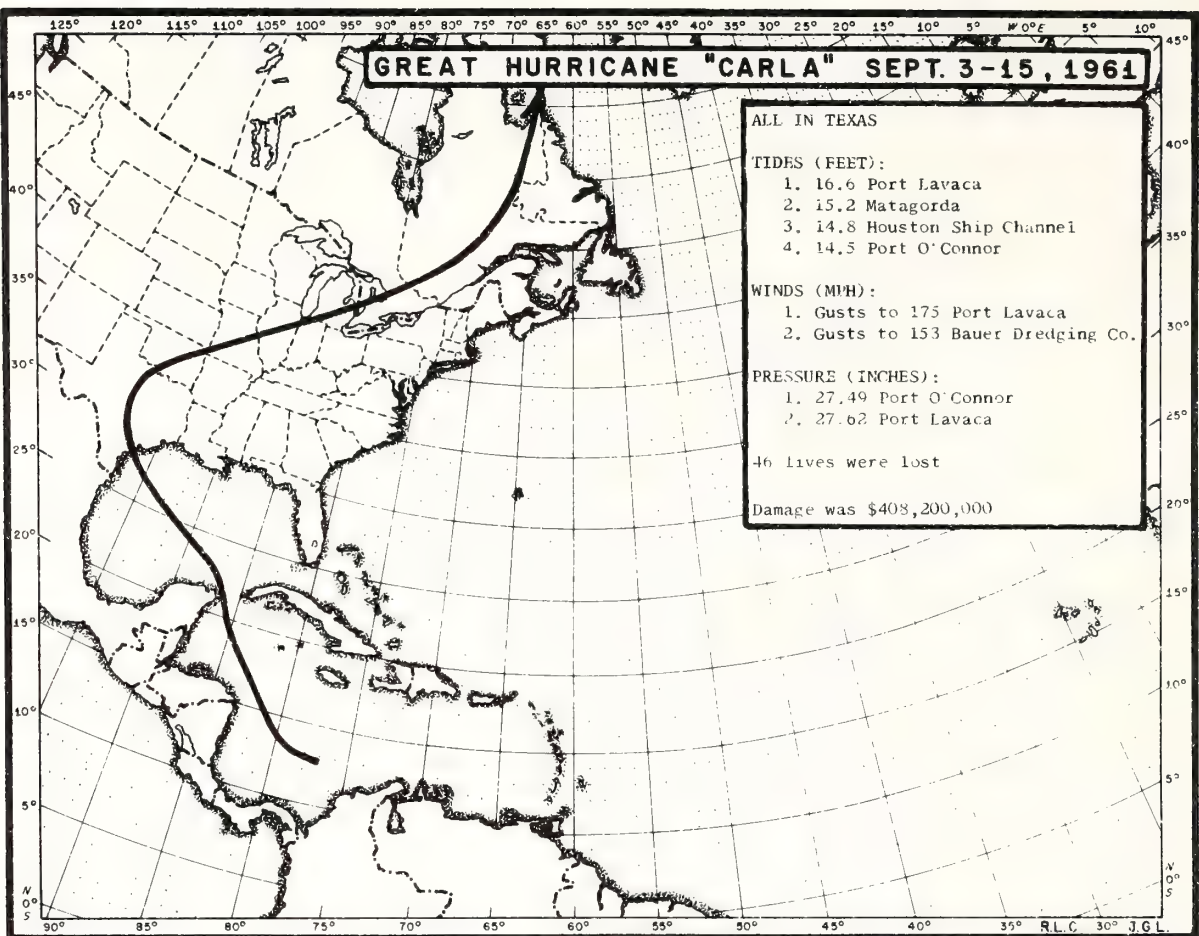




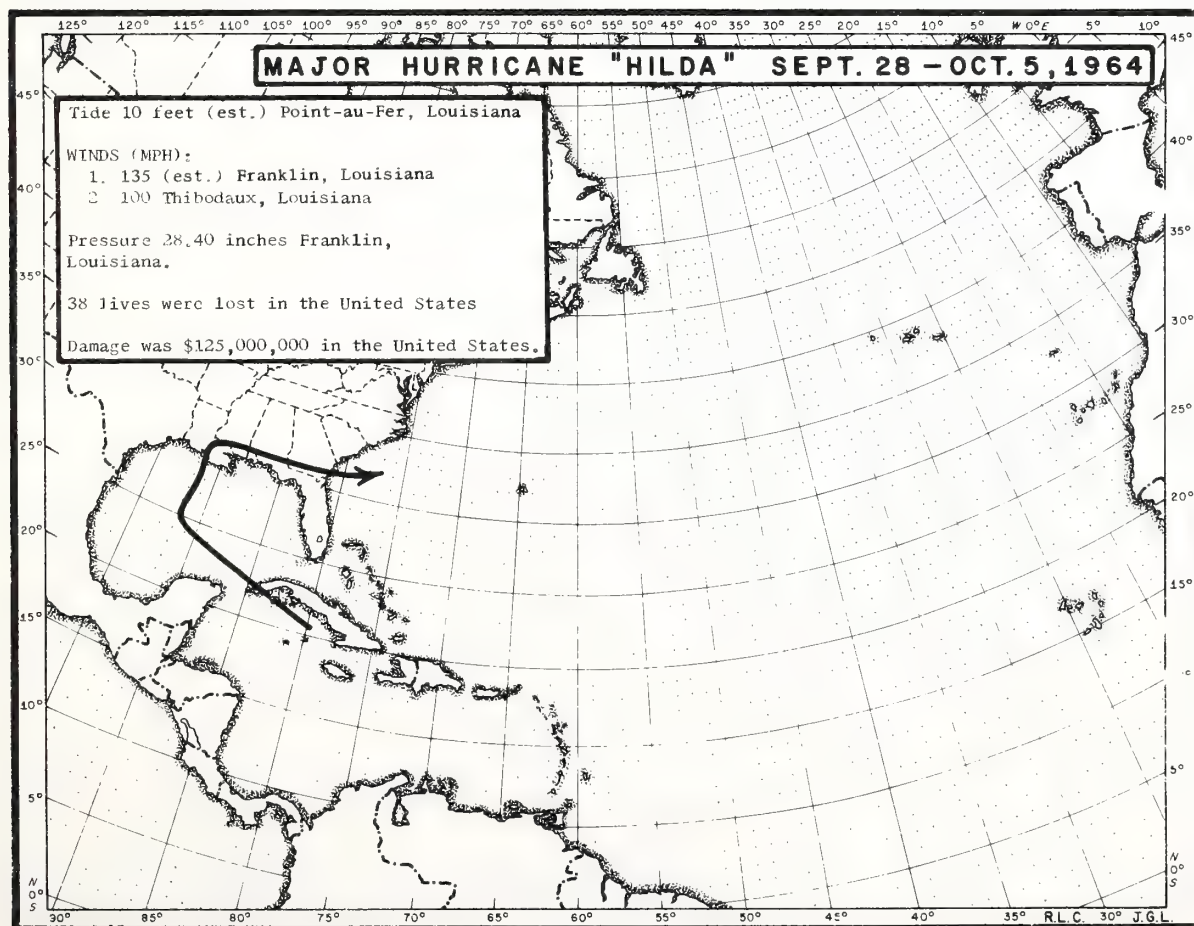
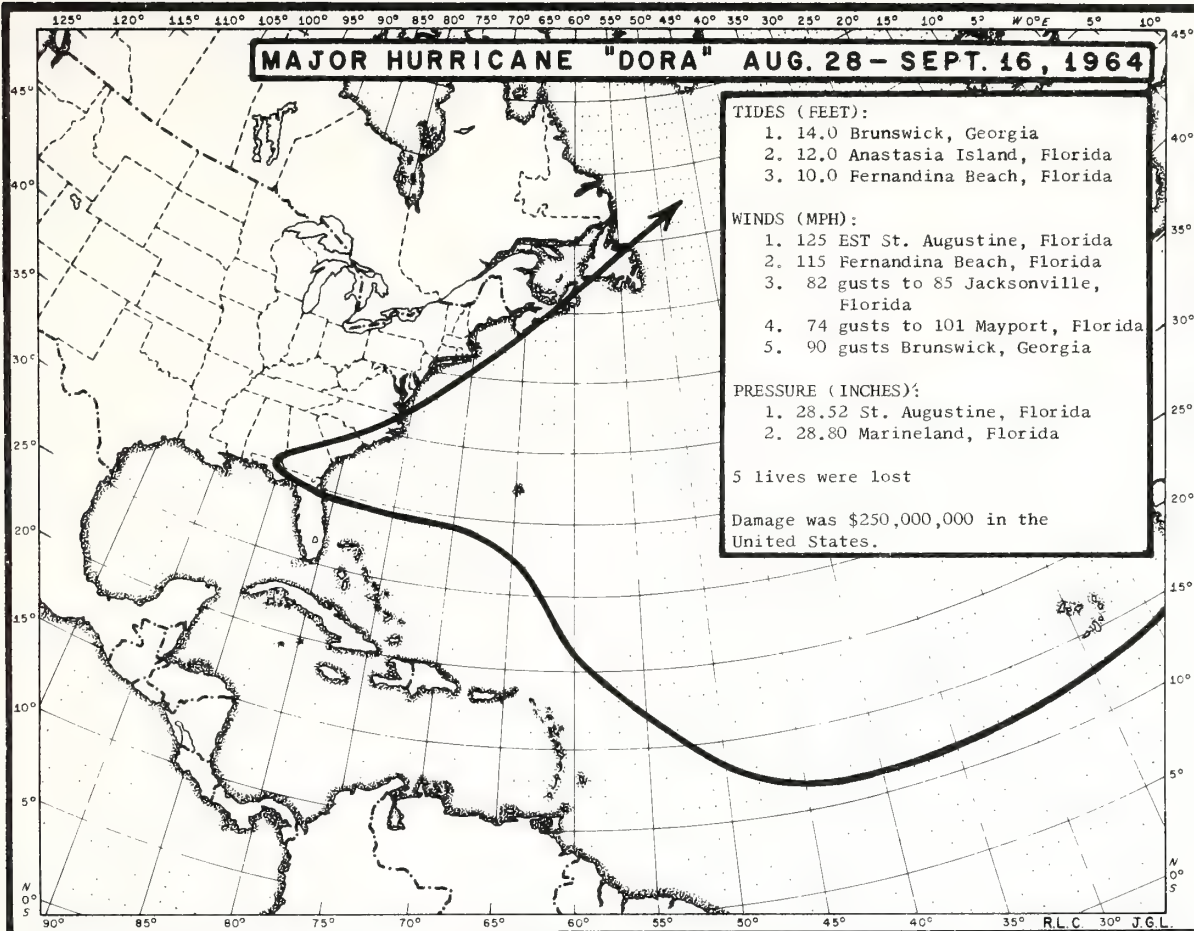


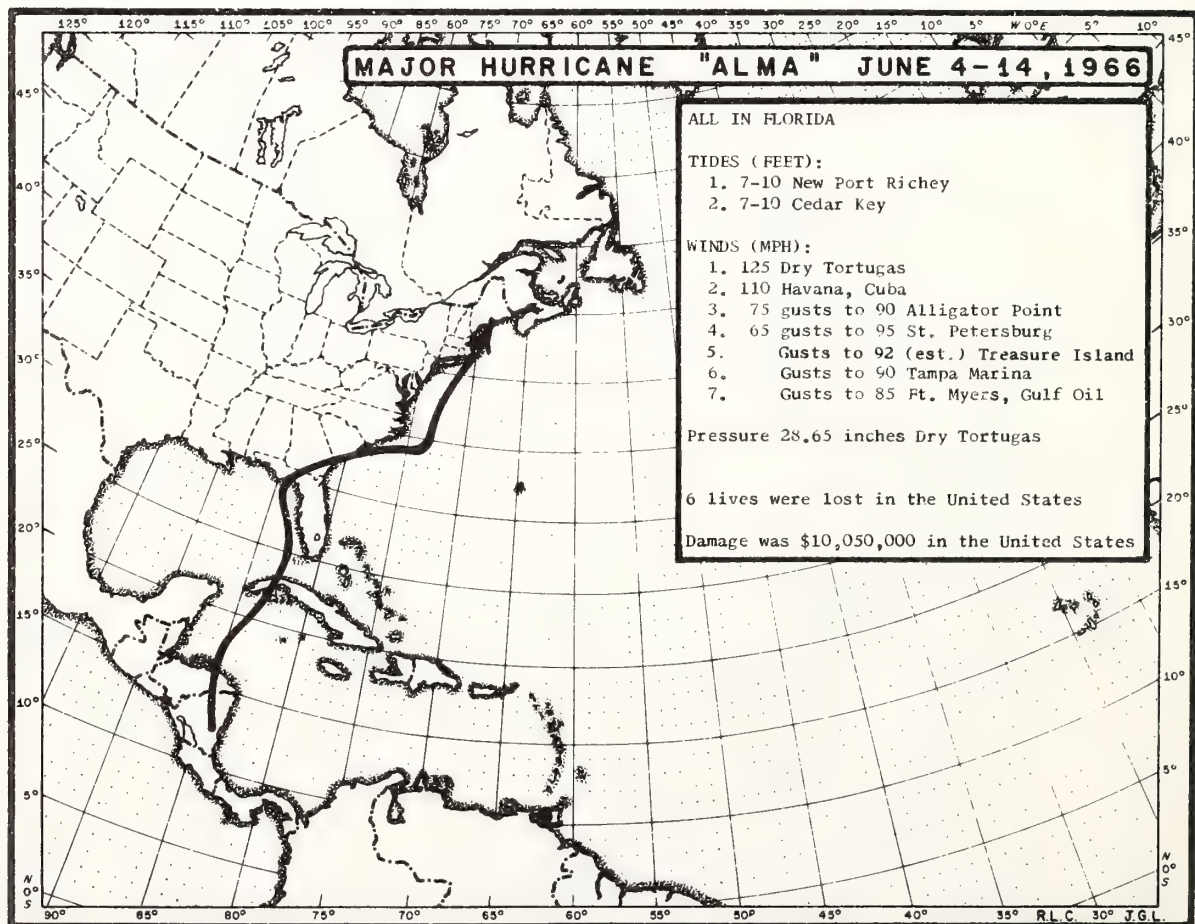
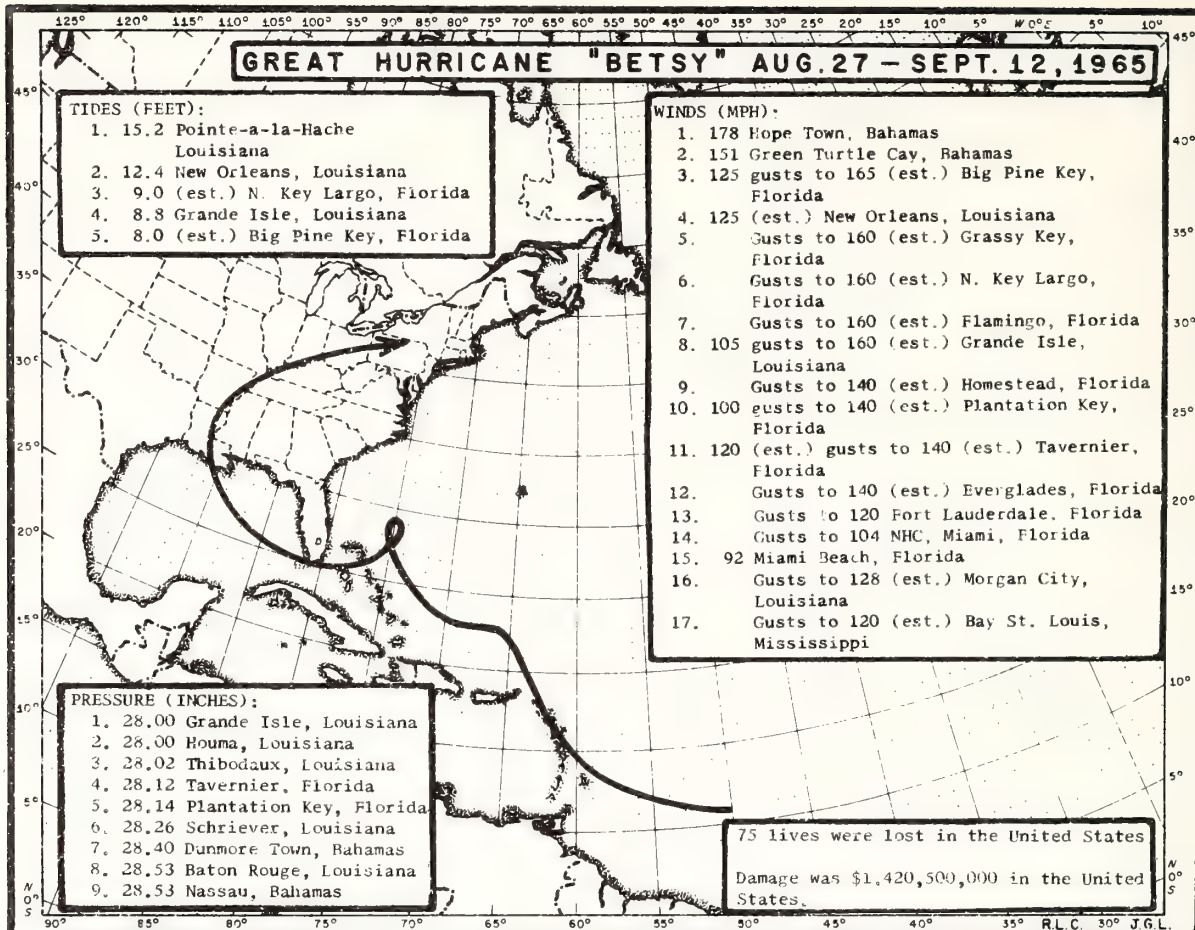




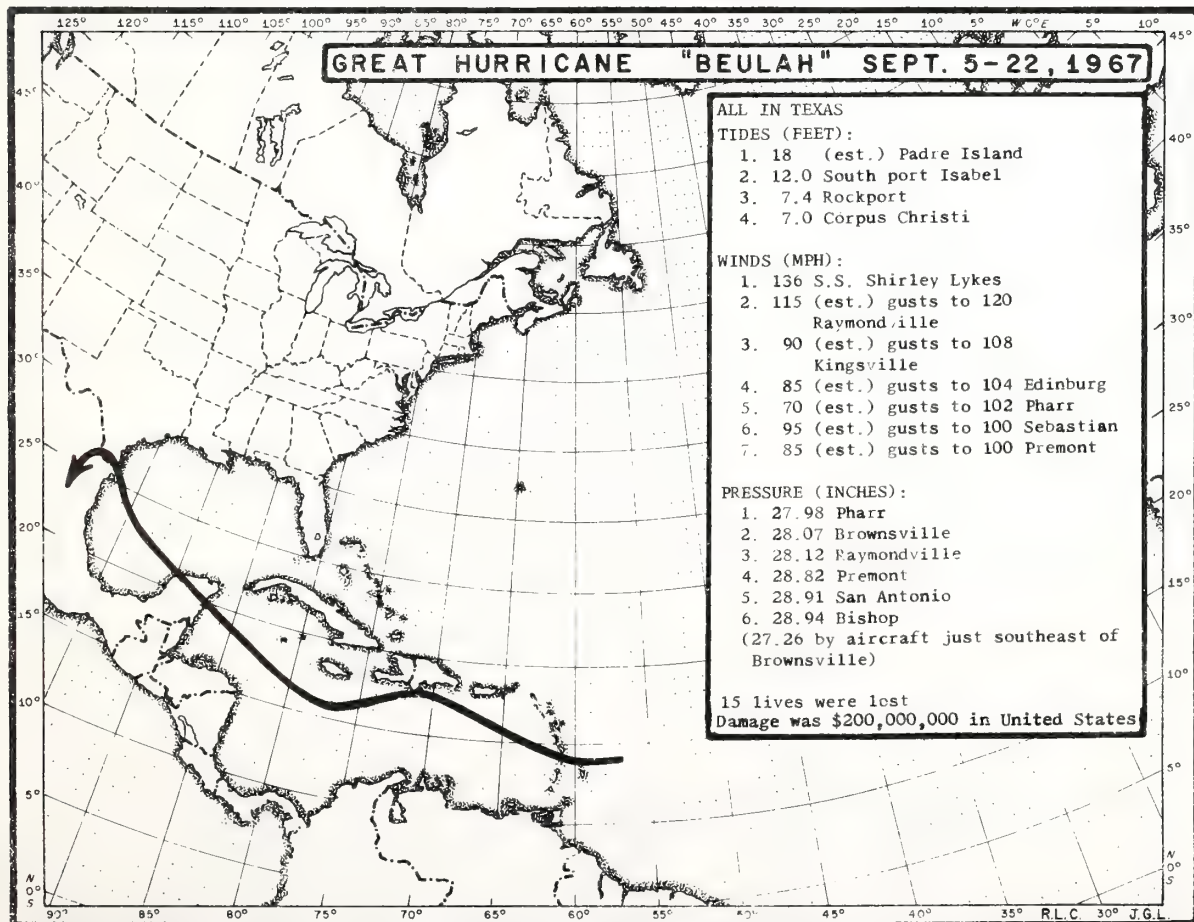
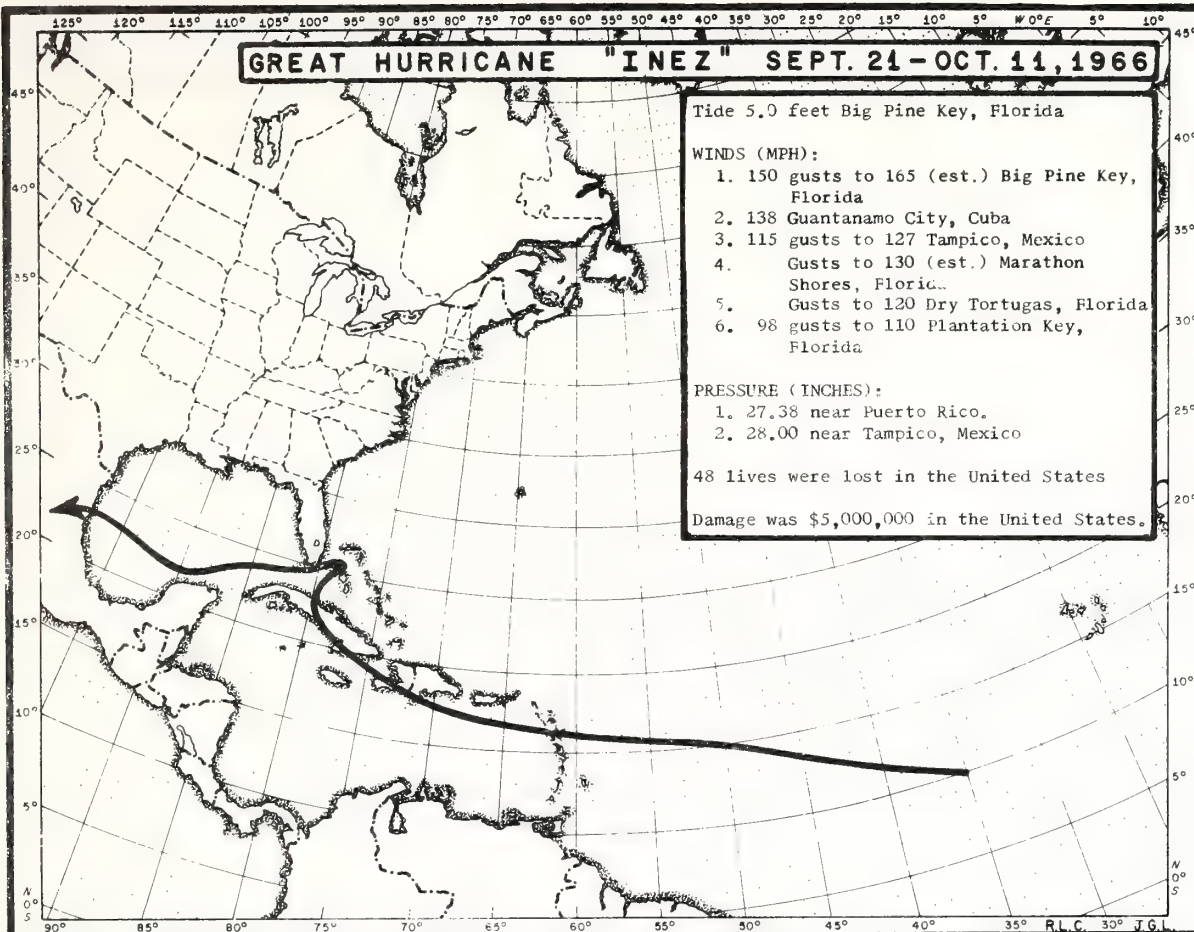


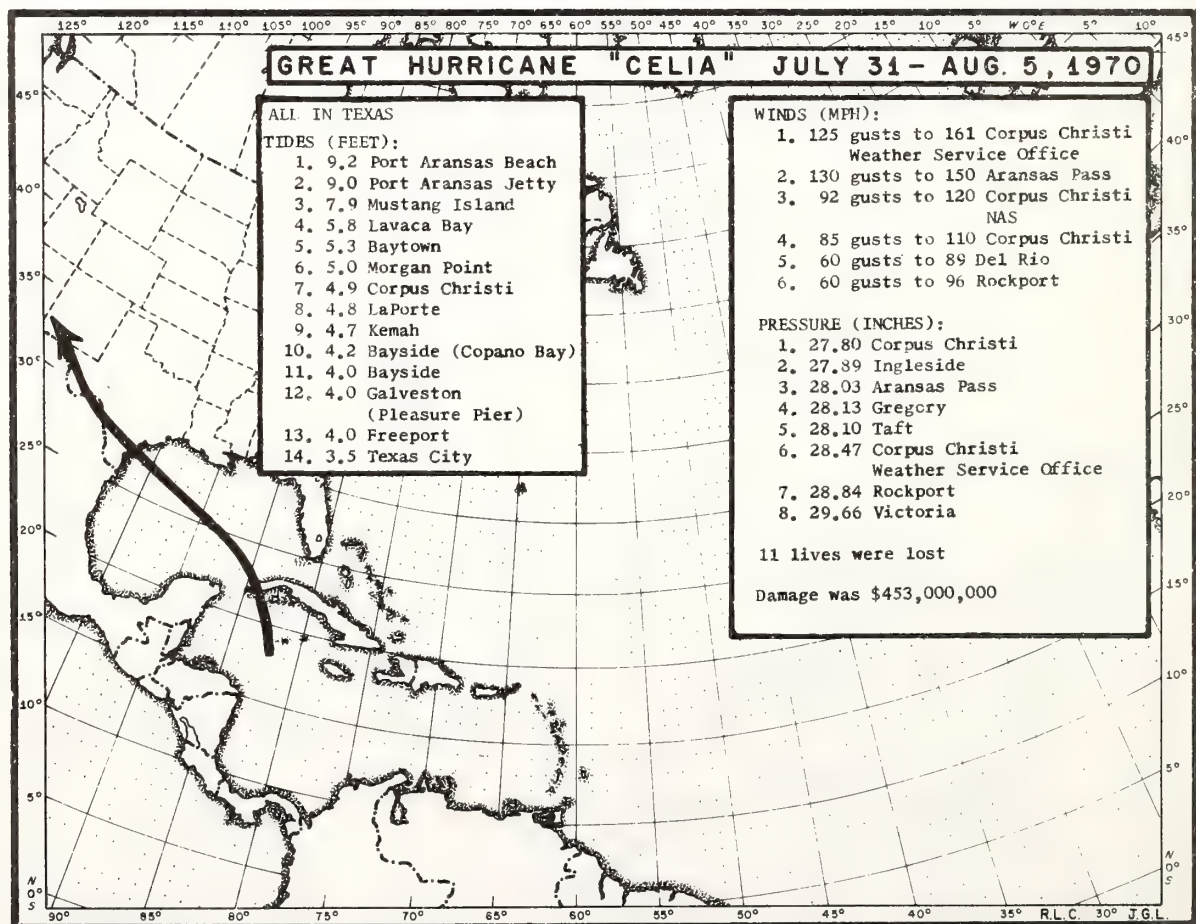
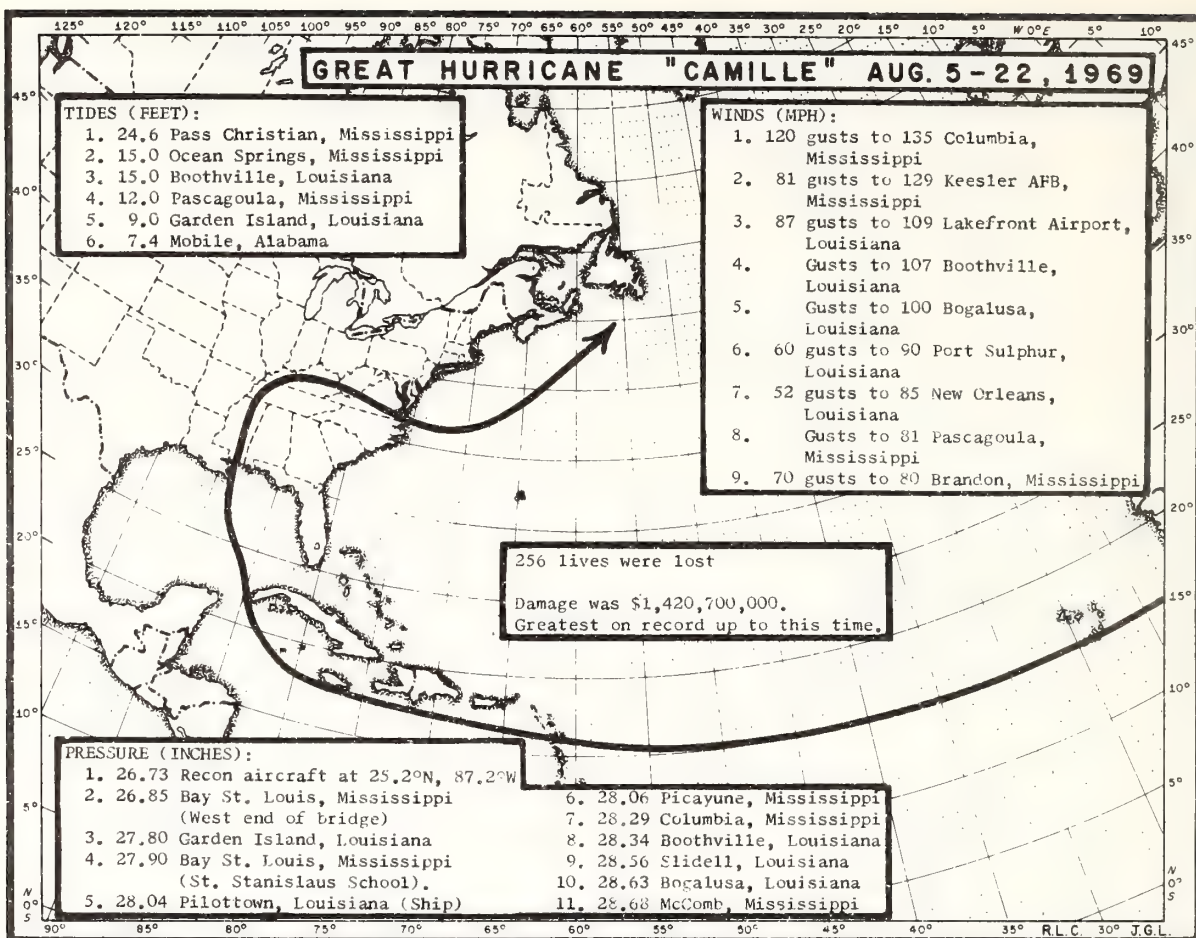


























PENN STATE UNIVERSITY LIBRARIES



A000072049631